2010

Proceedings of the 2010 Monitoring Research Review:
Ground-Based Nuclear Explosion Monitoring Technologies

Vol. I

Proceedings of the 2010 Monitoring Research Review: Ground-Based Nuclear Explosion Monitoring Technologies

September 21–23, 2010

Orlando, Florida

Volume I

Overview
Seismic Regional Characterizationand Wave Propagation
Seismic Event Detection and Location
Seismic Identification and Source Characterization

Approved for Public Release; further dissemination unlimited.

National Nuclear Security Administration

LA-UR-10-05578

To view these Proceedings online, visit
https://na22.nnsa.doe.gov/mrr/2010

ACKNOWLEDGEMENTS

The National Nuclear Security Administration (NNSA) and the Air Force Research Laboratory (AFRL) gratefully acknowledge the important contributions of the following people for their work to produce the ***Proceedings of the 2010 Monitoring Research Review: Ground-Based Nuclear Explosion Monitoring Technologies***.

Authors of papers for excellent research, technical documentation, and cooperation with electronic submission processes.

Dr. Anton M. Dainty, Mr. Robert J. Raistrick, Dr. Frederick R. Schult, AFRL/RVBYE, and ***Ms. Doris Richards***, 66 ABG/PA, for review and clearance of abstracts and papers related to AFRL contracts.

Dr. Stanley D. Ruppert, Lawrence Livermore National Laboratory (LLNL), for assistance in ensuring that the CDs could be read on a variety of platforms and for burning the CDs.

Ms. Brenda DeVargas, Los Alamos National Laboratory (LANL), for composition of the hardcopy covers and the CD label.

Ms. Eileen F. Patterson, LANL, for technical editing of papers.

Mr. Marvin A. Wetovsky, LANL, managing editor of the Proceedings.

Ms. Leslie A. Casey, NNSA, for review and clearance of abstracts and papers related to NNSA contracts and for NNSA overall support of the Proceedings.

Dr. Sanford (Sandy) Ballard, Sandia National Laboratories (SNL), for providing the 3D Earth model image on the CD label.

Ms. Mary L. Girven, SNL, for making everyone's job easier with web-based technology for abstract and paper submission, on-line review and approval tools, and creation of the master files for the hardcopy, CD, and website versions of the proceedings.

Ms. Guadalupe (Lupe) Massoth and ***Mr. Terry W. Spaulding***, SNL, for providing assistance to Mary Girven on website development and help in creating the master files.

Dr. William R. Walter and ***Dr. Stephen C. Myers***, LLNL; Dr. ***Dale N. Anderson*** and ***Mr. Ward L. Hawkins***, LANL; ***Dr. Theodore W. Bowyer*** and ***Dr. Martin E. Keillor***, Pacific Northwest National Laboratory; and ***Dr. Christopher J. Young***, SNL, for a myriad of internal management and technical reviews of NNSA abstracts and papers.

PREVIOUS PROCEEDINGS

Year	Title of the Proceedings
2009	Proceedings of the 2009 Monitoring Research Review: Ground-Based Nuclear Explosion Monitoring Technologies
2008	Proceedings of the 30th Monitoring Research Review: Ground-Based Nuclear Explosion Monitoring Technologies
2007	Proceedings of the 29th Monitoring Research Review: Ground-Based Nuclear Explosion Monitoring Technologies
2006	Proceedings of the 28th Seismic Research Review: Ground-Based Nuclear Explosion Monitoring Technologies
2005	Proceedings of the 27th Seismic Research Review: Ground-Based Nuclear Explosion Monitoring Technologies
2004	Proceedings of the 26th Seismic Research Review: Trends in Nuclear Explosion Monitoring
2003	Proceedings of the 25th Seismic Research Review: Nuclear Explosion Monitoring: Building the Knowledge Base
2002	Proceedings of the 24th Seismic Research Review: Nuclear Explosion Monitoring: Innovation and Integration
2001	Proceedings of the 23rd Seismic Research Review: Worldwide Monitoring of Nuclear Explosions
2000	Proceedings of the 22nd Annual DoD/DoE Seismic Research Symposium: Planning for Verification of and Compliance with the Comprehensive Nuclear-Test-Ban Treaty (CTBT)
1999	Proceedings of the 21st Seismic Research Symposium: Technologies for Monitoring the Comprehensive Nuclear-Test-Ban Treaty

Table of Contents — Volume I

1. Overview 1

1-01 **Casey, L. and R. Bell**
Nuclear Explosion Monitoring Research and Development Roadmaps 3

1-02 **Grenard, P. and T. Steeghs**
Science and Technology Foresight for the Provisional Technical Secretariat of the Comprehensive Nuclear-Test-Ban Treaty Organization 14

2. Seismic Regional Characterization and Wave Propagation 19

2-01 **Ammon, C., M. Maceira, and M. Cleveland**
3D Modeling of Iran and Surrounding Areas from Simultaneous Inversion of Multiple Geophysical Datasets 21

2-02 **Ballard, S., M. Begnaud, C. Young, J. Hipp, M. Chang, A. Encarnacao, C. Rowe, W. Phillips, and L. Steck**
A Global 3D P-Velocity Model of the Earth's Crust and Mantle for Improved Event Location — SALSA3D 31

2-03 **Chen, P., Y. Chen, and W. Chan**
Joint Inversion for Crustal and Upper Mantle Shear-Wave Velocity and Attenuation Structure in Eastern Eurasia Using Three-Dimensional Full-Wave Frechet Kernels 40

2-04 **Fisk, M. and W. Phillips**
A Stepwise, Iterative Procedure to Constrain Stress Drop, Regional Attenuation Models, and Site Effects 57

2-05 **Gritto, R., M. Sibol, P. Caron, H. Ghalib, R. Herrmann, G. Aleqabi, B. Ali, and A. Ali**
Crustal Velocity Models of the Zagros-Bitlis Zone from Body- and Surface Wave Analyses 67

2-06 **Hauser, J., K. Dyer, M. Pasyanos, H. Bungum, J. Faleide, and S. Clark**
Development and Tuning of a 3D Stochastic Inversion Methodology to the European Arctic 77

2-07 **Julia, J., A. Nyblade, A. Rodgers, and E. Matzel**
Developing Regionalized Models of Lithospheric Thickness and Velocity Structure Across Eurasia and the Middle East from Jointly Inverting P-Wave and S-Wave Receiver Functions with Rayleigh Wave Group and Phase Velocities 87

2-08 **Maceira, M., H. Zhang, R. Modrak, C. Rowe, and M. Begnaud**
Advanced Multivariate Inversion Techniques for High Resolution 3D Geophysical Modeling 97

2-09 **Mackey, K., H. Hartse, K. Fujita, M. Pasyanos, and M. Begnaud**
Seismic and Geophysical Characterization of Northern Asia 108

2-10 **Martin, R., L. Gulen, Y. Sun, and M. Toksoz**
The Crustal and Mantle Velocity Structure in Central Asia from 3D Travel Time Tomography 118

2-11 **Masters, T., Z. Ma, G. Laske, and M. Pasyanos**
LITHO1.0: An Updated Crust and Lithosphere Model of the Earth 128

2-12 **Mayeda, K. and W. Phillips**
Transitioning the Coda Methodology to Full 2-D for P and S Codas 138

2-13 **Miller, K., M. Arrowsmith, W. Phillips, S. Harder, L. Worthington, A. Sheehan, and M. Anderson**
Assessment of Regional Explosion Discriminants Using Datasets of Unparalleled Spatial Sampling: The Big Horns Array Seismic Experiment (BASE) 145

2-14 **Nabelek, J., S. Carpenter, P. Monigle, J. Braunmiller, and W. Phillips**
Source and Path Calibration in Regions of Poor Crustal Propagation Using Temporary, Large-Aperture, High-Resolution Seismic Arrays 150

2-15 **Nowack, R., W. Chen, J. Griffin, A. Bakir, and T. Tseng**
The Propagation of Pn in Western China 161

2-16 **Pollitz, F., J. Rubinstein, and W. Ellsworth**
Analysis and Modeling of the Wavefield Generated by Explosions at the San Andreas Fault Observatory at Depth 170

2-17 **Reiter, D., W. Rodi, and S. Myers**
Estimating the Uncertainty and Predictive Capabilities of Three-Dimensional Earth Models 180

2-18 **Rodgers, A., O. Vorobiev, N. Petersson, B. Sjogreen, and W. Foxall**
Progress in Three-Dimensional Simulations of Explosions and Earthquakes 188

2-19 **Sandvol, E., X. Bao, J. Ni, T. Hearn, and W. Phillips**
High-Resolution Seismic Velocity and Attenuation Models of Western China 197

2-20 **Savage, B., D. Peter, B. Covellone, A. Rodgers, and J. Tromp**
Next Generation, Waveform Based Three-Dimensional Models and Metrics to Improve Nuclear Explosion Monitoring in the Middle East 207

2-21 **Sen, M., J. Pulliam, U. Dutta, R. Ghosh, R. Gok, and M. Pasyanos**
Seismic Velocity Estimation in the Middle East from Multiple Waveform Functionals: P & S Receiver Functions, Waveform Fitting, and Surface Wave Dispersion 214

2-22 **Song, X., Z. Xu, L. Zhu, and Y. Zhou**
Joint Inversion of Crustal and Uppermost Mantle Structure in Western China 224

2-23 **Zhang, J., P. Gerstoft, and S. Taylor**
Body-Wave Arrivals from Seismic Noise 232

3. Seismic Event Detection and Location 247

3-01 **Bergman, E., E. Engdahl, M. Ritzwoller, and S. Myers**
Earthquake Location Accuracy in the Arabian-Eurasian Collision Zone 249

3-02 **Brazier, R., K. Boomer, S. Myers, A. Nyblade, and J. Kokoska**
Establishing and Validating Empirically-Based Ground Truth Criteria for Seismic Events Located Using Regional Networks 259

3-03 **Carr, D., P. Baldwin, S. Knapp-Kleinsorge, H. Milburn, and D. Robinson**
A Laser Interferometric Miniature Seismometer 268

3-04 **Fourguette, D., M. Otugen, L. Larocque, G. Ritter, J. Meeusen, and T. Ioppolo**
Optical MEMS-Based Seismometer "WhiG 272

3-05 **Garcia, C., G. Onaran, B. Avenson, B. Yocom, and N. Hall**
Micro-Seismometers via Advanced Meso-Scale Fabrication 280

3-06 **Kvaerna, T., S. Gibbons, D. Harris, and D. Dodge**
A Matched Field Processing Framework for Coherent Detection Over Local and Regional Networks 289

3-07 **Myers, S., G. Johannesson, and N. Simmons**
Bayesloc Multiple-Event Location Applied to a Global Data Set 299

3-08 **Myers, S., M. Begnaud, S. Ballard, A. Ramirez, W. Phillips, M. Pasyanos, H. Benz, and R. Buland**
A Regional Seismic Travel Time Model for North America 308

3-09 **Ringdal, F., D. Harris, T. Kvaerna, and S. Gibbons**
Expanding Coherent Array Processing to Larger Apertures Using Empirical Matched Field Processing 318

3-10 **Ritzwoller, M., M. Barmin, A. Levshin, and Y. Yang**
Epicentral Location of Regional Seismic Events Based on Empirical Green's Functions from Ambient Noise 328

3-11 **Rodi, W., D. Reiter, S. Myers, and N. Simmons**
A Unified Approach to Joint Regional/Teleseismic Calibration and Event Location with a 3D Earth Model 338

3-12 **Simmons, N., S. Myers, and G. Johannesson**
Global-Scale P-Wave Tomography Designed for Accurate Prediction of Regional and Teleseismic Travel Times for Middle East Events 348

4. Seismic Identification and Source Characterization 359

4-01 **Anderson, D., H. Patton, S. Taylor, and J. Bonner**
Isolating Source Information in mb and Ms with Model-Based Corrections: New mb Versus Ms Discriminant Formulations 361

4-02 **Brunish, W., W. Hawkins, D. Coblentz, H. Patton, J. Zucca, J. Sweeney, C. Carrigan, T. Antoun, C. Seifert, K. Wohletz, C. Bradley, A. Sussman, T. Bowyer, R. Corbell, R. Abbott, C. Snelson, and P. Lee**
Source Physics Experiments at the Nevada Test Site 370

4-03 **Dreger, D., S. Ford, and W. Walter**
Identifying Isotropic Events Using a Regional Moment Tensor Inversion Technique 381

4-04 **Ford, S., W. Walter, S. Ruppert, E. Matzel, T. Hauk, and R. Gok**
Toward an Empirically-Based Parametric Explosion Spectral Model 390

4-05 **Julia, J., A. Nyblade, R. Gok, W. Walter, L. Linzer, and R. Durrheim**
Developing and Exploiting a Unique Dataset from South African Gold Mines for Source Characterization and Wave Propagation 398

4-06 **Koch, K.**
Re-Examination of Surface Wave Magnitude Estimates for the North Korean Event of 25 May 2009 408

4-07 **Leidig, M., B. Stump, W. Walter, A. Stroujkova, X. Yang, and J. Bonner**
Examination of P/S Spectral Ratios for Small Explosions at Local Distances and Interpretation of Moment Tensors Estimated from Near-Source Data 416

4-08 **Martin, R., P. Boyd, A. Stroujkova, M. Leidig, L. Liu, J. Lewkowicz, and J. Bonner**
Correlating Near-Source Rock Damage from Single-Hole Explosions to Seismic Waves 427

4-09 **Mayeda, K., L. Malagnini, W. Walter, and R. Gok**
Improved High Frequency Discrimination: A New Approach to Correct for Regional Source Scaling Variations 437

4-10 **Murphy, J. and T. Bennett**
An Analysis of the Seismic Source Characteristics of Explosions in Low-Coupling Dry Porous Media 446

4-11 **Murphy, J., B. Kohl, J. Stevens, T. Bennett, and H. Israelsson**
Exploitation of the IMS and Other Data for a Comprehensive, Advanced Analysis of the North Korean Nuclear Tests 456

4-12 **Pasyanos, M., W. Walter, E. Matzel, S. Ford, R. Gok, and A. Rodgers**
Calibration of Attenuation Structure in Eurasia to Improve Discrimination and Yield 466

4-13 **Patton, H.**
Explosion Source Model Development in Support of Seismic Monitoring Technologies: Apparent Explosion Moment and Prospects for Moment-Based Yield Estimation 475

4-14 **Phillips, W., X. Yang, R. Stead, M. Begnaud, and K. Mayeda**
Model Development for Broad Area Event Identification and Yield Estimation 486

4-15 **Randall, G. and H. Hartse**
Identification of Deep Earthquakes 495

4-16 **Rougier, E., C. Bradley, H. Patton, and E. Knight**
Numerical Simulations of Cavity Radius in Granite: Cavity Behavior as a Function of Scaled Depth of Burial 504

4-17 **Sammis, C., H. Bhat, and A. Rosakis**
Micromechanical Damage Mechanics at High Loading Rates 513

4-18 **Stevens, J. and H. Xu**
Wave Propagation from Complex 3D Sources Using the Representation Theorem 519

4-19 **Stroujkova, A., J. Bonner, R. Herrmann, and D. Anderson**
Rayleigh and Love Wave Magnitudes 529

Overview

NUCLEAR EXPLOSION MONITORING RESEARCH AND DEVELOPMENT ROADMAPS

Leslie A. Casey and W. Randy Bell

Sponsored by the National Nuclear Security Administration

ABSTRACT

In the past ten years, significant progress has been made in nuclear explosion monitoring (NEM) through research and development (R&D) with regard to detection, location and identification, however substantial improvements are yet possible. Today, there is increasing interest in both current and planned NEM R&D technology particularly in light of its relevance to the Comprehensive Nuclear-Test-Ban Treaty (CTBT). At this juncture, the Ground-based Nuclear Explosion Monitoring R&D (GNEM R&D) roadmaps are particularly pertinent because they build upon decades of NEM accomplishments (https://na22.nnsa.doe.gov/mrr) to map future R&D themes. Indeed, the GNEM R&D mission, an essential program within the National Nuclear Security Administration's Office of Nuclear Detonation Detection (NA-222), is, "…to develop, demonstrate, and deliver advanced technologies and systems to operational monitoring agencies to fulfill US monitoring requirements and policies for detecting, locating, and identifying nuclear explosions" (Strategic Plan, 2004). Work sponsored by GNEM R&D and collaborators is world-class; conducted by scientists and engineers in national laboratories, universities, and private industry in partnership with international researchers. Waveform and radionuclide technology roadmaps are organized according to four program elements: source physics, signal propagation, sensors, and signal analysis. These elements were chosen to capture the full breadth of the physical representation of signals observed in the environment. Within each element, R&D themes and metrics are presented as illustrative of future directions. The roadmaps show the way forward to attain the goals of the program namely to: perform innovative scientific research, deliver capability-enhancing technologies to monitoring agencies and to motivate and nurture human capital to meet future monitoring challenges.

OBJECTIVE

The objective of this paper is to convey the central themes in the GNEM R&D technology roadmaps. Two high-level categories of roadmaps capture the signals of interest to the ground-based program: waveform and radionuclide. Utilizing scientific and operational-based program elements and associated technical themes, this roadmapping effort, builds on a continuous succession of past deliberate activities, step-by-step over decades, resulting in scientific and technical achievement, propelling the focus on the future. In the drive to lower detection thresholds, reduce location uncertainty and improve event identification, decades of concerted, peer-reviewed efforts in NEM R&D has paid off attaining a high-level of technical sophistication. In fact, compared to just ten years ago, significant progress has been made in key operational functions (detection, location and identification) and the roadmaps described here are very likely to make similar advancements over the decade to come. These roadmaps outline a way forward to ensure success. In fact, a deciding factor for program element and theme selection was the ability to project forward to credible, mission-inspired, pathways and end-products, thus providing potential topics for future proposal calls, guiding researchers, enabling collaborations with similarly driven agencies, as well as informing treaty policy makers.

RESEARCH ACCOMPLISHED

The progression of NEM R&D themes, starting with simple, empirical approaches to present day almost-real-time, entirely digital methodologies, and finally, projecting to tomorrow's technologies is established in these roadmaps. They intend to build upon the foundation and elaborate important ideas established at the 26th Seismic Research Review, in a paper titled, *Trends in Nuclear Explosion Monitoring* (Andersen et al., 2004) that focused on trends in monitoring agreements, science, technology and instrumentation.

NEM R&D waveform and radionuclide technology themes are organized into four program elements: source physics, signal propagation, sensors, and signal analysis. These program elements form the foundation for the roadmaps and, because of major inherent differences between waveform and radionuclide R&D; separate roadmaps were developed for each. Finally, themes and metrics serve as both a guide for researchers and a gauge to assess the merit of new approaches.

GNEM R&D goals are to: perform innovative scientific research, deliver capability-enhancing technologies to monitoring agencies and to motivate and nurture human capital to meet future monitoring challenges. The roadmap is intended to focus and stimulate innovation, enhancing delivery of products and attracting top scientists.

R&D Themes, Goals and Metrics

Delivering state-of-the-art products to operational monitoring systems to improve NEM proficiency is a major goal of the GNEM R&D program. The expectation is that much of this improvement will come from a better understanding of the science behind the generation, propagation, sensing, and interpretation of seismic, infrasound, hydroacoustic and radionuclide signals. To structure, plan and communicate future research advances, a simple four element schema was identified comprised of common elements of both operational and observational considerations. Figure 1 is a diagram of the four program elements displaying both operational and scientific attributes.

The first program element, Source Physics, aims to better understand the underlying principles and mechanisms behind all potential NEM sources with particular attention to complex interactions with the local source-medium (geology, structure, tectonics and emplacement conditions). These interactions can greatly affect the signals before they propagate to the sensors either through the atmosphere or through the Earth. As the signals from that source travel outward, the second program element, Signal Propagation, covers the critical factors that modify, in any way, the signal timing, amplitude and frequency content between the source and the sensor.

Next, these signals are recorded as data at very sensitive instruments carefully installed around the globe. This part of the process is captured in the Sensors program element, where sensors collect the continuous data (signals) that will be processed to detect, locate, and identify events of monitoring interest. The sensors program element addresses continued improvement in sensor size, weight, and lifecycle costs as well as noise reduction, emplacement conditions and system performance optimization. Finally, signals created by sources, propagated through the solid Earth, oceans, or atmosphere, and recorded by sensors must be processed to form hypotheses of possible nuclear events. We refer to this final processing step as the Signal Analysis program element.

These four elements provide a framework capable of capturing the full scope of the GNEM R&D mission, and can be thought of as a high-level amalgamation of nuclear explosion monitoring physical environments with a generalization of the operational systems.

In reality, few projects fit neatly into one program element, nor are the paths from R&D to operational applications simple: most products take several years from development of an idea to operational incorporation. Interactions between the operations leaders and staff and researchers are frequent and significant in order to achieve a successful final product delivery. None the less, the program element framework provides a useful way to view and understand our program. In this way the four program elements of Source Physics, Signal Propagation, Sensors and Signal Analysis bring planning together to improve nuclear monitoring capability. This synthesis is reflected in past and projected future improvements in overall monitoring of event detection, location, and identification as broadly portrayed in Figures 2, 3 and 4.

Each program element is composed of several R&D themes and most themes are related to or dependent on the results from other themes. Themes can span decades, some current themes have been active for more than 12 years while others will start activity in the next few years depending on the results of other themes. Themes are dynamic and can be modified, added and deleted. For each theme we have R&D metrics where appropriate to guide researchers in their work. Themes and R&D directions are reviewed annually in conjunction with the budget process and are the result of a vigorous on-going discussion between program managers, operational leaders and staff, national laboratory researchers, collaborators, and national and international nuclear explosion monitoring experts.

Source Physics R&D Themes and Metrics for Waveform Technologies

Source Physics R&D themes are focused on the ultimate technical goal of providing a physical basis for predicting the seismic signals emitted by all source types (e.g. earthquakes, explosions, mining blasts, etc) in a variety of geologic, tectonic and man-made emplacement settings. For explosions, the complexity of the source and the need for far more sophisticated models, especially for S wave generation, drives future R&D in: model synthesis, numerical simulations using realistic material models, and field experimentation, with underlying theoretical work supporting the overall development.

Model synthesis emphasizes analytical source models that build on past models and incorporate new information from other R&D. Improved source discrimination, yield estimation, and source-to- receiver waveform modeling capabilities at low yields and broad areas are monitoring goals of the final synthesis product. An over-arching metric for the synthesis is the ability to predict and match observed seismic signals for all distance ranges and across the entire seismic frequency band.

Numerical simulations and field experimentation test and validate source parameter scaling laws, tie near-source phenomenology to seismic measurements, fill knowledge gaps, and test and validate the overall performance of the models. These efforts and theoretical work provide a foundation for interpreting signals in the context of the source, its emplacement, and the generation processes of the surrounding source medium, including material damage, relaxation of pre-stress, material anisotropy, and wave propagation through heterogeneous media with irregular interfaces. Yield scaling and micro to macroscopic scaling of material behaviors relevant to seismic wave generation are important aspects of theoretical work.

R&D themes (and associated metrics) are identified below for various seismic sources and monitoring applications with focus on the underlying principles of Waveform Source Physics described above (WSO).

WSO1. New and more effective methods to identify sources of waveform signals (Metric: Improved identification of sources),

WSO2. Predict nuclear explosion seismic S-wave amplitudes near the source for all emplacements (Metric: Explosion models that better match observables),

WSO3. Tune earthquake seismic amplitude models to their tectonic setting (Metric: Improved earthquake models that better match observables),

WSO4. Predict industrial explosion local and regional seismic amplitudes (Metric: New mine blast models that better match observables),

WSO5. Predict local and regional seismic signals from the collapse of underground cavities (Metric: New collapse models that better match observables), and

WSO6. Calculate energy partitioning for sources near earth-water-air interfaces (Metric: Improved models that better match observables).

Signal Propagation R&D Themes and Metrics for Waveform Technologies

Many factors control the timing, amplitude and frequency content of propagating waveform signals. Foremost among these is the heterogeneity of the Earth's crustal velocity and attenuation.. In real application, other factors arise and must be considered, such as, processor and algorithm optimization. For seismic waveforms this includes improved understanding of the subsurface density, wave velocities and associated attenuation. For infrasound this includes understanding the velocity profile and dynamics of the atmosphere, which is in constant motion and has daily and seasonal variations. For hydroacoustic this includes improved understanding of the velocity profile of the oceans which undergoes seasonal variations as well as the bathymetry. The major goal of Signal Propagation is improved waveform signal prediction which impacts event detection, location identification and magnitude/yield estimation. R&D themes (and associated metrics) for Waveform Signal Propagation (WSP) are:

WSP1. Improve travel time predictions (Metric: Improved travel time and dispersion predictions),
WSP2. Improve amplitude modeling (Metric: Improved amplitude predictions), and
WSP3. Predict travel-time, amplitude and full waveform signals from these models (Metric: Improved synthetic waveforms that better match observables).

Sensors R&D Themes and Metrics for Waveform Technologies

Sensitive instrumentation is needed to detect extremely small (< nanometer displacements) signals and the Sensors program element is focused on improving sensitivity, signal-to-noise ratio, frequency bandwidth and operational and implementation issues of these sensors. The existing installed sensor systems, especially seismometers, have outstanding response characteristics and consequently are not the focus of this program element (see Figures 2 and 5). Sensor R&D is currently developing Micro-Electro-Mechanical Systems (MEMS) technology for local monitoring situations. MEMS requirements have been developed by working expert groups and continue to drive the innovation (see Table 1). MEMS as well as other types of miniature seismometers are predominantly funded by Small Business Innovation Grants (SBIR) with some GNEM R&D support. A particularly vexing challenge is overcoming the $1/f$ noise restriction for any small reference mass. Deploying local networks has several troublesome issues: optimal spatial distribution, inter-sensor and station communications, on-board processing, and, of course, long-term power, weight and size constraints. Therefore, Waveform Sensor (WSE) R&D themes (and associated metrics) include development, network configuration analyses, and testing facility support, namely:

WSE1. Build new short period (SP) micro seismometers and micro acoustic sensors (Metric: Design and build low power (<100 mW) micro-seismometers with internal noise levels below the reference low noise models (USGS for seismic, Bowman for infrasound) in the frequency range of approximately 0.2 to 40 Hz and high dynamic range (> 110 dB)),
WSE2. Prototype local monitoring sensor system (Metric: Demonstrate local monitoring system performance),
WSE3. Develop sensor network deployment software (Metric: Demonstrate capability to accurately model local network performance prior to deployment), and
WSE4. Maintain a sensor testing and evaluation facility (Metric: Provide testing and evaluation for data acquisition systems for waveform technologies).

Signal Analysis R&D Themes and Metrics for Waveform Technologies

The Signal Analysis program element is meant to include all signal processing techniques that are applied to data to detect and characterize events of interest for nuclear explosion monitoring. In an operational network, each and every sensor is interrogated, separately, to discern signals of interest, then these are associated into hypothetical events, and finally, magnitudes of the events are estimated, along with an estimate of the likely source type (e.g., earthquake or explosion). This is all done in as close to real-time as possible. So, in some ways, Signal Analysis covers a broad range which we choose to divide into two categories: Signal Processing and Results. Signal Processing is concerned with manipulating the data to enhance and find signals of interest, while the Results portion covers the higher-level processes used to generate source hypotheses (location, size, event type). For these types of processes, the refined measurements are compared to values from synthetic signals calculated using a model of the Earth, and uncertainties of source parameters are estimated.

This is a very rich set of techniques spanning signal enhancement (filtering, beaming, rotation, principal component analysis, waveform correlation, etc.), signal detection, parameter measurement, signal association, event location, magnitude/yield determination, and event identification. The desired product is a high-quality, comprehensive list of well-described, possible nuclear events. Because direct evidence is seldom available, a further challenge is to provide rigorous uncertainty estimates for each event parameter. Also, because earthquakes are so much more common than explosions and thus dominate the typical set of signals on any given day, a large proportion of signal analysis work focuses on identifying and screening the signals from earthquakes. Waveform Signal Analysis (WSA) R&D themes (and associated metrics) include:

WSA1. Improve the robustness and accuracy of parameter estimation (Metric: Demonstrate improved parameter and uncertainty estimates),
WSA2. Develop new waveform parameters (Metric: Demonstrate improved monitoring capability due to new waveform parameters),
WSA3. Improve parameter-based methods for monitoring (Metric: Improved detection, location, and/or identification), and
WSA4. Improve waveform-based methods for monitoring (Metric: Improved detection, location, and/or identification).

Source Physics R&D Themes and Metrics for Radionuclide Technologies

Quite different from seismic signals, which begin as a release of energy within the environment, a radionuclide event is the release of radioactive atoms. Radionuclide sources include nuclear explosions, normal or anomalous reactor operations, and releases from other nuclear industry, particularly medical isotope production. These overlay on natural radioactivity such as primordial isotopes (e.g., potassium, uranium, and thorium and their decay products) and isotopes produced from the interactions of cosmic rays with the atmosphere (e.g., ^{7}Be and ^{24}Na). The R&D themes (and associated metrics) for Radionuclide Source Physics (RSO) are:

RSO1. Determine the risk of innocuous background false alarms (Metric: Calculate risk),
RSO2. Improve knowledge of subsurface gas transport (Metric: Reduce the number of samples by an order of magnitude), and
RSO3. Determine the amount of radionuclides produced in various nuclear testing conditions (Metric: Improve input to geologic and atmospheric transport models).

Signal Propagation R&D Themes and Metrics for Radionuclide Technologies

While radionuclides can move in subterranean water, the dominant source propagation for radioactive atoms in the context of NEM is atmospheric transport. Atmospheric transport modeling (ATM) is central to weather prediction and therefore has large national and international academic research and operations support. The excellent state of ATM, the existing R&D support by other agencies like NOAA and NASA and the highly capable operational CTBT ATM capability are reasons that GNEM R&D is a user of ATM rather than a supplier. Signal Propagation R&D for radionuclides is not part of the GNEM R&D program, but advances at the Comprehensive Nuclear-Test-Ban Treaty Organization (CTBTO) in conjunction with their partnership with the World Meteorological Organization, are still part of the drivers for research and require thoughtful coordination. In light of this, there is an overall theme (and associated metric) for Radionuclide Signal Propagation:

RSP1. Fine tune atmospheric modeling by bettering local sources (Metric: Reduce uncertainty in the deduced release point for radionuclides).

Sensors R&D Themes and Metrics for Radionuclide Technologies

Sensors are the cornerstone of the Radionuclide part of the GNEM R&D Program. Sensors for radionuclide are complete sampler/analyzers rather than simply a transducer. The systems definitions encompass automatic collection of particulate material or gases, chemical processing if required, then measurements of temperatures, pressures and radioactive decay. Research funded by this program has broken scientific barriers in field and laboratory sensitivity, created whole new areas of scientific measurements of the environment, and then driven accuracy and precision to finer and finer levels.

Sensors, defined broadly here to include a sampler/analyzer system complete with radiometric measurement, are the main focus of the radionuclide part of the GNEM R&D program. Science breakthroughs in Sensors have enabled

science breakthroughs in Signal Processing, and Source Physics as well. In a sense, these advances (and Signal Propagation advances at the CTBTO and elsewhere) are now driving the next generation of science in Sensors.

Radionuclide Sensor (RSE) R&D themes (and associated metrics) include:

RSE1. More sensitivity, (Metric: Increase sensitivity to aerosols and short-lived xenons by an order of magnitude),
RSE2. More xenon for less energy, less liquid nitrogen, in less size, or with less adsorbent material, (Metric: Increase xenon yield while reducing complexity)
RSE3. Improve transfer of collected radionuclides into the radiation detector, (Metric: Improve radionuclide detection sensitivity by a factor of 2X)
RSE4. Higher uptime and less maintenance, (Metric: Meet or exceed an operation uptime of 95%), and
RSE5. Solving near-field radionuclide measurement and operations problems, including On-Site Inspection (Metric: Demonstrate technologies)

Signal Analysis R&D Themes and Metrics for Radionuclide Technologies

Radionuclide signal analysis is also divided into two topics: signal processing and results. The primary radionuclide analysis is of the decay information for atoms in a sample, a so-called nuclear spectrum. Gamma-rays from particulates are recorded in a histogram, and this is a mature scientific technique, in the science community at large including CTBTO. Noble gas collection and analysis is a new field, and this program continues to contribute greatly to establishing a regular analysis algorithm for the coincidence spectrum created by the emission of beta particles and gamma rays in Xe decay, known as beta-gamma spectrum.

To turn these measurements into useful information, 'screening' in the CTBT context, it is necessary to compare the measurement to previous measurements at this or other locations to determine if it is anomalous (in size and in frequency of detection – has this isotope been detected often at this size before?). It is also critical for noble gas isotopes to compare the ratio of isotopes, if more than one is detected, with that expected from medical isotope and reactor emissions. For example, the IMS detected a pair of xenon isotopes at a Japanese station shortly after the 2009 DPRK event. The ratio of isotopes indicated decayed reactor emissions however, and the signal was confidently rejected as not being nuclear explosion related.

The users cannot make use of the Sensor program element without signal processing. The GNEM R&D program began by simply using the gamma-ray spectroscopy capabilities available commercially and within the National labs; entirely adequate to perform basic signal processing for particulates. As noble gas systems became useful, signal processing was done by hand, as particulate signal processing was in the 1950's. A rapid evolution of signal processing for beta-gamma spectra, using modern tools and techniques of nuclear and particle physics brought about a basic xenon analysis scheme which is being actively refined today. Coincidence signal processing for particulates is now in development to support the multi-crystal germanium detector CASCADES for laboratory use.

Future research will be toward refined screening for both radionuclide and xenon data, as well as the new area described as 'network analysis' in which many stations results on many days are combined with the source-receptor strength fields to create a wholly new product, the maximum release possible from a suspected site as a function of time. This was a key result of DPRK 2009 analysis. Radionuclide Signal Analysis (RSA) R&D themes (and associated metrics) include:

RSA1. Develop methods and techniques to increase the sensitivity and selectivity of radionuclide detection (Metric: Improve radionuclide detection sensitivity and selectivity by an order of magnitude or more),
RSA2. Improve discrimination of detected signals from background with algorithms (Metric: Demonstrate refined algorithms), and
RSA3. Evaluation of intra-station dependencies to maximum network capabilities (Metric: Improved understanding of global coverage).

The aim of the GNEM R&D themes is to improve monitoring overall and Figures 2, 3 and 4 illustrate progress over five decades. By and large, Source Physics will provide a deeper understanding of the processes inherent in the explosion mechanisms which will enable lower detection thresholds, improved location accuracy and yield

estimates. Success with Signal Propagation themes will reduce location error; improve attenuation models and thus improving discrimination, detection and yield estimation. Better, in-close Sensors will lower detection thresholds, and improve signal-to-noise ratios allowing for better timing and thus locations. Finally, progress in Signal Analysis themes will allow full signal processing furthering operations while opening new opportunities for extracting even more information from these complex data.

CONCLUSIONS AND RECOMMENDATIONS

The central scientific and technical themes of the Ground-based Nuclear Explosion Monitoring R&D roadmaps were portrayed and R&D metrics stated to help guide research progress. Four scientific and operational-based program elements (Source Physics, Signal Propagation, Sensors and Signal Analysis) with associated technical themes, build on a continuous series of scientific and technical achievements that lowered detection thresholds, reduced location uncertainty and improved event identification. The program is poised to deliver another giant step in operational effectiveness similar to the one in the 1990's related to improvements in event location and this roadmap delineates a way to get there and provides the scientific foundation and wherewithal to ensure success. These roadmaps are reviewed annually in conjunction with the budget process. We invite comments on the GNEM R&D roadmaps and your comments may be sent at any time to Leslie.Casey@nnsa.doe.gov.

ACKNOWLEDGEMENTS

It is a great privilege to work in an important area of national security in support of operational organizations. We thank the Air Force Technical Applications Center for being a worthy customer in their role as the U.S. National Data Center in the context of the CTBT, and thank the Air Force Research Laboratory for being a good partner in R&D. We also thank the researchers who eagerly contribute their talent, work long hours, and inspire us all with their passion for the GNEM mission.

REFERENCES

Anderson, D. N., R. Willemann, H. Miley, C. L. Edwards, P. B. Herrington, J. M. Harris, J. C. Wehlburg, D. B. Harris, J. J. Zucca, and L. A. Casey (2004). Trends in Nuclear Explosion Monitoring, in *Proceedings of the 26th Seismic Research review – Trends in Nuclear Explosion Monitoring*, LA-UR-04-5801, Vol. 1, pp. 3–15.

Nuclear Explosion Monitoring Research and Engineering Program Strategic Plan, DOE/NNSA/NA-22-NEMRE 2004, https://na22.nnsa.doe.gov/gndd/StrategicPlan.

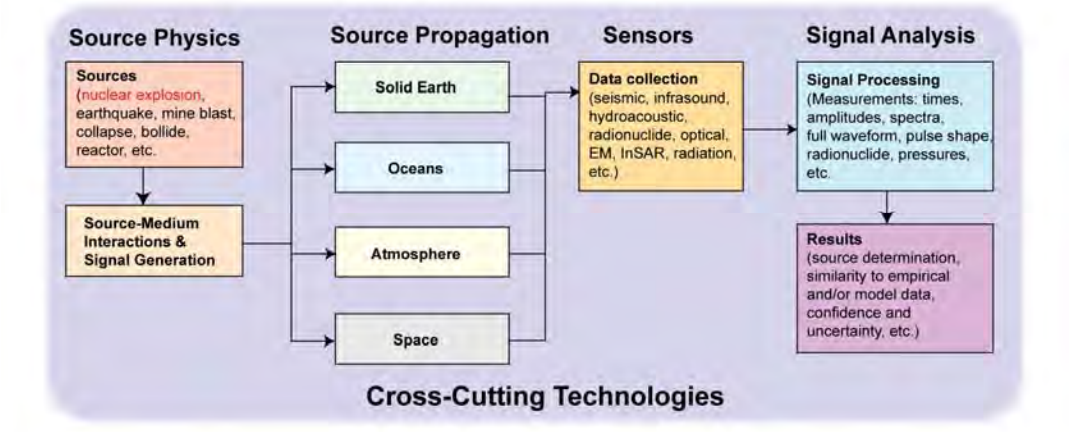

Figure 1. GNEM R&D program elements were chosen as a full scope representation of GNEM processes and are shown in a context of operational data and process flow.

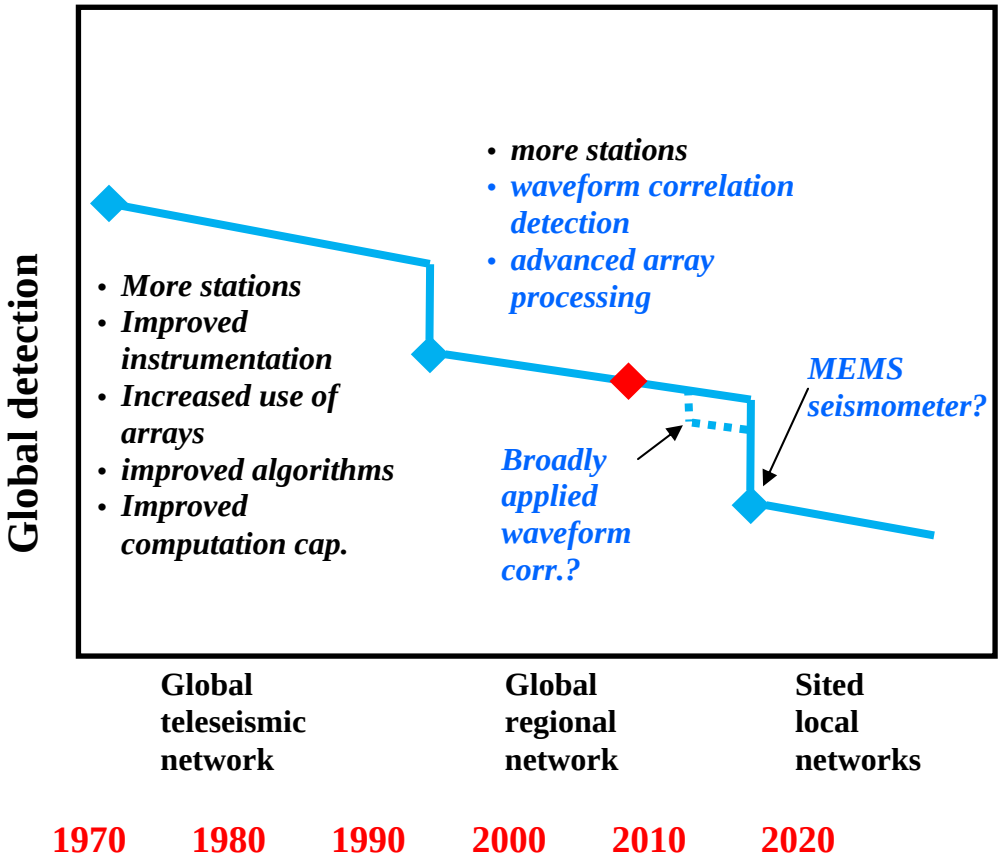

Figure 2. Progress in GNEM R&D detection metric is shown from 1970s to 2020. Detection improvements are a function of several factors the major being to add more stations closer to where you want to monitor. Improved instrumentation, algorithms, and analyses methods have made a difference.

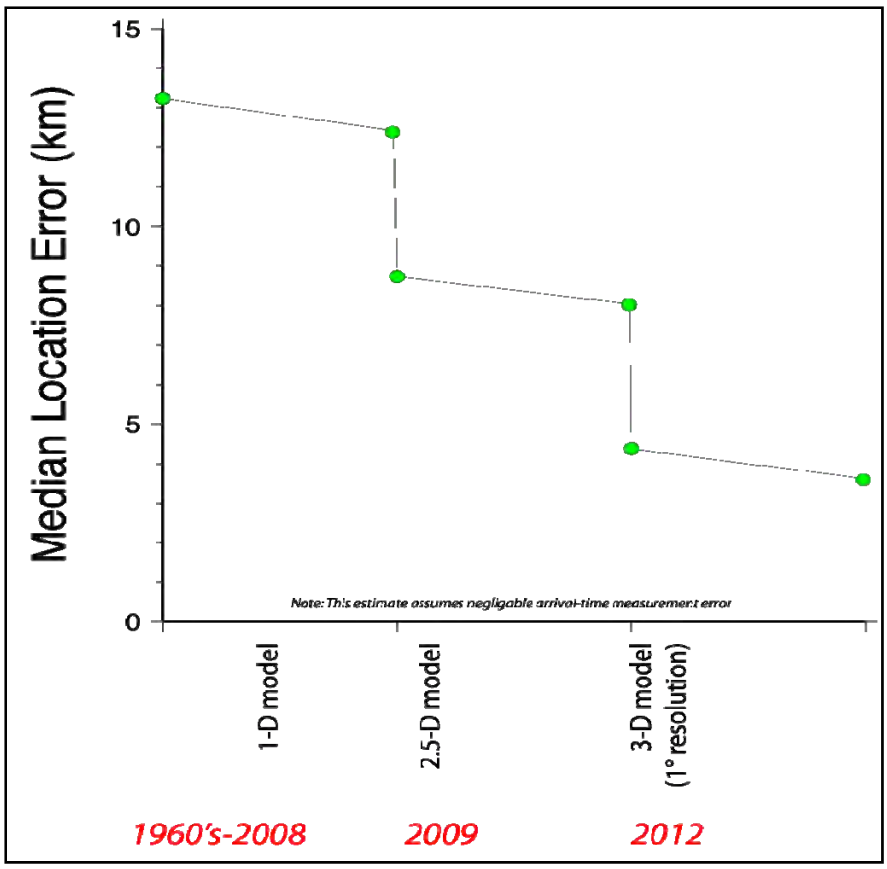

Figure 3. Location past, present and future progress chart. These results are applicable only for small tests (<~4.5) in broad tectonic regional discrimination.

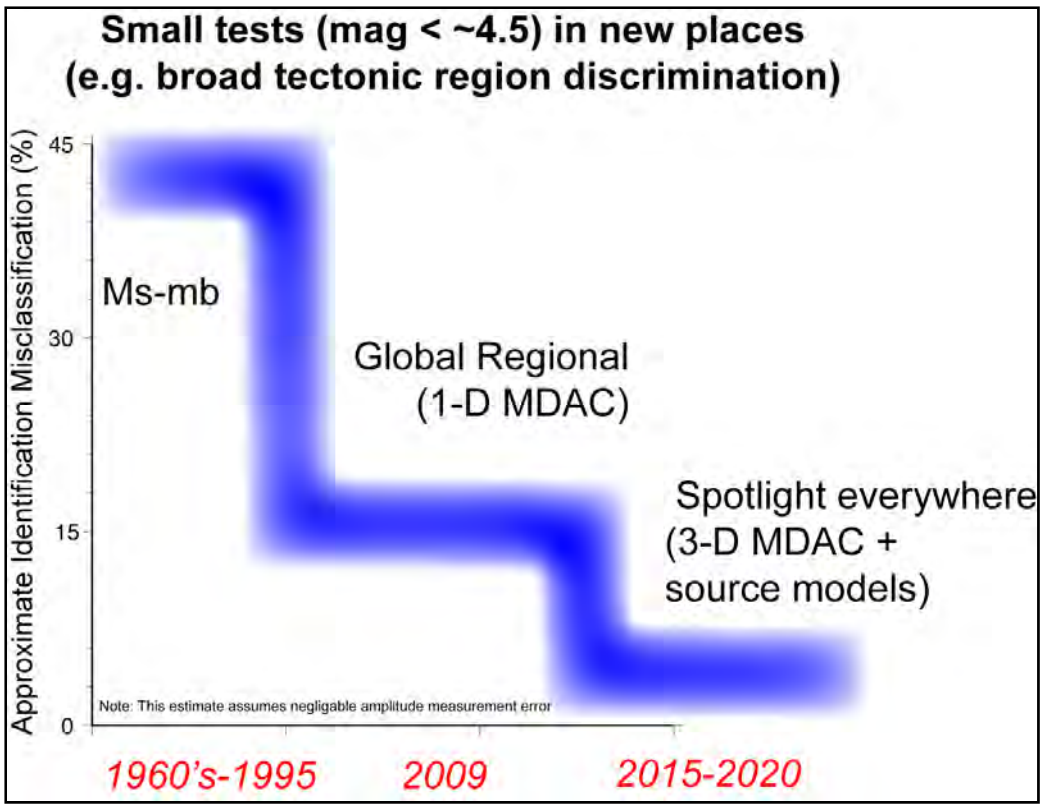

Figure 4. Identification past, present and future progress chart. Applicable only for small tests (<~4.5) in broad tectonic regional discrimination.

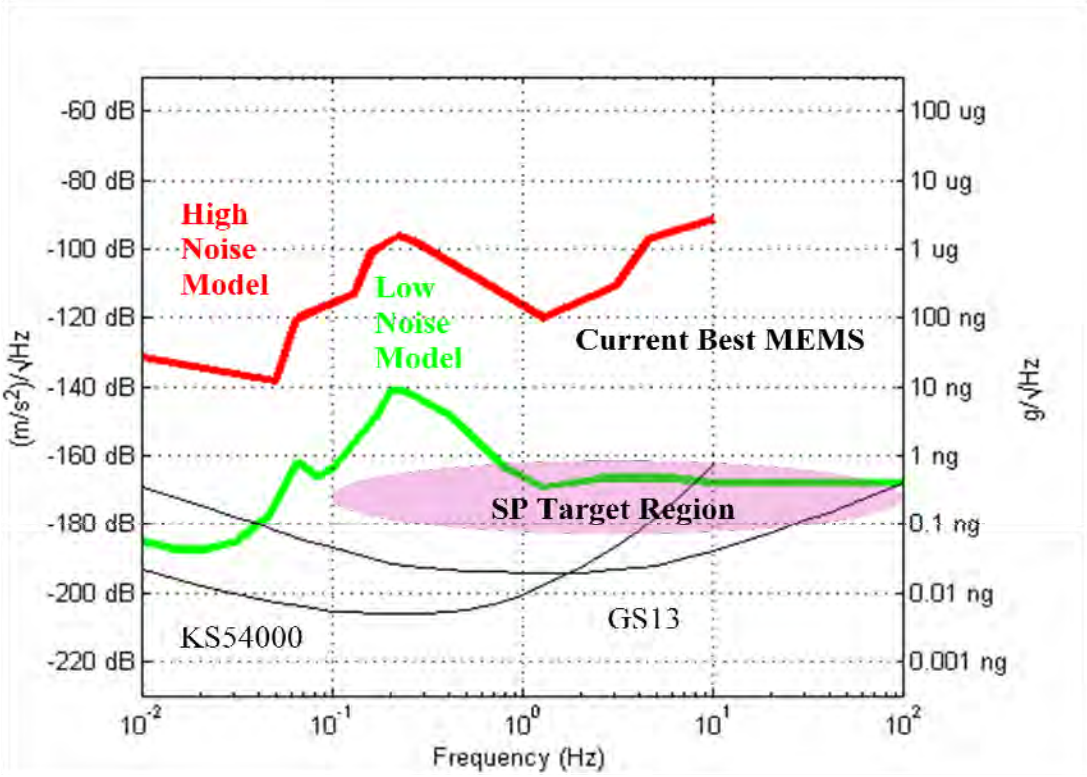

Figure 5. Seismometer R&D is directed and constrained by Earth noise. USGS High Noise (red) and Low Noise (green) models are shown with current capabilities and future targets.

Table 1. MEMS weak motion accelerometers requirements.

Noise	< 1 ng/√Hz
Bandwidth	SP: 0.1 Hz to 10's Hz LP: < 0.01 Hz to 1's Hz BB: 0.01 Hz to 10's Hz
Peak Acceleration	< 0.25 g
Dynamic Range	>120 dB

SCIENCE AND TECHNOLOGY FORESIGHT FOR THE PROVISIONAL TECHNICAL SECRETARIAT OF THE COMPREHENSIVE NUCLEAR-TEST-BAN TREATY ORGANIZATION

Patrick Grenard and Philippe Steeghs

Provisional Technical Secretariat of the Comprehensive Nuclear-Test-Ban-Treaty Organization

ABSTRACT

The Provisional Technical Secretariat (PTS) of the CTBTO has engaged in a Technology Foresight exercise aiming to mobilize the wider science and technology community in support of its mission to nurture and grow the technological capabilities of its verification systems and operations. In this context the PTS is currently working towards the establishment of a technology development strategy and a plan for the implementation of that strategy. The primary objective of the strategy is to structure the current portfolio of technology development activities as well as to provide guidance for future initiatives. A second objective is to promote communication and create a common understanding of technology development issues between the PTS and the wider science and technology community. The starting point is an evaluation of the results of the International Scientific Studies (ISS) project that were presented at the ISS Conference in June 2009. In addition, a critical technology study is being carried out in order to identify relevant wider scientific and technological trends and developments. This paper reports on the status of the Technology Foresight project and outlines the technology development strategy that is currently being formulated by the PTS.

OBJECTIVES

The primary goal of the technology development strategy is to grow the capabilities of the CTBT verification regime and to promote the efficient utilization of advances in science and technology. However, a number of issues that are pertinent to the mission and operations of the CTBTO need to be taken into consideration. Firstly, the PTS needs to prepare itself for the unique challenges and opportunities that are emerging from long-term continuous monitoring operations on a global scale. The IMS/IDC infrastructure is unique in the scope and scale of its mission, which brings some very specific challenges for the adoption of new technologies. Requirements on the longevity of infrastructure and continuity of operations are examples. Technology development should also contribute to increasing the efficiency and sustainability of systems and operations. Expanding the capabilities of the CTBT verification system needs to go hand-in-hand with efforts towards greater efficiency and sustainability. In addition, the technology development strategy should persistently express that transparency, neutrality, and reliability of CTBT verification technology and methods are central themes. The mission of the CTBTO requires the highest standards with respect to the validation and quality of data and products.

TECHNOLOGY FORESIGHT

Questions related to the positioning of CTBTO within a changing environment go well beyond the initial "bottom-up" approach of looking into emerging technologies of relevance to CTBTO's mission. Most likely, such an activity would require some scenario development work with more than just the CTBTO community in order to better specify potential future requirement profiles of CTBTO to which the evolution of the Science &Technology portfolio of CTBTO would then have to respond and conform.

In order to develop a broader perspective of the future role of the CTBTO verification regime within a changing global context, the PTS is engaging in an extended effort to reach out to, and to incorporate scientific and technological expertise from, the CTBTO community as well as personnel outside of CTBTO.

This Technology Foresight effort is essentially based on four elements: a collaborative electronic forum, focused surveys, technology workshops and bibliometric studies.

Technology Foresight Communication System

A new interactive forum for the exchange of information and ideas on Technology Foresight related to CTBTO has been developed and is available for use. The forum, called the Technology Foresight Communication System (TFCS), can be found at http://www.ctbto.org/expert-area/technology-foresight-communicationsystem/. It contains information, documents, surveys and discussion boards related to the PTS technology foresight effort.

Surveys

As part of the Technology Foresight effort, the PTS is conducting surveys to solicit expert opinions on the future of technology related to the IMS. The first of these surveys was carried out on modeling and computing applications across all the IMS technologies. Subsequent rounds of surveys are planned that will further investigate specific applications of modeling and computing, as well as more general trends, in particular technological fields including seismology, infrasound, and atmospheric sciences. Surveys evaluating the relevance and functionality of OSI techniques applied to different scenarios are also planned.

Technology Workshops

Technology workshops sponsored by external institutions and supported by the PTS have proved to be very effective at bringing together groups of experts from science, technology and industry to focus on topics of particular interest to the PTS. Workshops specific to each of the four monitoring technologies, Seismic, Hydroacoustic, Infrasound and Radionuclide, have been held over the years, typically with a declared theme to focus attention on a particular topic. There have been a number of OSI broad technical workshops as well. A new series of Science and Technology Foresight Workshops are planned, focused not on individual monitoring technologies, but on cross-cutting topics of relevance to the PTS. The output of these workshops will be in the form of advice and recommendations to the PTS on key developments in science and technology that should be considered for adoption by the PTS over the next decade, as they mature. The following topics of interest have already been identified: sources of energy, sensors and digitizers, wave propagation, automation and information processing, human system interfaces, and modeling.

Other forums are necessary, such as contracted studies and design competitions, to ensure that the PTS continues to engage with the applied science and technology communities.

Bibliometric Analysis

A particularly successful element of the Technology Foresight efforts has been the adoption of Bibliometric Survey & Analysis of the world's scientific literature. This foresight method systematically identifies highly relevant articles from many thousands of possible publications, whose authors represent key clusters of experts who could assist the CTBTO in technology foresight. To date, bibliometric analyses have been done on two topics: modeling of propagation phenomena related to event characterization and development of autonomous marine measurement systems with special consideration of hydroacoustics. In addition, a bibliometric analysis of technical and scientific underground nuclear explosion literature has been carried out in the OSI field, which has resulted in a portfolio of OSI-relevant technical background information.

TECHNOLOGY DEVELOPMENT

In the phase of the build-up of the verification systems and operations, technology development has been largely requirements based: technology needs to be developed and deployed to meet the requirements that have been the outcome of the design and specification process. On the whole, the aims and scope of technology development are narrowly defined by what is dictated by the operational requirements.

In the coming years the technology development will gradually shift from the present focus on meeting requirements towards increasing capabilities and preparing for the adoption of new technologies. This shift requires awareness of on-going scientific developments as well as the ability to identify promising new technology at an early stage. This awareness needs to come from involvement with the scientific community. In addition, mechanisms need to be in place to provide active support for the deployment of promising new technologies. In technology areas that have a significant application outside the nuclear explosion monitoring area, especially in seismology, rapid technological progress is being made. The efforts of the PTS will be largely directed towards how to leverage this progress for increasing the capabilities of its systems and operations. In other areas, there may be limited or only incremental progress because of an absence of commercial markets and/or limited application besides nuclear explosion monitoring. In these areas the PTS seeks to serve as a catalyst for developments and be an active supporter of innovation.

For the first phases of new technology development, the PTS depends on the work carried out at universities and institutions that engage in basic research. Key contributions are provided by the nuclear explosion monitoring research that takes place in national laboratories and research networks. However, the PTS also seeks to stimulate technology development by instrumentation providers. Thus, in early stage technology development the PTS takes the role of a potential end-user. In the later phases of technology development the PTS has the possibility to intensify its involvement. For instance, demonstration and validation projects can make use of PTS test facilities and data, such as the recently opened infrasound test-bed at the Conrad Observatory. In addition, the PTS seeks to contribute with its continually increasing experience gained from operating and sustaining its verification systems.

Ultimately the robustness and the performance of an evolving infrastructure integrating new developments will be evaluated within the PTS Performance Monitoring and Testing Framework. While still under development this framework provides a structure for testing and monitoring the verification system processes and elements, ultimately leading to their commissioning.

Scenarios and Major Challenges for Technology Development

At the current stage of development of the monitoring infrastructure, the design of the majority of system components is reaching maturity. Significant improvements in overall system performance can be expected to emerge through exploitation of synergies between monitoring technologies. In the long-term, major improvements may arise from integration of the measurement process with data exploitation using sophisticated modeling and automated learning strategies. The main challenge that lies ahead is to develop the methodology and tools to support this development.

However, integrating measurements and information extraction will require a major overhaul of certain parts of the system. At the same time, backward compatibility needs to be guaranteed. For instance, the current way the

waveform database is structured does not lend itself very well to application of advanced Machine Learning methods. However, changing the structure of the database without compromising other parts of the system holds a formidable design challenge.

Improvements in sensors will not only result in better data quality but will at the same time result in a significant increase in data rates and number of detections that need to be processed. Specifically, for hydroacoustic and infrasound data processing, an important issue is reduction of environment noise and the development of an effective approach to signal classification. A similar challenge lies ahead for the radionuclide technologies, where there exists a great need for better background and signature models.

For the On-Site Inspection (OSI) component of the verification regime the main goal for further technology development is the development of mechanisms to take systematic and evidence-based decisions in the planning and execution of an inspection. The creation of signature models that can be used to reliably parameterize geophysical measurements for an underground nuclear explosion is still a hard problem. In addition there is a need to integrate the different technologies with the operational concepts for an on-site inspection, e.g., the establishment of criteria, tools, and methods for choosing data acquisition parameters and effective sampling strategies.

Exploiting Synergies and Integration

The current global monitoring system is set-up as a one-way serial “pipeline” process in which data are created from measurements, followed by data transmission from the sensor station to the data center. In the second stage the information is extracted and reviewed. At several instances models are being used, for instance earth models from which seismic travel time corrections are derived. At present, the measurements and information derived from the data are not explicitly incorporated in the models or used to update and refine models. As a consequence, there is no formal strategy to utilize the vast amount of information from the present and past measurements to improve the monitoring system. The same applies to on-site inspection technologies, where an integration of the measurements coming from the different technologies into the OSI search logic is needed. A central theme of the technology development strategy is the transition from a sequential, “stovepipe” approach into an interconnected system, with several feedback loops. In the shorter term, improvements can be realized through partial integration. An example of a first step in a more integrated approach is to implement data fusion algorithms at an early stage of the data processing pipeline. For instance, joint infrasound and seismic data exploitation may result in significant gains in efficiency of the event screening process.

Beyond the current development horizon one could foresee a transition into a deeply integrated monitoring system operating in a closed loop that links the utilization of sophisticated environmental models in data exploitation with adaptive sensing and automated instrument calibration. Such an integrated system would support an implicit learning process: the sensor and environment models are continuously updated with information that is contributed by new data interpretation and background noise measurements.

At present, the integration of the data from the different sensor types takes place in the last stage of the process. A more effective data exploitation could be achieved if measurements from one sensor could be used to cue a detection and classification process for another sensor. For instance, earthquakes and explosions near the surface can be detected both in seismic and infrasound data. If event detections in both seismic and infrasound measurements could be associated as coming from the same source in an early stage this could result in reduction of the effort needed in the event screening phase. A similar concept could be envisaged for joint exploitation of seismic and hydroacoustic data. This would represent a big improvement when considering the information to be facilitated to the operations support center in a very brief time lapse in case of an OSI.

Another example of improvements that may be realized through further integration is in using additional measurements to improve instrument performance. For instance, atmospheric pressure variations can in certain cases have a detrimental effect on seismometer noise performance. The barometric pressure is measured by infrasound sensors, and hence data from a collocated infrasound sensor may be used to attribute and correct for this effect of the atmospheric pressure on seismometer performance. Similar synergies may be attainable in the integration of the atmospheric modeling—currently performed in support of the interpretation of radionuclide measurements—and the creation of infrasound propagation models. For the particular case of an OSI, the systematic integration of the analysis of the different geophysical techniques allowed by the Treaty would constitute a major development.

Goals for Technology Development

In follow-up to the present strategy development, an implementation plan will be established. Although the PTS is still in the early phase of the Technology Foresight project, some of the intermediate and end-goals of the technology development are already taking form.

Example long term goals: Establishment of a deeply integrated system with long-term memory, utilizing sophisticated models that are generated and maintained using measurements taken by the system itself.

Example intermediate term goals: Waveform event detection and classification takes place using advanced Machine Learning methods. Sophisticated earth, atmosphere, and ocean models are used in support of detection and localization. Creation of a comprehensive spatial and temporal radionuclide background model.

Example short term goals: Establishment of the groundwork for implementation of a Machine Learning approach. Initiate and evaluate data fusion strategies. Implement modern waveform classification tools for infrasound and hydroacoustic data.

CONCLUSIONS AND RECOMMENDATIONS

The PTS is currently reviewing its technology development strategy. Apart from laying the groundwork for sustaining and growing the technological capabilities of its verification systems, a major goal of the Technology Foresight project is to further build relations with the scientific community and to intensify its participation in the nuclear explosion monitoring research networks.

One long-term goal for technology development may be aimed at transitioning the present sequential and highly modular data acquisition and exploitation process into an integrated system that utilizes its own measurements and data to guide autonomous and highly automated operations. Several promising areas for research and development to support such a transition have been identified. For instance, promising results have been obtained with Machine Learning methods in data exploitation, which makes this a key area for further development. Other areas that have been targeted for further analysis are concepts for autonomous platforms, sensors with highly automated self-calibration and noise mitigation capabilities. A general issue that has been singled out as important is the utilization of sophisticated modeling concepts and tools throughout the system.

In the shorter-term there are significant gains to be expected from focused efforts to deploy available technologies and to exploit synergies between the different verification technologies. An example is to work towards more effective tools to support event screening through the joint exploitation of seismic, hydro-acoustic, and infrasound data, or the development of mechanisms for the integration of on-site inspection technologies.

In the first stages of implementation, growing the technology development capabilities and infrastructure will be highly placed on the agenda. With the establishment of a seismic and infrasound test facility at Conrad Observatory in Austria and the creation of an open access virtual Data Exploitation Center (vDEC) in the foreseeable future the first steps have been taken to build the infrastructure to support and stimulate cooperative technology development activities

REFERENCES

Science for Security – International Scientific Studies Conference – Preparatory Commission for the Comprehensive Nuclear-Test-Ban-Treaty Organization (CTBTO) – September 2009

Seismic Regional Characterization and Wave Propagation

3D MODELING OF IRAN AND SURROUNDING AREAS FROM SIMULTANEOUS INVERSION OF MULTIPLE GEOPHYSICAL DATASETS

Charles J. Ammon[1], Monica Maceira[2], and Michael Cleveland[1]

Penn State[1] and Los Alamos National Laboratory[2]

Sponsored by the Air Force Research Laboratory[1] and the National Nuclear Security Administration[2]

Award Nos. FA8718-09-C-0007[1] and LA09-BAA09-12-NDD03[2]
Proposal No. BAA09-12

ABSTRACT

The objective of this work is to help improve seismic monitoring technology through the development and application of advanced multivariate inversion techniques to generate realistic, comprehensive, and high-resolution 3D models of the seismic structure of the crust and upper mantle that satisfy independent geophysical datasets. Our focus is on the region surrounding Iran from the east coast of the Mediterranean in the west, to Pakistan in the east, an area of prime importance to NEM, and a region with adequate calibration events to validate our model and to quantify its accuracy. Specifically, we are working to integrate surface-wave dispersion, receiver function, and satellite and ground-based gravity observations to help constrain the shallow seismic structure in the Arabian-Eurasian collision zone. Building on our earlier work combining receiver functions and surface wave dispersion, and surface-wave dispersion and gravity, we plan to continue to integrate geophysical data sets to create more broadly compatible earth models. We also explore geologically based smoothness constraints to help resolve sharp features in the underlying shallow 3D structure.

OBJECTIVES

The National Nuclear Security Administration (NNSA) and Air Force Research Laboratory (AFRL) have decided to investigate 3D modeling as part of the effort to improve knowledge of Earth's compressional and shear velocity structure. Such knowledge will help reduce uncertainty in our ability to accurately detect, locate, and identify small (mb < 3.5) seismic events, which in turn will lead to improved capabilities for nuclear explosion monitoring (NEM). For seismically active areas, with good ground-truth event coverage, earth models with limited accuracy can be corrected by interpolating results from nearby 'ground truth' events (using the kriging methodology) making it possible to detect, locate, and identify events even with limited resolution of Earth's structure. However, such approaches are less effective for smaller events, and event location and characterization remains a challenge for aseismic regions. To improve monitoring capability in such instances, we must develop better seismic earth models.

The objective of this work is to help improve seismic monitoring technology through the development and application of advanced multivariate inversion techniques to generate realistic, comprehensive, and high-resolution 3D models of the seismic structure of the crust and upper mantle that satisfy independent geophysical datasets. Our focus is on the region including and surrounding Iran (Figure 1) from the east coast of the Mediterranean in the west, to Pakistan in the east, an area of prime importance to NEM, and a region with adequate calibration events to validate our models and to quantify their accuracy.

Background

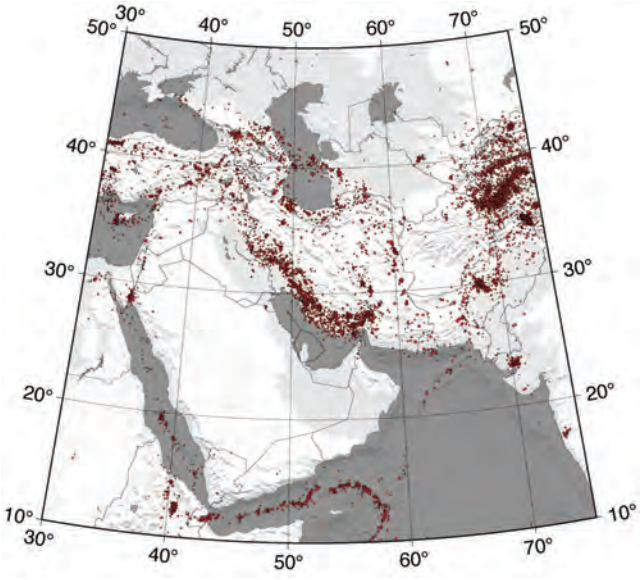

Figure 1 Map of focus region show with topographic and bathymetric shading and moderate to large earthquake locations (magnitudes ≥ 3.5 from 1990 to Spring 2008). The region contains the Arabian plate and the middle segment of the Alpine to Himalyan collision zone, which is constructed primarily of Phanerozoic terranes amalgamated onto southern Eurasia during the closing of the Tethys Ocean.

Estimating subsurface geologic variations is a challenge. Seismologists have worked on the problem for more than a century (e.g., Milne, 1899; Macelwane and Sohon, 1936; Dahlen and Tromp, 1999). As data quantity has increased and data quality and computational ability have improved, we have made important advances in our understanding of the subsurface. Our best knowledge applies to the shallowest regions as well as depths with the sharpest global interfaces (sediment-basement contacts, the base of the crust, base of the mantle, and transitions near 410 km and 660 km depths), where resolution is improved as a result of the strong interactions of seismic body waves with sharp geologic transitions (e.g., Helmberger, 1968; Langston, 1979; Shearer, 1991; Lay et al., 2004). We have also done well modeling regions with smooth velocity changes such as the lower mantle, which allows us to exploit the information in teleseismic body-wave travel times to locate seismic sources reasonably well (e.g., Kennett, 1991). Still, many details within and just beneath the lithosphere elude us. We have been able to surmise that geologic variations here are substantial, and we know that they frustrate attempts to use robust observations such as regional seismic travel times to locate events in many parts of the Earth (e.g., Bondar et al., 2004).

Travel-time based tomography (e.g., Nolet, 2008) opened the doors to 3D imaging but the models remain blurry, often suffer from interpretational ambiguity, and are not easily used to predict other, independent seismic observations. From our own analyses (Maceira et al., 2005; Maceira and Ammon, 2009), we have seen how high-resolution surface-wave tomography fails to produce the extremes in seismic shear-wave speed that are evident from independent observations. In particular, achieving a model with low enough seismic wave speeds within the Tarim Basin to match seismograms from high-quality observations remains an issue. Waveform tomography methods improve the situation somewhat, including information from both the amplitude and phase of the signal, but restriction of these methods to lower frequency bands limits the resolution of the methods and the substantial

computation requirements of these methods limit their application. More recent finite-frequency methods (e.g., Zhou et al., 2004; Dahlen and Zhou, 2006, Nolet, 2008) and adjoint methods (e.g., Tarantola, 1984; Tromp et al., 2008) offer more complete approaches to computing sensitivity kernels. But even these approaches face limits imposed by data bandwidth. In any event, such fully 3D waveform methods could benefit greatly from accurate, if approximate, starting models derived from more piecewise interpretation of seismic observables combined with other observations.

RESEARCH ACCOMPLISHED

Much of our effort during the first year of this project has been on the software development, although we have completed preliminary inversions that we present below with little discussion. At this point we caution readers about using or interpreting these preliminary earth models – they will improve. We begin with a simple conceptual illustration of the challenges we address and conclude with a discussion of accomplishments and plans for the second year of work.

Combining Gravity, Rayleigh-Wave Dispersion, and P-wave Receiver Function Observations

Inversion of surface wave dispersion observations is a standard method for estimating 3D shear velocity structure of Earth's crust and upper mantle. Nevertheless, it is well known that traditional state-of-the-art inversion techniques suffer from poor resolution and nonuniqueness, especially when a single surface-wave mode is used (Huang et al., 2003). This is particularly true at shallow depths where the shorter periods, which are primarily sensitive to upper crustal structures, are difficult to measure and especially true in tectonically and geologically complex areas. On the other hand, regional gravity inversions have the greatest resolving power at shallow depths since gravity anomalies decrease in amplitude and wavenumber bandwidth with increasing depth. Gravity measurements also supply constraints on rock density variations. Thus by combining surface-wave dispersion and gravity observations in a single inversion, we can obtain a self-consistent high-resolution 3D shear-velocity/density model with increased resolution of shallow geologic structures. Receiver function analysis (Langston, 1979) is a well-established tool for imaging relatively sharp changes in the subsurface structure that nicely complements information contained in surface-wave dispersion (e.g., Julià et al., 2000).

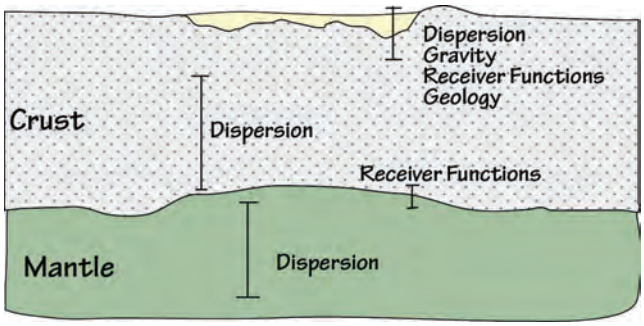

Figure 2 Conceptual illustration of the primary sensitivities of different data sets to the different depths of the lithosphere in a simultaneous inversion of surface-wave dispersion, gravity, and receiver-function observations. The crust shown contains a large basin (yellow). The receiver functions provide information on strong velocity contrasts such as the crust-mantle transition and near-surface structures; the spatially filtered gravity provides constraints on near-surface structures; and dispersion provides information on the absolute seismic velocities throughout the structure. Note that this cartoon is conceptual, the sensitivity of the data is more subtle than shown.

To improve our view of the earth structure within the focus region, we are working to combine receiver functions with surface-wave dispersion and gravity observations. The combination of receiver functions with tomographically localized surface-wave dispersion is well established (e.g., Julià et al. 2000). The integration of gravity observations with surface-wave dispersion is a more recent development (e.g., Maceira and Ammon, 2009), but these data are a good match. To a large part, the gravity observations add important constraints on the location of strong shallow heterogeneity to the information on smooth variations found in period-dependent dispersion maps. The choice of a density-velocity relationship can be subjective (Julià et al., 2004; Brocher, 2005; Maceira and Ammon, 2009), but testing the sensitivity of the results to a range of relations is not a challenge. To isolate gravity signatures associated with density variations (as opposed to dynamic and flexure variations) we plan to filter the gravity signals to include short wavenumbers sensitive to the crust. These concepts are summarized conceptually in Figure 2, which shows the regions of the lithosphere most sensitive to the different data that we employ.

To construct an approximate 3D model of the lithosphere, we use a hybrid 1D-3D inversion. In many tomography analyses, dispersion variations are converted to shear-velocity variations by inverting dispersion curves extracted from the tomographic model for a localized 1D structure. Smoothness constraints are applied to reduce cell-to-cell

shear-velocity fluctuations in the resulting composite 3D structure. Since gravity observations can be efficiently modeled using prisms they provide direct information on cell-to-cell density variations. In a particular cell, surface wave dispersion can be inverted simultaneously with receiver functions (surface or downward-continued signals). In regions with receiver function overlap, multiple signals can be combined to produce a structure that matches compatible features in several receiver functions. Because of the hybrid nature of the inversion, the resulting model is an approximation to the true 3D structure, but we can use to provide a starting point for future full 3D waveform-based inversions of the subsurface.

Preliminary Application to the Iranian Plateau and Surrounding Regions

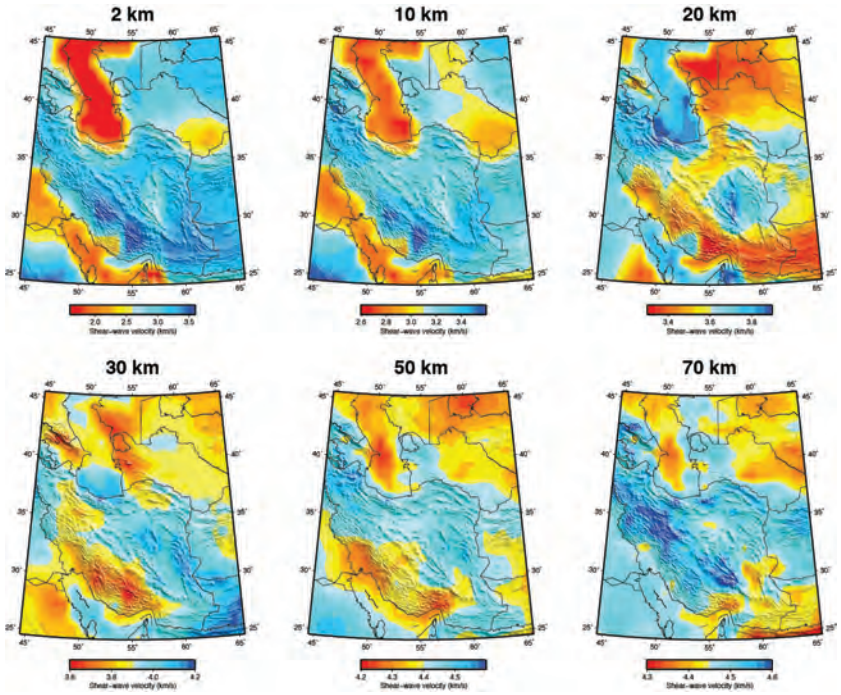

Figure 3. Results of a preliminary inversion of Rayleigh-wave dispersion and Bouguer gravity observations to estimate shear-velocity beneath the focus region. The inversion was performed using the existing SVD-based approach and took about 36 hours to compute on a high-end workstation. This result is preliminary and should not be used for specific interpretation. The extreme slow values for the shallow Caspian Sea are obvious; deeper values, particularly those with high wavenumbers are likely artifacts. The inversion weighted observations at shorter periods much more than longer-period observations.

A large component of the proposed work involves improving current software to allow more easy extension to larger focus areas and more flexible incorporation of additional data. For example, the earlier work in Maceira and Ammon (2009) blended gravity and surface-wave observations to produce a shear-velocity/density model for central Asia, but did not include receiver-function information. Our inversion is a straightforward composite of coupled and uncoupled linearized inversions of nonlinear data and model relationships. The preliminary results we present below do not have the gravity wavenumber filters applied. We rely on the dispersion models from the University of Colorado group (Ritzwoller and Levshin, 1998; Levshin et al., 2001, 2002) for the preliminary results, but we will include other measures as the project proceeds. Figure 3 is a plot of first-order shear-velocity variations beneath the study region. These are preliminary results, so we invest little space interpreting the variations. We started the inversion using only Rayleigh-wave dispersion in the period range from 7 to 200 seconds (with more weight on the shorter periods). Figure 4 shows example fits to the dispersion values and the Bouguer gravity variations. As seen in earlier studies (Maceira and Ammon, 2009) the addition of the gravity information produces little change to the overall fit of the dispersion values, but substantially improves the fit to the observed surface gravity signals.

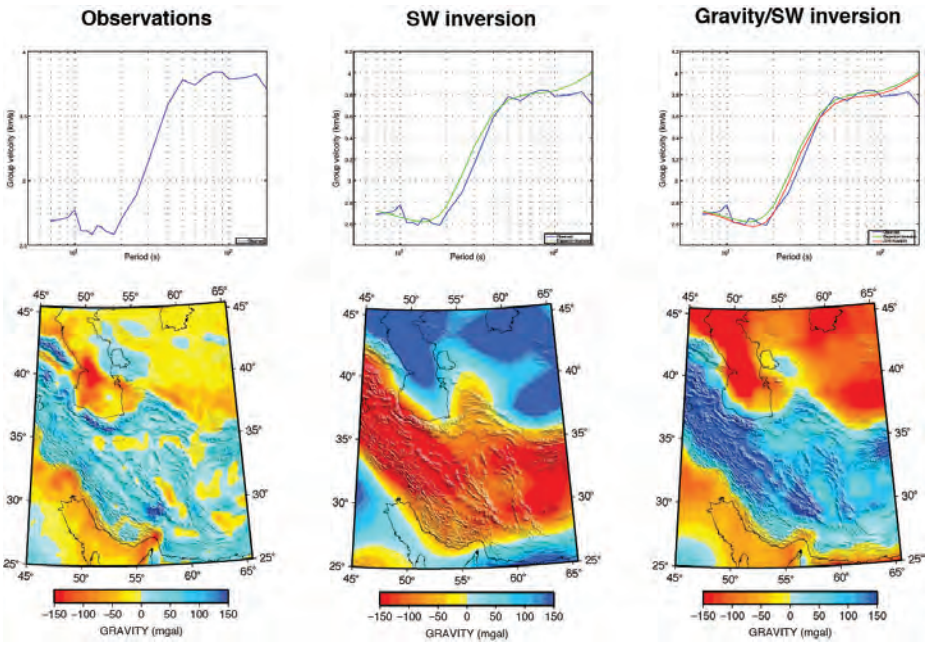

Figure 4. Sample dispersion (top) and Bouguer gravity (bottom) for the preliminary inversion. As for other regions (Maceira and Ammon, 2009), the inclusion of gravity observations produces a much better fit to the observed gravity variations with little change to the Rayleigh-wave fit. Note that the gravity in this inversion was not filtered to emphasize shorter wavelength variations in the gravity to focus on near-surface variations.

Software Development Progress

A large component of the proposed work involves improving current software to allow more easy extension to larger focus areas and more flexible incorporation of additional data. For example, the earlier work in Maceira and Ammon (2009) blended gravity and surface-wave observations to produce a shear-velocity/density model for central Asia, but did not include receiver function information. Our inversion is a straightforward composite of coupled and uncoupled linearized inversions of nonlinear data and model relationships. In essence we construct a large set of coupled data and constrain equations into the form $Gm = d$, where the model parameters are in m, observations and constraint information is in d, and the system matrix, G, contains partial derivatives and coefficients of constraint equations.

The existing inversion tool used a singular value decomposition (SVD) to invert the system matrix, G. The SVD is superb numerical choice for matrix inversion and problem analysis but the simplest implementations require substantial quantities of core memory and computational time as the problem grows large. To reduce these requirements we have replaced the SVD with Page and Saunders (1982) LSQR conjugate-gradient based routine. We adopted the LSQR function from the Association for Computing Machinery (ACM) FORTRAN implementation last modified in 1994 (http://toms.acm.org/). Although well known to seismic tomographers (Pavlis, 1988; Nolet, 1993), the benefits of the LSQR algorithm may be less familiar to those working on multi-dataset inversion tools. The key advantage is that the system matrix, G, need never be stored in memory. G can be stored on the disk as it is constructed one row at a time. The LSQR user need only develop a subroutine that computes $y = G\,y + y$ and $x = G^T x + x$, for vectors x and y provided during the inversion of G. G can be written to disk by saving only the nonzero columns of each row of the matrix and the associated indices of the nonzero columns. Not only do you save storage and input-output time, you also avoid waste by not multiplying numbers by zero. In our early experiments, we have saved roughly an order of magnitude in computation time (measured on a relatively simple desktop workstation). The great reduction in computation time allows more experimentation with and assessment of the model.

Example Rayleigh-Wave Dispersion Receiver Function Coupled Inversion

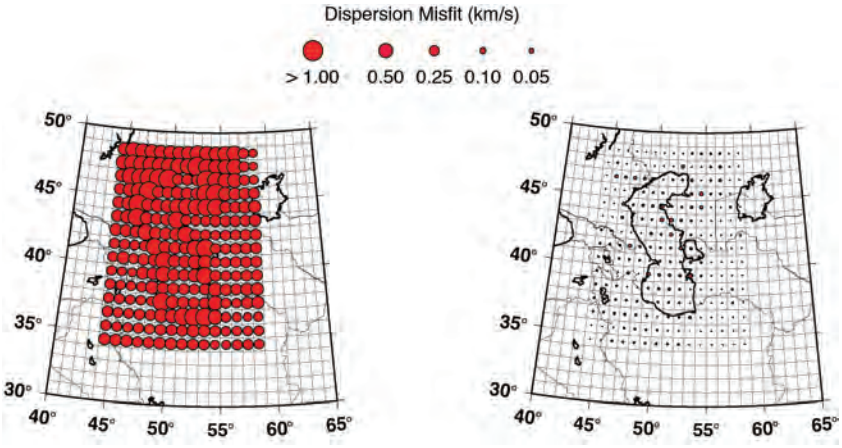

Figure 5. Initial (left) and final (right) dispersion misfit associated with the example subregion inversion of dispersion only. The initial model consists of a simple "continental" model and a Caspian Sea model. The initial misfits are large, but the convergence is reasonable to mean misfit values near or below 0.05 km/s.

To illustrate the result of combining surface-wave dispersion and receiver functions in a coupled inversion of cells for an approximation to a 3D model, we selected a small, but interesting region of the focus area that includes the Caspian Sea. The Caspian Sea region is an area of complex geologic structure (e.g., Mangino and Priestly, 1998) and significantly low shear velocities. The sub region is shown in Figure 5, which also shows the misfit to the dispersion values for each cell. As above, the dispersion values are from the University of Colorado tomographic effort (Ritzwoller and Levshin, 1998; Levshin et al., 2001, 2002). The initial misfits are large, but the inversion converges nicely to reasonable fits after four iterations (final). Two depth slices of the corresponding shear-velocity model (initial and final) are shown in Figure 6. The interpolation and contouring algorithm had some trouble with the rough initial model that contained two structures, one for region within the Caspian Sea and another for the rest of the model. We applied a simple Laplacian smoothing between adjacent cells so the resulting model remains smooth.

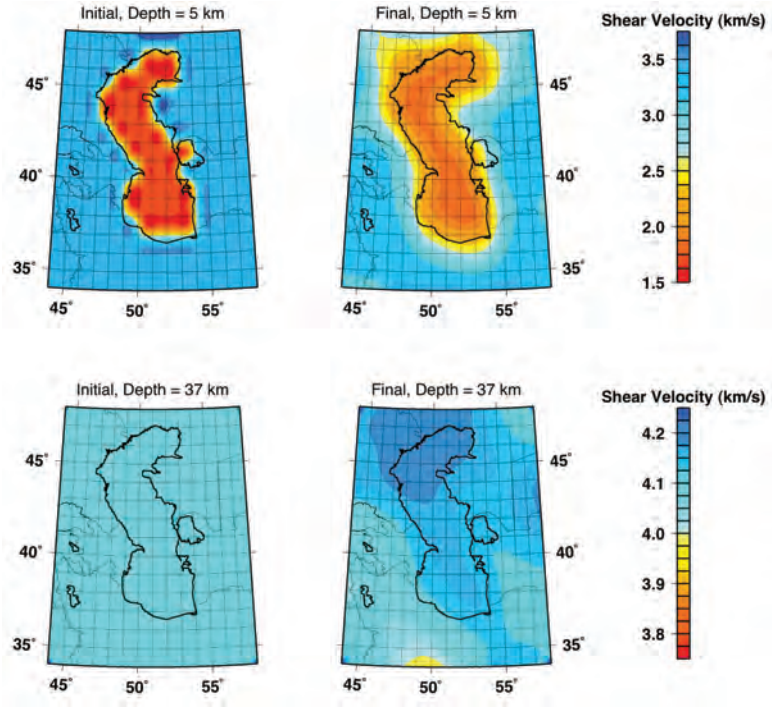

Figure 6. Initial (left) and final (right) shear-velocity values associated with the example subregion inversion of dispersion only for the upper and lower crust or upper mantle region of the model. The interpolation distorts the rough initial model producing artifacts that are absent when the inversion is complete and the model is smoother (we use a 1° cell dimension for the inversion).

Next, we added one receiver function to the dispersion data and repeated the 3D shear-velocity inversion. The receiver function was digitized from Mangino and Priestly (1998), and includes samples the structure in our cell with the lower left corner at 53E and 40N (Figure 7). Figure 7 is a plot of the initial and final dispersion fits, which show little change from those without the receiver function. The initial and final fit to the receiver function are shown in Figure 8. The effect of including the receiver function is to thicken the crust and better define the crust-mantle boundary. The net result is a decrease in the velocity at the depth slice near 37 km. Two depth slices of the corresponding shear-velocity model (initial and final) are shown in Figure 9. The thickening of the crust near the receiver function observation is clearly visible in the deeper slice through the model (compare Figure 6 and Figure 9). The fit to the receiver function is not perfect and the spread of the slower deep crustal speeds into the Caspian region does not make sense geologically.

These effects are driven by the simple Laplacian smoothness requirements placed on the 3D model.

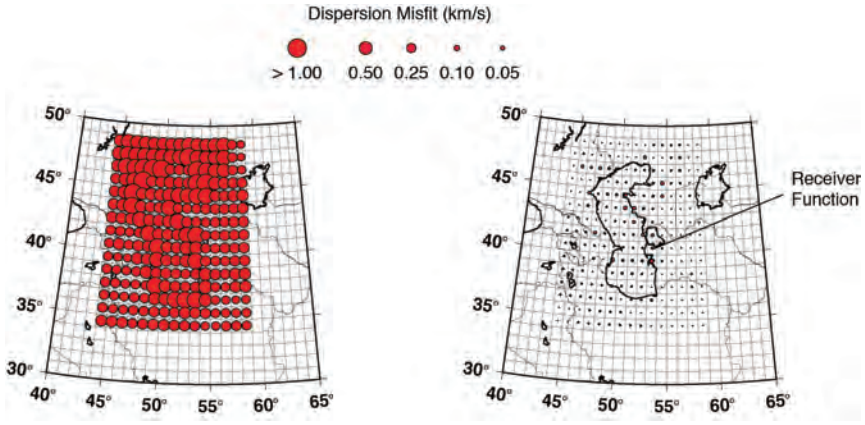

Figure 7. Initial (left) and final (right) dispersion misfit associated with the example subregion inversion of dispersion and a receiver function. The initial model consists of a simple "continental" model and a Caspian Sea model. The initial misfits are large, but the convergence is reasonable to mean misfit values near or below 0.05 km/s. The cell containing the isolated receiver function is labeled.

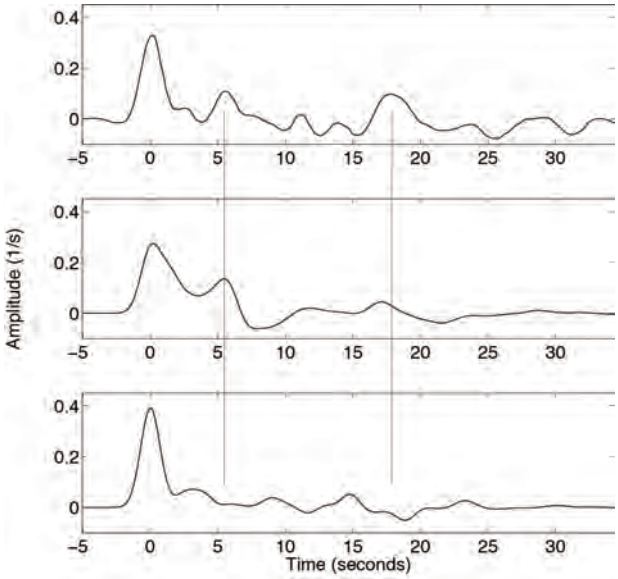

Figure 8. Observed (top), final prediction (middle) and initial prediction (bottom) of the receiver functions from the inversion shown in Figure 4. Vertical lines show the arrivals most likely associated with the crust-mantle transition. Although the final fit is certainly not perfect, note the improvement in timing of the main crustal conversion and reverberation (vertical lines) from the initial to final models.

Including Geologic Information

To produce models that have realistic 'sharp' boundaries requires that we include independent information on the location of those boundaries. Such information is available (for the shallow part of the model) in independent data sets such as gravity, surface geologic maps, and even something as simple as topography. As part of this work, we plan to resolve sharp features by adapting our imaging algorithms to allow the inclusion of geologic information on the location and nature of the boundary into shear-velocity inversions that permit such features (implemented through custom geologic smoothness constraints that allow velocities to be de-correlated across major geologic transitions). Including a priori information into an inversion is obviously only as good as the information that is included. Thus the inclusion of this type of information into the reconstruction of shear-velocity models of the

subsurface must proceed carefully and include documentation of the importance of the assumed a priori information on the resulting model.

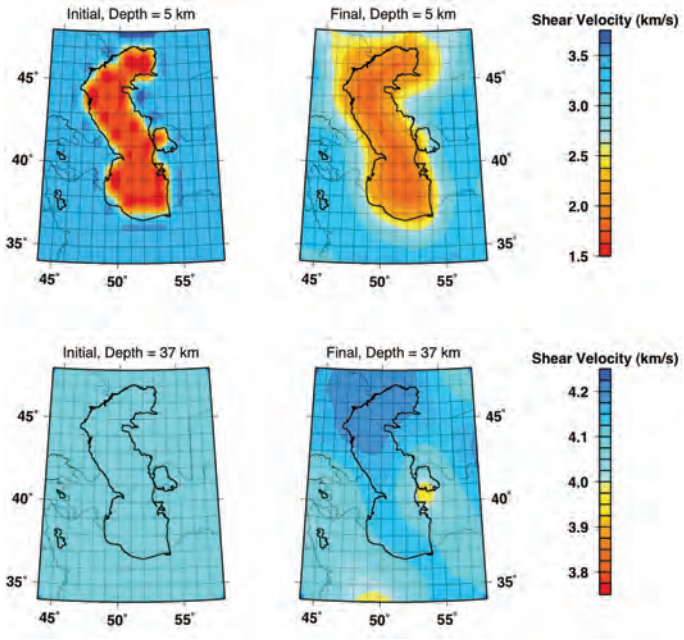

Figure 9. Initial (left) and final (right) interpolated shear-velocity values associated with the example subregion inversion of dispersion and a receiver function. The addition of the receiver function improves the estimate of crustal details. Please note the dramatic difference in the velocity scales shown to the right of each pair of images. The interpolation distorts the rough initial model producing artifacts that are absent when the inversion is complete and the model is smoother (we use a 1° cell dimension for the inversion).

We have made progress on including this type of information into the inversion, but have not finished debugging this component of the software. We expect that uncoupling the structures beneath a region of the Caspian Sea and its eastern margin will for example, allow a better fit to the KRF receiver function and decrease the leaking of receiver function model information into the model beneath the Caspian Sea. Implementation of these smoothing constraints requires more work, but in the end includes more information in the shear-velocity model reconstruction, and hopefully leads to improved regional earth models.

CONCLUSIONS

We have initiated a two-year project to map the subsurface geologic variations using seismic dispersion, gravity, and receiver-function observations. We face significant challenges in our efforts to include effective point constraints on structure (receiver functions) with the spatially continuous surface-wave tomography and gravity observations. Our work complements ongoing work at LANL to integrate body-wave travel times into the same formalism. The basic philosophy is that models that explain more data are better. The ultimate utility of the derived earth models is to provide improved predictive capabilities for routine seismic analyses and to provide adequate starting models for 3D waveform inversion approaches.

ACKNOWLEDGEMENTS

We thank the scientists, engineers, and technicians that have created the seismic-recording systems and networks that provide excellent broad-band seismic observations. In particular, we thank the USGS and the IRIS Consortia (NSF) who share information and data with the global community in an effective and efficient manner. We also thank the many international groups involved in collecting and sharing quality seismic observations. We also thank Wessel and Smith (1991), the developers of the Generic Mapping Tools software, which we use to create many of the illustrations of our research.

REFERENCES

Bondar, I., S. C. Myers, R. E. Engdahl, and E. A. Bergman (2004). Epicentre accuracy based on seismic network criteria, *Geophys. J. Int.* 156: 483–496.

Brocher, T. A. (2005). Empirical relations between elastic wavespeeds and density in the earth's crust, *Bull. Seismol. Soc. Am*. 95: (6), 2081–2092.

Dahlen, F. A. and J. Tromp (1999). *Theoretical Global Seismology*. Princeton University Press, Princeton, NJ, 1025 pp.

Dahlen, F. A. and Y. Zhou (2006). Surface-wave group-delay and attunuation kernels, *Geophys. J. Int*. 165: 545–554.

Helmberger, D. (1968). The crust-mantle transition in the Bering Sea, *Bull. Seismol. Soc. Am*. 58: 179–214.

Huang, Z., W. Su, Y. Peng, Y. Zheng, and H. Li (2003). Rayleigh wave tomography of China and adjacent regions, *J. Geophys. Res*. 108: doi:10.1029/2001JB001696.

Kennett, B. L. N. and E. R. Engdahl (1991). Traveltimes for global earthquake location and phase identification, *Geophys. J. Int*. 105: 429–465.

Langston, C. A. (1979). Structure under Mount Rainier, Washington, inferred from teleseismic body waves, *J. Geophys. Res.* 84: 4749–4762.

Lay, T., E. J. Garnero, and S. Russell (2004). Lateral variation of the D'' Discontinuity beneath the Cocos Plate, *Geophys. Res. Lett*. 31: L15612, doi:10.1029/2004GL020300.

Levshin, A. L., M. H. Ritzwoller, M. P. Barmin, and J. L. Stevens (2001). Short period group velocity measurements and maps in central Asia, in *Proceedings of the 23rd Seismic Research Review: Worldwide Monitoring of Nuclear Explosions*, LA-UR-01-4454, Vol. 1, pp. 258–269.

Levshin, A. L., J. L. Stevens, M. H. Ritzwoller, and D. A. Adams (2002). Short-period (7-s to 15-s) group velocity measurements and maps in central Asia, in *Proceedings of the 24th Seismic Research Review– Nuclear Explosion Monitoring: Innovation and Integration*, LA-UR-02-5048, Vol. 1, pp. 97–106.

Liang, C., X. Song, and J. Huang (2004). Tomographic inversion of Pn travel times in China, *J. Geophys. Res*. 109: B11304, doi:10.1029/2003JB002789.

Maceira, M. and C. J. Ammon (2009). Joint Inversion of Surface Wave Velocity and Gravity Observations and its Application to Central Asian Basins Shear Velocity Structure, *J. Geophys. Res.* 114: B02314, doi:10.1029/2007JB005157.

Maceira, M, S. R. Taylor, C. J. Ammon, and X. Yang (2005). High-resolution Rayleigh wave slowness tomography of central Asia, *J. Geophys. Res*. 110: doi:10.1029/2004JB003429.

Macelwane, J. B. and F. W. Sohon (1936). *Introduction to Theoretical Seismology, Part I, Geodynamics*. John Wiley and Sons, Inc., New York, 336 pp.

Mangino, S. and K. Priestley (1998). The crustal structure of the southern Caspian region, *Geophys. J. Inter*. 133: (3), 630–648.

Milne, J. (1899). *Earthquakes and Other Earth Movements* (4th Edition). D. Appleton and Company, New York, 376pp.

Nolet, G. (1993). Solving large linearized tomographic problems, in *Seismic Tomography - Theory and Practice*, edited by H. M. Iyer and K. Hirahara, pp. 227–247, Chapman & Hall, London.

Nolet, G. (2008). *A breviary of seismic tomography : imaging the interior of the earth and sun*, xiv, 344 p. pp., Cambridge University Press, Cambridge, UK; New York.

Pavlis, G. L. (1988). Vector and matrix manipulation algorithms, in *Seismological Algorithms, Computational Methods and Computer Programs*, edited by D. J. Doornbos, pp. 403–426, Acadmeic Press Limited, San Diego, CA.

Ritzwoller, M. H., and A. L. Levshin (1998), Eurasian surface wave tomography: Group velocities, *J. Geophys. Res*. 103: 4839–4878.

Shearer, P. M. (1991). Constraints on upper mantle dscontinuities from observations of long-period reflected and converted phases, *J. Geophys. Res*. 96: 18147–18182.

Tarantola, A. (1984). Inversion of seismic reflection data in the acoustic approximation, *Geophysics* 49: 1259–1266.

Tromp, J., D. Komatisch, and Q. Liu (2008). Spectral-element and adjoint methods in seismology, *Communications in Comp. Physics* 3: 1–32.

Wessel, P., and W. H. F. Smith (1991). Free software helps map and display data, *EOS, Trans. of Am. Geophys. Union*, 72: 441–445.

Zhou, Y. F. A. Dahlen, G. Nolet, and G. Laske (2004). Finite-frequency effects in global surface-wave tomography, *Geophys. J. Int*. 163: 1087–1111.

A GLOBAL 3D P-VELOCITY MODEL OF THE EARTH'S CRUST AND MANTLE FOR IMPROVED EVENT LOCATION -- SALSA3D

Sanford Ballard[1], Michael A. Begnaud[2], Christopher J. Young[1], James R. Hipp[1], Marcus Chang[1], Andre V. Encarnacao[1], Charlotte A. Rowe[2], W. Scott Phillips[2], and Lee K. Steck[2]

[1]Sandia National Laboratories and [2]Los Alamos National Laboratory

Sponsored by the National Nuclear Security Administration

Award Nos. DE-AC04-94AL8500/SL09-3D Earth-NDD02[1], and DE-AC52-06NA25396/LA09-IRP-NDD02[2]

ABSTRACT

To test the hypothesis that high quality 3D Earth models will produce seismic event locations which are more accurate and more precise, we are developing a global 3D P wave velocity model of the Earth's crust and mantle using seismic tomography. In this paper, we present the most recent version of our model, SALSA3D (SAndia LoS Alamos) version 1.4, and demonstrate its ability to reduce mislocations for a large set of realizations derived from a carefully chosen set of globally-distributed ground truth events.

Our model is derived from the latest version of the Ground Truth (GT) catalog of P and Pn travel time picks assembled by Los Alamos National Laboratory. To prevent over-weighting due to ray path redundancy and to reduce the computational burden, we cluster rays to produce representative rays. Reduction in the total number of ray paths is > 55%. The model is represented using the triangular tessellation system described by Ballard et al. (2009), which incorporates variable resolution in both the geographic and radial dimensions. For our starting model, we use a simplified two layer crustal model derived from the Crust 2.0 model over a uniform AK135 mantle. Sufficient damping is used to reduce velocity adjustments so that ray path changes between iterations are small. We obtain proper model smoothness by using progressive grid refinement, refining the grid only around areas with significant velocity changes from the starting model. At each grid refinement level except the last one we limit the number of iterations to prevent convergence thereby preserving aspects of broad features resolved at coarser resolutions. Our approach produces a smooth, multi-resolution model with node density appropriate to both ray coverage and the velocity gradients required by the data. This scheme is computationally expensive, so we use a distributed computing framework based on the Java Parallel Processing Framework, providing us with ~400 processors. Resolution of our model is assessed using a variation of the standard checkerboard method, as well as by directly estimating the diagonal of the model resolution matrix based on the technique developed by Bekas, et al.

We compare the travel-time prediction and location capabilities of this model over standard 1D models. We perform location tests on a global, geographically-distributed event set with ground truth levels of 5 km or better. These events generally possess hundreds of Pn and P phases from which we can generate different realizations of station distributions, yielding a range of azimuthal coverage and proportions of teleseismic to regional arrivals, with which we test the robustness and quality of relocation. The SALSA3D model reduces mislocation over standard 1D ak135, especially with increasing azimuthal gap. The 3D model appears to perform better for locations based solely or dominantly on regional arrivals, which is not unexpected given that ak135 represents a global average and cannot therefore capture local and regional variations.

INTRODUCTION

The evolving U.S. monitoring needs require accurate location of smaller and smaller events. Given the limited station coverage of a typical global monitoring network, such as the International Monitoring System (IMS), it is likely that such events will be detected by a small number of stations, quite possibly with a poor network geometry. For locating such events, it is essential to have extremely high fidelity travel time predictions, particularly at regional distances where lateral heterogeneity can be significant. Accurately accounting for lateral heterogeneity implies using 3D models of the Earth to calculate travel times, but relatively few of the available 3D Earth models are appropriate for high fidelity travel time prediction, and it is unclear whether any of those that are appropriate actually improve event locations. Thus, we are developing our own global 3D P wave velocity model of the Earth's crust and mantle -- SALSA3D (SAndia LoS Alamos 3D) -- using seismic tomography based on a carefully assembled data set of P phase travel times collected by LANL over the past decade. An important difference between our effort and previous efforts is that our model was produced specifically for improving event location; the model provides potentially valuable information about the structure of the Earth, but this is not our focus. Hence, all decisions about data processing and tomography were made with this goal in mind.

In this paper, we present the most recent version of our model, SALSA3D version 1.4, and demonstrate its ability to reduce mislocations for a large set of realizations derived from a carefully chosen set of globally-distributed ground truth events.

DATA SET

The data used for the tomographic inversion was collected by LANL over the past decade and includes events categorized with a ground truth (GT) level of 25 km or better (Bondár et al., 2004). Arrivals for these GT events were merged from various sources in order to produce a single set of arrivals for each event with redundancies removed, maximizing the available arrivals for each event (Begnaud, 2005). Regional Pn and teleseismic P arrivals were extracted for use in the tomography and resulted in ~119K events, ~12K stations, and almost 12 million individual ray paths (Figure 1). Geographically focused component data sets include USarray and the Deep Seismic Soundings in the former Soviet Union (e.g., Li and Mooney, 1998). To prevent over-weighting due to ray path redundancy and to reduce the computational burden, we cluster rays to produce representative rays, thereby reducing the total number of ray paths by 55%.

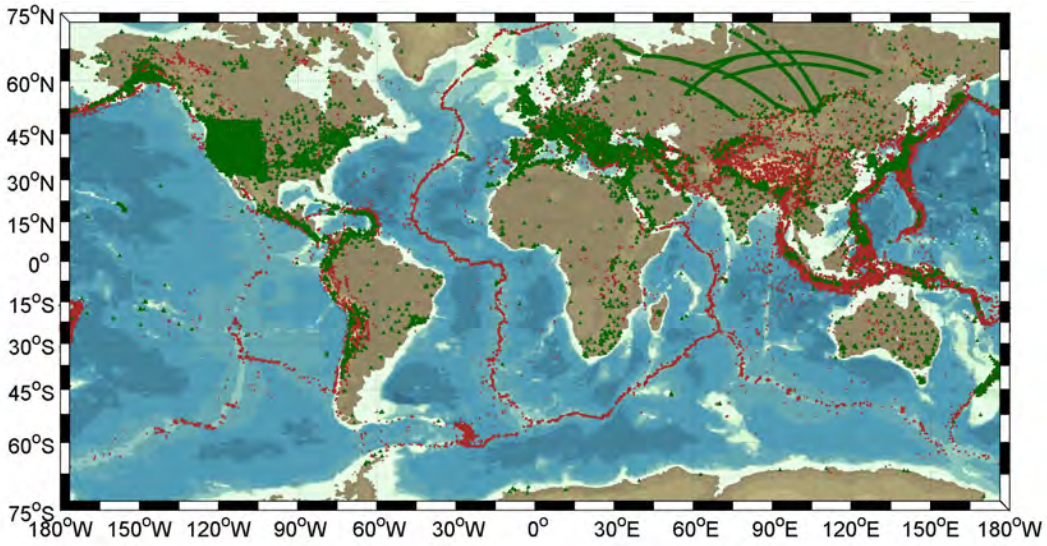

Figure 1. Stations and events used for the global tomography inversion. These data were collected by LANL over the past decade and are all categorized with a ground truth level of 25 km or better.

TOMOGRAPHIC INVERSION

We use the LSQR algorithm of Paige and Saunders (1982) to invert the data to find the P wave velocity distribution in the mantle that optimally reduces the misfit between observed and predicted travel times for P and Pn phase arrivals. Our starting model for the inversion consists of a modified version of the Crust 2.0 model (Laske and Masters, 1997, Laske et al., http://igppweb.ucsd.edu/~gabi/crust2.html) overlaying an AK135 mantle. We modify Crust 2.0 by combining their six layers into just two. The crust is damped heavily in the inversion so it changes very little. We retrace the rays at each of 16 iterations using the pseudo-bending algorithm (Um and Thurber, 1987, Zhao and Lei, 2004, Ballard et al., 2009). During early iterations, the mantle is moderately damped to discourage the inversion from progressing too rapidly but then damping is relaxed in later iterations. Adding regularization constraints to the data kernal matrix is not required during the inversion since it is accomplished by beginning with a coarse grid that is progressively refined several times during the inversion (Simmons et al., 2009).

ADAPTIVE GRID REFINEMENT

P wave velocity in our model is stored on a 3D grid of nodes that has variable resolution in both geographic and radial dimensions. Our basic starting point is a 2 dimensional, multi-level triangular tessellation of a unit sphere (Wang and Dahlen, 1995, Ballard et al., 2009). We assign a tessellation with 8° triangles to the lower mantle, a tessellation with 4° triangles to the transition zone and upper mantle, and a third tessellation with variable resolution to all crustal layers. The crustal tessellation (not shown) has 2° triangles in oceanic regions, 1° triangles in most continental regions, and 0.5° triangles in the United States where the additional resolution is warranted due to the dense station coverage afforded by the USArray. The two tessellations in the mantle are refined, in both the geographical and radial dimensions, during the progress of the tomographic inversion. Figure 2 illustrates the final geographic node configuration of the tessellation assigned to the transition zone and upper mantle. 4° triangles in relatively aseismic parts of the world remain unrefined in the final, model, but the grid is refined down to triangles as small as 0.5° in areas with dense seismicity or stations, or both.

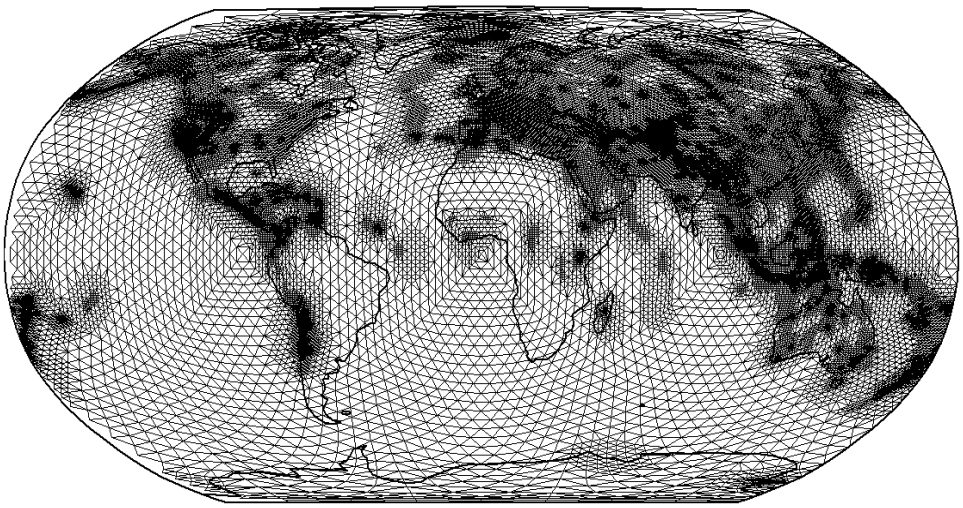

Figure 2. The final grid for the transition zone and upper mantle with triangle sizes ranging from 0.5° to 4°. The grid for these layers in the starting model consisted entirely of 4° triangles.

VELOCITY MODEL

A small portion of the global range of our model is illustrated in Figure 3 and Figure 4. The images reveal many tectonic features of the Earth. Major cratons in Siberia, North America, Southern Africa and Australia are all characterized by P wave velocities that are relatively fast compared to AK135. Tectonically active areas such as western North America and the Mediterranean region are relatively slow, as are the mid-ocean ridges in the Pacific, Atlantic and Indian Oceans. In subduction zones beneath the Andes, Sumatra and New Zealand we see fast oceanic slabs being subducted beneath the adjacent continents. The stagnant subducted slab beneath Japan is particularly evident in Figure 4. Very fast material is evident in the upper mantle beneath Tibet and slow velocity anomalies appear in the Red Sea region.

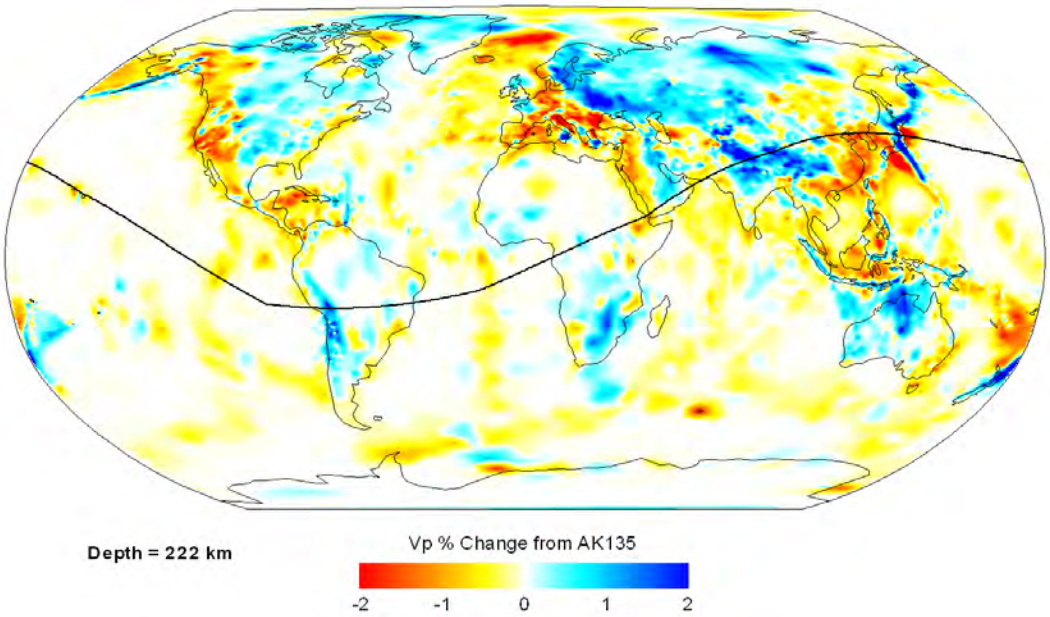

Figure 3. Map of the % difference in P wave velocity between SALSA3D and AK135 at a depth of 225 km in the upper mantle. The black line shows the position of the approximate great circle path of the cross section shown in Figure 4.

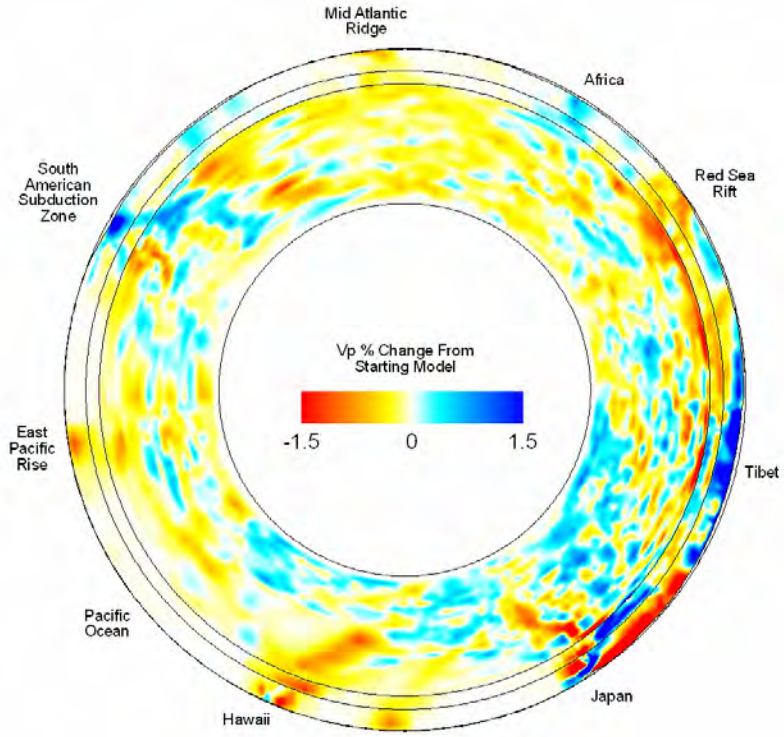

Figure 4. Cross section through SALSA3D at the location shown by the black line in Figure 3.

RESOLUTION TESTS

Images of tomographic models can provide important insight into fundamental questions about the structure of the Earth, such as the fate of subducting slabs. However, when interpreting these images, one must consider the

resolution of the tomographic inversion. For large models like ours, this can be a computationally challenging problem. A standard way to estimate model uncertainty is to create known detailed velocity structures (often "checkerboard" patterns), use these to create synthetic observations for the actual data paths, and then to invert these synthetic observations to see how much of the known structure can be recovered. This technique measures the theoretical resolution possible given the ray coverage (i.e. it is based entirely on ray geometries). The actual resolution is something less than this because the observations themselves will have errors.

We adopt the checkerboard technique here, though our pattern is slightly different, consisting of equal sized alternating velocity triangles, so that we can maintain the same feature size regardless of latitude (the rectangular latitude/longitude checkers used by many researchers actually get smaller towards the poles). Our checkers represent deviations relative to our final tomographic model so that the ray paths will be as realistic as possible. For the same reason, our checkers have relatively small deviations (+/- 1%) relative to the background model.

As expected given the ray coverage (Figure 1), our model resolution varies strongly both laterally and with depth. Resolution is best for Asia, due to the excellent coverage provided by the LANL GT data set. Resolution is best in the upper portion of the lower mantle, due to the large number of teleseismic raypaths in our dataset that bottom near this depth.

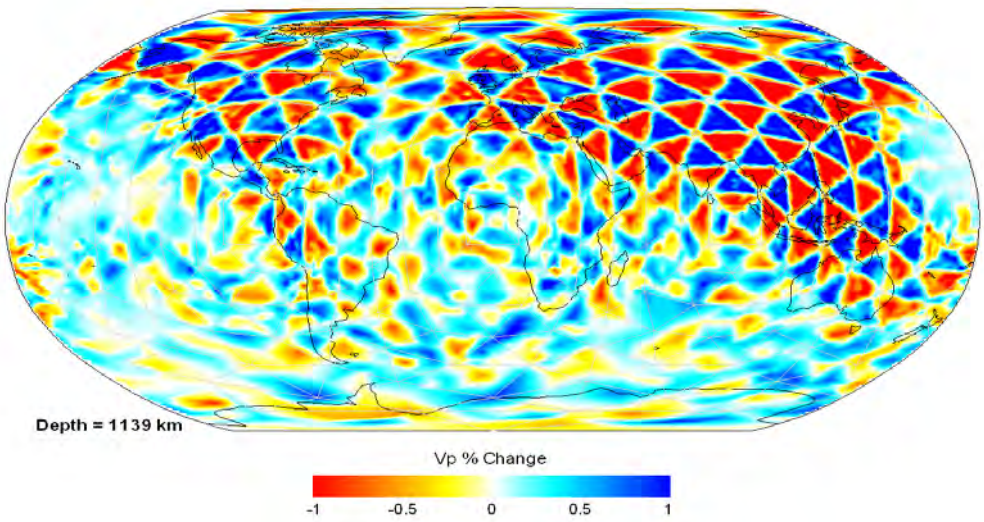

Figure 5. Results of the Chinese checkerboard test at a depth of 1139 km in the shallow part of the lower mantle.

TRAVEL TIME RESIDUAL REDUCTION

To evaluate the ability of our model to accurately predict observed source-receiver seismic travel times, we define a set of 19 polygons that surround areas of contiguous seismicity around the world (Figure 6). For each of the 49 seismic stations in the IMS primary network we compute the mean absolute residual (absolute value of observed minus predicted travel time) for all of the events in each polygon using the AK135 model (Kennett et al., 1995) and using SALSA3D. For computing the AK135 travel times we used the Taup Toolkit software package (Crotwell et al., 1999). The results, illustrated in Figure 7, indicate that SALSA3D produces travel time residuals that are smaller than those produced by AK135 more that 92% of the time.

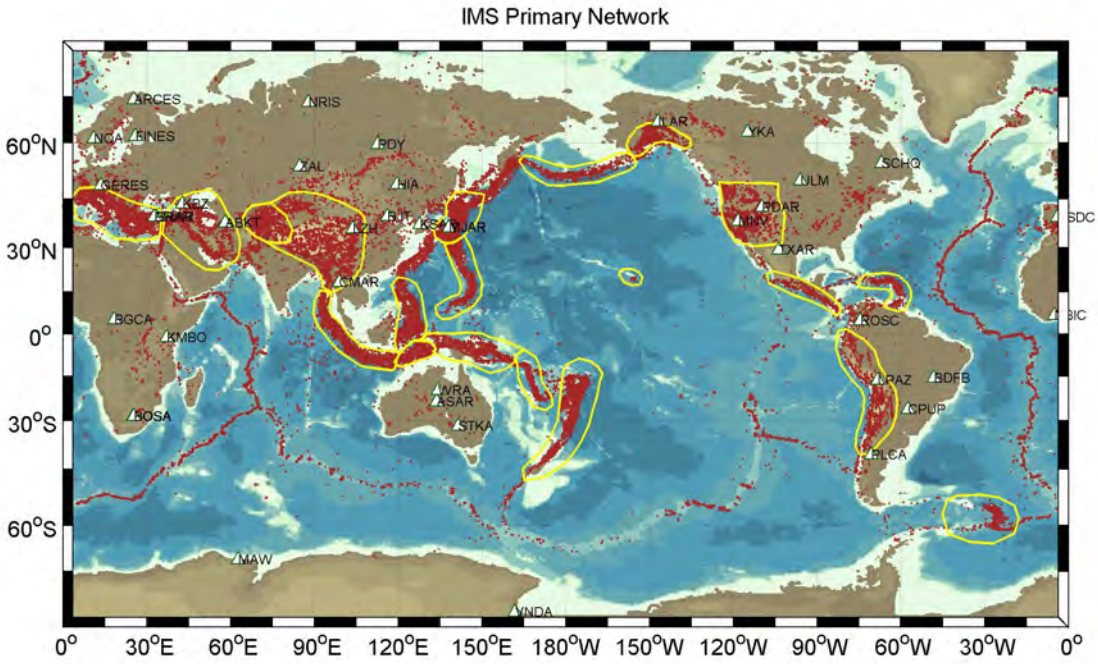

Figure 6. Map of the locations of the 49 IMS primary network stations and the 19 seismic regions selected for travel time residual analysis.

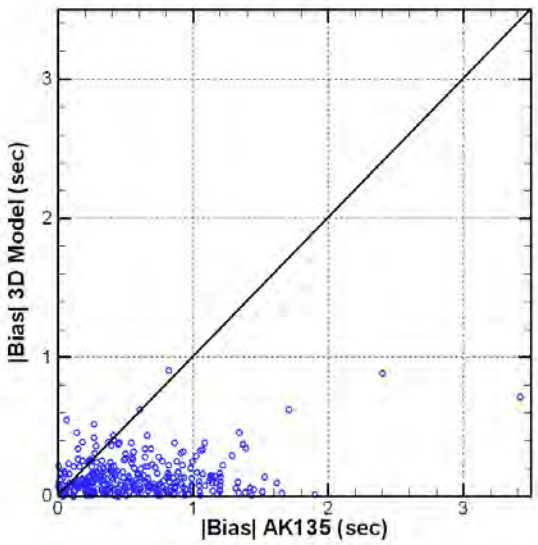

Figure 7. Median absolute value of residual computed with AK135 vs the same value computed with SALSA3D. Each point represents a single station-region pair.

LOCATION IMPROVEMENT

To test the location accuracy of the SALSA3D model, we selected a set of GT5 or better events from throughout Eurasia that contained enough Pn and P arrivals to be able to create a set of random realizations of differing station coverages. 42 events in Eurasia were initially selected and modified from the location test set of Myers et al. (2010), pulling data from the LANL GT database (Figure 8).

For each event, 5 random selections of P and Pn arrivals were made for each target number of arrivals from 5 to 50 (incremented by 1). The total number of realizations was 9585 (one event did not have 50 available phases).

Our event clustering process performed prior to the tomography significantly reduces any circularity issues despite the lack of a formal event segregation procedure.

We relocated each realization with the standard 1D AK135 model (Kennett et al, 1995) and our global SALSA3D tomography model. For AK135, we used the appropriate ellipticity/station corrections and the default model error. For SALSA3D, an estimated model error was used based on a summary standard deviation of residuals with distance. Results were evaluated based on median mislocations with the total number of phases, azimuthal gap, and the relative number of teleseismic P versus regional Pn.

Figure 9 shows the median mislocation of the relocated random realizations with azimuthal gap. At small azimuthal gaps, the median mislocation for the 3D model is slightly reduced over AK135, but the good station coverage produces accurate locations for either model. As the azimuthal gap increases, the use of the 3D model results in a greater reduction in mislocation over the 1D AK135 model by as much as a ~10 km.

Figure 10 shows the median mislocation using different combinations of P and Pn arrivals. The maximum number of any arrival set is 50. The SALSA3D model has an overall lower median mislocation. The combination of equal numbers of Pn and P arrivals results in the highest median mislocation values for the 1D AK135 model. This demonstrates the problems combining regional and teleseismic arrivals when using a model not designed for such a purpose. The results using the 3D model do not show this higher median mislocation in the area of equal P and Pn, indicating reduced problems with combining regional and teleseismic phases. Notice that results with fewer phases (< 10) clearly demonstrate improvement by the 3D model, as expected.

Figure 8. Validation events for location testing. 42 GT5 or better events were selected within Eurasia in order to produce a random data set of varying station/data configurations in which to test the location accuracy of the 3D model. The events were selected from Myers et al. (2010) with a few additional to improve spatial coverage.

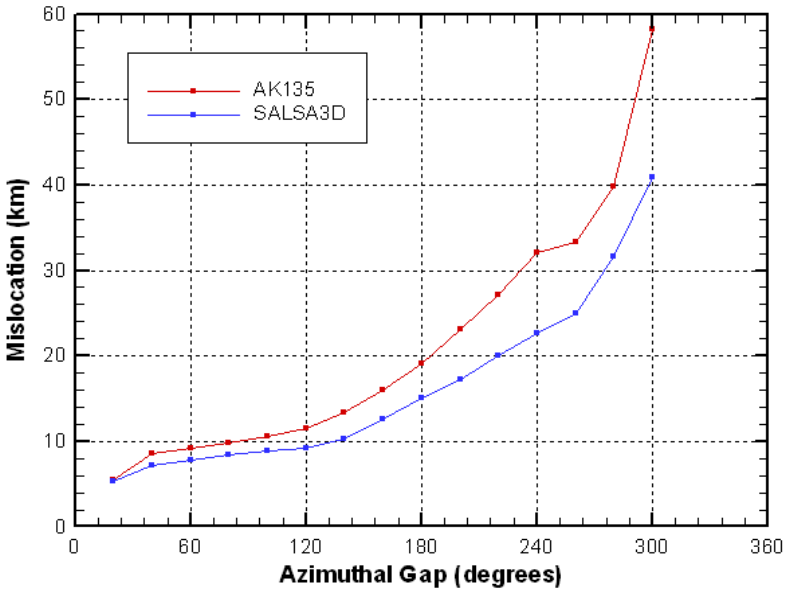

Figure 9. Median mislocation versus azimuthal gap for the location improvement testing using the random realizations of the 42 events shown in Figure 8.

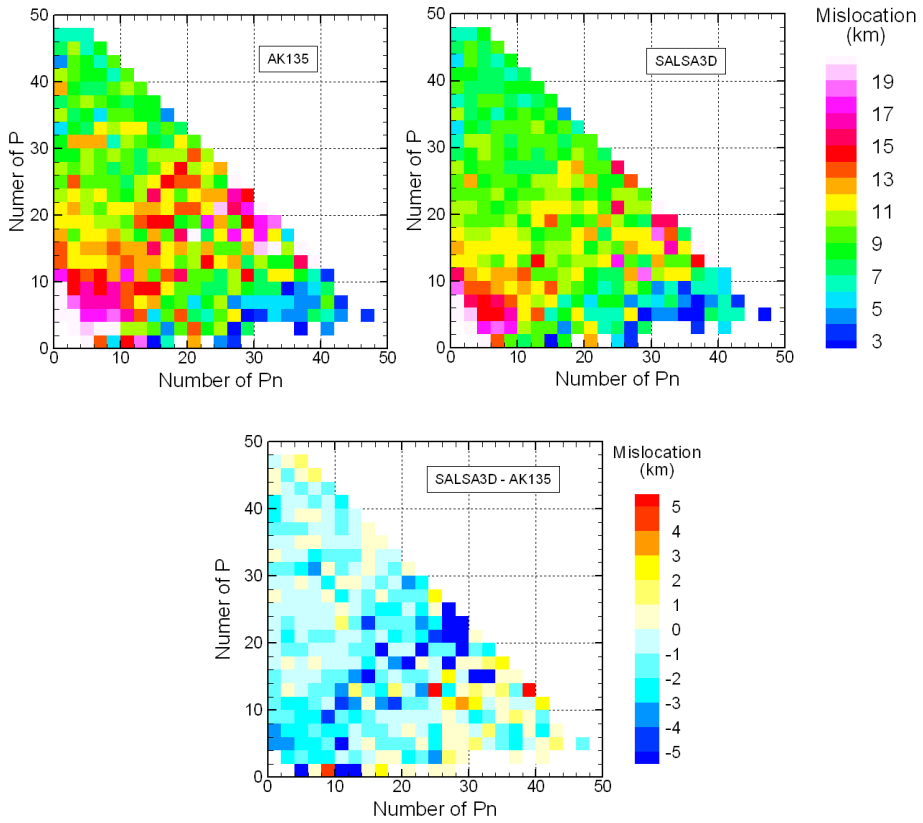

Figure 10. Median mislocation with varying number of P and Pn arrivals for the random realization location tests (bin size =2). The AK135 model results (top left) display higher mislocation values than the SALSA3D model (top right). The higher mislocation values at approximately equal numbers of P and Pn arrivals seen in the AK135 results are not observed for the 3D model. The mislocation difference between the models (bottom) shows that the 3D model is performing significantly better than AK135 for the majority of phase combinations.

CONCLUSION

In this paper, we have presented the latest version of SALSA3D, the Sandia-Los Alamos global tomography 3D P-velocity model of the crust and mantle. Our model is multi-resolution, with the resolution determined dynamically as part of the tomographic inversion. Additional nodes are added where ray coverage is high and velocity gradients are significant; other areas maintain the starting grid sampling. SALSA3D images many well-established features within the Earth, such as subducting slabs and continental roots, and is generally consistent with other recent global and regional models. Resolution, as established by checkerboard tests, is highly variable both laterally and with depth, with the best resolution in Asia and Europe in the upper part of the lower mantle.

More important than the structural features in the model is the fact that SALSA3D provides compelling improvement in travel time prediction and in event location compared to AK135. Evaluating performance for the IMS primary network, travel time residuals grouped by station and geographic region show clear improvements for virtually all combinations spanning a variety of distances and tectonic regions. Event location improvement is evaluated by re-locating multiple realizations from a set of 42 well-characterized events in Europe and Asia. SALSA3D improves locations only slightly when the number of stations is large, but as the number of phases drops, the 3D model does significantly better. Further, because our model is developed to fit both P and Pn data, it performs well with regional data, teleseismic data, or a combination of the two.

REFERENCES

Ballard, S, J. R. Hipp, C. J. Young, 2009, Efficient and accurate calculation of ray theory seismic travel time through variable resolution 3D earth models, *Seismol. Res. Lett*. 80: 989–999.

Begnaud, M. L. (2005). Using a dedicated location database to enhance the gathering of ground truth information, Los Alamos National Laboratory document LA-UR-04-5992, 22 pp.

Bondár, I., S. C. Myers, E. R. Engdahl, and E. A. Bergman (2004). Epicentre accuracy based on seismic network criteria, *Geophys. J. Int.* 156: 483–496.

Crotwell, H.P., T.J. Owens, and J. Ritsema (1999). The TauP toolkit: flexible seismic travel-time and ray-path utilities, *Seism. Res. Lett*. 70: 154–160.

Kennett, B.L.N., E.R. Engdahl, R. Buland (1995). Constraints on seismic velocities in the Earth from taveltimes, *Geophys. J. Int*. 122: 108–124.

Laske, G. and T.G. Masters (1997), A global digital map of sediment thickness, *EOS Trans*. AGU, 78, F483.

Laske, G., T. G. Masters and C. Reif, CRUST 2.0: A New Global Crustal Model at 2x2 Degrees, http://igppweb.ucsd.edu/~gabi/crust2.html.

Li, S., and W. D. Mooney (1998). Crustal structure of China from deep seismic sounding profiles, in *Proceedings of the 7th international symposium on Deep seismic profiling of the continents*, Asilomar, CA, United States, *Tectonophysics* 288: 105–113.

Myers, S. C., M. L. Begnaud, S. Ballard, M. E. Pasyanos, W. S. Phillips, A. L. Ramirez, M. S. Antolik, K. D. Hutchenson, G. S. Wagner, J. J. Dwyer, C. A. Rowe, and D. R. Russell (2010). A crust and upper mantle model of Eurasia and North Africa for Pn travel time calculation, *Bull. Seismol. Soc. Am*. 100: 2, 640–656.

Simmons, N. A., S. C. Myers and A. Ramirez (2009). Multi-Resolution Seismic Tomography Based on a Recursive Tessellation Hierarchy, in *Proceedings of the 2009 Monitoring Research Review: Ground-Based Nuclear Explosion Monitoring Technologies*, LA-UR-09-05276, Vol. 1, pp. 211–220.

Um, J. and C. H. Thurber (1987). A fast algorithm for two-point seismic ray tracing, *Bull. Seismol. Soc. Am*. 77: 972–986.

Zhao, D. and J. Lei (2004), Seismic ray path variations in a 3D global velocity model, *Phys. Earth Planet In*. 141: 153–166.

Wang, Z., and F. A. Dahlen (1995), Spherical-Spline Parameterization of Three-Dimensional Earth Models, *Geophys. Res. Lett*. 22: (22), 3099–3102.

JOINT INVERSION FOR CRUSTAL AND UPPER-MANTLE SHEAR-WAVE VELOCITY AND ATTENUATION STRUCTURE IN EASTERN EURASIA USING THREE-DIMENSIONAL FULL-WAVE FRÉCHET KERNELS

Po Chen[2], Youlin Chen[1], and Winston Chan[1]

Array Information Technology[1] and University of Wyoming[2]

Sponsored by the Air Force Research Laboratory

Award No. FA9453-10-C-0215
Proposal No. BAA10-06

ABSTRACT

We aim to map the lateral variations of crustal and upper-mantle shear-wave velocity β and shear attenuation ($1/Q_\mu$) in eastern Eurasia using a new joint inversion procedure based on three-dimensional (3D) sensitivity (Fréchet) kernels. In the first year of this project, we analyzed thousands of Rayleigh wave recordings with periods longer than ~15 s, derived from more than 250 regional and near-teleseismic earthquakes that occurred within our study region (10°–60°N, 70°–140°E). The data were recorded on the broadband seismic stations in this region, including the Chinese National Digital Seismic Network. The seismograms were evaluated for signal-to-noise within the band of interest (10–80 mHz) by comparing the records to complete synthetic seismograms computed using a 3D reference model derived from receiver-function analysis. We then made mutually consistent measurements of frequency-dependent phase-delay time and amplitude anomalies for surface waves by cross-correlation between records and synthetics. We used the spectral-element code to compute the 3D Fréchet kernels of these travel-time and amplitude anomalies to both the elastic shear-wave speeds β and shear-wave quality factor Q_μ values. Our starting model for Q_μ was extracted from a recent global model of upper-mantle attenuation. The frequency-dependent travel-time and amplitude anomalies were jointly inverted for 3D models of both elastic and anelastic structures. This coupled inversion allowed us to account for the effects on amplitudes from elastic heterogeneities such as scattering, focusing and defocusing, as well as the effects of anelastic dispersion on the travel times. Our primary models provide lateral resolution of about 400 km in the crust and upper mantle. In the crust, high values of Q_μ are concentrated in eastern China, extending southward from the North China craton, while a clear low-Q anomaly exists in the crust beneath northern Tibet. In the upper mantle, the model is characterized by a lithosphere with very high Q values ranging from 250 to 400, underlain by a low-Q asthenosphere with Q_μ of 60–100. The lateral variation of the upper-mantle Q_μ perturbation appears to correlate with the lateral variation in the inverted shear-velocity perturbation.

OBJECTIVES

The objectives of this project are to jointly invert for 3D seismic velocity and shear attenuation for the crust and upper mantle in eastern Eurasia using 3D full-wave Fréchet kernels. In this study, we analyze broadband surface waves from regional earthquakes, recorded on stations of the Chinese National Digital Seismic Network (CNDSN) and IRIS Global Seismic Network (GSN), and measure amplitude and phase residuals of these waveforms with respect to synthetics calculated from a 1D reference Earth model that represents the eastern Eurasia region using the Generalized Seismological Data Functionals (GSDF) method. These observations are then inverted for a 3D tomographic model of shear velocity (β) and shear attenuation ($1/Q_\mu$), using 3D Fréchet kernels that fully account for the effects of both elastic and anelastic structure on the amplitude and phase measurements. By jointly inverting for β along with $1/Q_\mu$, we remove much of the uncertainty associated with focusing and defocusing that is typically found in previous attenuation models. Our inverted attenuation perturbation (δQ_μ^{-1}) has a spatial correlation with our inverted shear-velocity perturbation ($\delta\beta$), which may suggest that the lateral variation in attenuation in the crust and upper mantle in eastern Eurasia is a result of temperature variation.

RESEARCH ACCOMPLISHED

Background

The eastern part of the Eurasian continent is characterized by a complex tectonic history. This region is composed of three major Precambrian cratons with very different origins: the Sino-Korean craton, the Yangtze craton, and the Tarim craton (Figure 1).

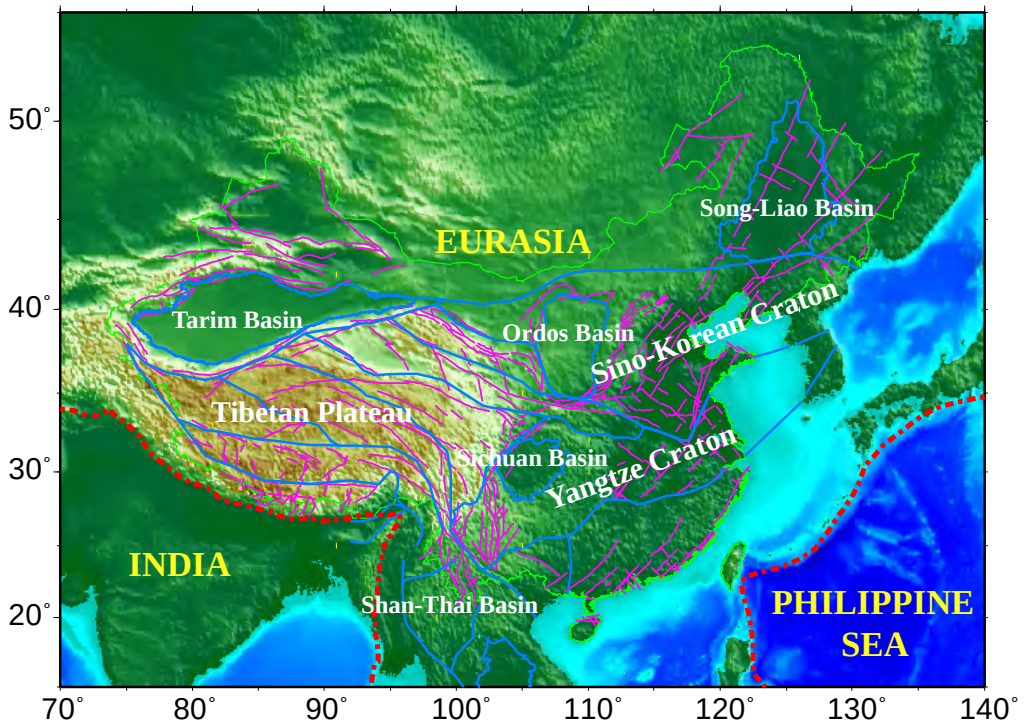

Figure 1. Tectonic setting in eastern Eurasia. Active faults are shown as purple lines and tectonic sutures are shown in blue lines. This part of Eurasia is being pushed in the south by the Indian plate and in the east and southeast by the Pacific and Philippine Sea plates, respectively.

The modern tectonics in this region is the result of a long and complicated evolution history of collision, underthrust, and suture between different tectonic blocks (e.g., Molnar and Tapponnier, 1975; Yin and Nie, 1996; Yin and Harrison, 2000; Vermeesch 2003). A good tomographic image of the crustal and upper-mantle structure would be very helpful in understanding these complexities. Indeed this region has been the focus in many previous regional and global tomographic studies of seismic velocity structures using surface waves (e.g., Song et al., 1991; Wu et al., 1997; Xu et al., 2000; Shapiro and Ritzwoller, 2002; Friederich, 2003; Huang et al., 2003; Lebedev and Nolet, 2003), S_n waves (e.g., Ritzwoller et al., 2002; Pei et al., 2007), receiver functions (e.g., Wu et al., 2001; Zou and Chen, 2003; Xu et al., 2006; Chen et al., 2010), and body-wave travel times (Sun and Toksöz., 2006; Sun et al., 2008).

Attenuation ($1/Q$) tomography for anelastic structure may provide additional constraints for the tectonics in eastern Eurasia. Considering the different sensitivities of seismic velocity and Q to temperature and composition (e.g., Karato, 1993; Faul and Jackson, 2005), a joint interpretation of both attenuation and velocity models would be very helpful in distinguishing the effects of thermal and chemical heterogeneities. Q is known to vary widely in continental regions, making its reliable estimates critically important but also quite difficult. Q is also frequency dependent, which makes it difficult to determine whether Q estimates derived from different phases with different frequency characteristics are a result of intrinsic frequency dependence or differences in structural sampling. Finally, Q estimates are derived from seismic amplitudes, which are also strongly dependent on elastic effects such as wavefield focusing and scattering. We address the difficulties in attenuation tomography by applying a unified waveform analysis and inversion method to simultaneously infer 3D seismic velocity and attenuation structures.

Waveform Data

We adopt broadband waveforms recorded on CNDSN stations, complemented by those on IRIS-GSN stations. Since the 1990s, the China Earthquake Administration (CEA) has made a great effort to upgrade its seismic instruments from analog to digital in order to establish a modern seismic network at a national level. The effort resulted in the number of modern digital seismic stations in the backbone network of China increasing from 11 GSN stations in the 1990s to 75 stations established in the early 2000s and the current 145 stations deployed since 2007.

Most CNDSN stations are equipped with the Chinese broadband seismographs, such as JCZ-1, CTS-1, and FBS-3, which have been well calibrated and tested by the Chinese seismological community (e.g., Lin, 2001; Zhao et al., 2001; Xie and Zhao, 2003). All of these instruments are broadband and have velocity-flat response. The upper bounds of their bandwidths are over 20 Hz, and the lower bounds are down to 360 seconds. The sampling rates are 50 samples per second, and the dynamic ranges are greater than 120 dB. In this study, we have included waveform data from 68 CNDSN stations, which increases the total number of stations in our tomography region from 46 to 114 (Figure 2). All of these 68 stations were updated in early 2000s and have accumulated large volumes of high-quality waveform data.

Seismograms from 848 earthquakes with $5.0 \leq \mathrm{Mw} \leq 6.5$ and occurring in the region 10°N–60°N and 70°E–140°E from 2000 to 2008 (Figure 2) are selected, and those with sufficiently high signal-to-noise ratio are processed. The two horizontal components are rotated into the radial and transverse directions. The resulting seismograms are then low-pass filtered using a 4th-order Butterworth filter with corner frequency at 50 mHz. Examples of the processed vertical-component observed seismograms from an Mw5.9 earthquake occurring in 2005 and recorded at 18 CNDSN stations are shown in Figure 3.

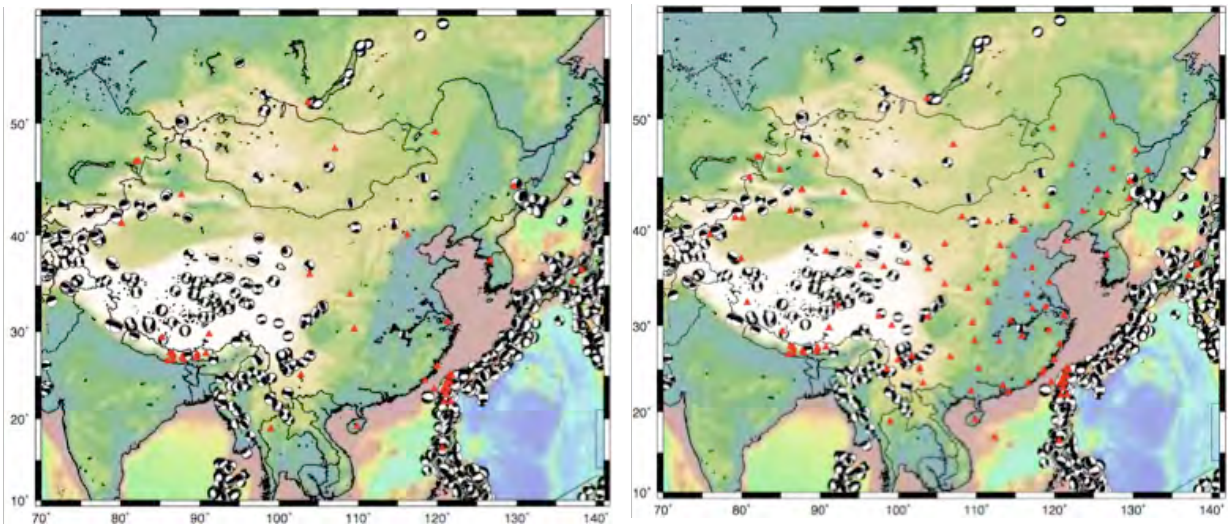

Figure 2. Station coverage within our tomography region with (right) and without (left) the CNDSN stations. Red triangles: Seismic stations, 41 in left panel and 114 in right panel. Beach balls: Harvard CMT solutions of 848 earthquakes with M_w>5.0 from year 2000 to 2008. Background color shows topography.

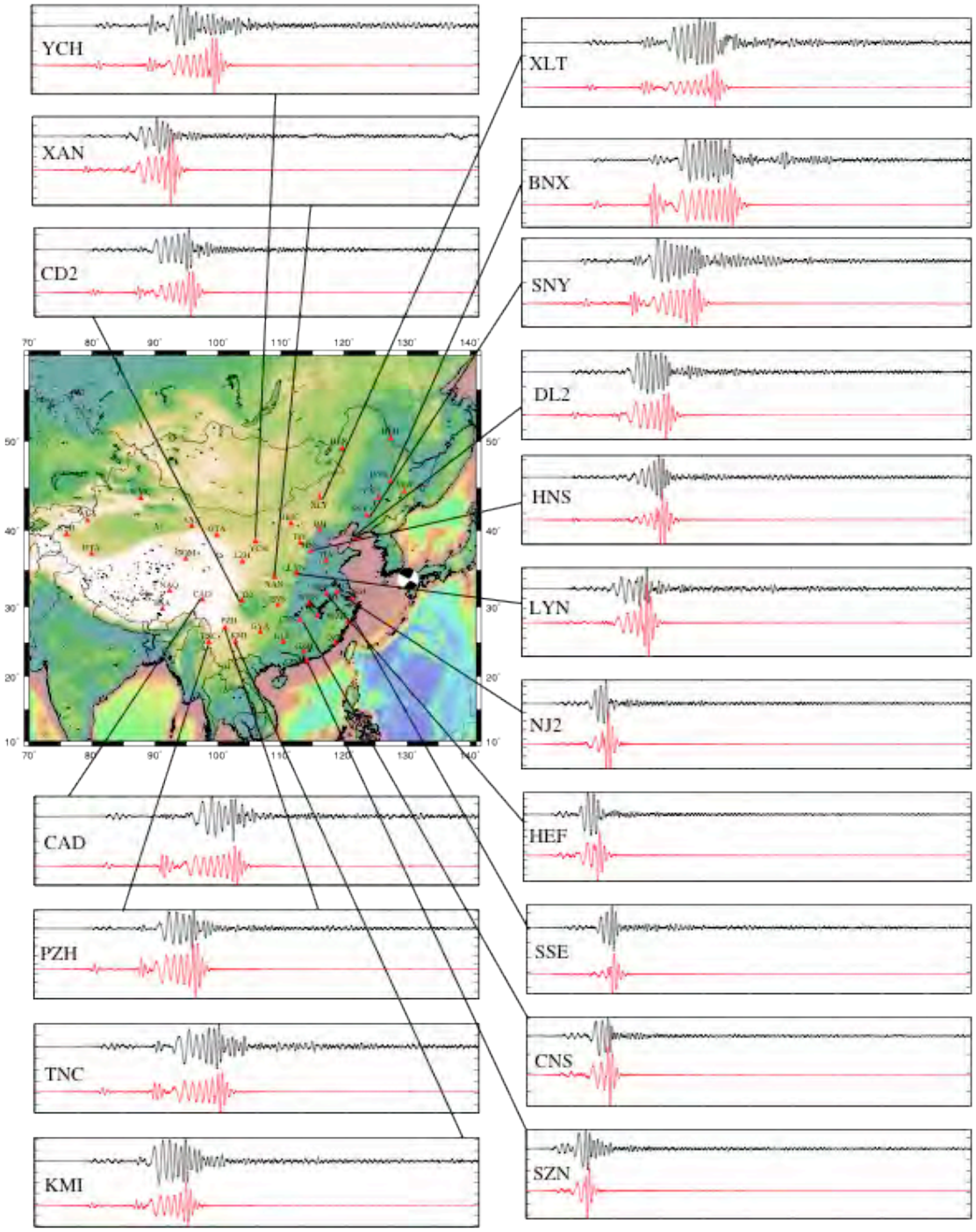

Figure 3. Examples of observed (black) and synthetic (red) vertical-component seismograms at 18 CNDSN stations. The seismograms have been low-pass filtered using a Butterworth filter with a corner at 50 mHz. The synthetics were computed using the 1D structure model, as shown in Figure 4, and a normal-mode summation code. The focal mechanism of the earthquake is obtained from the Harvard CMT catalog.

Methodology

We formulate our tomography as an optimization problem, in which we optimize the Earth structure model **m** to minimize an objective function defined in terms of the misfit between the observation and the model prediction with three regularization terms:

$$\chi^2 = \|\mathbf{d}\| + \lambda_1 \|\mathbf{m}\| + \lambda_2 \|\mathbf{Lm}\| + \lambda_3 \|\mathbf{m}_0 - \mathbf{m}\|. \quad (1)$$

Here the first term on the right-hand side quantifies waveform misfit between observed and synthetic seismograms, the second term regularizes the amplitude of the model, the third term regularizes the smoothness of the model, and the fourth term is used to impose additional constraints on certain portions of the model or to force the solution toward a certain direction. The Lagrangian multipliers $\lambda_{1,2,3}$ control the trade-off between fitting the seismic data and the three regularization terms.

Reference Model and Synthetic Seismogram

In the current study, we adopt a 1D structure model (Figure 4) as our reference model. The velocity model was constructed from a composition of iasp91 for mantle shear and compressional velocities and Crust 2.0 (Laske et al., 2001) for local crustal velocity perturbations. The attenuation model was composed of a mantle Q_μ profile extracted from the recent global attenuation model (Dalton and Ekström, 2006) and a crustal Q_μ profile derived from analysis of regional phases (Jemberíe and Mitchell, 2004). In order to accomplish our purpose of full 3D tomography, we will adopt a 3D reference model over eastern Eurasia derived from receiver function analysis made on each station.

For such a spherically symmetric reference earth model, complete synthetic seismograms can be computed using normal mode superposition (Dalen and Tromp, 1998). Centroid moment tensor (CMT) solutions from the global CMT catalog are used as our source models for computing synthetics. The calculated synthetic seismograms are convolved with corresponding instrument responses. Figure 3 shows a comparison between some vertical-component synthetic seismograms and their corresponding observed seismograms. For frequency up to 50 mHz, our synthetic seismograms generally provide sufficiently good fit to the observed seismograms, which indicates that our composite 1D structure model provides a good reference model for our tomographic inversion.

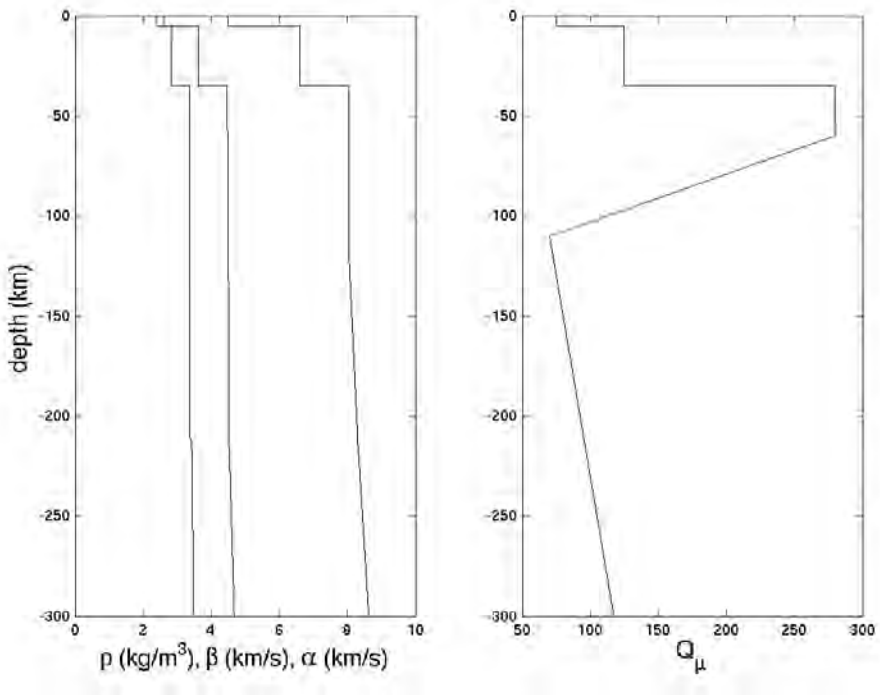

Figure 4. The 1D reference structure model used in our inversion. Left: The density, shear- and compressional-wave speeds as functions of depth. Right: Shear-attenuation quality factor as a function of depth.

Generalized Seismological Data Functionals (GSDF)

The misfit measurement **d** in Equation (1) is defined as the frequency-dependent phase-delay time and amplitude reduction time introduced in Gee and Jordan (1992) under the term Generalized Seismological Data Functionals (GSDF). The GSDF measurements generalize the classic travel-time and t^* measurements to better capture differences in the shapes of the waveforms.

In the frequency domain, we can map the synthetic waveform $u_i(\omega)$ into the observed waveform $\overline{u}_i(\omega)$ using two frequency-dependent, time-like quantities: the phase-delay times $\delta\tau_p(\omega)$ and the amplitude-reduction times $\delta\tau_q(\omega)$:

$$\overline{u}_i(\omega) = u_i(\omega)\exp\left\{i\omega\left[\delta\tau_p(\omega) + i\delta\tau_q(\omega)\right]\right\}. \quad (2)$$

To make the GSDF measurements, we first segment the complete synthetic seismogram to isolate the wave group that is to be measured. The isolated wave group is termed "isolation filter" (Figure 5b), which can contain any types of seismic phases. The isolation filter is then cross-correlated with both the observed seismogram and the complete synthetic seismogram (Figures 5c and d). The resulting cross-correlagrams are then windowed around zero-lag and narrow-band filtered at a set of frequencies of interest. After the narrow-band filtering operation, the resulting cross-correlagrams can be well parameterized using a five-parameter Gaussian wavelet (Gabor function). The amplitude and phase differences between the data and the synthetic wavelets provide us the frequency-dependent phase-delay measurements $\delta t_p(\omega_n)$ and amplitude anomaly $\delta t_q(\omega_n)$ at each narrow-band filtering frequency ω_n (Figures 5e and g). The misfit measurements of $\delta t_x(\omega_n)$ (x = p, q) are weighted averages of $\delta\tau_x$ over narrow frequency-bands centered on the narrow-band filtering frequency ω_n. The effects of the averaging introduced by our measurement procedure are completely accounted for in our full-wave Fréchet kernels (Chen et al., 2010).

The GSDF analysis has several advantages that are important to our tomographic inversion. First, a direct benefit of using frequency-dependent cross-correlation measurements is that the spatial sampling patterns of the associated Fréchet kernels are also frequency-dependent (Figure 6), which provides more spatial resolution than the kernels for a single broadband cross-correlation measurement (Gaherty et al., 1996; Katzman et al., 1998; Chen et al., 2007). Second, as shown in Figure 5c (green line), these frequency-dependent GSDF measurements can effectively capture the shape of the waveforms if the sampling in frequency domain is dense enough. Third, these GSDF measurements are well suited for the tomographic inverse problem. In particular, their linearization is based on the Rytov approximation, which is valid for large *accumulative* phase shifts as long as the phase perturbation *per wavelength* is small (Chernov, 1960; Snieder and Lomax, 1996).

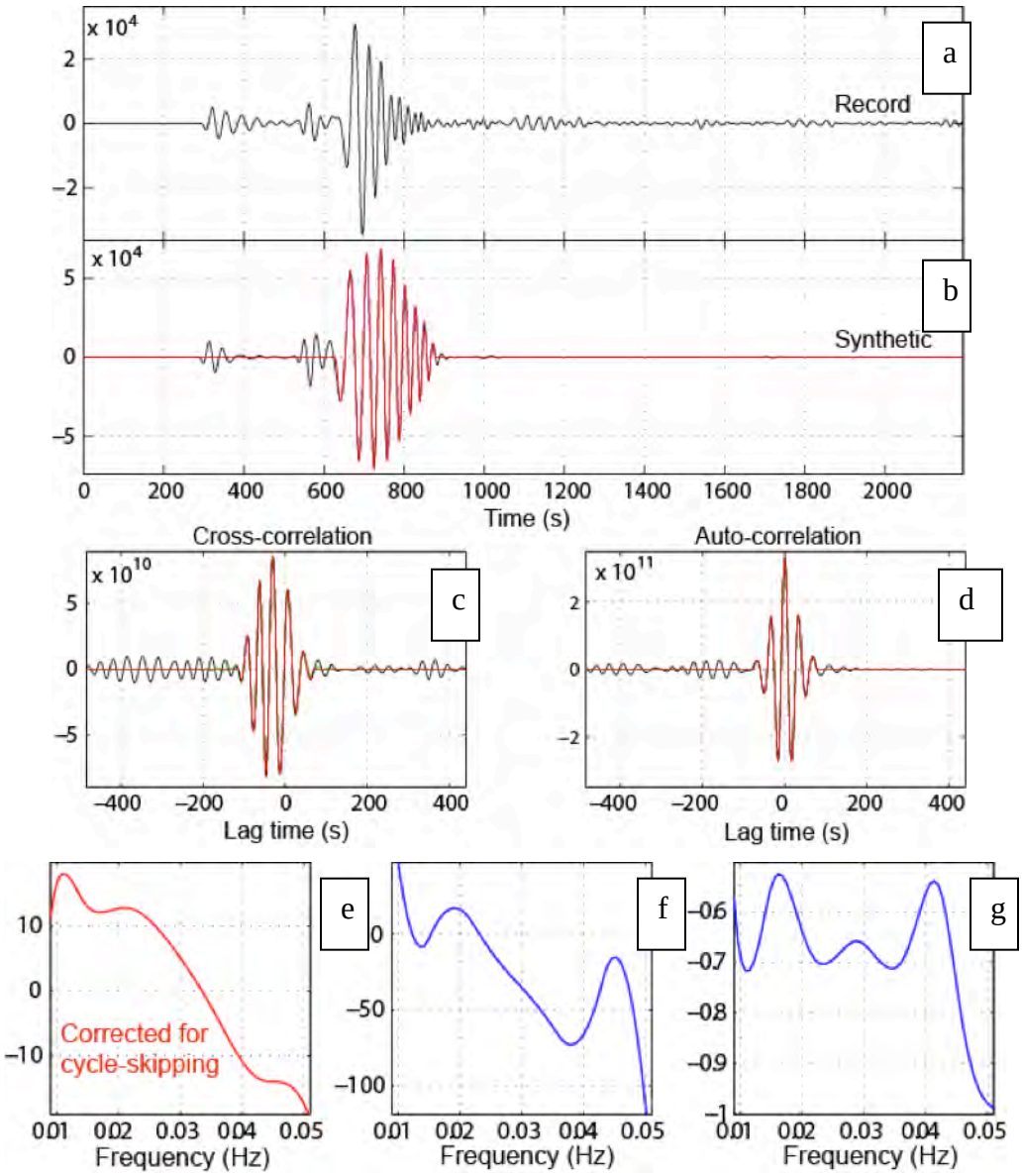

Figure 5. Our waveform analysis procedure, which follows Gee and Jordan (1992), for extracting frequency-dependent phase-delays and amplitude anomalies from waveforms. (a) Observed seismogram. (b) Synthetic seismogram (black) and the isolation filter (red), which includes the surface wave. (c) Cross-correlagram between the isolation filter and the observed seismogram (black), the windowed cross-correlagram (red) and the one recovered from the synthetic by applying the frequency-dependent phase-delay and amplitude anomaly using the right-hand side of Equation 2 (green). (d) Cross-correlagram between the isolation filter and the complete synthetic seismogram (black) and the windowed cross-correlagram (red). (e) Frequency-dependent phase-delay time. (f) Frequency-dependent group-delay time. (g) Frequency-dependent amplitude anomaly.

Three-Dimensional Full-Wave Fréchet Kernel

In this study, we adopt the normal-mode coupling theory (Zhao et al., 2000; Zhao and Jordan, 2006) for computing Fréchet kernels of our frequency-dependent GSDF measurements. The mode-coupling approach is a complete full-wave method and provides accurate 3D Fréchet kernels for any arrivals in both far field and near field in 1D reference models.

Following the notation in Zhao and Jordan (2006), the Born approximation to waveform perturbation can be expressed as

$$\delta\mathbf{u}(\mathbf{r}_R, t; \mathbf{r}_S) = \int_{\oplus}\int_{-\infty}^{\infty} [\nabla\mathbf{G}_0(\mathbf{r}_R, \tau; \mathbf{r})] : \delta\mathbf{\Lambda}(\mathbf{r}) : [\nabla\mathbf{u}_0(\mathbf{r}, t-\tau; \mathbf{r}_S)]\, d\tau\, d^3\mathbf{r}, \quad (3)$$

where $\delta\mathbf{\Lambda}(\mathbf{r})$ represents perturbations in structural parameters, $\mathbf{G}_0(\mathbf{r}_R, \tau; \mathbf{r})$ is the Green's tensor from the scattering point $\mathbf{r}$ to the receiver location $\mathbf{r}_R$, and $\mathbf{u}_0(\mathbf{r}, t-\tau; \mathbf{r}_S)$ is the forward wavefield from the source location $\mathbf{r}_S$ to the scattering point $\mathbf{r}$. It would take some time if both the Green's tensor and the forward wavefield were computed by normal-mode summation, and since we need to compute the kernels for a large number of points in space, this can make the whole calculation impractical for tomography. So our approach is to compute the Green's tensors in the reference model for a densely populated grid points, and store all the Green's tensors in a database. Then, when we need to compute the kernel for an arbitrary measurement, we can simply find the appropriate Green's tensors in the database and retrieve them. This makes the kernel calculations practical for tomography.

Figure 6 shows examples of our 3D full-wave Fréchet kernels for a shallow earthquake at 21-km depth. These kernels are computed for GSDF measurements at 20 mHz and 40 mHz made on the vertical-component Rayleigh wave. The figure shows cross sections of the kernels near the surface, and we can see that the symmetry across the source-receiver great-circle path is broken by the radiation pattern from the CMT solution. The width of the Fresnel zone depends on the frequency at which the measurements are made and is narrower at higher frequency. The kernels of the amplitude measurements with respect to P- and S-wave speeds allow us to correctly account for elastic effects on amplitudes, such as focusing/defocusing, in our velocity-attenuation joint inversion.

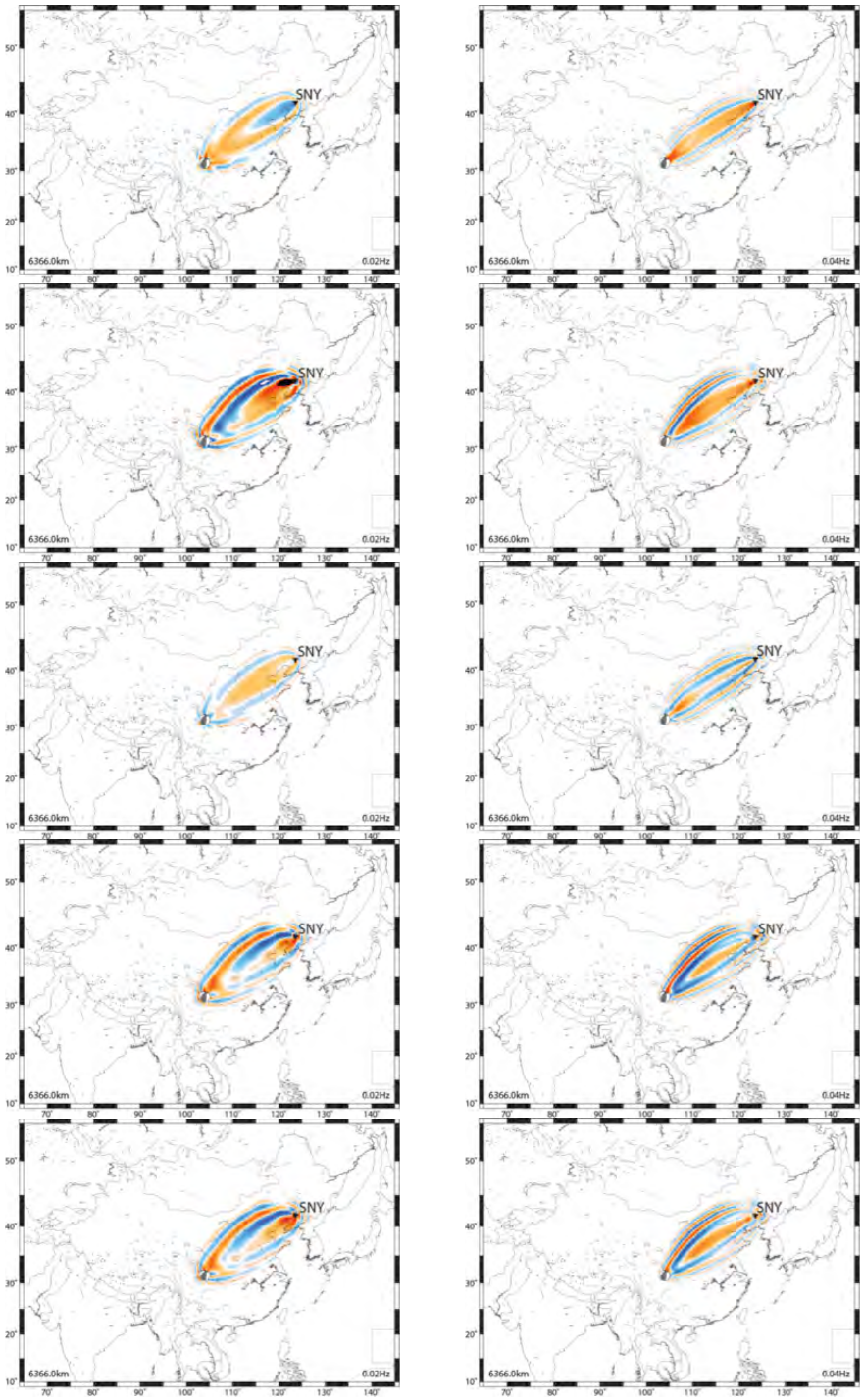

Figure 6. Examples of our 3D full-wave Fréchet kernels for an earthquake at 21-km depth. The left column shows the kernels for phase-delay and amplitude anomaly measured at 20 mHz, and the right column shows the kernels for measurements made at 40 mHz. The top two rows show the kernels for phase-delay measurements with respect to P- and S-wave speeds. The next three rows show kernels for amplitude anomalies with respect to P- and S-wave speeds and shear attenuation ($1/Q_\mu$). The beach ball shows the CMT solution for the earthquake.

Inversion

Optimizing Equation (1) using the Gauss-Newton algorithm requires the solution of the Gauss-Newton normal equation, which can be obtained by solving the following linear system:

$$\begin{bmatrix} \mathbf{C}_{\mathrm{d}}^{-1/2}\mathbf{A} \\ \mathbf{C}_{\mathrm{m}}^{-1/2} \end{bmatrix} \delta\mathbf{m} = \begin{bmatrix} \mathbf{C}_{\mathrm{d}}^{-1/2}\mathbf{d} \\ 0 \end{bmatrix} \tag{4}$$

by using the LSQR algorithm (Paige and Saunders, 1982). Here matrix **A** contains the sensitivity kernels for each misfit measurement, $\delta\mathbf{m}$ is the model parameter vector, **d** is the misfit measurement data vector, $\mathbf{C}_{\mathrm{d}}^{-1/2}$ is a data-weighting matrix, and $\mathbf{C}_{\mathrm{m}}^{-1/2}$ is a "roughing operator," which is a linear combination of the Laplacian operator (Constable et al., 1987; Sambridge, 1990) and the identity operator, i.e., $\mathbf{C}_{\mathrm{m}}^{-1/2} = \theta(\mathbf{I} + \lambda\nabla^2)$. Using this definition of the "roughing operator," we impose our prior information on the inversion; i.e., we assume that in the absence of any other information, the model perturbation is smooth and small.

Effect of P-wave Speed on Rayleigh Waves

We are mainly concerned with S-wave speed and shear attenuation ($1/Q_\mu$), and most of our GSDF measurements are made on surface waves. It has been recognized for many years that the P-wave speed, especially the P-wave speed in the crust, affects the surface wave phase and group velocities. But to our knowledge, the effect of P-wave speed on Rayleigh waves has not been explicitly considered in surface wave tomography so far. In Figure 7, we illustrate the effect of P-wave speed on Rayleigh waves through an example.

Figure 7 shows two pairs of Rayleigh waves in two different frequency bands at 60 degrees distance. In each pair, the black line is the Rayleigh wave for model AK135, and the red line is the Rayleigh wave for a model that is obtained by replacing the P-wave structure in the upper 800 km of AK135 with the corresponding P-wave structure in PREM. So there is no difference in S-wave speed between the two structure models, but we see that the Rayleigh waves are shifted by about 8 seconds. This example demonstrates that surface wave phase-delay anomalies may come entirely from perturbations in P-wave speed. So in this study, we take the P-wave speed into account for Rayleigh wave measurements. Examples of our full-wave Fréchet kernels for Rayleigh wave phase-delay and amplitude measurements with respect to P-wave speed are given in Figure 6.

Resolution Analysis

The modeling domain is from 0.5°N to 69°N in latitude, from 54.5°E to 157°E in longitude and from 0 km to 300 km in depth (Figure 8). The entire modeling domain is discretized into 0.5-degree by 0.5-degree cells horizontally and divided unevenly into 23 layers vertically, resulting in 645,955 blocks. Considering perturbations in P- and S-wave speeds and shear attenuation ($1/Q_\mu$), the total number of model parameters is 1,937,865. In this study, we used surface waves from 1,707 source-station paths that provide excellent coverage of our modeling domain. For each surface wave, we made GSDF measurements at nine frequencies evenly distributed from 10 mHz to 50 mHz, with 5 mHz intervals, resulting in 15,363 frequency-dependent phase-delay measurements and amplitude anomalies. The resulting linear system as specified in Equation (4) was then solved using a parallelized LSQR subroutine from the PETSc parallel scientific computing library (Balay et al., 2004).

To investigate the resolution of our inversion, we carried out a series of checkerboard tests with different cell sizes. An example of our checkerboard tests is shown in Figure 8. The recovery of the checkerboard pattern is better at shallower depths. The resolution for P-wave speed becomes worsening at and below about 66-km depth, while the resolution for S-wave speed and shear attenuation remains good in easternmost part of the model down to at least 300 km. The results of these checkerboard tests suggest that the smallest horizontal scale that our inversion can resolve is around 600 km.

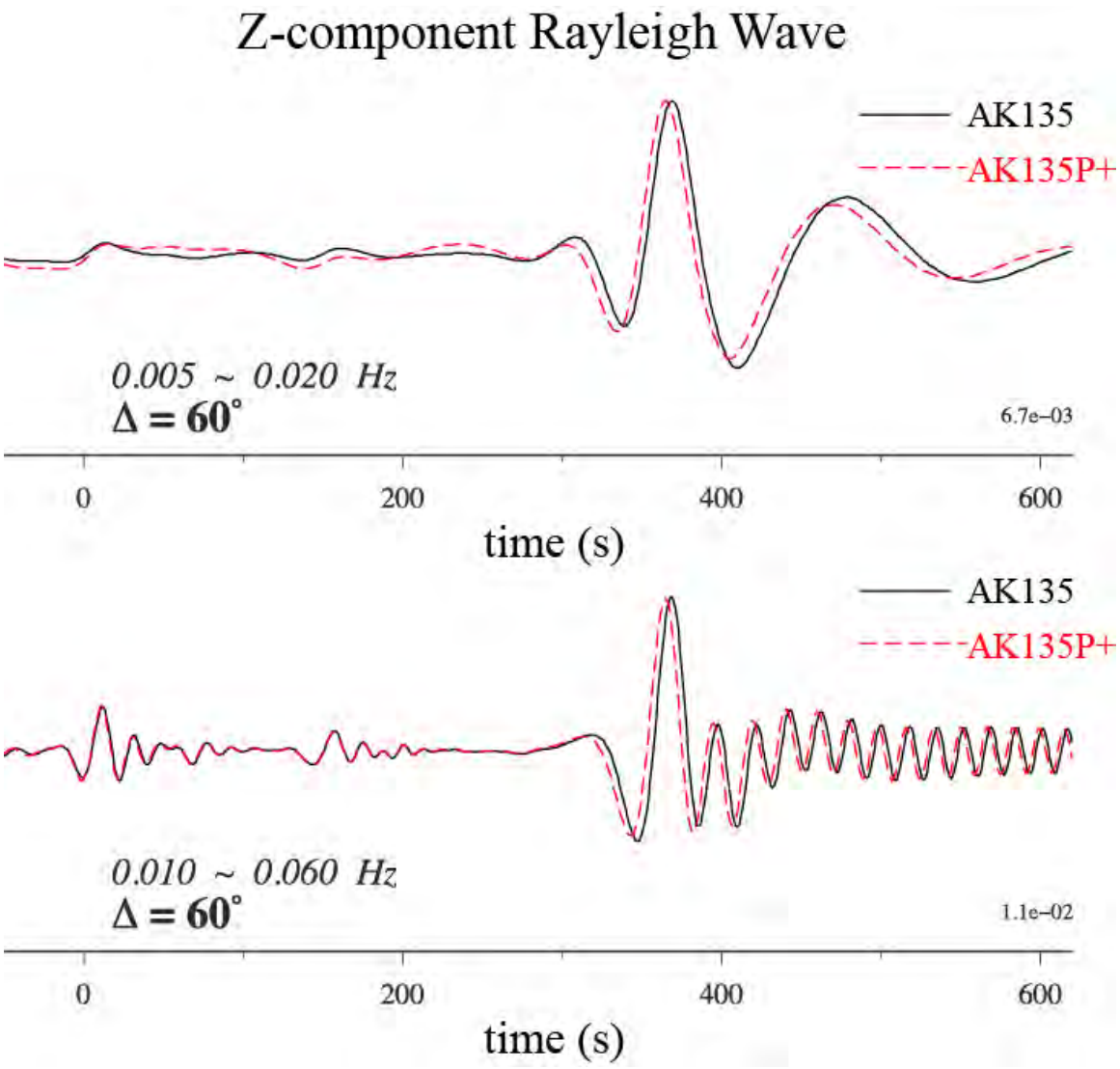

Figure 7. The effect of P-wave speed perturbation on Rayleigh wave phase-delay time. Black lines: Rayleigh waves generated using AK135. Red lines: Rayleigh waves generated using a model AK135P+ obtained by replacing the upper-800-km P-wave speed in AK135 with that of PREM. Upper plot: The two Rayleigh waves band-pass filtered from 5 mHz to 20 mHz. Lower plot: The two Rayleigh waves band-pass filtered from 10 mHz to 60 mHz.

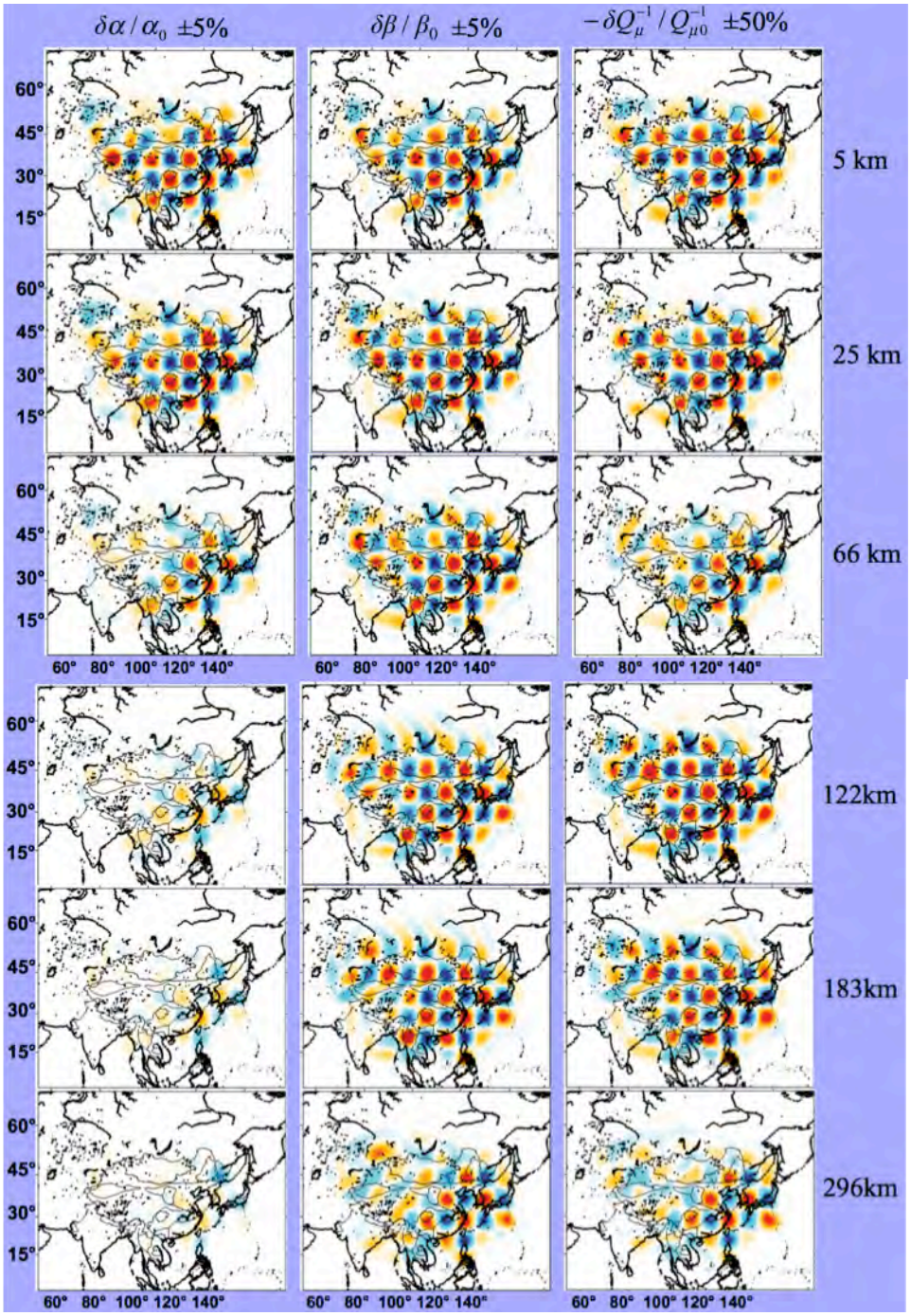

Figure 8. An example of our resolution tests showing the recovery of checkerboards for P- (left column) and S-wave (middle column) speeds and shear attenuation (right column) at six different depths. The input checkerboard has 5% perturbation for P- and S-wave speeds and 50% perturbation for shear attenuation.

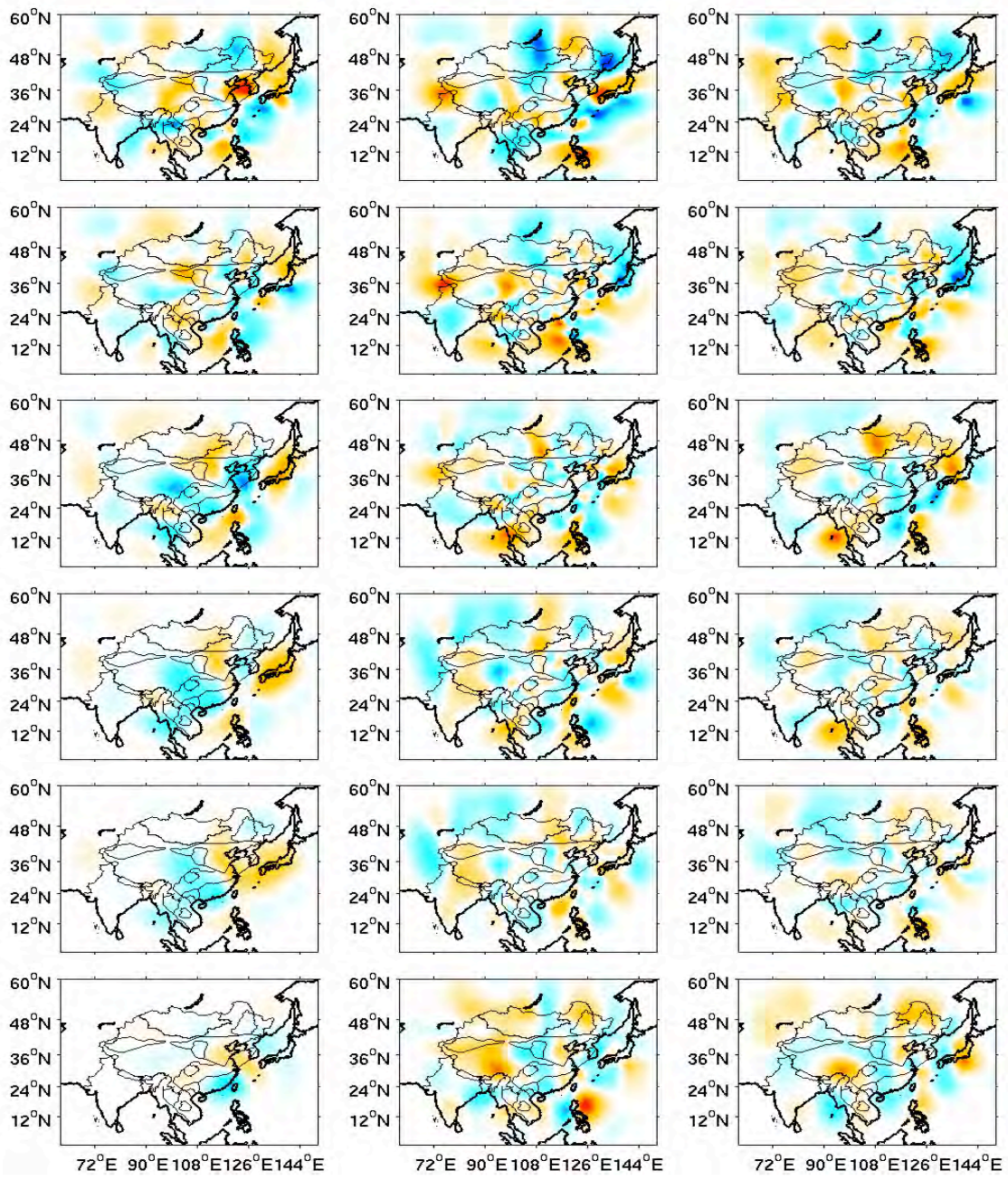

Figure 9. Our tomography models for the perturbations of P- (left column) and S-wave (middle column) speeds and shear attenuation (right column) at six different depths. There seems to be an overall positive correlation between S-wave speed and Q_μ. We see that the blue high-speed region corresponds to the blue region for low attenuations in the model, and we see the low S-speed region corresponds to high attenuation in the Q_μ model. There doesn't seem to be such correlation between the P- and S-wave speed models.

CONCLUSIONS AND RECOMMENDATIONS

The shear-velocity and shear-attenuation perturbations obtained from our preliminary inversion (Figure 9) seem to be geologically plausible. A major feature of our inverted Q_μ perturbation is that at shallower depth in the lithosphere, the average perturbation is positive, while at larger depths in the asthenosphere, the average perturbation is negative. This inverted Q_μ perturbation seems to enhance the depth gradient that already exists in our 1D reference model (Figure 4). In lower crust to upper mantle, the lateral variation of the inverted Q_μ perturbation shows a strong negative anomaly in northern Tibet and increases towards south and east. This lateral variation in Q_μ perturbation also seems to correlate with the lateral variation in the inverted shear-velocity perturbation. This result seems to be consistent with the conclusion reached by Xie (2006) based on spectral analysis on Pn arrivals from 1 to 10 Hz. In Xie (2006) this lateral variation of attenuation was interpreted as a result of temperature variation in the mantle lid under Tibet; i.e., the temperature in the mantle lid under northern Tibet is abnormally high and causes partial melting while it is abnormally low under southern and eastern Tibet due to the underthrusting Indian lithosphere.

In this study we have derived a 3D shear velocity and attenuation model for eastern Eurasia by inverting frequency-dependent phase-delay and amplitude anomalies measured on surface waves. Compared with previous surface wave tomographic inversions in the same region, we have made four major improvements in our approach. First, by including seismic stations from the CNDSN, we greatly enhanced source-station path coverage for our tomography region, which proved to be essential in improving the resolution of our inversion results. Second, the GSDF analysis provides an effective means to utilize waveform data. In particular, it converts waveform misfits, which are highly nonlinear with respect to structural parameters, into frequency-dependent phase-delays and amplitude anomalies, which are only weakly nonlinear and can be effectively linearized with respect to structural parameters. Third, by including both P- and S-wave speeds together with shear attenuation in a joint inversion, we were able to correctly account for the effect of P-wave speed on Rayleigh wave phase-delays and elastic effects on surface wave amplitudes. Fourth, we have developed an efficient algorithm for computing 3D full-wave Fréchet kernels based on the Green's tensor database, which is computed by normal-mode summation and accounts for the full physics of wave interactions in a 1D earth model, including non-ray theoretic effects such as diffraction and near-field effects.

REFERENCES

Balay S., K. Buschelman, V. Eijkhout, W. D. Gropp, D. Kaushik, M. G. Knepley, L. C. McInnes, B. F. Smith, and H. Zhang (2004). PETSc Users Manual, *ANL-95/11—Revision 2.1.5, Argonne National Laboratory*. http://www.mcs.anl.gov/petsc.

Chen, Y., F. Niu, R. Liu, Z. Huang, H. Tkalčić, L. Sun, and W. Chan (2010). Crustal structure beneath China from receiver function analysis, *J. Geophys. Res.* 115: B03307, doi:10.1029/2009JB006386.

Chen, P., L. Zhao, and T. H. Jordan (2007). Full-3D tomography for crustal structure in Los Angeles basin area, *Bull. Seism. Soc. Am*. 97: 1094–1120.

Chernov, L. A. (1960). Wave Propagation in a Random Medium. McGraw-Hill.

Constable, S. C., R. L. Parker, and C. G. Constable (1987). Occam's inversion: A practical algorithm for generating smooth models from electromagnetic sounding data. *Geophys.* 52: 289–300.

Dahlen, F. A. and J. Tromp (1998). Theoretical Global Seismology. Princeton, NJ: Princeton University Press.

Dalton, C. A. and G. Ekström (2006). Global models of surface wave attenuation, *J. Geophys. Res.* 111: B05317, doi:10029/2005JB003997.

Faul, U. H. and I. Jackson (2005). The seismological signature of temperature and grain size variations in the upper mantle, *Earth Planet. Sci. Lett*. 234: 119–134.

Friederich, W. (2003). The S-velocity structure of the east Asian mantle from inversion of shear and surface waveforms, *Geophys. J. Int.* 153**:** 88–102.

Gaherty, J. B., T.H. Jordan, and L .S. Gee (1996). Seismic structure of the upper mantle in a central Pacific corridor, *J. Geophys. Res.* 101: 22,291–22,309.

Gee, L. S. and T. H. Jordan (1992). Generalized seismological data functionals, *Geophys. J. Int*. 111: 363–390.

Huang, Z., W. Su, Y. Peng, Y. Zheng, and H. Li (2003). Rayleigh wave tomography of China and adjacent regions, *J. Geophys. Res.* 108: B2, 2073, doi 10.1029/2001JB001696.

Jemberíe, A. L. and B. J. Mitchell (2004). Shear-wave Q structure and its lateral variation in the crust of China and surrounding regions, *Geophys. J. Int*. 157: 363–380.

Karato, S. (1993): Importance of anelasticity in the interpretation of seismic tomography, *Geophys. Res. Lett.* 20: 1623–1626.

Katzman, R., L. Zhao, and T. H. Jordan (1998). High-resolution, two- dimensional vertical tomography of the central Pacific mantle using *ScS* reverberations and frequency-dependent travel times, *J. Geophys. Res.* 103: 17,933–17,971.

Laske, G., G. Masters and C. Reif (2001). CRUST 2.0, A new global crustal model at 2x2 degrees, http://igppweb.ucsd.edu/~gabi/crust2.html.

Lebedev, S. and G. Nolet (2003). Upper mantle beneath southeast Asia from S velocity tomography, *J. Geophys. Res.* 108: B1, 2048, doi 10.1029/2000JB000073.

Lin, S. (2001). Comparison of digital and analog seismic recordings, *Seism. Geomagnetic Obser. Res.* 22: 57–62 (in Chinese).

Molnar, P. and P. Tapponnier (1975). Cenozoic tectionics of Asia: Effects of a continental collision. *Science* 189: 419–426.

Paige, C. C. and M. A. Saunders (1982). LSQR: Sparse linear equations and least squares problems. *ACM Trans. Math. Software* 8: 195–209.

Pei, S., J. Zhao, Y. Sun, Z. Xu, S. Wang, H. Liu, and C. A. Rowe (2007). Upper mantle seismic velocities and anisotropy in China determined through Pn and Sn tomography, *J. Geophys. Res.* 112**:** B05312, doi 10.1029/2006JB004409.

Ritzwoller, M. H., M. P. Barmin, A. Villasenor, A. L. Levshin, and E. R. Engdahl (2002). Pn and Sn tomography across Eurasia to improve regional seismic event locations, *Tectonophys.* 358: 39–55.

Sambridge, M. S. (1990). Non-linear arrival time inversion: Constraining velocity anomalies by seeking smooth models in 3-D. *Geophys. J. Int.* 102: 653–677.

Shapiro, N. M. and M. H. Ritzwoller (2002). Monte Carlo inversion for a global shear velocity model of the crust and upper mantle, *Geophys. J. Int.* 151 88–105.

Snieder, R. and A. Lomax (1996). Wavefield smoothing and the effect of rough velocity perturbations on arrival times and amplitudes. *Geophys J. Int.* 125: 796–812.

Song, Z. H., C. Q. An, G. Y. Chen, L. H. Chen, Z. Zhuang, Z. W. Fu, and J. F. Hu (1991). Study on 3-D velocity structure and anisotropy beneath the west China from the Love wave dispersion, *Acta Geophys. Sin.* 34: 694–707 (in Chinese).

Sun, Y. and M. N. Toksöz (2006). Crustal structure of China and surrounding regions from P wave traveltime tomography, *J. Geophys. Res.* 111: B03310, doi 10.1029/2005JB003962.

Sun, Y., M. N. Toksöz, S. Pei, and F. D. Morgan (2008). The layered shear-wave velocity structure of the crust and uppermost mantle in China. *Bull. Seism. Soc. Am.* 98: 746–755; DOI: 10.1785/0120050222.

Vermeesch, P. (2003). A second look at the geologic map of China: The "Sloss approach," *Int. Geol. Rev*, 45: 119–132, doi:10.2747/0020-6814.45.2.119.

Wu, F. T., A. L. Levshin, and V. M. Kozhevnikov (1997). Rayleigh wave group velocity tomography of Siberia, China and vicinity, *Pure Appl. Geophys.* 149: 447–473.

Wu, J. P., Y. H. Ming, and C. Y. Wang (2001). The S wave velocity structure beneath digital seismic stations of Yunnan province inferred from teleseismic receiver function modelling, *Chin. J. Geophys.* 44: 237–243.

Xie, J. (2006). Pn attenuation beneath Tibetan plateau, *Bull. Seismol. Soc. Am*. 97: 2040–2052; DOI: 10.1785/0120070016.

Xie, C. and A. Zhao (2003), A preliminary analysis on the waveform and magnitude from the digital and analog recordings at Huichang seismic station, *Seism. Geomagnetic Obser. Res.* 24: 39–44 (in Chinese).

Xu, G., G. Li, S. Wang, H. Chen, and H. Zhou (2000). The 3-D structure of shear waves in the crust and mantle of east continental china inverted by rayleigh wave data, *Chin. J. Geophys.* 43: 376–384.

Xu, M., L. Wang, J. Liu, K. Zhong, H. Li, D. Hu, and Z. Xu (2006). Crust and uppermost mantle structure of the Ailaoshan-Red River fault from receiver function analysis, *Sci. China Ser. D: Earth Sci.* 49: 1043.

Yin, A. and T. M. Harrison (2000). Geologic evolution of the Himalayan-Tibetan orogen, *Annu. Rev. Earth Planet. Sci*. 28: 211–280, doi:10.1146/annurev.earth.28.1.211.

Yin, A. and S. Y. Nie (1996). A Phanerozoic palinspastic reconstruction of China and its neighboring regions, in *The Tectonic Evolution of Asia*, A. Yin and T. M. Harrison, Eds. New York, NY: Cambridge University Press.

Zhao, Y., J. Jia, J. Xue, G. Liu, X. Meng, Y. Wang, and N. Song (2001). Comparison of digital and analog data from the seismic networks in Shanxi province, *Earthquake in Shanxi*, 106: 40–44 (in Chinese).

Zhao, L., T. H. Jordan, and C. H. Chapman (2000). Three-dimensional Fréchet differential kernels for seismic delay times, *Geophys. J. Int*. 141: 558–576.

Zhao, L. and T. H. Jordan (2006), Structural sensitivities of finite-frequency seismic waves: A full-wave approach. *Geophys. J. Int.* 165: 981–990.

Zou, Z. and X. Chen (2003). Mapping the crustal S-wave velocity structure by using the SV component receiver function method, *Acta Seism. Sinica* 16: 16–25.

A STEPWISE, ITERATIVE PROCEDURE TO CONSTRAIN STRESS DROP, REGIONAL ATTENUATION MODELS, AND SITE EFFECTS

Mark D. Fisk[1] and W. Scott Phillips[2]

Alliant Techsystems[1] and Los Alamos National Laboratory[2]

Sponsored by Air Force Research Laboratory[1] and National Nuclear Security Administration[2]

Contract Nos. FA8718-09-C-0005[1] and LA09-BAA09-01-NDD03[2]

ABSTRACT

Accurate corrections for attenuation, geometrical spreading, source size, and site effects are needed for reliable use of regional seismic phases for discrimination and magnitude estimation. Without constraints, the full parameter space has many tradeoffs and instabilities that can lead to significant errors. We are developing a stepwise, iterative procedure, utilizing constraints, to provide more accurate parameter estimates. As a starting point, we use spectral ratios of regional phases for nearby events of different moments to eliminate path and site effects, yielding more reliable estimates of the source parameters. As shown by Schaff and Richards (2004) and Fisk et al. (2008), there are many pairs of nearby similar events throughout Eurasia available for this analysis. We then correct the spectra for source effects to be able to estimate more reliable distance and site corrections, adopting this same basic approach to constrain remaining tradeoffs. A key element of this effort is incorporation of coda envelope measurements, along with spectra of direct regional phases. The stability of coda allows the analysis to be applied to event pairs that are non-similar and may be separated by, e.g., up to 50 km, greatly augmenting those that can provide accurate source terms. We have acquired from IRIS a very large dataset of three-component regional seismic recordings for events listed in the USGS PDE from 1989 to 2009 that have epicenter estimates within 50 km of another event, with at least 0.7 magnitude units difference, and the larger event of each pair at least mb 5. The set includes over 46,000 such pairs, corresponding to about 9,400 unique events. We have processed 599,226 waveforms to compute spectra of direct Pn, Pg, Sn, and/or Lg phases (of the order of 2,000,000 spectra) and coda envelopes in 16 frequency bands (about 10,000,000 envelopes). We have computed and fit a relative Brune (1970) source model to network-median relative spectra for all 46,000 pairs. We have reviewed and compared relative spectra and model fits for direct phases and coda to assess the reliability of the estimated source parameters, the dependence on station coverage and event similarity, and effects of various data quality issues. We present several cases, corroborating the stability of coda, showing very comparable source terms estimated from coda and direct-phase for many, even for single stations for well-recorded, similar event pairs, and good agreement with available published studies that used dense local networks. The comparisons also highlight the complementary benefit of using multiple, independent measurements of coda and direct phases, which have led to improvements in the processing both (e.g., better fitting methods, restricting the data to those of higher quality using a magnitude-distance criterion, and flagging discrepancies, often due to data quality issues, for review). These collective processing and review efforts have led to a large, reliable set of source terms. We then show how the source-corrected spectra are used to estimate distance and site corrections. We also plan to use coda measurements to independently estimate and validate the site terms. We describe plans to partition the uncertainties and their correlation lengths for use in Bayesian methods to interpolate grids of stress drop, geometrical spreading, and Q estimates, and to merge our results with previous developments at Los Alamos National Laboratory (LANL).

OBJECTIVES

We are developing, applying, and evaluating methods to improve the accuracy of attenuation models, geometrical spreading, site terms, and their uncertainties for regional phases in Eurasia, by constraining trade-offs among the parameters at various stages of the analysis. The approach is to break up traditional grid-search inversions, which are known to have many trade-offs and instabilities (cf. Fisk and Phillips, 2009), into manageable pieces, canceling out certain physical effects (e.g., distance and site) to allow reliable estimation of others (e.g., source), and then correcting for the latter to then estimate reliable parameters for the former. We are processing spectra of direct phases and coda envelope measurements to augment and corroborate source terms and to independently estimate site terms. We also plan to use multiple methods to estimate the correction parameters and to validate the results at key stages. We plan to partition the uncertainties and their correlation lengths, interpolate grids of stress drop, geometrical spreading, and Q estimates, and merge our results with amplitude tomography developments at LANL. We will evaluate the corrections and uncertainties using two large datasets and cross-validation methods.

RESEARCH ACCOMPLISHED

Following Sereno et al. (1988), Taylor and Hartse (1998), Taylor et al. (2002), and numerous others, the amplitude spectrum for a given phase and station, for event i, may be modeled by

$$A_i(f) = S_i(f;M_0, f_c(\sigma_b^{(0)}, \psi))G(r_i;r_0, \eta)\exp\left(-\frac{\pi f^{1-\gamma}}{Q_0 \nu} r_i\right)P(f;a, b) \quad , \qquad \text{(EQ 1)}$$

where $S_i(f)$ is the source spectrum with seismic moment M_0 (and radiation pattern terms) and corner frequency f_c (which may be parameterized in terms of M_0, stress drop $\sigma_b^{(0)}$ or apparent stress, and a scaling parameter ψ), r_i is epicentral distance, $P(f)$ is a frequency-dependent site term, $Q_0 f^{\gamma}$ represents anelastic attenuation, ν is group velocity, and $G(r, r_0)$ represents frequency-independent geometrical spreading, inversely proportional to distance to a power η, beyond a reference distance r_0. The objective is to accurately estimate the parameters shown in red.

Constrained Inversion Approach

Instead of performing a grid search for all parameters simultaneously, we start by using relative spectra for event pairs with similar locations and focal mechanisms (assessed by waveform cross-correlations), but different moments, to factor out path and site effects and obtain reliable estimates of the source terms. Once accurate source terms are estimated, the source-corrected spectra can be used to estimate the distance and site terms. That is, for a pair of nearby earthquakes with similar radiation patterns, the relative spectra for a given seismic phase type is modeled by

$$\frac{A_1(f)}{A_2(f)} = \frac{S_1(f)}{S_2(f)} = \frac{M_0^{(1)}[1 + (f/f_c^{(2)})^2]}{M_0^{(2)}[1 + (f/f_c^{(1)})^2]} \quad . \qquad \text{(EQ 2)}$$

This approach requires many similar pairs. Schaff and Richards (2004) showed that there are indeed many such pairs. In addition, Mayeda et al. (2007) showed that coda is less sensitive to focal mechanism, event separation, and station coverage. This allows the requirement of similar events to be relaxed, greatly augmenting the number of pairs for which source terms can be estimated. Thus, in addition to using relative spectra of direct regional phases, we compute coda envelopes, using the processing method as Mayeda et al. (2003) and Phillips et al. (2008). We then compute a pseudo relative spectrum as the median ratio of coda envelopes in 16 frequency bands. For example, Figure 1 shows relative spectra of Pn, Sn, Lg, and coda, along with source model fits for an earthquake pair. Note that the relative coda spectrum, just using MK31 three-component (3C) data, is nearly the same as the network results for coda and direct phases using 19 regional stations. Spectra of direct phases and coda envelopes each have distinct advantages (discussed further below); their independence corroborates estimated source terms or helps identify problems.

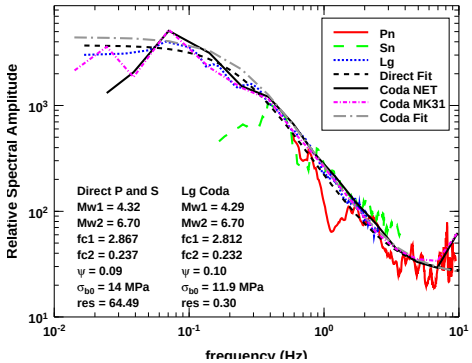

Figure 1. Network-median relative spectra of Pn, Sn, Lg, and Lg coda (using 19 stations and just MK31) for an event pair in southwestern Siberia. Model fits and estimated source parameters agree very well.

As an initial comparison, we estimated source terms from direct phases and coda for a cluster of about 100 events in southern Russia. Figure 2 shows that the estimates of moments and corner frequencies are similar. To assess the reliability of the resulting path corrections using these independent source estimates, we corrected Lg spectra at 23 stations using source estimates from direct phases or coda. Figure 3 shows the source-corrected Lg spectra at BRVK, along with fits of the combined site and distance terms. Figure 4 compares Q estimates, showing that the results using source terms from coda or direct phases are highly correlated. We have yet to treat site effects, so these estimates will likely change, but the relative corrections, using independent source estimates from coda and direct phases, are very consistent.

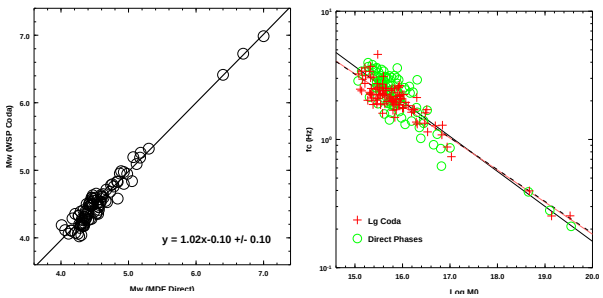

Figure 2. Comparison of Mw estimates (left) and corner-frequency scaling (right), independently estimated from direct phases and Lg coda.

Large-Scale Processing

We acquired regional data from IRIS for events listed in PDE from 1989 to 2009 that have epicenter estimates within 50 km of another event, a magnitude difference of at least 0.7 m.u., and the larger event of each pair at least mb 5. The set includes 46,495 such pairs, corresponding to 9,395 unique events, shown in Figure 5. Also shown are IRIS stations and ray paths with data, indicating good coverage for much of Eurasia. Unlike tomography, our approach does not require crossing ray paths to estimate model parameters of Eq. (1), providing constraints for many paths and extending calibration to the edges of Eurasia (e.g., Russia, India, and the Arabian Peninsula). We automatically processed about 2,000,000 spectra of regional phases and about 10,000,000 coda envelopes, computed network-median relative spectra, and fit Eq. (2) to over 46,000 pairs, without restricting to similar event pairs. We computed waveform cross-correlations for all pairs that can be used to assess the similarity of mechanisms for cases where results from direct phases and coda disagree. We have reviewed the results for master events of mb 5.5 and larger and are completing the review for the remaining master events.

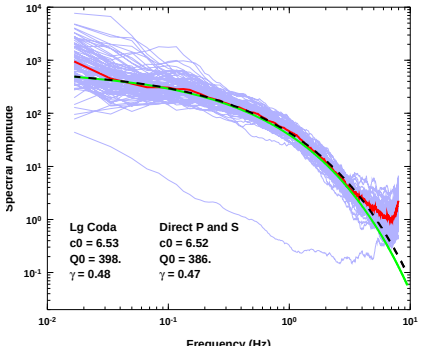

Figure 3. Source-corrected Lg spectra at BRVK for 100 events in the cluster (blue), the median (red), and Q model fits (black dashed and green) using source corrections from direct phases and coda, respectively.

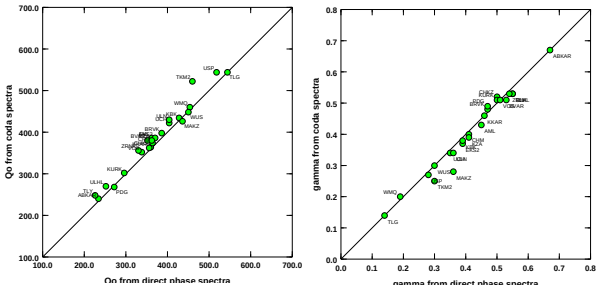

Figure 4. Comparison of Q_0 (left) and γ (right; exponent of frequency-dependent Q) estimates from coda versus direct phases, showing good agreement.

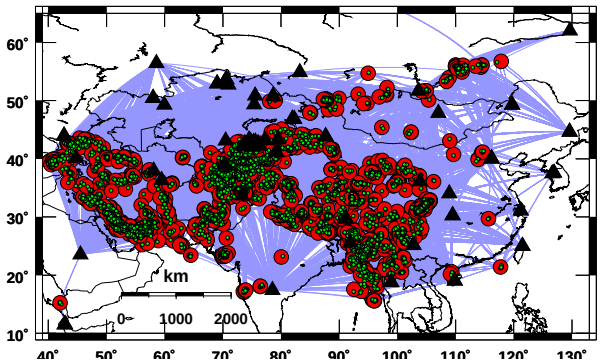

Figure 5. Map of earthquakes listed in the PDE from 1989 to 2009; red circles correspond to mb>5 events within 50 km of smaller events (green circles). Also shown are ray paths for which regional seismic data are available from IRIS stations (triangles).

Figure 6 compares preliminary estimates of source parameters from direct phases versus coda. Moments of the large master events are fixed, using values in the PDE; they were not used in the linear regression (left plot), which shows very good overall agreement. There are clearly discrepancies, particularly for the corner frequencies, which we are investigating/reconciling.

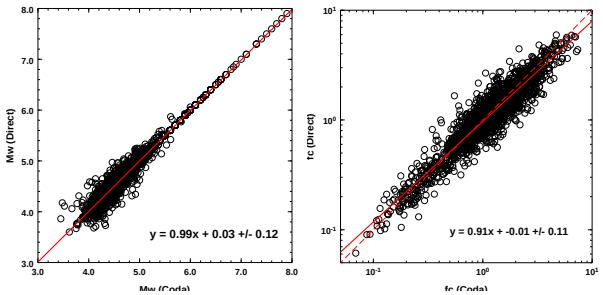

Figure 6. Preliminary estimates of Mw and corner frequency from direct phases versus coda.

Detailed Examinations

Because automatic processing is needed for this very large data set, to build confidence in the procedure and the resulting source terms, we compared coda and direct results in detail for many cases and to published results. Here we show some that highlight the dependence of the results on station coverage and the benefits of using both direct phases and coda. For example, coda results at even a single station are often comparable to network results, as illustrated in Figure 1. Since not all pairs are equally well recorded or similar, an important question is how sensitive direct-phase results are. We examine this for progressive cases, starting with an ideal one. Figure 7 shows the locations of a large, similar pair recorded by 19 stations within 14º. The left plot of Figure 8 shows the network-median relative spectra and source model fits for this pair. The coda and direct Lg relative spectra are remarkably similar, even for subtle Lg fluctuations above 1 Hz. It can be argued that the direct-phase results are so consistent because the events were well recorded. However, the right plot of Figure 8 shows that the coda and direct results also agree just using station CHKZ. Figure 9 shows estimated corner frequencies versus log moment for each of 19 stations. Except for data quality issues at three stations for coda and one for direct Lg, the single-station results agree very well. Clipping at MK31 for the Mw 6.7 event has a greater effect on direct Lg, leading to a discrepancy (Figure 10). Data quality issues at a small fraction of stations do not impact the network median, but could affect the results if recorded by fewer stations. The discrepancy of source terms from coda and direct phases can flag such problems, without having to examine many thousands of waveforms.

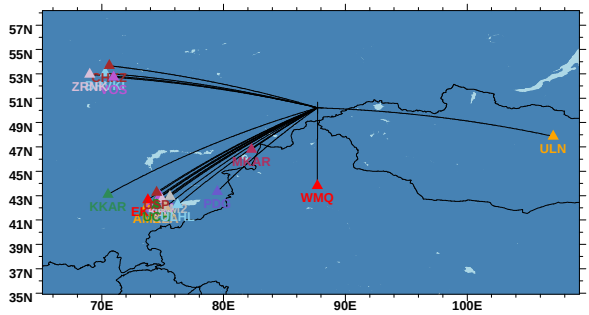

Figure 7. Locations of an event pair in southern Russia and regional stations with recordings.

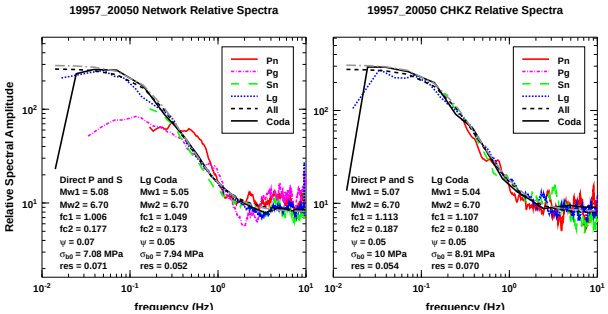

Figure 8. Relative spectra from direct phases and Lg coda, and source model fits and parameter estimates using 19 stations (left) and just using CHKZ (right).

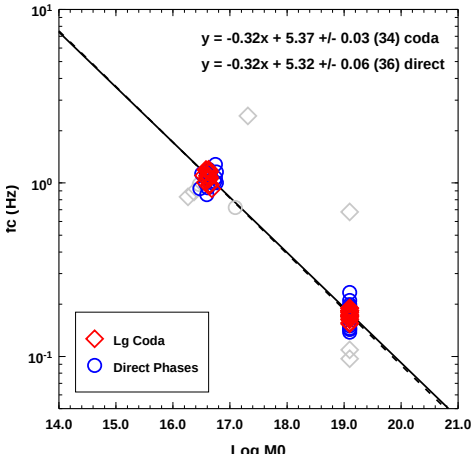

Figure 9. Single-station estimates of corner frequency versus log moment and scaling relations (linear fits) from direct phases and Lg coda. Gray markers correspond to stations with data quality problems.

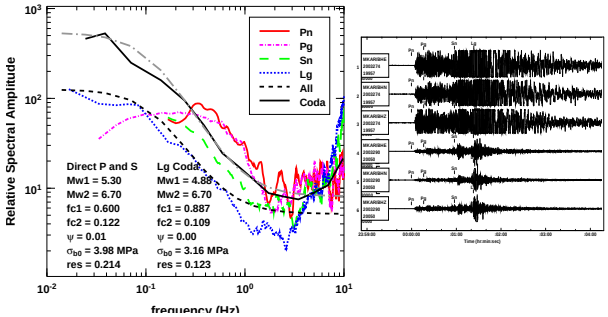

Figure 10. Relative spectra from direct phases and Lg coda at MK31 (left), which disagree due to clipping for the larger event (right).

As a less ideal case, Figure 11 depicts two earthquakes at the Lop Nor test site (LNTS), smaller (Mw 5.5/4.2) than the first case and recorded out to 20º. Figure 12 shows relative spectra at MAKZ and NIL. For NIL, the direct-phase results agree with MAKZ and network results. Lg coda has poor SNR for this path, illustrating how direct P and S phases complement coda. Figure 13 shows single-station estimates of corner frequencies versus moment. Coda results have less scatter, but the direct-phase results are similar. Figure 14 shows single-station f_c estimates versus distance. Even requiring SNR>3, data quality degrades for longer paths/smaller events, causing biases and apparent distance dependence. Using a magnitude-distance criterion (e.g., Phillips et al., 2008) to restrict the data to higher quality generally improves the results, as illustrated in Figure 15 for LNTS.

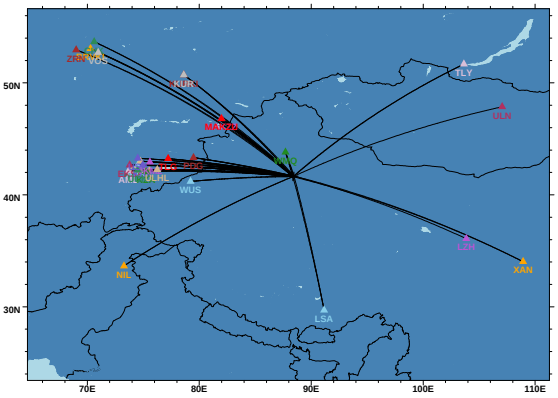

Figure 11. Locations of an earthquake pair during January 1999 at LNTS and regional stations.

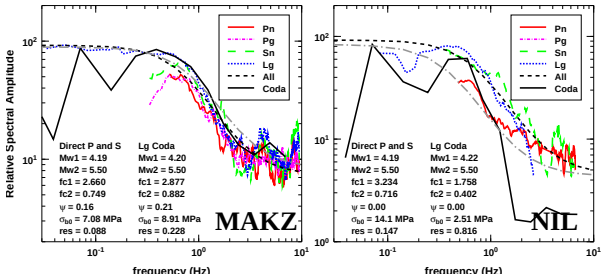

Figure 12. Relative spectra and source model fits at MAKZ (left) and NIL (right) for the LNTS pair.

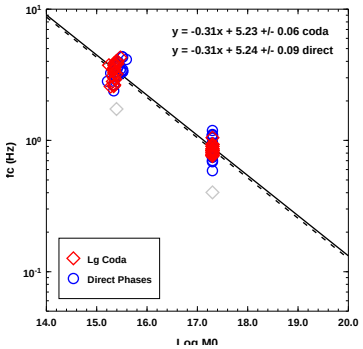

Figure 13. Estimates of corner frequency versus log moment from direct phases and Lg coda at each station using a pair of events at LNTS. The NIL coda result is an outlier.

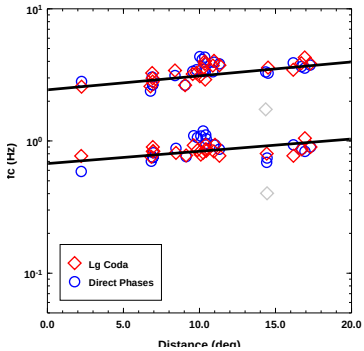

Figure 14. Single-station estimates of corner frequency versus distance to each station for the LNTS pair, showing apparent trends.

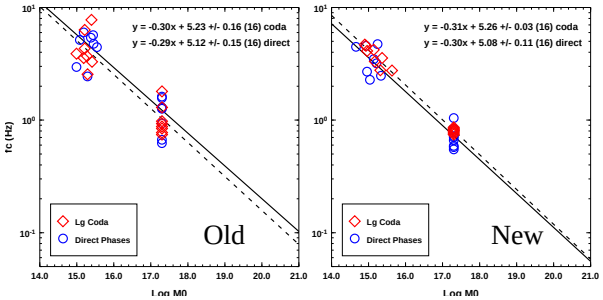

Figure 15. Source parameter estimates for 8 crustal pairs near LNTS using all regional data (left) and restricting the data by magnitude/distance (right).

A sequence of Bhuj earthquakes is interesting because: (1) IRIS data are available from only 3 regional stations (Figure 16); (2) direct Lg is clipped at HYB for the main shock; (3) one NIL channel is missing; (4) Lg does not propagate efficiently to ABKT (Δ = 1980 km); and (5) many aftershocks occurred throughout the crust. Thus, this is a case of very limited data and source variability. Figure 17 shows relative spectra for one pair, using only NIL data for direct Lg, and NIL and HYB data for Pn, Sn and coda. The magnitude-distance criterion excludes ABKT for all but the largest events. Figure 18 shows estimates of source parameters. From the fits, using 1-3 regional stations, we estimate fc = 0.072, 0.084 Hz for the main shock from coda and direct phases. Using 8 local stations, Bodin and Horton (2004) estimate static stress drop of 16-20 MPa, giving fc = 0.066-0.071 Hz. Thus, using very limited data, our results are consistent with GT source information. The scatter and bias for the smaller events (Figure 18) are due to a combination of varying locations, depths, mechanisms, and SNR effects.

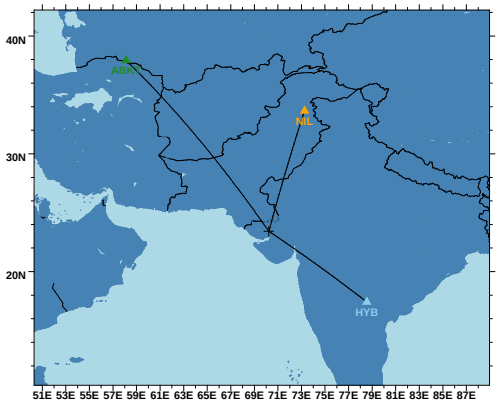

Figure 16. Locations of Bhuj, India earthquakes with regional recordings by ABKT, HYB, and NIL.

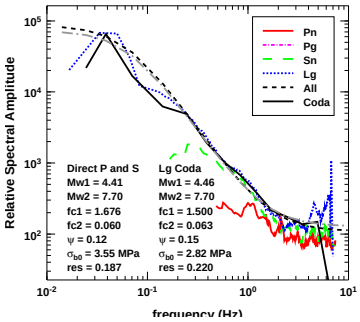

Figure 17. Relative spectra and model fits for a Bhuj pair, using NIL data for direct Lg and NIL and HYB data for other phases.

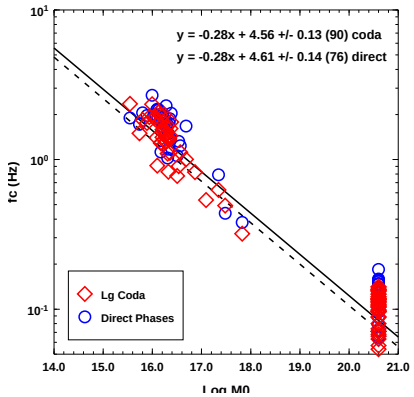

Figure 18. Estimates of f_c versus log M_0 for Bhuj events. Linear regressions were weighted by moment.

I also processed a pair of earthquakes near Wells, NV that are reported to have strong source directivity. They were recorded by several permanent broadband networks and 400 portable broadband USArray stations with 70-km spacing. Using stations at more typical regional distances (Figure 19), 22 with good data, Figure 20 (left) shows that network-median relative spectra from direct phases and coda agree quite well, even for Pn (often the most variable) over frequencies with adequate SNR. Our Mw estimates of 4.27 and 4.29 for the smaller event, fixing Mw 5.8 for the larger, agree with estimates of 4.3 and 5.8 by Mendoza and Hartzell (2009), who used a finite-fault method. They estimated static stress drop of 7.2 MPa for the larger event, noting that it is higher than expected for the Basin and Range, equivalent to f_c = 0.39 Hz. I obtain f_c estimates of 0.29-0.31 Hz from coda and direct phases.

There are many cases for which the source parameters estimated from coda and direct phases agree very well, typically for event pairs with similar mechanisms. It is also interesting to examine discrepancies of coda and direct results. Figure 21 depicts the location of one such cluster of 10 events in Kazakhstan, near the Caspian Sea.

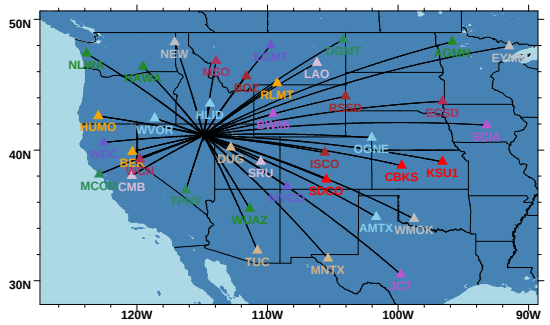

Figure 19. Locations of earthquakes near Wells, Nevada and 39 stations at regional distances.

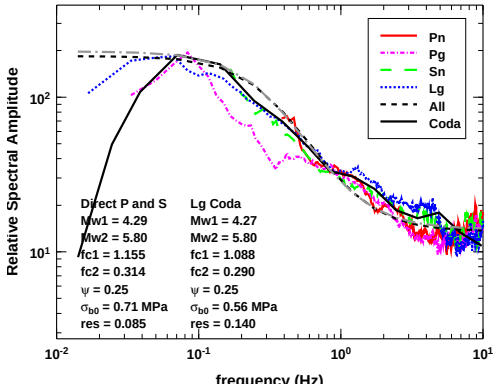

Figure 20. Relative spectra, model fits, and source parameter estimates for a pair of Wells earthquakes.

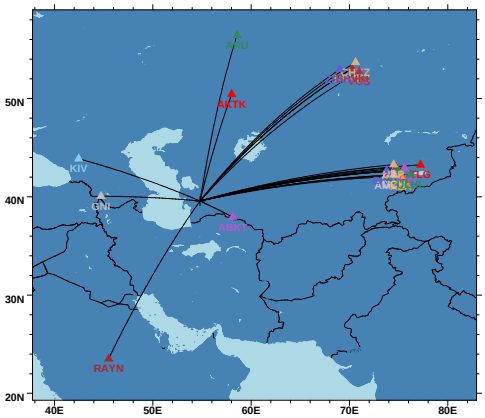

Figure 21. Locations of a cluster of earthquakes near the Caspian Sea and recording regional stations.

Figure 22 (left) shows corner frequency estimates versus log M_0 from all 10 pairs; the direct-phase results exhibit much more scatter and bias than coda. Figure 22 (right) shows the results for the events with waveform cross-correlations greater than 0.6. The coda results are very similar in both cases, illustrating its stability to source effects. The direct-phase results have much less scatter and bias by restricting to similar pairs.

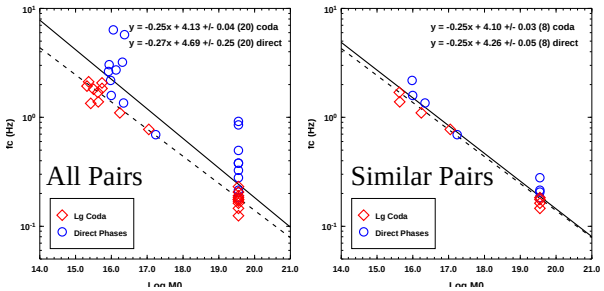

Figure 22. Estimates of source parameter for a cluster in Kazakhstan, using 10 events within 50 km of the master (left) and restricting the events to those with similar waveforms/mechanisms (right).

As a final case, Figure 23 depicts a cluster in Myanmar. Figure 24 shows estimates of corner frequencies versus log moment using up to 5 stations; 5 of 11 coda results are outliers due to data quality issues. When excluded, the coda results are tighter than those from direct phases, as seen for many cases, but can be more prone/sensitive to data quality problems because measurement windows are longer, increasing the probability of including spurious signals, and SNR is lower than direct Lg.

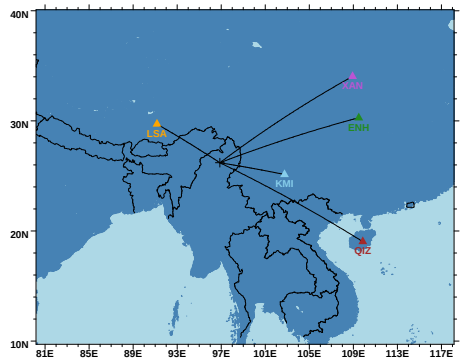

Figure 23. Location of an Mw 5.9 earthquake in Myanmar and 5 regional stations with recordings.

For example, an Mw 5.0 event occurred 13 minutes after the largest (Mw 5.9); its signals are in the coda of the preceding event (Figure 25), which biases the estimates of source parameters for both events of the pair. The corner-frequency estimates from coda for this pair are the most inconsistent with all of the other results. The results from direct Lg are also biased some, but not nearly as much because it has higher SNR.

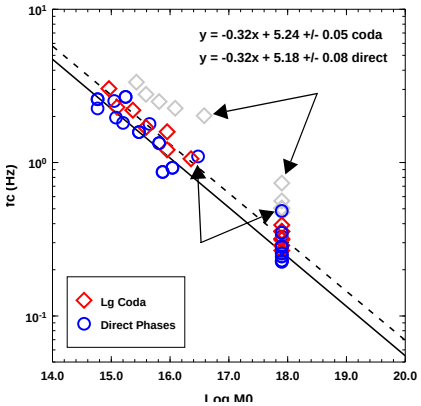

Figure 24. Estimates of corner frequency versus log moment and scaling relations from direct phases and Lg coda, using data from up to five common stations. Gray markers are outliers of the coda results.

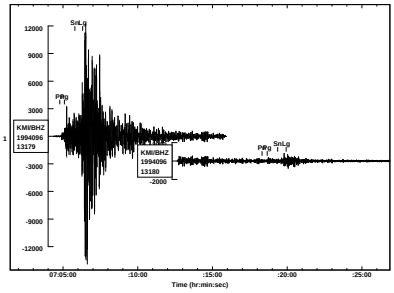

Figure 25. KMI data for two events in the Myanmar cluster, separated in time by about 13 minutes.

Comparisons of Preliminary Q Parameters

Now that we are establishing a large set of corroborated source terms, the next step is to fit the source-corrected spectra to estimate the distance and site terms. For paths from LNTS to regional stations, we compared our Q_0 estimates for Pn, Sn, Lg to those computed as averages of Q_0^{-1} along the paths from tomography by Dr. Phillips. Our results were generated using only one pair at LNTS. Figure 26 shows examples of source-corrected spectra for various phases and fits, giving estimates of effective Q parameters. Figure 27 compares Lg Q_0 estimates for 24 stations, which agree well for stations in Kazakhstan and Kyrgyzstan. Our average Lg Q_0 for these paths is 442 versus 478 from tomography. Our Lg Q_0 estimates are 18-32% lower than those from tomography for TLY, NIL, LZH, ULN, and WMQ, paths for which stations are sparse. We are using more data to improve and validate these initial results. It is interesting that we obtain similar results for many stations using a single pair with well-constrained source terms, which can be used to constrain tomography, particularly for paths with sparse coverage.

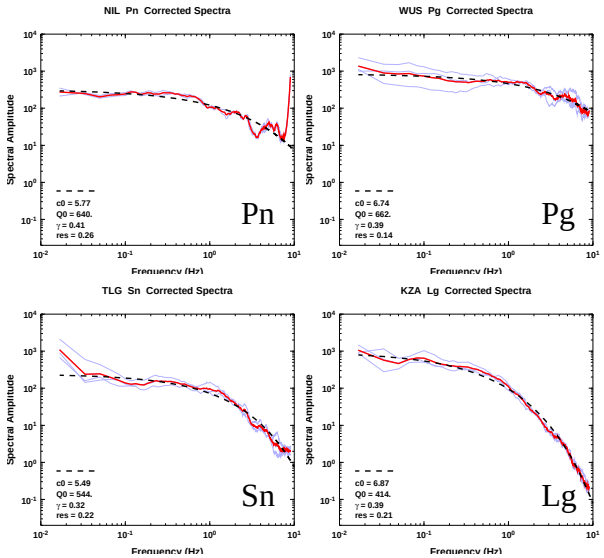

Figure 26. Examples of source-corrected spectra and Q model fits using a pair of LNTS earthquakes.

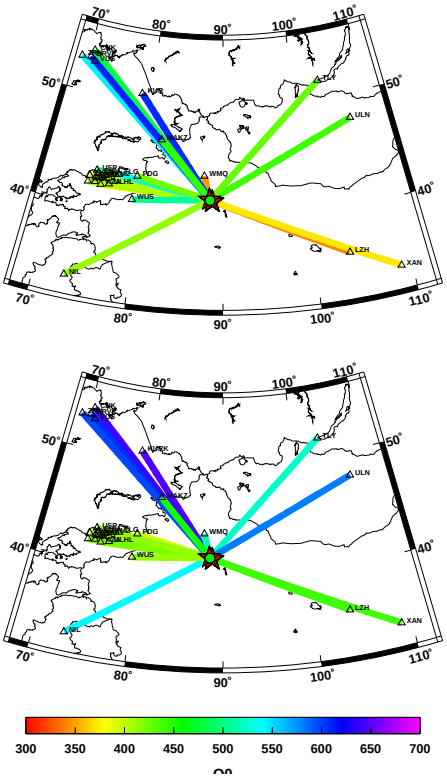

Figure 27. Effective Lg Q_0 for paths from LNTS to regional stations from our analysis (top) and based on amplitude tomography (bottom).

Figure 27 shows effective Lg Q_0 estimates for selected paths to MAKZ and MKAR, illustrating systematic path variations. We still need to treat frequency-dependent site effects, which will affect the Q estimates; however, the estimates of source terms and Q for these paths can help constrain amplitude tomography work at LANL, providing the most immediate benefit to existing efforts.

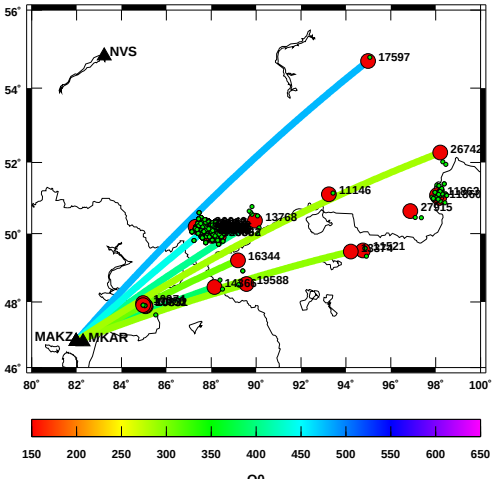

Figure 28. Effective Lg Q_0 for paths to MAKZ and MKAR, using source corrections estimated from various pairs/clusters.

Next Steps

By first eliminating path and site effects, using an EGF approach, accurate source terms can be estimated for events with suitable data. These terms and fits of source-corrected spectra (e.g., Figure 26) completely calibrate all combined physical effects over a broad spectral range for relevant paths. For isolated clusters, the fits do not provide independent estimates of Q, spreading, and site parameters. We are extending the constrained approach to eliminate remaining trade-offs. For example, site effects have frequency dependence that, if inaccurately treated, can adversely impact Q estimates. An approach that imposes a constraint is to use relative spectra for clusters with similar paths, but different distances from a station, to factor out the site term and estimate of Q for that path. Figure 29 illustrates this approach. It shows the ratio of the median source-corrected spectra for two clusters along a path to MAKZ. This factors out the site term, and the spreading terms are different constants, independent of frequency. Thus, the estimate of Q has no trade-off with source, site, or geometrical spreading effects. Assuming the effective Q is relatively constant over a path, the ratio of source-corrected median spectra for the two clusters is simply modeled by

$$\log(\tilde{A}_1/\tilde{A}_2) = \frac{\pi f^{1-\gamma}}{Q_0 v}\Delta r \ , \qquad \text{(EQ 3)}$$

where Δr is the separation of the clusters. Fitting this expression to empirical spectral ratios (dashed curve in Figure 29) gives constrained estimates of Q_0 and γ (e.g., Lg $Q_0 = 546$) for the path.

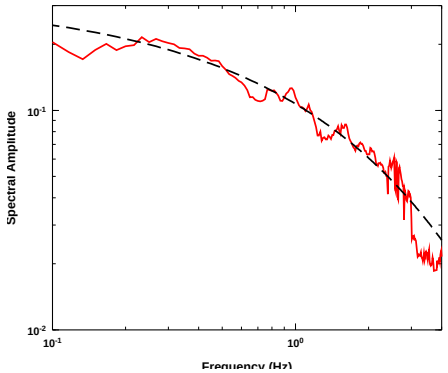

Figure 29. Ratio of source-corrected median spectra for two clusters along a great-circle path to MAKZ. The relative spectrum factors out the site term and allows a robust estimate of Q for this path.

Now correcting the source-corrected spectra for Q, the remaining frequency dependence is due to site effects. Once this is done for at least one path, the frequency-dependent site term may be estimated and fixed, under a typical assumption that $P(f)$ is independent of azimuth. We can then estimate Q for all paths with available data. The other assumption is that a suitable path exists for a given station along which Q is fairly constant. We are investigating its validity for stations of interest.

CONCLUSIONS AND RECOMMENDATIONS

We are developing and testing methods to constrain source, distance, and site corrections for regional phases. We have processed 20 years of IRIS data for Eurasia. A significant aspect has been incorporating coda measurements to corroborate, augment, and improve source estimates from direct phases. Coda is generally more stable, allowing estimates for more pairs that do not have similar mechanisms or that are not as well recorded. Source terms estimated from relative coda envelopes

generally have lower variance than those from spectra of direct phases. However, they often compare very well, even for single stations, for similar pairs with good data. Our results also agree with published studies based on dense local networks, for the Bhuj cluster with very limited regional data and for Wells events that have source directivity effects. Examples shown highlight that direct phases can be variable for non-similar event pairs and coda results can be more prone to data quality issues. Note that processing a data set of this size requires a high degree of automation; it is impractical to examine all of the data. Agreement of the coda and direct-phase results help to validate the source terms. Discrepancies flag various (e.g., data quality) problems that need to be treated. Because reliable source terms are an important foundation for this effort, significant efforts have been made to compare coda and direct results and improve the processing of both. We plan to finish reviewing the source terms and quantify their uncertainties.

Amplitude tomography is a major, ongoing calibration effort at LANL. Our source terms can be used in the near term as quasi ground truth for tomographic inversions, both to validate existing grids and to improve them by imposing constraints. We plan to use cross-validation methods to start testing improvements to tomographic grids. We also plan to progress to the next phase of this project, using source-corrected spectra and additional constraints (e.g., as illustrated by Eq. (3) and Figure 29) to estimate reliable path and site terms. Other key aspects of this work are to partition the uncertainties, validate the distance and site corrections, and also merge them with amplitude tomography.

ACKNOWLEDGMENTS

Seismic data from IRIS were used in this study.

REFERENCES

Bodin, P., and S. Horton (2004). Source parameters and tectonic implications of aftershocks of the Mw 7.6 Bhuj earthquake of 26 January 2001, *Bull. Seismol. Soc. Am.*, 94: 818–827.

Bodin, P., L. Malagnini, and A. Akinci (2004). Ground-motion scaling in the Kachchh Basin, India, deduced from aftershocks of the 2001 Mw 7.6 Bhuj earthquake, *Bull. Seismol. Soc. Am.*, 94: 1658–1669.

Brune, J. N. (1970). Tectonic stress and the spectra of seismic shear waves from earthquakes, *J. Geophys. Res.*, 75: 4997-5009.

Fisk, M. D., G. D. McCartor, and S. R. Taylor (2008). Robust Magnitude, Distance, and Path-Specific Corrections for Regional Seismic Phases by Constrained Inversion and Enhanced Kriging Methods, ATK/NCR-0608-501, Final Report.

Fisk, M. D. and W. S. Phillips (2009). A Stepwise, Iterative Procedure to Constrain Stress Drop, Regional Attenuation Models, and Site Effects, in *Proceedings of the 2009 Monitoring Research Review: Ground-Based Nuclear Explosion Monitoring Technologies*, LA-UR-09-05276, Vol. 1, pp. 52-61.

Mayeda, K. M., A. Hofstetter, J. L. O'Boyle, and W. R. Walter (2003). Stable and Transportable Regional Magnitudes Based on Coda-Derived Moment-Rate Spectra, *Bull. Seismol. Soc. Am.*, 93: 224-239.

Mayeda, K. M., L. Malagnini, and W. R. Walter (2007). A new spectral ratio method using narrow band coda envelopes: evidence for non-self-similarity in the Hector Mine sequence, *Geophys. Res. Lett.*, 34: L11303.

Mendoza, C., and S. Hartzell (2009). Source analysis using regional empirical Green's functions: The 2008 Wells, Nevada, earthquake, *Geophys. Res. Lett.*, 36, L11302, doi:10.1029/2009GL038073.

Phillips, W. S., R. J. Stead, G. E. Randall, H. E. Hartse and K. Mayeda (2008). Source effects from broad area network calibration of regional distance coda waves, in *Scattering of Short Period Waves in the Heterogeneous Earth*, H. Sato and M.C. Fehler, Editors.

Schaff, D. P. and P. G. Richards (2004). Repeating seismic events in China, *Science*, 303: 1176-1178.

Sereno T. J., S. R. Bratt and T. C. Bache (1988). Simultaneous inversion of regional wave spectra for attenuation and seismic moment in Scandinavia, *J. Geophys. Res.*, 93: 2019-2035.

Taylor, S. R., and H. E. Hartse (1998). A procedure for estimation of source and propagation amplitude corrections for regional seismic discriminants, *J. Geophys. Res.*, 103: 2781-2789.

Taylor, S. R., A. A. Velasco, H. E. Hartse, W. S. Phillips, W. R. Walter, and A. J. Rodgers (2002). Amplitude corrections for regional seismic discriminants, *Pure and Appl. Geophys.*, 159: 623-650.

CRUSTAL VELOCITY MODELS OF THE ZAGROS-BITLIS ZONE FROM BODY- AND SURFACE WAVE ANALYSES

Roland Gritto[1], Matthew S. Sibol[1], Pierre Caron[1], Hafidh A. A. Ghalib[1], Robert B. Herrmann[2], Ghassan I. Aleqabi[3], Bakir S. Ali[4], Ali A. Ali[5]

Array Information Technology[1], Saint Louis University[2], Washington University in Saint Louis[3], Sulaimaniyah Seismological Observatory[4], Baghdad Seismological Observatory[5]

Sponsored by Air Force Research Laboratory

Award No. FA8718-10-C-0003

ABSTRACT

Results of crustal studies obtained with seismic data from the Northern Iraq Seismic Network (NISN) are presented. NISN has operated ten broadband stations in north-eastern Iraq since late 2005 and was supplemented by the five-element broadband Iraq Seismic Array (KSIRS) in 2007. In the past two years, the former Iraq Seismic Network (ISN) was reestablished with the deployment of six broadband stations throughout Iraq. The aim of the present study is to derive models of the local and regional crustal structure of the Middle East, including Eastern Turkey, Iraq and Iran. To achieve this goal, we derive crustal velocity models using surface - and body wave analyses. The velocity models will eventually be used to obtain accurate hypocenter locations and event focal mechanisms. At present we have analyzed over 3,000 surface wave dispersion curves from about 200 events throughout the Middle-East. NISN data were augmented by waveforms from IRIS including those published by the neighboring Syrian, Iranian and Turkish networks. Our Rayleigh wave velocity analysis resulted in a clear demarcation of the tectonic features in the region. The results show a thick (10-15km) sedimentary layer that overlays the crystalline basement and a Conrad and Moho discontinuities at depths of 20-25km and 45-55km, respectively. The results also show that the Arabian plate exhibits higher shear-wave velocities than found across the Turkish and Iranian plateaus; imprint of the Zagros Mountain roots extends down as deep as the Moho; and that the tectonic boundaries along the Dead Sea, Taurus and Zagros are more pronounced with depth describing a 60km or thicker Arabian plate. Current work involving body wave velocity tomography modeling is intended to improve the resolution of the obtained velocity model and extend it across the region from Iran across Iraq into Eastern and Central Turkey.

OBJECTIVES

Through collaboration with the Sulaimaniyah Seismological Observatory, Erbil Seismological Observatory, Iraqi Meteorological Organization and Seismology, and the University of Baghdad, Array Information Technology (AIT) has collected over 1 TB of continuous digital broadband seismic data as a result of the successful deployment throughout northern Iraq of ten three-component stations that comprised NISN. Since late 2005, these data have yielded over 3,000 well located events. Additional broadband data have been provided by a seismic array (KSIRS) recently installed in northeast Iraq and from the newly refurbished stations of Iraq Seismographic Network (ISN). A wealth of seismic bulletins and waveforms for over 30,000 events is also provided by the Iranian Seismological Center (IRSC) of the Institute of Geophysics at the University of Tehran, and the International Institute of Earthquake Engineering and Seismology under Iran's Ministry of Science Research and Technology. The combination of these datasets provides an unprecedented database to perform a variety of in-depth and detailed seismological studies on Iraq, Iran and neighboring countries.

The objectives of the current project include the development of high-resolution crustal and upper mantle velocity models based on a combination of the available seismic datasets. The intention is to improve the resolution of existing regional models to derive a detailed structure of the tectonics of the Middle East including the Arabian Peninsula and the Zagros Thrust Zone. In the current paper, we present results of our Rayleigh surface wave analysis and provide an outlook of our current project of 3-D P- and S-wave body-wave tomography.

RESEARCH ACCOMPLISHED

Translational and rotational interaction between the Arabian, African and Eurasian plates over time has resulted in a challenging seismotectonic framework that is least understood in the Middle East region, in particular. Sea floor spreading along the Red Sea and Gulf of Aden, transform faulting along the Dead Sea and Own fracture zone, and compressional suture zones form the seismic and tectonic boundaries between the Arabian plate and the Iranian and Turkish plateaus creating the Bitlis/Zagros fold zone along the northern boundary of Iraq and the western boundary of Iran. The geography of this region is presented in Figure 1, where major tectonic features and plate boundaries are noted for reference. Until recently, the tectonic structure of this collision was not well understood. Theories included continental subduction or delamination of the Arabian plate (Rotstein and Kafka, 1982), continental thickening of the Eurasian plate (Dewey et al., 1986), or a combination of these processes. Reilinger (2008) presented GPS measurements of the velocity field of the Arabian Peninsula. The results, comprised of measurements from 1988 through 2005 and presented in Figure 2, indicate a counter-clockwise rotation of the Arabian Peninsula, relative to the Iranian and Turkish plateaus. In order to verify plate boundaries, crustal thickness, collision zones and spreading centers associated with the plate rotation observed at the Earth surface Raleigh wave tomography was conducted throughout the Middle East.

Seismic waveform data were collected by NISN, the International Institute of Earthquake Engineering and Seismology (IIEES), Incorporated Research Institutions for Seismology (IRIS) and Observatories and Research Facilities for European Seismology (ORFEUS). The station locations and epicenters used for the surface tomography study are presented in Figure 3. The surface wave dispersion analysis was performed using the multiple filter technique (MFT) to determine group velocity dispersion curves. This analysis yields the variation of Rayleigh wave group velocities at given periods along the propagation path from the epicenter to the recording station. During our study, we calculated 4,215 dispersion curves of which 3,663 were utilized in the results presented here. The spatial distribution of the 3,663 ray paths is indicated by the light blue lines in Figure 3. It can be seen that the ray density is highest in the center of the Zagros thrust zone, where the concentration of seismicity and stations is highest. Given the density of paths, a 1°x1° grid was used to develop a detailed map of the lateral and vertical variation of shear-wave velocities in the Middle East.

The second step, after deriving dispersion curves for all ray paths, uses the grid dispersion inversion (GDI) technique to determine single dispersion curves for each 1°x1° grid cell. Once the single dispersion curves are determined, the shear velocity as a function of depth is estimated in each cell using the program SURF96 (Herrmann, 2006). An example of a dispersion curve inversion fit for a fundamental Rayleigh wave and an estimate of its associated velocity as a function of depth is presented in Figure 4. The velocity inversion as a function of depth is based on an initial starting model indicated by the dashed blue line. It can be seen that the

inversion changes the velocity model only where supported by measured data. In the current case of a well fitted dispersion curve between 5 and 60 sec, the resolved depth range is limited to the crust and upper mantle to a depth of approximately 60 km (red line). Because the measured periods support velocity estimates down to the upper mantle only, it is important that the starting model reaches much deeper into the mantle. Such an approach will avoid large oscillations in the velocity estimates at depth, which may adversely affect estimates in the crust and upper mantle.

The results of the velocity inversion are presented in Figure 5. The figure shows a set of horizontal depth slices from 5 – 80 km throughout the Middle East representing the spatial distribution of the shear wave velocity. At shallow depth (5 km) the sedimentary basins in western Iraq and along the Euphrates and Tigris Rivers in central Iraq are clearly visible. Furthermore, the thick sedimentary basin below the southern Caspian Sea is apparent by its low shear wave velocities down to 20 km depth. The Arabian Shield, in the western peninsula, is demarked by higher shear wave velocities than the Foredeep (compare to Figure 1) with its thicker sediments along the eastern half of the peninsula at depths of 5–20 km. At a depth range from 20–30 km the spreading center in the Red Sea is visible by higher shear wave velocity indicating the presence of magmatic rocks. An interesting feature is the strike of the spreading center which does not follow the orientation of the Read Sea, but transects the region from Eritrea to north-western Saudi Arabia. The Zagros thrust zone is demarked by lower than average velocities along the axis of the Mountain range down to 55 km. The lower velocities are a manifestation of the tectonic forces that compress and fracture the rocks while lifting the Zagros Mountains and the Iranian Plateau. The resolution of the current study is reached at a depth of approximately 60 km, as indicated by the velocity depth profile in Figure 4. An overall velocity increase at 20 km depth may indicate the transition from crystalline to basaltic rocks (Conrad discontinuity), while the transition from crustal to mantle rocks (Moho discontinuity) is suggested by velocity increases between 45 and 50 km. In addition, the maps show that the Arabian plate exhibits higher shear-wave velocities than found across the Turkish and Iranian plateaus.

The results of the three-dimensional depth distribution of fixed shear wave velocity values are presented in Figure 6. The maps help to display the depth dependence of various terrains encountered in the Middle East. As such, the Arabian Shield is clearly distinct from the Foredeep extending to a depth of 20 km. Similarly, the root of the Zagros thrust zone can be recognized down to a depth of approximately 50 km. It is noted that this structure does not extend southward to the Makran mountain range. The strike of the Red Sea rift system is clearly visible in the maps denoting shear wave velocities of 3.8 km/s and 3.9 km/s and is oriented at an angle to the axis of the Red Sea. The deepest structures visible in the maps are indicated by the blue colored features surrounding the Arabian Peninsula at 60 – 65 km depth. The associated velocities of 4.0 km/s and 4.1 km/s suggest the presence of crustal rocks. This feature follows the tectonic boundaries along the Red Sea, the Dead Sea, the Taurus and the Zagros mountains. Therefore, it may demark the boundary of the Arabian Plate (compare to boundary indicated by yellow line in Figure 1) while indicating a thickness of about 60 km. However, these interpretations need to be viewed with caution as the limit in resolution of our study is reached at 60 km, as mentioned above.

CONCLUSIONS AND RECOMMENDATIONS

The current study generated results with significantly detailed tectonic structures of the crust in the Middle East. The main findings include a sedimentary column with a thickness of 5 – 10 km, while Conrad and Moho discontinuities were found at 20 km and 45 - 50 km depth, respectively. The thickness of the crust beneath the Arabian Peninsula is suggested to be about 60 km, which is the limit of depth resolution of the current study. Stable and well resolved features include the extent of the Zagros thrust zone down to the Moho and the Red Sea spreading center with its axis rotated counter clockwise to the axis of the Red Sea. Furthermore, the observed shear wave velocities of the Turkish Plateau to the north of the Taurus Mountains and of the Iranian Plateau to the east of the Zagros Mountains are generally lower than those of the Arabian Peninsula.

It should be noted that the presented results were obtained by combining seismic waveform data from Iraqi (NISN) and Iranian (IIEES) networks supported by IRIS and ORFEUS stations throughout the region. However, contributions from similar efforts along the various boundaries of the Arabian plate are as important to the stated objectives of better understanding the seismicity and seismotectonics of the greater Middle East region and should be pursuit in the future.

At present, efforts are under way to perform P- and S-wave tomographic studies of the crustal structure in the Middle East. These efforts will include a region including central and eastern Turkey, Iraq and Iran. Waveform analysis of NISN data from 2006 through 2008 has been completed and will be supported by data from IRIS and ORFEUS stations throughout the region. The goal is to complement the results of the surface wave analysis by increasing the resolution and detail of the imaged crustal structures.

REFERENCES

Dewey J. F., Hempton M. R., Kidd W. S. F. and Sengor A. M. C. (1986). Shortening of continental lithosphere; the neotectonics of eastern Anatolia, a young collision zone, eds. Coward M.P. et al., *Geol. Soc. Spec. Pub.*, 19: 3–36.

Herrmann, R. B. (2006). Surface waves, receiver functions and crustal structure, in Computer Programs inSeismology, Version. 3.30, Saint Louis University, St. Louis, MO (URL: http://www.eas.slu.edu/People/RBHerrmann/CPS330.html).

Reilinger, R. E. (2009). Seismotectonics of the Arabian Plate and its Boundaries III, *Eos Trans. AGU*, *90*(52), Fall Meet. Suppl., Abstract T54C-2011.

Rotstein Y. and A. L. Kafka (1982), Seismotectonics of the southern boundary of Anatolia, eastern Mediterranean region: subduction, collision, and arc jumping, *J. Geophys. Res.* 87: 7694–7706.

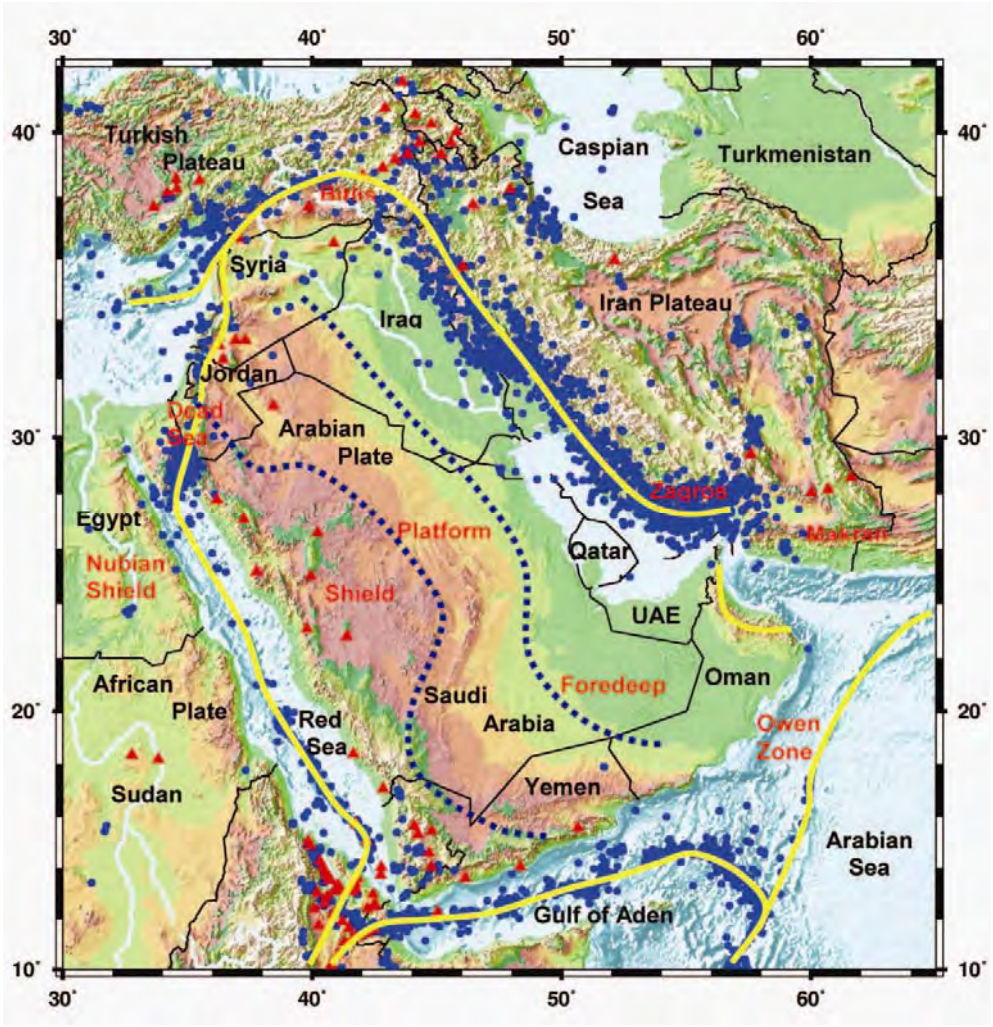

Figure 1. Map of the Arabian Peninsula and surrounding regions. The major geographic, tectonic and geologic features are labeled. The plate boundaries are marked with yellow lines. Earthquakes and volcanoes are shown as blue circles and red triangles, respectively. The depicted seismicity is for the time period between 1975 and 2001 for events of Mb ≥ 4.0.

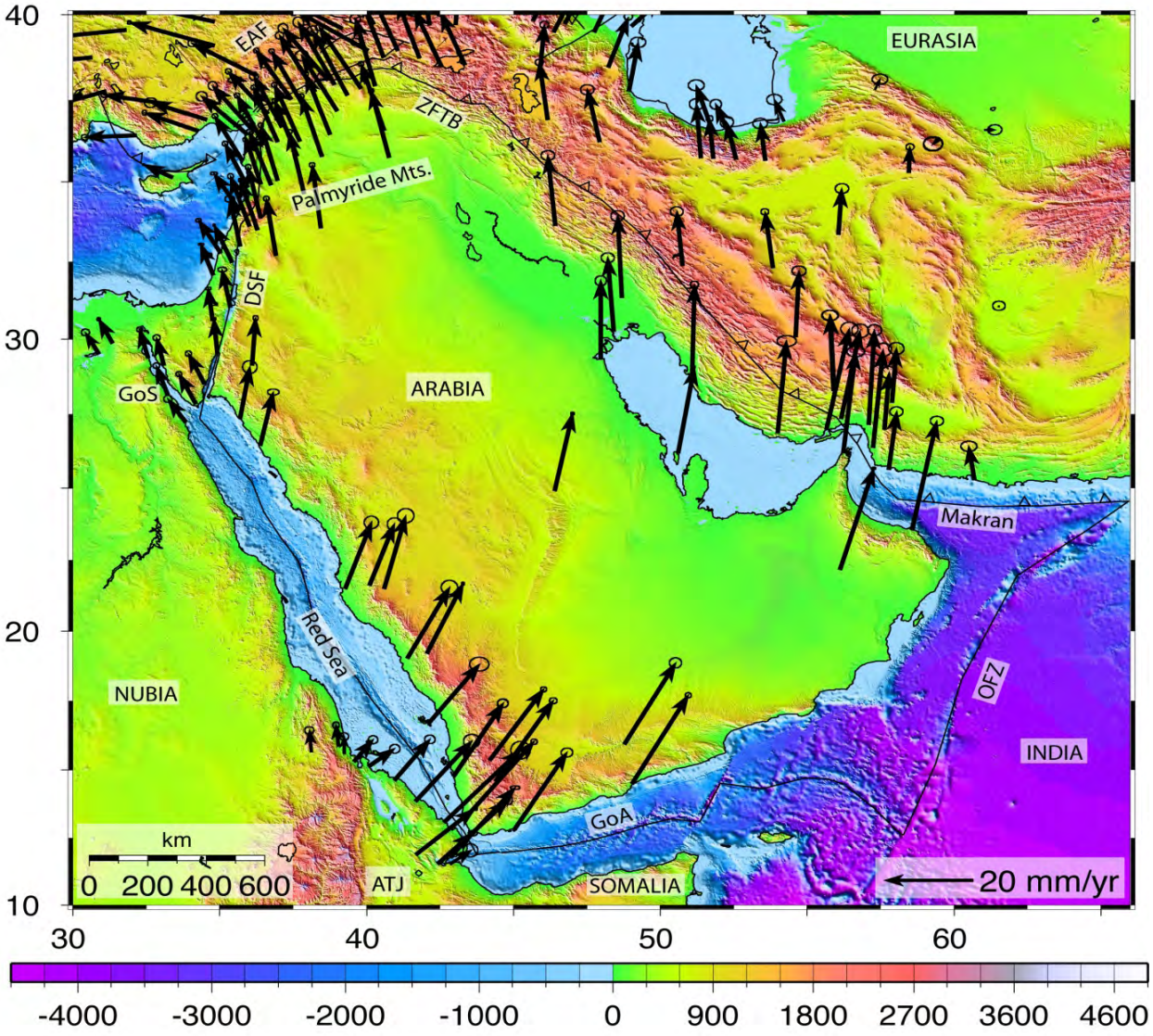

Figure 2. GPS-derived velocity field of the Arabian, African and Eurasian plates, showing counter-clockwise rotation of the Arabian Peninsula with a velocity of 20 – 30 mm/yr (Reilinger et al., 2008).

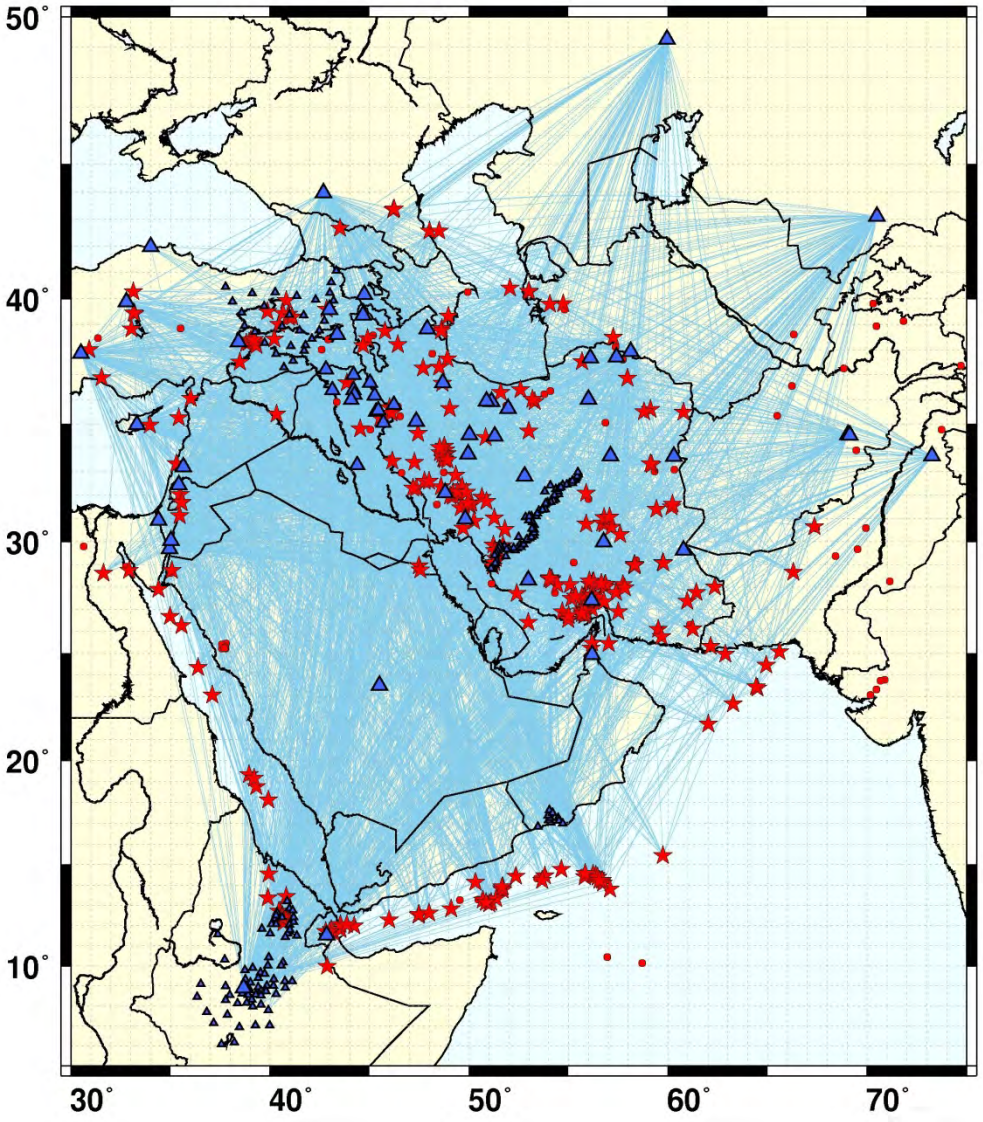

Figure 3. Mixed path dispersion curve coverage of the study area. A total of 262 earthquakes, denoted by red stars, were used for the surface wave analysis. The large blue triangles indicate the locations of the NISN, IRIS, ORFEUS, and IIEES seismic stations where the analyzed waveforms were recorded.

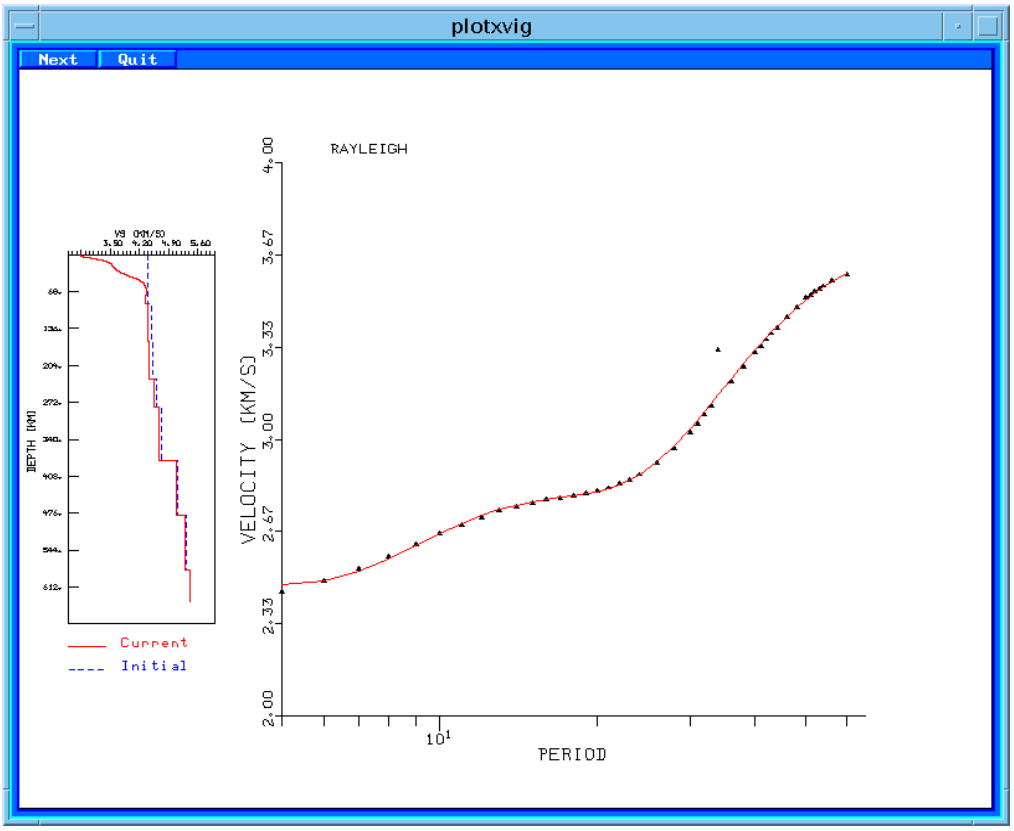

Figure 4. Example of dispersion curve inversion (right) and estimation of corresponding velocity model (left) along a ray path from epicenter to recording station. The black triangles (right) depict the observed dispersion curve data resulting from MFT, while the red line represents is the best dispersion curve fit. The velocity depth model (left) is characterized by its starting model, shown by the blue dashed line, and the resulting velocity profile given by the solid red line.

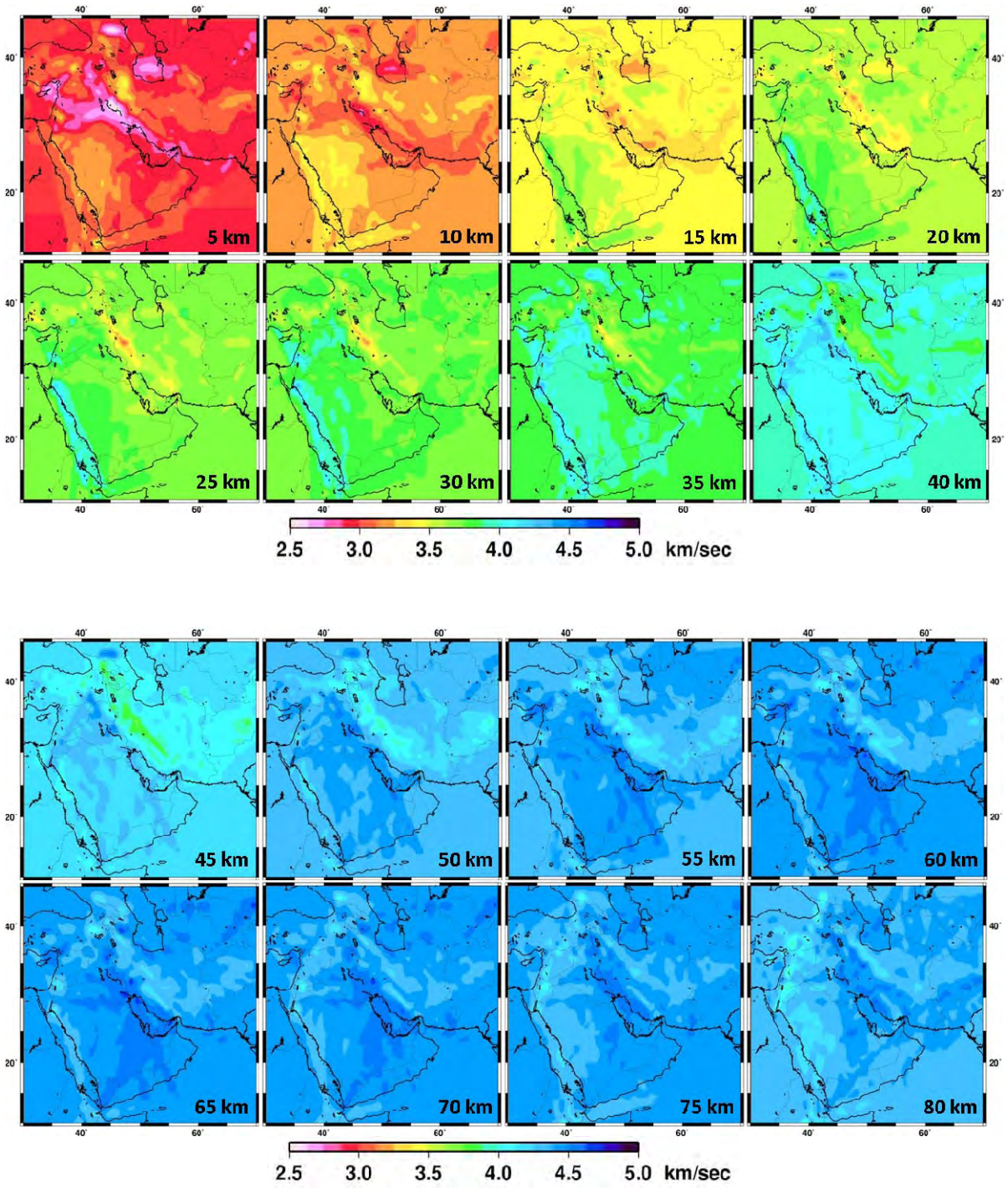

Figure 5. Maps showing the three-dimensional shear wave velocity variations in the Middle East for selected depths (5-80 km) derived from Rayleigh surface wave dispersion curves.

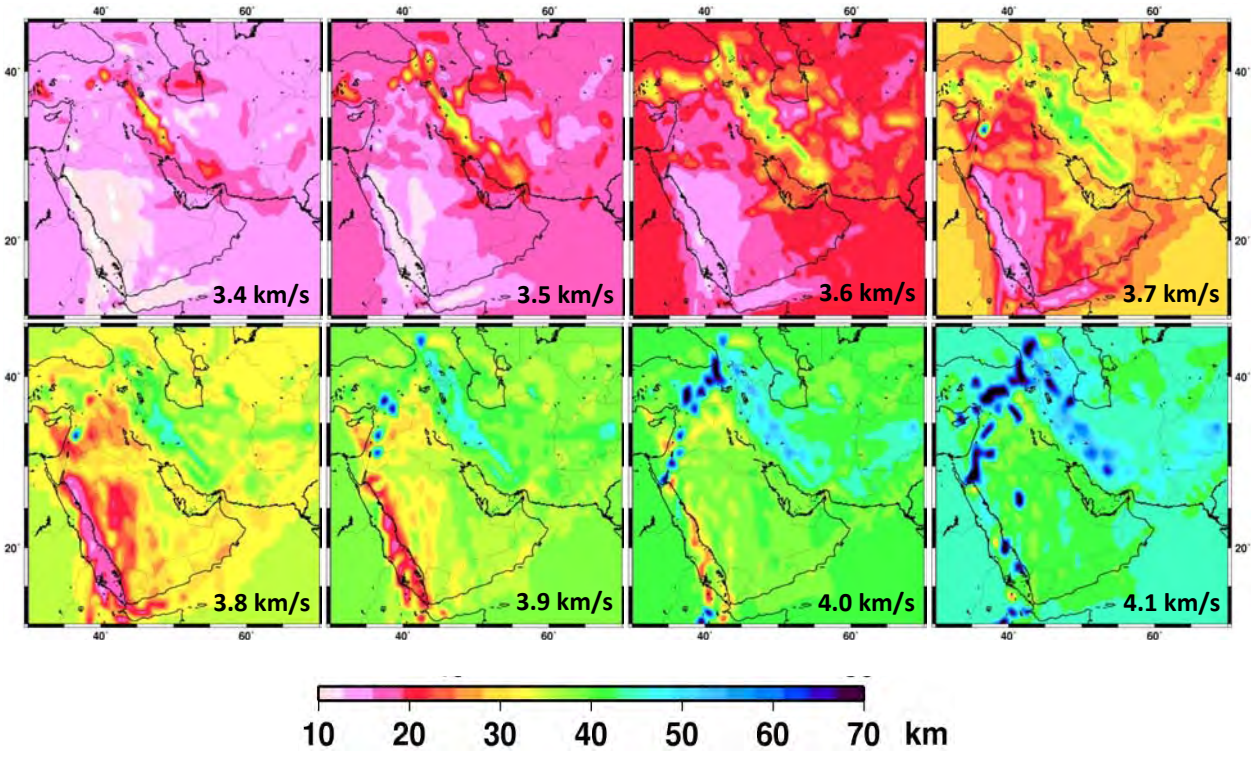

Figure 6 Maps showing the three-dimensional depth distribution of fixed shear wave velocity values (3.4 – 4.1 km/s) in the Middle East. A depth color scale is shown at the bottom.

DEVELOPMENT AND TUNING OF A 3D STOCHASTIC INVERSION METHODOLOGY TO THE EUROPEAN ARCTIC

Juerg Hauser[1], Kathleen M. Dyer[2], Michael E. Pasyanos[2], Hilmar Bungum[1], Jan Inge Faleide[3], and Stephen A. Clark[3]

NORSAR[1], Lawrence Livermore National Laboratory[2], and University of Oslo[3]

Sponsored by the National Nuclear Security Administration

Award Nos. DE-AC52-08NA28651 and DE-AC52-07NA27344
BAA08-38

ABSTRACT

The development of three-dimensional (3D) seismic models for the crust and upper mantle has traditionally focused on finding one model that provides the best fit to the data, while observing some regularization constraints. Such deterministic models, however, ignore a fundamental property of many inverse problems in geophysics: nonuniqueness. It is likely that if a model can be found to satisfy given datasets, an infinite number of alternative models will exist that satisfy the datasets equally well. Our solution to the inverse problem of developing a seismic model for the Barents Sea, given various datasets, is therefore a probabilistic model, a posterior distribution of models that satisfy the data to the same degree. We use a Markov Chain Monte Carlo algorithm to sample the unknown posterior distribution, which describes the ensemble of models that are in agreement with prior information and the datasets. An example of prior information used in this work is the extent of regions with limited sediment coverage. The datasets we use are thickness constraints, velocity profiles, gravity data, surface-wave group velocities, and body-wave travel times. The model introduced here for the crust and upper mantle structure of the European Arctic is parameterized by a set of one-dimensional (1D) models positioned at the nodes of an arbitrary mesh. Two linear functions in the sediment layer, three in the crystalline crust, and three in the mantle are used to describe the seismic parameters (i.e., Vp, Vs, and density) as a function of depth. This allows changes of seismic parameters within the sediments, the crystalline crust, and the upper mantle without introducing artificial discontinuities that would result from parameterizing the structure using layers with constant seismic parameters. The samples drawn from the posterior distribution using a Markov Chain Monte Carlo technique form our probabilistic model. Analyzing this ensemble of models that fit the data allows us to estimate a mean model and the standard deviation for the model parameters, i.e., their uncertainty. Maps of sediment thickness and thickness of the crystalline crust derived from the posterior distribution are in good agreement with knowledge of the regional tectonic setting. The predicted uncertainties, which are equally important as the absolute values, correlate well with the variation in data coverage and data quality in the region. The real power of a probabilistic model, however, lies in predicting observables and their uncertainties. A probabilistic model allows estimation of seismic-event location uncertainties that take into account uncertainties in the velocity model and the inability to absolutely identify the onset of the arrival associated with a phase.

OBJECTIVES

The area of interest for this study is the European Arctic, in particular the Barents Sea and surrounding regions such as the Norwegian-Greenland Sea, the Southern Eurasian Basin, Novaya Zemlya, the Kara Sea, the East European Lowlands, the Kola Peninsula, and the Arctic plate boundary (Figure 1). The complex geology of the region, encompassing oceanic crust, continental shelf regions, rift basins, and old cratonic crust and the nonuniform coverage of the region by data with varying levels of uncertainty, makes the European Arctic a challenging setting for any imaging technique and therefore an ideal environment for the development and application of a probabilistic approach to seismic imaging.

The aim of this study was to develop a probabilistic seismic model, i.e., sample the posterior distribution consisting of the ensemble of models that are all in agreement with the data. The datasets used in this work are thickness constraints, velocity profiles, gravity data, surface-wave group velocities, and body-wave travel times. The stochastic inversion methodology that has been further developed in this study has been used previously by Pasyanos et al. (2006) to derive a geophysical model for the Yellow Sea and Korean Peninsula region, given surface-wave group velocities, body-wave travel times, receiver functions, and gravity data.

The project has achieved three objectives. First, we have developed a probabilistic seismic model for the European Arctic that not only harnesses the information available in more datasets than used in previous models but also employs an improved model parameterization. Second, we have shown how a probabilistic model can be used in seismic monitoring to estimate location uncertainties that are caused by model uncertainties. Third, the introduction of improved forward solvers, an arbitrary mesh, and linear transitions to represent structure will facilitate the application of the methodology to other regions.

RESEARCH ACCOMPLISHED

The development of a probabilistic seismic model for the European Arctic involved improving the methodology employed by Pasyanos et al. (2006). The introduction of a new model parameterization (Figure 2) that allows for an arbitrary mesh and uses two linear transitions in the sediments and three in the crystalline crust and upper mantle to represent the seismic parameters (Vp, Vs, and density) made it necessary to develop new forward solvers for the various datasets. The parameterization of structure associated with every 1D model represents a trade-off between trying to describe the structure as accurately as possible and limiting the number of parameters to avoid having to search a model space that is unnecessarily large. The parameters are not completely independent of each other due to the constraints imposed on the prior distribution (see below). The node spacing of 83 km was chosen based on the expected resolution of the data and the computational resources available.

When developing regional seismic models, one often uses layers with constant seismic parameters to represent structure (e.g. Pasyanos et al., 2006 and Ritzmann et al., 2007). For deep sedimentary basins like the East Barents Sea Basin, however, the rate of increase of Vp, Vs, and density decreases with depth, and the seismic parameters at the bottom of the basin are comparable to those of the underlying basement. Two layers that allow for a linear increase of the seismic parameters allow us to model this behavior better than two layers with constant seismic parameters.

The datasets used in this study were described in a previous MRR contribution (Hauser et al., 2009). We therefore focus here on the probabilistic model, its application, and the inversion methodology.

Markov Chain Monte Carlo Algorithm

The Markov Chain Monte Carlo (MCMC) algorithm employed here is a derivative of the Metropolis algorithm by Metropolis et al. (1953) as described by Mosegaard and Tarantola (1995). MCMC algorithms sample the model space at a rate proportional to the posterior probabilities, a process known as importance sampling, thereby empirically reconstructing the unknown posterior distribution. They achieve this by moving through model space according to the posterior probabilities for these models, thereby performing a guided search and focusing on regions that better fit the prior information and the data. In contrast, a Monte Carlo algorithm samples the model space purely randomly. The definition of which models are accessible from a given model when constructing the Markov Chain is critical for the success of a probabilistic inversion. If we perturb the model too much, we will be sampling the model space randomly instead of performing a guided search. On the other hand, if we perturb the model too little, we might not explore the model space sufficiently.

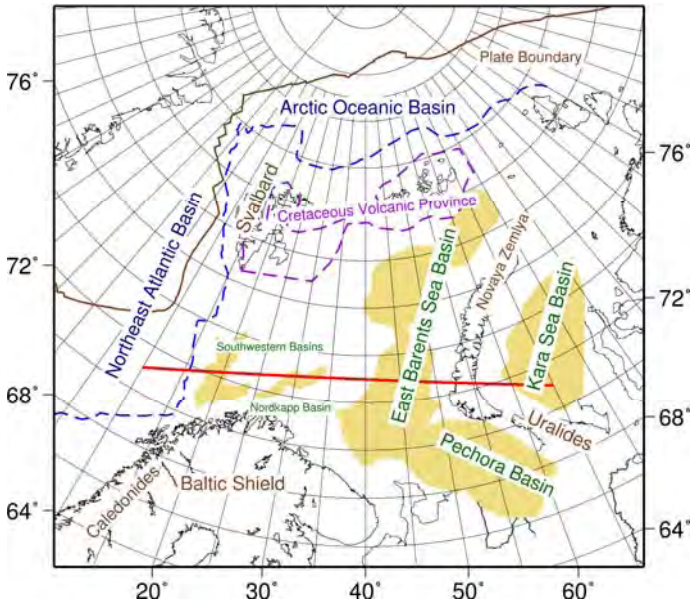

Figure 1. Simplified tectonic map of the region after Ritzmann et al. (2007) and Bird (2003). The plate boundary is given by the brown line and the continent-ocean boundary by the dashed blue line. Beige areas represent the major sedimentary basins in the region. The cross section along which we will examine our probabilistic model in Figure 5 is outlined in red.

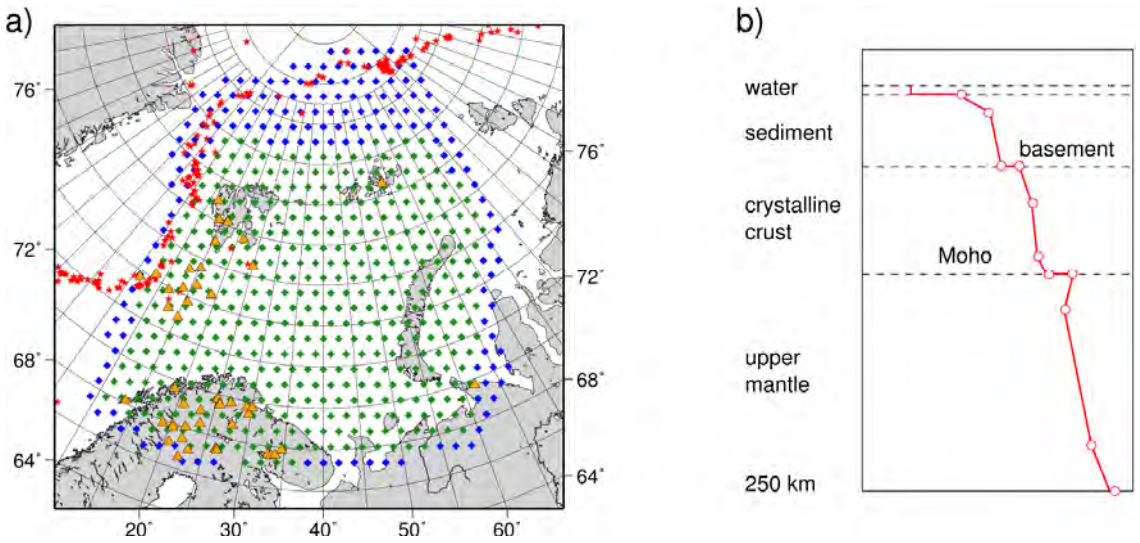

Figure 2. Parameterization of the target region for this study. (a) The red stars are the earthquakes in the target region, according to the Global CMT catalog (1971–2008), and seismic stations used in this study are marked by orange triangles. The blue and green diamonds show the distribution of the 1D profiles used to describe the structure. For the blue diamonds, the starting model is based on CRUST 2.0 (Bassin et al., 2000); for the green diamonds, it is based on the crustal model of Ritzmann et al. (2007) and the mantle model of Levshin et al. (2007). (b) Diagram showing the constant gradient parameterization used to describe the seismic parameters as a function of depth.

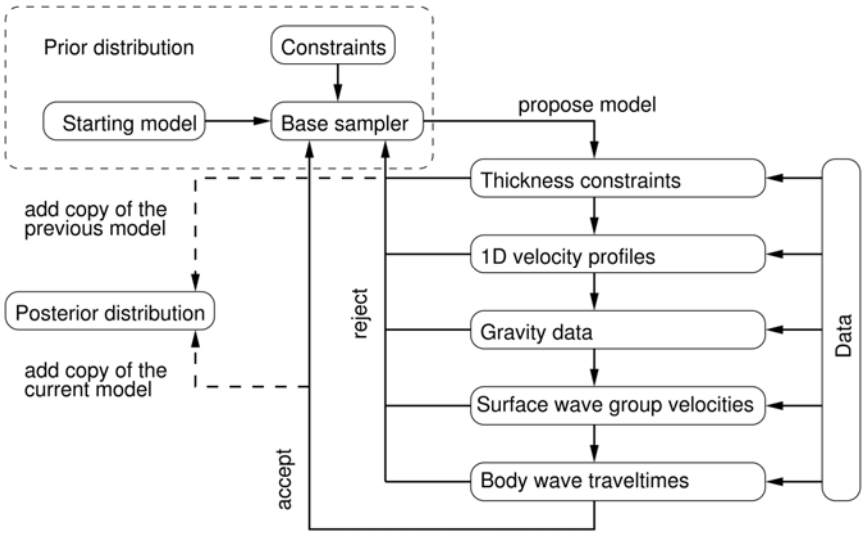

Figure 3. Flowchart showing the MCMC inversion methodology used to derive the probabilistic model.

As mentioned before, the success of an MCMC methodology relies partly on a mechanism for generating plausible models based on the prior information. In a Bayesian formulation, this process is known as sampling the prior distribution. The prior distribution is given by the starting model and constraints for the individual parameters. The most-basic constraints are the upper and lower limits and the standard deviation for the normal distribution, from which we randomly draw new model parameters when perturbing the model. More sophisticated constraints employed in this study are ranges for acceptable Vp/Vs and Vp/density ratios, a positive velocity contrast imposed across the Moho interface and across the interface between the sediments and the crystalline crust, and a limit on the maximum decrease of seismic parameters with increasing depth. Plausible ranges for seismic parameters in the area of interest and the relationship between them were derived from previous studies covering the region, in particular from Breivik et al. (2002).

Our MCMC algorithm shown in Figure 3 has two major components: (1) the base sampler, which proposes new models by randomly perturbing the current model, while observing the rules for the prior distribution; and (2) the datasets against which proposed models are tested. If all the models proposed by the base sampler are accepted, one recovers the prior distribution. The aim is to recover the posterior distribution, and proposed models are therefore tested against data. The datasets are tested in sequence, and a proposed model is added to the posterior set if it fits the data equally well or better for all the stages than the previous model that was added to the posterior set. A model with a worse fit to the data might also be accepted to the posterior set but with a probability dependent on the decrease in fit relative to the previous accepted model. In other words, the worse the fit to the data the more likely it is that the model is rejected. Accepting models with a worse fit to the data with a certain probability means that an MCMC algorithm can avoid a situation where the guided search might get trapped in a local minimum. For each chain we also randomly swap a subset of nodes in the starting model to ensure that we are exploring the model space sufficiently.

Probabilistic Seismic Model

Two separate runs of our MCMC algorithm with different seeds for the random number generator were used to generate our probabilistic model. In practice this means that we have explored the model space with two different chains starting at different points in model space. Once convergence is reached, however, the two chains are statistically similar. Our probabilistic model is based on a combination of the last 1/3 of the two chains, with each consisting of 12,000 iterations. Our samples of the posterior distribution are given by 4,000 models, where every second model is taken from the same chain, thus we are mixing the chains. We determined an average model to compare the results of this study to other studies of the same region. The real power of a probabilistic model lies however in the fact that it describes the distribution of models that fit the data, as we will see later in the location example.

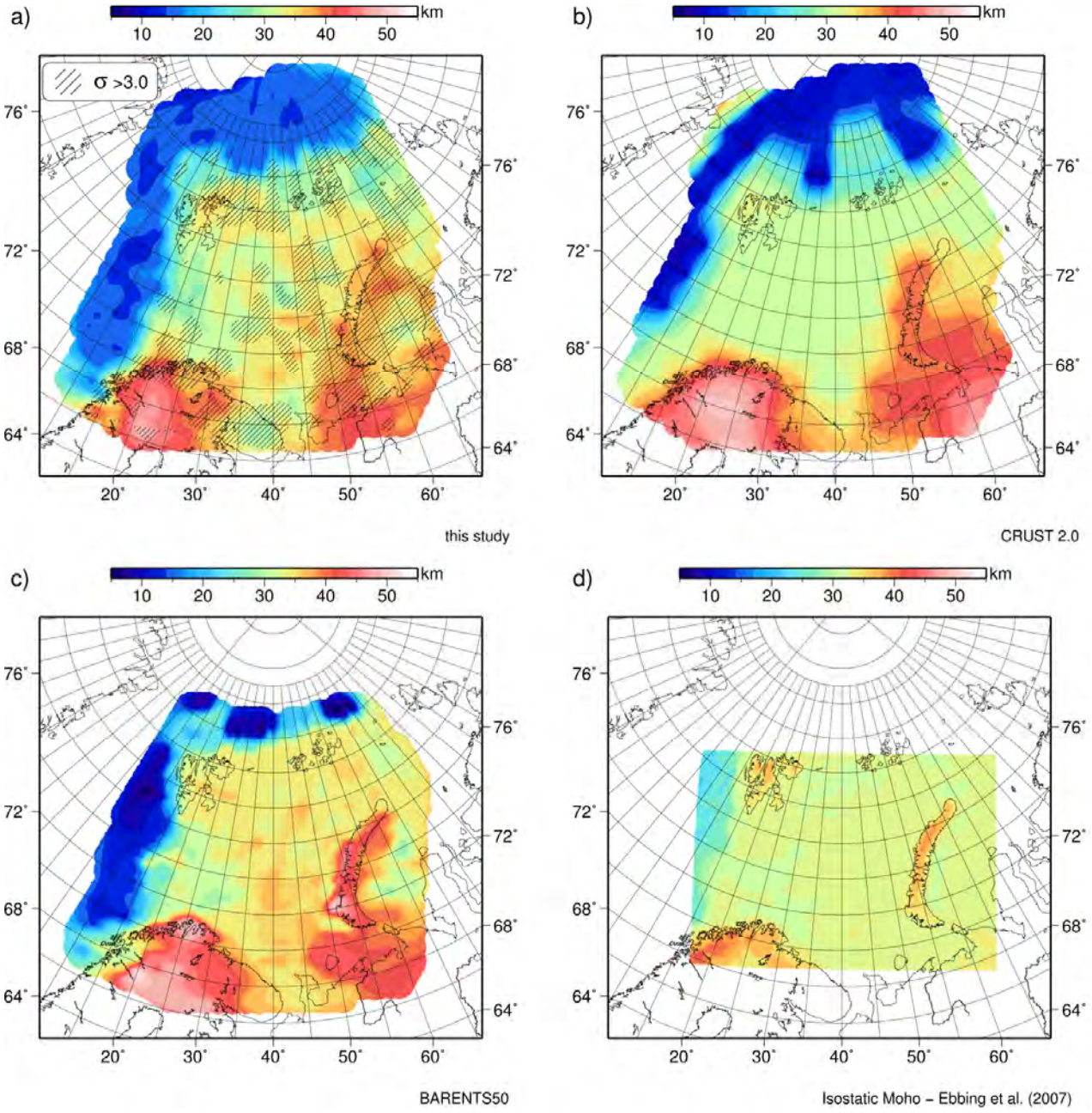

Figure 4. Depth to Moho: (a) Mean model obtained in this study, (b) CRUST 2.0 after Bassin et al. (2000), (c) BARENTS50 after Ritzmann et al. (2007), and (d) isostatic Moho of Ebbing et al. (2007).

Figure 4 shows the depth to Moho in this study, CRUST 2.0 (Bassin et al., 2000), BARENTS50 (Ritzmann et al., 2007) and for an isostatic Moho computed by Ebbing et al. (2007). It is important to keep in mind that the different models have different spatial resolutions; our model, for example, has a node spacing of 83 km, while CRUST 2.0 uses a 2-by-2–degree grid. This makes it necessary to resample the models for this comparison. Unlike the other models, our probabilistic model also provides estimates for the uncertainties, thus we can compute a standard deviation in addition to the mean of our samples of the posterior distribution. We have hatched the areas where the standard deviation on the Moho exceeds 3 km, indicating where this parameter is poorly constrained. The models are generally similar, with some notable differences. For example, most models see more complexity within the major tectonic provinces than the relatively simple CRUST 2.0 model. Also, the Moho recovered by BARENTS50 appears more detailed than the Moho recovered in the present study. This comes as no surprise when one takes into

account that BARENTS50 has a spatial resolution of 50 km. The models differ the most from each other around Novaya Zemlya and in the Kara Sea. It is interesting that this is also where the uncertainties in the depth to Moho are generally larger than 3 km in our study. The isostatic modeling of Ebbing et al. (2007) suggests, as expected, a shallower and smoother Moho than the other, seismically based models.

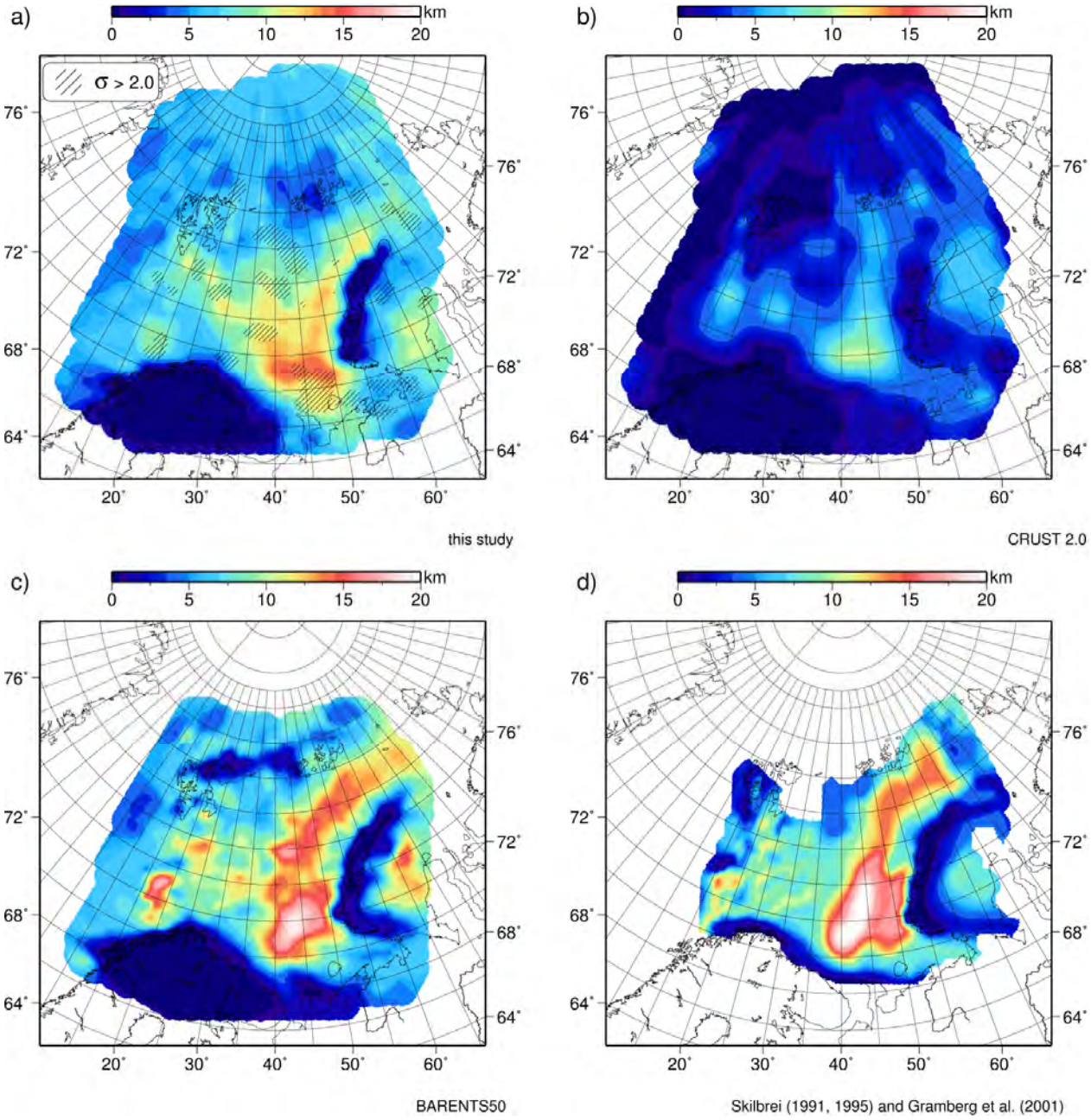

Figure 5. Depth to basement: (a) Mean model obtained in this study, (b) CRUST 2.0 after Bassin et al. (2000), (c) BARENTS50 after Ritzmann et al. (2007), and (d) compilation of depth to basement by Smelror et al. (2009), based on the work by Skilbrei (1991,1995) and Gramberg et al. (2001).

A similar comparison among the models for the depth to basement is given in Figure 5. Here we compare the mean of our probabilistic model with CRUST 2.0 (Bassin et al., 2000), BARENTS50 (Ritzmann et al., 2007) and a compilation of depth to basement by Smelror et al. (2009) derived from magnetic and seismic data based on the work by Skilbrei (1991,1995) and Gramberg et al. (2001). We have again hatched areas in our map indicating

regions with poor constraint, where the standard deviation in depth to basement exceeds 2.0 km. In contrast to the different Moho results, the depth-to-basement topography varies significantly among the studies. There are differences in the overall depth and shape for the major basins between our study and the other studies. In a deep basin the sediments at the bottom of the basin become chemically compacted or weakly metamorphosed, making their seismic parameters comparable to those of the underlying basement. This means that datasets used in this study are not very sensitive to the position of this interface between the sediments and the crystalline crust. This also correlates with the relatively large uncertainties for the southern end of the East Barents Sea Basin.

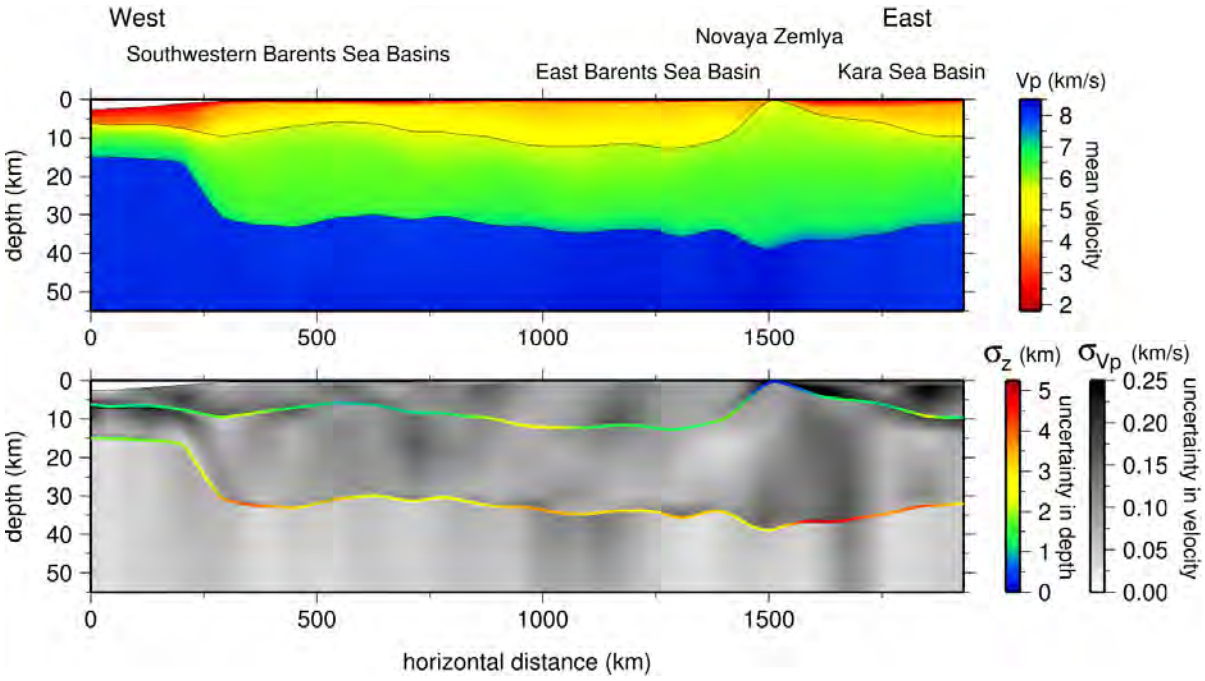

Figure 6. West-east cross section along the great circle path shown in Figure 1. The top panel shows Vp, and the bottom panel shows the uncertainty in Vp. In the bottom panel, interfaces are colored according to the uncertainty in depth.

Figure 6 shows a west-to-east cross section through our probabilistic model. Unlike cross sections farther north across the western continental margin, we find a relatively rapid transition in crustal thickness and see an increase in crustal thickness associated with Novaya Zemlya. The highest uncertainty in depth to Moho lies below the Kara Sea. This is related to the weak constraints on the Moho here: gravity data and a velocity profile with a relatively high uncertainty, with no body waves sampling the Moho. We clearly recover the East Barents Sea and Kara Sea basin. The sedimentary basins in the southwestern Barents Sea, on the other hand, are only 10s of kilometers wide. The node spacing of 83 km used in this study means that we cannot recover these basins. What we are able to recover is the fact that the sedimentary layer is on average thicker if there are several sedimentary basins a few 10s of kilometers wide.

The sediments on the epicontinental Barents Shelf have significantly higher velocities than sediments covering the oceanic crust. This feature of our model can be linked to the uplift of the region in the Neogene and the repeated phases of glaciation in the Barents Sea during the late Pliocene and Pleistocene (Smelror et al., 2009). Uplift and glaciation cause erosion of the sediments covering the Barents Shelf and the deposition of large amounts of young sediments into major submarine fans along the western and northern margin. These young sediments are less consolidated and have, as a consequence, lower seismic velocities when compared to the older sediments covering the Barents Shelf. The uppermost sediments in the Kara Sea Basin show slightly lower velocities than the uppermost sediments in the East Barents Sea Basin. This correlates with the interpretation that only during the maximum extent of glaciation in the late Pleistocene did the ice sheet reach into the Kara Sea (Smelror et al., 2009). Sediments in the Kara Sea have therefore experienced less erosion, leaving less compacted sediment exposed at the seafloor, possibly together with deposits from other periods of glaciation.

Probabilistic Earthquake Location

The nonlinear problem of seismic event location using body-wave travel times is often solved using nonlinear iterative approaches. However, a poor station distribution and a complex 3D velocity structure contribute to the nonlinearity of the location problem and create potential instabilities. The potential failure of linearization, together with the need for more comprehensive location uncertainty information in the form of a probability density function, has led to the formulation of numerous probabilistic approaches (e.g., Kennett and Sambridge, 1992; Billings, 1994; Lomax et al., 2000). Location uncertainty is caused by pick uncertainties (i.e., the inability to accurately estimate onset time for a phase) and uncertainties in the velocity models. Most estimates for location uncertainty do not however take into account the uncertainties in the model used to predict the travel times. They are solely based on pick uncertainties. A probabilistic model, on the other hand, allows a prediction of observables and their uncertainties.

The distribution of an observable (i.e., its value and uncertainty), given a probabilistic model, can be recovered by calculating its values for every model belonging to the posterior set that defines the probabilistic model. Similarly, it is possible to obtain an estimate for the location uncertainty of a seismic event due to model uncertainty by locating the event for all the models that compose the posterior set. Here we use an MCMC approach to approximate the posterior distribution for the origin time and location of an earthquake. The maximum of the posterior distribution then defines the hypocenter location and origin time.

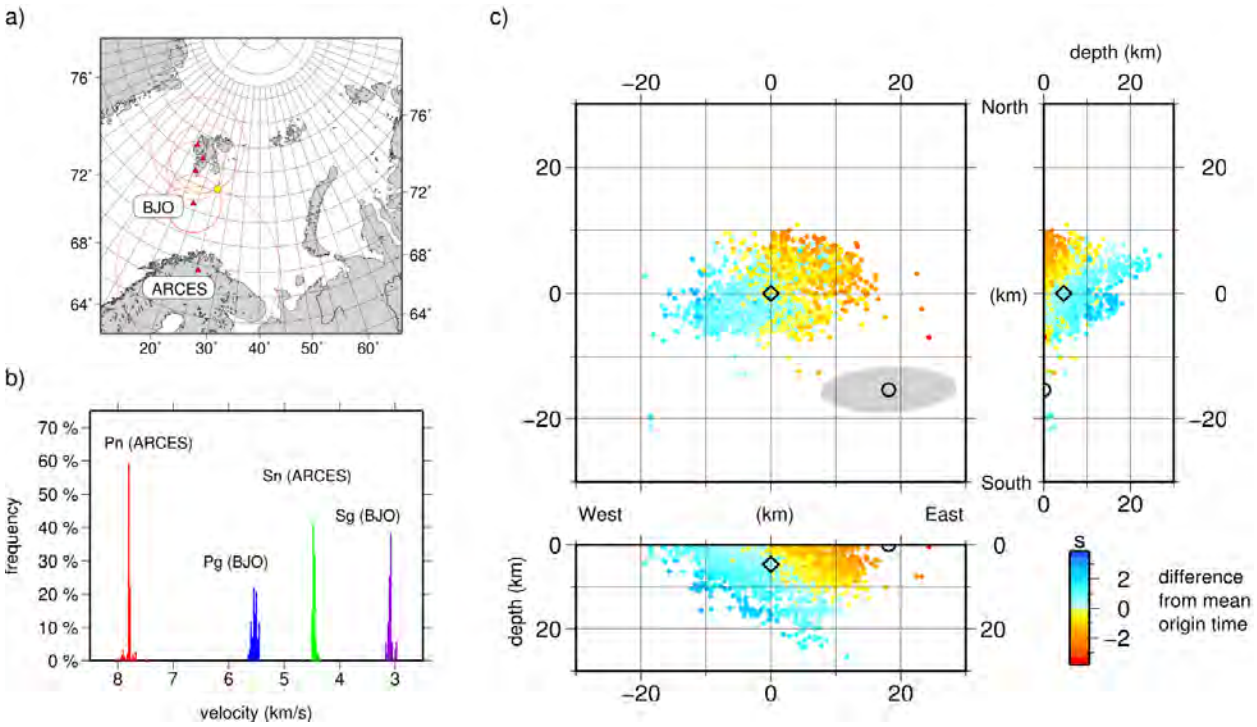

Figure 7. Probabilistic location of an earthquake, taking model uncertainties into account: (a) station distribution, (b) distribution of average path velocities for regional phases for two stations used in the location example, and (c) hypocenter and origin time of the earthquake computed for each of the 4,000 models forming our probabilistic model. The mean location is given by the black diamond. The points are colored according to the deviation from the mean origin time of our set of locations. The black circle marks the location of the event computed using a 1D velocity model and a fixed depth of 0 km, and the error ellipse is given by the gray shaded area.

We use an earthquake in the western Barents Sea to investigate the influence of model uncertainties on location uncertainties. Figure 7a shows the station distribution, and Figure 7b shows the distribution of the mean path velocities, between the event and two selected stations. For longer paths that reside primarily in the mantle, the mean velocity is less influenced than for shorter paths that reside in the crust. We have located the earthquake for each of

the 4,000 models in the posterior distribution. Figure 7c shows the 4,000 locations obtained and thereby provides an estimate for the location uncertainty from model errors alone, together with an event location obtained using a regional 1D velocity model. All stations available for the location of this event lie to the west of the earthquake. This results in both the error ellipse for the 1D velocity model solution and the cloud of locations being elongated in the west-east direction. We observe a linear trend between late deep-event locations to the southwest and early shallow locations to the northeast. Bondár et al. (2004) showed that for excellent station coverage, depth and origin time are more sensitive to the velocity model than the epicenter location. We find that for an uneven station distribution as shown here, the epicenter location seems to be equally sensitive to the velocity model as to the origin time and depth.

CONCLUSIONS AND RECOMMENDATIONS

We have successfully employed a probabilistic approach for the development of a data-driven regional seismic model for the European Arctic. We have compared the mean model of our posterior distribution with other models that cover the region and find that it captures the features that can be resolved with a node spacing of 83 km. Our probabilistic model not only provides images of the subsurface, together with estimates of uncertainties, it also allows for the prediction of observables and uncertainties. This can be used to derive seismic event location uncertainties from model uncertainties and can in the future be used for location algorithms that take model uncertainties in addition to uncertainties in onset time into account.

The introduction of an arbitrary mesh to represent structure means that future applications of the methodology could include optimizing the mesh as part of the inversion. Trans-dimensional MCMC algorithms (e.g., Green, 1995) provide a framework for situations where the optimum number and distribution of model parameters is unknown. Such an algorithm would allow optimizing the distribution and number of nodes used to describe structure as part of the inversion and thereby account for the differences in data quality and data density between the eastern and western part.

The success of a probabilistic technique for the development of a regional seismic model relies on a mechanism to propose plausible models. In this context, choosing plausible ranges for the ratios between seismic parameters is as important as the ranges for individual values. Ultimately, one is only interested in testing models for their fit to the data if they are plausible from a geological, geodynamical, and compositional point of view. The primary application of the type of models developed here is the location of seismic events. On the other hand, a probabilistic framework where we would invert for composition and temperature instead of velocity and density is feasible and could be a valuable tool for understanding the nature of the upper mantle in the European Arctic and in particular of the eastward-dipping high-velocity anomaly under the Barents Sea and Kara Sea (Ritzmann and Faleide, 2009).

ACKNOWLEDGEMENTS

We thank NOTUR (The Norwegian Metacenter for Computational Science) and the University of Oslo for providing the computational resource on the Titan III high-performance computing facilities. We thank Stephen Myers (Lawrence Livermore National Laboratory) for contributing the ground-truth data and NGU (The Geological Survey of Norway) for providing the depth-to-Moho and depth-to-basement data shown in Figures 4d and 5d. We also thank Johannes Schweitzer (NORSAR) for contributing the P observation from deep seismic experiments.

REFERENCES

Bassin, C., G. Laske, and G. Masters (2000). The current limits of resolution for surface wave tomography in North America, *EOS Trans. AGU* 81: F897.

Billings, S. (1994). Simulated annealing for earthquake location, *Geophys. J. Int.* 118: 680–692.

Bird, P. (2003). An updated digital model of plate boundaries, *Geochem. Geophys. Geosyst.* 4: 1027, doi:10.1029/2001GC000252.

Bondár, I., S. Myers, E. Engdahl, and E. Bergman (2004). Epicentre accuracy based on seismic network criteria, *Geophys. J. Int*., 156: 483–496, doi:10.1111/j.1365-246X.2004.570 02070.x.

Breivik, A., R. Mjelde, P. Grogan, H. Shimamura, Y. Murai, Y. Nishimura, and A. Kuwano (2002). A possible Caledonide arm through the Barents Sea imaged by OBS data, *Tectonophys.* 355: 67–97.

Ebbing, J., C. Braitenberg ,and S. Wienecke (2007). Insights into the lithospheric structure and the tectonic setting of the Barents Sea region by isostatic considerations, *Geophys. J. Int.* 171: 1390–1403, doi:10.1111/j.1365-246X.2007.03602.x.

Gramberg, I. S., V. Y. Glebovsky, G. E. Grikurov, V. L Ivanov, E. A. Korago, M. K. Kos'ko, S. P. Maschenkov, A. L. Piskarev, Y. E. Pogrebitsky, Y. V. Shipelkevitch, and O. I. Suprunenko (2001). Eurasian arctic margin: Earth science problems and research challenges, *Polarforschung* 69: 3–25.

Green, P. (1995). Reversible jump Markov chain Monte Carlo computation and Bayesian model determination, *Biometrika* 82: 711–732.

Hauser, J., K. Dyer, M. E. Pasyanos, H. Bungum, J. I. Faleide, and S. A. Clark (2009). Development and tuning of a 3-D stochastic inversion methodology to the European Arctic, in *Proceedings of the 2009 Monitoring Research Review*: *Ground-Based Nuclear Explosion Monitoring Technologies*, LA-UR-09-05276, Vol. 1, pp. 73–83.

Kennett, B. L. N. and M. Sambridge (1992). Earthquake location—Genetic algorithms for teleseismic location, *Phys. Earth Planet. Inter.* 75: 103–110.

Levshin, A., J. Schweitzer, C. Weidle, N. Shapiro, N. Maercklin, and M. Ritzwoller (2007). Surface wave tomography for the Barents Sea and surrounding regions, *Geophys. J. Int*. 170: 441–459, doi:10.1111/j.1365-246X.2006.03285.x.

Lomax, A., J. Virieux, P. Volant, and C. Berge (2000). Probabilistic earthquake location in 3D and layered models: Introduction of a Metropolis-Gibbs method and comparison with linear locations, in *Advances in Seismic Event Location*, C. H. Thurber and N. Rabinowits, Eds. Dordrecht, Netherlands: Kulwer.

Metropolis, N., A. Rosenbluth, M. Rosenbluth, A. Teller, and E. Teller (1953). Equation of state calculations by fast computing machines, *J. Chem. Phys*. 21: 1087–1092.

Mosegaard, K. and A. Tarantola (1995). Monte Carlo sampling of solutions to inverse problems, *J. Geophys. Res*. 100: B7, 2,431–12,447.

Pasyanos, M. E., G. A. Franz, and A. L. Ramirez (2006). Reconciling a geophysical model to data using a Markov Chain Monte Carlo algorithm: An application to the Yellow Sea-Korean Peninsula region, *J. Geophys. Res.* 111: B03313, doi:10.1029/2005JB003851.

Ritzmann, O. and J. Faleide (2009). The crust and mantle lithosphere in the Barents Sea/Kara Sea region, *Tectonophys.* 470: 89–104, doi:10.1016/j.tecto.2008.06.018.

Ritzmann, O., N. Maercklin, J. I. Faleide, H. Bungum, W. D. Mooney, and S. T. Detweiler (2007). A 3D geophysical model for the crust in the greater Barents Sea region: Model construction and basement characterization. *Geophys. J. Int*. 170: 417–435, doi: 10.1111/j.1365-246X.2007.03337.x.

Skilbrei, J. (1991). Interpretation of depth to the magnetic basement in the northern Barents Sea (south of Svalbard), *Tectonophys.* 200: 127–141.

Skilbrei, J. (1995). Aspects of the geology of the southwestern Barents Sea from aero-magnetic data, *NGU Bull.* 427, 64–67.

Smelror, M. O., O. Petrov, G. B. Larsen, and S.Werner (2009). *Geological History of the Barents Sea*. Geological Survey of Norway.

DEVELOPING REGIONALIZED MODELS OF LITHOSPHERIC THICKNESS AND VELOCITY STRUCTURE ACROSS EURASIA AND THE MIDDLE EAST FROM JOINTLY INVERTING P-WAVE AND S-WAVE RECEIVER FUNCTIONS WITH RAYLEIGH WAVE GROUP AND PHASE VELOCITIES

Jordi Julià[1], Andrew A. Nyblade[1], Arthur J. Rodgers[2], and Eric Matzel[2]

Penn State University[1] and Lawrence Livermore National Laboratory[2]

Sponsored by National Nuclear Security Administration

Award Nos. DE-AC52-09NA29322[1] and LL09-BAA09-13-NDD03[2]
Proposal No. BAA09-13

ABSTRACT

The main goal of this project is to develop regionalized models of lithospheric velocity structure for a wide variety of tectonic regions throughout Eurasia and the Middle East. We expect the regionalized models will improve the ability of the National Nuclear Security Administration (NNSA) labs to predict travel times for local and regional phases, such as Pg, Pn, Sn and Lg, as well as travel times for body waves at upper-mantle triplication distances in both seismic and aseismic regions. The models have been developed following a two-step approach: (i) first, one-dimensional (1D) velocity models for select broadband stations are obtained by jointly inverting P- and S-wave receiver functions and fundamental-mode group and phase dispersion velocities, and (ii) regionalized velocity models are then constructed by combining the 1D joint inversion models within each tectonic region and validated through regional waveform modeling. The velocity models thus obtained will also help inform and strengthen ongoing and future efforts within the NNSA labs to develop 3D velocity models for Eurasia and the Middle East, and will assist in obtaining model-based predictions where no empirical data are available and for improving locations from sparse networks.

During the first year of this project, we have developed 1D velocity models for 54 locations in Europe and 10 locations in the Middle East. Receiver functions were computed from teleseismic P- and S-waveforms recorded at open broadband stations and archived at the Data Management Center of the Incorporated Research Institutes for Seismology (IRIS-DMS), while dispersion velocities were obtained from an independent surface-wave tomography study for Eurasia and North Africa. Due to a combination of short recording time-windows and inefficient recording of teleseismic S-waves, some locations in Western Europe did not yield reliable S-wave receiver function estimates. To improve coverage in the Middle East, we also computed receiver functions at broadband stations from the Israel National Seismic Network, made available through the GEOFON program. The joint inversion models reveal important differences in lithospheric structure between the cratonic regions of Eastern Europe and the tectonic regions of Western Europe and the Middle East. Lithospheric structure in Eastern Europe is generally characterized by a gradual increase in seismic velocity with depth and no sharp velocity decrease down to maximum inversion depths of ~250 km. In contrast, the lithospheric mantle in Western Europe and the Middle East displays relatively sharp velocity variations, defining low-velocity zones of varying thicknesses, depths, and minimum velocities.

We are now combining the 1D velocity models obtained from the joint inversion of P- and S-wave receiver functions and dispersion velocities to construct regionalized velocity models for the tectonic regions of Europe and the Middle East. We have also identified a number of regional events in the Lawrence Livermore National Laboratory (LLNL) Ground-Based Nuclear Explosion Monitoring (GNEM) Seismic Research Database with well-determined source parameters and broadband recordings with ray-paths predominately in a single tectonic region (pure path propagation) to validate the regionalized velocity models. During the next year, we will continue the development of 1D velocity models from the joint inversion of receiver functions and dispersion velocities at open broadband stations in Asia and the construction and validation of regionalized velocity models for the corresponding tectonic regions.

OBJECTIVES

The main objective of this project is to develop new velocity models for Eurasia and the Middle East that improve the ability of the NNSA labs to predict travel times for local and regional phases, such as Pg, Pn, Sn and Lg, as well as travel times for body waves at upper-mantle triplication distances in both seismic and aseismic regions. The models are being developed by combining multiple seismic datasets through a joint inversion scheme that integrates the complementary constraints conveyed by each dataset while bridging resolution gaps among them. We are placing special emphasis on constraining the velocity structure of the lithospheric mantle, the thickness of the lithosphere, and the structure of the low-velocity zone under the lithosphere, as models that parameterize the upper mantle as infinitely thick cannot accurately model rays that penetrate below the lithosphere.

The seismic datasets contributing to the new velocity models include P-wave receiver functions (PRFs), S-wave receiver functions (SRFs), Rayleigh-wave group velocities, and Rayleigh-wave phase velocities. All datasets are sensitive to S-wave velocity structure, but are sensitive to complementary aspects of that structure. PRFs constrain detailed crust and uppermost mantle structure through S-P travel times and velocity contrast across discontinuities; SRFs constrain detailed lithospheric mantle structure, including lithospheric thickness, through P-S travel times and velocity contrasts across discontinuities; and surface-wave dispersion velocities constrain large-scale average velocity structure at frequency-dependent depth ranges across the crust and upper mantle. The combination produces S-wave velocity-depth profiles where the high-resolution details constrained by the receiver functions are superimposed on a background velocity model constrained by the dispersion velocities (Julià et al., 2000).

The velocity models are being developed following a two-step approach. In the first step, PRFs and SRFs obtained at individual broadband stations are jointly inverted with tomographic Rayleigh-wave dispersion velocities from independent surface-wave studies to develop local 1D velocity-depth profiles at each location. In the second step, the local 1D models are combined within geologic/tectonic terrain defined in published terrain maps, such as the WENA and UNIFIED models of Pasyanos et al. (2003, 2004), to produce regionalized velocity models of the crust and upper mantle for each terrain. The regionalized models represent the average velocity structure within the corresponding tectonic/geologic region.

The regionalized models are evaluated through 1-D waveform modeling for events with well-determined source parameters (depth, seismic moment, and focal mechanism) and broadband recordings with ray paths predominately in a single tectonic/geologic region. The model validation effort focuses on regions where there is good event-station coverage (i.e., pure path propagation within a region) over a range of local and regional distances and also includes an investigation of the misfits between data and synthetics to understand how the regionalized models need to be perturbed to improve the fits in phase and amplitude.

In addition to improving the ability of the NNSA labs to predict local and regional phase travel times in Eurasia and the Middle East, the regionalized velocity models will also help inform and strengthen ongoing and future efforts to develop 3-D velocity models for Eurasia and the Middle East. What is also important is that the new velocity models will assist in obtaining model-based predictions where no empirical data are available (e.g., Flanagan et al., 2006) and in improving locations from sparse networks (e.g., Schultz et al., 1998; Myers and Schultz, 2000).

RESEARCH ACCOMPLISHED

During the first year of application of this project, we have developed local 1D models for open broadband stations in Europe and the Middle East (Figure 1). We have concentrated on permanent broadband stations with operating times over 5 years in order to develop robust receiver function averages and to be able to inspect for azimuthal variations around the station. Using large datasets is especially important for obtaining reliable SRF estimates, as events must be within epicentral distance ranges that are narrower than those for PRFs (Wilson et al., 2006), and the deconvolution process is more unstable.

Data Gathering

Broadband seismic waveforms for computation of PRFs and SRFs were downloaded from the IRIS-DMC using the SOD utility (Owens et al., 2004) for all open broadband stations in Europe and the Middle East. For PRFs we selected events with magnitudes above 5.5 and sources at epicentral distances between 30^o and 90^o, and events with magnitudes above 6.0 and sources at epicentral distances between 60^o and 85^o were considered for SRFs. These

distance ranges keep the teleseismic P- or S-wave from interfering with other teleseismic arrivals and are commonly utilized for receiver function computation (e.g., Julià et al., 2008; Hansen et al., 2007).

The majority of the stations archived at the IRIS-DMC are contributed from temporary IRIS PASSCAL-type deployments, with short operation times, and concentrate on small geologic/tectonic regions, mostly in Europe. As a result, the station coverage of Eurasia and the Middle East is quite uneven and can be quite sparse in some areas. This problem is especially critical for the Middle East, where only 6 permanent broadband stations are available at the IRIS-DMC. To alleviate this situation, we downloaded data from the GEOFON data center for four additional open broadband stations operated by the Israeli Seismic Network. Overall, a dataset of 88,530 P-waveforms and 9,279 S-waveforms recorded at 64 broadband stations was assembled.

Fundamental-mode, Rayleigh-wave group velocities in Europe and the Middle East were obtained from the surface-wave tomography study of Pasyanos (2005). In that study, local dispersion curves were obtained for Eurasia, the Middle East, and North Africa by inverting fundamental-mode, Rayleigh-wave group velocities measured along more than 30,000 source-station paths with a conjugate-gradient method with variable smoothness. The resulting surface-wave tomography maps highlight lateral variations across the region for periods between 7 and 100 s, with a resolution approaching 1º.

Regional events with ray paths contained within terrains defined in the UNIFIED and WENA models are now being identified for Europe and the Middle East. These events will be utilized to evaluate the average velocity models that will be developed for the geologic/tectonic terrains from the local 1D models.

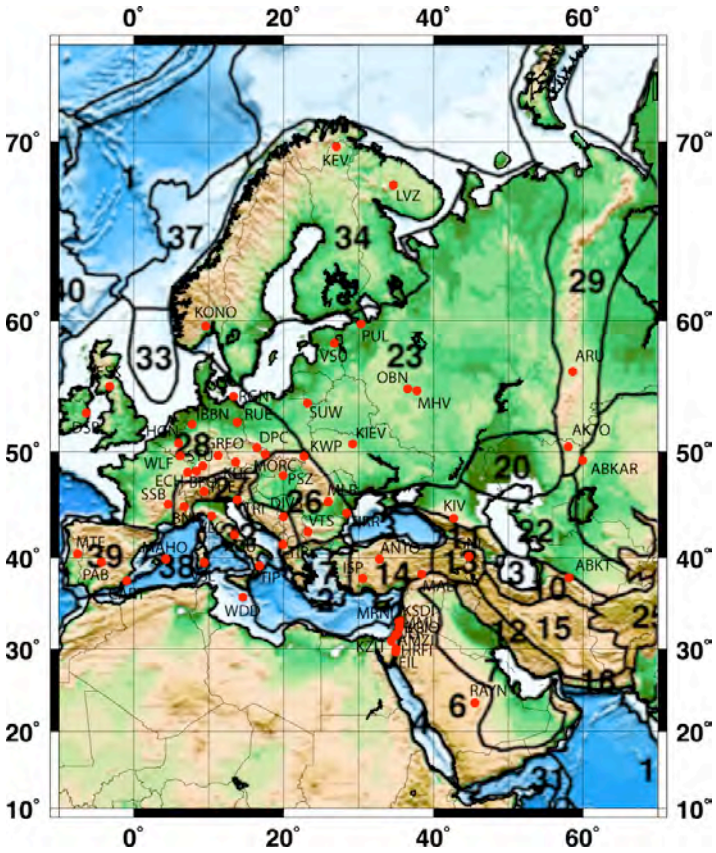

Figure 1. Topographic map of Europe and the Middle East showing the open broadband stations analyzed so far and the WENA/UNIFIED regions as defined in Pasyanos et al. (2003; 2004)

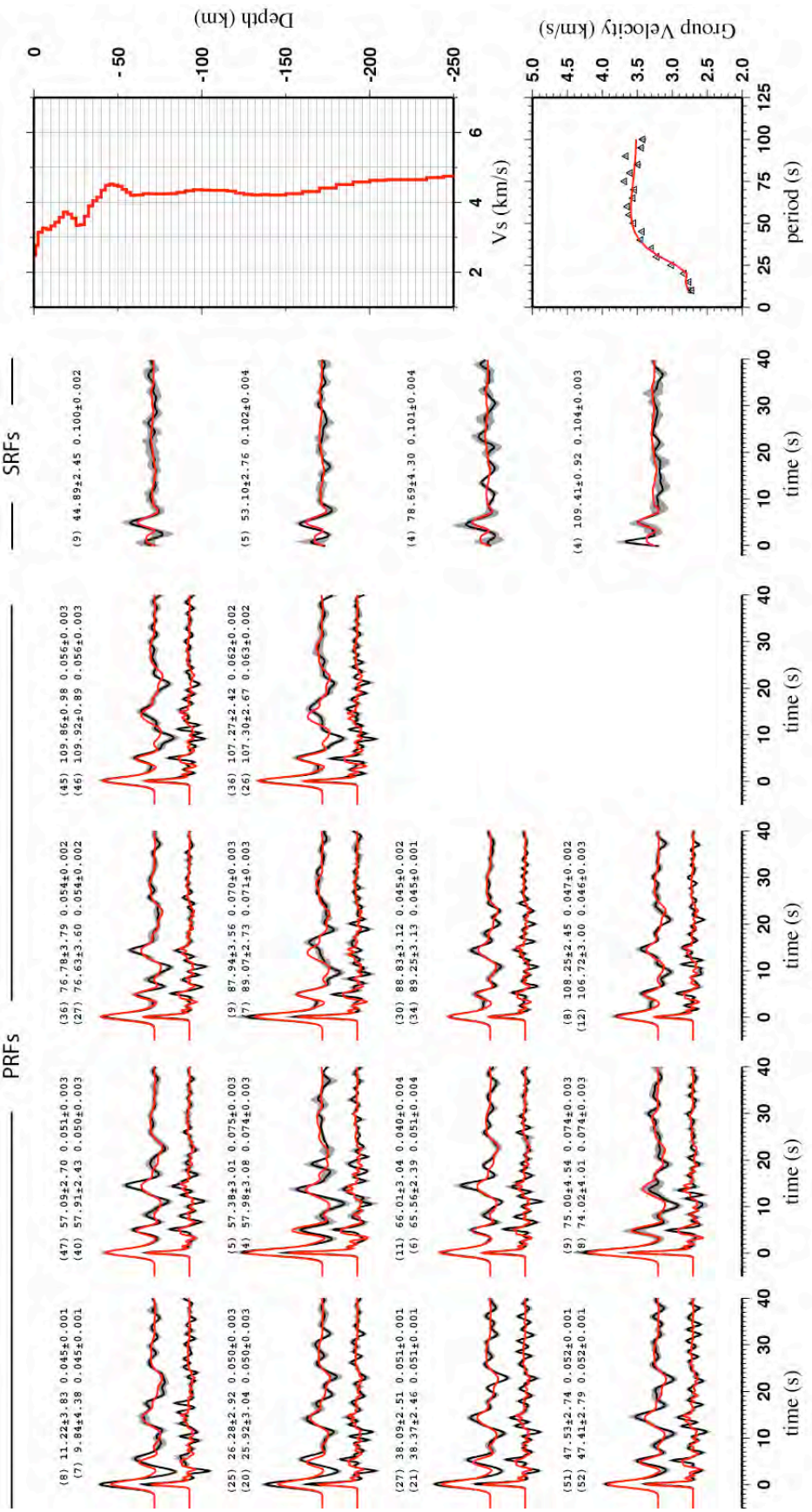

Figure 2. Joint inversion results for station MALT, in southern Turkey. The left panels are the observed (black) and predicted (red) PRFs at two overlapping frequency bands of fc<0.5 Hz and fc<1.2 Hz, the middle panels are the observed (black) and predicted (red) SRFs. The upper-right panel is the inverted model, and the bottom-right panel are the observed (triangles) and predicted (red line) dispersion velocities. The grey shadows surrounding the observed PRFs and SRFs and the vertical lines across the dispersion measurements are the 1σ-confidence bounds. The number of waveforms (n), average back-azimuth and standard deviation in deg (baz±1σbaz), average ray-parameter and standard deviation in s/km (rayp±1σr) is indicated on top of each receiver function panel.

Receiver Function Computation

Computation of PRFs was performed in the ZRT system by deconvolving the vertical component of the teleseismic P-waveforms from the corresponding radial component (e.g., Langston, 1979). Prior to deconvolution, the waveforms were windowed 10 s before and 110 s after the teleseismic P-wave arrival, detrended, tapered, and decimated to 10 samples per second (s.p.s.). The waveforms were low-pass filtered at 8 Hz before decimation to avoid aliasing and high-pass filtered above 0.05 Hz to remove low-frequency noise. PRFs were computed at two overlapping frequency bands of $f < 1.2$ Hz and $f < 0.5$ Hz. The combination of high and low frequencies provides constraints on velocity structure at different wavelengths and helps discriminate sharp boundaries from gradational transitions (Owens and Zandt, 1985; Julià, 2007). The deconvolution operation was applied using the iterative, time-domain deconvolution of Ligorría and Ammon (1999), with 500 iterations.

Transverse PRFs were also obtained by deconvolving the vertical component of the teleseisimc P-waveforms from the corresponding transverse component. Transverse PRFs are not used to constrain our local 1D models, but they offer a good dimensionality check on the structure under the station. For 1D structures the transverse receiver function should be identically zero; if the signal in the transverse PRF is comparable to that of the radial PRF, the model is not 1D (or anisotropic), and modeling of the radial PRF cannot be achieved through simple 1D velocity models.

On the other hand, SRFs were obtained in the local ray-coordinate (LQT) system by deconvolving the SV component of the teleseismic S-waveforms from the corresponding P component (Farra and Vinnik, 2000). The waveforms were windowed 100 s before and 12 s after the teleseismic S-wave arrival, detrended, tapered, and decimated down to 10 s.p.s. Similar to PRFs, the waveforms were low-pass filtered at 8 Hz to avoid aliasing and high-pass filtered above 0.05 Hz. Following standard practices in SRF computation (e.g., Hansen et al., 2007), the waveforms were time-reversed and polarity-flipped. Again, the deconvolution operation was performed through the iterative, time-domain deconvolution of Ligorría and Ammon (1999), with 500 iterations.

In general, we observed that the deconvolution process for S-waveforms is more unstable than for P-waveforms. We attribute this instability to the fact that Sp conversions happen within the coda of the teleseismic P-wave and to the difficulty in isolating the teleseismic S-wave pulse from other teleseismic phases (SKS, SKKS, SP) and from crustal reverberations. Given the relatively narrow range of epicentral distances suitable for SRF computation (60^o to 85^o), we decided to focus on stations with long operating times to obtain reliable SRF averages and robustly constrain lithospheric and sublithospheric structure.

A first-pass quality control was applied to the computed PRFs and SRFs by requiring that the convolution of the receiver functions with the corresponding vertical waveforms (PRFs) or SV waveforms (SRFs) reproduced 85% or more of the original radial and P-waveforms, respectively. The remaining receiver functions were then further inspected for visual stability and waveform consistency. Overall, we obtained 15,517 high-frequency PRFs ($f < 1.2$ Hz), 14,244 low-frequency PRFs ($f < 0.5$ Hz), and 965 SRFs ($f < 0.5$ Hz) for the selected 64 broadband stations in Eurasia and the Middle East.

Local 1D Velocity Models

Local 1D velocity models have been developed for Europe and the Middle East by jointly inverting PRFs and SRFs with Rayleigh-wave group velocities from the tomographic study of Pasyanos (2005) for S-wave velocity structure. Rayleigh-wave phase velocities will be added at a later stage. The velocity models are parameterized as a stack of thin layers down to ~400-km depth, with layer thicknesses ranging from 1.0 km for sedimentary structures, to 2.5 km for the crust and uppermost mantle (down to 60-km depth), 5.0 km for lithospheric mantle (down to 150-km depth), and 10.0 km for deeper structures. Layer thicknesses and Vp/Vs ratios are fixed for each layer during the inversion process, and densities are obtained from P-wave velocities through an empirical relationship (Berteussen, 1977). The models are parameterized down to ~400 km depth but only structure for the top 250 km is inverted for. Seismic velocities for layers deeper than 400 km are fixed to PREM values (Dziewonski and Anderson, 1981) in order to account for partial sensitivity of the long-period dispersion velocities to deep structure (Julià et al, 2003).

The joint inversion procedure utilized follows the iterative, linearized approach of Julià et al. (2003). The approach is described by the following system of equations:

$$\begin{bmatrix} \sqrt{\frac{p}{w_s^2}}\,D_s \\ \sqrt{\frac{q}{w_b^2}}\,D_b \\ \sigma\Delta \\ \Lambda \end{bmatrix} \vec{m} = \begin{bmatrix} \sqrt{\frac{p}{w_s^2}}\,\vec{r}_s \\ \sqrt{\frac{q}{w_b^2}}\,\vec{r}_b \\ \vec{0} \\ A\,\vec{m}_a \end{bmatrix} + \begin{bmatrix} \sqrt{\frac{p}{w_s^2}}\,D_s \\ \sqrt{\frac{q}{w_b^2}}\,D_b \\ \vec{0} \\ \vec{0} \end{bmatrix} \vec{m}_o$$

where D_s and D_b are partial derivative matrices for the dispersion and the receiver function estimates, respectively, r_s and r_b are the corresponding vectors of residuals, w_s^2 and w_b^2 are weights that equalize the datasets, the vector m contains the velocities of fixed thickness layers overlying a half-space, and m_0 contains an initial estimate for the velocities. The matrix Δ constructs the second difference model and makes the resulting profiles vary smoothly, and the diagonal matrix W contains constraint weights to the *a priori* velocity values m_a. The influence factor p controls the trade-off between fitting the receiver functions and the dispersion curves, and the smoothness parameter σ controls the trade-off between fitting the data and model smoothness. The values of these parameters are determined empirically by performing suites of inversions. The parameter q = 1-p, with $0 \le p \le 1$, so that p = 0 means inverting receiver function data only and p = 1 means inverting dispersion data only. The weights w_s^2 and w_b^2 are computed as $N\sigma^2$, where N is the number of data points and σ^2 is the variance of the observations.

The development of the 1D local models is illustrated in Figure 2, which displays the joint inversion results for the GEOFON station MALT in southern Turkey. The observations consist of 28 PRF averages (14 at frequencies < 1.2 Hz; 14 at frequencies < 0.5 Hz), 4 SRF averages (at frequencies < 0.5 Hz), and 1 dispersion curve (fundamental-mode Rayleigh-wave group velocity) extracted from the tomographic cell in Pasyanos (2005) enclosing the station. The different PRF and SRF averages are point-to-point stacks from teleseismic waves approaching the recording station from different directions and at different incidence angles. The starting model consisted of a simple gradational crust overlying PREM, which converged to a stable solution after six iterations with the aid of depth-dependent smoothing constraints on the profiles (σ = 0 .5 down to 100 km; σ = 1.0 underneath).

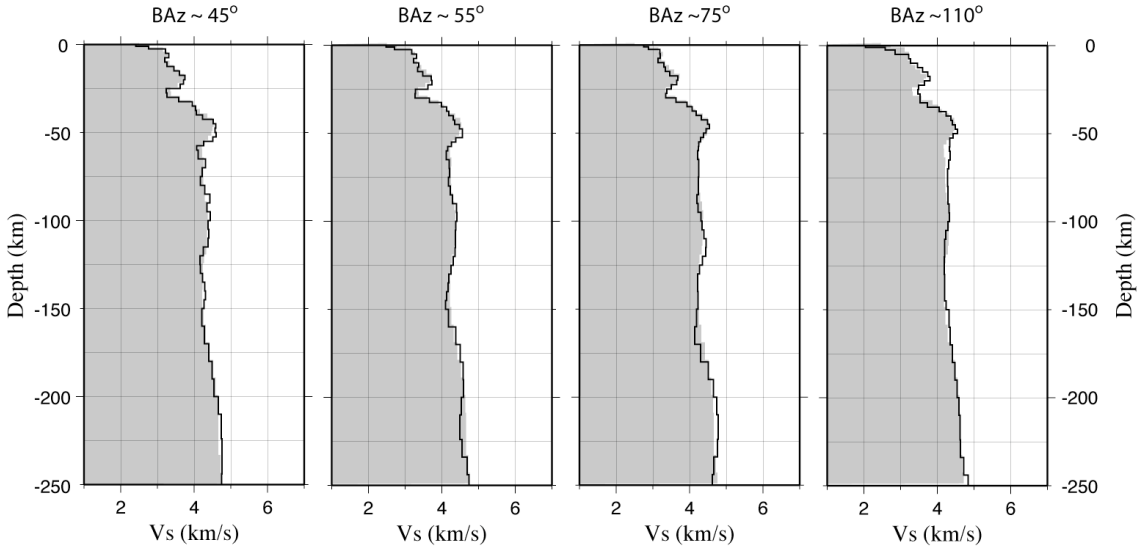

Figure 3. Velocity models corresponding to 4 separate joint inversions using PRF and SRF averages sampling at ~45°, ~55°, ~75°, and ~110° from the recording stations. The dispersion velocities constraining the velocity models were the same. The grey shade is the average velocity model displayed in Figure 2.

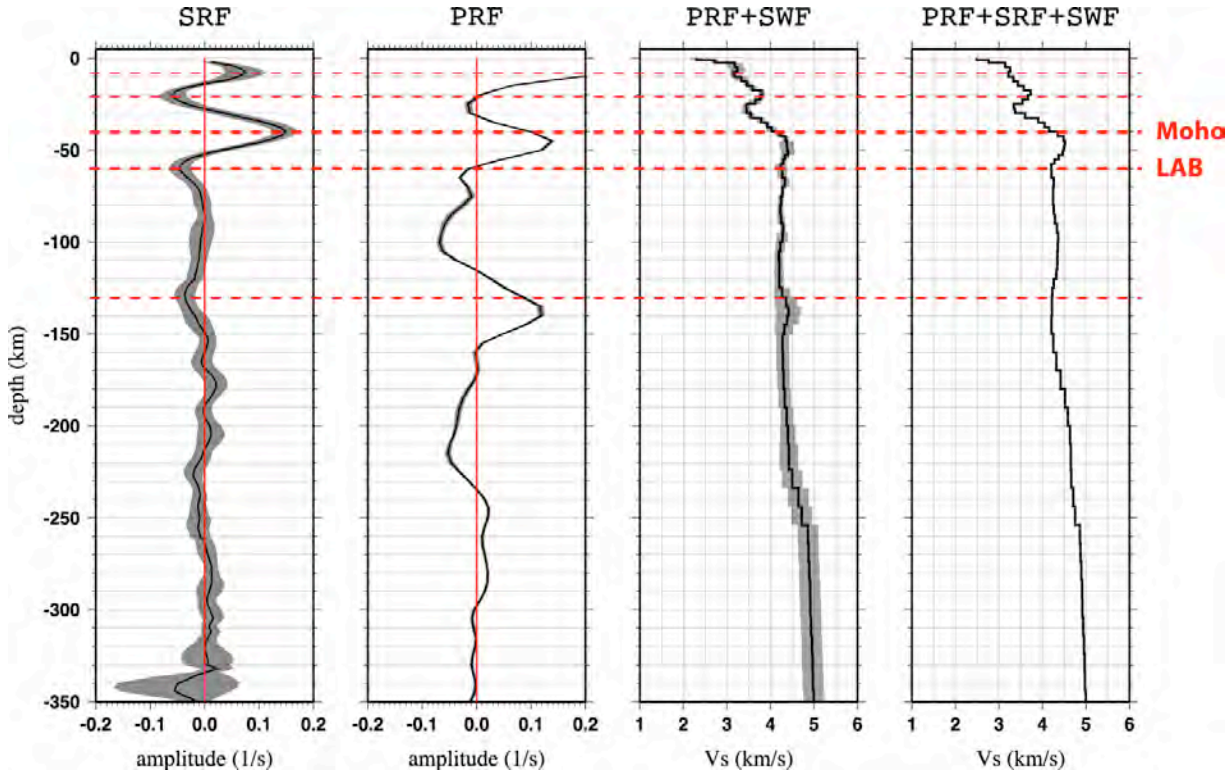

Figure 4. Correlation between joint inversion models with and without SRF constraints and depth-migrated PRF and SRF stacks for station MALT. The grey band in the SRF panel denotes the 1σ-confidence bounds for the SRF stack, and the grey band in the PRF+SRF panel denotes the 1σ-confidence bounds for the velocity model. The red dashed lines mark the statistically significant peaks and troughs in the SRFs.

The comparison between observations and predictions is excellent for the dispersion velocities, but some discrepancies are observed for the receiver functions. These discrepancies are the result of azimuthal variations in velocity structure around the station. The main features in all datasets, nonetheless, are satisfactorily accounted for, and the resulting velocity model can be regarded as a representative average. The main features of the velocity-depth profile for station MALT include (i) a ~40-km-thick crust, (ii) a low-velocity zone centered at ~25-km depth, (iii) a thin upper mantle lid (10–15 km thick), (iv) a shallow LAB (at ~55-km depth), and (v) a gradual velocity increase between 150- and 180-km depth back to PREM values. In order to check the robustness of those features and also to assess the degree of azimuthal heterogeneity around the station, we performed separate joint inversions for select PRF and SRF averages (Figure 3). The resulting velocity models show that, although the details may vary among the models, all the features are required to explain each of the separate inversions.

It is important to realize that the structure in the lithospheric mantle is strongly influenced by the constraints conveyed by the SRF average. This is illustrated in Figure 4, which displays the joint inversion model in Figure 2, along with depth-migrated PRF and SRF stacks (frequencies < 0.5 Hz) and the velocity model resulting from jointly inverting the PRF averages with the dispersion velocities (without the SRF contribution). The figure shows that the velocity decrease at 55-km depth correlates with the downswing (S-to-P conversion) in the SRF average at similar depths but that it was not required to explain the PRF average. It also shows that the velocity increase at ~130-km depth observed in the joint inversion model with no SRF data is removed with the addition of this dataset. Also, note that the crustal structure does not differ much with and without the contribution of the SRF data.

Some stations did not yield enough SRF waveforms to compute reliable SRF averages; therefore, the velocity models were developed without SRF constraints. This can introduce artifacts in the lithospheric structure due to partial modeling of crustal reverberations with Ps conversions in the mantle. These models will be down-weighted during the development of the average regional velocity models for the geologic/tectonic terrains.

Regional Velocity Models

We are now developing average velocity models for the WENA/UNIFIED terrains displayed in Figure 1 from the local 1D velocity models developed so far for Europe and the Middle East. Figure 5 displays the velocity models for region No. 23, approximately coinciding with Eastern Europe. The models display significant variation in crustal structures but a more-or less-homogeneous lithospheric mantle characterized by the absence of a clear LAB (down to the maximum resolvable depth of ~250 km).

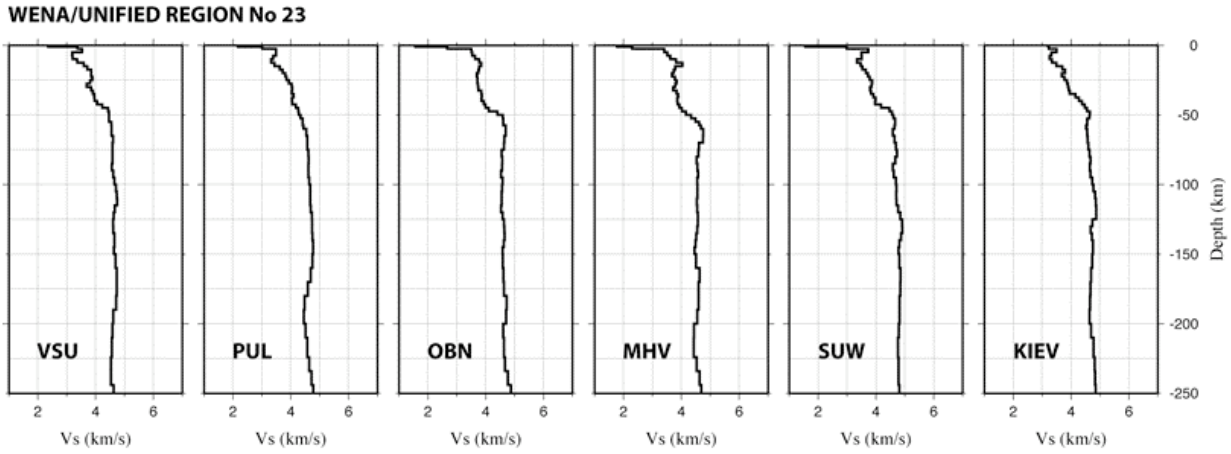

Figure 5. Local 1D velocity models for all the stations enclosed in the WENA/UNIFIED region No. 23 (Figure 1). Two of the models, PUL and KIEV, did not produce stable SRFs and were constrained from PRFs and dispersion only. Note that all the models constrained with SRF data are characterized by the absence of a LAB down to 250 km depth.

CONCLUSIONS AND RECOMMENDATIONS

We have developed local 1D velocity models for 64 permanent broadband stations in Europe and the Middle East by jointly inverting PRFs, SRFs, and fundamental-model, Rayleigh-wave group velocities. The data for PRF and SRF computation was downloaded from open stations at the IRIS DMC (60) and GEOFON (4) data archives, and the group velocities were obtained from the independent tomographic study of Pasyanos (2005). The inclusion of SRF waveforms into the joint inversion has proven critical to robustly constrain lithospheric thickness and lithospheric velocities.

The sampling of the WENA/UNIFIED tectonic models provided by the permanent broadband stations archived at the IRIS-DMC is quite uneven. Station coverage is best in the terrains of Western Europe, and it degrades towards Eastern Europe and the Middle East. Two possibilities for alleviating this situation include (i) obtaining data from permanent broadband stations freely available at other data centers (e.g., GEOFON, ORFEUS) and (ii) developing velocity models from temporary networks in terrains where the sampling from permanent stations is poor. As mentioned above, additional station coverage for the Middle East has been obtained from the Israeli Seismic Network through the GEOFON data center. Due to the larger instability of the deconvolution process in SRF computation, developing local 1D velocity models from temporary deployments will require combining data from several stations.

Stations in Western Europe are somewhat more inefficient in recording teleseismic S-waves than stations in Eastern Europe and the Middle East. As a result, a number of velocity models had to be developed with no SRF constraints or with less-robust SRF averages. To augment the dataset, we will investigate the use of SKS waves for SRF computation, which has shown some promise in other regions such as South Africa (Wittlinger and Farra, 2007) or South America (Heit et al., 2007).

ACKNOWLEDGEMENT

We would like to thank the IRIS-DMC and GEOFON data center for their role in the archiving and distribution of seismic data utilized for this project.

REFERENCES

Berteussen, K. A. (1977). Moho depth determinations based on spectral ratio analysis of NORSAR long-period P-waves, *Phys. Earth Planet. Inter*. 31: 313–326.

Dziewonsky, A. M. and D. L. Anderson (1981). Preliminary reference earth model, *Phys. Earth and Planet. Inter.* 25: 297–356.

Farra, V. and L. Vinnik (2000). Upper mantle stratification by P and S receiver functions, *Geophys. J. Int.* 141: 699–712.

Flanagan, M., S. Myers, and K. Koper (2006). Regional travel-time uncertainty and seismic location improvement using a three-dimensional a priori velocity model, *EOS Trans. AGU* 87: S31B–0194.

Hansen, S., A. Rodgers, S. Schwartz, and A. Al-Amri (2007). Imaging ruptured lithosphere beneath the Red Sea and Arabian Peninsula, *Earth Planet. Sci. Lett.* 259: 256–265.

Heit, B., F. Sodoudi, X. Yuan, M. Bianchi, and R. Kind (2007). An S receiver function analysis of the lithospheric structure in South America, *Geophys. Res. Lett.* 34: L143078, doi:10.1029/2007GL030317.

Julià, J. (2007). Constraining velocity and density contrasts across the crust-mantle boundary with receiver function amplitudes, *Geophys. J. Int.* 171: 286–301.

Julià, J., C. J. Ammon, R. B. Herrmann, and A. M. Correig (2000). Joint inversion of receiver function and surface wave dispersion observations, *Geophys. J. Int.* 143: 99–112.

Julià, J., C. Ammon, and R. Herrmann (2003). Lithospheric structure of the Arabian Shield from the joint inversion of receiver functions and surface-wave group velocities, *Tectonophysics* 371: 1–21.

Julià, J., M. Assumpção, and M. Rocha (2008). Deep crustal structure of the Paraná Basin from receiver functions and Rayleigh-wave dispersion: Evidence for a fragmented cratonic root, *J. Geophys. Res*. 13: B08318, doi:10.1029/2007JB005374.

Langston, C. (1979). Structure under Mount Rainier, Washington, inferred from teleseismic body waves, *J. Geophys. Res.* 84: 4749–4762.

Ligorría, J. and C. Ammon (1999). Poisson's ratio variations of the crust beneath North America, *Seism. Res. Lett.* 89: 1395–1400.

Myers, S. and C. Schultz (2000). Improving sparse network seismic location with Bayesian kriging and teleseismically constrained calibration events, *Bull. Seis. Soc. Am*. 90: 199–211.

Owens, T. J., H. P. Crotwell, C. Groves, and P. Oliver-Paul (2004). Standing order for data, *Seism. Res. Lett.* 75: 515–520.

Owens, T. J. and G. Zandt (1985). The response of the continental crust-mantle boundary observed on broadband teleseismic receiver functions, *J. Geophys. Res.* 12: 705–708.

Pasyanos, M., W. Walter, and M. Flanagan (2003). Geophysical models for nuclear explosion monitoring, in *Proceedings of the 25th Seismic Research Review—Nuclear Explosion Monitoring: Building the Knowledge Base*, LA-UR-03-6029, Vol. 1, pp.125–134

Pasyanos, M., W. Walter, M. Flanagan, P. Goldstein, and J. Bhattacharyya (2004). Building and testing an a priori geophysical model for western Eurasia and North America, *Pure Appl. Geophys.* 161: 235–281.

Pasyanos, M. (2005). A variable resolution surface wave dispersion study of Eurasia, North Africa, and surrounding regions, *J. Geophys. Res.* 110: doi: 10.1029/2005JB003749.

Schultz, C., S. Myers, J. Hipp, and C. Young (1998). Nonstationary Bayesian kriging: A predictive technique to genereate spatial corrections for seismic detection, location, and identification. *Bull. Seis. Soc. Am*. 88: 1275–1288.

Wilson, D., D. Angus, J. Ni, and S. Grand (2006). Constraints on the interpretation of *S*-to-*P* receiver functions, *Geophys. J. Int*. 165: 969–980.

Wittlinger, G. and V. Farra (2007). Converted waves reveal a thick and layered tectosphere beneath the Kalahari super-craton, *Earth Planet. Sci. Lett*. 254: 404–415.

ADVANCED MULTIVARIATE INVERSION TECHNIQUES FOR HIGH RESOLUTION 3D GEOPHYSICAL MODELING

Monica Maceira[1], Haijiang Zhang[2], Ryan T. Modrak[1], Charlotte A. Rowe[1], and Michael L. Begnaud[1]

Los Alamos National Laboratory[1] and Massachusetts Institute of Technology[2]

Sponsored by the National Nuclear Security Administration

Award No. DE-AC52-06NA25396/LA09-3D Inv-NDD02

ABSTRACT

To meet the United States Government nuclear explosion monitoring requirements with high confidence, the Air Force Technical Applications Center needs new and improved capabilities for analyzing regional seismic, teleseismic, and infrasound event data. Recently, the National Nuclear Security Administration has decided to investigate three-dimensional (3D) modeling in an effort to further improve knowledge of the compressional and shear-velocity structure as well as reduce uncertainty and more accurately detect, locate, and identify small (body wave magnitude m_b<4) seismic events. For seismically active areas, inaccurate models can be corrected using the kriging methodology; therefore, it is possible to detect, locate, and identify large events even with limited resolution models. This is not necessarily the case for smaller events, however, and it is even more of a challenge for aseismic regions. On the other hand, improving near-regional to local monitoring demands that we address the Earth's heterogeneities and 3D complexities.

Motivated by the shortcomings of existing single-parameter inversion methods in accurate prediction of other geophysical parameters, this research was mainly focused during its first year on the development of advanced multivariate inversion techniques to generate a realistic, comprehensive, and high-resolution 3D model of the seismic structure of the crust and upper mantle that satisfies multiple independent geophysical datasets. During its second year, we have focused on the efficient implementation of the newly developed technique. Application to different areas around the globe with different sets of observations allows us to study sensitivities, trade-offs, and possible improvements of the methodology. We present 3D seismic velocity models of the crust and upper mantle beneath several regions, resulting from the simultaneous and joint use of seismic body-wave arrival times, surface-wave dispersion measurements, and gravity data. The joint inversion takes advantage of strengths of individual datasets and is able to better constrain the velocity models from shallower to greater depths. Combining three different datasets to jointly invert for the velocity structure is equivalent to a multiple-objective optimization problem. Because it is unlikely that the different "objectives" (data types) would be optimized by the same parameter choices, some trade-off between the objectives is needed. The optimum weighting scheme for different data types is based on relative uncertainties of individual observations and their sensitivities to model parameters.

OBJECTIVES

The ultimate goal of this study is to improve our knowledge of the 3D compressional and shear-velocity structure and enable us to reduce uncertainty and more accurately detect, locate, and identify small (body-wave magnitude m_b<4) seismic events, and therefore improve our capabilities for nuclear explosion monitoring (NEM). This project specifically improves seismic monitoring technology through the development and application of advanced multivariate inversion techniques to generate a realistic, comprehensive, and high-resolution 3D model of the seismic structure of the crust and upper mantle that satisfies numerous independent geophysical datasets.

RESEARCH ACCOMPLISHED

This is the second year of a three-year project. During the first year and motivated by the shortcomings of existing single-parameter inversion methods in accurate prediction of other geophysical parameters (e.g. Julià et al. 2000, 2003; Maceira, 2006; Maceira and Ammon, 2006), we focused on the development of advanced multivariate inversion techniques to generate a realistic, comprehensive, and high-resolution 3D model of the seismic structure of the crust and upper mantle that satisfies multiple independent geophysical datasets (Maceira et al, 2009). In particular, we developed a method to simultaneously and jointly invert four different datasets: surface-wave dispersion measurements, teleseismic P-wave receiver functions, gravity observations, and body wave (both P and S phases) travel-time arrivals. Surface wave dispersion measurements are primarily sensitive to seismic shear wave velocities. Theoretically, the dispersion curve is a nonlinear function of shear wave velocity and/or compressional wave velocity and density of the media (Bucher and Smith, 1971). However, it has been proved (Takeuchi and Saito, 1972; Aki and Richards, 1980) that the sensitivity to the P-wave velocity is significantly smaller than the sensitivity to the S-wave velocity. Also the sensitivity function for the density is smaller than the one for the shear-wave velocity (Bache et al., 1978; Tanimoto, 1991). Therefore, shear velocity variations are usually the model parameters in inversion studies of surface-wave dispersion. But, at shallow depths, it is difficult to obtain high resolution and constrain the structure. This is because the longer the period, the deeper the surface-wave energy penetrates, so shorter periods are primarily sensitive to upper crustal structures. But short periods are difficult to measure, especially in tectonically and geologically complex areas. On the other hand, gravity inversions have the greatest resolving power at shallow depths since gravity anomalies decrease in amplitude and increase in wavelength with increasing depth. And gravity measurements supply constraints on rock density variations. In addition, surface-wave dispersion measurements are primarily sensitive to vertical shear-wave velocity averages; while body wave receiver functions are sensitive to shear-wave velocity contrasts and vertical travel-times. Addition of the seismic travel-time data helps to constrain the shear wave velocities both vertically and horizontally in the model cells crossed by the ray paths. Thus by combining these four complimentary datasets into a single inversion, we can obtain a self-consistent 3D seismic velocity-density model with increased resolution of shallow geologic structures. Our final algorithm is a modification of the Maceira and Ammon (2009) joint-inversion code, in combination with the regional version of the double-difference (DD) tomography program *tomoDD* (Zhang and Thurber, 2003, 2006), with a fast LSQR solver operating on the gridded values jointly.

During this second year, we have focused on the efficient implementation of this newly developed technique. Application to different areas around the globe with different sets of observations allows us to study sensitivities, trade-offs, and possible improvements of the methodology. We present here 3D seismic velocity models of the crust and upper mantle beneath several regions, resulting from the simultaneous and joint use of seismic body-wave arrival times, surface-wave dispersion measurements, and gravity data.

East Africa Rift System

Knowledge of crustal and upper mantle structure is of importance for understanding East Africa's geodynamic evolution and for addressing broader questions about the causes of continental breakup. Though recent investigations have yielded improved characterizations of the rift zone, questions remain concerning the distribution of velocity anomalies (e.g., Julià et al., 2005), extent of lithospheric thinning (e.g., Weeraratne et al., 2003), and temporal variation in rift evolution (e.g., Ebinger, 1989). Key to resolving these questions are better constrained seismic models. We decided to test our joint inversion methodology in this region due to its scientific significance and because of a more practical reason: the unprecedented opportunity of getting a handle on on-land Bouguer gravity observations. Benefits of our joint inversion approach appear pronounced when working with regions of strong lateral contrast as found in central Asia (Maceira and Ammon, 2009). In applying the joint-inversion

technique to East Africa, we solve for velocity structure in an area with less lateral heterogeneity but great tectonic complexity. To increase the effectiveness of the technique in this region, we explore gravity-filtering methods and test different velocity-density relations (the relationship between the independent datasets is always one of the difficulties with simultaneous joint inversions).

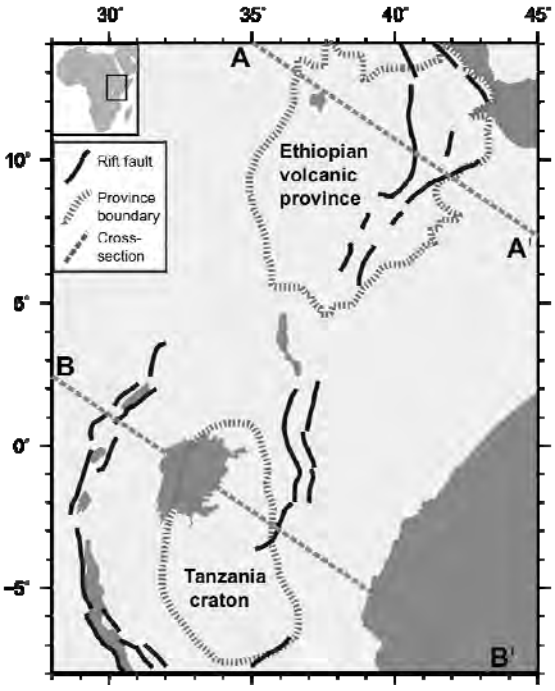

Figure 1. We distinguish between Ethiopia and Tanzania as distinct portions of the larger rift system. The Ethiopian volcanic province (after Keranen et al., 2009) spans the northern portion of the rift system. The Tanzania craton (after Nyblade and Brazier, 2002) marks the southern portion of the rift system (rift lies for the most part along the edges of the craton).

The area for the inversion spans the broad uplifted region from Ethiopia at one end to Kenya, Uganda, and Tanzania at the other (Figure 1). Near the northern boundary of our study area, the Main Ethiopia Rift meets the incipient Red Sea and Gulf of Aden spreading ridges. At the opposite end, the rift system splits into distinct western and eastern branches, which largely sidestep the Archean Tanzania craton. Recent inversions of East Africa have employed body waves (e.g., Benoit et al., 2006), surface waves (e.g., Weeraratne et al., 2003), receiver functions, or some combination of these (e.g., Julià et al., 2005; Keranen et al., 2009). Although useful comparisons can be drawn between the Ethiopian and Tanzanian portions of the rift system, most tomographic studies to date have focused exclusively on one section or the other. The current inversion, in contrast, is carried out over a wider area than most previous studies, allowing straightforward comparison between these two distinct portions of the rift system.

Fundamental-mode Rayleigh wave group velocity estimates with periods from 7 s to 150 s were obtained from Pasyanos and Nyblade (2007) for the inversion. Though less detailed than images from local seismic arrays (e.g., Prodehl et al., 1997), these estimates span a broader spatial and period range. Gravity data for the inversion were derived from the Gravity Recovery and Climate Experiment (GRACE) (Tapley et al., 2005). Comparison of GRACE-converted Bouguer anomalies with values from a proprietary gravity compilation showed close agreement between the two datasets; in light of this similarity, we chose the GRACE data because of their more uniform coverage.

We developed and implemented a method to increase the usefulness of gravity data by filtering the Bouguer anomaly map. Though commonly applied in gravity forward modeling (e.g., Simiyu and Keller, 1997) such techniques have not to our knowledge been used in previous joint inversion studies (e.g., Lees and VanDecar, 1991; Zeyen and Achauer 1997; Tiberi et al., 2003; Maceira and Ammon, 2009). Figure 2a suggests possible benefits of filtering. In this figure, results from the inversion using group velocities only (solid line) provide the starting model for the joint inversion (dashed line). Comparison of the two profiles suggests that the addition of unfiltered gravity data contributes little in the way of distinguishing between features at different depths. Rather than improving resolution at shallow depths as desired, features in the unfiltered gravity data are smeared into the mantle; moreover, within the mantle the two profiles are offset by a roughly constant amount, suggesting that gravity data provide inadequate constraints on mantle anomalies. Examination of additional profiles shows that these problems, likely exacerbated by East Africa's pronounced long-wavelength Bouguer components (Girdler, 1975), are pervasive throughout the study area. In response, we employ filtering methods to remove the long-wavelength gravity components, reducing the tendency of crustal gravity features to be smeared into the mantle. To balance the change to the observed gravity values brought on by filtering, we reduce the contribution to the predicted gravity values from blocks below 60 km, corresponding to the portion of the Bouguer anomaly signal we attempt to suppress. Finally, while allowing velocity structure above 60 km to vary freely, below 60 km we induce agreement between the joint inversion results and the initial model by imposing stronger a priori model constraints. In the application of the described technique, problems of depth correlation associated with filtering make our choice of depth cutoff (60 km) somewhat subjective. This disadvantage, however, is likely outweighed by the reduction in smearing of the gravity signal

suggested by Figure 2b. Although filtering removes potentially useful information on mantle structure, the remaining short-wavelength signal can be assigned with greater reliability within the crust, avoiding the mutually degrading effects of smearing between crust and mantle. To remove the long-wavelength components from the Bouguer gravity map, we follow Tessema and Antoine (2004), who use an upward continuation method and demonstrate correlation with crustal geology.

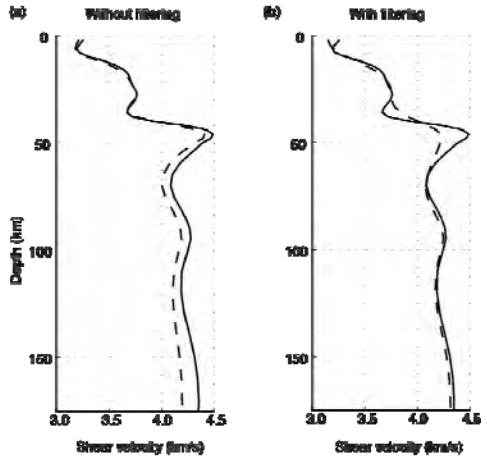

Figure 2. One-dimensional profiles from a representative cell in our model. Comparison shows results from an inversion of group velocities only (solid lines) and from joint inversion (dashed lines). (a) Without gravity filtering, results point to an inability to distinguish between density anomalies at depth. (b) With gravity filtering, the two profiles agree less closely at crustal depths and more closely over mantle depths.

Previous inversions have incorporated gravity data by formulating the forward problem in two steps: (1) velocity variations are mapped to density variations and (2) density variations are mapped to gravity anomalies. While the second mapping is mathematically straightforward, the first necessitates use of empirical formulae. Perhaps because empirical mappings between density and P-wave velocity (e.g., Birch's law) are more familiar than mappings between density and S-wave velocity, previous studies have relied on the former together with ad hoc scaling to obtain S-wave velocities. Here, we eliminate the need for such scaling by adopting a direct mapping between density and S-wave velocity. Given the variability in Poisson's ratio for rift zones (e.g., Dugda et al., 2005), this new mapping provides the proper framework for allowing spatial V_P/V_S variability, which we envision developing in future inversions.

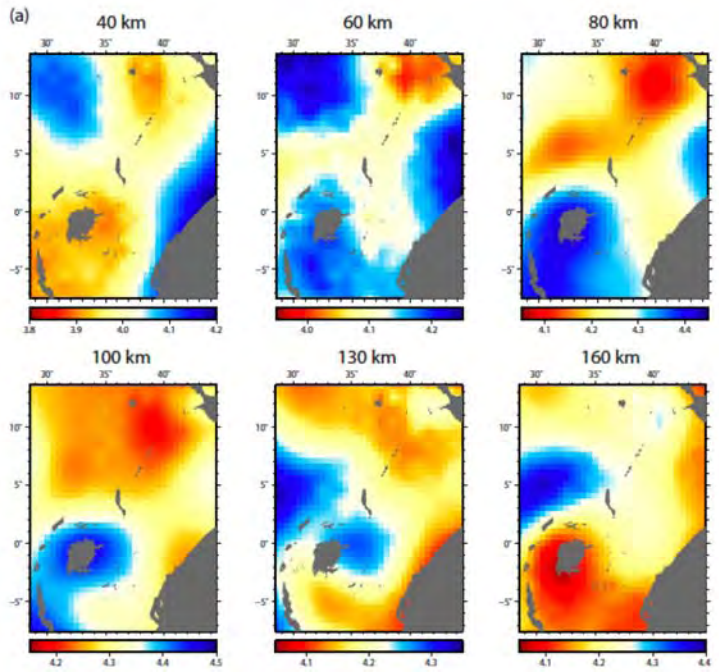

Figure 3. Horizontal cross sections at various depths through the 3D shear velocity model (velocity units: km/s).

Figure 3 shows the 3D S-wave velocity model obtained from the joint inversion. Two sets of velocity anomalies, one beneath Ethiopia and the other beneath the Tanzania craton, stand out among the most prominent features. Beneath Ethiopia a distinct low-velocity anomaly is observed over a depth of 30–150 km. Though the existence of lower-than-average shear-wave velocities in the uppermost mantle beneath Ethiopia matches a variety of previous results (e.g., Keranen et al., 2009), controversy exists regarding velocity structure at greater depths. Such disagreement may in part reflect differences in methodology. While surface wave studies (e.g., Ritsema and van Heijst, 2000) have often failed to resolve low velocities beneath Ethiopia at depths greater than 170 km, body-wave investigations (e.g., Benoit et al., 2006) have imaged low velocities extending as deep as 400 km. As a result of upward trajectories associated with incoming rays, body-wave studies may tend to underestimate velocity deviations and smear velocity structure (see Weeraratne et al., 2003, for analysis based on observations from East Africa). From these considerations, it seems likely that the true vertical extent of the low-velocity anomaly beneath Ethiopia lies between the shallower and deeper values

predicted using surface-wave and body-wave methodologies, respectively. Besides the low-velocity anomaly beneath Ethiopia, prominent velocity excursions also occur beneath Tanzania. As shown in Figure 3, we resolve high velocities below the craton over a depth of 50–130 km. Contiguous to this high-velocity zone, a low-velocity anomaly emerges at a depth of 140 km. Although the upper part of this low-velocity anomaly is well constrained by the long-period Rayleigh wave group velocities used in the inversion, sensitivity kernels suggest resolution drops off below 175 km. This juxtaposition of high and low shear-wave speeds appears consistent with the hypothesis, discussed in detail by Weeraratne et al. (2003), of a hot mantle plume impeded by cool, stable, overlying cratonic lithosphere. In the following particulars, we obtain close agreement with Weeraratne et al. (2003): (1) the low-velocity anomaly beneath the craton originates at around 140 km, (2) the anomaly lies squarely beneath the craton, and (3) deviations from background shear velocities reach as much as 5% over the depths displayed in Figure 3. Additionally, our results allow comparison between the rift structures of Ethiopia and Tanzania. In obtaining data from Pasyanos and Nyblade (2007), we use group velocities derived not only from local stations and events, but also from stations and events distributed across surrounding tectonic plates. Though the resulting continental-scale maps possess less detail than local-scale group-velocity maps, their wider spatial coverage allows straightforward comparison between distinct portions of the rift system. As a result, we find that uppermost mantle shear velocities beneath Ethiopia appear much slower than those beneath Tanzania. While the presence of shallow low velocities beneath Ethiopia can be explained in terms of lithospheric erosion or magma-assisted rifting (e.g., Dugda et al., 2007; Ebinger and Casey, 2001), the absence of shallow low velocities beneath Tanzania suggests an alternate mechanism of extension. Such differences may stem in part from inherited rheology, as related for example to the high-velocity zone observed beneath Tanzania. Finally, though a common origin below 175 km cannot be ruled out, no evidence is found to suggest the various low-velocity anomalies in Figure 3 merge continuously at depth. Indeed, low velocities beneath Ethiopia appear diffuse and diminished by 160 km, suggesting the existence of a seismic velocity discontinuity separating the low-velocity anomaly beneath Ethiopia from the one below Tanzania.

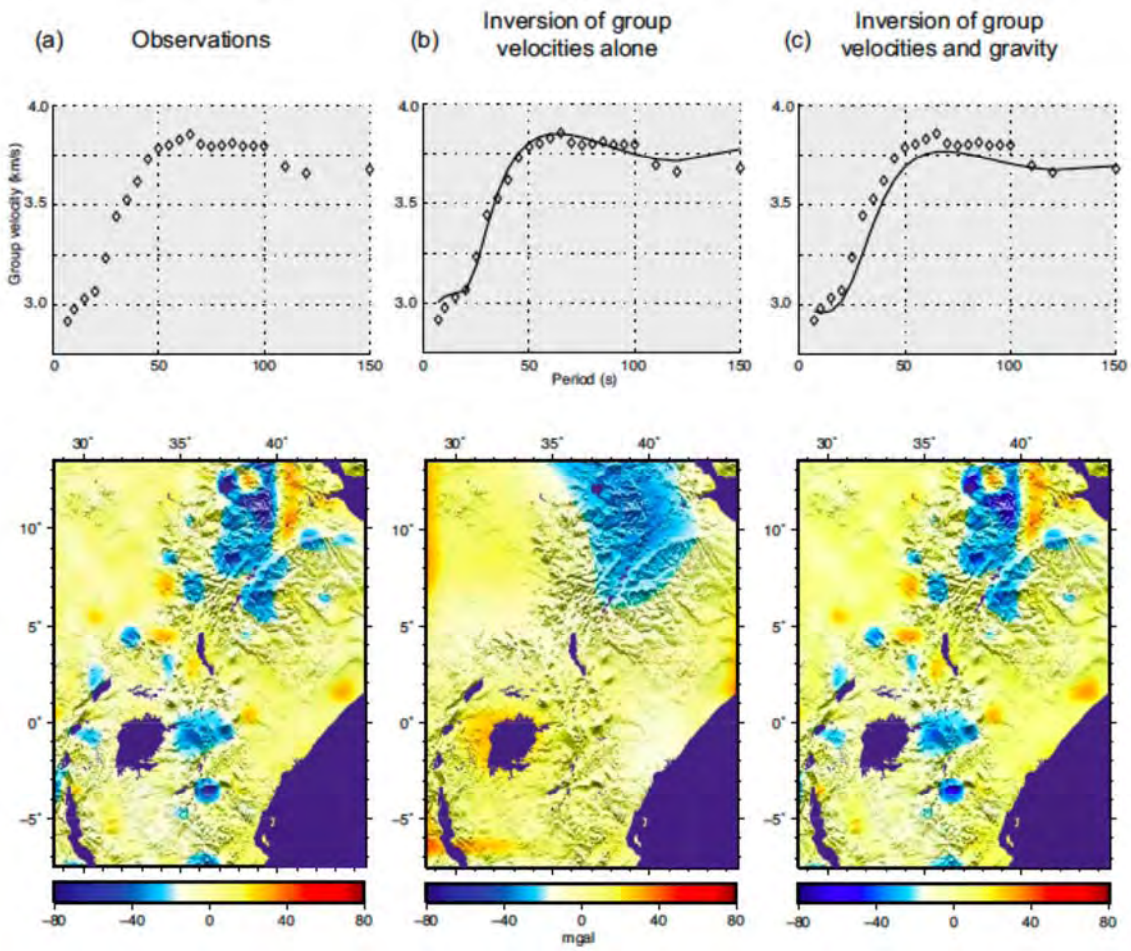

Figure 4. Fit to data from inversion of surface-wave dispersion only and from joint inversion. (a) Top: Group velocities from a representative cell in our model. Bottom: Filtered Bouguer anomalies. (b) Top: Group velocity fit obtained from the inversion of group velocities only. Bottom: Gravity fit from the same inversion. (c) Top: Group velocity fit obtained from joint inversion. Bottom: Gravity fit from joint inversion.

In the inversion carried out in central Asia by Maceira and Ammon (2009), addition of gravity data dramatically improved the fit to the Bouguer anomalies without significantly degrading the fit to the group velocities. Figure 4 demonstrates this result for the current study area as well. Although it is well known that problems of nonuniqueness make gravity data easier to match than seismic data, several observations provide confidence in our methodology's robustness. These include the simultaneous fit to both datasets shown in Figure 4 as well as other changes resulting from the addition of gravity data. Compared with results from the inversion of group velocities only, the joint-inversion methodology provides increased effectiveness in capturing Moho depth and improved resolution of uppermost mantle detail, including sharper delineation of the Tanzania craton in the vertical cross sections and in the horizontal cross section at 60 km. The resolved extent of the high-velocity cratonic region accords well with previous tomographic images (e.g., Figure 11 of Weereratne et al., 2003) and with geodynamic models suggesting strain localization in zones of weakness surrounding the craton (e.g., Nyblade and Brazier, 2002).

Utah Geothermal Field

The Cove Fort-Sulphurdale geothermal area is located in the transition zone between the Basin and Range to the west and the Colorado Plateau to the east (Figure 5). We have collected various geophysical data around the geothermal field, including heat flow (Henrikson and Chapman, 2002), gravity (Pan American Center for Earth and Environmental Studies (PACES) available at http://gis.utep.edu), seismic surface-wave phase and group velocity

maps (Yang et al., 2008), and seismic body-wave arrival times that were assembled from seismic waveforms recorded by the University of Utah Seismograph Stations (UUSS) regional network for the past 7 years and the recent EArthscope/USArray phase data. All of these geophysical datasets have different strengths for characterizing subsurface structures and properties. Combining these data through a coordinated analysis and, when possible, by joint inversion provides a detailed model of the Cove Fort geothermal region.

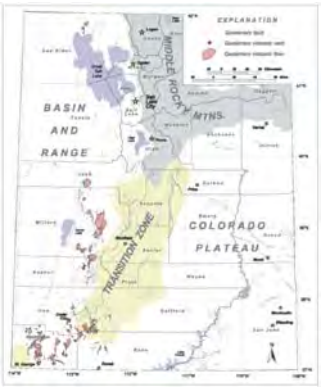

Figure 5. Utah simplified geological map (after Stokes, 1977; Hecker, 1993)

Various geophysical datasets indicate that beneath the Cove Fort-Sulphurdale geothermal resource there is a strong anomaly of low seismic velocity, low gravity, and high electrical conductivity that correlates with the high surface heat flow. This suggests that there is a heat source in the crust beneath the geothermal field. We collected first P-arrival data from more than 6500 earthquakes in the Utah region. Each event has at least six arrivals for reliably determining its location. We apply the DD seismic tomography method (Zhang and Thurber, 2003) to simultaneously determine an initial velocity structure and earthquake locations. The finite-difference travel-time calculation method of Podvin and Lecomte (1991) is used to calculate travel times between events and stations. On the preliminary regional seismic velocity map computed this way, we can also identify some other low-velocity anomalies, indicating other potential geothermal prospects. We decided to apply our joint inversion methodology to produce a better-constrained velocity structure of the Utah area, which will be very helpful for characterizing and exploring existing and potential geothermal reservoirs in the area.

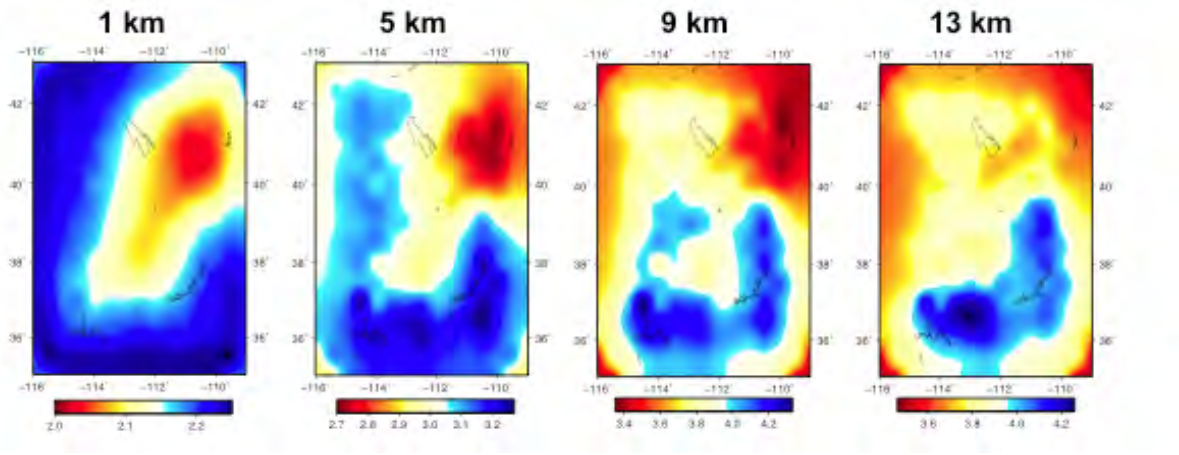

Figure 6. Shear-wave velocity model at constant depth slices. The depth of each image is shown at the top of each map (velocity units: km/s).

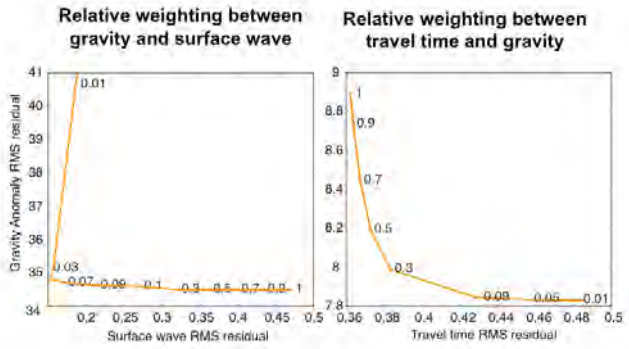

Figure 7. Trade-off curves between surface-wave and gravity data residuals (left) and between travel time and gravity data residuals (right).

Figure 6 shows the results from using the surface and gravity data to jointly determine the shear-velocity (Vs) model. Combining both datasets to jointly invert for the velocity structure is equivalent to a multiple-objective optimization problem. Because it is unlikely that the different "objectives" (data types) would be optimized by the same parameter choices, some trade-off between the objectives is needed. The optimum weighting scheme for different data types is based on relative uncertainties of individual observations and their sensitivities to model parameters. Here we determine their relative weightings through a trade-off analysis of surface-wave residual and gravity data residual (Figure 7). As a result, the model optimally fits both the surface wave and gravity data. In this study, the surface wave is weighted 50 times of the gravity data (1:0.02). Compared to the inversion using only the surface wave data, at shallow depths (e.g., 1 and 5 km), the Vs model better delineates the low-velocity anomaly. The first-order horizontal and vertical smooth weighting are also applied to constrain the model during the joint inversion. After three iterations of joint inversion, the surface-wave data residual is close to zero and the gravity data residual decreases ~90%.

Preliminary joint inversion results using seismic travel time and gravity data (Figure 8) indicate strong low velocity anomalies in middle crust beneath some known geothermal sites in Utah.

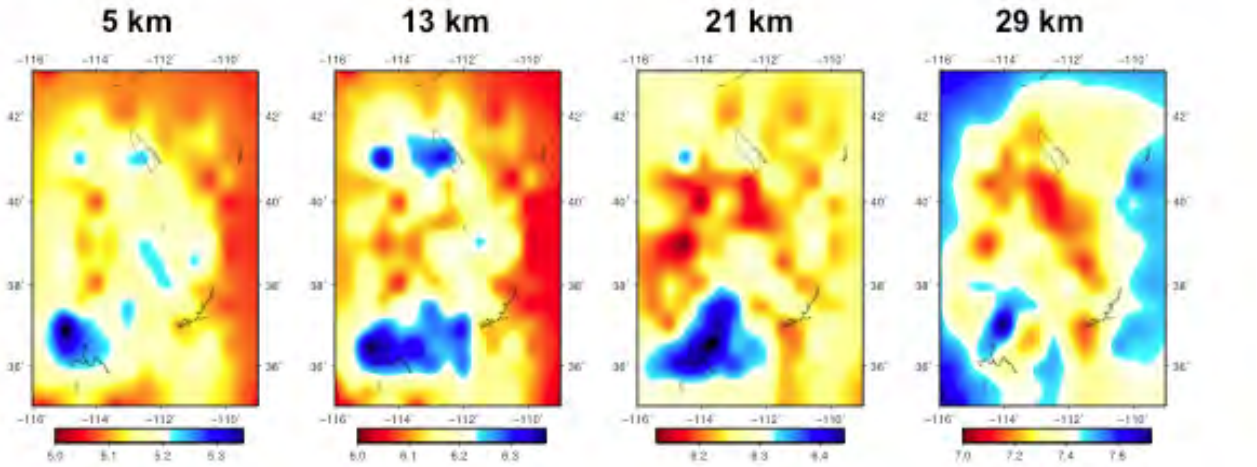

Figure 8. Compressional wave velocity model at constant depth slices. The depth of each image is shown at the top of each map (velocity units: km/s).

CONCLUSIONS AND RECOMMENDATIONS

This is the second year of a three-year project to map the 3D seismic structure of the crust and upper mantle using simultaneous joint inversion of surface-wave dispersion, gravity, receiver function, and travel-time observations. Geophysical models play an important role in ground-based nuclear explosion monitoring (GNEM). To more confidently and accurately detect, locate, and identify small seismic events, better high-resolution 3D structural models are needed. Therefore, the ongoing research directly addresses this challenge, and our results are also of fundamental importance for understanding the geodynamic evolution and formation of continents, as well as the processes acting within and on the continental lithosphere.

We are now focusing on developing 3D models for different areas for which we have different sets of observations. This approach allows us to study sensitivities, trade-offs, and possible improvements of our methodology. We have presented here models obtained for the East Africa Rift System and the Utah geothermal area (more areas of interest to the GNEM program will be shown at the MRR 2010 meeting). By tailoring our methodology to these two different areas, we have learned that besides enhancing resolution at short wavelengths, use of filtered gravity anomalies may help distinguish between anomalies at different depths. We have also tested different relations between seismic velocities and density and concluded that a relation where no a priori Poisson's ratio assumptions are needed (e.g., D. G. Harkrider's) is more beneficial. Future work will involve validation of these 3D models through the use of the spectral element method and full waveform comparisons.

ACKNOWLEDGEMENTS

Special thanks to Cindy Ebinger for kindly providing us with her gravity measurements. We thank Mike Pasyanos for allowing us to use their tomographic maps for this research. Special thanks also to D. G. Harkrider for providing us with valuable relationships between seismic velocities and density. Thanks to Chuck Ammon for valuable insights. We thank the scientists, engineers, and technicians that have created the seismic recording systems and networks that provide excellent broadband seismic observations. In particular, we thank the USGS and the IRIS Consortia (NSF) who share information and data with the global community in an effective and efficient manner. Thanks to Paul Wessel and Walter Smith (1995) for developing and maintaining their Generic Mapping Tool (GMT) that we use to create many of the illustrations used in our research. Our thanks to M. Wetovsky for editorial assistance.

REFERENCES

Aki, K. and P. G. Richards (1980*). Quantitative Seismology: Theory and Methods*, San Francisco, CA: W. H. Freeman.

Bache, T. C., W. L. Rodi, and D. G. Harkrider (1978). Crustal structures inferred from Rayleigh-wave signatures of NTS explosions, *Bull. Seismol. Soc. Am.* 68: 1399–1413.

Benoit, M. H., A. A. Nyblade, and J. C. VanDecar (2006). Upper mantle P-wave speed variations beneath Ethiopia and the origin of the Afar hotspot, *Geology* 34: 329–332.

Bucher, R. L. and R. B. Smith (1971). Crustal structure of the eastern Basin and Range province and the northern Colorado Plateau from phase velocities of Rayleigh waves, in *The Structure and Physical Properties of the Earth's Crust*, Geophysical Monograph. Series, Vol. 14, J. G. Heacock, Ed. Washington, D.C.: AGU.

Dugda, M. T., A. A. Nyblade, and J. Julià (2007). Thin lithosphere beneath the Ethiopian Plateau revealed by a joint inversion of Rayleigh wave group velocities and receiver functions, *J. Geophys. Res*. 112: B08305, doi:10.1029/2006JB004918.

Dugda, M. T., A. A. Nyblade, J. Julià, C. A. Langston, C. J. Ammon, and S. Simiyu (2005). Crustal structure in Ethiopia and Kenya from receiver function analysis: Implications for rift development in eastern Africa, *J. Geophys. Res.* 110: B01303, doi:10.1029/2004JB003065.

Ebinger, C. J. and M. Casey (2001). Continental breakup in magmatic provinces: An Ethiopian example, *Geology*, 29: 527–530.

Ebinger, C. J. (1989). Tectonic development of the western branch of the East African rift system, *Geol. Soc. Am. Bull.* 101: 885–903.

Girdler, R. W. (1975). The great negative Bouguer anomaly over Africa, *EOS Trans. AGU* 56: 516–519.

Hecker, S. (1993). Quaternary tectonics of Utah with emphasis on earthquake-hazard characterization, Utah Geological and Mineral Survey Bulletin 127.

Henrikson, A. and D. S. Chapman, 2002. Terrestrial heat flow in Utah, open report, Dept. of Geology and Geophysics, Univ. Utah.

Julià, J., C. J. Ammon, R. B. Herrmann, and A. M. Correig (2000). Joint inversion of receiver function and surface wave dispersion observations, *Geophys. J. Int*. 143: 99–112.

Julià, J., C. J. Ammon, and R. B. Herrmann (2003). Lithospheric structure of the Arabian shield from the joint inversion of receiver functions and surface wave dispersion, *Tectonophys.* 371: 1–21.

Julià, J., C. J. Ammon, and A. A. Nyblade (2005). Evidence for mafic lower crust in Tanzania, East Africa, from joint inversion of receiver functions and Rayleigh wave dispersion velocities, *Geophys. J. Int.* 162: 555–569.

Keranen, K. M., S. L. Klemperer, J. F. Lawrence, J. Julia, and A. A. Nyblade (2009). Low lower crustal velocity across Ethiopia: Is the Main Ethiopian Rift a narrow rift in a hot craton? *Geochemistry, Geophysics, Geosystems* 10: 121.

Lees, J. M. and J. C. VanDecar (1991). Seismic tomography constrained by Bouguer gravity anomalies: Applications in western Washington, *Pure Appl. Geophys*. 135: 31–52.

Maceira, M. (2006). Surface waves, Earth structure, and seismic discrimination, Ph.D. thesis, Pennsylvania State University.

Maceira, M. and C. J. Ammon (2006). Joint inversion of surface wave velocity and gravity observations and its application to Central Asian basins shear velocity structure, *Seismol. Res. Lett*. 77: 297.

Maceira, M. and C. J. Ammon (2009). Joint inversion of surface wave velocity and gravity observations and its application to Central Asian basins shear velocity structure, *J. Geophys. Res*. 114: B02314, doi:10.1029/2007JB005157.

Maceira, M., C. Rowe, H. Zhang, R. Modrak, M. Begnaud, L. Steck, G. Randall, and X. Yang (2009). Advanced Multivariate Inversion Techniques for High Resolution 3D Geophysical Modeling, in *Proceedings of the 2009 Monitoring Research Review: Ground-Based Nuclear Explosion Monitoring Technologies*, LA-UR-09-05276, Vol. 1, pp. 121–130.

Nyblade, A. A. and R. A. Brazier (2002). Precambrian lithospheric controls on the development of the East Africa rift system, *Geology* 30: 755–758.

Pasyanos, M. E. and A. A. Nyblade (2007). A top to bottom lithospheric study of Africa and Arabia, *Tectonophys.* 444: 27–4.

Podvin, P. and I. Lecomte (1991). Finite difference computation of travel times in very contrasted velocity models: A massively parallel approach and its associated tools, *Geophys. J. Int*. 105: 27–84.

Prodehl, C., J. R. R. Ritter, J. Mechie, G. R. Keller, M. A. Khan, B. Jacob, K. Fuchs, I. O. Nyambok, J. D. Obel, and D. Riaroh (1997). The KRISP 94 lithospheric investigation of southern Kenya—the experiments and their main results, *Tectonophys.* 278: 121–147.

Ritsema, J. and H. van Heijst (2000). New seismic model of the upper mantle beneath Africa, *Geology* 28: 63–66.

Simiyu, S. M. and G. R. Keller (1997). An integrated analysis of lithospheric structure across the East Africa plateau based on gravity anomalies and recent seismic studies, *Tectonophys.* 278: 291–313.

Stokes, W. L. (1977). Subdivisions of the major physiographic provinces in Utah, *Utah Geol. 4* 1: 1–17.

Takeuchi, H. and M. Saito (1972). Seismic surface waves, in *Methods of Computational Physics*, B. A. Bolt, Ed. New York, NY: Academic.

Tanimoto, T. (1991), Waveform inversion for three-dimensional density and S-wave structure, *J. Geophys. Res.* 96: 8167–8189.

Tapley, B. D., S. Bettadpur, J. C. Ries, P. F. Thompson, and M. M. Watkins (2005). GRACE measurements of mass variability in the Earth system, *Science* 305: 503–505.

Tessema, A. and L. A. G. Antoine (2004). Processing and interpretation of the gravity field of the East African Rift: Implication for crustal extension, *Tectonophys*. 394: 87–110.

Tiberi, C., M. Diament, J. Déverchère, C. Petit-Mariani, V. Mikhailov, S. Tikhhotsky, and U. Achauer (2003). Deep structure of the Baikal rift zone revealed by joint inversion of gravity and seismology, *J. Geophys. Res*. 108: B3, 2133, doi:10.1029/2002JB001880.

Weeraratne, D. S., D. W. Forsyth, and K. M. Fischer (2003). Evidence for an upper mantle plume beneath the Tanzanian craton from Rayleigh wave tomography, *J. Geophys. Res*. 108: 2427, doi:10.1029/2002JB002273.

Wessel, P. and W. H. F. Smith (1995). New version of the Generic Mapping Tools released, *EOS Trans. AGU* 76: 329.

Yang, Y., M. H. Ritzwoller, F.-C. Lin, M. P. Moschetti, and N. M. Shapiro (2008). Structure of the crust and uppermost mantle beneath the western United States revealed by ambient noise and earthquake tomography, *J. Geophys. Res*. 113: B12310, doi:10.1029/2008JB005833.

Zeyen, H. and U. Achauer (1997). Joint inversion of teleseismic delay times and gravity anomaly data for regional structures, in *Upper Mantle Heterogeneities from Active and Passive Seismology*, K. Fuchs Ed. Dordrecht, Netherlands: Kluwer Academic Publishers.

Zhang, H. and C. Thurber (2006). Development and applications of double-difference tomography, *Pure App. Geophys.* 16:, 373–03, doi:10.1007/s00024-005-0021-y.

Zhang, H. and C. H. Thurber (2003). Double-difference tomography: The method and its application to the Hayward Fault, California, *Bull. Seism. Soc. Am.* 93: 1875–1889.

SEISMIC AND GEOPHYSICAL CHARACTERIZATION OF NORTHERN ASIA

Kevin Mackey[1], Hans Hartse[2], Kazuya Fujita[1], Michael Pasyanos[3], and Michael Begnaud[2]

Michigan State University[1], Los Alamos National Laboratory[2], and Lawrence Livermore National Laboratory[3]

Sponsored by the National Nuclear Security Administration

Award Nos. DE-AC52-09NA29323[1], DE-AC52-06NA25396[2], and DE-AC52-07NA27344[3].
Proposal No. BAA09-19

ABSTRACT

We have begun a major research effort consisting of a combination of seismic field deployments, historical seismic data retrieval, and seismic data analysis to further improve the calibration of northern Asia for nuclear explosion monitoring purposes. This project builds off previous work, and is a cooperative effort between Michigan State University (MSU), Los Alamos National Laboratory (LANL), Lawrence Livermore National Laboratory (LLNL), and several seismic networks in Russia and Japan. The geographic scope of this project covers Russia from the Urals to the Bering Strait and from the Arctic Ocean to the North Korean border. We are expanding our unique data set on earthquakes and nuclear and industrial explosions. Combining historic datasets with data from approximately 50 existing Russian and MSU/Russian and Japanese/Russian digital seismic stations, new deployments, and geologic information, we will substantially increase ground truth data and our understanding of the seismicity, velocity structure, explosion discrimination, and wave propagation characteristics in northern Asia. Our work will further improve location and detection and discrimination capabilities, crustal and upper mantle structure, wave propagation, and natural seismic source characteristics of northern Asia.

Our initial work on this project covers several aspects.

- Updated our seismicity map and seismic database for eastern Russia through 2009. This update has added many thousands of events with associated bulletin information (phase arrival times, amplitude measurements, etc.). We are extending the map to cover the Altai-Sayan network.
- Targeted research on active faulting in the Nera Basin and the Moma Range by combining hypocenter locations, satellite and field analysis of fault scarps, and geomorphological analysis of geologic structures and river drainage.
- Continued our efforts to digitize and analyze historic seismograms from Soviet Peaceful Nuclear Explosions (PNEs) and analyze seismograms from more recent nuclear explosions in Asia.
- Made dispersion measurements for hundreds of paths and have used them to update group velocity maps of the region from 10 to 150 seconds period, which will be used to characterize the complex lithospheric structure of our study area.
- Re-examined mining explosion contamination present in eastern Russian seismic bulletins based on event time of day.
- We have improved the GT locations of the Yakutian PNEs, with most now classified as GT-1 or GT-0. Previously, actual errors for published locations were up to 40km.

OBJECTIVES

The objectives of this project are to characterize the seismicity and geophysical parameters of northern Asia.

RESEARCH ACCOMPLISHED

Expansion of the Eastern Russia Seismicity Map and Database

We continue the development of our seismicity map and database for eastern Russia. Specifically for this project, we have begun to expand project coverage further west to include the Altai-Sayan seismic network (Figure 1). Our seismicity map of eastern Russia has been previously presented on numerous occasions (see Mackey et al., 2007 and Mackey et al., in press). In addition to event locations, our database will also be expanded with phase data from the network.

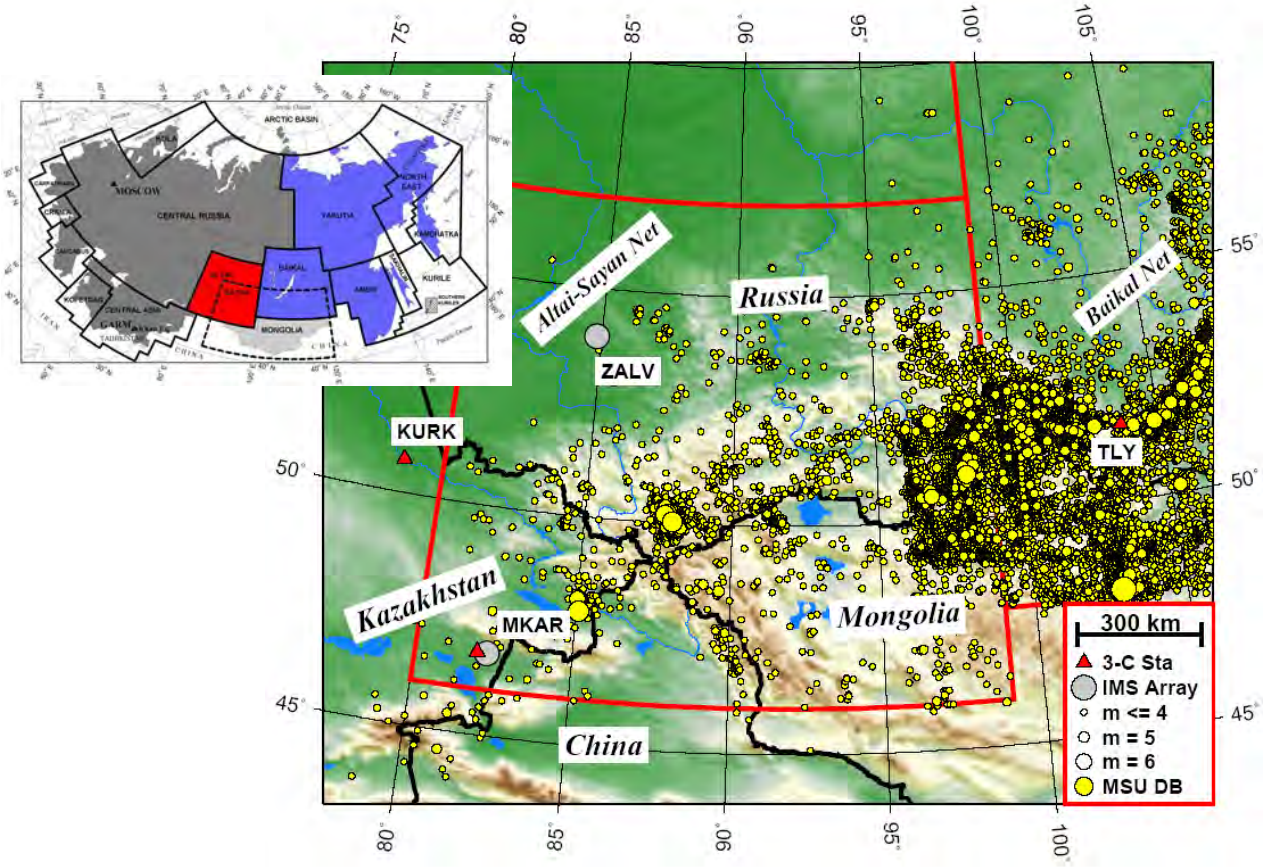

Figure 1. Seismicity of the Altai-Sayan seismic network, covering intermittent years between 1990 and 2010. High event densities east of 96°E are due to overlapping network coverage from the Baikal network. Total, there are about 37,000 events plotted on this map. Inset shows the location of the Altai-Sayan seismic network (red) relative to the existing MSU seismic database (blue).

Surface Wave Studies

For improving the quality of our surface wave studies, we have improved our path coverage of regions north of 60°N in eastern Russia. Figure 2 shows a path map of surface wave dispersion measurements in our study region. Blue paths are the background dispersion paths, while the magenta paths indicate new dispersion measurements made in the past year. Most new data shown here were obtained from IRIS. Additional waveforms recorded at several other broadband stations (not shown) have been acquired, but are not yet integrated into the study.

Figure 3 is a plot of 80 second Rayleigh wave tomography. Rayleigh waves in this period are sensitive to upper mantle structure, particularly the upper mantle shear-wave velocity and lithospheric thickness. Interestingly, we see

a couple of key features. First, is the fast velocity signature of the Central Siberian Platform (shown in blue), which has faster mantle velocities and a thicker lithospheric lid. We see slow Rayleigh wave velocities along both the back-arc regions of the Pacific subduction zones and the Lake Baikal Rift. While it appears that the boundaries between these somewhat correspond to the boundaries of the microplates, it is our intention to use significantly more data from the region to define these boundaries in finer detail.

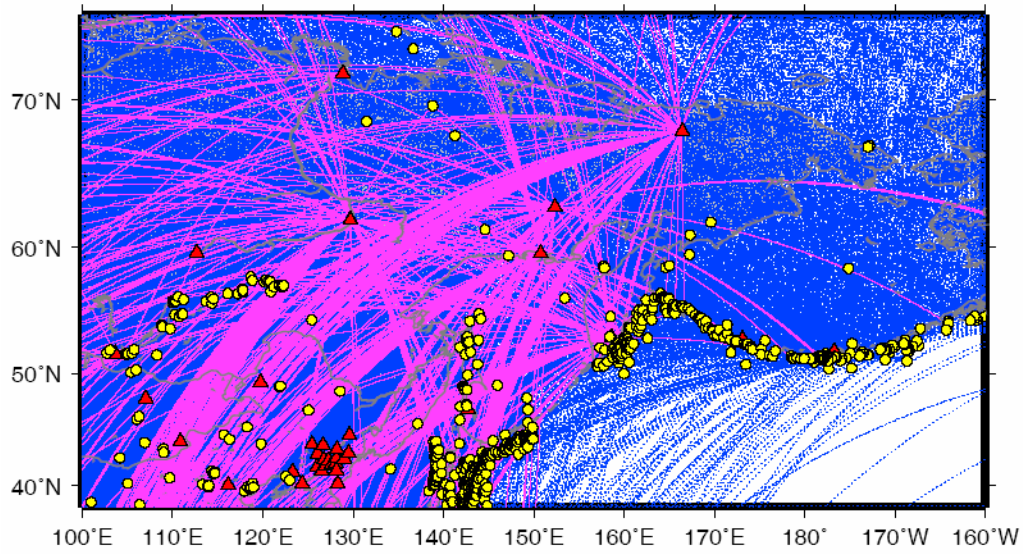

Figure 2. Path coverage in eastern Russia for 80.0 second Rayleigh wave surface wave studies. Pink shows newly acquired paths, while blue indicate earlier measurements. Events and stations used are shown as yellow circles and red triangles, respectively.

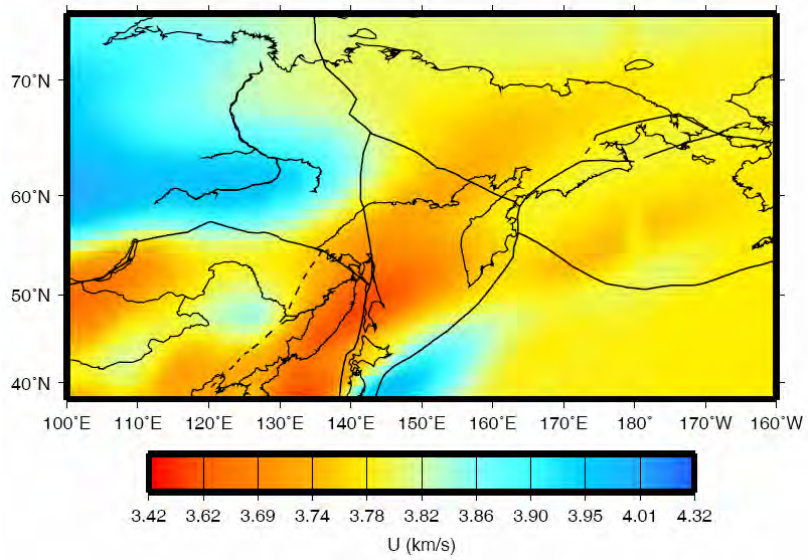

Figure 3. 80.0 second Rayleigh wave tomography of eastern Russia. Main features of note are high velocities associated with the Siberian Platform and lower velocities associated with the Baikal Rift zone and back-arc regions of the pacific subduction zones.

Seismograms of the 2009 DPRK Nuclear Explosion

On 25 May, 2009, North Korea detonated its second nuclear test. This test was recorded moderately well across continental eastern Russia by stations of the Russian regional seismic networks. Figure 4 shows a record section of seismograms primarily from the Magadan and Yakutsk regions. Paths transiting the back-arc regions of the pacific

subduction zones to stations in Kamchatka did not record the explosion as clearly (Figure 5). Within Kamchatka, stations either along the central axis of the peninsula or close to the western coast recorded the explosion better than stations along the eastern coast. This suggests that the subduction zone processes interferes with good transmission of the seismic signal from North Korea.

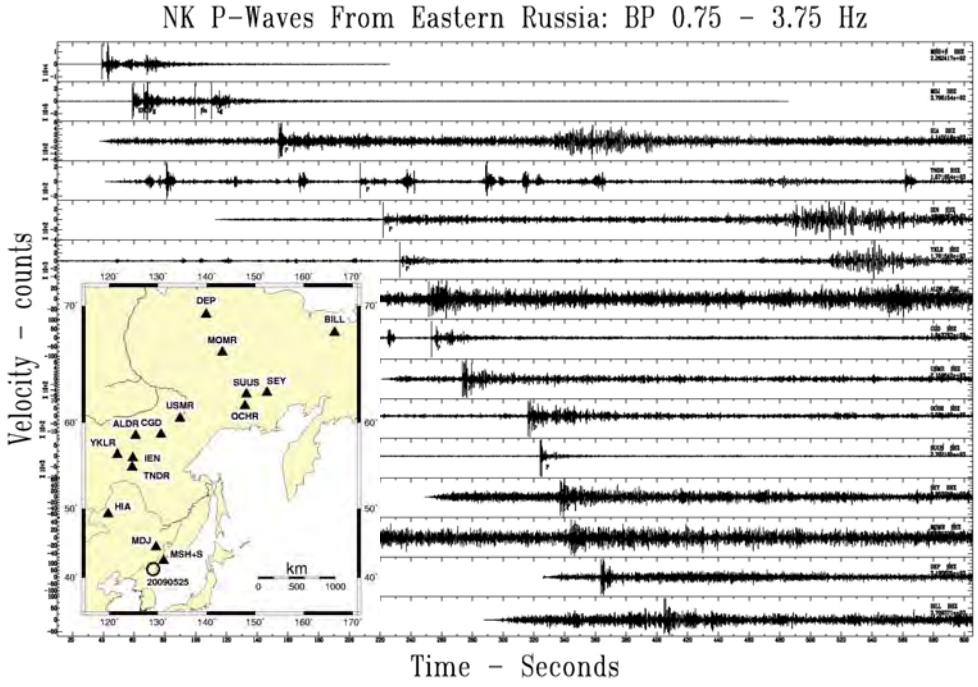

Figure 4. Vertical component seismograms from continental eastern Russia of the 2009 DPRK nuclear test. Traces are bandpass filtered from 0.75-3.75 Hz. Index map on inset.

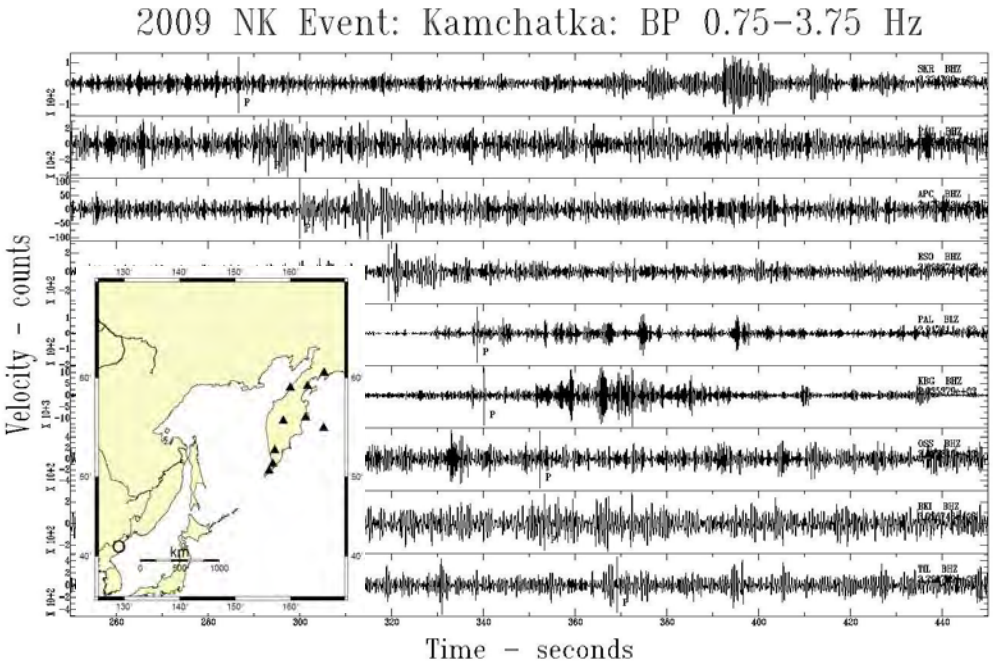

Figure 5. Vertical component seismograms from Kamchatka, Russia of the 2009 DPRK nuclear test. Traces are bandpass filtered from 0.75-3.75 Hz. Index map on inset. Stations either along the central axis of the peninsula (third and fourth traces from the top) or close to the western coast (fifth trace from top) recorded the explosion better than stations along the eastern coast.

Improved Ground-Truth for Yakutian PNEs

The monitoring community has generally accepted the source coordinates for PNEs presented in Sultanov et al. (1999) as representing ground truth, although in reality there remains considerable variability in location quality. Working from recent Russian literature, we present revised coordinates here for PNEs detonated in Yakutia (see Figure 5 inset), with revised coordinates generally at either a GT-0 or GT-1. The Yakutian PNEs can be divided into two categories; those detonated for Deep Seismic Sounding (DSS) geophysical surveys, and those detonated for industrial applications such as oil recovery or dam construction. Locations cited by Sultanov et al. (1999) for PNEs associated with industrial applications are derived from seismically determined parameters and are poor, with errors up to 40km. We summarize each of these below. Deep seismic sounding associated events appear accurate to the GT-1 level or better, and are not discussed in detail other than minor corrections as listed in Table 1. Regarding Yakutian PNEs, Fujita (1995) presented an overview and provided preliminary estimates on their locations based on Russian publications from the mid-1990s. Mackey et al. (2009) discussed, and summarized here, Crystal, Craton-3, and Horizon-3 in detail using a combination of satellite images and newly released Russian papers. Mackey et al., (2005) discussed Neva-1 and the Neva-2 series on the basis of Soviet military topographic maps.

On October 2, 1974, a small (1.7 kt) explosion, "Crystal," was detonated near the Udachnyi diamond mine to create a foundation for a tailings storage pond dam. The epicenter cited by Sultanov et al. (1999) is taken from the International Seismological Center (ISC) Bulletin with coordinates of 66.1°N and 112.65°E. Fujita (1995) cited the location of the detonation as on the "left bank of the Ulakhan-Bysyttaakh stream, 2.5 km north of the town." Examination of this site using Google Earth imagery reveals a circular dome (Figure 6). According to Gedeonov et al. (1997), in 1992 the crater was covered with an artificial mound about 300 m in diameter and 7-20 m in height, consistent with the Google Earth image. This site falls approximately 40 km north-northwest from the location given by Sultanov et al. (1999). The center of the dome is located at 66.4573±0.0001°N, 112.3989±0.0001°E. Although this is one of the smallest and most poorly recorded PNEs in this region, it now must be considered the best located.

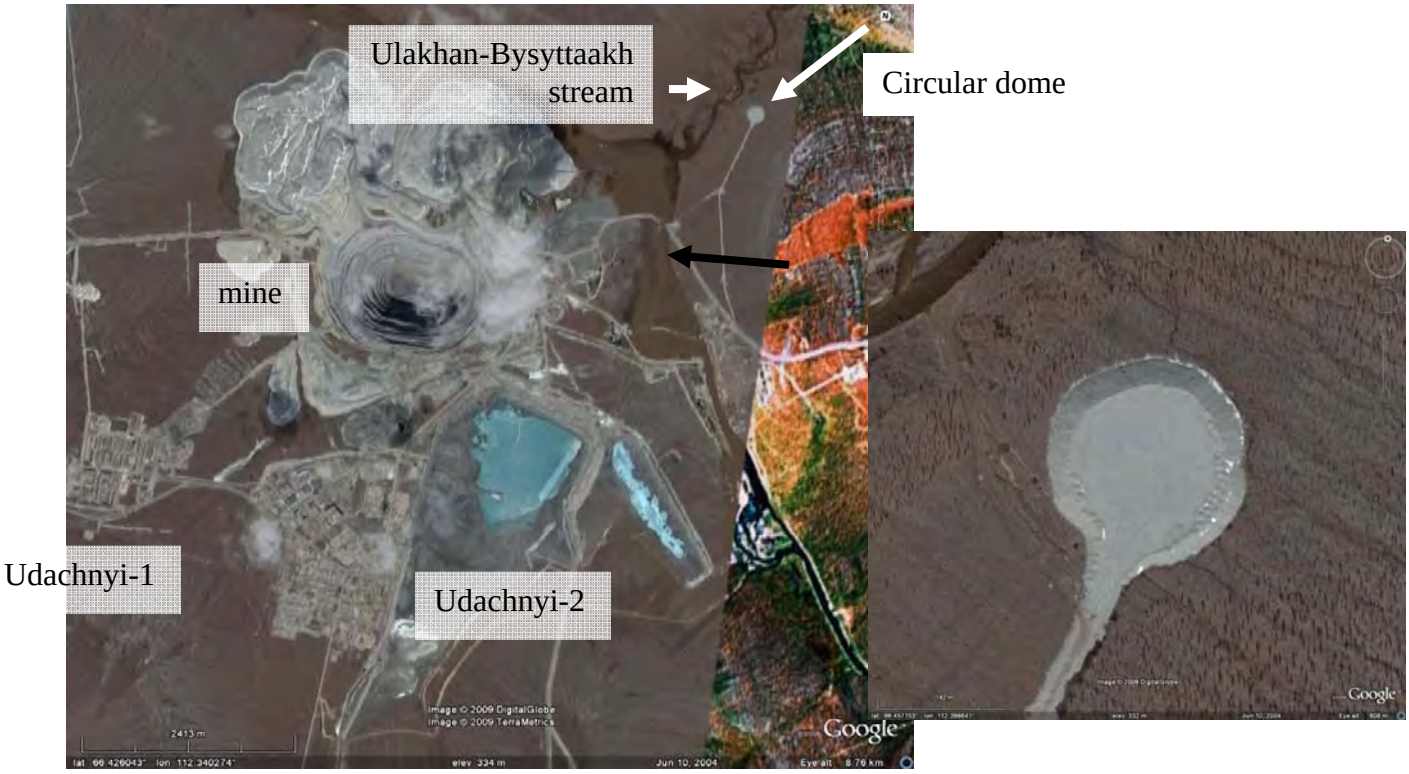

Figure 6. Google Earth image of the Udachnyi Mining complex and encapsulated crater from the Crystal PNE (circular dome). The inset shows a close-up of the site.

The Neva series of PNEs as well as Oka, Sheksna, and Vyatkta were detonated primarily to enhance oil recovery in the Central Botuobuya Oil and Gas field (Figure 7). The locations of these detonations were given in Burtsev (1993) in terms of distance from Tas-Yuryakh settlement. It has been unclear whether the distances were as "the crow flies" or distance along a connecting road. Mackey et al. (2005) used the direct line distance to suggest that the Neva-2 sequence was detonated along the Telgespit River, southeast of its confluence with the Uspun (Figure N2a). Mikulenko et al. (2006) present a map (Figure N2b) showing the details of the locations of the nuclear detonations in the Butuobaya area. Using this map and distances from Burtsev (1993), we examined the detonation sites in detail on satellite imagery. The Neva-2 series events are located almost exactly as predicted by Mackey et al. (2005, Figure 8).

Mikulenko et al. (2006) place the Neva-2 series sites on the east bank of the Telgespit River where satellite imagery reveals a series of disturbed areas that corresponds to almost the exact location predicted by Mackey et al. (2005) (Figure N4). This confirms that the distances presented in the various Russian publications represent straight-line distances, and we have used this to locate the other PNEs, both in the Central Botuobuya region as well as Craton-4 and Kimberlite-4, below, which are given distances from specific settlements.

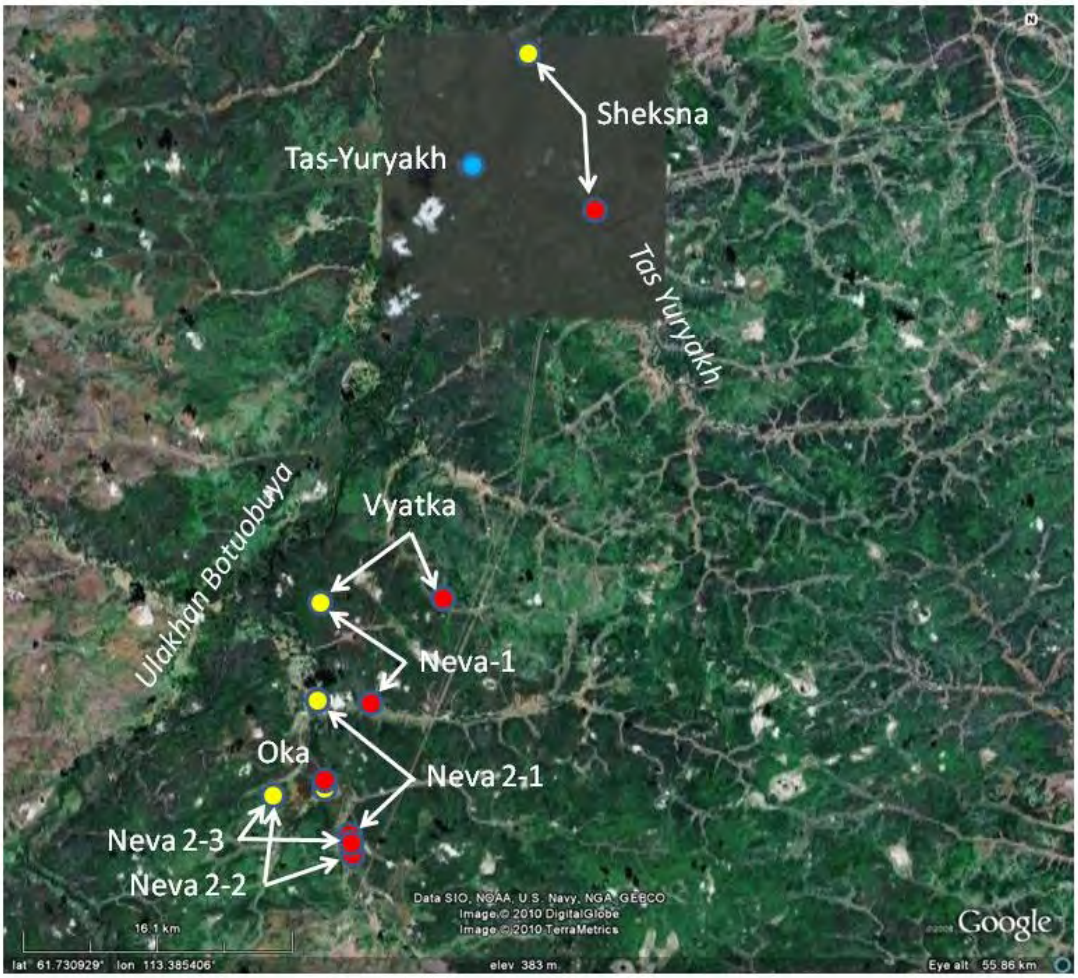

Figure 7. Satellite image of the Central Botuobuya Oil and Gas field. Locations of the Neva series of PNEs as given by Sultanov et al. (1999; yellow) ISC (orange), and in this report (red) also shown. Tas-Yuryakh shown as blue dot. The locations by Sultanov et al. (1999) are essentially the same as ISC for the Neva 2 series.

Neva 2-1 is the northernmost of the cluster, Neva 2-2 is the southernmost, and Neva 2-3 is in between. Table 1 presents our estimates of the location of the Neva 2 series and determinations from other sources. These are a significant improvement over Sultanov et al. (1999) and the ISC. Neva 2-3 was detonated with the intent of creating an underground oil storage facility.

Oka was detonated on November 5, 1976, 38 km from Tas-Yuryakh (Burtsev, 1993). Mikulenko et al. (2006) place the site on the west bank of the Telgespit, just below its confluence with the Uspun River (Figure 8b). Examination of satellite imagery shows a disturbed area with many roads leading to it as well as a larger area of apparently disturbed ground along the Uspun (Figure 10a). Based on the figure from Mikulenko et al. (2006, Figure 8b), which places the borehole below the confluence of the two rivers, we select the northern site; however, from a distance viewpoint, both are essentially 38 km from Tas-Yuryakh. The two sites are less than 300 m apart, and the coordinates reported by Sultanov et al. (1999) are in between.

Neva-1 was detonated on October 10, 1982, 31.5 km from Tas-Yuryakh. Mikulenko et al. (2006) place it along the Kudulakh River, 2.75 km above its confluence with the Telgesit (Figure 8b). There is a cleared area with apparent road access from the south (Figure 10b). This site is closer to 32.5 km from Tas-Yuryakh. An alternate possibility, a cleared formerly swampy area, located about 2 km to the north, would not fit the Mikulenko et al. (2006) map. In the absence of additional information, we suggest this is the possible site. Sultanov places Neva-1 close to the ISC coordinates (Figure 7). This is the most poorly located of the Botuobuya PNEs.

A.

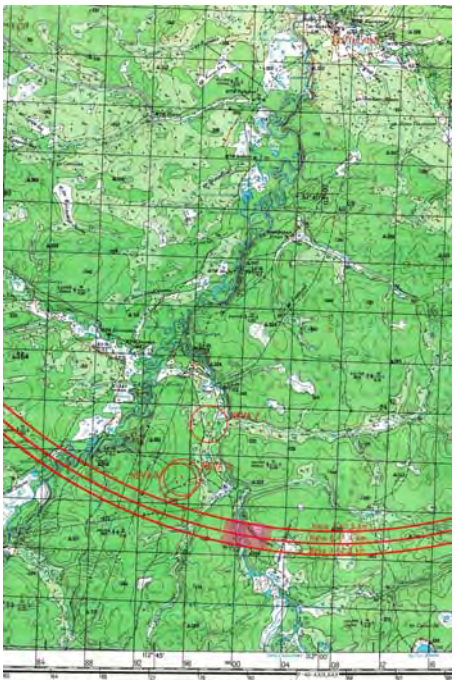

B.

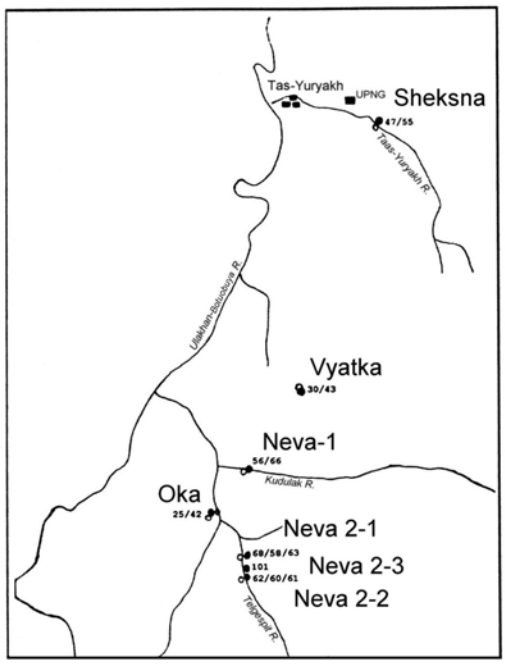

Figure 8. a) Location of Neva-2 series (pink area) as predicted by Mackey et al. (2005) based on direct-line distance (red arcs) from Tas-Yuryakh as reported by Burtsev (1993) and Tsyganov (1993). b) Location of PNEs in the Central Botuobuya Oil and Gas field as published in Mikulenko et al. (2006). Black dots represent PNE locations.

Vyatka was detonated on October 7, 1978, 26 km from Tas Yuryakh. There is a disturbed area visible in satellite imagery (Figure 11a) exactly 26 km from Tas Yuryakh along the Uspun stream at the relative location indicated on the Mikulenko et al. (2006) map (Figure 8b). Our proposed location is about 6 1/2 km east of the location given in Sultanov et al. (1999), which is located at the same coordinates as they propose for Neva-1.

Sheksna was detonated on October 7, 1979, 7.2 km from Tas-Yuryakh. Examination of the locality identified by Mikulenko et al. (2006; Figure 8b), a small area of disturbed ground is found (Figure 11b) approximately 7.2-7.6 km from Tas-Yuryakh (depending on starting point). Another area of disturbed ground, farther southeast along the

present highway, is even further from Tas-Yuryakh. This location is significantly south-southeast of the ISC, PDE, and Sultanov et al. (1999) locations (Figure 7), which are to the north of Tas-Yuryakh and far away from the Tas-Yuryakh River; the Mikulenko et al. (2006) map is unambiguous about the location of Sheksna close to the river.

Figure 9. Detail of the Telgespit River valley 40 km from Tas-Yuryakh showing disturbed areas proposed to be the detonation sites (red dots) of the Neva 2 series of PNEs in 1987.

a). **b).**

Figure 10. a) Proposed location of Oka (arrow) and location from Sultanov et al. (1999; yellow dot). b) Region along Kudulakh River above its confluence with the Telgespit showing possible location (arrow) for Neva-1. The Sultanov et al. (1999) location is off the map.

a) **b)**

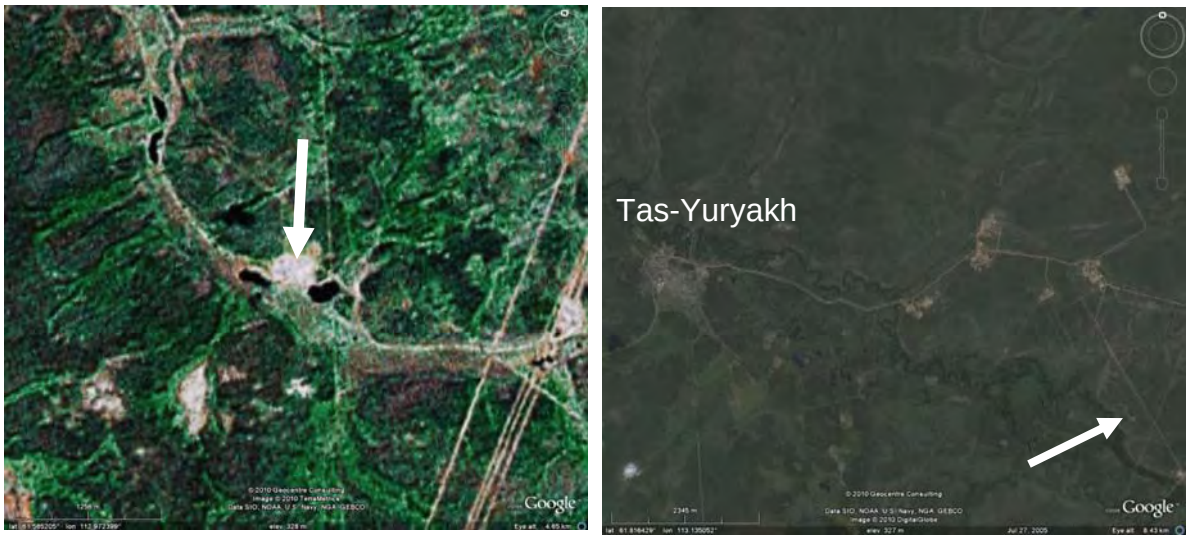

Figure 11. a) Satellite image of the proposed location of Vyatka (arrow). b) Tas-Yuryakh and vicinity showing the proposed site of Sheksha (arrow).

Craton-3 was detonated on August 24, 1978, and also produced radioactive contamination. Sultanov et al. (1999) lists coordinates of 65.925°N, 112.338°E, and a depth of 577 m. Gedeonov et al. (1997) gives a detailed map which yields coordinates of 65.9249± 0.0005°N, 112.3330± 0.0005°E, within 400 m of the Sultanov et al. (1999) coordinates. The description in Burtsev (1993) of the event being on the left-bank of the Chukuka stream, and hence the Fujita (1995) epicenter, is erroneous.

Horizon-4 was detonated on August 12, 1975. A crater-like feature visible in satellite imagery on the north bank of the Erikit, the location described in Burtsev (1993), is suggested to be the site of Horizon-4 (Table 1). The resolution is insufficient to be certain of the site and there is another crater-like feature in close proximity, thus there may be uncertainty on the order of a km.

Kimberlite-4 was detonated on August 12, 1979. Mikulenko et al. (2006) and papers in Burtsev (1993) place the site as being on the shores of Lake Daban, 27-28 km from Tuobuya. A disturbed area visible in satellite imagery at the south end of the lake (Table 1); the coordinates from Sultanov et al. (1999) are in a forested area.

Craton-4 was detonated on August 9, 1978. The detonation site is given in papers in Burtsev (1993) and Mikulenko et al. (2006) as being 12 km from Lake Nidzhili and 19 km from Aryktakh. In addition, a map of radiation sampling in Burtsev (1993) can be scaled to fit a lake near these coordinates. A disturbed area corresponding to the map location is suggested to be the detonation site (Table 1). There are some other disturbed areas within 300 m, thus a small amount of uncertainty remains.

For the PNEs of the Central Botuobuya region, Sultanov et al. (1999) have located Oka very well, but differ significantly (5 to 10 km) for the others. The conformity of satellite imagery, the map presented in Mikulenko et al. (2006), and the distance from Tas-Yuryakh (always within 1 km in a direct-line) gives us confidence about our proposed coordinates for these PNEs. For other PNEs in Yakutia, the Sultanov et al. (1999) coordinates are very close (< 1 km) to our final coordinates for proposed sites (Table 1), except for Crystal. Table 1 also includes our estimates of their GT classification. We suggest that the revised coordinates supersede those found in Sultanov et al. (1999) in future GT studies.

Table 1. Revised GT locations of Yakutia PNEs.

PNE	Proposed Coordinates		Sultanov Coordinates		Difference (km)	Proposed GT
	Latitude (ºN)	Longitude (ºE)	Latitude (ºN)	Longitude (ºE)		
Crystal	66.4573	112.3989	66.10	112.65	41.4	GT0
Neva 2-1	61.4316	112.8867	61.50	112.85	7.8	GT0
Neva 2-2	61.4185	112.8904	61.45	112.80	6.1	GT0
Neva 2-3	61.4288	112.8878	61.45	112.80	5.2	GT0
Oka	61.4606	112.8592	61.458	112.860	0.3	GT1
Neva-1	61.5006	112.9110	61.55	112.85	6.4	GT5
Vyatka	61.5562	112.9915	61.55	112.85	7.5	GT0
Sheksna	61.7683	113.1625	61.85	113.10	9.7	GT0
Craton-3	65.9249	112.3330	65.925	112.338	0.2	GT0
Horizon-4	70.7635	126.9520	70.763	126.953	0.0	GT1
Kimberlite-4	61.8000	122.4159	61.803	122.430	0.8	GT0
Craton-4	63.6800	125.5289	63.678	125.522	0.4	GT0

CONCLUSIONS AND RECOMMENDATIONS

This project will improve our knowledge on many geophysical aspects of northern Asia. As summarized here, this is inclusive of seismic characterization, surface wave tomography, analysis of nuclear explosion seismograms, and improving the GT classification of events.

REFERENCES

Burtsev, I. S. (editor), (1993). *Radiation Contamination of the Territory of the Sakha Republic (Yakutia): Problems of Radiation Safety*: Ministry of Public Health of the Sakha Republic (Yakutia), Yakutsk, 254 pp. (in Russian).

Fujita, K. (1995). Peaceful nuclear explosions in the Sakha Republic (Yakutia): *Seismol. Res. Lett.*. 66: (3), 20–24.

Gedeonov, A. D., I. N. Kuleshova, E. R. Petrov, M. L. Savopulo, V. Y. Shkroev, B. N. Shuvalov, V. G. Alexeev, V. I. Arkhipov, and I. S. Burtsev (1997). Plutonium in soils, bottom sediments and lichen near peaceful nuclear explosion sites in the Republic of Sakha (Yakutia): *J. Radioanal. Nucl. Chem*. 221: 85–92. (in Russian).

Mackey, K. G., K. Fujita, H. E. Hartse, R. J. Stead, L. K. Steck, L. V. Gunbina, N. Leyshuk, S. Shibaev, B. M. Koz'min, V. S. Imaev, E. Gordeev, V. Chebrov O. Masal'ski, N. Gileva, V. A. Bormatov, A. A. Voitenok, Y. Levin, and T. Fokina, (*in press*). Seismicity Map of Eastern Russia, 1960-2010. *Seismol. Res. Lett.*

Mackey, K. G., H. E. Hartse, L. K. Steck, R. J. Stead, C. A. Rowe, K. Fujita, and L. Gutirrez (2007). Seismic characterization of northeast Asia, in *Proceedings of the 29th Monitoring Research Review: Ground-Based Nuclear Explosion Technologies,* LA-UR-07-5613, Vol. 1:, pp. 123–132.

Mikulenko, K. I., A. I. Chomchoev, and S. P. Gotovtsev (2006). *Geologic-Geopgraphical Conditions for Conducting and the Consequences of Underground Nuclear Explosions on the Territory of the Sakha Republic (Yakutia)* . Ministry for the Protection of Nature of the Sakha Republic (Yakutia), Yakutsk, 195 pp. (n Russian).

Sultanov, D. D., J. R. Murphy, and K. D. Rubinstein (1999). A seismic source summary for Soviet peaceful nuclear explosions, *Bull. Seismol. Soc. Am.* 89: 640–647.

THE CRUSTAL AND MANTLE VELOCITY STRUCTURE IN CENTRAL ASIA FROM 3D TRAVEL TIME TOMOGRAPHY

Randolph J. Martin[1], Levent Gulen[2], Youshun Sun[2], M. Nafi Toksöz[2]

New England Research[1] and Massachusetts Institute of Technology[2]

Sponsored by the National Nuclear Security Administration

Award No. DE-AC52-08NA28751

ABSTRACT

The lithospheric structure in Central Asia features large blocks such as the Indian plate, the Afghan block, the Turan plate, and the Tarim block. This geologically and tectonically complicated area is also one of the most seismically active regions in the world. We developed *P*- and *S*-wave velocity structures of Central Asia in the crust using the travel-time data from Kyrgyzstan, Tajikistan, Kazakhstan, and Uzbek Republic. We chose the events and stations between 32N65E and 45N85E and focused on the areas of Pamir and western Tianshan. In this data set, there are more than 6000 *P* and *S* arrivals received at 80 stations from about 300 events. Double difference tomography is applied to relocate events and to determine seismic velocities simultaneously. Our results provide an improved earthquake location and high resolution crustal structure in this region.

To extend the model deeper into the mantle through the upper mantle transition zone, ISC/EHB data for *P* and *PP* phases are combined with the ABCE data. To counteract the "smearing effect," the crust and upper mantle velocity structure, derived from regional travel-times, is used. An adaptive grid method based on ray density is used in the inversion. Regional teleseismic tomography provides a high-resolution, 3-D *P*-wave velocity model for the crust, upper mantle, and the transition zone. The crustal models correlate well with geologic and tectonic features. The upper mantle tomograms show the images of Tian Shan. The slab geometry is quite complex, reflecting the history of the changes in the plate motions.

OBJECTIVES

The main goal of this project is to develop a database consisting of: new waveform data, seismic event catalogs, and information on the geology and active tectonics in the Central Asian region. Over the past years, we have collected geologic, geophysical, seismic event catalog and phase arrival data from local networks in the Caucasus region; this project extends the work into the CASRI (Central Asia Seismic Research Initiative) region (Kazakhstan, Kyrgyzstan, Uzbekistan, and Tajikistan). The new database is crucial in generating a detailed crust and mantle structure model and characterizing seismic wave propagation and attenuation in Central Asia. The local seismic networks, calibration events, improved crust and mantle structure models and better location algorithms (e.g., multiple-event grid search, double difference methods) will improve the event locations. This new database will form the basis for mitigating earthquake hazard in Central Asia, and it will aid in the monitoring of these regions of strategic interest to U.S. national security.

RESEARCH ACCOMPLISHED

The Regional Tectonic Setting

The active tectonics of Asia is predominantly the result of the continental collision and the continuing continental convergence between the Indian and the Eurasian Plates. As a result, large scale structures such as the Himalayas, Tibet, Hindu Kush-Pamir, and Zagros have been produced by the collision and the post-collisional convergence.

The India-Eurasia collision is also accommodated by major thrusting and crustal shortening as evidenced by the high elevation and compressional structures such as the Himalayas, Hindu Kush-Pamir, and the Tien Shan and Zagros region (Figure 1). An alternative model suggesting that the mode of continental deformation can be explained by continuum mechanics was proposed to explain the continental deformation of Asia (England and Houseman, 1986; Houseman and England, 1993). This alternative model assumes that the collision and convergence of the Indian and Eurasian Plates are mainly accommodated by lithospheric thickening, and the resultant increased gravitational body forces drive the active tectonics of Asia. The Global Positioning System measurements and crustal rheology modeling in Asia provide evidence that the deformation in the shallow brittle crust occurs on a distributed network of faults, and some regions, such as the Tarim Basin, the Ordos and South China, behave as rigid blocks; however, deformation of a continuous medium at depth is the best description of the present day tectonics of Asia (Royden et al., 1997; Wang et al., 2001; Calais et al., 2003; Zhang and Gan, 2008). The *Pn* and *Sn* tomographic models (Figure 1) show the heterogeneities below the crust that correlate well with the subduction zones, rigid blocks and other tectonic features.

The countries that are within the interest area of the CASRI project are primarily affected by the tectonic deformations and associated seismic activity of the Tien Shan and the Pamir-Hindu Kush regions. Since we have covered the Neotectonic analysis of the Tien Shan region previously (Martin et al., 2009) we will briefly summarize the active tectonics of the Pamir-Hindu Kush region in this paper.

The Pamir-Hindu Kush Region

The Pamir-Hindu Kush region is located at the western syntaxis of the Himalayan belt and it has an elevation of 4000–5000 m. This orojenic syntaxis consists of several terrains that were accreted to the southern margin of Asia during the Paleozoic-Mesozoic closure of the Tethys Ocean (Tapponnier et al., 1981; Burtman and Molnar, 1993; Yin and Harrison, 2000; Schwab et al., 2004; Robinson et al., 2007). Before the India-Asia continental collision took place about 45–50 my ago, the Pamir region was an Andean-style plate margin. The post-collisional indentation of the Indian Plate into the Eurasian Plate caused intense deformation and crustal shortening and created major thrusts and strike-slip faults bounding the region (Figure 2). The Main Pamir Thrust forms the northern boundary separating the Pamirs from the Tien Shan. The left-lateral strike-slip Darvaz-Karakul Fault Zone marks the boundary in the west between the Tadjik Depression and the Pamirs. The right-lateral strike-slip Karakorum fault zone forms the eastern boundary that separates the Pamirs from the western Kunlun and the Tarim Basin (Molnar and Tapponnier, 1978). The Main Pamir Thrust has been interpreted to have accommodated about 300 km of crustal shortening, and additionally, at least 300 km of shortening was also accommodated internally by thrusting and faulting within the Pamirs during the Cenozoic (Burtman and Molnar, 1993).

The Pamir-Hindu Kush region has high seismic activity and many large earthquakes have occurred in the region. The focal mechanism solutions for the earthquakes in this region indicate predominantly thrust events, as would be expected, and some strike-slip events along major shear zones that form the boundaries of the region.

The most interesting aspect of the Pamir-Hindu Kush seismicity is that this region is one of the most active regions of intermediate depth seismicity. Many studies have been carried out to evaluate the seismicity of the Pamir-Hindu Kush region (Chatelain et al., 1980; Roecker 1982; Fan and Ni, 1989; Burtman and Molnar, 1993; Fan et al., 1994; Pegler and Das, 1998). More recently, seismic tomographic studies of the mantle structure beneath the Pamir-Hindu Kush region have revealed that the intermediate depth seismicity is the result of the existence of two opposing sense subduction zones (Freiderich, 2003; Kumar et al., 2005; Koulakov and Sobolev, 2006; Negredo et al., 2007). The Indian lithosphere subducts steeply northward beneath the Hindu Kush, and the Asian lithosphere subducts southward beneath the Pamirs; the interface of the two converging lithospheres, at mantle depths beneath the Pamir-Hindu Kush region, forms the zone of intermediate depth seismicity.

Travel-Time Data

An important task under this project is to collect arrival time data from seismic stations situated in the Central Asia. A significant number of these stations are in networks whose data are not available from global data centers such as IRIS (Incorporated Research Institutions for Seismology) or ISC (International Seismological Centre). Figure 3 shows seismic stations in the region from which we have obtained data either through data centers or by bilateral arrangements. In the previous studies of this region, teleseismic data and surface wave data were the main data sources. Although teleseismic data provide us with much information about the mantle, shallow structure is still unclear. The horizontal resolution is also limited by available periods of surface waves. Therefore, we use the local and regional travel times to invert for the 3-D crustal velocity structure in this region. We selected the stations and events between 32°N-65°E and 45°N-85°E where there are 68 stations and 220 events (Figure 3). More than 2200 P-wave phase picks are employed in the inversion. The average grid spacing is 100 km and the inverted grids lay on six layers. The source-station ray paths are also shown in Figure 3 and the ray density is dense enough to obtain good tomographic resolution.

***P*- and *S*-Wave Travel-Time Tomography of the Crust and Upper Mantle**

A high-resolution tomographic model for the heterogeneous crust is constructed by iterative, non-linear tomography. To generate adequate starting models for the nonlinear inversion, we combine pertinent information from global (Mooney et al., 1998; Stevens et al., 2001; Ritzwoller et al., 2002), regional, and local crust and uppermost mantle models. Next, we use the adaptive moving window (AMW) approach (Sun et al., 2004, 2008) to obtain crustal velocities and *Pn* and *Sn* models from a 1-D Monte Carlo inversion of local ($\leq 20°$) arrival time data in the whole region, building these into the next model (Model #2). The third step is a tomographic inversion of the local and regional arrival time data for 3-D variations in the *P*- and *S*-wave speed, using Model #2 as the initial input model.

For this purpose we use a modified version of Zhao's tomographic method (Zhao et al., 1992, 1994; Zhao, 2001; Sun and Toksöz, 2006), which allows for 3-D velocity variations everywhere in the model and can accommodate velocity discontinuities. The velocity structure is discretized using a 3-D grid. The velocity perturbation at each point is calculated by linear interpolation of the velocity perturbations at surrounding (adjacent) grid nodes. The velocity perturbations at grid nodes are the unknown parameters for the inversion procedure. To calculate travel-times and ray paths accurately and rapidly, the pseudo-bending technique (Um and Thurber, 1987) is used iteratively. We correct for station elevations by including station correction terms in the inversion. The nonlinear tomographic problem is solved by repeated linear inversions. At each iteration, perturbations to hypocentral parameters and velocity structure are determined simultaneously.

Starting from the *P* and *S* models obtained from the above strategy, we apply an adaptive-mesh double-difference tomography method to the newly assembled data set to further improve event locations and velocity models (Zhang and Thurber, 2003; 2006). In this approach, the configuration of model cells is adjusted to sampling density to stabilize the inversion and (locally) optimize spatial resolution. Figure 4 shows the *P* and *S* travel-time, distance graphs, and *P*-wave travel-time residual distribution before and after the 3-D inversion. The standard deviation improved from 2.1 seconds to 0.9 seconds as a result of the 3-D inversion.

Figure 5 shows *Pn* and *Sn* structure and Figures 6 and 7 show the tomographic results obtained for the Central Asian crustal structure. Since most phase arrivals are *Pn*, the layers around the Moho (50 km and 70 km) are imaged with the best resolution. In addition, the shallower structure can also be recovered along the China boundary. Figure 8 shows the upper mantle velocity structure at the depths of 100, 200, 400, and 600 km obtained by the double difference tomography method.

CONCLUSIONS

Our results show strong crust and mantle heterogeneities in Central Asia. The low velocity zones are found near the Tien Shan, northern Pamirs, and Tajik depression, whereas high velocity anomalies exist beneath the southern Pamir, Kazakh shield, and the Tarim basin. High velocities delineate the subduction zones and active or fossil slabs.

The Moho depth in the region is about 70 km. There are areas such as the western Tarim Basin where the Moho discontinuity is much shallower

The extension of the velocity models into the mantle transition zone is accomplished by adding the teleseismic data from the 1964–2008 ISC/EHB database, which contains over 10 million P-wave travel-times, and from datasets obtained by the various national data centers.

REFERENCES

Burtman, V. S. and P. Molnar (1993). Geological and geophysical evidence for deep subduction of continental crust beneath the Pamir, *Geol. Soc. Am. Spec. Paper* 281, 76 p.

Calais, E., M. Vergnolle, V. San'kov, A. Lukhnev, A. Miroshnitchenko, S. Amarjargal, and J. Déverchère (2003). GPS measurements of crustal deformation in the Baikal-Mongolia area (1994-2002): Implications for current kinematics of Asia, *J. Geophys. Res.* 108: doi:10.1029/2002JB002373.

Chatelain, J. L., S. W. Roecker, D. Hatzfeld, and P. Molnar (1980). Microearthquake seismicity and fault plane solutions in the Hindu Kush region and their tectonic implications, *J. Geophys. Res.* 85: 1365–1387.

England, P. and G. Houseman (1986). Finite strain calculations of continental deformation: 2. Comparison with the India-Eurasia collision zone, *J. Geophys. Res.* 91: 3664–3676.

Fan, G. and J. F. Ni (1989). Source parameters of the 13 February Karakoram earthquake, *Bull. Seismol. Soc. Am.* 79: 945–954.

Fan, G., J. F. Ni, and T. C. Wallace (1994). Active tectonics of the Pamirs and Karakorum, *J. Geophys. Res.* 99: 7131–7160.

Friederich, W. (2003). The S-velocity structure of the east Asian mantle from inversion of shear and surface waveforms, *Geophys. J. Int.* 153: 88–102.

Houseman, G. and P. England (1993). Crustal thickening versus lateral expulsion in the India-Asia continental collision, *J. Geophys. Res.* 98: 12,233–12,249.

Koulakov, I. S. and V. Sobolev (2006). A tomographic image of Indian lithosphere break-off beneath the Pamir-Hindukush region, *Geophys. J. Int*. 164: 425–440.

Kumar, P., X. Yuan, R. Kind, G. L. Kosarev (2005). The lithosphere-asthenosphere boundary in the Tien Shan-Karakoram region from S receiver functions: Evidence for continental subduction, *Geophys. Res. Lett.* 32: doi: 10.1029/2004GL022291.

Martin, R. J., M. N. Toksoz, L. Gulen, Y. Sun (2009). Extension of the CauSIN Study into Central Asia: Final Report, Contract No. De-AC52-04NA25612.

Molnar, P. and P. Tapponnier (1978) Active tectonics of Tibet, *J. Geophys. Res.* 83: 5361–5375.

Mooney, W.D., G. Laske, and G. Masters (1998). CRUST 5.1: A global crustal model at 5°× 5°, *J. Geophys. Res.* 103: 727–747.

Negredo, A. M., A. Replumaz, A. Villasenor, and S. Guillot (2007). Modeling the evolution of continental subduction process in the Pamir-Hindu Kush region, *Earth Planet. Sci. Lett*. 259: 212225.

Pegler, G. and S. Das (1998). An enhanced image of the Pamir-Hindu Kush seismic zone from relocated earthquake hypocenters, *Geophys. J. Int*. 134: 573–595.

Ritzwoller, M.H., M. P. Barmin, A. Villasenor, A. L. Levshin, and E. R. Engdahl (2002). Pn and Sn tomography across Eurasia to improve regional seismic event locations, *Tectonophysics* 358: 39-55.

Robinson, A. C., A. Yin, C. E. Manning, T. M. Harrison, S. H. Zhang, and X. F. Wang (2007). Cenozoic evolution of the eastern Pamir: Implications for strain-accommodation mechanisms at the western end of the Himalayan-Tibetan orogen, *Geol. Soc. Am. Bull*. 119: doi: 10.1130/B25981.1

Roecker, S. W. (1982). Velocity structure of the Pamir-Hindu Kush region: possible evidence of subducted crust, *J. Geophys. Res*. 87: 945–959.

Royden, L.H., B.C. Burchfiel, R.W. King, E. Wang, Z. Chen, F. Shen, and L. Yuping (1997). Surface deformation and lower crustal flow in eastern Tibet, *Science* 276: 788–790.

Schwab, M., L. Ratschbacher, W. Siebel, M. McWilliams, V. Minaev, V. Lutkov, F. Chen, K. Stanek, B. Nelson, W. Frisch, and J. L. Wooden (2004). Assembly of the Pamirs: Age and origin of magmatic belts from the southern Tien Shan to the southern Pamirs and their relation to Tibet, *Tectonics* 23: doi:1029/2003TC001583.

Stevens, J. L., D. A. Adams, and G. E. Baker (2001). Improved surface wave detection and measurement using phase-matched filtering with a global one-degree dispersion model, in *Proceedings of the 23rd Seismic Research Review: Worldwide Monitoring of Nuclear Explosions*, LA-UR-01-4454, Vol. 1, pp. 420–430.

Sun, Y., L. Xu, S. Kuleli, F. D. Morgan, and M. N. Toksöz (2004). Adaptive moving window method for 3-D P-velocity tomography and its application in China, *Bull. Seismol. Soc. Am*. 94: 740–746.

Sun, Y. and M. N. Toksöz (2006). Crustal structure of China and surrounding regions from P wave traveltime tomography, *J. Geophys. Res*. 111: doi:10.1029/2005JB003962.

Sun, Y., M. N. Toksöz, S. Pei, D. Zhao, F. D. Morgan, and A. Rosca (2008). S-wave tomography of the crust and uppermost mantle in China, *J. Geophys. Res*. 113: doi:10.1029/2008JB005836.

Tapponnier, P., M. Mattauer, F. Proust, and C. Cassaigneau (1981). Mesozoic ophiolites, sutures, and large scale tectonic movements in Afghanistan, *Earth Planet. Sci. Lett*. 52: 355–371.

Um, J. and C. Thurber (1987). A fast algorithm for two-point seismic ray tracing, *Bull. Seismol. Soc. Am*. 77: 972–986.

Wang, Q. P. Zhang, J. T. Freymueller, R. Bilham, K. M. Larson, X. Lai, X. You, Z. Niu, J. Wu, Y. Li, J. Liu, Z. Yang, and Q. Chen (2001). Present-day crustal deformation in China constrained by Global Positioning System measurements, *Science* 294: 574–577.

Yin, A. and T. M. Harrison (2000). Geologic evolution of the Himalayan-Tibetan Orogen, Annu. Rev. *Earth Planet. Sci*. 28: 211–280.

Zhang, H. and C. Thurber (2003). Double-Difference Tomography: The Method and Its Application to the Hayward Fault, California, *Bull. Seismol. Soc. Am*. 93: doi: 10.1785/0120020190.

Zhang, H. and C. Thurber (2006). Development and applications of double-difference tomography, *Pure Appl. Geophys*. 163: doi:10.1007/s00024-005-0021-y.

Zhang, P.-Zh. and W. Gan (2008). Combined model of rigid-block motion with continuous deformation: Patterns of present-day deformation in continental China, in Burchfiel, B.C., and Wang, E., Eds., Investigations into the Tectonics of the Tibetan Plateau, *Geol. Soc. Am*. Special Paper 444, 59–71, doi:10.1130/2008.2444.

Zhao, D. (2001). Seismic structure and origin of hotspots and mantle plumes, *Earth Planet. Sci. Lett*. 192: 251–265.

Zhao, D., A. Hasewaga, and S. Horiuchi (1992). Tomographic imaging of P and S wave velocity structure beneath northeastern Japan, *J. Geophys. Res*. 97: 19909–19928.

Zhao, D., A. Hasegawa, and H. Kanamori (1994). Deep structure of Japan subduction zone as derived from local, regional and teleseismic events, *J. Geophys. Res*. 99: 22313–22329.

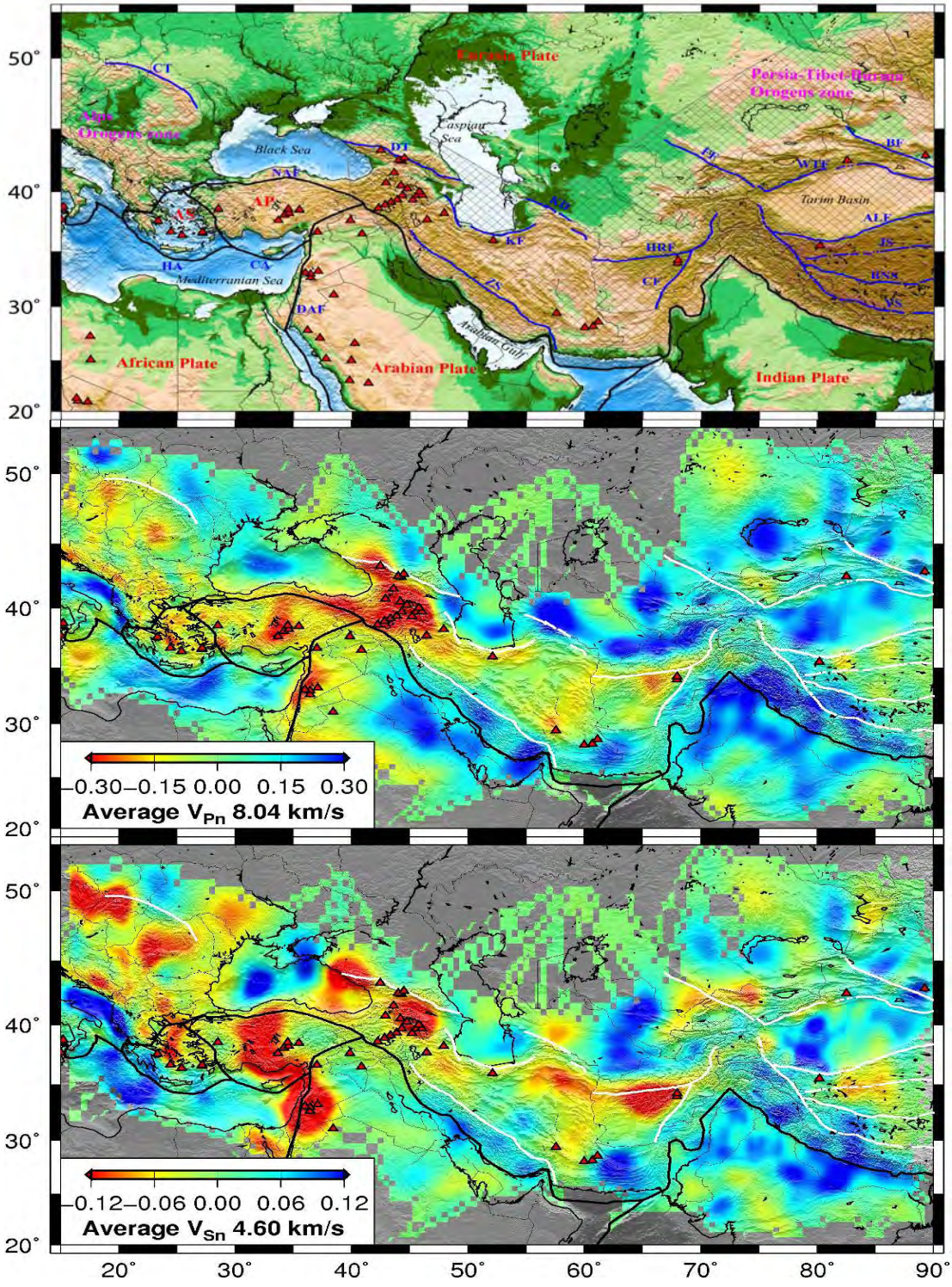

Figure 1. Simplified tectonic map (top) and imaged *Pn* (middle) and *Sn* velocity lateral variations from Alps to Himalaya region. The dark lines show the plate boundaries and the red triangles are volcanoes. ALF: Altyn fault; AF: Anatolian Fault; AP: Anatolian plate; AS: Aegean sea plate; BF: Boluokenu fault; BNS: Bangong-Nujiang suture; CA: Cyprean arc; CF: Chaman fault; CT: Capathians thrust belt; DSF: Dead Sea Fault; DT: Dagestan thrust belt; FF: Fergana Fault; HA: Hellenic arc; HRT: Hari Rod fault; KD: Kopeh Dagh fault; JS: Jinsha river suture; KF: Khazar fault; WTF: Western Tianshan faults; YS: Yalong-zangbo suture; ZS: Zagros Suture.

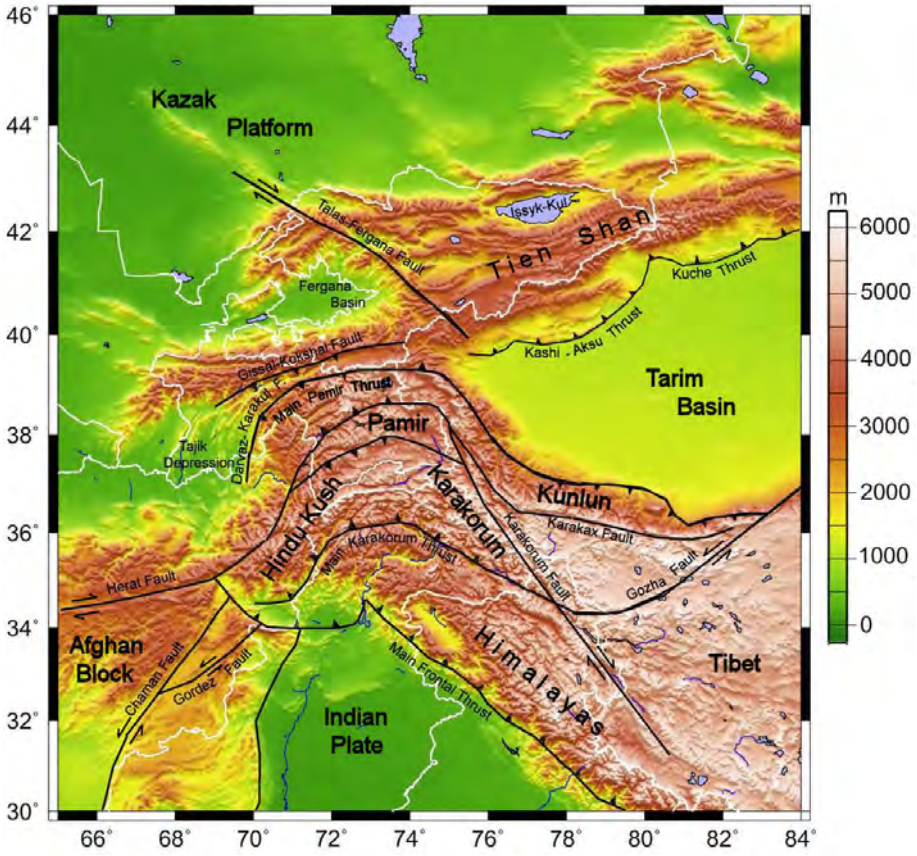

Figure 2. Map of the Pamir-Hindu Kush and surrounding areas showing major tectonic features.

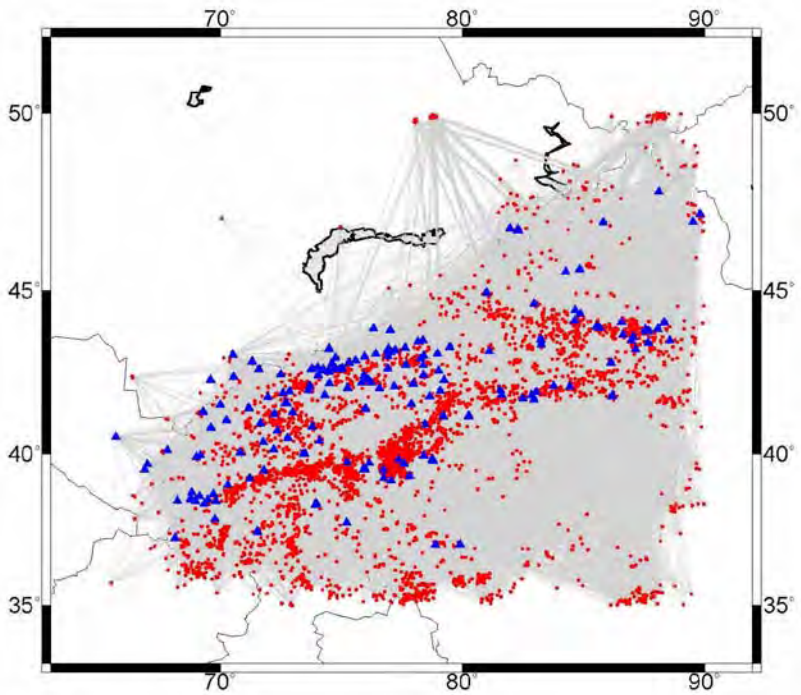

Figure 3. Ray path distribution in Central Asia. The stations are shown with blue triangles and the events are shown with red dots.

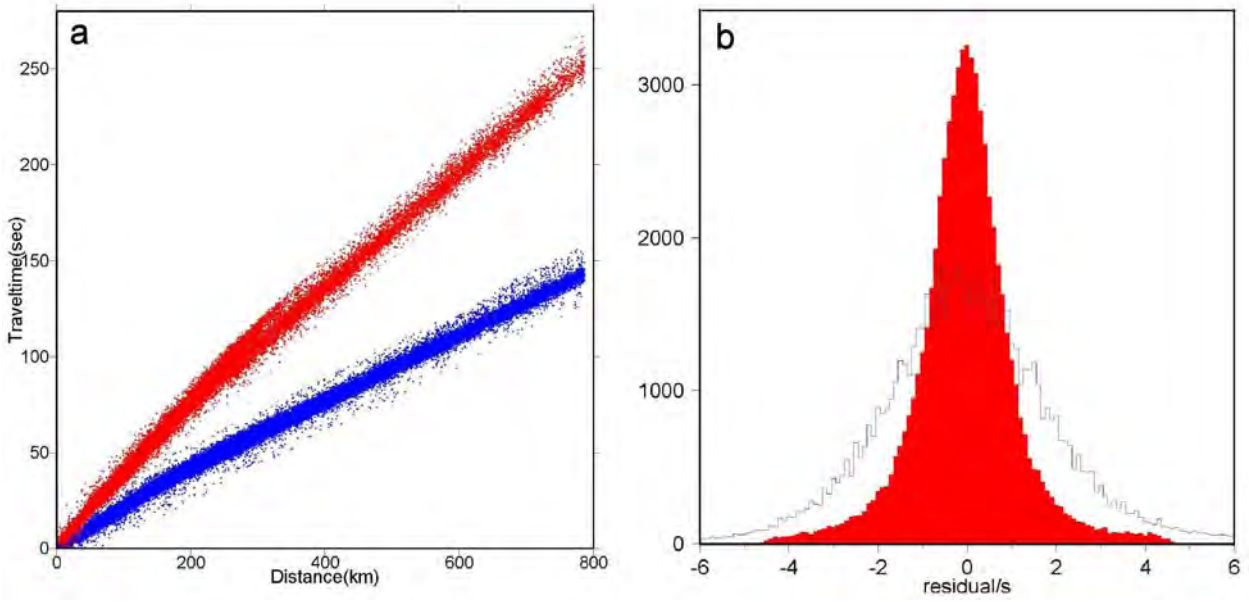

Figure 4. (a) *P* and *S* travel time distribution in the study area. (b) *P*-wave travel time residual distribution before and after (red) 3-D inversion. The standard deviation decreased from 2.1 seconds to 0.9 seconds.

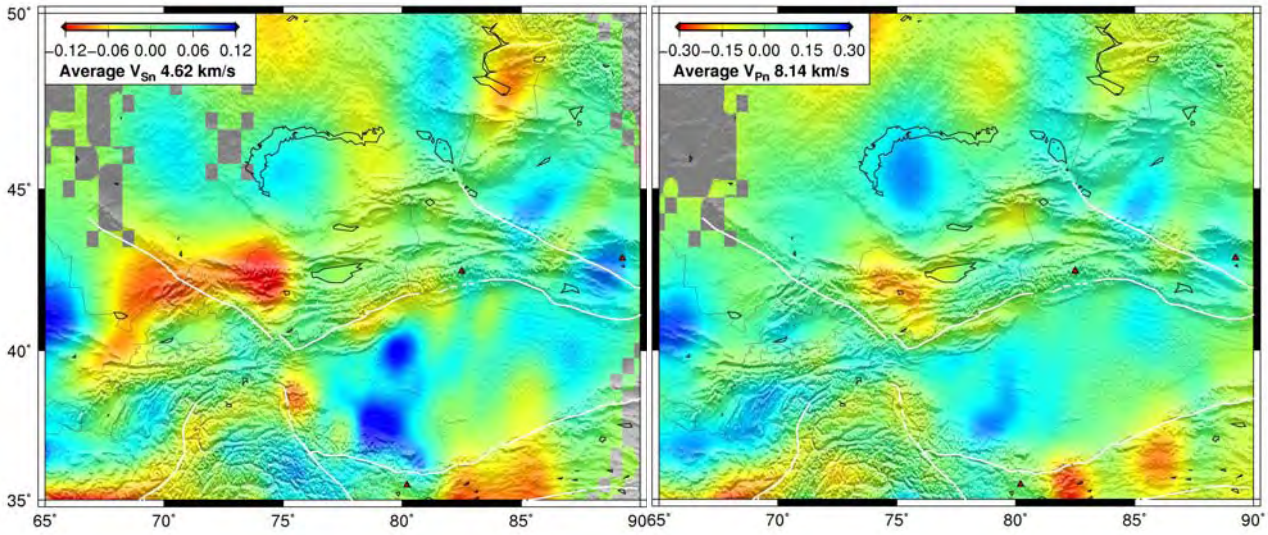

Figure 5. Imaged *Pn* (left) and *Sn* velocity lateral variations of the Central Asia region.

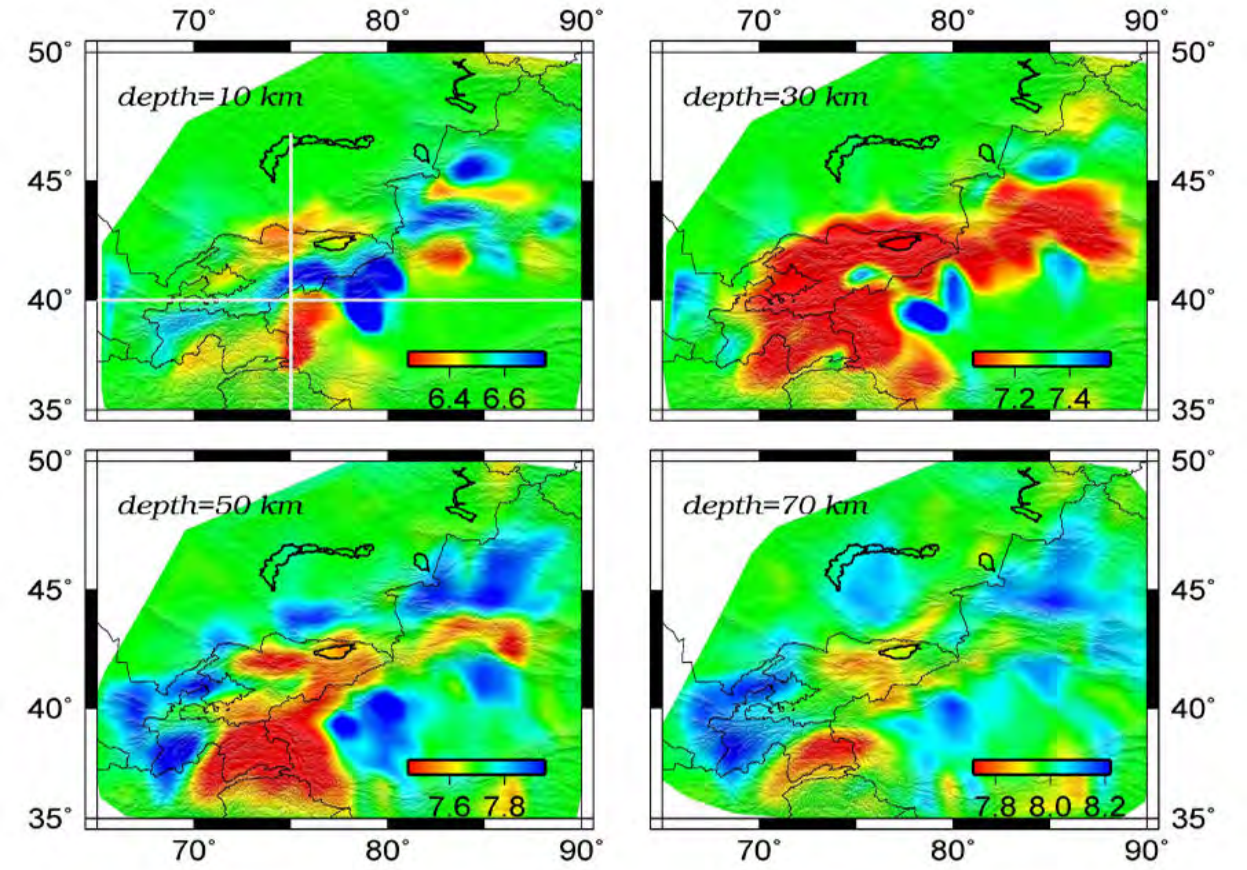

Figure 6. 3-D P-wave velocity structure for different depths in Central Asia. These maps were generated by assuming different P-wave reference velocities for each depth.

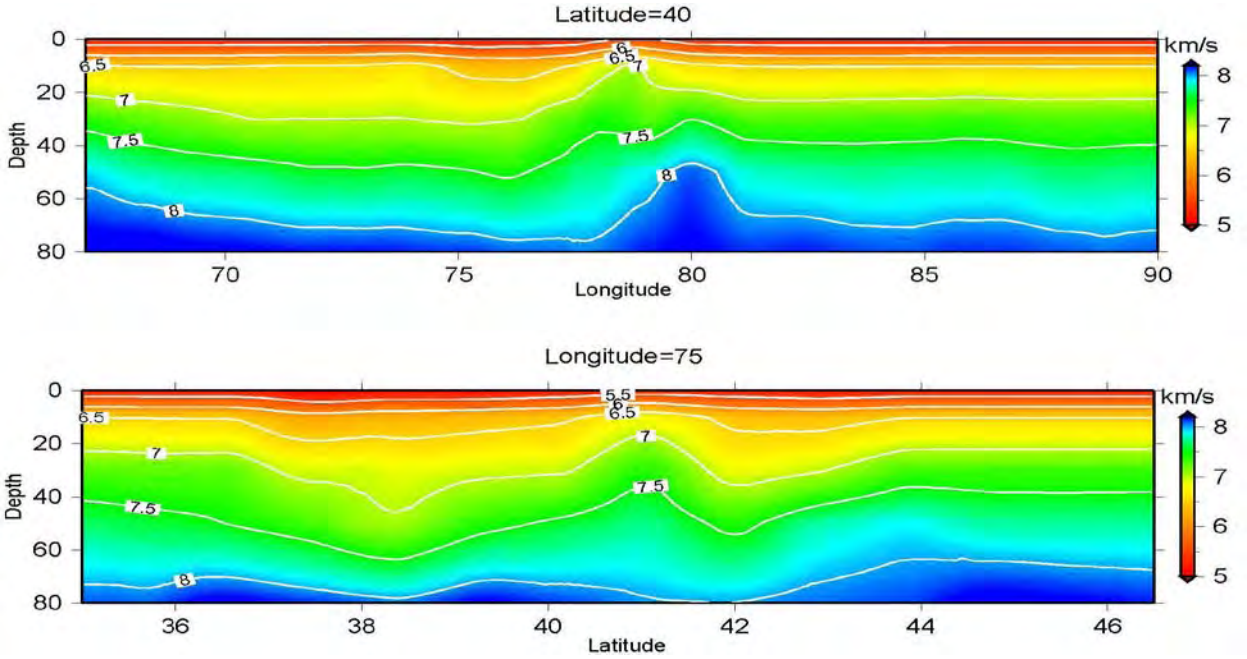

Figure 7. Vertical velocity profiles (the locations are shown in Figure 6).

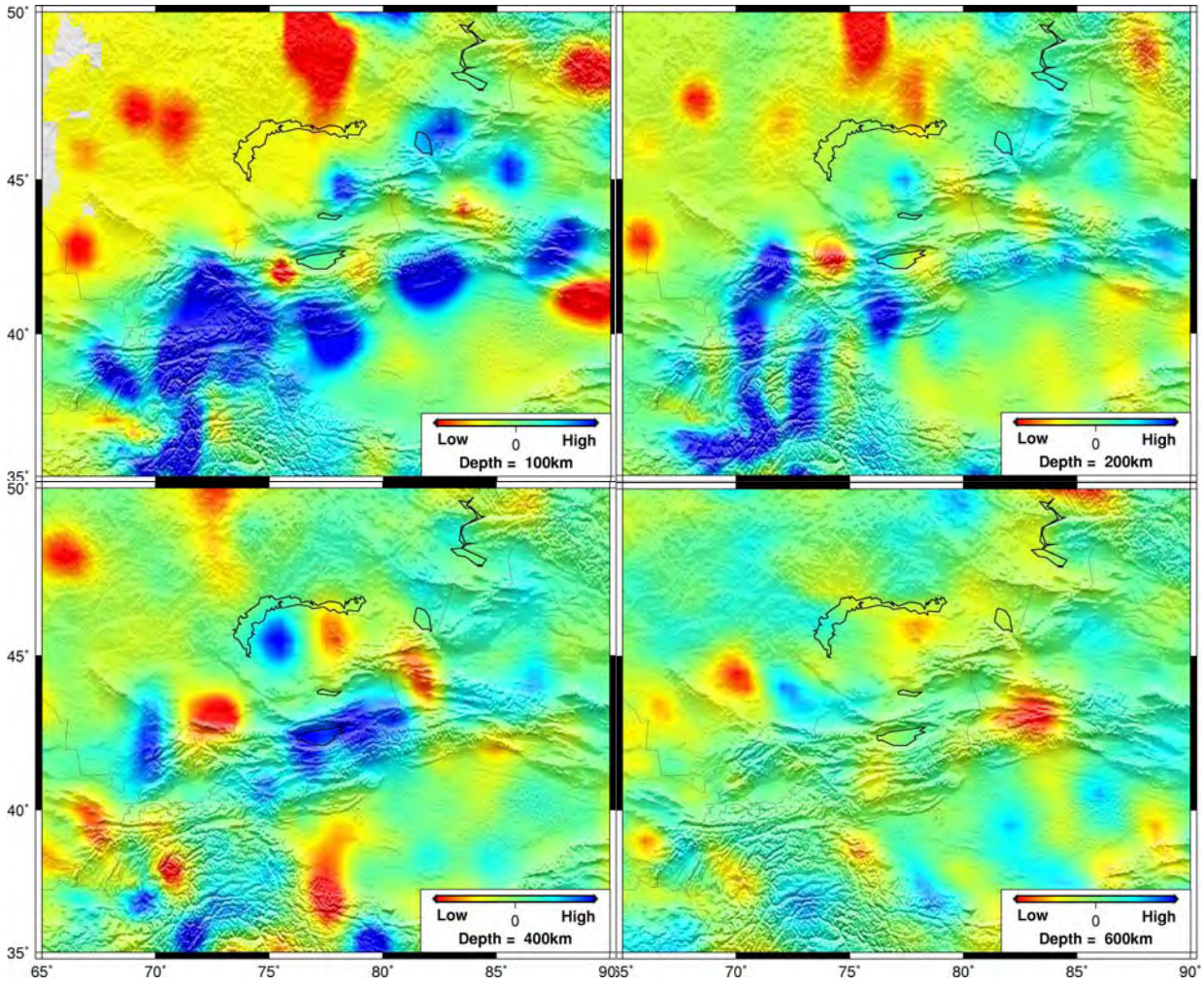

Figure 8. Upper mantle velocity structure at the depths of 100, 200, 400, and 600 km obtained by the double difference tomography method.

LITHO1.0: AN UPDATED CRUST AND LITHOSPHERE MODEL OF THE EARTH

T. Guy Masters[1], Zhitu Ma[1], Gabi Laske[1], and Mike Pasyanos[2]

University of California San Diego[1] and Lawrence Livermore National Laboratory[2]

Sponsored by the Air Force Research Laboratory

Award Nos. FA8718-09C-0008 and DE-AC52-07NA27344
Proposal No. BAA09-32

ABSTRACT

We are developing LITHO1.0: an updated crust and lithosphere model of the Earth. The overall plan is to take the popular CRUST2.0 model—a global model of crustal structure with a relatively poor representation of the uppermost mantle—and improve its nominal resolution to 1 degree and extend the model to include lithospheric structure. The new model, LITHO1.0, will be constrained by many different datasets, including extremely large new datasets of relatively short-period group velocity data measured with a new technique which are sensitive to lid properties as well as crustal thickness and average crustal properties. Other datasets include (but are not limited to) compilations of receiver function constraints and active source studies.

This year, most progress was made on surface-wave measurements. We use a cluster analysis technique to measure surface-wave group velocity from 10mHz to 40mHz . We use all the LH data from the Data Management Center (DMC) of Incorporated Research Institutions for Seismology (IRIS) between 1976 and 2007. The Rayleigh wave group velocity dataset is complete. The current dataset has about 330000 measurements for each of 10 mHz and 20mHz , 210000 for 30mHz , and 45000 for 40mHz . We also include some BH data from Program for Array Seismic Studies of the Continental Lithosphere (PASSCAL) in the southern hemisphere and the Portable Observatories for Lithospheric Analysis and Research Investigating Seismicity (POLARIS) network to increase ray coverage. Initial inversions of the datasets show features consistent with geophysical observation. Some artifacts are found in the ocean regions at high frequencies due to limited ray coverage. A solution we are currently pursuing is to implement an a priori group velocity model based on the age of oceanic lithosphere, which will be used to constrain the inversions where necessary.

We anticipate the new model will provide a much more accurate representation of regional phases, including the propagation of Pn and Sn phases, which strongly depend on lid structure. The new model will also provide a good starting point for more-accurate regional models using specialized datasets that can then be naturally embedded in a global model.

OBJECTIVES

The main objective is to take the popular CRUST2.0 model—a global model of crustal structure with a relatively poor representation of the uppermost mantle—and improve its nominal resolution to 1 degree and extend the model to include lithospheric structure. The new model, LITHO1.0, will be constrained by many different datasets, including extremely large new datasets of relatively short-period group velocity data measured with a new technique, which are sensitive to lid properties as well as crustal thickness and average crustal properties. Other datasets include (but are not limited to) compilations of receiver function constraints and active source studies.

RESEARCH ACCOMPLISHED

Global Surface Wave Group Velocity Datasets

Surface-wave group velocity measurements have been made for many decades, and most algorithms are based on the one first introduced by Dziewonski et al. (1969), which uses a suite of Gaussian narrow pass-band filters to generate a set of frequency-dependent envelope functions. The group arrival time is taken to be the peak of the envelope function. Further developments of this technique are described in Levshin et al. (1992), which introduces some interactive techniques to improve the measurements (see also Keilis-Borok, 1989). Levshin and co-workers have made many such measurements, and these have been used in both regional (Ritwoller and Levshin, 1998; Ritzwoller et al., 2001; Villasenor et al., 2001; Levshin et al., 2001) and global (Ritzwoller et al, 2002; Shapiro and Ritzwoller, 2002) inversions for group velocity maps and near-surface structures. The interactive nature of this algorithm makes construction of large datasets very time consuming, though the recent global analyses have about 100,000 measurements per frequency (Ritzwoller et al., 2002).

Here, we describe a different technique to measure the relative group arrival times of surface wave packets, which allows very efficient construction of large data sets. We have applied the technique to all LH data at the IRIS DMC from events larger than Ms = 5.5 between 1976 and 2007. We also include some BH data from PASSCAL experiments in the southern hemisphere and the POLARIS network to increase ray coverage. The Rayleigh wave group velocity data set is complete from 10mHz to 40mHz. The current data set has about 330000 measurements for each of 10mHz and 20mHz, 210000 for 30mHz, and 45000 for 40mHz. We have also performed a ray-theoretical inversion of the data for group velocity perturbation maps to allow us to estimate the internal consistency of the data. The data are surprisingly well fit by this simple inversion even though, as previously shown (e.g., Ritzwoller and Levshin, 1998), perturbations in group velocity reach 30% at 50 seconds and are bigger at shorter periods. Similar datasets for Love waves are under construction and are complete for data through 2005.□□

Our method starts in a similar fashion to the traditional group velocity measurement in that we apply a narrow-band Gaussian filter to the data and compute the envelope function (after correcting to a common instrument response and for the source phase). The difference is that we choose only one pass band and compute the envelope functions of all records for an event. We then treat these envelope functions in the same way as we do body waveforms in our cluster-analysis technique (Reif et al., 2001, Houser et al., 2008).

The first hundred envelope functions for an event are plotted in Figure 1. The envelope functions are displayed centered on their predicted group arrival time and are ordered by distance. This example is for Rayleigh waves band-passed with a center frequency of 20mHz and a bandwidth of 5mHz . Note how similar to each other most of the envelope functions are, and while this particular sample has only a couple of examples, shifts in the envelope functions of over 200 seconds from the expected arrival times are not uncommon.

We consider all records in the distance range of 20 to 160 degrees, though waveforms tend to be distorted for short-period waves propagating long distances. Measurements are made interactively, and the user first picks a desired time window for cross-correlation. Cross-correlation functions for every trace with every other trace are computed using a time domain method, and the (positive) peaks in the cross-correlation function that contain the differential time and scaling information between the traces are identified. Using cluster analysis (e.g., Hartigan, 1975), the stations are sorted by the similarity of their waveforms, and a cluster tree is plotted that shows at what level of correlation the various groups may be joined. The user then selects a minimum correlation coefficient to use as a cutoff for the cluster divisions. There is a tradeoff between having a large number of clusters with highly similar waveforms and a smaller number of clusters with less-correlated waveforms.

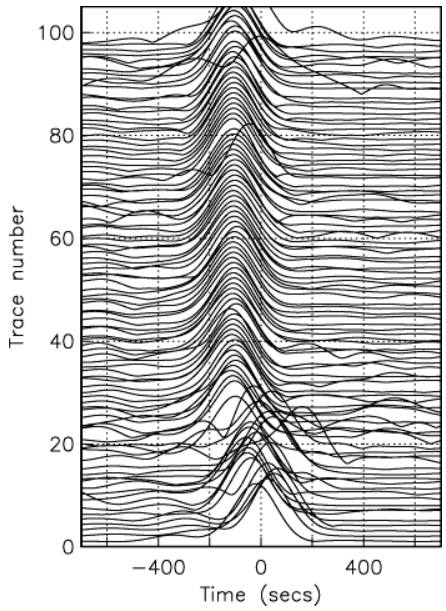

Figure 1. The first 100 envelope functions for an event on 2003:8, ordered by distance and aligned on the expected group arrival time. This example is for 50-second Rayleigh waves and demonstrates how similar envelope functions are, even though they occasionally are delayed by more than 200 seconds.

Optimal time shifts for the stations within each cluster are then obtained using a weighted least squares method that also returns error estimates based on the internal consistency of the time shifts (VanDecar and Crosson, 1990). These error estimates are often grossly optimistic, so we get an independent estimate of true errors using the consistency of group arrival times at closely spaced stations.

The clustering is illustrated in Figure 2. The left side shows the waveforms, which have been organized into clusters, the right hand side shows the cluster tree that governs the clustering. The user determines the degree of clustering with a vertical cursor (see figure caption).

Experiments with spherical-Earth synthetic waveforms suggest that envelope shape should correlate well at all distances and, in practice, many of the envelope functions for an event cross-correlate extremely well with each other, sometimes allowing over 200 relative group arrival times to be estimated simultaneously. Experiments with synthetic seismograms also show that the algorithm gives accurate, unbiased estimates of relative group arrival times. For events with variable waveforms (due to low signal, source directivity effects, overtone contamination, etc.), the clustering allows efficient isolation of those waveforms with simple envelope functions without prescreening of the data. This lack of need to prescreen the data is essential when dealing with very large datasets. It is important to note that we keep only those measurements for clusters with simple envelope shapes (about 20% of the data at long periods and less than 10% of the data at short periods). This may help explain why very simple ray-theory-based inversions of the data are extremely successful at explaining the measurements (see below)

When we compute the envelopes, we also measure the peak arrival time of the envelope and the centroid frequency of the spectrum. The relative arrival times are best fit to the measured peak arrival times to determine a set of absolute group arrival times. The centroid frequency is taken to be a better estimate of the frequency of the actual measurement than the center of the Gaussian filter (Shapiro and Singh, 1999) and varies from record to record. It is typically about 2% higher than the filter center.

Comparison with Previous Datasets

We compare the new dataset with another large, global group velocity dataset from the Colorado group (henceforth cub) though our current dataset (henceforth ucsd) is about a factor of 4 larger in size. The cub dataset was measured using traditional measurement techniques, and there was no correction for source phase that might account for some discrepancies at the longer periods (Levshin et al., 1999). At 20mHz , there are 330,000 ucsd measurements and about 85000 cub measurements, of which only 24,300 overlap.

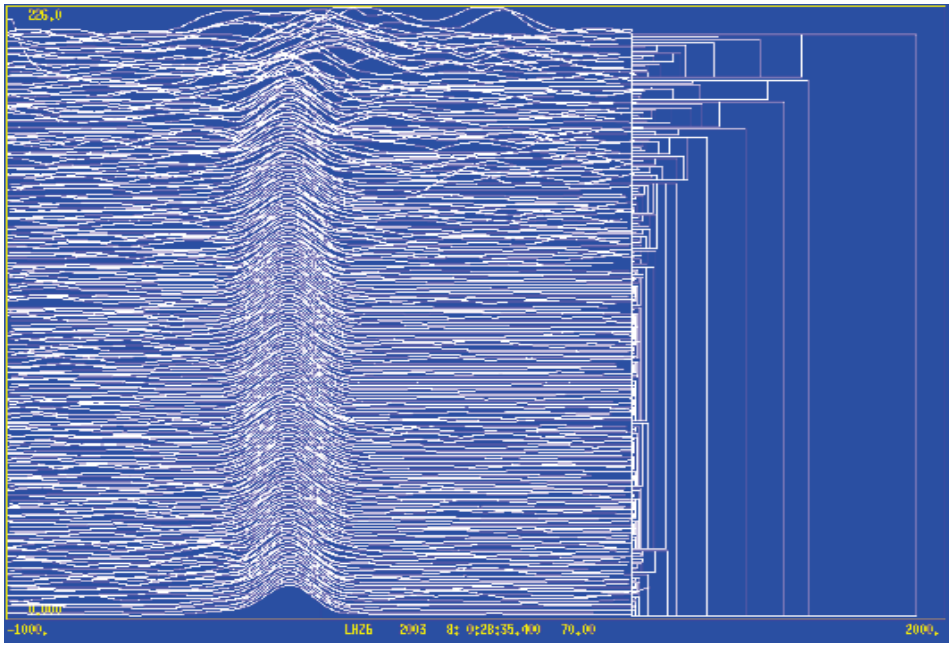

Figure 2. Screen capture of all envelope functions for 50-second Rayleigh waves between distances of 20 and 160 degrees for an event on 2003:8, after clustering. The left side shows the aligned traces sorted by degree of similarity into clusters. The tree diagram on the right allows the user to decide how finely clustering needs to be done. A vertical cursor is used to do this—as the cursor is moved to the left of the cluster tree plot, the waveforms are divided into smaller and smaller clusters. In this case, the cursor would be clicked close to the left, dividing the waveforms into one or two large clusters, leaving a group of uncorrelated traces near the top of the plot. Once the level of clustering has been chosen, the differential times between traces in each cluster are remeasured using cross correlation.

Since the precision of apparent group velocities is a strong function of distance, we compare group arrival times that are expected to be of similar precision regardless of distance. There are some uncertainties here because our measurements are each from slightly different frequencies while we believe that the cub group interpolates their group velocity curves to the desired frequency. However, the average offset between the two datasets is only 2 seconds, which is much smaller than our measurement precision.

The scaled median absolute deviation (SMAD) of the difference between group arrival time residuals is about 12 seconds. This is larger than we expected and about 50% larger than our inferred measurement precision at this frequency (about 7 seconds—obtained by looking at arrival times at nearby stations). This discrepancy is also bigger than the expected effect of including the source phase shift (from measurements on synthetics, we find that the source phase can lead to a time error of about 7 seconds at 10mHz and about 4 seconds at 20mHz). On the other hand, we should point out that the measurement discrepancy is much smaller than the signal in the actual data (Figure 3). Indeed, group velocity maps made using the two different datasets are extremely similar. The fact that there is no systematic difference between the datasets means that they can be combined in an inversion, and we find that maps made from the combined datasets fit both datasets almost as well as maps made from the separate datasets.

Estimation of Group Velocity Maps

To evaluate the internal consistency of our group arrival time measurements, we have performed a simple inversion, based on ray theory assuming great circle propagation. We discretize the Earth's surface into equal area cells of 1 or 2 degrees in dimension at the equator. Sampling of the Earth is quite nonuniform, though most cells have more than 500 hits, and all cells have more than 100 hits (Figure 4). Some cells in the western U.S. have over 10,000 hits, suggesting that more-sophisticated inversions could use a finer parameterization in this region or one using a variable tessellation, as is used in other tomographic inversions. Coverage in most of Eurasia is excellent.

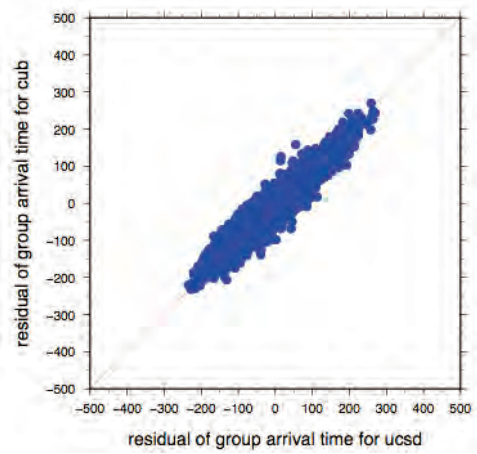

Figure 3. Scatter plot of the residual of group arrival time for ucsd and cub data set at 20 mHz .

The data are inverted using LSQR (Paige and Saunders, 1982) with a light smoothing constraint on the first lateral derivative of structure. Convergence is fast, reflecting the well-conditioned nature of the inversion. The resulting maps (Figure 5) are similar to the global maps of Shapiro and Ritzwoller (2002) or the regional maps of Ritzwoller and Levshin (1998) but show more detail and higher amplitudes. We suspect this is because the greater number of data used here means that less smoothing is required.

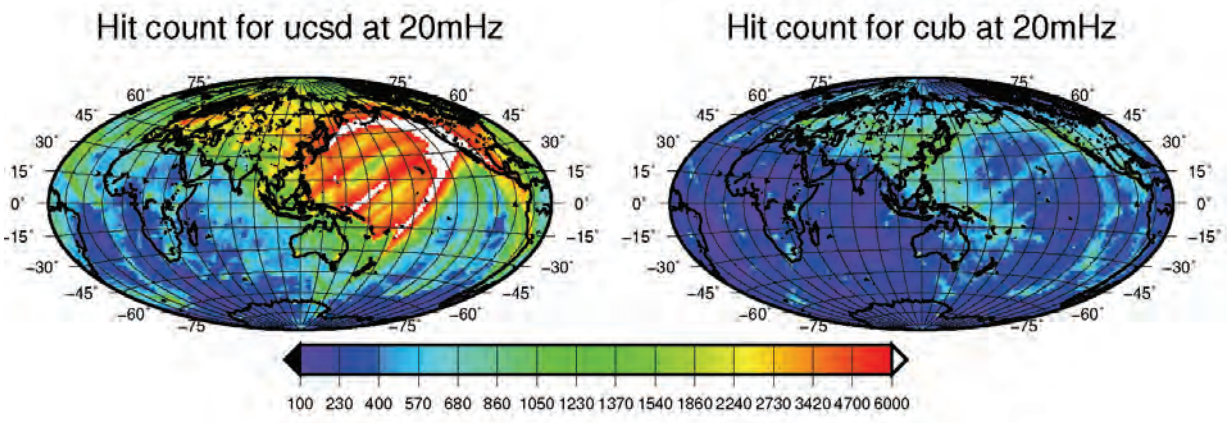

Figure 4. Hit count for the ucsd and cub datasets. Notice that all cells have more than 100 hits for both datasets, though the cub dataset focuses more on Eurasia.

Consider the map at 20mHz . Clearly, the biggest signal in continental regions is due to variations in crustal thickness. Most extreme group velocity variations occur under Tibet (30%) and under the Andes. This is not surprising since the sensitivity of 50-second Rayleigh waves peaks at 70–100 km, so we are actually seeing a crust-mantle signal. Other continental signals seem associated with hot spots (East Africa). The signal in oceanic regions is also interesting, with extremely slow regions associated with back-arc basins (e.g., the Lau basin) and some hot spots (e.g., Galapagos) but not others (Iceland, Hawaii). Some parts of the East Pacific Rise are clearly very slow, and there is a perceptible slow anomaly associated with the Australian-Antarctic discordance.

Currently, we have produced Rayleigh wave group velocity maps between 10mHz and 40mHz at frequency increments of 2.5mHz. These maps are extremely good representations of the group arrival time data, typically giving variance reductions of well over 90% (Figure 6). In some ways, this is surprising since we are using a very simple theory to model the data, and we have performed many tests to detect possible biases. These include using finite frequency kernels (Dahlen and Zhou, 2006) for the longer periods (Masters et al, 2005, 2006), doing surface wave ray tracing at shorter periods to check the effect of large velocity perturbations, making measurements from SEM synthetics and inverting them in a variety of ways, etc. Surprisingly, simple great-circle ray theory is usually

adequate—possibly because our measurement technique selects only those surface wave packets whose envelopes are simple in shape.

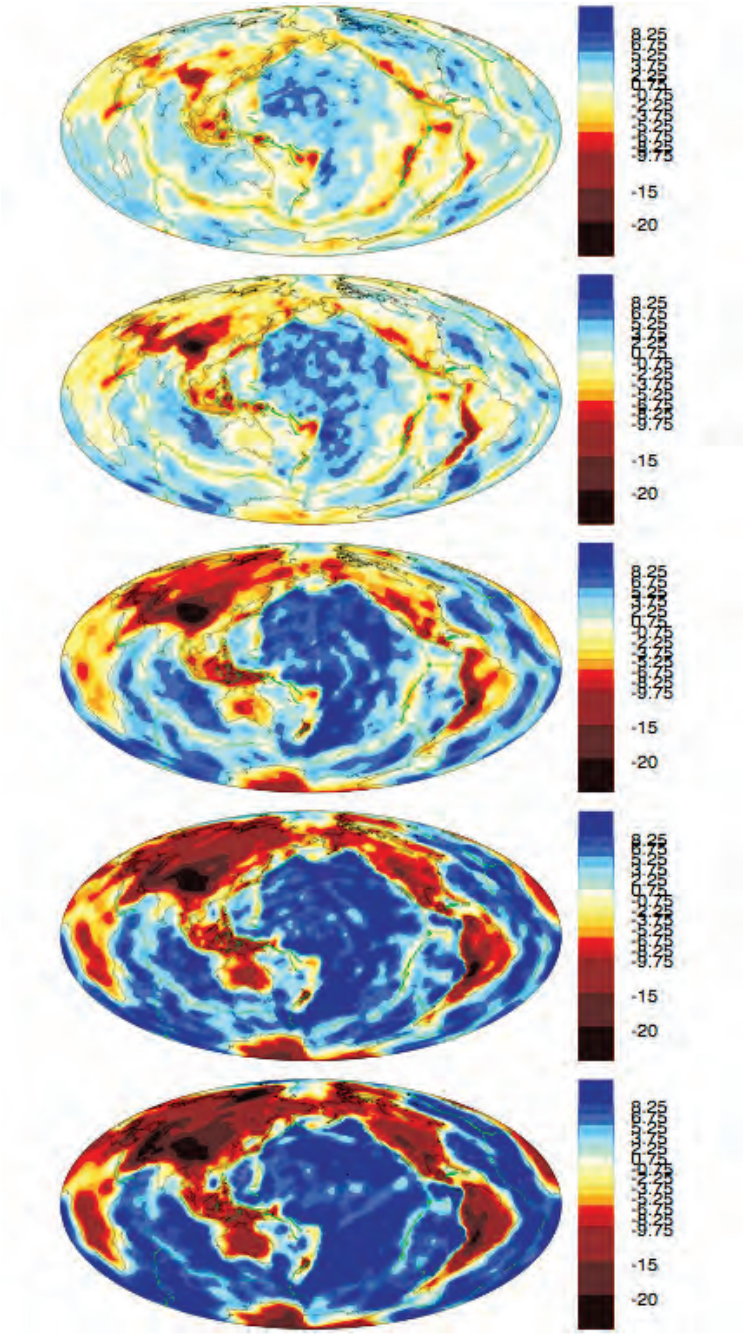

Figure 5. Group velocity perturbation maps at frequencies, from top to bottom, 15mHz, 20mHz, 25 mHz, 30mHz, and 35mHz.

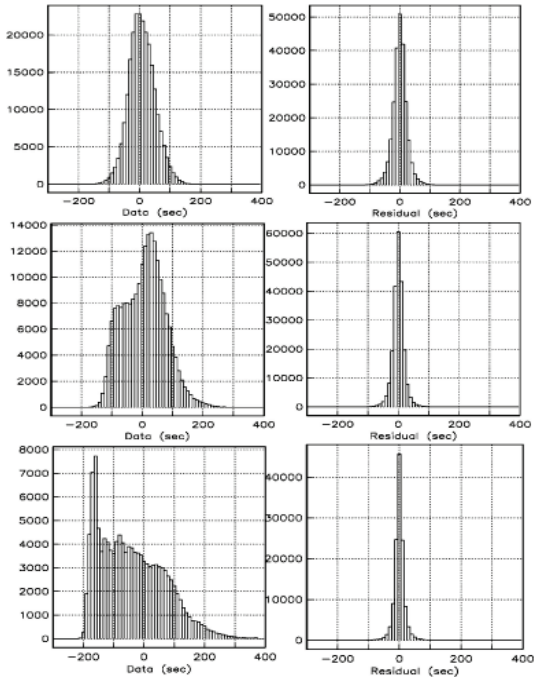

Figure 6. Histograms of group arrival time residuals before and after inversion. Top: 10mHz, variance reduction is 76%; middle 20mHz, variance reduction is 94%; bottom 30mHz, variance reduction is 98%.

Constraining Group Velocity Maps Using Physical Models

In recent years, there have been several attempts to relate seismic data directly to the parameters of a physical model (e.g., Goes et al., 2000; Cammarano et al., 2003; Shapiro and Ritzwoller, 2004). While there is no "simple theory" of continental structure, the half-space cooling model of oceanic lithosphere and its variants suggest that we might be able to predict group velocities in oceanic regions quite accurately. We are motivated to include such physical models because, at short periods, group velocity measurements are difficult to make for long paths, with the result that several parts of the ocean basins are not well constrained.

When the maps shown in Figure 5 are binned by oceanic lithospheric age, they produce quite simple variations of group velocity with age up to about 120Ma. Older regions show much greater variability, particularly at short periods, where the group velocity tends to be lower than expected (Figure 7). This suggests that thermal rejuvenation of old oceanic lithosphere is quite common, but it also suggests that a physical model could be successful up to ages of about 120Ma. Several attempts to predict oceanic structure as a function of lithospheric age have been made, with perhaps the most-sophisticated thermodynamic models being those of Stixrude and Lithgow-Bertelloni (2005). Some of these studies (e.g., Shapiro and Ritzwoller, 2004) have had to resort to introducing a baseline shift so that the physical models predict group velocities in accordance with those shown in Figure 7. We find this to be rather unsatisfactory. The models of Stixrude and Lithgow-Bertelloni (2005) also show complex structure in the lid due to phase transitions in feldspar and spinel (using a pyrolite composition). There is no seismic evidence for such complex structure, which would be consistent with the likely scenario that the uppermost mantle is depleted. We therefore parameterize our model with a crust (taken from CRUST2.0), which we take to first order to be independent of age. With careful attention to physical dispersion effects (since Q in the asthenosphere is very low), we modified the QL6 attenuation model (Durek and Ekstrom, 1996) and find that a model based on pyrolite and a cooling half-space thermal profile (Figure 8) can reproduce the data in Figure 7 quite well.

The Q value in our model at 100km depth is very close to other Q models, such as Romanowicz (1996), but the predicted attenuation for surface waves is stronger than the model from Dalton and Ekstrom (2006). While these results are preliminary (e.g., future models will take account of what we know about Pn and Sn in ocean basins and allow for variations in lid structure), they do suggest that the models can provide a basis for constraining inversions at the shorter periods, where the unconstrained inversions are less precise.

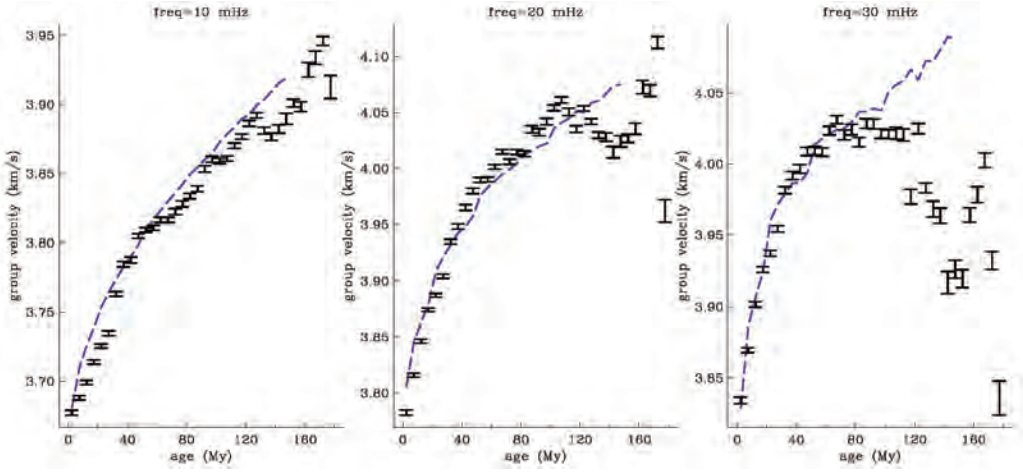

Figure 7. Group velocity maps binned by lithosphere age for 10, 20, and 30mHz. The error bars indicate the standard deviation of the mean of each bin. The dashed line shows the predicted group velocity from our physical model with a modified QL6 attenuation model.

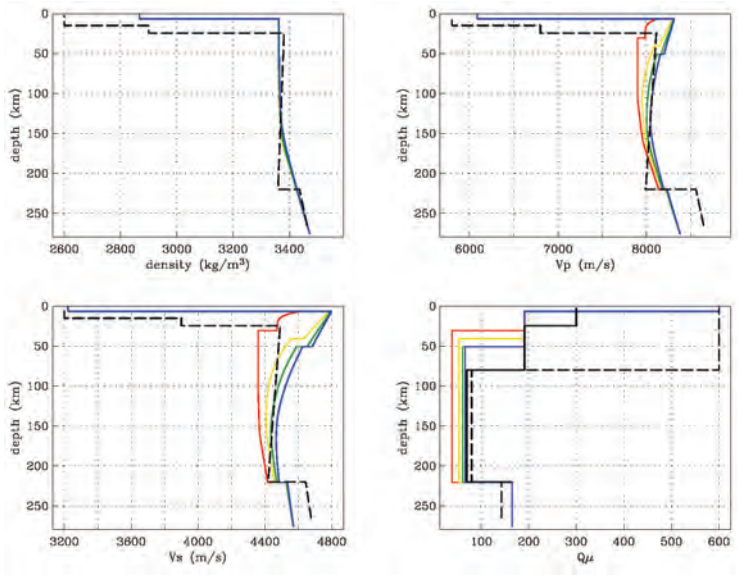

Figure 8. Vp,Vs, density, and Q models that produce the group velocity shown in Figure 7. Colored lines show depth profiles for different ages (Red: 1My, Yellow: 50My, Green: 100My, Blue: 150My). The dashed line is the PREM model. The solid black line in the plot of Q value is the QL6 model.

CONCLUSIONS AND RECOMMENDATIONS

We have completed the construction of a new large global dataset of Rayleigh wave group arrival times using a new efficient measurement technique and have evaluated the data by constructing group velocity maps using simple ray theory.

Comparisons of the data with datasets of previous workers show no bias in the data, but measurement discrepancies are about 50% larger than we would expect, based on estimates of precision of the measurements. While part of this discrepancy can be ascribed to source effects, we are uncertain what causes the remainder of the discrepancy. The measurement discrepancies are much smaller than the signal in the data, and the group velocity maps that we generate are capable of explaining almost all the signal in the data.

At short periods, we find that parts of the ocean basins are not well sampled, and we use the longer-period data to construct a physical model of oceanic structure that accurately predicts the age dependence of group velocity out to about 120Ma. Such models can be used as loose constraints on the short-period inversions. They can also be used to identify and evaluate apparent deviations in group velocity from the basic physical model.

The next step in this project is to finalize the group velocity maps and do a formal resolution and error analysis at each period. We have recently adapted the technique to vary the Gaussian filter until the centroid frequency for each spectrum matches the target frequency. Preliminary results show that the refinement makes very little difference to the final maps.

We are also close to completing the equivalent dataset for Love waves, which will be subject to the same analysis described above.

ACKNOWLEDGEMENTS

The data used in this research is obtained from IRIS Data Management Center and Canadian National Seismograph Network. We thank M. H. Ritzwoller and A. L. Levshin for personal communications.

REFERENCES

Cammarano, F., S. Goes, P. Vacher, and D. Giardini (2003). Inferring upper-mantle temperatures from seismic velocities, *Phys. Earth Planet. Int.* 138: 197–222.

Dahlen, F. A. and Y. Zhou (2006). Surface wave group delay and attenuation kernels, *Geophys. J. Int.* 165: 545–554.

Dalton, C. A. and G. Ekstrom (2006). Global models of surface wave attenuation, *J. Geophys. Res.* 111: B05317, doi:10.1029/2005JB003997.

Dziewonski, A. M., S. Bloch, and M. Landisman (1969). A technique for the analysis of transient seismic signals, *Bull. Seism. Soc. Am.* 59: 427–444.

Durek, J. and G. Ekstrom (1996). A radial model of anelasticity consistent with long-period surface-wave attenuation, *Bull. Seism. Soc. Am.* 86: 144–158.

Goes, S., R. Govers, and P. Vacher (2000). Shallow mantle temperatures under Europe from P and S wave tomography, *J. Geophys. Res.* 105: 11,153–11,169.

Hartigan, J. A. (1975). *Clustering Algorithms*. New York, NY: John Wiley & Sons, Inc.

Houser, C., G. Masters, P. Shearer, and G. Laske (2008). Shear and compressional velocity models of the mantle from cluster analysis of long-period waveforms, *Geophys. J. Int.* (in press).

Keilis-Borok, V. I., Ed. (1989). Seismic Surface Waves in Laterally Inhomogeneous Earth. Doredrecht, Neterlands: Kulwer.

Levshin, A., L. Ratnikova, and J. Berger (1992). Peculiarities of surface wave propagation across central Eurasia, *Bull. Seism. Soc. Am.* 82: 2464–2493.

Levshin, A. L., M. H. Ritzwoller, and J. Resovsky (1999). Source effects on surface wave group travel times and group velocity maps, *Phys. Earth Planet. Int.* 115: 293–312.

Levshin, A. L., M. H. Ritzwoller, M. P. Barmin, A. Villasenor, and C. A. Padgett (2001). New constraints on the Arctic crust and uppermost mantle: Surface wave group velocities, Pn, and Sn, *Phys. Earth Planet. Int.* 123: 185–204.

Masters, G., D. Kane, J. Morrow, Y. Zhou, and J. Tromp (2005). Measurement and interpretation of surface wave group arrival times, *EOS Trans. AGU* 86: fall meeting supplement; abstract S42A-05.□□

Masters, G., Y. Zhou, and J. Tromp (2006). Measurement and interpretation of surface wave group arrival times, *EOS Trans. AGU* 87: fall meeting supplement; abstract S54B-01.

Paige, C. C. and M. A. Saunders (1982). LSQR: An algorithm for sparse linear equations and sparse least squares, *TOMS* 8: 43–71. □□

Reif, C., G. Masters, G. Laske, P. Shearer, and M. Flanagan (2001). Joint inversions for velocity and discontinuity structure in the mantle, *EOS Trans. AGU* 82: F888, fall meeting supplement.□□

Ritzwoller, M. H. and A. L. Levshin (1998). Eurasian seismic tomography: Group velocities, *J. Geophys. Res*. 103: 4838–4878

Ritzwoller, M. H., N. M. Shapiro, A. L. Levshin, and G. M. Leahy (2001). The structure of the crust and upper mantle beneath Antarctica and the surrounding oceans, *J. Geophys. Res*. 106: 30645–30670.

Ritzwoller, M. H., N. M. Shapiro, M. P. Barmin, and A. L. Levshin (2002). Global surface wave diffraction tomography, *J. Geophys. Res*. 107: 2335.

Romanowicz, B. (1995). A global tomographic model of shear attenuation in the upper mantle, *J. Geophys. Res*. 100: 12,375–12,394.

Shapiro, N. M. and S. K. Singh (1999). A systematic error in estimating surface-wave group-velocity dispersion curves and a procedure for its correction, *Bull. Seism. Soc. Am*. 89: 1138–1142.

Shapiro, N. M. and M. H. Ritzwoller (2002). Monte-Carlo inversion for a global shear velocity model of the crust and upper mantle, *Geophys. J. Int*. 151: 88–105.

Shapiro, N. M. and M. H. Ritzwoller (2004). Thermodynamic constraints on seismic inversions, *Geophys. J. Int*. 157: 1175–1188.

Stixrude, L. and C. Lithgow-Bertelloni (2005). Mineralogy and elasticity of the oceanic upper mantle: Origin of the low-velocity zone, *J. Geophys. Res*. 110: B03204, doi:10.1029/2004JB002965.

VanDecar, J. C. and R .S. Crosson (1990). Determination of teleseismic relative phase arrival times using multi-channel cross correlation and least squares, *Bull. Seism. Soc. Am*. 80: 150–169.□□

Villasenor, A., M. H. Ritzwoller, A. L. Levshin, M. P. Barmin, E. R. Engdahl, W. Spakman, and J. Trampert (2001). Shear velocity structure of Central Eurasia from inversion of surface wave velocities, *Phys. Earth Planet. Int.* 123: 169–184.□□

TRANSITIONING THE CODA METHODOLOGY TO FULL 2-D FOR *P* AND *S* CODAS

Kevin M. Mayeda[1] and W. Scott Phillips[2]

Weston Geophysical[1] and Los Alamos National Laboratory[2]

Sponsored by the Air Force Research Laboratory[1] and the National Nuclear Security Administration[2]

Award No. FA9453-10-C-0255
Proposal No. BAA10-72

ABSTRACT

Over the past decade, we have developed and implemented an empirically-based regional shear wave coda methodology that provides unprecedented amplitude stability for events at local and regional distances. In regions of interest, small-scale 1-D coda calibrations have proven sufficient and result in very low variance estimates. For the broader, increasingly complex regions, it is unfeasible to perform a patch-work of small-scale 1-D calibrations due to lack of stations and events. As a first attempt at the problem, we have embarked upon 2-D path (Q) corrections. However, this has proven insufficient and it is clear that 2-D variations in the *other* coda calibration parameters are significant and their inclusion in the coda method is necessary to significantly reduce variance in broad-area coda calibrations. Specifically, lateral variations in coda shape (envelope decay), peak velocity, including coda type, and site-transfer corrections must be accounted for. Our objective is to improve the regional methodology for both *P*-coda and *S*-coda by upgrading models and transitioning to full 2-D. For example, the parameterization of the synthetic coda envelope shapes has been based on a simplistic single-scattering formulation for a homogeneous full-space. We plan to test formulations that better predict the effects of multiple scattering as well as develop 2-D empirical models. Increasingly, monitoring needs require both local and broad-area regional to far-regional calibration, usually in complex regions where we observe frequency-dependent phase blockage. For example, regions of the Middle East and Central Asia, including the Iranian plateau, present strong 2-D variations in attenuation and phase blockage effects, and we must adjust to the dominant coda type on the fly. The recent North Korean nuclear test illustrates that even a seemingly simple geological region requires 2-D corrections for L_g-coda. The highest valuable deliverable from this project will be a general 2-D coda methodology that significantly reduces amplitude variance in complex tectonic regions for both *P*-coda and *S*-coda.

OBJECTIVES

The regional shear-wave coda methodology has evolved over time; originally inspired by Aki's (1969) local single-scattering model, the method has undergone some recent modification, but is mostly used under the assumption of 1-D, radial symmetry centered on each station. The methodology has had great success at local and near-regional distances for simple regions, based on crustal *S* and L_g coda types, and at longer distances for small source regions such as test sites and aftershock zones, using codas associated with *P*, S_n or L_g, depending on the dominant coda type for each individual path. Despite recent successes with small-scale 1-D coda calibrations, there are a number of reasons to make significant enhancements to the coda methodology to encompass laterally complex regions. This project is timely because 1-D coda techniques have been implemented in a number of small regions of interest, however there is a need to extend to the broader regions, which have larger lateral complexity. Regions that have been calibrated under the 1-D assumption (Mayeda et al., 2003) have either been small and/or uniformly complicated (e.g., Yellow Sea/Korean Peninsula (YSKP), Bhuj aftershock zone, India, Persian Gulf, eastern Mediterranean, Italian Alps, California Coast ranges) or broad regions that are more or less uniform (e.g., European Arctic, Anatolian plateau, South African craton).

In each of the above-mentioned cases, we recognize that performance was limited mostly by oversimplified parameterization and that better results could have been obtained. For example in the YSKP region, calibration to the east of the peninsula requires completely different velocity, coda shape, and attenuation corrections because the path is dominated by oceanic S_n propagation, whereas the YSKP is comprised of L_g continental propagation. In fact, the recent North Korean tests illustrate this point as we found partial blockage for paths towards the south because of short (but significant) propagation through the oceanic crust that reduced broadband amplitudes by nearly a factor of two-to-three on the L_g coda (SRP presentation by K. Mayeda, March 2007). This effect was critical for yield estimation work and will be equally critical in other areas of low crustal *Q* and L_g blockage, such as the Iranian plateau. For example, the Anatolian plateau is geophysically complicated, but for lower frequencies, between 0.05 and ~1 Hz, the whole region can be treated as if it were homogeneous (e.g., Eken et al., 2004). However for the higher frequencies, 2-D corrections are required for path corrections, envelope shapes (due to varying S_n and L_g levels, and subsequent coda, and peak envelope velocity.

It has been suggested by the authors that the coda is insensitive to the source radiation pattern, while others suggest the inclusion of this term in any coda formulation. The following example would argue for the former, namely that the coda is insensitive to the source radiation pattern. We illustrate the stability of the coda using the recent 2008 Wells, Nevada sequence. Figure 1 shows amplitude ratios between the mainshock and an aftershock at 3.5-Hz for direct Lg and coda as recorded by US Array stations at roughly 200 km distance. For the coda source ratios, we see almost no variation in sharp contrast with direct Lg.

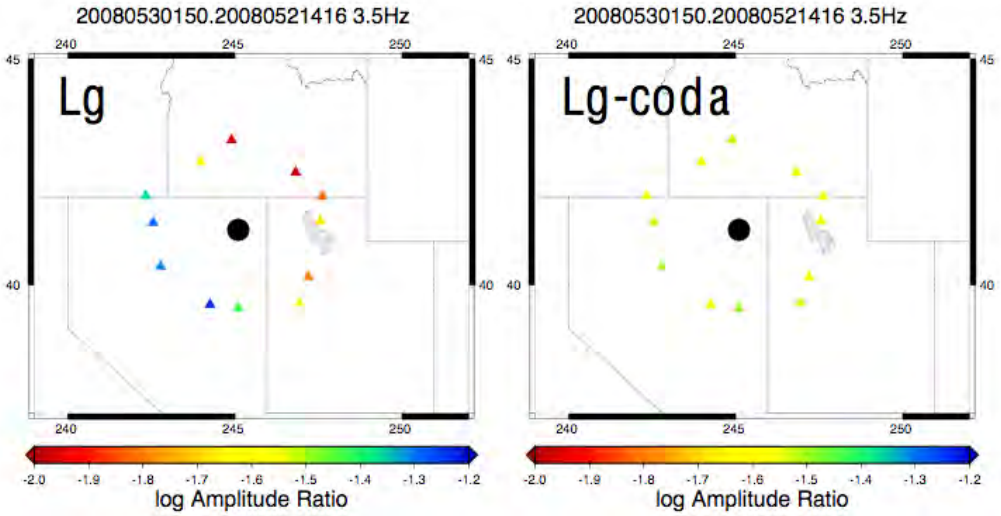

Figure 1. Coda amplitude ratios between the Wells, Nevada mainshock and an aftershock at 3.5-Hz are shown for 12 U.S. Array stations at roughly 200 km distance. The point of this figure is to show the large variation for direct Lg on the left due to differences in source radiation, versus the minimal variation in source ratio for the Lg-coda on the right.

More recently, Mayeda et al. (2005) compared 1-D versus 2-D path corrections on coda and direct S/L_g waves using moderate-sized earthquakes with long codas in the California Coast Ranges. The improvement found for 2-D path corrections for coda was roughly 30%. This was an average measure; the improvement was expected to be greater for the most anomalous regions, such as the high attenuation, seismically active area surrounding the Geysers, allowing more accurate recovery of source spectra for those regions. This situation is similar to the Korean peninsula, where we expect to see only modest improvement between 1-D and 2-D approaches on average, but dramatic improvement for critical paths through anomalous regions such as oceanic crust. Furthermore, the early coda showed significant variation from station-to-station in the California study. When event size decreases, we must rely on shorter length coda and therefore it is critical to know the early envelope shape. For example, we find that the early coda decay for event-station pairs that are confined to the Sierra batholith have lower decay rate than those that sample the Great Valley (Figure 2). However, in their 2005 study, Mayeda et al. assumed the ***same*** envelope shape and velocity for ***every*** station (1-D assumption), independent of azimuth or location. Therefore, the inclusion of ***both*** 2-D path ***and*** 2-D envelope shape, velocity, and site-transfer would have reduced the variance well below the previous 30%, which only included 2-D path corrections. We note however, that the purpose of that study was only to test the effects of 2-D path corrections, with everything else, such as velocity, envelope shape and transfer function being held to 1-D radially symmetric.

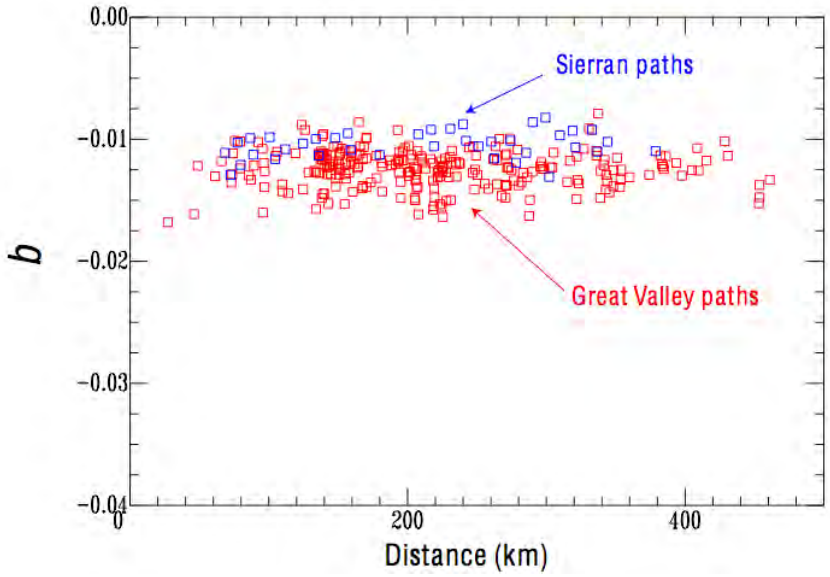

Figure 2. Coda shape parameter, *b*, taken for stations situated in the Sierra Nevada (CMB, ORV, KCC) for 1.5-2.0 Hz for events in northern California Coast Ranges. Event-station pairs that are confined to the Sierra Nevada batholith (blue) exhibit lower coda decay than event-station pairs that traverse the Great Valley (red). This clearly shows 2-D variations in coda envelope shape. See Equation 1.

Since the Mayeda et al. (2005) study assumed the same envelope shape function for all 16 broadband stations, the errors would certainly increase as the event size decreases (e.g., Figure 5) if regional variations in coda shape remain unaccounted for.

In addition, path lengths were on average, relatively short for the California Coast Range study. For the case of central Asia, the same 2-D path correction methodology results in much larger improvement, but again, this is for larger events with ample coda.

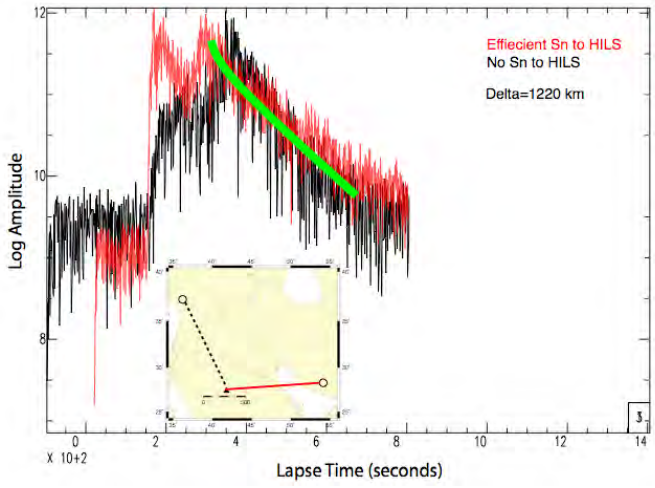

Figure 3. Middle East example of 2-3 Hz envelopes for two events recorded at station HILS on the Saudi Peninsula. The event from south-central Anatolian plateau has L_g coda whereas the event from southern Iranian plateau has S_n coda. A simple 1-D calibration for this region would introduce significant error because velocity, shape, and path effects are different.

With regard to Asia and the Middle East, we are also faced with mixing of phase types in addition to strong lateral changes in attenuation. We need to improve the coda method so that it is general enough to handle any region, including those that have lateral changes in phase type and/or blockage. This will require enhancing all aspects of coda calibration to full 2-D. Figure 3 illustrates such a case where we have two events recorded by station HILS located on the Saudi peninsula. For one event there is clear L_g and associated coda, whereas the path from the southern Iranian plateau has only S_n and its coda. This will require spatial and/or azimuthally varying parameters to account for this since a 1-D approach will introduce error. Even small error is intolerable as we are going to extra effort to calibrate coda in order to take advantage of the higher accuracy and precision relative to direct wave methods.

The motivation for making a change to the methodology is quite simple. First, regions of monitoring interest are generally tectonically complex and in fact, most appear to require 2-D corrections for velocity, path, and envelope function. Figure 4 shows a result of coda wave Q for central Asia (Q from amplitude decrease with distance, rather than temporal decay of coda) and illustrates the strong lateral changes that need to be accounted for. The partial blockage for paths from the Korean test can be seen in the Q map, although the smoothness enforced on this large-scale result decreases it's effectiveness for such short paths. We will test the application of similar, 2-D tomographic techniques on other coda parameters (i.e., peak velocity, envelope shape, and transfer function).

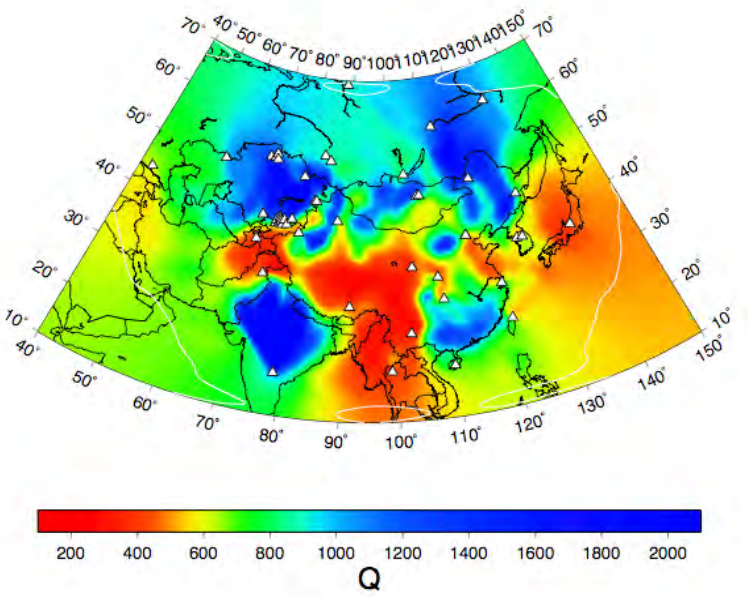

Figure 4. Coda wave apparent *Q* for central Asia for the 0.7-1.0 Hz band. This 2-D inversion was performed over a very broad region and emphasizes the need for 2-D path corrections. Stations are represented by triangles and a liberal model error (1/*Q*) indicating raypath coverage is represented by the white contour. *Q* becomes poorly resolved as the coverage contour is approached.

Second, regional seismic assets are usually sparse or on the periphery of the region-of-interest and amplitude stability as well as sufficient signal-to-noise ratio is always an issue, especially for smaller yield events. Because of this, more emphasis must be placed on the early coda, which historically has been avoided. The often used rule-of-thumb of measuring the coda after '*twice the S-wave travel-time*', is just that, a rule of thumb with empirical rather than theoretical basis. However, as Figure 5 shows, the early coda still provides more stable estimates than the direct wave and should be used to lower our measurement threshold.

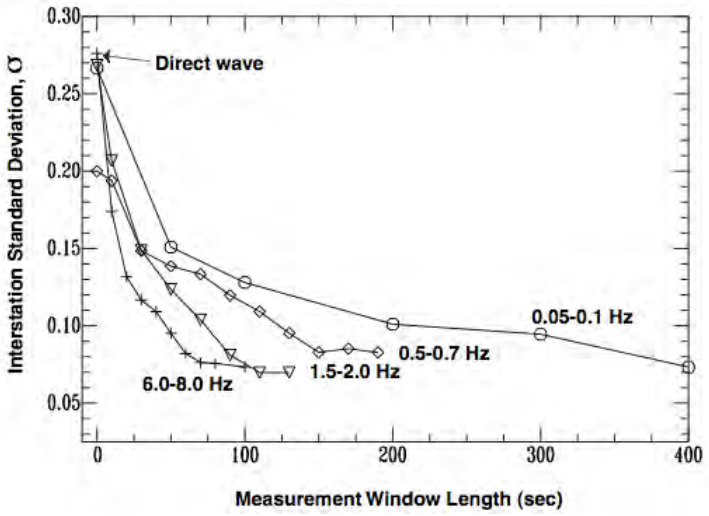

Figure 5. Interstation standard deviation, σ, is shown for a range of frequencies as a function of coda measurement window length using Gulf of Aqaba earthquakes. For longer periods, the critical window length, where reduction in scatter is minimal, becomes larger, ranging from about 80 seconds at 6.0–8.0 Hz to about 400 seconds for 0.05–0.1 Hz (from Mayeda et al., 2003). We will apply the same approach to local data in a variety of different tectonic settings to derive 'averaged' curves. We note that twice the *S*-wave travel time for this dataset is at ~150 seconds.

RESEARCH ACCOMPLISHED

As this award was funded in the spring of 2010, the authors have not started working on this project due to prior programmatic commitments. We instead, list out the proposal objectives that we plan to work on later in the Fall. The proposal objectives are straightforward and can be broken down into two parts. First, we will transition the 1-D coda methodology to a full 2-D capability including both P-coda and S-coda, with the ability to account for frequency-dependent phase blockage, as well as 2-D variations in peak envelope velocity and site-transfer corrections. Second, we will improve upon the way we make amplitude measurements and tie to an absolute scale. This will include improved synthetic envelope functions and fitting, which to date has been overly simplified using a model derived for a homogeneous full-space (i.e., the single-scattering model). For example, Figure 6 shows synthetic envelope fits using Equation 1 to observed data from the eastern Anatolian plateau. Note that the actual data has extra curvature starting at around ~120 seconds from the origin time which is not predicted in the model. The curvature could result from multiple scattering, or from increasing importance of mantle (S_n) coda with lapse time.

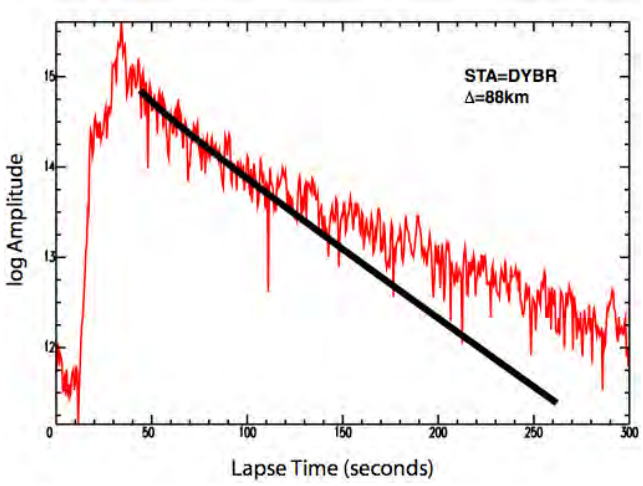

Figure 6. Example narrowband envelope from the eastern Anatolian plateau (red) illustrating that the calibrated synthetic coda envelope (black) does a poor job at longer lapse times (> ~120 seconds). The synthetic was based on an average using many events in the region, but we clearly see that for this station-event path, the model does not perform well and suggests we need 2-D envelope functions.

Unfortunately, the current envelope formulation does not account for the increased curvature. We will experiment with other formulations, such as the addition of another exponential term in Equation 1 as well as using multiple scattering formulations from the literature (e.g., see Sato and Fehler, 1998). For example, adding an additional exponential term that starts later in the coda at time t_c with a different decay rate, c, could be used.

$$A_c(f, t, r) \approx H(t - t_s) \cdot (t - t_s)^{-\gamma(r)} \exp\left[-b(r) \cdot (t - t_s)\right] + \exp\left[-c(r) \cdot (t - t_c)\right] \qquad (1)$$

In addition, for calibration earthquakes we will tie our distance-corrected amplitudes to theoretical source spectra under different source-scaling assumptions derived from *a priori* assumptions or independent source scaling studies.

CONCLUSIONS AND RECOMMENDATIONS

The applications and benefits are several-fold. First, we believe that the proposed changes to the coda methodology will provide significant improvement for complex, broad area calibrations, NOT simply an incremental improvement. This is timely since the community is embarking on calibrating complex broad regions, in contrast to the past coda applications, which were smaller in scale and complexity. We have tested the effects of only applying 2-D path corrections to a number of regions (central Asia, western North America, and recently the Middle East)

and we find that the other coda calibration parameters have very large, lateral variations (e.g., coda envelope shape, peak velocity and site-transfer). Since a patch-work of small-scale 1-D coda calibrations is unfeasible in most regions of monitoring interest, our proposal for full 2-D coda parameterization should significantly reduce amplitude variance for discrimination, magnitude and yield estimation. We will develop a generalized 2-D coda methodology that accounts for lateral variations in path effects, peak envelope velocity, envelope shape, and site-transfer corrections. The coda models for both *P*-codas and *S*-coda from both small and broad regions will be seamlessly tied to each other and most importantly, constructed in an identical manner that is internally consistent. In addition to the above-mentioned 2-D improvements, new synthetic envelope functions for amplitude fitting will lower amplitude variance, especially for events where signal-to-noise ratio is low.

REFERENCES

Aki, K. (1969), Analysis of the seismic coda of local earthquakes as scattered waves, *J. Geophys. Res*. 74: 615–631.

Eken, T., K. Mayeda, A. Hofstetter, R. Gök, G. Örgülü and N. Turkelli (2004). An application of the coda methodology for moment-rate spectra using broadband stations in Turkey, *Geophys. Res. Lett*. 31: 11, L11609.

Mayeda, K., A. Hofstetter, J.L. O'Boyle, and W.R. Walter (2003). Stable and transportable regional magnitudes based on coda-derived moment-rate spectra, *BSSA* 93: 224–239.

Mayeda, K. L. Malagnini, W. S. Phillips, W. R. Walter, D. Dreger (2005). 2-D or not 2-D, that is the question: A northern California test, *Geophys. Res. Lett*. February, Doi:10.1029/2005GL022882.

Mayeda, K., L. Malagnini, W.R. Walter, A new spectral ratio method using narrow band coda envelopes: Evidence for non-self-similarity in the Hector Mine sequence, *Geophys.Res. Lett.*, doi:10.1029/2007GL030041, 2007.

Sato, H. and Fehler, M. (1998). Seismic wave propagation and scattering in the heterogeneous earth, AIP Press, *Modern Acoustics and Signal Processing*.

ASSESSMENT OF REGIONAL EXPLOSION DISCRIMINANTS USING DATASETS OF UNPARALLELED SPATIAL SAMPLING: THE BIG HORNS ARRAY SEISMIC EXPERIMENT (BASE)

Kate C. Miller[1], Marie D. Arrowsmith[2], W. Scott Phillips[2], Steven H. Harder[3], Lindsay L. Worthington[4], Anne F. Sheehan[5], and Megan L. Anderson[6]

Texas A&M University[1], Los Alamos National Laboratory[2], University of Texas at El Paso[3], University of Colorado[5], and Colorado College[6]

Sponsored by the Air Force Research Laboratory and the National Science Foundation

NSF Award Nos. EAR-0843835[4], EAR-0843657[6], and EAR-0843889[7]
AFRL/NNSA Award Nos. FA9453-10-C-0214[1] and DE-AC52-06NA25396[2]
Proposal No. BAA10-31

ABSTRACT

Discrimination of regional earthquakes, single-fired explosions, and delay-fired mining explosions is dependent upon separation of path and source. Waveforms of regional events are typically sparsely sampled in space, with individual observations being separated by hundreds of kilometers, thus complicating the process of separating source and path effects. In this work, we are taking advantage of data being collected for the Big Horns Array Seismic Experiment (BASE), an EarthScope project funded by the National Science Foundation (NSF), to investigate the degree of spatial sampling of the seismic wavefield needed to characterize three-dimensional (3D) wave propagation effects in a complex regional setting and the implications for regional discrimination. BASE consists of a hybrid active/passive short-term seismic deployment that greatly increases the spatial sampling of the seismic wavefield in north-central Wyoming, a region with abundant natural and man-made events. Our goal is to fully assess the performance of regional seismic discriminants as they are applied to earthquakes, contained single-fired explosions, delay-fired mining explosions, and mining collapses using the unprecedented spatial sampling presented by the BASE dataset.

The centerpiece of USArray, one component of the NSF-sponsored EarthScope program, is the Transportable Array (TA) a rolling 70 km grid of over 400 broadband seismic stations that is already producing more densely sampled wavefields. BASE is designed to embed seismic instrumentation from the Flexible Array (FA) within the TA in order to construct complete 3D structural models of the region around the Big Horn Mountains, in conjunction with known geologic structures. The deployment, which is occurring in three phases that began in the summer of 2009 and will continue into the fall of 2010, has five main components. The first is a ca. year-long deployment of 39 broadband systems to infill the TA in the vicinity of the Big Horn Mountains to achieve an average spacing of 35 km. The second is an array of 170 short-period instruments that are being deployed along a grid of five lines with a station spacing of 5 to 10 km. The third component consists of three 5-element regional seismic arrays that are being deployed to assess the role of arrays in signal detection and characterization for discrimination purposes. These arrays will in place for 6 months, beginning in May. In July 2010, an active-source seismic experiment consisting of two profiles with 1850 “Texan” seismographs deployed at 0.1 to 0.5 km and up to 20 large (500–2000 lb) single-fired shots are being conducted. The seismic signals from the shots will also be recorded by the passive arrays. Finally, 850 Texan seismographs will be deployed for two weeks along the short-period grid in passive mode to achieve a nominal station spacing of 1 km.

Analysis plans include calculation of two-dimensional (2D) and 3D velocity models of the crust and upper mantle and a 2D amplitude tomography. The resulting Q models will be used to estimate amplitude corrections that will be applied to the observational data prior to the discrimination analysis. Results from this study will allow us to quantify the degree of regionalization and instrumentation necessary for successful discrimination in a tectonically complex region. This result will provide a basis for assessing regional discrimination performance in areas with substantially reduced datasets.

OBJECTIVES

The primary objective of the work being performed under this contract is to quantify the degree of regionalization and instrumentation necessary for successful discrimination in a tectonically complex region. Ultimately, this result will provide a basis for assessing regional discrimination performance in areas with substantially reduced datasets. To date, our work is entirely focused on collecting a large and diverse seismic dataset in north-central Wyoming, during a field season that stretches from May to October 2010.

The work for this contract piggybacks on a project sponsored by the EarthScope program of the NSF, known as BASE—the Big Horns Array Seismic Experiment. The focus of the NSF proposal is on imaging the deep structure of basement-cored arches in order to understand the mechanisms of formation of the Rocky Mountains. Other science goals of the NSF project center on the nature of faults at depth in the crust and on questions about crustal rheology. In addition to producing velocity models of the crust and upper mantle, the seismic-imaging experiment will determine whether faults continue as sharp features at depth or whether they spread into a broader zone of ductile deformation.

RESEARCH ACCOMPLISHED

At the time of the submission deadline for the meeting proceedings, the fieldwork for this contract was in full gear. Thus, this paper focuses primarily on the nature of the field experiment.

BASE is designed to embed seismic instrumentation from the EarthScope FA within the EarthScope TA in order to construct complete 3D structural models of the region around the Big Horn Mountains of Wyoming, in conjunction with known geologic structures. The TA is a rolling 70-km grid of over 400 broadband seismic stations that is the centerpiece of the USArray component of the NSF-sponsored EarthScope program. The TA is deployed in north-central Wyoming and southern Montana until early fall of 2010. The BASE deployment of FA instruments, consists of three phases that began in the summer of 2009 and that continues into the fall of 2010. The deployment can be divided into five components described below and illustrated in Figure 1.

The first component is a ca. year-long deployment of broadband stations designed to infill the TA in the vicinity of the Big Horn Mountains to achieve an average spacing of 35 km. Installation of these stations, using CMG-3T broadband seismometers, took place during the summer and fall of 2009; 39 CMG-3T broadband seismometers were installed in the Big Horn region. Of these, 27 stations were placed in locations that densify the grid of transportable array stations in the area. Another 12 were placed on transect lines (Figure 1). The broadband stations all have Quanterra Q330 data loggers sampling at 50 Hz. Stations were oriented using an Octans, a high-precision fiber-optic gyrocompass. These stations will remain in place until fall 2010.

The second component consists of 170 short-period seismometers deployed along five transects at 4 to10 km spacing, as well as three mini-arrays at the ends and in the middle of the main E-W transect (line M, Figure 1). Seventy short-period seismometers were deployed in April, 35 in May, and the remaining sites in June.

In July 2010, an active-source seismic experiment, the third component, will be conducted (Figure 1). This effort will consist of 1850 “Texan” seismographs deployed along one E-W and one NW-SE transect. Seismometer spacing will range from 0.1 to 0.5 km. Twenty large (500–2000 lb) single-fired explosions will be recorded along the active source lines. The shots will also be recorded by the broadband and short-period arrays.

Following the active source experiment, the Texan seismometers will be redeployed in passive source mode along the five transects shown in Figure 1. Station spacing is 1 km. Eight hundred fifty Texans will be deployed in passive mode for two weeks (instrument/battery swaps every 4–5 days). The single-fired shots at mines will be fired into this array.

A day’s worth of recording at a TA station near Big Horn, Wyoming (Figure 2), demonstrates the nature of the data that will be collected at each seismometer site. Recordings of teleseisms, regional earthquakes, and mine blasts are expected to be common. This will provide a rich dataset for discrimination analysis.

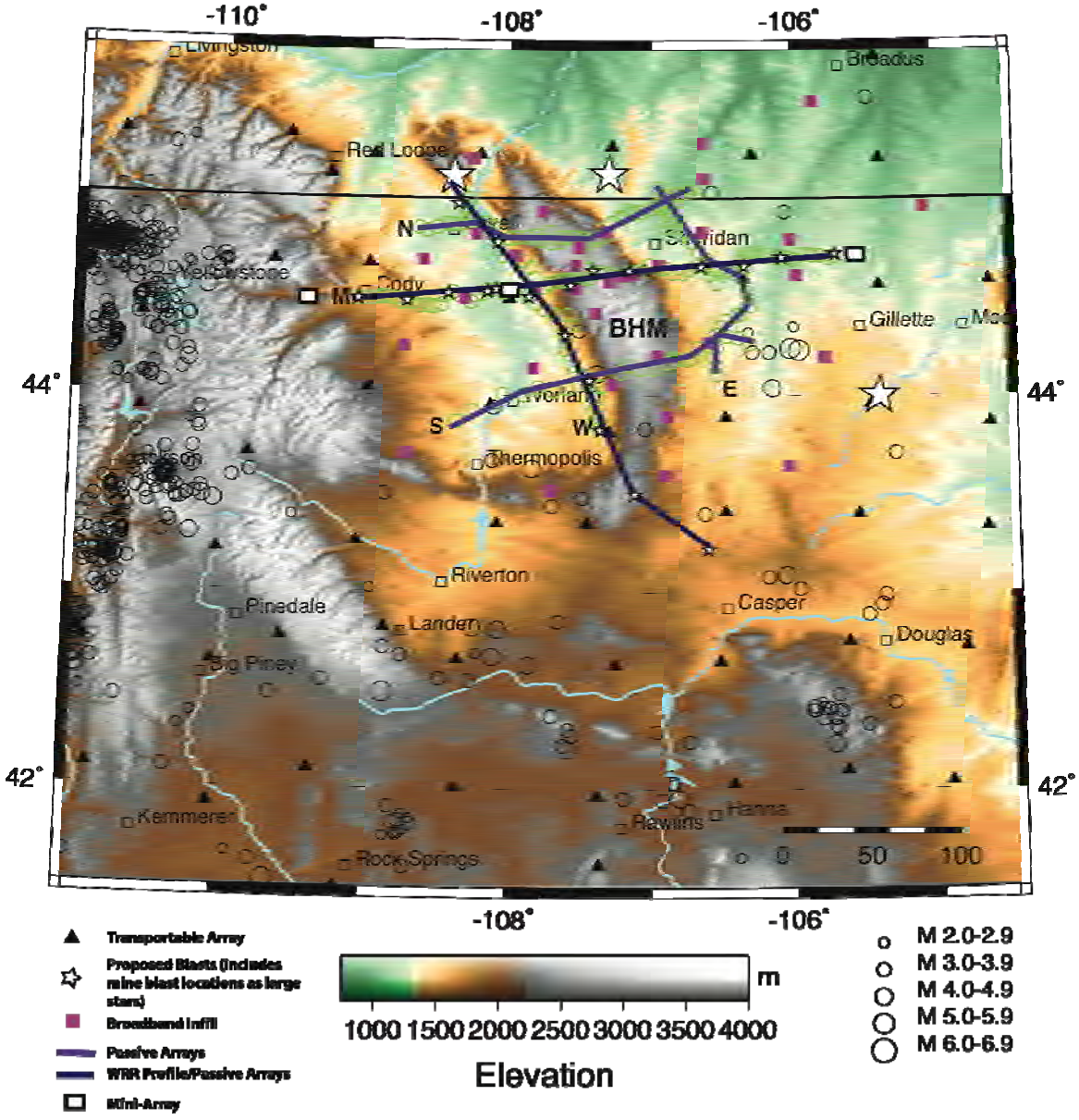

Figure 1. Topographic map of north-central Montana showing seismic experiment geometry and regional seismicity. A total of 27 broadband stations (pink squares) infills the EarthScope TA stations (black triangles). A total of 182 temporary stations (green circles), including 12 with broadband sensors, are deployed along the five array lines at 4- to 10-km intervals. Three mini-arrays are located along the central transect. Single-fired shots (small white stars) are to be fired into 1850 Texans deployed along transects with shots. Subsequently, 850 Texans will be deployed along all transects for 2 weeks, to record passively and infill the array lines to a station spacing of 1 km.

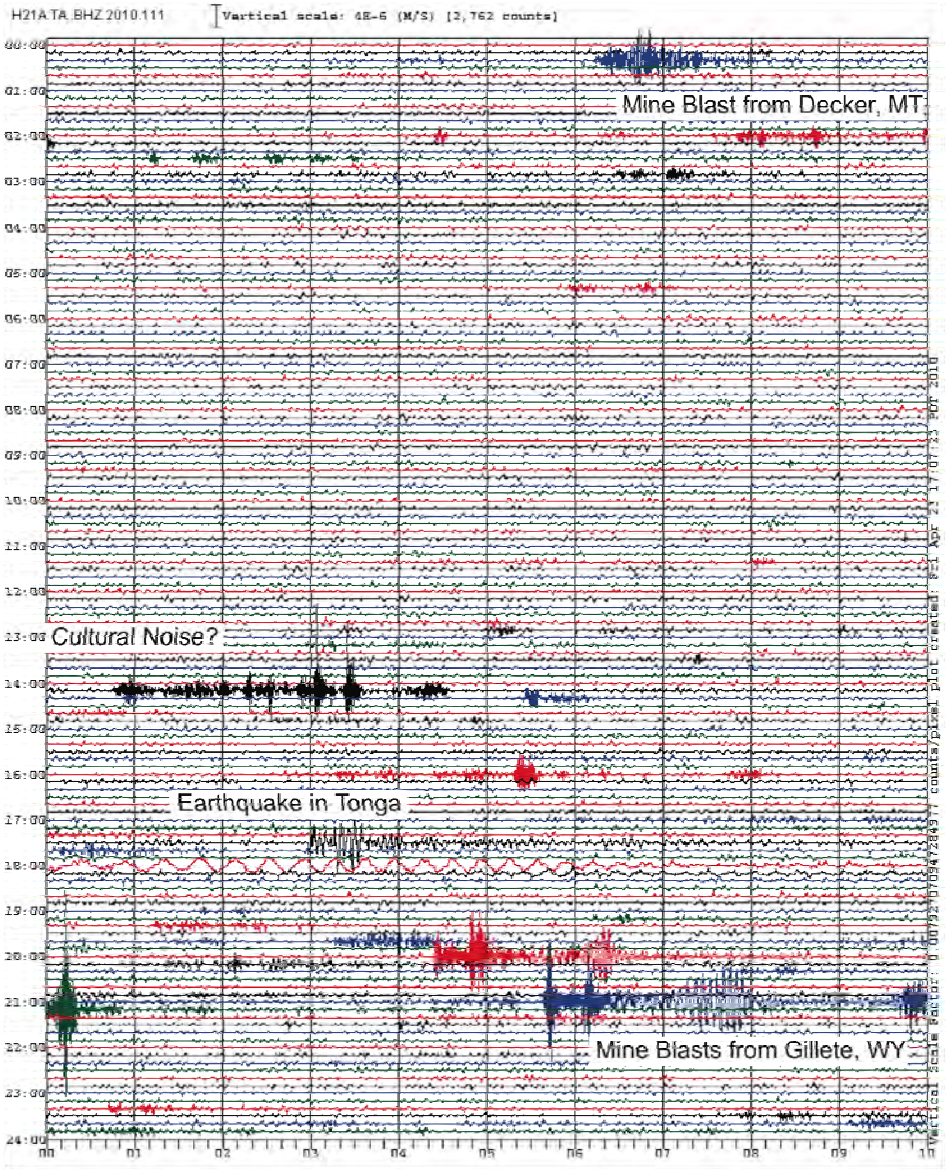

Figure 2. Typical day of seismicity recorded at a TA station at Big Horn, Wyoming. Each line displays 10 minutes of ground motion.

CONCLUSIONS AND RECOMMENDATIONS

As the field work for this project is just underway, it is still too early to draw any detailed conclusions. Analysis plans for the dataset include calculation of 2D and 3D velocity models of the crust and upper mantle and a 2D amplitude tomography. The resulting Q models will be used to estimate amplitude corrections that will be applied to the observational data prior to the discrimination analysis. These detailed regional models, combined with the dense spatial sampling of BASE, will put us in an excellent position to be able to quantify the degree of regionalization and instrumentation necessary for successful discrimination in a tectonically complex region.

ACKNOWLEDGEMENTS

We thank the NSF, IRIS, the PASSCAL instrument center, Bighorn National Forest, Bureau of Land Management, and private landowners for their support. We also thank all the student volunteers from across the country that helped deploy seismometers.

SOURCE AND PATH CALIBRATION IN REGIONS OF POOR CRUSTAL PROPAGATION USING TEMPORARY, LARGE-APERTURE, HIGH-RESOLUTION SEISMIC ARRAYS

John L. Nabelek[1], Seth Carpenter[1], Patrick W. Monigle[1], Jochen Braunmiller[1], and W. Scott Phillips[2]

Oregon State University[1] and Los Alamos National Laboratory[2]

Sponsored by Air Force Research Laboratory and the National Nuclear Security Administration

Contract No. FA8718-09-C-0004
Proposal No. BAA09-28

ABSTRACT

Broadband seismic data acquired during the Hi-CLIMB experiment are used to study seismic events and path propagation in the Nepal Himalaya and the south-central Tibetan Plateau. The 2002–2005 experiment consisted of 233 stations along a dense 800 km linear north-south array extending from the Himalayan foreland into the central Tibetan Plateau. The main array was flanked by a 350 km x 350 km sub-array in southern Tibet and central and eastern Nepal. The dataset provides an opportunity to obtain seismic event locations for ground truth (GT) evaluation, to determine source parameters, and to study distance evolution of seismic coda for yield estimation in low Q regions.

In year two of the project we concentrated on refining hypocenter locations and magnitude estimates in Tibet near the Hi-CLIMB stations. Better event locations are primarily due to improvements in crustal models and to eliminating spurious events and arrivals. The dataset now holds over 34,000 events with ~8,900 defined by more than 30 phase arrivals, which we consider well located. In southern Tibet, many well-located earthquakes occur in the lower crust and upper mantle. Abundant seismicity north of the Yarlung Tsangpo Suture, however, occurs primarily in the upper-most crust in extensional grabens and along strike-slip faults connecting them. Many initial event magnitudes were contaminated by arrivals from closely following, larger events during times of vigorous seismicity. Use of vertical component data consistently underestimates the S arrival amplitude, which led to systematically underestimated magnitudes. Using only P-arrivals eliminated contamination and provided a much cleaner magnitude dataset, which can be uniformly converted to S-based magnitude by adding a constant 0.7 to compensate for the average S-to-P amplitude ratio for earthquakes with double-couple mechanisms. This corrected P-derived M_L is consistent with M_w from low-frequency regional moment tensor analysis we have performed on larger events in our dataset.

In-depth analysis focused on seismicity along the Pumqu-Xianza Rift (PQX) (~30ºN, 88ºE) an area of known geothermal activity and exceptionally high rate of seismicity. Hi-CLIMB stations operating in the region from July 2004 to August 2005 recorded over 500 well-located earthquakes near the PQX compared to only 11 events listed in the USGS NEIC catalog for the same region. The USGS locations show a systematic west-southwest bias of up to ~40 km compared to locations based on automatic P- and S-phase picks from local stations, which are tightly clustered and ~20 km west of the central PQX. Epicenters from manual phase picking differ by only a few km from the automatic locations confirming their overall quality. Manually derived hypocenter depths of ~10 km are consistent with regional moment tensor depths of 36 larger ($3.5 \leq M_w \leq 4.8$) earthquakes recorded by Hi-CLIMB. All source mechanisms show ~N-S oriented normal faulting with a shallow west-dipping nodal plane. Based on event locations, source mechanisms, and Google imagery showing no prominent scarps in the immediate vicinity of the earthquakes, we favor a scenario of rupture along the eastern PQX rift boundary fault, a west-dipping low-angle normal fault and the most prominent feature on the Google imagery.

OBJECTIVES

The broadband dataset from the 2002–2005 Hi-CLIMB seismic array in the Himalayan-Tibetan collision zone is unique in its large aperture and dense station spacing. The purpose of our research is to improve source and path calibration in regions of poor crustal propagation to enhance the monitoring community's capabilities to estimate magnitude and yield of future nuclear tests in low Q and highly scattering environments. We have three linked objectives. The first is to obtain high-precision ground-truth seismic event hypocenters. The second is to provide seismic moment and independent depth estimates from waveform modeling of local and regional earthquakes. The third is to determine the distance evolution of seismic coda, utilizing the quasi-continuous control offered by the dense, laterally large network, important for low Q areas. In the second year of the project, efforts concentrated on (i) improving the seismic event database obtained from automatic phase picking and event association, (ii) improving consistency and reliability of the local magnitude estimates, and (iii) in-depth analysis for absolute event location and moment tensor analysis focusing initially on a small area, the Pumqu-Xianza rift in southern Tibet.

RESEARCH ACCOMPLISHED

Data

The Hi-CLIMB broadband seismic experiment (Nabelek et al., 2005; 2009a) in Nepal and the south-central Tibet consisted of 233 sites with each site occupied for 12-20 months (Figure 1). Station spacing along the ~800-km long north-south array covering the India-Eurasia collision zone from the Ganges foreland into the Tibetan Plateau was 3-4 km in the south and about 8 km north of the Yarlong-Tsangpo suture. Lateral deployments in Nepal and southern Tibet with 30-40 km station spacing improve earthquake location capabilities and provide wave propagation control for the transition from the foreland into the plateau. Data were recorded continuously at 50 and 40 sps. The Hi-CLIMB data provide a unique opportunity to study small sized seismic events at unprecedented accuracy in central Asia.

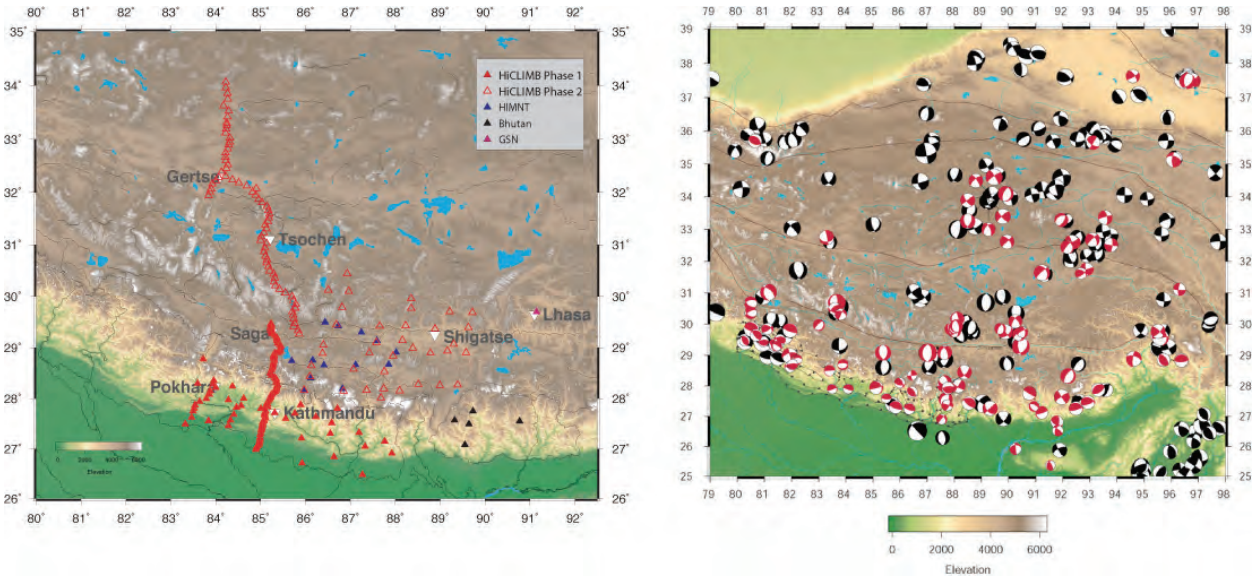

Figure 1. Left. Map of Hi-CLIMB (red triangles) 233 station seismic network, and HIMNT (blue triangles) (Sheehan et al., 2004) and Bhutan (black triangles) (Velasco et al., 2007) broadband temporary seismic networks also available for this study. Purple triangle: Permanent broadband station in Lhasa. Right. Regional moment tensors (red: Burtin, 2005; Baur, 2007; Monigle et al., 2009) and Global CMTs (black). We completed analysis of 170+ larger events in the Tibet region using high-quality waveforms. The 150+ Hi-CLIMB solutions contain events as small as M_w = 3.5. 166 CMTs, mainly for M_w>5.0, exist for 1976-2005.

We had already performed regional moment tensor analysis in the Himalayan-Tibetan region for ~150 selected larger earthquakes (Burtin, 2005; Burtin et al., 2005; Baur, 2007) using the full waveform inversion code of Nabelek and Xia (1995). Results (Figure 1, Nabelek et al., 2009b) illustrate that our efforts substantially expand the region's moment tensor catalog; our database also includes most events analyzed by de la Torre et al. (2007). Analysis suggests a depth resolution for shallow crustal events on the order of ±5 km and an estimated M_w uncertainty of ±0.1-0.2 units with currently used velocity models and event locations. Additional moment tensors were obtained for the Pumqu-Xianza Rift (~ 30ºN, 88ºE) (see below) where we have good event location control, a significant number of events with similar-looking waveforms spanning a wide size range, and good recording geometry that allows testing of parameter resolution and evaluating of velocity-depth models for seismogram calculation.

Event Detection and Location

In year two of the project we concentrated on refining hypocenter locations and magnitude estimates in Tibet near the Hi-CLIMB stations. The entire Hi-CLIMB waveform database (1.4 TB) has been organized using the Antelope software developed by Boulder Real Time Technologies (BRTT). We used the Antelope modules for automatic detection and arrival time picking, event-arrival association and event location. Requiring low detection (3.0 STA/LTA ratio) and association (7 and more phases constitute an event) thresholds implemented to obtain a dataset as complete as possible resulted in an initial database of almost 110,000 declared events for the second half of the experiment (15 months from June 2004 to August 2005) or on average ~240 per day.

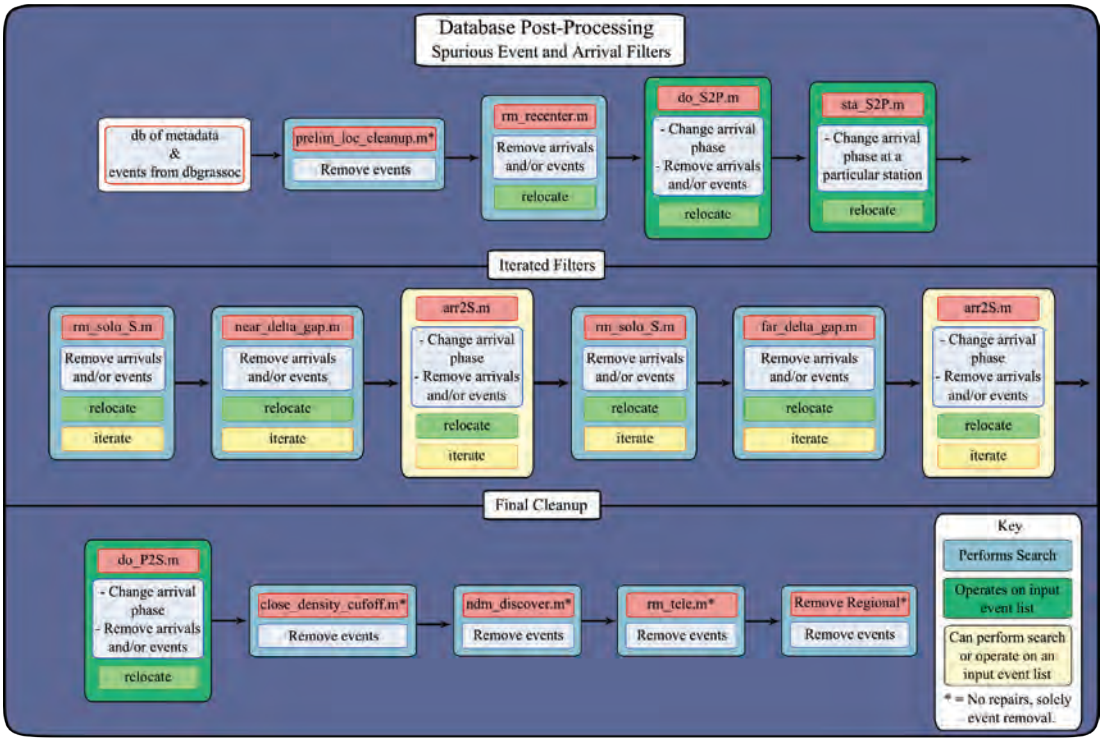

Figure 2. Simplified flowchart showing database post-processing steps performed to clean up the associated event table. Processing steps fall into two groups: (1) removing or reassigning phase picks to obtain a more consistent set of phase picks for an event leading to an improved location (green box "relocate") or (2) removing spurious events for which the set of phase picks could not be fixed (blue box "Remove events"). Details are described in Carpenter (2010).

The large number of events rendered manual inspection unfeasible and we spent considerable effort to develop modules to weed out spurious detections as well as erroneous phase and event associations to automate data management. Figure 2 shows a simplified flowchart of post-processing steps that implement simple logic considerations about what constitutes a valid seismic event. For example, we expect that stations close to an

epicenter record an event and that stations close to each other either all (or most) record an event or do not. Many problems stemmed from wrong phase association caused by simultaneously occurring events in different locations within the Hi-CLIMB array region, misplaced seismicity from the great 2004 Sumatra earthquake sequence or incorrectly associating P arrivals as S arrivals, or vice versa. We tested phase arrivals for each event and removed spurious arrivals or switched mis-associated arrivals (e.g., S- to P-phase) to improve the consistency of the phase-arrival set for an event; if this was impossible, we removed events entirely.

The resulting automatic preliminary event database contains more than 34,000 seismic events, with about 8,900 defined by more than 30 P and S arrivals. Figure 3 shows a subset of 4,500 well located events with at least 30 defining arrivals and local magnitude $M_L(P) \geq 2.0$, which is a relevant cut-off for monitoring purposes ($M_L(P)$ is defined below). The automatic locations utilize many S-arrivals, constraining the epicenters, and correlate with geologic structures seen in satellite imagery suggesting they are quite accurate; for some events the USGS PDE locations show a mismatch of up to 50 km (see Pumqu-Xianza section below for quantitative analysis of PDE and automatic location bias). Most shallow seismicity north of the Yarlung-Tsangpo suture (north of 29.5°N) is in an area not investigated by most other previous experiments. The most prolific source region was the Payang Basin (near 30º-31ºN, 84ºE), with almost 10,000 events following M_w>6 main shocks in July 2004 and April 2005, respectively (Figure 4); the extreme number of events immediately after the main events actually was one of the primary reasons for phase misassignments requiring database post-processing (Figure 2). Vigorous seismicity (1,600+ events) was also observed from the vicinity of the Pumqu-Xianza Rift (~30ºN, 88ºE).

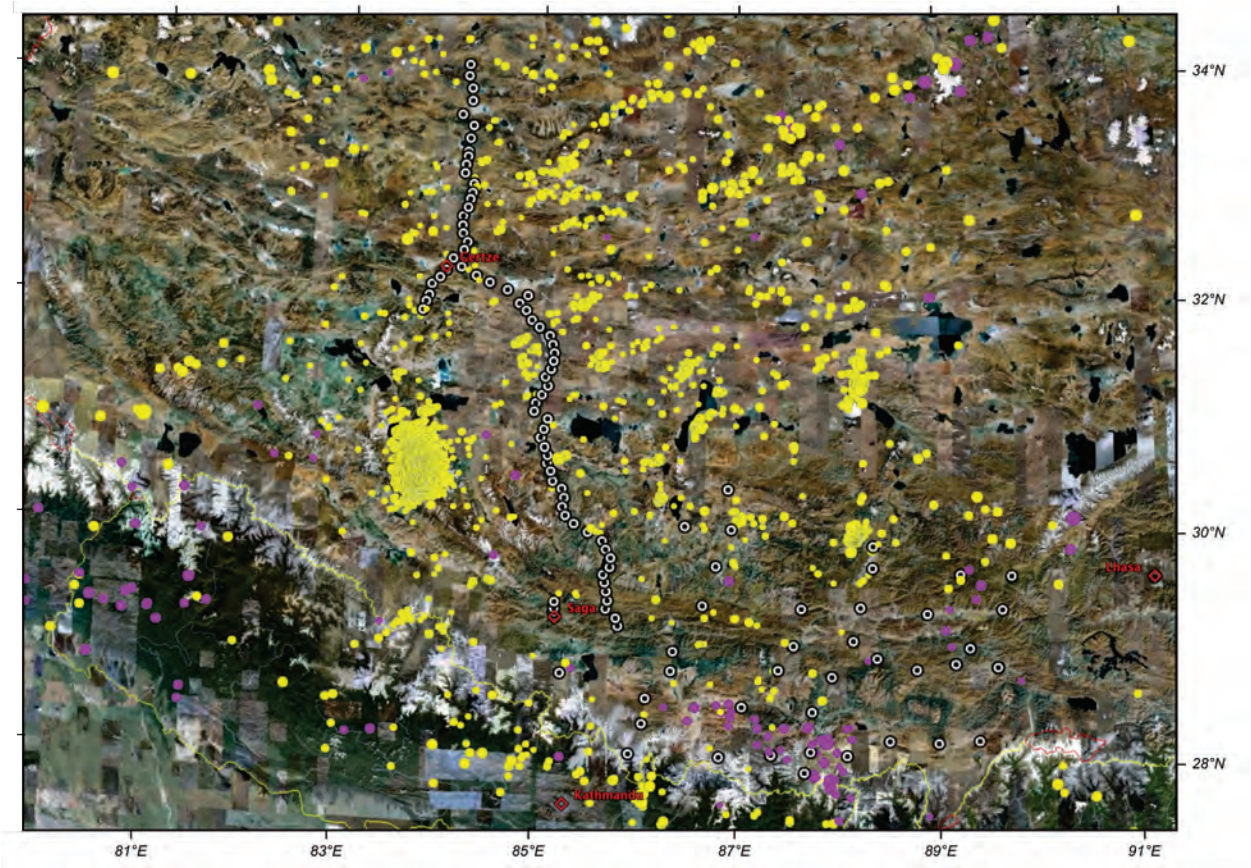

Figure 3. Preliminary epicenter map (colored circles) for 15-month period covering the second half of Hi-CLIMB (recording stations black circles). Over 34,000 events have been located. We plot 4,500 events with at least 30 P and S arrivals and $M_L(P) \geq 2.0$. Yellow are crustal events and purple are upper mantle events. The numerous shallow events north of the Yarlung-Tsangpo suture (>29°N) have not been covered by previous experiments.

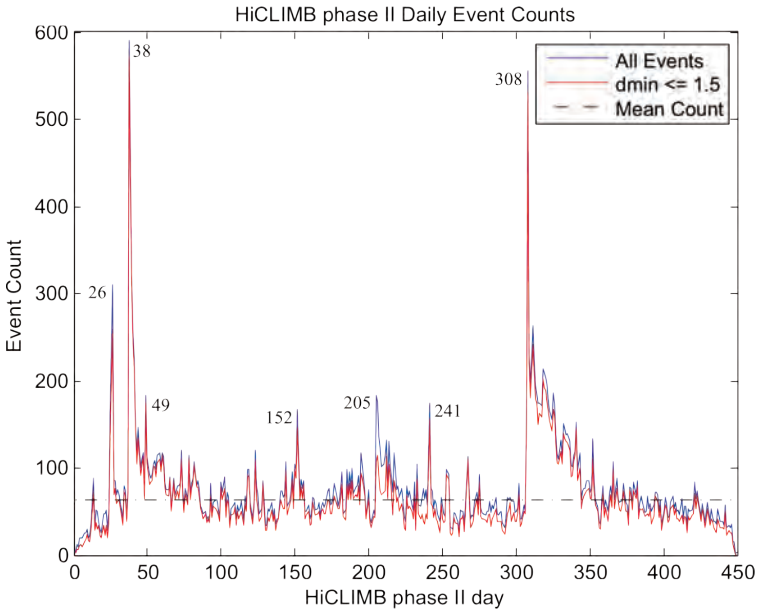

Figure 4. Events per day in the 34,000+ Hi-CLIMB phase II database (June 2004 – August 2005). Peaks at day 38 and 308 are immediate aftershocks of Payang Basin M 6+ main shocks. Day 26 and 49 peaks are partially due to elevated seismicity in the Pumqu-Xianza Rift. Red shows event counts with closest station 1.5º or less away from an event, blue are all events. The peak at day 205 is due to the 2004/12/26 M_w=9.1 Sumatra-Andaman earthquake about 20º SE from the array; its aftershocks were very well-recorded by the Hi-CLIMB array, however, automated processing encountered difficulties determining correct slowness and/or depth resulting in a significant number of events being mislocated inside or near the array requiring database post-processing (Figure 2).

Efforts will now concentrate on identifying potential GT5 events and to determine their locations based on manually picked phases with careful consideration on depth and absolute location uncertainties as required. This work will include improving crustal structural models. Selected small events near the dense array will be analyzed in conjunction with the GT location effort (e.g., to obtain independent depth estimates) and the requirements of the coda wave modeling (e.g., to provide seismic moment over a range of event sizes for calibration of absolute spectral levels from coda to bands approaching those used for yield estimation).

Local Magnitude

We used the Antelope module dbml to calculate local magnitude (M_L) from the vertical component seismograms for all events in the database with epicenter-station distances of 600 km or less. Usually M_L is determined from the maximum amplitudes on Wood-Anderson-equivalent horizontal seismograms with the maximum amplitude corresponding to an S-phase. We thus originally defined the time window to be 1.5 times the S-P-time for a given station-event distance to obtain the amplitudes. However, during times of vigorous seismicity, we often encountered contamination by arrivals from closely following, larger events (Figure 5). Another complication arises from using vertical component data that underestimate the S arrival amplitude, which led to systematically underestimated magnitudes.

In order to avoid both problems, we decided to estimate event size from a short time window containing only P waves (0.25 S-P-time, Figure 5). This approach eliminated contamination and provided a much cleaner magnitude dataset. Using the average expected S-to-P amplitude ratio of $(v_p/v_s)^3 \approx 5$ for earthquakes with a double-couple mechanism provides a physics-based approach to convert to S-based magnitude by simply adding a constant value of 0.7. We call this (corrected) magnitude M_L(P).

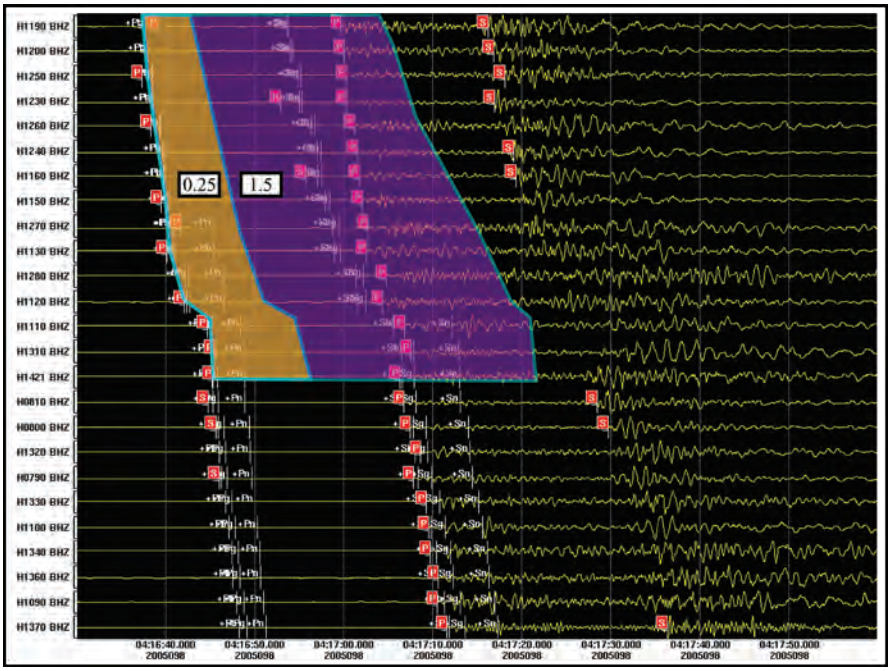

Figure 5. Wood-Anderson equivalent waveforms for 90 seconds of data from April 8, 2005, about 8 hours after an M=6+ earthquake in the Payang Basin. A small event (first set of arrivals) is followed by a much stronger event (second set of P arrivals) within 1.5 times its S-P-time (purple area). The M_L for the first event based on the long time window is about 2 magnitude units too large. Another problem, apparent for the second event, is that vertical seismograms underestimate the amplitude of S-phases, which are predominantly recorded on horizontal components; in this case the S-to-P amplitude ratio is about 2 compared to the expected value of ~5. We decided to determine magnitudes from a short window containing only the P arrival (0.25 S-P-time shown in brown).

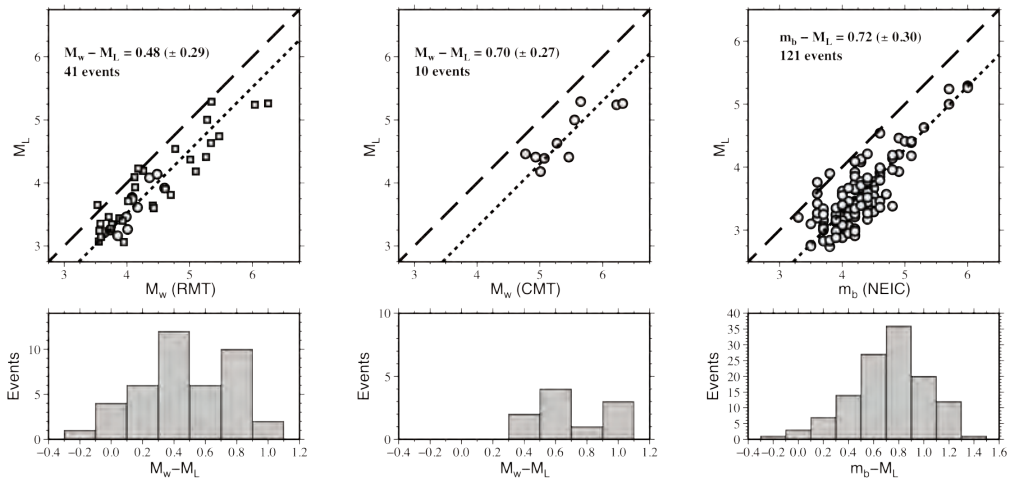

Figure 6. Magnitude comparison. M_L is local magnitude based on P wave amplitudes determined during automatic processing. M_w(RMT), M_w(CMT), m_b(NEIC) are moment magnitude from regional moment tensor inversion, Global CMT analysis, and USGS NEIC body wave magnitude, respectively. Shown are common events. The average underestimation of uncorrected M_L of 0.5, 0.7, and 0.7, respectively, is consistent with the expected theoretical bias due the use of P instead of S waves. The scatter around the average (short dashes, long dashes correspond to one-to-one correspondence) is similar to scatter observed when regressing other magnitudes relative to each other (e.g., Braunmiller et al., 2005).

We found our $M_L(P)$ (P-wave M_L + 0.7) is consistent with the moment magnitude M_w determined from low-frequency regional moment tensor analysis for 41 common events, the average $M_L(P)$-M_w(RMT) difference is 0.2 units (Figure 6). We also compared $M_L(P)$ with Global CMT M_w and USGS PDE body wave magnitude m_b, which for moderate event sizes is close to M_w. We found on average $M_L(P)$ matches exactly both teleseismic estimates (Figure 6).

Low-Angle Normal Faulting in the Pumqu-Xianza Rift

Seismicity north of the Yarlung-Tsangpo Suture in the Lhasa Terrane of southern Tibet occurs primarily along N-S trending grabens. In-depth analysis concentrated on particularly focused seismicity along the Pumqu-Xianza rift (PQX) (Figure 7) an area of known geothermal activity and exceptionally high rate of seismicity that initiated in 1980 following an M_S 6.2 earthquake in the northern part of the rift. Hi-CLIMB stations operating in the area from July 2004 to August 2005 recorded over 500 well-located earthquakes near the PQX rift compared to only 11 events, ranging in magnitude (m_b) from 4.0 to 4.8, listed in the USGS NEIC catalog.

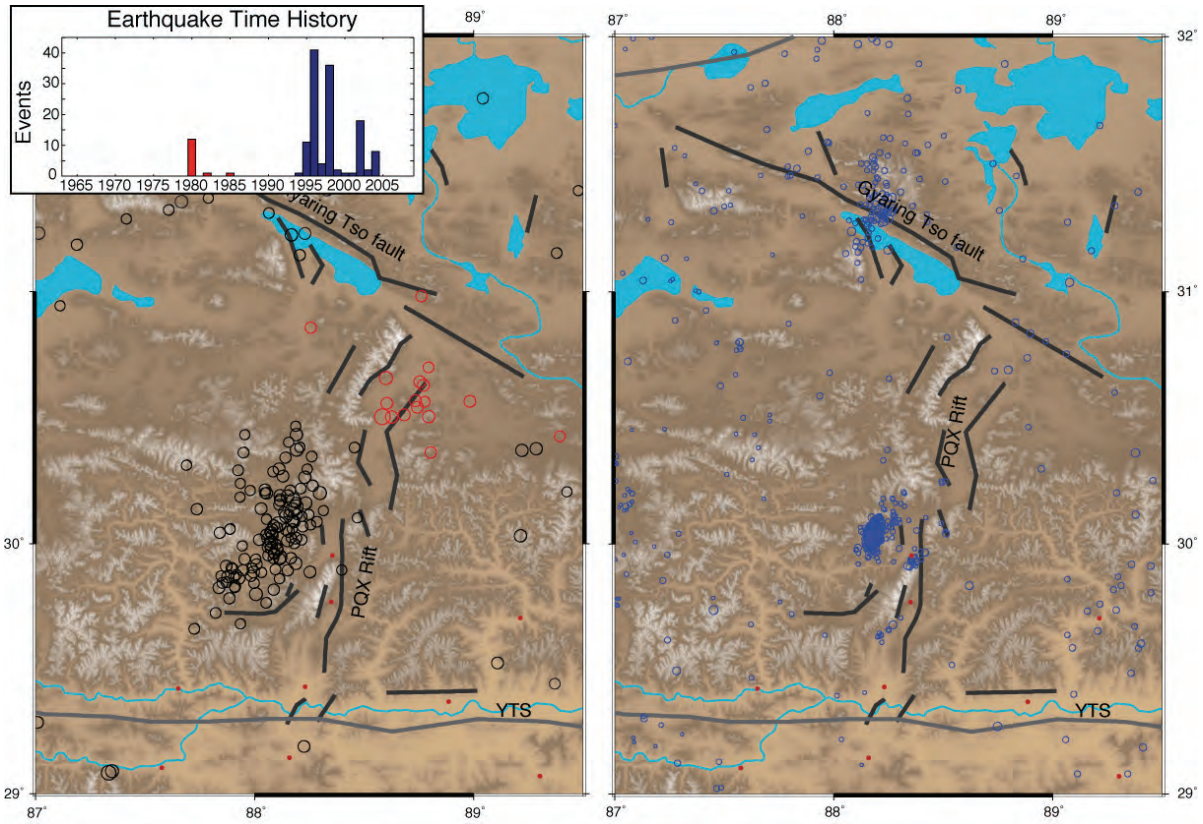

Figure 7. Left. Map and time history (inset) of 1963-2009 seismicity ($m_b \geq 4.0$). An M_S 6.2 event in 1980, the largest historic PQX event, initiated activity in the northern rift (red). After a ~10 year hiatus, activity started in the central part (black). Right. Hi-CLIMB seismicity. Shown are 500+ high-quality epicenters (blue) for events from July 2004 to August 2005, when close-by sites (red) operated, based on at least 20 automatic phase picks. Note tight event cluster at 30ºN about 20 km west of the graben.

Locations with local Hi-CLIMB stations reveal a systematic west-southwest bias of the routine NEIC epicenter locations that can reach up to ~50 km (Figure 8). The Hi-CLIMB locations based on automatic P- and S-phase pick are closer to the rift and cluster near the central PQX. Manual phase picking for selected events verified the high

automatic location quality with epicenter differences of only a few kilometers (Figure 8). Manual locations include a larger number of phase picks, in particular, many more S picks from close-by stations that provide strong epicenter and depth control. The resulting hypocenters cluster very tightly west of the central PQX (triangles in Figure 8) near ~10 km depth. The cluster technically does not satisfy GT5 criteria (e.g., Bondar et al., 2004), even though the closest site is ~20 km from the epicenters, because of the large ~150º azimuthal gap since the events occurred at the northern terminus of the lateral array.

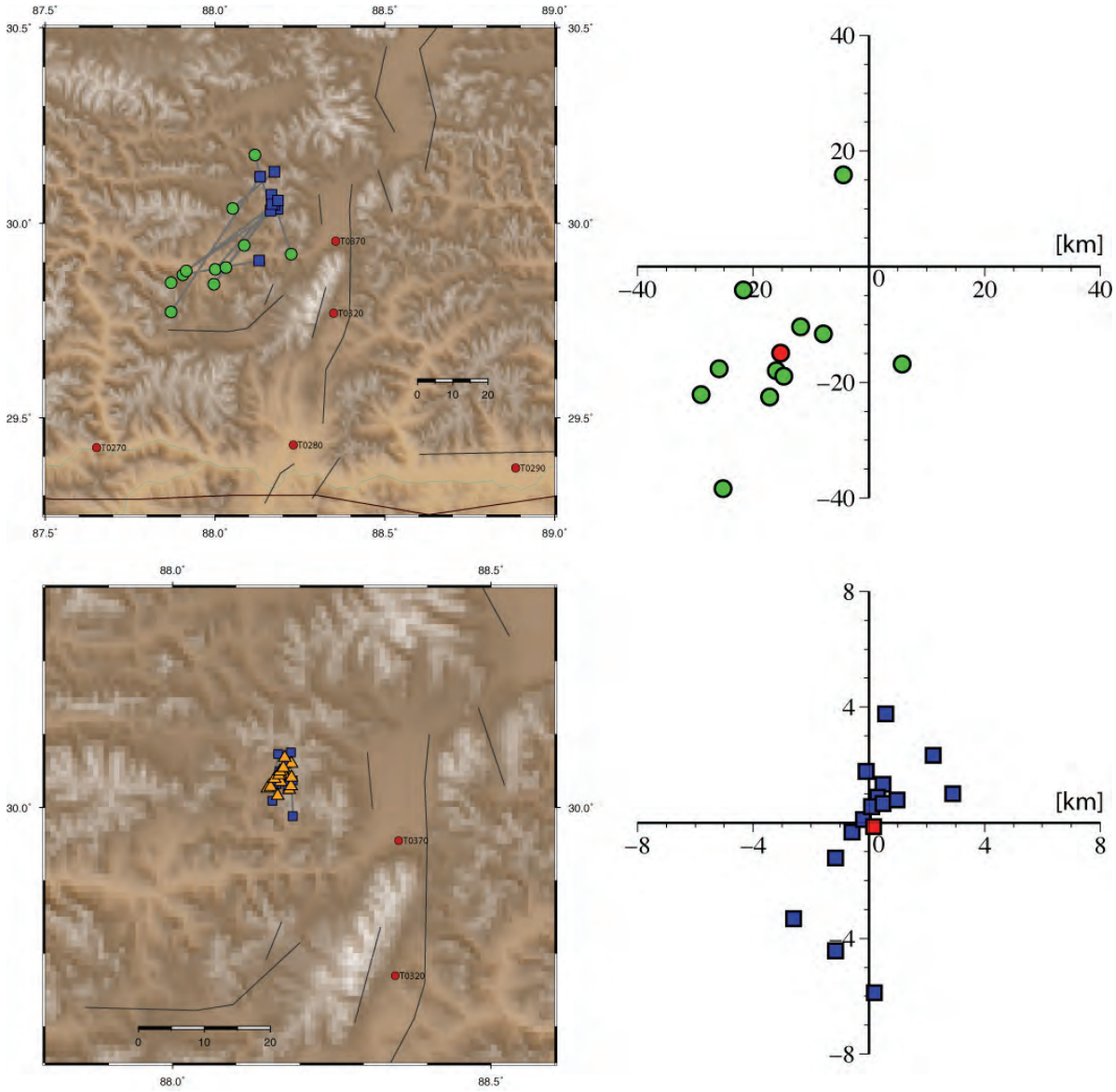

Figure 8. Comparison of NEIC (green circles), automatic Hi-CLIMB (blue squares), and manual Hi-CLIMB (orange triangles) earthquake locations for the PQX reveals (top) a general SW NEIC location bias that can reach more than 40 km (average value for 11 common events is 25 km) and (bottom) a close correspondence of locations based on automatic and manual P- and S-phase picks, respectively (average epicenter difference for 15 events is 2 km). The closest Hi-CLIMB station (red circles) is about 20 km east of the epicenters. Right shows (top) NEIC relative to automatic Hi-CLIMB location (at center), and (bottom) automatic relative to manual Hi-CLIMB location (at center). Red symbols are "centroid" shifts of ~20 km to the SW and ~0 km, respectively.

However, the manual hypocenter depths of ~10 km are consistent with shallow 6-9 km depths (with uncertainties probably on the order of ±3 km) from regional moment tensor analysis of 36 larger ($3.5 \leq M_w \leq 4.8$) earthquakes from modeling Hi-CLIMB data (Figure 9) (Baur, 2007; Monigle et al., 2009). This suggests that actual hypocenter resolution for events from July 2004 to August 2005, for which location and waveform modeling were performed, is close to GT5. All source mechanisms show ~N-S oriented normal faulting with a ~25-30º shallow west-dipping nodal plane. Solutions for events when sites east of 86º E were operating are highly consistent suggesting a small rupture area in agreement with the tight epicenter cluster from earthquake location.

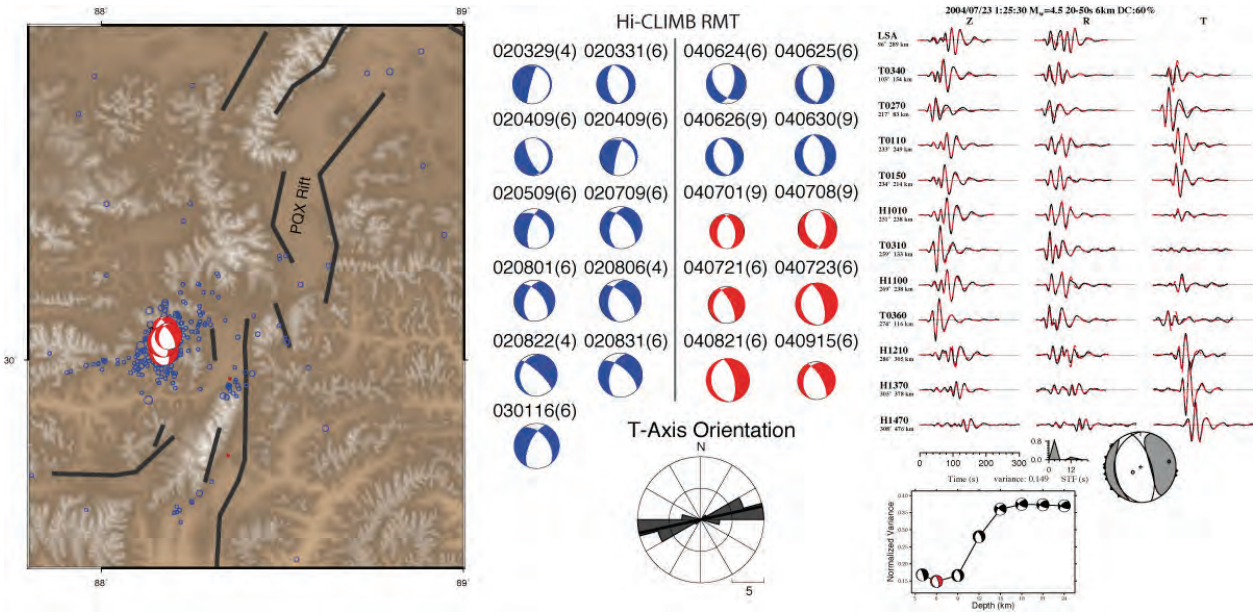

Figure 9. Left. Hi-CLIMB epicenters (blue) plotted with corresponding regional moment tensors (red) when close-by sites operated. Center. Selected fault plane solutions from regional moment tensor analysis. Red are best-constrained events in terms of location and moment tensor because of operating close-by sites; blue are events before local sites where installed. Right. Example of waveform fit (black observed, red synthetic, shown are only selected sites) for a M_w=4.5 event. All events are constrained by a large number of three-component waveforms from at least 20 stations. All solutions are consistent with shear faulting, are shallow, and indicate normal faulting along a N-S to NNW-SSE trending fault.

Based on event locations, source mechanisms, and Google imagery showing no prominent scarps in the immediate vicinity of the earthquakes, we favor a scenario of rupture along the eastern PQX rift boundary fault, a west-dipping low-angle normal fault and the most prominent feature on the Google imagery. The N-S extent of the cluster coincides with the dimensions (~20 km) of the basin, just east of the event-cluster, which forms a short, bounded rift segment. Combining the consistent observations leads to a preferred interpretation of active low-angle normal faulting. Physically, low-angle faulting is difficult to achieve unless the stress field is rotated or resolved shear stress is very low. Presence of fluids, likely in this geothermal region, could possibly achieve both. Globally, our study is one of the first to document possible low-angle faulting. Given uncertainties in location, depth, and dip and choice of nodal plane, other scenaria cannot be ruled out. The fault could be steeply east dipping or could have occurred on an unidentified west-dipping fault west of the PQX. Surface morphology, however, supports neither alternative.

Initial results were presented at the 2009 AGU meeting (Monigle et al., 2009). We are currently finalizing absolute and relative locations based on manual P- and S-phase picks for prominent events during the 2002-2005 sequence to test our initial interpretation.

CONCLUSIONS AND RECOMMENDATIONS

The Hi-CLIMB broadband seismic dataset provides the opportunity for ground truth location, source parameter determination and studying distance evolution of seismic coda in central Asia. The dataset reveals an abundance of seismic events not included in any other catalog. We developed modules to clean up the automatic event location database that eliminate spurious phase arrivals leading to improved locations, or, where this was impossible, remove spurious events entirely. The resulting database contains over 34,000 events with almost 9,000 based on 30 or more P and S arrivals. Initial M_L determination indicated systematic underestimation and frequent contamination of smaller events by later, larger events due to the high level of seismicity. Instead of determining M_L from S phases, we implemented a local magnitude based on P wave amplitudes $M_L(P)$ and use a simple, physics-based conversion to obtain regular M_L. We analyze the vigorous seismicity near the Pumqu-Xianza Rift for precise hypocenter locations and regional moment tensor determination to evaluate events for GT-locations. Knowledge gained from the small Pumqu-Xianza area will be transferred to GT-location determination and evaluation in other areas covered by the Hi-CLIMB array. The GT level locations and moment tensor depths will contribute to SLBM tomographic efforts, allow evaluation of depth for crustal models, and enhance model accuracy throughout central and southern Asia and, in general, will contribute to the National Nuclear Security Administration (NNSA) Knowledge Base.

REFERENCES

Baur, J. (2007). Seismotectonic analysis of the Himalayan-Tibetan collision zone from regional seismic moment tensor analysis with Hi-CLIMB data, *M.Sc. thesis, Oregon State University, Corvallis, Oregon*, 276 pp.

Bondar, I., S. C. Myers, E. R. Engdahl, E. A. Bergman (2004). Epicentre accuracy based on seismic network criteria, *Geophys. J. Int*. 156: 483–496, doi: 10.1111/j.1365-246X.2004.02070.x, 2004.

Braunmiller, J., N. Deichmann, D. Giardini, W. Wiemer, and the SED Magnitude Working Group (2005). Homogeneous moment-magnitude calibration in Switzerland, *Bull. Seis. Soc. Am.*, 95, 58-74, doi: 10.1785/0120030245.

Burtin, A. (2005). Seismotectonics of the Himalayan arc from regional seismogram moment tensor inversion, *Internship Report, Oregon State University, Corvallis, Oregon*, 42 pp.

Burtin, A., J. Nábělek, J. Baur, and J. Vergne (2005). Evidence for the decoupling of stress above and beneath the Main Himalayan Thrust, *Eos Trans. Am. Geophys. Union* 86: (52): Fall Meet. Suppl., Abstract T43A-1379.

Carpenter, S. (in prep. 2010). *M.Sc. thesis, Oregon State University, Corvallis, Oregon*.

De la Torre, T. L., G. Monsalve, A. F. Sheehan, S. Sapkota, and F. Wu (2007). Earthquake processes of the Himalayan collision zone in eastern Nepal and the southern Tibetan Plateau, *Geophys. J. Int.* 171: 718-738, doi: 10.1111/j.1365-246X.2007.03537.x

Monigle, P. W., J. Nábělek, J. Braunmiller, S. Carpenter, and J. R. Baur (2009). Earthquake activity along the Pumqu-Xianza rift (Tibet) and its tectonic implications, *Eos Trans. AGU*, 90(52), Fall Meet. Suppl., Abstract T43C-2111.

Nábělek, J. and G. Xia (1995). Moment-tensor analysis using regional data: application to the 25 March 1994 Scotts Mills, Oregon earthquake, *Geophys. Res. Lett.* 22: 1316.

Nábělek, J., J. Vergne, G. Hetenyi, and the Hi-CLIMB Team (2005). Project Hi-CLIMB: a synoptic view of the Himalayan collision zone and southern Tibet, *Eos Trans. Am. Geophys. Union* 86: (52): Fall Meet. Suppl., Abstract T52A-02.

Nábělek, J., G. Hetényi, J. Vergne, S. Sapkota, B. Kafle, M. Jiang, H. Su, J. Chen, B.-S. Huang, and the Hi-CLIMB Team (2009a). Underplating in the Himalaya-Tibet collision zone revealed by the Hi-CLIMB experiment, *Science* 325: 1371, doi: 10.1126/science.1167719.

Nábělek, J. L., J. Braunmiller, and W. Scott Phillips (2009b). Source and path calibration in regions of poor crustal propagation using temporary, large-aperture, high-resolution seismic arrays, in *Proceedings of the 2009 Monitoring Research Review: Ground-Based Nuclear Explosion Monitoring Technologies*, LA-UR-09-05276, Vol. 1, pp. 158-165.

Sheehan, A. F., G. Monsalve, C. Rowe, and M. Begnaud (2004). Ground truth in central Asia from in-country networks, in *Proceedings of the 26th Seismic Research Review: Trends in Nuclear Explosion Monitoring*, LA-UR-04-5801, Vol. 1, pp. 338–345.

Velasco, A. A., V. L. Gee, C. Rowe, D. Grujic, L. S. Hossister, D. Hernandez, K. C. Miller, T. Tobgay, M. Fort, and S. Harder (2007). Using small, temporary seismic networks for investigating tectonic deformation: Brittle deformation and evidence for strike-slip faulting in Bhutan, *Seis. Res. Lett.* 78: (4) 446-453, doi: 10.1785/gssrl.78.4.446.

THE PROPAGATION OF *Pn* IN WESTERN CHINA

Robert L. Nowack[1], Wang-Ping Chen[2], Jessica D. Griffin[1], Ali C. Bakir[1] and Tai-Lin Tseng[2]

Purdue University[1] and University of Illinois[2]

Sponsored by the Air Force Research Laboratory

Award No. FA8718-08-C-0025
Proposal No. BAA08-42

ABSTRACT

The propagation of *Pn* in Western China is investigated with regional events recorded by the Himalyan-Tibetan Continental Lithosphere during Mountain Building (Hi-CLIMB) array in Tibet. Seismic attributes, including arrival times, Hilbert envelope amplitudes, and instantaneous and spectral frequencies, are used to study how the crustal and upper-mantle velocity and attenuation structure affects the propagation of *Pn* arrivals in Tibet. We have constructed more than 30 high-quality regional seismic profiles, and of these, 12 events have been selected with excellent crustal and *Pn* arrivals for further analysis. Regional travel times recorded by the Hi-CLIMB array are utilized to constrain the large-scale velocity structure in the region, with four near regional events to the array used to constrain the crustal structure. The travel times from the far regional events indicate that the Moho beneath the southern Lhasa terrane is up to 75 km thick, with *Pn* velocities greater than 8 km/s. In contrast, the data sampling the Qiangtang terrane north of the Bangong-Nujiang suture shows thinner crust with Pn velocities less than 8 km/s. This is consistent with the virtual seismic profile results of Tseng et al. (2009) of the teleseismic *SsPmp* phase recorded along the Hi-CLIMB array. Nonetheless, there is additional variability of the regional travel-time data suggesting further 3D complexities. Seismic amplitude and frequency attributes have been extracted from the crustal and *Pn* wave trains, and these data are compared with numerical results for models with upper-mantle velocity gradients and attenuation, which can strongly affect *Pn* amplitudes and pulse frequencies. The numerical modeling is performed using the complete spectral element method (SEM), where the results from the SEM method are in good agreement with analytical and reflectivity results for different models with upper-mantle velocity gradients. The approach we are following is to have the analysis of *Pn* seismic attributes be largely data driven to investigate the effects of large-scale lithospheric structure, velocity gradient heterogeneities, and attenuation in Tibet.

OBJECTIVES

We are investigating the propagation of regional *Pn* waves recorded by the Hi-CLIMB array in Tibet. Considering the station spacing (3 to 8 km) and large aperture (800 km) of the Hi-CLIMB seismic experiment, our objective is to use these densely recorded data to construct a self-consistent model of *Pn* propagation over a large region in western China. In turn, a better understanding of the effects of *Pn* propagation from analysis of the data will improve frequency-dependent attenuation models of regional *Pn* phases. This will lead to a clearer separation of elastic and anelastic effects in a laterally varying crust and upper mantle, eventually eliminating the assumption of a simplified, frequency-independent geometric spreading component.

RESEARCH ACCOMPLISHED

We have constructed more than 30 high-quality seismic profiles recorded on the Tibet Hi-CLIMB array (Nabelek, et al., 2005) and from these, 12 have been selected for further analysis. Similarities in the seismic profiles for events in clusters are outstanding. About two-thirds of the larger earthquakes have fault-plane solutions available in the global Harvard Centroid Moment Tensor (CMT) catalog (Dziewonski et al., 1981) and the report by Baur (2007). For those without fault plane solutions, we have identified several additional events that can be resolved using regional waveforms recorded by Hi-CLIMB stations for their appropriate azimuthal coverage. The fault-plane solutions that cannot be obtained through this method have been estimated based on geologic structures or historic solutions.

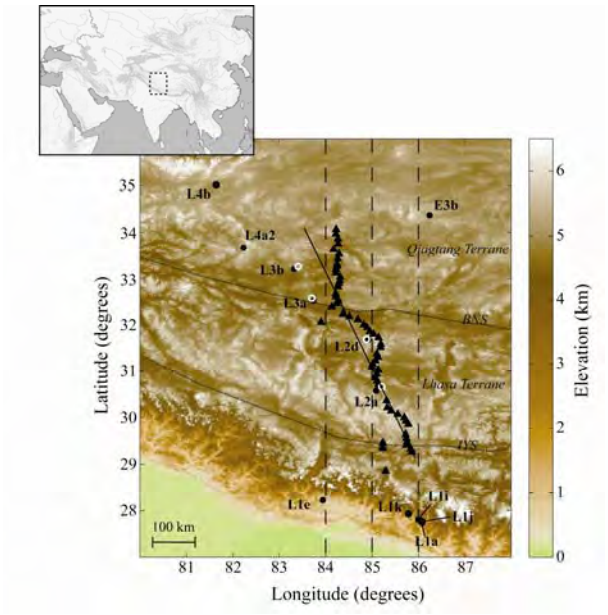

Figure 1. Map of the stations of the Hi-CLIMB array in Tibet (triangles) and the epicenters of the selected regional earthquake sources (circles). Black circles are the hypocenters reports by the PDE catalogs and Engdahl et al. (1998), and the white circles are the epicenters nearest to the array that have been relocated in this study. The dashed lines indicate the locations of north-south slices of the P-wave velocities from travel-time modeling, with the East Line at 84 degrees, the Central Line at 85 degrees, and the West Line at 86 degrees in longitude.

Regional events recorded by the Tibet Hi-CLIMB array with locations approximately in line with the array have been chosen for analysis here and are shown in Figure 1. However, other events in specific terranes have also been identified for later processing. Four of the in-line events have epicenters less than 200 km from the Hi-CLIMB array, and these events were relocated with data from the Hi-CLIMB array using the earthquake location program HYPOINVERSE-2000 (Klein, 2002). The locations of selected in-line events are shown in Figure 1, using the Engdahl et al. (1998) or the Preliminary Determination of Epicenters (PDE) catalogs for all events except the four nearby events (L2a, L2d, L3a, and L3b), which were relocated using Hi-CLIMB data. These relocations improved the fit to the travel-times but moved the epicenters on average of about 5 km. For more-distant events in Tibet, a

focal depth normalization procedure was used since events on the Tibetan plateau are dominantly less than 15 km in focal depth (e.g., Molnar and Chen, 1983; Chen and Molnar, 1983; Langin et al., 2003).

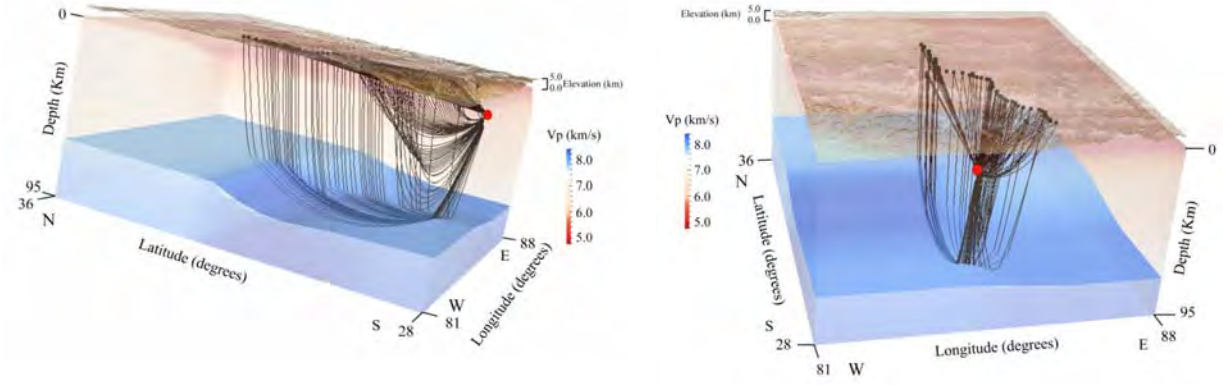

Figure 2. Ray diagrams calculated using the 3D ray-tracer cathode ray tube (CRT) for the Event L1E located by the red dot.

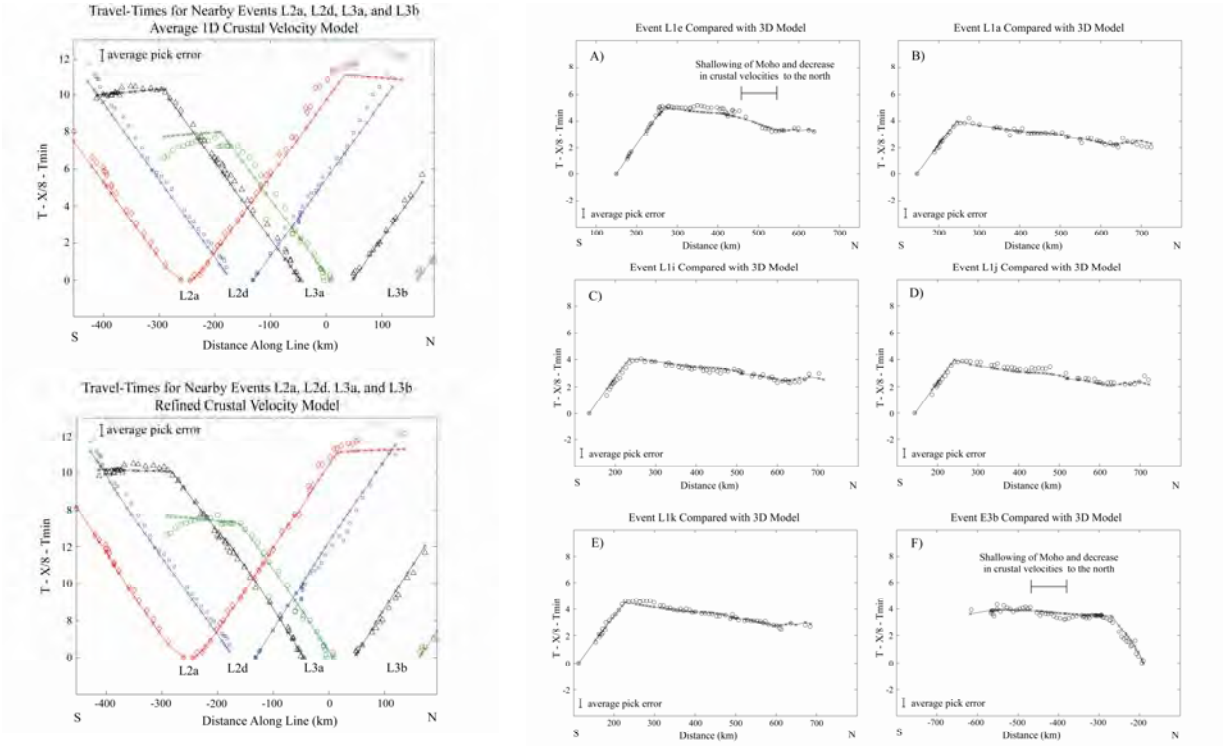

Figure 3. The left two plots show the observed first-arrival travel times and the calculated travel times (lines and crosses) for the relocated nearby events using the average 1D crustal model on top and the refined crustal velocity model on the bottom. The right plots show observed P-wave travel times (circles) and calculated travel times (lines and crosses) for the far-regional events: (A) L1e, (B) L1a, (C) L1i, (D) L1j, (E) L1k, and (F) E3b.

Figure 2 shows ray diagrams calculated using the 3D ray-tracer CRT (Cerveny et al., 1988) for the Event L1e shown by the red circle. The left plot is viewed from the west, and the right plot is viewed from the south. The blue top surface indicates the structure of the Moho used for the 3D model. The left top plot of Figure 3 shows the observed P-wave travel times for the relocated nearby Events L2a, L2d, L3a, and L3b, compared with the calculated travel times using the average 1D crustal velocity model. The left bottom plot of Figure 3 shows the observed travel times

of the first-arrival P waves for the nearby events, compared with the calculated travel times of the refined, laterally varying crustal velocity model. The right plots of Figure 3 show the observed P-wave travel-times (circles) for the far-regional Events (A) L1e, (B) L1a, (C) L1i, (D) L1j, (E) L1k, and (F) E3b. The *Pn* travel-times for these events were used to constrain the Moho structure and *P*-wave velocities in the upper mantle for this part of the Tibetan Plateau. The lines and crosses in each of the far-regional travel-time plots are the calculated travel-times using the inferred 3D regional velocity model.

Figure 4 shows plots of the 3D Moho and upper-mantle velocity structure found in this study from the modeling of near and far regional travel-time data for this region of the Tibetan Plateau, as viewed from (A) the west and (B) the south (Griffin et al, 2010). The upper-mantle velocities are higher and the Moho deeper beneath the southern portion of the plateau south of the Bangong-Nuijang suture (BNS), and upper-mantle velocities are lower and the Moho is shallower north of the BNS. These results are similar to those found by Tseng et al. (2009) using virtual seismic profiles from the *SsPmP* teleseismic phase and by Nowack et al. (2010) using Gaussian beam migration of teleseismic receiver functions. Other structure controls on the structure have been found by Hung et al. (2010) using finite frequency tomography of teleseismic arrival times, and for anisotropic structure of the upper mantle by Chen et al. (2010).

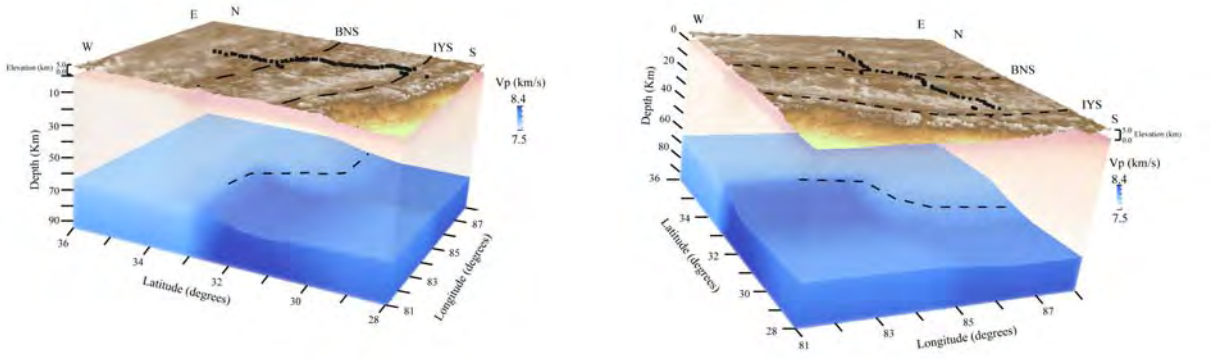

Figure 4. The 3D Moho and upper-mantle velocity structure found in this study for the region of the Hi-CLIMB array, with the left plot showing a view from the west and the right plot showing a view from the south.

The *Pn* phase is typically not a simple head wave but is composed of a complex set of interfering waves when there is a positive velocity gradient with respect to depth below the Moho interface (Cerveny and Ravindra, 1971; Hill, 1971; Menke and Richards, 1980). These interfering waves can also simply result from the spherical nature of the Earth (Hill, 1973; Sereno and Given, 1990, Yang et al., 2007), which gives an effect equivalent to a velocity gradient in a corresponding flattened Earth model. How observed amplitudes of refracted waves change over distance supports the interpretation that these arrivals are composed of diving and interference waves and is in contrast to a pure head wave (Braile and Smith, 1975). To account for the intricate nature of *Pn* propagation, we are applying SEM (Komatitsch and Vilotte, 1998; Komatitsch et al., 2005), as well as asymptotic ray/beam methods. In contrast, alternatives such as the reflectivity method are restricted to 1D media. SEM can be applied in 2D or 3D and implemented in parallel using message passing interface (MPI) on large-cluster computing. Here we are applying a 2D viscoelastic SEM code. As a practical measure, essential features of *Pn* waveforms are being distilled into seismic attributes, including arrival times, envelopes of wave amplitudes, and pulse frequencies for modeling.

To test the effects of upper-mantle velocity gradient, Moho topography, and lateral velocity variation on *Pn* propagation, we designed two velocity models. The left plot of Figure 5 shows the P-wave velocity model for a laterally homogeneous flat model with an upper-mantle velocity gradient of .004 1/s and has a crustal layer above a half space, with the Moho at 70 km depth. The right plot of Figure 5 shows a simplified 2D slice of a model derived from the 3D travel-time modeling, using regional data from the Hi-CLIMB array. Both the crust and the upper mantle have velocity gradients with depth and velocities that change laterally. The Moho changes in depth from 73.4 km on the left side of the model to 64.3 km on the right side of the model.

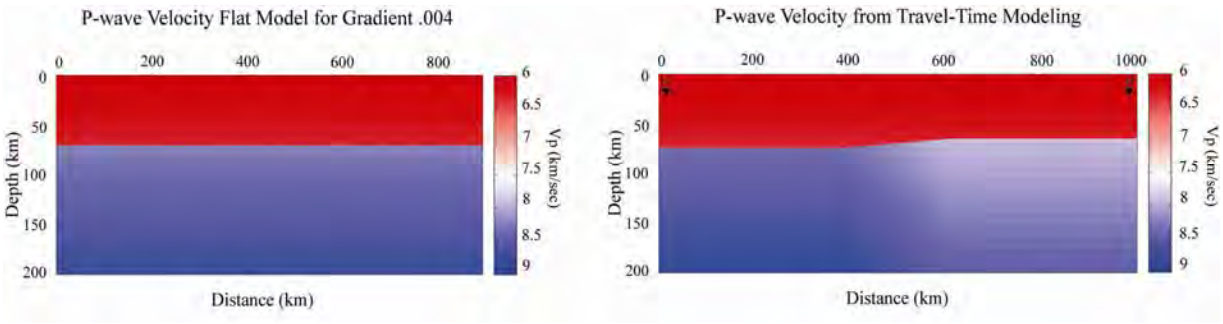

Figure 5. The left plot shows the P-wave velocities for a simple layer over a gradient with an upper-mantle velocity gradient of .004 1/s. The right plot shows a simplified P-wave velocity model from travel-time modeling of regional events from Hi-CLIMB, showing a step in the Moho.

Figure 6 shows the first arrival amplitudes for several laterally homogeneous models with different upper-mantle velocity gradients of 0, 0.002, 0.004, and 0.006 1/s. The case where the upper-mantle gradient is .004 1/s is the model shown in Figure 5 (left plot). As seen in Figure 6, when there is no upper mantle gradient, the *Pn* pulse amplitudes decrease with distance from 300 to 800 km. For an upper-mantle velocity gradient greater than .004, the *Pn* pulse amplitudes increases for this distance range.

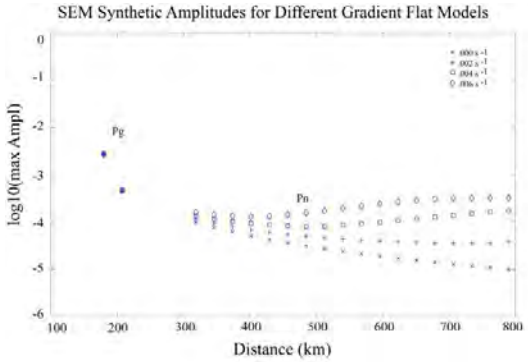

Figure 6. SEM synthetic P-wave amplitudes for several velocity models with different upper-mantle velocity gradients of 0.0, 0.002, 0.004, and 0.006 1/s.

Figure 7 shows the amplitudes computed for the velocity model shown in the right plot of Figure 5, with a step in the Moho that approximately satisfies the general shape of the Hi-CLIMB travel-time data. The blue curve is for source B near 1000 km and recorded to the south in Figure 5 (right plot); the red curve is for source A near 0 km and recorded to the north in Figure 5 (right plot). The synthetic amplitudes suggest that the amplitudes should relatively increase with distance for the *Pn* branch for source B, resulting from the step in the Moho for the particular upper-mantle velocity gradient. However, for source A, the *Pn* amplitudes should relatively decrease with amplitude, resulting from the step in the Moho. Thus, using events at different locations to the north and south of the Hi-CLIMB array, one should be able to identify the large-scale structural features.

In order to analyze the amplitude and pulse frequency data from Hi-CLIMB, we must first define several 2D cross sections from the derived 3D velocity model from travel-time modeling in order to compare with the 2D SEM results. In addition, an Earth-flattening transformation must be applied to use the 2D SEM modeling. Also, the 2D SEM amplitudes must be approximately corrected for out-of-plane spreading to compare with the observed amplitude data. The locations of the cross sections are shown in map view in Figure 1. The West Line along 84 degrees, Central Line along 85 degrees, and East Line along 86 degrees are used to model seismic attributes for event gathers L1e, group (L1a, L1i, L1j, L1k), and E3b, respectively. The earth-flattened models along these three lines are shown in Figure 8.

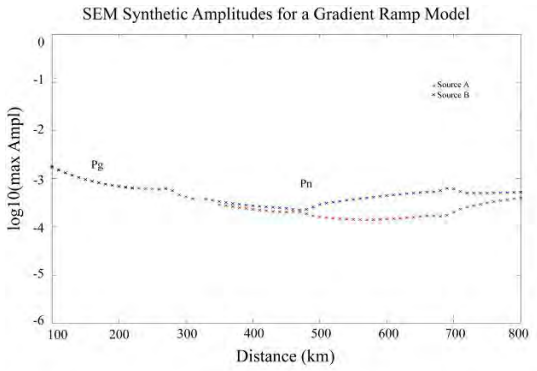

Figure 7. SEM synthetic amplitudes for a step in the Moho, as shown for the right plot in Figure 5. The blue curve is for source B near 1000 km in Figure 5 (right plot) and recorded to the south, and the red curve is for source A near 0 km and recorded to the north in Figure 5 (right plot).

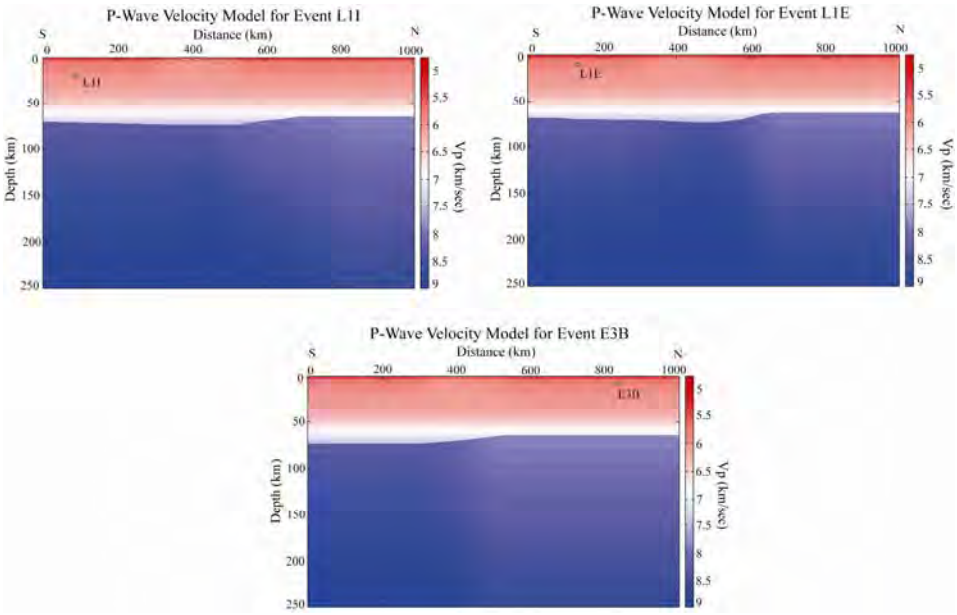

Figure 8. The top left plot shows the Earth-flattened Central Line through the 3D velocity model for Event L1i, the top right plot shows the Earth-flattened West Line though the 3D velocity model for Event L1e, and the lower plot shows the Earth-flattened East Line through the 3D velocity model for Event E3b.

We initially need to match the observed travel times on each event gather using the approximate 2D slices that have been Earth flattened. The upper left plot of Figures 9 and 10 show the travel-time comparisons for Events L1i and L1e, respectively. As can be seen in the travel-time comparisons, the 2D SEM calculations with the models given in Figure 8 do a reasonably good job at fitting the travel times.

For the upper right plots in the Figures 9–10, the observed Hilbert envelope amplitudes for the P-wave pulses are then compared with those calculated from the 2D SEM code. In order to make the comparison with the observed data, the 2D amplitudes are approximately corrected to account for out-of-plane spreading. However, for future research these results will need to be compared with 3D SEM calculations. For Events L1i and L1e, the *Pn* waves across the Moho step from a deeper Moho to a shallower Moho. From the synthetic results shown in Figure 7, this will result in a lowering in the amplitudes at larger offsets, resulting from the large-scale structural effects for events to the south. From the observed amplitudes for Events L1i and L1e shown in Figures 9 and 10, there are relatively

lower amplitudes at offsets between 500 to 600 km. Note that the observed amplitudes were only selected if there was no interference with later arrivals, and also reliable pulse frequencies could be estimated.

The SEM modeling includes the finer-scale upper-mantle velocity gradients that are initially taken from the 3D velocity model and are similar to those found by Phillips et al. (2007). The velocity gradients are also similar to those found by Myers et al. (2010) in the southern Lhasa terrane but are larger than those given by Myers et al. (2010) for the northern Qiangtang terrane. However, the upper-mantle speeds from the travel-time modeling of Hi-CLIMB *Pn* data are more similar to the results found by Phillips et al. (2007), as well as to other recent travel-time modeling studies on the Tibetan Plateau, including Liang and Song (2006), Sun and Toksoz (2006), and Hearn et al. (2004).

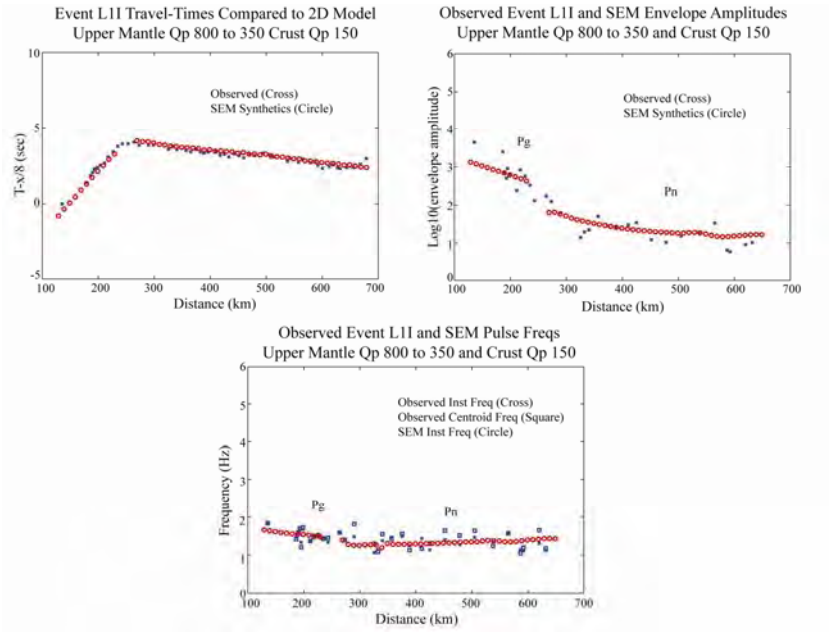

Figure 9. Seismic attribute comparisons for Event L1i between observed and calculated SEM attributes. The travel times are shown in the upper left plot, the pulse amplitudes are shown in the upper right plot, and the pulse frequencies are shown in the lower plot.

For the Lhasa terrane in the southern Tibet, the structural velocity model seems to account for a good portion of the amplitude signature for Events L1i and L1e, with larger Q values to the south of the BNS. However, the upper-mantle Q values for the Qiangtang terrane are around 350 for the L1I an L1E profiles at frequencies near 1.5 Hz. For Event E3b, we are still re-evaluating the focal mechanism, but initial modeling has somewhat lower upper mantle Q values in the Qiangtang terrane at frequencies near 1.5 Hz. These variations can be related to different ray paths for Event E3b to the north and for Events L1i and L1e to the south (Figure 1). Nonetheless, these upper-mantle Q values for the Qiangtang terrane are consistent with the range of Q values found by Xie (2007).

The pulse-broadening estimates are shown in the lower plots of Figures 9–10, where the observed values are given for both the instantaneous and spectral centroid frequencies. The calculated pulse frequencies are shown using the instantaneous frequencies. In Figures 9 and 10, the pulse frequencies are shown for Events L1i and L1e, and a reasonably good agreement is found between the observed and calculated values. For Event E3b, there are still some slight discrepancies with the calculated pulse frequency values for the *Pn* branch, which are somewhat higher than the observed values. This discrepancy might suggest a somewhat-lower upper-mantle velocity gradient in the northern Qiangtang terrane, possibly more similar to that found by Myers et al. (2010). However, this might also decrease the calculated amplitudes compared to the observed values. In any case, further tests on this are being investigated, and the focal mechanism for Event E3b is also being re-evaluated.

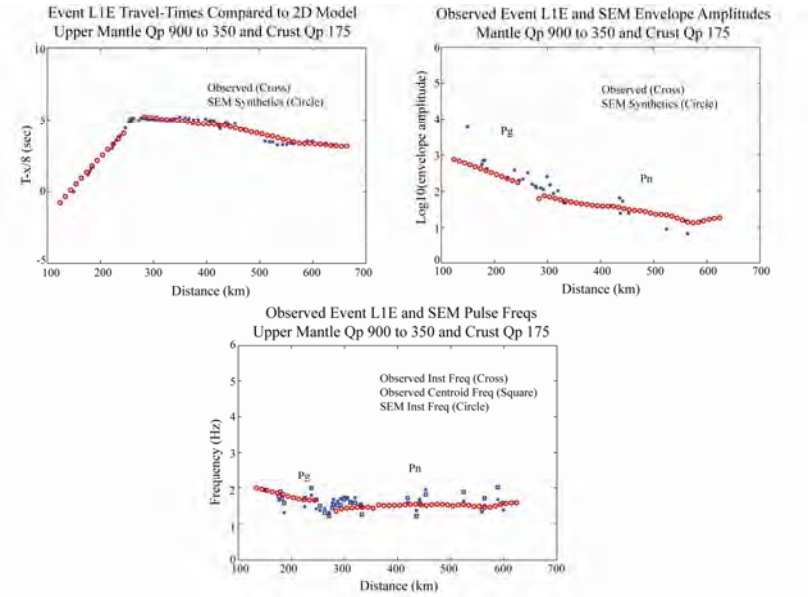

Figure 10. Seismic attribute comparisons for Event L1e between observed and calculated SEM attributes. The travel times are shown in the upper left plot, the pulse amplitudes are shown in the upper right plot, and the pulse frequencies are shown in the lower plot.

CONCLUSIONS AND RECOMMENDATIONS

We have assembled a number of record sections from regional events recorded by the Hi-CLIMB array. For several events nearby the Hi-CLIMB array, we have relocated the events using Hi-CLIMB data. From these record sections, seismic attributes of the *Pn* phase have been extracted from the data, including arrival times, envelope amplitudes, and instantaneous and spectral pulse frequencies. Several nearby events to the Hi-CLIMB array have been used to constrain crustal velocities from the crustal branches. For the *Pn* phases, the travel times have been modeled using 3D ray tracing in order to constrain the large-scale structural features, including Moho depths, upper-mantle velocities, and velocity gradients. Numerical modeling has been performed using SEM for selected regional event gathers in order to estimate the effects of large-scale velocity structure and attenuation on the extracted seismic attributes.

REFERENCES

Baur, J. R. (2007). Seismotectonics of the Himalayas and the Tibetan Plateau: Moment tensor analysis of regional seismograms, M.S. thesis, Oregon State University.

Braile, L. W. and R. B. Smith (1975). Guide to the interpretation of crustal refraction profiles, *Geophys. J. R. Astr. Soc.* 40: 145–176.

Cerveny, V., L. Klimes, and I. Psencik (1988). Complete seismic-ray tracing in three-dimensional structures, in *Seismological Alogorithms.* London: Academic Press.

Cerveny, V. and R. Ravindra (1971). *Theory of Seismic Head Waves*. University of Toronto Press.

Chen, W. P. M. Martin, T. L. Tseng, R. L. Nowack, S. Hung, and B. Huang (2010). Shear-wave birefringence and current configuration of converging lithosphere under Tibet, *Earth Planet. Sci. Lett.*, 295, 297-304.

Chen, W.-P., and P. Molnar (1983). Focal depths of intracontinental and intraplate earthquakes and their implications for the thermal and mechanical properties of the lithosphere, *J. Geophys. Res.* 88: 4183–4214.

Dziewonski, A. M., T.-A. Chou and J. H. Woodhouse (1981). Determination of earthquake source parameters from waveform data for studies of global and regional seismicity, *J. Geophys. Res.* 86: 2825–2852.

Engdahl, E. R., R. D. van der Hilst, and R.P. Buland (1998). Global teleseismic earthquake relocation with improved travel times and procedures for depth determination, *Bull. Seism. Soc. Am.* 88: 722–743.

Griffin, J. D., R. L. Nowack, T. L. Tseng, and W. P. Chen (2010). Modeling of three-dimensional regional velocity structure using wide-angle seismic data from the Hi-CLIMB experiment in Tibet, *Seism. Res. Lett.* 81: 373.

Hearn, T. M., S. Wang, J. F. Ni, Z. Xu, Y. Yu, and X. Zhang (2004). Uppermost mantle velocities beneath China and surrounding regions, *J. Geophys. Res.* 109: B11301.

Hill, D. (1971) Velocity gradients and anelasticity from crustal body-wave amplitudes, *J. Geophys. Res.* 76: 3309–3325.

Hill, D. (1973). Critically refracted waves in a spherically symmetric radially heterogeneous Earth model, *Geophys. J. R. Astr. Soc.* 34: 149–177.

Hung, S. H., W. P. Chen, L. Y. Chiao, and T. L. Tseng (2010). First multi-scale, finite frequency tomography illuminates 3-D anatomy of the Tibetan Plateau, *Geophys. Res. Lett.* 37: doi:10.1029/2009GL041875.

Klein, F. (2002). HYPOINVERSE-2000 (4/2002 vers.) [Computer Software]. Menlo Park, CA: U.S. Geological Survey.

Komatitsch, D. and J. P. Vilotte (1998). The spectral element method: An efficient tool to simulate the seismic response of 2D and 3D geological structures, *Bull. Seismol. Soc. Am.* 88: 368–392.

Komatitsch, D., S. Tsuboi, and J. Tromp (2005). The spectral-element method in seismology, in *Seismic Earth: Array Analysis of Broadband Seismograms*, Geophysical Monograph Series, Vol. 157, A. Levander and G. Nolet, Eds. Washington, DC: American Geophysical Union.

Liang, C. and X. Song (2006). A low velocity belt beneath northern and eastern Tibetan Plateau from *Pn* tomography, *Geophys. Res. Lett.* 33: L22306.

Langin, W. R., L. D. Brown, and E. A. Sandvol (2003). Seismicity of central Tibet from Project INDEPTH III seismic recordings, *Bull. Seism. Soc. Am.* 93: 2146–2159.

Menke, W. H. and P. G. Richards (1980). Crust-mantle whispering gallery phases—A deterministic model of teleseismic Pn wave-propagation, *J. Geophys. Res.* 85: 5416–5422.

Molnar, P. and W.-P. Chen (1983). Depths and fault plane solutions of earthquakes under the Tibetan plateau, *J. Geophys. Res.* 88: 1180–1196.

Myers, S. M. L. Begnaud, S. Ballard, M. E. Pasyanos, W. S. Phillips, A. L. Ramirez, M. S. Antolik, K. D. Hutchenson, J. J. Dwyer, C. A. Rowe, and G. S. Wagner (2010). A crust and upper-mantle model of Eurasia and North Africa for *Pn* travel-time calculation, *Bull. Seism. Soc. Am.* 100: 640–656.

Nabelek, J., W. P. Chen, M. R. Pandey, J. Mei, J. Chen, B. S. Huang, and the Project Hi-CLIMB Team (2005). Hi-CLIMB: A high-resolution seismic profile across the Himalayas and Southern Tibet, IRIS Annual Report, Washington DC.

Nowack, R. L., W .P. Chen, and T. L. Tseng (2010). Application of Gaussian beam migration to multi-scale imaging of the lithosphere beneath the Hi-CLIMB array in Tibet, *Bull. Seism. Soc. Am.* 100: 1743–1754.

Phillips, W. S., M. L. Begnaud, C. A. Rowe, L. K. Steck, S. C. Myers, M. E. Pasyanos, and S. Ballard (2007). Accounting for lateral variations of the upper mantle gradient in *Pn* tomography studies, *Geophys. Res. Lett.* 34: doi:10.1029/2007GL029338.

Sereno, T. J. and J. W. Given (1990), *Pn* attenuation for a spherically symmetric Earth model, *Geophys. Res. Lett.* 17: 1141–1144.

Sun, Y. and M. N. Toksoz (2006). Crustal structure of China and surrounding regions from *P*-wave travel-time tomography, *J. Geophys. Res.* 111: B03310.

Tseng, T. L., W. P. Chen, and R .L. Nowack (2009). Northward thinning of the Tibetan crust revealed by virtual seismic profiles, *Geophys. Res. Lett.* 36: L244304, doi:10.1029/2009GL040457.

Xie, J. (2007). *Pn* attenuation beneath the Tibetan Plateau, *Bull. Seism. Soc. Am.* 97: 2040–2052.

Yang, X., T. Lay, X. B. Xie, and M. S. Thorne (2007). Geometric spreading of *Pn* and *Sn* in a spherical earth model, *Bull. Seism. Soc. Am.* 97: 2053–2065.

ANALYSIS AND MODELING OF THE WAVEFIELD GENERATED BY EXPLOSIONS AT THE SAN ANDREAS FAULT OBSERVATORY AT DEPTH

Fred Pollitz, Justin L. Rubinstein, and William L. Ellsworth

U. S. Geological Survey

Sponsored by the National Nuclear Security Administration

Award No. DE-AI52-09NA29328
Proposal No. BAA09-69

ABSTRACT

Surface array and deep borehole recordings of chemical explosions in the near-source (0-20 km) region are studied to better understand the radiated wavefield, and in particular the generation of S-waves by explosions. More than 120 explosions have been conducted in the immediate vicinity of the San Andreas Fault Observatory at Depth (SAFOD) between 2002 and 2006 as part of a comprehensive program to determine the crustal structure and precise location of shallow microearthquakes near the deep drill holes at SAFOD. The data set features more than 70 high-quality digital surface and shallow borehole stations within 10 km of SAFOD; extensive observation of the downgoing wavefield by up to 80 3-component geophones deployed at depths of up to 2.7 km in the SAFOD boreholes; and 86 shot points, including 17 shot points located within a few tens of meters of seismic stations, creating an extensive set of reciprocity observations. Shallow crustal earthquakes have also been extensively observed by the recording networks.

We compare these observations with synthetic seismograms generated using published 3-D crustal models for SAFOD to test prevailing hypotheses of S-wave generation. The methods include a combination of basic source characterization (i.e., point sources represented by a moment tensor), imaging of scattering sources, non-linear wave generation associated with the initial shock wave, and non-linear free surface effects. We compute high-frequency synthetic seismograms in 3-D laterally heterogeneous structure using a new approach based on coupled normal modes. Applying the pure path approximation to a suitably smooth representation of the 3D structure and appropriately revising the eigenfrequencies of the normal modes, amounting essentially to a phase shift of each seismic arrival, reduces the non-linearity of the seismogram with respect to structural parameters. Following this, we apply the Born approximation to the remaining smooth structure (accounting for focusing / defocusing and refraction effects) and non-smooth structure, thus accounting for scattering from relatively short-wavelength structure. Limitations of this approach include:

1. A locked mode approximation must be employed (i.e., an artificial boundary at depth is introduced) in order to keep the number of mode branches reasonably bounded.
2. The effects of multiple scattering, which may affect the amplitude of direct-wave arrivals as well as the character of the coda waves, are not accounted for, since non-smooth structure is implemented with a single-scattering formalism

Keeping the limitations in mind, we apply our method to ~ 4 Hz wave propagation using SAFOD borehole seismometers and the Parkfield Array Seismic Observatory (PASO) array (Thurber et al., 2004). Initial modeling using a smooth 3-D model augmented by random structure shows that observed extended coda following the direct *S* arrival are partially explained by scattering from short-wavelength structure. However, additional structure (e.g., sharp lateral or horizontal discontinuities) may be necessary to explain the precise character of observed coda. We note that *P* coda is typically strong and complicates the identification of *S*-wave energy. We employ polarization analysis to guide the identification of *S* waves. Bearing the above in mind, preliminary analysis of 13 chemical shots during the 2006 PASO-TRES experiment suggests that direct *S*, when it can be unambiguously identified, is polarized as dominantly SV energy. This suggests that the chemical explosions transmit an effective vertical-force component in addition to an isotropic component.

OBJECTIVES

The principal objective of the work being undertaken is to better characterize and understand the generation of *S* waves from explosive sources. The amplitudes of *S* waves are commonly used as a discriminant between explosion- and earthquake-generated sources, in that explosion sources primarily produce *P* waves. Thus, characterizing how *S* waves may be generated by explosive sources is critical to improving explosion discrimination criteria. In this project, we focus on *S* waves generated in the near-source region (0-20 km).

Here we explore the generation of *S* waves from explosive sources using a data set consisting of explosion source data from the San Andreas Fault Observatory at Depth (SAFOD) project (Zoback, et al., 2010). These sources were used by the SAFOD project for site characterization and tomographic imaging, but also can be used for studying shear-wave generation and scattering. This dataset consists of over 120 explosions recorded on a large collection of instruments, both short period and broadband instruments at the surface and at depth. Shots were fired in holes of 5 to 100 feet deep, with shot size ranging between 2 and 100 kg. The shots used high-velocity explosives, such that source durations were very short. Additionally, there were multi-level (32- and 80-instrument) arrays installed in the SAFOD Pilot and Main holes at different times, which can be used to monitor the evolution of the wavefield over short distances.

We explore the generation of shear waves in the near-source region from two directions in the work described here. First, we have developed a methodology for synthesizing seismograms that is less computationally expensive than standard methods and simulates the scattered wavefield. Comparing these synthetic seismograms with observed explosion sources and earthquake sources on the myriad instruments we have available will hopefully show whether shear waves are generated in the near-source region and if so, where and how they are generated as well. The second direction with which we study the generation of shear waves is through examination of the Paulsson Geophysical Service Incorporated (PGSI) multi-level instrument array that was deployed directly below explosion sources. Examining amplitudes, arrival times, and polarizations we hope will reveal how, when and where shear waves are generated within 2 km of explosive sources.

RESEARCH ACCOMPLISHED

Methodology for Scattering of High-Frequency Waves

High-frequency seismic waves recorded at the surface are highly scattered. The prolonged nature of the *P* and *S* codas can be explained as the presence of scattered energy (e.g., Aki & Chouet, 1975). In order to study high frequency wave propagation in a heterogeneous crust, we have developed a new method to synthesize high-frequency seismograms using scattering theory in the context of coupled normal modes (e.g., Friederich, 1999). An expedient in applying coupled mode theory is the use of path-dependent reference models, which account to a large extent for the nonlinear dependence of the seismic waveforms with respect to the overall structure (e.g., Meier et al., 1997). This expedient is akin to the Rytov approximation (e.g., Snieder & Lomax, 1996), which accounts for the first-order shift in arrival times of propagating waves arising from a component of structure. The phase shift for a (path-dependent) spherically symmetric perturbation is already known in analytical form in terms of a perturbation to the mode eigenfrequency, and we shall refer to it as the pure-path approximation. The pure-path approximation represents the effect of smooth structure on the full wavefield to first order, and the leading term of our representation of the synthetic wavefield employs this approximation. Application of the Born approximation using the pure-path-approximated full wavefields accounts for scattering from remaining small-scale heterogeneities (as well as smooth heterogeneities which differ from the path average, leading to focusing and defocusing effects).

Figure 1 shows a ‘constant gradient model’ for the SAFOD area that we use as a reference structure, and Figure 2 shows the normal mode dispersion on this model. We illustrate the computational method with an example of scattering from a point heterogeneity. Figure 3 shows the incident and scattered wavefields resulting from an explosive point source placed at 3.5 km depth. The wavefield is shown on various vertical planes that intersect along a vertical line segment which contains the scatterer. The scattered displacement field on the $y = 0$ plane illustrate scattered P→P and P→SV waves that first appear after the incident *P* wave arrives at about 0.57 sec, and that on the $y' = 0$ plane illustrates scattered P→SH waves. The incident wavefields also display reflections of incident *P* off the free surface as well as the artificial boundary at 7 km depth, leading to the propagation of converted *P* and SV

waves. The interaction of these reflected waves with the scatterer just begins to develop at the last plotted snapshot at t = 1.2 sec.

Wave Propagation Through the SAFOD Crustal Volume

An extract of the 3-D Zhang et al. (2009) v_p model projected over a 8 × 8 km^2 map area is shown in Figure 4. We use this and their corresponding v_s model, combined with a density- v_p relationship (Brocher, 2005), to derive a 3-D model of lateral variations in density and elastic parameters. (Figure 1 shows the lateral average of this 3-D model.)

We compare synthetic velocity seismograms with observed seismograms for a small shallow earthquake, Md = 1.2, that occurred in 2002 on the San Andreas Fault in the region of maximum horizontal velocity gradient in the model. Figure 5 shows observed and synthetic seismograms filtered at 4 Hz at 26 PASO sites in order of increasing distance from the source. For the synthetics we use either the Born-scattering wavefield (pure path + scattering terms; continuous green traces) or the leading term (pure path term only; dashed red traces) and implement the source as a point horizontal shear dislocation on a N40◦W vertical plane at 3.7 km depth. The arrival times of the *S* waves are roughly matched by the models, though the initial *S* waveform is difficult to match. Comparing the synthetics with pure path + scattering terms (solid green curves) with those involving only the pure path term (dashed red curves), the main effects of scattering are focusing / defocusing and lateral refraction. For example, from the simulations we can see that the *S* wave has undergone focusing at RCKY (i.e., the data has higher amplitude than the simulation) and defocusing (the data has lower amplitude than the simulation) at HOTF and CRAK. The synthetics do not capture the extended coda waves generally observed for ~1 sec after the *S* arrival. This is to be expected from seismic wave propagation through the relatively smooth Zhang et al. (2009) structure, which primarily modifies the phase and amplitude of the arrivals but does not produce significant coda waves.

It is well known that coda following direct *P* and *S* arrivals at relatively high frequencies (> 1 Hz) are produced by scattering from relatively short wavelength structure (Aki, 1969, 1973), and this scattering process also leads to apparent attenuation of the direct arrivals (Aki & Chouet, 1975; Aki, 1980; Wu, 1982). Several studies have implemented short-wavelength structure in terms of a random media with scale lengths of a fraction of a wavelength of the dominant high-frequency waves (e.g., Frankel & Clayton, 1986). As one example, we implement a simple random medium by adding a random component of shear modulus to the original seismic structure. This structure is converted into corresponding perturbations in v_s and v_p assuming that the v_p / v_s ratio equals its original value in each cell. Synthetics using the velocity model with randomized perturbations (not shown) have coda durations matching those observed, but their amplitudes still do not match observations.

Near-field *S*-wave generation is further illuminated by observations of near-surface explosions recorded by SAFOD downhole arrays. Shots conducted during the November 1-2, 2006 virtual earthquake experiment at several PASO stations were recorded by a three-component seismometer in the SAFOD main hole at 2.654 km depth below the surface. Figure 6 shows an observed velocity seismogram from a ~10 m deep chemical shot at KOOL (solid curve) compared with the Born-scattering wavefield. The transverse component contains a moderate amount of energy that cannot be explained by scattering from the smooth Zhang et al. (2009) structure. On the vertical and cylindrical-radial components, the direct arrival (in both observed and synthetic seismograms) is a combination of direct *P* and pP, and the later arrival is pS reflected off the free surface. These arrivals are a common feature of near-surface explosions generated both with and without surface topography (e.g., Xie et al., 2005; He et al., 2008). Figure 7 confirms that these phases are generated by a near-surface explosion with flat topography, imparting downgoing SV energy into the crust. The character of these free-surface reflections is important because they and other phases (e.g., Rg) generated in the near field contribute to Lg wave propagation (e.g., He et al., 2008). Continued work with our approach and other numerical wave-computation approaches can further quantify the effect of near-source scattering, including surface topography. In addition, the near-surface zone is probably more heterogeneous than the deeper zone, enhancing multiple scattering.

Very Near-Source (<3000m) Generation of *S* Waves

The seismometers in the (PGSI) array have proven to be instructive in constraining where *S* waves are generated by small, contained explosions. The PGSI array contains eighty levels, spaced at 15-meter intervals, each with a 3-component 15 Hz seismometer. This pipe-deployed array uses a flexible bladder to hydraulically clamp the seismometer to the steel casing in the well. During deployment of the array 6 small shots (5 to 10 lbs buried 10 to

15 ft below the surface) were fired from a shot point 40 m from the well-head. This permits wave propagation to be tracked for the entire 2700 meters that the array occupied (Figures 8, 9). The upper ~100 intervals are in a near-vertical section of well, with very small offset from the shot-points. Given this source-receiver geometry, we don't expect to see *S* waves radiated in the downward direction, unless symmetry is broken at the shot-point.

Visual examination of the wavefield shows that the *S* waves present in the wavefield recorded on the downhole string are very weak (Figures 8, 9). First, we note that amplitudes on the radial (near vertical component) are much larger than anything on the horizontal components. Since the array is vertical in its upper half and the shot point is at near zero offset, the vertical ground motion should contain only P waves and any *S* should be on the two horizontal components. At the upper ~40 stations, we identify waves traveling at a velocity close to the computed *S* velocity of 1747 m/s ($1/\sqrt{3}$ times the observed *P* velocities of 3025 m/s) only on the vertical channel (Figure 8a). These *S* waves have a zero-offset intercept of about 0.5s after the origin time. Clearly they cannot be directly radiated by the source and, thus must be converted waves. We cannot clearly identify energy arriving on the horizontal components that has the appropriate moveout for *S* waves radiated by the source. In addition to energy strongly coming in at the computed *P* velocities, we can see clear reflections from the bottom of the well (Figure 8a) and some very late arriving waves with very slow velocities (~350 m/s and ~1500 m/s). These very slow waves appear to be tube waves (White and Lessenger, 1988).

CONCLUSIONS AND RECOMMENDATIONS

Since scattering is a major component of the high-frequency wavefield, it is critical to include it in the generation of high-frequency synthetics. We have explored a new method of synthesizing seismograms based on using coupled normal modes which allows for the simulation of first-order scattering. Using this method at ~4 Hz we generally reproduce the arrival time of the initial *S* arrival, but observed S (and P) arrivals have more complicated waveforms and are typically followed by coda waves. Waveforms and coda duration are difficult to match with a model of wave propagation through a smooth 3D medium. Adding random noise to the velocity model that we use improves the match to the duration of the coda, indicating that much of the *S* waves generated near to explosive sources are generated from scattering. This is further supported from data coming from the PGSI deployment, where there is scant evidence for *S* waves at stations directly below the explosions where there will be less scattered energy. Continuing work will focus on (1) the implementation of other numerical seismic wave propagation algorithms (e.g., finite element), (2) imaging techniques to characterize the sources of scattered energy from PASO array recordings, and (3) source modeling at relatively long period to characterize the amount of non-isotropic energy radiating from the chemical sources.

REFERENCES

Aki, K., (1969). Analysis of seismic coda of local earthquakes as scattered waves, *J. Geophys. Res.* 74: 615–631.

Aki, K., (1973). Scattering of P waves under the Montana LASA, *J. Geophys. Res.* 78: 1334–1346.

Aki, K., (1980). Scattering and attenuation of shear waves in the lithosphere, *J. Geophys. Res.* 85: 6496–6504.

Aki, K. & Chouet, L. B., (1975). Origin of coda waves: Source, attenuation, and scattering effects, *J. Geophys. Res.* 80: 3322–3342.

Friederich, W., (1999). Propagation of seismic shear and surface waves in a laterally heterogeneous mantle by multiple forward scattering, *Geophys. J. Int.* 136: 180–204.

He, Y., Xie, X.-B., and Lay, T., (2008). Explosion-source energy partitioning and Lg-wave excitation: Contributions of free-surface scattering, *Geophys. J. Int.* 98: 778–792.

Meier, T., Lebedev, S., Nolet, G., & Dahlen, F., (1997). Diffraction tomography using multimode surface waves, *J. Geophys. Res.* 102: 8255–8267.

Snieder, R. & Lomax, A., (1996). Wavefield smoothing and the effect of rough velocity perturbations on arrival times and amplitudes, *Geophys. J. Int.* 125: 796–812.

Thurber, C., S. Roecker, H. Zhang, S. Baher, and W. Ellsworth (2004). Fine-scale structure of the San Andreas fault zone and location of the SAFOD target earthquakes, *Geophys. Res. Lett.*, L12S02, doi:10.1029/2003GL019398.

Thurber, C. H., Zhang, H.,Waldhauser, F., Hardebeck, J., Michael, A., & Eberhart-Phillips, D., (2006). Three-dimensional Compressional Wavespeed Model, Earthquake Relocations, and Focal Mechanisms for the Parkfield, California, Region, *Bull. Seismol. Soc. Am.* 96: S38-S49S49, doi: 10.1785/0120050825.

White, J.E. and Lessenger, M.A., (1988), Caliper effect on borehole coupling, *Exploration Geophys.* 19: 201–205.

Wu, R.-S., (1982). Attenuation of short-period seismic waves due to scattering, *Geophys. Res. Lett.* 9: 9–12.

Xie, X.-B., Ge, Z., and Lay, T., (2005). Investigating explosion source energy partitioning and Lg-wave excitation using a finite-difference plus slowness analysis method, *Bull. Seismol. Soc. Am.* 95: 2412–2427.

Zhang, H., Thurber, C., & Bedrosian, P., (2009). Joint inversion for Vp, Vs, and Vp/Vs at SAFOD, Parkfield, California, *Geochem. Geophys. Geosyst.*, 10, Q11002, doi:10.1029/2009GC002709.

Zoback, M., S. Hickman, W. Ellsworth, (2010), Scientific Drilling into the San Andreas Fault Zone (2010), *Eos, Trans. Am. Geophys. Un.*, 91: 197, doi:10.1029/2010EO220001.

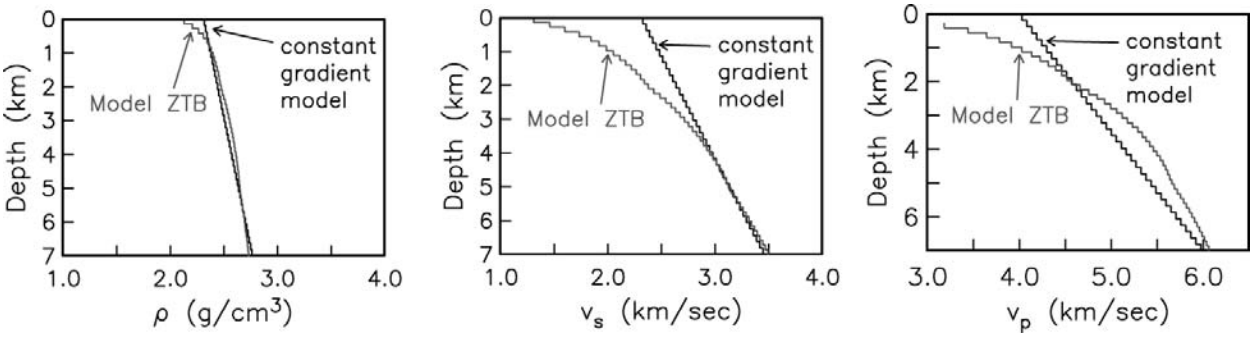

Figure 1. Density and seismic velocities as a function of depth on a synthetic reference model with a constant velocity gradient and the laterally averaged velocities on the Zhang et al. (2009) 3D model of the SAFOD area.

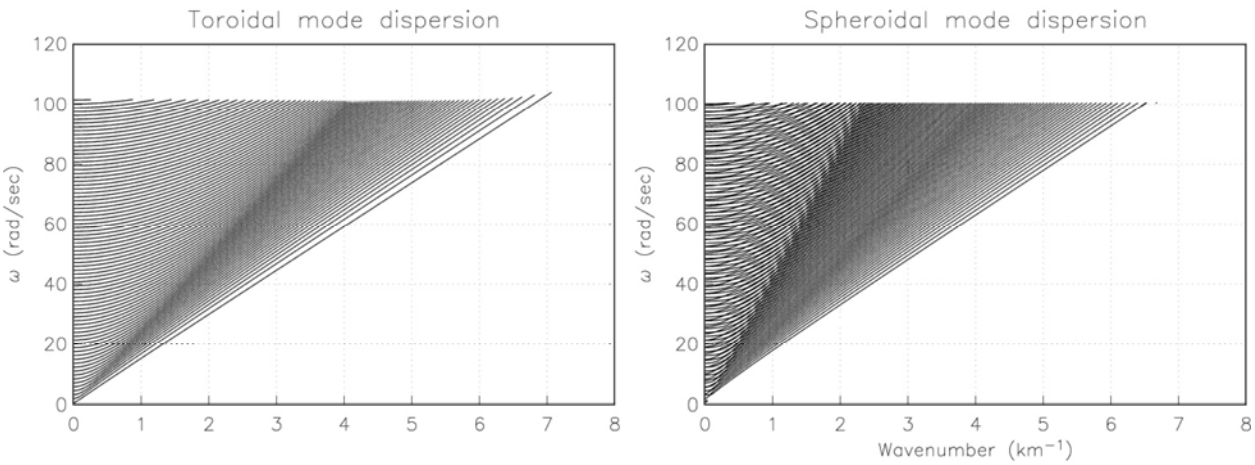

Figure 2. Eigenfrequencies of spheroidal and toroidal modes as a function of wavenumber on the synthetic model shown in Figure F1.

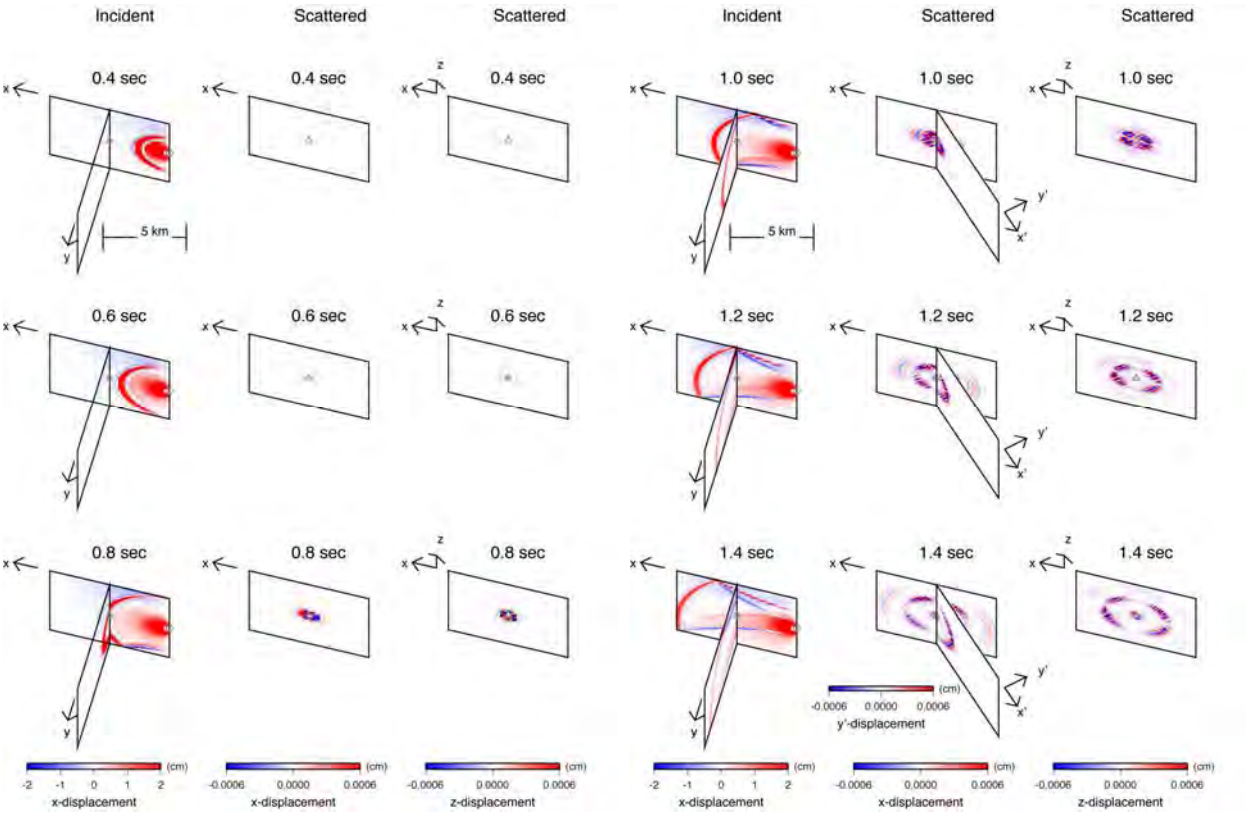

Figure 3. Incident and scattered displacement fields on various vertical sections resulting from an explosive source at depth 3.5 km (gray circle). The incident displacement field interacts with a point scatterer at depth 3.5 km (gray triangle) 4 km from the source. For the incident wavefield, the x− horizontal displacement field is shown on the x = 0 and y = 0 planes. For the scattered wavefield, the x− and z−components are shown on the y = 0 plane, and the transverse component scattered displacement field is shown on the y' = 0 plane, which makes a 45° angle with each of the other planes. The three planes intersect at a vertical line segment which passes through the scatterer.

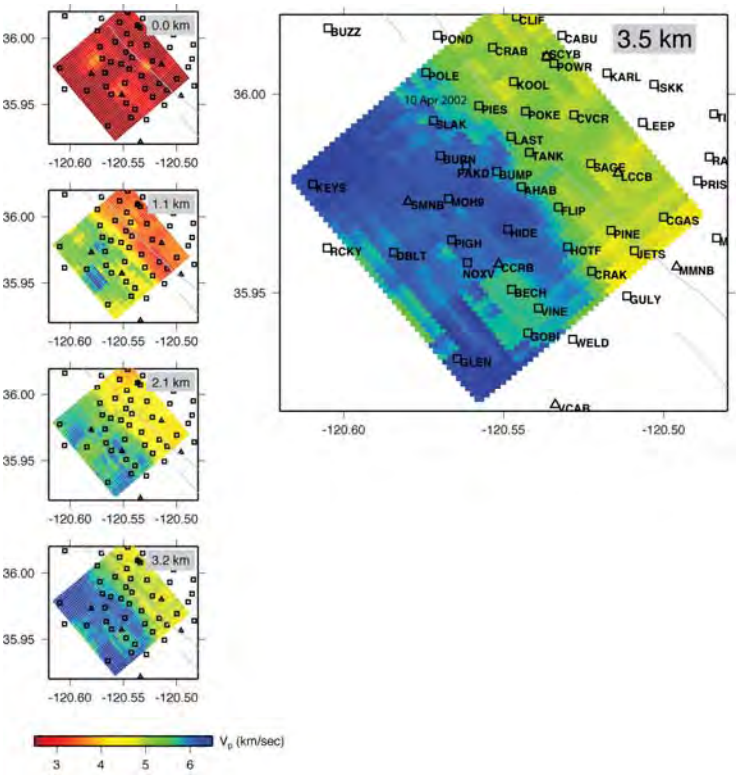

Figure 4. Subset of V_p structure in the SAFOD area (Zhang et al., 2009) on a 3D volume of dimensions 8 × 8 km2 (in map view) ×4.0 km in depth. Squares and triangles denote PASO and HRSN stations, respectively. Location of the M=1.5 10 April 2002 earthquake (depth = 3.5 km) is indicated with text.

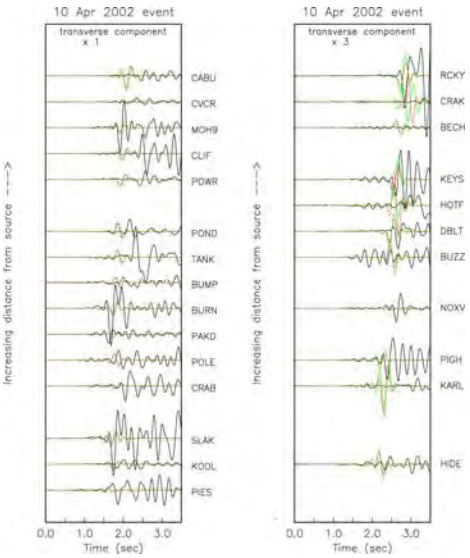

Figure 5. Transverse-component velocity seismograms at PASO stations for the April 10, 2002 event at 3.7 km depth (Thurber et al., 2003) (in black) compared with synthetic velocity seismograms. The synthetics in continuous green are calculated using the 3D Zhang et al. (2009) tomographic model and filtered at 4 Hz. The synthetics in dashed red are calculated using the pure path term only. The observed seismograms are band-pass filtered between 0.2 and 4 Hz. The right column shows more distant stations than the left column – the synthetics in the right column have been multiplied by 3 to help match the recordings.

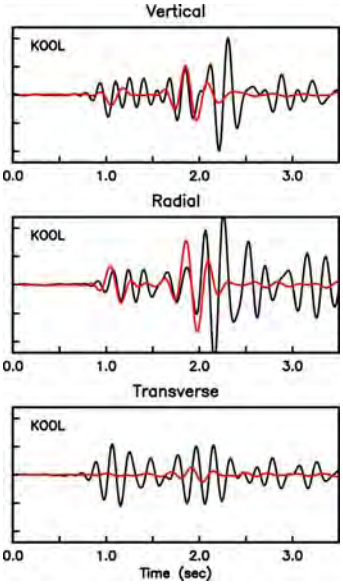

Figure 6. Observed (black) and synthetic (red) seismograms for a surface chemical explosion at KOOL recorded in the SAFOD main hole at depth 2.654 km below the surface.

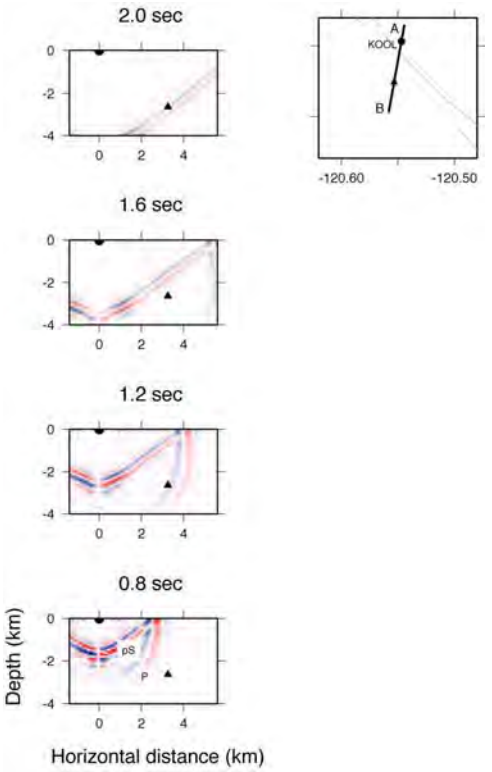

Figure 7. Cylindrical-radial component of synthetic wavefield generated by explosion at 0.01 km depth (indicated by black circle) at the location of PASO site KOOL, indicated by "A". The synthetics are generated with pure path term only in the Zhang et al. (2009) model. The location of the main-hole seismometer is indicated by the black triangle "B". Grey lines indicate faults.

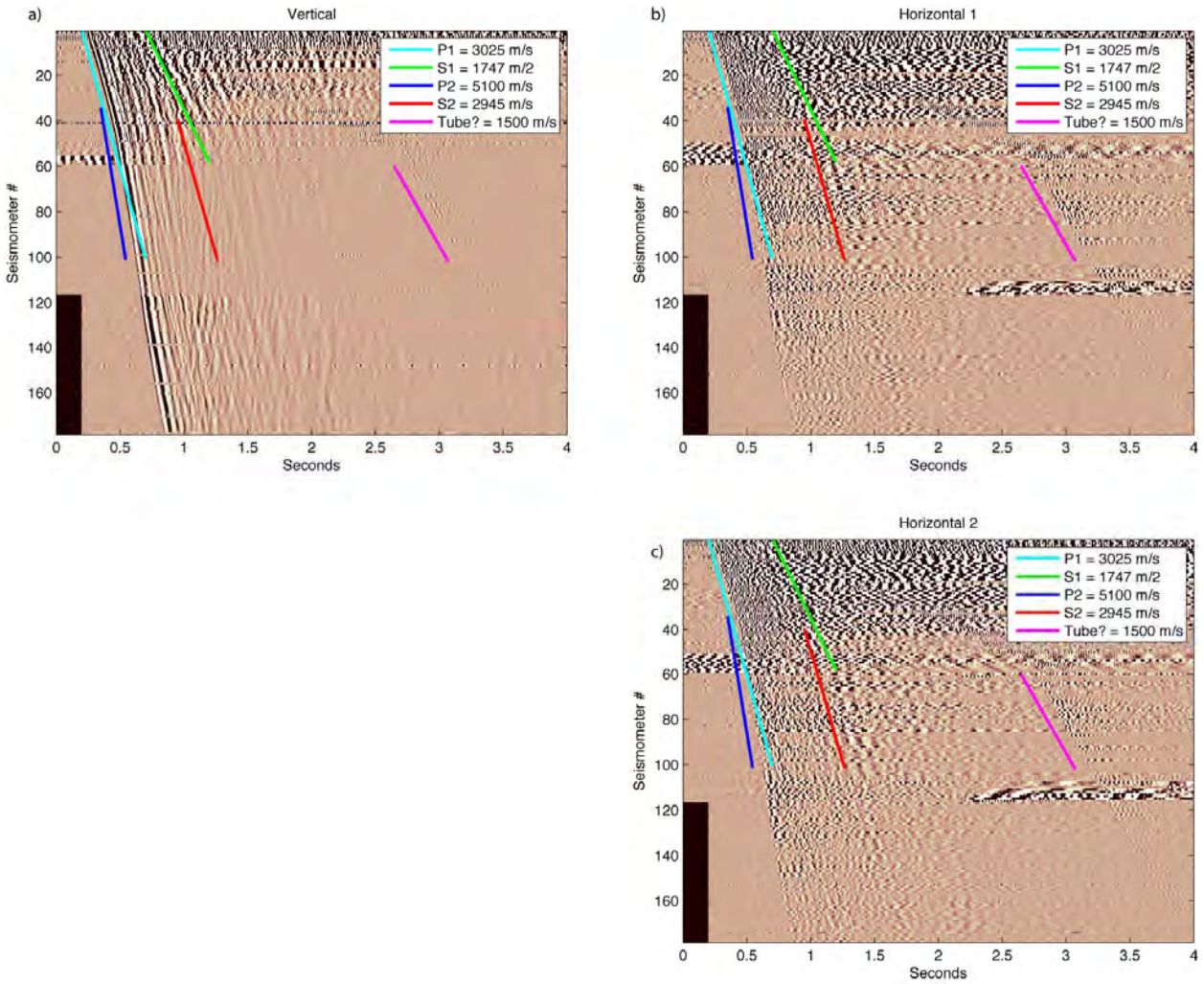

Figure 8: Seismic gathers for the PGSI array spanning the length of the well. Three different shots have been merged so that these records span the well. Amplitudes are all normalized to the same value. The well is near vertical for stations 1-100, where it makes an abrupt turn, thus we cannot interpret across this boundary. Station spacing is 15m, so depth of the sensors can be easily computed. The initial *P* arrival can be clearly identified on the vertical component, and the velocity of this is indicated with cyan and blue lines with the appropriate slope – these are placed before the arrival so that they can be seen. An assumed *S* velocity is also shown for the two observed *P* velocities and is indicated with green and red lines. Arrivals with the upper *S* velocity can be seen on the vertical component, but they arrive more than 0.5 seconds after the *P* arrival. What appears to be a tube wave is also seen much later, as indicated by the magenta line, this can be seen on all components.

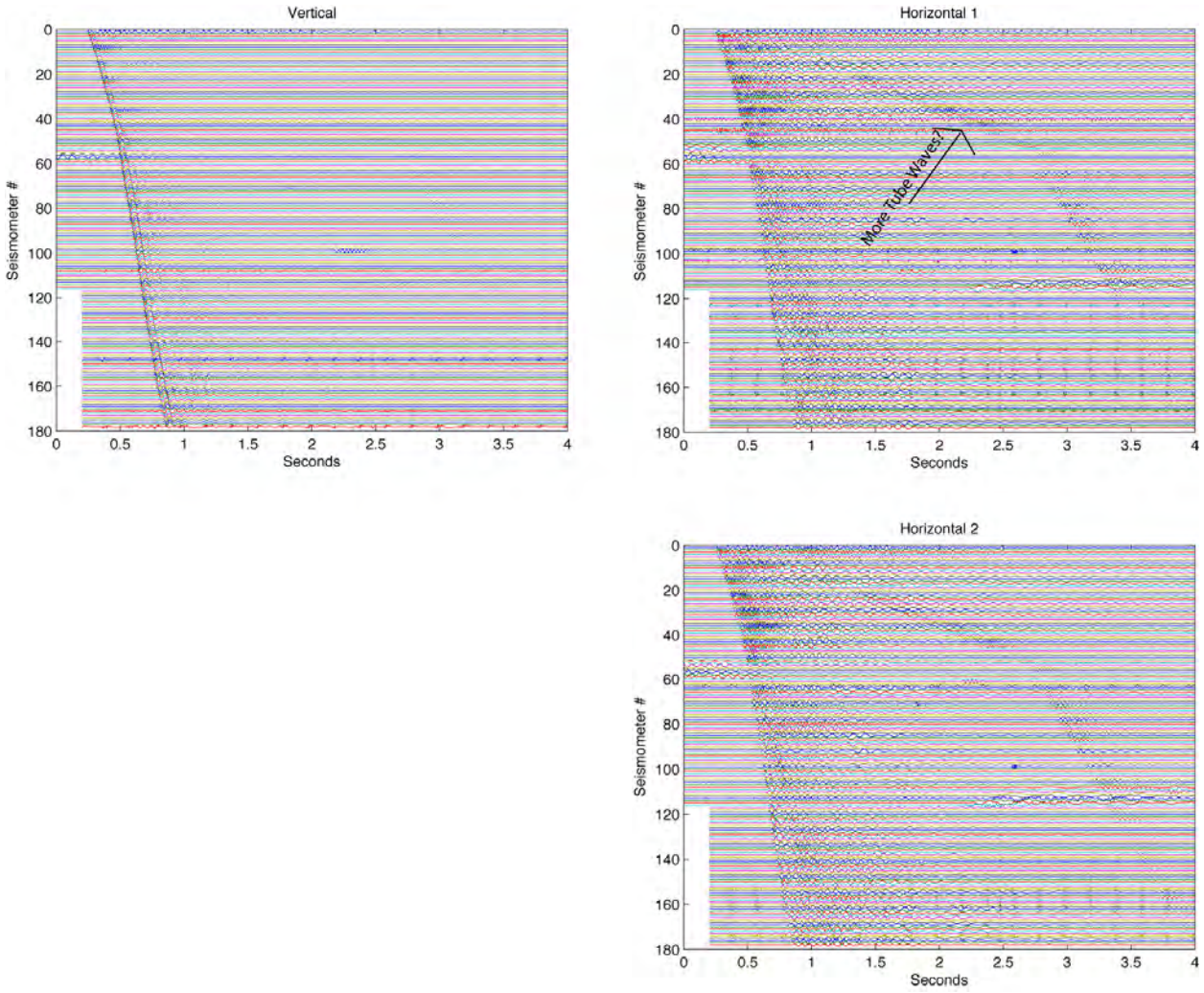

Figure 9: Seismic gather for the PGSI array spanning the length of the well. Amplitudes for each trace are normalized, relative amplitudes from trace to trace are not meaningful. The *P* arrival is very simple and is much larger than anything else on the vertical trace (and even larger than anything on the horizontal components, but due to scaling this cannot be seen here). In addition to the arrivals visible in Figure 8, there is an incredibly slow arriving phase (~350 m/s) that appears to connect to what we believe to be a tube wave at lower depths, this is indicated on the first horizontal component.

ESTIMATING THE UNCERTAINTY AND PREDICTIVE CAPABILITIES OF THREE-DIMENSIONAL EARTH MODELS

Delaine T. Reiter[1], William L. Rodi[2], and Stephen C. Myers[3]

Weston Geophysical Corp.[1], Massachusetts Institute of Technology[2], and Lawrence Livermore National Laboratory[3]

Sponsored by the Air Force Research Laboratory and the National Nuclear Security Administration

Award Nos. FA8718-09-C-0013[1,2] and DE-AC52-07NA27344LL09[3]
Proposal No. BAA09-73

ABSTRACT

In recent years many models of 3-D seismic velocity structure in Eurasia have been developed, using a variety of techniques and data. Most of these models are not accompanied by quantitative estimates of uncertainty, either in the model parameters themselves (e.g., seismic velocities) or in geophysical observables predicted by the models (e.g., body-wave travel times). Moreover, the various 3-D models produced by these studies have not been compared to one another in their predictive capabilities in any meaningful way within the monitoring research community. To address these issues we are developing and applying evaluation metrics that robustly quantify and compare the uncertainty and predictive capabilities of 3-D seismic velocity models.

There are two major elements in our approach. First, we are performing a comprehensive evaluation of a set of velocity models for Eurasia based on previously developed data misfit and event mislocation metrics. We are using a ground-truth (GT) data set available at the International Seismic Centre (ISC). We discuss some of the difficulties involved in reconciling discrepancies between the parameterization and coverage of various models available to the research community, and compare some of the standard metrics we have been able to derive for these models.

Second, we are investigating a new approach to evaluating velocity models based on a Bayesian framework for model uncertainty in the travel-time tomography problem. Bayesian analysis provides a regimen for deriving posterior model uncertainty that combines prior model uncertainty with the information from travel-time data. Our new approach focuses on the prior model uncertainty. Following concepts used in the kriging method, we are representing prior model uncertainty with geostatistical parameters that characterize the Earth's 3-D velocity heterogeneity relative to a given reference model. These parameters include the velocity variance, which quantifies the strength of velocity heterogeneity, and vertical and horizontal correlation lengths, which quantify the spatial smoothness of velocity heterogeneity. We assume these parameters vary with position in the Earth. Our approach is to estimate the geostatistical parameters from observed travel-time residuals, relative to a reference model of interest, by fitting the parameters to the second-order sample statistics of the residuals. Our premise is that the estimated parameters will be a rigorous metric for evaluating the reference model, at least in comparison to competing reference models. Further, the estimated geostatistical parameters describing velocity uncertainty can be mapped to prediction errors on travel times and other observables, providing further model evaluation metrics. Our preliminary efforts in developing this approach consist of fitting velocity variances and correlation lengths to AK135 residual statistics derived from events in Eurasia and Africa.

OBJECTIVES

The main objective of our research project is to develop and apply meaningful measures of the predictive capabilities of 3D Earth models. We will specifically focus on seismic velocity models, although our general approach should be applicable to models of other geophysical parameters such as attenuation and density.

Our project consists of two major elements. First, we are collecting a set of regional 3D velocity models for Asia and are performing a comprehensive and methodical evaluation of them using data misfit and event mislocation metrics. These metrics are already generally accepted as informative, if not complete, measures of the prediction capability of Earth models. Metrics will be evaluated for each model based on a common ground-truth data set comprising GT5 events and their arrival picks. A large part of this effort will be to establish rigorous validation tests, employing standardized methods for model parameterization, forward modeling (e.g., ray tracing), and event relocation. The tools we need for these tests are available to us in-house from our previous tomography and location projects.

The second element of our project is the investigation of a new approach for estimating the predictive capability of 3D velocity models. Our approach will convert the uncertainty in the parameters of a 3D velocity model, as a function of position in the Earth, into the uncertainty in travel-time or other geophysical predictions. To do this requires covariance modeling capabilities we have developed for travel times in an earlier project (Rodi and Myers, 2008) and which can be extended to other observables given appropriate model sensitivities.

RESEARCH ACCOMPLISHED

Three-Dimensional Velocity Models of the Crust and Upper Mantle

One of our first tasks has been to collect 3D regionalized velocity models from their authors and format them in a way that makes comparisons straightforward. Our test-bed model for the project is JWM, the *J*oint *W*eston/*M*IT inversion model (Reiter and Rodi, 2009). JWM is result of a joint inversion of regional P travel times and Rayleigh fundamental-mode group velocities. It consists of the P and S velocities and density of the crust and upper mantle for a broad region of Asia (defined in a geographic box from 0 – 60°N, 30 – 120°E). In addition to the JWM model, we have obtained the CUB2.0 surface-wave inversion model (Ritzwoller et al., 2002) with density; the Stevens et al. (2008) surface-wave inversion model, and a new joint inversion model (LLNL G3D) from Nathan Simmons and Stephen Myers at LLNL. We also have access to several *a priori* regionalized models, such as the Unified Model from LLNL (Begnaud et al., 2004; Pasyanos et al., 2004). We continue to seek models from other researchers, but many are not available for our use at this time.

In Figure 1 we display map-view slices from four of the models in our study. The Generic Mapping Tool (GMT) package (Wessel and Smith, 1995) was used to plot the P and S velocities at a depth of 120 km, using the same color map for each model. Prior to creating this plot, the models were reformatted to a common geographic representation and then interpolated to a depth-slice grid. The different panels in Figure 1 offer a direct comparison of the models and illustrate their similarities and differences. For example, JWM and CUB2.0 are similar to each other in the strength of heterogeneity at this upper-mantle depth, particularly in the southwestern corner of the model. CUB2.0 is defined on a 2°x2° grid, which produces a smoother result compared to the other models. The LLNL G3D inversion model appears to have similar patterns of heterogeneity as the CUB2.0 and JWM models, but its heterogeneity strength is significantly smaller. The *a priori* LLNL Unified model is least like the others in pattern and heterogeneity strength – we note that this model is equivalent to the 3SMAC model (Nataf and Ricard, 1996) at this depth. We do not show the Stevens et al. (2008) model here, since we have not yet converted it to our in-house format.

While the models may be quite different in snapshot form, they can often perform like each other in travel-time prediction and location tests, as we will see in a later section. We are investigating the behavior of the 3D models using different forward modeling techniques, in an attempt to determine how and why they differ.

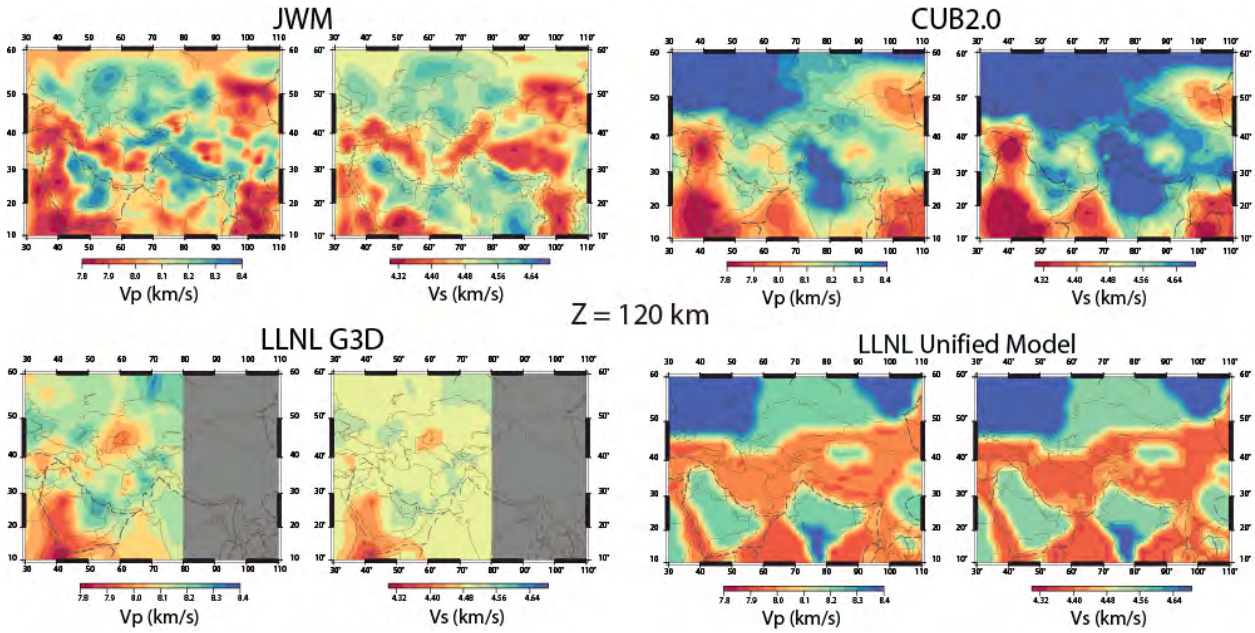

Figure 1. Map-view slices of P and S velocity from four of the regional 3-D velocity models in our study. The depth slices from each model are taken at Z=120 km depth, and the color scale is the same in each panel. The LLNL G3D model extends only to 80°E, and we plotted it to that longitude, leaving the remainder of the box empty.

Validation Data: Ground-Truth Explosions and Earthquakes

To evaluate models with respect to one another, we require a high-quality set of GT events whose epicentral locations are known precisely. We used the new catalog of GT0-5 reference events (Bondàr and McLaughlin, 2009) hosted by the ISC (http://www.isc.ac.uk). This global database includes more than 7,000 events whose epicentral location accuracy is known to at least 5 km. GT events with well-established locations and origin times have been used by multiple authors to validate velocity models (Ritzwoller et al., 2003; Flanagan et al., 2007). We filtered the new IASPEI Reference Event List (REL) for events in our study region and found 248 GT(0–5) explosions and 348 GT5 earthquakes, most of which are in specific geographic clusters. From these events we extracted the defining regional P and S arrival-time picks in the IASPEI REL that were used to develop the GT locations.

Even though the IASPEI REL bulletin represents a significant improvement over previous GT databases, we found that additional grooming was required to eliminate inconsistent arrivals. For example, we eliminated observations with clearly misidentified phase arrivals in crossover distances between various travel-time branches. In addition, we filtered out arrivals from distances less than 0.5°, since they do not sample a significant portion of our models. Following these simple filtering exercises, we examined the earthquake and explosion event clusters in the data and found repeated station-to-event phase readings that occurred over time. Most of these revealed consistent travel-time readings, especially for the first arriving P phases. However, at some distances and for some paths there were inconsistencies that made the readings unreliable. We illustrate this in Figure 2, where we plotted two examples of station-to-event paths that occur multiple times in the REL database: the Degelen nuclear explosion cluster with paths to station PSH in central Pakistan, and the Chinese Lop Nor test site explosions to station ZAK in Russia. For the Degelen example there are 27 P phase picks in the REL bulletin, with a mean epicentral distance between station and event of 16.4°. In the AK135 model the travel time for this path averages 232 s (using the exact GT hypocenters) with a standard deviation of .44 s. The mean of the observations is 231 s, but the standard deviation is 3.0 s. The same phenomenon is seen with the other example path, albeit with the S arrival and many fewer phase picks (5) in the bulletin. These large values of standard deviations in the travel times make it impossible to compare the validity of different velocity models along the paths, since many models can fit a travel time to within ±3.0 s. To date we have dealt with this problem by eliminating any phase paths in the REL arrival database that have standard deviations greater than 1.5 s for P or 2.0 s for S.

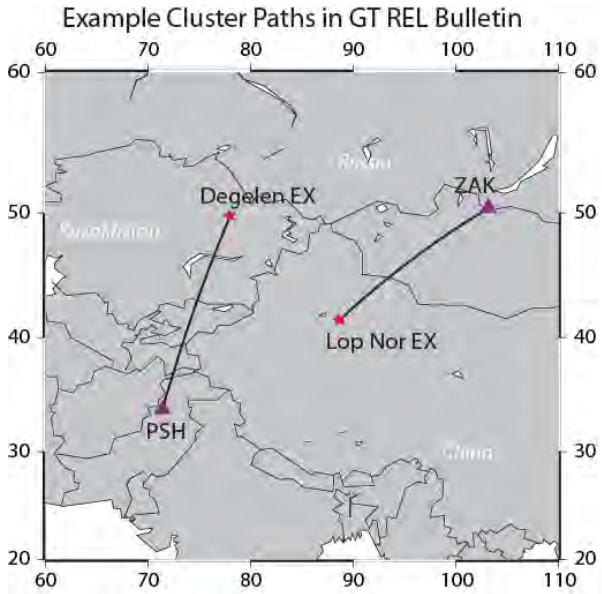

Degelen to PSH
P bulletin picks = 27

	Mean value	Std Dev
Δ	16.38°	0.03°
Esaz	200.0°	0.13°
Bulletin TT	231 s	3.0 s
AK TT Pred	232 s	.44 s
JWM TT Pred	230 s	.44 s

Lop Nor to ZAK
S bulletin picks = 5

	Mean value	Std Dev
Δ	13.4°	0.01°
Esaz	43.9°	0.06°
Bulletin TT	341 s	3.5 s
AK TT Pred	342 s	.40 s
JWM TT Pred	347 s	.40 s

Figure 2. Examples of persistent inconsistencies in the GT reference event database. On the left are two station-event paths that occur multiple times in the database; on the right are the statistics associated with the readings for the two paths. The standard deviations of the observations (Bulletin TT vs. AK TT Pred) indicate either pick errors or phase misidentifications that corrupt the GT phase bulletin.

Using the filtering criteria described above we derived a validation data set of 9,242 P-wave and 2,214 S-wave regional arrivals observed at stations within a latitude-longitude box defined by (0-60° N, 30-120° E). The great-circle raypath coverage for the P and S GT observations is shown in Figure 3. The GT data ray paths sample only a limited portion of the study region, which illustrates the difficulty of validating a model with travel times alone. However, the IASPEI REL database is currently the best available resource we have to demonstrate the performance of the 3D models.

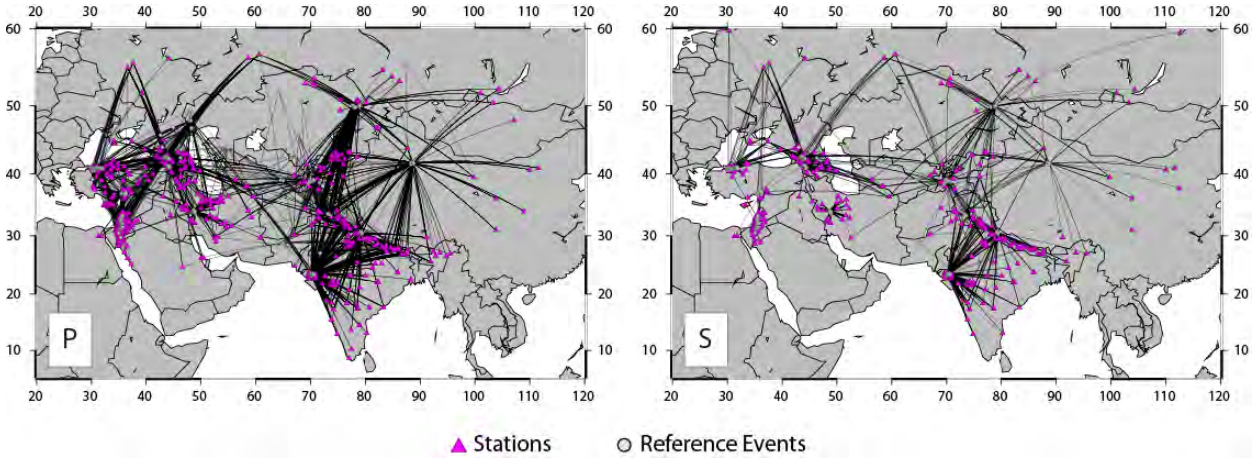

Figure 3. Great-circle raypath coverage for the P (top) and S (bottom) paths in the IASPEI REL ground-truth database. Stations are represented by purple triangles and events by gray circles. Note the sparse coverage over the area of the regional 3D models.

Validation Exercise: Regional Travel-Time Prediction

One of the first assessments we make of the 3D models involves measuring their ability to accurately model the regional travel-time data. As noted by other authors, improved travel-time prediction is the most direct way to estimate the quality of a 3D model, because it eliminates the effects of network geometry and variable pick quality.

One of the more difficult questions we are addressing in our project is how to present the model fits in a coherent and meaningful fashion. There are many ways to examine residuals; for example, on a station-by-station or event cluster basis (e.g. Flanagan et al., 2007), or through spatial patterns as a function of distance and station (e.g., Murphy et al., 2005), or by the fits to empirical phase path anomalies (e.g., Ritzwoller et al., 2003). Figure 4 represents one way to present travel-time fits to the regional P data in the GT database relative to a model. For this figure we binned the data as a function of event-to-station distance and the absolute value of the residual. By defining a visually distinct color scale and the bin sizes (here set to 0.25° in distance and 0.5 seconds in residual size), we can examine a distance-based measure of the fit; however, we remove any sense of the spatial/geographic variation or dependence of the model fits. Nevertheless, we can make some general observations about the models from these plots. The P residuals with respect to the AK135 model (Figure 4a) show a distinct pattern that is due to the tectonics of the study region. As noted in Ritzwoller et al. (2003), the increase in spread at the longer regional distances is likely due to some ray paths bottoming well below the bottom of the crust and encountering low velocity zones. The residuals plotted in Figure 4b-e show that all of the 3D models fit the GT observations better than AK135, particularly at the shorter distances (<8°). There are some differences between the 3D models at the longer distances, but this type of plot tends to mask much of the variation that is due to paths that cross differing tectonic regimes. It is remarkable that while Figure 1 implies the significant differences in the models, the travel-time predictions and subsequent residuals do not show the same variability when they are presented in this manner.

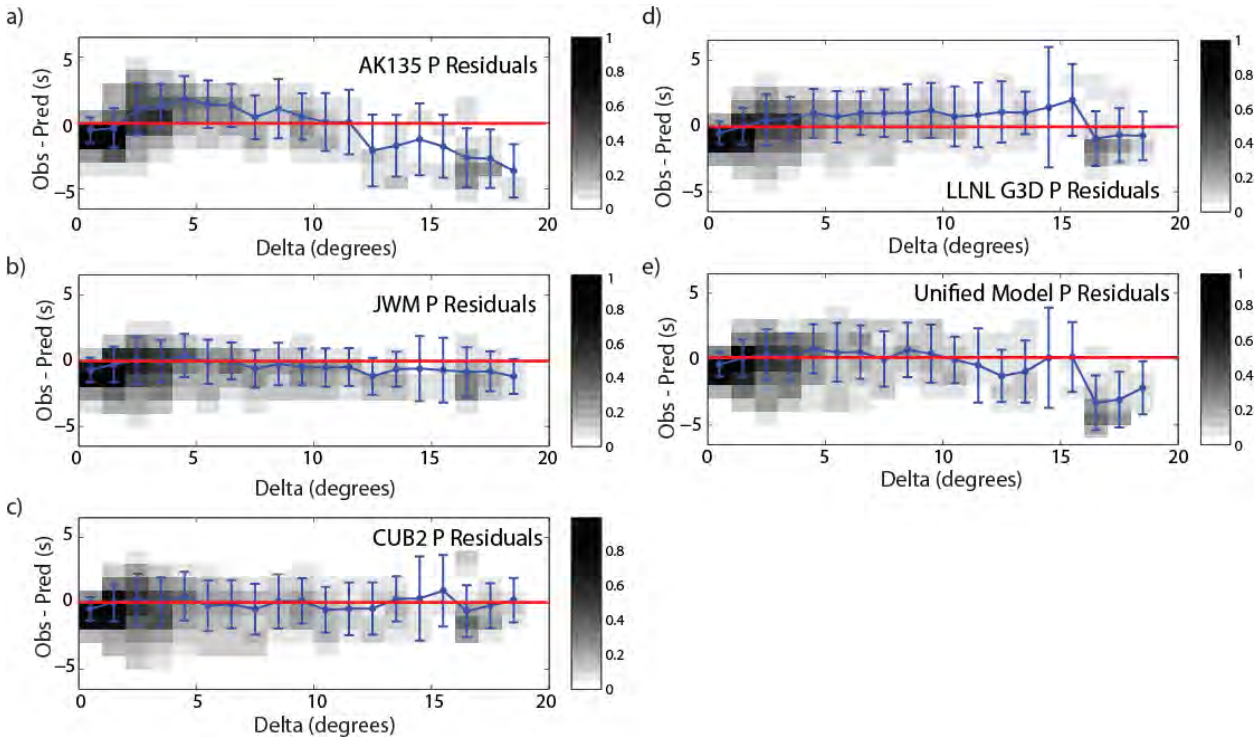

Figure 4. Ground-truth residuals for the P arrivals in our GT database, binned according to station-to-event distance and residual (intervals of 0.25° in distance and 0.5 seconds in residual size). The bin hit counts are plotted with the nonlinear color scale at the side of each subplot; the blue error bars indicate the mean and one standard deviation of the residuals at 1° intervals. Residuals with respect to five models are shown: a) AK135; b) JWM; c) CUB2.0; d) LLNL G3D; and e) Unified Model.

Evaluation of Velocity Models Based on Model Uncertainty Analysis

For the second task in our project we are investigating a new approach to evaluating velocity models based on the analysis of model uncertainty. The approach is formulated within a Bayesian framework as it applies to the travel-time tomography inverse problem. Bayesian analysis provides a regimen for deriving posterior model uncertainty that combines prior model uncertainty with the information from travel-time data. Our new approach focuses on the prior model uncertainty. Following concepts used in the kriging method, we are linking prior model uncertainty to geostatistical parameters that describe the difference between the Earth's true velocity distribution and that of a given reference model. These parameters include the velocity variance, which quantifies the strength of velocity heterogeneity, and vertical and horizontal correlation lengths, which quantify the spatial smoothness of velocity heterogeneity. We assume these parameters vary with position in the Earth.

Our approach is to estimate the geostatistical parameters from observed travel-time residuals relative to a reference model of interest. This entails fitting the parameters to the second-order statistics of the residuals, such as sample variances, covariances, variograms, etc. Our premise is that the estimated parameters will be a rigorous metric for evaluating the reference model, at least in comparison to competing reference models. The estimated geostatistical parameters would also provide a meaningful prior uncertainty for use in a tomographic inversion of the data, although this is not the primary purpose of the approach. A forward model for the estimation problem is available in the results of a previous project which developed theoretical techniques for calculating travel-time variances and covariances given assumed geostatistical parameters for velocity (see Rodi and Myers, 2008).

Our initial efforts with this approach have focused on fitting velocity variance profiles to an empirical estimate of travel-time variance vs. epicentral distance, derived from a statistical analysis of travel-time residuals relative to the AK135 reference model. Using the method of Rodi and Myers (2008), we computed theoretical travel-time variance curves for the six velocity variance profiles listed in Table 1. In conjunction with each profile, the following velocity correlation lengths were assumed: a lateral correlation length of 300 km everywhere, and a vertical correlation length of 17.5 km in the crust and 60 km in the mantle.

For instance, we can use this approach to examine the dependence of travel-time variance on distance. To illustrate this concept, we consider a linear array of 70 stations equally spaced from 0.5° to 35° in epicentral distance from a nominal event, at a common azimuth from the event. The resulting 70x70 travel-time covariance matrix reveals the dependence of travel-time variance on distance and of travel-time correlation on distance and distance separation between stations. We computed the travel-time covariances using the AK135 reference model (Kennett et al., 1995) and fixed correlation lengths (300 km horizontal, 17.5 and 60 km vertical). We then modeled six cases of slowness standard deviations in the crust and mantle, using the parameters shown in Table 1.

Table 1. Assumed velocity standard deviation for modeling travel-time variances.

	Case A	Case B	Case C	Case D	Case E	Case F
Crust	3%	3%	6%	12%	12%	12%
Moho - 210 km	1.5%	2%	2%	2%	2%	1.5%
210 km - 410 km	1.5%	2%	2%	2%	1%	1.5%
> 410 km	1.5%	1%	1%	1%	0%	0%

Figure 5 shows the calculated travel-time standard deviation for the six cases as blue circles. Each panel shows the travel-time standard deviations (blue circles), which are the square-roots of the diagonal elements of the 70x70 covariance matrix. Discontinuities in standard deviation are evident at certain distances. These are directly related to discontinuities in the ray parameter of first arriving P waves, as predicted by the AK135 model. The red line in each panel of Figure 5 is an empirical relation inferred from travel-time residual statistics derived from the LLNL ground-truth database (Ruppert et al., 2005). First-arriving P-waves were used for events meeting the GT criteria of Bondàr et al. (2004) or whose location was constrained by non-seismic means (e.g., known explosions, mine collapses, earthquakes with InSar signals). We used a methodology similar to Flanagan et al. (2007) to assess travel-time model error. We began by selecting only stations with sufficient data for distance-dependent variance estimation (at least 10 arrivals in each 1° event-station bin). For each station, we assessed pick (random) error by computing the standard deviation of residuals for clusters of events within 20 km of one another. The random error for many event clusters was used to determine pick error as a function of station-event distance. We subtracted

distant-dependent pick error variance from travel-time residual variance to estimate distance-dependent model-error variance. The final curve was obtained as an average of the model-error curve for stations throughout Eurasia and Africa.

Comparing the six panels in Figure 5, it is clear that the theoretical calculations (blue circles) for Case E give the best overall fit to the empirical curve over the regional and teleseismic distance range. Large velocity heterogeneity in the crust (12%) is needed to predict the large travel-time model-error variance observed at short distances. To match the peak variance at 15° requires 2% heterogeneity at the top of the mantle (1.5% is too small: Case F). Given the high crustal heterogeneity, the relatively small variance at teleseismic distances is best fit by the velocity standard deviation below 210 km depth and setting it to zero below the 410-km discontinuity. In other words, the observations suggest that velocity heterogeneity in the Earth is highly concentrated at shallow depths.

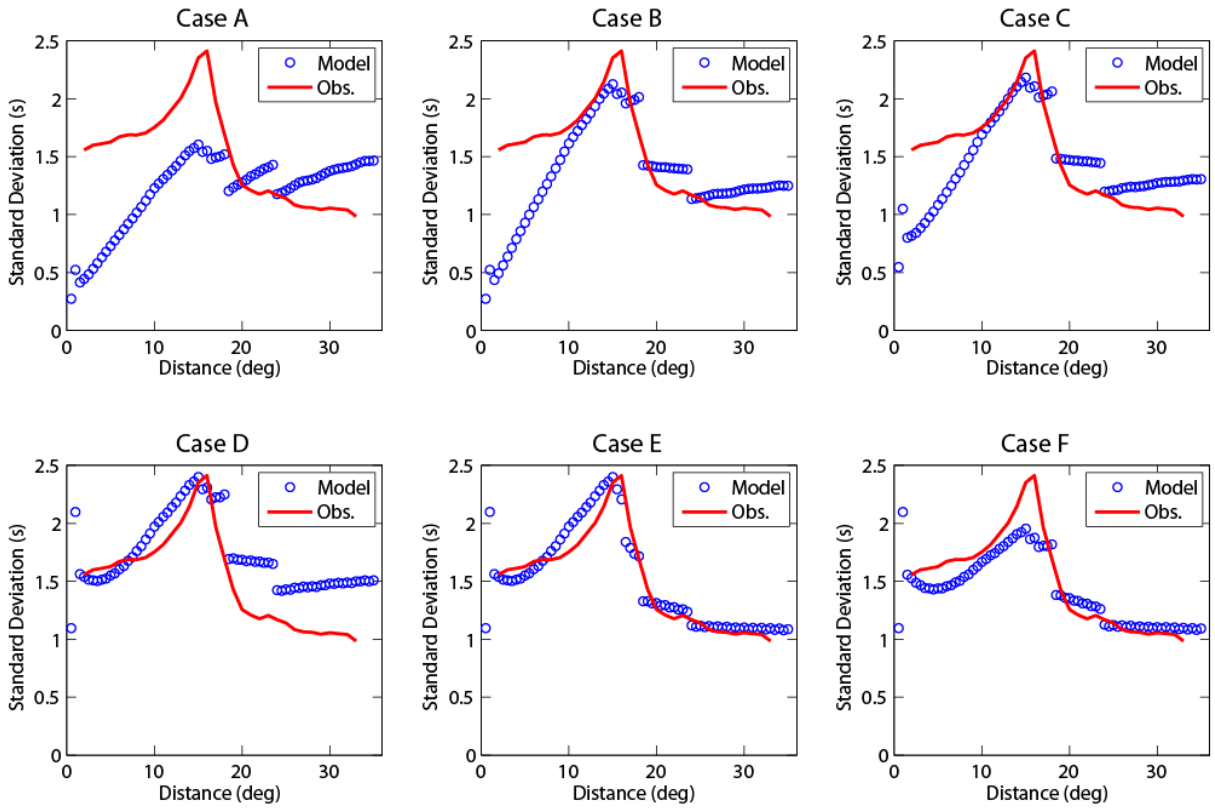

Figure 5. Standard deviation of travel-time model error versus epicentral distance for six cases of geostatistical parameters. The cases differ in the velocity standard deviations assigned to the crust and mantle, as enumerated in Table 1. The horizontal correlation length was set to 300 km; the vertical correlation length was 17.5 and 60 km in the crust and mantle, respectively.

CONCLUSIONS AND RECOMMENDATIONS

The main objective of our research project is to develop and apply meaningful measures of the predictive capabilities of 3-D Earth models. As part of this work, we are performing a comprehensive and methodical evaluation of a set of regional velocity models for Asia based on data misfit and event mislocation metrics. These metrics are already generally accepted as informative, if not complete, measures of the prediction capability of Earth models. We are currently working with five 3D regional velocity models of the crust and mantle and will develop our techniques so that they are easily applicable to others that become available.

In another task we are developing a new method to evaluate models based on the analysis of their uncertainty. We are currently formulating this estimation problem in a more formal way and reviewing statistical methodologies for variance estimation that may apply to the problem. To date, we have formulated theoretical solutions in terms of

maximum-likelihood and Bayesian variance estimation but have not identified many practical numerical techniques for computing such solutions. The crux of the difficulty is that travel-time residuals mapped from velocity heterogeneity (via raypath integration) have non-stationary statistics.

REFERENCES

Begnaud, M. L., C. A. Rowe and L. K. Steck (2004). Validating three-dimensional velocity models in China and East-Asia for use in regional seismic event location, *EOS Trans. AGU*, Fall Meet. Suppl.

Bondár, I., and K. L. McLaughlin (2009). A new ground truth data set for seismic studies, *Seismol. Res. Lett.* 80: 465–472.

Bondár, I., S. C. Myers, E. R. Engdahl, and E. A. Bergman (2004). Epicentre accuracy based on seismic network criteria *Geophys. J. Int.* 156: 483–496.

Flanagan, M. P., S. C. Myers, and K. D. Koper (2007). Regional travel-time uncertainty and seismic location improvement using a three-dimensional a priori velocity model, *Bull. Seismol. Soc. Am*. 97: 804–825.

Murphy, J. R., W. Rodi, M. Johnson, D. D. Sultanov, T. J. Bennett, M. N. Toksöz, et al. (2005). Calibration of International Monitoring System (IMS) stations in Central and Eastern Asia for improved seismic event location, *Bull. Seismol. Soc. Am*. 95: 1535–1560.

Nataf, H.-C., and Y. Ricard (1996). 3SMAC: an a priori tomographic model of the upper mantle based on geophysical modeling, *Phys. Earth and Planet. Int.* 95: 101–122.

Pasyanos, M. E., W. R. Walter, M. P. Flanagan, P. Goldstein, and J. Bhattacharyya (2004). Building and testing an a priori geophysical model for Western Eurasia and North Africa, *Pure Appl. Geophys*. 161: 234–281.

Ritzwoller, M. H., N. M. Shapiro, M. P. Barmin and A. L. Levshin (2002). Global surface wave diffraction tomography, *J. Geophys. Res*., 107**,** doi: 10.1029/2002JB001777.

Ritzwoller, M. H., N. M. Shapiro, A. L. Levshin, E. A. Bergman, and E. R. Engdahl (2003). Ability of a global three-dimensional model to locate regional events, *J. Geophys. Res*. 108: 2353, doi:10.1029/2002JB002167.

Rodi, W. L., and S. C. Myers (2008). Modeling travel-time correlations based on sensitivity kernels and correlated velocity anomalies, in *Proceedings of the 30th Monitoring Research Review: Ground-Based Nuclear Explosion Monitoring Technologies*, LA-UR-08-05261,Vol. 1, pp. 475–484.

Reiter, D. T., and W. L. Rodi (2009). Validated 3D velocity models in Asia from joint regional body- and surface-wave tomography, *Final Report*, Contract FA8718-04-C-0027, AFRL-RV-HA-TR-2009-1009.

Ruppert, S. D., D. A. Dodge, A. B. Elliott, M. D. Ganzberger, T. F. Hauk, and E. M. Matzel (2005). Enhancing seismic calibration research through software automation and scientific information management, in *Proceedings of the 27th Seismic Research Review: Ground-based Nuclear Explosion Monitoring Technologies*, LA-UR-05-6407, Vol. 2, pp. 937–945.

Stevens, J. L., H. Xu, J. W. Given, and G. E. Baker (2008). Development of surface wave dispersion and attenuation maps and improved methods for measuring surface waves, *Final Report*, Contract FA8718-05-C-0023, AFRL-RV-HA-TR-2008-1106.

Wessel, P., and W. H. F. Smith (1995). New Version of the Generic Mapping Tools Released, *EOS Trans. AGU*, 76: 329.

PROGRESS IN THREE-DIMENSIONAL SIMULATIONS OF EXPLOSIONS AND EARTHQUAKES

Arthur J. Rodgers, Oleg Vorobiev, N. Anders Petersson, Bjorn A. Sjogreen, and William Foxall

Lawrence Livermore National Laboratory

Sponsored by the National Nuclear Security Administration

Award No. DE-AC52-07NA27344/LL09-Simulation-NDD02

ABSTRACT

We report results of simulations of explosion- and earthquake-generated wave propagation in three-dimensional (3D) earth models. Computer codes at Lawrence Livermore National Laboratory (LLNL) model the nonlinear (hydrodynamic) and linear (anelastic) response of the earth to arbitrary forcing with material properties varying in 3D. In order to simulate the ranges and frequencies of interest to nuclear explosion monitoring, we run simulations on massively parallel computers at LLNL, often on hundreds or thousands of CPUs. Simulations broadly cover three thrust areas: (1) nonlinear shock-wave (hydrodynamic) modeling of explosions; (2) near-field elastic modeling of explosions, including free-surface topography; and (3) regional-scale modeling of earthquakes and explosions. Hydrodynamic simulations are performed with GEODYN, an Eulerian finite volume code for modeling shock-waves in earth materials. Local and near-regional scale elastic simulations are performed with WPP, a Cartesian finite difference code for seismic wave modeling. Regional simulations are performed with SPECFEM_3D_GLOBE, a code based upon the spectral element method in spherical geometry. These capabilities are joined for modeling explosion ground motions to local distances with a one-way coupling to pass hydrodynamic motions from GEODYN to WPP. We continue to improve these capabilities to support nuclear explosion monitoring research, for example, to study special events and/or understand specific phenomena of seismic sources and wave propagation.

In the last year, we have made progress in each thrust. We have worked to facilitate hydrodynamic modeling and pass motions from GEODYN to WPP. We are modeling the HUMBLE REDWOOD series of explosions in order to validate material models and one-way coupling of GEODYN to WPP. We have done extensive calculations of the effect of free-surface topography on shallow explosions. We show that shear waves can be very effectively generated by P-to-S scattering by surface topography, and the P-coda and Rg wave spectra are shaped by the source spectrum. Regional simulations of earthquakes near the North Korean nuclear test site show that 3D models can predict the waveforms at near-regional distances. The 2009 nuclear test can be modeled with a pure explosion plus a small double-couple (10% M_0 of the explosion) composed of strike-slip mechanisms, consistent with nearby earthquakes.

OBJECTIVES

Advances in numerical methods for modeling seismic wave excitation and propagation and ever more powerful parallel computers are making it easier to simulate ground motions on the scale lengths (domain sizes) and frequencies (resolutions) of importance to nuclear explosion monitoring. The objective of this research is to develop and improve methods for seismic simulation in fully 3D earth models to improve nuclear explosion monitoring. Specifically, research is directed along three thrusts: modeling of shock-wave propagation with hydrodynamic methods; modeling of elastic propagation near shallow explosions and earthquakes, including the effect of 3D volumetric structure and free-surface topography; and regional broadband waveform modeling. This effort relies on numerical methods for 3D wave phenomena implemented in computer codes running on massively parallel computers. These capabilities allow us to investigate source and propagation phenomenology of explosion sources and understand waveform data from specific events of interest.

RESEARCH ACCOMPLISHED

In the following sections we describe research accomplished on several tasks.

Modeling the HUMBLE REDWOOD Explosions

We performed preliminary modeling of the HUMBLE REDWOOD series of explosions. These explosions were conducted above and below the ground surface and were recorded by seismic (ground motion) and acoustic (air blast) sensors (Foxall et al., 2010). The purpose of this experiment was to develop methods for yield estimation of explosions that are not fully contained and require joint consideration of the amplitudes of the air blast and seismic waves. We are working on coupled modeling of the explosive source with GEODYN (to simulate the shock wave in solid earth and the air above) with motions subsequently passed to WPP for seismic wave propagation, as described in Rodgers et al. (2009). The preliminary modeling shown here is for one of the contained explosions (5 m depth of burial) and was performed to evaluate how well purely elastic modeling and a preliminary seismic model predict the recorded response.

Figure 1a shows the experimental configuration, with the explosion shot points and recording stations for weak motions (velocity sensors). The experiments involved strong motion (accelerometer) and air-blast (acoustic) sensors as well, but we do consider those data in this study. Figure 1b shows the preliminary model for shear wave speeds. The orientation of the basement was determined from seismic refraction data. We maintained this geometry of alluvium-basement interface, modified the velocities, and compared the simulated ground motions with the recorded ground motions. Modeling was done with an isotropic (explosion) buried source and purely elastic propagation.

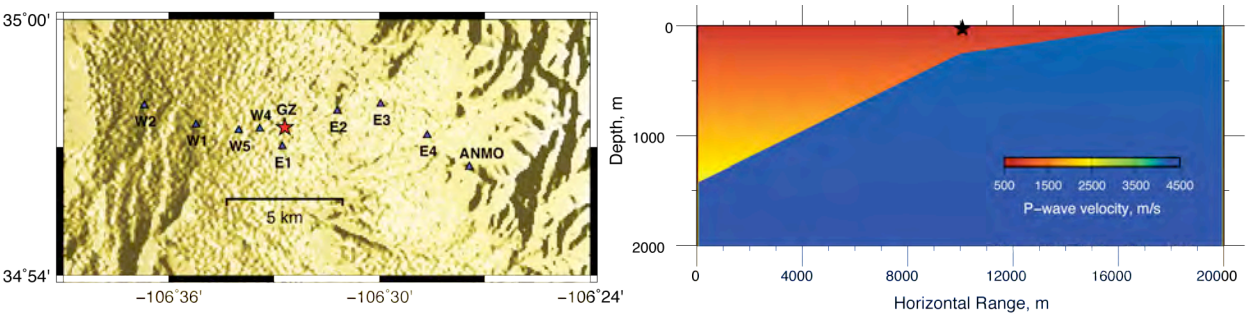

Figure 1. (a) Map of the HUMBLE REDWOOD experiment, with shot points and seismic weak motions recording stations (triangles) overlain on surface topography. (b) Vertical cross section of the preliminary velocity model showing the P-wave speeds. In both panels the star indicates the shot point.

Figure 2 shows the comparison of the recorded (blue) and simulated (red) vertical component, ground velocity time histories for shot HR1-G (5 m depth of burial). The recorded and simulated ground motions were filtered 0.3–1.0 Hz. The shot occurred over a change in the dip of the basement, thus the near-surface structure is quite different between the east and west. These differences are apparent in the recorded motions, which show different

arrival times (note group velocity indications) and a simpler response for the western stations, composed of a P- and S-wave (Rg), and for the eastern stations, which show a very long duration surface wave. The surface wave to the eastern stations appears to be attenuated relative to the simulated response. Attenuation was not included in the simulations; however, not surprisingly it appears to be important for propagation in the alluvium. At higher frequencies the model fit becomes worse, suggesting that the source model, as well as attenuation, needs to be considered. The model could certainly be improved to predict the arrival times, dispersions, and amplitudes.

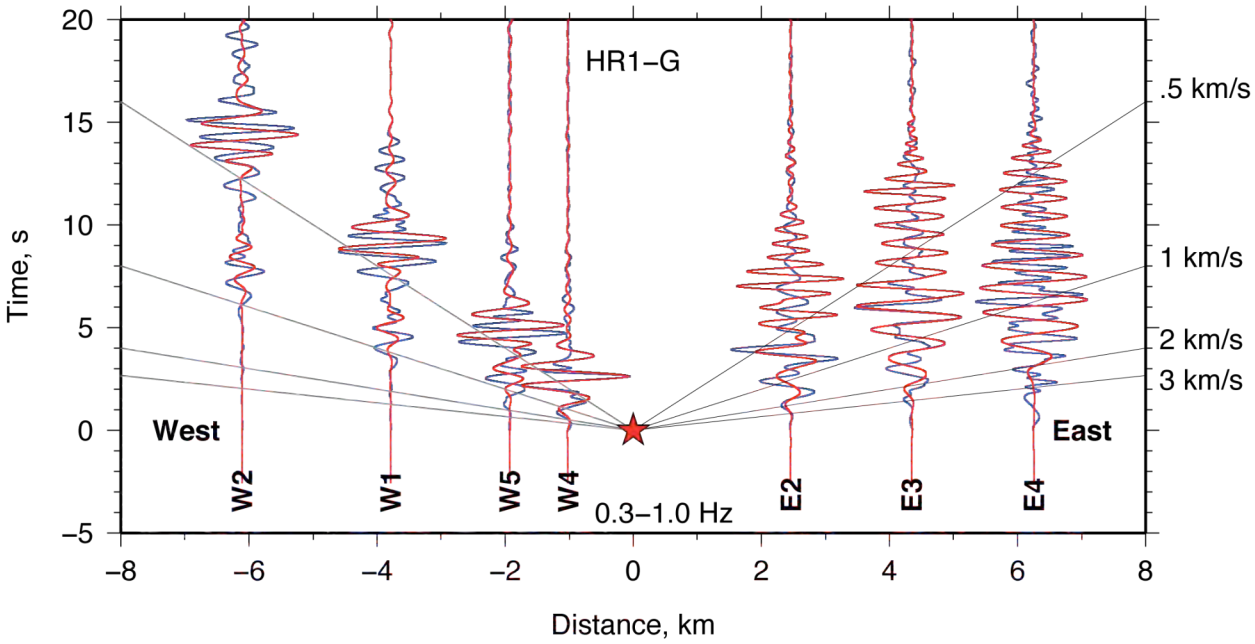

Figure 2. Comparison of observed (blue) and synthetic (red) vertical component ground velocity time histories for HUMBLE REDWOOD shot HR1-G, plotted as record section. The data and synthetics are filtered between 0.3–1 Hz. Gray lines indicate the 3-, 2-, 1-, and 0.5-km/s group velocities in both directions.

Topographic Scattering and Shear-Wave Generation Near Shallow Explosions

In the last year simulations were performed of the 2006 and 2009 North Korean nuclear tests, using reported locations and including the effect of free-surface topography on wavefield (Rodgers, 2010; Rodgers et al., 2010a,b). We modeled the near-field response for a domain covering 40 km around the source. Simulations were performed at high resolution (up to 8 Hz) to capture the frequencies of interest for regional high-frequency discrimination and yield estimation. Figure 3 shows the study area, surface topography, and reported locations of the explosions.

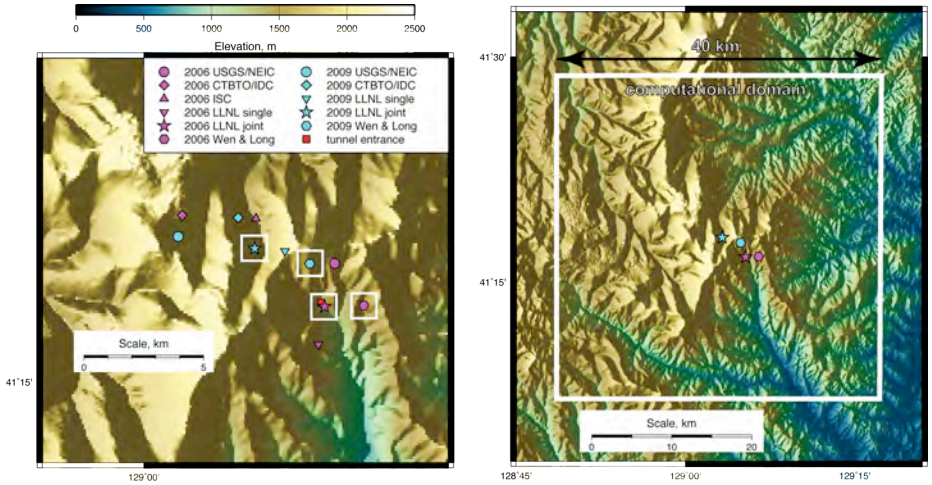

Figure 3. (left) Reported locations of 2006 (magenta) and 2009 (cyan) North Korean nuclear tests. (right) Computational domain for elastic simulations, including free-surface topography (color scale).

The simulations used a homogeneous half-space model but included the actual free-surface topography from the Shuttle Radar Topography Mission, with 90-meter resolution (Farr et al., 2007). The inclusion of rough free-surface topography has a strong effect on the ground motion. Figure 4a shows an image of the vertical component velocities for the flat and topographic cases, using the LLNL location of the 2009 event. The flat response is very simple, with outward-propagating P and Rg waves. Notice that the topographic case shows strong azimuthal variations before the waves have traveled more than 3 km (1 s). A strong distortion in the wavefield is caused by the steep slope to the southwest of the shot point, and this results in a large-amplitude Rg at later times and farther distances (indicated by the arrow in Figure 4a). At longer times the topographic response shows strong scattering of P-to-Rg energy. Much of the energy between P and Rg travels with the Rg velocity.

When the same source (isotropic moment tensor, depth of 600 m) is used, but at four different locations, the response can be quite different. Figure 4b shows the vertical-component ground-velocity responses for four different locations: LLNL and Wen and Long (2010) for the 2006 and 2009 events. This indicates that the response is strongly impacted by the topography. In further analysis we showed that the amplitudes of downward-propagating waves can be affected with focusing and defocusing by topographic features, causing variations of a factor of 2 or more and leading to an effective asymmetric radiation pattern (Rodgers et al., 2010b).

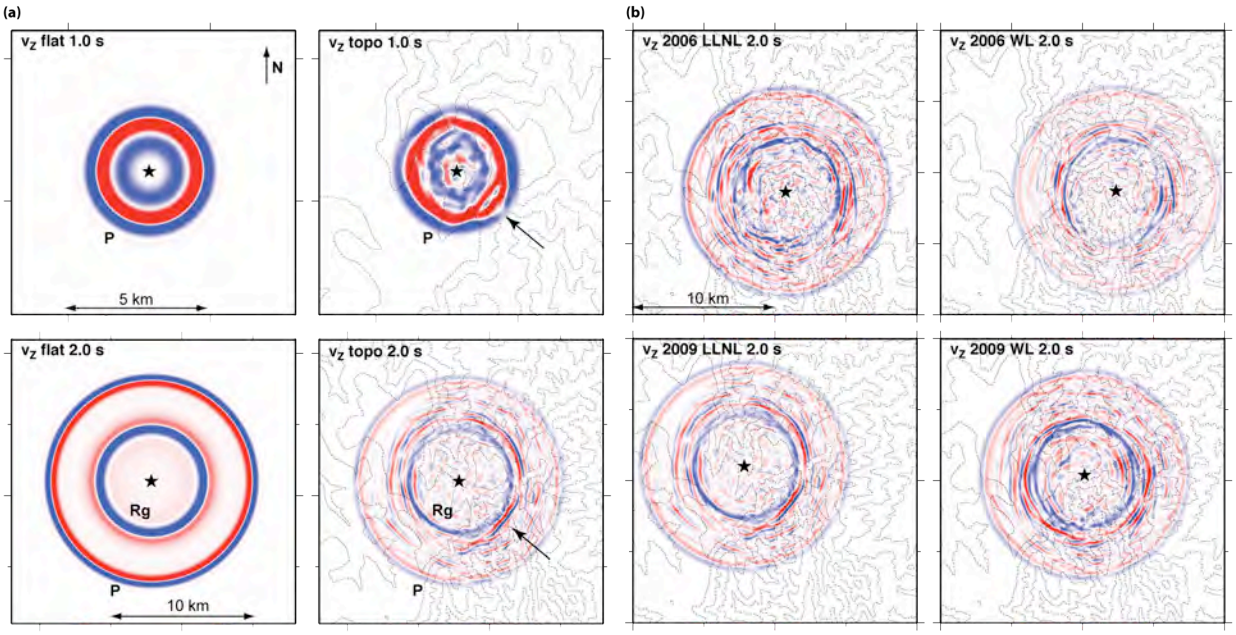

Figure 4. (a) Vertical-component ground velocity at two time steps (1 and 2 s, note different scales) for the flat (left) and topographic (right) cases, assuming the LLNL location of the 2009 event. (b) Vertical-component ground velocity at 2 s after the event for four different locations, LLNL and WL (Wen and Long, 2010), for the 2006 and 2009 events.

Variability in the wave field seen in Figure 2 is clear in the ground-motion time histories as well. Figure 5 shows the three-component ground velocities for the vertical, radial, and transverse components recorded at 10 km for two filter bands 0.5–2 Hz and 2–8 Hz. For reference, the motions for the flat case are also shown. Note that below 2 Hz the topographic response is similar to the flat case, but above 2 Hz topographic scattering causes significant complexity in the wave field, particularly the P-wave coda (between P and Rg) and Rg. Also note that above 2 Hz the transverse component response can have amplitudes equal to that on the vertical and radial component. Note that the ground velocities plotted in full-field view in Figure 4 and as time histories in Figure 5 show higher-frequency response for the topographic cases than for the flat case, especially the Rg phase. P-to-S scattering by topography tends to capture high-frequency energy from the source and propagate it along the surface.

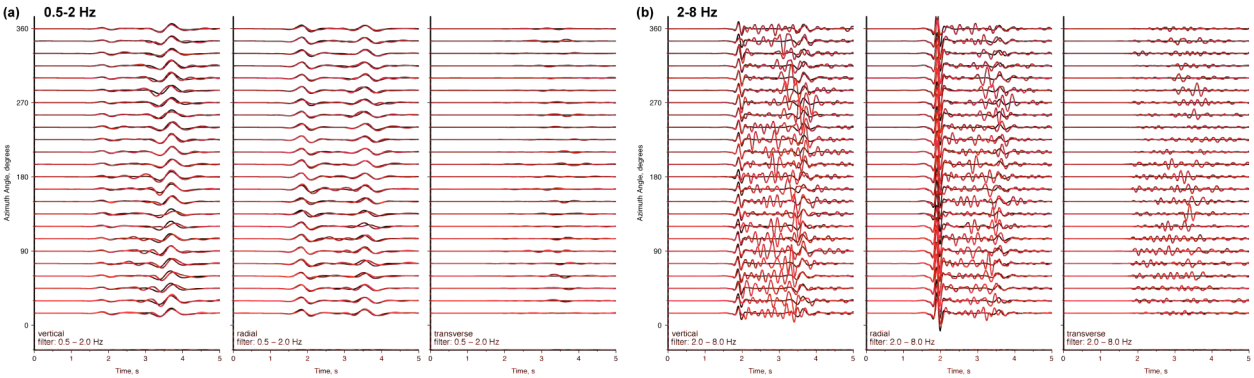

Figure 5. Ground-velocity time histories on the surface at 10 km as a function of azimuth filtered (a) 0.5–2 Hz and (b) 2–8 Hz for the vertical (left), radial (center), and transverse (right) components. The responses are plotted for the flat (black) and topographic (red) cases with the same amplitude scale for all three components and both filter bands.

In order to further understand the simulated response, we measured the spectral amplitudes of carefully windowed segments of the wavefield for the flat and topographic case. Figure 6a shows such an example, where the P, P-coda (energy between the P and Rg phases), and Rg phases are indicated by the color-coded windows for the flat and topographic cases. The Fourier spectral amplitudes are plotted in Figure 6b. Note that the P-wave spectra are nearly identical, with the topographic case slightly lower than the flat case. The P-wave coda in the topographic case is composed of P-to-P and P-to-Rg scattered energy and has a similar spectrum as the direct P-wave with modulation caused by path-specific scattering, while the amplitude of the P-wave coda for the flat case is very small in both the time and frequency domains. The Rg phase in the flat case is peaked at about 1.5 Hz and falls off very quickly with increasing frequency. However, in the topographic case, the Rg phase has the low-frequency spectral amplitude of the Rg in the flat case (i.e., peaked between 1–2 Hz) plus the high-frequency spectral amplitudes of the P-wave. These spectral measurements show how the Rg waves in the topographic case have the low-frequency spectral characteristics of the Rg phase for the flat earth and high-frequency spectral characteristics of the P-wave. P-coda waves have the spectral characteristics of the direct P-wave. Scattering of P-to-Rg can increase amplitudes of regional S-wave, particularly Lg, and will require further study to understand the propagation mode of this enhanced S-wave energy from explosion sources.

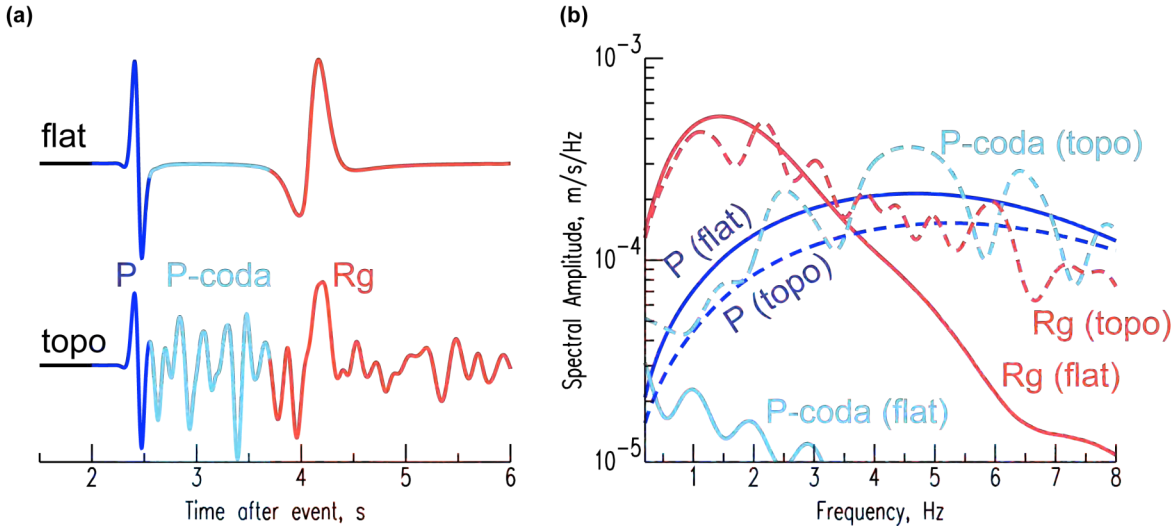

Figure 6. (a) Vertical-component velocity time series for the flat (top) and topographic (bottom) cases, with the direct P (blue), P-wave coda composed of scattered energy (cyan) and Rg (magenta). (b) The Fourier amplitude spectra for the six colored waveform segments shown in (a) for the flat (solid lines) and topographic (dashed lines) cases. Note that the P-coda spectrum for the topographic case is similar to the direct P-wave, and the Rg spectrum for the topographic case is composed of the Rg spectra from the flat case for low frequencies plus the P-wave spectrum for high frequencies.

Regional Waveform Modeling and a Double-Couple Component from the 2009 North Korean Nuclear Test

We modeled the 2006 and 2009 North Korean nuclear tests and nearby earthquakes using the 3D *s29ea* (Kustowski et al., 2008) models. Calculations were made with SPECFEM3D_GLOBE, the spherical geometry spectral element method (Komatitsch and Tromp, 1999) code distributed by the Computational Infrastructure for Geodynamics (CIG, 2010). Figure 7a shows a map of the events and stations used in this analysis. Double-couple focal mechanisms for the regional earthquakes were estimated with the Cut-and-Paste method (Zhao and Helmberger, 1994; Zhu and Helmberger, 1996), which is based on a grid search using Green's functions from a plane-layered (one-dimensional, [1D]) model. Using the double-couple solutions for the earthquakes, we computed the response at regional stations. Figure 7b shows the fits to broadband waveform using the 3D *s29ea* model and our estimated source parameters for the two earthquakes at two stations (MDJ to the north and TJN to the south). Data and synthetics were filtered 0.02–0.07 Hz (14–50 s periods) and are plotted in absolute time and amplitude. Note that the waveforms are well fit

in this frequency band. This provides validation of the 3D seismic model and confidence that we can predict waveforms in this frequency band.

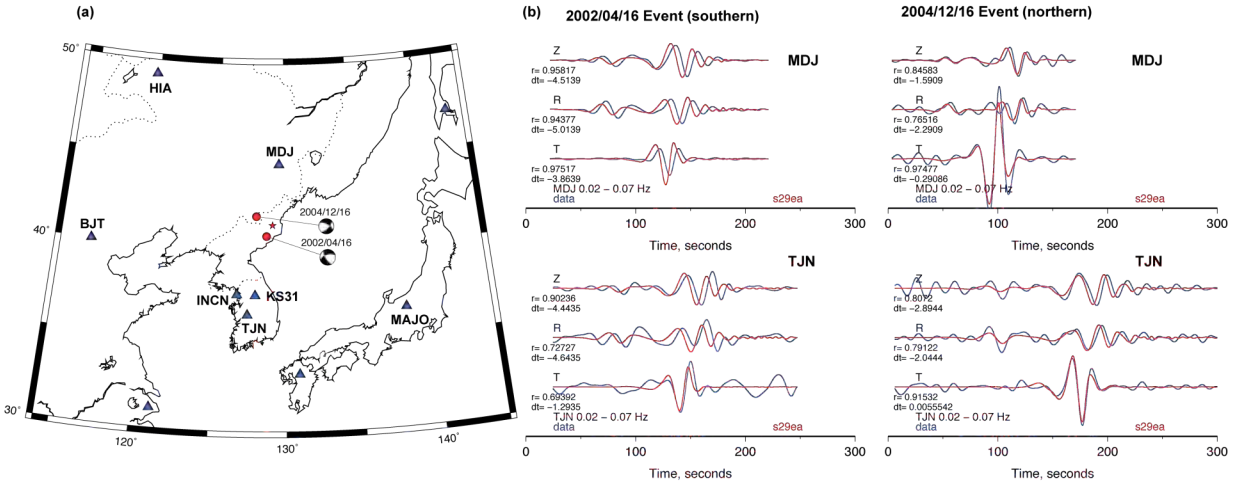

Figure 7. (a) Map showing the locations of the North Korean nuclear tests (stars) and nearby earthquakes (circles) and focal mechanisms, along with regional broadband stations (triangles). (b) Waveform fits for the two earthquakes at stations MDJ and TJN. Data (blue) and synthetics (red) were filtered 0.02-0.07 Hz and are plotted in absolute time and amplitude.

When the same 3D model is used to predict the waveforms from the larger May 25, 2009, North Korean nuclear test and the isotropic source model reported by Ford et al. (2009), we obtain good fits to the vertical and radial components (Figure 8a). Note, however, that the transverse components show an apparent Love wave not predicted by the source model or path propagation in the 3D. Analysis of the particle motion (not shown) at several regional stations indicates that the Love wave precedes the Rayleigh wave. We used the residual waveforms from the purely isotropic source to estimate a double-couple focal mechanism. This is reduced to estimating the source from the Love waves, which is highly nonunique due to the slow variation of the Love wave radiation pattern with azimuth. However, if the mechanism is constrained to be steeply dipping, we obtain a solution that is very consistent with the strike-slip mechanisms of the nearby earthquakes and does not degrade the fit to the Rayleigh waves on the vertical and radial components (Figure 8b). The source of the Love waves from the 2009 explosion is likely to be coincident in time and space with the explosion (isotropic) source and could be due to tectonic release or damage in the source zone (e.g., Ben-Zion and Ampuero, 2009).

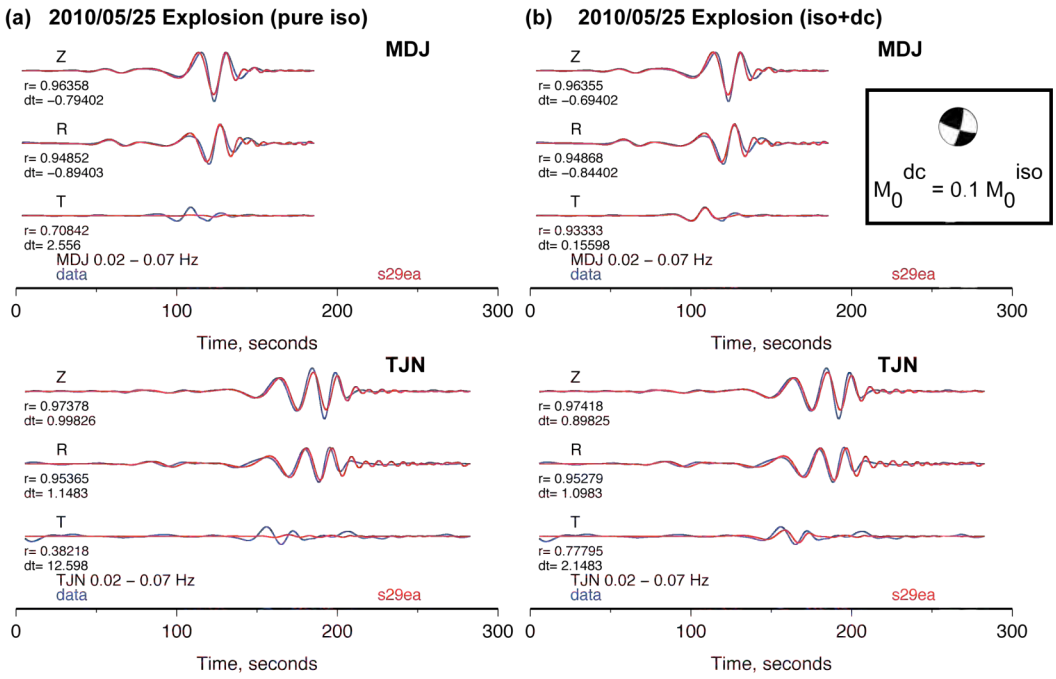

Figure 8. Waveform fits for the 2010/05/25 explosion at stations MDJ and TJN for (a) pure isotropic source and (b) isotropic and 10% double-couple source with the focal mechanism shown. Data (blue) and synthetics (red) were filtered 0.02–0.07 Hz and are plotted in absolute time and amplitude.

CONCLUSIONS AND RECOMMENDATIONS

We continue to make progress on numerical modeling of seismic ground motions to improve nuclear explosion monitoring. Advances in mathematical methods to represent the physics of shock- and seismic-wave excitation and propagation enhance our efforts. Over the last year we have performed studies on small explosions to model the near-field response (HUMBLE REDWOOD); shallow explosions in the presence of rough surface topography to understand how topography impacts the response (North Korean nuclear test site); and regional-scale (400–1000 km), long-period (14–50 s) earthquakes and nuclear explosions in North Korea to improve source estimates.

ACKNOWLEDGEMENTS

Arthur Rodgers is grateful for support as a Fulbright Scholar from the Council for International Exchange of Scholars and the Commission franco-américaine d'échanges universitaires et culture, to Michel Campillo for hosting him at the Laboratoire Géophysique Interne et Tectonophysique Université Joseph Fourier, Grenoble, France, and to LLNL for granting professional research and teaching leave. The authors thank Jeff Wagoner for assistance with topographic data from the Shuttle Radar Topography Mission project. We are grateful to the LLNL Laboratory Directed Research and Development program for support to develop the WPP code. The WPP code is open source and available with documentation from the LLNL website (Petersson, 2010). Spectral element calculations were made with SPECFEM3D_GLOBE, which is developed, maintained, and distributed by CIG. Simulations were performed on parallel computers operated by Livermore Computing using a Grand Challenge Allocation. Waveform data were obtained from the Incorporated Research Institutions for Seismology's Data Management System (IRIS-DMC) and organized in the LLNL Seismic Research Database by Stan Ruppert and Terri Hauk. Waveforms were extracted from the database and prepared for waveform modeling using dbtool, developed by Eric Matzel. Figures were made with the Generic Mapping Tool (GMT, Wessel and Smith, 1998). Seismogram plots were made with pssac2, developed by Lupei Zhu and Brian Savage. We are also grateful to Stephen Myers for communications about vertical-component ground-velocity responses from the LLNL location, shown in Figure 4a,b.

REFERENCES

Ben-Zion, Y. and J.-P. Ampuero (2009). Seismic radiation from regions sustaining material damage, *Geophys. J. Int.* 178: 1351–1356.

Computational Infrastructure for Geodynamics (2010). SPECFEM3D_GLOBE, www.geodynamics.org, accessed January 2010.

Farr, T. G., P. A. Rosen, E. Caro, R. Crippen, R. Duren, S. Hensley, M. Kobrick, M. Paller, E. Rodriguez, L. Roth, D. Seal, S. Shaffer, J. Shimada, J. Umland, M. Werner, M. Oskin, D. Burbank, and D. Alsdorf (2007). The Shuttle Radar Topography Mission, *Rev. Geophys.* 45: RG2004, doi:10.1029/2005RG000183.

Ford, S., D. Dreger, and W. Walter (2009). Source analysis of the Memorial Day explosion, Kimchaek, North Korean, *Geophys. Res. Lett.* 36: L21304, doi:10.1029/2009GL040003.

Foxall, B., R. Marrs, E. Lenox, R. Reinke, D. Seastrand, J. Bonner, K. Mayeda, and C. Snelson (2010). The HUMBLE REDWOOD seismic/acoustic coupling experiments: Joint inversion for yield using seismic, acoustic and crater data, *Seismo. Res. Lett.* 8: 315.

Komatitsch, D. and J. Tromp (1999). Introduction to the spectral-element method for 3-D seismic wave propagation, *Geophys. J. Int.* 139: 806–822.

Kustowski, B., G. Ekstrom, and A. Dziewonski (2008). The shear-wave velocity structure in the upper mantle beneath Eurasia, *Geophys. J. Int.* 174: 978–992, 10.1111/j.1365-246X.2008.03865.x.

Petersson, N. A. (2010). https://computation.llnl.gov/casc/serpentine/software.html (website).

Rodgers, A., O. Vorobiev, N. A. Petersson, and B. Sjogreen (2009). Simulation of seismic waves from underground explosions in geologic media, FY2009 progress report, Lawrence Livermore National Laboratory report LLNL-TR 420208

Rodgers, A. (2010). Simulation of seismic waves for nuclear explosion monitoring, Lawrence Livermore National Laboratory abstract, LLNL-ABS-422488, European Geophysical Union Annual Meeting, May 2–7, 2010, Vienna, Austria (submitted).

Rodgers, A., N. A. Petersson, and B. Sjogreen (2010a). Seismic simulations of recent DPRK nuclear explosions including the effects of free surface topography and 3D structure, abstract, Seismological Society of America Annual Meeting, April 20–23, 2010, Portland, OR, USA (submitted).

Rodgers, A., N. A. Petersson, and B. Sjogreen (2010b). Efficient generation of shear waves from shallow explosions by topographic scattering near the North Korean nuclear test site, *J. Geophys. Res.*(submitted).

Wen, L. and H. Long (2010). High-precision location of North Korea's 2009 nuclear test, *Seismo. Res. Lett.* 81: 26–29.

Wessel, P. and W. H. F. Smith (1998). New, improved version of Generic Mapping Tools released, *EOS Trans. Amer. Geophys. U.* 79: 579.

Zhao, L. S. and D. V. Helmberger (1994). Source estimation from broadband regional seismograms, *Bull. Seismo. Soc. Amer.* 84: 91–10.

Zhu, L. and D. V. Helmberger (1996a). Advancements in source estimation techniques using broadband regional seismograms, *Bull. Seismo. Soc. Amer.* 86: 1634–1641.

HIGH-RESOLUTION SEISMIC VELOCITY AND ATTENUATION MODELS OF WESTERN CHINA

Eric A. Sandvol[1], Xueyang Bao[1], James Ni[2], Tom Hearn[2], and Scott Phillips[3]

University of Missouri[1], New Mexico State University[2], and Los Alamos National Laboratory[3]

Sponsored by the Air Force Research Laboratory[1,2] and the National Nuclear Security Administration[3]

Award No. FA9453-10-C-0256
Proposal No. BAA10-61

ABSTRACT

Development of high-resolution seismic velocity and attenuation models of the Qinghai-Tibet Plateau and adjacent regions of western China are critical to monitoring efforts because of their close proximity (~380 km) to the nuclear test site at Lop Nur. Previous studies have demonstrated the great complexity in crustal and uppermost mantle seismic velocity structure and propagation characteristics. As a result, regional seismic phases show strong lateral variability in travel time, amplitude, and frequency content. New broadband stations in the region give unprecedented two-dimensional coverage of the northeastern portion of the Plateau. The NETS (North-Eastern Tibet Seismic experiment) and ASCENT (A Seismic Collaborative Experiment of Northern Tibet) arrays (5/07-6/09) consisted of more than 110 temporary broadband stations in the northeast Tibetan Plateau, Ordos Plateau, and Qaidam basin. We are using this data set to develop and calibrate high-resolution regional velocity and attenuation models of the crust and upper mantle for these regions. We have already worked with collaborators in China to construct a preliminary catalog of 400 well-located events within the northeastern Tibetan Plateau. Preliminary results of seismic attenuation studies show a remarkable correlation between Lg and Pg Q values and surface tectonics and crustal velocity estimates. These include relatively high Q values in the Qaidam basin and very low Q values in the Songpan-Ganzi and northernmost Qiangtang terranes.

OBJECTIVES

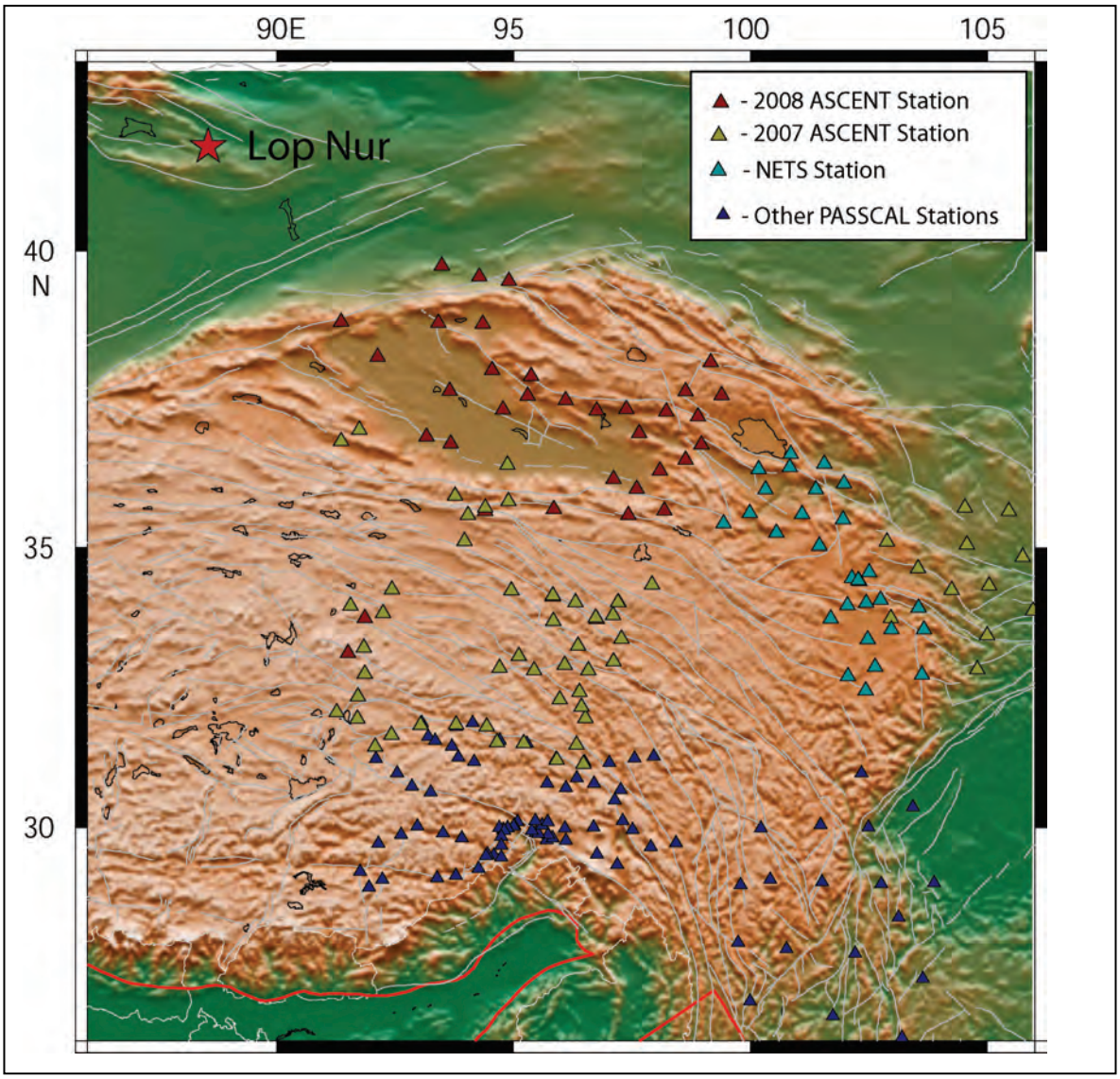

Figure 1. A regional topographic map showing the broadband stations (triangles) from all of the temporary networks that have been deployed across the Tibetan Plateau. The data from the newly available ASCENT and NETS networks are shown as dark red, yellow and cyan triangles. All remaining temporary stations are shown in dark blue. We have access to at least two years of data for all of these networks.

The objective of this project is to construct and validate both 3-D P wave and S wave velocity models and attenuation models (Pn, Pg, Sn, and Lg) for the crust and upper mantle in western China. This research will dramatically increase the seismic characterization of critical areas in western China. It will use new data collected by the 90-station ASCENT and 25-station NETS arrays (total 116 broadband stations; Figure 1) and integration of waveform data from broadband stations in western China suitable for surface wave tomography and attenuation studies. These data sets allow the application of new techniques designed to create robust models of seismic velocity and attenuation in which we reliably estimate the absolute amplitude of the velocity and Q variations across western China.

The ASCENT and NETS arrays (Figure 1) cover much of central northeastern Tibet and the Qaidam basin in Qinghai and Gansu provinces. The location of these arrays is ideal for studying aspects of monitoring research, namely the Chinese test site at Lop Nur and regions 400 km to the south. The initial installation in June 2007 covered the northeastern Tibet Plateau and part of Gansu province. This was fortuitous as it allowed us to widely record the May 12, 2008, Wenchuan earthquake and aftershocks. In August of 2008, these stations were moved to Qaidam Basin to better cover the northern Qinghai-Tibet Plateau. All stations are equipped with broadband CMG-3T, CMG-3ESP, and STS-2 sensors with continuous recording. Using both travel-time body and surface wave tomography, we are producing 3-D P and S wave velocity models and regional wave attenuation models for the crust and upper mantle. In the following sections we describe the data, Pn and Sn travel time tomography, short and long wavelength surface wave tomography, and regional wave attenuation modeling.

RESEARCH ACCOMPLISHED

Background

Tibet and surrounding areas have been the focus of many studies related to seismic wave propagation and velocity structure (Li et al., 2008; Tilman et al., 2000; Mitchell, 1997; Rodgers et al., 1997; Rapine et al. 2003b; McNamara et al., 1997). Here we summarize the current state-of-the-art knowledge of the seismic structure of the Tibetan Plateau and its relationship to tectonic hypotheses.

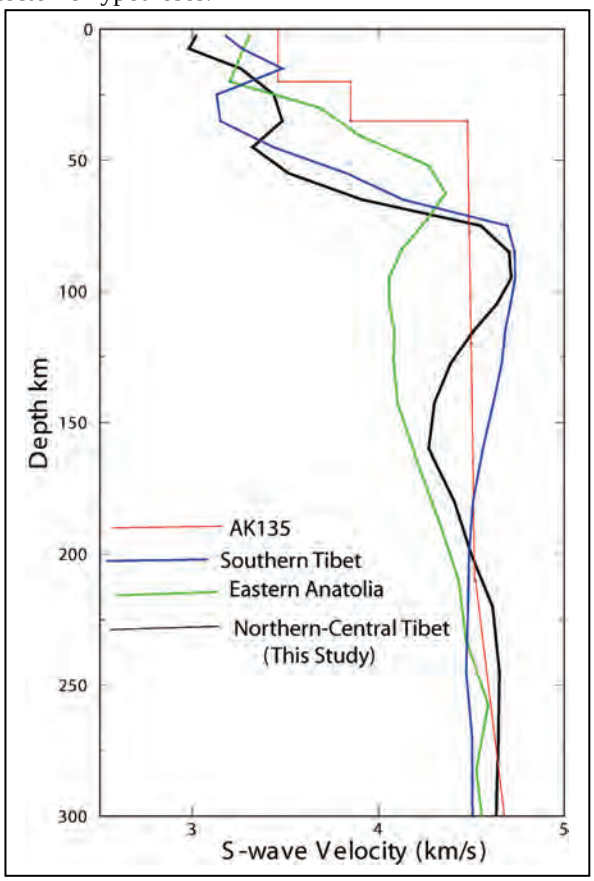

Figure 2. Velocity models from Rayleigh wave phase dispersion curves from the northern and southern Tibet as well as eastern Anatolia for comparison. The low velocities are most likely a result of anomalously slow velocities in the uppermost mantle beneath northern Tibet but not as low as seen in regions like eastern Turkey and the Basin and Range.

Recent P-wave tomography images of the Tibetan Plateau indicates that the Indian continental lithosphere underlies southern Tibet and that an estimated minimum of 1000 km of post-collisional convergence between India and Asia has occurred. The downwelling Indian lithosphere extends to depths near 400 km beneath central Tibet without significant internal deformation (Kind et al., 2002; Tilmann, et al., 2003; Kumar et al., 2006). Body wave and

surface wave studies have indicated a seismically low velocity and highly attenuating uppermost mantle for much of northern Tibet (Ni and Barazangi, 1983; McNamara et al., 1997; Rapine et al., 2003a). In contrast, in southern Tibet and the Qaidam basin (north of Kunlun fault), colder mantle has been implied (Ni and Barazangi, 1983, 1984; Tilmann et al., 2003; Galve et al., 2002; Li et al., 2008) (Figure 2). In southern Tibet, a variety of seismic observations (Alsdorf et al., 1998; Makovsky and Klemperer, 1999; Yuan et al., 1997; Kind et al., 2002; Tilmann, et al., 2003; Huang and Zhao; 2006; Li et al., 2008) and electrical conductivity (Wei et al., 2001) all point to a weak low-velocity middle crust (Nelson et al., 1996). The cause of this low-viscosity and low-velocity channel in the mid-crust is predominantly due to wet melting of the subducted Indian sediments and metasediments (Nelson et al., 1996; Cotte, 1999; Rapine et al., 2003b). The mid crustal low velocity zone is also the culprit of high attenuation of Lg waves in southern Tibet (McNamara et al., 1996; Reese et al., 1999; Xie, 2002a; Phillips et al., 2000, 2001, 2005). Lg attenuation is also observed beneath northern Tibet (Qiangtang terrane), but crustal velocities there are only about 8% lower than normal continental crust (Rapine et al., 2003a). The cause of such a high Lg attenuation is not completely understood, but it seems related to high temperature and a partially melted crust of northern Tibet (Hacker et al., 2000; Fan and Lay, 2003).

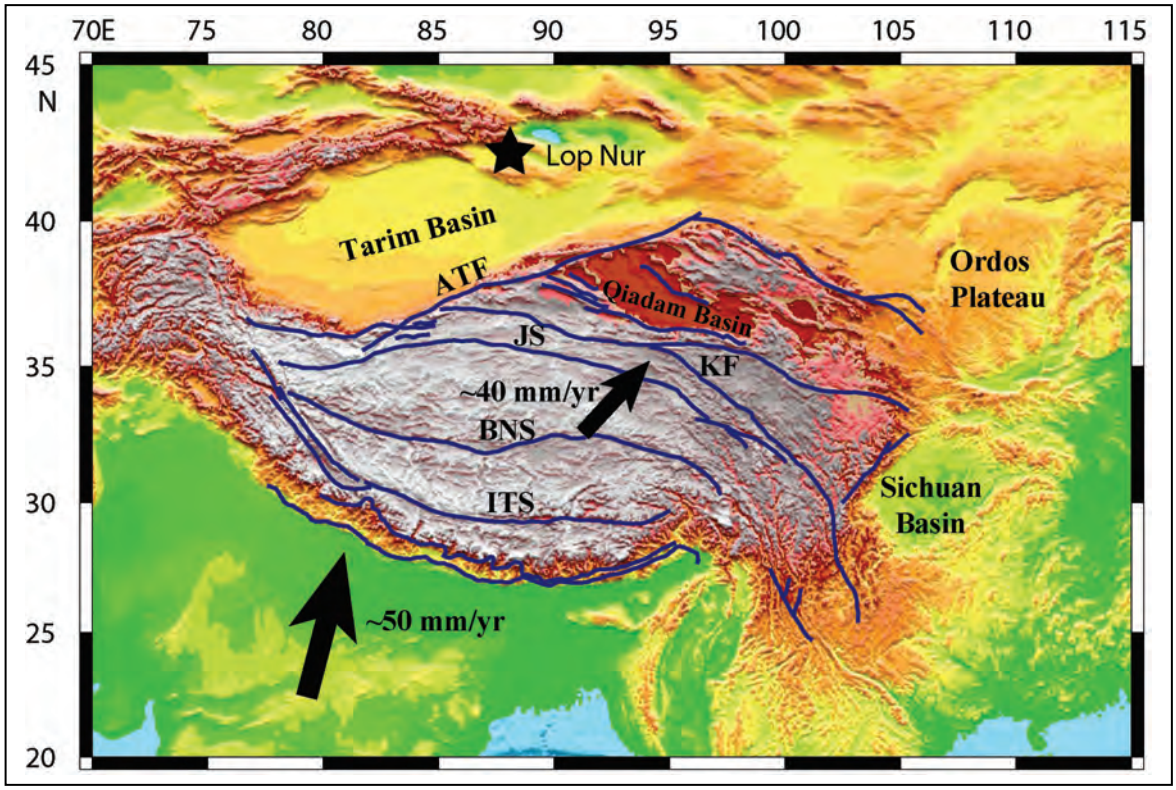

Figure 3. A simple tectonic map for the Tibetan Plateau. The major features shown are ITS- Indus Tsangpo Suture, BNS-Bangong-Nujiang Suture, ATF-Altyn Tagh Fault, KF-Kunlun Fault.

A maximum seismogenic thickness of 25 km (Langin et al., 2003) is observed for northern Tibet. The lithosphere thickness is about 140 km according to S-P converted phase (Kumar, et al., 2006); however, it could be thinner in the interior of the northern Plateau. Rayleigh wave phase velocity inversion indicates a lithosphere thickness of only about 120-140 km thick.

Attenuation and Amplitude Tomography Method

Attenuation tomography uses estimates of path-averaged attenuation to delineate laterally varying Q. This includes most spectral methods, which use the ratio of spectral slopes to estimate Q independent of wave amplitude (Zor et al., 2007). An example of attenuation tomography for Asia using coarsely spaced stations is shown in Figure 4 (Xie et al., 2006). We have used this method to create phase blockage maps for regions of the Middle East

(Sandvol et al., 2001). A major advantage of attenuation tomography is that it is a two-station method, and this allows the cancellation of all source effects and gives high quality estimates of path-Q; however, two-station methods require the two stations to be on the same raypath, and this requirement substantially reduces the amount of data that can be obtained. We are measuring attenuation with both the two-station method (Xie and Mitchell, 1990; Xie, 2002a; and Zor et al., 2007 for descriptions of the method, including rigorous error analysis) and reversed two station methods (Chun et al., 1987). The preliminary results of this method is shown in Figure 4. The reversed two station method eliminates site as well as source effects. Path averaged Q measurements are inverted tomographically to create a Q model. Using these methods and the newly collected data from the ASCENT arrays we have found that the attenuation structure of the Tibetan crust is far more complex than previously thought. It appears as if there are fairly large regions of low attenuation within Tibet with Q values exceeding 300.

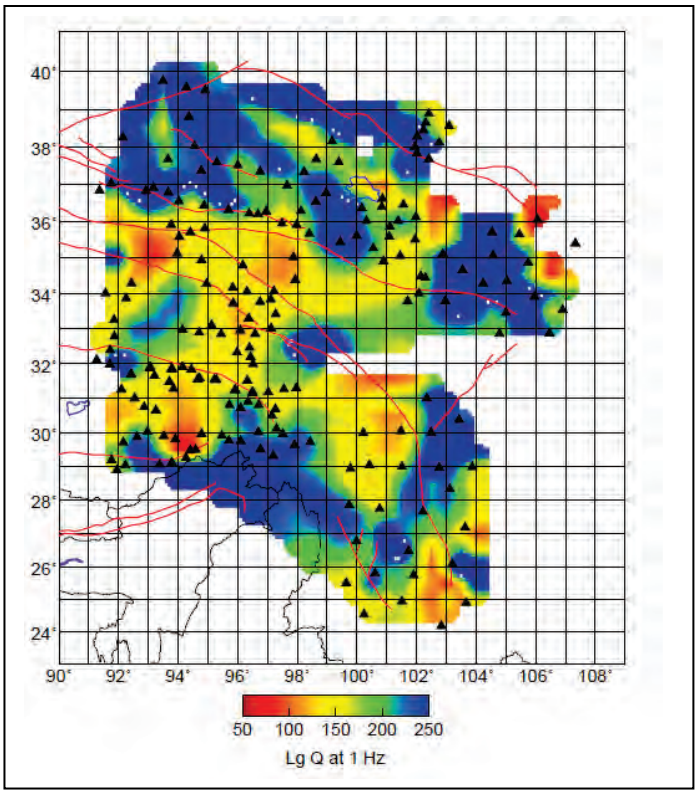

Figure 4. **A preliminary map of Lg Qo in the northeastern corner of the Tibetan Plateau based on two-station Lg spectral ratios applied to waveform data from a variety of 2-D networks spread across the eastern portion of the plateau. The black triangles are the ASCENT seismic stations and the major tectonic boundaries are show as red lines. This result suggests much more inter-plateau Lg Q heterogeneity that previously thought**.

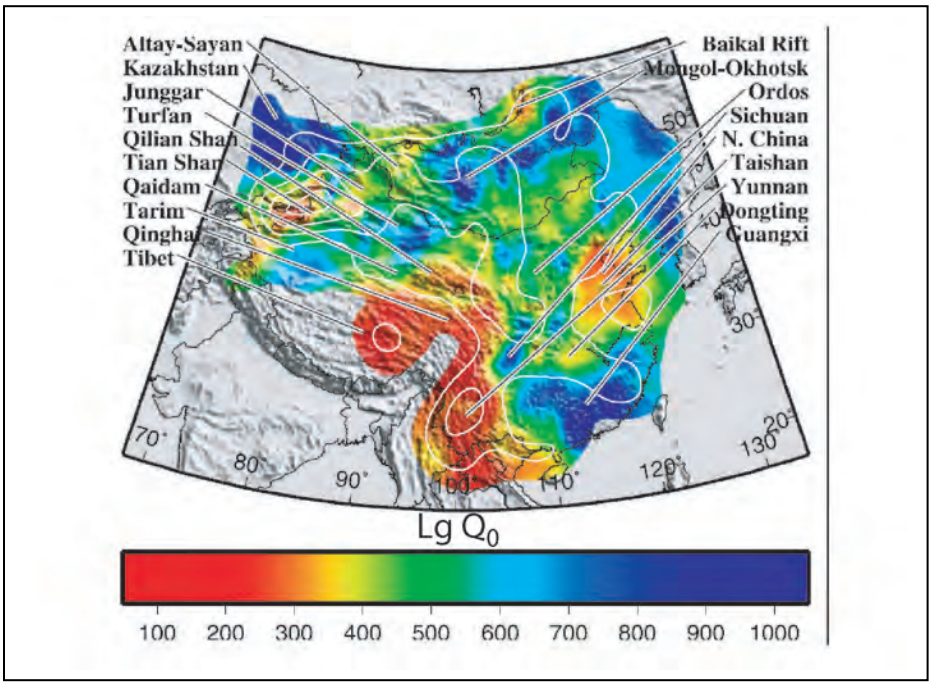

Figure 5. **Q estimated using 1-Hz Lg amplitudes obtained from digital waveform data (Phillips et al., 2005). White contours represent the model resolution at levels of 0.1, 0.2, 0.3, and 0.4.**

We are also investigating attenuation using amplitude tomography as well as attenuation tomography. Amplitude tomography uses raw amplitudes as opposed to Q-estimates based on spectral ratios. It assumes an isotropic source radiation pattern, and solves for source and site terms in addition to 2-D attenuation. Its advantage over attenuation tomography is that there is no two-station geometry requirement so that all recorded amplitudes may be used in the tomography. Examples of amplitude based tomography for Asia are shown in Figures 5 and 6 from Phillips et al. (2005), and Hearn et al. (2008a), respectively. The amplitude tomography method has proven successful and performs well even for lower quality data sets such as the surface-wave amplitudes archived by the International Seismological Centre (Hearn, 2008b). Constraints from high quality path averaged Q such as those described above, can be incorporated into the inversion.

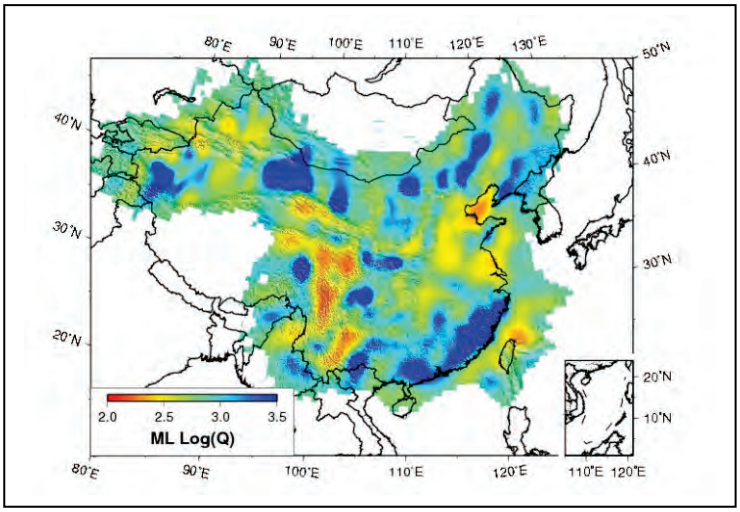

Figure 6. **Q estimated using 1-Hz maximum amplitude measurements collected for ML magnitude estimation (Hearn et al., 2008a).**

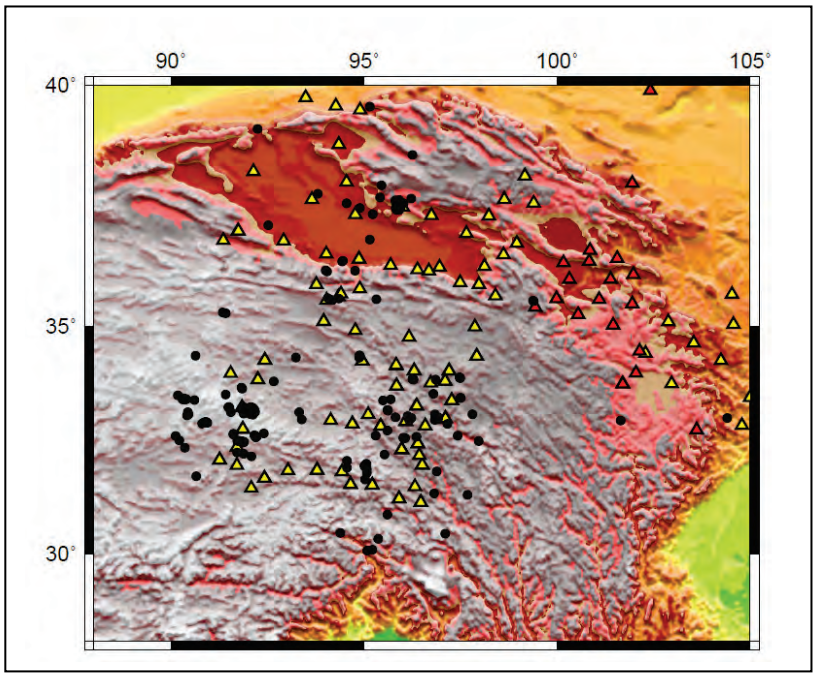

Figure 7. **A plot of the 450 well located local and regional earthquakes recorded by the 2007-2009 combined INDEPTH-IV/ASCENT arrays. The black dots are the earthquakes and the yellow triangles are the stations used to locate the events**.

Seismic Event Location

Our collaborators at Peking University have already conducted a thorough review of all of the continuous data from the ASCENT arrays and have located a total of 592 regional earthquakes for the period of May 2007 to June 2009 (Figure 7). The even distribution of these earthquakes in the study area is compatible with the hypothesis of continuous deformation of the Tibetan Plateau from GPS observations. Our network recorded a Ms = 6.3 event in the Qaidam Basin and this region was recently struck by a damaging Ms = 7.1 earthquake near Yushu. The vast majority regional earthquakes are broadly scattered in the depth range of 8-10 km, but no event deeper than 35 km. This observation strongly supports the existence of a hot and weak lower crust beneath the Qaidam Basin, the Qilian Mountains and the 5 km elevated northeastern Tibetan Plateau. The crustal seismogenic zone appears slightly thicker beneath the northeastern Tibetan Plateau than in southern Tibet, reflecting a difference in both the rheological structure of the crust and the amount of stress that the crust is experiencing. The absence of lower crustal and uppermost mantle earthquakes in northeastern Tibet is consistent with a hot asthenosphere mantle upwelling under the Qiangtang and Songpan-Ganze terranes, associated with regional convective removal of lithosphere. In contrast to southernmost Tibet, this part of northeastern Tibet has no evidence of any type of continental subduction of Asian continent beneath the northeastern Tibetan margin. The present tectonics of northeastern Tibet is mainly controlled by trans-extensional deformation that is associated with the strike-slip Kunlun and Altyn Tagh.

CONCLUSIONS AND RECOMMENDATIONS

In this project, we are processing a large set of new broadband waveform data to obtain both seismic velocity and attenuation results for major portions of western China. The resulting tomographic models shown in Figures 4 through 6 clearly show the variation in Lg Q across the boundary between the Qaidam basin and the northern Tibetan Plateau. The Lg Q_o values are generally higher outside the high elevation regions of the Tibetan Plateau than the surrounding regions. Other studies have similarly concluded that Lg propagation in the Tibetan Plateau is usually blocked or highly attenuated. We also observe substantial variation in Pg and Lg Q_o values within the Tibetan Plateau itself; for example, we observe higher values along the Bangong-Nujiang suture and along the eastern syntaxis of the Plateau.

High Lg attenuation within the Tibetan Plateau (Q_o ~100–200) may be caused by a combination of scattering and intrinsic attenuation. Scattering attenuation is due to the large strike slip faults like the Kunlun and the intrinsic attenuation could be due to crustal partial melting in northernmost Qiangtang terrane. However, we observe that most of the rapid changes in Lg Q occur across major fault zones or sutures suggesting that scattering due to structural changes in the crust plays an important role in Lg attenuation. By quantifying anisotropic Q we can help to distinguish between scattering and intrinsic Q in this tectonically complex region. Furthermore, we recommend the use of multiple Q techniques in these seismically complex regions in order to formulate a robust attenuation model. This approach, utilizing both two station, reversed two station, and single event-station pairs should help us not only to define the shape of the attenuation anomalies but also to constrain the size of the anomalies. These models should ultimately help to create transportable, physically based discriminants for much of western China.

ACKNOWLEDGEMENTS

We would like to thank Yongshun "John" Chen and the entire geophysics team at Peking University for their help on the deployment and maintenance of the INDEPTH-IV/ASCENT seismic arrays as well in the deployment of their own equipment. We would also like to thank IRIS-PASSCAL for the loan of the equipment for many of these seismic stations and their assistance in maintaining this large array.

REFERENCES

Alsdorf, D., Brown, L., Nelson, K.D., Makovsky, Y., Klemperer, S.L., and Zhao, W.J. (1998). Crustal deformation of the Lhasa terrane, Tibet plateau from INDEPTH deep seismic reflection profiles, *Tectonics* 17**:** 501–519.

Chun, K., G. F. West, R. J. Kokoski, and C. Samson (1987). A novel technique for measuring Lg attenuation - results from eastern Canada between 1 to 10 Hz, *Bull. Seismol. Soc. Am* **77**(2): 398–419, doi:10.1785/0120080316.

Cotte, N., H. Pedersen, M. Campillo, J. Mars, J. F. Ni, R. Kind, E. Sandvol, and W. Zhao (1999). Determination of the crustal structure in southern Tibet by dispersion and amplitude analysis of Rayleigh waves, *Geophysical Journal International*, 138(3), 809-819, doi:10.1046/j.1365-246x.1999.00927.x. [online] Available from: http://blackwell-synergy.com/doi/abs/10.1046/j.1365-246x.1999.00927.x

Fan, G.W., and Lay, T. (2003). Strong Lg wave attenuation in the Northern and Eastern Tibetan Plateau measured by a two-station/two-event stacking method, *Geophys. Res. Lett.* 30**:** doi:10.1029/2002GL016211.

Galve, A., Sapin, M., Hirn, A., Diaz, J., , J.-C., Laigle, M., Gallart, J., Jiang, M. (2002). Complex images of Moho and variation of Vp/Vs across the Himalaya and South Tibet, from a joint receiver-function and wide-angle-reflection approach, *Geophys. Res. Lett.* 29 (24): 35–1.

Hacker, B.R., Gnos, E., Ratschbacher, L., Grove, M., McWilliams, M., Sobolev, S.V., Wan, J., and Wu, Z. (2000). Hot and dry deep crustal xenoliths from Tibet, *Science* 287: 2463–2466.

Hearn, T.M., Wang, S., Pei, S., Xu, Z., Ni, J., and Y. Yu, Y. (2008a). Seismic amplitude tomography for crustal attenuation beneath China, *Geophys. J. Int.* 174: 223–234, doi: 10.1111/j.1365-246X.2008.03776.x, 2008

Hearn, T.M. (2008b). Surface-wave attenuation from ISC Bulletin data, presented at 2008 SSA meeting, *Seismol. Res. Lett.* 79**:** 339, Meeting Abstract.

Huang, J., and Zhao D. (2006), High-resolution mantle tomography of China and surrounding regions, *J. Geophys. Res.*, 111**,** B09305, doi:10.1029/2005JB004066.

Kind, R.,Yuan, X., Saul, J., Nelson, D., Sobolev, S. V., Mechie, J., Zhao, W., Kosarev, G., Ni, J., Achauer, U., Jiang, M. (2002). Seismic images of crust and upper mantle beneath Tibet: Evidence for Eurasian plate subduction, *Science*, 298: 1219–1221.

Kumar, P., Yuan, X., Kind, R., Ni, J. (2006). Imaging the colliding Indian and Asian lithospheric plates beneath Tibet, *J. Geophys. Res.* 111**:** B06308, DOI:10.1029/2005JB003930.

Langin, W. R., Brown, L.D., Sandvol, E. A., and Project INDEPTH Team (2003). Seismicity of central Tibet from INDEPTH III seismic recordings, *Bull. Seismol. Soc. Am.* 93: 2146–2159.

Li, C., Van der Hilst, R.D., Meltzer, A.S., Sun, R., and Engdahl, E.R. (2008). Subduction of the Indian lithosphere beneath the Tibetan Plateau and Burma, *Earth and Planetary Science Letters,* 274**:** 157–168.

Makovsky, Y., and Klemperer, S. (1999). Measuring the Seismic Properties of Tibetan Bright Spots: Evidence for Free Aqueous Fluids in the Tibetan Middle Crust, *J. Geophys. Res.* 104**:** 10795–10825.

McNamara, D.E., Owens, T.J., and Walter, W.R. (1996). Propagation characteristics of Lg across the Tibetan Plateau, *Bull. Seismol. Soc. Am.* 86**:** 457–469.

McNamara, D. E., Walter, W.R., Owens, T.J., and Ammon, C. J. (1997). Upper mantle structure beneath the Tibetan Plateau from Pn travel time tomography, *J. Geophys. Res*. 102: 493–505.

Nelson, K., W. Zhao, L. Brown, J. Kuo, J. Che, X. Liu, and SL (1996), Partially molten middle crust beneath southern Tibet: synthesis of project INDEPTH results, *Science* 274: 1684–1688. [online] Available from: http://www.sciencemag.org/cgi/content/abstract/274/5293/1684

Ni, J., and Barazangi, M. (1983). High-frequency seismic wave propagation beneath the Indian Shield, Himalayan Arc, Tibetan Plateau and surrounding regions: High uppermost mantle velocities and efficient SN propagation beneath Tibet. *Geophys. J. Royal Astron. Soc.* 72**:** 665–689.

Mitchell, B. (1997). *Lg* coda Q variation across Eurasia and its relation to crustal evolution, *J. Geophys. Res* 102**:** 22,767–22,779.

Phillips, W.S., Hartse, H.E., Taylor, S.R., and G.E. Randall,G.E. (2000). 1 Hz Lg Q Tomography in central Asia, *Geophys. Res. Lett*. 27: 3425–3428.

Phillips, W. S., Hartse, H. E., Taylor, S. R., Velasco, A. A., and Randall, G.E. (2001). Application of regional phase amplitude tomography to seismic verification, *PAGEOPH* 158**:** 1189–1206.

Phillips, W.S., Hartse, H.E., and J.T. Rutledge, J.T. (2005). Amplitude ratio tomography for regional phase Q, *Geophys. Res. Lett*. 32: doi:10.1029/2005GL023870.

Rapine, R., and Ni, J.F. (2003a). Propagation characteristics of Sn and Lg in Northern China and Mongolia, *Bull. Seismol. Soc. Am.* 93: 939–945.

Rapine, R., Tilmann, F., West, M., Ni, J., and Rodgers, A. (2003b). Crustal structure of northern and southern Tibet from a surface wave dispersion analysis, *J. Geophys. Res.*, 108, *2120*, doi:10.1029/2001JB000445.

Reese C., Papine, R., and Ni, J. (1999). Lateral variation of Pn and Lg attenuation at the CDSN station LSA, *Bull. Seismol. Soc. Am.,* 89, 325–330.

Rodgers, A. R., Ni, J.F., and Hearn, T.M. (1997). Propagation Characteristics of Short-Period Sn and Lg in the Middle East, *Bull. Seismol. Soc. Am.* 87, 396-413.

Sandvol, E., Al-Damegh, K., Calvert, A., Seber, D., Barazangi, M., Mohamad, R., Gok, R., Turkelli, N., and Gurbuz, C. (2001). Tomographic imaging of Lg and Sn propagation in the Middle East, *Pure Appl. Geophys.* 158: 1121–1163.

Tilmann, F., Ni, J., and INDEPTH III Seismic Team (2003). Seismic imaging of the downwelling Indian lithosphere beneath central Tibet. *Science* 300**,** 1424–1427.

Wei, W., M. Unsworth, A. Jones, J. Booker, H. Tan, D. Nelson, L. Chen, S. Li, K. Solon, P. Bedrosian, S. Jin, M. Dang, J. Ledo, D. Kay, and B. Roberts (2001). Detection of widespread fluids in the Tibetan crust by magnetotelluric studies., *Science* (New York, N.Y.), 292(5517), 716-9, doi:10.1126/science.1010580. [online] Available from: http://www.ncbi.nlm.nih.gov/pubmed/11326096

Xie, J. and Mitchell, B.J. (1990). Attenuation of multiphase surface waves in the Basin and Range province, Part 1: Lg and Lg coda. *Geophys. J.* 102: 121–138.

Xie, J. (2002a). Lg Q in the Eastern Tibetan Plateau, *Bull. Seismol. Soc. Am* 92: 871–876.

Xie, J., Wu, Z., Liu, R., Schaff, D., Liu, Y., and Liang, J. (2006). Tomographic regionalization of crustal Lg Q in eastern Eurasia, *Geophys. Res. Lett.* 33: L03315, doi:10.1029/2005GL024410.

Yuan, X., Ni, J., Kind, R., Sandvol, E., Mechie, J. (1997). Lithospheric and upper mantle structure of southern Tibet from a seismological passive source experiment, *J. Geophys. Res.* 102: B 12, 27491–27500.

Zor, E., E. Sandvol, J. Xie, N. Türkelli, B. Mitchell, A. Gasanov, and G. Yetirmishli.,(2007). Crustal Attenuation within the Turkish Plateau and Surrounding Regions, *Bull. Seismol. Soc. Am.* 97: 151–161.

NEXT GENERATION, WAVEFORM BASED THREE-DIMENSIONAL MODELS AND METRICS TO IMPROVE NUCLEAR EXPLOSION MONITORING IN THE MIDDLE EAST

Brian Savage[1], Daniel Peter[2], Brian Covellone[1] Arthur Rodgers[3], and Jeroen Tromp[2]

University of Rhode Island[1], Princeton University[2], and Lawrence Livermore National Laboratory[3]

Sponsored by the Air Force Research Laboratory and the National Nuclear Security Administration

Award Nos. FA8718-08-C-0009[1,2] and DE-AC52-07NA27344[3]
Proposal No. BAA08-79

ABSTRACT

Improvements to current wave speed models of the Middle East requires confidence in sources and recordings, along with a methodology to directly improve 3D wave speed models. Recordings of seismic waves traversing the region from Tibet to the Red Sea are the principal metric in guiding improvements to the current wave speed model using adjoint waveform tomography. To avoid a mapping of source errors, including incorrect depths and faulting mechanisms, into the new wave speed model, a rigorous characterization of each source within the current wave speed model was undertaken. Source depths and paths near nodal planes are particularly error prone as small changes may severely affect the resulting wavefield. As these sources have been evaluated, regions requiring refinement will be highlighted using adjoint tomography methods based on spectral-element simulations (Komatitsch and Tromp, 1999).

Following source evaluations using teleseismic body waves (Kikuchi and Kanamori, 1982) and regional surface and body waves (Zhao and Helmberger, 1994), we reinterpreted a large, well-recorded subset of 201 events (1990–2007) through a direct comparison between data and synthetics based upon a centroid moment tensor inversion (Liu et al., 2004). Evaluation was done using both a 1D reference model (Dziewonski and Anderson, 1981) at periods greater than 80 seconds and a 3D model (Kustowski et al., 2008) at periods of 25 seconds and longer. The final source reinterpretations within the 3D model define a source database and the initial starting point for the adjoint tomography. Transitioning from a 1D to 3D wave speed model shows dramatic improvements when comparisons are done at shorter periods (25 s). Synthetics from the 1D model were created through mode summation while those from the 3D model were created using the spectral-element method.

To further assess errors in source depth and focal mechanism, comparisons between the three methods were made. These comparisons help to identify problematic stations and sources that may bias the final solution. Estimates of standard errors were generated for each event's source depth and focal mechanism to identify poorly constrained events. The final, well-characterized set of sources and stations is currently used to iteratively improve the wave speed model of the Middle East. After a few iterations during the adjoint inversion process, the sources will be reexamined and relocated to further reduce mapping of source errors into structural features.

Finally, efforts continue to update the current wave speed model using adjoint tomography. Initial inversion iterations have guided the measurements, model smoothing and filtering to produce the accurate and relevant improvements to the initial model. Event kernels can now be computed "quickly" at the n-th iteration and invert for a new $(n+1)$-th wave speed model of the Middle East. As demonstrated with previous adjoint tomography experiments (Tape et al., 2009), each iteration only improves the model progressively, and relies on successive iterations to reduce variance and improve the fitting of data to synthetics. Exploiting the source database with multiple adjoint inversions at shorter and shorter periods will refine the wave speed structures of the Middle East.

OBJECTIVES

Improving models of 3D wave speeds within the greater Middle East, from the Turkish Plateau to the eastern edge of Tibet (Figure 1), will enhance our ability to discriminate between natural and man-made events, locate these events, identify source depths, and determine magnitudes. Current wave speed models of the Middle East will be improved through an adjoint tomography method (Tromp et al., 2005) by a comparison of seismic phase and amplitude data. The initial step towards our adjoint tomography model involves the development of a database of relocated and characterized set of sources and waveforms. Events were re-inverted in 1D and 3D wave speed models and agree fairly well with currently available solutions and across wave speed models. The adjoint tomography method (Tromp et al., 2005) uses full seismic waveforms as a measure of misfit of the current model iteration. Differences between data and synthetics are used to create adjoint sources and generate sensitivity kernels required to update the wave speed model. A first set of test iterations towards an improved wave speed model of the Middle East will be presented here and a final model built on the foundation of the seismic waveform database will be distributed to the community.

RESEARCH ACCOMPLISHED

Event Characterization

Using the CMT inversion methodology of Liu et al. (2004), ~200 events in the Middle East were re-characterized using the 1D PREM model (Dziewonski and Anderson, 1981) at periods of 80 seconds and longer and within a 3D wave speed model (S2.9EA) (Kustowski et al., 2008) at much shorter period, 25 seconds. Initially, the procedure of processing large amounts of data, comparing these to synthetics, and reevaluating the source parameters and locations needed to be assessed and streamlined. This procedure, accomplished through the 1D long period modeling, needed to be straightforward and able to avoid problematic areas, as the initial 3D event re-evaluation requires more demanding computational efforts. Further source evaluations in updated wave speed models will occur two to three more times during the adjoint inversion. Problematic events and stations were subsequently screened out within this procedure before building the final waveform data set. Problematic stations and waveforms with dropouts and poorly characterized amplitude responses can negatively influence a CMT inversion, and these stations were removed before any 3D CMT inversions or adjoint inversions were performed.

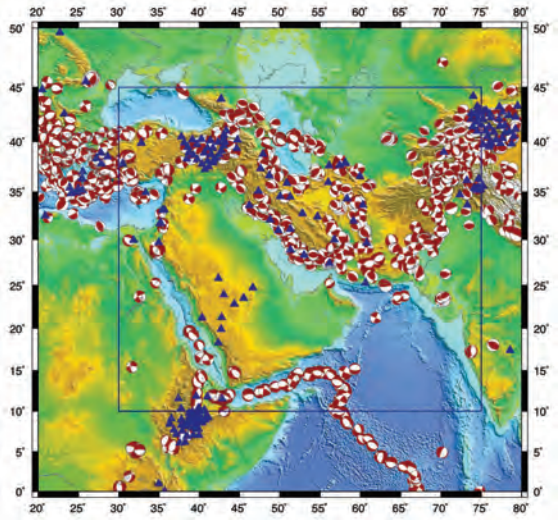

Figure 1. Map of the available sources and stations in the Middle East for the adjoint tomography inversion.

Solutions using the long period 1D model are shown in Figure 2 (left) and within the 3D wave speed model (right). Faulting parameters agree reasonably well with those from the Global CMT Project, but depths are biased towards the surface when using the 1D model. This is most likely due to the 3D model corrections used at the Global CMT Project or reduced depth sensitivity when using longer period records. However, depths compare well between the 3D solutions and the Global CMT Project. Solutions match reasonably well when using either 1D or 3D wave speed models, but the 3D wave speed synthetics use a much smaller minimum period, 25 seconds, that incorporates complicated body wave arrivals and more pronounced surface wave arrivals and dispersion.

Figure 3 displays vertical component data (black) and synthetics (red) for a single event on 2005/03/13 in the southern Zagros Mountains recorded by two stations (KURK.II and KIEV.IU) to the north. Synthetics from the 1D PREM model at long and short periods are displayed in the first two columns of Figure 3. At long periods, the data and synthetics are relatively simple, with identifiable, small amplitude body wave arrivals and much larger amplitude, fundamental mode, surface wave arrivals. Synthetics match the absolute arrivals times rather well, but

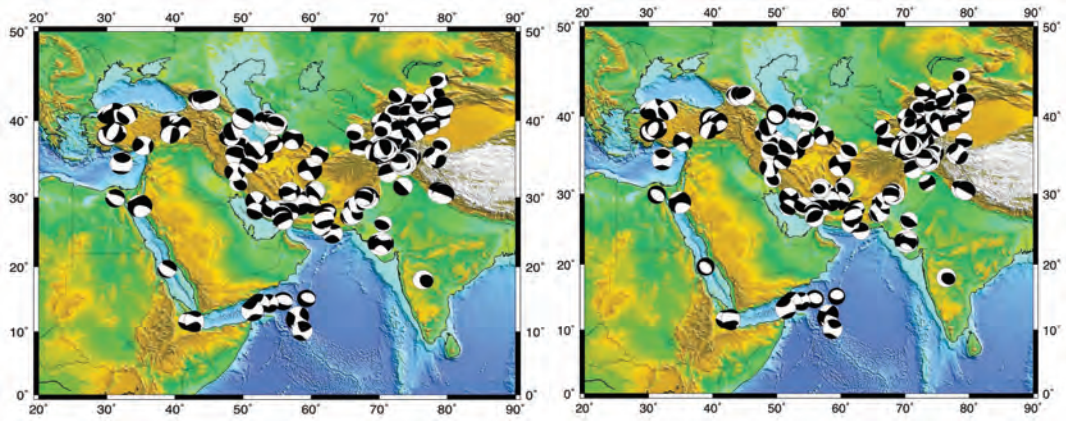

Figure 2. Comparison of solutions using a 1D wave speed model at 80 s, left, and the 3D model at 25 s, right. Fault plane solutions are constrained to be zero trace and the depth is also solved for. Solutions do not change when using either model, but depths do show systematic variation. The fault plane solution catalog includes ~200 events.

the amplitudes differ for each station at the longest period, 80 seconds. As shorter periods are included, middle column at 25 seconds, the 1D synthetics display simple arrivals but the data starts to show dispersion due to traversing the continent (see 800 to 1100 seconds for station KURK.II.LHZ and 1000 to 1400 seconds for station KIEV.IU.LHZ). Body wave arrivals also show more complex propagation as compared to the 1D synthetics, including larger amplitudes and longer duration coda (see 600 to 700 seconds for KURK.II.LHZ and 700 to 900 for KIEV.IU.LHZ in Figure 3 middle column). Simulations using the S2.9EA model (Kustowski et al., 2008) model reproduce the recorded data more closely than the 1D model at 25 seconds, Figure 3 right column. Use of the 3D wave speed model provides a more robust, shorter period estimation of the faulting parameters without losing the essential, long period estimate of the moment / magnitude. The more complex propagation paths, represented by the waveform coda in the data and now the synthetics, do not influence the estimates of source epicenter, faulting parameters, and more importantly source depth.

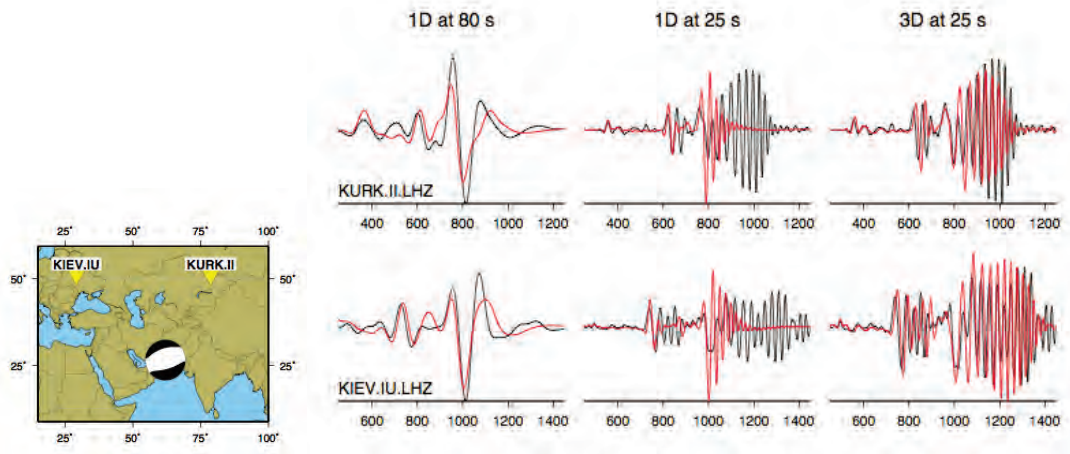

Figure 3. Comparison of vertical data (black) and synthetics (red) at 80 s and 25 s using a 1D and 3D wave speed model. The event and stations are located on the map, left. Use of the 3D wave speed model improves the match between the data and synthetics, specifically the body wave arrivals and the surface wave dispersion.

Adjoint Inversions and Model Updates

Using the discrepancies between the observed and synthetic seismograms, an event kernel can be constructed for each source solution using the adjoint method (Tromp et al. 2005). The sum of all these event kernels guides model updates of the current iteration. Measurements are made automatically between the data and synthetics using the Flexwin tool (Maggi et al., 2009), creating isolated data windows and metrics that are then used in the creation of the adjoint source. Windows, and their adjoint sources, are not constrained to any specific seismic phase or time window and only use well matched data-synthetic pairs. Adjoint sources along with the reconstructed, full synthetic wavefield are propagated in reverse time through the current iteration wave speed model to identify locations in the model requiring improvement. Interactions between the adjoint sources and the time-reversed wavefield, integrated over time, generate kernels specific to each measurement, e.g., a simple difference between the data and synthetics. Such kernels can be created using individual, isolated measurements or for each event with a large number of back-propagated adjoint sources to create event kernels. Event kernels are then summed volumetrically to produce Frechet derivates which are used to update the wave speed model.

In a first attempt, our updates to the wave speed model use a steepest descent method with tight controls on the magnitude of the update. Examples of the first two adjoint iterations to the shear wave speed model are displayed in Figure 4. The maximum change in the model update is limited to 3% based on comparisons between data and synthetics from a set of test events not used in the inversion. The shear wave speed model oscillates between the first and second inversion, Figure 4. This is most likely due to the improvement methodology, smoothing the largest differences between data and synthetics, which dominate the model update. With each iteration of these initial tests, finer scale structure begins to appear and the large-scale oscillations disappear. Successive iterations also introduce higher frequencies into the inversion not present during previous iterations.

Total updates for the shear wave speed relative to the initial model are displayed in Figure 5 with a maximum change of 5%. The oscillation seen in Figure 4 is not apparent in the total model updates indicating its source is most likely the removal of the largest data/synthetic discrepancies. As with Figure 4, more updates provide finer structure as higher-frequency signals are added to the inversion. The total misfit between the data and synthetics as measured by metrics from FLEWIN (time shift, amplitude ratio, and cross-correlation value) all show progressive

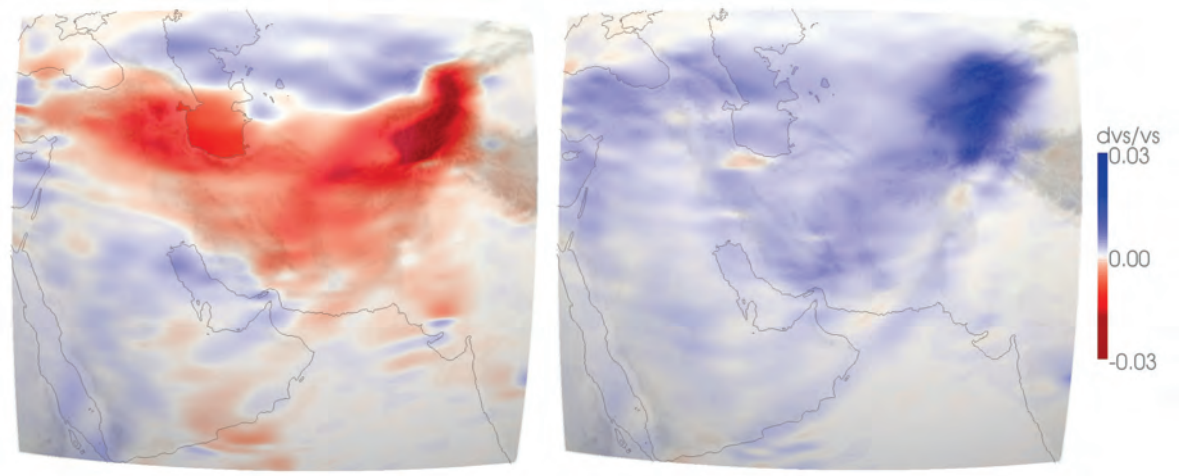

Figure 4. Adjoint model iteration updates 1 and 2, left and right, for the shear wave speed at 50 km depth. Maximum update value shown is +- 3% with blue indicating increases in wave speed.

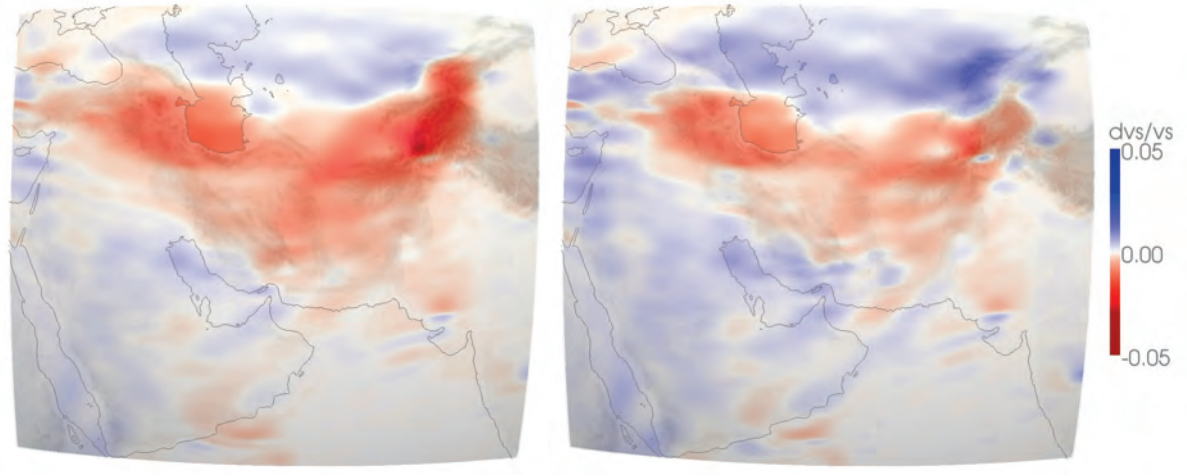

Figure 5. Adjoint model iterations 1 and 2, left and right, for the shear wave speed at 50 km depth relative to the initial 3D model. Maximum difference shown for updates is +- 5% with blue indicating faster wave speeds.

improvement to the synthetics relative to the data for each iteration.

A comparison between the total model updates and the initial model (S2.9EA) perturbations show similar features, see Figure 6. The initial model in central Asia at 50 km depth shows faster wave speeds caused primarily by thick, cold lithosphere. Further to the south, into the Zagros Mountains where a large amount of continental deformation and crustal thickening is occurring, the wave speeds are substantially slower. This Asian north-to-south, fast-to-slow wave speed pattern in the initial model is mirrored in the second model iteration, right panel Figure 5. Similar behavior was identified in other finite-frequency tomography experiments (Montelli et al., 2004). Wave speed perturbations in the initial model are amplified when using sensitivity kernels based on a finite-frequency approach rather than an approximation, either classical ray theory or surface wave sensitivities kernels.

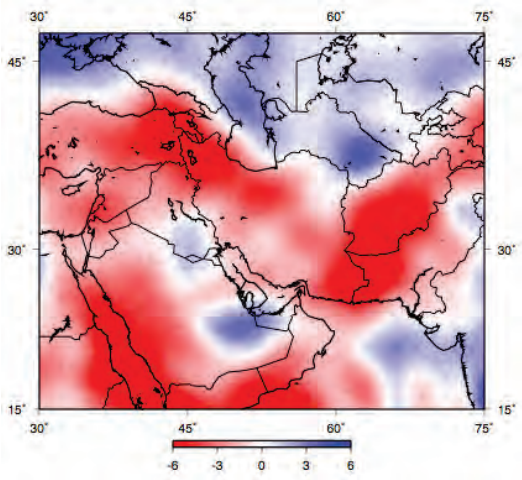

Figure 6. Initial Model shear wave speed variations +- 6% compared to the average value at 50 km depth.

Updates to the model also include density and compressional components. Compressional updates are shown in Figure 7; density is not shown. The initial 3D compressional wave speed model was scaled in the initial model from the 3D shear wave speed by a constant factor. Shear wave speeds in S2.9EA were derived from a large number of Love, Rayleigh, and shear body waves and was not directly constrained by seismic data. A comparison between the compressional adjoint results and the initial model can be difficult as the ratio between shear and compressional wave speeds can vary due to

chemistry. All adjoint iterations for compressional wave speeds show a much slower upper mantle beneath much of the Middle East than indicated by S2.9EA. Updates to the model at long wavelengths for these initial iterations are

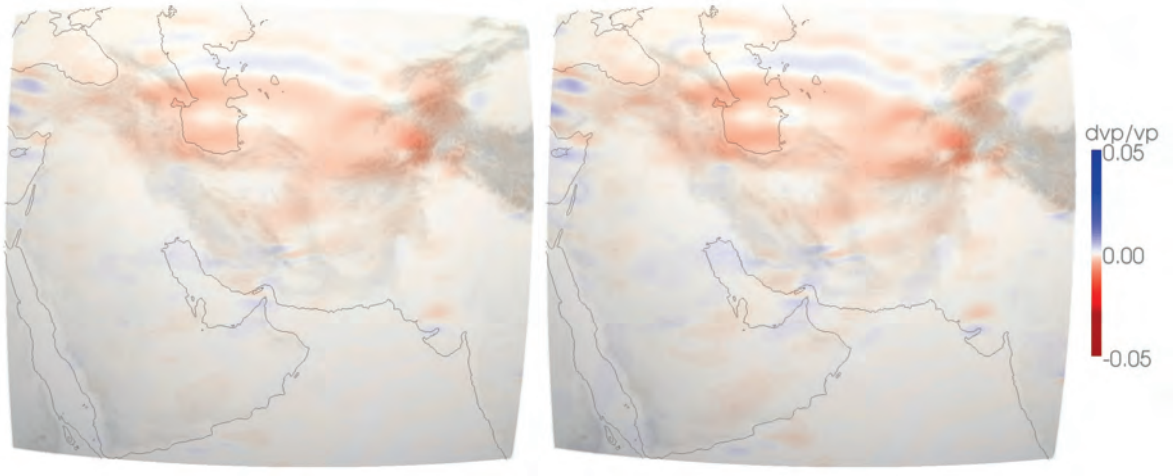

Figure 7. Compressional wave speed updates, same as for Figure 5.

predominately controlled by Rayleigh waves (shear and compressional surface wave) as the initial S2.9EA model fit the Love waves (shear only surface waves) better.

CONCLUSIONS AND RECOMMENDATIONS

Initial adjoint iterations to update a wave speed model of the Middle East have shown improvements to the model based on data / synthetic comparisons and expected behavior when introducing a finite-frequency tomographic approach. Before iterations began, a seismic waveform database with ~200 reinterpreted sources in the Middle East was compiled to avoid the mapping of source errors into wave speed structure. All sources in the database agree with previously published solutions and between the methodologies used: CAP (Zhao and Helmberger, 1994), teleseismic (Kikuchi and Kanamori, 1982) and a CMT inversion (Liu et al., 2004). Initial comparisons between data and synthetics computed from the initial 3D model S2.9EA (Kustowski et al., 2008) at 25 seconds and longer show reasonable agreement and a general improvement over the 1D PREM model (Dziewonski and Anderson, 1981).

To further improve the fit between data and synthetics, the adjoint inversion methodology was implemented to iteratively update the 3D wave speed model (Tromp et al., 2005). Following an initial set of iterations, the wave speed model was updated in a manner consistent with the finite-frequency tomographic techniques and the constraints on the initial wave speed model. Regions of wave speed perturbations have increased in magnitude from the initial to the second iteration as physics of wave propagation were incorporated into the inversion; see, e.g., the northern portion of the model in stable Asia (Figure 5, shear component). Compressional wave speed estimates also improved from increased use of Rayleigh waves and relaxing constraints between shear and compressional wave speeds. Our recommendations for a robustly constrained 3D wave speed model in the Middle East include using quality controlled seismic waveform data from well-constrained sources and use of a physics based tomographic technique to improve upon existing 3D models.

REFERENCES

Dziewonski, A., and D. Anderson (1981). Preliminary reference Earth model, *Phys. Earth. Planet. Int.* 25: 297–356.

Kikuchi, M., and H. Kanamori (1982), Inversion of complex body waves, *Bull. Seismol. Soc. Am.* 72: (2), 491–506.

Komatitsch, D., and J. Tromp (1999). Introduction to the spectral-element method for 3-D seismic wave propagation, *Geophys. J. Int.* 139: 806–822.

Kustowski, B., G. Ekstrom, and A. Dziewonski (2008). The shear-wave velocity structure in the upper mantle beneath Eurasia, *Geophys. J. Int.* 174: 978–992, 10.1111/j.1365-246X.2008.03865.x.

Liu, Q., J. Polet, D. Komatitsch, and J. Tromp (2004). Spectral-Element Moment Tensor Inversions for Earthquakes in Southern California, *Bull. Seismol. Soc. Am.* 94: (5), 1748–1761, 10.1785/012004038.

Maggi, A., C. Tape, M. Chen, D. Chao, and J. Tromp (2009). An Automated time-window selection algorithm for seismic tomography, *Geophys. J. Int.* 178: (1), 257–281, 10.1111/j.1365-246X.2009.04099.x.

Montelli, R., G. Nolet, F. Dahlen, G. Masters, E. Engdahl, and S. Hung (2004). Finite-Frequency Tomography Reveals a Variety of Plumes in the Mantle, *Science* 303: (5656), 338–343.

Tape, C., Q. Liu, A. Maggi, and J. Tromp (2009). Adjoint tomography of the Southern California crust, *Science*, 325: 988–992.

Tromp, J., C. Tape, and Q. Liu (2005). Seismic tomography, adjoint methods, time reversal and banana-doughnut kernels, *Geophys. J. Int.* 160: (1), 195–216.

Zhao, L., and D. Helmberger (1994). Source estimation from broadband regional seismograms, *Bull. Seismol. Soc. Am.* 84: (1), 91–104.

SEISMIC VELOCITY ESTIMATION IN THE MIDDLE EAST FROM MULTIPLE WAVEFORM FUNCTIONALS: P & S RECEIVER FUNCTIONS, WAVEFORM FITTING, AND SURFACE WAVE DISPERSION

Mrinal K. Sen[1], Jay Pulliam[2], Utpal Dutta[3], Ranjana Ghosh[1], Rengin Gök[4], and Michael Pasyanos[4]

The University of Texas at Austin[1], Baylor University[2], University of Alaska, Anchorage[3], and Lawrence Livermore National Laboratory[4]

Sponsored by the National Nuclear Security Administration

Award Nos. DE-AC52-09NA29327 and DE-AC52-07NA27344
Proposal No. BAA09-58

ABSTRACT

We demonstrated that SPL waveform data, together with associated phases, are able to constrain crustal and upper mantle seismic wave velocity structures. Forward modeling is done using a reflectivity algorithm and optimization is carried out using an algorithm called very fast simulated annealing (VFSA). The code runs efficiently on multiple processors using MPI routines. The advantages of VFSA include

- It is derivative free and therefore, the objective function can be changed to include disparate datasets without any changes in the algorithm, and
- Models from multiple VFSA runs can be used to obtain estimates of uncertainty.

We are currently developing a new algorithm to derive crustal velocity structure by modeling SPL wavetrains, surface wave dispersion and receiver function data from collocated source-receiver pairs. Optimization is done using a three part objective function given by

$$Error = a_1 \| \mathbf{d}^{obs}_{SPL} - \mathbf{d}^{syn}_{SPL} \|_p + a_2 \| \mathbf{d}^{obs}_{dispersion} - \mathbf{d}^{syn}_{dispersion} \|_p + a_3 \| \mathbf{d}^{obs}_{receiverfucntion} - \mathbf{d}^{syn}_{receiverfucntion} \|_p, \quad (1)$$

where a_1, a_2 and a_3 are the relative weights of different data and p is the norm used to measure data misfit. The algorithm is very general in that the weights can change with iteration and p can take different values for the three different parts of the objective function. Note that the same model is used to compute synthetic SPL waveform, surface waves and receiver function data.

Since SPL calculation takes the longest, the reflectivity calculation is distributed over ray-parameters using MPI calls. On the other hand, one node each is allocated to compute surface wave dispersion and receiver function, resulting in efficient load balancing. The following issues are currently being investigated:

- Types of objective functions to be used,
- Values of weights assigned to different data types,
- Influence of different datasets on the derived model estimates.

The algorithm will be applied to data recorded at broadband seismic stations in the Middle East, an area of strategic interest and one for which there exist previous results of surface wave dispersion and receiver function m modeling. We have developed statistical tools, including estimates of the Posterior Probability Density (PPD) functions and parameter correlation matrices, which allow us to evaluate the uniqueness and physical feasibility of resulting models. These tools will allow us to evaluate the relative strength of constraints placed on model parameters by each type of data in addition to the portions of the model that are well- or poorly constrained.

OBJECTIVES

One goal of the BAA to which this proposal responds is to develop optimal procedures for the use of multiple datasets. Due to the inherent variability, inconsistency, and peculiarities of disparate datasets and the well-known nonlinearity and non-uniqueness associated with geophysical modeling, such procedures must include methods for evaluating the performance and contribution of each dataset to the final results.

Our approach makes use of quantitative assessment tools and a well-developed Bayesian approach to explore and evaluate each step of the modeling process, rather than to simply toss all constraints into a simultaneous fitting procedure to find the single solution that satisfies particular criteria. The procedure we propose, best characterized as velocity analysis via optimization, is analogous to velocity analysis in exploration seismology, rather than "inversion". It will provide quantitative error measures of structural parameter estimates that can then be translated to earthquake location errors, and thus guide seismologists toward the most effective and efficient ways to improve model reliability.

RESEARCH ACCOMPLISHED

We have made substantial progress in developing, testing, and applying the method for waveform modeling via global optimization described above (Gangopadhyay et al., 2007; Pulliam and Sen, 2005; Pulliam et al., 2006). Earlier we developed, with Lian-She Zhao and Cliff Frohlich, a VFSA-based inversion algorithm for P-wave receiver functions (Zhao and Frohlich, 1996; Zhao et al., 1996). Additional tools we developed include a fast, parallelized reflectivity code that incorporates anisotropic model parameters, additional global optimization methods based upon genetic algorithms, and numerous imaging algorithms.

Specifically with regard to waveform modeling: We developed a code that computes synthetic seismograms with a parallelized reflectivity method and fits the observed waveforms by global optimization. Our method also computes the Posterior Probability Density (PPD) function and correlation matrix, to evaluate the uniqueness of the resulting models, and the trade-offs between individual model parameters therein. We applied the code to determine the crust and upper mantle structure beneath permanent broadband seismic stations in Africa using teleseismic earthquakes (M 5.5-7.0 and 200-800 km focal depth) recorded at these stations. We modeled the S, SP, SsPmP, and shear-coupled PL waves from these earthquakes and our P- and S-wave velocity models compare well with, and in some cases improve upon the models obtained from other existing methods. We obtained P- and S-wave velocities simultaneously and our use of the shear-coupled PL phase wherever available improved constraints on the models of the lower crust and upper mantle(Gangopadhyay et al., 2007).

During the past year, we have accomplished the following tasks listed below. Later we describe these in detail.

1. testing of waveform, surface wave dispersion and receiver function modeling codes using identical inputs,
2. development of a joint inversion code using all three different types of data sets,
3. extensive testing of objective functions appropriate for each data set,
4. efficient parallelization of the joint inversion code,
5. extensive testing with synthetic data, and
6. preliminary tests with a data set from the middle east.

Joint Modeling of Multiple Datasets

There are several advantages to jointly modeling multiple datasets. First, each data functional has unique sensitivities to Earth structure. For example, receiver functions are primarily sensitive to shear wave velocity contrasts and vertical traveltimes while surface wave dispersion measurements are sensitive to vertical shear wave velocity averages (Julia et al., 2000). Full waveform modeling of S, Sp, SsPmP phases, in contrast, are more sensitive compressional wave velocity contrasts and vertical traveltimes; adding SPL to the modeling improves senstivity to the uppermost mantle shear wave structure and to velocity contrasts across the Moho (Gangopadhyay et al., 2007). The amplitudes and signal-to-noise characteristics of waves that produce these data functionals depend on several factors, including epicentral distance, event focal depth, fault mechanism and radiation patterns, source time function, properties of the intervening Earth structure (including attenuation, low velocity zones, velocities, heterogeneity, and anisotropy), and characteristics of the recording seismometer. Since regions of high seismicity are highly restricted, many stations are not well situated to record appropriate events. An algorithm that incorporates multiple data types is more widely applicable than one that relies solely on a single type.

However, with these advantages come some disadvantages. For example, combining disparate data types requires great care in their treatment and assessment (Roy et al., 2005). Benefits of additional data may be null if the method used to model them preferentially fits one type. Or, worse, minimizing an inappropriate criterion in conjunction with

incompatible data may "split the difference" between them to choose a model that is wholly inaccurate and inappropriate for its intended purpose. If the model is to be used for regional or local earthquake locations, for example, it would be a mistake to rely on the best fit to surface wave dispersion. The judgment and experience of seismologists who keep a clear eye on their goal is critical, and this experience must be combined with rigor in the computational modeling. This experience and judgment can be incorporated after the fact, as is sometimes the case with, for example, the smoothing applied to 3D tomographic models but it is usually better to acknowledge the "prior" explicitly at the outset. This is one advantage of the Bayesian approach that we propose here. While priors are sometimes referred to pejoratively as "bias", their explicit statement during the formulation of the modeling algorithm forestalls serious criticism and enables a clear, quantitative discussion of "bias".

Next, as a general rule of thumb, a greater number of data functionals incorporated into modeling will result in a broader range of model parameter sensitivities, and it will be less likely that a linear inversion approach will be adequate. This is unfortunate because linear approaches are much more tractable and straightforward than nonlinear methods. But only a broad search of the model space will demonstrate whether a linear approach is valid. Non-linear global optimization algorithms require no change in the algorithm to include multi-part objective function with different norms. A variety of methods for nonlinear inversion are now available and the only real cost for conducting a thorough search and finding the single best-fitting model is in computational effort and complexity. The downside is that theoretically exact methods for assessing model uncertainties and model reliability are not generally tractable, and approximate methods result in significantly greater cost and complexity than is required to find the best-fitting model alone. Nevertheless, our previous work has demonstrated that useful methods are indeed tractable, and the method we propose will add only marginal increases in computation time.

While surface wave dispersion and receiver functions have been modeled jointly (Ammon et al., 2005; Ammon et al., 2004; Cakir and Erduran, 2004; Chang et al., 2004; Dugda and Nyblade, 2006; Herrmann et al., 2001; Julia et al., 2000; Julia et al., 2005; Lawrence and Wiens, 2004; Ozalaybey et al., 1997; Tkalcic et al., 2006), no study has, to our knowledge, incorporated waveform constraints such as S, Sp, SsPmP, and Shear-coupled PL. Further, none has conducted a thorough, nonlinear assessment of the constraints provided by each functional.

Multi-Objective Optimization for Multiple Datasets

The primary goal of our current project is to develop a tool for estimating crustal structure that can explain surface wave dispersion, receiver function and full waveform modeling. Thus our optimization algorithm is expected to minimize misfit of each of the datasets using three different objective or cost functions. The process of optimizing systematically and simultaneously a collection of objective functions is called multiobjective optimization (MOO) or vector optimization. The general MOO is posed as follows:

$$\underset{\mathbf{m}}{\textit{Minimize}}\ \boldsymbol{F}(\mathbf{m}) = \left[\boldsymbol{F}_1(\mathbf{m}), \boldsymbol{F}_2(\mathbf{m}), ..., \boldsymbol{F}_{\boldsymbol{k}}(\mathbf{m})\right]^{\boldsymbol{T}}, \tag{2}$$

where **m** is the model vector, and *k* is the number of objective functions. The objective function is minimized subject to some constraints. In our application, we use standard constraints such as bounds and negativity.

Contrary to single-objective optimization, an MOO may be considered more of a concept than a definition. Typically, with noisy data there is no single global solution and it is often necessary to determine a set of points that all fit a predetermined definition for an optimum. This is commonly done using what is known as Pareto optimality (Pareto 1906) defined as follows.

Definition: A model **m*** belonging in the model space is said to be Pareto optimal if and only if there does not exist any other model **m** in the model space such that $\boldsymbol{F}(\mathbf{m}) \le \boldsymbol{F}(\mathbf{m}^*)$, and $\boldsymbol{F}_{\boldsymbol{i}}(\mathbf{m}) \le \boldsymbol{F}_{\boldsymbol{i}}(\mathbf{m}^*)$ for at least one function.

We often use a *Global criterion* in search for models belonging to Pareto set, which is a scalar function that mathematically combines multiple objective functions; it may or may not involve preference of one or the other.

Objective Function

We use the following objective function which outputs a single scalar value.

$$Error = a_1 \| \mathbf{d}^{obs}_{SPL} - \mathbf{d}^{syn}_{SPL} \|_p + a_2 \| \mathbf{d}^{obs}_{dispersion} - \mathbf{d}^{syn}_{dispersion} \|_p + a_3 \| \mathbf{d}^{obs}_{receiverfucntion} - \mathbf{d}^{syn}_{receiverfucntion} \|_p . \tag{3}$$

This general objective function allows for different measures of error and different weights to the datasets. There are at least three fundamental issues that we need to address:

1. What measures of error do we use? Can they be different for different datasets?
2. Can we use simple differences?
3. How do we choose the three weights?

Question (3) does not generally have a straightforward answer. The weights have to be determined by trial and error. One important consideration in defining the global objective function for MOO is to ascertain that no individual objective function introduces more impact than the others unless so desired. To address this, we use the following normalized objective function defined in Sen and Stoffa (1995)

$$\boldsymbol{Error} = 1 - \frac{2\sum \left| \boldsymbol{d}_{\boldsymbol{obs}}^{\boldsymbol{i}} - \boldsymbol{d}_{\boldsymbol{syn}}^{\boldsymbol{i}} \right|^{\alpha}}{\sum \left| \boldsymbol{d}_{\boldsymbol{obs}}^{\boldsymbol{i}} + \boldsymbol{d}_{\boldsymbol{syn}}^{\boldsymbol{i}} \right|^{\alpha} + \sum \left| \boldsymbol{d}_{\boldsymbol{obs}}^{\boldsymbol{i}} - \boldsymbol{d}_{\boldsymbol{syn}}^{\boldsymbol{i}} \right|^{\alpha}}, \tag{4}$$

where the sum is taken over all the data points and the parameter α is equivalent to norm.

Initially we chose α=1 for all three objective functions. Note that the SPL and receiver function make use of waveform data while the dispersion curve is fairly simple. The objective function corresponding to the surface wave disersion is smoothly varying and therefore, we chose α=0.5 to introduce more sensitivity. With these choices of α values and normalized objective functions as defined in the above equation, we employ equal weights to all three parts of the objective function.

There are several advantages to jointly modeling multiple datasets. First, each data functional has unique sensitivities to Earth structure. For example, receiver functions are primarily sensitive to shear wave velocity contrasts and vertical traveltimes while surface wave dispersion measurements are sensitive to vertical shear wave velocity averages (Julia et al., 2000). Full waveform modeling of S, Sp, SsPmP phases, in contrast, are more sensitive compressional wave velocity contrasts and vertical traveltimes; adding SPL to the modeling improves senstivity to the uppermost mantle shear wave structure and to velocity contrasts across the Moho (Gangopadhyay et al., 2007). Mutually satisfying constraints imposed by the three datasets may constrain a larger subset of model parameters than a single set alone, resulting in a single model that better represents the true structure.

Optimization and Parallelization

Having defined the objective function, we employ VFSA for optimization (Pulliam and Sen, 2005; Sen and Stoffa 1995). Note that VFSA causes no difficulties since we do not require computing derivatives. As used in Pulliam and Sen (2005), we use a parallel optimization code for MOO as well. Note that the most expensive computation element is that of SPL waveform by the reflectivity method and therefore, the reflectivity computation is distributed over multiple nodes. Since surface wave dispersion and receiver function computations are fairly fast, we distribute those to one node each and thus achieve reasonable load balancing.

Results from a Synthetic Experiment

We generated synthetic S-waveform for three component seismograms, surface wave dispersion and receiver function for a simple six layer model. This dataset is then used as observation for optimization. Our model's search parameters are Vp, Vs, and layer thickeness for the six layers. We use search bounds for the three model parameters, as shown in Fig 1(a). Figures 1, 2, and 3 show results from our inversion experiments using three different combination of weights, namely, (1) receiver function 0, dispersion 0, SPL 1; (2) receiver function 0, dispersion 1, SPL 1, and (3) receiver function 1, dispersion 0, SPL 1.

Thus Figure 3 corresponds to the case where all three datasets are weighed equally. The results show a mean model and posterior variances corresponding to different model parameters (see Pulliam and Sen 2005 for more details on this). Note that we run multiple VFSA with different starting models and use all the models to characterize uncertainty. In other words, we attempt to sample many models from the Pareto set. The impact of different weights is fairly obvious in the three figures. It seems SPL data has the most impact; by setting SPL=1 and the other two to zeros, we are able to obtain reasonable fit of surface wave dispersion and receiver function. When all the weights are set equal to one, we are able to match all three datasets and reproduce the model fairly well.

CONCLUSIONS AND RECOMMENDATIONS

We have developed a parallel VFSA based multi-objective optimization code that can be used to obtain crustal velocity structures by modeling SPL waveform, receiver function and surface wave dispersion data. The code has been tested successfully with a simple synthetic example. We will continue to test our code using more realistic synthetics and will then apply extensively to several datasets from the Middle East.

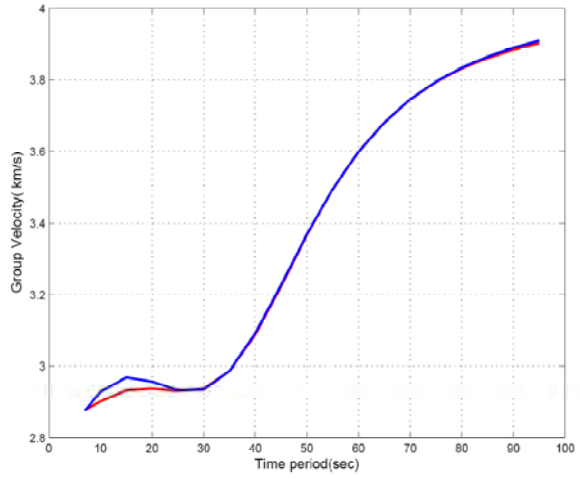

(a)

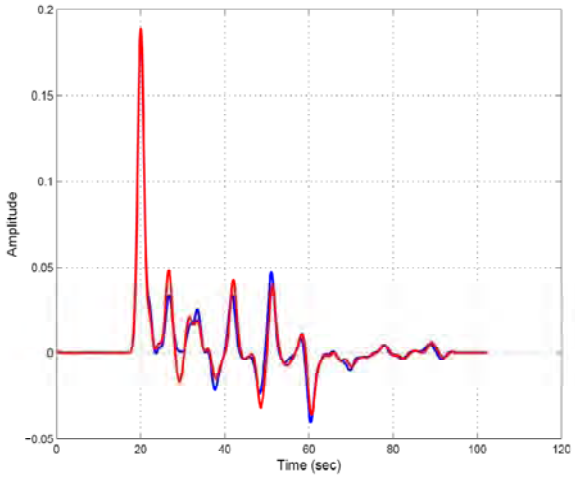

(c)

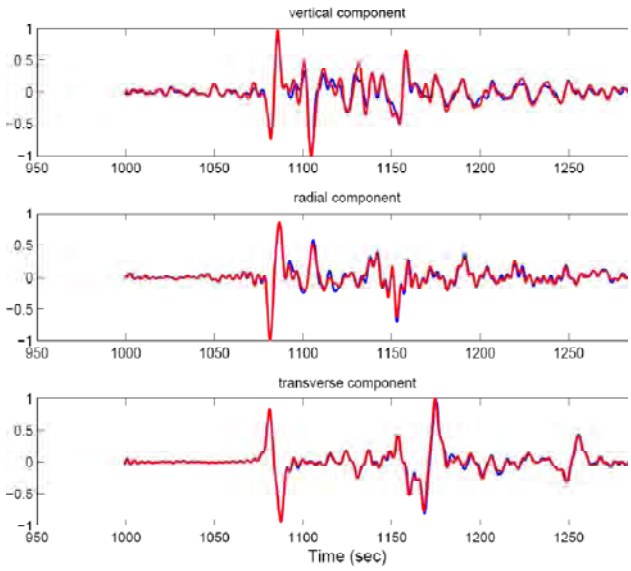

(b)

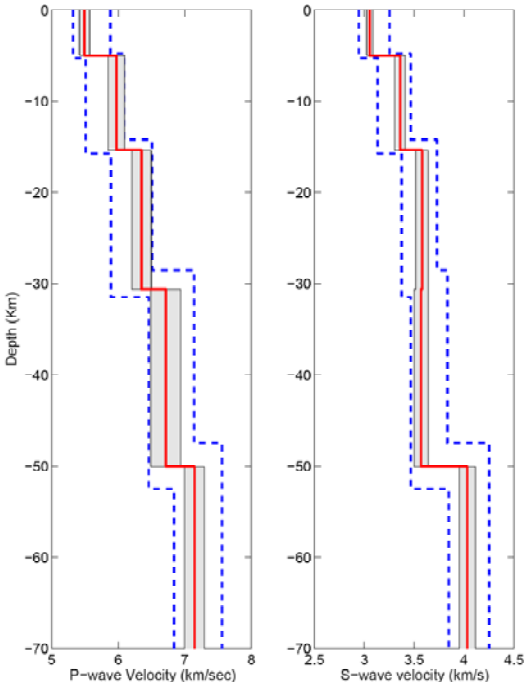

(d)

Figure 1. Results from joint inversion code: the weight for SPL data was set equal to one; the other two weights are zero. (a) surface wave dispersion, (b) SPL waveforms, (c) receiver function, (d) model fit. In figures (a)-(c), blue is the observed data and red the synthetic data. In figure (d), blue dotted lines are the model bounds; mean estimated model is the red line and the grey area is the uncertainty in the estimated model.

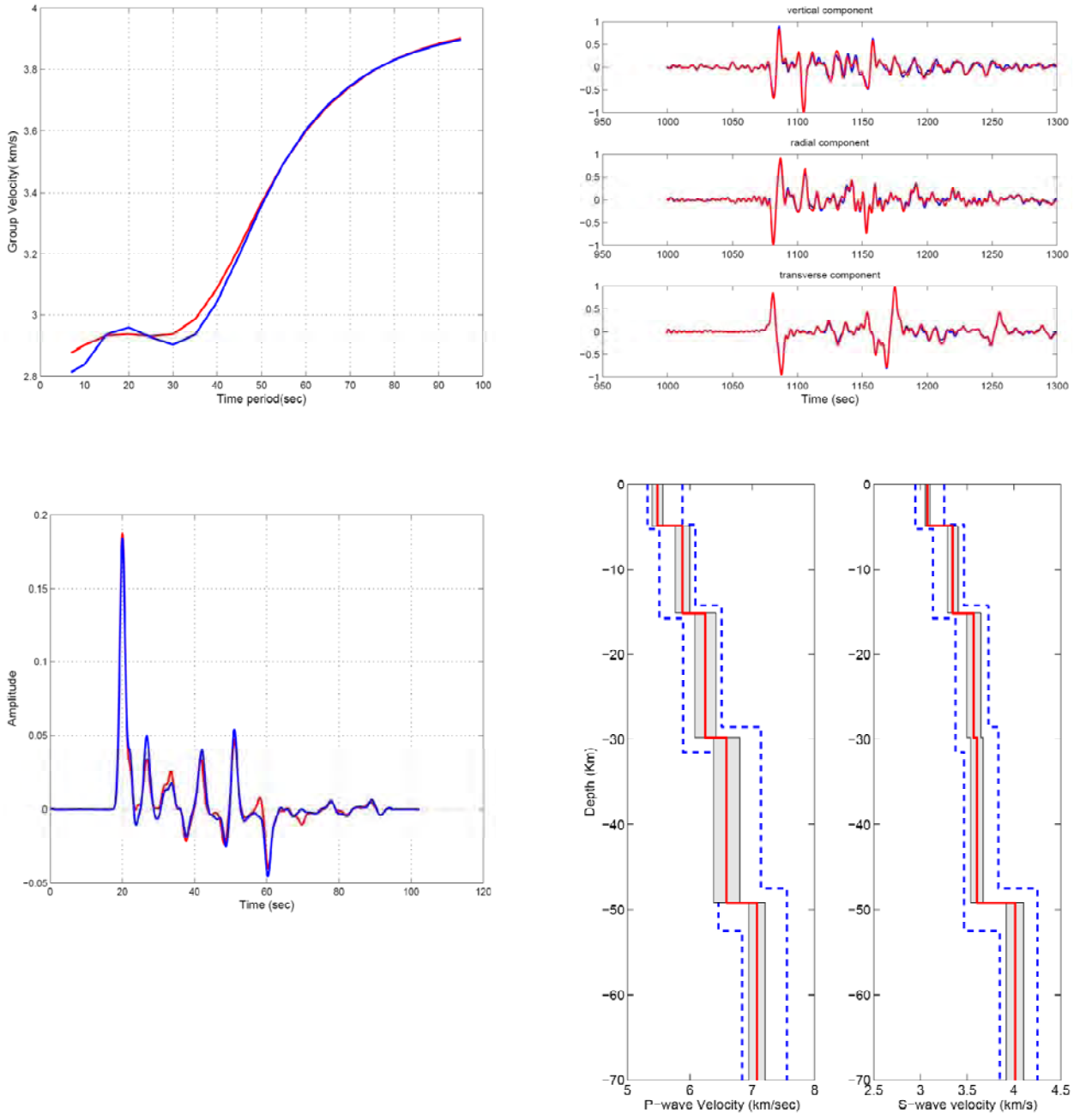

Figure 2. Results from joint inversion code: the weights for SPL and receiver function data were set equal to one only. (a) surface wave dispersion, (b) SPL waveforms, (c) receiver function, (d) model fit. In Figures (a)-(c), blue is the observed data and red the synthetic data. In Figure (d), blue dotted lines are the model bounds; mean estimated model is the red line and the grey area is the uncertainty in the estimated model.

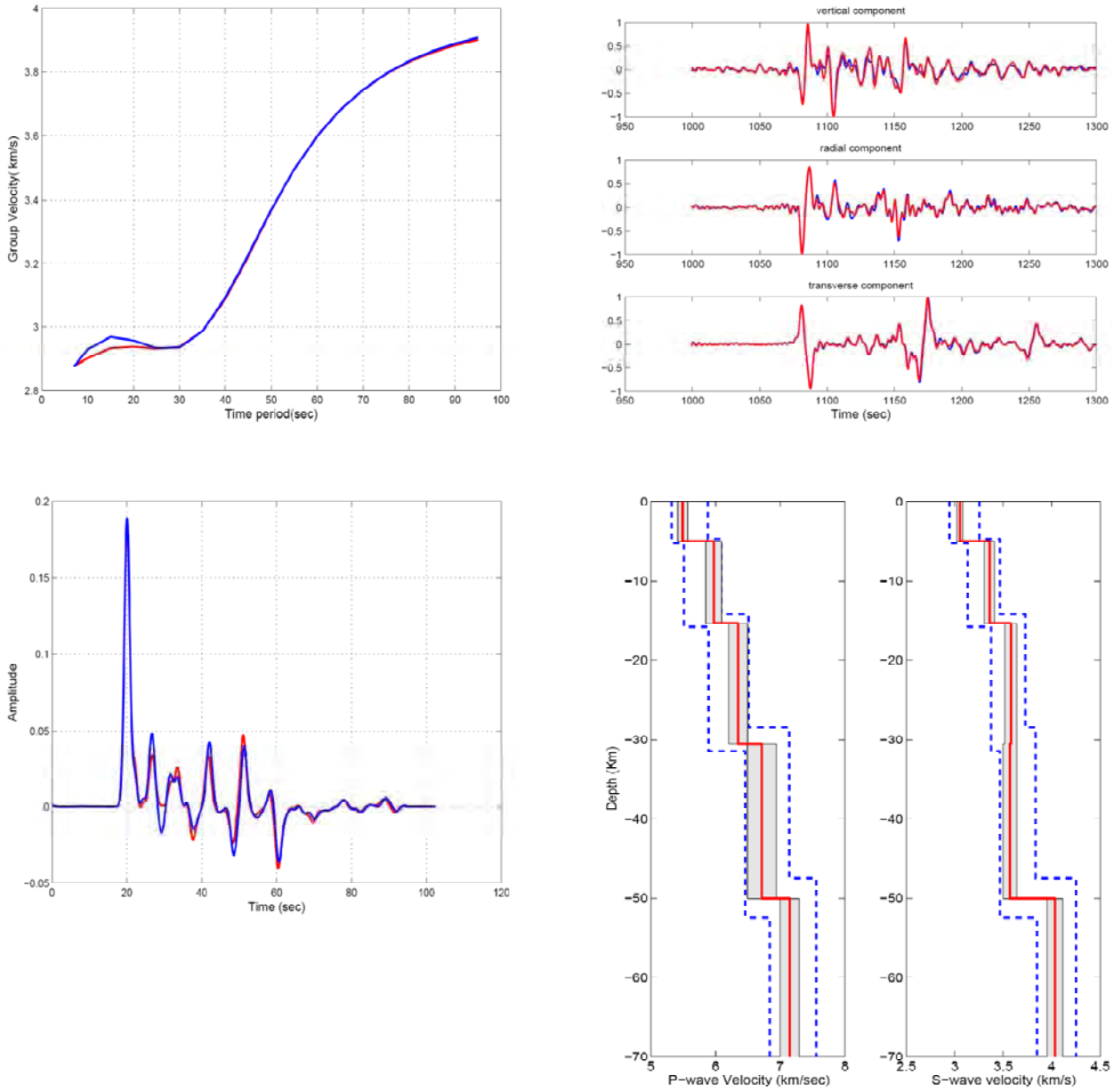

Figure 3. Results from joint inversion code: all threee weights were set equal to one. (a) surface wave dispersion, (b) SPL waveforms, (c) receiver function, (d) model fit. In Figures (a)-(c), blue is the observed data and red the synthetic data. In Figure (d), blue dotted lines are the model bounds; mean estimated model is the red line and the grey area is the uncertainty in the estimated model.

REFERENCES

Ammon, C.J., M. Kosarian, R. Herrmann, M. Payanos, W. Walter, W. Sevilla, and G. Randall (2005). Simultaneous Inversion of Receiver Functions and Surface-Wave Dispersion Measurements for Lithospheric Structure Beneath Asia and North Africa, in *Proceedings of the 27th Seismic Research Review: Ground-Based Nuclear Explosion Monitoring Technologies*, LA-UR-05-6407, Vol. 1, pp. 3–12.

Ammon, C.J., M. Kosarian, R. Herrmann, M. Payanos, W. Walter, and H. Tkalcic (2004). Simultaneous Inversion of Receiver Functions, Multi-mode Dispersion, and Travel-time Tomography for Lithospheric Structure Beneath the Middle East and North Africa, in *Proceedings of the 26th Seismic Research Review—Trends in Nuclear Explosion Monitoring*, LA-UR-04-5801, Vol. 1, pp. 17–28.

Cakir, O. and Erduran, M. (2004). Constraining crustal and uppermost mantle structure beneath station TBZ (Trabzon, Turkey) by receiver function and dispersion analyses. *Geophys. J. Int*., 158(3): 955-971.

Chang, S.-J., Baag, C.-E. and Langston, C. (2004). Joint analysis of teleseismic receiver functions and surface wave dispersion using the genetic algorithm. *Bull. Seismol. Soc. Am*. 94:(2): 691–704.

Dugda, M. and Nyblade, A. A. (2006). New constraints on crustal structure in eastern Afar from the analysis of receiver functions and surface wave dispersion in Djibouti. *Geological Society of London Special Publications*, 259: 239–251.

Gangopadhyay, A., Pulliam, J. and Sen, M. K. (2007). Waveform Modeling of Teleseismic S, SP, SsPmP, and Shear-Coupled PL Waves for Crust and Upper Mantle Velocity Structure Beneath Africa. Geophys. J. Int., 170: 1210–1226.

Herrmann, R. B., Ammon, C. J. and Julia, J. (2001). Application of joint receiver-function surface-wave dispersion for local structure in Eurasia, in *Proceedings of the 23rd Seismic Research Review: Worldwide Monitoring of Nuclear Explosions*, LA-UR-01-4454, Vol. 1, pp. 46–54.

Julia, J., Ammon, C.J., Herrmann, R.B. and Correig, A.M. (2000). Joint inversion of receiver function and surface wave dispersion observations. *Geophys. J. Int*., 143(1): 99-112.

Julia, J., Ammon, C. J. and Nyblade, A. A. (2005). Evidence for mafic lower crust in Tanzania, East Africa, from joint inversion of receiver functions and Rayleigh wave dispersion velocities, Geophys. J. Int.. Blackwell Science for the Royal Astronomical Society, the *Deutsche Geophysikalische Gesellschaft and the European Geophysical Society*, International, International, pp. 555.

Lawrence, J.F. and Wiens, D.A. (2004). Combined Receiver-Function and Surface Wave Phase-Velocity Inversion Using a Niching Genetic Algorithm: Application to Patagonia. *Bull. Seismol. Soc. Am*. 94: (3), 977–987.

Ozalaybey, S., Savage, M.K., Sheehan, A.F., Louie, J.N. and Brune, J.N. (1997). Shear-wave velocity structure in the northern Basin and Range province from the combined analysis of receiver functions and surface waves. Bull. *Seismol. Soc. Am*. 87: (1): 18–199.

Pareto, V. (1906) Manuale di Economica Politica, Societa Editrice Libraria. Milan; translated into English by A.S. Schwier as Manual of Political Economy, edited by A.S. Schwier andA.N. Page, 1971. New York: A.M. Kelley.

Pulliam, J. and Sen, M.K. (2005). Assessing Uncertainties in Waveform Modeling of the Crust and Upper Mantle, in *Proceedings of the 27th Seismic Research Review: Ground-Based Nuclear Explosion Monitoring Technologies*, LA-UR-05-6407, Vol. 1, pp. 152–160.

Pulliam, J., Sen, M. K. and Gangopadhyay, A. (2006). Determination of Crust and Upper Mantle Structure Beneath Africa Using a Global Optimization-Based Waveform Modeling Technique, in *Proceedings of the 28th Seismic Research Review: Ground-Based Nuclear Explosion Monitoring Technologies*, LA-UR-06-5471, Vol. 1, pp. 196–208.

Roy, L., Sen, M. K., Stoffa, P. L., McIntosh, K. and Nakamura, Y. (2005). Joint inversion of first arrival travel time and gravity data. *J. Geophys and Eng*, 2: 277–289.

Sen, M. K. and Stoffa, P. L. (1995). Bayesian inversion in geophysics, Union of Geodesy and Geophysics; XXI General Assembly, Boulder, CO, pp. 9.

Shibutani, T., Sambridge, M. and Kennett, B. (1996). Genetic algorithm inversion for receiver functions with application to crust and uppermost mantle structure beneath eastern Australia. *Geophys. Res. Lett*., 23: 1829-1832.

Tkalcic, H. et al. (2006). A multistep approach for joint modeling of surface wave dispersion and teleseismic receiver functions: Implications for lithospheric structure of the Arabian Peninsula. *J. Geophys. Res*., 111(B11311): 10.1029/2005JB004130.

Zhao, L.-S. and Frohlich, C. (1996). Teleseismic body waveforms and receiver structures beneath seismic stations. *Geophys. J. Int*., 124: 525–540.

Zhao, L.-S., Sen, M.K., Stoffa, P. and Frohlich, C. (1996). Application of very fast simulated annealing to the determination of the crustal structure beneath Tibet. *Geophys. J. Int*. 125: 355–370.

JOINT INVERSION OF CRUSTAL AND UPPERMOST MANTLE STRUCTURE IN WESTERN CHINA

Xiaodong Song[1], Zhen Xu[1], Lupei Zhu[2], and Yuming Zhou[2]

University of Illinois at Urbana-Champaign[1] and Saint Louis University[2]

Sponsored by the Air Force Research Laboratory

Award No. FA9453-10-C-0216
Proposal No. BAA10-55

ABSTRACT

In seismic inversion, trade-offs between model parameters are well known. To resolve the ambiguity and to improve resolution, a combination of different datasets that have sensitivities to different parameters is required, or a priori constraints have to be imposed. The objective of this research is to develop joint-inversion methods involving P travel times (including secondary P), receiver functions, and surface-wave dispersion measurements from ambient noise correlation and apply them to the western China region to obtain 3D models of P and S structures of the crust and upper mantle.

Our joint inversions are done in two steps. First, we jointly invert P travel-time datasets that include first-arriving Pg and Pn and secondary crustal direct P waves. This gives us a 3D model of crustal Vp, a Pn velocity map, a Moho depth map, and Pn station delays. Inclusion of secondary crustal direct P waves improves the resolution of lower crust, and the joint inversion allows the separation of crustal velocities and Moho depth variation. Second, we combine the P model and Pn station delays from the first step with receiver functions and Rayleigh-wave dispersion measurements to invert jointly for S wave structure and Moho depth. Adding well-constrained P model and Pn station delays will help the joint inversion of receiver functions and surface-wave dispersions to find the right S model when the crustal Vp/Vs ratio is not known, which is often the case.

This is the first year of the project. We report progress made on the following two areas: (1) development of joint-inversion methods and (2) new dispersion measurements and dispersion maps from a combination of both ambient noise data.

OBJECTIVES

The objective of this research is to develop joint-inversion methods involving P travel times, receiver functions, and surface-wave dispersion measurements from ambient noise correlation and to apply them to the western China region to obtain 3D models of P and S structures of the crust and upper mantle.

RESEARCH ACCOMPLISHED

Join Inversion Methods

Trade-offs between model parameters are well known in seismic inversions. To resolve the ambiguity and to improve resolution, a combination of different datasets that have sensitivities to different parameters is required, or a priori constraints have to be imposed. For example, it has long been recognized that the teleseismic P receiver functions are primarily sensitive to shear-wave velocity (Vs) contrasts and depth-velocity product and not the velocity alone (Ammon et al., 1990). On the other hand, surface waves are primarily sensitive to the vertical shear-velocity averages. Thus, joint inversion (or analysis) of receiver functions and surface-wave dispersions has now been commonly used to resolve depth resolution of Vs structure (e.g., Julia et al. 2000; Ozalaybey et al., 1997). Similarly, crustal thickness estimated using only the delay time of Moho P-to-S converted phase (Ps) relative to P at the receiver trades off strongly with crustal Vp/Vs ratio, which can be remedied using later converted phases (Zhu and Kanamori, 2000).

Our joint inversions are done in two steps. First, we jointly invert our P travel-time datasets, including first-arriving Pg and Pn, and secondary crustal direct P. This gives us a 3D model of crustal Vp, a 2D Pn velocity map, a Moho depth map, and Pn station delays. Second, we combine the P model and Pn station delays from the first step with receiver functions and Rayleigh-wave dispersions to invert jointly for S wave structure and Moho depth.

Step 1. Joint inversion of Pg, Pn, and secondary crustal P for crustal P velocities, Moho depths, and Pn velocities

We have recently designed an iterative scheme to invert jointly for the velocities of the whole crust and the Pn waves as well as the Moho depth and have found it to be highly effective (Xu and Song, 2009). The method uses crustal Pg waves, head waves Pn, and secondary direct P waves at distances greater than the Pn and Pg crossover distance. These secondary arrivals are often very energetic and are quite abundant in earthquake bulletins (Figure 1). The advantage of a joint inversion approach is several-fold. First, Pn waves and secondary P waves at distances greater than the crossover distance provide constraint on crustal velocity in the lower crust. Second, with the resolution of 3D P velocity structure of the whole crust, Moho depth variation can be separately parameterized and simultaneously solved in the inversion. Third, with improved determination of Moho depth, different types of P waves can be better separated in the inversion iterations, thus reducing the contamination of P waves in the crust from Pn waves.

The joint inversion is a highly iterative. The gist includes rejecting bad data and sorting out different phases (Pg, Pn, secondary crustal P), effective ray tracing, formulating joint inversion of velocities and Moho, iterative selection of data with the improved models, and treatments on the inversion process (derivation of 1D model, parameterization, regularization and smoothing, and minimizer and linear-system solver). We use a spherical-coordinate 3D ray tracer that is based on a modification of the pseudo-bending ray (PBR) tracing method proposed by Koketsu and Sekine (1998). The joint inversions are formulated as follows:

Residual for Pg wave traveling from event j to station k can be approximated in the following linear form

$$r_{jk} = T_{jk}^{obs} - T_{jk}^{pred} = \sum_n \left(-\frac{dl}{v} \right) \left(\frac{\Delta v}{v} \right). \quad (1)$$

Residual for Pn wave traveling from event j to station k can be approximated as

$$r_{jk} = T_{jk}^{obs} - T_{jk}^{pred} = \sum_{n1}\left(-\frac{dl}{v}\right)\left(\frac{\Delta v}{v}\right)_m + \sum_{n2}\left(-\frac{dl}{v}\right)\left(\frac{\Delta v}{v}\right)_r + \eta\Delta h_k + \Delta t_j, \quad (2)$$

where the first the term on the right-hand side is the mantle contribution, and the second term is the contribution of velocity perturbation in the crust of the receiver side. The third term is the contribution of Moho depth variation at the receiver side. The combination of the 2nd and 3rd terms represents the station delay as in Equation 1. The last term is the event delay representing the uncertainty of event location, origin time, and Moho depth variation at the source side.

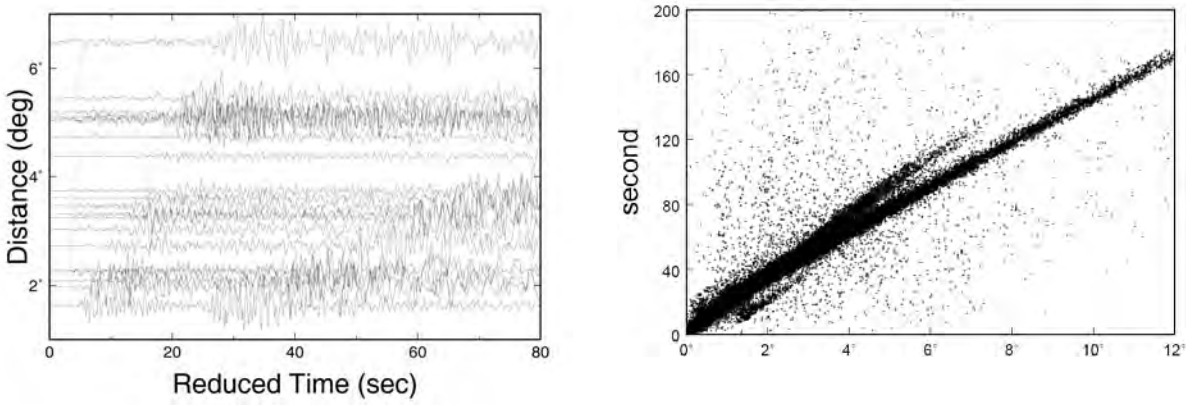

Figure 1. (Left) Example seismograms from Sichuan and Yunnan stations at regional distances. The travel time is reduced by 8 km/s. The lines show our travel-time picks. The nearly vertical line indicates first-arriving Pn waves. The second line indicates clear and strong secondary arrivals. The slowness is about 6.0 km/s. They are direct P waves turning at mid to lower crust. (Right) Raw travel-time picks from stations at Sichuan and Yunnan region. Data are from the Annual Bulletins of Chinese Earthquakes and Sichuan and Yunnan provincial earthquake bulletins. Note clear secondary arrivals, after Pn, at distances from 4 to 7 degrees.

Step 2. Joint inversion of receiver functions, surface wave dispersions, and Pn station delay for S velocities and Moho

The combination of receiver functions and surface-wave dispersions bridges some resolution gaps associated with each individual dataset (e.g., Julia et al. 2000; Ozalaybey et al., 1997). Figure 2 shows an example of joint inversion of receiver function and surface-wave dispersions at an INDEPTH station.

However, important ambiguity remains. In the P receiver function, the Moho P-to-S converted phase (Ps) is generally the strongest. The Moho depth determined from the Ps delay (relative to P) trades off strongly with crustal Vp/Vs ratio. Multiple converted phases would help resolve the ambiguity (Zhu and Kanamori, 2000), but they are usually more difficult to identify. Sensitivity tests (Figures 3–4) suggest that adding well-constrained P information will help the joint inversion of receiver function and surface-wave dispersion to find the right S model when the Vp/Vs ratio is not known, which is often the case. Two types of P information from Step 1 can be used in the joint inversion of receiver functions and surface waves for S structure. One is to use directly the crustal P velocities under the station derived from the 3D P model. Another type of P information is the Pn station delay time, which provides a constraint on Moho depth and average crustal velocity.

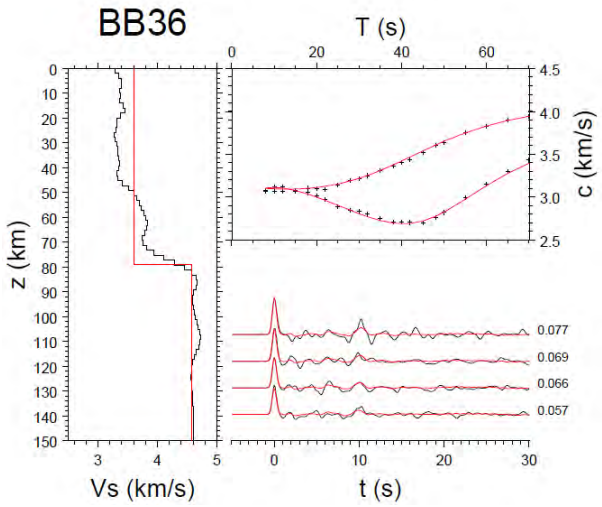

Figure 2. An example of joint inversion of receiver function and surface-wave dispersions. The left panel shows the S velocity model (black lines) from the inversion and the H-k stacking result (red lines). The right panel shows receiver function and surface-wave dispersion fits, black representing data and red representing prediction from the obtained S velocity model. The Vp/Vs ratios are fixed using the values obtained from the H-k stacking results.

A. Vp is known. **B**. Wrong Vp/Vs

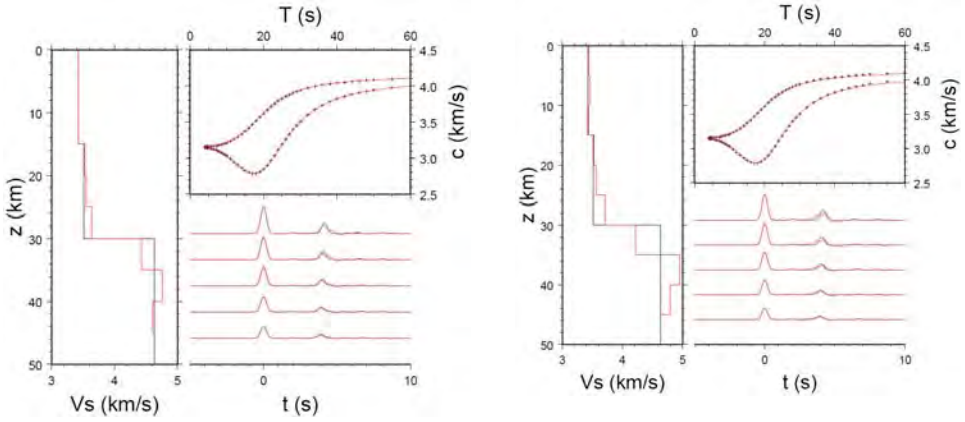

Figure 3. Tests on joint inversion of receiver functions and surface-wave dispersions, with and without prior knowledge of Vp structure. (A) Vp is set to the true values. Inverted Vs (red) matches the input model (black) relatively well. (B) Vp/Vs ratio is set to 1.7 (compared with the average 1.8 of the input model). Inverted Vs does not match the input as well as in (A), while the fits to dispersions (upper right) and receiver functions (lower right) are similar.

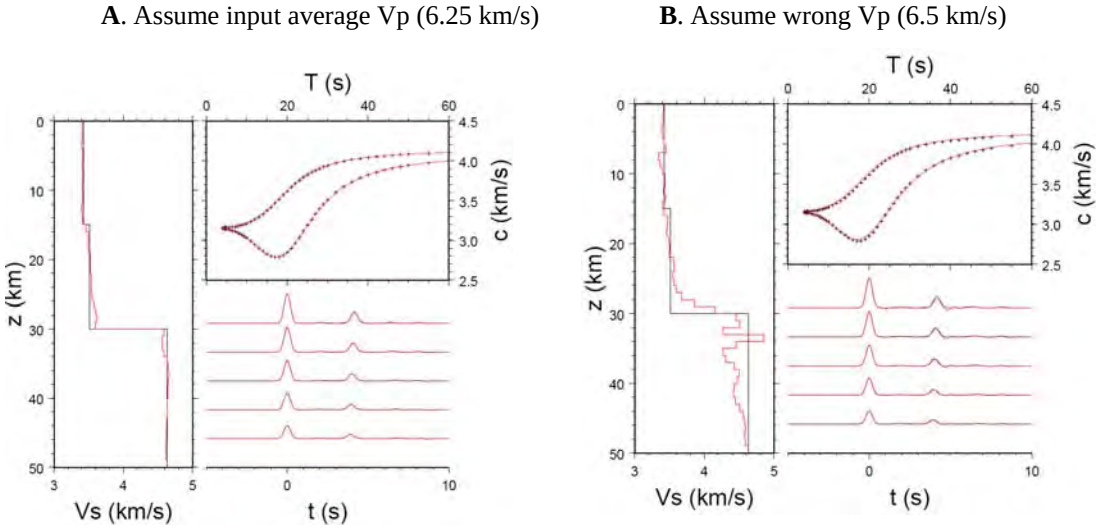

Figure 4. Synthetic tests on combining Pn station delay with receiver functions and surface-wave dispersion for a joint inversion. The input model is listed in Table 1. (A) Correct average crustal Vp (6.25 km/s) is assumed, which would yield the correct Moho depth (30 km) from Pn station delay. (B) Average crust Vp is assumed to be a wrong value of 6.5 km/s, yielding Moho depth of 33.3 km from Pn station delay. The S structure recovered in B is considerably poorer than in A and has a Moho (slightly less than 30 km) inconsistent with the Pn Moho (33.3 km).

New Dispersion Measurements and Dispersion Maps

Over the last few years, we have been working on ambient noise tomography of China (Zheng et al., 2008; Song et al., 2009). Recently, we have made a major effort to increase dispersion measurements by including stations over a long period of time and by including traditional earthquake data (Figure 5). For empirical Green's functions (EGFs), we have a total of 528 stations. The data are from 18 months of continuous data from the Chinese National Seismic Network (CNSN) (48 stations) and all the continuous broadband and long-period data in our study region available from 1991 to 2007 from permanent global and regional network stations as well as temporary Program for the Array Seismic Studies of the Continental Lithosphere (PASSCAL) stations from the Incorporated Research Institutions for Seismology Data Management Center (IRIS DMC). The earthquake data include events for all the stations from 155 earthquakes in our study region with depth shallower than 40 km and magnitude larger than 5.5 from 2000 to 2007. We also included event data recorded by CNSN stations for another 197 earthquakes with magnitude from 5.0 to 5.5 in the same depth range and time period.

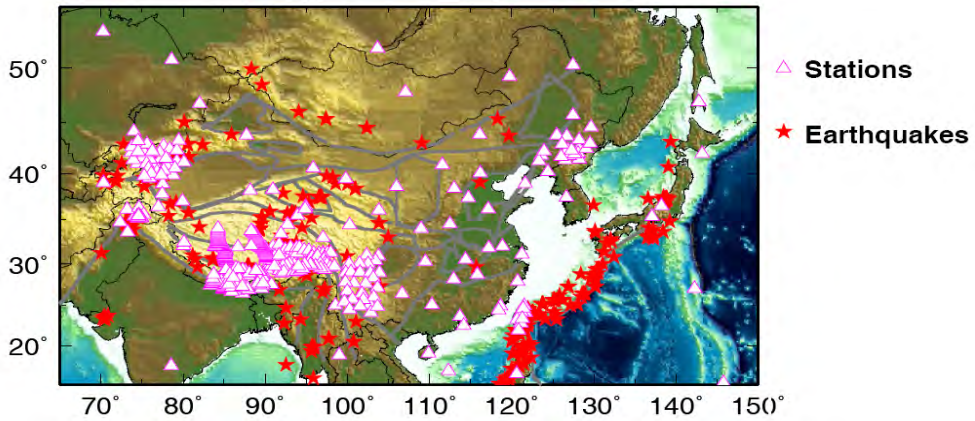

Figure 5. Distributions of stations (triangles) and earthquakes (stars) used in our study.

The EGFs are obtained using procedures from Bensen et al. (2007) and both group- and phase-velocity dispersion curves are measured from the EGFs using a frequency-time analysis (Levshin and Ritzwoller, 2001). For earthquake data, only group-velocity dispersion curves of earthquake data are measured in the same way. The new dataset has a maximum of ~35000 measurements for group velocity and ~22500 measurements for phase velocity at s period of 20 s (Figure. 6). We increase our total number of measurements by four times in this process.

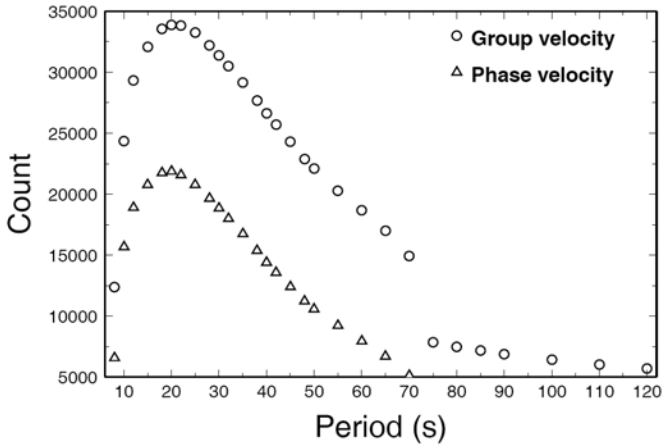

Figure 6. Distribution of Rayleigh group (open circles) and phase (open triangles) dispersion measurements for different periods. Note that the EGFs from both ambient noise correlation and earthquake data are included in Rayleigh group measurements up to 70 s. Only earthquake data are used for group dispersion measurements for periods longer than 70 s. To avoid initial phase ambiguity, earthquake data are not used in phase dispersion measurements.

Dispersion maps at different periods are constructed by minimizing the following equation:
$\min (\|\mathbf{Am}-\mathbf{r}\|^2+\lambda^2\|\mathbf{m}\|^2+\varphi^2\|\mathbf{Lm}\|^2)$.

The first term is a data misfit, in which **m** is the parameter vector, **A** is the coefficient matrix, and **r** is the vector of travel-time residuals. The second term is the model regularization with a damping parameter of non-zero real number λ. The third term is the smoothing constraint with non-zero real number φ. The smoothing operator **L** is the Laplacian operator (Lees and Crosson, 1989).

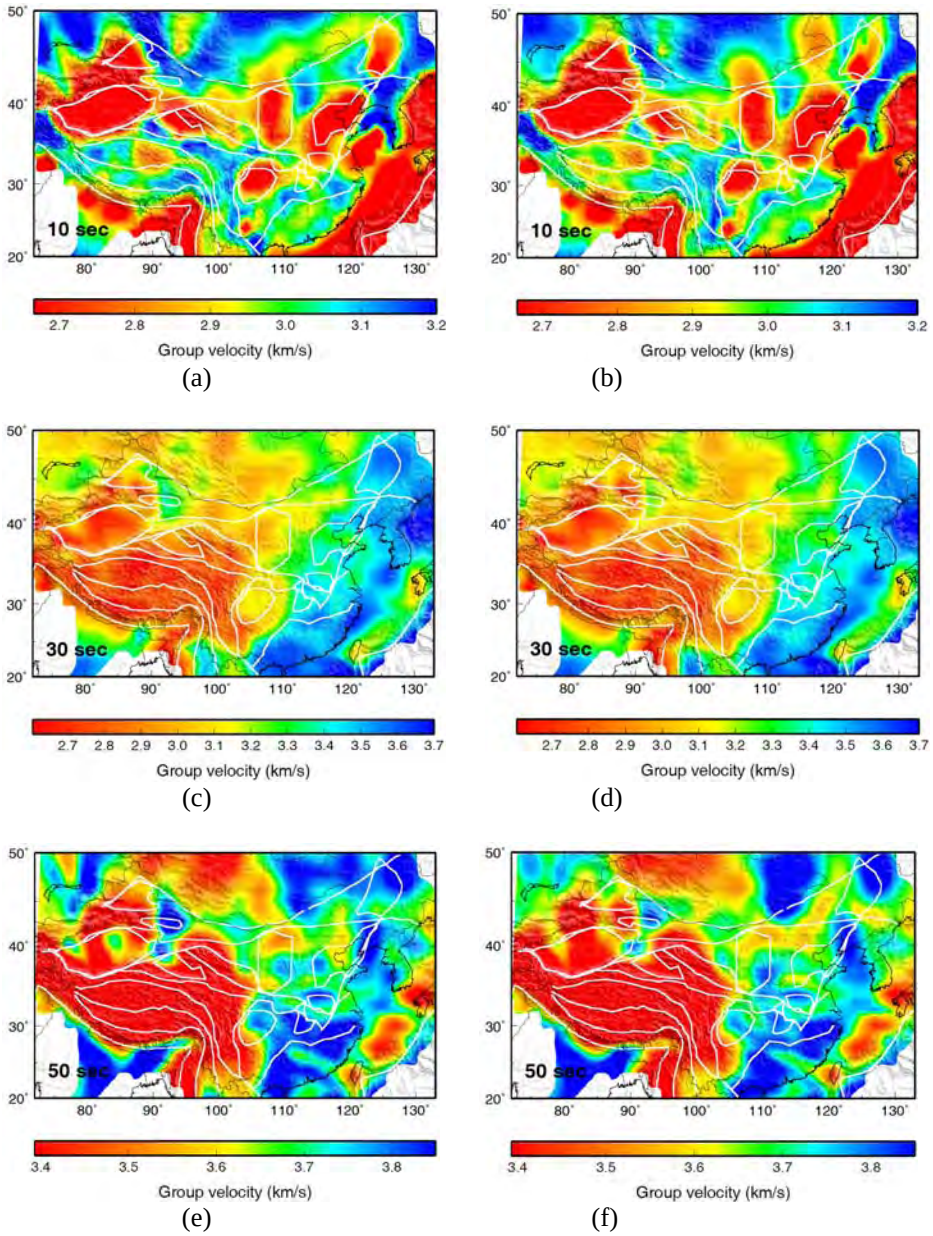

Figure 7. Group velocity maps at 10, 30, and 50 s, using EGFs and earthquake data (left) and earthquake data only (right). Results from two different datasets are generally compatible.

Examples of new dispersion maps are shown in Figure 7. Earthquake data account for about 50% of total group velocity measurements for periods from 8 to 70 s. We compare group velocity dispersion maps from earthquake data and the results using the whole dataset. The images are generally compatible (Figure 7). All large-scale major features are similar, e.g., low velocity in the sediment basin at short periods, a low-velocity zone throughout the Tibetan Plateau, and an eastern-western velocity contrast at mid periods, although there are differences in detailed structures.

CONCLUSIONS AND RECOMMENDATIONS

Our effort so far has focused on two areas. One is the joint inversion methods, which are done in two steps. The first step is to derive a joint P model from first-arriving Pg and Pn and secondary crustal direct P waves. The method has been demonstrated to be highly effective. The second step is to combine the P model and Pn station delays from the first step with receiver functions and Rayleigh-wave dispersion measurements to invert jointly for S wave structure and Moho depth. Another major effort is to increase dispersion measurements by including stations over a long period of time and by including traditional earthquake data. We increase the total number of dispersion measurements by four times. We have obtained a new set of dispersion maps. Maps from ambient noise data and earthquake data are highly compatible, both showing robust major features; thus, the combination greatly increases the resolution of the dispersion maps.

REFERENCES

Ammon, C. J., G. E. Randall, and G. Zandt (1990). On the nonuiqueness of receiver function inversions, *J. Geophys. Res.* 95: 15303–15318.

Benson, G. D., M. H. Ritzwoller, M. P. Barmin, A. L. Levshin, F. Lin, M. P. Moschetti, N. M. Shapiro, and Y. Yang (2007). Processing seismic ambient noise data to obtain reliable broad-band surface wave dispersion measurements, *Geophys. J. Int.* 169: 1239–1260.

Julia, J., C. J. Ammon, R. B. Herrmann, and A. M. Correig (2000). Joint inversion of receiver functions and surface-wave dispersion observations, *Geophys. J. Int*. 143: 99–112.

Lees, J. M. and R. S. Crosson (1989). Tomographic inversion for three-dimensional velocity structure at Mount St. Helens using earthquake data, *J. Geophys. Res*. 94: 5716–5728.

Levshin, A. L. and Ritzwoller, M. H. (2001). Automated detection, extraction, and measurement of regional surface waves, *Pure Appl. Geophys.* 158: 1531–1545.

Koketsu, K. and S. Sekine (1998). Pseudo-bending method for three-dimensional seismic ray tracing in a spherical Earth with discontinuities, *Geophys. J. Int*. 132: 339–346.

Ozalaybey, S., M. K. Savage, A. F. Sheehan, J. N. Louie, and J. N. Brune (1997). Shear-wave velocity structure in the northern basin and range province from the combined analysis of receiver functions and surface waves, *Bull. seism. Soc. Am*. 87: 183–189.

Song, X. D., Z. J. Xu, X. L. Sun, S. H. Zheng, Y.J . Yang, and M. H. Ritzwoller (2009). Surface wave dispersion measurements and tomography from ambient seismic noise correlation in China, in *Proceedings of the 2009 Monitoring Research Review: Ground-Based Nuclear Explosion Monitoring Technologies*, LA-UR-09-05276, Vol. 1, pp. 221–229.

Xu, Z. and X. D. Song (2009). Joint inversion for crustal and Pn velocities and Moho depth for eastern margin of Tibetan Plateau, *Tectonophys.* (in press).

Zheng, S. H., X. L. Sun, X. D. Song, Y. J. Yang, and M. H. Ritzwoller (2008). Surface wave tomography of China from ambient seismic noise correlation, *Geochem. Geophys. Geosyst*. 9: Q05020, doi:10.1029/2008GC001981, 2008.

Zhu, L. P. and H. Kanamori (2000). Moho depth variation in southern California from teleseismic receiver functions, *J. Geophys. Res*. 105: 2969–2980.

BODY-WAVE ARRIVALS FROM SEISMIC NOISE

Jian Zhang[1], Peter Gerstoft[1], Steven R. Taylor[2]

University of California, San Diego[1] and Rocky Mountain Geophysics, LLC[2]

Sponsored by Air Force Research Laboratory

Contract No. FA8718-07-C-0005

ABSTRACT

Array analysis of body-wave seismic noise has the potential to be very useful in improving body-wave tomography of Earth structure, just as noise cross-correlation methods have recently proven successful in surface-wave tomography. Beamforming of seismic noise recorded in southern California reveals *P*-wave arrivals from distant storms in open oceans. In this case, the noise can be processed using cross-correlation among different station pairs and optimal *P*-wave relative arrival times can be estimated using the same approach traditionally used to analyze earthquake arrival times.

Using three storms in the Gulf of Mexico, the Western Pacific (near Japan), and the South Pacific (near Fiji) respectively, we demonstrate that travel-time anomalies can be obtained from *P* waves generated by a distant storm, and that they are similar to those obtained from using an earthquake close to the storm. Our results suggest using oceanic storms as additional seismic sources for resolving *P*-wave travel-time anomalies.

The accurate identification of *P*-wave microseism source areas is also useful to monitor ocean wave-wave interactions due to tropical cyclones. Nonlinear wave-wave interactions generate double-frequency (DF) microseisms, which include both surface waves (mainly Rayleigh-type) and compressional (*P*) waves. Although it is unclear whether DF surface waves generated in deep oceans are observed on land, we show that beamforming of land-based seismic array data allows detection of DF *P* waves generated by ocean waves from Super Typhoon Ioke in both pelagic and coastal regions.

Two distinct spectral bands associated with different *P*-wave source locations are observed. The short-period DF band (0.16–0.35 Hz) is dominated by *P* waves generated in the deep ocean by local wind seas under the storm. In contrast, *P* waves in the long-period DF band (0.1–0.15 Hz) are weaker and generated closer to the coast of Japan from swell interactions.

OBJECTIVES

Our objective is to seek turning storm-generated body-wave seismic noise into relative arrival time estimates, and thus improving traditional body-wave tomography by filling the azimuthal gaps of seismic sources. We also tend to determine if deep-ocean source areas of microseismic *P* waves can be definitively identified using frequency-domain beamforming of land-based seismic array data, and to distinguish distinct SPDF and LPDF *P*-wave microseism source areas through spectral analysis of the beamformer outputs.

RESEARCH ACCOMPLISHED

Resolving *P*-Wave Travel-Time Anomalies using Seismic Array Observations of Oceanic Storms

This section is based on Zhang et al. (2010a). Since the pioneering studies by K. Aki and colleagues in the mid 1970s (Aki et al., 1976, 1977; Husebye et al., 1976), teleseismic *P*-wave travel-time anomalies derived from using earthquakes have been providing the data for inferring three-dimensional (3-D) velocity heterogeneities beneath seismic networks or arrays, i.e., regional/local body-wave tomography. However, inhomogeneous data coverage, particularly the absence of both earthquakes and seismic instruments in many open oceans, has long been a challenge for seismic imaging. For teleseismic body-wave tomography, this may result in poor coverage of certain directions. Studies of phase delay times across southern California, for instance, have been hampered by azimuthal gaps to the south and northeast (e.g., Humphreys and Clayton, 1990; Polet, 2007). Thus, additional seismic sources, if available, could help fill azimuthal gaps in the data. An alternative to earthquakes (and/or controlled sources) is storms. Hiding in microseisms there are non-pulse-like yet coherent *P* waves that are generated by oceanic storms, which can be revealed by seismic array observations. *P* waves from storms have been reported as early as in the late 1960s (Toksoz and Lacoss, 1968; Lacoss et al., 1969; Haubrich and McCamy, 1969), but then received little attention until Hurricane Katrina "hit" California and Gerstoft et al. (2006a) were able to characterize and back-project the hurricane-generated *P* waves with beamforming of seismic noise recorded at the Southern California Seismic Network (SCSN). Modern array techniques now have allowed the accumulation of more observations of *P* waves that can be associated with sea states and even specific storms (Gerstoft et al., 2008; Koper and de Foy, 2008; Landes et al., 2008; Koper et al., 2009; Zhang et al., 2009).

Noise cross-correlation (NCC) of coherent *P* waves such as those observed in Gerstoft et al. (2006a and 2008) at the SCSN can therefore be used to measure the time lag of *P* arrivals between a pair of stations, and thus lead to estimates of relative *P*-wave arrival times across an array from distant noise sources. These relative arrival times, if accurate enough, contain information about seismic velocity anomalies under the array. This suggests that it may be possible to supplement earthquake data with *P*-wave microseisms from areas of active storms, for performing regional body-wave tomography of crust and upper-mantle structure. It should be noted that NCC processing has recently become popular in extracting Green's functions from seismic noise (Shapiro and Campillo, 2004; Snieder, 2004; Wapenaar, 2004; Sabra et al., 2005a), which has made possible the use of ambient noise for surface-wave tomography (Shapiro et al., 2005; Sabra et al., 2005b; Yao et al., 2006, 2008; Kang and Shin, 2006; Yang et al., 2007, 2008; Moschetti et al., 2007; Lin et al., 2007, 2008; Liang and Langston, 2008; Zheng et al., 2008).

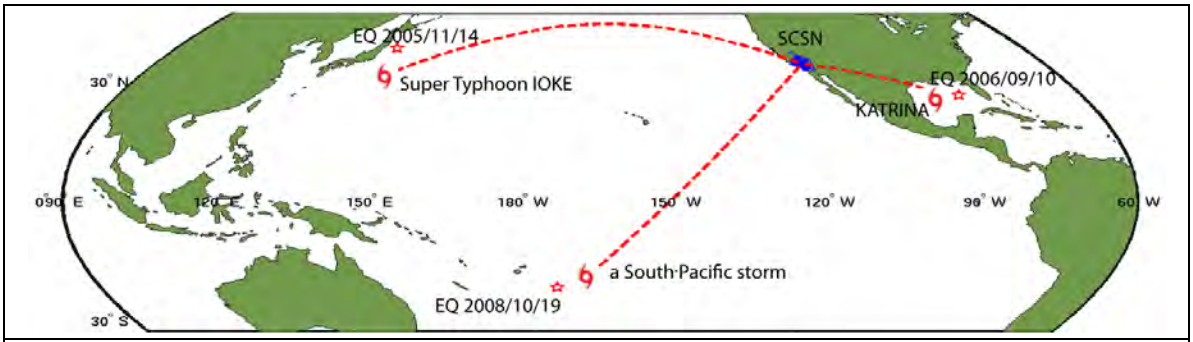

Figure 1. Locations of the SCSN, Hurricane Katrina (schematic), an Mw 5.9 earthquake on September 10, 2006, Super Typhoon Ioke (schematic), an Mw 7.0 earthquake on November 14, 2005, a South Pacific storm (schematic), and an Mw 6.9 earthquake on October 19, 2008. The dashed lines indicate the great circle paths of the *P* waves from the storms to the SCSN.

We demonstrate in this paper that the delay times measured from NCC processing of *P* waves from storms, which are "bias events" in terms of extracting Green's function for surface-wave tomography, can in fact provide travel-time anomaly information for teleseismic body-wave tomography. In particular, we identify and characterize the direct *P*-wave arrivals observed at the SCSN from three storms (see Figure 1) – Hurricane Katrina in the Gulf of Mexico, Super Typhoon Ioke in the Western Pacific (near Japan), and a storm in the South Pacific (near Fiji). We then validate the basic approach by following VanDecar and Crosson (1990) to obtain relative arrival times. For each storm we calculate the *P*-wave travel-time anomalies beneath southern California, and compare the result with that derived from using an earthquake close to the storm. It is noteworthy that these storms are at relatively great distances from the SCSN (~ 27–78^o), so that the *P*-wave arrivals can be approximated as plane waves, just as is commonly done when using earthquakes in teleseismic tomography.

Our analysis starts with array beamforming for identifying *P*-wave arrivals in seismic noise, as well as their sources. We use continuous vertical-component data (sampled at 1 s) recorded at the SCSN for the time window covering Hurricane Katrina's landing (August 28–29, 2005), and also for the whole year of 2006. Note that a 1-s sample rate allows faster beamforming yet is sufficient for identifying coherent microseisms. The data are truncated to no more than half of the daily standard deviations to mitigate contamination from occasional large-amplitude events (e.g., earthquakes). Beamforming is done within each 3-hour window for each 0.02-Hz bandwidth (details in Gerstoft et al., 2006a, 2008). By comparing the beamformed source regions with the ocean-wave hindcast data (Tolman, 2005), many *P*-wave events in the microseisms during 2006 are found to be due to specific storms. These storms, plus Katrina, serve as candidates for the NCC processing. For each storm we then compute the NCC time series (time lags up to 400 s, using data sampled at 0.05 s) among all station pairs and construct range-time plots to show propagating waves. Note that the ranges are the station separations projected along the storm direction, obtained from the beamformer output. We use a passband of 0.18–0.25 Hz for the NCC processing, in order to focus on the *P*-wave microseisms.

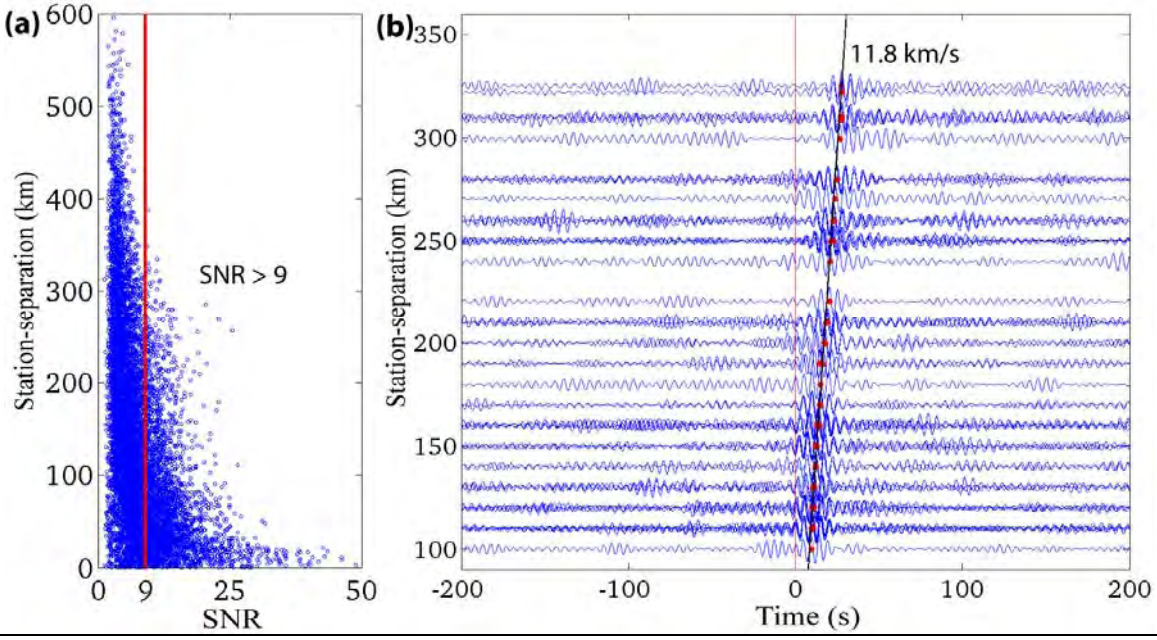

Figure 2. Delay- time measurements from using Hurricane Katrina. (a) SNR vs. station-separation (projected along 100^o). The vertical line indicates a SNR of 9. (b) Range-time representation of the noise cross-correlation (NCC) time series for sample station pairs with SNR > 9. Dots in (b) mark the delay-time measurements (offsets of the NCC peaks) of *P* waves for each pair of stations. The thick line indicates an 11.8 km/s plane wave.

A typical storm suitable for travel-time analysis should reach a sufficient signal-to-noise ratio (SNR) for its NCC peaks, so as to show up as an apparent propagating wave associated with its *P*-wave speed from beamforming. We define the SNR as the ratio of the peak in the *P*-arrival window (+/- 20 s of the plane-wave arrival as derived from beamforming) to the standard deviation for a "noise-only" window (300–400 s of an NCC time series). For example

in Fig. 2b, a propagating *P* wave from Katrina can be clearly seen in the range-time representation of the NCC time series of 400 station pairs (only a fraction is shown) with a SNR above 9, calculated for 1-day data (UTC 18:00 August 28 to UTC 18:00 August 29, 2005). Besides the SNR criterion, we apply a cutoff range over 100–400 km, given that there is an ambiguity between *P*-wave and coastal surface-wave arrivals at shorter ranges, and that times at longer ranges may not be well represented by the plane-wave assumption. In addition to Katrina, we have collected two more storms in 2006 (Fig. 1) for performing relative arrival-time measurements. For each of them, the *P*-wave delay time of each station pair is simply the offset of the maximum of the NCC function, e.g., see the dots in Fig. 2b. Instead of 1-s data for beamforming analysis, however, here we use the data sampled at 0.05 s for picking the peak times of the NCC functions, in order to obtain the delay-time estimates with a higher precision. Moreover, we select only delay-time measurements within +/- 2 s relative to the plane-wave arrival times approximated by the beamforming result. This criterion can remove large outliers, yet still covers the magnitude of typical regional travel-time anomalies.

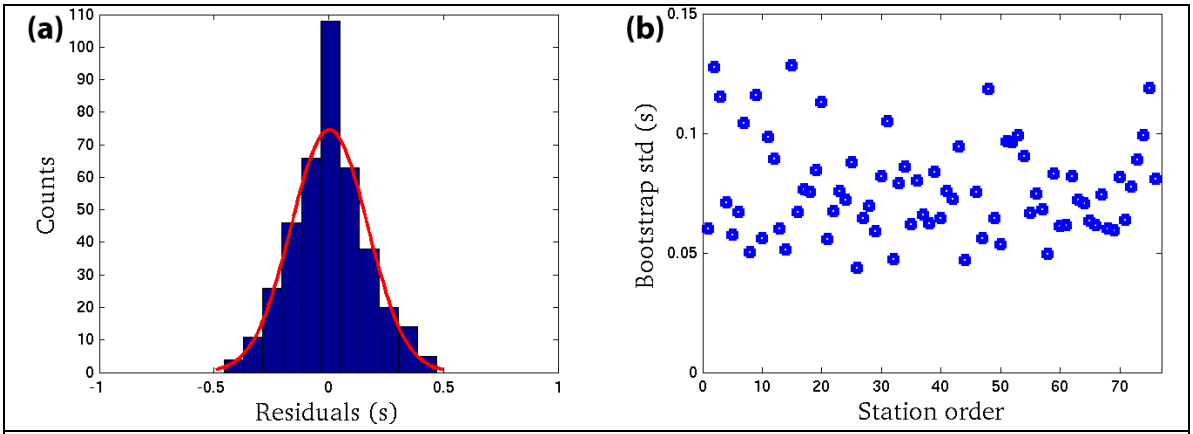

Figure 3. Least-squares residuals and uncertainty estimation in differential times obtained from using Hurricane Katrina. (a) Histogram of equation residuals derived from the best-fitting solutions, showing a Gaussian-like distribution. The curve indicates a fitted normal distribution. (b) Bootstrap-resampling derived timing uncertainties of the *P*-wave relative arrival times for each station.

Our approach of determining travel-time anomalies follows VanDecar and Crosson [1990]. We optimize relative arrival-time estimates through using least squares to solve an overdetermined system of delay-time equations, assuming that errors in the NCC derived delay times are primarily random in nature. For station pairs with a sufficient SNR, we generate equations given by $t_i - t_j = \Delta t_{ij}$. This system is expressed as $A \cdot t = \Delta t$. A is a $M \times N$ sparse coefficient matrix, where M is the number of equations and N is the number of stations. The i^{th} and j^{th} columns of A in a row associated with Δt_{ij} are 1 and -1 respectively, while the other columns are zeros, and we add the constraint equation $\sum t_i = 0$ to force the arbitrary mean of the relative arrival times to be zero. Note that $N < M < (N-1) \cdot N/2 + 1$, as only the pairs with SNR above a certain criterion are used. A standard least-squares fit $t^{est} = A^{+} \cdot \Delta t$, where the pseudoinverse $A^{+} = (A^T \cdot A)^{-1} \cdot A^T$, can be found by applying singular value decomposition (SVD) and truncating small singular values. We repeat the procedure by removing outliers, i.e., the station pairs with a residual over 3 times the standard deviation of all residuals. Typically a stable solution is obtained after 4 iterations. For large systems in which SVD becomes computationally impractical, iterative methods such as the conjugate gradient algorithm LSQR of Paige and Saunders [1982] can be used to find the solution t^{est}.

We have found that the equation residuals $res_{ij} = \Delta t_{ij} - (t_i^{est} - t_j^{est})$ derived from the best-fitting solutions are nearly Gaussian-type distributed. An example is shown in Fig. 3a for the Katrina result. This suggests that the least-squares solutions can provide reasonable estimates of the relative arrival times. In addition, to evaluate the accuracy of the least-squares estimates of the relative *P* arrival times using seismic noise, we perform a statistical resampling analysis (i.e., the "bootstrap" method, Efron, 1982; Shearer, 1997; Waldhauser and Ellsworth, 2000) by replacing

the equation residuals with a randomly chosen set of residuals from the best fitting solutions. The process is then repeated 200 times, and the standard deviation of these bootstrap outputs provides an estimate of the timing uncertainty for each station. Fig. 3b shows, for an example of the Katrina, that a level of 0.1 s in timing errors can be reached, which should be sufficient for resolving typical *P*-wave travel-time anomalies on the order of 1 s.

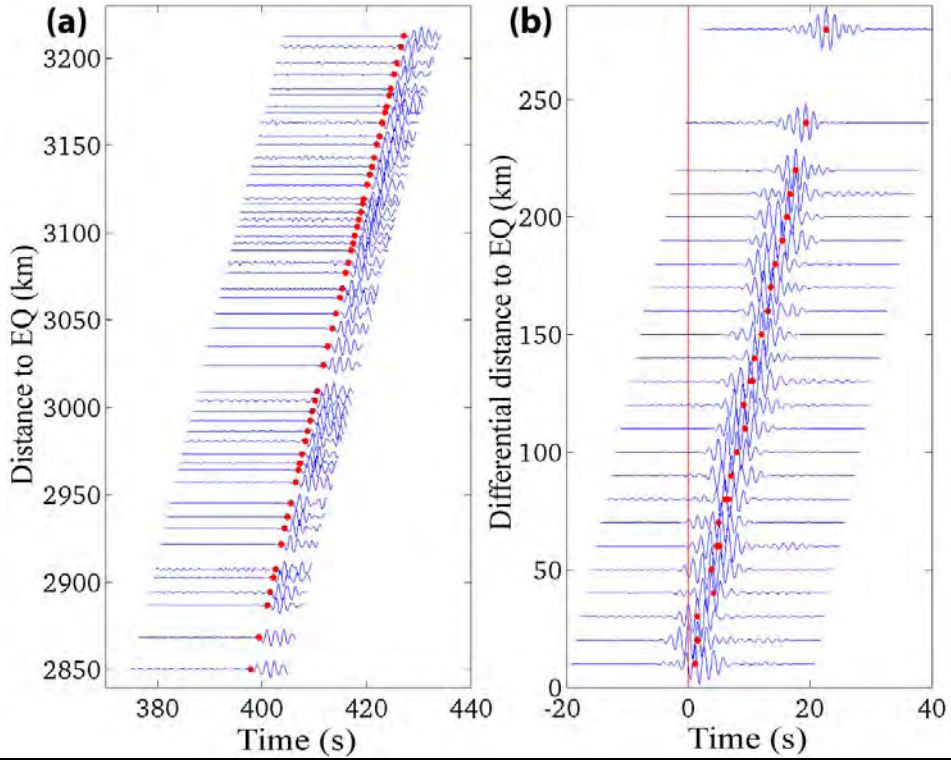

Figure 4. Delay-time measurements from using EQ 2006/09/10. (a) Waveforms of the *P*-wave arrivals at the sample SCSN stations from EQ 2006/09/10. Dots mark the *ak135*-predicted travel times at each station. (b) Range-time representation of the earthquake waveform cross-correlation time series for sample station pairs. Dots mark the delay-time measurements (offsets of the cross-correlation peaks).

To demonstrate the accuracy of the approach for using *P*-wave noise from the three storms, for each one we find an appropriate earthquake (Fig. 1) that is close to the storm and big enough to produce clear *P* pulses at the SCSN stations. We process the earthquake data in the same manner as described above. The principal difference to the NCC processing is that the cross-correlation using the earthquake signals takes advantage of the waveform similarity of the direct *P* arrivals in a short time-window, unlike using non-pulse-like noise, which requires coherence in a relatively long time-window. An example range-time plot of pulse-like *P*-wave arrivals and the waveform cross-correlation traces (only a fraction) is shown in Fig. 4 for an earthquake near Katrina (EQ 2006/09/10).

We then compare the results obtained from using storms and earthquakes respectively, for the relative *P*-wave arrival-time estimates, and accordingly for the *P*-wave travel-time anomalies as well. Anomalies are calculated as the zero-mean difference between the relative arrival-time estimates and the modeled relative arrival times. Upon choosing a reference arrival-time model, an earthquake can be regarded as a point source and thus the modeled arrival times can be calculated using the earthquake location and a standard Earth model, e.g., *ak135* (Kennett et al., 1995). When using a storm, the source point of its peak *P*-wave energy may be approximated by the location of the peak beam power. Thus the modeled arrival times can be calculated in the same way as is used for an earthquake. Alternatively the azimuth-slowness beam can provide a plane-wave reference model of the relative arrival times from a storm, without the need for a precise source location. We have noticed that the two methods result in very similar anomaly patterns.

The first comparison is shown in Fig. 5 for Hurricane Katrina (~ 27° away from the SCSN) and an Mw 5.9 earthquake that occurred in the Gulf of Mexico on September 10, 2006 (see Fig. 1 for the storm and earthquake locations). The relative *P* arrival times estimated by using Katrina noise and their residuals relative to a plane-wave arrival (with an apparent speed of 11.8 km/s and a back-azimuth of 100°) are shown in Figure 5a and c respectively. Similarly, the estimates using the earthquake and their residuals relative to the *ak135*-predicted arrival times are shown in Figure 5b and d respectively. It can be seen that the travel-time anomalies obtained from using Katrina-generated *P* waves are well correlated with those from an earthquake in the same source region. For example, the slow anomalies at the Mojave Desert side of the San Andreas Fault (SAF) and the Los Angeles basin (see Fig. 5f for the basic geological features) are observed both from Katrina (Figure 5c), and EQ 2006/09/10 (Figure 5d). To quantify this, the correlation coefficient between the two anomaly patterns is 0.62, with a significance level over 99%, calculated by using the noise vs. earthquake anomalies at 80 common stations (see also a scatter-plot in Figure 5e).

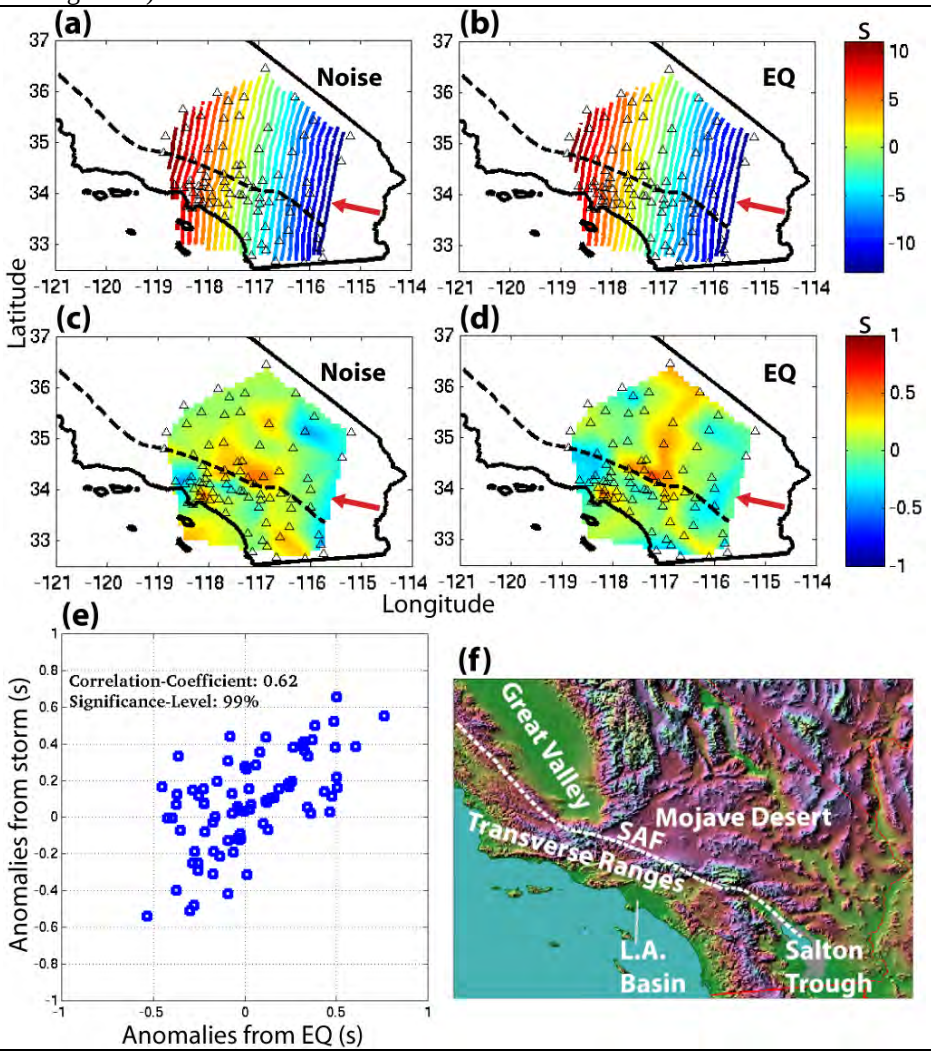

Figure 5. Relative *P* arrival times in southern California as determined by using (a) Katrina, compared with those as determined by using (b) EQ 2006/09/10. Maps are also shown for *P* travel-time anomalies obtained from (c) subtracting a plane wave (100° in back-azimuth and 11.8 km/s in speed) from the NCC-derived arrival times in (a), compared with those obtained from (d) subtracting the *ak135*-predicted arrivals of EQ 2006/09/10 from the EQ-derived arrival times in (b). The used stations (triangles) and the San Andreas Fault (SAF) trace (dashed) are indicated in the maps. Arrows indicate the direction of the *P*-wave arrivals. (e) Scatter plot of EQ-determined anomalies vs. noise-determined anomalies at all common stations. (f) A topographic map showing the basic geological features of southern California.

We find that this approach also works well for storms at longer distances. The second example is given in Fig. 6 by repeating the above procedure for Super Typhoon Ioke during September 5, 2006, which was ~ 75° away from the SCSN. Ioke appears in the beamformer output with a slowness of 0.051 s/km (19.6 km/s) and a back-azimuth of 300°. An Mw 7.0 earthquake near Japan on November 14, 2005 (Figure 1) is used to show a comparison of its *P*-wave relative arrival-time estimates with those obtained from using Ioke-generated *P* waves. Lastly we show in Fig. 7 the anomaly pattern from using a South Pacific storm (~ 78° away from the SCSN) during July 1, 2006, compared with that from an Mw 6.9 earthquake near Fiji on October 19, 2008, (Figure 1). This South Pacific storm appears in the beamformer output with a slowness of 0.05 s/km (20 km/s) and a back-azimuth of 228°. In Figures 6 and 7 respectively, once again a good correlation between the noise- and earthquake-derived anomaly patterns is directly visible in the map and quantified in the scatter plot. Typical agreement can be seen over regions such as the Great Valley, the Transverse Ranges, and the Salton Trough, further proving that *P*-wave travel-time anomalies can be resolved by using storms. Although beyond the scope of this work, one may also notice the large variation of the anomaly pattern obtained from events (either storms or earthquakes) with different directions and/or distances. Across the Salton Trough, for instance, Figure 6 shows fast anomalies whereas a slow pattern can be seen in Figure 7. Such differences can be used to image the heterogeneities at depth using tomographic inversion methods.

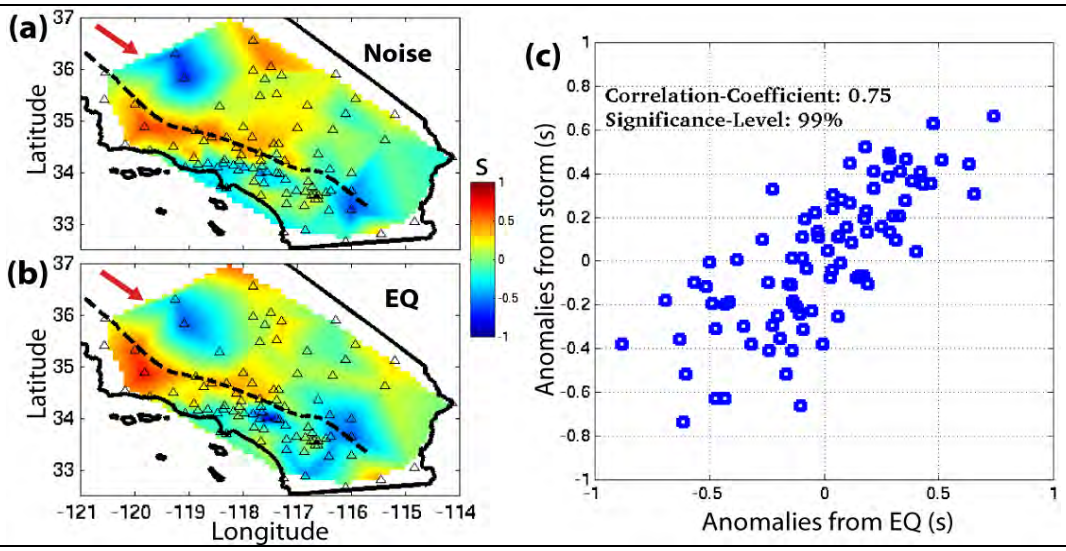

Figure 6. Comparison of the result from using (a) Super Typhoon Ioke with that from using (b) EQ 2005/11/14, and thus their scatter plot (c), similar to Fig. 5c – e.

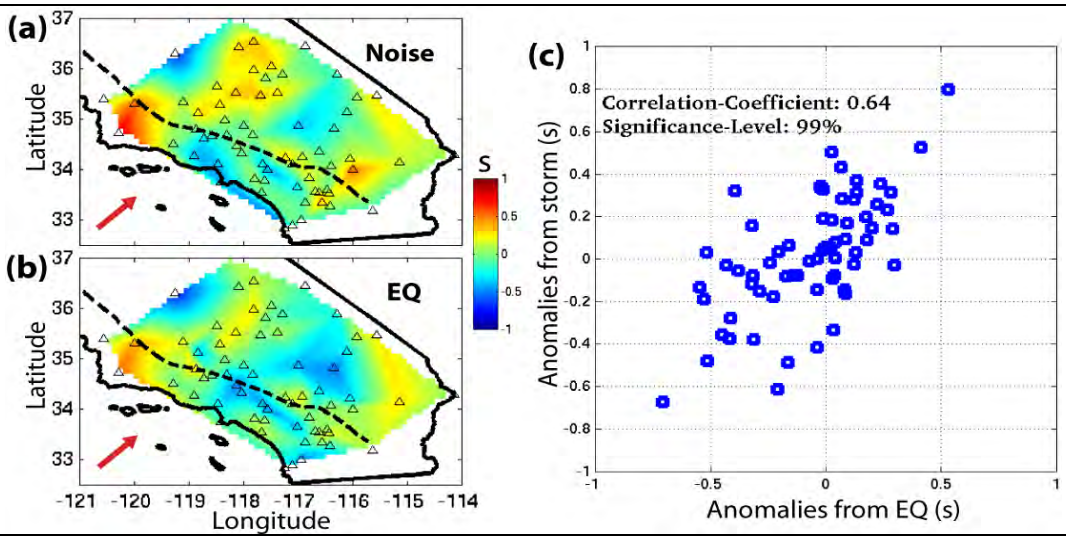

Figure 7. Comparison of the result from using (a) a South Pacific storm with that from using (b) EQ 2008/10/19, and thus their scatter plot (c), similar to Fig. 5c – e.

Pelagic and Coastal Sources of *P*-Wave Microseisms: Generation under Tropical Cyclones

This section is based on Zhang et al. (2010b). Strong coherent *P* waves generated under Super Typhoon Ioke (Figure 8a) are revealed and traced back to their origin locations via array beamforming of the microseisms recorded at the SCSN and the Hi-net respectively. First we focus on the SPDF band (about 0.16–0.35 Hz), as the power of *P*-wave beams peaks around 0.2 Hz. Tests show that *P*-wave energy is below the array noise floor at frequencies greater than 0.35 Hz. The trace of *P*-wave source locations, derived from using data at the SCSN, follows the path of Ioke (Figure 8b; typical beamformer output is shown in the insert). The source locations can also be identified using data from 79 southern stations of the Hi-net (Figure 8c), although the precision is relatively poor, in part due to the array geometry and the relatively short distance of Ioke from the array. Comparison of the *P*-wave source paths with the track of Ioke indicates that these *P* waves originated in the deep ocean near Ioke. This provides evidence that nonlinear wave-wave interactions in deep oceans generate *P*-wave microseisms that can be observed by land stations.

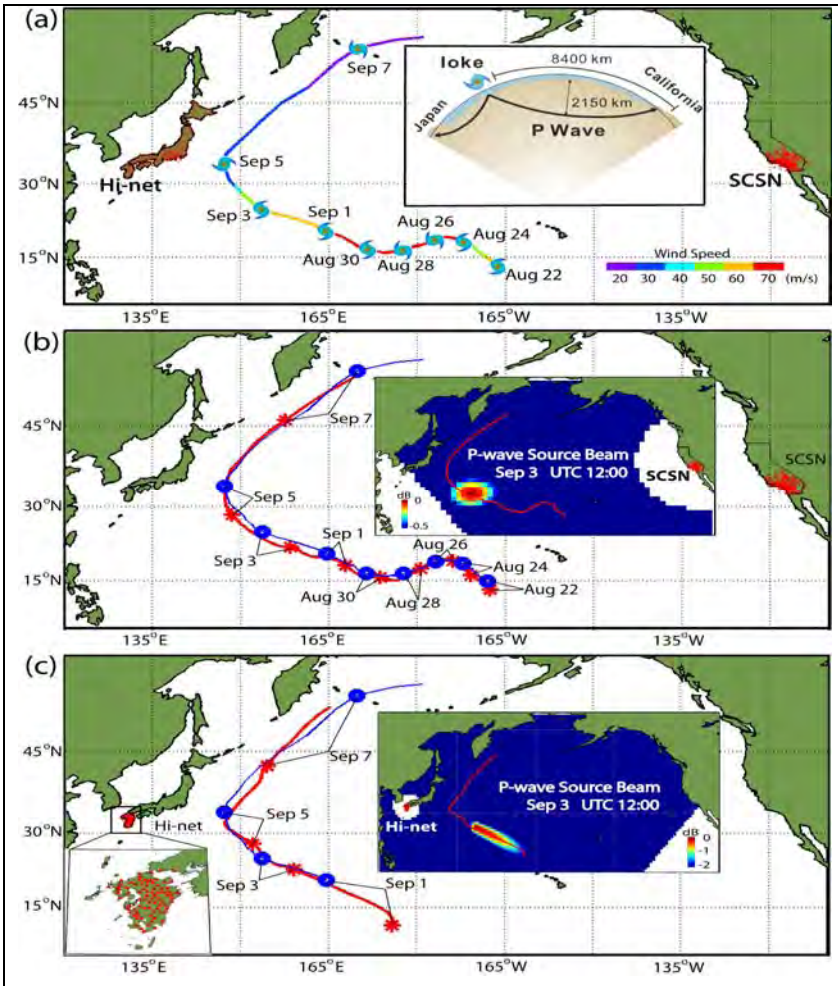

Figure 8. Pelagic *P*-wave microseism sources tailing Super Typhoon Ioke. (a) Locations of the two arrays (SCSN and Hi-net, red), and the best-track of Super Typhoon Ioke (August 22 – September 7, from National Hurricane Center http://www.nhc.noaa.gov/) with wind speed indicated (color scale) and a schematic of *P*-wave ray paths from Ioke to California and Japan (insert). (b) Tracks of Ioke (blue) and Ioke-generated SPDF *P*-wave sources (red) using the SCSN stations. Locations of *P*-wave sources (*) and storm centers (o) are marked every second day. The insert shows *P*-wave beamformer output on 3 September. (c) Similar to (b), but for the beamformer outputs (September 1–7) from using 79 of the southernmost Hi-net stations.

Surface waves might be generated in deep water near Ioke. A strong localized cyclone that has not yet interacted with the coast should provide a likely scenario for deep-water generation of SPDF surface waves. Deep-water SPDF *P* waves from Ioke were observed in this study, and Bromirski et al. (2005) observed deep-water SPDF microseisms at the ocean bottom. However, and in contrast, deep-water generated surface waves from Ioke were not identified with the land array data, consistent with studies indicating that non-coastal DF surface-wave microseisms are not observed at land stations (Bromirski, 2001; Bromirski and Duennebier, 2002; Gerstoft and Tanimoto, 2007).

Although the source locations of SPDF *P* waves correlate well with the track of Ioke, they do not necessarily coincide with the locations of the storm center. Despite beamforming bias due to Earth structure heterogeneity, the locations of the *P*-wave peak beam (thus the field of wave-wave interactions) tend to trail Ioke, i.e., in the storm's wake (Figures 8b and 1c), as also observed by Haubrich and McCamy (1969). Opposing waves may develop behind a storm when it overrides its waves. For example, the western quadrant of Ioke forces wind waves southward. If the storm is moving northward faster than the ocean gravity waves propagate, southward traveling wind waves could interact with previously generated northward propagating wind waves at locations behind the storm. However, during August 22 – September 4, *P* waves at 0.2 Hz were generated near Ioke even when the storm propagation speed was less than the group speed of the deep-water ocean waves at 0.1 Hz, i.e., ~ 8 m/s [$c_{group} = g/(4\pi f)$]. This suggests that there must be some wave-wave interactions due to the inhomogeneity of local wave fields even when the storm is stationary.

Power of the SPDF *P* waves generated by Ioke provides a proxy of the intensity of wave-wave interaction under the storm. We made a correction of the SPDF *P*-wave beam power by considering the distance-dependent geometric spreading for *P* waves in a spherically symmetric Earth (Shearer, 2009). The corrected *P*-wave power is compared with the Ioke propagation speed (estimated from the best-track locations at each 6-h time step) and the maximum wind speed (Figure 9), giving correlation-coefficients of 0.72 and -0.66 respectively. Stronger *P* waves were generated when Ioke propagated faster, suggesting that a faster-moving storm may simply increase the area of wave-wave interactions. The lack of positive correlation between the *P*-wave power and wind speed is consistent with the most intense wave-wave interactions occurring not directly under the storm, but after the waves have propagated some distance where they interact with previously generated waves. However, multiple factors may contribute to the intensity of wave-wave interaction. The magnitude and frequency of ocean waves generated by storms is a function of the wind speed, duration, and fetch, each of which vary. In addition, the estimate of *P*-wave energy generated by the storm can be biased due to scattering and lateral structure dependence of attenuation along the storm track.

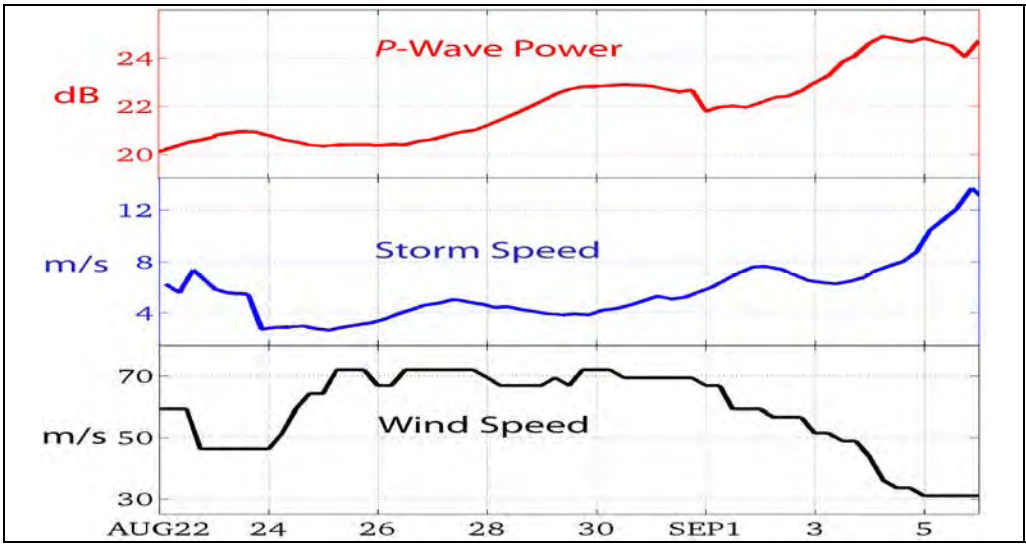

Figure 9. *P*-wave power (estimated using the peak amplitudes of beamformer outputs and corrected for distance-dependent geometric spreading) compared with storm propagation speed and wind speed.

Mid-ocean sites exhibit concentrations of DF microseism energy in the SPDF band associated with local wind seas, and in the swell-generated LPDF band linked to near-coastal wave activity (Bromirski et al., 2005). This can be clearly seen in the spectral variation sampled at three F-net stations in Japan (Figures 10a–d) when nearby Ioke transited northwards (September 2–6). Both surface waves and *P* waves likely contribute to the microseism levels observed, although their respective contributions to each band are not known. The different levels of power near 0.2 Hz at the three stations result from their proximity to Ioke and the storm strength at its closest approach to the Japanese coast, with a significant contribution from the storm-associated wave-wave activities at nearby shorelines. Because swell propagates with less dissipation, the differences in the LPDF band between the stations are less. The presence of strong SPDF *P*-wave component in microseisms is also consistent with Tanimoto et al. (2006), who

found that Rayleigh waves appear less dominant above about 0.2 Hz, potentially because of a strong *P* wave contribution.

Swell wave-wave interactions can occur distant from storms, i.e., when incident swell interacts with swell from coastal reflections or from another storm system. This suggests that the Ioke-generated swell may generate *P* waves in the LPDF band distant from the storm. Two relatively distinct *P*-wave source regions are identified for the LPDF and SPDF bands. The beams were calculated and stacked over the 0.10–0.13 Hz, 0.13–0.16 Hz, and 0.18–0.21 Hz when Ioke was weakening. LPDF *P*-wave microseisms tend to be generated closer to the coast (Figure 10e), which is clearly distinct from the deep-ocean SPDF *P*-wave source area near the storm (Figure 10g). Note that the power of the LPDF *P* waves is much less than the SPDF *P* waves. Relatively little *P*-wave energy was generated in the mid-range DF band (Figure 10f), in agreement with the spectral minimum in this band (Figures 10b–d and Bromirski et al. [2005]).

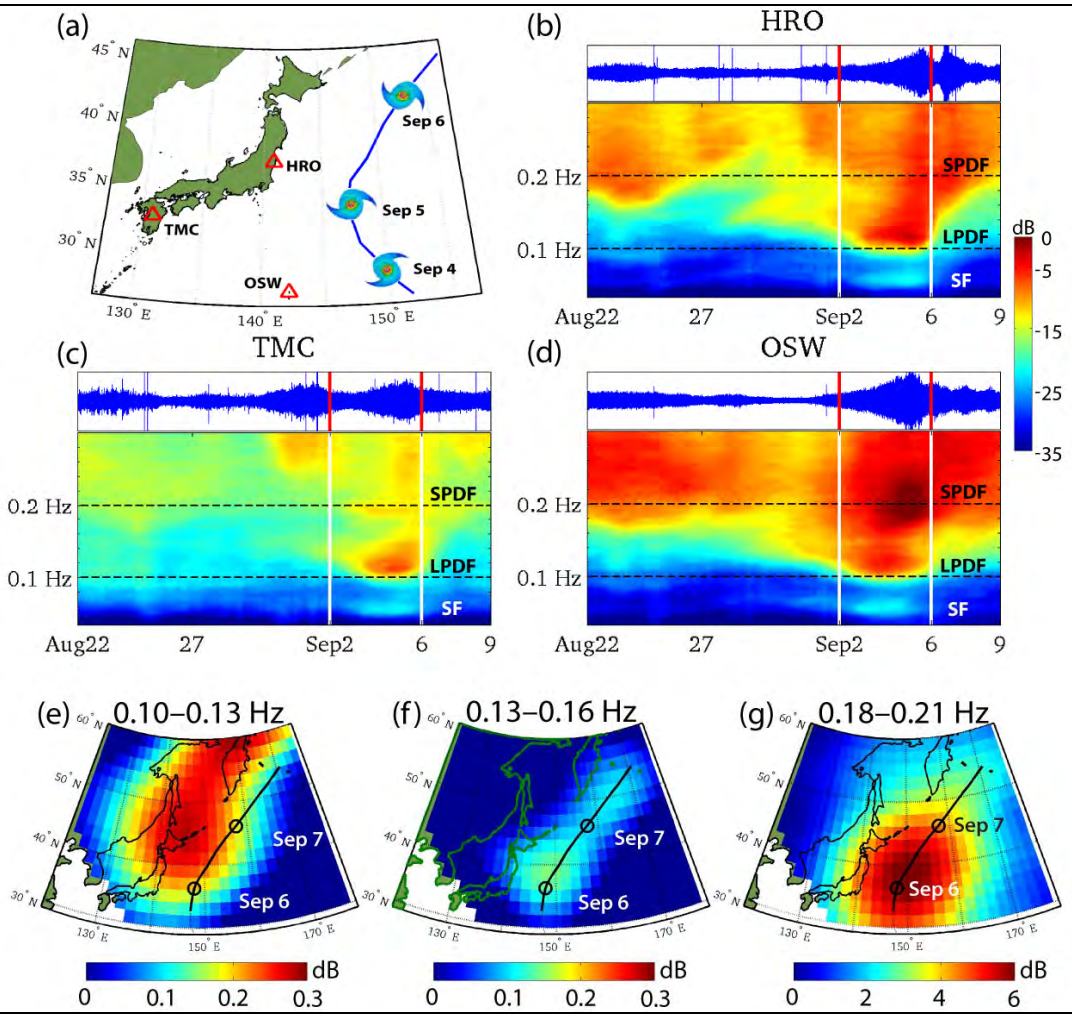

Figure 10. Spectral partitioning of microseismic *P* waves and their sources. (a) Locations of three individual stations (triangles) and track of Ioke (blue trace). (b–d) Vertical-component time series and spectrograms of the data form HRO, TMC, and OSW. Bands associated with single frequency (SF), long-period double frequency (LPDF), and short-period double frequency (SPDF) microseisms are indicated. Beamformer outputs of *P*-wave sources using the SCSN data are shown for three frequency bands: (e) LPDF, 0.10–0.13 Hz, (f) 0.13–16 Hz, and (g) SPDF, 0.18–0.21 Hz. The beam is averaged over UTC 12-h September 5 through September 7. The trace and circles indicate the temporal locations of the SPDF *P*-wave sources. Note that the beam power is significantly higher in the SPDF band.

Observations over the whole year 2006 show a seasonal variability of *P*-wave microseism source areas. The dominant SPDF *P*-wave source areas occur in deep oceans (Figure 11a, see also Gerstoft et al., 2008), correlating well with ocean wave height (Tolman, 2005). LPDF *P*-wave microseisms have a stronger coastal component (Figure 11b), generated along Pacific coastlines all year long. In summer, intense wave activity across the South Pacific dominates *P*-wave microseism generation in both bands. In winter, the North Atlantic is also a strong LPDF *P* source region. It is interesting that the Hawaiian Island chain seems to be a hotspot of coastal wave-wave interaction that generates LPDF *P*-wave microseisms in addition to surface waves (Bromirski et al., 2005), as observed for each month in Figure 11b.

For point sources at selected global locations (crosses in Fig. 11 c and 4d), we construct a synthetic beam neglecting amplitude differences, by modeling phase responses corresponding to the travel times at each station, i.e., $\sum_k \exp(i\omega\, \mathbf{t}_{lat[k],lon[k]})$, where $\mathbf{t}_{lat[k],lon[k]}$ describes the travel times from the k^{th} point source to each array stations. Excluding the Hawaiian Island chain, LPDF *P*-wave source areas are modeled for summer and winter months respectively (Fig. 11c and 4d). The simulations do not show significant beamformer leakage near Hawaii, in contrast to the local maximum near Hawaii observed in the real data (Fig. 11b). This suggests that the wave-wave interaction observed near Hawaii is not a processing artifact.

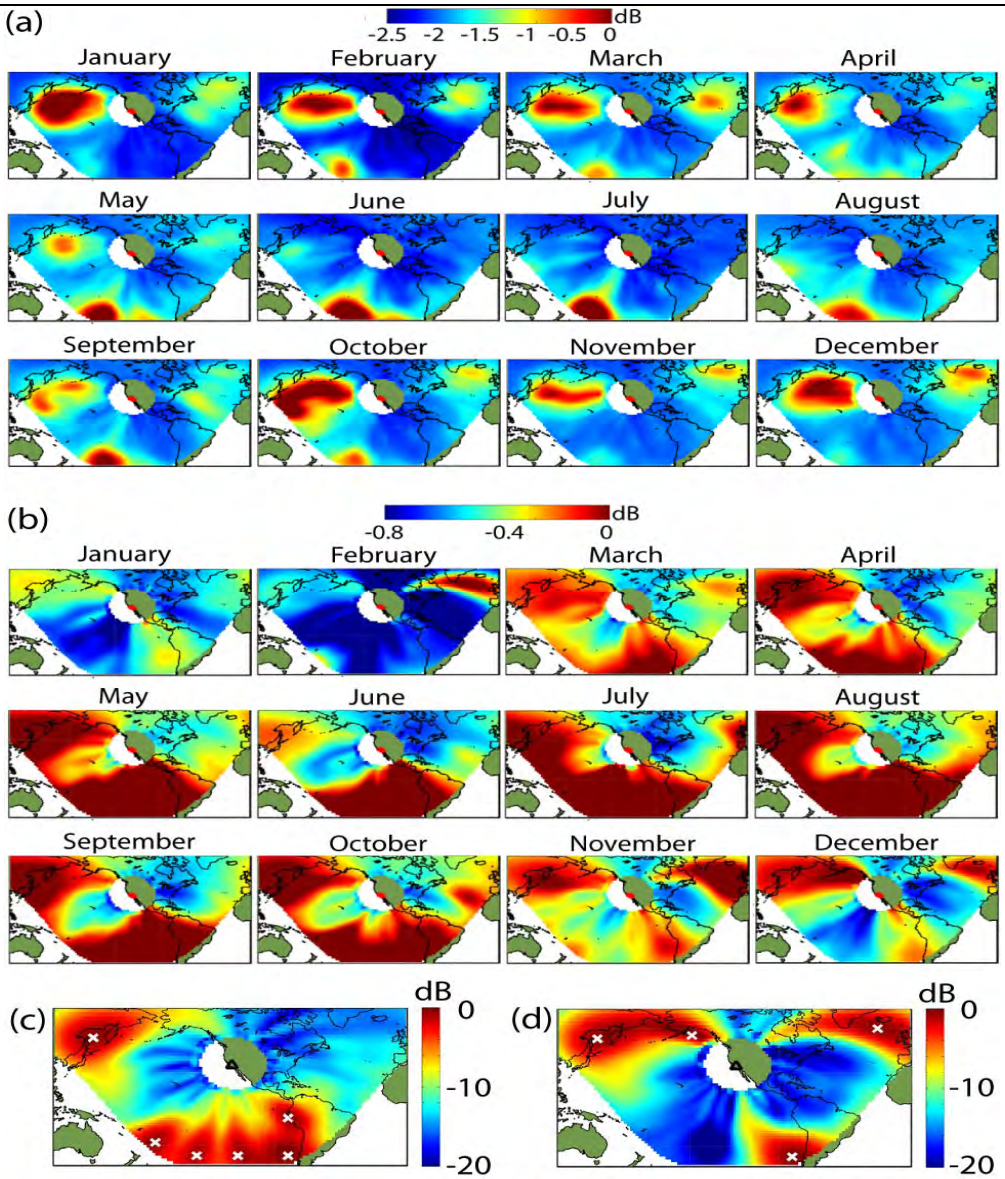

Figure 11: ***P*-wave microseism source areas from monthly averaged beamformer outputs using the SCSN data in 2006. (a) SPDF (0.18–0.25 Hz) *P*-wave source areas. (b) LPDF (0.10–0.13 Hz) *P*-wave source areas. The dB scales are independent for SPDF and LPDF bands. (c) Synthetic LPDF *P*-wave beams for summer months, excited by spatially distributed point sources at selected locations (crosses). (d) Synthetics for winter months**.

CONCLUSIONS AND RECOMMENDATIONS

Using the *P*-wave microseisms of pelagic origin recorded in southern California and generated by Hurricane Katrina, Super Typhoon Ioke, and a South Pacific storm, we have extracted accurate relative *P*-wave arrival times. In practice, a candidate storm is analyzed via array beamforming. Once strong *P* waves are identified and characterized, NCC processing is conducted for obtaining the delay times of *P* arrivals between each pair of stations. Determination of relative arrival times is then realized by solving timing residual equations using least squares. The *P*-wave travel-time anomalies derived from distant storms are similar to those obtained from earthquakes close to the storms. This indicates that oceanic storms may contribute to tomography by providing additional teleseismic sources for imaging Earth structure. Improvements in regional body-wave tomography may come from using oceanic sources that can fill azimuthal gaps in the earthquakes recorded in a particular region.

Beamforming of land-based seismic array data shows clear evidence of deep-ocean origins of SPDF (0.16–0.35 Hz) *P*-wave microseisms due to nonlinear wave-wave interactions of local wind seas near storms. Weaker *P*-wave microseisms are also observable in the LPDF (0.1–0.13 Hz) band, likely associated with swell interactions near the coastlines. These observations show that wave-wave interactions under tropical cyclones may be tracked using land-based seismic arrays. Surface waves generated under the storm were not observed. Further studies with higher density arrays are needed to conclusively determine if surface-wave DF microseisms generated in deep oceans are observed on land.

ACKNOWLEDGEMENTS

The seismic data were from the Southern California Earthquake Data Center (www.data.scec.org), and the National Research Institute for Earth Science and Disaster Prevention in Japan.

REFERENCES

Aki, K., A. Christoffersson, and E. S. Husebye (1976). Three-dimensional seismic structure of the lithosphere under Montana LASA, *Bull. Seismol. Soc. Am*. 66: 501–524.

Aki, K., A. Christoffersson and E.S. Husebye (1977). Determination of the 3-dimensional seismic structure of the lithosphere. *J. Geophys. Res.* 82: 277–296.

Bromirski, P. D. (2001). Vibrations from the "Perfect Storm", *Geochem. Geophys. Geosyst.* 2(7), doi:10.1029/2000GC000119.

Bromirski, P. D. and F. K. Duennebier (2002). The near-coastal microseism spectrum: Spatial and temporal wave climate relationships, *J. Geophys. Res*. 107(B8), 2166, doi:10.1029/2001JB000265.

Bromirski, P. D., F. K. Duennebier, and R. A. Stephen (2005). Mid-ocean microseisms, *Geochem. Geophys. Geosyst*. 6, Q04009, doi:10.1029/2004GC000768.

Burg, J. P., and G. C. Burrell (1967). Analysis of K-line wavenumber spectra from the TFO long noise sample, Special Report of *AFTAC Project VT/4053*, *23*.

Cessaro, R. (1994). Sources of primary and secondary microseisms, *Bull. Seismol. Soc. Am.* 84: 142–148.

Chevrot, S., M. Sylvander, S. Benahmed, C. Ponsolles, J. M. Lefevre, and D. Paradis (2007). Source locations of secondary microseisms in western Europe: Evidence for both coastal and pelagic sources, *J. Geophys. Res*. 112: B11301, doi:10.1029/2007JB005059.

Efron, B. (1982). The jackknife, the bootstrap, and other resampling plans. *SIAM*, Philadelphia.

Gerstoft, P., M. C. Fehler, K. G. Sabra (2006a). When Katrina hit California, *Geophys. Res. Lett.* 33: L17308, doi:10.1029/2006GL027270.

Gerstoft, P., K. G. Sabra, P. Roux, W.A. Kuperman, and M. C. Fehler (2006b). Green's functions extraction and surface-wave tomography from microseisms in southern California, *Geophysics* 71: SI23–SI31.

Gerstoft, P., and T. Tanimoto (2007). A year of microseisms in southern California, *Geophys. Res. Lett.* 34: L20304, doi:10.1029/2007GL031091.

Gerstoft, P, P. M. Shearer, N. Harmon, and J. Zhang (2008). Global *P*, *PP*, and *PKP* wave microseisms observed from distant storms, *Geophys. Res. Lett*. 35: L23306, doi:10.1029/2008GL036111.

Guitton, A., and W. W. Symes (2003). Robust inversion of seismic data using the Huber norm, *Geophysics* 68: 1310–1319.

Haubrich, R. A., and K. McCamy (1969). Microseisms: Costal and pelagic sources, *Rev. Geophys.* 7: 539–571.

Humphreys, E. D., and R. W. Clayton (1990). Tomographic image of the southern California mantle. *J. Geophys. Res*. 95: 19, 725–19 746.

Husebye, E. S., A. Christoffersson, K. Aki, and C. Powell (1976). Preliminary results of the 3-dimensional seismic structure of the lithosphere under the USGS Central California Seismic Array. *Geophys. J. Roy. Astron. Soc.* 46: 319–340.

Kang, T. S. and J. S. Shin (2006). Surface-wave tomography from ambient seismic noise of accelerograph networks in southern Korea, *Geophys. Res. Lett.* 33: L17303.

Kedar, S., M. Longuet-Higgins, F. Webb, N. Graham, R. Clayton, and C. Jones (2008). The origin of deep ocean microseisms in the North Atlantic Ocean, *Proc. R. Soc., Ser. A.*, 464: 777–793, doi:10.1098/rspa.2007.0277.

Kennett, B. L. N., E. R. Engdahl, and R. Buland (1995). Constraints on seismic velocities in the Earth from travel times, *Geophys. J. Int.* 122: 108–124.

Koper, K. and B. de Foy (2008). Seasonal anisotropy of short-period seismic noise recorded in south Asia, *Bull. Seismol. Soc. Am.* 98: 3033–3045.

Koper, K., B. de Foy, and H. M. Benz (2010). Composition and variation of noise recorded at the Yellowknife seismic array, 1991-2007, *J. Geophys. Res*., doi:10.1029/2008JB006307.

Lacoss, R. T., E. J. Kelly, and N. M. Toksoz (1969). Estimation of seismic noise structure using arrays, *Geophysics* 34: 21–38.

Landes, M., F. Hubans, N. M. Shapiro, A. Paul, and M. Campillo (2010). Origin of deep ocean microseisms by using teleseismic body waves, *J. Geophys. Res*., doi:10.1029/2009JB006918.

Liang, C., C. A. Langston (2008). Ambient seismic noise tomography and structure of east North America. *J. Geophys. Res.* 113: (B3), B03309, doi:10.1029/2007JB005350.

Lin, F.-C., M. H. Ritzwoller, J. Townend, S. Bannister, and M. K. Savage (2007). Ambient noise Rayleigh wave tomography of New Zealand, *Geophys. J. Int.* 170(2), 649–666.

Lin, F.-C., M. P. Moschetti, and M. H. Rizwoller (2008). Surface wave tomography of the western United States from ambient seismic noise: Rayleigh and Love wave phase velocity maps, *Geophys. J. Int.* 173(1), 281–298.

Longuet-Higgins, M. S. (1950). A theory of origin of microseisms, *Philos. Trans. R. Soc. London, Ser. A.*, 243: 1–35.

Moschetti, M. P., M. H. Rizwoller, and N. M. Shapiro (2007). Surface wave tomography of western United States from ambient seismic noise: Rayleigh wave group velocity maps, *Geochem. Geophys. Geosys*. 8, Q080101, doi:10.1029/2007GC001655.

Paige, C. C., and M. A. Saunders (1982). LSQR: Sparse linear equations and least squares problems. ACM Transactions on Mathematical Software 8/2, 195–209.

Polet, J. (2007). A map of relative *P* wave delay times across southern California, *Geochem. Geophys. Geosys*. 8, Q10003, doi:10.1029/2007GC001626.

Sabra, K. G., P. Gerstoft, P. Roux, W. A. Kuperman, and M. C. Fehler (2005a). Extracting time-domain Greens function estimates from ambient seismic noise, *Geophys. Res. Lett.* 32: L03310, doi:10.1029/2004GL021862.

Sabra, K. G., P. Gerstoft, P. Roux, W. A. Kuperman, and M. C. Fehler (2005b). Surface wave tomography from microseisms in southern California, *Geophys. Res. Lett.* 32: L14311, doi:10.1029/2005GL023155.

Shapiro, N. M., and M. Campillo (2004). Emergence of broadband Rayleigh waves from correlations of the ambient seismic noise, *Geophys. Res. Lett.* 31, L07614, doi:10.1029/2004GL019491.

Shapiro, N. M., M. Campillo, L. Stehly, and M. H. Ritzwoller (2005). High-resolution surface-wave tomography from ambient seismic noise, *Science* 307: 1615–1617.

Shearer, P. M. (1997). Improving local earthquake locations using the L1 norm and waveform cross correlation: application to the Whittier Narrows, California, after shock sequence, *J. Geophys. Res.* 102: 8269–8283.

Shearer, P. M. (2009). *Introduction to Seismology*, Cambridge University Press, Cambridge, UK.

Snieder, R. (2004). Extracting the Green s function from the correlation of coda waves: A derivation based on stationary phase, *Phys. Rev.* E 69: 046610.

Stehly, L., M. Campillo, N. M. Shapiro (2006). A study of the seismic noise from its long-range correlation properties, *J. Geophys. Res.* 111: B10306, doi:10.1029/2005JB004237.

Sutton, G. H., and N. Barstow (1990). Ocean-bottom ultralow-frequency (ULF) seismo-acoustic ambient noise: 0.002 to 0.4 Hz, *J. Acoust. Soc. Am.* 87: 2005–2012.

Tanimoto, T. (2007). Excitation of microseisms, *Geophys. Res. Lett.* 34: L05308, doi:10.1029/2006GL029046.

Tanimoto, T., S. Ishimaru, and C. Alvizuri (2006). Seasonality in particle motion of microseisms, *Geophys. J. Int.*, 166: 253–256, doi:10/1111/j/1365-246X.2006.02931.x.

Toksoz, N. M., and R. T. Lacoss (1968). Microseisms: Mode structure and sources, *Science* 159: 872–873. doi: 10.1126/science.159.3817.872.

Tolman, H.L. (2005). Manual and wave user system documentation of WAVEWATCH-III, NOAA, Camp Springs, Md. (Available at http://polar.ncep.noaa.gov/)

Tsai, V.C. (2009). On establishing the accuracy of noise tomography travel-time measurements in a realistic medium, *Geophys. J. Int.* 178: (3), 1555–1564.

VanDecar, J. C., and R. S. Crosson (1990). Determination of teleseismic relative phase arrival times using multi-channel cross-correlation and least squares, *Bull. Seismol. Soc. Am.* 80: 150–169.

Waldhauser, F., and W. L. Ellsworth (2000). A double-difference earthquake location algorithm: method and application to the northern Hayward fault, California, *Bull. Seismol. Soc. Am.* 90: 1353–1368.

Wapenaar, K. (2004). Retrieving the elastodynamic Green's function of an arbitrary inhomogeneous medium by cross correlation, *Phys. Rev. Lett.* 93: 254301.

Yang, Y., M. H. Ritzwoller, A. L. Levshin, and N. M. Shapiro (2007). Ambient noise Rayleigh wave tomography across Europe, *Geophys. J. Int.* 168: 259–274.

Yang, Y., A. Li, and M. H. Ritzwoller (2008). Crustal and uppermost mantle structure in southern Africa revealed from ambient noise and teleseismic tomography, *Geophys. J. Int.* 174: 235–248.

Yang, Y., and M. H. Ritzwoller (2008). Characteristics of ambient seismic noise as a source for surface wave tomography, *Geochem. Geophys. Geosyst.* 9, doi:10/1029/2007GC001814.

Yao, H., R. D. van der Hilst, and M. V. de Hoop (2006). Surface-wave array tomography in SE Tibet from ambient seismic noise and two-station analysis: I – Phase velocity maps, *Geophys. J. Int.* 166: 732–744.

Yao, H., C. Beghem, and R.D. van der Hilst (2008). Surface-wave array tomography in SE Tibet from ambient seismic noise and two-station analysis: II – Crustal and upper mantle structure, *Geophys. J. Int.* 173: 205–219.

Yao, H., and R. D. van der Hilst (2009). Analysis of ambient noise energy distribution and phase velocity bias in ambient noise tomography, with application to SE Tibet, *Geophys. J. Int.*, in press.

Zhang, J., P. Gerstoft, and P. M. Shearer (2009). High-frequency *P*-wave seismic noise driven by ocean winds. *Geophys. Res. Lett.* 36, L09302, doi:10.1029/2009GL037761.

Zhang, J., P. Gerstoft, and P. M. Shearer (2010a). Resolving P-wave travel-time anomalies using seismic array observations of oceanic storms, *Earth Planet. Sci. Lett.* 292: 419–427, doi:10.1016/j.epsl.2010.02.014.

Zhang, J., P. Gerstoft, and P. D. Bromirski (2010b). Pelagic and coastal sources of P-wave microseisms: Generation under tropical cyclones, *Geophys. Res. Lett.*, in press.

Zheng, S., X. Sun, X. Song, Y. Yang, and M. H. Ritzwoller (2008). Surface wave tomography of China from ambient seismic noise correlation, *Geochem. Geophys. Geosyst.* 9, Q0502, doi:10.1029/2008GC001981.

Seismic Event Detection and Location

EARTHQUAKE LOCATION ACCURACY IN THE ARABIAN-EURASIAN COLLISION ZONE

Eric A. Bergman[1], Eric R. Engdahl[1], Michael H. Ritzwoller[1], and Stephen C. Myers[2]

University of Colorado[1] and Lawrence Livermore National Laboratory[2]

Sponsored by the Air Force Research Laboratory and the National Nuclear Security Administration

Award Nos. FA8718-08-C-0020[1] and DE-AC52-07NA27344[2]
Proposal No. BAA08-69

ABSTRACT

An extensive and high-quality data set of earthquake locations, many of them calibrated to $GT5_{90}$ levels of accuracy, is being compiled for the region that expresses the continental collision between the Arabian and Eurasian plates, with the primary goal of obtaining improved resolution of the crustal and upper mantle velocity structure through tomographic imaging. A specialized multiple event relocation algorithm is used to calibrate clusters of earthquakes, using several kinds of calibration data, including near-source seismic observations, InSAR data on source location and mechanism, and mapped faulting. Although our data set of calibrated locations (880 events in 21 calibrated clusters) is substantial, compared to what is available for most other regions of the Earth, it is still small in comparison with the full catalog of earthquake locations (~26,000 events) in the region which can be used for tomographic studies. Our strategy is to use the observed arrival times from GT5 events set to study regions in which the ray path coverage is dense enough, and to use these calibrated travel times for validation in regions for which it is necessary to use arrival time data from uncalibrated sources for tomography. In addition to providing data sets for tomography, the calibrated earthquake locations provide insight into the performance of permanent seismic networks that monitor the region. The location accuracy of two global networks and two regional networks, is investigated by comparing their locations with the calibrated locations (the subset of 684 events meeting $GT5_{90}$ criteria) determined in this project. Earthquake locations in this region which are based on regional and teleseismic arrival time data are systematically biased to the southwest and have a 90% location accuracy of 18-23 km, with the lower value achievable by applying limits on secondary azimuth gap. The two regional seismograph networks achieve a 90% accuracy level of 22 and 36 km, respectively. One regional network actually operated as a set of independent subnetworks until 2006 and suffers from a very imbalanced distribution of stations, such that the 90% level of accuracy exceeds 100 km during that time. In broad terms, location accuracy in the region using 1-D travel time models and single event location procedures, is presently limited to about 20 km at the 90% level of accuracy (i.e., $GT20_{90}$). The tendency for routinely-determined epicenters to be biased to the south can be explained as a consequence of the fact that there are far more seismic stations in the northern hemisphere, relative to the study region, and that the true travel times are larger than the theoretical ones, yielding positive travel-time residuals. The inversion for location tends to push an event further away from the bulk of seismic stations, i.e., to the south.

OBJECTIVES

This research has the goal of developing in-country datasets that can be used to improve ground-based monitoring capabilities in the study region, in particular by providing information needed to develop and test more accurate travel time models for seismic phases that propagate in the crust and upper mantle in the region that expresses the continental collision between the Arabian and Eurasian plates. The main thrust of this project is developing high quality data sets for tomography. The research presented here, however, deals with an assessment of the current level of location accuracy in the region of interest from several permanent seismic networks.

As part of this project we are conducting detailed analyses of clusters of earthquakes with a multiple event relocation method that has been developed to determine calibrated locations that meet or exceed $GT5_{90}$ levels of accuracy. The success of this analysis usually depends on the availability of near-source data, such as temporary deployments of seismometers for aftershock studies and geological field work after large earthquakes. In-country data sets therefore play a critical role in this kind of analysis. In the region of interest we have developed 21 calibrated earthquake clusters, containing 880 events; 684 of these events qualify as $GT5_{90}$ locations. We compare the epicenters (we do not consider focal depth or origin time) reported in two global seismic catalogs and two regional seismic catalogs with the GT5 locations to gain an understanding of the average level of location accuracy of different networks and also to reveal any evidence for systematic mis-location. All locations in this study, for the multiple event relocation analysis used to determine GT5 locations or the catalogs used for comparison, are based on 1-D Earth models, although the models may differ from cluster to cluster and from catalog to catalog.

The global catalogs considered in this study are those of the International Seismological Centre (ISC) and a version of the well-known EHB catalog (Engdahl et al., 1998) that has been carefully reviewed for the region of interest. The two regional catalogs are those published by the International Institute for Earthquake Engineering and Seismology (IIEES) and the Iranian Seismological Centre (IRSC). The IRSC is contained within the Institute of Geophysics of the University of Tehran. The IIEES catalog is based on data from the Iranian National Seismic Network (INSN), consisting of 16 broadband (Güralp CMG-3T seismometers, Güralp digitizers), real-time satellite-telemetered stations. Most stations have been installed since 2000. The IRSC catalog is based on data from the Iranian Seismic Telemetry Network (ISTN). The ITSN consists of 73 three-component short-period (Kinemetrics SS-1), digital, telemetered stations organized in 10 subnetworks. Timing corrections, based on GPS, are applied at the subnetwork recording centers. The earliest installations, for the Tehran and Tabriz subnetworks, occurred in 1995. Until 2006 the subnetworks operated largely autonomously, producing their own bulletins. Since then, all subnetwork data are transmitted to the IRSC where a national bulletin is prepared. The IRSC and IIEES catalogs used for this study can be considered almost completely independent, each utilizing only data from their own network and their own location procedures. In recent years the IRSC has sometimes included a few readings from the IIEES network to improve azimuthal coverage.

RESEARCH ACCOMPLISHED

Calibrated Earthquake Clusters

Our method of determining ground-truth quality calibrated locations is based on multiple event analysis, for which we use the Hypocentroidal Decomposition (HDC) algorithm described by Jordan and Sverdrup (1981). The code has been extensively modified to incorporate features that are relevant to the calibrated location problem, especially in the area of incorporating empirical (data-derived) estimates of arrival time uncertainty, and the results have been extensively tested through intercomparisons with other methods of location (e.g., Rodi et al., 2002, Bondár et al., 2008) and with GT0 data sets. Details have been discussed in previous presentations over the past decade. The calibration process itself can be done in two ways (categorized as “direct” and “indirect”), as discussed in previous presentations, but it almost always depends on near-source observations that can constrain the epicenter (or other hypocentral parameters) of at least one event in the HDC cluster. Near-source seismic observations are required to minimize the unknown biasing effect of using theoretical travel times in the location algorithm that do not adequately reproduce the travel times of seismic phases in the crust and upper mantle of the source region.

This requirement generally means using arrival time data only at distances inside the Pg/Pn crossover distance. Because HDC analysis tightly constrains the relative locations of all events in the cluster, the entire cluster can be shifted in space and time to best fit the available calibration data from near-source observations.

The 21 calibrated earthquake clusters used in this study are shown in Figure 1. The statistics of the calibrated clusters are presented in Table 1.

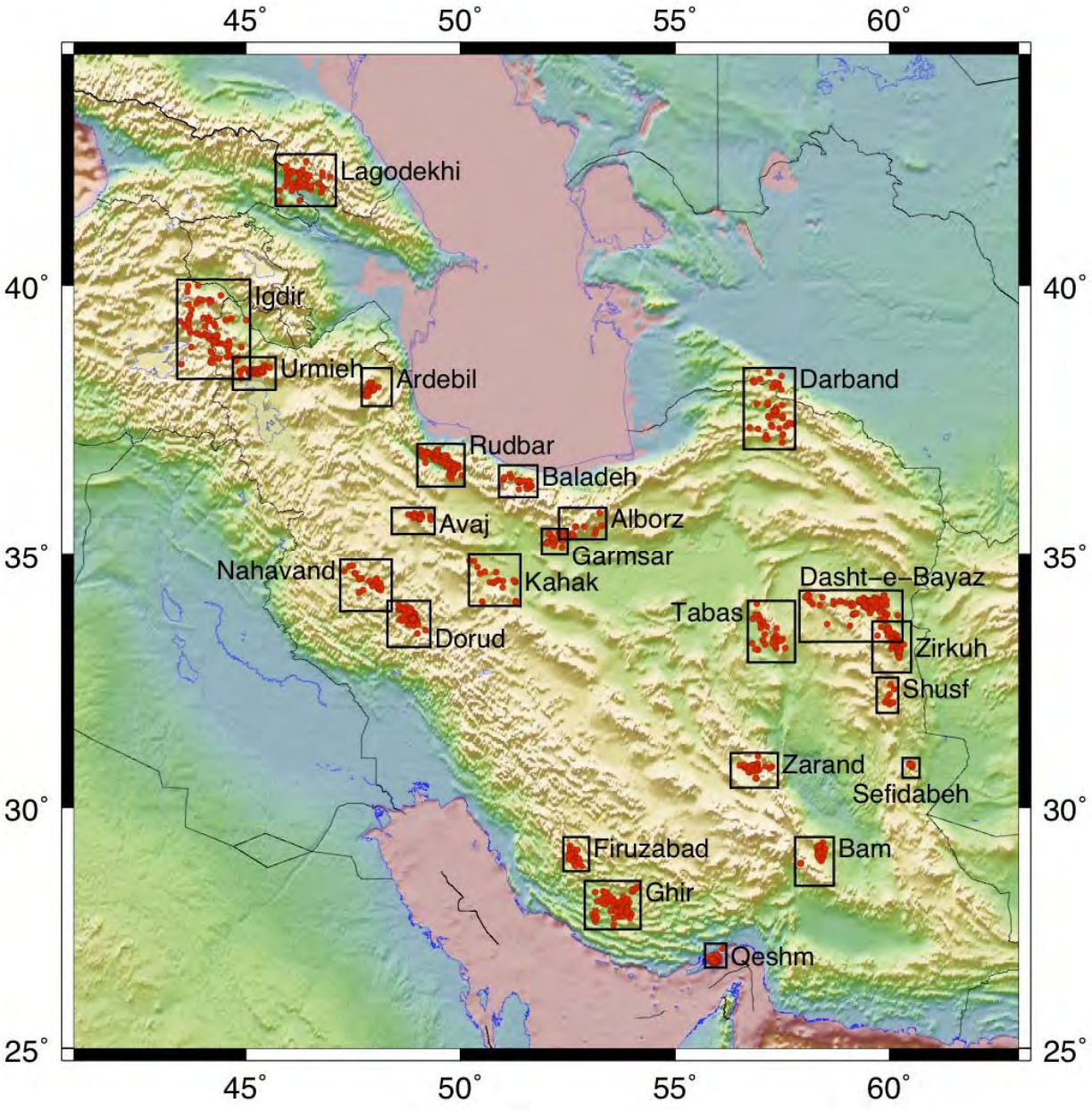

Figure 1. Locations of earthquake clusters whose locations have been calibrated using near-source data.

Table 1. Earthquake clusters for which a calibration analysis was made. "GT5" and "GT3" are the number of events that qualify as $GT5_{90}$ or better and $GT3_{90}$ or better. "Direct" and "Indirect" indicate different methods of calibration (see text). "Cal. Level" is the level of uncertainty of the calibration process, in km. "Seismic" is the number of seismic calibration events used for calibration. "InSAR" is the number of InSAR analyses or instances of mapped faulting used for calibration. "OT" indicates that the origin time is calibrated.

Name	Events	GT5	GT3	Direct	Indirect	Cal. Level	Seismic	InSAR	OT
Alborz	11	11	11	•		1.6			•
Ardebil	19	16	0	•		3.6			•
Avaj	17	16	1		•	4.3	1		•
Baladeh	25	23	20	•		2.2			•
Bam	31	18	2		•	3.2	1	1	•
Darband	44	41	17	•		2.9			•
Dasht-e-Bayaz	101	44	0		•	4.7	3	3	•
Dorud	80	77	63	•		1.8			•
Garmsar	16	16	15	•		1.3			•
Ghir	67	51	23		•	2.8	2	1	•
Igdir	71	47	1	•		3.1			•
Kahak	18	17	9	•		2.6			•
Lagodekhi	44	36	19	•		2.4			•
Qeshm	93	89	20	•		3.3			•
Rudbar	81	78	58		•	1.8	3		•
Sefidabeh	7	7	6		•	3.1	1	1	•
Shusf	7	4	1		•	4.1		1	
Tabas	30	14	2		•	4.4	2		•
Urmieh	26	25	0	•		3.5			•
Zarand	49	44	7		•	3.1	1	1	•
Zirkuh	43	10	0		•	5.1	2		•
Total	880	684	275	11	10				

Location Accuracy of Regional Networks

IIEES

The IIEES catalog has been published since July 2004 and is based on arrival time data only at INSN stations, which have increased in number from 13 in July 2004 to 16 in September 2007. The IIEES catalog contains 188 events that are also contained in our set of $GT5_{90}$ events. Most (160) of the events occurred since the beginning of 2005 when network operations became routine. For each match, we have calculated the distance and azimuth of the IIEES location with respect to the $GT5_{90}$ location. These vectors are shown in Figure 2a.

The median mislocation is only 5.1 km, showing that many IIEES locations are quite accurate. Based on median

mislocation, the IIEES catalog would be rated the most accurate of the catalogs analyzed. However the distribution is quite long-tailed and a significant number of IIEES locations have large mislocations (Figure 3a). At the 90% level, IIEES locations are accurate at about 22 km. The statistics of the mislocations for the IIEES catalog are summarized in Table 2.

IRSC

Because the ISTN is organized in 10 subnetworks, the detection and location capability is quite variable, geographically. Moreover, the IRSC did not publish a unified "network" catalog until the beginning of 2006. Prior to then, locations are published for the individual subnetworks, based in most cases only on the data of that subnetwork. Thus there are many cases of multiple subnet locations of the same event. Subnet locations can be quite accurate for events inside the network, but the majority of IRSC locations before 2006 are for the case when the event is outside the network. It is well known that this inevitably leads to large errors in location. For this reason we have split the IRSC catalog into two parts for comparison with our $GT5_{90}$ locations:

- IRSC1: 538 events prior to 2006. All subnetwork solutions for the same event are retained.
- IRSC2: 82 events since 2006.

The mislocation vectors for the IRSC1 and IRSC2 data sets are shown in map view in Figure 2 and histograms of the mislocation distances is shown in Figure 3. The median mislocation for IRSC1 and IRSC2 is 31.3 and 19.6 km, respectively (Table 2), confirming our expectation that pre-2006 locations will be less accurate is strongly confirmed. At the 90% level, the location accuracy of the IRSC1 and IRSC2 is 123 and 36 km, respectively.

Even the recent IRSC2 catalog is significantly less accurate than the IIEES catalog. While some of the difference may be attributed to smaller sample size for IRSC2 which is based mainly on events from two calibrated clusters (Figure 2), we believe that the main factor is the unbalanced distribution of the ISTN stations. Because the stations are grouped tightly into subnetworks, the effective number of stations for location in many parts of the region is far less than the total number of stations would imply, and the distribution of those subnetworks does not provide adequate azimuthal coverage for many seismic source regions. Recently, the IRSC has begun incorporating some readings from INSN stations in their processing, and this should help improve location accuracy, as should the recent installation of new stations in the east and southeast of the country.

It is ironic that the ITSN, which has been the most important source of phase arrival data for many of our calibration studies, itself provides the least accurate locations of any of the networks considered.

Location Accuracy of Global Networks

ISC

The ISC catalog contains 501 of the events in common with our $9GT_{50}$ data set. 12 of the missing events occurred later than the most recent ISC Bulletin available at the time of analysis (June 2006); the remainder are smaller events which depend on data from the regional networks to obtain a stable solution. Mislocation vectors are shown in Figure 2, and a histogram of mislocation distances is shown in Figure 3. The median mislocation is 10.6 km (Table 2). At the 90th percentile, the location accuracy is about 23 km, about the same as the IIEES.

EHB-Iran

The "EHB-Iran" catalog for this comparison is based on our carefully-reviewed catalog of the region of interest, not the standard EHB catalog that is widely distributed. The 546 events considered are those that meet a secondary azimuth gap of 180° or better, based on all available arrivals from the ISC, PDE, and regional networks. Secondary azimuth gap is the largest azimuth gap filled by a single station. They have been located with the standard EHB methodology using all arrivals. In contrast, the "standard" EHB catalog is based on arrivals only at teleseismic distances (> 28°). Based on the 90% level of accuracy, the EHB-Iran catalog provides the lowest level of location

bias (18 km) of the four networks examined (Table 2), although the median mislocation of 9.1 km is not as good as that of the IIEES catalog. The map and histogram of mislocations are shown in Figures 2d and 3d, respectively. The fact that the EHB-Iran catalog has fewer events with very large mislocations than any of the other catalogs is primarily due to the selection criterion on secondary azimuth gap.

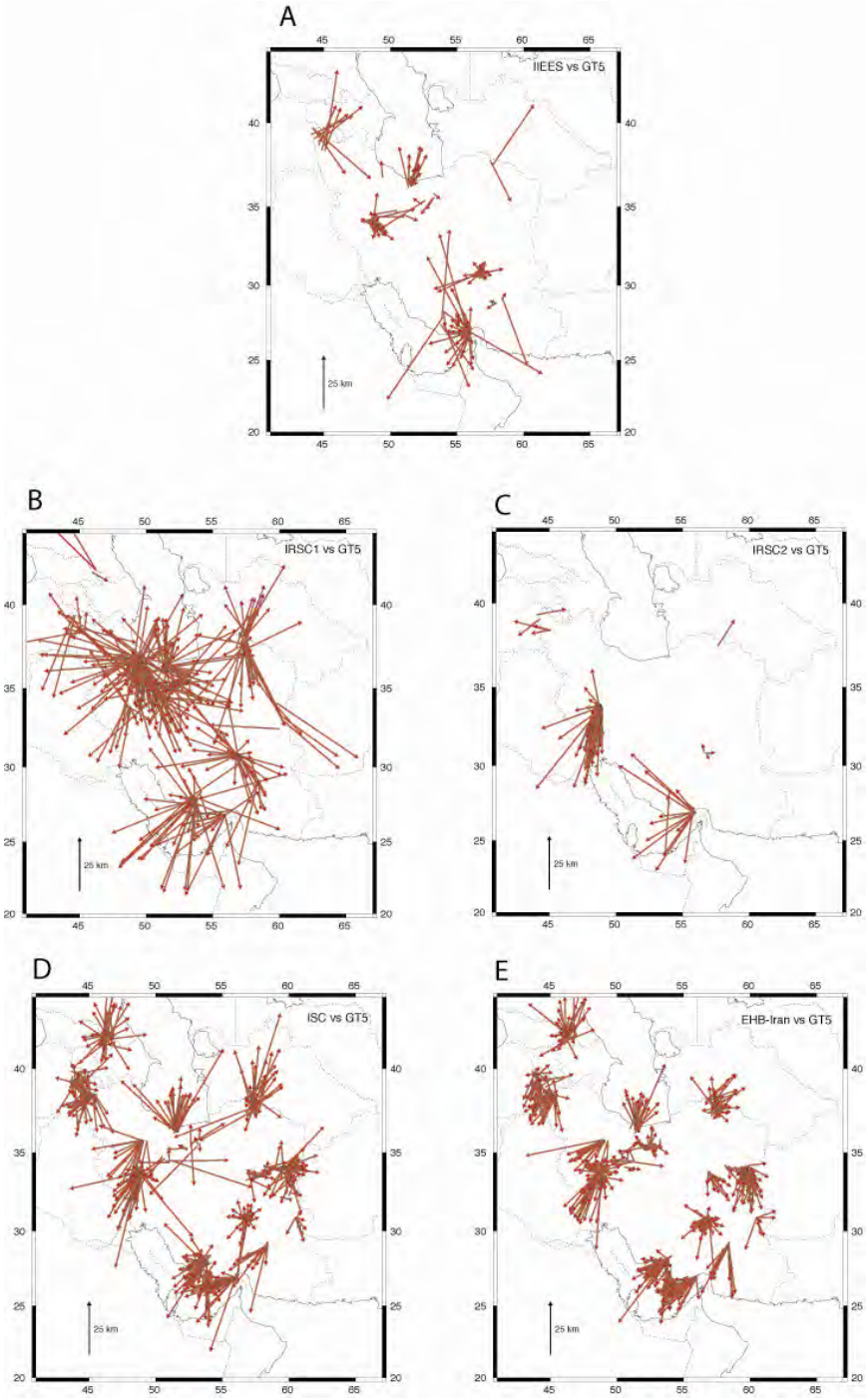

Figure 2. Mislocation vectors for locations for different catalogs, in comparison with corresponding GT5 locations. Only vectors with length less than 50 km are plotted.

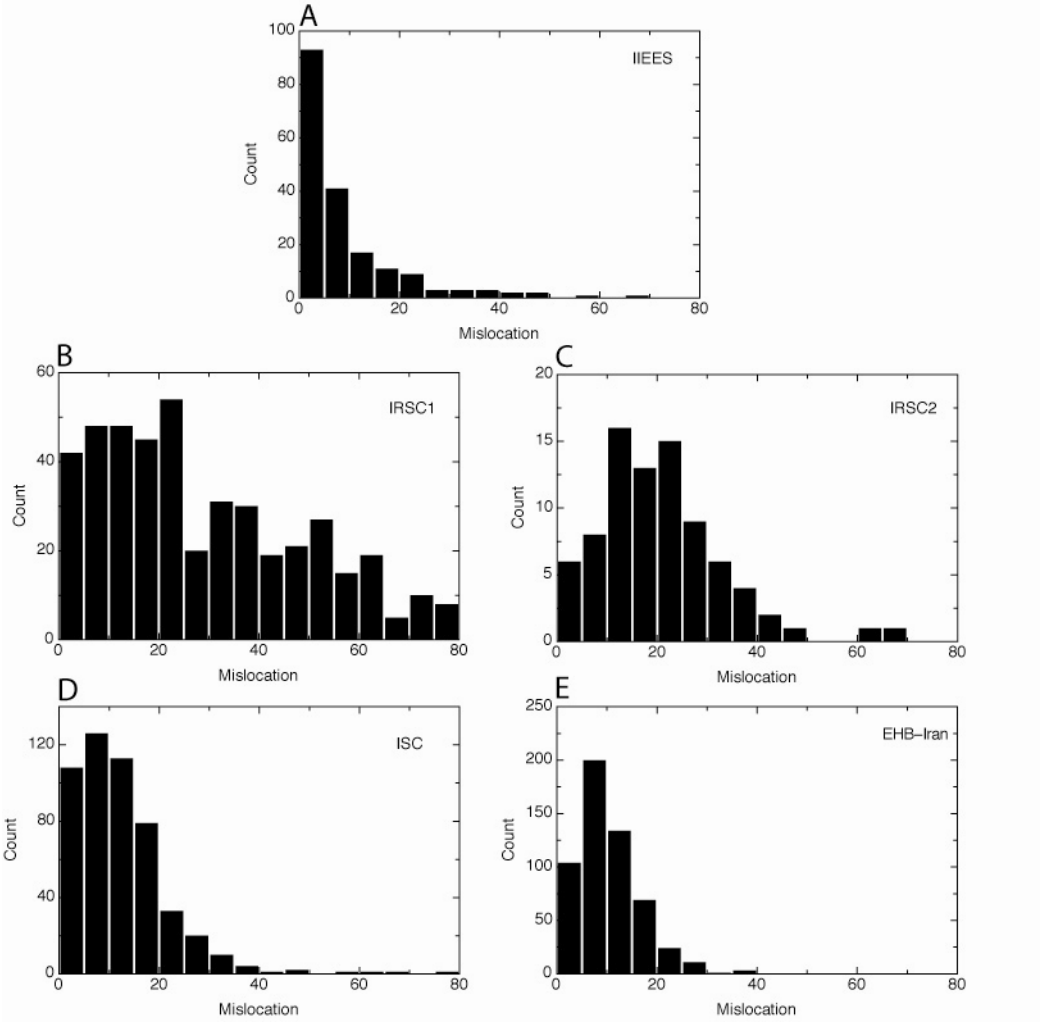

Figure 3. Histograms of mislocation distances of the different catalogs relative to the GT5 data set.

Table 2. Statistics of mislocation vectors of several seismic networks compared with the set of corresponding GT5 locations.

	# Samples	Median (km)	Mean (km)	90% (km)	Max (km)
IIEES	188	5.1	10.1	22	87
IRSC1	538	31.3	49.3	123	275
IRSC2	82	19.6	21.0	36	67
ISC	501	10.6	12.6	23	170
EHB-Iran	546	9.1	10.3	18	38

Azimuthal Bias in Locations

To explore the possibility of a systematic direction of location bias, we made sector plots of the mislocation vectors for each catalog (Figure 4). All the networks considered exhibit a tendency for systematic bias in certain directions, driven by the convolution of station geometry with the distribution of seismicity in the region, and scaled by the appropriateness of the travel time model used for location.

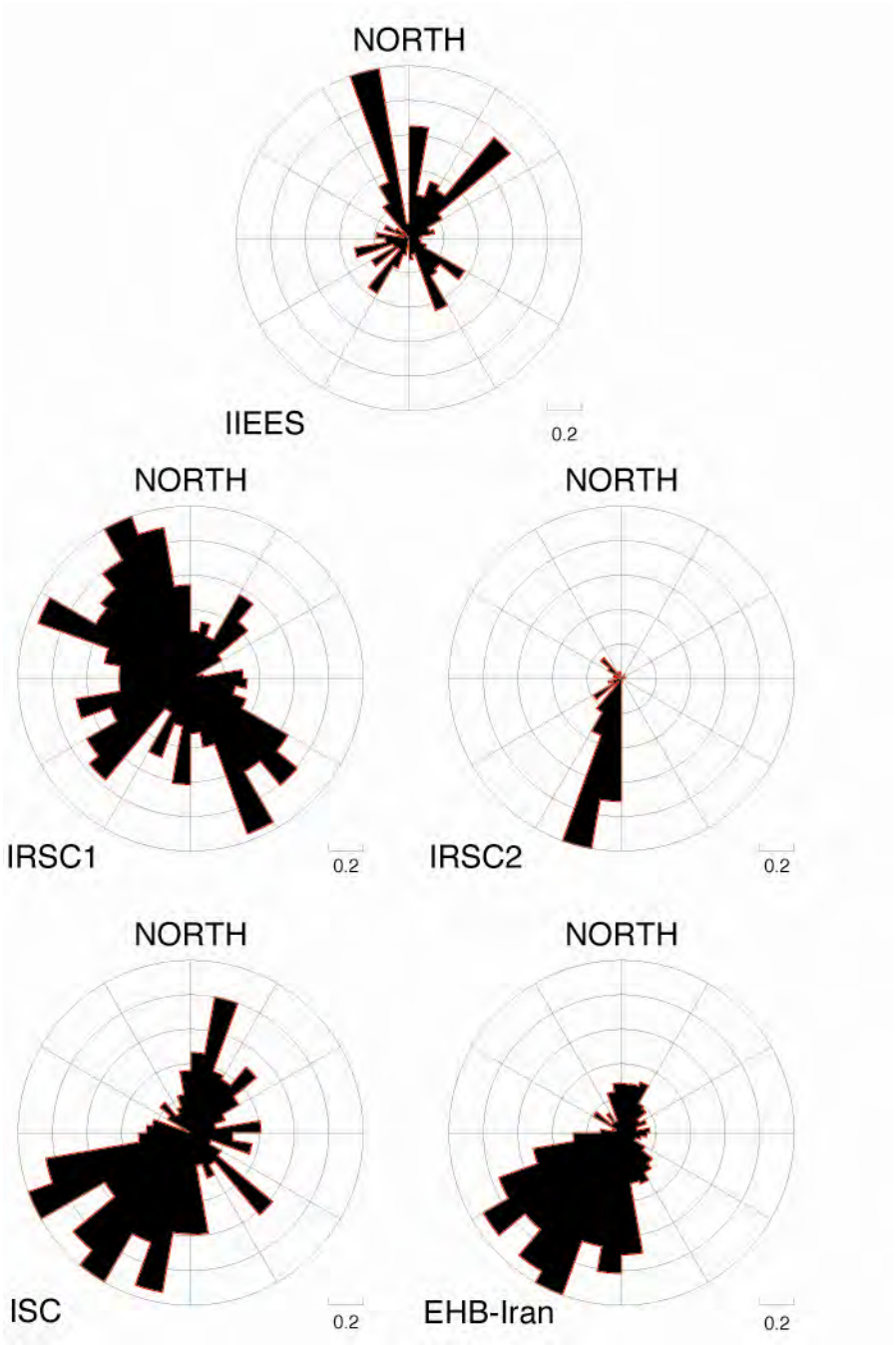

Figure 4. Sector diagrams of the azimuth of mislocation for the different catalogs. Sectors are 30° in azimuth.

The number of mislocation vectors in each sector is normalized to the most populous sector.

The IIEES catalog tends to be biased to the north, and probably represents a tendency for epicenters to be pulled toward the bulk of the stations. The IRSC1 (pre-2006, subnetwork solutions) catalog shows a strong NW-SE trend for mislocations. It may be that this pattern is the sum of two patterns such as is seen for the IIEES catalog, dominated by the frequent seismic activity in the NW-SE trending Zagros region. Some subnetworks of the ISTN see more events to the northwest and some see more events to the southeast. The sector plot for the IRSC2 catalog (post-2006) is dominated by a single calibrated cluster (Dorud), for which IRSC locations were systematically too far south, but this should not be taken to represent the performance of the ISTN network in all parts of the region. The two catalogs (ISC and EHB-Iran) that are based largely on teleseismic and far-regional phase readings both exhibit a strong tendency to mislocate events to the southwest. This is especially true of the EHB-Iran catalog, from which the grossest consequences of poor azimuthal coverage and large outlier readings have been removed. What remains is a signal that is the result of a significant and regionally-consistent departure of real Earth structure in the study region from that assumed in the theoretical travel-time model used for location. All EHB-Iran locations are based on the ak135 model (Kennett et al., 1995); all ISC locations in this comparison are based on the Jeffreys-Bullen tables (ISC has recently begun using ak135).

In broad terms the systematic direction of mislocation can be summarized as a consequence of the fact that there are far more seismic stations in the northern hemisphere, relative to the study region, and that the true travel times are larger than the theoretical ones, yielding positive travel-time residuals (Figure 5). The inversion for location tends to push the event further away from the bulk of seismic stations, i.e., to the south. The EHB-Iran catalog simply ignores the worst cases of poor azimuthal distribution, but it cannot correct the fundamental imbalance of global station distribution.

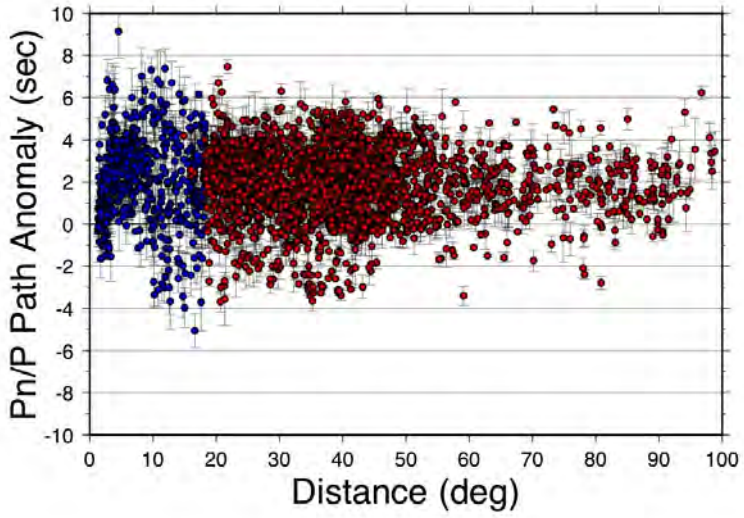

Figure 5. Empirical path anomalies for Pn (blue) and P (red) phases for $GT5_{90}$ events in the study region, calculated as the difference between the observed travel time of the phase arrival from a calibrated location (including origin time) and the theoretical travel time calculated with the ak135 velocity model. On average over the entire epicentral distance range, ak135-derived travel times are about 2 seconds faster than the travel times derived from calibrated locations.

CONCLUSIONS AND RECOMMENDATIONS

880 earthquakes in 21 clusters have been analyzed using a multiple event relocation technique for calibrated locations that remove most of the systematic bias in single-event locations done with regional and teleseismic data. 684 of these calibrated events have location uncertainties that qualify them as $GT5_{90}$ or better. By comparing these

locations with those from the catalogs of global and regional networks (all of which are based on 1-D Earth models), we investigate the location accuracy of those networks in the region. Earthquake locations in the study region which are based on regional and teleseismic arrival time data (ISC and EHB) are systematically biased to the southwest and have a 90% location accuracy of 18-23 km, with the lower value achievable by applying limits on secondary azimuth gap. Iranian seismograph networks have operated both as regional networks (IIEES and the IRSC since 2006) and local networks (IRSC prior to 2006). The IIEES catalog achieves the best location accuracy in this category, with a 90% accuracy level of 22 km. The IRSC network, even in recent years, when all the subnetwork data have been combined, suffers from a very imbalanced distribution of stations and achieves a 90% level of accuracy of 36 km. When IRSC subnetworks are used independently to locate earthquakes, as was typically the case prior to 2006, location accuracy at the 90% level exceeds 100 km. The IIEES catalog has a systematic location bias towards the north. The data for the IRSC catalog are inadequate for an analysis of systematic mislocation directions. In broad terms, location accuracy in the study region using 1-D travel time models and single event location procedures, is presently limited to about 20 km at the 90% level of accuracy (i.e., $GT20_{90}$). These results emphasize the importance of developing improved velocity models for the region which can more reliably predict seismic travel times at regional distances. The data set of calibrated earthquake locations assembled for this study has exceptional value as a validation tool for such efforts.

ACKNOWLEDGEMENTS

We gratefully acknowledge the assistance and advice of colleagues in the region who helped us to acquire and evaluate the various data sets that were used. We acknowledge Istvan Bondàr and Bill Rodi for many useful discussions on statistical aspects of earthquake location accuracy.

REFERENCES

Bondár, I., E. A. Bergman, E. R. Engdahl, B. Kohl, Y.-L. Kung, and K. McLaughlin (2008). A hybrid multiple event location technique to obtain ground truth event locations, *Geophys. J. Int*. 175: 185–201.

Engdahl, E. R., R. D. Van der Hilst and R. P. Buland (1998). Global teleseismic earthquake relocation with improved travel times and procedures for depth determination, *Bull. Seismol. Soc. Am.* 88: 722–743.

Jordan, T. H. and K. A. Sverdrup (1981). Teleseismic location techniques and their application to earthquake clusters in the south-central Pacific, *Bull. Seismol. Soc. Am.* 71: 1105–1130.

Kennett, B. L. N., E. R. Engdahl, and R. P. Buland (1995). Constraints on seismic velocities in the Earth from traveltimes, *Geophys J. Int.* 122: 108–124.

Rodi, W., E. R. Engdahl, E. A. Bergman, F. Waldhauser, G. Pavlis, H. Israelsson, J. Dewey, and M. Toksöz (2002). A new grid-search multiple event location algorithm and a comparison of methods, in *Proceedings of the 24th Seismic Research Review – Nuclear Explosion Monitoring: Innovation and Integration*, LA-UR-02-5048, Vol. 1, pp. 403–411.

ESTABLISHING AND VALIDATING EMPIRICALLY-BASED GROUND TRUTH CRITERIA FOR SEISMIC EVENTS LOCATED USING REGIONAL NETWORKS

Richard Brazier[1], KB Boomer[2], Steven Myers[3], Andrew Nyblade[1], and Jennifer Kokoska[2]

The Pennsylvania State University[1], Bucknell University[2],
and Lawrence Livermore National Laboratory[3]

Sponsored by the Air Force Research Laboratory and the National Nuclear Security Administration

Award Nos. FA9453-10-C-0211[1,2], LL-10-BAA10-420NDD03[3]
Proposal No. BAA10-42

ABSTRACT

Determining accurate seismic locations with representative uncertainty estimates is of fundamental importance to ground-based nuclear explosion monitoring, including the assignment of accurate ground truth (*GT*) levels. The monitoring community relies on selection criteria for classifying seismic events at the *GT*5 level, which specifies the absolute location and depth errors as being less than 5 kilometers. Regional-network locations are currently validated at the $GT20_{90\%}$ level, which does not satisfy the requirement for $GT5_{95\%}$ validation for inclusion in the NNSA Knowledge Base.

Our recent work testing the existing *GT* criteria against *GT0* mine events in southern Africa recorded on a sparse regional network shows that the *GT* criteria presently used by the community are overly restrictive. Consequently, there are likely many *GT5* events recorded by regional networks that do not appear in *GT5* catalogs, including events in strategically important areas. To identify these events and get them added to the *GT5* catalogs, new criteria for acquiring location ground truth from regional networks need to be developed that both account for the complexities in Earth structure beneath a network, and the fact that through careful phase picking, high quality travel time measurements can be obtained.

Using the methodologies developed by Bondár et al. (2004) and our empirically based ground truth criteria for the Kaapvaal Craton in southern Africa, (Boomer et al., 2010), we have obtained preliminary criteria for Main Ethiopian Rift based on reference events from the EAGLE refraction line shots and phase II and III stations. This new criterion has the potential to add 70 events to the Ground Truth database.

OBJECTIVES

Determining accurate seismic locations with representative uncertainty estimates is of fundamental importance to ground-based nuclear explosion monitoring, including the assignment of accurate ground truth (*GT*) levels. The monitoring community relies on selection criteria for classifying seismic events at the *GT*5 level, which specifies the absolute location and depth errors as being less than 5 kilometers. Regional-network locations are currently validated at the $GT20_{90\%}$ level, which does not satisfy the requirement for $GT5_{95\%}$ validation for inclusion in the NNSA Knowledge Base.

Our recent work testing the existing global *GT* criteria against *GT0* mine events in southern Africa recorded on a sparse regional network shows that the global *GT* criteria (Bondár et al., 2004; Bondár and McLaughlin, 2009) presently used by the community may be overly restrictive in some regions, at least for regions with relatively homogeneous crustal and upper mantle structure (Boomer et al., 2010). Consequently, there are likely many *GT5* events recorded by regional networks that do not appear in *GT5* catalogs, including events in strategically important areas.

The objective of this project is to develop new criteria for acquiring location ground truth from regional networks that both account for the complexities in Earth structure beneath a network, and the fact that through careful phase picking, high quality travel time measurements can be obtained. Empirically based ground truth criteria (*EBGT*) will be developed for the Main Ethiopian Rift and the Tibetan Plateau, which are both regions with more complex structures than southern Africa.

The *EBGT5* criteria for these two regions, when combined with the criteria already obtained for the Kaapvaal Craton, will enable us to compare regionally-developed criteria against the existing global criteria for a range of tectonic settings (i.e., stable craton, plateau within a collisional zone, and an active rift). We anticipate that as the level of heterogeneity in the geologic structure increases, at some point the regional *EBGT* criteria will become similar to the global 2004 and 2009 criteria. Once the *EBGT* criteria appropriate for each tectonic setting has been established, in the second part of this project we will apply them to several datasets from eastern Turkey, the Arabian Peninsula, the Tibetan Plateau, and Kyrgyzstan with the goal of identifying new *GT5* events. In addition, we will use a correlation method between observed and synthetic seismograms to improve the precision of the arrival time measurements, thus further improving the location accuracy of the events we anticipate adding to the *GT5* catalog.

RESEARCH ACCOMPLISHED

The deliverables for the first year of this project include the development of *EBGT5* criteria for the Main Ethiopian Rift and the Tibetan Plateau.

Geological Background and Data Sources

The Main Ethiopia Rift is geologically very complex, and the well determined crustal and upper mantle studies from several seismic investigations have revealed heterogeneity in structure both across and along the rift. We are using the data set from the 2003 Ethiopia-Afar Geoscientific Lithosphere Experiment (EAGLE; Maguire et al., 2003) to obtain *EBGT5* criteria for this rift. The data set includes a combined active-passive source seismic experiment, where 25 large shots were well recorded across the refraction profiles as well as by a local/regional network of 80 broadband stations (see Figure 1). Arrival times from these shots were provided by Keranen et al. (2004). Station dependant velocity models were adapted from EAGLE refraction studies (Maguire et al., 2006) and receiver function models from Dugda et al. (2005). In addition, Keir et al. (2006) provide a seismicity study of the rift using the broadband stations, listing over 2000 local events; the Ethiopian Broadband Seismic Experiment recorded over 400 local and regional events on 25 broadband seismic stations between 1999 and 2001 (Brazier et al., 2008).

The Tibetan Plateau resulted from a continent-continent collision between the Indian and Eurasian plates, creating an uplifted region (5 km of topography in places) that is 550-1200 km wide with crustal thickening of up to ~70 km. The crust and upper mantle structure of the plateau is arguably much more complicated than for the Kaapvaal Craton yet less complicated than the Main Ethiopian Rift, and includes a number of prominent suture zones.

The International Deep Profiling of Tibet and the Himalaya (INDEPTH III) project conducted a 400 km long passive-active seismic project across the Tibetan Plateau using 50 shots, each of at least 50 kg. At the conclusion of the active-source experiment, many broadband stations remained in place to record naturally occurring seismic events. Langin et al. (2003) provided a seismicity study of the local and regional events recorded by the project and a catalog of 267 local and regional events, many of them with magnitudes larger than 3 (see Figure 2). Waveforms and arrival times for all 50 shots have been collected for broadband and refraction lines stations; a selection will be used as reference events and the rest will be used as a validation data set.

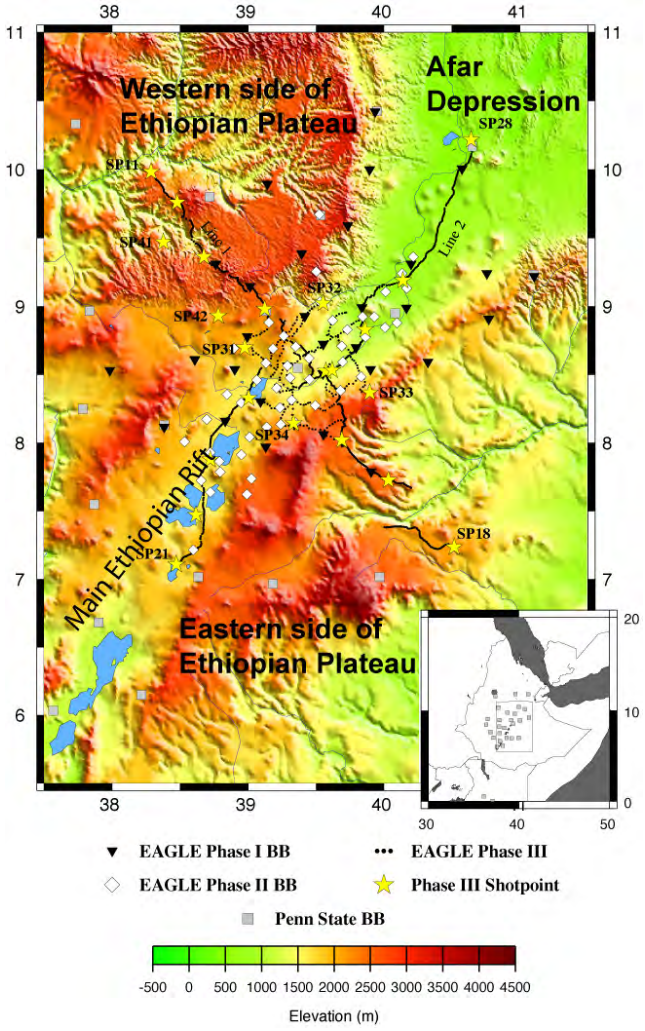

Figure 1. Map of central Ethiopia showing the location of seimic stations and shotpoints for the January, 2003, EAGLE project (figure from Maguire et al., 2003). The insert map shows location of broadband stations operated in the Ethiopia Broadband Seismic Experiment, 2000-2002 (Nyblade and Langston, 2002).

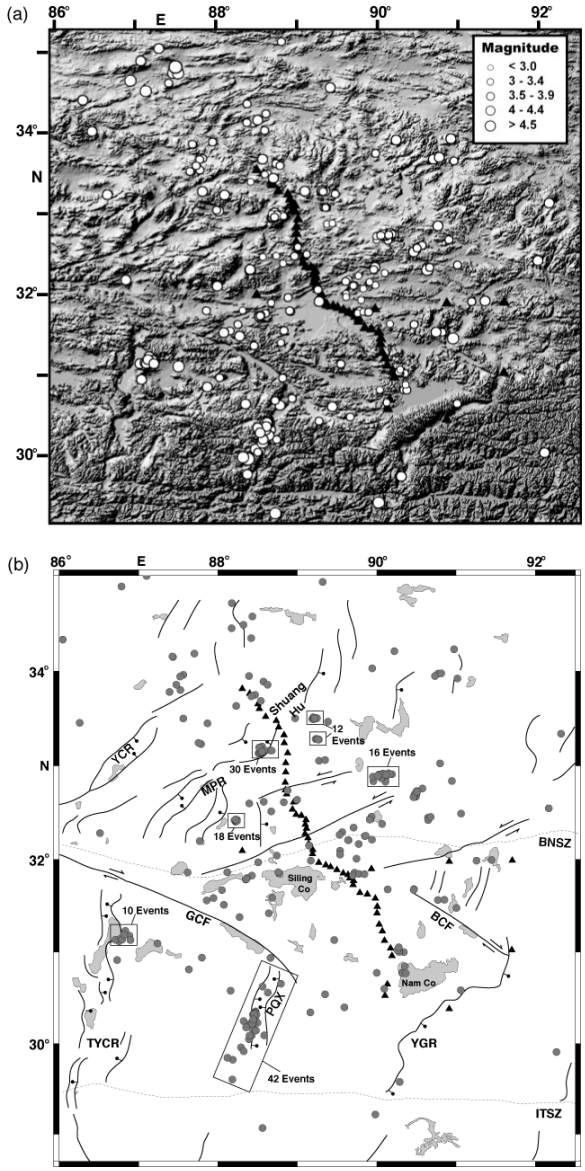

Figure 2. Maps showing local and regional seismicity from the INDEPH III project in the Tibetan Plateau (figure taken from Langin et al., 2003). Seismic station locations are shown with triangles, and epicentral locations with circles.

Development of existing *GT* criteria

Bondár et al. (2004) explore the use of network coverage as a metric for assessing location accuracy. In their work, network coverage was quantified by measuring not only the primary but also the secondary azimuthal gap. By restricting the primary gap to less than 110° and the secondary gap to less than 120° (160° for local networks), selection criteria (see Table 1) were developed to classify an event location as being accurate within 5 km (or 20 km, locally) with 95% (or 90%) confidence ($GT5_{95\%}$, $GT20_{90\%}$, respectively). As these criteria are based on the global *Pg/Pn* crossover distance of 250 km, they may not be representative of the local velocity structure and thus may lead to phase identification errors.

In 2009, Bondár and McLaughlin modified the selection criteria using a 150 km *Pg/Pb* crossover to relocate over 90 *GT*0 reference events, in part to address the concern over phase identification errors (Table 1). A new network

quality metric ΔU was introduced as a means to assess the uniformity of azimuthal coverage. This metric is similar to the Kolmogorov-Smirnov test of whether the station azimuths are uniformly distributed in a circle around the epicenter. Bondár and McLaughlin found that networks with values of ΔU less than 0.35 tend to provide *GT*5 candidates. As with the 2004 selection criteria, these modified criteria were developed using events recorded on a large number of local and regional recording stations with travel times reported in bulletins. Bondár and McLaughlin (2009) also simulate sparse networks and select the 20 most representative network geometries in developing their modified criteria.

Using a local *Pg/Pn* crossover distance of 215 km, Boomer *et al.* (2010) develop *EBGT* criteria for the Kaapvaal Craton. Networks with a primary gap greater than 202° yielded mislocations in excess of 40 km, which were considered to be obvious outliers. Further, due to the homogeneous crustal structure, secondary gap did not provide additional constraint. Unlike the regions used to develop the 2004 and 2009 criteria, the Kaapvaal Craton was measured with a sparse network, with some of the larger mine-related events (e.g. *GT*0 events) recorded on 16 or fewer stations.

Table 1: Existing epicentral location accuracy criteria

Network	Distance Range	Primary Azimuthal Gap	Secondary Azimuthal Gap	Number of stations within specified distance			GT level
				Between Pg/Pn crossover and 1000km	< Pg/Pn crossover	< Minimum Distance	
Local[a]	0°-2.5°	110°	160°		10	1 < 30km	$GT5_{95\%}$
Near Regional[a]	2.5°-10°		120°	10			$GT20_{90\%}$
Teleseismic[a]	28°-91°		120°				$GT25_{90\%}$
Kaapvaal EBGT[b]	0-215km	202°			8	1 < 78 km	$GT3_{95\%}$
Network	**Distance Range (degrees)**	**Network Metric**		**Number of stations within specified distance**			**GT level**
				Between 150km and 1000km	**< 150km**	**< 10km**	
Local[c]	0°-1.35°	< 0.35			5	1	$GT5_{95\%}$

Notes: [a]Bondár *et al.* 2004
[b]Boomer *et al.* 2010
[c]Bondár and McLaughlin, 2009

The re-sampling method often used in developing selection criteria (e.g. Bondár et al., 2004; Yang et al. 2006; Bondár and McLaughlin, 2009) is bootstrapping in which $k \leq n$ arrival times are sampled with replacement from the set of n available arrival times. Sampling with replacement is used to ensure independent samples, and, particularly when there are a large number of possible elements (e.g., arrival times), a large number of realizations can easily be achieved. The EBGT Kaapvaal Craton criteria were developed using a similar statistical re-sampling technique, the jackknife method. This approach considers all possible subsets of the $k \leq n$ arrival times, permitting the determination of criteria based on the number of recording stations.

Empirically Based Ground Truth Criteria for the Main Ethiopian Rift

Preliminary $EBGT5_{95\%}$ criteria have been developed for the Main Ethiopian Rift using two shots centrally located at the crossing of the refraction lines. Both these shots were recorded on over 600 stations including the broadband and refraction line stations. Three bootstrap samples, each based on 10,000 realizations of k = 7, 8 or 9 arrival times, were used to develop these criteria. Networks were quantified based on maximum epicentral distance and the network quality metric ΔU.

The criteria require that the maximum epicentral distance be less than 180 km, the local *Pg/Pn* crossover distance, and that $\Delta U < 0.45$. Scatter plots in Figure 3 and the empirical cumulative distribution functions in Figure 4 demonstrate that the estimated mislocation error is less than 5km, with 95% confidence, when $\Delta U < 0.45$ and the maximum epicentral distance is less than the local *Pg/Pn* crossover distance. Using the network quality metric with a lower threshold, such as $\Delta U < 0.35$, yielded a lower mislocation error. However, as these are preliminary results based on only two shot points, the conservative threshold of 0.45 is suggested. These results yield a set of preliminary empirically based ground truth criteria for the Main Ethiopian Rift (see Table 2).

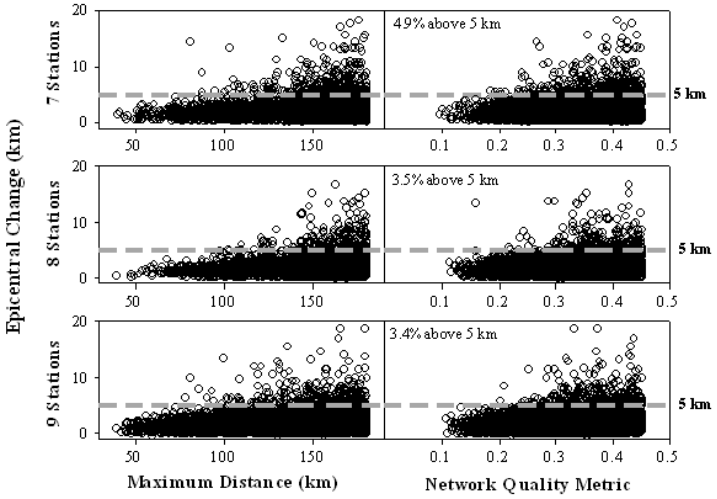

Figure 3. Maximum epicentral distance (< 180 km) and the network quality metric (< 0.45) versus change in epicentral distance for 7 to 9 stations. The *GT*5 levels are indicated and the % of data with change > 5 km is noted for ΔU.

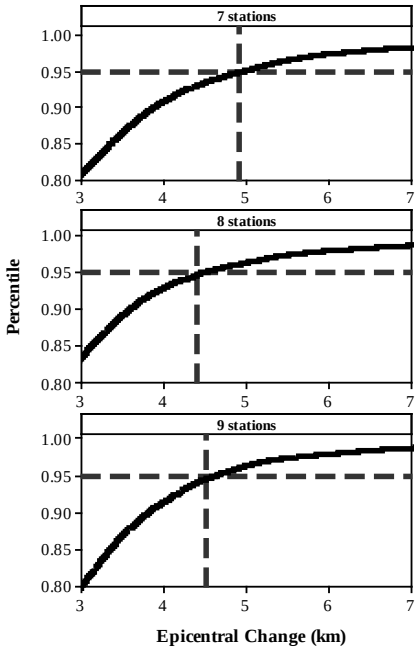

Figure 4: Empirical cumulative distribution functions demonstrate that the 95th percentile for absolute epicentral change is less than 5 km for 7, 8, and 9 arrival times.

Table 2: Preliminary $EBGT5_{95\%}$ criteria for the Main Ethiopian Rift

N° of stations within 180 km	One-sided 95% Confidence Interval (km)			Network Quality Metric Maximum
	Epicentral Change	Depth Change	Time Change	
7	[0, 4.9)	[0, 10.9)	[0, 0.86)	0.45
8	[0, 4.4)	[0, 10.2)	[0, 0.85)	
9	[0, 4.5)	[0, 8.5)	[0, 0.81)	

As an extension of the criteria in Table 2, the concept of using the degree of network azimuthal uniformity was explored by examining two well-established goodness-of-fit significance tests for the analysis of circular data. The Kuiper test (Kuiper, 1960; Fisher, 1993) is an analog of the Kolmogorov-Smirnov test in that it measures the maximum positive and negative difference between the empirical azimuthal distribution and a uniform distribution. It is more sensitive to differences between the empirical and expected (i.e., uniform) distributions than a standard Kolmogorov-Smirnov test. Values of the test statistics, V, greater than 1.747 suggest a network does not have an azimuthally uniform distribution. Related to the primary azimuthal gap, the circular range test calculates the length of the smallest arc, *w*, which contains all the observations (Mardia, 1972). With 8 arrival times, values of $w < 158°$ (equivalently, primary azimuthal gaps greater than 202°) suggest the stations are too clustered to represent a uniform distribution.

Figure 5 shows the empirical cumulative distribution of estimated mislocations for networks (within 180 km) with (i) $\Delta U < 0.45$ (solid black), (ii) $V < 1.747$ (dashed red) and (iii) $w > 158$ (dotted green). Our preliminary results suggest that $EBGT5_{95\%}$ criteria can be obtained using both these tests. An advantage of using a significance testing approach is that thresholds are based on statistical theory, and thus are not subjectively chosen. More work is needed to explore how clustering of stations within an azimuthal distribution impacts the effectives of such statistics for quantifying network quality.

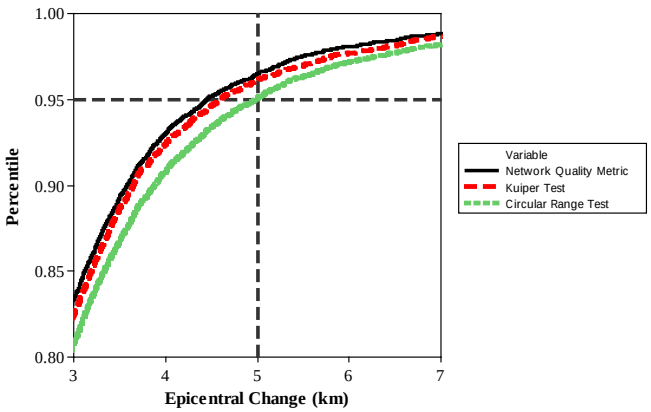

Figure 5. The 95th percentiles for estimated epicentral mislocation based on 8 arrival times using (i) the network quality metric ΔU, (ii) Kuiper V statistic, and (iii) circular range *w* statistics suggest these possible $EBGT5_{95\%}$ criteria.

CONCLUSIONS AND RECOMENDATIONS

The preliminary $EBGT5_{95\%}$ criteria for the Main Ethiopian Rift will be extended to include four more reference shots in different geological settings. There is a good potential for the addition of *GT5* events to the NNSA Knowledge Base; as many as 70 of the 450 local and regional events recorded on the Ethiopian Broadband Seismic Experiment network meet the preliminary criteria.

Collecting the arrival times and waveforms for refraction shots recorded as part of the INDEPTH III project will now be followed by careful picking and locating of the chosen reference shots. In addition, the regional empirically based criteria will continue to be compared with the existing global 2004 and 2009 criteria to assess whether there is a level of homogeneity in the geologic structure signally that the global criteria are overly restrictive or a level of heterogeneity at which no gains are made by developing regional criteria.

ACKNOWLEDGEMENTS

We thank K. Keranen for her assistance with EAGLE shot information and Incorporated Research Institutions for Seismology Data Management Center (IRIS) for data access.

REFERENCES

Bondár, I., S. C. Myers, E. R. Engdahl and E. A. Bergman (2004). Epicenter accuracy based on seismic network criteria, *Geophys. Jour. Int.* 156: 483–496.

Bondár, I, and K. L. McLaughlin (2009). A new ground truth data set for seismic studies, *Geophys. Res. Lett.* 80: 465-472.

Boomer, K., R. Brazier, and A. Nyblade (2010). Empirically-based ground truth criteria for seismic events located using regional networks with application to southern Africa, *Bull. Seismol. Soc. Am.* 100: 8–21.

Brazier R. A., Q. Miao, A. A. Nyblade, A. Ayele, and C. A. Langston (2008). Local magnitude scale for the Ethiopian Plateau, *Bull. Seismol. Soc. Am.* 98: 2341-2348, doi: 10.1785/0120070266.

Bump, H. A., and A. F. Sheehan (1998). Crustal thickness variations across the northern Tien Shan from teleseismic receiver functions**,** *J. Geophys. Res.* 25: 1055–1058.

Dugda, M. T., A. A. Nyblade, J. Julia, C. A. Langston, C. J. Ammon, and S. Simiyu (2005). Crustal structure in Ethiopia and Kenya from receiver function analysis: Implications for rift development in eastern Africa, *J. Geophys. Res.*, 110: B01303.

Efron, B. and G. Gong (1983). A leisurely look at the bootstrap, the jackknife, and cross-validation, *Amer. Statist.* 37: 36–48.

Fisher, N. I. (1993). Statistical Analysis of Circular Data, *Cambridge University Press*, 277pp.

James, D. E., M. J. Fouch, J. C. VanDecar, S. van der Lee and Kaapvaal Seismic Group (2001). Tectospheric structure beneath southern Africa, *Geophys. Res. Lett.* 28: 2485–2488.

Keir, D., G.W. Stuart, A. Jackson and A. Ayele (2006). Local Earthquake Magnitude Scale and Seismicity rate for Ethiopia, *Bull. Seismol. Soc. Am.* 96: 2221–2230.

Keranen K., S. Klemperer,R. Gloaguen, L. Asfaw, A. Ayele, C. Ebinger, T. Furman, S. Harder, G. Keller, G. Mackenzie, P. Maguire, and G. Stuart (2004). Three-dimensional seismic imaging of a protoridge axis in the Main Ethiopian Rift, *Geology (Boulder),* 32: 949–952.

Kuiper, N. H. (1960). Tests concerning random points on a circle, *Koninklijke Nederlandse Akademie Van Wetenschapen, Proceedings Series A*, 63: 38–47.

Langin, W.R., L.D. Brown, and E. A., Sandvol (2003). Seismicity of central Tibet from Project INDEPTH III seismic recordings, *Bull. Seismol. Soc. Am.* 93: 2146–2159.

Maguire, P.K.H, and 15 other authors (2003). Geophysical project in Ethiopia studies continental breakup, *Eos, Trans. AGU,* 84: 337–343.

Maguire, P K H, Keller, G R; Klemperer, S L, Mackenzie, G D, Keranen, K; Harder, S, O'Reilly, B, Thybo, H, Asfaw, Laike M, Khan, M A, Amha, M. (2006). Crustal structure of the northern Main Ethiopian Rift from the EAGLE controlled-source survey: A snapshot of incipient lithospheric break-up, *Geological Society Special Publications*, 259: 269–291.

Mardia, K.V. (1972) *Statistics of Directional Data*. Academic Press, 357pp.

Nyblade, A.A., and C. A. Langston (2002). Broadband seismic experiments probe the East African rift, *EOS, Transactions AGU*, 83: 405–408.

Yang, X., I. Bondár, J. Bhattacharyya, M. Ritzwoller, N. Shapiro, M. Antolik, G. Ekström, H. Israelsson, and K. McLaughlin (2004). Validation of regional and teleseismic travel-time models by re-locating ground-truth events, *Bull. Seismol. Soc. Am.*, 94: 897–919.

A LASER INTERFEROMETRIC MINIATURE SEISMOMETER

Dustin W. Carr, Patrick C. Baldwin, Shawn A. Knapp-Kleinsorge, Howard Milburn, and David Robinson

Symphony Acoustics, Inc.

Sponsored by the National Nuclear Security Administration

Award No. DE-FG02-08ER85108.001

ABSTRACT

The threat of nuclear proliferation remains a critical issue in our society. Prevention requires knowledge, and there is no greater indicator of the capability and intent of a nation than observation of actual detonation tests being conducted. Ground-based monitoring systems have proven to be very capable in identifying nuclear tests and can provide somewhat precise information on the location and yield of the explosive device. Making these measurements, however, currently requires very expensive and bulky seismometers that are difficult to deploy in places where they are most needed. A high-performance, compact device can enable rapid deployment of large-scale arrays, which can in turn be used to provide higher-quality data during times of critical need.

During our Phase I Small Business Innovation Research (SBIR) work, we designed and built a seismic sensor prototype that is 40 times smaller than existing state-of-the-art sensors. This acceleration sensor integrates optoelectronics, passive optics, and micromechanical structures in a compact assembly that is robust and extensible to manufacturing. The use of an optical interference transducer provides very high gain in the displacement measurement, which in turn leads to mechanical design parameters that are optimal for miniaturization without performance being sacrificed.

We extended this work in the first year of our Phase II research. Compact sensors were assembled in a robust connectorized housing. This sensor demonstrated substantial progress towards the goal of a very low noise seismometer, with a noise floor approaching –150 dB/Hz relative to 1 m^2/s^4. These prototypes shed light on the remaining issues to be addressed in order to reduce the noise to the target level of –168 dB/Hz from 0.1 Hz to 40 Hz. We need improvement in our sensor control electronics, in addition to compensation for the nonlinear optical response curve. These improvements will be implemented in the next prototypes to be built by the end of FY 2010.

OBJECTIVES

This goal of this work is to create a much smaller seismic sensor that is optimized for nuclear test ban treaty monitoring. Such a device would substantially reduce the deployment cost for temporary or permanent monitoring stations. The ultimate objective, as defined by the National Nuclear Security Administration (NNSA) in the original call for proposals, is to make a 1" sensor with performance that is equivalent to or better than the new low-noise model from 0.2 to 40 Hz, with a digital output and total power consumption of 100 mW. Such a device would represent a tremendous advance in the state of the art.

The technical objectives of our 2-year Phase II research, as established in our original proposal, are as follows:

1. Refine our sensor designs from Phase I so that they may extend to N-layer normal mode (NLNM**)** limited performance, along with the commensurate testing and verification procedures necessary to prove this performance.
2. Establish robustness and reliability testing for this new technology to enhance the opportunity for rapid acceptance in the marketplace.
3. Execute field tests using arrays of devices (10 to 100), in collaboration with systems-integration companies and/or government test facilities.
4. Establish collaborations with chip manufacturers and system integrators to create a digital output sensor that can be rapidly deployed in arrays.
5. Packaging of a compact, 3-axis digital sensor prototype that can be operated in any orientation and meets the specifications as spelled out by the Department of Energy.

RESEARCH ACCOMPLISHED

We did not explicitly separate the above objectives into yearly segments, but instead we presented a continuous 2-year plan for the accomplishment of these objectives. However, success of the first objective was determined to be the most important to focus on early in the project, as the sensor performance is the driver for all other progress. We successfully progressed through the design phases for the sensor, housing, and electronics. We designed a robust sensor with a standard connector that could survive in harsh environments. We then established a test plan for in-house testing, and we acquired the necessary data-acquisition and reference-sensor components that are required for this task. We then built several sensors and tested them. Our initial measurements showed a higher-than-expected noise floor but still a 10 dB improvement over our Phase I prototypes.

Our Phase I protoypes were very good for miniature seismometers, but they were still about 25 dB higher than the targeted noise floor. Those prototypes were intended to be a significant advance forward, and they were indeed about 30 dB better than previous attempts to make robust compact accelerometers. We began Phase II with a design phase to address the issues identified with the Phase I prototypes. We made numerous design changes in order to make improvements in the device noise floor. We increased our proof mass substantially and modified our spring design to increase sensitivity, while reducing our noise floor. These design changes resulted in the theoretical physical noise limits, defined by the mechanical thermal noise and the photodiode shot noise, being pushed to below the target levels.

We designed a housing made from anodized aluminum. A connector from Fischer was used for all of the I/O. This circular connector is the smallest that is readily available, while still meeting the requirements of robustness. It is a watertight, submersible connector (IP68). We also acquired custom cables built by Fischer. The completed sensor design is shown in Figure 1, along with a photo of an assembled device.

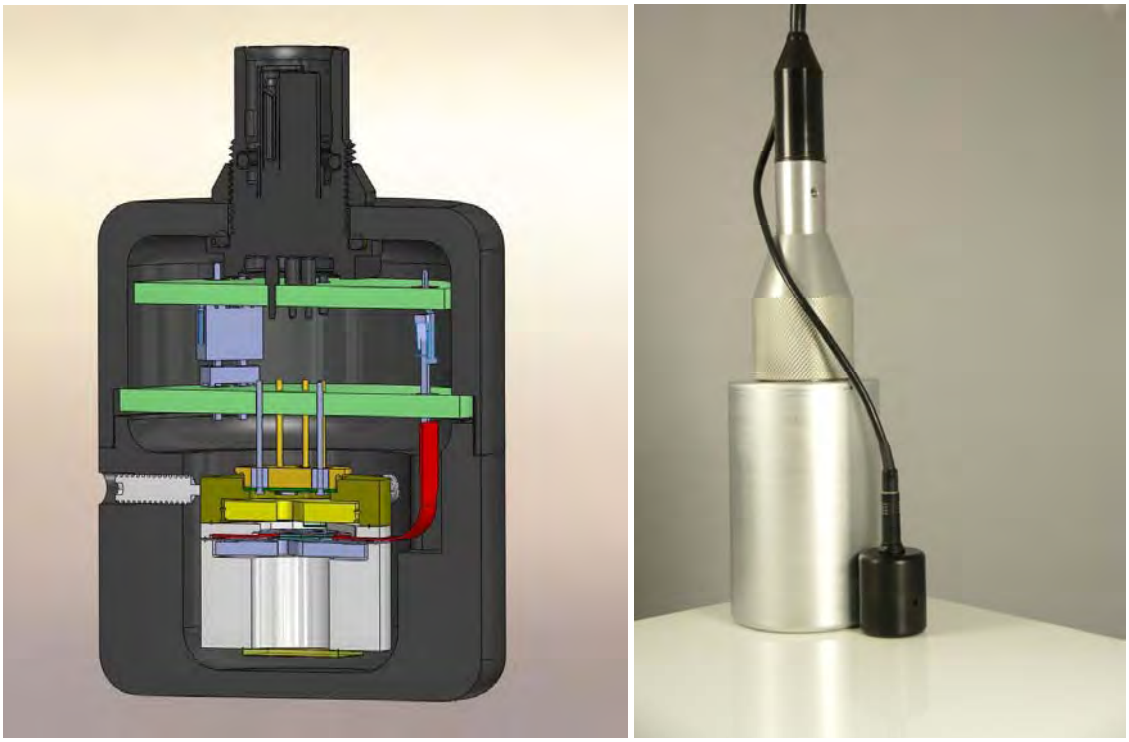

Figure 1. Left is a modeled cross-sectional view showing the sensor capsule, electronics, and housing. On the right is a completely assembled sensor, placed next to a 1-Hz geophone for reference.

The noise performance of the SA1210 was a considerable step forward, although we still have some ways to go before we achieve low-noise model performance. In Figure 2, we compare the low-frequency noise performance of devices from Phase I with the most recent devices from Phase II. The noise is dominated by our implementation of a mass-centering control loop that operates at very low frequencies to maintain the sensor at an optimal operating point. We are also impacted by the temperature sensitivity of the sensor and the very short time constant of the thermal coupling between the outer housing and the sensor capsule. As such, low-frequency noise measurements are usually dominated by ambient temperature fluctuations, an issue that would be greatly reduced in a typical shallow borehole deployment. Nonetheless, we are substantially altering the sensor design to eliminate these thermal issues.

The nonlinearity of the optical signal also must be accounted for, as aliased high-frequency signals (>100 Hz) can produce noise in the baseband. Since we are developing our own digital output implementation, compensation for this will be straightforward.

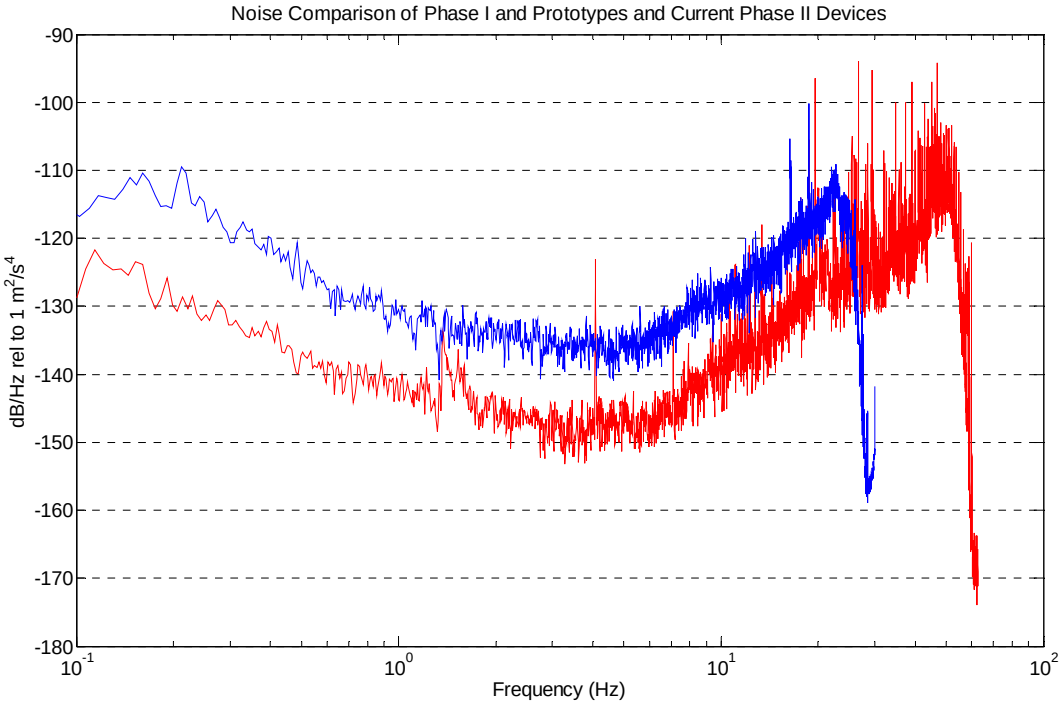

Figure 2. A comparison of the noise floor of our Phase I devices and our most recent Phase II devices. Above a few Hz, the ambient noise dominates in both spectra.

CONCLUSIONS AND RECOMMENDATIONS

The full SBIR project funding arrived very late in the fiscal year, which slowed our progress considerably. We are now developing a single-axis design that would more readily extend to three axes, in an effort to make rapid progress over the coming months. We have a good grasp of the various sources of noise in the sensor, and recent experiments indicate that we will be able to come very close to NLNM performance over the desired bandwidth.

ACKNOWLEDGEMENT

The authors would like to thank Darren Hart of Sandia National Laboratories for many useful discussions about the testing and deployment of sensors in the field.

REFERENCES

Carr, D., G. Bogart, S. Goodman, P. Baldwin, and D. Robinson (2008). A laser interferometric miniature seismometer in *Proceedings of the 30th Monitoring Review: Ground Based Nuclear Explosion Monitoring Technologies*, LA-UR-08-05261, Vol. 1, pp. 376–384.

Peterson, J. (1993). Observations and modeling of seismic background noise, Department of the Interior, U.S. Geological Survey open-file report, *OFR 93-322*.

OPTICAL MEMS-BASED SEISMOMETER "WhiGS"

Dominique Fourguette[1], Volkan Ötügen[2], Liane M. Larocque[1], Greg A. Ritter[1], Jason J. Meeusen[1], and Tindaro Ioppolo[2]

Michigan Aerospace Corporation[1] and Southern Methodist University[2]

Sponsored by the National Nuclear Security Administration

Award No. DE-FG02-08ER85099

ABSTRACT

Low-yield man-made seismic activity is difficult to detect and most often occurs in remote areas where seismic detection is weak. The Whispering Gallery mode based Seismometer (WhiGS), is an optical Micro-Electro-Mechanical System based (MEMS) instrument. The seismometer is a three-axis instrument, is compact, has low power consumption and is capable of unattended operation.

WhiGS exploits morphology-dependent optical resonance shifts in small dielectric spheres (<1 mm in diameter). These optical resonances, called whispering gallery modes (WGM), are extremely narrow, making the transducer highly sensitive to force ($< 10^{-9}$ Newtons). The MEMS sensing element in this seismometer has demonstrated an optical Q-factor of 10^7. As a result, the instrument is capable of measuring accelerations as low as 10 nano-g.

The engineering model to demonstrate the performance of the instrument has been built. Tests have demonstrated the sensitivity of the instrument. The development of the electronics is underway.

OBJECTIVES

Michigan Aerospace Corporation, in collaboration with Southern Methodist University, is developing a compact Whispering Gallery Seismometer (WhiGS). The sensing principle of the seismometer exploits the morphology-dependent optical resonance shifts of dielectric spheres to detect ground motion. These optical resonances are extremely narrow, making the transducer highly sensitive to ground motion. The small dielectric spheres are easily packaged into a small instrument capable of measuring accelerations as low as 10 nano-g.

The optical MEMS sensing element, typically a microsphere (with diameters in the range 200 to 1000 μm), is weakly coupled to an optical fiber, as shown in Figure 1a. The optical fiber, which carries light from a tunable laser, serves as an input/output port for the microsphere. When the microsphere comes into contact with an exposed section of the fiber core, light is coupled into the outer layer of the sphere, (Figure 1b). Its resonances are observed as sharp dips in the transmission spectrum as depicted in Figure 1d. When the sphere is compressed (as shown in Figure 1c), the wavelength of the resonances shifts.

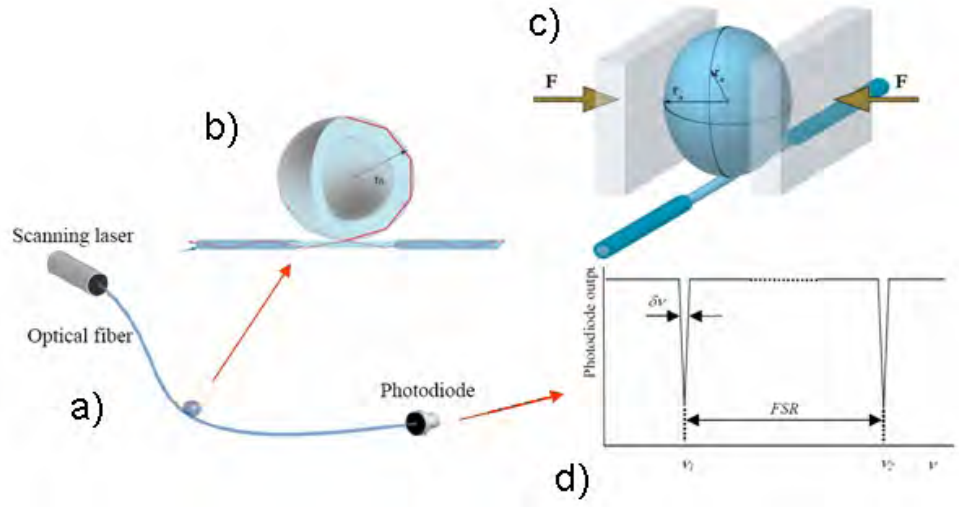

Figure 1: Principle of the WGM pressure-induced wavelength shift $\delta\nu$.

These optical resonances, also known as the "whispering gallery modes" (WGM), are extremely narrow and hence are highly sensitive to any morphological change in the microsphere. Other micro-resonator geometries, such as micro-discs, can be used as sensing elements in place of the microspheres.

The objectives include the fabrication of the dielectric microspheres, engineering model fabrication and preliminary tests, and instrument fabrication.

Objective 1:
The first objective of this effort is the experimental investigation of WGM characteristics of different-sized spheres (ranging from ~ 200 μm and 1 mm) and the fabrication of the microspheres. The candidate material to be used for the spheres is PDMS (commercially known as Sylgard 184). Different percentage of additives (cure agent) will be used to obtain different elastic modulus values and optical characteristics in order to determine the force sensitivity ranges that can be achieved and their suitability for the seismometer to be developed.

Objective 2:
The second objective was the fabrication of the engineering model to demonstrate the seismometer principle.

Objective 3:
The third objective entails the fabrication of the seismometer prototype.

RESEARCH ACCOMPLISHED

The transducer uses morphology-dependent optical resonances described by Benner and Hill (1988), WGMs in this case, investigated by Guan et al. (2006), to measure minute shape variations in dielectric spheres squeezed between the mass and the instrument base. Current studies by SMU using 0.7 mm spheres of another polymer, polydimethylsiloxane (PDMS), indicate that a force resolution of 10^{-8} N is possibly exploiting the same sensing principle. The dependence of the wavelength on the force is expressed as:

$$\delta F = \frac{\lambda}{Q}\left(\frac{d\lambda}{dF}\right)^{-1} \qquad (1)$$

where Q is the quality factor. The table below shows change of wavelength with force applied (dλ/dF) and the force resolution for several different sphere materials and dimensions. Polymer base-to-cure agent ratios of up to 60:1 were used in this investigation ($\frac{d\lambda}{dF} = 181 pm/\mu N$, ***Table 1***).

Our goal at onset of the program was to demonstrate the validity of the proposed concept using a bench test. To do so, a spring-proof mass assembly was designed, fabricated and tested to verify that

- The bandwidth extends over 40 Hz
- The spring is compliant enough to compress the sensing elements, i.e., the polymer microspheres
- And, the spheres register noticeable wavelength shifts at nano-g's acceleration.

The conceptual design of one axis of the seismometer is shown in Figure 2. The opto-mechanical assembly of the seismometer is composed of the spring-proof mass assembly and a polymer microsphere positioned between the proof mass and the seismometer base and an optical fiber to couple infrared light into the equatorial region of the microsphere. As the proof mass is set in motion by ground motion, the proof mass compresses a polymer microsphere. The morphological deformation of the microsphere under compression shifts the naturally occurring optical resonances in the sphere, proportionally to the physical deformation. The Q-factor of these optical resonances is ~10^7 thus providing the ability to detect acceleration as small as 10 nano-g.

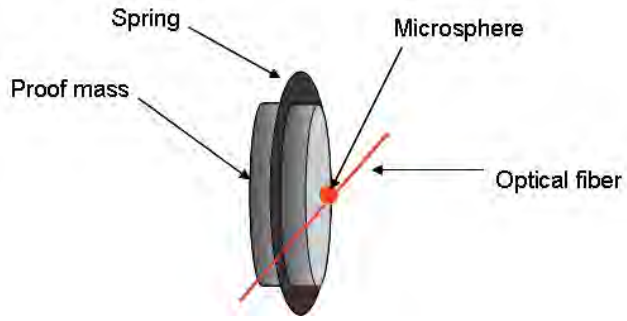

Figure 2. Whispering gallery mode based seismometer principle.

Table 1 lists the optimal characteristics for damping and sensitivity.

Table 1: Parameters for the mechanical design

Parameters	
Mass (kg)	0.01
Stiffness (N/m)	631
Resistance Constant (kg/s)	0.5
Sphere: PDMS	181 pm/μN
Q Factor (Mechanical)	5
Decay Modulus (s)	0.04

Spring Design

Finite element analysis was used to determine the optimal shape of the spring and the displacement. The spring must be sufficiently compliant to extend over a few nanometers and yet be stiff enough to ensure a flat response up to 40 Hz. The results of the spring design and deformation model is presented in Figure 3. The spring is composed of leaves that extend in the normal direction out of the plane of the spring. This design ensured radial stability under the gravitational acceleration. The thickness of the spring and the width of the slots define the spring stiffness, and two spring thicknesses were investigated.

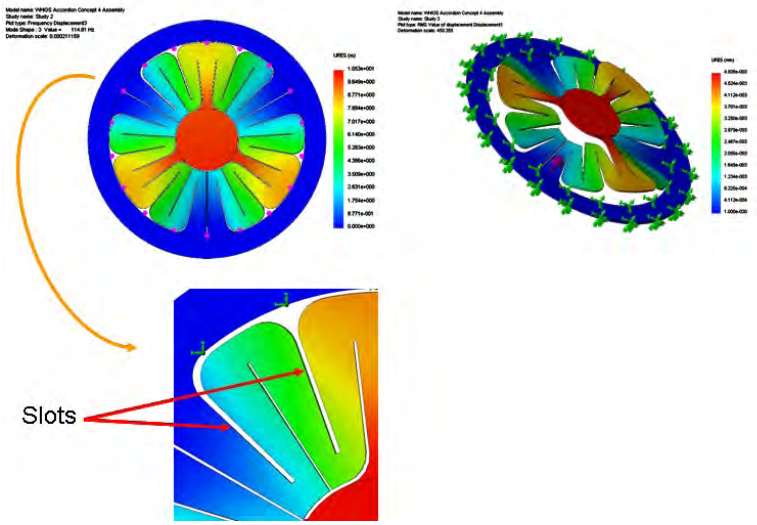

Figure 3. SolidWorks analysis of the spring design and deformation under static load.

Microsphere Fabrication

Our collaborator at Southern Methodist University, Professor Ötügen and his team, fabricated and delivered polymer (PDMS: polydimethylsiloxane) microspheres with curing agent ratios from 10:1 to 60:1. The curing agent ratio determines the hardness of the microsphere, 10:1 being the hardest. Figure 4 shows the microspheres held at the end of a fiber and a close up view of one of the spheres.

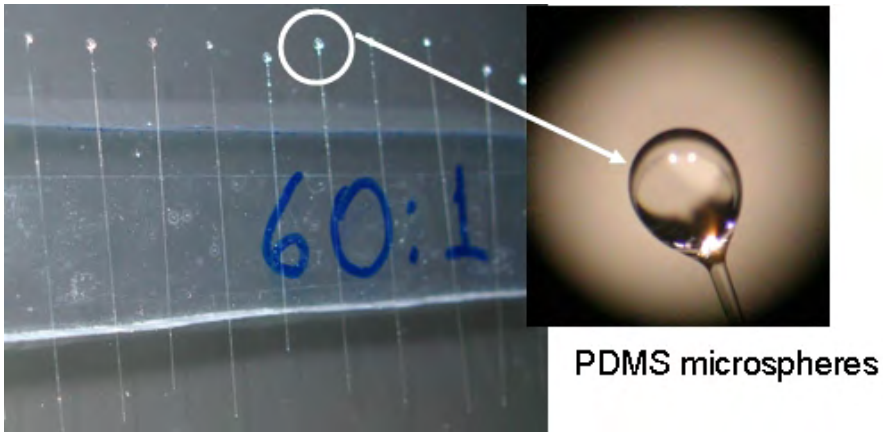

Figure 4 PDMS Spheres.

Accelerometer Design and Engineering Model

A prototype spring-proof mass assembly was fabricated and tested. Figure 5 shows a photograph of a spring and proof mass for the seismometer. The spring diameter is 0.88" (22 mm), thus very compact. The proof mass is 10 gm and fabricated out of tungsten. Springs of two different stiffness and slot widths were fabricated for testing.

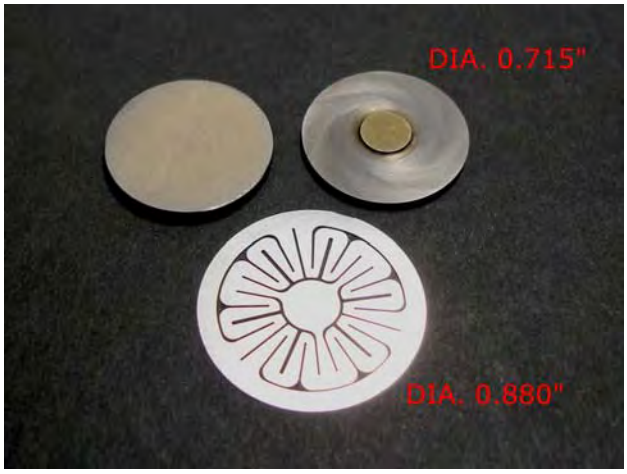

Figure 5 Spring and proof masses.

Test Results

A test rig, shown in Figure 6, was set up to measure the spring stiffness. The stiffness was measured by mass loading the spring with calibrated masses (against the gravitational acceleration) and measuring the elongation using a proximity sensor (placed under the spring). The results are shown in Figure 7. The spring stretched by 3.8 micrometer/gram, which provides a spring stiffness of 2.58×10^3 kg/s^2. For a proof mass of 10 gm, the resonant frequency is 80 Hz, sufficiently above the desired cut-off bandwidth at 40 Hz for the instrument. The spring elongation is a few hundred picometers, sufficient to generate a measurable shift in the whispering gallery mode resonance.

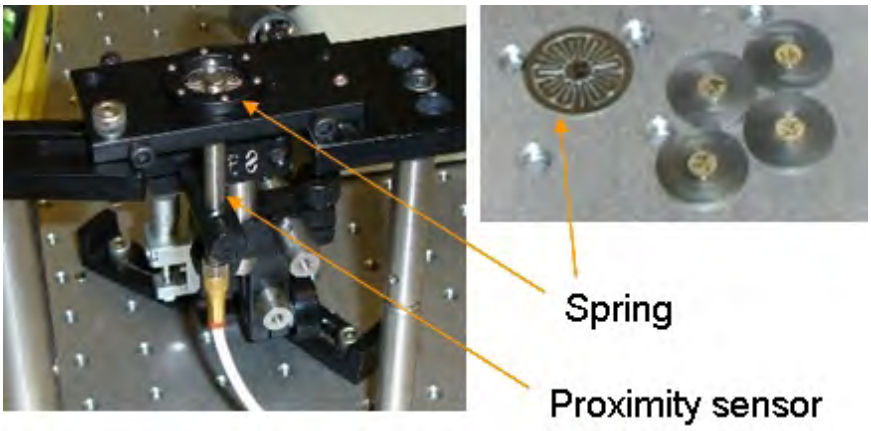

Figure 6. Test rig to measure the spring stiffness. (The tapped holes on the optical table are 1 inch apart).

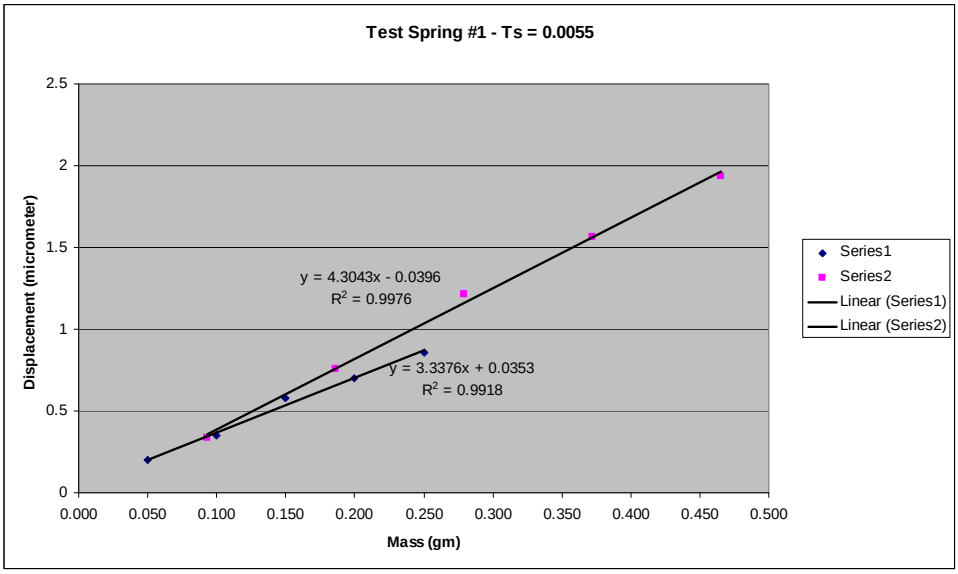

Figure 7. Test results to asses the stiffness of two springs.

Electronics

The development of the electronics entails the programming of an FPGA to digitize the output of the photodiode detector and track the resonance shifts caused by the deformation of the polymer microspheres under compression. The laser, laser driver and controller, fibers and photodiode detectors were assembled to characterize the laser performance and operating characteristics.

The laser has an integrated bias-t network inside the package that allows the use of an RF port on our laser diode holder to modulate the laser instead of using the modulation port on the laser controller. The lower cutoff frequency was near 650kHz therefore a capacitor was replaced to drive it with frequencies above 50kHz. The FPGA is currently being programmed for analog to digital conversion of the photodiode output.

The role of the processing electronics consists of identifying an optical resonance in the microsphere and tracking the wavelength shift of that resonance caused by the microsphere deformation, as shown in Figure 8. The processor instructs the driver controller to scan the current of the laser, and therefore the wavelength. The processor selects a resonance (dip in the detector output), and then instructs the driver controller to scan around the resonance. Once the processor is “locked” around a resonance, the current is dithered around that value.

Space conservation is paramount in the design of this small seismometer. The easiest way to conserve space is to reduce the number of pins and traces required for the circuit. All the components have been selected based on pin count and power dissipation. An analog-to-digital converter will be sampling the waveform detected from the photodiode. Parts are readily available with our constraints which dissipate roughly 3-5mW of power. The analog-to-digital converter would ideally be a serially-operated device to conserve the number of pins required for it to operate. Examples of such devices would be the AD7694 or the AD7685. A Field Programmable Gate Array (FPGA) was selected for this application (ACTEL Igloo Series). Assuming a 1-MHz internal clock rate and complexity similar to some of our other designs, the Igloo FPGA is expected to consume no more than 5mW of power. If for some reason the clock rate had to be increased to 5 MHz, the estimated power consumption would increase to about 15 mW (Table 2).

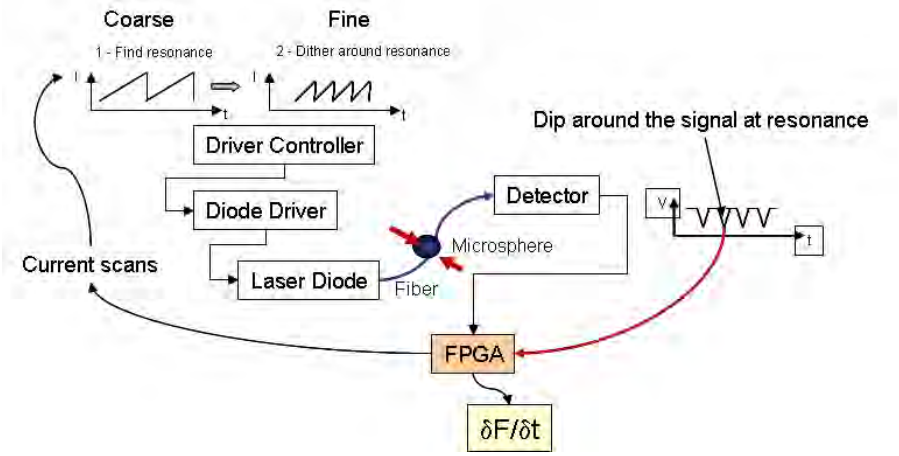

Figure 8. Functional diagram for the sensing element.

Table 2: Dissipation of the seismometer electronics components

Component	Dissipation (mW)
Laser Diode Controller	45
TEC Controller	100
Processor	15
Total	160

Our next effort entails installing a microsphere next to the proof mass and shaking the test assembly, as shown in the schematic in Figure 9. A shaker was purchased to test the instrument prototype.

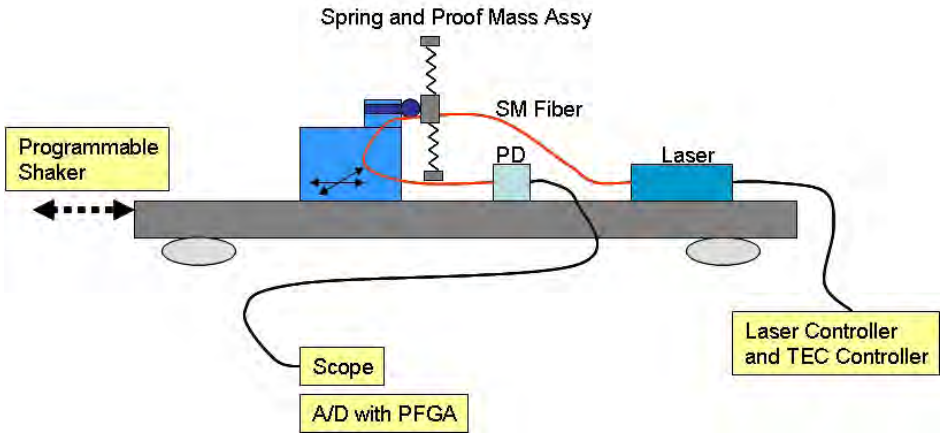

Figure 9. Schematic of test bench.

CONCLUSIONS AND RECOMMENDATION

The sensitivity of the sensing element was demonstrated using an engineering model. Results of photodiode outputs during acceleration will be pursued next.

REFERENCES

Benner, R. E.and S. C Hill (1988). Morphology-dependent Resonances, in *Optical effects Associated with Small Particles*, P.W. Barber and R.K. Chang, Eds., *Advanced Series in Applied Physics*, World Scientific.

Guan, G., S. Arnold and M. V. Ötügen, (2006). Temperature Measurements Using a Micro-Optical Sensor Based on Whispering Gallery Modes, *AIAA Journal* 44: 10, 2385–2389.

Ioppolo, T., U. K. Ayaz, U. K., and M. V. Ötügen (2009). High-resolution whispering gallery mode force micro-sensor based on polymeric spheres, Paper 2009-1450, 47th AIAA Aerospace Sciences Meeting and Exhibit, Orlando, FL.

MICRO-SEISMOMETERS VIA ADVANCED MESO-SCALE FABRICATION

Caesar T. Garcia, Guclu Onaran, Brad Avenson, Bryan A. Yocom, and Neal A. Hall

Silicon Audio, LLC

Sponsored by the National Nuclear Security Administration

Award No. DE-FG02-08ER85106

ABSTRACT

The Department of Energy (DOE) and the National Nuclear Security Administration (NNSA) seek revolutionary innovations with respect to miniature seismic sensors for the monitoring of nuclear detonations. Specifically, the performance specifications are to be consistent with those obtainable by only an elite few products available today, but with orders of magnitude reduction in size, weight, power, and cost. The proposed commercial innovation calls upon several advanced fabrication methods and read-out technologies being pioneered by Silicon Audio, including the combination of silicon microfabrication, advanced meso-scale fabrication and assembly, and the use of advanced photonics-based displacement / motion detection methods. Early Phase II development has demonstrated 1) verified and repeatable sub 2ng/√Hz noise floor from 5 to 100Hz, 2) compact integration of 3-axis prototypes and 3) robust deployment exercises. Ongoing developments are focusing on low frequency challenges, low power consumption, ultra-miniature size, and low cross axis sensitivity. Successful implementation will result in a demonstration unit roughly the size of a 9-volt battery with the ability to address advanced national security needs of the DOE/NNSA. Additional applications envisioned include military/defense, scientific instrumentation, oil and gas exploration, inertial navigation, and civil infrastructure monitoring.

OBJECTIVES

The DOE/NNSA seeks revolutionary innovations with respect to miniature seismic sensors for the monitoring of nuclear detonations. Specifically, the performance specifications are to be consistent with those obtainable only by a few elite products available today, but with orders of magnitude reduction in size, weight, power, and cost. The specific sensor specifications solicited are as follows:

- Size – less than 1 in^3
- Power – less than 100 mW
- Sensor self noise – below USGS NLNM, or approximately 0.5 ng/√Hz
- Dynamic range at least 120 dB over a frequency band of 0.2 to 40 Hz.

In a prior review (Hall, 2008), we summarized basic design considerations for any proposed technology aiming to meet the aforementioned specifications. In particular, it was shown that meeting the noise requirement demands both a) ultra-low thermal mechanical noise from the seismometer proof mass, and b) high resolution displacement measuring capability of the proof mass motion. As an example, a design with a 2 gram proof mass and 50 Hz open loop resonant frequency may be considered. In this case, achieving the required 0.5 ng/√Hz acceleration noise requires a resonance quality factor, *Q*, of 100 and an ultra-low displacement resolving capability of 50 fm/√Hz (Hall, 2008). The high resonance *Q*, in-turn, requires the use of closed-loop feedback altered dynamics to realize the desired flat frequency response of the sensor. This discussion provides the motivation for Silicon Audio's proposed design innovation, which calls upon advanced meso-scale fabrication of mechanical proof-mass elements, photonics-based displacement / motion detection, micro-scale optoelectronic integration, and the integration of closed-loop sensing modalities for high stability and high dynamic range. In subsequent sections, results are presented which demonstrate this approach.

Sensor Schematic

Phase I prototypes demonstrated the viability of a sensor system similar to that shown in Figure 1. The present design, which has been field tested and demonstrates sub 2ng/√Hz noise, is summarized in the following figure.

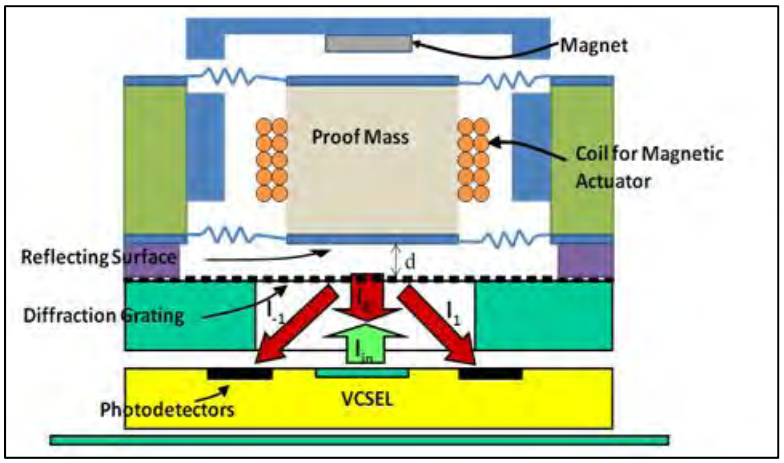

Figure 1. Schematic of a photonics based motion detection principle in development. Light from a semiconductor laser such as a vertical cavity surface emitting laser (VCSEL) illuminates a diffraction grating fabricated on silicon. A portion of the incident light reflects directly off of the grating fingers, while the remaining light travels in between the grating fingers and to the proof mass and back to accrue additional phase. A diffracted field results consisting of a zero and higher orders whose angles remain fixed, but whose intensities are modulated by the relative distance between the proof mass and grating with the sensitivity of a Michelson type interferometer.

A sensing method very similar to that summarized in the caption of Figure 1 has been demonstrated and described in detail in prior developments (Lee et al., 2004; Hall et al., 2007; Hall, et al., 2008). The diffraction grating in this

system serves the function of an optical beamsplitter, directly reflecting half of the incident light while passing the remaining half to travel to the proof-mass and back to accrue additional phase. Being an optical interference based approach, the displacement resolving capability of the method is of very high fidelity – on the order of 20 fm/√Hz when using small 500μW semiconductor lasers. The intrinsic open loop dynamic range of this approach (i.e., clip level) is limited to approximately λ/4, where λ is the optical wavelength. This corresponds to the peak-to-trough range of an interference cycle (i.e., fringe cycle) and is approximately 212 nm for an 850 nm wavelength semiconductor laser. Considering that 20 fm displacement can be resolved over a 1 Hz bandwidth, the intrinsic dynamic range is then 140 dB. Over the 40 Hz measurement bandwidth of interest, the open-loop dynamic range is 124 dB.

It is important that the interferometer be operated at a point of quadrature (i.e., a point of maximum slope and linearity on the interference curve). Figure 2 helps to clarify this by summarizing the theoretically predicted relationship between light intensity of the diffracted beams labeled in Figure 1 vs. the gap distance "d" also labeled in Figure 1. The center beam modulation is complementary to the sum of the exterior beams. Therefore, one can use the difference signal (in practice this is done by simple photocurrent subtraction), as the seismometer output signal. The linear operating region is highlighted in the figure. The slope of this curve is the displacement sensitivity of the detection method (after amplification through a photocurrent-to-voltage amplifier, the unit of the y axis is volts, and the sensitivity is therefore expressed in V/m).

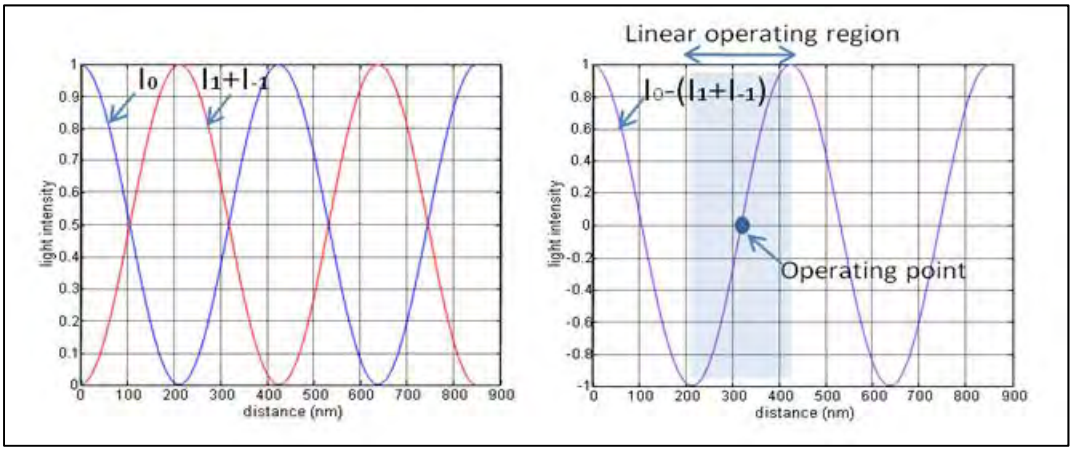

Figure 2. (left) Theoretically predicted relationship between the diffracted beams labeled in Figure 2 vs. gap distance "d" labeled in Figure 2. (right) The difference signal is then used to detect the proof mass motion within a single interference fringe.

Operation about a point of quadrature (i.e., the operating point labeled in Figure 2) is maintained by direct actuation of the proof mass using magnetic actuation. In addition, dynamic actuation of the proof mass also enables closed-loop measurement modalities. Closed loop operation is critical in high performance accelerometers, as the high *Q* of the open loop system required for low thermal noise must be electronically compensated for via feedback-altered-dynamics to achieve the desired flat frequency response (Liu and Kenny, 2001).

RESEARCH ACCOMPLISHED

In this report we present work related to mechanical and optical design optimization and demonstration of small (coke can size), fully integrated, 3-component sensor prototypes with 2ng/√Hz noise floor.

Design of Mechanical and Optical Systems

Using finite element analysis (FEA), a model has been constructed to analyze the mechanical aspects of the system. This model, shown in Figure 3, was first used to extract the higher order modes of the spring-mass system. These higher modes can become problematic for two reasons. First, it can be shown that cross axis sensitivity is adversely affected by these modes which tend to rock and respond to off-axis excitation. Secondly and perhaps less obviously, higher order modes limit the achievable bandwidth of the closed loop system and pose challenging demands on

closed loop stabilization circuitry[1]. By pushing these modes to higher frequencies, away from the fundamental mode of interest, these two problems can be overcome. Several iterations of spring design led to the current 4-arm structure shown. Using FEA tools, the frequencies of problematic higher order modes discovered in Phase I prototypes were positioned from a factor of 5 to a factor of 65 times the fundamental mode of interest.

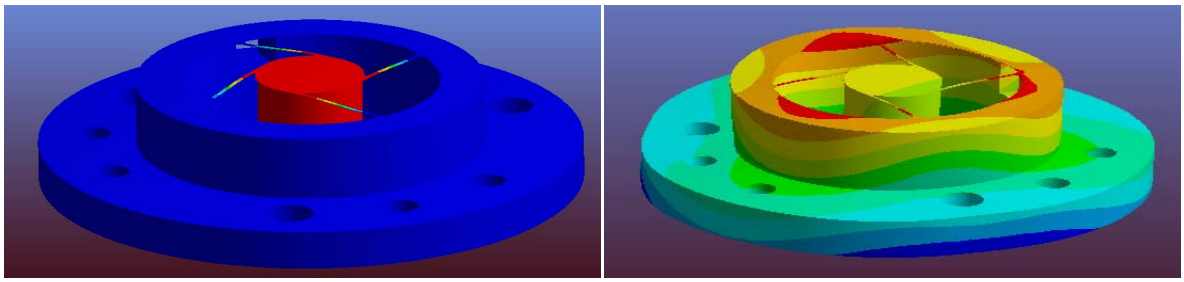

Figure 3. (left) FEA modal analysis used to isolate fundamental mode from higher order modes by a factor of 65. (right) FEA thermal analysis simulating temperature induced proof mass deflection.

A second FEA analysis studied the effects of temperature on low frequency signal drift which is believed to be the dominant source of *1/f* noise. Sensitivity of a Michaelson Interferometer depends on both wavelength, λ, and gap distance, d, labeled in Figure 1. Because both of these parameters are subject to change with temperature, it is possible to null out their effects on sensitivity by setting $\Delta d/d=\Delta\lambda/\lambda$ where Δ indicates a temperature induced change. The values of λ and $\Delta\lambda$ are provided by VCSEL manufacturers, and d is a known design parameter, approximately 25µm. Solving the relationship above leads to a desired Δd value on the order of 1nm/°C. FEA modeling of earlier designs predicted Δd values near 100nm/°C while the newer 4-arm design predicts a much improved value of approximately 10nm/°C with future designs anticipated to go even lower. In practice, the easiest way to measure the effectiveness of this design approach is to monitor the coil actuation signal as a function of temperature since this signal is tasked with compensating for any sensitivity drift left uncancelled. Experiments are presently underway to verify the effectiveness of this design.

Equally valuable insight into the optical system is gained by rigorous modeling efforts using custom Fourier Optics based simulations in combination with off the shelf ray-tracing optical modeling CAD tools. OSLO ray-tracing optical modeling software package was used to construct an accurate model of the complete optical system, including a diverging Gaussian source and monochromatic aberrations of lenses. Results from these simulations led to the conclusion that initial estimations of the focal plane location based on first order paraxial approximations were off by 15% leading to less than optimal tolerance to misalignment and optical surface flatness resulting in reduced modulation efficiency. Critical components of the CAD model are labeled in Figure 4.

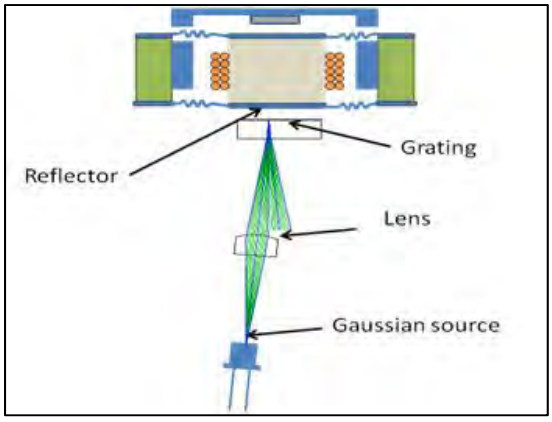

Figure 4: Computer aided optical modeling software improves upon first order paraxial assumptions by 15% to provide accurate focal plane prediction.

[1] Higher order modes can vibrate 180 degrees out of phase with the fundamental mode of interest. When doing so, they confuse the sign of gains in the proportional, integral, and derivative blocks of the proof mass control. This, in turn, can lead to positive rather than negative feedback which causes instability.

Detailed interactions of incident light with the grating/reflector/proof-mass sub-system cannot be studied with macro ray-tracing tools. A custom Fourier Optic diffraction simulation code was developed in Matlab for this purpose. This code, unlike the previous diffraction simulation mentioned in prior reviews (Garcia, 2009; Hall, 2008), was designed to account for relative tilt between grating and reflector planes as well as their absolute separation, *d* (labeled in Figures 1 and 5 (left)). The goal of these simulations is to generate sensor designs that maintain high optical modulation efficiency, which is defined by the peak-to-trough swing resulting from interference in the diffracted beams. Higher modulation efficiency yields higher output sensitivity and lower sensor self noise. The theoretical curves in Figure 2 display a modulation of 100%. In practice, achieving high modulation efficiency requires careful design.

Variables affecting modulation efficiency are highlighted in Figure 5 (left). These include incident beam angle, β, reflector tilt angle, α, and stand-off distance between the grating surface and the reflector, *d*. This stand-off, *d*, is also highlighted in the complete sensor schematic of Figure 1. Another important variable is the numerical aperture of the system, which is a measure of the cone angle of the incident beam focused onto the plane of the diffraction grating. The incident beam at the plane of the grating is focused, but because of the finite stand-off, *d*, and finite cone angle, the reflector plane is not illuminated with a focused beam. This is addressed in our model by defining a virtual source behind the reflector. Simulation results are presented in Figure 5 (right) for a fixed angle of incidence (β =2.5°) and a fixed cone angle of 5° full width at half maximum (FWHM). The contours represent various levels of modulation efficiency, 0.9 being the best defined in the figure and 0.1 being the worst. The modulation efficiency ratio is seen to be a function of α and *d*.

The choice of distance *d* is influenced by mechanical criteria in addition to optical design criteria. For example, *d* affects the damping dynamics of the proof mass structure due to squeeze film effects. For fixed *d*, the simulation results allow one to study the effect of reflector tilt on modulation ratio. The black solid lines in Figure 5 (right) highlight another fundamental design constraint, namely, the reflector should not touch the grating surface. For example, for a reflector diameter equal to 3mm, all possible designs lie to the right of the solid line in the figure. Understanding from this modeling is critical in prototyping and also in studying manufacturing and assembly tolerances in production.

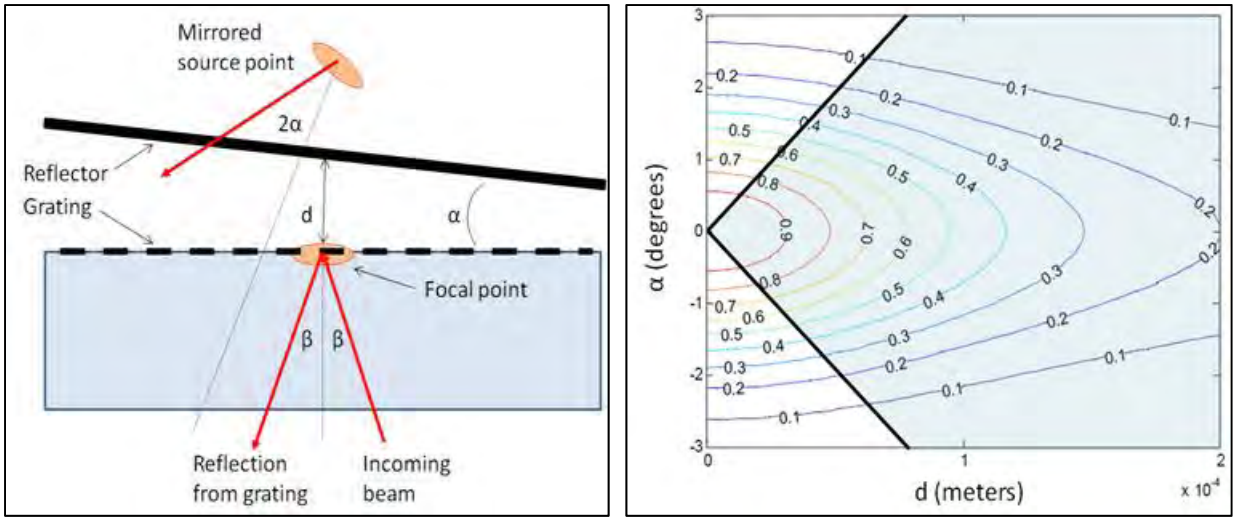

Figure 5. (left) Schematic illustrating relevant tilt angles. (right) Typical result assuming 2.5° incident beam angle (β) and cone angle of 5° FWHM showing contour lines of constant modulation ratio. In this figure a 3mm diameter reflector will limit access to the shaded region of the plot.

Field Testing of Three Axis Prototypes

Silicon Audio has successfully built and tested several 3-axis prototypes. These beta prototypes were designed to demonstrate the current state of the development effort and to address unanticipated challenges associated with building and testing a 3-axis seismometer. The compact design is roughly the size of a 12-oz coke can and incorporates a Galperin sensor orientation, semi-closed loop force feedback operation, automatic mass centering, and clip level stabilization. In Figure 6, a CAD image (left) is shown along with an actual photograph (right) of the field tested "GeoLight" prototype.

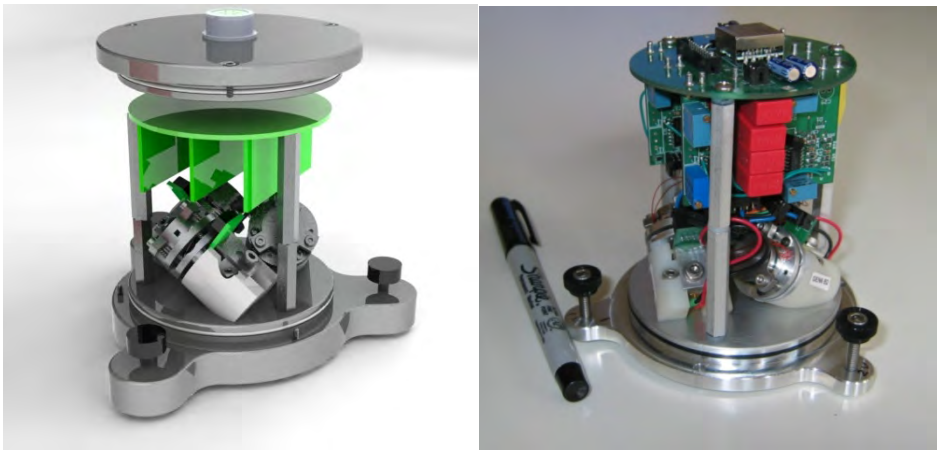

Figure 6. (Left) CAD image of GeoLight prototype along with (right) actual field tested prototype.

Prior to field testing, frequency response measurements of single axis sensors were measured (see Figure 7). In this measurement an excitation signal is provided using the sensor's magnetic coil input while the output signal is detected optically. This measurement highlights a useful self-test capability that can be performed in-situ to monitor each device's frequency response. In addition to testing sensor dynamics, large force excitations can be used to traverse multiple interference fringes (see Figure 2), which enable absolute displacement sensor calibration owing to the fixed optical wavelength. The flattened response is attributed to closed-loop feedback altered dynamics which are summed together with the external excitation signal at the coil input (see Garcia, 2009). Here, the *Q* factor is reduced from roughly 100 down to critical damping.

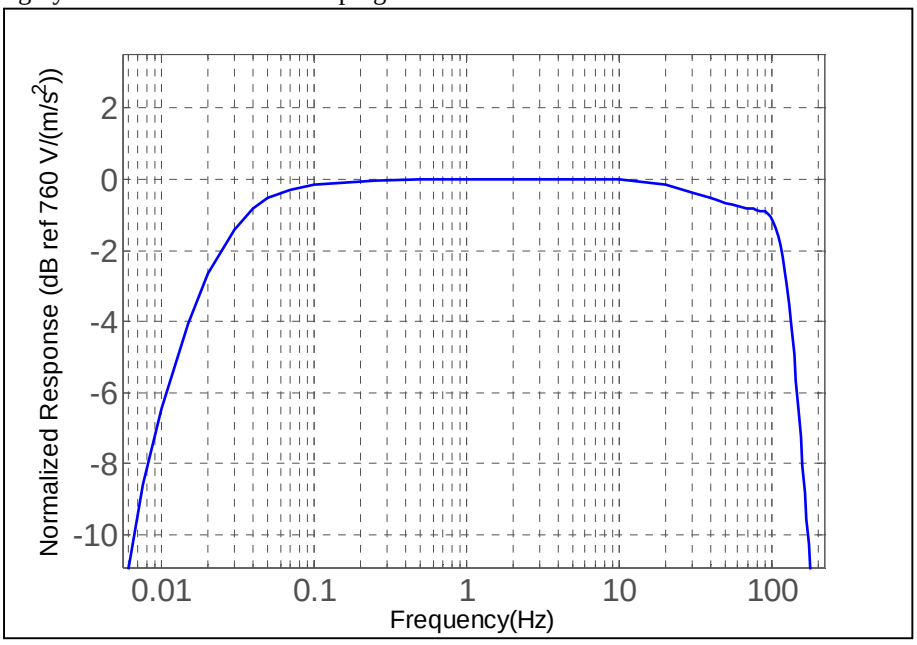

Figure 7: Frequency response measured using magnetic coil self excitation and optical detection capabilities.

During a field test at the USGS Albuquerque Seismology Laboratory (ASL), these prototypes were tested alongside a calibrated Stekheisen STS-2 broadband seismometer. Both instruments were connected to a Quanterra digitizer sampling at 200 Hz and left to record data overnight. Sensor noise floor was assessed using data captured during a non-event period. Initial results, summarized in Figure 8, reveal that at frequencies greater than 3Hz the GeoLight prototype accurately resolves the 2ng/√Hz background noise of the test site (e.g., -154 dB level in Fig x). Below 3Hz, *1/f* noise begins to dominate. Still, the early stage prototype is able to resolve a portion of the microseism peak between 0.1-0.3Hz, at a level of -130 dB or approximately 20ng/√Hz .

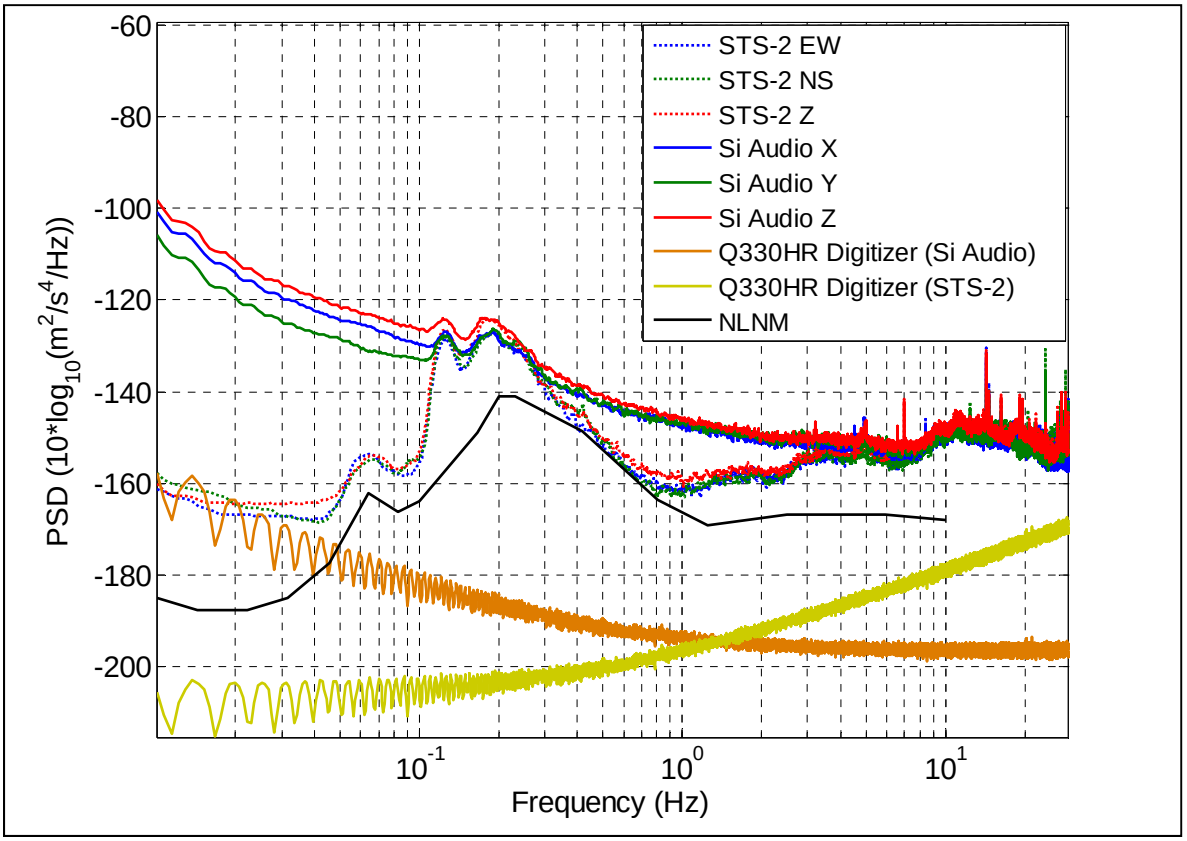

Figure 8: Noise measurement made during visit to USGS ASL demonstrating Silicon Audio's miniature 3-axis GeoLight prototype detecting down to site noise at 3 Hz and above and capturing portions of the 0.2 Hz microseism. Sources of *1/*f noise at lower frequencies are presently being addressed. For comparison, the NLNM is included as are the digitizer noise levels.

During overnight noise testing, an earthquake originating off the cost of Tarapaca, Chile (UTC 2010/05/06 02:42:47) was recorded. The velocity waveforms of the P-wave arrival are plotted in Figure 9. Excellent matching among all 3 axes can be seen between the GeoLight prototype and the STS-2 calibrated reference.

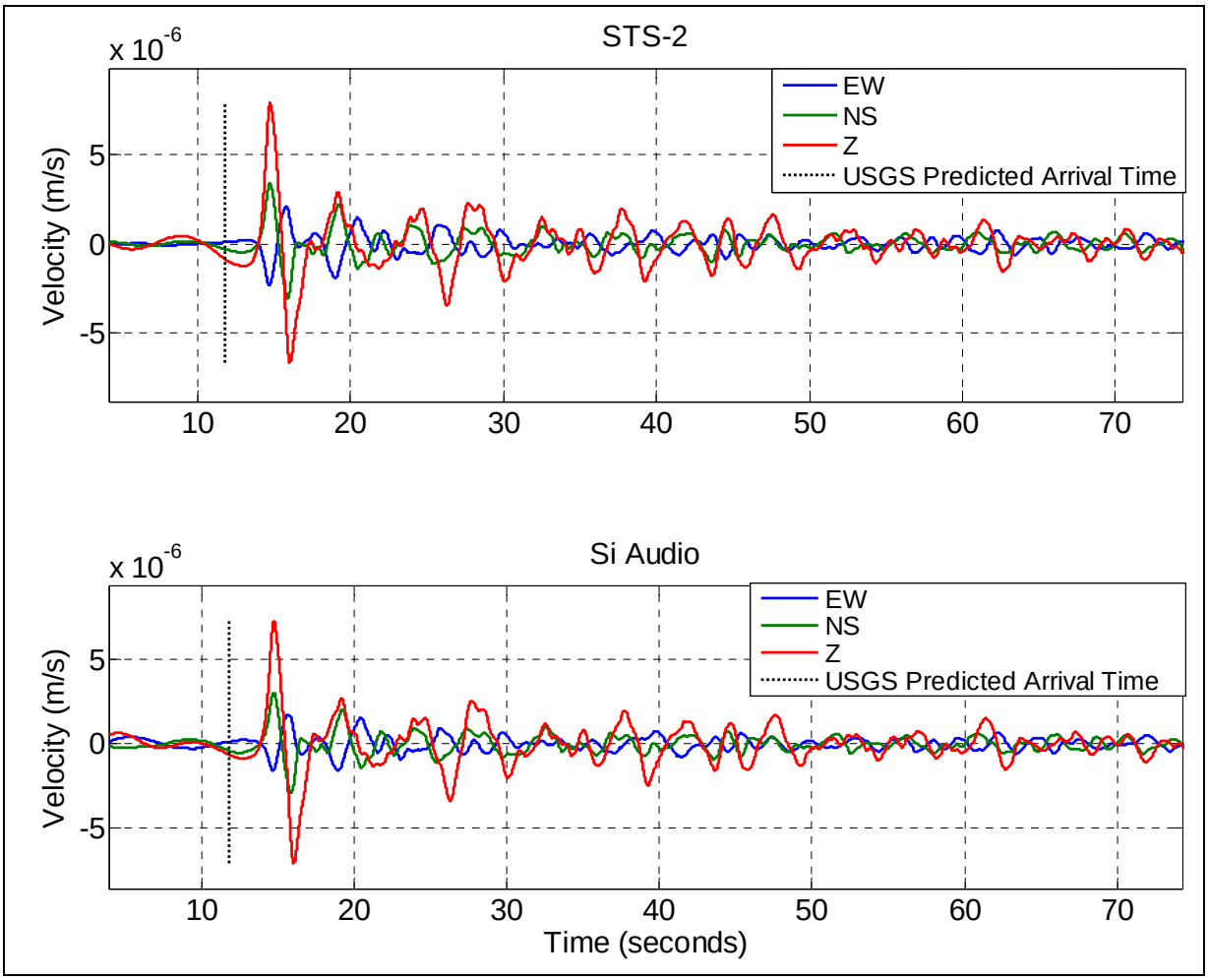

Figure 9: P-wave arrival of Tarapaca, Chile event recorded by STS-2 and by Silicon Audio's GeoLight prototype during testing visit to USGS ASL, May 3-6th 2010.

CONCLUSIONS AND RECOMMENDATIONS

Silicon Audio is addressing the NNSA's rigorous seismometer specifications using an approach that combines silicon micromachined optical elements, integrated semiconductor lasers, photo detection electronics, and meso-scale proof mass structures. This review article focused on a grating based implementation and significant accomplishments were discussed; improved dynamic and optical modeling capabilities, and demonstration of 3-axis prototypes. Future developments will focus primarily on improved noise performance in the 100mHz-5Hz band, low power operation <100mW, and further miniaturization. We envision complete units integrated into a 3-axis sensor package roughly the size of a 9-volt battery.

ACKNOWLEDGEMENTS

The authors graciously thank the NNSA and the DOE SBIR program for support. We also thank the University of Texas, Institute of Geophysics for assistance with Phase I and Phase II field test demonstrations. Finally, we would like to thank Bob Hutt and his team at the USGS Albuquerque Seismology Lab for their assistance with Phase II field testing.

REFERENCES

Hall, N. A. (2008). Micro-seismometers via advanced mesoscale fabrication, in *Proceedings of the 30th Monitoring Research Review: Ground-Based Nuclear Explosion Monitoring Technologies*, LA-UR-08-05261, Vol. 1, pp. 610–614.

Hall, N. A., M. Okandan, R. Littrell, B. Bicen, and F. L. Degertekin (2007). Micromachined optical microphones with low thermal-mechanical noise levels, *J. Acous. Soc. Am*. 122 (4): 2031–2037.

Hall, N. A., M. Okandan, R. Littrell, D. K. Serkland, G. A. Keeler, and K. Peterson (2008). Micromachined accelerometers with optical interferometric read-out and integrated electrostatic actuation, *J. Microelectromech. Syst*. 17 :(1), 37–44.

Hobbs, P. C. D. (1997). Ultrasensitive laser measurements without tears, *Applied Optics* 36: (4): 903–920.

Lee, W., N. A. Hall, et al. (2004). Fabrication and characterization of a micromachined acoustic sensor with integrated optical readout. IEEE Journal on Selected Topics in Quantum Electronics 10: (3), 643–651.

Liu, C. H. and T. W. Kenny (2001). A high-precision, wide-bandwidth micromachined tunneling accelerometer, *J. Microelectromech. Syst*. 10: (3) 425–433.

Garcia, C. T., Onaran, G., Avenson, B., Ellis, M., and N. A. Hall (2009). Micro-Seismometers via Advanced Mesoscale Fabrication. in *Proceedings of the 2009 Monitoring Research Review: Ground-Based Nuclear Explosion Monitoring Technologies*, LA-UR-09-05276, Vol. 1, pp. 330–337.

A MATCHED FIELD PROCESSING FRAMEWORK FOR COHERENT DETECTION OVER LOCAL AND REGIONAL NETWORKS

Tormod Kværna[1], Steven J. Gibbons[1], David B. Harris[2] and Douglas A. Dodge[3]

NORSAR[1], Deschutes Signal Processing, LLC[2], and Lawrence Livermore National Laboratory[3]

Sponsored by the Air Force Research Laboratory and the National Nuclear Security Administration

Award Nos. FA9453-10-C-0209[1,2] and LL10-BAA10-20-NDD03[3]
Proposal No. BAA10-20

ABSTRACT

The objective of this one-year feasibility study is to develop a data-adaptive matched field procedure to detect coherently and incoherently across networks of stations at local and regional distances. The detector will extend the current matched field processing approach, which classifies events on the basis of observations of first-arriving P-waves, to detection using the entire waveform. The framework is based upon a narrowband signal representation that we believe exposes invariant spatial and temporal correlation structure of network signals from repeating sources.

During the first months of the contract period, we have implemented a prototype matched field (MF) algorithm for detection processing using the full event waveforms. We have initially tested and validated the algorithm with regional events on the Kola Peninsula, for which good ground truth information is available and where signals from repeating sources are observed by network stations and arrays at distances of interest. We will continue testing of the prototype matched field detector on larger datasets from the Kola Peninsula and assess the performance against ground truth information and benchmarks set by correlation detectors and empirical matched field processing event classification studies. This algorithm will become an important part of a general detection framework to estimate autonomously the correlation structure of signals from repeating sources while processing continuous data streams. The framework will be tested for its ability to derive detectors adapted to the correlation structure of repeating sources using networks in Fennoscandia and the Korean peninsula.

In parallel, we have worked on the preparation of a database of continuous waveforms from the network of stations on and surrounding the Korean peninsula. We have obtained seismic event bulletins from KIGAM (the Korea Institute of Geology, Mining and Materials) in addition to the International Data Centre (IDC) Reviewed Event Bulletin, the preliminary determination of epicenters (PDE) bulletin from the USGS, and the bulletin of the International Seismological Center (ISC). However, it is almost guaranteed that the majority of small, repeating, industrial events will not be present in these event lists. We have therefore performed a single-array detection procedure on the KSRS teleseismic array in South Korea targeted at identifying regional events from repeating sources. The main purpose of this is to identify sources of repeating seismicity against which the new algorithms can be evaluated. The initial power detection procedure applies an incoherent detection scheme which calculates continuous spectral estimates of single channels and then forms beams of transformed spectrograms. This method has the advantage that it detects phases which are rich in high frequency energy, at which coherent processing on the KSRS array fails. Coherent processing in the 2-4 Hz band does usually provide fairly robust and accurate estimates of the slowness, even though the signal-to-noise ratio (SNR) in this frequency band is usually too low to provide a good detector with a low false alarm rate. This procedure of incoherent detection and coherent parameter estimation appears to provide an extensive bulletin of well-defined events at regional distances which fall into clusters. The detections which do belong to the same groupings are currently being clustered using the standard multi-channel correlation detectors, followed by f-k analysis post-processing to further validate the detections.

OBJECTIVES

The objective of this one-year feasibility study is to develop a data-adaptive matched field procedure to detect coherently and incoherently across networks of stations at local and regional distances:

- The detector will extend the current matched field processing approach, which classifies events on the basis of observations of first-arriving P-waves, to detection using the entire waveform.
- The framework will be based upon a narrowband signal representation that exposes invariant spatial and temporal correlation structure of network signals from repeating sources, even in the presence of source-time history variation. It is anticipated that familiar waveform correlation detectors and alternative temporally or spatially incoherent detectors will emerge as special cases of the proposed architecture.
- The specific form of the detector that emerges will depend upon the details of correlation structure present in the signal data. The architecture will be tested initially against events on the Kola Peninsula, for which good Ground Truth information is available and where signals from repeating sources are observed by network stations and arrays at distances of interest.

Once the basic detection algorithm has been developed and tested, a previously developed autonomous calibration framework will be adapted to drive the detector. The new detector will replace correlation and subspace detectors currently employed in that framework. As the framework operates and collects events from sources of repeating seismicity, the general network covariance will be estimated and used to update individual detectors to match the observed correlation characteristics of signals they are designed to detect. As more events are detected, the covariance estimates will be updated and used to adapt detectors to be more finely tuned to their targets. Once the framework is complete, it will be applied to the Korean Peninsula. The framework will be applied using data from several different time periods, mainly during time intervals when existing bulletins contain high numbers of seismic events in the regions of interest. Data intervals surrounding the known nuclear tests will be included.

RESEARCH ACCOMPLISHED

Types of sources and their bearing upon detector architecture

Correlation, subspace and matched field detectors offer advantages of great sensitivity at a low false alarm rate and the ability to wrap detection, association, location and identification functions into a single operation. These advantages are a consequence of the fact that the detectors are highly tuned to the characteristics of one particular source. The premise of this project is that repeated observations of waveforms from a given source can be used automatically to tune a detector to match the spatial and the statistical temporal structure of the waveforms generated by the source. Figure 1 illustrates two sources with substantially different temporal statistical structure. The top set of traces depicts waveforms from 10 consecutive explosions at a munitions demolition site in Finland observed at the ARCES array center element. The salient feature of these waveforms is that they are nearly identical. A waveform correlator (subspace detector of rank one) is the optimum detector for events of this source. The bottom set of traces shows waveforms from 10 consecutive explosions at the underground Kirovsk mine. The waveforms of this set vary considerably, so that the optimum detector is a higher-rank subspace detector or a matched field detector.

We seek a single model for both sets of observations, and, hence, a single framework for optimized detectors of both source types. Because the sources are approximately point sources, we assume that a fixed set of Greens functions describe propagation from each source to the observing array. The Greens functions are deterministic, but unknown, though subject to calibration. We assume the variation appears in the source time history and mechanisms of the sources, which we consider to be stochastic. In the case of the Finnish explosions, source variance is very low and the source is nearly deterministic. In the case of the Kirovsk explosions, source variance is substantially higher.

Matched field detectors are designed for sources like the Kirovsk mine, as they are insensitive to variations in source time history. They operate on a narrowband signal representation, where the bandwidth is chosen to be narrow

enough to wash out the effects of the source forcing functions. For a sufficiently narrow band centered on frequency ω_i, the vector of signals $\mathbf{r}_i(t)$ observed across an array or network is, approximately:

$$\mathbf{r}_i(t) \approx F(\omega_i)\mathbf{g}(t,\omega_i) \tag{1}$$

This model assumes that the source forcing function $f(t)$ has a very short duration $\Delta t \ll {}^{1}/_{\Delta\omega}$, where $\Delta\omega$ is the width of the narrow bands. Here $\mathbf{g}(t,\omega_i)$ is the vector of Greens functions describing propagation to the collection of sensors from the source, also filtered into the band centered on ω_i, and $F(\omega_i)$ is the Fourier transform of $f(t)$. Matched field detectors operate by correlating a template with the signal in each frequency band, then combining the result over frequency bands. The statistical (covariance) structure of the source waveforms governs the combination over bands: incoherent in the case of a source like the Kirovsk mine, coherent in the case of a source like the Finnish demolition site.

The templates are obtained from an eigendecomposition of the covariance function for the observations:

$$\mathbf{C_{ij}}(t_1,t_2) = E\{\mathbf{r}_i(t)\mathbf{r}_j^H(t)\} \approx \mathbf{g}(t,\omega_i)E\{F(\omega_i)F^*(\omega_j)\}\mathbf{g}^H(t,\omega_j) \tag{2}$$

The essential feature of this covariance function is the behavior of different frequency components for the two source types. For the Kirovsk source, we anticipate independence among frequency bands:

$$E\{F(\omega_i)F^*(\omega_j)\} = \delta_{ij}\,E\{|F(\omega_i)|^2\} \tag{3}$$

i.e., $E\{F(\omega_i)F^*(\omega_j)\} = 0$ whenever $i \neq j$. For the Finnish demolition source, we anticipate high correlation among different frequency bands, i.e. $E\{F(\omega_i)F^*(\omega_j)\} \neq 0$.

The form of the detector requires some explanation. First, we restructure the narrowband signals into a single vector:

$$\mathbf{r}(t) = \begin{bmatrix} \mathbf{r}_1(t) \\ \vdots \\ \mathbf{r}_i(t) \\ \vdots \end{bmatrix} \tag{4}$$

and the covariance function into a matrix:

$$\mathbf{C}(t_1,t_2) = \begin{bmatrix} \mathbf{C_{11}}(t_1,t_2) & \mathbf{C_{12}}(t_1,t_2) & \cdots \\ \mathbf{C_{21}}(t_1,t_2) & \mathbf{C_{22}}(t_1,t_2) & \cdots \\ \vdots & \vdots & \ddots \end{bmatrix} \tag{5}$$

The covariance matrix has a Karhunen-Loeve representation:

$$\mathbf{C}(t_1,t_2) = \sum_p \lambda_p \boldsymbol{\phi}_p(t_1)\ \boldsymbol{\phi}_p^H(t_2) \tag{6}$$

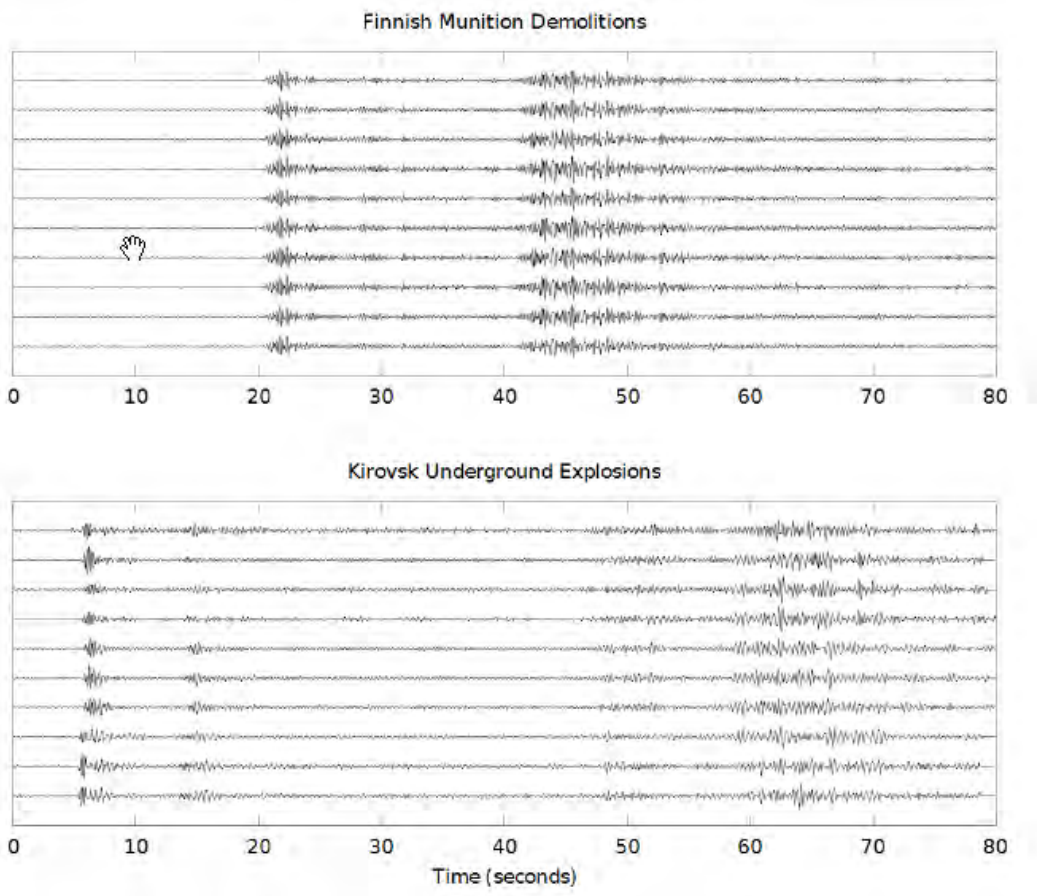

Figure 1. Representative waveforms from two different sources types: 10 consecutive explosions from a munitions demolition site in Finland and 10 consecutive explosions from the Kirovsk underground mine in the Khibiny Massif. Note the similarity of the munitions shots and the variation among the Kirovsk shots.

The detection statistic computed by the matched field detector is given by:

$$d(t) = \sum_{p} \left| \int \boldsymbol{\phi}_p^H(\tau)\mathbf{r}(t+\tau)d\tau \right|^2 \tag{7}$$

In the Kirovsk case, it is approximately true that any particular $\boldsymbol{\phi}_p$ will contain a contribution from only one frequency band. Consequently the contributions from different frequency bands will be summed incoherently. In the case of the Finnish demolition site, any particular $\boldsymbol{\phi}_p$ will contain contributions from many or all frequency bands and contributions from different frequency bands will be summed coherently in the detection statistic.

An automated system to design a detector appropriate to a particular source will begin by estimating the covariance matrix $\mathbf{C}(t_1, t_2)$ from many observations of waveforms from that source. The correlation kernel $\boldsymbol{\phi}_p$ will be estimated from the sample covariance matrix and will automatically assume the structure of a waveform correlator or an incoherent matched field detector depending upon the statistical characteristics of the source. Our intention is that, over time, as many observations are acquired, the detector will tune itself to the statistical characteristics of the source.

We plan to try two initialization strategies, starting with a single event observation for a particular source. The first strategy may begin with a correlation detector defined by the one available waveform and, by setting the detection threshold low, attempt to acquire more events to define the covariance matrix. This strategy obviously would work perfectly for the Finnish munitions explosions, but may fail for the Kirovsk mine shots with their considerable waveform variability. The second strategy will use the single observation to define the spatial structure of the signal across the array, but will force incoherence across frequency bands to suppress dependence on the source time history. This approach will provide a more general detector with the prospect of acquiring enough events to define the statistical structure of sources like the Kirovsk mine.

Implementing and testing a prototype Matched Field Detector

Priority during the first phase of this project has been given to implementation and testing of a prototype Matched Field (MF) detector. The prototype software is written in Matlab and provides a convenient tool for experiments. We have initially tested and validated the algorithm with regional events on the Kola Peninsula, for which good ground truth information is available and where signals from repeating sources are observed by network stations and arrays at distances of interest. In Figure 2 we show the result from processing of a 3-hour data interval using the new prototype MF detector software. Notice the peaks of the detection statistic associated with known blasts in the Kirovsk mine.

In order to facilitate further testing and experiments, we have implemented access to NORSAR's large database of continuous seismic data into the MF detector software. This is demonstrated in Figure 3 which shows results from processing of a recent 3-hour time interval from the ARCES array starting at 12 UTC on 10 April 2010. This first version of the MF detector software will be subjected to further validation and testing using ARCES recordings of mining events from the Kola Peninsula. In particular we will address aspects of the detector normalization, design of detector templates from event ensembles and threshold setting for triggering of events.

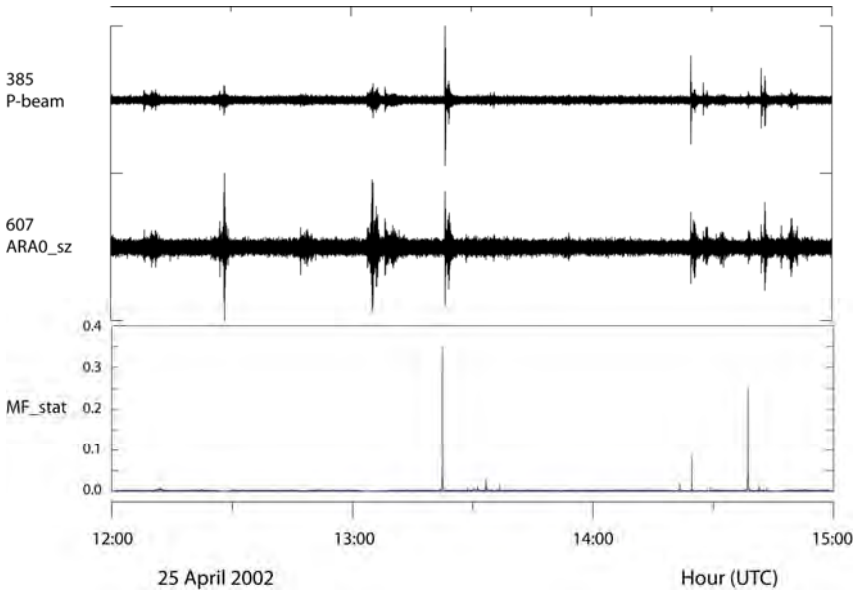

Figure 2. Result from the application of the prototype implementation of the full-waveform MF detector to three hours of data from the ARCES array on 25 April 2002. The detector was designed using observations of 114 explosions at the Kirovsk mine, which is one of the five closely spaced mines on the Khibiny Massif on the Kola Peninsula. The three largest peaks correspond to three Kirovsk explosions. The processing frequency band was 2.5 - 12.5 Hz, which the detector breaks into 33 narrow sub-bands.

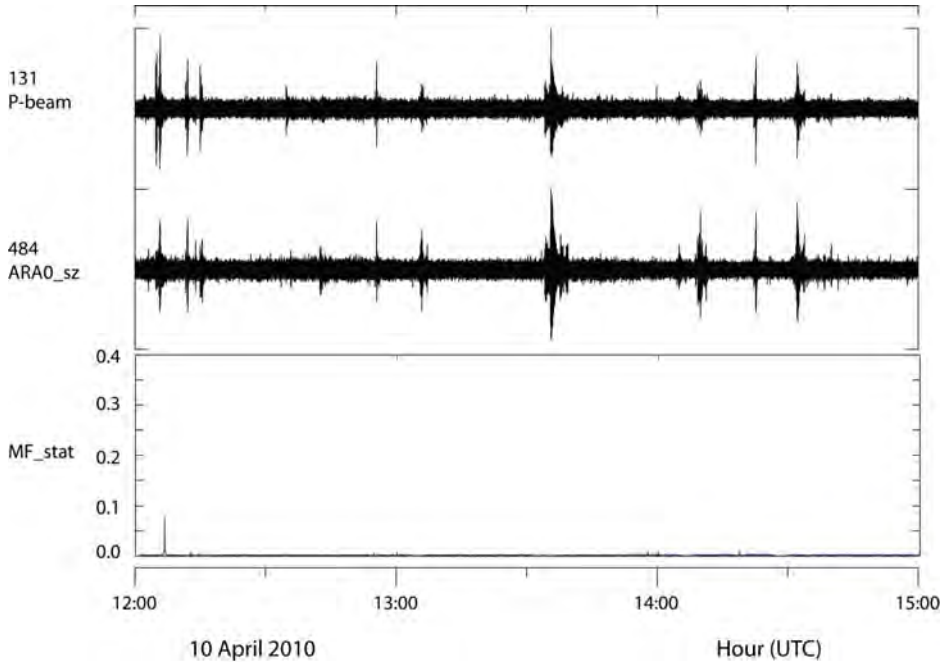

Figure 3. Result from the application of the new prototype MF detector to three hours of data from the ARCES array on 10 April 2010, again using the 114 explosions at the Kirovsk mine for designing of the detector. The peak just after 12 UTC corresponds to signals from a small event most likely located in one of the mines of Khibiny Massif. We do not currently have Ground Truth information for this event.

Preparation of a Database of Continuous Waveforms from the Network of Stations Surrounding North Korea

While the matched field detection architecture is currently being tested on datasets in the European Arctic, it is an important part of the current project to apply the algorithms to a region of programmatic interest: the Korean Peninsula. The closest two IRIS 3-component stations to the test site are INCN (Inchon, Republic of Korea, IRIS-USGS network) and MDJ (Mudanjiang, China, IC network). Data from these two stations have been archived back to January 1, 2006, although older archives may be accessed if this is deemed necessary. As the Norwegian NDC, NORSAR has access to data from the USRK, KSRS, and MJAR arrays from the IDC in Vienna. All current holdings from these stations have now been obtained. The geography of the stations in relation to the test site is displayed in Figure 4.

We have obtained seismic event bulletins from KIGAM in addition to the IDC Reviewed Event Bulletin, the PDE bulletin from the USGS, and the bulletin of the ISC. However, it is almost guaranteed that the majority of small, repeating, industrial events will not be present in these event lists.

We start by attempting to bootstrap lists of seismic events from repeating industrial sources.

Most of the signals from such events are characterized by high frequency regional phases. We begin with the KSRS array (since this has the longest history of continuous data), a teleseismic array over which signals are fairly incoherent above 4 Hz. This has the consequence that beamforming at the frequencies with the greatest SNR leads to substantial beam-loss, and that slowness estimates in these frequency bands are often qualitatively misleading. In order to detect the high frequency regional phases with a low false alarm rate, we use the spectrogram beamforming (incoherent) method described in Gibbons et al. (2008) - see Figure 5. Despite the typically low SNR in the 2-4 hz frequency band, the slowness estimates made in this band do appear to be fairly stable.

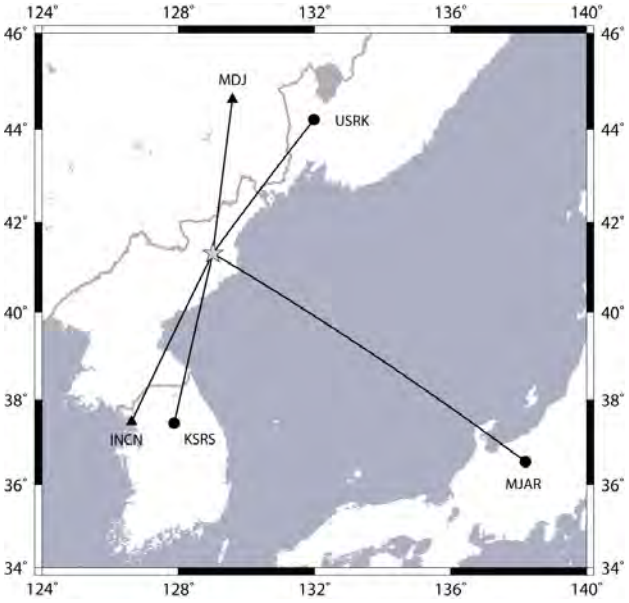

Figure 4.
Location of the IMS arrays KSRS (Wonju, South Korea), USRK (Ussirusk, Russian Federation), and MJAR (Matsushiro, Japan) and the IRIS 3-component stations INCN (IU network) and MDJ (IC network). The star denotes the location of the DPRK nuclear test site.

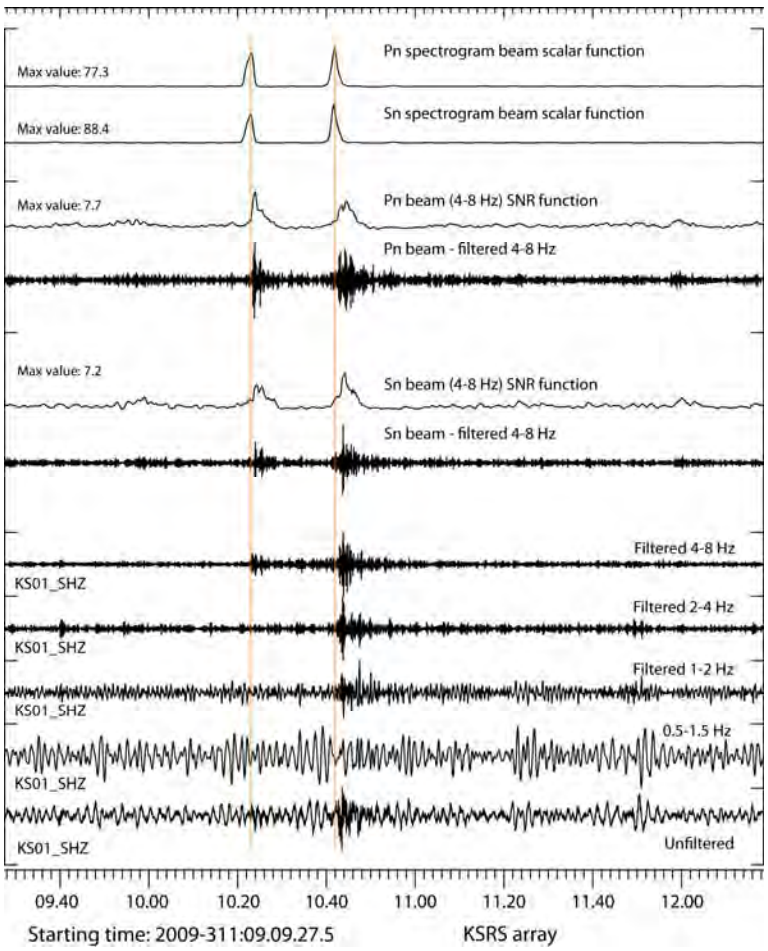

Figure 5.
An example of the detection of a P and S phase for an event within regional distances of the KSRS array. The only frequency band at which a reasonable SNR is attained is the 4-8 Hz band. The beamforming of transformed spectrograms described by Gibbons et al. (2008) provides a promising detection statistic for these phases, as shown in the upper two traces of the figure.

The detection lists obtained using this procedure are now complete from 2006 to the present day. A procedure of taking a single event, running a correlation detector, removing all of the power detections which are confidently associated with these correlation detections, and then spawning a new correlation detector from an event in the pool of remaining detections, is currently underway. We hope that, when completed, this will give quite a comprehensive list of sources of repeating seismicity within regional distances of KSRS. So far, a small number of clusters have been investigated using correlation detectors and four of these are displayed, together with the full set of automatic event locations, in Figure 6. In situations where multiple correlation detectors have common events, output from the different templates will be compared. This may indicate that events originate from a large source region and that several correlation templates are necessary to characterize the source. Such instances will be an interesting point of comparison for the new detection architecture.

Waveforms from events assigned to the four clusters displayed on the map are shown in Figure 7. It is clear that even these four clusters alone show significant variation in the both waveform amplitudes, SNR, and waveform semblance. Results of the detector and cluster analysis will be addressed in the next phase of the project.

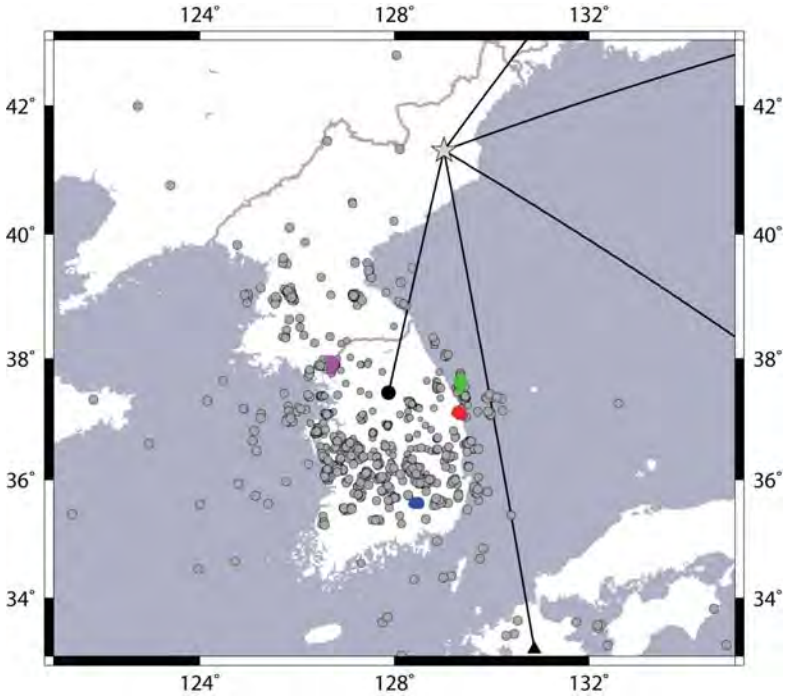

Figure 6. Fully automatic event location estimates using only regional P and S detections on the KSRS array (marked by the black circle at the center of the map). Given that the event locations at this stage are fully automatic, some of the events shown may be spurious associations. However, there are clearly many clusters of events and location estimates for four groups of events found to correlate are displayed in four different colors. The compactness of the automatic estimates within these event clusters gives some confidence about the robustness of the automatic phase detection and estimation procedure. The color-coded clusters on the map are associated with correlations with master events as follows:
red (2006-307:20.30.24, 37.100 N, 129.252 E), blue (2006-308:09.05.26, 35.610 N, 128.408 E), green (2006-308:02.57.19, 37.593 N, 129.388 E), magenta (2006-310:03.07.22, 37.940 N, 126.794 E).

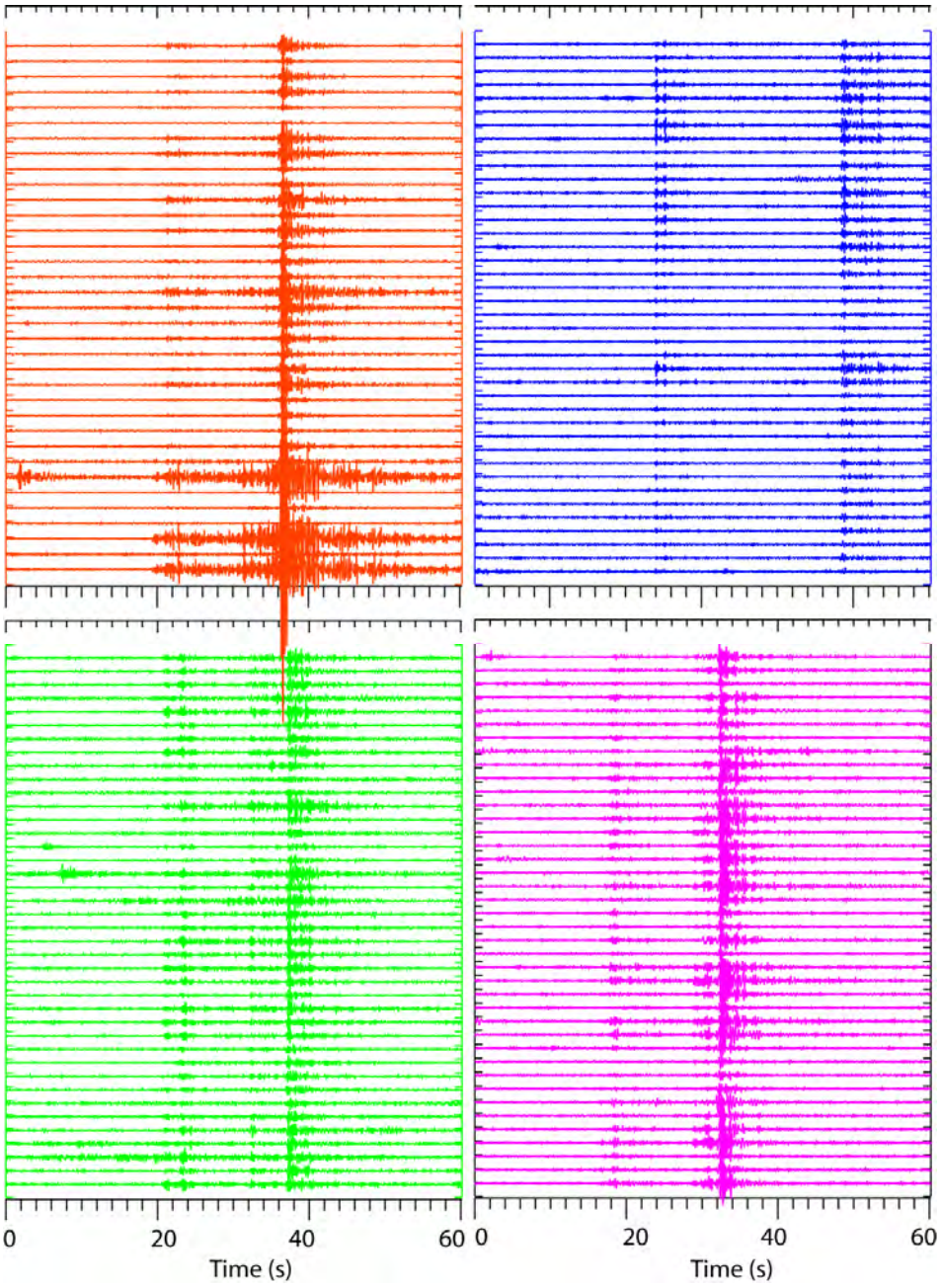

Figure 7. Waveforms from the KS01_SHZ instrument, aligned according to the times of best correlation coefficient for 40 events from each of the clusters displayed in Figure 6 in the appropriate color.

CONCLUSIONS AND RECOMMENDATIONS

In the development of the processing system, we plan to try two initialization strategies, starting with a single event observation for a particular source. The first strategy may begin with a correlation detector defined by the one available waveform and, by setting the detection threshold low, attempt to acquire more events to define the

covariance matrix. The second strategy will use the single observation to define the spatial structure of the signal across the array, but will force incoherence across frequency bands to suppress dependence on the source time history. The applicability of these strategies is expected to depend on the degree of waveform variability of the events from the repeating source in question.

During the first few months of this project, we have achieved the following results:

We have evaluated a prototype matched field (MF) detector on ARCES data for well constrained mining events on the Kola Peninsula. The results are very promising, and the initial version of the MF detector will be subjected to further validation and testing using this data set. In particular we will address aspects of the detector normalization, design of detector templates from event ensembles and threshold setting for triggering of events.

We have collected seismic array and 3-component data for stations on or surrounding the Korean Peninsula. From the IDC of the CTBTO, we have obtained KSRS array data from November 2006 to the present day, USRK data from 2008 to the present day, and also MJAR data (Matsushiro array, Japan) from 2005 to the present day. The IRIS 3-component stations MDJ (IC network) and INCN (IU network) have been obtained from the IRIS Data Management Center for the years 2006 to the present day (older data is available in the archives and may be collected should this be deemed to be of interest).

We have performed a single-array detection procedure on the KSRS teleseismic array in South Korea targeted at identifying regional events from repeating sources. The main purpose of this is to identify sources of repeating seismicity against which the new algorithms can be evaluated. The initial power detection procedure applies the method of Gibbons et al. (2008)—an incoherent detection scheme which works by calculating continuous spectral estimates of single channels and then forming beams of transformed spectrograms. This method (which has been used in operational mode on the NORSAR array) has the advantage that it detects phases which are rich in high frequency energy, at which coherent processing on the array fails. Coherent processing in the 2-4 Hz band does usually provide fairly robust and accurate estimates of the slowness, even though the SNR in this frequency band is usually too low to provide a good detector with a low false alarm rate. This procedure of incoherent detection and coherent parameter estimation appears to provide an extensive bulletin of well-defined events at regional distances which fall into clusters. The detections which do belong to the same groupings are currently being clustered using the standard multi-channel correlation detectors with f-k analysis post-processing (Gibbons and Ringdal, 2006).

ACKNOWLEDGEMENTS

We are grateful to the IRIS DMC for data from the INCN and MDJ 3-component stations which belong to the networks IU and IC respectively. Array data was obtained from the IDC of the Comprehensive Nuclear-Test-Ban Treaty Organization (CTBTO) in Vienna, Austria. All maps have been produced using GMT software (Wessel and Smith, 1995).

REFERENCES

Harris, D. B. and T. Kvaerna (2010). Superresolution with seismic arrays using empirical matched field processing, accepted for publication, *Geophys. Jour. International.*

Harris, D. B. and D. Dodge (2010). An autonomous system for grouping events in a developing aftershock sequence, accepted for publication *Bull. Seismol. Soc. Am.*

Gibbons, S. J. and F. Ringdal (2006). The detection of low magnitude seismic events using array-based waveform correlation, *Geophys. J. Int.* 165: 149–166.

Gibbons, S. J., F. Ringdal and T.Kværna, (2008). Detection and characterization of seismic phases using continuous spectral estimation on incoherent and partially coherent arrays, *Geophys. J. Int*. 172: 405–421.

Wessel, P. and Smith, W. H. F. (1995). New version of the generic mapping tools, *EOS Trans., Am. geophys. Union.*, 76: 329.

BAYESLOC MULTIPLE-EVENT LOCATION APPLIED TO A GLOBAL DATA SET

Stephen C. Myers, Gardar Johannesson, and Nathan A. Simmons

Lawrence Livermore National Laboratory

Sponsored by the National Nuclear Security Administration

Award No. DE-AC52-07NA27344/LL10-DM4TT-NDD02

ABSTRACT

We extend the Bayesloc seismic multiple-event location algorithm for application to global arrival time data sets. Bayesloc is a formulation of the joint probability distribution across multiple-event location parameters that includes hypocenters, travel time corrections, pick precision, and phase labels. Stochastic priors may be used to constrain any of the Bayesloc parameters. Markov Chain Monte Carlo (MCMC) sampling is used to draw samples from the joint probability distribution, and the posteriori samples are summarized to infer conventional location parameters such as the hypocenter. The first application is to a data set consisting of all well-recorded events in the Middle East and the most well-recorded events in 5° bins globally. This sampling strategy is designed to provide the ray coverage needed to determine lithospheric-scale structure in the Middle East using the complementary ray geometry provided by regional (sub-horizontal) and teleseismic (sub-vertical) ray paths, and to determine a consistent – albeit lower resolution – image of global mantle structure. The data set consists of 5401 events and 878,535 arrivals of P,Pn, pP, sP, and PcP recorded at 4606 stations. Relocated epicenters are an average of 16 km from bulletin locations. Although epicenter priors are not used, epicenters are found to be within 5.6 km from those that are known to within 1 km (e.g., peaceful nuclear explosions). Much of the improvement in location accuracy is attributed to dynamic assessment of data precision, which factors into data weights. Location accuracy will improve when location priors are used. For arrivals labeled *P*, *Pn*, and *PcP*, ~92%, ~90%, and 96% are properly labeled with probability > 0.9, respectively. Incorrect phase labels are found to be erroneous at rates of 0.6%, 0.2%, 1.6%, and 2.5% for *P*, *Pn*, *PcP*, and depth phases (*pP* and *sP*), respectively. Labels found to be incorrect, but not erroneous, were reassigned to another phase label. *P* and *Pn* residual standard deviation with respect to *ak135* travel times are dramatically reduced from 3.45 seconds to 1.01 seconds. Simmons et al. (2010, these Proceedings) use the Bayesloc-processed data set in a global tomographic study, which reduces residual standard deviation to 0.53 seconds (consistent with pick error). This result suggests that the dominant contribution to global bulletins residuals is location and picks errors, not travel time prediction errors due to 3D structure. Modeling the whole multiple-event system results in exceedingly accurate locations and an internally consistent data set that is ideal for tomography and other travel time calibration studies.

OBJECTIVES

Production of high-quality data sets for calibration of seismic travel times remains a painstaking and costly endeavor. The value of meticulous data analysis is beyond reproach, but the number and coverage of events with accurate locations and carefully measured seismic-phase arrival times is not sufficient for either development of high-fidelity (3-dimensional) models or comprehensive empirical calibration. Although regional and global bulletins of seismic data provide excellent data coverage, these databases are contaminated by inaccurate and spurious entries.

This project adapts the Bayesloc method (Myers et al., 2007, 2009) of multiple-event location for application to global data sets. Using the updated Bayesloc algorithm, we simultaneously relocate events, assess pick precision, estimate path-specific travel time corrections, and probabilistically assess phase labels to produce an accurate and consistent global bulletin. Bayesloc allows prior constraints on any aspect of the multiple-event system, enabling direct utilization of previous work that statistically characterizes the accuracy of event hypocenters and picks (e.g., Bondár et al., 2004; Bondár and McLaughlin, 2009). Simultaneous analysis if the whole data set allows robust estimation of travel time corrections, probabilistic phase labels (including outlier identification), and assessment of pick precision. Travel-time corrections mitigate location bias and probabilistic assessment of pick error optimizes data weighting. The posteriori bulletin is, on the whole, the most accurate set of global locations available with self-consistent arrival-time picks and phase labels. Therefore, the posteriori bulletin is ideal for tomographic studies.

RESEARCH ACCOMPLISHED

Bayesloc

Bayesloc is a statistical model of the multiple event system that includes event locations, travel-time corrections, assessments of arrival-time measurement (pick) precision, and phase labels. The overarching statistical model is

$$p(o,x,T,W,\delta,\phi \mid a,w) = p(a \mid o,T,W,\phi)\, p(T(x) \mid F(x),\delta,W)\, p(W \mid w,a,T(x)) \\ p(x,o)\, p(\phi)\, p(\delta)\, p(W \mid w) / p(a), \quad (1)$$

where *o* represents event origin times, *x* represents event locations, *T* is the collection of travel times from each event to each station for each phase (model prediction plus correction), *W* is the collection of all phase labels, ϕ is the collection of arrival-time precision parameters, δ is a collection of travel-time corrections, *a* and *w* are the collection of arrival times and phase labels. Equation 1 decomposes the inversion of arrival time data to solve for the components of the multiple-event system (left-hand side of equation 1), into a collection of "forward" problems and priors (right-hand side of equation 1). Specifically, the first term (right-hand side) computes the probability of observing the collection of arrivals given a set of hypocenters, travel times, phase labels, and pick precisions. The second term computes the probability of all travel times, given a model-based prediction, a collection of corrections, and the phase labels. The third term computes the probability of the true phase labels given a set of input phase labels, the observed arrivals, and the corrected travel times. The fourth, fifth, sixth, and seventh terms are prior constraints on hypocenters, arrival-time measurement precision, travel-time corrections, and input phase labels, respectively. The denominator is the probability over all arrival data, which serves as normalization. Analytical expressions for each term in equation 1 are provided in Myers et al. (2007, 2009).

Bayesloc uses the MCMC method to sample the joint probability of the multiple-event system (Gelman et al., 2004). Sampling the probability function is accomplished by starting with an initial configuration of the system, then proposing a new configuration that is consistent with prior information. The proposal process is random in the absence of prior information. The probability of each multiple-event configuration is computed using the forward calculations afforded by equation 1. A proposed configuration is always accepted as the new "state" of the system if the probability is greater than the current state. If the probability of the proposed state is lower than the current state, then the new state is accepted at a rate specified by the ratio of the probability for the proposed state and the current state. The process of proposing and accepting/rejecting configurations is continued until adequate sampling of the joint probability density is achieved (typically 10,000 to 20,000 samples). Graphical examination of the MCMC samples can be used to assess the non-parametric probability density, or an analytical form (e.g., Gaussian) may be used to summarize the MCMC samples. For example, the mean or mode of *lat* and *lon* samples for given event may be used to compute an epicenter, and *lat* and *lon* covariance estimates may be used to estimate an uncertainty ellipse.

Modifications to Bayesloc

Myers et al. (2007, 2009) implement simple adjustments to the travel-time curve and a zero-mean collection of station terms to robustly correct for gross prediction errors. That formulation is suitable for event clusters, where a station term can adequately capture deviations from the travel-time curve. In order to apply Bayesloc to a broad-area data set, the travel-time corrections must be path specific. As such, we recast the Bayesloc travel-time correction as,

$$\delta_{ijW} = T_{ijW} - F_{ijW} = \alpha_W + \alpha_i + \alpha_j + \alpha_{iW} + \alpha_{jW} + \beta_W \left\| x_i - s_j \right\|, \quad (2)$$

where δ is the travel-time correction, T is the corrected travel time, F is the model-based travel time, and α terms are static corrections. β is an adjustment to the slope of the travel-time curve with x and s representing event and station positions, respectively. The double bars indicate a norm giving event-station distance. Subscripts i, j, and W are indices for event, station, and phase, respectively. We further constrain the collection of station and event terms (α_i, α_j) to be zero mean with respect to the corrected travel-time curve ($F_w + \alpha_w, + b_w \|x_i - s_j\|$) and the station-phase and event-phase terms (α_{iw}, α_{jw}) are constrained to be zero mean with respect to their station and event terms. Decomposition of terms in this way allows robust determination of station and event corrections, and refinement of event-phase and station-phase corrections is possible if sufficient data are available.

Data Set

For the first application of Bayesloc to a broad-area data set we have gathered an extensive list of events throughout the Middle East that is complemented by approximately 5° sampling (~550 km spacing) of global events. This sampling strategy is designed to provide the ray coverage needed to determine lithospheric-scale structure in the Middle East using the complementary ray geometry provided by regional (sub-horizontal) and teleseismic (sub-vertical) ray paths, and to determine a consistent—albeit lower resolution—image of global mantle structure. Simmons et al. (2010, these Proceedings) report on the tomography study using the data resulting from Bayesloc relocation and processing.

We relocate 5401 events using 878,535 *P*, *Pn*, *pP*, *sP*, and *PcP* arrivals recorded at 4606 stations (Figure 1). Table 1 lists the number of arrivals for each phase. Event locations and arrival times for Middle East events are from the LLNL database (Ruppert et al., 2005), which is a compilation of global and regional bulletins as well as ~20,000 travel-time measurements at regional stations (*Pn*) made by LLNL staff. The global *P*-wave data set is from Engdahl et al. (1998), referred to hereafter as the EHB data set. Event selection from the EHB data set is based on the number of associated *P*-phases. After ordering events by the number of P-phases, the event having the most *P*-phases is selected, and all remaining events within 5° epicenter distance from the selected event are removed from the list. The procedure is repeated until the list is exhausted. In order to preserve the depth sampling afforded by the EHB bulletin, geographic event sampling is conducted in depth bins with lower bounds of 35 km, 75 km, 150km, 300 km, 450 km, and 700 km.

Table 1. Number of picks for each event and summary of posteriori assessment of phase labels.

Phase	Number of picks	Estimated standard deviation	Phase label retained with prob.>0.9	Input label is most probable	Most probably erroneous.
P	817,552	0.74 s	92%	96%	0.6%
Pn	42,327	0.90 s	90%	98%	0.2%
pP	10,524	1.60 s	90%	95%	2.1%
sP	4,992	2.22 s	92%	97%	2.6%
PcP	3,140	1.83 s	96%	98%	1.6%

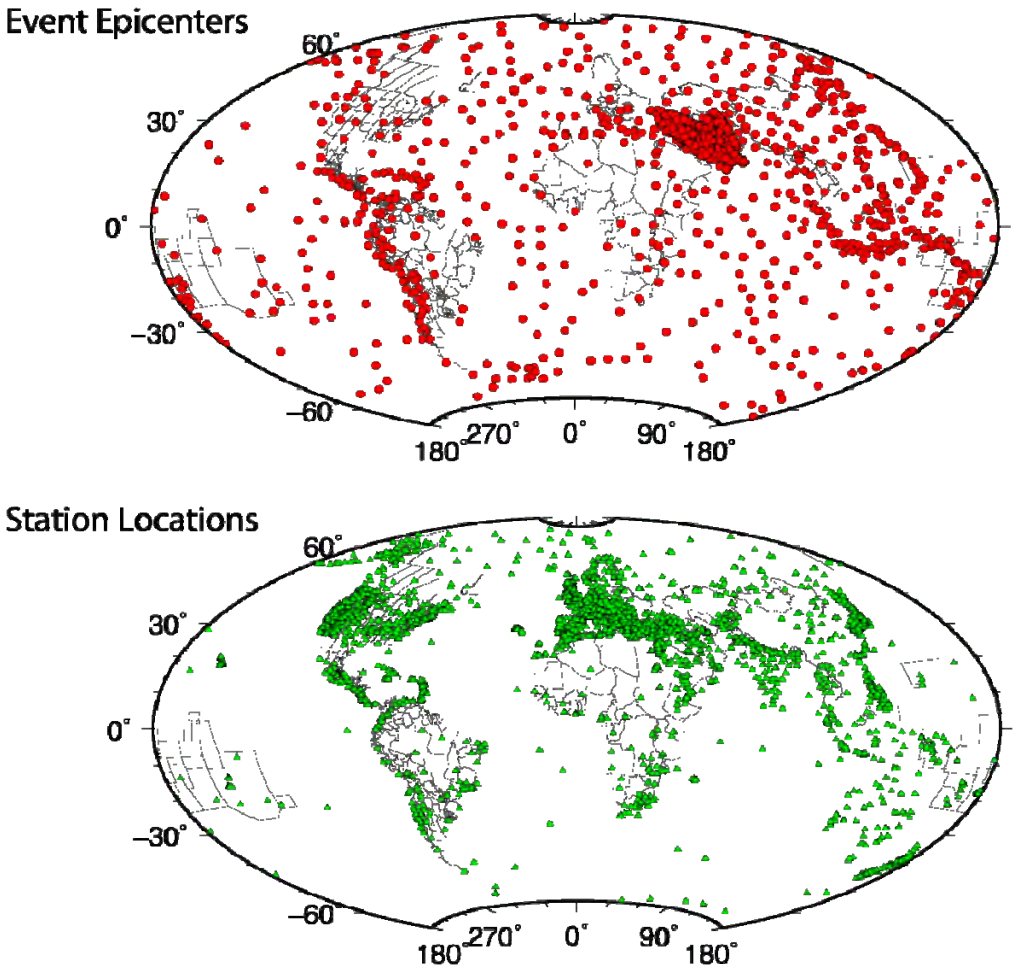

Figure 1. Event epicenters and station locations. All well-recorded events in the Middle East are considered and global event sampling is approximately 5°. Global sampling is performed independently in event depth intervals down to 700 km (see text). The resulting data set provides horizontal and vertical ray coverage through the Middle East, which is used by Simmons et al. (2010, these Proceedings) in a tomographic study.

Bayesloc Relocation

The joint posteriori distribution is determined using 4 Markov Chains. For this data set the starting position is the station location with the earliest pick. Starting depths were set to 15 km, except for events with EHB locations greater than 100 km, in which case the EHB depth was used as the starting depth. EHB depths were determined by scrutinizing depth phases, including depth phases that pass through the oceanic water column, suggesting that event depths in subduction zones are well constrained. Therefore, in addition to starting the MCMC chain at the input depth, we place 5 km standard deviation prior constraints on EHB depths greater than 70km.

Prior constraints on travel-time corrections are based on prediction errors assessed by Engdahl et al. (1998) and our own experience (Flanagan et al., 2007; Myers et al., 2010). We place tight prior constraints on the shift to the travel-time curve for teleseismic phases (*P*, *pP*, *sP*, *PcP*), because the absolute travel time for these phases is established using nuclear explosions with known origin times, as well as events recorded by local networks with well-constrained origin times. A prior with standard deviation of ±5 seconds is imposed on the regional *Pn*-phase. These constraints force the average travel time to be consistent with the model used for teleseismic travel-time prediction (*ak135*; Kennett et al, 1995). Myers et al. (2007) demonstrate that adjustments to the slope of the travel-time curves are robustly determined with large data sets and are, therefore, not needed in this case. As such, we allow phase velocity for all phases to vary by a factor of 3. Priors on the standard deviation of event, station, event-phase, and station-phase corrections are uninformative, but recall that the collection of each parameter must be

zero mean. Priors on the measurement precision are also uninformative, so data weighting is entirely determined by adapting precision parameters to fit data distributions during the MCMC sampling.

Relocation Results

The results presented here are averages of the last 12,000 of 15,000 MCMC samples. The first 3,000 samples ("burn in") are used to find the neighborhood of the mode of the posteriori distribution and to adapt MCMC sampling. As such the, first 3,000 samples are not necessarily representative of the joint probability density. The samples are non-parametric in nature, but we summarize many of the samples by assuming a Gaussian distribution. The Gaussian assumption allows hypocenters to be represented using conventional parameters, including epicenter ellipses.

Figure 2 shows epicenter shifts for all of the global events and a representative sampling of events in the Middle East. Epicenters shift by 16 km on average relative to the input bulletin locations, and regional trends in the vector directions are evident. Eight of the events in the global data set are listed in the IASPEI Reference Event List (Bondár and McLaughlin, 2009) with location accuracy of 1 km or better, and the average difference between reference epicenters and Bayesloc epicenters is 5.6 km. If this level of accuracy holds for the events with less well-known locations, this suggests that the Bayesloc locations are substantially more accurate than the bulletin location given that the average epicenter shift is ~16 km. However, more testing is needed to further quantify Bayesloc epicenter accuracy.

Figure 3 shows the location of the May 28, 1998, Pakistan nuclear explosion and Bayesloc location predictions. The event was well recorded, but station sampling is not geographically even. Residual travel times at European stations with respect to the known location, which is based on satellite imagery (Albright et al., 1998), are negative (fast). The predominance of European stations with biased negative residuals results in a northward bias in the location when the ak135 model is used (mislocation of 10.1 km). Because the prediction errors are biased (not completely random), the resulting epicenter error ellipse does not cover the true location (Figure 3). Bayesloc travel-time corrections mitigate travel-time prediction bias, resulting in an epicenter error of 4.5 km. Modeling all components of the location system, including pick and model error, results in a reduction of the epicenter error ellipse area from 207 km^2 to 70 km^2. Perhaps more importantly, the Bayesloc error ellipse covers the known location because the marginal probability of the event location integrates over the joint probability of all other multiple-event parameters.

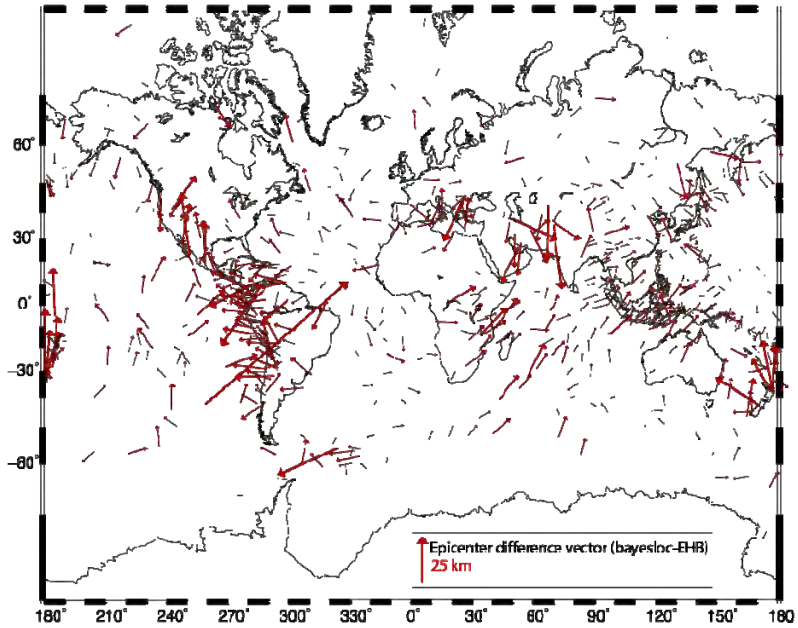

Figure 2. Epicenter relocation vectors. The tail of each vector is at the starting location based on the EHB and LLNL bulletins. Vector length is scaled by the magnitude of the epicenter shift (see inset scale), and vector orientation is in the direction of epicenter shift.

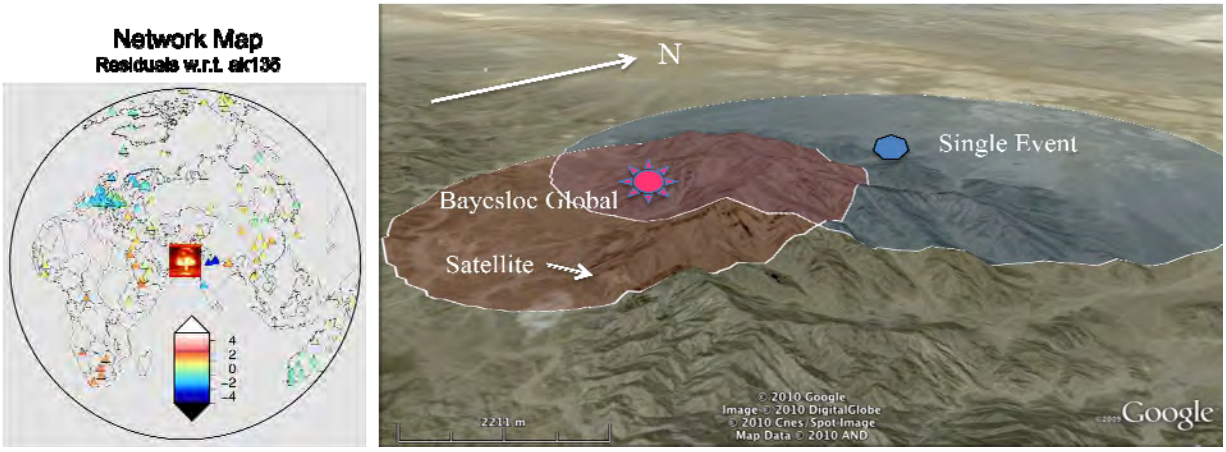

Figure 3. Single-event and Bayesloc global relocation of the May 28, 1998 Pakistan nuclear test. Bayesloc mislocation is 4.5 km with epicenter error ellipse area of 70 km^2. Single event mislocation is 10.1 km with epicenter error ellipse area of 207 km^2. The satellite location is from Albright et al., 1998.

We imposed tight priors on the shift of travel-time curves for teleseismic phases (*P*, *PcP*, *pP*, *sP*). Loose priors were used on the slope (travel time/distance) of the teleseismic travel-time curves but posteriori changes to the travel-time slope were insignificant. A loose prior ±5 seconds was used for the regional phase (*Pn*) travel times, and the posteriori shift of the *Pn* curve is 0.42 seconds. The slope of the *Pn* curve changes significantly and equates to *Pn* phase velocity of 8.16 km/s compared to 8.05 km/s in ak135. In summary, the *Pn* phase travels faster horizontally through the upper mantle than the global average, but *Pn* travel times are delayed relative to the global average due to thick crust.

Figure 4 is a Gaussian representation of the posteriori data precision for each phase. In this case prior information on the pick error was not used, resulting in a pure data-driven assessment of the precision for each phase. The errors are relative to the corrected travel times, but we did include the 0.42 second shift in the *Pn* travel-time prediction to show the significance of the shift with respect to the overall Pn distribution. *P* is found to be most precisely timed, followed by *Pn, pP, PcP, and sP*. Summary of the posteriori pick error is provided in Table 1.

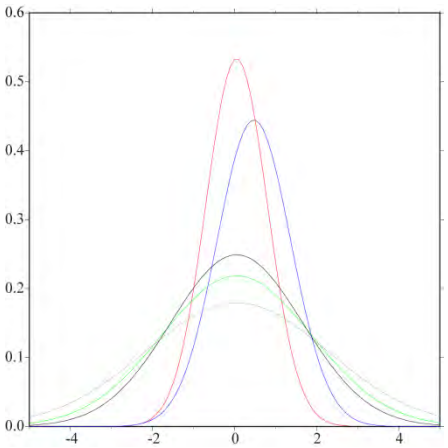

Figure 4. Gaussian representation of posteriori measurement error distribution. *P*=red, *Pn*=blue, *PcP*=green, *pP*=black, and *sP*=grey. The 0.42 second shift of *Pn* travel prediction is included. Standard deviation of measurement error for each pick is also tabulated in Table 1.

MCMC sampling includes testing alternate phase labels for each arrival datum. The phase labels that increase overall probability are more likely to be accepted, and posteriori probability is assessed by counting the number of times a label is accepted. Posteriori summary statistics for each phase are listed in Table 1. The 4th column of Table 1 lists the percentage of instances where the input and posteriori phase label agree and the posteriori probability of the phase label is greater than 0.9. The results suggest that input phase labels are correct, with high confidence, in about 90% of the instances for this data set. The 5th column lists the percentage of instances where the input and most likely posteriori phase label agree. The 6th column lists that percentage of instances where the posteriori phase label was deemed "erroneous", i.e., the provided arrival time did not match the timing for any of the phases considered in this study. The results also suggest that the first-arrival, *P* and *Pn* phases, are not likely to be erroneous, but the rate of erroneous data entries for later-arriving phase – *pP*, *sP*, *and PcP* – is from 1% to 2%. The difference between columns 5 and 6 is the rate of misidentified phases, i.e., valid arrivals with the wrong phase assignment. For example, approximately 3% of reported *P* phases are mislabeled. Detailed examination of the Bayesloc output finds that if a *P* phase is relabeled it is most likely to be relabeled as a depth phase. The depth phase *pP* is also commonly relabeled as either another depth phase or as *P*. Figure 5 shows an example of phase relabeling with waveforms added to substantiate the Bayesloc result. Clearly the removal of one *P* phase is correct, and relabeling the *pP* arrival to *sP* appears reasonable given the apparent arrival of the true *pP* phase that precedes the relabeled phase.

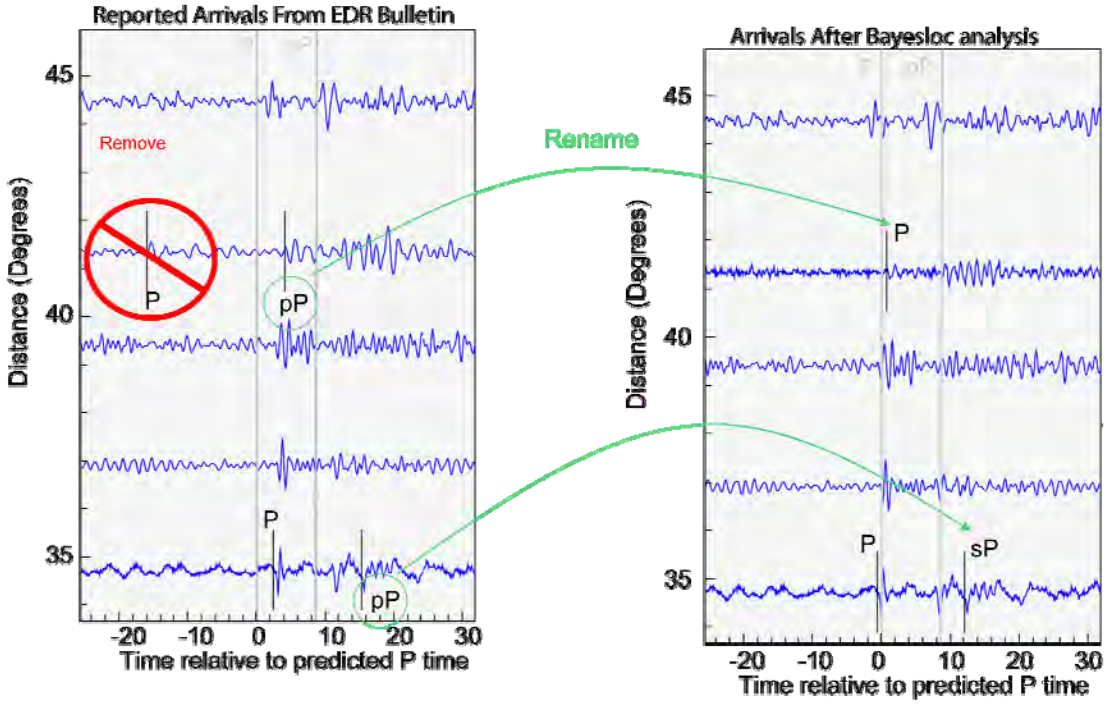

Figure 5. Example of phase re-labeling. In this case, posteriori labels have probability greater than 0.9. Validation of phase relabeling using waveform data suggests that posteriori labels are correct. The data shown here are a small subset of the data for this particular event.

Figure 6 plots posteriori precision (1/variance) for the 3 components of the Bayesloc error model. Low precision indicates that no configuration of the multiple-event system could be found to precisely fit the data for the tested station, phase, or event. High precision indicates precise data fit. The precision of each arrival-time datum is the product of station, phase, and event terms. Posteriori precision is dominated by pick (measurement) error, but also includes other errors that are not accounted for in the travel-time correction. The *P* phase is found to be the most precise, followed by *Pn*, *PcP*, *pP*, and *sP* (also see Table 1). Stations show the largest variability in precision: arrival time data are very consistent at some stations and inconsistent at others. Likewise, arrival times are more consistently fit by corrected travel-time predictions for some events. A possible reason for this is that some events (e.g., explosions) are more impulsive, as noted by Bondár et al. (2004). Variable data precision is used to weight the

penalty for data misfit. Therefore, Bayesloc relocations and travel-time corrections are weighted to fit high-precision stations and events by design.

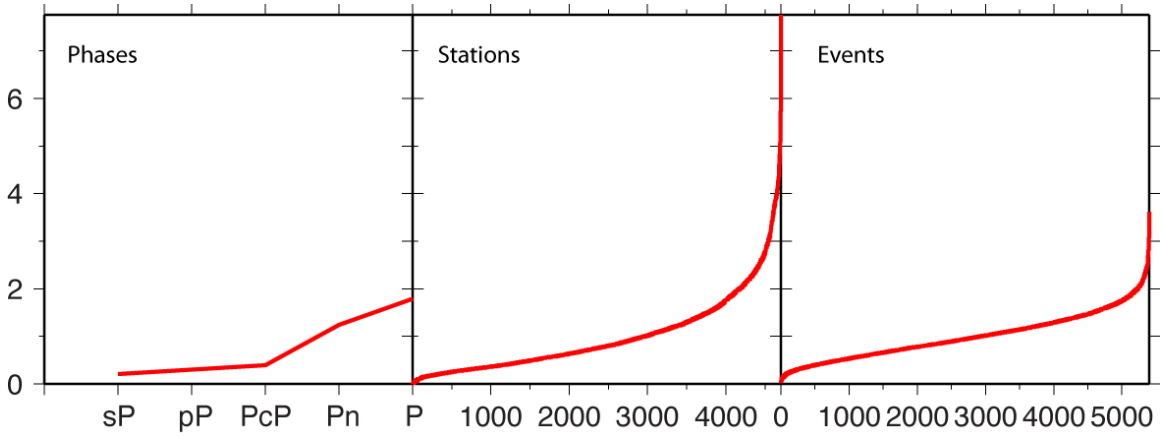

Figure 6. Posteriori precision (1/variance) for phases, stations, and events. Phases, stations, and events are ordered from least precise to most precise. See text for discussion.

Bayesloc posteriori residual standard deviation for the first-arriving *P* wave (*P* and *Pn*) is more than a factor of 3 smaller than input residual standard deviation. Figure 7 shows the density of residual occurrence as a function of distance for input data and Bayesloc output. Approximately 4% of the data are removed since the phases were not confidently determined. The result in Figure 7 suggests that the dominant contribution to global bulletin residuals is location and picks errors, rather than the effects of 3D velocity heterogeneity. At teleseismic distances, the residual distribution shows a slight negative trend, as well as patterns within the body of the residual distribution. *Pn* residuals exhibit a distinct negative trend, consistent with the Bayesloc correction to the *Pn* travel-time curve. The *Pn* distribution after trend removal is slightly larger than the distribution for teleseismic *P*, because of increased pick error and extreme lateral heterogeneity in the Middle East region. Simmons et al. (2010, these Proceedings) use the Bayesloc output as input to 3D tomography. With respect to the 3D velocity model, residuals are 0 mean and standard deviation is reduced to 0.53 seconds. Moreover, the residual trends seen in Figure 7 are removed when travel times are predicted on the basis of the new global tomography model.

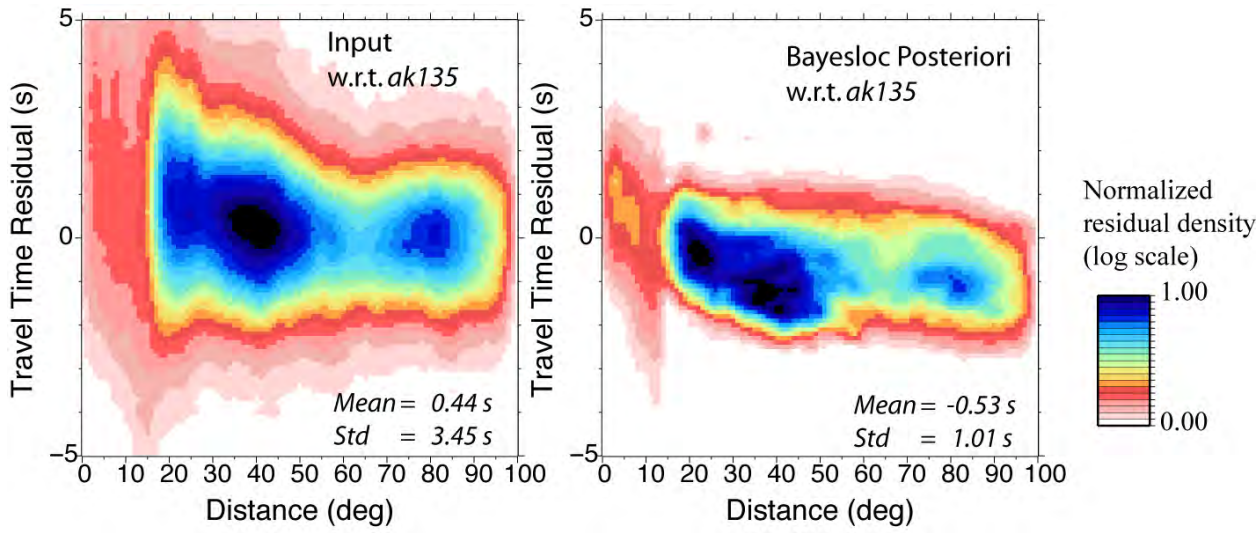

Figure 7. Input and output (posteriori) residual occurrence (density). See text for details.

CONCLUSIONS AND RECOMMENDATIONS

We have made modifications to the Bayesloc multiple-event algorithm that enable application to a global arrival time data set. The first application is to a data set with approximately 5° event spacing globally, to which we add all well-recorded events in the Middle East. Bayesloc relocated epicenters are, on average, 16 km from global bulletin locations (Figure 2). Measured against events that are known to within 1 km, Bayesloc epicenter errors are 5.6 km on average. For the *P* phase: 92% of the bulletin phase labels are confidently determined to be correct; 4% have a significant probability of being improperly labeled, but the input label is the most likely choice; 3.4% are most likely mislabeled; and 0.6% are confidently determined to be erroneous. Analysis for other phases is listed in Table 1. Data precision is decomposed into event, station, and phase components. *P*-phase arrivals are found to be the most precise, followed by *Pn*, *pP*, *PcP*, and *sP*. The most variability in precision is seen for stations, reinforcing common knowledge that some stations are very good and others are not. The range in precision for events is intermediate between stations and phases (Figure 6). Residual standard deviation for the *P* and *Pn* phases is reduced from 3.45 seconds to 1.01 seconds (Figure 7). Reduction in residual magnitude includes identification of outliers and arrivals with ambiguous phase labels. Simmons et al. (2010, these Proceedings) use the posteriori Bayesloc data set for global-scale tomography and demonstrate how the data consistency yields markedly detailed velocity structure beneath the Middle East region. After tomography, residual standard deviation for *P* and *Pn* is 0.53 seconds, which is consistent with Bayesloc assessment of pick error.

ACKNOWLEDGEMENTS

We thank our LLNL colleagues for day-to-day interactions and support. Thanks also to Bill Rodi for numerous, wide-ranging conversations on the location problem.

REFERENCES

Albright, D., Gay, C., and Pabian, F. (1998). New details emerge on Pakistan's nuclear test site, Earth Observation Magazine, December.

Bondár, I., S. C. Myers, E. R. Engdahl, and E. A. Bergman (2004). Epicenter accuracy based on seismic network criteria, *Geophys. Jour. Int.* 156**:** 483–496.

Bondár, I., and K. L. McLaughlin (2009). A new ground truth data set for seismic studies, *Seismol. Res. Lett.* 80: 3.

Flanagan, M. P., S. C. Myers, and K. D. Koper (2007). Regional travel-time uncertainty and seismic location improvement using a 3Dimensional *a priori* velocity model, *Bull. Seismol. Soc. Am.* 97:804–825.

Engdahl, E. R., R. van der Hilst, and R. Buland (1998). Global Teleseismic Earthquake Relocation with Improved Travel Times and Procedures for Depth Determination, *Bull. Seismol. Soc. Am.* 88: 722–743.

Gelman, A., Carlin, J. B., Stern, H. S., and Rubin, D. B. (2004). Bayesian Data Analysis (2nd ed.). Boca Raton, Florida: Hapman and Hall/CRC.

Kennett, B.J.N., E.R. Engdahl and R. Buland (1995). Constraints on seismic velocities in the Earth from traveltimes, *Geophys. J. Int,* 122: 108–124.

Ruppert, S., D., Dodge, A. Elliott, M. Ganzberger, T. Hauk and E. Matzel (2005). Enhancing seismic calibration research through software automation and scientific information management, in *Proceedings of the 27th Seismic Research Review: Ground-Based Nuclear Explosion Monitoring Technologies*, LA-UR-05-6407, Vol. 2, pp. 937–945.

Myers, S. C., G. Johannesson, and W. Hanley (2009). Incorporation of probabilistic seismic phase labels into a Bayesian multiple-event seismic locator, *Geophys. J. Int*. 177: 193–204.

Myers, S. C., G. Johannesson, and W. Hanley (2007).A Bayesian hierarchical method for multiple-event seismic location, *Geophys. J. Int*. 171: 1049–1063.

Myers, S.C., M. L. Begnaud, S. Ballard, M. E. Pasyanos, W. S. Phillips, A. L. Ramirez, M. S. Antolik, K. D. Hutchenson, J. Dwyer, and C. A. Rowe, and G. S. Wagner (2009). A crust and upper mantle model of Eurasia and North Africa for Pn travel time calculation, *Bull. Seismol. Soc. Am*., 100: 640–656.

A REGIONAL SEISMIC TRAVEL TIME MODEL FOR NORTH AMERICA

Stephen C. Myers[1], Michael L. Begnaud[2], Sanford Ballard[3], Abelardo L. Ramirez[1], W. Scott Phillips[2], Michael E. Pasyanos[1], Harley Benz[4], Raymond P. Buland[4]

Lawrence Livermore National Laboratory[1], Los Alamos National Laboratory[2], Sandia National Laboratory[3], National Earthquake Information Center[4]

Sponsored by the National Nuclear Security Administration

Award Nos. DE-AC52-07NA27344[1], DE-AC52-06NA25396[2], and DE-AC04-94AL8500[3]

ABSTRACT

We extend the Regional Seismic Travel Time (RSTT) tomographic effort to North America. In previous work we developed a real-time method to capture the 1st-order effects of 3-dimensional crust and upper mantle structure on RSTTs. The model parameterization is a global tessellation of nodes with a velocity profile at each node. Interpolation of the velocity profiles generates a 3-dimensional crust and laterally variable upper mantle velocity. The upper-mantle velocity profile at each node is represented as a linear velocity gradient, which enables travel time computation in approximately 1 millisecond. Fast computation allows the model to be used in routine analyses and in operational monitoring systems. Model velocities are optimized for travel-time prediction using a tomographic formulation that adjusts the mantle velocity at the Moho, the mantle velocity gradient, and the average crustal velocity. After tomography across Eurasia, rigorous tests find that *Pn* travel time residuals are reduced from a standard deviation of approximately 1.75 seconds (ak135 model) to approximately 1.25 seconds. Further, location error is consistently reduced by approximately 45% for events located using the *Pn* phase. For North American tomography we begin by reconciling North American seismic bulletins. To these bulletins we add high-quality data sets that improve data coverage and data quality, including arrival times reported by the Array Network Facility for USArray stations. In the western United States, USArray provides unprecedented data coverage with station spacing of approximately 70 km. The National Earthquake Information Center (NEIC) researchers contribute unique ground-truth data sets that have been culled over decades. NEIC data is particularly helpful in eastern North America, where the seismicity rate is low. Arrival-time measurements from all sources are re-associated, and event locations that are best constrained by seismic data are relocated using all available arrivals. Events with known locations, e.g., explosions, are not relocated and these events help to establish absolute travel time accuracy. Seismic locations are evaluated against network coverage criteria to estimate hypocenter accuracy. The full error budget for each travel time – hypocenter uncertainty and arrival-time measurement uncertainty – is evaluated to provide a datum-specific uncertainty that establishes weighting in the tomographic inversion. Model validation includes prediction of travel times, as well as relocation of ground-truth events to measure location accuracy. Neither the travel time validation data nor the location validation data are used in the tomographic inversion.

OBJECTIVES

Monitoring seismic events at ever-lower magnitude thresholds requires the utilization of seismic stations that are close to the event. The proliferation of seismic stations across the globe results in lower seismic detection thresholds because more stations are likely to be at regional distance to an event. However, utilization of arrival time data at regional distances often results in degraded location accuracy, because large variations in regional crust and upper-mantle structure can result in large travel time prediction errors.

In previous work we successfully developed an operations-oriented method to account for the 1st-order effects of 3-dimensional crust and upper mantle structure on RSTTs (Myers et al., 2010). The RSTT model parameterization is a global tessellation of nodes, so any model in RSTT format is inherently global in extent and a regional travel time can be computed anywhere for the dominant regional phases (*Pn*, *Pg*, *Sn*, and *Lg*). However, in order to improve travel time prediction accuracy over conventional methods, the model must be "tuned" along each ray path. RSTT model tuning is accomplished by first constructing a best approximation to the 3-dimensional structure of the Earth's crust and upper-most mantle based on existing models. Model velocity – but not layer interfaces – are then adjusted using tomographic imaging methods to further improve prediction accuracy. RSTT model refinement was conducted first over the ~1/4 of the globe containing Eurasia and North Africa (Myers et al., 2010; Figure 1). RSTT tomography across Eurasia and North Africa results in a factor ~2 improvement in location accuracy.

Here we extend RSTT tomography to North America. By extending tomography to North America we address the need to improve global tomographic coverage, which is desirable for CTBT monitoring, and we motivate RSTT use at the NEIC, whose primary interest is monitoring earthquakes in the continental U.S.

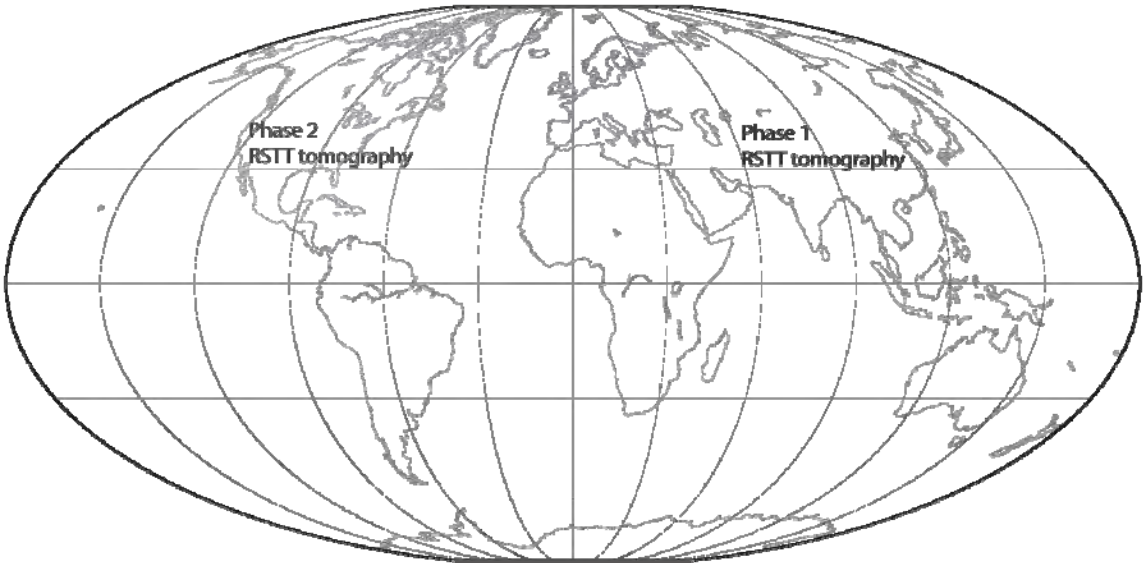

Figure 1. Phased approach for applying RSTT tomography, with the end goal of producing a global model for the universal prediction of regional phases. Phase 1 is complete, and Phase 2 would be initiated under this proposal. (Reproduced from Myers et al., 2010)

RESEARCH ACCOMPLISHED

Work Plan

RSTT model refinement has 5 essential components. First, based on previously determined models, a prior model is built that includes lateral variability of the geologic layers that comprise the crust. The prior model also includes lateral variability of *P*-wave and *S*-wave velocity in the crustal layers and in the upper mantle. A good prior model is essential because the RSTT tomography inversion is invariably under determined, necessitating a model search in the neighborhood of the starting model. Second, a high-quality data set of event locations and arrival-time observations is compiled for use in tomography and for model validation. Third, tomographic inversion is used to adjust model velocities so that travel time predictions are in agreement with the high-quality data set. Layer boundaries are not adjusted in the tomographic inversion because RSTT data sets cannot adequately resolve the trade-off between boundary depth and velocity. Fourth, assessment of travel time error is accomplished by comparing model predictions to the validation data set (not used in tomography). The fifth step is model validation, in which events with known locations are relocated to measure location accuracy and compare observed location error with estimates derived from model uncertainty.

To date, we have completed the data compilation effort, begun evaluation of the CRUST2.0 starting model, and conducted preliminary tomographic inversions. We report on the data set and on our preliminary findings.

Model Parameterization

Myers et al. (2010) provide a detailed description of RSTT model parameterization, travel time calculation, and tomographic formulation, and we provide a brief review here. Crust and upper mantle velocity structure are represented using radial velocity profiles at geographically distributed nodes (Figure 2). The nodes form a triangular tessellation that seamlessly covers the globe. Node spacing is approximately 1° for the model presented here. Node spacing may be adjusted as needed, and we plan to investigate the use of 0.25° node spacing in North America that may be warranted by outstanding data coverage in the western U.S. Velocity interfaces are defined by the radial distance from the center of the Earth, which allows us to explicitly build the GRS80 ellipsoid (Moritz, 1980) into the model and obviate travel-time corrections for ellipticity.

We adopt the velocity versus depth profile in the crust from Pasyanos et al. (2004), which includes model layers for water, 3 types of sediments, upper crystalline crust, middle crust, and lower crust (Figure 2). The crustal layers overlay a mantle velocity profile that is simplified to two parameters: velocity at the Moho and a linear velocity gradient with depth. By interpolating model parameters from surrounding nodes – layer thickness, velocity, and mantle gradient – we generate a continuous model of the 3-D crust and laterally varying upper mantle.

Travel Time Calculation

Parameterization of upper mantle velocity with a linear gradient facilitates an approximation for *Pn* travel time that enables real-time computation (~1 millisecond). Computation of *Pn* travel time at near-regional distance (<700 km) commonly assumes that the *Pn* phase propagates as a head wave, with a ray-path that follows the contour of the Moho (e.g. Hearn, 1984). The head wave assumption results in poor travel time prediction at far-regional distance (>~700 km) because the *Pn* ray can dive appreciably into the mantle due to a positive velocity gradient with depth and Earth sphericity (e.g,. Zhao and Xie, 1993; Ritzwoller et al., 2003; Hearn et al., 2004). To more accurately predict *Pn* at far-regional distances, Zhao (1993) and Zhao and Xie (1993) employ a constant linear velocity gradient in the upper mantle for the whole study area.

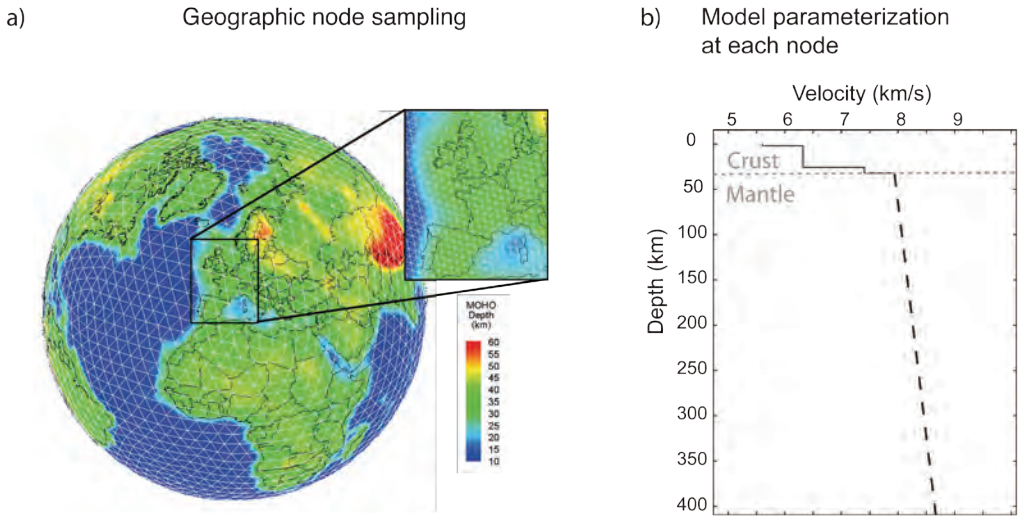

Figure 2. Global model parameterization. a) An example tessellation with approximately 5° grid spacing. The inset shows the 1° used in this study. Color indicates Moho depth of the starting model. b) An example velocity/depth profile as defined at each node. The mantle portion of the profile is specified by the velocity at the crust/mantle interface and a linear gradient. (Reproduced from Myers et al., 2010)

The Zhao (1993) and Zhao and Xie (1993) travel-time calculation is similar to the widely used approach of Hearn (1984), with an additional term (γ) introduced to account for diving rays. The travel-time calculation is

$$TT = \sum_{i=1}^{N} d_i s_i + \alpha + \beta + \gamma \qquad (1)$$

where *d* and *s* are the distance and slowness (taken as 1/velocity below the Moho) in each of the *i* segments comprising the great-circle path between Moho pierce points near the event and station, α and β are the crustal travel times at the source and receiver, and γ (described below).

From Zhao (1993) and Zhao and Xie (1993),

$$\gamma = \frac{c^2 X_m^3}{24 V_0} \qquad (2)$$

where X_m is the horizontal distance traveled in the mantle, and V_0 is a regional average of mantle velocity at the Moho. $c = g * s + 1/r$, where 1/r is an Earth flattening correction and r is the radius at which a ray enters and exits the linear velocity gradient, g (Helmberger, 1973; Zhao and Xie, 1993). This approximation is valid when $ch << 1$, where h is the bottoming depth of the ray in a linear velocity gradient.

We use a spatially varying mantle velocity gradient, *c* (Phillips et al., 2007), and we calculate γ by averaging *c* along the ray track. V_0 remains an average *Pn* velocity over the whole model, which allows us to take advantage of linear tomographic inversion methods (see below). Tests find that using a global average for V_0 introduces negligible travel-time error when *Pn* velocities range from 7.5 km/s to 8.3 km/s.

Data

Ongoing GNEM R&D integration efforts include the collection of seismic bulletins that comprise the vast majority of events and arrival time measurements that are available in North America. To these ongoing efforts we add additional high-quality data sets that provide coverage in specific areas. The USarray project (http://www.iris.edu/USArray/researchers/data.html) is providing unprecedented coverage with station spacing of approximately 70 km. The transportable USarray is a staged deployment that began on the west coast of the U.S. and is steadily moving eastward. USarray currently straddles the Rocky Mountain front

and the Great Plains. The transportable array is scheduled to reach the Eastern US in 2013. Because of the dense station spacing, arrival time measurements of regional distance events at USArray stations can constrain short wavelength lateral variations in the crust and upper mantle. We have loaded the arrival time measurements from the Array Network Facility (http://anf.ucsd.edu) into the GNEM R&D database and reconcile the events/arrivals with existing holdings. Second, NEIC researchers have collected unique ground truth data sets in North America, particularly in the Eastern U.S. The NEIC data have been integrated/reconciled with GNEM R&D holdings in a similar fashion as the ANF data.

Data processing follows the procedure outlined in Myers et al. (2010). Epicenter accuracy for each event in the reconciled bulletin is assessed using the network coverage criteria of Bondár et al. (2004). We further add non-seismic constraints based on known explosion locations, ground displacement from interferometric synthetic aperture radar (InSAR), and mine locations. To diminish the possibility of introducing travel times for phases that interact with velocity discontinuities at ~410 km and ~660 km, the maximum event-station distance range is set to 15°. The minimum event-station distance range is determined by the post-critical refraction for a wave interacting with the Moho. In practice, the minimum distance varies from tens of km in the ocean (thin crust) to approximately 200 km in regions of thick crust.

Because the goal of this work is to produce a model for *Pn* travel-time prediction for real-time monitoring, it is important that *Pn* prediction error is unbiased relative to teleseismic *P*-wave prediction error. Previous efforts have achieved unbiased *Pn* error by using an *ad hoc* travel time correction (Yang et al., 2004). To achieve unbiased *Pn* error, we recomputed each event origin time using at least 10 *P*-wave arrivals. The hypocenter is then fixed during the tomographic procedure, which forces *Pn* prediction error to be unbiased relative to teleseismic P-wave error.

All picks are evaluated against an uncertainty budget that accounts for event mislocation, a global average of *ak135* prediction uncertainty, and arrival-time measurement uncertainty (See Myers et al., 2010). Following removal of local outliers, we produce summary rays for each station by averaging residuals for events that are within 0.25° of one another (Figure 3).

For North America we begin with 80728 *Pn* paths. Outlier removal reduces the number of paths to 70514, of which 7575 are set aside for validation. Use of summary rays reduces the number of paths from 62939 to 35736. The standard deviation of the initial *Pn* data set (80728 paths) is 2.71 seconds with a mean of 0.81 seconds. After outlier remove the standard deviation is reduced to 2.35 seconds with a mean of 0.78 seconds.

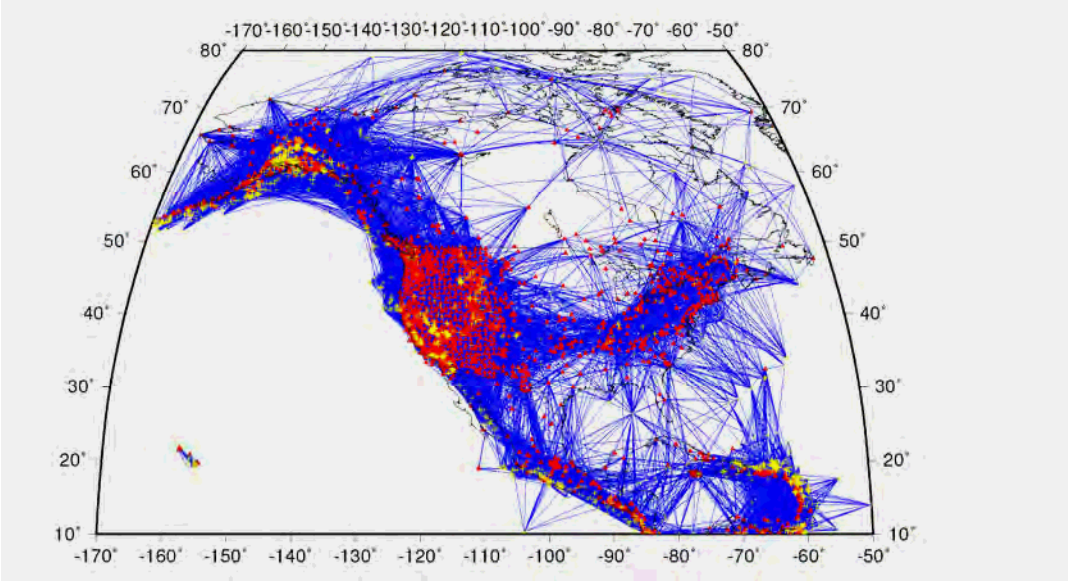

Figure 3. RSTT *Pn* summary ray paths for North America. Stations are red triangles and events are yellow "pluses".

Tomography

The *Pn* travel time (Equation 1) lends itself to a linear tomographic formulation. Because our primary objective is to improve travel-time prediction, we avoid the use of parameters that would not be part of a subsequent travel-time calculation (e.g. event and station time terms). In matrix form, the tomographic system of equations is:

$$\begin{bmatrix} x_1^1 & \cdots & x_N^1 & -\frac{x_1^1 (X_m)^3}{24 V_o X_m} & \cdots & -\frac{x_N^1 (X_m)^3}{24 V_o X_m} & \sum_{p=1}^{Q} \frac{l_{1p}^1}{v_{1p}} & \cdots & \sum_{p=1}^{Q} \frac{l_{Np}^1}{v_{Np}} \\ \vdots & & & & \ddots & & & & \vdots \\ x_1^K & \cdots & x_N^K & -\frac{x_1^K (X_m)^3}{24 V_o X_m} & \cdots & -\frac{x_N^K (X_m)^3}{24 V_o X_m} & \sum_{p=1}^{Q} \frac{l_{1p}^K}{v_{1p}} & \cdots & \sum_{p=1}^{Q} \frac{l_{Np}^K}{v_{Np}} \\ & & & & & \text{Regularization} & & & \end{bmatrix} * \begin{bmatrix} s_1 \\ \vdots \\ s_N \\ c_1^2 \\ \vdots \\ c_N^2 \\ a_1 \\ \vdots \\ a_N \end{bmatrix} = \begin{bmatrix} t^1 \\ \vdots \\ t^K \\ \text{Regularization} \end{bmatrix} \quad (3)$$

where

t = *travel time*
s = *mantle slowness below the Moho (a.k.a. Pn slowness)*
x = *Pn distance (or weight) for each model node*
c = *normalized velocity gradient, v=vo(1+cz)*
X_m = *length of Pn ray path in the mantle*
Vo = *average Pn velocity*
v = *velocity of a crustal layer*
k = *index on K paths (travel-time observations)*
p = *index on Q crustal layers*
l = *length of the ray path in a specified crustal layer (determined by layer thickness and ray parameter in Equations (2) and (3)).*
a = *node-specific adjustment to the slowness of each crustal layer (crustal modifier).*

The tomographic equation solves for the model slowness below the Moho, *s* (a.k.a. *Pn* slowness), the square of mantle velocity gradient, c^2, and a scalar adjustment to crustal slowness, *a*. The formulation in Equation 3 is similar to the approach presented in Phillips et al. (2007), with the difference that we use a scalar adjustment to the slowness of the crustal stack, as opposed to a time term, to account for travel-time errors in crustal legs of the *Pn* ray. The crustal legs can impart as much or more error on the travel time prediction as the travel time in the mantle. Because our goal is to accurately predict subsequent travel times using the tomographic model, it is important to fold all adjustments affecting travel time into the model, rather than absorb the error in a time term that is discarded and will not be used in subsequent travel time prediction.

Preliminary Results

Initial tomgraphic inversions for North America are consistent with the broad trends in previous studies (Figures 4, 5, and 6). The mantle velocity at the Moho approaches 8.3 km/s across much of the Canadian Shield and drops to between 8.0 km/s and 8.15 km/s in the Eastern U.S. (Figure 4). West of the Rocky Mountain Front, velocity drops abruptly below 8 km/s, with low-velocity anomalies of approximately 7.7 km/s in some places.

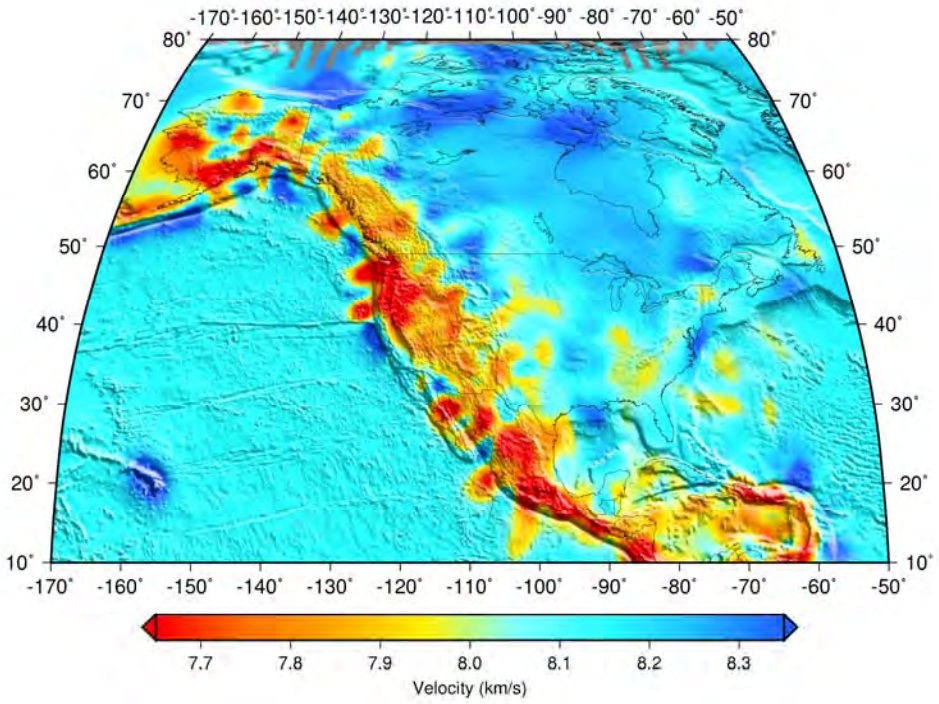

Figure 4. Mantle velocity at the Moho. RSTT tomography is consistent with the known pattern of upper-mantle velocity: very fast across the Canadian Shield; fast across the eastern U.S., and slow west of the Rocky Mountain Front.

The pattern of velocity gradient in the mantle is dominated by oceanic subduction (Figure 5). Subduction of high velocity oceanic lithosphere creates complex three-dimensional structure that cannot be fully captured by the RSTT model parameterization. However, the first-order effect on *Pn* travel times is early arrival at far-regional distances when rays dive into the mantle and preferentially channel through the high-velocity ocean lithosphere. RSTT captures this travel-time effect with a strong velocity gradient, as seen in southern Alaska, the Pacific Northwest, southern Mexico, and the Caribbean. Other areas of high gradient include the Wyoming Archean terrain and the central U.S. We expect the Canadian Shield have a strong velocity gradient, but the tomographic data set, which only has a few long paths across the Canadian Shield, is not suited to resolve mantle gradient in the Canadian Shield. In subsequent inversions we may force a high gradient in the Canadian Shield.

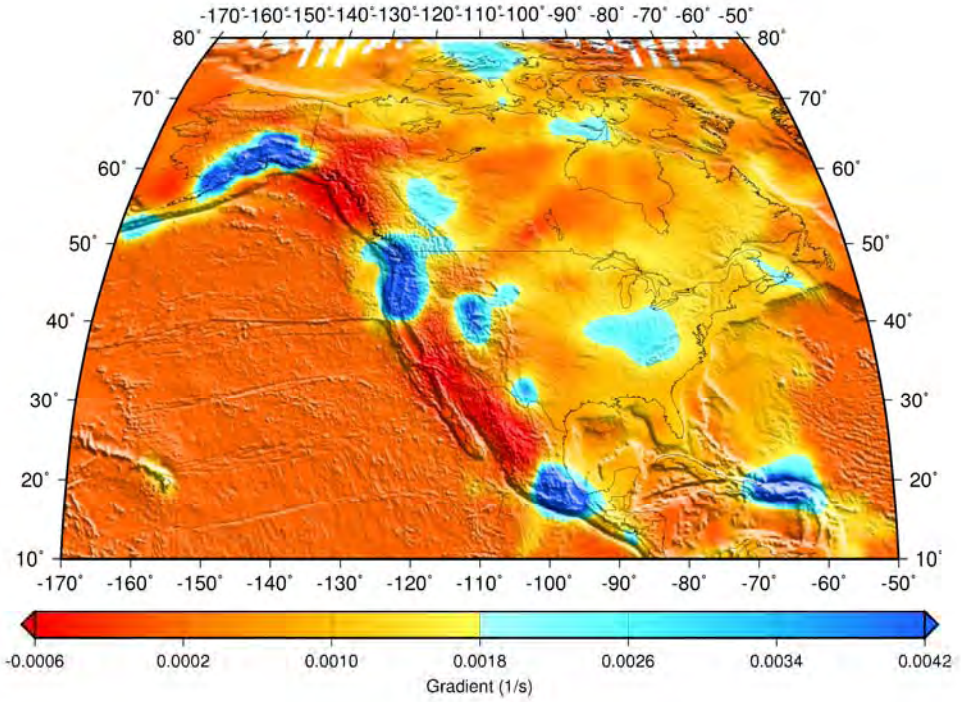

Figure 5. Mantle velocity gradient. Subduction zones are characterized with a high velocity gradient.

Figure 6 shows the modification to crustal slowness (*a* in equation 3). The *Pn* data set does not provide resolution of each of the 7 layers that comprise the RSTT crust, so we solve for a single modification to crustal slowness at each node that is uniformly applied each crustal layer. Increases in crustal velocity (negative *a* values) are seen in California and Idaho. Decreases in crustal velocity are seen in the Colorado Plateau, Wyoming, and the Wrangle Mountains of Alaska. The crustal velocity does not change significantly throughout eastern North America.

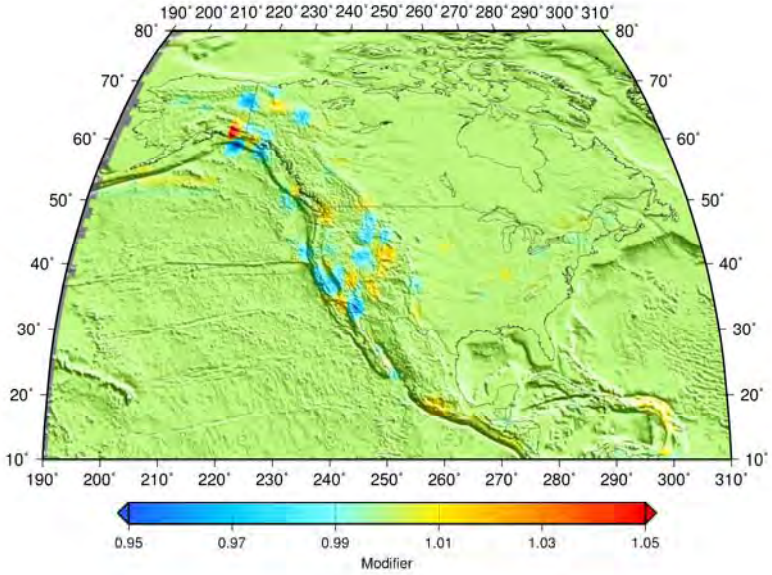

Figure 6. Modification of crustal slowness. This term adjusts the slowness (1/velocity) of the whole crustal stack.

Validation

We leave out 10% of the tomographic data for use in non-circular validation tests. The validation data provides sampling across North America, so residual summary statistics are a good measure of expected model performance in monitoring systems. Figure 7 shows travel time error as a function of distance for the *ak135* model, and the RSTT model. In this case error is represented as the average residual in successive distance bins. Similar to the Eurasia results, *ak135* uncertainty is approximately 2 seconds at near-regional distance and increases rapidly beyond 5° to a maximum of almost 3 seconds at far-regional distance. The RSTT model is significantly improved over *ak135* by reducing the overall travel time prediction error down to approximately 1.5 seconds. The trend of increasing residuals as a function of distance is still evident in the preliminary model.

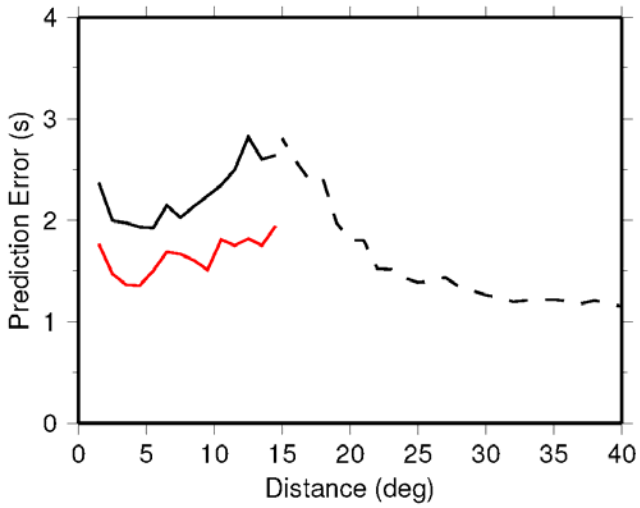

Figure 7. *Pn* travel time prediction error as a function of distance for North American validation data set: black line is ak135, red line is RSTT.

CONCLUSIONS AND RECOMMENDATIONS

We have completed the data compilation needed to extend RSTT tomography to North America. That effort includes integration into our database of data provided by the NEIC and picks provided by the Array Network Facility for USArray stations. The integrated data have been relocated and epicenter accuracy criteria applied. Pick outliers have been identified based on overall statistics and comparison with neighboring data. Summary rays for the Pn data (Figure 3) provide excellent ray coverage across western North America, good coverage across the eastern U.S., poor coverage across central and eastern Canada.

Preliminary tomographic results use a starting model that is based on CRUST2.0. We find that modification to CRUST2.0 are needed. Nonetheless, preliminary tomographic results are consistent with known velocities for major tectonic provinces. Tests of travel-time prediction based on a validation data set (Figure7) show approximately 25% reduction in the standard deviation of residuals.

ACKNOWLEDGEMENTS

We thank our colleagues and collaborators at AFTAC, who worked closely with us at the formative stages of the RSTT project.

REFERENCES

Bondár, I., S. C. Myers, E. R. Engdahl, and E. A. Bergman (2004). Epicenter accuracy based on seismic network criteria, *Geophys. Jour. Int*., 156**,** 483–496.

Bondár, I., K. L. McLaughlin (2009). A New Ground Truth Data Set For Seismic Studies, *Seismol. Res. Lett*. 80: 3.

Hearn, T. M. (1984). Pn travel times in southern California, *Jour. Geophys. Res*. 89: 1843–1855.

Hearn, T. M., S. Wang, J. F. Ni, Z. Xu, Y. Yu, and X. Zhang (2004). Uppermost mantle velocities beneath China and surrounding regions, *J. Geophys. Res*. 109: B11301, doi:10.1029/2003JB002874.

Helmberger, D. V. (1973). Numerical seismograms of long-period body waves from seventeen to forty degrees, *Bull. Seismol. Soc. Am*. 63: 633–646.

Hestenes, M. R., and E. Stiefel (1952). Methods of conjugate gradients for solving linear systems, *J. Res. Nat. Bur. Stand*., 49 (6).

Johnson, M., and C. Vincent (2002). Development and testing of a 3-D velocity model for improved event location: A case study for the India-Pakistan region, *Bull. Seismol. Soc. Am*. 92: 2893–2910.

Kennett, B. J. N., E. R. Engdahl and R. Buland (1995). Constraints on seismic velocities in the Earth from traveltimes, *Geophys. J. Int*, 122: 108–124.

Moritz, H. (1980). Geodetic reference system 1980. Bull. Geodesique. Paris, 54 (3).

Myers, S.C., M. L. Begnaud, S. Ballard, M. E. Pasyanos, W. S. Phillips, A. L. Ramirez, M. S. Antolik, K. D. Hutchenson, J. Dwyer, and C. A. Rowe, and G. S. Wagner (2009). A crust and upper mantle model of Eurasia and North Africa for Pn travel time calculation, *Bull. Seismol. Soc. Am*. 100: 640–656.

Pasyanos, M. E., W. R. Walter, M. P. Flanagan, P. Goldstein, and J. Bhattacharyya (2004). Building and testing an a priori geophysical model for western Eurasia and North Africa, *Pure. Appl. Geophys*. 161: 235–281.

Phillips, W. S., M. L. Begnaud, C. A. Rowe, L. K. Steck, S. C. Myers, M. E. Pasyanos, and S. Ballard (2007). Accounting for lateral variations of the upper mantle gradient in Pn tomography studies, *Geophys. Res. Lett*. 34: doi:10.1029/2007GL029338, 2007.

Steck, L. K., C. A. Rowe, M. L. Begnaud, W. S. Phillips, V. L. Gee, and A. A. Velasco (2004), Advancing seismic event location through difference constraints and three-dimensional models, in *Proceedings of the 26th Seismic Research Review - Trends in Nuclear Explosion Monitoring*, LA-UR-04-5801, Vol. 1, pp. 346–355.

Yang, X., I. Bondár, J. Bhattacharyya, M. Ritzwoller, N. Shapiro, M. Antolik, G. Ekstro¨m, H. Israelsson, and K. McLaughlin (2004). Validation of Regional and Teleseismic Travel-Time Models by Relocating Ground-Truth Events, *Bull. Seismol. Soc. Am*. 94: 897–919.

Zhao, L.-S. (1993). Lateral variations and azimuthal isotropy of *Pn* velocities beneath Basin and Range province, *J. Geophys. Res*. 98: 22,109–22,122.

Zhao, L.-S., and J. Xie (1993). Lateral variations in compressional velocities beneath the Tibetan Plateau from Pn traveltime tomography, *Geophys. J. Int*. 115: 1070–1084.

EXPANDING COHERENT ARRAY PROCESSING TO LARGER APERTURES USING EMPIRICAL MATCHED FIELD PROCESSING

Frode Ringdal[1], David B. Harris[2,3], Tormod Kværna[1], Steven J. Gibbons[1]

NORSAR[1], Lawrence Livermore National Laboratory[2], and Deschutes Signal Processing LLC[3]

Sponsored by the Air Force Research Laboratory and the National Nuclear Security Administration
Award Nos. FA8718-08-C-0007[1,3] and DE-FC52-06NA27324[2]
Proposal No. BAA08-39

ABSTRACT

Matched field processing, a method developed in underwater acoustics to detect and locate targets, has been adapted to classify transient seismic signals arising from mining explosions and other sources of recurring seismicity. Empirical matched field processing (EMFP) uses observations of historical events to calibrate the amplitude and phase structure of wavefields incident upon an array aperture for particular repeating sources. The objective of this project is to determine how broadly applicable the method is and to understand the phenomena that control its performance. EMFP has been evaluated using seismic arrays and networks in Central Asia which comprise a wide spectrum of sensor geometries. These range from medium aperture arrays (e.g., MKAR and BVAR), to teleseismic arrays and networks (e.g., KNET and KURK), through to very large aperture virtual networks consisting of arrays and single-site stations separated by distances of several hundreds of kilometers. The region studied is also of interest given the large number of sources of repeating industrial events and regions of diffuse seismicity.

Multitaper methods have been used to calculate narrow frequency-band spectral covariance matrices for short data segments. Windows of the order 3 seconds are typically used in classical f-k analysis, and calculating the empirical steering vectors from data segments of this length allows a direct comparison between matching statistics from theoretical and empirical steering vectors. Using first P-arrivals from events at the Kara Zhyra mine near Semipalatinsk, observed on the MKAR and ZALV arrays, we have demonstrated that the empirical matched field statistics are significantly greater than those obtained for plane-wavefront models. The gain is greatest for high frequencies, at which coherent processing is difficult even on these relatively small aperture arrays. We have also demonstrated that the performance using empirical steering vectors calibrated from single events is frequently comparable to that possible using vectors calibrated from ensembles of many events. This indicates that the method is applicable to sources of interest from which only single events have been observed.

The sensitivity of the spectral covariance estimates to the exact positioning of the data-window has been investigated. For 3-second windows surrounding P-arrivals, the resulting matched field statistics appear to be almost unaffected by shifts of over a second. This has the consequences that the method can be applied to signals with fairly uncertain onset times, and that a single-phase matched field detector can be formulated where the covariance estimates on the incoming data need not be evaluated more often than once per second. Detection runs have been performed for Kara Zhyra events using only 3-second P-phase matched field templates on MKAR, ZALV, and a wide-aperture network comprising both arrays (where time-shifts are applied prior to calculating the spectral covariance matrix). In all three cases, values of the matched field statistic exceeding the background level significantly were only recorded on a very limited number of occasions. All were at characteristic times of day, and all were accompanied by additional evidence, both from correlation detectors and signals at a closer station (KURK), that the detected signal did indeed come from the target source region. A P-phase matched field detector was run using templates from single after-shocks of the M=7.4 October 8, 2005, Kashmir earthquake for both KNET (with staggered time-windows) and the KKAR array. Significant values of the matched field statistic were obtained for both sensor geometries on multiple occasions, at times consistent with events from the same source region. The source region within which events can be associated using EMFP is likely to decrease as the sensor network aperture increases. Consequently, an unequivocal matched field identification over a very large aperture sensor array is likely to attribute a signal to a specific source region with a greater degree of confidence than when a small aperture array is used.

OBJECTIVE

The objectives of this project are

- To investigate the limits of empirical matched field processing and other coherent array detection and parameter estimation methods as receiver aperture size increases from a few kilometers to many hundreds of kilometers.
- To investigate techniques for extending the geographical source-region footprint over which empirical matched field processing and other coherent calibrated methods apply.

We began by reanalyzing data from the European Arctic in order to reconfirm the potential of empirical matched field processing that has been indicated by our work under a previous contract. We then proceeded to study the central Asia region to assure programmatic relevance and to exploit the large belts of natural and man-made seismicity to test the applicability of the technique to diffuse seismicity.

RESEARCH ACCOMPLISHED

Throughout this study, we consider exclusively seismic data from arrays and networks. If $\underline{\boldsymbol{x}}_m$ denotes the coordinates of sensor *m* relative to some reference site, then we denote the time-series recorded at this site by $r_m(t) = r(t, \underline{\boldsymbol{x}}_m)$. If *N* denotes the number of sensors in our array then, for a given frequency ω, one can form the $N \times N$ spatial covariance matrix, $\underline{\boldsymbol{R}}(\omega)$, of which the element R_{nm} is given by

$$R_{mn}(\omega) = \left(\int r(t, \underline{\boldsymbol{x}}_m) e^{-i\omega t} dt \right) \left(\int r(t, \underline{\boldsymbol{x}}_n) e^{i\omega t} dt \right) \tag{1}$$

Given the relative transience of seismic signals, it is understood that $\underline{\boldsymbol{R}}(\omega)$ should be calculated on a relatively short data segment (at most a few seconds for high frequency studies of regional events).

The complex *N*-vector $\underline{\boldsymbol{\varepsilon}}(\omega, \underline{\boldsymbol{s}}) = \left[e^{-i\omega \underline{\boldsymbol{s}} \cdot \underline{\boldsymbol{x}}_1}, \quad \cdots, \quad e^{-i\omega \underline{\boldsymbol{s}} \cdot \underline{\boldsymbol{x}}_N} \right]^T$ describes a wavefield over the array at the frequency ω with the ε_m defining the time-delays (phase shifts) and amplitudes for the waveforms at the *N* sites. If *H* denotes the Hermitian transpose, then a scalar of the form

$$\hat{P}(\underline{\boldsymbol{\varepsilon}}(\omega)) = \frac{\underline{\boldsymbol{\varepsilon}}(\omega)^H \underline{\boldsymbol{R}}(\omega) \underline{\boldsymbol{\varepsilon}}(\omega)}{\mathrm{tr}\left\{ \underline{\boldsymbol{R}}(\omega) \right\}} \tag{2}$$

provides a measure of how consistent the data (from which $\underline{\boldsymbol{R}}(\omega)$ is calculated) are with the wavefield hypothesis defined by $\underline{\boldsymbol{\varepsilon}}(\omega, \underline{\boldsymbol{s}})$.

Given the broadband nature of the majority of the seismic signals examined, it is usual to consider a wide-band statistic, summed incoherently over a range of *K* frequency bands:

$$\hat{P}(\underline{\boldsymbol{\varepsilon}}([\omega_1 : \omega_K])) = \sum_{k=1}^{K} a_k \frac{\underline{\boldsymbol{\varepsilon}}(\omega_k)^H \underline{\boldsymbol{R}}(\omega_k) \underline{\boldsymbol{\varepsilon}}(\omega_k)}{\mathrm{tr}\left\{ \underline{\boldsymbol{R}}(\omega_k) \right\}} \tag{3}$$

where $\underline{\boldsymbol{\varepsilon}}(\omega_1 : \omega_K)$ comprises *K* complex vectors of length *N*: the so-called steering vectors for each of the *K* frequencies. The coefficients a_k are weights which ensure normalization of the broadband statistic:

$$\sum_{k=1}^{K} a_k = 1. \tag{4}$$

The most obvious solution is to set $a_k = 1/K$ (for all *k*) for a simple mean, although non-uniform coefficients may be preferable due to signal-to-noise considerations or stability.

In the most straightforward wavefield parametrization, the plane wavefront assumption, we assume that the waveforms on all sensors are identical except for the time-delay and that the arrival time at sensor *m* is specified by

$$t_m = t_0 - \underline{\boldsymbol{s}} \cdot \underline{\boldsymbol{x}}_m \tag{5}$$

where t_0 is the arrival time at the array reference site (with coordinate vector $\underline{\boldsymbol{x}}_0$) and the slowness vector

$\underline{\boldsymbol{s}} = (s_x, s_y)$ is related to the backazimuth Θ and the apparent velocity v_{app} by

$$s_x = s\sin(\Theta), \quad s_y = s\cos(\Theta), \quad \text{and} \quad s = 1/v_{\text{app}}. \tag{6}$$

In this case, our theoretical steering vector $\underline{\boldsymbol{\varepsilon}}$ is given by

$$\underline{\boldsymbol{\varepsilon}}(\omega, \underline{\boldsymbol{s}}) = \left[e^{-i\omega\underline{\boldsymbol{s}}\cdot\underline{\boldsymbol{x}}_1}, \quad \cdots, \quad e^{-i\omega\underline{\boldsymbol{s}}\cdot\underline{\boldsymbol{x}}_N}\right]^T \tag{7}$$

and the statistic evaluated over our *K* specified frequencies is

$$\hat{P}(\ \underline{\boldsymbol{\varepsilon}}([\omega_1 : \omega_K], \underline{\boldsymbol{s}})\ ) = \sum_{k=1}^{K} a_k \frac{\underline{\boldsymbol{\varepsilon}}(\omega_k, \underline{\boldsymbol{s}})^H \underline{\boldsymbol{R}}(\omega_k)\underline{\boldsymbol{\varepsilon}}(\omega_k, \underline{\boldsymbol{s}})}{\text{tr}\left\{\underline{\boldsymbol{R}}(\omega_k)\right\}} \tag{8}$$

Deviations of the wavefield from the predicted plane wavefront model will lead to a reduction in the value of the expression in Equation (8). The steering vector, $\underline{\boldsymbol{\varepsilon}}(\omega)$, which optimizes the value of the quadratic form in Equation (3) is the principal eigenvector of the matrix $\underline{\boldsymbol{R}}(\omega)$. In empirical matched field processing (EMPF), it is anticipated that the spatial structure of an incoming wavefront over a sensor array from a source of repeating seismicity will be approximately the same for each event. Therefore, if a covariance matrix $\underline{\boldsymbol{R}}(\omega, \alpha)$ is measured for an arrival from a source of interest (denoted by α) then the principal eigenvector $\underline{\boldsymbol{\varepsilon}}(\omega, \alpha)$ is likely to constitute an empirical steering vector which will provide a better match than the closest theoretical (plane-wave) steering vector, given that differences in amplitude and deviations in phase-shifts resulting from diffraction and scattering will be accounted for in the spectral covariance matrix estimate.

There may be many occurrences, α_i, of a given arrival from subsequent events at the site of interest. In this case, it may be desirable to use many different observations on which to base our EMFP spatial template. We could form an ensemble covariance matrix, $\underline{\boldsymbol{R}}(\omega, \boldsymbol{\alpha})$, from the single arrival covariance matrices, $\underline{\boldsymbol{R}}(\omega, \alpha_i)$, with

$$\underline{\boldsymbol{R}}(\omega, \boldsymbol{\alpha}) = \sum_{\alpha_i \in \boldsymbol{\alpha}} w_i \underline{\boldsymbol{R}}(\omega, \alpha_i) \tag{9}$$

where the w_i are weights which define the contribution for each of the single arrival covariance matrices. Forming the ensemble covariance matrix may provide a more stable estimator of the optimal empirical steering vector for the arrival by reducing the variability in the single arrival matrices. On the other hand, there is a danger that the ensemble covariance matrix will be degraded by the inclusion of arrivals from too great a diversity of sources (for example, a larger source region than was at first anticipated). In such a case it may be better to consider multiple steering vectors, each calculated from a single arrival. Ringdal et al. (2009) show an example of how source classification performance improved significantly by constructing two separate ensemble estimates from the individual observations. Cluster analysis on the single arrival covariance matrices is necessary before forming the covariance matrix in Equation 9.

Given that we may normalize any covariance matrix $\underline{\boldsymbol{R}}(\omega)$, to have unit trace (either prior to or after the forming of an ensemble covariance matrix), we can express our ensemble and single observation matched field estimators for the source region α as

$$\hat{P}(\ \underline{\boldsymbol{\varepsilon}}([\omega_1 : \omega_K], \boldsymbol{\alpha})\ ) = \sum_{k=1}^{K} a_k \underline{\boldsymbol{\varepsilon}}(\omega_k, \boldsymbol{\alpha})^H \underline{\boldsymbol{R}}(\omega_k)\underline{\boldsymbol{\varepsilon}}(\omega_k, \boldsymbol{\alpha}) \tag{10}$$

and

$$\hat{P}(\ \underline{\boldsymbol{\varepsilon}}([\omega_1 : \omega_K], \alpha_i)\ ) = \sum_{k=1}^{K} a_k \underline{\boldsymbol{\varepsilon}}(\omega_k, \alpha_i)^H \underline{\boldsymbol{R}}(\omega_k)\underline{\boldsymbol{\varepsilon}}(\omega_k, \alpha_i) \tag{11}$$

respectively. Here, the steering vectors $\underline{\boldsymbol{\varepsilon}}(\omega_k, \boldsymbol{\alpha})$ and $\underline{\boldsymbol{\varepsilon}}(\omega_k, \alpha_i)$ are respectively the principal eigenvectors of ensemble covariance matrices, $\underline{\boldsymbol{R}}(\omega_k, \boldsymbol{\alpha})$, and single arrival covariance matrices, $\underline{\boldsymbol{R}}(\omega, \alpha_i)$.

If the eigenspectrum of the covariance matrix is dominated by a single eigenvalue, then it is very likely that the principal eigenvector will provide a good representation of an arrival. If the wavefield at a given time is not well represented by a simple wavefront, the eigenspectrum is not likely to be dominated by one eigenvalue and a subspace approach may be more appropriate where we consider a signal-space spanned by more than one eigenvector. Our single-band steering vector $\underline{\boldsymbol{\varepsilon}}(\omega_k)$ then has to be a linear combination of the eigenvectors corresponding to the *L* largest eigenvectors of the template covariance matrix: $\underline{\boldsymbol{e}}_1, \cdots, \underline{\boldsymbol{e}}_L$. If the $\underline{\boldsymbol{e}}_i$ form the columns of the $N \times L$ steering

matrix $\underline{\underline{\boldsymbol{E}}}$, with

$$\underline{\varepsilon}(\omega_k) = \underline{\underline{\boldsymbol{E}}}\ \underline{\boldsymbol{v}} \tag{12}$$

then the vector of coefficients, $\underline{\boldsymbol{v}} = [v_1, \cdots, v_L]^T$, subject to $\underline{\boldsymbol{v}}^H \underline{\boldsymbol{v}} = 1$, is the principal eigenvector of the $L \times L$ matrix $\underline{\underline{\boldsymbol{E}}}^H \underline{\underline{\boldsymbol{R}}}\ \underline{\underline{\boldsymbol{E}}}$. L is referred to as the rank of the matched field statistic.

One of the most appealing features of empirical matched field processing (EMFP) is the expectation that, due to the narrow-band nature, the method will be far less sensitive to differences in the source-time function. Ripple-firing practices can cause significant problems for the classical correlation detectors (e.g., Gibbons and Ringdal, 2006) due to significant waveform variation from event to event. The spectral covariance matrices encode the spatial structure of the wavefield over the receiver aperture far more than the temporal structure and work on quarries on the Kola Peninsula (Harris and Kværna, 2010, Ringdal et al., 2009) has demonstrated that EMFP can provide excellent source classification for ripple-fired events, despite significant waveform diversity.

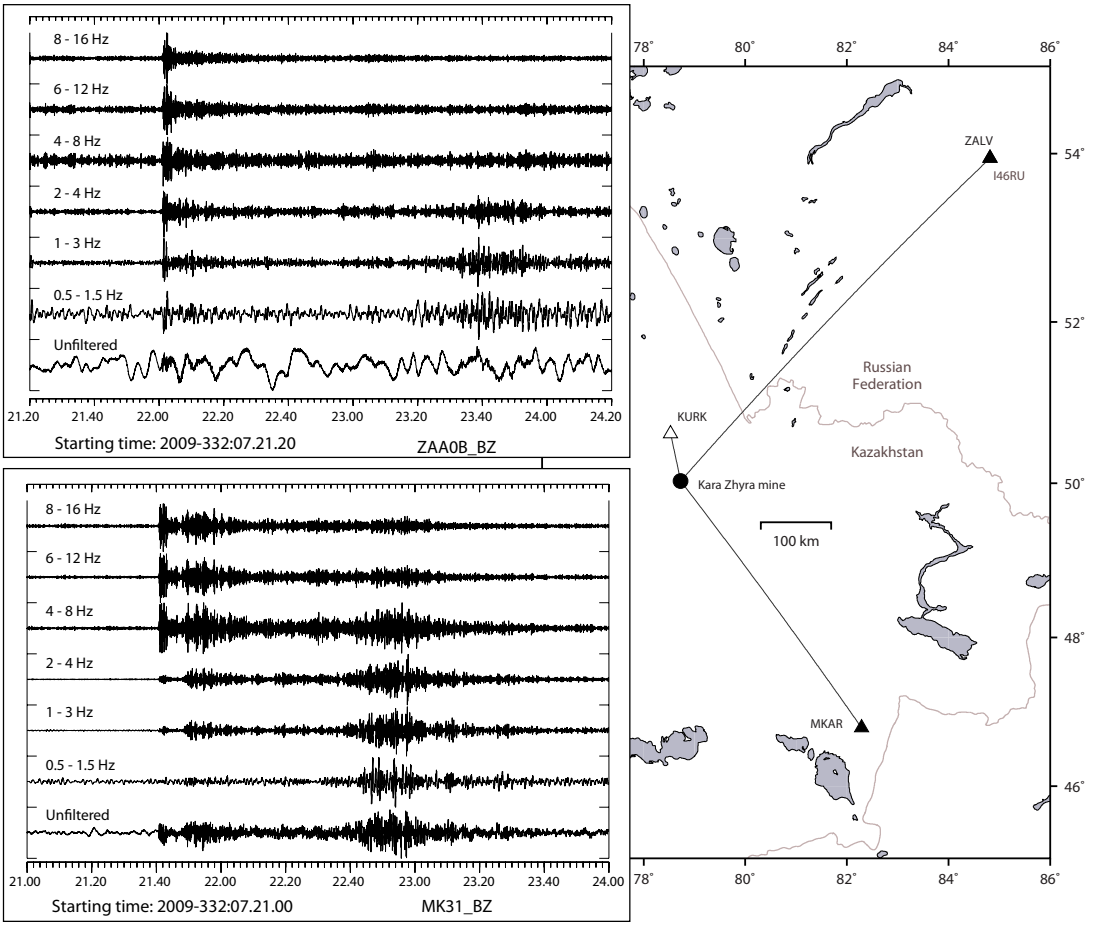

Figure 1. Location of the Kara Zhyra mine in Eastern Kazakhstan with respect to the MKAR and ZALV arrays (at 445 km and 600 km respectively). Waveforms from the vertical component broadband sensor at both arrays are shown at the times and in the frequency bands indicated.

Figure 1 displays the locations of two primary seismic arrays in central Asia in relation to a source of repeating seismic events. Both arrays consist of 9 sites over an aperture of ~5 km over which coherent processing of higher frequencies (> 4 Hz) demonstrably fails (Ringdal et al., 2009). The wavefield characteristics vary greatly between the two arrays. The only impulsive arrival at ZALV is Pn; Lg is highly emergent and there is no clear Sn onset. At MKAR, there are clear Pn and Pg onsets and high amplitude Lg. Pn is a very high frequency arrival and is often estimated poorly due to a low SNR below 4 Hz. The Pg arrival has far more low frequency energy. An event on October 28, 2009, was confirmed to have occurred at the mine and an extensive search using multiple correlation detectors on all available

arrays, followed by careful analysis of the signals at the closest station (KURK), provided a large database of events which were likely to have come from that source. For each event, a spectral covariance matrix and corresponding eigenvectors were evaluated for analyst-picked Pn arrivals at both the MKAR and ZALV arrays. We chose a window length of 121 samples (3.0 seconds) and 19 discrete frequencies from 2.0 to 8.0 Hz. The multitaper (Thomson, 1982) software described by Prieto et al. (2009) was used to construct the covariance matrices. An ensemble covariance matrix was also constructed for each of the two arrays, taking care to account properly for missing or corrupted data channels for a number of events.

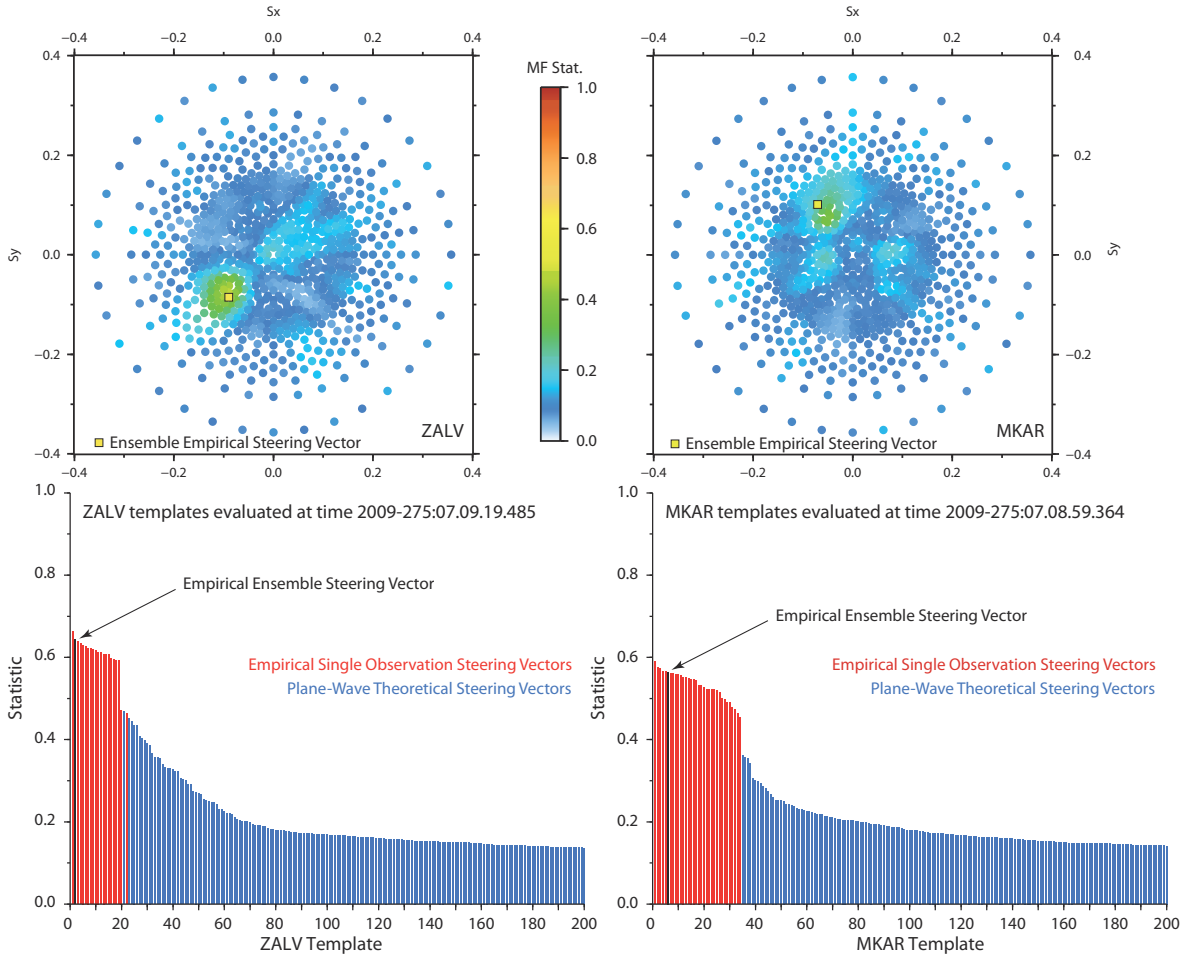

Figure 2. Matched field statistics for the specified times at ZALV and MKAR for Pn arrivals from an event assumed to originate close to the Kara Zhyra mine in Eastern Kazakhstan. Both theoretical plane wave steering vectors (blue), single observation empirical matched field steering vectors (red) and ensemble matched steering vectors (black) are used. The bars in the lower panels are rearranged in descending order of the matched field statistic.

For a number of candidate arrivals, the matched field statistic (an arithmetic mean across all frequency bands) was evaluated against steering vectors as displayed in Figure 2. The theoretical plane-wave, single observation empirical, and ensemble matched field statistics are as given in equations 8, 11, and 10 respectively. The upper panels of Figure 2 show the deployment in slowness space of the theoretical plane-wave steering vectors. Empirical steering vectors were only calculated for phase arrivals for which a clear onset could be picked by an analyst and the calculations displayed in Figure 2 are limited to events where the SNR on the array beam exceeds 20. In almost all cases, the matched field statistics for the empirical steering vectors (red/black) is considerably higher than that for the theoretical steering vectors (blue). The improvement is greater for MKAR than for ZALV, probably due to the high frequency content of the MKAR signals (for which the theoretical steering vectors perform poorly). The plot of matched field statistic as a function of slowness indicates local maxima close to the theoretical slowness vector; more clearly defined for ZALV than for MKAR over this frequency range.

The slowness plots also suggest a strategy for the calculation of f-k spectra in routine processing. A matched field statistic should be evaluated over a dense slowness grid (as is typically done today) but, in addition, a number of empirical steering vectors for repeatedly observed arrivals should augment the slowness space, labelled with the corresponding theoretical slowness vectors. Should an empirical steering vector attain a higher matched field statistic than any of the theoretical steering vectors, the corresponding theoretical slowness vector should be returned. Given a suitably dense coverage of empirical slowness vectors, this could remove the need to apply Slowness and Azimuth Station Corrections (SASCs). A final observation from Figure 2 is that essentially every one of the single-observation empirical matched field steering vectors performs significantly better than the best theoretical steering vector. EMFP can therefore be expected to perform well even for situations in which only a single observation is available. The evaluation of the matched field statistic for a given steering vector against the current covariance matrix is very rapid and it could be envisaged that huge numbers of steering vectors could be processed for each covariance matrix without the computational demands becoming prohibitive. The ensemble covariance matrices in these cases do perform well and it may be advisable to use empirical steering vectors both from ensemble estimates and from single observations.

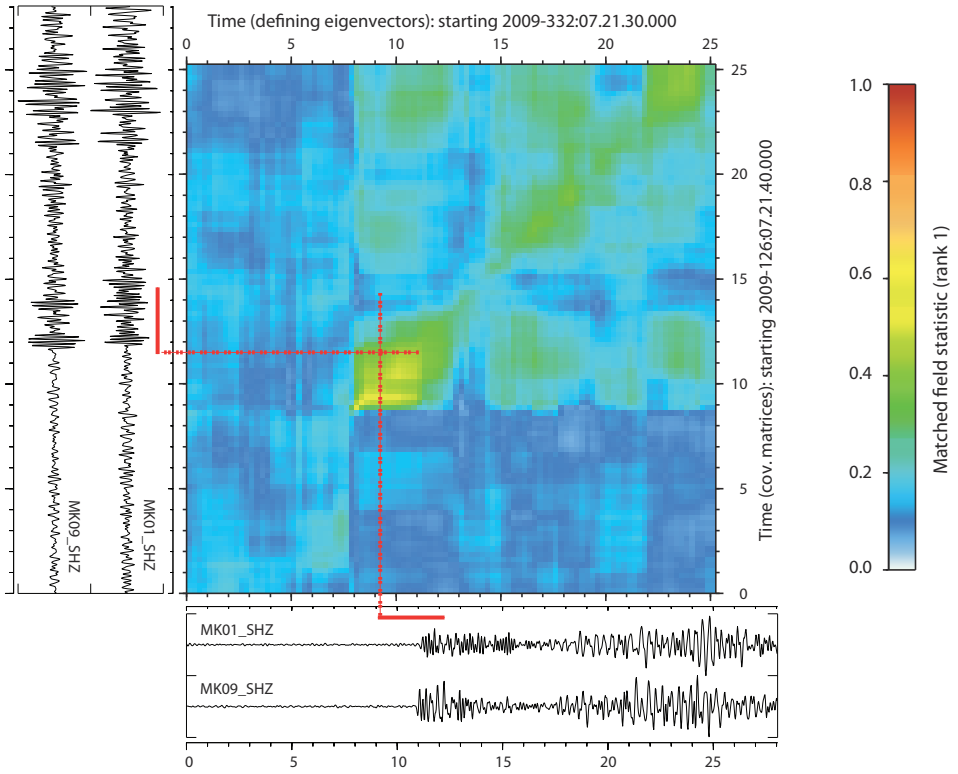

Figure 3. Matched field statistics as a function of data-window positioning for two events from the Kara Zhyra mine recorded at Makanchi. The x-axis of the grid indicates the starting time of the 3 second (121 sample) long data-window from which the (single event, single phase) empirical steering vector is calculated. The colors of the pixels for that value of x indicate the values of the matched field statistic evaluated against a data-window starting at the time indicated by the y coordinate. For example, the intersection of the dashed red lines indicates the value of the rank-1 statistic obtained using the spectral covariance matrix evaluated for the data segment covered by the vertical solid red bar against an empirical steering vector calculated from the template indicated by the horizontal red bar.

All of the matched field statistics presented so far have been evaluated over data segments carefully selected by an analyst. How sensitive are the results to the positioning of the data window? The three-second window chosen here is typical of the classical f-k analysis performed on small and medium aperture arrays and, given the relative transience of seismic phases, a significant increase in the data window length is probably not advisable. The uncertainties associated with arrival time estimates can be significant, especially for low SNR signals, and the method may be of limited applicability in automated processes if the matched field statistic varies greatly within the uncertainty of the phase arrival estimate.

Figure 3 displays the matched field statistic as a function both of time of the template window (for the calculation of the empirical steering vector) and of the time of the data window. The transience of the statistic is evident and it is clear that there is a modulation as the statistic is evaluated over time-intervals with different degrees of coherence. (For example, the matched field statistic for the Pg phase of event 2 using the Pn empirical steering vector for event 1 is considerably higher than for the coda immediately following the Pn arrival.) However, it appears that the matched field statistic is significantly greater than the background level for a duration long enough to cover the uncertainty surrounding the arrival time estimate. The variability will clearly change from arrival to arrival, and from array to array, although the results displayed here appear to be fairly representative of a wide range of phases observed.

The time dependence indicated in Figure 3 suggests that, for a continuous evaluation of a matched field statistic against a set of reference steering vectors, an evaluation of the data covariance matrix every second is probably sufficient. A more frequent evaluation of the spectral covariance matrix is likely to lead to a significantly higher computational expense without a signficant gain in performance. This provides for the possibility of a single-phase matched field detector to find the occurrences of incoming wavefields resembling a previously observed template. This is analogous to the correlation detectors except for that we are seeking primarily a spatial wavefield structure over the array and not necessarily a temporal wavefield structure.

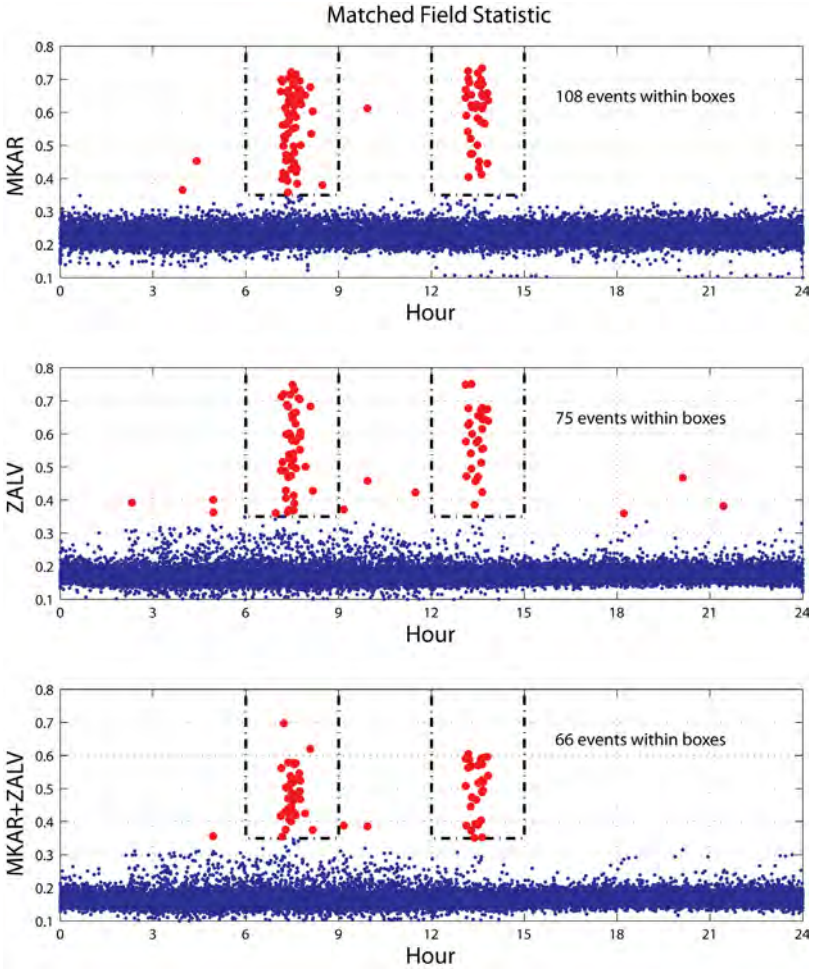

Figure 4. Matched field statistics from empirical steering vectors from a single Kara Zhyra event as function of time of day from the array configurations as displayed from January 1, 2009, to December 31, 2009. Each point indicates the maximum value obtained in a 20 minute segment (and so multiple events within the same data window would not be resolved). Values greater than 0.35 are highlighted. The covariance matrices for the two-array matched field calculation in the lowermost panel are calculated using a 20.0 second delay imposed on the ZALV waveforms relative to the MKAR waveforms.

Figure 4 shows the results of using the single-phase EMFP detector to identify Pn arrivals from Kara Zhyra events, at both MKAR, ZALV, and a virtual network consisting of the two arrays with the ZALV waveforms moved forward by 20 seconds to compensate the longer travel-time. The matched field statistic was evaluated every second for the calendar year 2009, for the three array configurations, using the empirical steering vectors from the ensemble covariance matrices. Every point shown in the plot is the maximum value obtained within predefined 20 minute segments. From the time-of-day plots, it does not appear that many triggers have occurred outside of two very narrow time-zones in the day, indicating that these matched field statistics may constitute a detector with a low false alarm rate. The virtual wide-aperture array works quite well (despite capturing slightly fewer events than the single array processes). The distribution of points for the two-array system follows very closely the results of the ZALV array which may indicate that, at some times, the covariance matrix is likely to be dominated by the contributions from channel pairs within one of the arrays. It is also possible that the single arrays cannot resolve between events from distant extremes of an extended source region since the relative phase-shifts are very small, whereas the two-array system is sensitive to far smaller changes of source region. This is identical to what is observed using the multi-channel waveform correlation detector. On a small-aperture array, detections of some significance can occur when an unrelated wavefront approaches from a similar direction to the master event. On a large array or network, it is almost impossible to get a trigger at all sites simultaneously and the detector responds to events from a much smaller source region.

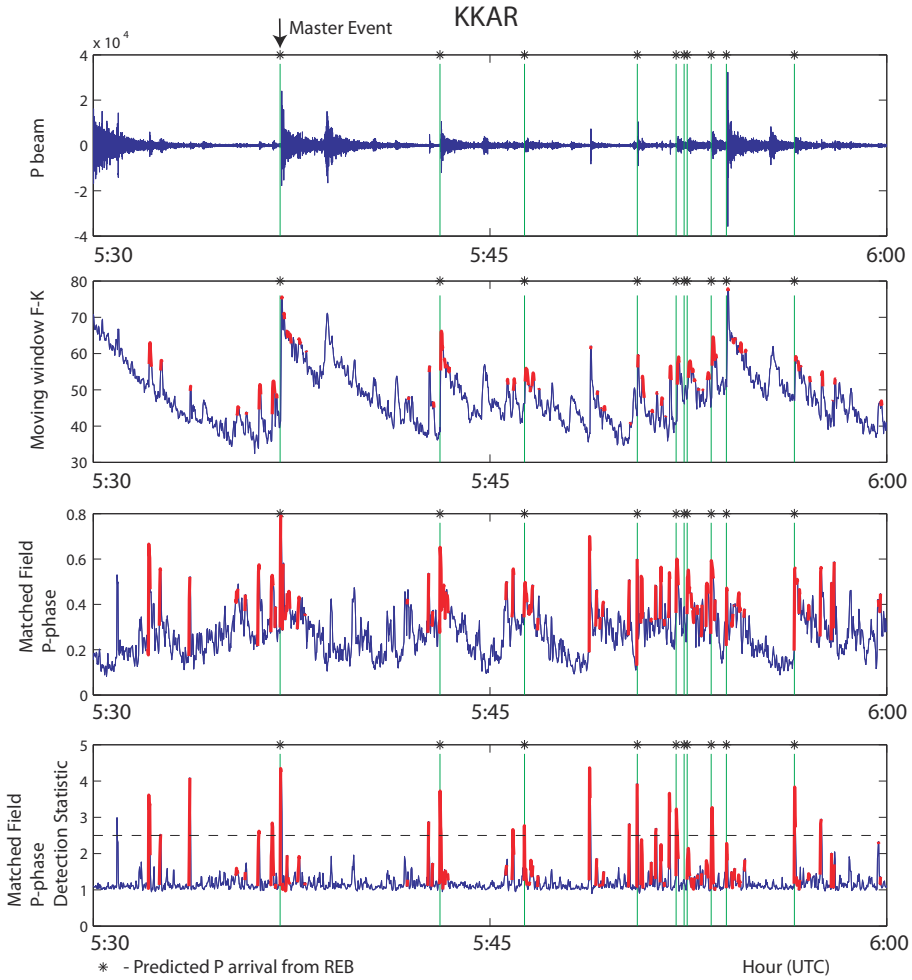

Figure 5. Panels displaying different processing attributes for a 30 minute long window of data from the KKAR array on October 8, 2005. Red parts of the traces indicate that the slowness vector from moving window F-K analysis is consistent with the P-phase of the master event. The lowermost trace shows the mean values over the narrow frequency bands where the matched field statistics for the different bands have been transformed using the procedure of Gibbons et al. (2008).

Figure 5 shows matched field statistics as a function of time for a 30 minute segment of data from the KKAR array in the aftermath of the M=7.4 Kashmir event of October 8, 2005, (at a distance of approximately 1000 km). Using a Pn arrival for a single aftershock to develop an empirical steering vector, the continuous matched field statistic attains a peak close to the first Pn arrival for each aftershock from this extended source region, diminishing throughout the coda. The transformed narrowband matched field trace appears to be a much more easily interpreted detection statistic than the simple matched field statistics (third trace) and this method may help greatly in the rapid identification of first arrivals in an extensive aftershock sequence. Performing the same calculation over the large aperture KNET network (but with time-shifts of up to several seconds provided a priori between the different stations) provided clear detections for a number of events, although far fewer than at the medium aperture KKAR array. This again suggests that the larger aperture network provides a sensitive coherent detector for events from a more limited source region.

CONCLUSIONS AND RECOMMENDATIONS

We have demonstrated that EMFP provides an effective means of identifying signals from sources of repeating seismicity. The matched field statistics obtained using empirical steering vectors, derived from previous observations of arrivals from the target site, are significantly higher than those obtained using the optimal theoretical steering vectors since deviations from the plane wavefront model are accounted for in the formulation. The improvement is greatest for higher frequencies and for larger aperture arrays over which classical array processing is made difficult or impossible due to waveform dissimilarity between the different sites.

If the theoretical steering vectors provided for scans of slowness-space in classical f-k analysis are augmented by empirical steering vectors from sources of repeating seismicity, this could provide “instant identification” of phases from known sources and may also circumvent the need for applying Slowness and Azimuth Station Corrections (SASCs).

The multitaper methods for spectral estimation appear to provide very stable estimates of the narrow-band phase and amplitude differences between different channels when only short duration waveform segments are to be used.

EMFP is applicable to sites of interest for which only a single observation is available. It is clearly an advantage to have numerous observations for estimation of the variability and a reduction of the “noise” in the matched field templates. However, using empirical steering vectors calculated from a single observation appears to give significantly better performance than the best theoretical steering vector.

The matched field statistics obtained for a typical 3-second long data segment appear to be sufficiently insensitive to the exact starting time of the selected data-windows that uncertainty in arrival time picking should not usually be an issue. In particular, for the application of EMFP as a continuous signal detector, it has been deemed that estimating a spectral covariance matrix every second on the incoming data is probably sufficient. We have demonstrated a successful application of EMFP for detecting occurrences of routine mining blasts at the Kara Zhyra mine in Eastern Kazakhstan on three different array configurations: the MKAR and ZALV arrays, and a virtual wide-aperture network comprising both arrays.

EMFP can be extended to far larger sensor apertures than are amenable to classical coherent array processing, although increasing the size of the receiver aperture reduces the size of the source region which can be monitored effectively. This has both advantages and disadvantages; a large network can provide a highly sensitive monitoring capability for a limited source region. A medium aperture array is likely to provide coverage of a greater source region with a somewhat higher false alarm rate if only a very limited source region is to be observed.

We have demonstrated that a transformation applied to continuous matched field statistic traces for narrow frequency bands can provide a very effective identification of arrivals in extensive aftershock sequences. This may contribute to a dramatic improvement of how efficiently such aftershock sequences can be classified.

ACKNOWLEDGEMENTS

We are grateful to the National Data Center in Kazakhstan for permission to use the data from the Kazakh seismic arrays. We are grateful to Prof. Germán Prieto of Universidad de los Andes, Bogotá, for making available the source code and documentation for the Multitaper Spectral Analysis code. We thank the IRIS DMC and the KN network for making continuous data from the KNET stations available.
All maps produced using GMT software (Wessel and Smith, 1995).

REFERENCES

Gibbons, S. J. and Ringdal, F. (2006). The detection of low magnitude seismic events using array-based waveform correlation, *Geophys. J. Int.,* 165: 149–166.

Gibbons, S. J., Ringdal, F., and Kværna, T. (2008). Detection and characterization of seismic phases using continuous spectral estimation on incoherent and partially coherent arrays, *Geophys. J. Int.*, 172: 405–421.

Harris, D. B. and Kværna, T. (2010). Superresolution with Seismic Arrays using Empirical Matched Field Processing, *Geophys. J. Int.* (in press).

Harris, D. B., F. Ringdal, E. O. Kremenetskaya, S. Mykkeltveit, J. Schweitzer, T. F. Hauk,V. E. Asming, D. W. Rock and J. P. Lewis (2003). Ground-truth Collection for Mining Explosions in Northern Fennoscandia and Russia, in *Proceedings of the 25th Seismic Research Review - Nuclear Explosion Monitoring: Building the Knowledge Base*, Los Alamos National Laboratory, LA-UR-03-6029, Vol. 1, pp. 54–62.

Hartse, H. E., Randall, G. E., and Arrowsmith, S. J. (2008). Regional Event Identification Research in Asia, in *Proceedings of the 30th Monitoring Research Review, Ground-Based Nuclear Explosion Monitoring Technologies*, LA-UR-08-05261, Vol. 1, pp. 615–624.

MacCarthy, J. K., Hartse, H., Greene, M., and Rowe, C. (2008). Using Waveform Cross-Correlation and Satellite Imagery to Identify Repeating Mine Blasts in Eastern Kazakhstan, in *Seism. Res. Lett.* 79: 393–399.

Prieto, G. A., Parker, R. L. and Vernon, F. L. (2009). A Fortran 90 library for multitaper spectrum analysis, in *Computers and Geosciences*, 35: 1701–1710.

Ringdal, F., Harris, D. B., Kværna, T., and Gibbons, S. J. (2009). Expanding Coherent Array Processing to Larger Apertures Using Empirical Matched Field Processing, in *Proceedings of the 2009 Monitoring Research Review, Ground-Based Nuclear Explosion Monitoring Technologies*, LA-UR-09-05276, Vol. 1, pp. 379–388.

Thomson, D. J. (1982), Spectrum estimation and harmonic analysis, in *Proc. IEEE,* 70:1055–1096.

Wessel, P. and Smith, W. H. F. (1995), New version of the generic mapping tools, *EOS Trans., Am. Geophys. Un*., 76: 329.

EPICENTRAL LOCATION OF REGIONAL SEISMIC EVENTS BASED ON EMPIRICAL GREEN'S FUNCTIONS FROM AMBIENT NOISE

Michael H. Ritzwoller, Mikhail P. Barmin, Anatoli L. Levshin, and Yingjie Yang

University of Colorado at Boulder

Sponsored by the National Nuclear Security Administration

Award No. DE-AC52-09NA29326
Proposal No. BAA09-52

ABSTRACT

The purpose of this research is to develop and test a novel method of regional seismic event location based on exploiting Empirical Green's Functions (EGF) that are produced from ambient noise. Elastic EGFs between pairs of seismic stations are determined by cross-correlating long ambient noise time-series recorded at the two stations. The EGFs principally contain Rayleigh and Love wave energy and our focus is placed on utilizing these signals between 5- and 15-sec periods. By comparing the tabulated EGFs in the frequency-time domain with similarly transformed records of seismic events (earthquakes, explosions, mine collapses) obtained by a network of remote stations, we have tested the method by locating events in the western USA for which other methods provide accurate locations (Californian Ground Truth earthquakes, the mine collapse in Utah). Data from the EarthScope USArray were used primarily. The location errors for GT1 earthquakes in California and the Crandall mine collapse in Utah were on average less than 1 km with origin time errors less than 1 s. These results were described in detail in Ritzwoller et al. (2009). During the past year we continued to refine the method and evaluate its capabilities. The ability of this approach to locate seismic events using a limited number of recording stations with significant open azimuth has been shown. We applied this method to less ideal environments locating small seismic events with magnitude 3.0-3.7 in Utah, with location accuracy better than 0.5 km relative to the University of Utah network locations. The effects of unknown source mechanism and depth on location were studied and are presented here. All research to date is described in detail by Barmin et al. (2010). Future work will continue to refine the location procedure and explore it ability to constrain depth and the moment tensor using ambient noise.

OBJECTIVES

The purpose of this research is to improve seismic event location accuracy and event characterization by exploiting EGFs that emerge by cross-correlating long time sequences of ambient noise observed at pairs of seismic stations. Because ambient noise EGFs are dominated by surface waves, the method uses surface wave energy for location purposes. Present efforts apply Rayleigh wave EGFs from 5 to 15 sec period to the epicentral location problem. The method of epicentral location as well as proof-of-concept applications for a series of seismic events in the western US have been described by Ritzwoller et al. (2009) and more recently and completely by Barmin et al. (2010). During the past year we continued to refine the method, estimated its ability to locate events with smaller magnitudes ($3 < M < 4$), and investigated the intrinsic limitations of the method as a function of number of recording stations and open azimuth. In addition, the effects of unknown source mechanism and depth on location were studied. Future work will continue to refine the location procedure and explore the ability to constrain depth and the moment tensor using ambient noise.

RESEARCH ACCOMPLISHED

1. Methodology

The main features of the epicentral location method based on ambient noise EGFs are as follows:

a) We assume that inside of “the region of interest” where seismic events may occur, a temporary dense local array, termed the **base stations**, is deployed. Second, there is a more distant permanent (but potentially sparse) regional network of stations termed the **remote stations** (Figure 1). Using what are now well established methods (e.g., Bensen et al. (2007), the EGFs from every base to every remote station are computed. At this stage of the project, we use only vertical-to-vertical components of EGFs, which are dominated by Rayleigh waves.

b) The amplitude spectra of EGFs and events recorded at remote stations are normalized without changing the phase spectra. This is done by replacing the amplitude spectrum of the event record with the amplitude spectrum of the EGF, or by replacing both the EGF and event record’s amplitude spectrum with the square root of the product of the amplitude spectrum of the event and the EGF.

c) The set of these EGFs is transformed by means of frequency-time analysis (FTAN) as described by Levshin et al.(1971, 1980) into two-dimensional (frequency-time) representations of signal power in a period band and group velocity window corresponding to the fundamental mode of Rayleigh wave in the continental crust. Typically, we select a period range of 5-15 s and a group velocity range of 2.5-4.0 km/s.

d) We cover the "region of interest" by a grid of points whose spacing depends on the density of the base stations array. For each grid point we calculate the so-called **Composite EGFs (CEGFs)** by transforming and stacking the individual EGFs for a given remote station over the base stations. The transformation is done by rescaling the FTAN-diagrams in time according to the distance between a grid point and a remote station. At this stage of the method's development we assume that group velocity in the selected period range does not depend on frequency, and do not use the phase velocity information.

e) The same transformation is applied to the signals recorded by all remote stations. Now for each grid point and each remote station we have an FTAN-diagram of the CGF and the event record. An example of this pair of diagrams is shown in Figure 2a.

f) The next step is cross-correlation in the time domain of the two types of FTAN-diagrams: from event records at all remotes stations and CEGFs for all points of the grid. The time delays of the maximum amplitudes of the cross-correlation functions (Figure 2b) are found and used to construct a quadratic functional of residuals similar to that used in body wave hypocentral location. The grid point with the minimal value of this functional is considered as the epicenter, and the average value of the residuals at this point provides an estimate of the origin time.

g) The confidence ellipse for the position of the epicenter is constructed following the method of Flinn (1965).

2. Location of weaker events in Utah

Ritzwoller et al. (2009) demonstrated the application of the method to GT1 earthquakes in California with $4 < M_b < 5$ and found that average mislocation for these events was about 1 km. To investigate how the method works when applied to events smaller than about magnitude 4.0, we applied it to locate smaller events ($3 < mb < 4.0$) that occurred in Utah in 2007 and 2008. The location parameters used in this test were: grid size 200 m, ρ_1=400 km, ρ_2=100 km. These events were well located and characterized by the University of Utah Seismic Stations (UUSS) and by the Department of Earth and Atmospheric Sciences at Saint Louis University (SLU) (J. C. Pechmann, see Acknowledgements). Information about these events is given in Table 1. The configuration of stations is shown in Figure 3a and an example of location for one of these earthquakes is given in Figure 3b. Average mislocation is less than 500 m, which indicates the method appears to work well with little modification for events with magnitudes between 3.0 and 4.0. The smaller mislocation for the Utah events compared with the California events may be due to source depth, as these smaller events may be either shallower or deeper than the earthquakes in California. The effect of event depth on mislocation is discussed further in section 3. The location method may be able to be improved further by tuning the band width of the method to the magnitude of the event.

3. Accuracy of location

A number of effects on the accuracy of location are discussed in this section. A more complete discussion is presented by Barmin et al. (2010).

a) **Technical Effects**:There are a number of technical variables that affect the accuracy of locations. We have used EGFs and event seismograms with a time sampling rate of 1 sps, which leads to errors up to 0.5 s in timing of the resulting correlograms. Increasing sampling rates to 10 sps improves the location of well located events but has little effect for events mislocated by 1 km or worse. The size of the spatial grid spacing also affects accuracy, of course.

b) **Observational Network:** The number of remote stations and their geometry relative to the located events are important factors in location accuracy. To evaluate how the number of remote stations and their azimuthal distribution influence location accuracy we focus tests on the TA station S10A in Central Nevada as a virtual earthquake (Figure 4a). Using a jack-knife procedure, we systematically reduced the number of remote stations participating in the location from 126 to 10, while preserving a more or less homogeneous azimuthal coverage. This procedure included 10 runs for each given number of remote stations, but with different ensembles of stations selected. In order to remove the effect of grid increment, we performed locations on a very fine grid (25 m). The average of the mislocations for the 12 runs is shown in Figure 4b as a function of the number of stations, presented with standard deviations. Note that the expected location error is less than 600 m even when the number of remote stations reduces to 10. Mislocation asymptotically approaches about 250 m, for large number of stations and low open azimuth, which we take as the practical limit for the current location algorithm when source mechanism and depth are eliminated. This residual error appears to be determined largely by time discretization (1 sps here).

We have also systematically investigated the effect of open azimuth by eliminating remote stations in azimuthal sectors that vary in size from 30° to 240°. The azimuthal position of each sector of a given size was changed 12 times by shifting the central azimuth of the sector by 30°. The average mislocations for 12 runs as a function of open azimuth plotted with the standard deviations are shown in Figure 4c. As with most location methods, open azimuth is more important than number of remote stations for location accuracy. In particular, as open azimuth grows above about 240°, location accuracy degrades rapidly. As long as open azimuth is less than 240°, however, location errors are expected to be less than 500 m and approach 250 m as open azimuth shrinks.

c) **Event Source Mechanism and Depth:** The most significant physical effects on location accuracy are source mechanism and depth. EGFs determined from ambient noise correspond to surface sources with a predominant source mechanism close to a vertical force. The event seismograms, however, may result from different types of sources at different depths; e.g., earthquakes within Earth's crust, volcanic explosions, meteoritic impacts, explosions, mine collapses, or other human-related excitation processes. The radiation pattern of Rayleigh wave excited by an earthquake is defined by a complex function $E(\omega, h, \boldsymbol{M})$, which depends on the frequency ω, the source moment tensor $\boldsymbol{M}$ and depth h as well as local structure, and is quite variable. The function $\arg(E(\omega))$ is the so-called the source phase, and its derivative with ω is the source group time shift. Because the envelopes of event records and EGFs are what we compare in the frequency-time domain to determine the epicenter, it is group time shift (rather than source phase) that is the relevant effect of event mechanism and depth. Levshin et al. (1999) discuss group time shifts expected for different types of events in detail, and we only summarize briefly here.

(1) Group time delays are generally much smaller than the source phase delays. This is because the phase delays tend to change relatively slowly with frequency and is one of the reasons we have ignored phase information in the current version of the location method. Nevertheless, group time delays are not negligible and can bias locations.

(2) Group time shifts are anti-symmetric in epicenter to station azimuth; i.e., changing azimuth by 180º changes only the sign of the delay. Group time shifts differing in azimuth by 180º, therefore, will constructively interfere. Thus, averaging residuals over azimuth while searching for the source position only partially suppresses the effect of group time delays on location.

(3) For events at the free surface, group time delays are zero for any source mechanism due to the zero amplitude of tangential stress near the free surface. For very shallow depth events (less than 1 km) group time delays will be very small. Thus, shallow events will have small location bias due to source mechanism. This is probably why the Crandall Canyon Mine collapse (see Pechmann et al. (2007)) and small event #3 in Utah (Table 1) were located so well.

(4) For some mechanisms, such as a pure normal, pure thrust, or a pure strike-slip, group time delays are exactly zero. For pure normal and thrust faults (45º dip and 90º slip) the real part of the expression for te radiation term E is zero. For pure strike-slip faults (90ºdip and 0º slip), the imaginary part of E (traction at the surface) is zero. In these cases, arg(E) and the frequency derivative of arg(E), which is the group time delay, will be zero. As discussed by Levshin et al. (1999), the source mechanism for most crustal earthquakes is relatively close to these pure mechanisms.

These observations demonstrate that the epicentral location method based on the envelope of ambient noise EGFs will be biased minimally by events that are near the surface or that possess nearly strike-slip, thrust, or normal faulting mechanisms. It remains to be determined numerically how bias sets on as events deepen and mechanisms diverge from these pure types. Numerical simulations of group time delays for events between depths of 2 and 20 km show significant variability with depth, azimuth from the source, and period. Because source mechanisms at these depths typically are close to pure strike-slip, thrust, or normal fault mechanisms, they create very small group delays (from 0 to 1 s) at periods between 6 and 15 s. More complicated mechanisms, however, can create delays up to (3-4) s, depending on azimuth, depth and period. To quantify group time shifts for a variety of source mechanisms and depths for crustal events we computed simulated Green's functions for a laterally homogeneous model typical of central Nevada (Shapiro and Ritzwoller, 2002) using a surface wave 1-D synthetic code. The base and remote stations used are those shown in Figure 4a. The simulated Green's functions correspond to a vertical force acting at the Earth's surface. We also calculated simulated event seismograms at remote stations for four events with a fixed geographical position within the base network. These events have the source mechanisms shown in the upper part of Figure 5. These mechanisms are similar to pure normal (red) and thrust (green) faults, a vertical thrust fault (navy blue), and a strike-slip fault (light blue), but the corresponding angles characterizing the double couple mechanism (dip and rake) are 15º-20º different from the pure mechanisms, which is sufficient to produce a significant group time shift. The polar diagrams in Figure 5a show the azimuthal distribution of group time residuals for the corresponding mechanisms with source depths of 2, 5, and 10 km. Note that our location method is based on cross-correlating frequency-time diagrams between 7 and 15 s periods. Thus, the results in Fig. 5a are frequency averaged.

Applying our location technique to the simulated data we find errors in source locations as a function of source depth for the four mechanisms, as seen in Figure 5b. Shallow focus events (depths less than about 1 km) produce very small group time shifts and, therefore, minimal location bias. Similarly, events deeper than about 7 km have location errors smaller than 500 m, at least given the period band of this study (7-15 s). Generally, events with mechanisms similar to thrust or normal faults will have a larger mislocation than those similar to strike-slip. Therefore, non-strike-slip earthquakes with depths between 1 and 5 km provide the greatest challenge for our method.

Our current method is integrated over frequency and it is possible that in the location process the observation of the azimuthal distribution of the group time residuals as a function of period may be used to provide information about the accuracy of the epicentral location or provide information about source depth. Figures 6- 8 present polar diagrams of theoretical group time shifts as a function of period for three event depths for the same mechanisms as in Figure 5. These results indicate that the azimuthal patterns of group time shifts tend not to change appreciably with period, but the amplitudes can vary strongly. Thus, in the location procedure, the observation of frequency-independent group time residuals is evidence that the epicenter of the event has not been strongly biased by source

mechanism. Conversely, the observation of strong frequency-dependence is evidence that the epicenter may be biased, but that the event probably occurred between depths of about 1 and 5 km.

4. Further directions for the method's improvement

Among possible directions for improvement which we plan to investigate during the coming year are:

(1) The refinement of the EGFs' database by using more detailed time discretization and phase match filtering procedures for improving the signal-to-noise ratio;
(2) applying frequency-dependent group time transformation of the FTAN-diagram of the EGFs and the event records;
(3) incorporation of phase information and the transformation of EGFs into Composite EGFs based on tomographic group and phase velocity maps for the region of interest (e.g., Moschetti et al., 2007; Lin et al., 2008);
(4) the application of information about the frequency-dependence of the residuals to provide information about the source depth and mechanism;
(5) considering not only vertical but also transverse components of the EGFs which are dominated by Love waves.

Many parameters define the technical instantiation of the method, such as the frequency band, group velocity window, base/remote station geometry, the spatial grid, and the time series sampling rate. These parameters can be varied systematically to tune the method to different observational settings and for events of different magnitude and character.

CONCLUSIONS AND RECOMMENDATIONS

The method to locate the epicenter of regional seismic events based on the envelope of Empirical Green's Functions determined from ambient seismic nosie which has been described here and by Barmin et al. (2010) has several features that make it a useful addition to existing location methods.

- Its accuracy does not require knowledge of Earth structure.
- It works for weak events where the detection of body wave phases may be problematic.
- The empirical Green's functions (EGFs) computed during a temporary deployment of a base network (such as the USArray Transportable Array or PASSCAL deployments) may be applied to events that occurred earlier or later than the temporary network using permanent remote stations even when the temporary stations are not present.

In addition, the method has several evident limitations.

- It requires a relatively dense base network within an area of interest for at least a few months.
- It provides the best accuracy when the frequency derivative of the source phase is relatively small; for example, when the source mechanism is a vertical force or a center of compression, when the source depth is less than 1 km or more than 5 km, or when the source mechanism is nearly purely strike-slip, thrust, or normal.

The technique described here is the first attempt at such a nonstandard approach to locate regional events using ambient noise EGFs.

ACKNOWLEDGEMENTS

The facilities of the IRIS Data Management System, and specifically the IRIS Data Management Center, were used to access the waveforms and metadata required in this study. The IRIS DMS is funded by the National Science Foundation and specifically the GEO Directorate through the Instrumentation and Facilities Program of the National Science Foundation under Cooperative Agreement EAR-0552316. We are grateful to Drs. J. C. Pechmann and W. S. Arabasz (University of Utah) for their help in identifying well located events in Utah.

REFERENCES

Barmin M. P., A. L. Levshin, Y. Yang, and M. H. Ritzwoller (2010). Epicentral location based on Rayleigh wave Empirical Green functions from ambient noise, submitted to *Geophys. J. Int*.

Bensen, G.D., M.H. Ritzwoller, M.P. Barmin, A.L. Levshin, F. Lin, M.P. Moschetti, N.M. Shapiro, and Y.Yang (2007). Processing seismic ambient noise data to obtain reliable broad-band surface wave dispersion measurements, *Geophys. J. Int.*,169 (3): 1239–1260, DOI:10.1111/j.1365-246X.2007.03374.x.

Flinn, E.A. (1965). Confidence regions and error determinations for seismic event locations. *Rev. Geophys*. 3: 157–185.

Levshin, A. L., T. B.Yanovskaya, A. V. Lander, B. G. Bukchin, M. P. Barmin, L. I. Ratnikova, and E. N. Its (1989). *Seismic Surface Waves in Laterally Inhomogeneous Earth*, (V.I. Keilis-Borok, Ed.), Kluwer Academic Publishers. Dordrecht/Boston/London.

Levshin,A.L., M.H. Ritzwoller, and J.S. Resovsky (1999). Source effects on surface wave group travel times and group velocity maps*, Phys. Earth Planet. Inter*.,115: 293–312.

Lin, F., M. P. Moschetti,and M. H. Ritzwoller (2008). Surface wave tomography of the western United States from ambient seismic noise: Rayleigh and Love wave phase velocity maps, *Geophys. J. Int.*, 173(1), pp. 281-298, doi:10.1111/j1365-246X.2008.03720.x.

Moschetti, M. P., M. H. Ritzwoller, and N. M. Shapiro (2007). Surface wave tomography of the western United States from ambient seismic noise: Rayleigh wave group velocity maps, *Geochem., Geophys., Geosys.*, 8: Q08010, doi:10.1029/2007GC001655.

Pechmann, J. C., W. I. Arabasz, K. L. Pankow, R. Burlacu,and M. K. McCarter (2007). Seismological report on the 6 Aug 2007 Crandall Canyon Mine Collapse in Utah, *Seismol. Res. Lett.*, 79: (5) 620–636.

Ritzwoller, M.H., M. P. Barmin, A.L. Levshin, and Y.Yang (2009). Epicentral location of regional seismic events based on empirical Green functions from ambient noise**,** in *Proceedings of the 2009 Monitoring Research Review: Ground-Based Nuclear Explosion Monitoring Technologies*, LA-UR-09-05726, Vol. 1, pp. 389–398.

Shapiro, N.M. and M.H. Ritzwoller (2002). Monte-Carlo inversion for a global shear velocity model of the crust and upper mantle, *Geophys. J. Int.* 151: 88-105.

Table 1. UUSS and SLU event parameters for earthquakes in Utah.

event #	Date (y/m/d)	Time(h:m:s)	latitude	longitude	Depth (km)	mb	Error (km)	Error (s)
1	2007/08/18	13:16:13.46	38.070	-113.323	9.0*	3.65*	0.42	0.4
2	2007/11/05	21:48:00.61	39.346	-111.648	15.0*	3.76*	0.41	0.4
3	2008/02/01	21:36:54.23	41.809	-112.218	0.18	3.59	0.40	2.0
4	2008/02/01	3:26:01.41	41.690	-111.143	8.5	3.37	0.47	0.6

* Depth and magnitude are from SLU.

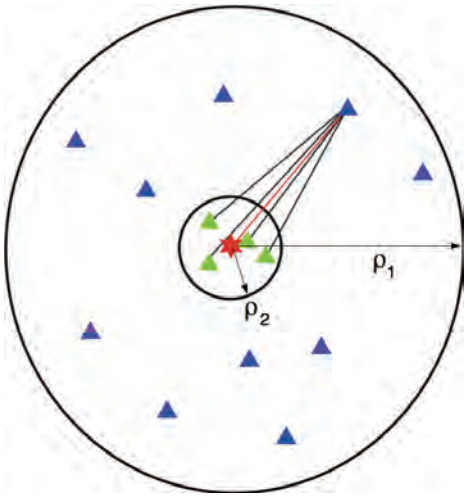

Figure 1. Schematic observational setting. A relatively dense set of temporary "base stations" (green triangles) encompasses the source region of interest (event is denoted by the red star). A sparse set of permanent "remote stations" (blue triangles) lies farther from the epicentral region.

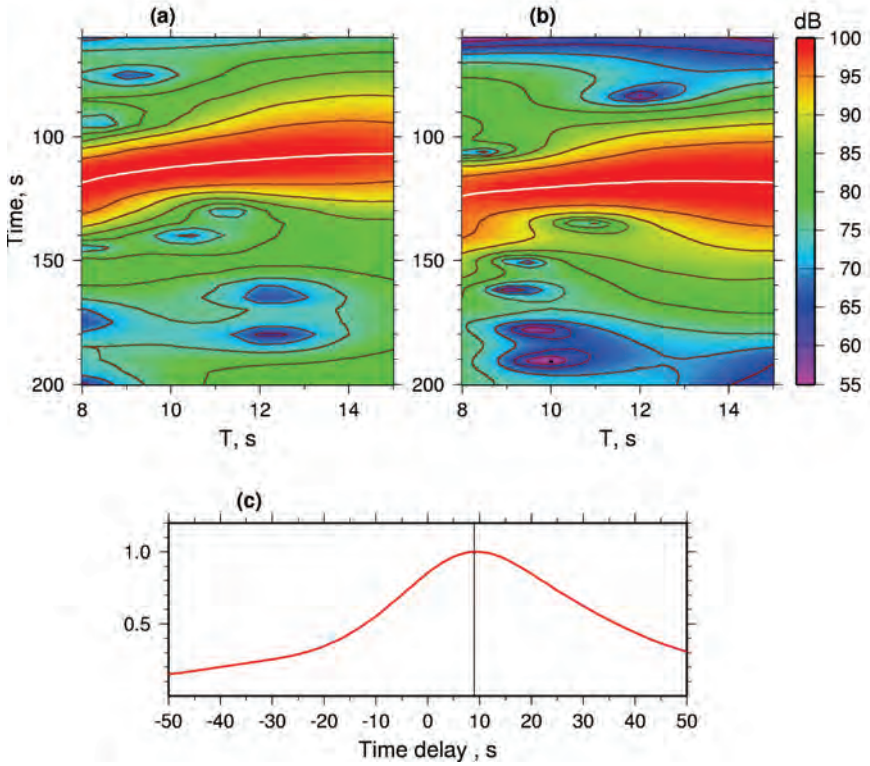

Figure 2. Illustration of location procedure based on cross-correlation of frequency-time (FT) representations of an event record and a Composite EGF. (a) FT-diagram of the event record for USArray Transportable Array station T14A following the Crandall Canyon Mine collapse (Pechmann et al., 2007) and the selected grid point. (b) FT-diagram of the Composite EGF for the same station and the same grid point. (c) Cross-correlogram of the two FT-representations in (a) and (b) showing a time delay of the maximum around 10 s.

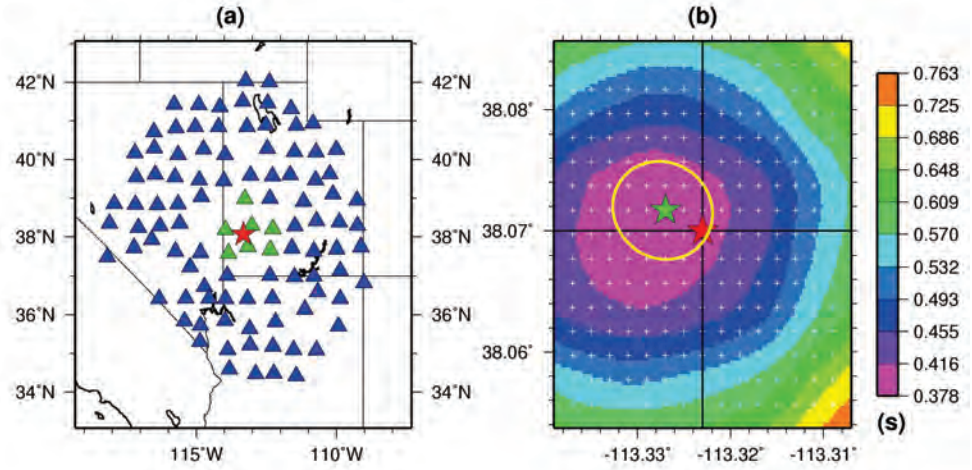

Figure 3. Location of event on 2007/08/18 (#1 in Table 1) in Utah. (a) Station configuration and misfit surface for the location (a) Symbols: base stations (green triangles), remote stations (blue triangles), and event location (red star). (b) Map of residuals: our event location (green star), UUSS location (red star), the 90% confidence ellipsoid (yellow line). Grid spacing of 200 m.

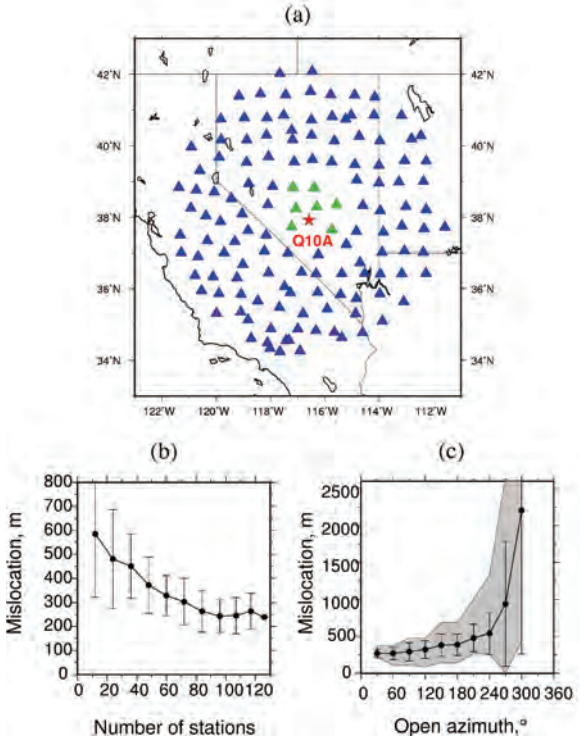

Figure 4. Location error as a function of the number of remote stations and azimuthal coverage. (a) Location of stations and virtual event (TA station Q10A): base stations (green triangles), remote stations (blue triangles), red star is the virtual source; (b) Effect of varying the number of remote stations on location accuracy; (c) Effect of the azimuthal coverage on location accuracy. Shaded domain covers all solutions for twelve realizations of each open azimuth. Error bars are 1standard deviation.

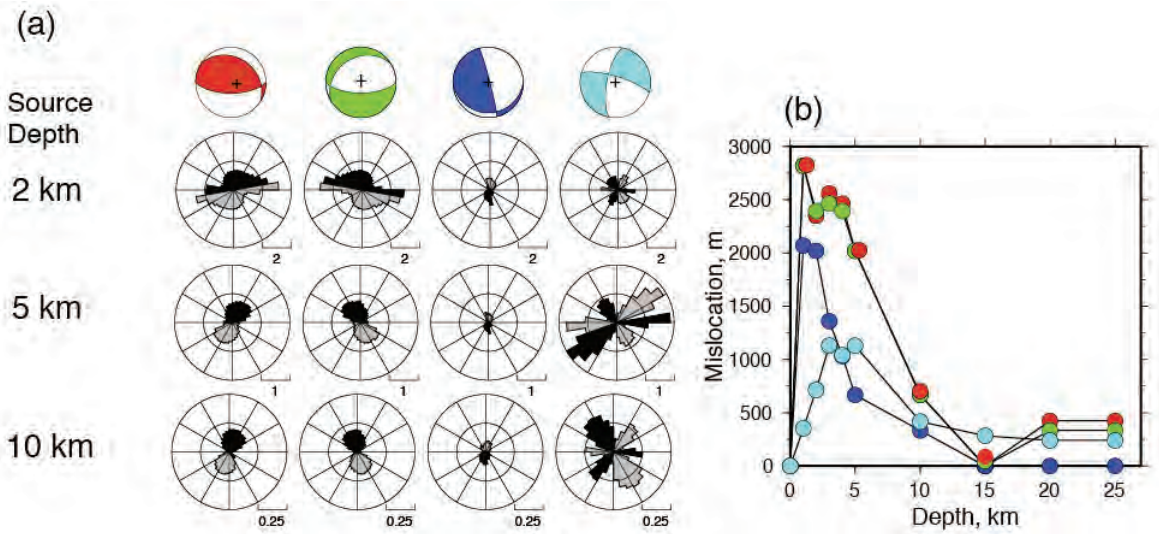

Figure 5. Simulation of the effect of source mechanism and depth on group time shifts and mislocation. Combination of base-remote stations used in the numerical simulation is shown in Figure 3a. (a) Source mechanisms (upper) and corresponding polar diagrams of group time residuals (lower) for the indicated source depths. Mechanism: red, near normal fault; green, near thrust fault; navy, near vertical thrust fault; light blue, near strike-slip fault. (b) Event mislocation for the four different source mechanisms as a function of depth. Symbol colors correspond to the source mechanisms shown in (a).

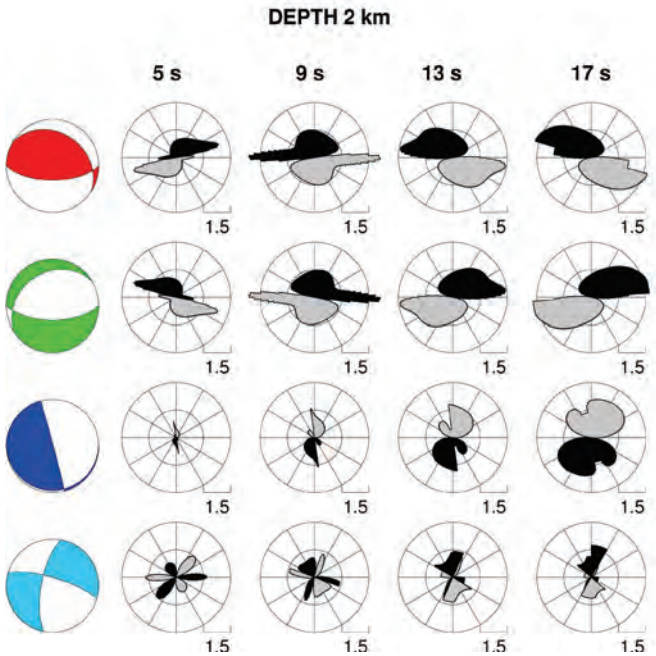

Figure 6. Theoretical prediction of group time delays at different periods for earthquakes at 2 km depth. Azimuthal dependence of group time delays are presented for four periods for four different source mechanisms (the same as in Figure 5). The size of the time delays scale according to the bar at the lower right hand side of each component of the figure, in seconds.

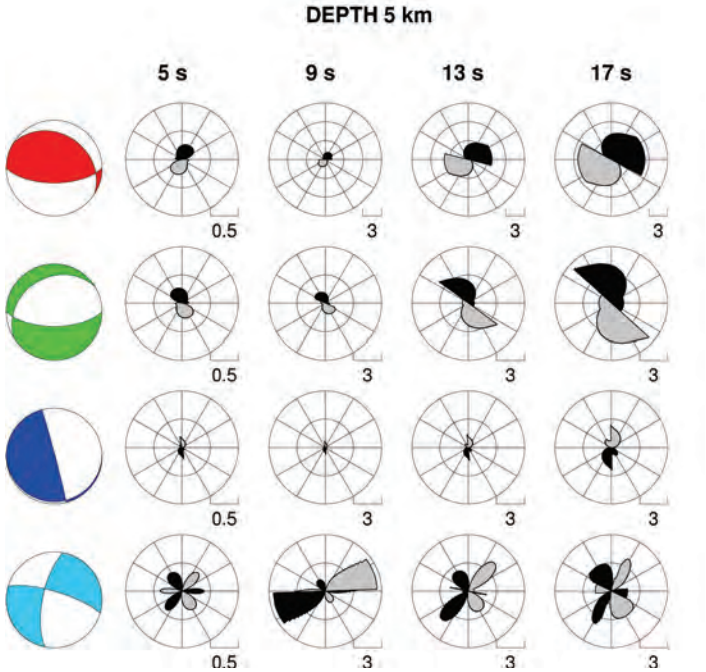

Figure 7. Theoretical prediction of group time delays at different periods. Same as Figure 6, but for events at 5 km depth.

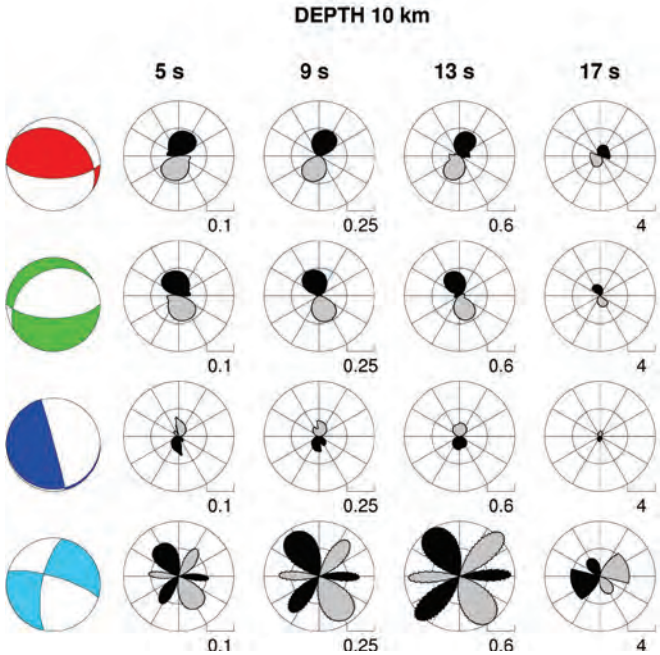

Figure 8. Theoretical prediction of group time delays at different periods. Same as Figure 6, but for events at 10 km depth.

A UNIFIED APPROACH TO JOINT REGIONAL/TELESEISMIC CALIBRATION AND EVENT LOCATION WITH A 3D EARTH MODEL

William L. Rodi[1], Delaine T. Reiter[2], Stephen C. Myers[3], and Nathan A. Simmons[3]

Massachusetts Institute of Technology[1], Weston Geophysical Corporation[2], and
Lawrence Livermore National Laboratory[3]

Sponsored by the National Nuclear Security Administration

Award Nos. DE-AC52-08NA28539[1, 2] and DE-AC52-07NA27344[3]
Proposal No. BAA08-19

ABSTRACT

This project is investigating the problem of locating seismic events from combined data sets of regional and teleseismic arrival times, based on the use of a unified 3D model of the Earth's velocity structure to predict travel times for both types of data. Inherent to this problem is the joint tomographic calibration of the Earth model with both regional and teleseismic ground-truth data. The goal of the unified approach is to remove the inconsistencies that result when travel-time predictions are performed with a mixture of separately calibrated regional and global models and empirical corrections, which can lead to degradation in event location accuracy. Additionally, the unified approach provides a rigorous framework for choosing optimal relative weighting of different types of data used in locating an event.

We are addressing a number of practical difficulties that arise in the pursuit of a unified location/calibration capability. One is to develop fast and accurate raytracing techniques for modeling different types of seismic arrivals. A second is the computational challenge of performing joint tomographic calibration with very large numbers of data and model parameters. We are considering various strategies for reducing the problem size, such as averaging data from proximate events and stations, and for breaking the calibration problem into equivalent sub-problems by region or depth range. The calculation of model uncertainty, and its translation to travel-time prediction uncertainty, provides optimal data weighting for locating events, but adds greatly to the computational challenge.

A significant computational savings, in both calibration and location, is achieved by employing a linearized approximation to travel-time calculations, obtained by integrating the slowness function of a 3D model along ray paths computed in a 1D reference model. While this approximation is not adequate for regional travel times, we have performed numerical experiments that indicate it is quite accurate for teleseismic travel times, as judged by comparing to travel times calculated with a highly accurate raybending method. We have also continued numerical experiments, initiated last year, with joint regional/teleseismic travel-time tomography built on the linearized forward model for teleseismic data. The results to date indicate that biases between regional and teleseismic travel-time predictions, which create difficulties for an event location algorithm, are removed by the joint calibration process.

OBJECTIVE

Previous studies have demonstrated that 3D models of crust and upper mantle velocity structure predict significantly more accurate travel times for regional seismic phases than do 1D global models, leading to more accurate locations for small, regionally recorded events (e.g., Ryaboy et al., 2001; Murphy et al., 2005; Flanagan et al., 2007; Reiter and Rodi, 2009). However, it is not uncommon to also observe teleseismic arrivals from small events of monitoring interest, at least in part of the teleseismic distance range. While adding teleseismic to regional data should in theory improve event locations even further, it has not always been the case in practice. For example, Yang et al. (2004) found that event locations obtained by combining regional and teleseismic data were only more accurate than locations found from the separate data sets if they corrected for a bias between teleseismic and regional travel-time predictions, each made from a different 3D model: CUB1.0 (Ritzwoller et al., 2002) for regional, and J362D28 (Antolik et al., 2003) for teleseismic. The correction they inferred is small (0.79 s), but even small, systematic shifts in teleseismic travel times can induce large location errors owing to the high apparent velocity of teleseismic waves.

We are investigating a methodology for seismic event location based on the principle that travel times for all seismic phases should be predicted consistently with a single 3D Earth model. This unified modeling approach would be applied as the forward model in locating events from combined sets of regional and teleseismic data. Moreover, the 3D model would be calibrated with regional and teleseismic ground-truth data in a joint tomographic analysis. A unified approach to location and travel-time calibration is not a new concept and, in fact, has been the approach taken with 1D Earth modeling for many decades. Applying the approach to 3D Earth models, however, presents many strategic and computational challenges, which this project is attempting to address.

RESEARCH ACCOMPLISHED

Our project is focusing on the development of a prototype capability for event location and travel-time calibration with 3D Earth models, applicable to regional and teleseismic data. Our goal is not to develop a complete and operations-ready 3D capability but rather to demonstrate the value and practicality of the unified approach. The following sections describe our progress to date in developing two key components of the approach: 3D travel-time calculation and joint regional/teleseismic tomography.

Travel-Time Linearization

A number of numerical methods are available for raytracing and travel-time calculation in 3D Earth models, such as the finite-difference eikonal method (e.g., Podvin and Lecomte, 1991), fast marching (Rawlinson and Sambridge, 2004), and two-point raybending (e.g., Um and Thurber, 1987). Given the computational intensity of these full 3D methods, many applications, such as global tomography with teleseismic data, have used approximate travel times calculated with linearization around a 1D reference model. In this approximation, the travel time T through a 3D model of interest is obtained by integrating the model's slowness function along the Fermat raypath computed in a different, reference model velocity model:

$$T \approx \int d\mathbf{x}\, a(\mathbf{x}; v_{\mathrm{ref}})\, v^{-1}(\mathbf{x}) \qquad (1)$$

where $\mathbf{x}$ is the position vector; $v(\mathbf{x})$ is the 3D velocity function of interest; and $a(\mathbf{x}; v_{\mathrm{ref}})$ is a sensitivity distribution concentrated on the Fermat raypath evaluated in the reference velocity function, $v_{\mathrm{ref}}(\mathbf{x})$. When $v_{\mathrm{ref}} = v$, T is exact. When v_{ref} is 1D, linearization of travel times offers great computational advantages in both computation time and storage. It also greatly simplifies the computation of times for secondary arrivals.

Rodi et al. (2009) conducted a preliminary investigation of the accuracy of travel-time linearization in 3D velocity models. Their experiments involved the computation of P-wave travel times for various paths in southern Asia through the JWM model of Reiter and Rodi (2009). Linearized times, using reference rays for model AK135 (Kennett et al., 1995), were compared to travel times calculated with the Podvin-Lecomte (P-L) finite-difference method, with the presumption that the latter are more accurate and can be used to judge the adequacy of linearization. The numerical tests reported last year showed that linearization about AK135 was very inaccurate for computing travel times at regional distances, as expected, but seemed to be a good approximation at teleseismic distances except for some bothersome artifacts related to shallow velocity structure. The tests were not definitive, however, because the accuracy of the

P-L times, which are also approximate, was not known. Moreover, the JWM model is the same as AK135 below a depth of 410 km, weakening the tests.

We have continued this investigation of travel-time linearization with the aim of getting a more definitive assessment of its accuracy. The new tests we report here involve three main changes from our preliminary tests. First, the calculations were performed with the 3D velocity model taken to be a portion of Lawrence Livermore National Laboratory's (LLNL's) recently developed G3D-LLNL global tomographic model (Simmons et al., 2010), which has 3D velocity anomalies throughout the crust and mantle. Second, we modified our algorithm for computing linearized travel times to be more accurate when reference rays traverse low velocity, shallow layers in the 3D model.

In a third departure from our earlier investigation, we used highly accurate raybending calculations as the benchmark for assessing the accuracy of linearization. The raybending calculations through G3D-LLNL were performed by LLNL using an algorithm they adapted from the 3D raytracing procedure of Zhao (1992) and Zhao and Lei (2004). This technique combines the pseudo-bending method for continuous media, developed by Um and Thurber (1987), and refraction (Snell's law) at velocity discontinuities. The specific approach is outlined in Simmons et al. (2009).

Our new tests considered travel times between various station locations and a 3D grid of event locations. The event grid covers the box 15°–55° N, 30°–80° E (roughly, the Middle East) at 1° spacing, but contains only a few event depths between the surface and 120 km. We performed calculations for four station locations, one at each corner of the event grid and each at zero depth. We will refer to these as Station NW, etc.

Figure 1 compares travel times calculated through G3D-LLNL (with raybending) to those calculated through AK135. We see that the effects of 3D velocity structure in G3D-LLNL on regional times is several seconds. The 3D effects on teleseismic travel times (distance greater than ~23 deg) are smaller but still significant. For the same stations and grid of surface events, Figure 2 shows the discrepancy between travel times calculated through G3D-LLNL with raybending and with linearization around AK135, i.e. integrating the slowness function of G3D-LLNL along rays generated in AK135. Given the high accuracy of the raybending method, the travel-time discrepancy plotted in Figure 2 can be interpreted as the error in the linearization calculations. The same results are shown geographically in Figure 3.

Figures 2 and 3 demonstrate that the errors in linearized Pn times can be very large, as much as 30 s for some paths (not seen in the plots due to clipping). The errors at teleseismic distances are much smaller, being generally well below 0.5 s. However, it is notable in Figure 3 that the largest errors in linearized times for these surface events correlate with the areas having the lowest near-surface velocities, i.e. the oceans. For deeper events, the surface-related artifacts disappear (Figure 4). While in practice we do not need to be concerned with event locations in oceans and slow sediments, we are still investigating whether our ray integration scheme may be undersampling thin, low velocity layers in the 3D model, or whether we have simply reached a situation in which linearization is not adequate.

Figures 2–4 also show that the errors in linearized teleseismic times are predominantly negative, which seemingly violates Fermat's Principle. One explanation for the negative bias is a quirk in our experiments whereby the effects of the Earth's ellipticity were calculated differently in the raybending and linearization methods. We may also be seeing the above-mentioned problems with thin, low-velocity layers beneath the stations (rather than the events).

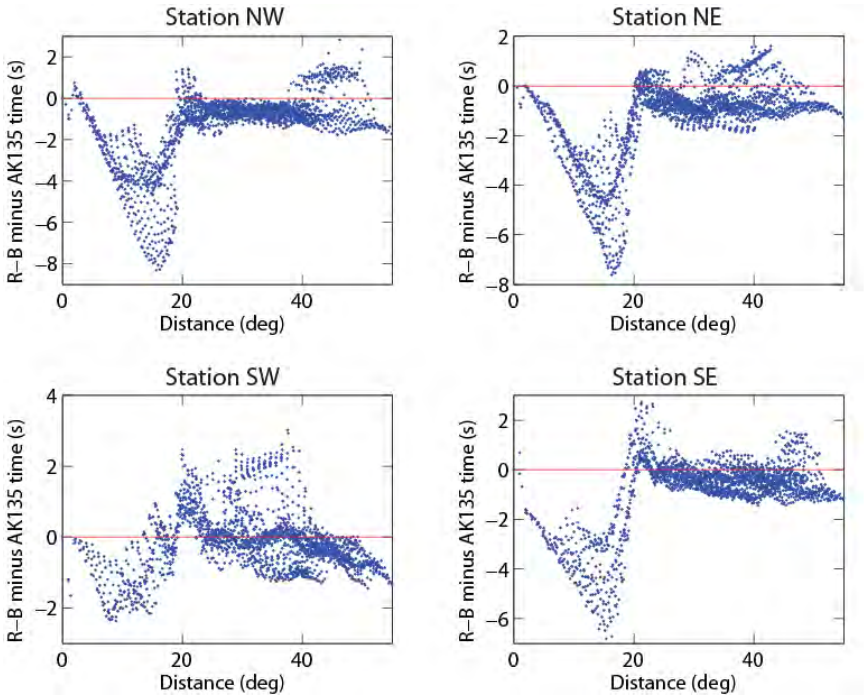

Figure 1. Difference between travel times through models G3D-LLNL and AK135, calculated between each of four stations and a grid of surface events. The G3D-LLNL times were calculated with raybending; AK135 times were calculated analytically. The time differences are plotted as a function of epicentral distance.

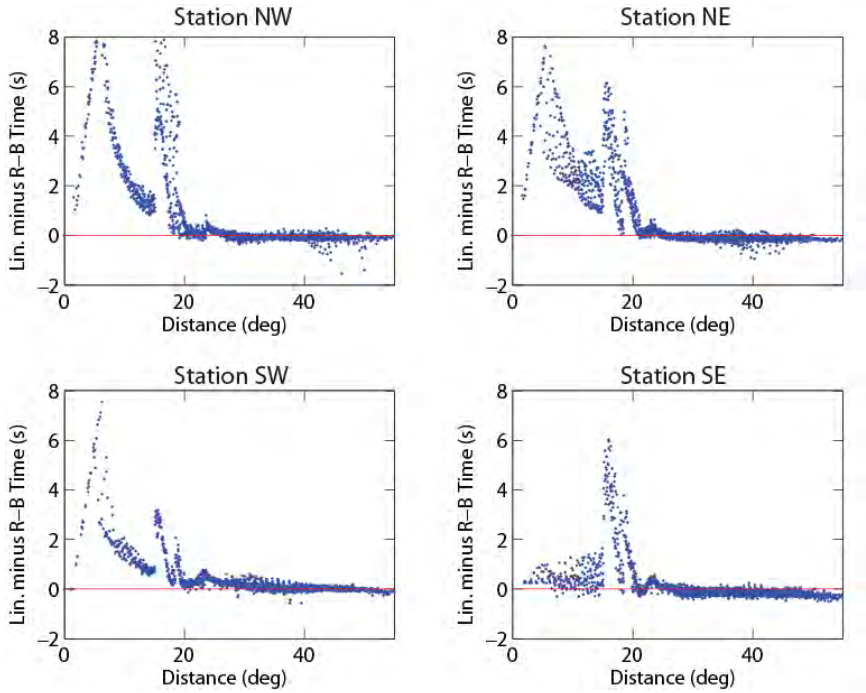

Figure 2. Discrepancy between travel times calculated through model G3D-LLNL with two methods: raybending and linearization relative to AK135 rays. Each panel shows the discrepancy vs. distance for paths from one of the corner stations to the geographic grid of surface events. The travel-time scale has been clipped at 8 sec.

Joint Regional/Teleseismic Tomography

Rodi et al. (2009) reported on preliminary tests of joint regional/teleseismic calibration, whereby the JWM model of southern Asia derived by Reiter and Rodi (2009) was updated through linearized tomography applied to a combination of regional and teleseismic P-wave travel times. Linearized tomography uses Equation (1) to model travel times. For teleseismic times, we take the reference velocity model to be AK135, which our numerical experiments have shown to be adequate. The same experiments showed that linearization about AK135 is not adequate for regional travel-time calculation; therefore, we used JWM as the reference model for regional times.

The regional data set used in the joint calibration tests was identical to that used by Reiter and Rodi (2009) in constructing JWM. Two teleseismic data sets were considered, both extracted from the EHB database (Engdahl et al., 1998) and both including arrivals only in the epicentral distance range 35°–65°. In the first teleseismic data set (termed TelE), the stations were restricted to be located in or near the JWM study region, i.e., in the box 0°–60° N, 30°–120° E. The event locations were unrestricted (except for the distance criterion) and fell primarily outside this box. The second data set (TelS) restricted the events to be within the study box and accepted all stations obeying the distance criterion. The regional and both teleseismic data sets included only events which have EHB focal depths less than 200 km and which are deemed well-located in accordance with criteria described by Reiter and Rodi (2009). To reduce the size and redundancy of the data sets, individual events were lumped into summary events in the same manner as done for JWM, with each summary event being a node on a 0.5° geographic grid and an irregular depth grid.

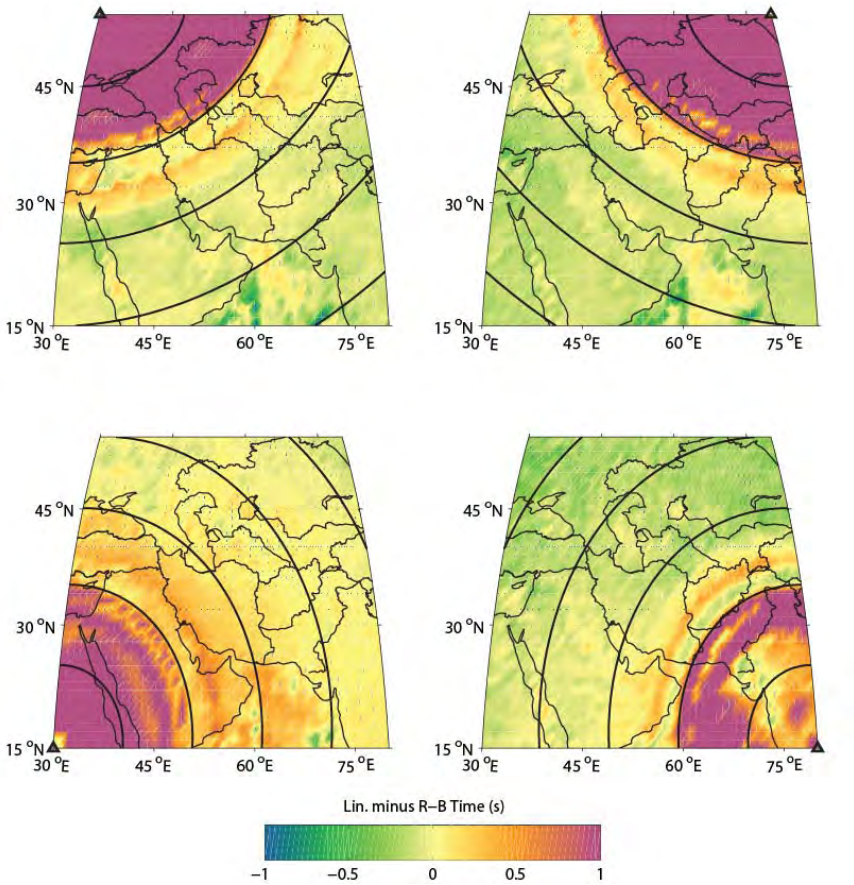

Figure 3. Discrepancy between travel times calculated through model G3D-LLNL with raybending and linearization. The discrepancies shown are the same as in Figure 2 but plotted as a function of the epicenter of the surface events. The travel-time scale has been clipped at -1 and +1 sec.

We have repeated these experiments using our improved algorithm for computing linearized travel times, and with upgraded teleseismic data sets. The teleseismic data were extracted from the updated EHB database distributed by the International Seismological Centre (http://www.isc.ac.uk/EHB/index.html). The new database included two additional years (2005 and 2006) as well as additional arrivals for years prior to 2005. After forming summary events, data set TelE contained 411,232 teleseismic P arrivals for 15,576 summary events and 900 stations. TelS contained 360,706 arrivals from 4,253 summary events and 2,846 stations. The teleseismic data sets are considerably larger than the regional data set, which contains 104,065 arrivals (>99% being the Pn phase) from 3,689 summary events and 603 stations. These data-set sizes approach the capacity of our current tomography software, which is why we considered teleseismic events and stations separately, and why we capped epicentral distances at 65°.

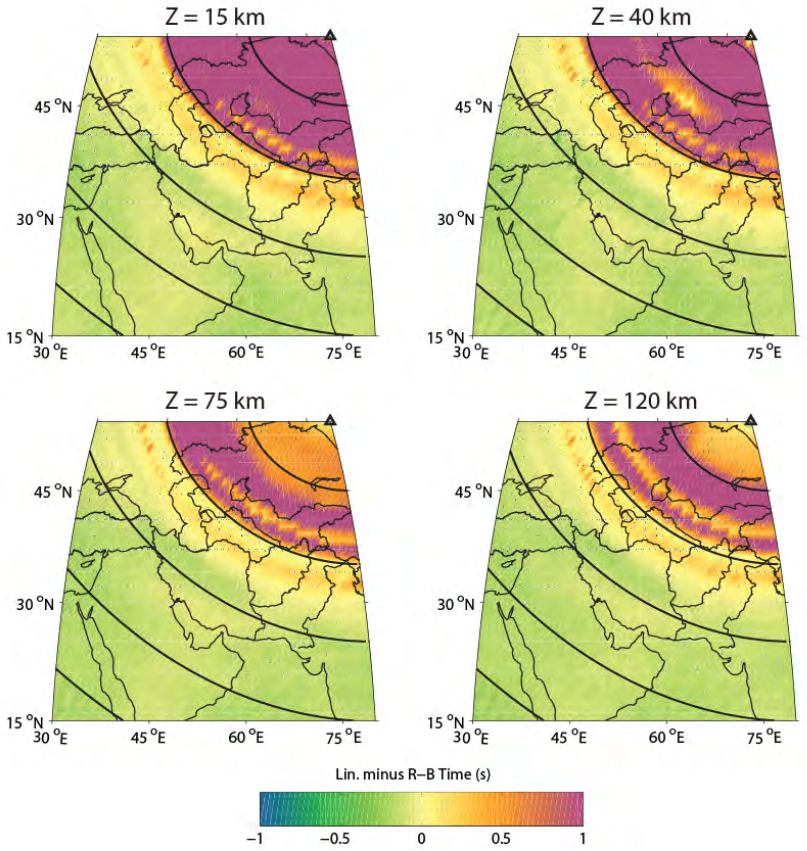

Figure 4. Discrepancy between travel times calculated through model G3D-LLNL with raybending and linearization. Each panel shows the discrepancy for paths from Station NE to a geographic grid of events at the labeled focal depth (*z*).

Figure 5 shows a vertical slice through each of two joint regional/teleseismic tomography models, corresponding to the two versions of the teleseismic data set that were combined with the common regional data set. The model obtained with TelE as the teleseismic data set is labeled JWM_TelE, and the other model as JWM_TelS. Both models are displayed as deviations from JWM. We see that the models are quite similar to each other, and overall have lower velocities than JWM. The largest differences from JWM occur at depths below 200 km, where the P velocity is significantly slower.

The reason for the lower mantle velocities in JWM_TelE and JWM_TelS is clear if we compare their travel-time residuals to those of JWM. Figure 6 displays separate histograms of regional (left) and teleseismic (right) residuals for each joint inversion model (red lines), compared in each case to the corresponding histograms for JWM (blue lines). We see that JWM yields regional residuals with a mean near zero but teleseismic residuals with a large positive mean: 1.8 s for the TelE residuals and 1.6 s for the TelS residuals. Both joint inversion models maintain the unbiased fit to the regional data and yields zero-mean teleseismic residuals as well. Each joint regional tomography

removed the teleseismic travel-time bias of JWM by lowering the P velocity below 200 km depth, in a way that preserved the fit to the Pn data.

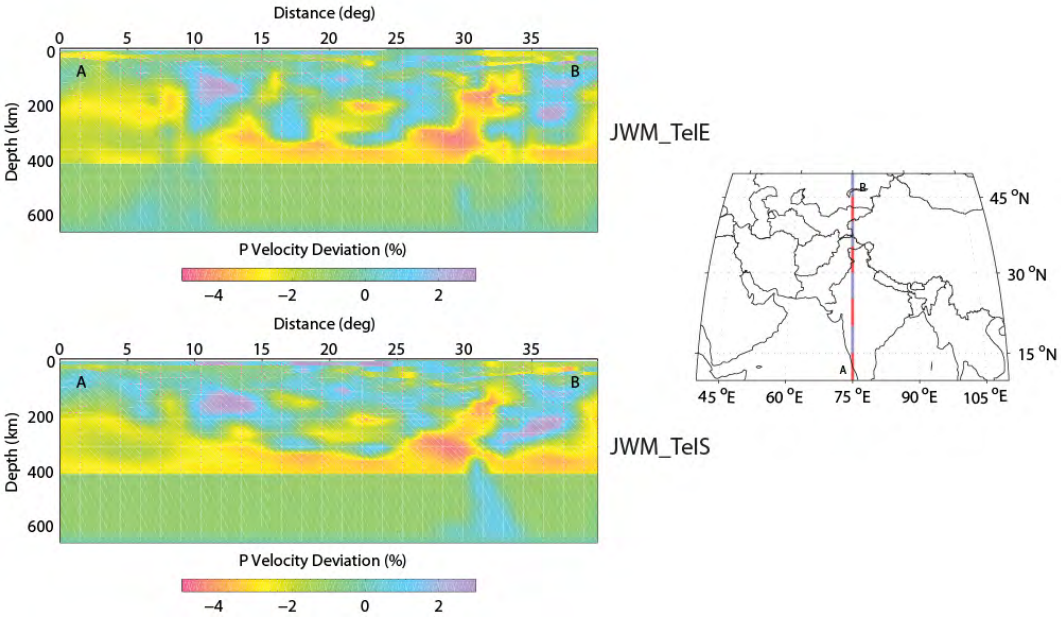

Figure 5. A vertical section through two 3D P velocity models obtained by joint inversion of regional and teleseismic P-wave travel times, each shown in terms of its velocity deviation from model JWM. The top model (JWM_TelE) used teleseismic data from local stations and teleseismic events, while the bottom model (JWM_TelS) used teleseismic data from local events and teleseismic stations. The regional data were the same in both cases and are from stations and events inside the model region. Note that the color scale for velocity deviation is asymmetrical (shifted toward negative deviations).

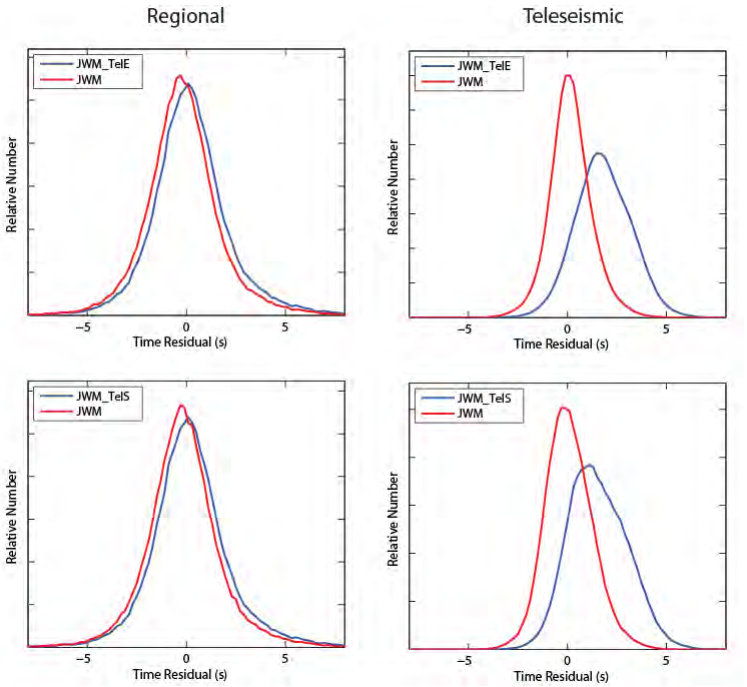

Figure 6. *Red lines*: Distributions of regional (left) and teleseismic (right) travel-time residuals for models JWM_TelE (top panels) and model JWM_TelS (bottom panels). The teleseismic data set is TelE (teleseismic events) for the top-right panel and TelS for the bottom-right panel. *Blue lines:* Analogous distributions for model JWM.

Joint Tomography with Hypocenter Relocation

The above tomography results and those presented in Rodi et al. (2009) do not account for the effect of event mislocations on the velocity model. We have addressed this by extending our tomography algorithm to allow event hypocenters and origin times to vary, in accordance with specified prior errors. We followed the approach developed by Spencer and Gubbins (1980) and Pavlis and Booker (1980), whereby a projection operator is applied to the travel-time residual vector and its sensitivity matrix to remove patterns in the residuals that can be explained by perturbing the hypocenters and origin times of the events. Departing from the original formulations of the approach in terms of matrix inversion, we implemented the projection operations within the conjugate gradients technique we use for computing tomographic models.

To test the new capability, we repeated the two joint regional/teleseismic tomography experiments of the previous section, allowing variable event locations with a prior hypocentral uncertainty of 10 km (epicenter and depth) and origin time uncertainty of 2 s (all at 95% confidence). Figure 7 shows a slice through the resulting inversion models (called JWM_TelE_loc and JWM_TelE_loc). We see that model JWM_TelE_loc deviates much less from JWM than did model JWM_TelE (Figure 5 top vs. Figure 7 top), showing that perturbations to the teleseismic event locations can fit a significant portion of the JWM residuals. Models JWM_TelS_loc and JWM_TelS are less different. However, as before, both joint inversion models reconcile the regional/teleseismic travel-time bias of JWM, as seen in Figure 8. We also see that the residual histograms for JWM_TelE_loc, and to a lesser extent JWM_TelS_loc, are more peaked than before as a result of allowing perturbations in the event locations.

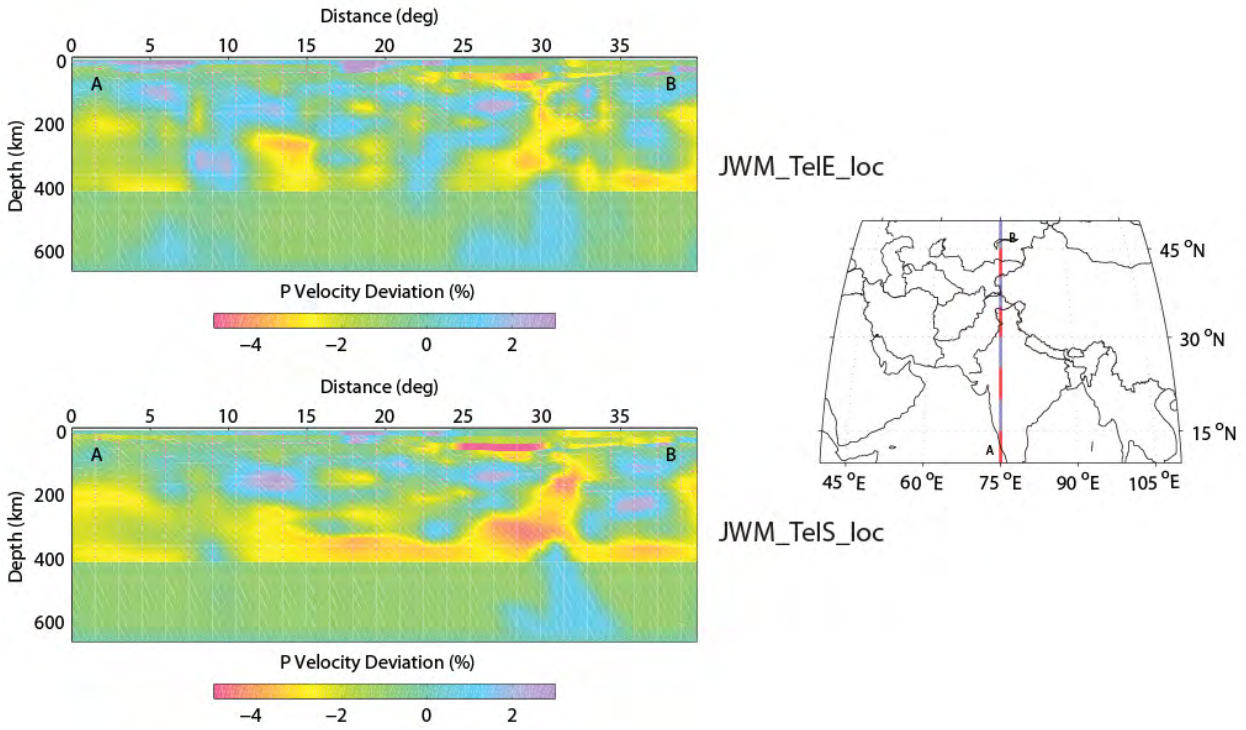

Figure 7. A vertical section through two 3D P velocity models (JWM_TelE_loc and JWM_TelS_loc) obtained by joint inversion of regional and teleseismic P-wave travel times, each shown in terms of its velocity deviation from model JWM. This figure is analogous to Figure 5 except that the joint inversion models were obtained in conjunction with linearized hypocenter relocation.

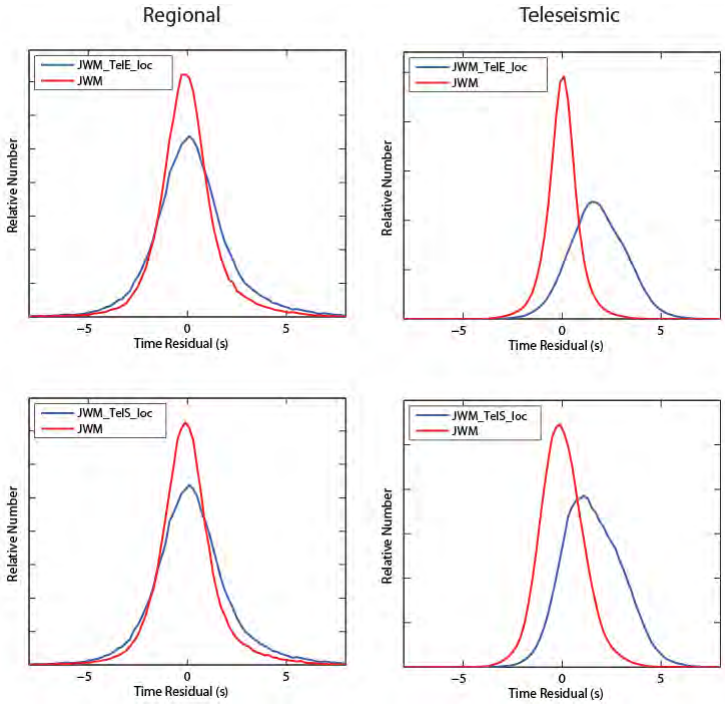

Figure 8. ***Red lines*****: Distributions of regional (left) and teleseismic (right) travel-time residuals for models JWM_TelE_loc (top panels) and model JWM_TelS_loc (bottom panels).** ***Blue lines:*** **Analogous distributions for model JWM.**

CONCLUSIONS AND RECOMMENDATIONS

We continue to develop and improve the tools needed to perform event location and travel-time calibration with regional and teleseismic arrival-time data, based on a unified 3D Earth model for travel-time calculation. Our latest numerical raytracing experiments show that the errors in linearized teleseismic travel-time calculations are 0.5 s or less, which is adequate for location and calibration but large enough to warrant further effort on making the errors even smaller. The use of linearization for travel-time prediction vastly reduces the computational requirements of a unified approach.

Our latest tests of joint regional/teleseismic tomography confirm the value of this approach in generating a 3D Earth model that predicts consistent travel times for regional and teleseismic P waves. The tests also show that accounting for event mislocations in the tomographic procedure does affect the velocity model that results, implying that location uncertainty must be quantified accurately in order to properly resolve the location/velocity trade-off. The use of secondary seismic phases (e.g. surface reflections and S phases) may ultimately address this problem. We are attempting to increase the capacity of our tomography algorithm significantly in order to handle much larger, multiple-phase data sets in a desktop computing environment.

REFERENCES

Antolik, M., Y. J. Gu, G. Ekström and A. M. Dziewonski (2003). J362D28: a new joint model of compressional and shear velocity in the Earth's mantle, *Geophys. J. Int*, 153: 2, 443–466.

Engdahl, E. R., R. van der Hilst and R. Buland (1998). Global teleseismic earthquake relocation with improved travel times and procedures for depth determination, *Bull. Seismol. Soc. Am*. 88: 722–743.

Flanagan, M. P., S. C. Myers and K. D. Koper (2007). Regional travel-time uncertainty and seismic location improvement using a three-dimensional a priori velocity model, *Bull. Seismol. Soc. Am*. 97: 804–825.

Kennett, B. L. N., E. R. Engdahl and R. Buland (1995). Constraints on the velocity structure in the Earth from travel times, *Geophys. J. Int*. 122: 108–124.

Murphy, J. R., W. Rodi, M. Johnson, et al. (2005). Calibration of International Monitoring System (IMS) stations in central and eastern Asia for improved seismic event location, *Bull. Seismol. Soc. Am*. 95: 1535–1560.

Pavlis, G. L., and J. R. Booker (1980). The mixed discrete continuous inverse problem: application to the simultaneous determination of earthquake hypocenters and velocity structure, *J. Geophys. Res*. 85: 4801–4810.

Podvin, P., and I. Lecomte (1991). Finite difference computation of traveltimes in very contrasted velocity models: a massively parallel approach and its associated tools, *Geophys. J. Int*. 105: 271–284.

Rawlinson, N., and M. Sambridge (2004). Wave front evolution in strongly heterogeneous layered media using the fast marching method, *Geophys. J. Int*. 156L: 63–647.

Reiter, D. T., and W. L. Rodi (2009). Validated 3D velocity models in Asia from joint regional body- and surface-wave tomography. *Final Report*, Weston Geophysical Corporation, AFRL-RV-HA-TR-2009-1009.

Ritzwoller, M. H., N. M. Shapiro, M. P. Barmin and A. L. Levshin (2002). Global surface wave diffraction tomography, *J. Geophys. Res*. 107: doi: 10.1029/2002JB001777.

Rodi, W. L., D. T. Reiter, S. C. Myers and N. A. Simmons (2009). A unified approach to joint regional/teleseismic calibration and event location with a 3D Earth model, in *Proceedings of the 2009 Monitoring Research Review: Ground-Based Nuclear Explosion Monitoring Technologies*, LA-UR-09-05276, Vol. 1, pp. 399–407.

Ryaboy, V., D. R. Baumgardt, P. Firbas, et al. (2001). Application of 3-D crustal and upper mantle velocity model of North America for location of regional seismic events, *Pure and Appl. Geophys*. 158: 79–103.

Simmons, N. A., S. C. Myers, and G. Johannesson (2010). Global-scale P-wave tomography designed for accurate prediction of regional and teleseismic travel times for Middle East events, in preparation.

Simmons, N. A., S. C. Myers and A. Ramirez (2010). Multi-resolution seismic tomography based on recursive tessellation hierarchy, these Proceedings.

Spencer, C., and D. Gubbins (1980). Travel time inversion for simultaneous earthquake location and velocity structure determination in laterally varying media, *Geophys. J. R. Astr. Soc*. 63: 95–116.

Um, J., and C. H. Thurber (1987). A fast algorithm for two-point seismic ray tracing, *Bull. Seismol. Soc. Am*. 77: 972–986.

Yang, X. P., I. Bondàr, J. Bhattacharyya, et al. (2004). Validation of regional and teleseismic travel-time models by relocating ground-truth events, *Bull. Seismol. Soc. Am*. 94: 897–919.

Zhao, D., A. Hasegawa and S. Horiuchi (1992). Tomographic imaging of P and S wave velocity structure beneath Northeastern Japan, *J. Geophys. Res*. 97: B13, 19909–19928.

Zhao, D. and J. Lei (2004). Seismic ray path variations in a 3D global velocity model, *Phys. Earth. Planet. Int.* 141: 153–166.

GLOBAL-SCALE *P*-WAVE TOMOGRAPHY DESIGNED FOR ACCURATE PREDICTION OF REGIONAL AND TELESEISMIC TRAVEL TIMES FOR MIDDLE EAST EVENTS

Nathan A. Simmons, Stephen C. Myers, and Gardar Johannesson

Lawrence Livermore National Laboratory

Sponsored by the National Nuclear Security Administration

Award No. DE-AC52-07NA27344/LL09-3Dseismic-NDD02

ABSTRACT

A global-scale *P*-wave tomography model of the crust and mantle is constructed. The model depicts both large-scale tectonic/dynamic features, as well as detailed upper mantle heterogeneities beneath the greater Middle East region. Fully three-dimensional ray tracing is employed to achieve accurate travel-time predictions of a suite of *P* and P_n arrivals, necessitating the characterization of irregular and discontinuous boundaries. Therefore, we explicitly represent undulating seismic discontinuities in the crust and upper mantle within a spherical tessellation modeling framework. The tessellation-based model architecture is hierarchical in that fine node sampling is achieved by recursively subdividing a base-level tessellation. Determining the required node spacing to effectively model a given set of data is problematic, given the uneven sampling of seismic data and the differing wavelengths of actual seismic heterogeneity. To address this problem, we have developed an inversion process called *Progressive Multi-level Tessellation Inversion* (PMTI) that exploits the hierarchical nature of the tessellation-based design and is well-suited for modeling a mixture of teleseismic and regional data. PMTI allows the data to determine the level of model complexity by progressively solving for shorter wavelength structure, thereby robustly imaging regional trends and allowing localized details to emerge where resolution is sufficient. Using the PMTI approach, we have developed a global-scale *P*-wave model that simultaneously predicts teleseismic *P* and P_n travel times for events occurring throughout the Middle East. The tomographic image provides a new glimpse of the complex upper mantle velocity anomalies associated with the convergence of the Arabian and Indian plates with Eurasia along the Tethyan margin.

OBJECTIVES

Travel time predictions based on global tomography models can improve seismic event location accuracy (e.g., Antolik et al. 2001, 2003). However, *P*-wave models, derived from teleseismic data, lack detailed structures in the upper mantle and generally do not accurately predict regional travel times as a result. Regional-scale models of upper mantle P-wave velocity structure are therefore essential for locating small seismic events. Detailed upper mantle P-wave velocities may be interpreted from surface wave solutions with some success (e.g., Ritzwoller et al. 2003); however these solutions are not specifically optimized for the prediction of P_n travel times. Additionally, hybrid combinations of independent regional and teleseismic models tend to be inconsistent since the predicted teleseismic (i.e., *P*) and regional (i.e., P_n) travel times often conflict (Yang et al. 2004). At a minimum, baseline travel time shifts must be determined through the calculation of travel time correction surfaces in order to reduce the 1st-order regional-teleseismic travel time inconsistencies generated by the hybrid models.

The objective of this project is to further advance event monitoring capabilities, through the generation of a seamless model of the Earth's crust and mantle that is capable of self-consistently predicting regional and teleseismic travel times as accurately as possible. Effectively, this requires simultaneous modeling of detailed upper mantle heterogeneities to adequately predict regional phases such as P_n and lower mantle structures to predict teleseismic travel times. It is also highly desirable to develop a model and techniques that reduce the need for numerous travel time corrections (e.g., crustal corrections, Earth's ellipticity, etc.) and/or massive travel time lookup tables. In this report, we present our progress toward the development of a global 3-D seismic event monitoring model.

RESEARCH ACCOMPLISHED

We have established a set of global 3-D tomographic model design components and procedures including a statistical event location/data culling process and a novel inversion technique that is specifically designed to exploit the hierarchical nature of our tessellation-based model representation. We apply our modeling procedures to produce a global-scale model of *P*-wave velocity structure based upon *P* and P_n travel times from >4,000 Middle East events and an additional ~1,000 globally-distributed seismic events. The new tomographic image contains large-scale features seen in most modern global tomographic models, but also contains previously un-imaged details of the Arabia plate beneath Eurasia. The model is consistent with geology and predicts >800,000 *P* and P_n travel times to with 0.53 seconds standard deviation when statistics-based data corrections are considered.

Model Representation and Inversion Technique

Our model parameterization is based on triangular tessellations of a spherical surface. Spherical tessellation parameterizations have been employed for multiple geophysical applications including mantle convection simulations (Baumgardner and Frederickson 1985), magnetic field modeling (Constable et al. 1993), and the basis for representation of Earth's seismic velocity structure (e.g., Wang and Dahlen 1995; Chiao and Kuo 2001; Ishii and Dziewonski 2002; Ballard et al. 2009; Myers et al. 2010). The primary purpose for employing spherical tessellations is to generate a mesh of nearly evenly spaced nodes (or knots), therefore preventing the polar distortion effects of a latitude-longitude grid. Building a spherical tessellation mesh involves recursive subdivision of triangular facets of an initial polyhedron (in our case, an icosahedron) into smaller sub-triangles whose vertices are projected onto a unit sphere (Figure 1). Each sub-division of a triangular facet ('*parent*') produces 4 triangular facets ('*daughters*') and thus increases the number of nearly evenly spaced vertices. We refer to each tessellation recursion as a '*Level*' starting with the initial object (Level 1; Figure 1) up to Level *N*, where *N* is some maximum recursion level. For example, a Level 7 recursion results in node spacing of approximately 1° when an icosahedron is used as the initial object. Although the tessellation meshes represent simple sphere-like surfaces, they form the basis of an aspherical Earth representation in this study. See Ballard et al. (2008, 2009) and Simmons et al. (2009) for more information on the model design and communication.

The tomographic imaging procedure developed for this project, PMTI, is designed with the same underlying philosophy as the wavelet and multi-grid approaches described in Chiao and Kuo (2001) and Zhou (1996), respectively. Specifically, the PMTI technique circumvents the need for predefining variable resolution scales through the hierarchical expression of higher resolution solutions as perturbations to lower resolution models. The most notable difference of PMTI from the wavelet and multi-grid approaches is that model components are found *progressively* through inversions of tomographic systems built upon successively finer parameterizations defined by

a hierarchy of tessellation grids. Therefore, multiple parameter grids with different node densities are not considered simultaneously and wavelet transforms are unnecessary. Each successive model component is added to the previous solution to form a total model field. As with the wavelet and multi-grid approaches, the data drive the resulting variable resolution scales and finer detail structures emerge from the regional trends only where it is necessary to explain the given set of observations. The PMTI process is described at a high level by the following algorithm:

$$\mathbf{x}_1 = \mathbf{A}_1^{-1}\mathbf{b}$$
$$\mathbf{b}_1 = \mathbf{b} - \mathbf{A}_1\mathbf{x}_1$$
$$for\ i = 2 \ldots N$$
$$\mathbf{x}_i = \mathbf{x}_{i-1}^{*} + \mathbf{A}_i^{-1}\mathbf{b}_{i-1}$$
$$\mathbf{b}_i = \mathbf{b} - \mathbf{A}_i\mathbf{x}_i$$
$$end$$

Beginning with the initial travel time residuals (**b**) and sensitivity kernels defined at the lowest resolution level ($\mathbf{A}_1$), an initial slowness perturbation model ($\mathbf{x}_1$) is determined through an inversion process. The initial travel time residuals are subsequently reduced by the residuals predicted by the lowest-resolution solution to produce a new data vector, $\mathbf{b}_1$. An inversion is then performed on the basis of sensitivity kernels defined at the next resolution level ($\mathbf{A}_2$) and the reduced data vector ($\mathbf{b}_1$). The total slowness perturbation model ($\mathbf{x}_2$) accumulates by summing the interpolated model from the previous step ($\mathbf{x}_1^*$) and the higher resolution solution based on the remaining travel time signals ($\mathbf{A}_2^{-1}\mathbf{b}_1$). All subsequent inversions operate on data vectors reduced by the previous solution ($\mathbf{b}_{i-1}$) to produce slowness perturbations relative to the previous model. Therefore, if a low-resolution solution accounts for all of the travel time signal, the total slowness model ceases to accumulate additional slowness perturbations.

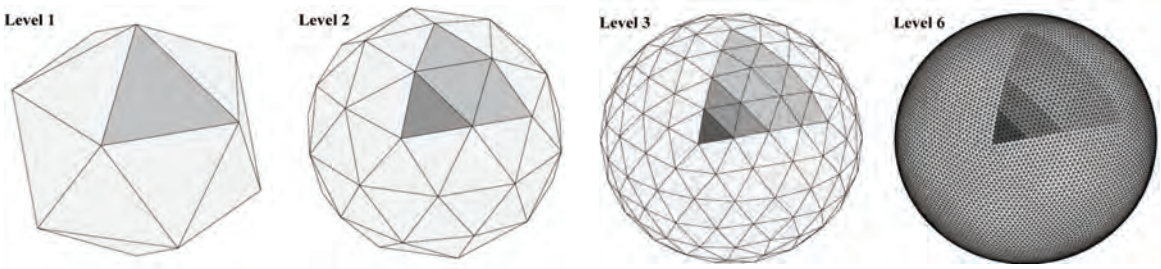

Figure 1. Spherical tessellation grids and parent-daughter triangle relationships. The initial object (a regular icosahedron; Level 1) consists of 20 triangular faces and 12 distinct vertices. The triangular faces (parents) are recursively subdivided into smaller triangles (daughters) and the vertices are normalized to the unit sphere. Each recursion represents a level in the tessellation hierarchy and parent-daughter triangle relationships are indexed for efficient communication. Triangular regions are shaded simply for visual orientation of the parent-daughter regions and sub-regions.

To evaluate the behavior of the PMTI approach, we devised a 3-D synthetic test bed to explore the intricacies of the imaging procedure. The synthetic model domain consists of 3 triangular depth slices with nodes defined by a tessellation procedure up to the Level 5 (Figure 2). We chose to mimic complex, sub-crustal *P* -wave velocity structure with two dominant characteristic wavelengths. Specifically, the synthetic model consists of a long-wavelength regional velocity trend with short-wavelength details embedded within the center of model domain (Figure 2, left). The chosen ray path configuration consisted of clusters of regional phases (sub-lateral travel direction) and teleseismic paths (near vertical travel direction). The ray path density is highly heterogeneous and random noise was added to imitate a realistic shallow mantle imaging problem.

Inversions were performed directly (simple least-squares at the highest tessellation level) and with the PMTI procedure for comparison. A representative solution from a single realization (paths shown in Figure 2 and 20% RMS noise added) is shown in Figure 3. For the simple (or direct) inversion, we incorporated damping and smoothing operators independently and optimized the regularization weights to find the solutions closest to the known solution (based on RMS model misfit). With damping alone, detailed structures emerge where there are a large number of crossing paths (Figure 3; SIMPLE damping). However, instead of recovering the long-wavelength

regional trend, isolated velocity structures are generated without a smooth transition through unresolved regions. In regions with only near-vertical paths (teleseismic phases), circular velocity structures are generated since there is no sensitivity to surrounding nodes. In regions with only bundles of sub-horizontal paths (regional phases), linear velocity anomalies are evident. Such isolated velocity blobs and streaks are undesirable since they may result in geological misinterpretations and also pose serious problems when computing travel times with 3-D ray paths. Alternatively, simple inversion with a first-order smoothing operator (with an optimum weight) recovers the long-wavelength regional trend, but fails to recover fine details where information is sufficient (Figure 7; SIMPLE smoothing). This smooth solution is also undesirable since we would prefer to take full advantage of the resolvability of dense data packets.

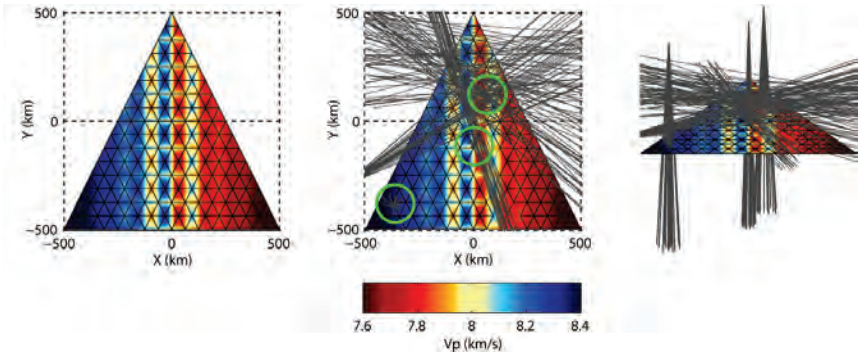

Figure 2. Synthetic tomography scenario imitating a combination of regional and teleseismic phases and complex shallow upper mantle velocity structure parameterized by a triangular tessellation with 5 hierarchical levels. (left) Synthesized velocity structure with a regional trend (from left to right) and embedded, small-scale velocity heterogeneities. (center) Map view of synthetic ray path coverage consisting of several clusters of sub-horizontal regional phase ray paths and 3 clusters of near-vertical teleseismic ray paths (highlighted with green circles). (right) 3-D view of the synthesized ray path coverage.

Using the PMTI approach, the long-wavelength velocity structure is established with the first inversion based on nodes defined by the first level tessellation (Figure 3; PMTI Level 1). Note that only simple damping is used as regularization. The Levels 2-4 PMTI solutions adjust the model only slightly, relative to the Level 1 solution. The minor model variation provided by these intermediate steps is due to the synthetic velocity model design with only two dominant characteristic wavelengths. In the final PMTI stage (Level 5 inversion), detailed structures emerge from the underlying long-wavelength velocity trend (Figure 3; PMTI Level 5). The detailed anomalies are most refined where data coverage is dense and ray path travel directions are diverse. It should be noted that the slight changes through the first 3 progressions demonstrates the potential pitfalls of an alternative imaging procedure involving dynamic mesh refinement (e.g., Sambridge and Faletič 2003). A dynamic mesh refinement procedure would likely cease to insert new model nodes, thereby never recovering the fine (yet resolvable) details. Our tests also reveal that the PMTI solution is less dependent on the choice of damping weight than a simple direct inversion. While it is true that a similar model could be recovered through a simple inversion with combined damping *and* smoothing, regularization weights would need to be fine-tuned in order to best match the known solution. In a real scenario, however, the 'true' solution is never known.

The PMTI approach has important advantages over other inversion techniques, especially when considering extreme spatial resolvability variations. If the travel time observations cannot be explained by a long-wavelength velocity trend in a particular region, detailed anomalies emerge from the background velocity model. Therefore, the 'resolution level' is predicated by the data without any user intervention. Dynamic mesh refinement (or adaptive meshing) is one such method of intervention whereby the addition or subtraction of model parameters occurs based on some user-defined criteria, thus generating an irregular grid. Aside from the additional complexity of establishing and communicating with a model based on an irregular grid, our synthetic example demonstrates other potential pitfalls of a dynamic/adaptive mesh refinement approach (Figure 3). For example, if we chose to refine the mesh from one inversion step to the next based on model movement, the imaging process would cease after the inversion based on the nodes defined by the Level 2 triangular tessellation (see Figure 3). This cessation could be prevented through knowledge of the data density (e.g., hit count criteria). However, hit count does not necessarily reflect resolvability since ray paths are commonly bundled providing limited additional constraints on lateral velocity

variations. For ultra-high resolution modeling with a global basis (<0.5° node spacing), adaptive meshing may be required to limit the size of the tomographic systems of equations. For our initial global model design however, we find that irregular meshing is unnecessary.

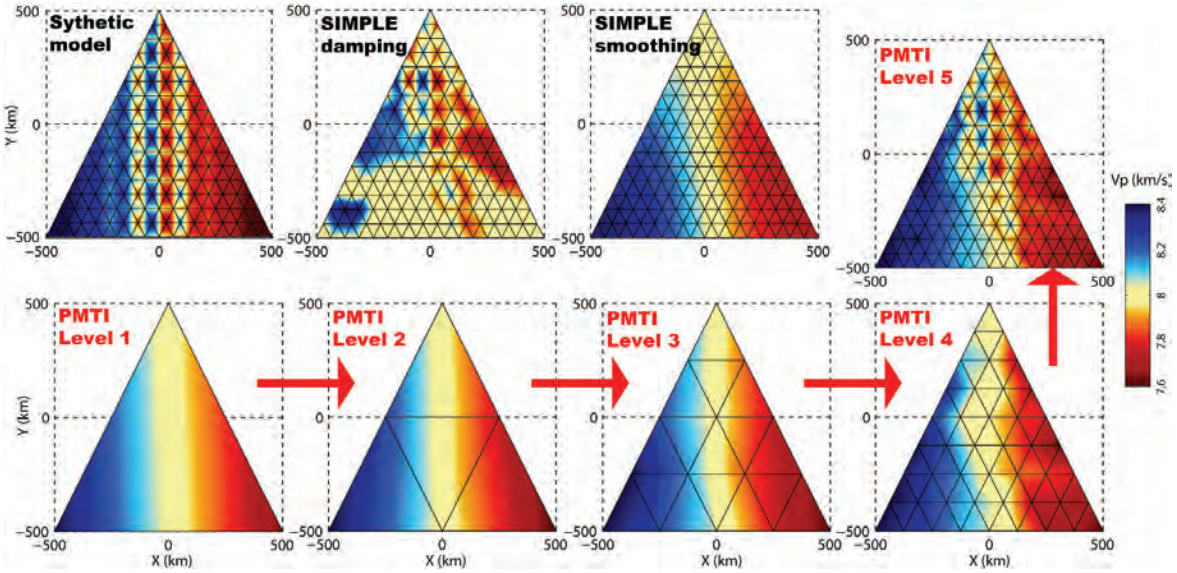

Figure 3. Representative tomography solutions for the synthetic tomography scenario shown in Figure 2. (top row) Synthetic model and 3 possible solutions using different approaches and regularization. With simple inversion and damping ('SIMPLE damping'), detailed structures emerge where there are sufficient crossing paths and isolated velocity structures are generated where there are gaps in ray path coverage. Simple inversion with a first-order smoothing operator ('SIMPLE smoothing') recovers the long-wavelength regional trend, but fails to recover fine details. Using the PMTI approach ('PMTI Level 5'), the regional trend is recovered and details emerge where there is sufficient ray path coverage (in the northern portion of the model space). (bottom row) The accumulation of velocity structure through the PMTI process.

Travel Time Data and Event Locations

We compiled a Middle East-centric set of teleseismic *P* and regional P_n travel time measurements from a subset of our local database at Lawrence Livermore National Laboratory (Ruppert et al. 2005) and the publicly available Engdahl-van der Hilst-Buland (EHB) catalog (Engdahl et al. 1998). The data selection criteria were: 1) all available *P* and P_n travel time measurements from seismic events occurring within the greater Middle East region, and 2) teleseismic *P* measurements from globally distributed events with the largest number of recordings within 5° lateral bins and 7 depth bins from the surface to 700 km depth. In total, we consider 5,401 events (~4,000 within the Middle East) recorded at approximately 4,500 seismic stations around the globe. The data consist of ~800,000 *P* arrivals from globally distributed events and stations, and ~43,000 P_n arrivals to stations within the Middle East (Figure 4). Although the compiled dataset is global in extent, more than 60% of the data are from events occurring within the Middle East and/or arrivals to one of the 600+ seismic stations within the region. Ray path hitcount calculations reveal that most of the shallow upper mantle in the Middle East region is sampled by more than 1,000 *P* and 100 P_n paths providing excellent constraints on detailed velocity structure (Figure 4).

We adapted a multi-event location algorithm, initially designed to simultaneously locate event clusters, to handle a global distribution of seismic events (Myers et al. 2007, 2009). The algorithm, called *BayesLoc*, is a multi-event location algorithm that operates within a hierarchical Bayesian statistical framework. The process entails generating numerous realizations of event hypocenters, origin times, phase labels, and travel time curves using a Markov Chain Monte Carlo (MCMC) sampling scheme. Using prior statistical models, the process allows for complete statistical characterization of the multi-event problem and thus develops a joint posterior distribution of all elements involved. The *BayesLoc* algorithm simultaneously determines event location probability regions, identifies likely outlier arrival time data (inconsistent with the total population), re-labels misidentified seismic phases, and adjusts travel

times based on statistically likelihood. The net result of the procedure is a set of event locations and travel times such that the spread of the travel time residuals relative to the 1-D AK135 (Kennett et al. 1995) velocity model is minimal (Figure 5).

In terms of data variance, the apparent travel time residual signal of the raw data (based on the original event locations) is ~12 times larger than the signal based on the *BayesLoc* event locations. This suggests that a tremendous amount of the apparent signal associated with the raw event locations is not due to 3-D velocity structure, but rather hypocenter mis-location, mis-identified seismic phases and arrival time pick errors. The total signal reduction signifies the improved data consistency that *BayesLoc* provides, but another important aspect is the shift of the mean from a positive 0.44 seconds to a negative 0.53 seconds. This mean shift and the residual trend with distance (see Figure 5) have tremendous implications on the absolute velocity structure needed to explain the data. Hypocenter locations based on single-event location procedures often do not recover such trends; particularly when assuming a location such that the residual travel times are zero-mean.

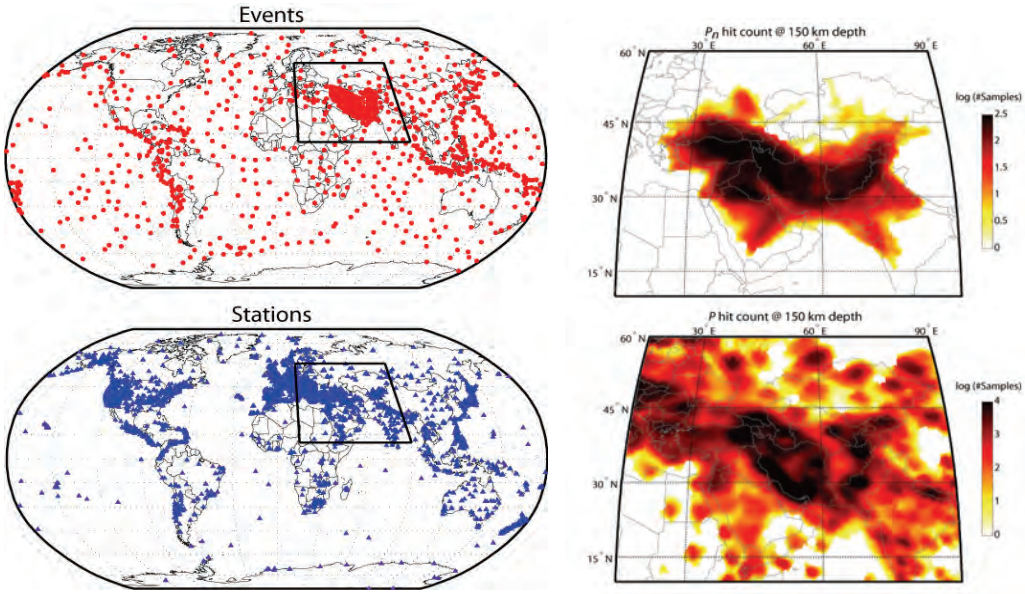

Figure 4. (left column) Selected seismic events (5,401) and stations (4,500) around the globe. (right column) P_n and teleseismic *P* hitcount in the outlined region at a depth of 150 km.

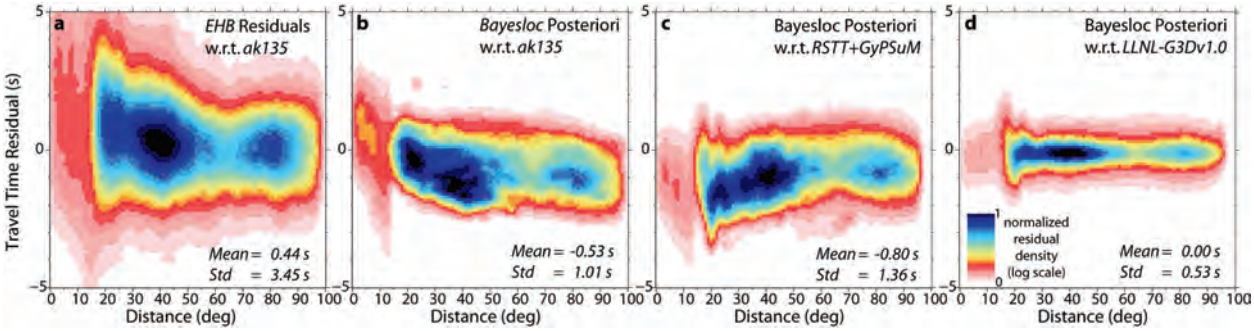

Figure 5. Travel time residuals for the compiled *P* and P_n data set. Residual travel times are plotted as a function of great circle distance in terms of point density on a normalized log scale. (a) Travel time residuals for the initial EHB bulletin and LLNL data set with respect to (w.r.t.) the AK135 1-D velocity model. (b) Travel time residuals w.r.t. AK135 after *BayesLoc* processing. (c) Residuals based on *BayesLoc* processed data relative to the hybrid regional-teleseismic velocity model described in the text (RSTT+GyPSuM). (d) Travel time residuals w.r.t. to the global 3-D *P* wave model constructed in this study (*LLNL-G3Dv1.0*).

3-D Ray Tracing and Sensitivity Definitions

We have adapted a 3-D ray tracing procedure specifically tailored to communicate with the aforementioned tessellation-based model design. The general approach we have taken is based on the techniques originally conceived by Zhao et al. (1992) to model direct arrivals within a subduction zone and extended to teleseismic phases by Zhao and Lei (2004). The procedure combines pseudo-bending in continuous media (Um and Thurber 1987) while simultaneously satisfying Snell's Law at discontinuous interfaces through an iterative process. One major shortcoming of this general approach is the inability to find global minimum travel times and paths for complex regional phases such as P_n. We have therefore adapted the procedure to find such global minima by considering multiple starting ray path configurations. A similar adaptation has recently been developed by Ballard et al. (2009) where the computational process was designed within a distributed computing environment.

In our specific approach, we initially create several crude 3-D ray path estimates based on an imposed set of rules for a given source-receiver configuration. Each of the initial paths is perturbed with a limited set of pseudo-bending iterations and discontinuity piercing point adjustments as described in Zhao et al. (1992). Rather than performing ray path adjustment iterations until convergence, we cull out paths that provide travel times within some tolerance of the minimum time achieved by the full set of perturbed paths (we chose a 1 second tolerance). Ray path adjustment iterations are then performed on the remaining paths until the minimum travel time is attained. The paths that generate the minimum time within a secondary time tolerance (we chose 0.2 seconds) are accepted and used in the development of model space sensitivity kernels. For example, near the upper mantle transition zone crossover distance range (~18° distance for a surface event), ray paths traveling through the shallow upper mantle and below transition zone discontinuities are accepted if they satisfy the minimum time tolerance criterion. By accepting all paths that produce near-minimum travel times, we directly address the multi-pathing problem. Additionally, model sensitivity may be distributed over a wide depth range as opposed to two (or more) distinct geological units in a pure multi-pathing scenario (see the example in Figure 6). Thus, the issue of interdependence of velocity structure and ray path is mitigated.

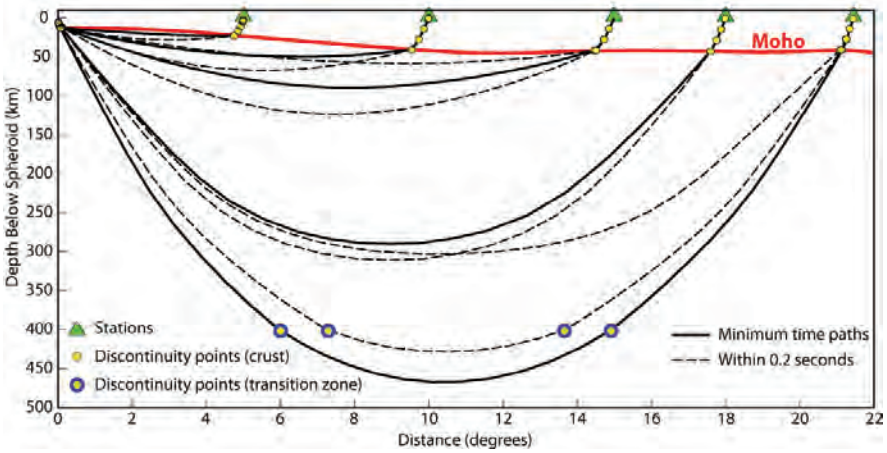

Figure 6. Example 3-D ray paths calculated through the global velocity model constructed in this study. Sensitivity is spread across broad depth zones and/or multiple model units to mitigate the problem of interdependence of paths and velocity structure as well as multi-pathing.

Inversion Procedures and Results

We designed a starting model by combining the Regional Seismic Travel Time (RSTT) model (Myers et al. 2010) and the global joint seismic-geodynamic image called GyPSuM (Simmons et al. 2010). The crust and upper mantle velocity model is represented by 33 layers (including 7 crustal units) with a lateral spacing of ~1° (Level 7 tessellation) and the lower mantle is represented by 25 layers with a lateral spacing of ~2° (Level 6 tessellation). In total, the crust and mantle *P*-wave velocity structure is defined at ~1.6 million points (1.35 million points in the crust and upper mantle; 250,000 points in the lower mantle). Sensitivities to each of the model nodes defined in the starting solution (RSTT+GyPSuM) were determined based on the calculated 3-D ray paths and model space sensitivity definitions described in the previous section. For the inverse problem, we chose to combine certain layers

to limit the number of free parameters and account for limited resolvability in particular depth zones. Specifically, sensitivities to all nodes representing the crust (as defined in the full hybrid model) were summed along the geocentric vertices to define a single set of sensitivity kernels associated with the crust. Therefore, tomographic inversion results in slowness perturbation updates for the entire crustal stack at each lateral position instead of determining model updates within each individual crustal layer. The upper mantle sensitivities were condensed in a similar fashion creating 9 total inversion layers in the crust and upper mantle with an average depth spacing of ~80 km. The lower mantle sensitivities were only slightly condensed providing an average depth spacing of just over 100 km. In total, the node sensitivities defined for the starting model were condensed from 55 model layers and ~1.6 million nodes to 31 layers and ~600,000 free parameters to be determined in the tomographic inversion process.

Global-scale velocity model updates were determined by carrying out the PMTI procedure where successive inversions were performed using the LSQR algorithm (Paige and Saunders 1984). We initiated the progression by solving for model updates at nodes defined by tessellation Level 4 vertices (~8° lateral node spacing) followed by Levels 5,6 and 7 (4°, 2° and 1° node spacing, respectively). We chose not to begin the progressive inversion below Level 4 to limit structural leakage across drastically different tectonic environments. In addition, we chose not to adjust the depth resolution during the progression. A global damping operator was employed as regularization and the damping weight was chosen based on the trade-off of model norm and data misfit (L-curve analysis).

Owing to the substantial non-linearity of ray paths and velocity structure for regional phases, P_n ray paths and sensitivity kernels were re-computed after one complete PMTI cycle and the inversion procedure was performed again. After the 2nd inversion cycle, P_n ray paths were computed once again to test for convergence. It was concluded that most minimum-time ray paths did not change appreciably; and paths that noticeably changed, did not generate substantially different travel time predictions relative to the previous stage. It is our conclusion that the sensitivity definitions, which include multi-pathing and broadened kernels, mitigate the non-linear path-velocity interdependence issues to a large degree. However, we are cautious about generalizing this observation to every scenario and region.

The final *P* -wave model, *LLNL-G3Dv1.0*, predicts the *BayesLoc* posteriori data to within 0.53 seconds standard deviation (Figure 5). This equates to ~72% variance reduction relative to *BayesLoc* posteriori travel times predicted with AK135 (1.01 second standard deviation). The initial bulletin data (without *BayesLoc* statistical operations) are predicted to within 3.45 seconds standard deviation on the basis of the 1-D AK135 Earth model. The combination of *BayesLoc* processing and the *LLNL-G3Dv1.0* velocity model yields data fits on the order of 97% variance reduction relative to the initial data and AK135 (see Figure 5). Thus, the travel times for the ~800,000 *P* and ~43,000 P_n arrivals are predicted to extremely high degrees given the statistical corrections provided by *BayesLoc* and the 3-D velocity heterogeneities in the new global-scale tomographic model shown in Figures 7 and 8.

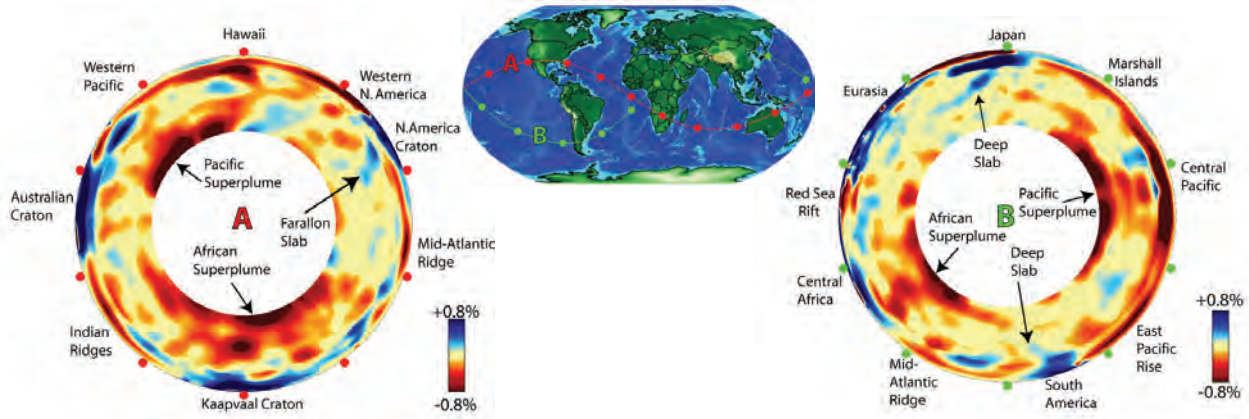

Figure 7. Selected 360° cross sections through the *LLNL-G3Dv1.0* velocity model. Most of the major features highlighted are also observed in the hybrid starting model based on the joint seismic-geodynamic image called GyPSuM (Simmons et al. 2010). However, a number of additional features are observed in the *LLNL-G3Dv1.0* model including deep slabs originating from the Japan subduction zone and detailed upper mantle structures beneath the Middle East region (see Figure 8).

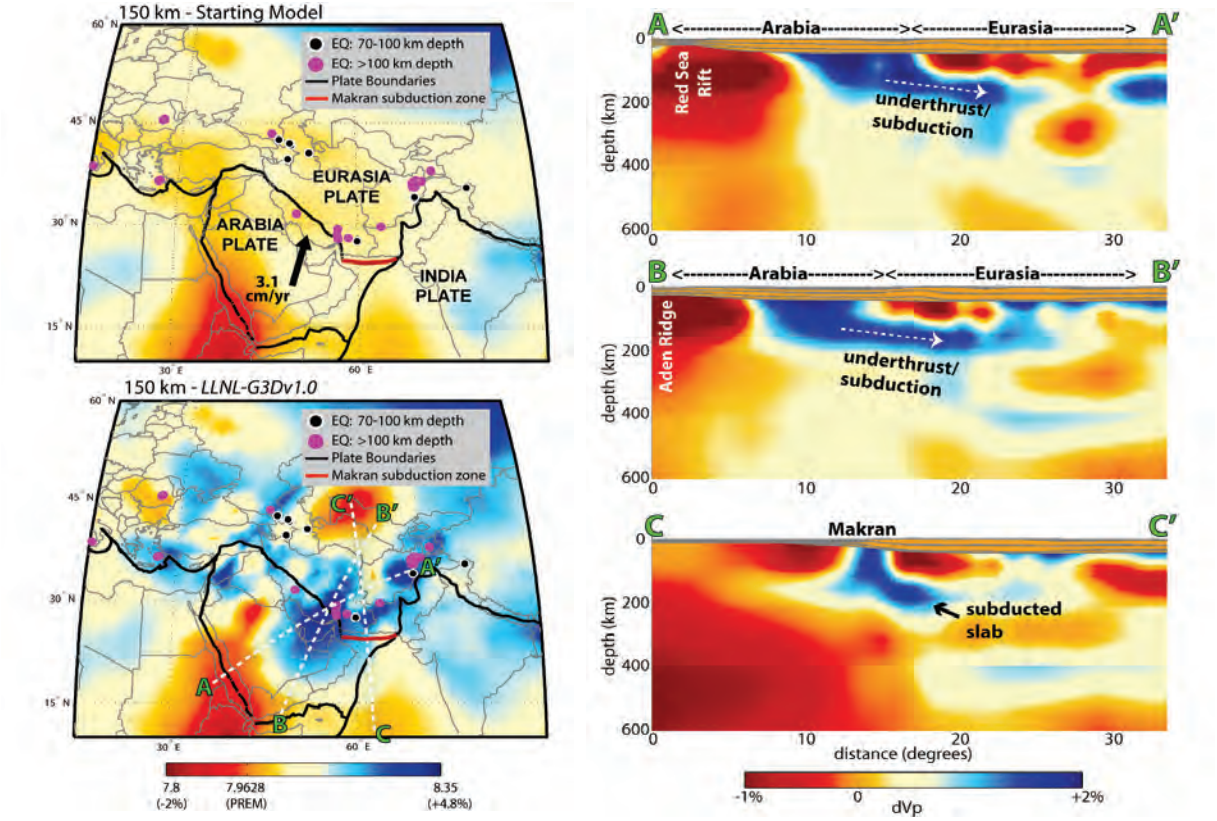

Figure 8. (left column) Close-up view of the *P* -wave velocity at 150 km depth from the *LLNL-G3Dv1.0* model. The final model differs dramatically from the starting solution in the shallow upper mantle beneath the Middle East region. Most notably, several high-velocity structures emerge beneath the region and correlate well with the location of deep earthquakes used in this study. (right column) Cross sections along the A-A', B-B' and C-C' transects. Velocity perturbations are relative to the global mean velocity anomalies in *LLNL-G3Dv1.0* at each depth. High-velocity structures extending from Arabia to beneath Eurasia represent underthrusted continental lithosphere along the western plate boundary and subducted oceanic lithosphere beneath the Makran region along the southern plate boundary.

CONCLUSIONS AND RECOMMENDATIONS

Our initial monitoring model, named *LLNL-G3Dv1.0*, is a global-scale tomographic model of *P* -wave velocity that predicts >800,000 *P* and >46,000 P_n travel times (mostly from Middle East events) to within 0.53 seconds standard deviation. The model is built with the tools and processes described in this report including: *BayesLoc* data processing, 3-D ray tracing with multi-pathing, and PMTI imaging. The current model consists of large-scale mantle structures such as spreading centers, cratons, superplumes and lower mantle slabs (generally observed in all modern global tomography models). In addition, the image depicts remarkably detailed structures in the upper mantle below the Middle East, owing to the dense data coverage in the region and data consistency yielded by the *BayesLoc* processing. In addition to predicting travel times, our model provides a new and important perspective of the upper mantle structures associated with convergence of the Arabia and India plates with Eurasia. In particular, we image the underthrusted continental Arabian lithosphere beneath Iran along the western Arabia-Eurasia plate boundary. In addition, the transition from continent-continent collision to subduction beneath the Makran region along the southern Arabia-Eurasia boundary is evidenced by the imaged structures in the *LLNL-G3Dv1.0* model. The next phase in this modeling effort will be to perform the same procedures described in the current study with a massive set of teleseismic *P* travel time data that are more globally distributed than the data considered herein. In conjunction, P_n travel time data from multiple regions will be considered simultaneously for the purpose of self-consistent travel time prediction at both regional and teleseismic distances.

REFERENCES

Antolik, M., G. Ekström and A. M. Dziewonski (2001), Global event location with full and sparse data sets using three-dimensional model of mantle *P* -wave velocity, *Pure Appl. Geophys*. 158: 291–317.

Antolik, M., Y. J. Gu, G. Ekström and A. M. Dziewonski (2003), J362D28: a new joint model of compressional and shear velocity in the Earth's mantle, *Geophys. J. Int*. 153: 443–466.

Ballard, S., J. Hipp, and C. Young (2008). Robust, extensible representation of complex Earth models for use in seismological software systems, in *Proceedings of the 30th Monitoring Research Review: Ground-Based Nuclear Explosion Monitoring Technologies*, LA-UR-08-05261, Vol. 1, pp. 347–355.

Ballard, S., J. R. Hipp and C. J. Young (2009), Efficient and accurate calculation of ray theory seismic travel time through variable resolution 3D Earth models, *Seis. Res. Lett*. 80(6): 990–1000.

Baumgardner, J. R. and P. O. Frederickson (1985), Icosahedral discretization of the two-sphere, *SIAM J. Numer. Anal*. 22(6): 1107–1115.

Chiao, L. -Y. and B. -Y. Kuo (2001), Multiscale seismic tomography, *Geophys. J. Int., 145*, 517–527.

Constable, C. G., R. L. Parker and P. B. Stark (1993), Geomagnetic field models incorporating frozen-flux constraints, *Geophys. J. Int.* 113: 419–433.

Engdahl, E. R., R. van der Hilst and R. Buland (1998). Global teleseismic earthquake relocation with improved travel times and procedures for depth determination, *Bull. Seismol. Soc. Am*. 88(3): 722–743.

Ishii, M. and A. M. Dziewonski (2002). The innermost inner core of the Earth: Evidence for a change in anisotropic behavior at the radius of about 300 km, *PNAS*, 99(22): 14026–14030.

Kennett, B. L. N., E. R. Engdahl and R. Buland (1995). Constraints on seismic velocities in the Earth from travel times, *Geophys. J. Int*. 122: 108–124.

Myers, S. C., G. Johannesson and W. Hanley (2007). A Bayesian hierarchical method for multiple-event seismic location, *Geophys. J. Int*. 171: 1049–1063.

Myers, S. C., G. Johannesson and W. Hanley (2009). Incorporation of probabilistic seismic phase labels into a Bayesian multiple-event seismic locator, *Geophys. J. Int*. 177: 193–204.

Myers, S. C., M. L. Begnaud, S. Ballard, M. E. Pasyanos, W. S. Phillips, A. L. Ramirez, M. S. Antolik, K. D. Hutchenson, J. J. Dwyer, C. A. Rowe and G. S. Wagner (2010a). A crust and upper-mantle model of Eurasia and North Africa for P_n travel-time calculation, *Bull. Seismol. Soc. Am*. 100(2): 640–656.

Paige, C. C. and M. A. Saunders (1982), LSQR: an algorithm for sparse linear equations and sparse least squares, *ACM Transactions on Mathematical Software*, 8: 43–71.

Ritzwoller, M. H., N. M. Shapiro, A. L. Levshin, E. A. Bergman and E. R. Engdahl (2003). Ability of a global three-dimensional model to locate regional events, *J. Geophys. Res*. 108(B7): doi: 10.1029/2002JB002167.

Ruppert, S., D., Dodge, A. Elliott, M. Ganzberger, T. Hauk and E. Matzel (2005). Enhancing seismic calibration research through software automation and scientific information management, in *Proceedings of the 27th Seismic Research Review: Ground-Based Nuclear Explosion Monitoring Technologies*, LA-UR-05-6407, Vol. 2, pp. 937–945.

Sambridge, M. and R. Faletič (2003). Adaptive whole Earth tomography, *Geochem. Geophys. Geosys*. 4(3): doi:10.1029/2001GC000213.

Simmons, N. A., S. C. Myers and A. Ramirez (2009). Multi-resolution seismic tomography based on a recursive tessellation hierarchy, in *Proceedings of the 2009 Monitoring Research Review: Ground-Based Nuclear Explosion Monitoring Technologies*, LA-UR-09-05276, Vol. 1, pp. 211–220.

Simmons, N. A., A. M. Forte, L. Boschi and S. P. Grand (2010). GyPSuM: A joint tomographic model of mantle density and seismic wave speeds, *J. Geophys. Res*. (under review).

Um, J. and C. Thurber (1987). A fast algorithm for two-point seismic ray tracing, *Bull. Seismol. Soc. Am*. 77: 972–986.

Wang, Z. and F. A. Dahlen (1995). Spherical-spline parameterization of three-dimensional Earth models, *Geophys. Res. Lett*. 22(22): 3099–3102.

Yang, X., I. Bondár, J. Bhattacharyya, M. Ritzwoller, N. Shapiro, M. Antolik, G. Ekström, H. Israelsson and K. McLaughlin (2004). Validation of regional and teleseismic travel-time models by relocating ground-truth events, *Bull. Seismol. Soc. Am*. 94(3): 897–919.

Zhao, D., A. Hasegawa, and S. Horiuchi (1992). Tomographic imaging of *P* and *S* wave velocity structure beneath northeastern Japan, *J. Geophys. Res*. 97: 19909–19928.

Zhao, D. and J. Lei (2004). Seismic ray path variations in a 3D global velocity model, *Phys. Earth Planet. Int*. 141: 153–166.

Zhou, H. -W. (1996). A high-resolution *P* wave model for the top 1200 km of the mantle, *J. Geophys. Res.* 101(B12), 27791–27810.

Seismic Identification and Source Characterization

ISOLATING SOURCE INFORMATION IN *mb* AND *Ms* WITH MODEL-BASED CORRECTIONS: NEW *mb* VERSUS *Ms* DISCRIMINANT FORMULATIONS

Dale N. Anderson[1], Howard J. Patton[1], Steven R. Taylor[1], and Jessie L. Bonner[2]

Los Alamos National Laboratory[1] and Weston Geophysical Corporation[2]

Sponsored by the National Nuclear Security Administration[1] and the Air Force Research Laboratory[2]

Award Nos. DE-AC52-06NA25396[1] and FA8718-09-C-0012[2]
BAA09-75

ABSTRACT

Path and signal processing corrections made to amplitudes give magnitudes *mb* and *Ms*, that in principle, have only source information. We propose the addition of a model-based magnitude prediction as a correction term, that is, a source correction in addition to path and signal processing corrections under the null (H0) hypothesis that a seismic event is a single-point fully contained explosion. This additional correction removes explosion source information from the *Ms* versus *mb* discriminant with the remaining source information represented as a constant. There are effects such as depth, focal mechanism, and local material properties that cannot easily be determined and mathematically included in amplitude corrections. We develop a mathematical model to capture these near source effects as random (unknown) giving an error partition of two sources: model inadequacy and station noise. This mathematical model is the basis for two new *Ms* versus *mb* discriminant formulations. Both methods are designed to utilize advances in source physics theory by using new source models to predict (correct) observed surface wave magnitudes. *The network average discriminant formulation includes source model error and magnitude correlation in the standard error (SE) of the discriminant, effectively placing a lower bound on the discriminant SE and accounting for scaling between Ms and mb. This new property of the Ms versus mb discriminant correctly reduces the SE only through network averaging of magnitudes. A second discriminant formulation derived from order statistics theory is potentially robust to station coverage for an event by basing discrimination on the maximum observed station Ms value.*

OBJECTIVES

When completed, this research will leverage advances in *Ms* signal processing into significant reformulations of the *Ms* versus *mb* discriminant to include: 1) a new correction for source in addition to established path corrections under the null hypothesis that a seismic event is an explosion, 2) a new sources-of-error model that correctly partitions total error between two components – model and background noise, and provides the correct formulation for scaling between *Ms* and *mb*, 3) and a new *Ms* versus *mb* discriminant formulation that can be robust to surface wave radiation pattern (station coverage) for earthquakes. We review progress to date on this research.

RESEARCH ACCOMPLISHED

An instrument-corrected amplitude spectrum can be thought of as a convolution between the source and the path. In the frequency domain this can be mathematically represented as

$$A(\omega, \Delta) = S(\omega)G(\Delta)P(\omega)B(\omega, \Delta) \quad , \tag{1}$$

where *S* is the source spectrum, *G* is geometrical spreading, *P* is the frequency-dependent site effect, and *B* is the an-elastic attenuation with function arguments epicentral distance Δ and angular frequency ω. Here we have split the path effect into three components: 1) a frequency independent geometrical spreading component, 2) a range independent and frequency dependent site effect, and 3) an an-elastic attenuation component.

The logarithm of both sides of Equation (1) gives

$$\log A(\omega, \Delta) = \log S(\omega) + \log G(\Delta) + \log P(\omega) + \log B(\omega, \Delta). \tag{2}$$

In general, to remove source, size and path trends in the data, we can correct the observed log $A_O(\omega,\Delta)$ spectrum so that

$$\log A_c(\omega, \Delta) = \log A_o(\omega, \Delta) - \log A(\omega, \Delta), \tag{3}$$

where log $A_C(\omega,\Delta)$ is the corrected spectrum. Equation (3) gives corrected magnitudes (residuals) *Y* that are then used to construct discriminants. Specifically, from Equation (3), the corrected magnitude *Y* is a log observed magnitude minus a model prediction of magnitude under the hypothesis that the event was generated by source $S(\omega)$ (e.g, single-point fully contained explosion). The residuals *Y* provide data (evidence) to test this hypothesis. Parseval's theorem provides the signal processing for magnitude calculations (total phase energy) in the time domain.

A baseline source model $S(\omega)$ will forecast estimates of *mb* and *Ms* for an event in question. Fully developed, the source model $S(\omega)$ is a linear superposition of two axisymmetric force systems for explosions conducted in hard rock. First, a monopole represents the explosion as a spherical source. Second, a compensated linear vector dipole (CLVD) with vertical axis in extension represents shock-induced, deep-seated tensile failure, a form of source medium damage (see Patton and Taylor (2008), and Ben-Zion and Ampuero (2009)). Both sources are assumed to be time and space coincident, and have a common Mueller and Murphy (1971) source function. The monopole source alone is used to forecast *mb*. *Ms* is forecast by half-space calculations of Rayleigh wave interference between the monopole and CLVD force systems (Patton and Taylor (2008)).

Estimates of *mb* and *Ms* and error bounds are derived from statistical analysis of model parameters. With density and P velocity fixed for hard rock, the model has four parameters: Poisson ratio ν, depth of burial *h*, yield *W*, and a low-frequency CLVD source strength to monopole parameter *K* developed in Patton and Taylor (2008). Independent observations constrain or bracket values for each parameter. Such observations might be drawn from site geology and tectonic history (ν), previous testing history (mature versus new test sites; *h*, *K*), and seismic measurements, both regional and teleseismic, of source size (*W*). The two discriminants developed here utilize a prediction of *mb* and *Ms* derived from a reasonable suite of models covering the parameter space. Thus, the discrimination methods developed in this paper have the potential to provide monitoring capability in settings with no explosion calibration data.

Consistent with the established approach to *Ms* versus *mb* discrimination, we develop the mathematics of two new discriminant formulations – a multi-station discriminant constructed from the network average of the corrected magnitudes *Y*, and a multi-station discriminant constructed from the maximum of station *Ms* values. Both discriminants are built from random effects analysis of variance (Scheffe (1959), Searle (1971) and Searle et al. (1992)) which has been applied to other path correction theories in seismology (e.g., Chen and Tsai (2002), Tsai and Chen (2003) and Tsai et al. (2006)). We model any remaining physical structure in corrected magnitudes as a source bias plus two random effect components – model inadequacy and station noise. This approach to *Ms* versus *mb* discriminant formulation properly forms the discriminant standard error with these two variance components. Model inadequacy decreases with scientific advances in source and path correction theory and improved calibration, and consistent with signal processing theory, station noise is reduced through station averaging in the network average formulation. The conceptual motivation for the new discrimination formulations is illustrated in Figure 1.

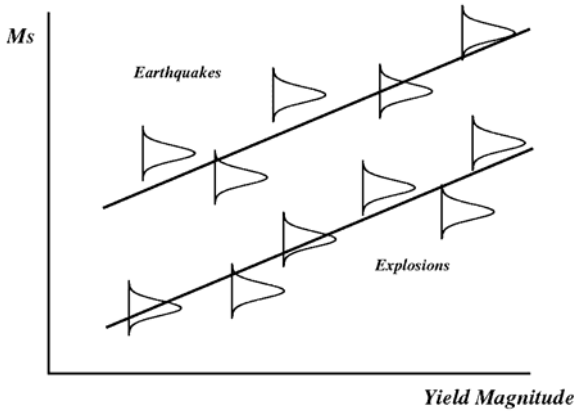

(a) Uncorrected Ms Magnitudes

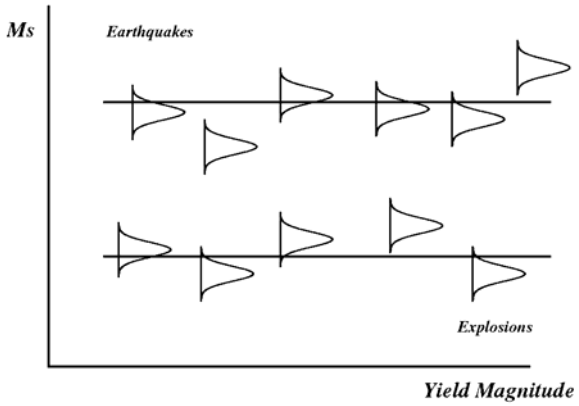

(b) Ms Magnitudes Corrected for $Yield\ Magnitude$

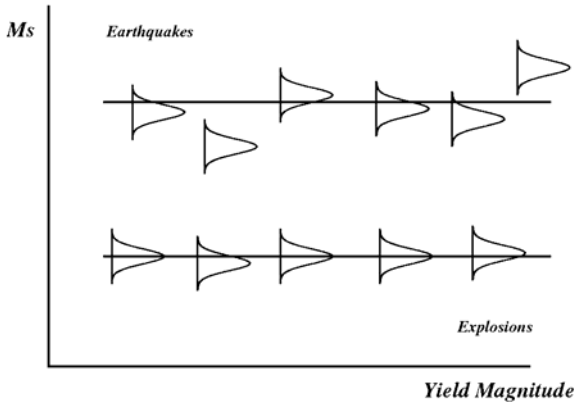

(c) Ms Magnitudes Corrected for $YieldMagnitude$ and $Source$

Figure 1. Conceptual illustration of corrections applied to *Ms* magnitudes, conditional on known *Yield Magnitude*. Normal curves represent the distribution of station *Ms* values. Figure 1(a) illustrates uncorrected *Ms* magnitudes. Figure 1(b) illustrates the event populations after correction for *Yield Magnitude* giving a significant reduction in model error. Figure 1(c) illustrates the event populations after correction for *Yield Magnitude* and additionally a *Source* correction (observed minus prediction). Note the additional reduction in model error and the significant source population separation.

Discriminant Formulation with Model Inadequacy and Station Noise Error Partition

Established signal processing treats amplitudes as lognormal distributed and therefore magnitudes are normally distributed. The conceptual representation of the proposed model is

$$Y = \log(\text{corrected amplitude}) = C(\text{source}) + Event + Noise, \quad (4)$$

where C(source) is a source constant, *Event* is a zero mean random effect that varies from event to event and represents model inadequacy from effects such as depth, focal mechanism, local material property and apparent stress variability, and *Noise* represents measurement and ambient noise, also with zero mean. This approach results in C(source) terms for earthquakes and explosions, with large differences in these terms indicative of good discrimination ability. In subsequent development, the hypotheses test that an event is a single point fully contained explosion will be mathematically represented in terms of these C(source) parameters. Equation (4) implies the expected value of Y is $\mathbf{E}\{Y\} = C(\text{source})$. In the development it is assumed that good signal processing practices have been applied giving high confidence in the quality of the observed amplitudes and calculated magnitudes.

For the mathematical statistics formulation of Equation (4), define the random variable Y_{ijk} to be a magnitude residual for source i=0,1 (explosion, earthquake), event j and station k (observed data are denoted y_{ijk}). The statistical linear model representation of Equation (4) is then

$$Y_{ijk} = \mu_i + E_j + \epsilon_{(ij)k} \quad j = 1, 2, \ldots m_i \quad k = 1, 2, \ldots n_{ij}. \quad (5)$$

Analogous to Equation (4), Equation (5) reads Y_{ijk} equals a source constant μ_i plus a random event adjustment E_j (source and path model inadequacy) plus a station noise adjustment $\varepsilon_{(ij)k}$. The subscript notation $(ij)k$ for $\varepsilon_{(ij)k}$ specifies that observed station noise (k) is different for each source and event combination (ij). Equation (5) is a standard mixed effects (random and fixed) linear model.

The E_j are modeled as independent normal random variables with zero mean and variance τ^2. The $\varepsilon_{(ij)k}$ are independent normal random variables with zero mean and variance σ^2. E_j and $\varepsilon_{(ij)k}$ are independent across all subscripts. This assumption is consistent with effects local to the source being uncorrelated with station noise.

Statistical Properties of a Network Magnitude Residual

For source i and event j, denote the $1 \times n_{ij}$ vector of magnitude residuals for n_{ij} stations as $\underline{Y}'_{ij}$. Then $\underline{Y}'_{ij}$ is multivariate normal with $1 \times n_{ij}$ mean vector $\underline{\theta}'_{ij}=(\mu_i, \mu_i, \ldots, \mu_i)$ and $n_{ij} \times n_{ij}$ covariance matrix

$$\Omega_{ij} = \begin{pmatrix} \tau^2+\sigma^2 & \tau^2 & \tau^2 & \cdots & \tau^2 \\ \tau^2 & \tau^2+\sigma^2 & \tau^2 & & \tau^2 \\ \tau^2 & \tau^2 & \ddots & & \vdots \\ \vdots & & & \tau^2+\sigma^2 & \tau^2 \\ \tau^2 & \cdots & \tau^2 & \tau^2 & \tau^2+\sigma^2 \end{pmatrix}. \quad (6)$$

The network magnitude residual is $Y_{ij}= \underline{1}' \underline{Y}_{ij} / n_{ij}$ is normal with mean μ_i and standard error $\tau^2+\sigma^2/n_{ij}$. Omitting the term E_j in Equation (5) implies that the magnitude residual at a station is μ_i plus station noise. This model formulation is fundamentally inconsistent with seismic observation. The standard error of Y_{ij} with E_j removed from Equation (5) is σ^2/n_{ij} (τ^2=0) and decreases as the number of stations n_{ij} observing an event increases. By not including the term E_j, effects such as depth, focal mechanism, local material property and apparent stress variability are not accounted for in the theoretical model representation of a magnitude, and this bias can never be diminished with a network average calculation. Equation (5) captures source and path model deficiencies as a random effect (E_j) and compensates for them as a component in the standard error of a discriminant. Also, the lower bound of a magnitude standard error, derived from Equation (5), is non-zero and therefore consistent with realistic seismic observation.

Another important property of this model is that a magnitude residual for a single event is correlated across stations. This correlation, $\tau^2/(\tau^2+\sigma^2)$ implies that large adjustment E_j increases correlation between stations because this

random adjustment is applied to all stations observing an event, that is, the station residuals stochastically move together. Small adjustment E_j implies the correction model is good and is conceptually equivalent to stations with incoherent noise. Small adjustment E_j also implies τ^2 is small and the standard error of Y_{ij} is fundamentally reduced through network averaging.

The corrected magnitudes *mb* and *Ms* can be correlated if they are both corrected for size in the source spectrum *S* with, for example, *Mw*. If *Ms* is corrected for size with *mb*, then these magnitudes will be uncorrelated. From Equation (5) the random mechanism causing this correlation is modeled with the E_j terms between magnitudes because these errors perturb the signal equally at all stations observing an event, and also the measured amplitudes. *This correlation is the mathematical mechanism that captures any scaling between magnitudes.* Extending Equation (5) to two corrected magnitudes $Y1_{ijk}$ (= Ms_{ijk}) and $Y2_{ijk}$ (= mb_{ijk}) with the $E1_j$ and $E2_j$ terms between magnitudes correlated (ρ) provides the statistical model to calculate the standard error of the multi-station discriminant given in the section that follows.

Network Average Discriminant Formulation

The *Ms* versus *mb* discriminant is constructed from a bivariate normal model of network magnitude residuals *Ms* and *mb*, with bias constants $\mu_{Ms}i$ and $\mu_{mb}i$, i=0,1 (explosion, earthquake). For an explosion, the network magnitude residual *Ms* is normal with mean μ_{Ms_0} and standard error $\tau^2_{Ms}+\sigma^2_{Ms}/n_{Ms}$ and *mb* is normal with mean μ_{mb_0} and standard error $\tau^2_{mb}+\sigma^2_{mb}/n_{mb}$. With the inclusion of correlation between model errors $E_{Ms}j$ and $E_{mb}j$, the standard error of the *Ms* versus *mb* discriminant is then

$$SE_{\bar{M}_s-\bar{m}_b} = \sqrt{\tau^2_{mb} + \frac{\sigma^2_{mb}}{n_{mb}} + \tau^2_{Ms} + \frac{\sigma^2_{Ms}}{n_{Ms}} - 2\,\rho\,\tau_{mb}\,\tau_{Ms}}\,, \qquad (7)$$

for both earthquakes and explosions. Equality of the standard error for both source types is an important model property because unlike discrimination analysis with unequal source variability, it ensures that an earthquake with an unusually strong earthquake-identifying discriminant value will not be identified as an explosion. This can occur with discrimination methods that model source variance as unequal – explosion calibration data can exhibit variability that is significantly larger than earthquake calibration data.

In an operational setting, physical correction theory will never be able to adjust amplitudes for all local systematic effects. As discussed previously, these local systematic effects are modeled as random, moving out to all stations (and therefore amplitudes), hence the correlation between a network of stations. As physical (source and path) corrections improve, the model inadequacy terms E_j will be small, giving small values of τ, and the covariance between amplitudes will be small. In the limit, this conceptually gives station discriminant scatter plots for explosions and earthquakes (populations) that are small shotgun patterns of data.

Centering relative to the explosion population means, the standardized discriminant is

$$Z_{\bar{M}_s-\bar{m}_b} = \frac{(\bar{mb}-\mu_{mb_0})-(\bar{Ms}-\mu_{Ms_0})}{\sqrt{\tau^2_{mb}+\sigma^2_{mb}/n_{mb}+\tau^2_{Ms}+\sigma^2_{Ms}/n_{Ms}-2\,\rho\,\tau_{mb}\,\tau_{Ms}}}\,, \qquad (8)$$

which is centered at zero for explosions and has a non-zero center for earthquakes. The advantage to centering relative to explosions is consistency with the monitoring position to assume all events are explosions and then prove otherwise with seismic signatures. From Equation (8), values of Z_{Ms-mb} greater than a decision threshold fail to reject the hypothesis that an event is a single-point fully contained explosion.

Statistical Properties of the Maximum of Magnitude Residuals

The energy radiation pattern of surface waves from a single-point fully contained explosion can be reasonably assumed to be azimuthally isotropic. With $\tau^2=\tau^2_{Ms}$ and $\sigma^2=\sigma^2_{Ms}$, Equation (6) gives the *Ms* covariance matrix for an event observed by n_{ij} stations. Make the assumption that corrections are of sufficient high quality to give $\tau^2_{Ms} \cong 0$. With this assumption, the observed station *Ms* are independent (uncorrelated) for an event, and the *Ms* population mean is zero for explosions and greater than zero for earthquakes. For source i, event j, $Max\{Ms_{ijk}\} < m \Leftrightarrow \{Ms_{ijk} < m;\ k = 1, n_{ij}\}$. Under the null (*H0*) hypothesis that a seismic event is a single-point fully contained explosion, surface

wave energy is azimuthally isotropic and observed station *Ms* have the same probability distribution and so the *H0* likelihood is

$$P(Ms_1 < m, \ldots, Ms_{n_{ij}} < m \mid H0) = P(Ms_1 < m \mid H0) \cdots P(Ms_{n_{ij}} < m \mid H0) = P(Ms_k < m \mid H0)^{n_{ij}}. \quad (9)$$

Order Statistics Discriminant Formulation

The energy radiation pattern of surface waves from an earthquake is not azimuthally isotropic. Some stations could be on an energy lobe and some could lie on an energy node. In an event identification setting the energy radiation pattern of an event will not be known. This means that a network average of station *Ms* values could be strongly influenced by nodal stations. For example, an earthquake with four nodal stations and one station on an energy lobe could look like an explosion with *Ms* versus *mb* network average discrimination.

The right hand side of Equation (9) provides the likelihood of the random variable $Max\{Ms_{ijk}\}$ under the null hypothesis of single-point fully contained explosion. A conservative alternative hypothesis (*Ha*) likelihood is provided by

$$P(Ms_k < m \mid Ha) \times P(Ms_k < m \mid H0)^{n_{ij}-1}, \quad (10)$$

that is, an *Ms* earthquake model at one station and an *Ms* explosion model for the other stations. The Neyman-Pearson likelihood ratio test reduces to; Reject *H0* if

$$ce^{\psi m} + \varphi(m)(n_{ij} - 1) > k, \quad (11)$$

where c, ψ and $\varphi(m)$ are a function of the null and alternative hypothesis parameter values. The function $\varphi(m) \in (0,1)$ and monotonic increasing, and so

$$ce^{\psi m} + \varphi(m)(n_{ij} - 1) > ce^{\psi m}. \quad (12)$$

From Equation (12), for a given value of k there are values of $m=Max\{Ms_{ijk}\}$ that will fail to reject *H0* with a conservative hypothesis test based on right side of Equation (12), yet reject if the test is based on the Neyman-Pearson test (left side of Equation (12). This is graphically shown in Figure 2. The conservative hypothesis test is of the form reject *H0* if $Max\{Ms_{ijk}\} > k$, and is conservative in the sense of "miss no explosions". $Max\{Ms_{ijk}\}$ *as a discriminant offers a cost efficient approach to discrimination in settings where path and source corrections are mature.*

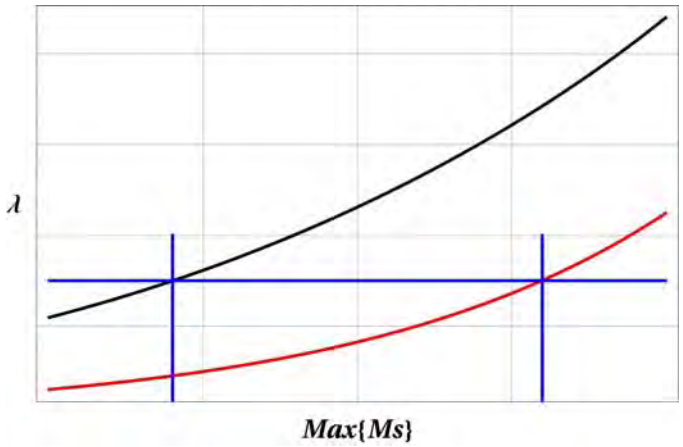

Figure 2. Graphic of the Neyman-Pearson (black) and conservative (red) likelihood ratio λ. The blue horizontal decision line projects a decision region for the discrimination *Max*(*Ms*). Values of *Max*(*Ms*) interior to this decision region reject H0 with Neyman-Pearson test and fail to reject H0 with the conservative test.

CONCLUSIONS AND RECOMMENDATIONS

The mathematical statistics of two new approaches to *Ms* versus *mb* discrimination are developed in this paper. Both methods are designed to utilize advances in source physics theory by using new source models to predict (correct) observed surface wave magnitudes. The network average discriminant formulation additionally includes source model error in the standard error (SE) of a discriminant effectively placing a lower bound on the discriminant SE. This new property of the *Ms* versus *mb* discriminant correctly reduces the SE only through network averaging of magnitudes. The order statistics discriminant formulation is potentially robust to station coverage for an event by basing discrimination on the maximum observed station *Ms* value. Validation analysis for these new formulations is in progress using global events reported in reported in Bonner et al. (2003), Bonner et al. (2006), Marshall and Bashman (1972). The Bonner et al. (2003) and Bonner et al. (2006) papers research and develop new signal processing theories for *Ms* that are design to Rayleigh wave energy from small magnitude events (stations close to source).

REFERENCES

Patton, H. J. and S. R. Taylor (2008). Effects of shock-induced tensile failure on mb-Ms discrimination: Contrasts between historic nuclear explosions and the North Korean test of 9 October 2006. *Geophys. Res. Lett.* , 35:L14301.

Ben-Zion, Y and J. P. Ampuero (2009). Seismic radiation from regions sustaining material damage. *Geophys. J. Int.* 178:1351–1356.

Mueller, R. A. and J. R. Murphy (1971). Seismic characteristics of underground nuclear detonations, part I: Seismic spectrum scaling. *Bull. Seismol. Soc. Am.* 67: 135–158.

Scheffe, H (1959). *The Analysis of Variance.* John Wiley & Sons, New York.

Searle, S. R. (1971). *Linear Models.* John Wiley & Sons, New York.

Searle, S. R., G. Casella, and C. E. McCulloch (1992). *Variance Components*. John Wiley & Sons, New York.

Chen, Y. H. and P. C. Tsai (2002). A new method of estimation of the attenuation relationship with variance components. *Bull. Seismol. Soc. Am.* 92: 1984–1991.

Tsai, P. C. and Y. H. Chen (2003). Reduction of ground motion variability using the variance components technique. *EOS Trans. AGU*, 84.

Tsai, P. C., YH Chen, and L Chia-Hsin (2006). The path effect in ground-motion variability: An application of the variance-components technique. *Bull. Seismol. Soc. Am.* 96:1170–1176.

Bonner, J. L., DG Harkrider, ET Herrin, S. A. Russell, IM Tibuleac, and RH Shumway (2003). Evaluation of short-period near-regional Ms scales for the Nevada test site. *Bull. Seismol. Soc. Am.* 93: 1–19.

Bonner, J. L., D. R. Russell, DG Harkrider, DT Reiter and RB Herrmann (2006). Development of a time-domain, variable-period surface-wave magnitude measurement procedure for application at regional and teleseismic distances, Part II: Application and Ms −mb performance. *Bull. Seismol. Soc. Am.* 96:678–696.

Marshall, P. D. and P. W. Basham (1972). Discrimination between earthquakes and underground explosions employing an improved Ms scale. *Geophys. J. R. Astr. Soc*. 29: 431–458.

SOURCE PHYSICS EXPERIMENTS AT THE NEVADA TEST SITE

Wendee M. Brunish[1], Ward L. Hawkins[1], David Coblentz[1], Howard J. Patton[1], John J. Zucca[2], Jerry J. Sweeney[2], Charles R. Carrigan[2], Tarabay H. Antoun[2], Carolyn E. Seifert[3], Kenneth H. Wohletz[1], Christopher R. Bradley[1], Aviva J. Sussman[1], Theodore W. Bowyer[3], Robert Corbell[4], Robert Abbott[4], Catherine M. Snelson[5], Ping Lee[5]

Los Alamos National Laboratory[1], Lawrence Livermore National Laboratory [2], Pacific Northwest National Laboratory[3], Sandia National Laboratories[4], Nuclear Security Technologies, Inc.[5]

Sponsored by the National Nuclear Security Administration

Award No. DE-AC52-06NA25946/NST10-NCNS-PD00

ABSTRACT

The U. S. capability to monitor foreign underground nuclear test activities relies heavily on measurement of explosion phenomena, including characteristic seismic, infrasound, radionuclide, and acoustic signals. Despite recent advances in each of these fields, empirical, rather than physics-based, approaches are used to predict and explain observations. Seismologists rely on prior knowledge of the variations of teleseismic and regional seismic parameters such as p- and s-wave arrivals from simple one-dimensional models for the teleseismic case to somewhat more complicated enhanced two-dimensional models for the regional case. Likewise, radionuclide experts rely on empirical results from a handful of limited experiments to determine the radiological source terms present at the surface after an underground test. To make the next step in the advancement of the science of monitoring we need to transform these fields to enable predictive, physics-based modeling and analysis.

The Nevada Test Site Source Physics Experiments (N-SPE) provide a unique opportunity to gather precise data from well-designed experiments to improve physics-based modeling capability. In the seismic experiments, data collection will include time domain reflectometry to measure explosive performance and yield, free-field accelerometers, extensive seismic arrays, and infrasound and acoustic measurements. The improved modeling capability that we will develop using this data should enable important advances in our ability to monitor worldwide for nuclear testing. The first of a series of source physics experiments will be conducted in the granite of Climax Stock at the NTS, near the locations of the HARD HAT and PILE DRIVER nuclear tests. This site not only provides a fairly homogeneous and well-documented geology, but also an opportunity to improve our understanding of how fractures, joints, and faults affect seismic wave generation and propagation. The Climax Stock experiments will consist of a 220 lb (TNT equivalent) calibration shot and a 2200 lb (TNT equivalent) over-buried shot conducted in the same emplacement hole. An identical 2200 lb shot at the same location will follow to investigate the effects of pre-conditioning.

These experiments also provide an opportunity to advance capabilities for near-field monitoring, and on-site inspections (OSIs) of suspected testing sites. In particular, geologic, physical, and cultural signatures of underground testing can be evaluated using the N-SPE activities as case studies. Furthermore, experiments to measure the migration of radioactive noble gases to the surface from underground explosions will enable development of higher fidelity radiological source term models that can predict migration through a variety of geologic conditions. Because the detection of short-lived radionuclides is essential to determining if an explosion was nuclear or conventional, a better understanding of the gaseous and particulate radionuclide source terms that reach the surface from underground testing is critical to development of OSI capability.

Note: The upcoming Nevada Test Site Source Physics Experiments (N-SPE) should not be confused with the 2003 Source Phenomenology Experiments (SPE) conducted in Arizona (Yang and Bonner, 2009).

OBJECTIVES

The Source Physics Experiments (N-SPE) will enhance the DOE National Nuclear Security Administration's (NNSA) efforts related to verification, arms control and nonproliferation, by providing computational improvements in our ability to predict ground motion, gas flow and nuclear cavity dynamics, and enhance our ability for near-field monitoring and on-site inspection. This predictive capability combined with advanced capabilities to compute synthetic seismograms through three-dimensional models of the earth will move monitoring science into a physics-based era. This capability should enable important advances in our ability to monitor worldwide for nuclear testing. Furthermore, the combination of the improved understanding of the source with the advanced ability to model synthetic seismograms in three-dimensional earth models should also lead to advances in the ability to locate and identify events. NNSA will conduct focused activities at the Nevada Test Site (NTS), which is the preferred location to conduct high-hazard experiments that are vital to our national security. Nuclear Security Technologies (NSTec), in its role as operations management for NTS will partner with the NNSA, and the DOE Nevada Site Office (NSO). The Defense Threat Reduction Agency (DTRA) will also play an important role in the N-SPE experiments. DTRA has expertise in the areas of explosive emplacement, detonation, and diagnostics, as well as in fielding instrumentation for recording explosion-related phenomena. This experiment series is sponsored by NA-22 (Nonproliferation and Verification Research and Development office), and provides an opportunity for collaborative experimentation at NTS among NSTec, and the NNSA National Laboratories, Lawrence Livermore National Laboratory (LLNL), Los Alamos National Laboratory (LANL), Pacific Northwest National Laboratory (PNNL), and Sandia National Laboratories (SNL) for addressing many national nuclear nonproliferation and security R&D "Theme Areas," such as the Comprehensive Nuclear-Test-Ban Treaty (CTBT), Fissile Material Cutoff Treaty (FMCT), Nuclear Forensics, and START. The first "Theme Area" of CTBT is being addressed through a series of source physics and on-site inspection experiments.

RESEARCH ACCOMPLISHED

Building on the accomplishments of previous relevant field experiments such as the Non-Proliferation Experiment (NPE, 1994) and the Arizona Source Phenomenology Experiments (Yang and Bonner, 2009), the N-SPE series of chemical explosions is designed to gather specific ground truth information. These data are needed to fill knowledge gaps in our understanding of shear-wave generation by explosions, for improving numerical analysis, and to test and validate seismic explosion source and wave propagation models. NNSA has begun a multi-year research program beginning in FY2010 with technologies to simulate complex phenomenologies associated with explosions conducted in realistic geologic media. The N-SPE research includes geophysical characterization, geodynamic modeling (including strong shock propagation, seismic wave generation, and seismic wave propagation), infrasound measurements, near-field monitoring technologies (including on-site inspection, hyperspectral imaging, lidar, and InSAR), electromagnetic sensors, and noble gas migration.

Key research objectives related to understanding the prompt nuclear explosion phenomena that can be addressed through NTS experiments include:

- Model validation, e.g., explosion source physics, coupling, s-wave generation, energy propagation, and gas migration,
- Effects of explosion emplacement configurations and conditions,
- Differentiation between conventional and nuclear explosions,
- Detection and analysis of radiation transport mechanisms,
- Detection of testing-related operations and facilities (machinery, infrastructure, etc.),
- Detection of electromagnetic signatures from nuclear-related work, and,
- Unification of local, regional, and global monitoring technologies.

Key technologies include:

- Seismic
- Infrasound
- Seismo-acoustics
- Radionuclide sampling (particulates and noble gases)
- Energetic particles
- Radiation survey (x-rays, gamma rays)
- Electro-Magnetic Pulse

Current monitoring systems, including those of the Comprehensive Nuclear-Test-Ban Treaty Organization (CTBTO), focus on long range monitoring of relatively large nuclear explosions. Near-field monitoring and OSI access to a suspected test site will greatly improve information about testing activities and phenomena, especially for smaller, nuclear and non-nuclear explosions. To be an effective deterrent, the OSI technologies and techniques need the benefit of scientific and operational credibility. This can only come through development and demonstration of capability.

Key research objectives related to post detonation evidence that can be addressed through NTS experiments include:

- Explosion effects detection and documentation,
- Methods to identify key inspection areas of interest
- Effectiveness of near-field monitoring and OSI geophysical techniques,
- Development and evaluation of prototype sensor systems,
- Advanced data analysis techniques that are faster, more sensitive, more selective,
- Performance estimation software development,
- Transport and deposition of materials of interest,
- Radionuclide sample collection and analysis at, or near, the collection site.

Key technologies include:

- Visual inspection,
- Geophysical techniques (seismic, electrical, magnetic, etc.) to detect surface and underground anomalies,
- Soil gas sampling and analysis,
- Environmental sampling and analysis,
- Radiation survey,
- Remote sensing techniques to support OSI,
- Collection of samples from strategic locations in a timely manner,
- Analysis of samples quickly and accurately, and
- Identification of morphological, chemical, and isotopic signatures.

Motivation and Opportunity

Monitoring and verification issues are a fundamental part of this NTS research. The NNSA laboratories possess an extensive collection of verification seismic data for near- and far-field seismic data, and the NTS provides the ideal setting for field experiments. The local seismic networks provide the basis for optimal sensor placement and performance specifications required for effective seismic monitoring. Electromagnetic pulse (EMP) and radionuclide sensor technology will be used in controlled source experiments to determine detection thresholds. Current lab expertise regarding ground-based visual observations, geophysical techniques, and other OSI supporting technologies such as hyperspectral imaging will significantly add to the US efforts in detection and monitoring. The ability of the U.S. to effectively verify nuclear testing treaties is heavily dependent on our experience, innovative application of technologies, and validation of those technologies via demonstration tests. The planned experiments involve moderate to large quantities (kilograms to 1000s of kilograms) of high explosives.

Source Physics Experiments

The N-SPEs will support computational improvements in our ability to predict ground motion, gas flow, nuclear cavity dynamics, and surface effects. The effective use of the limited testing resources will require predictive calculations and then a verification and validation component. The NNSA laboratories have a long history and extensive earth materials database to support explosive testing and experiments. Along with historic DoD study results (e.g. Defense Nuclear Agency (now DTRA) tests and Soviet data), the proposed work will advance our ability to model and predict phenomena from tests in various environments. Fundamental questions regarding the effects of depth of burial and the generation of shear waves by explosive sources will be answered through the combined experimental and computational research.

The source physics experiments will be well-instrumented with both near- and far-field measurements to provide an outstanding dataset that will allow us to advance our understanding of the basic physical processes that affect the seismic signal generated by an underground explosion. Time-domain reflectometry measurements will provide information about explosive performance and yield, and free-field accelerometers will provide information about

source conditions and strong shock propagation. Data collected from an extensive array of seismometers, with good azimuthal coverage, will give us the ground truth necessary to fully comprehend the mechanisms for shear wave generation. Additional instrumentation, including infrasound and EMP sensor, will further enhance our understanding of underground explosion phenomenology.

Development of high performance hydrodynamic modeling will allow us to predict and enhance our understanding of coupling experiments conducted in simple (e.g., Climax Stock) and complex (e.g., U16b) geologies. Experiment datasets will then be used to validate equations of state for hard rock, further populate parameter spaces (rock type, cavity geometry, source type, etc.), and improve the understanding of seismoacoustic coupling and propagation and its implications for monitoring explosions under the CTBT.

Experimental plan: The N-SPE is a series of physics experiments involving buried explosives. The N-SPE provides a unique opportunity to gather precise data on well-designed experiments to test and enhance our modeling codes.

The first source physics experiments will be conducted in the granite of Climax Stock, near the locations of the HARD HAT and PILE DRIVER nuclear tests (Figure 1). This site not only provides a fairly homogeneous and well-documented geology, but also an opportunity to improve our understanding of how fractures, joints, and faults affect seismic wave generation and propagation. The Climax Stock experiments will consist of a 220 lb (TNT energy equivalent) calibration shot and an over-buried 2200 lb (TNT energy equivalent) shot conducted in the same emplacement hole. Ideally, an identical 2200 lb follow-on shot would be conducted at the same location to investigate the effects of rock pre-conditioning.

Subsequent experiments in this series over the next few years will likely vary in source strength, emplacement configuration, sensor placements and be conducted in different geologic settings.

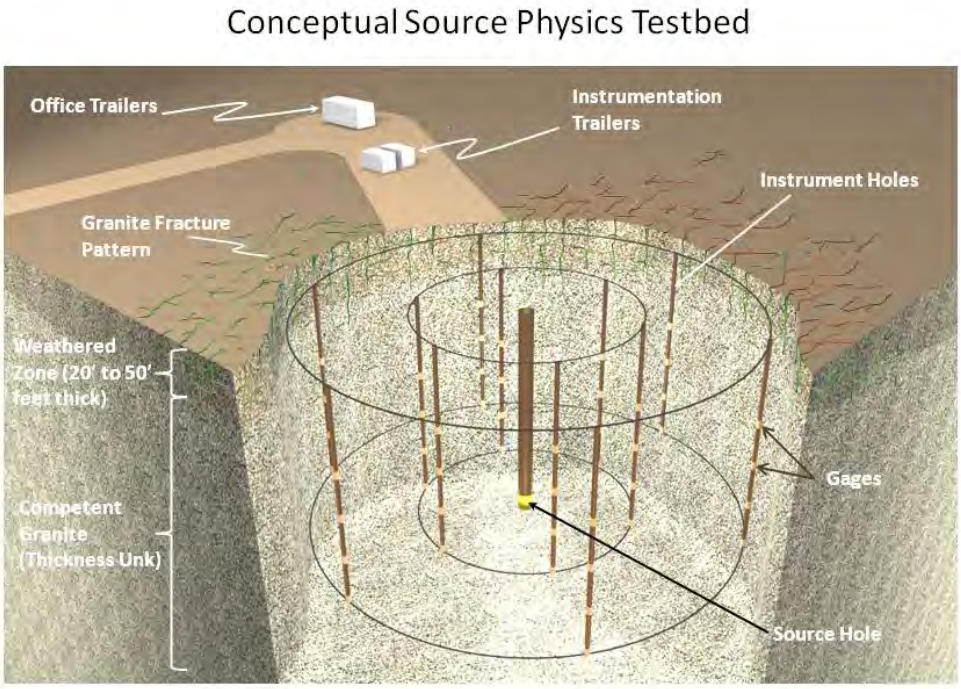

Figure 1. The first N-SPE test in Climax Stock granite will consist of a 65-meter deep emplacement hole and six instrument holes, three at 10 meters from the emplacement hole and three at 20 meters from the emplacement hole.

There are three major elements of the initial N-SPE efforts. These are geophysical characterization, hydrodynamic and seismic source modeling, and near-field monitoring technologies.

Geophysical characterization: Geophysical methods provide information about the physical properties of the subsurface. There are two general types of methods: 1) active, which measure the subsurface response to seismic, electromagnetic, and electrical energy; and 2) passive, which measure the earth's ambient magnetic, electrical, and gravitational fields. Geophysical methods fall into several broad categories including seismic methods (e.g., refraction, reflection, and tomography), ground-penetrating radar (GPR), electrical methods [e.g., electromagnetics (EM), electrical resistivity, induced polarization (IP) and self potential (SP)], and potential field methods (e.g., gravity, geoid, and magnetics). In addition, the tectonic history will be included for a comprehensive geophysical characterization.

Geophysical data are often difficult to interpret. For any given set of geophysical data a variety of subsurface conditions or parameter distributions can explain the data (i.e., solutions are not unique). The proper way to interpret geophysical data is to use the measured parameters as a description of a suite of solutions that can be used in combination with other site information (e.g., data from different geophysical methods, sampling and analytical tools, geological and historic records, anecdotal information) to arrive at the most plausible solution.

Figure 2. A variety of geologic and geophysical data will be combined to create a geologic framework model for the Source Physics Experiments in Climax Stock granite.

The interpretation of the geophysical data will be used to build a geologic framework model (Figure 2). This model will include stratigraphic layers, physical and material properties, ambient stresses, and surface topography. The model will then be meshed for use by the hydrodynamic modelers.

Modeling: Our goal is to develop analytical and simulation capabilities that will provide a physical basis for modeling the important facets of explosion phenomena (Figure 3). The important components of our approach include 1) utilizing three-dimensional fully-coupled strong motion hydrodynamic codes that will allow us to explicitly model near source finite displacement on faults as well as surface spall/slapdown (the gravitationally derived signal from lofted earth material) that is an important source of shear waves; 2) developing and implementing models that will allow us to realistically treat the microcrack releases that dominate near-source energy; 3) coupling the strong motion code to higher order spectral element codes with variable gridding to accurately model the effect of surface topography; 4) coupling our hydrodynamic calculations to seismic source models that utilize Compensated Linear Vector Dipole (CLVD) models in order to unequivocally separate source-generated shear waves from scattering-generated shear waves; and 5) using a coupled Eulerian Lagrangian approach to model decoupled shots or shots near voids or rubble columns where the momentum transfer at the air-rock interface plays a crucial role in energy coupling, shock propagation, and permeability to radioactive gases.

The combination of these efforts will provide a unique and unified capability to model nuclear explosions in realistic conditions including complex layering, uneven topography, pre-existing stresses, hard rock with fractures, joints, and faults, pre-conditioned rock, and cavities, rubble shields and other scenarios. All of these conditions are

extremely relevant to our efforts to understand and monitor underground nuclear test activities at test sites of interest.

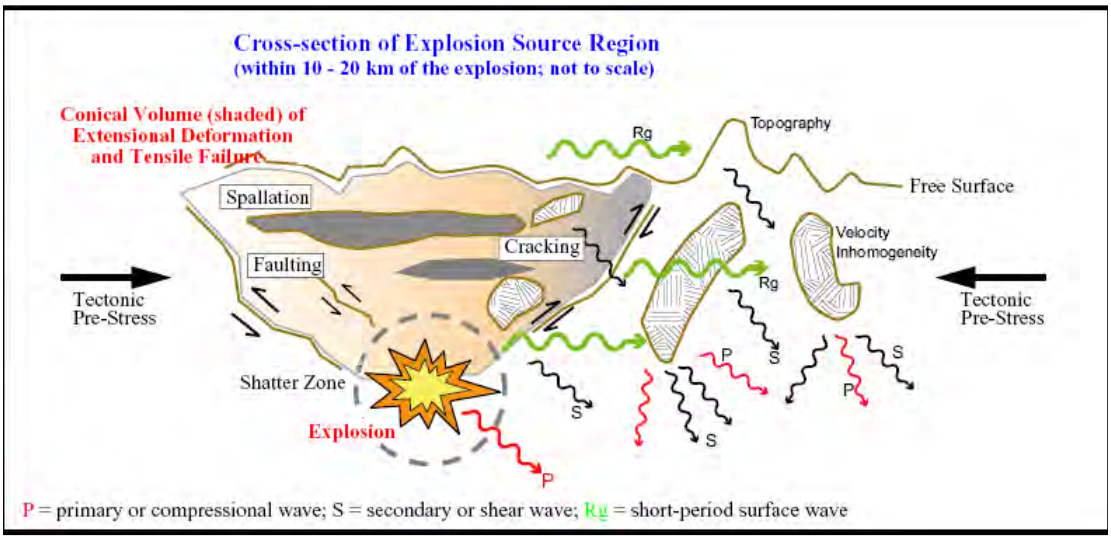

Figure 3. Currently employed simple seismic source models of nuclear explosions are inadequate for addressing the ever more challenging monitoring requirements. New models will include source complexities of tensile failure and near-source scattering.

Near-Field Monitoring and OSI Technologies: Experiments to investigate and validate near-field monitoring and OSI techniques will greatly enhance the understanding of the efficacy of these techniques. OSI is one of the verification elements specified in the CTBT. Once a general search area has been determined by other monitoring technologies (e.g., seismic), the challenge of OSI is to detect, identify, and describe features (Figure 4) in order to clarify whether that a nuclear explosion in violation of the CTBT has occurred. The treaty allows specific inspection techniques that must be applied during a limited time frame. OSI includes visual observation, geophysical, and radiological techniques. Visual observation also involves the identification and documentation of features and activities that are part of the support operations associated with nuclear testing. The conduct of a high explosive experiment at the NTS will be a surrogate to a nuclear test to determine the types of observables that are associated with the conduct of the explosion. Some of the OSI geophysical methods (active seismic, gravity, electrical, magnetic, etc.) are not well understood for OSI applications. Experiments to explore and validate techniques will greatly enhance the understanding of the efficacy of these techniques for OSI. NTS as a former nuclear explosion test site is uniquely suited to be a test bed for near-field monitoring and OSI verification techniques. The application of these techniques in conjunction with the enhanced understanding of field deployments issues will then become more effective in addressing the objective of the field activity. The general concept of operations for an OSI requires narrowing the possibly 1000-km^2 search area down to smaller, focused areas of interest, with the possibility of further selecting a specific site for drilling to obtain radioactive samples (Figure 5).

Visual observation (VO) methodologies can increase the effectiveness of OSI and will be integrated with an N-SPE. The specific objective is to calibrate near-field manifestation of visual observables by analyzing the degree of surface feature expression as a function of experimental design. To fully realize the results of N-SPE, assessments of the geological and geomorphological features are required to analyze source conditions. Changes in these characteristics that occur as a result of the experiments need to be thoroughly documented and quantified.

Passive seismology survey lines of seismometers over an explosion ground zero will be used to detect and record aftershocks. Data would be collected through the period where individual aftershocks can no longer be detected, but background noise levels will continue to be measured at individual stations to determine if an elevated background noise signature persists for a long time after detonation in the area near ground zero. An active seismic experiment

using either an explosive or non-explosive source, would establish the effectiveness of seismic instruments to detect and locate the damage zone of the explosion. Areal multispectral/infrared imagery can be acquired before and after an explosion to determine the usefulness of this type of imagery for detection of disturbed ground. Relatively shallow surveys with DC resistivity or electromagnetic methods after the explosion will provide an assessment of the contrast of electrical properties in the damage/rubble zone indicating the relative level of resolution of the technique for damage/rubble zone detection and characterization. These methods will provide baseline knowledge that will be valuable supporting information for the modeling efforts.

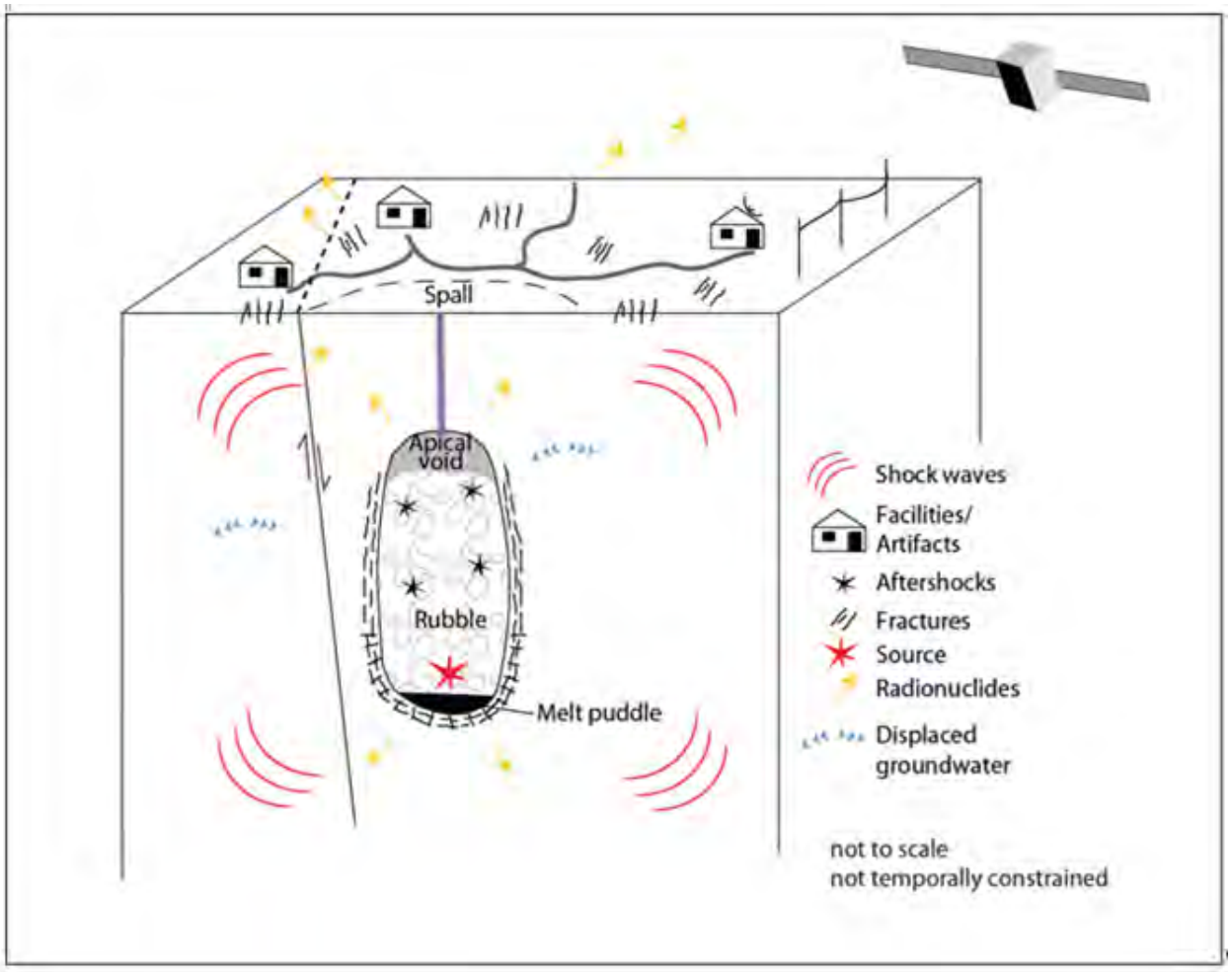

Figure 4. Potential observables from an underground nuclear explosion that may be detected and described using near-field monitoring and OSI technologies.

Hyperspectral Imaging, LIDAR and Laser scanning (HILL) is an especially powerful technology for evaluating transparency, quantifying N-SPE effects, and improving the effectiveness of OSI. HILL technology will provide and preserve a high-resolution, digital, dynamic-range, scale-variable dataset that has vast applications; for example, HILL data can be integrated with historical NTS data into a searchable, interactive observable phenomena atlas/database. Underground nuclear detonations can carry volatilized materials away from the source through fissures to the surface, Hyperspectral thermal imaging may also provide additional spectral signatures and emissivity changes that could result from disturbed soil.

Observable explosion effects are variable and depend upon several parameters including: emplacement site material properties, experiment design, explosive yield, depth of burial, and tamping. Consequently, N-SPE effects will

drastically range in scale and demonstrate the fact that an apparent lack of explosively produced effects may be a resolution artifact. Experimentation of HILL technology and further development will augment the systematics required to produce objective, repeatable, and quantifiable documentation during OSI. Given that NNSA laboratories possess a large collection of verification seismic data for near- and far-field seismic data, HILL technology is a complementary dataset that will allow for improved modeling and predictive capabilities. HILL technology would significantly reduce personnel time within potentially dangerous field situations, and provide a dramatic savings in person-hours and equipment/field costs. Current LANL expertise regarding ground-based visual observations and other field-based technologies will significantly add to the US ability for monitoring and transparency.

During near-field monitoring and on-site inspection the monitoring technologies and inspectors look for radioactive debris that has escaped an underground nuclear explosion and settled on the surface near and downwind of ground zero. For development of OSI capability, it is necessary to understand the surface source term created by short-lived particulate radioactive debris. There is much data available regarding the type and quantity of airborne particulate radioisotopes that were detected off-site during the era of nuclear testing at NTS. However, there is a dearth of data on near-field debris distributions for underground tests in which venting occurred.

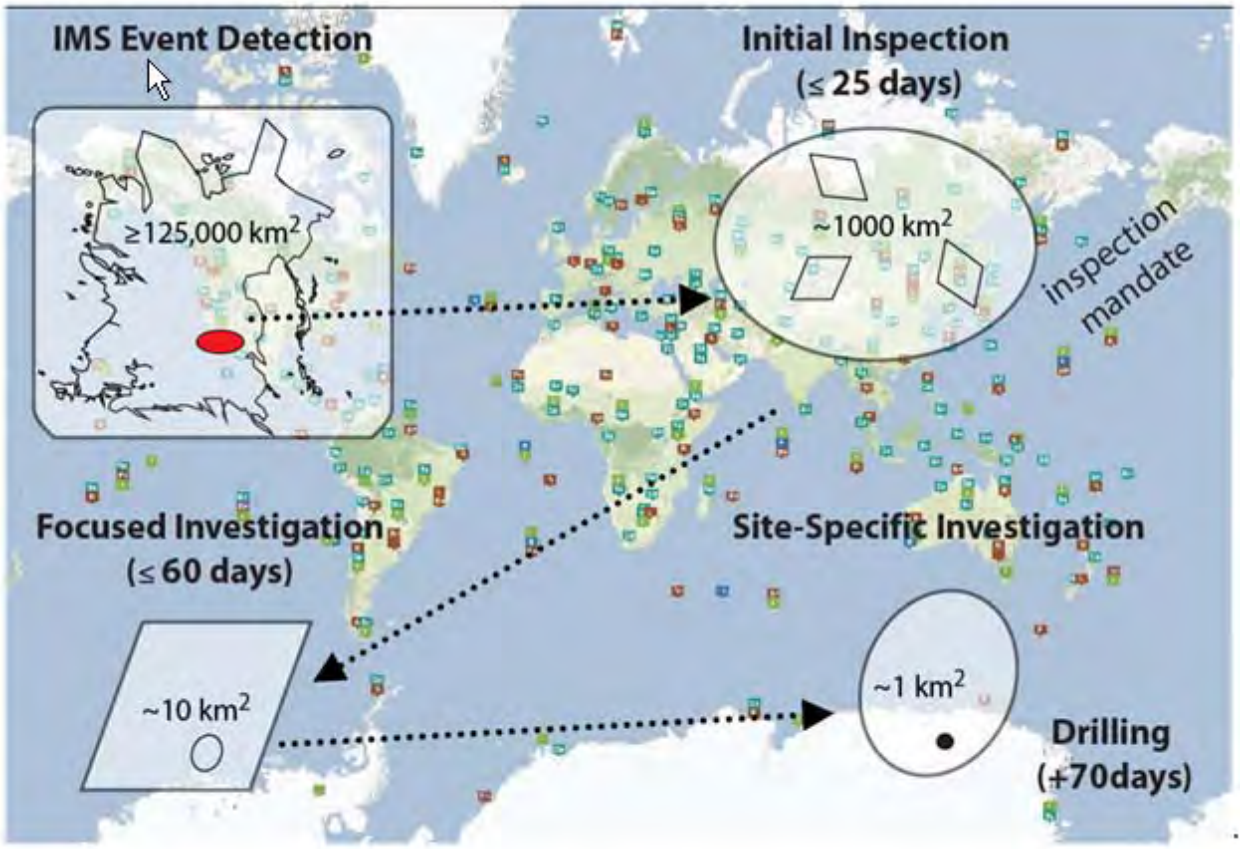

Figure 5. The primary objective of CTBT On-Site Inspection activities is collect evidence to clarify whether a nuclear test in violation of the treaty occurred. The concept of operations requires narrowing the search area (up to 1000^2 km) to identify areas for detailed investigation that includes sampling for radioactive gases and particulates in the soil. Drilling may also be conducted to search for underground radioactive material near a suspected test cavity.

Atmospheric transport and search methodology studies will help in determining instrument sensitivity requirements, developing concepts of operations, evaluating sampling methodologies, estimating instrument performance

(including spectral blinding techniques), and validating the list of relevant radionuclides for CTBT OSI. A release of short-lived isotopes (e.g., via shallow underground chemical explosion, direct spraying, or other controlled release) will be used for high-fidelity radiometric measurements at the surface with no permanent contamination introduced to the site. Radioactive debris will decay to below background levels within 1 year.

Various search strategies will be evaluated using gamma-ray spectroscopy equipment over the short-lived debris field via *in situ*, handheld, mobile, and aerial platforms. In addition, environmental sampling from the proposed site will occur before the execution of the experiment and then immediately after at predetermined locations. Sampling will consist of surface soil samples, swipes across exposed surfaces and continuous air sampling via a whole air particulate sampler. The samples will then be measured on existing spectrometry systems, including ultra-low-background gamma-ray detectors. Isotopes under consideration include a combination of treaty-relevant nuclides and other short-lived species that can be conveniently produced.

National Security Benefits of the N-SPE

The Source Physics Experiments will contribute significantly to our ability to detect, locate, identify and understand underground nuclear explosion phenomena. This understanding will assist the US in exploiting many data sources including: the International Monitoring System, the U.S. Atomic Energy Detection System, local and regional arrays, and National Technical Means. These experiments will add significantly to our predictive modeling capabilities and will greatly improve our understanding of emplacement, deployment, and processing techniques for sensors as well as the application of other monitoring technologies. Finally, the experiments proposed herein will greatly improve our ability to interpret, and potentially predict, signals from global events such as in the ever- expanding number of regions of interest for our national security.

The primary user of the increased understanding gained by this research is intended to be the Air Force Technical Applications Center (AFTAC) in their role as the US National Data Center. High performance modeling of the near source environment will give researchers improved source models which will translate into operational improvement for AFTAC's mission. Other potential users include other governmental agencies, such as the State Department for treaty verification (e.g., CTBT, TTBT and NPT), and DTRA for non-proliferation and site specific database development. It is expected that the user base will expand as more interests and applications arise as a result of greater understanding of source region effects on seismic radiation and general understanding of coupling, including near-field monitoring and OSI.

Seismic data are used by AFTAC to detect, locate, and identify earthquakes from explosions in their national mission of ground-based nuclear explosion monitoring (GNEM). Seismic yield estimation is an important function of their GNEM mission. Problems facing accurate yield estimation have new challenges due to (a) inherent difficulties monitoring broad areas, and (b) different approaches to testing taken by today's proliferant nations. A common thread in all of these challenges is greater uncertainty posed by unknowns surrounding geologic conditions of the source and uncertainty in the regional propagation effects. In the past, improvements in yield estimation for known test sites could be made through research that exploited empirical calibrations better. But today a proliferant nation by definition will not have tested many (or any) nuclear explosives. There is a great need to improve our yield estimation capabilities by developing a stronger physical basis for traditional and emerging methods. This includes and requires better understanding of how earth materials behave in the strong shock environment and how this behavior affects the propagated seismic wave field. These improved material models, implemented in numerical simulations of nuclear tests, will fill the gaps in our observationally based empirical models and, in doing so, make better quantification of error bounds and better corrections to yield estimates when information about source emplacement and geologic conditions is available.

Many data, analysis, and numerical simulation products coming out of N-SPEs will be integrated into a new explosion source model framework with the ultimate goal being a Source Prediction Capability for global monitoring applications (Figure 6). These experiments will also serve as the foundation for future efforts, including: the effect of different rock types at and near the source and along the propagation path, the range of energy densities and how this affects both containment prospects and detection probabilities, the effect of cavity geometry, explosive source equation of state and burn rate, and near-source phenomenology (including seismic wave conversion).

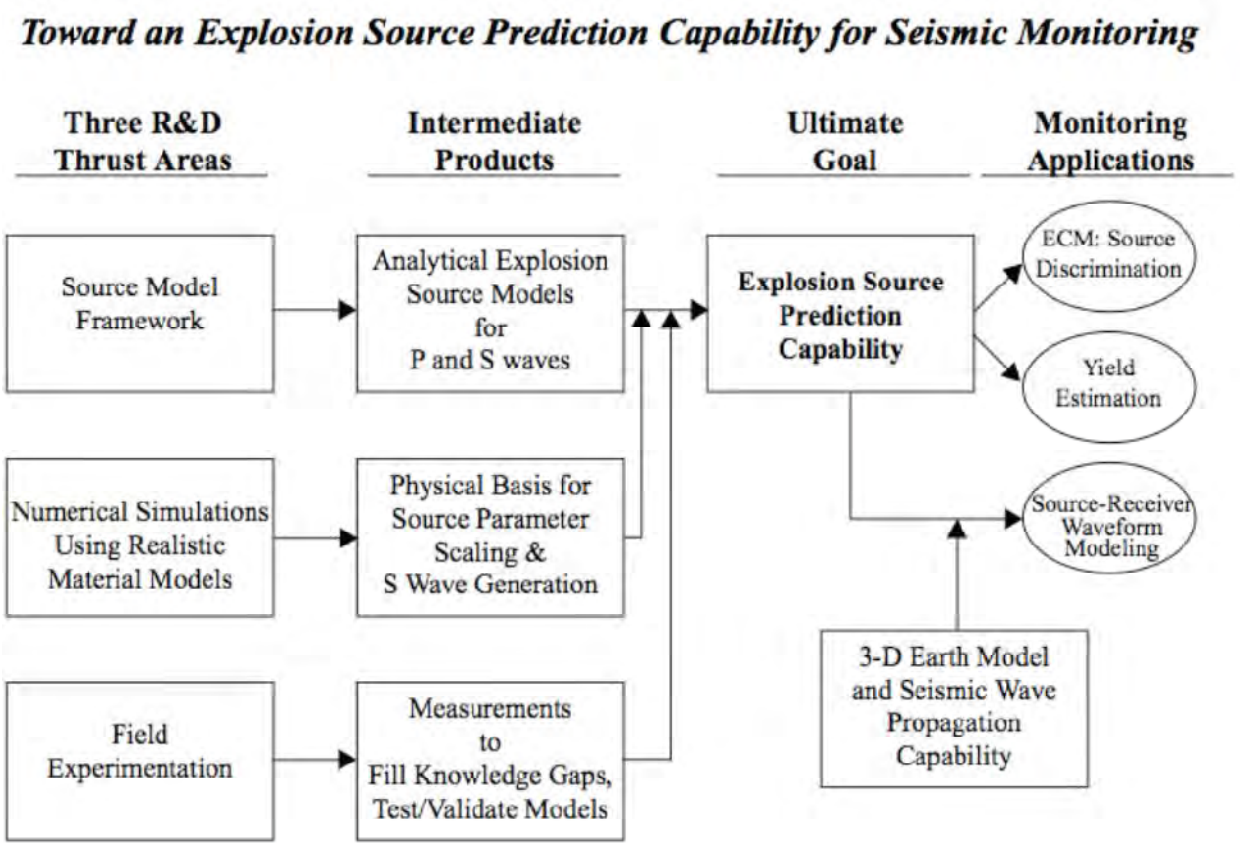

Figure 6. Source model development integrating data, analysis, and numerical simulation products resulting in an Explosion Source Prediction Capability for global monitoring applications including event identification, yield estimation, and end-to-end modeling for special event analysis.

CONCLUSIONS AND RECOMMENDATIONS

The execution, data collection and analysis, and modeling of the NTS Source Physics Experiments will produce results that will lead to significant improvements and breakthroughs in our capabilities and understanding in several areas:

- The experiments will provide valuable information about the expected detection threshold for events in hard rock with a number of monitoring technologies, utilized both separately and in combination, including seismoacoustic, radionuclide, geodetic, imaging, and electromagnetic methods.
- We will gain valuable experience in how to design and field sensors and sensor arrays, collect, process and analyze sensor data, and optimize the deployment and placement of sensors under a variety of conditions. It is expected that novel sensor technologies as well as modeling and signal processing techniques will be developed. Forensic analysis of all the signals will lead to a probabilistic approach to our capabilities and confidence in the event detection and discrimination.
- These experiments could serve to develop cost effective experimental designs for explosion monitoring and proliferation detection data acquisition. Over 20 years of proliferation and explosion monitoring research has led to scientific questions on theory and model development/validation that are best resolved with well designed experiments. Experimental cost efficiencies can only be realized with well-designed experimental campaigns that have multiple uses and are based on proven statistical experimental design theories. Properly applied, these theories target an experimental campaign to relevant research questions through a mathematical down select of less relevant questions.
- Development of greatly improved weapons effects modeling capabilities will be based on a better physical understanding of the behavior of explosives, rock, and man-made structures. Gaps in current datasets will

be filled in to provide a basis for dimensional analysis of the effects of: source size and geometry, burn rates, energy density, geologic setting, signal generation and propagation paths such that predictive capability can be improved for events in different geologic scenarios with varying sources, yields, and emplacement geometries. In particular, our plan to evaluate the modulating effects of the ambient tectonic stresses, inherited geologic features, and the effects of topography-induced anisotropic responses to shock propagation, will improve detection capabilities for any potential proliferant nations' test sites.

- In the absence of dynamic experimentation for stockpile stewardship, these experiments will also serve to continue improving our understanding of containing underground explosions with a rather unique approach to testing our numerical predictions, fielding of newer sensors and materials, and provide valuable first-hand experience for containment science.
- OSI is one of the critical verification elements for the CTBT. The challenge of OSI is to detect, identify, and describe features that may indicate that a nuclear explosion in violation of the CTBT has occurred. Experiments to investigate and validate near-field monitoring and OSI techniques will greatly enhance the understanding of the efficacy of these techniques.

ACKNOWLEDGEMENTS

Large field activities like the Source Physics Experiment require the cooperation of individuals from many organizations. We thank each of the team members for contributing their particular expertise to make the N-SPE benefit multiple objectives with each explosive shot.

REFERENCES

Symposium on the Non-Proliferation Experiment: Results and Implications for Test Ban Treaties, CONF-9404100, (1994), https://na22.nnsa.doe.gov/cgi-bin/prod/nemre/index.cgi?Page=Symposium+1994

Garwin, R. L., and F. N. von Hippel (2006). A Technical Analysis of North Korea's Oct. 9 Nuclear Test, Arms Control Today, November 2006.

Garbin, H.D. (1997). Diamond Fortune Seismic Attenuation Measurements, Sandia National Laboratory Report, SAND96-2544 UC-703.

National Academy of Sciences (2002). Technical Issues Related to the Comprehensive Nuclear Test-Ban-Treaty, *National Academy Press*, 2101 Constitution Avenue, N.W. Washington, D.C. 20418.

U.S. Congress, Office of Technology Assessment (1988). Seismic Verification of Nuclear Testing Treaties, OTA-ISC-361 (Washington, DC: U.S. Government Printing Office, May 1988).

Karlykhanov, N.G., et al., (2004). Magnetic Dipole Moment from a One-kiloton Underground Nuclear Explosion in a Cavity, J. *Appl. Mech. Tech. Phys*. 45: No. 3, 311–315.

Richards, P.G. and W. Kim, (2009) Monitoring for Nuclear Explosions, *Scientific American*, March 2009, Vol. 300, no 3, pp 64–71.

Yang, X. and J. L. Bonner, 2009 Characteristics of Chemical Explosive Sources from Time-Dependent Moment Tensors, *Bull. Seismol. Soc. Am*. 99: No. 1, pp. 36–51.

IDENTIFYING ISOTROPIC EVENTS USING A REGIONAL MOMENT TENSOR INVERSION TECHNIQUE

Douglas S. Dreger[1], Sean R. Ford[2], and William R. Walter[2]

Berkeley Seismological Laboratory[1] and Lawrence Livermore National Laboratory[2]

Sponsored by the National Nuclear Security Administration and the Air Force Research Laboratory

Award Nos. DE-FC52-06NA27324[1], FA9453-10-C-0263[1], and DE-FC52-07NA27344[2]
Proposal Nos. BAA06-42 and BAA10-76

ABSTRACT

We developed a regional distance seismic moment tensor inversion procedure, and a method for the evaluation of uncertainties that considers random errors, and systematic uncertainty due to assumed velocity model and the network coverage. The method provides a tool for the *a priori* evaluation of inversion capabilities for source-type identification and discrimination given a fixed recording network. In addition, the method allows for the determination of how recording networks can be optimized to improve source-type identification capability. In one study the deviatoric and isotropic source components for 17 explosions at the Nevada Test Site (NTS), as well as 12 earthquakes and 4 collapses in the surrounding region of the western US, were calculated using a regional time-domain full waveform inversion for the complete moment tensor (Dreger et al., 2008; Ford et al., 2008; Ford et al., 2009). The events separate into specific populations according to their deviation from a pure double-couple and ratio of isotropic to deviatoric energy. The separation allows for anomalous event identification and discrimination between explosions, earthquakes, and collapses. Confidence regions of the model parameters are estimated from the data misfit by assuming normally distributed parameter values. We developed a new Network Sensitivity Solution (NSS) in which the fit of sources distributed over a source-type plot (Hudson et al., 1989) show the resolution of the source parameters (Ford et al., 2010). The NSS takes into account the unique station distribution, frequency band, and signal-to-noise ratio of a given event scenario. The NSS compares both a hypothetical pure source (for example an explosion or an earthquake) and the actual data with several thousand sets of synthetic data from a uniform distribution of all possible sources. The comparison with a hypothetical pure source provides the theoretically best-constrained source-type region for a given set of stations, and with it one can determine whether further analysis with the data is warranted. We apply the NSS to a NTS nuclear explosion, and earthquake, the 1998 India nuclear test, as well as the 2006 and 2009 North Korean nuclear tests, and a nearby earthquake. The results show that explosions and earthquakes are distinguishable, however the solution space depends strongly on the station coverage. The NSS results for the 1998 India test classify it as anomalous but not to the same degree as found for the NTS and Korean cases. Large F-factor events such as the 1998 India test present additional challenges, however capability to discriminate would likely be improved with additional station coverage. Ongoing work will apply and refine these techniques using data from the Korean Peninsula, Kazakhstan, Middle East and the European Arctic.

OBJECTIVES

In contract DE-FC52-06NA27324 we examined the application of the time-domain full-waveform inversion of regional data for the complete moment tensor for source-type identification and discrimination (Dreger et al., 2008; Ford et al., 2008; Ford et al., 2009) and to develop a method of assessing uncertainty in solutions due to the recording geometry (Ford et al. 2010). By means of forward calculations the fit of thousands of possible moment tensor solutions, distributed over a Hudson et al. (1989) source-type plot, the classification of a given seismic event in terms of double-couple, non-double-couple, and isotropic components can be more thoroughly examined (Ford et al. 2010). Direct comparisons between the fit of such mechanisms can greatly aide in the classification of event type, and importantly present it in a manner that allows for the assessment of solution resolution and uncertainty in terms of station geometry. This contract has been completed.

In our new contract FA9453-10-C-0263 we build on our earlier results (DE-FC52-06NA27324, Dreger et al., 2008; Ford et al., 2010; Ford et al., 2009; Ford et al., 2008) to investigate whether source-type populations (explosion, collapse, earthquakes) that were found to be separated on a source-type plot for the Western US remain separated for other regions of the world. We will expand the database of studied invents to include natural and man-made seismicity from the Korean Peninsula, Kazakhstan, Middle East, and European Arctic. In each region we apply regional distance seismic moment tensor analysis, investigating aleatoric and epistemic (velocity model and network configuration) uncertainties. This regional characterization is a necessary first step toward developing a decision basis for utilizing moment tensor results for source-type identification and discrimination. In addition, we present results comparing different data windowing and component goodness of fit weighting strategies using the network sensitivity solution (NSS) framework (Ford et al., 2010) to improve the separation of event type, and to reduce tradeoff between non-double-couple solutions as represented on a source-type plot. Analysis procedures will be developed with synthetic cases and then applied to studied events.

RESEARCH ACCOMPLISHED

Introduction

Ford et al. (2009) calculated seismic moment tensors for 17 nuclear test explosions, 12 earthquakes, and 3 collapses in the vicinity of the Nevada Test Site in the Western US. They found that the relative amount of isotropic and deviatoric moment provided a good discriminant between the explosions and earthquakes. The observational work to describe the discriminant was accompanied by a theoretical study into the sensitivities of the method and it was found that the ability to resolve a well-constrained solution is dependent on station configuration, data bandwidth, and signal-to-noise ratio (SNR). It is difficult to state steadfast rules for what source-types can be resolved for all conditions, when different conditions lead to different levels of confidence in the solution. Therefore, in this study we develop a confidence analysis specific to the source type, station configuration and data SNR, which we call the NSS.

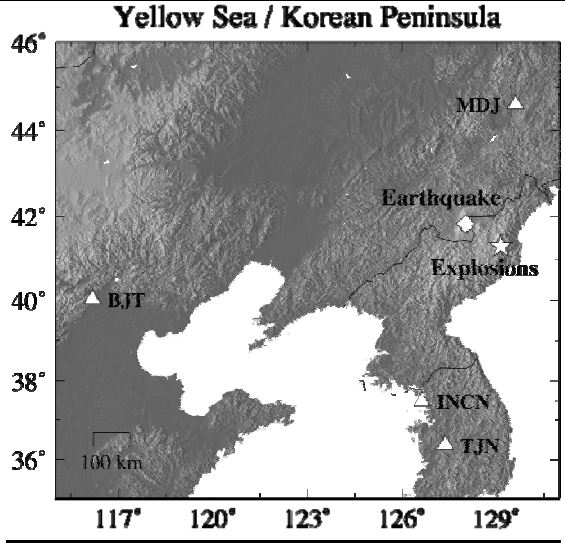

Figure 1. Map of the Yellow Sea / Korean Peninsula with the North Korea tests (5-point star) and nearby earthquake (diamond) as well as the stations used in their analysis (triangles).

There have been many attempts to understand error in seismic moment tensor inversions. Sileny and coathors have done extensive sensitivity testing of the methods they use to calculate the moment tensor. Sileny et al. (1992; 1994), Sileny (1998), Jechumtalova and Sileny (2001), Sileny and Vavrycuk (2002), and Sileny (2004) have collectively investigated the effects of incorrect event depth, poor knowledge of the structural model including anisotropy, noise, and station configuration on the retrieved solution. They found that for only a few stations with data of SNR>5 the moments of various components were sensitive to improper source depth and velocity model, but that the mechanism remained robust, and that spurious isotropic components may manifest in the solution if an isotropic medium assumption is made incorrectly. Roessler et al. (2007) confirm this last result. The probabilistic inversion method by Weber (2006) using near-field full-waveform data helped to inspire the approach taken in this study. Weber (2006) inverts for hundreds of sources using a distribution of hypocentral location based on *a priori* information.

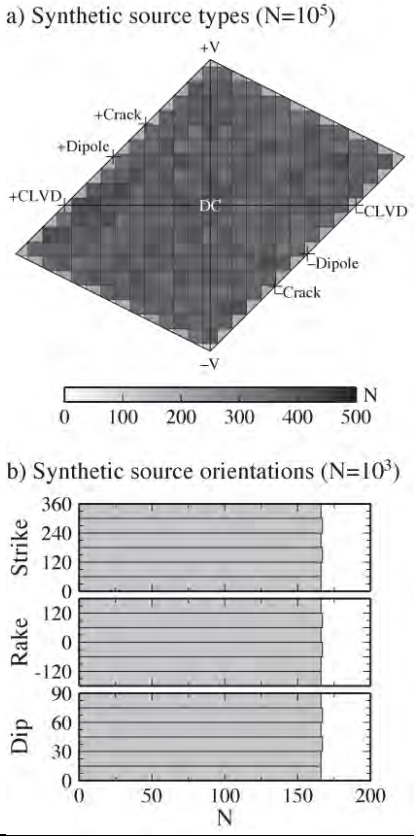

Figure 2. Synthetic sources. a) Source-type plot of synthetic source distribution. Gray scale gives the 0.1-unit smoothed number of events, and the white box outlines the sources described in b). b) Parameters of the synthetic sources contained in the white box in b).

Perturbations to the velocity model and noise are also added in the synthetic portion of the study. Empirical parameter distributions are then produced to assess the resolution. Mechanism distribution is plotted with a Riedesel and Jordan (1989) plot, which is also the preference of many of the previously mentioned studies. In the following study we will employ the source-type plot from Hudson et al. (1989), which is described in Ford et al. (2009). Further details of the inversion method and its practical implementation are also given in Ford et al. (2009).

Network Sensitivity Solutions (NSS)

The theoretical NSS tries to answer the question of how well a pure earthquake or explosion can be resolved with very high SNR data for the given event scenario (i.e., data bandwidth and station distribution). To do this we use the GFs to first produce data for a model event (earthquake or explosion) as well as a uniform distribution of synthetic sources representing all possible sources, where the moment of these sources is chosen so as to best fit the model event data. The source-type parameters (Hudson et al., 1989) are calculated for each of the thousands of synthetic sources (Figure 2a). Since the source-type plot does not account for total seismic moment (only relative moment) or source orientation, a single set of source-type parameters (one point on the source-type plot) can represent several sources. For example, a DC source with any strike, rake, or dip, will plot in the center of the source-type plot (Figure 2b). However, as one moves away from the center of the source-type plot (location of a DC mechanism), source orientation becomes less important to the seismic radiation so that the top and bottom of the plot are uniquely represented by an explosion or implosion, respectively.

The model event data d is then compared with the synthetic source data s and the fit for each comparison is quantified by the variance reduction VR

$$\mathrm{VR} = \left[1 - \frac{\sum_i (d_i - s_i)^2}{\sum_i d_i^2} \right] \times 100 \,. \quad (1)$$

where *i* are the displacements at all times for all components at all stations.

The VR for each synthetic source is calculated and plotted as a function of source-type parameter on the source-type plot. Since a single set of source-type parameters can represent many sources that could have varying levels of fit to the model event data (and therefore, VR), a moving-maximum window is used to smooth the VR distribution. The source-type plot empirical VR distributions are shown in Figure 2 for a small earthquake located in southeast China.

NSS for a Southeast China Earthquake

Figure 3 gives the theoretical and actual NSSs for the earthquake in China, as well as the waveforms for the data, Best-fit, Example, and Explosion models for comparison. The actual NSS for the earthquake (Figure 3b) shows a well-constrained region similar to the theoretical NSS (Figure 3a). The waveforms of the best-fit model (VR = 67%), shown in Figure 3c, fit the data just as well as a pure DC. This result gives us confidence that the MDJ2 model is a good 1-D approximation of the velocity structure in this region, as the expectation is that the small earthquake should be well represented by a double-couple point-source. Importantly, the analysis also shows that a pure explosion fails to fit the data yielding a best fit variance reduction of only 13%.

2006 North Korean Nuclear Test

The solution for the October 2006 explosion in North Korea is much less constrained than the Chinese earthquake due to the simpler radiation pattern. Normally, we would run the inversion without station BJT because the epicentral distance is more than 1000 km and performance of the simpler 1-D velocity model employed here degrades at such great distances. However, preliminary inspection of the theoretical NSS without BJT showed that the solution could not satisfactorily exclude DC sources. Although this understanding could be gained from simple inspection of the station configuration shown in Figure 1b, where without BJT all stations fall along one azimuth with π periodicity (a condition that can always fit the two-lobed Rayleigh radiation pattern of a 45-degree dip-slip mechanism), the example is still instructive for cases that are not so easily visually inspected. With station BJT, the high VR region has the shape typical of NTS events, illustrating the tradeoff between isotropic and vertical, compressive CLVD sources (e.g. Ford et al., 2010).

The addition of station BJT presents some additional problems for the actual NSS (Figure 4b). BJT is more than 1100 km away from the source, yet the displacement (2.24e-05 cm) is larger than that of station MDJ (2.04e-05 cm), which is only 371 km from the source. The usual method of weighting the data as a function of inverse distance caused the data from BJT to dominate the inversion, since there is only one station at this very great distance. As a corrective measure, we decreased the weight of data from BJT and produced the actual NSS in Figure 4b. As was stated in the discussion of the theoretical NSS, BJT is instrumental in constraining the source to be non-DC. Figure 4c shows that the Best DC model does not produce the observed Rayleigh amplitudes at BJT. Further, there is added confidence that the source is dominantly explosive because the Example mechanism, which fits the waveforms at a VR that is 3% less than the Best-fit model, produces a Love wave that is not observed at MDJ (Figure 4c).

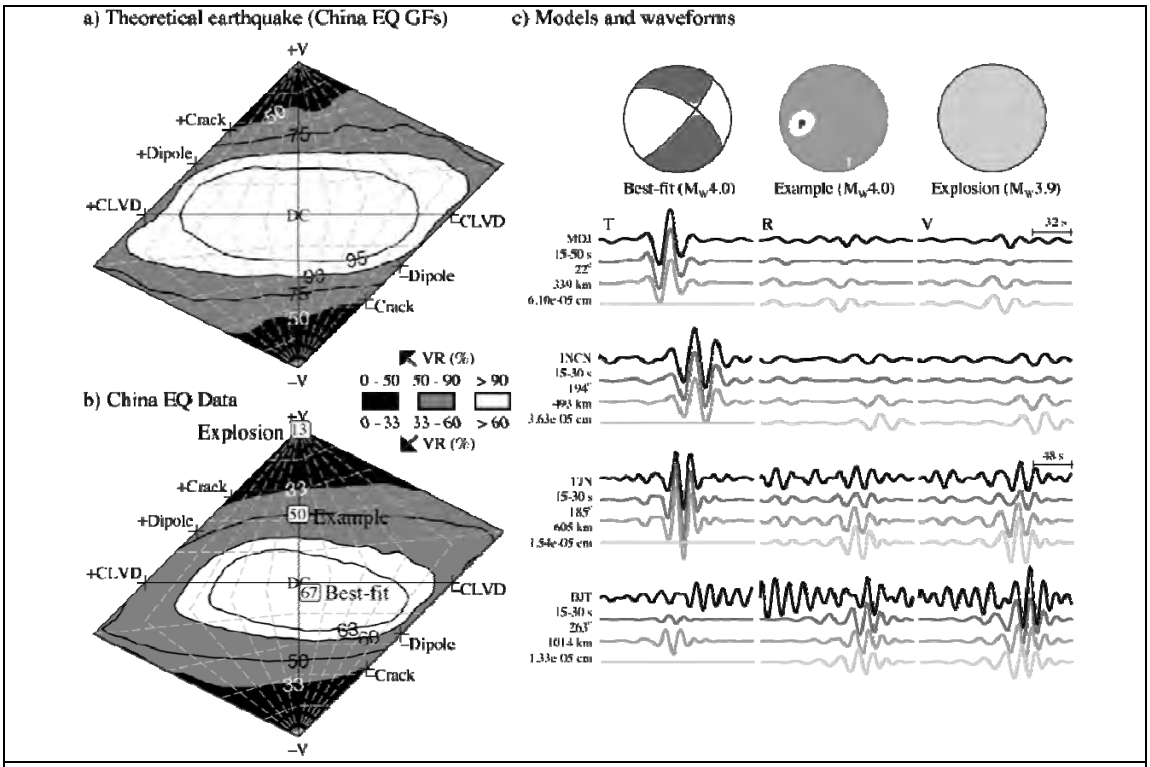

Figure 3. NSS for an earthquake (16 Dec 04) near the 2006 North Korea test location. a) Theoretical NSS using one hundred earthquakes with a uniform distribution of fault parameters where the Green's function is derived from the actual network setup and the data is noiseless. The best-fit model is a pure double-couple (DC) with a VR of 100%. Empirical distributions of other models and the corresponding VR are also given via contours on the source-type plot. b) Actual NSS using data from the China earthquake. The best-fit model with a VR of 67% along with other models and the corresponding VR distributions are shown. For comparison, an Example model (VR = 50%) and a pure Explosion model (VR = 13%) are also plotted and correspond with the models and waveforms given in c). c) Models corresponding to those plotted in b) and their respective forward-predicted waveforms as a function of color compared with the actual waveforms (black line). The left, middle, and right columns are the tangential (T), radial (R), and vertical (V) displacement waveforms, respectively. The text block to the left of the waveforms gives the station name, passband period (s), azimuth, epicentral distance (km), and maximum displacement (cm). The moment magnitudes of the models are also given below the mechanism.

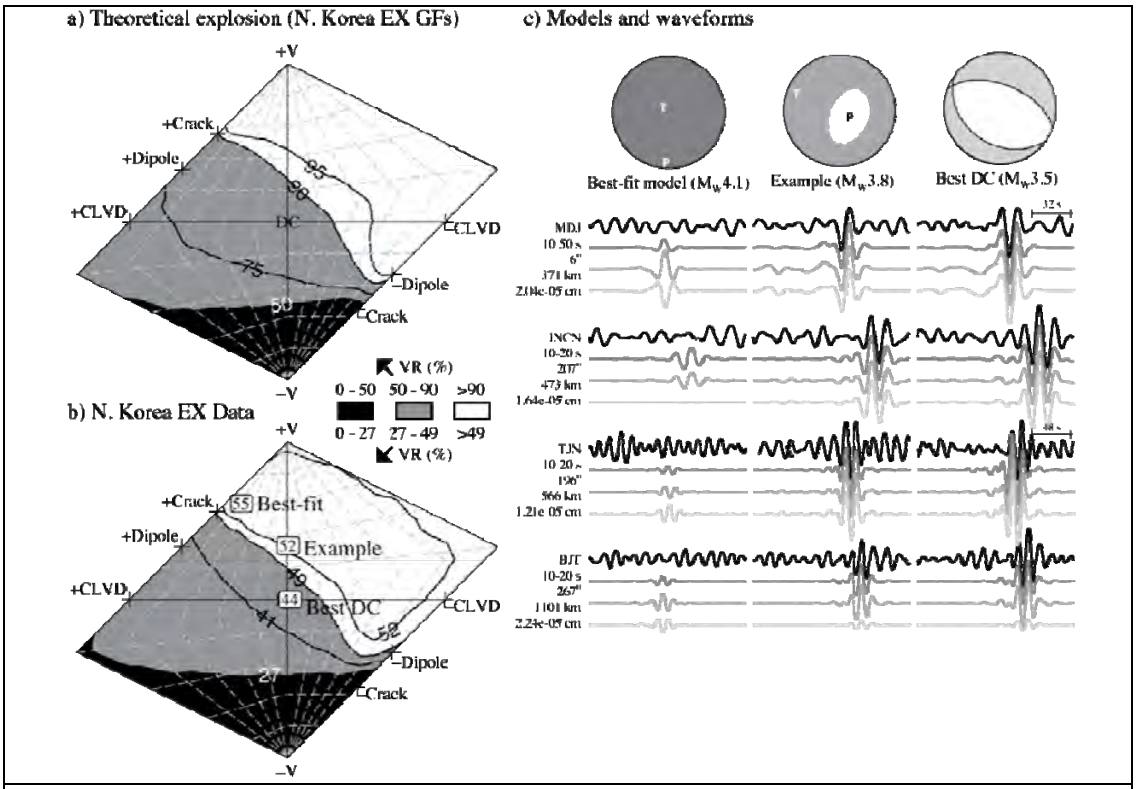

Figure 4. NSS for the first North Korea test (9 Oct 06, m_b4.2). a) Theoretical NSS for an explosion where the Green's functions are derived from the actual network setup and the data is noiseless. The best-fit model is an explosion with a VR of 100%. Empirical distributions of models and their corresponding VR are also given via contours on the source-type plot. b) Actual NSS using data from the North Korea test. The best-fit model with a VR of 55% along with other models and the corresponding VR distributions is shown similar to a). For comparison, an Example (VR = 52%) and a Best DC model (VR = 44%) are also plotted and correspond with the models and waveforms in c). c) Models corresponding to those plotted in b) and their respective forward-predicted waveforms as a function of color compared with the actual waveforms (black line). The left, middle, and right columns are the tangential (T), radial (R), and vertical (V) displacement waveforms, respectively. The text block to the left of the waveforms gives the station name, passband period (s), azimuth, epicentral distance (km), and maximum displacement (cm). The moment magnitudes of the models are also given below the mechanism.

2009 North Korean Test

The source type plot shown in Figure 5b shows that for Western US seismicity and NTS explosions that the two populations separate (Ford et al., 2009). The rectangles compare the solutions for the 2009 North Korean test were the number refers to the level of fit measured by a variance reduction. The fit to the waveforms for the corresponding source types is given in Figure 5a.

The pure explosion model for the 2009 test is able to fit the waveforms with a variance reduction of 75% and yields an isotropic moment of 1.8e22 dyne-cm (M_W4.1; all seismic moment values are calculated with the method of Bowers and Hudson, 1999). In contrast, the pure DC solution fits the data much worse at 52% with M_0 = 3.8e22 dyne-cm (M_W4.4). The fact that the single degree of freedom explosion model fits so much better than the four degree of freedom DC model is highly significant and indicates that such a comparison can be a useful discriminant. The strike, rake, and dip of the best-fit DC is 50°, -85°, and 10°.

Such a steep dip-slip mechanism is very rare and of all sources calculated by the Global CMT Project (globalcmt.org) less than 1.6% have dips less than 10°. This type of information can be used as an additional flag for anomalous sources. The differences in the fits between explosion (Best-iso) and DC (Best-DC) sources (Figure 5a) shows that the DC overpredicts the Love wave amplitude at almost all stations and underpredicts the Rayleigh wave amplitudes, especially at station INCN.

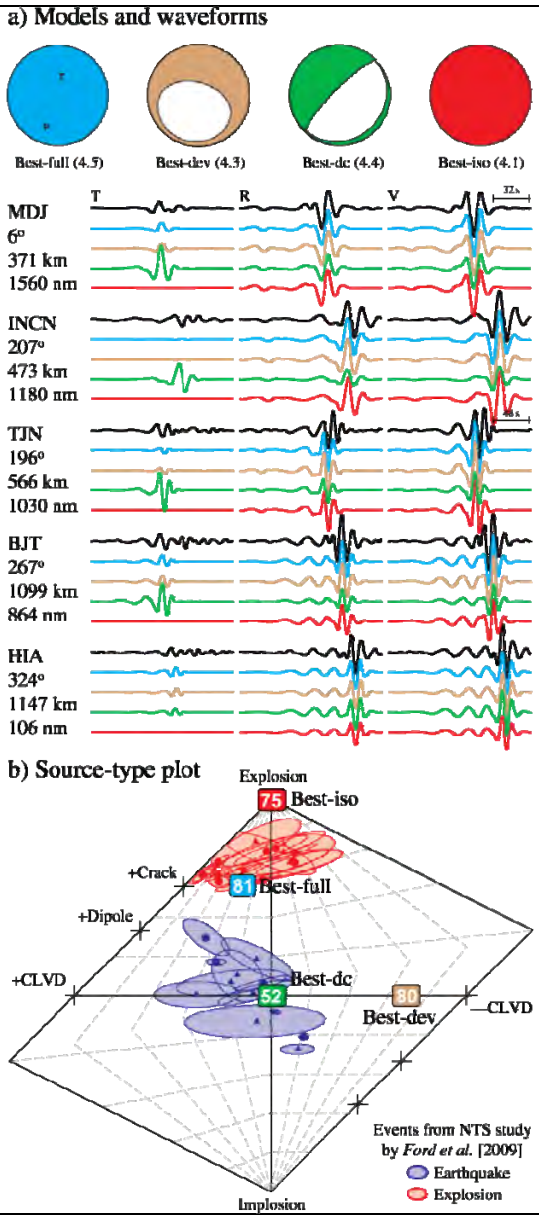

Figure 5. Source analysis of the Memorial Day Explosion, Kimchaek, North Korea (25 May 2009). Figure 1 shows the location of the event. a) Waveform fit for various source models. b) The level of fit (variance reduction) for the models in (a) are given in color-coded squares. These solutions are compared to populations of explosions and earthquakes for the Western US and Nevada Test Site (NTS) from Ford et al. (2009).

The full moment tensor inversion fits the data at 81% and yields an isotropic moment of 3.6e22 dyne-cm, and a total moment of 6.3e22 dyne-cm (M_W4.5). The deviatoric moment tensor inversion fits the data at 80% and a total moment of 3.2e22 dyne-cm (M_W4.3). If the deviatoric source is decomposed to a compensated linear vector dipole (CLVD; Knopoff and Randall, 1970) and DC sharing the same principal axes, then the source is 70% CLVD. The similarity in fits between the dominantly CLVD deviatoric source and dominantly isotropic full moment tensor shows that at shallow depths, a vertical CLVD mechanism can effectively mimic an explosion at the distances and periods analyzed here. This can be seen in the waveform comparison in Figure 5a. The full moment tensor isotropic moment is two times larger than the pure explosion indicating that the compound source of the full moment tensor solution (DC+CLVD+Isotropic) required to fit the Love waves also modifies the Rayleigh waves causing the isotropic component to increase to compensate. Some non-isotropic radiation is required to fit the observed Love waves as can be seen on the tangential component waveforms in Figure 5a.

Continuing Work

During FY2010-2011 we will continue to refine our methods, and apply them in other regions. This coming year we will investigate seismicity on the Korean Peninsula, and in Kazakhstan. Next year the analyses will focus on the Middle East and European Arctic regions. As part of this research we will further refine the NSS method for improved source-type identification and characterization of aleatoric and epistemic uncertainty. We will also investigate damped moment tensor techniques designed to stabilize inversions for shallow sources and to correct for free-surface vanishing-traction bias in moment tensor inversion results.

CONCLUSIONS AND RECOMMENDATIONS

Confidence in best-fit solutions for regional full-waveform moment tensor inversions is dependent on station configuration, data bandwidth, and signal-to-noise ratio (SNR). The best way to characterize that dependence is on a case-by-case basis, where each individual event scenario is analyzed. The network sensitivity solution (NSS) attempts to do this characterization and is introduced and implemented in this report for the Oct 06 North Korea test, a nearby earthquake in China, and the May 09 North Korea test. A more complete description of the method is presented in Ford et al. 2010. The theoretical network sensitivity solution provides solution confidence regions for ideal models (explosion or earthquake) with high SNR data. With this type of network sensitivity solution, one can learn if the station configuration and bandwidth is sufficient to resolve a given model. The actual network sensitivity solution assesses confidence using the actual data from the event. Goodness-of-fit for each model is parameterized with a percent variance reduction (VR), where the complete VR space can be mapped out on a source-type plot and the well-fit region of solutions is defined by a chosen threshold VR.

The theoretical network sensitivity solutions for the North Korea tests show a trade-off between CLVD and explosion, but the well-fit solution space is separated from a double-couple, indicating that an anomalous event can be resolved. In the case of the North Korea tests, a specific configuration using the very distant station BJT is required to rule out a DC solution. With some additional data weighting, the actual network sensitivity solution of the North Korea test also shows a tight region of well-fit solutions clustered between an opening crack and an explosion, though with the addition of just one more imaginary station, this region is made much smaller (Ford et al., 2010). The network sensitivity solutions for the earthquake in China provide high confidence in the best-fit solution, which is indistinguishable for a double-couple.

Modeling of low-frequency, regional distance waveforms identifies the 2009 event as primarily an explosion source. Comparison of pure explosion and pure double-couple models indicate that the simpler explosion model fits the waveform data substantially better than the higher degree of freedom double-couple model. While the source type is well determined, the isotropic moment of the full moment tensor inversion has some uncertainty and the M_W is between 4.4 and 4.6. The preferred scalar moment for the event is the isotropic moment of 1.8e+22 dyne-cm (M_W 4.1) of the pure explosion case. However, there are Love waves observed at several stations indicating that the source must have some non-isotropic component. This component could have been present in the previous 2006 test, but was masked by the noise.

ACKNOWLEDGEMENTS

We thank Bruce Julian for scripts to make the source-type plots.

REFERENCES

Bowers, D. and J. A. Hudson (1999). Defining the scalar moment of a seismic source with a general moment tensor, *Bull. Seismol. Soc. Am*. 89: (5), 1390–1394.

Dreger, D. S. , S. R. Ford, and W. R. Walter (2008). Source Analysis of the Crandall Canyon, Utah, Mine Collapse, *Science,* VOL 321, 217.

Ford, S., D. Dreger and W. Walter (2008). Source Characterization of the August 6, 2007 Crandall Canyon Mine Seismic Event in Central Utah, *Seism. Res. Lett*., 79, 637-644.

Ford, S. R., D. S. Dreger and W. R. Walter (2009). Identifying isotropic events using a regional moment tensor inversion, *J. Geophys. Res*., 114, B01306, doi:10.1029/2008JB005743.

Ford, S. R., D. S. Dreger and W. R. Walter (2010). Network sensitivity solutions for regional moment tensor inversions, *In Press Bull. Seismol. Soc. Am.*

Hudson, J. A., R. G. Pearce, R. G., and R. M. Rogers (1989). Source type plot for inversion of the moment tensor, *J. Geophys. Res*. 9: (B1), 765–774.

Jechumtalova, Z. and J. Sileny (2001). Point-source parameters from noisy waveforms: Error estimate by Monte-Carlo simulation, *Pure Appl. Geophys*. 158: 1639–1654.

Koper, K. D., R. B. Herrmann, and H. M. Benz (2008). Overview of Open Seismic Data from the North Korean Event of 9 October 2006, *Seismol. Res. Lett*., 79 (2), 178-185; doi:10.1785/gssrl.79.2.178.

Knopoff, L. and M. J. Randall (1970). The compensated linear-vector dipole; a possible mechanism for deep earthquakes, *J. Geophys. Res*. 75(26), 4957–4963.

Minson, S., and D. Dreger (2007). Stable inversions for complete moment tensors, Geophys J . Int ., 174, 585–592, doi:10.1111/j.1365-246X.2008.03797.x.

Riedesel, M. and T. H. Jordan (1989). Display and assessment of seismic moment tensors, *Bull. Seismol. Soc. Am*. 79: 85–100.

Sileny, J. (1998). Earthquake source parameters and their confidence regions by a genetic algorithm with a 'memory', *Geophys. J. Inter*. 134: 228–242.

Sileny, J. (2004). Regional moment tensor uncertainty due to mismodeling of the crust, Tectonophysics, 383: 133–147.

Sileny, J., P. Campus, and G. F. Panza (1996). Seismic moment tensor resolution by waveform inversion of a few local noisy records; I, Synthetic tests, *Geophys. J. Inter*. 126: 605–619.

Sileny, J., G. F. Panza, and P. Campus (1992). Waveform inversion for point source moment tensor retrieval with variable hypocentral depth and structural model, Geophysical Journal International, 109, 259–274.

Song, X. J., D. V. Helmberger and L. Zhao (1996). Broad-band modelling of regional seismograms; the basin and range crustal structure, *Geophys. J. Int*. 125: (1), 15–29.

Walter, W. R., K. D. Smith, J. L. O'Boyle, T. F. Hauk, F. Ryall, S. D. Ruppert, S. C. Myers, R. Abbot, and D. A. Dodge (2004). An assembled western United States Dataset for regional seismic analysis, LLNL, UCRL-TR-206630.

Walter, W., E. Matzel, M. Pasyanos, D. Harris, R. Gok, and S. Ford (2007). Empirical Observations of Earthquake-Explosion Discrimination Using P/S Ratios and Implications for the Sources of Explosion S-Waves, in *Proceedings of the 30th Monitoring Research Review: Ground-Based Nuclear Explosion Monitoring Technologies*, LA-UR-07-5613, Vol. 1, pp. 684–693, https://na22.nnsa.doe.gov/prod/researchreview/2007/PAPERS/03-20.PDF.

Weber, Z. (2006). Probabilistic local waveform inversion for moment tensor and hypocentral location, Geophysical Journal International, 165: 607–621.

TOWARD AN EMPIRICALLY-BASED PARAMETRIC EXPLOSION SPECTRAL MODEL

Sean R. Ford[1], William R. Walter[1], Stan D. Ruppert[1], Eric Matzel[1], Terri F. Hauk[1], and Rengin Gok[1]

Lawrence Livermore National Laboratory[1]

Sponsored by the National Nuclear Security Administration

Award No. DE-AC52-07NA27344/LL08-Parametrics-NDD02[1]

ABSTRACT

Small underground nuclear explosions need to be confidently detected and identified in regions of the world where they have never occurred. We are developing a parametric model of the nuclear explosion seismic source spectrum derived from regional phases (*Pn, Pg, Sn, and Lg*) that is compatible with earthquake-based geometrical spreading and attenuation. Earthquake spectra are fit with a generalized version of the Brune spectrum, which is a three-parameter model that describes the long-period level, corner-frequency, and spectral slope at high frequencies. These parameters are then correlated with near-source geology and containment conditions. There is a correlation of high gas-porosity (low strength) with increased spectral slope. However, there are trade-offs between the slope and corner-frequency, which we try to independently constrain using Mueller-Murphy relations and coda-ratio techniques. The relationship between the parametric equations and the geologic and containment conditions will assist in our physical understanding of the nuclear explosion source. The achievable goal of our parametric model development is to be able to predict observed local and regional distance seismic amplitudes for event identification and yield determination in regions with incomplete or no prior history of underground nuclear testing.

OBJECTIVES

We aim to develop a practical explosion source parametric spectral model, based on all available data, that describes nuclear explosion *P*- and *S*-wave source spectra for a variety of geologic and containment conditions. This approach follows the simple earthquake parametric spectral model based on Brune (1970), which is used for the MDAC approach (Walter and Taylor, 2002) to improve earthquake/explosion discrimination. In regions without prior explosions, the parametric model could be combined with earthquake-derived path corrections to predict explosion regional phase amplitudes, improve discriminants such as *P*/*S* ratios, and support identification procedures (e.g., Event Classification Matrix, [ECM]) that explicitly need to use explosion discriminant probability density functions.

It is well known that depth and near-source material properties can affect seismic estimates of explosion yield, and prior work at the Nevada Test Site (NTS) (e.g., Walter et al., 1995) has found that explosions in weak materials have lower corner frequencies and steeper spectral fall-offs for *P*-waves than is predicted by the standard Mueller and Murphy (1971) model. As part of this research, we hope to quantify these effects as a function of frequency and wave type. Additionally, many of the most effective regional discriminants (high-frequency *P*/*S* ratios) make use of *S*-waves, as do *S*-wave coda yield estimation techniques, yet there remain many questions about how to predict explosion *S*-wave amplitudes. The development of a combined *P*- and *S*-wave spectral model consistent with observed regional *P*-and *S*-wave data is a goal of this work.

RESEARCH ACCOMPLISHED

Introduction

In previous work that looked at low to high frequency ratios of regional phase (e.g., *Pn*, *Pg*, *Lg*) amplitudes to separate explosions from earthquakes at NTS, Walter et al. (1995) noted that the results showed a strong dependence on the source media properties. Nuclear tests in weak and/or high gas porosity media tended to have higher values and discriminate better from earthquakes than explosions in stronger and/or lower gas porosity media.

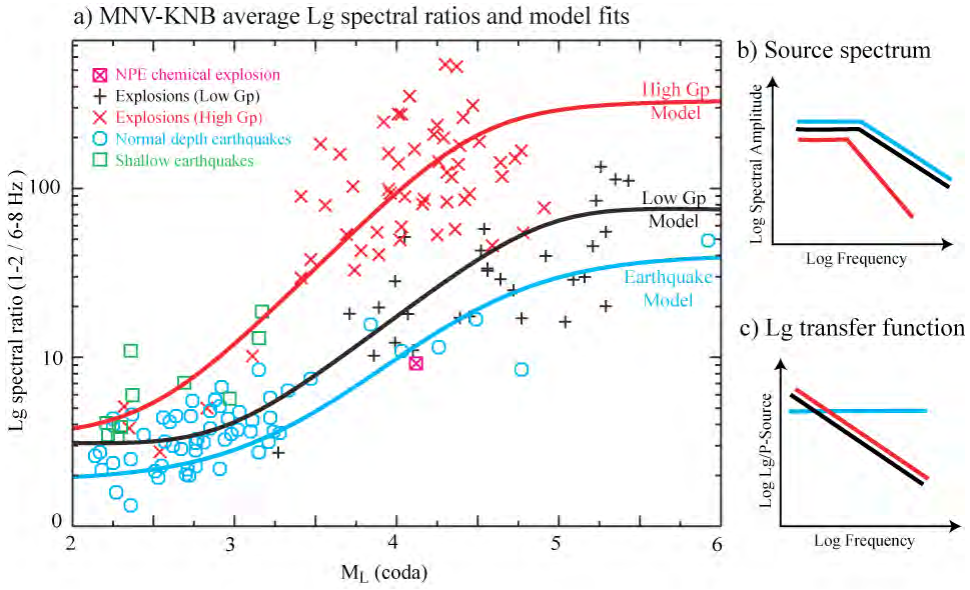

Figure 1. Simple first-order source model fits to low to high frequency spectral ratios of *Lg* amplitudes from Walter et al. (1995, Figure 8). Earthquake displacement spectra are fit with the Brune (1970) model (blue line), which is constant at low frequencies and falls off above a corner frequency as f^{-2}. Explosions are fit with two extremes of the Denny and Goodman (1990) model in order to investigate explosion dependence on emplacement material (namely, gas porosity [*Gp*]). The 'Low *Gp*' model (black line) has an effective fall-off similar to the earthquake model. The 'High *Gp*' model (red line) has a greater fall-off of f^{-3}.

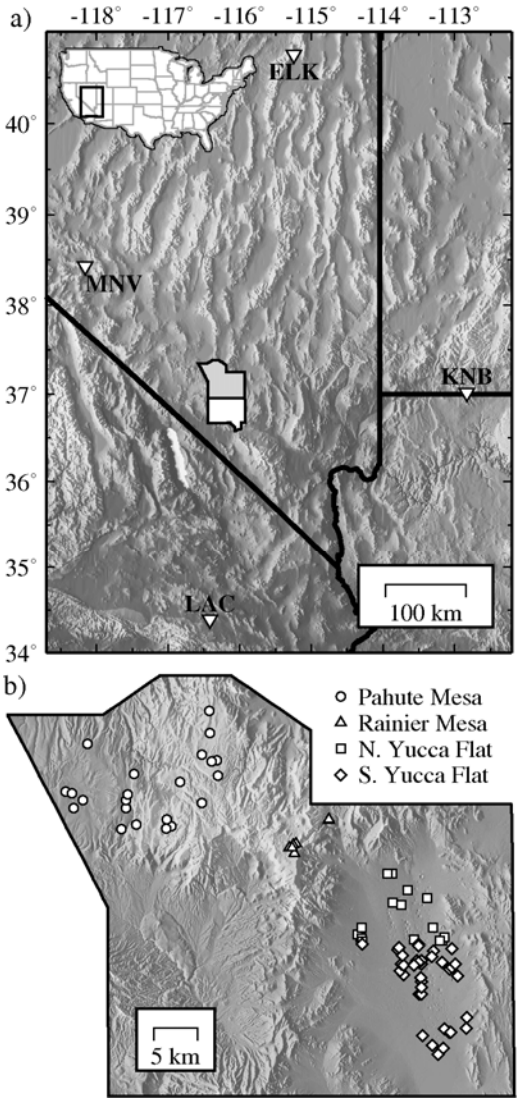

Figure 2. a) Regional map of stations used in the analysis. The location of the map within the continental US is given by the inset map. The NTS is outlined and the shaded section is shown in (b). b) Map of the northern NTS with explosion locations and Vergino and Mensing (1990) area designations.

For example, in Figure 1 the ratio of the *Lg* amplitude at 1–2 Hz compared with the amplitude at 6–8 Hz is shown as a function of magnitude. The earthquakes (blue circles and green squares) show the expected trend with magnitude going from a low value for small events when the corner frequency is above 8 Hz and both measurements are on the constant part of the source spectra that is proportional to moment. For large magnitudes, the source corner frequency drops below 1 Hz and then both measures are on the part of the source spectra that decays with frequency as f^{-2}, resulting in high spectral ratio values. As magnitude increases, the earthquakes follow a sigmoid curve as shown by the blue line, which is based on the Brune (1970) model. The explosions are split into two categories based on the source media, a high gas porosity (*Gp*) and low strength (defined as $\rho\alpha^2$, where ρ is density and α is the local compressional wave speed) group (red x) and low *Gp* high strength group (black crosses), and a clear difference between the two can be seen. In fact, the low *Gp* explosions reach spectral ratio values that imply much steeper falloff than f^{-2}.

To fit the explosion data, we used two extremes of the Denny and Goodman explosion model (1990), which has two corner frequencies. In the low *Gp* case we allowed the second corner to be at a higher frequency than the range of interest, giving an effective f^{-2} falloff. In the high *Gp* case we forced the corners to be the same, giving an f^{-3} falloff. In both cases we used the observed 3 Hz corner frequency of the 1993 Non-Proliferation Experiment (NPE), a kiloton chemical explosion and assumed the corner frequency scales with the cube root of M_L(coda). Given that a pure explosion should not generate *S*-waves, one way to think about the *Lg* spectral ratio is as the product of the *P*-wave source ratio and a transfer function ratio, where the transfer function is a representation of how efficiently the source generated *P*-waves are converted (by whatever means) into *S*-waves. We estimated the transfer function ratio as a function of frequency as shown in Figure 1, and then multiplied the *P*-wave based Denny-Goodman model curves by these factors and then compared them to the *Lg* spectral ratio in Figure 1. The result is a fairly reasonable first order fit to the data. Interestingly, since the explosion *Lg* transfer functions are larger than those for the earthquakes, it shifts the explosion *Lg* spectral ratios to relatively higher values than for the earthquakes, improving the discrimination performance of *Lg* spectral ratios over those of *Pn* alone (Walter et al. 1995, Figure 7).

While in this case, the Denny and Goodman (1990) model provides a reasonable fit to these NTS data, it is not clear how we would make use of it in other regions. Furthermore the limitation of only two choices of high frequency fall-off does not capture the full range of the observations. To develop a practical parametric source spectral model we want to be able to tie parameters like low-frequency level, corner-frequency and fall-off rate to

Table 1. NTS regional attenuation and geometric spreading parameters.

Phase	η	r_0 (km)	Q_0	γ
Pn	1.1	0. 001	210	0. 65
Pg	0.5	1 00	190	0 .45
Lg	0.5	1 00	200	0 .54

measureable properties like yield, depth, and media properties such as gas porosity, water content, and strength. In the next section we take a more general approach to fitting the NTS explosion data with a simple spectral model parameterized by a long-period level, corner-frequency, and high-frequency roll-off. We then relate these parameters for *Pn* spectra to source and medium properties. In the future we will perform similar analyses for *Pg* and *Lg* spectra.

Data and Methods

We employ the NTS explosion dataset of Walter et al. (2004), specifically the raw spectra of that dataset. Waveforms are de-meaned, de-trended and instrument corrected to acceleration. The signal is windowed with a 5% cosine taper that starts before the pick, where the time before the pick is 5% of the total time window. The Fourier transform is calculated and displacement spectra are obtained via double integration in the frequency domain. Finally, the resultant amplitude spectra are interpolated and smoothed to obtain a sampling period of 0.05 $\log_{10}$ Hz.

Spectra of each seismic phase for each explosion are calculated from the recordings of stations of the Livermore NTS Network, ELK (Elko, NV), KNB (Kanab, UT), LAC (Landers, CA), and MNV (Mina, NV). The locations of these stations relative to the NTS are given in Figure 2. These spectra are then corrected for geometrical spreading and regional, frequency-dependent attenuation of the form $Q = Q_0 f^{\gamma}$, where Q_0 is Q at 1 Hz and γ is the power-law dependence on frequency, f. We employ the Street et al. (1975) parametric form of geometrical spreading,

$$G(r) = \begin{cases} r^{-1}, & r < r_0 \\ 1/r_0 (r_0/r)^{\eta}, & r \geq r_0 \end{cases}, \qquad (1)$$

where r_0 is the distance at which the spreading transitions from spherical- to a cylindrical-type spreading and η is the distance dependence. The attenuation and spreading model parameters for each seismic phase are given in Table 1.

We require three of the four stations listed above to have recorded an event with a signal-to-noise ratio greater than two. We also inspect each spectra for non-stationary noise at high-frequency (typically >9 Hz) due to multi-band recording problems and restrict spectral fitting to bands unaffected by problems. The spectra are jointly fit with a simple parametric form given by

$$S(f) = \frac{S_0}{1 + (f/f_c)^{\psi}}, \qquad (2)$$

in a least-squares inversion that also provides standard error for each parameter estimate. Equation (2) describes the

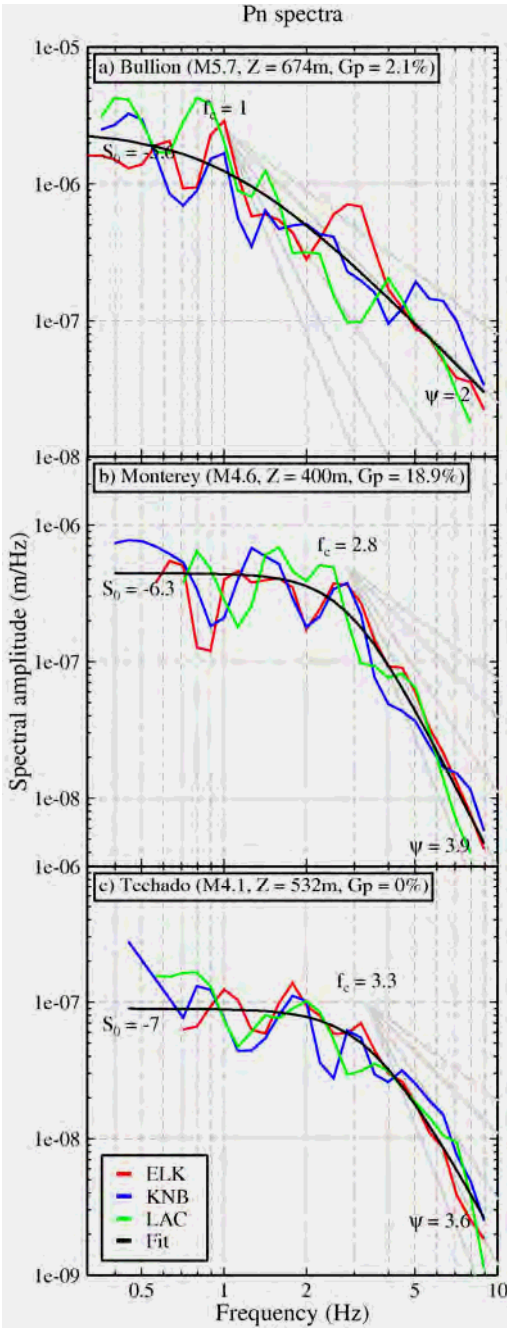

Figure 3. *Pn* spectra examples with the name, magnitude (where $M = m_b[Pn]$), depth (*Z*), and gas porosity (*Gp*) given in the subtitles. The long-period level (S_0), corner-frequency (f_c), and fall-off (ψ) are given in each plot, and the spectra are colored by station and the fit is shown in the legend in the lowermost plot. a) Spectra for an event with low *Gp* and ω^{-2} fall-off. b) Spectra for an event with high *Gp* and high fall-off. c) Spectra for an event with low *Gp* and high fall-off.

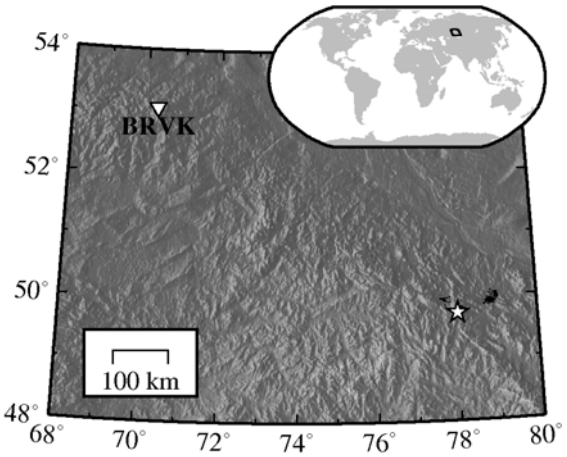

Figure 4. Regional map of station in Borovoye (BRVK) and recorded events in the archive (dots) along with the event shown in Figure 5 (star). The location of the map is given in the inset global map.

simplest behavior expected for seismic spectra. It has a constant level at low frequencies (S_0), which is proportional to static displacement, and falls off at high frequencies with a slope of $f^{-\psi}$ beyond a corner frequency f_c. Examples of the spectra and model fits are proportional to static displacement, and fall off at high frequencies with a slope of $f^{-\psi}$ beyond a corner frequency f_c. Examples of the spectra and model fits are given in Figure 3. BULLION (Figure 3a) is fit well with a standard f^{-2} (ψ=2) spectral fall-off, but MONTEREY (Figure 3b), detonated in weak material, requires a steeper fall-off where the best fit $\psi \approx 4$.

We plan to complement the NTS dataset with the Borovoye (BRV) archive that has recently been deglitched and response functions estimated (Richards and Kim, 2009). This archive could potentially provide 200 recordings of explosions at Semipalatinsk Test Site of the former Soviet Union (Figure 4). As an example, we plot the regional phase spectra of one of the explosions mapped in Figure 4 (shown by a star) in Figure 5. The attenuation and spreading model parameters used to correct these spectra are given in Table 2. The *Pn* and *Pg* spectra are fit with $\psi \approx 3$, whereas *Lg* fall-off is approximately $\psi \approx 2$.

The BRV regional seismic phase spectra, especially *Pn* and *Pg* (Figure 5a-b), show the trade-off in fitting the corner frequency and the roll-off. In this case a slightly smaller f_c would lead perhaps a more appropriate ψ of 2. Attempts to diminish this trade-off will be discussed in the next section.

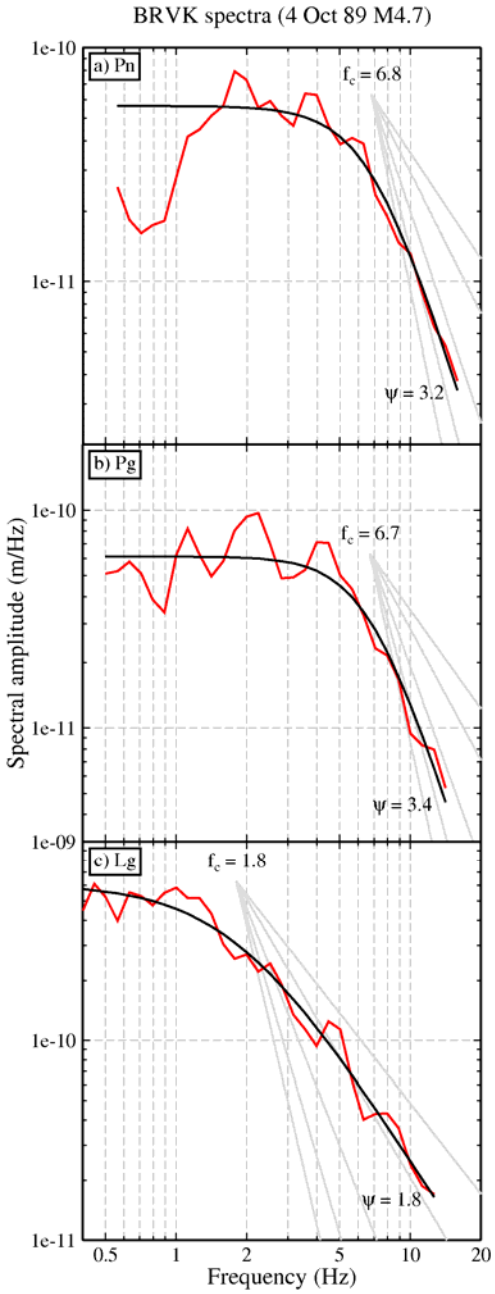

Figure 5. *Pn* spectra of example BRVK event (shown by star in Figure 4). Values given in each plot are defined in Figure 3.

Preliminary results

We present the results of fitting the *Pn* spectra for NTS explosions in Figure 6, where corner-frequency is plotted versus fall-off. There is a correlation between the two estimated parameters that is most probably related to the least-squares fitting of Equation (2) and not to any physical relationship. This trade-off can be seen graphically

Table 2. BRV regional attenuation and geometric spreading parameters

Phase	η	r_0 (km)	Q_0	γ
Pn	1.1	0.001	210	0.65
Pg	0.5	1.00	190	0.45
Lg	0.5	1.00	200	0.54

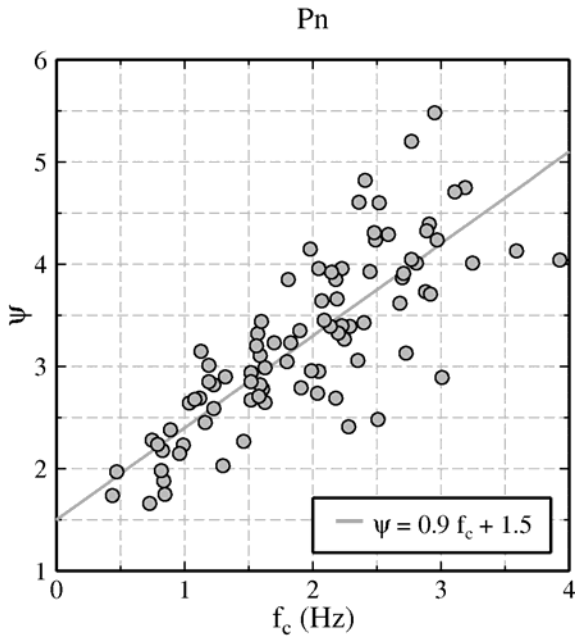

Figure 6. Correlation of estimated source parameters, corner-frequency (f_c) and fall-off (ψ) from Equation (2).

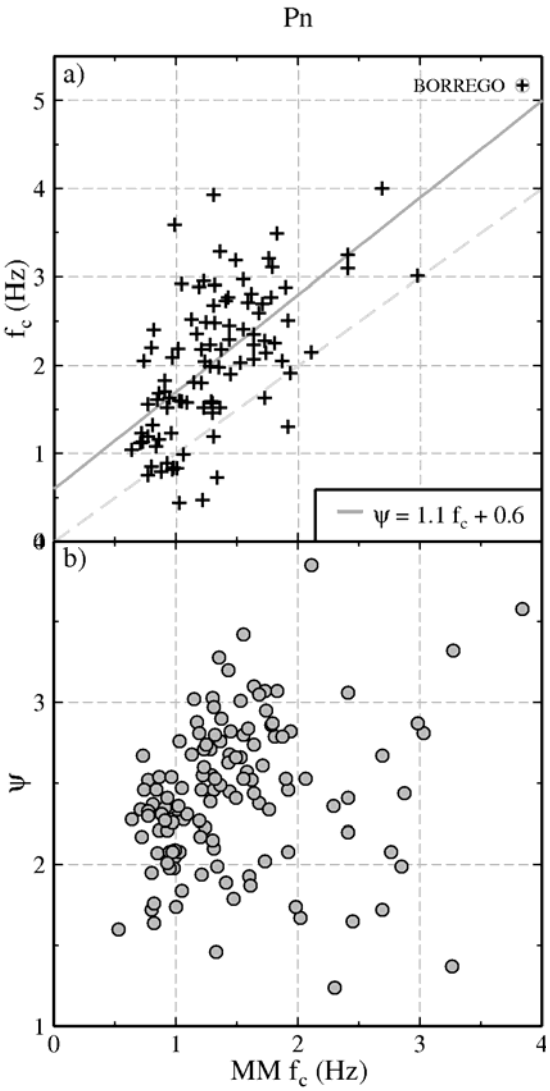

Figure 7. a) Corner-frequency (f_c) from the fits to Equation (2) compared with those predicted by Mueller and Murphy (1971), MM71 f_c. The linear relationship is given by the equation at the top of the plot and the slope is close to one. b) ψ obtained while fixing f_c in Equation (2) to the MM71 f_c. The correlation of the terms is reduced compared with Figure 6.

in the BRV spectra plotted in Figure 5. The trade-off could produce biased estimates of ψ, so we seek to constrain f_c in Equation (2) using the corner frequency predicted by Mueller and Murphy (1971) as parameterized by Stevens and Day (1985) for tuff/rhyolite. Figure 7a shows that the freely-fit f_c is well-correlated with the Mueller and Murphy (1971) predicted corner-frequency (MM f_c) and the slope is close to one. It can be made even closer by decreasing the reference elastic radius used to calculate the proportionality constant used in the Mueller and Murphy (1971) relationship. We set f_c = MM f_c in Equation (2) and estimate ψ. This new ψ is less correlated with MM f_c as shown in Figure 7b.

A least-squares regression of spectral fall-off (ψ) for *Gp* is given in Figure 8a, where the weights are given by the inverse variance of ψ estimated by the inversion. Figure 8b is the same, but uses the estimated ψ while fixing f_c as described previously. We also perform a comprehensive search for material property correlation with ψ, using several regressions on ψ for water content (S_W), gas porosity (*Gp*), density (ρ), compressional wave speed (α), compressional modulus ($\rho\alpha$), strength ($\rho\alpha^2$), depth, depth to water-table, and scaled depth-of-burial (sDOB = depth/yield$^{1/3}$). These geophysical parameters are taken from the database of Springer et al. (2002) and are reported to represent an integrated value over the source region. Yield was inferred from m_b(*Pn*) based on the Vergino and Mensing (1990) relationship at NTS. Using a step-wise regression criteria we found the most significant parameters in a linear regression model to be S_W, *Gp*, and sDOB.

We then perform a least-squares regression using these parameters weighted by the estimated inverse variance of ψ. The model is given by

$$\psi = 2.977 - 4.026Gp + 3.519S_w + 2.81\times10^{-3}\,sDOB\,. \qquad (3)$$

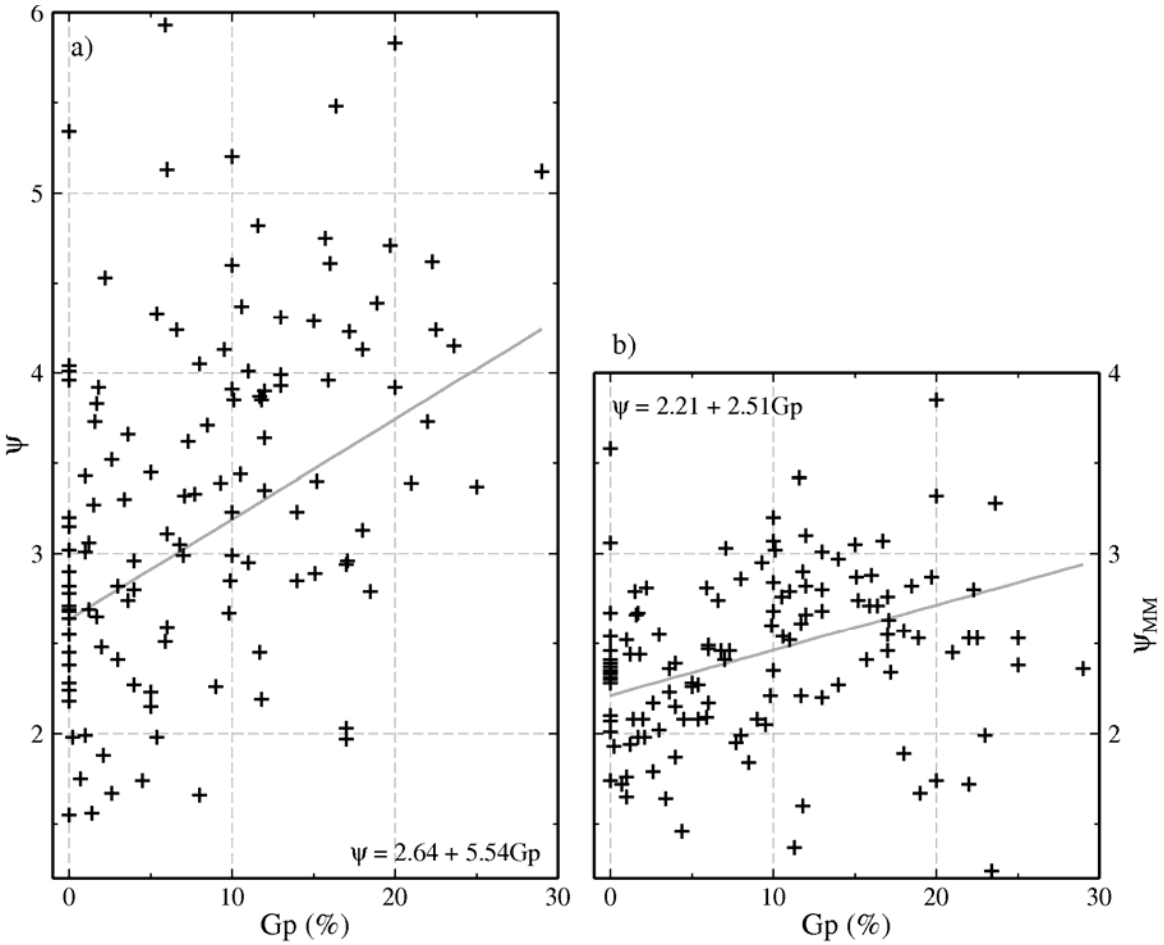

Figure 8. Fall-off (ψ) as a function of gas porosity (*Gp*) for a) unconstrained f_c and, b) f_c fixed to the MM71-predicted value. The best-fit relationship weighted by the inverse variance of the estimated ψ is given in the inset equation.

When we regress using ψ estimated while fixing f_c, we get a slightly different model given by

$$\psi = 1.823 + 0.433Gp + 1.710S_w + 2.21\times10^{-3}\,sDOB. \quad (4)$$

In new testing environments geophysical parameters such as gas porosity and water content may not be accessible. Using NTS geophysical data from Springer et al. (2002) we find that Gp is best approximated by ρ, α, and their interaction, $\rho\alpha$, also known as the compressional modulus. This relationship is given by

$$Gp = 1.266 - 5.437\times10^{-4}\rho - 3.776\times10^{-4}\alpha + 1.635\times10^{-7}\rho\alpha, \quad (5)$$

where is ρ is in kg/m^3 and α is in m/s.

CONCLUSIONS AND RECOMMENDATIONS

Our preliminary analysis of *Pn* spectra of NTS explosions shows that a simple spectral model with variable fall-off is appropriate, and the fall-off correlates well with material properties, gas porosity and water-content, and the scaled depth-of-burial. Corner-frequencies obtained with the variable fall-off model correlate with Mueller and Murphy (1971) corner-frequencies. If we use a smaller elastic radius than the one given for tuff, we believe we could match the trend of the Mueller-Murphy corner frequencies with a slope close to one.

Future Work

This initial *P*-wave spectral fitting focused on correlating material properties with the model parameters. We will perform similar analyses for NTS seismic phases, *Pg* and *Lg*, and compare the results with those presented above for *Pn*. We will make similar calculations for spectra at Borovoye. The comparison of seismic phases will allow for an examination of *P/S* scaling relationships, which can be compared with results from the Fisk (2007) study at NTS. The results of this study with a variable fall-off spectral model will be compared with other spectral models (e.g., Denny and Johnson [1991] and references therein). In addition, we will formally analyze the error and trade-offs in the estimated parameters of Equation (2).

REFERENCES

Baker, D., W.-Y. Kim, H. Patton, G. Randall, and P. Richards (2009). Improvements to a major digital archive of seismic waveforms from nuclear explosions: The Borovoye seismogram archive, in *Proceedings of the 2009 Monitoring Research Review: Ground-Based Nuclear Explosion Monitoring Technologies,* LA-UR-09-05276, Vol. 1, pp. 12–21.

Brune, J. N. (1970). Tectonic stress and the spectra of seismic shear waves from earthquakes, *J. Geophys. Res.* 75: 4997–5009.

Denny, M. D. and D. M. Goodman (1990). A case study of the seismic source function; SALMON and STERLING reevaluated, *J. Geophys. Res.* 95: 19705–19723.

Denny, M. D. and L. R. Johnson (1991). The explosion seismic source function: Models and scaling laws reviewed, in *Explosion Source Phenomenology*, eds. Taylor S. R. et al., AGU Monograph 65: 1–24.

Fisk, M. D. (2007). Corner frequency scaling of regional seismic phases for underground nuclear explosions at the Nevada Test Site, *Bull. Seismol. Soc. Am.* 97: 977–988.

Goldstein, P., S. P. Jarpe, K. M. Mayeda, and W. R. Walter (1994). Separation of source and propagation effects and regional distances, in *Proceedings of the Symposium on the Non-Proliferation Experiment: Results and Implications for Test Ban Treaties,* DOE-CONF-9404100, 6-272–6-276.

Mueller, C. S. and J. R. Murphy (1971). Seismic characteristics of underground nuclear detonations, Part I: Seismic spectrum scaling, *Bull. Seismol. Soc. Am.* 61: 1675–1692.

Stevens, J. L. and S. M. Day (1985). The physical basis of m_b:M_S and variable frequency magnitude methods for earthquake/explosion discrimination, *J. Geophys. Res.* 90: 3009–3020.

Street, R. L., R. B. Herrmann, and O. W. Nuttli (1975). Spectral characteristics of the Lg wave generated by central United States earthquakes, *Geophys. J. R. Astro.* 41: 51–63.

Vergino, E. S. and R. W. Mensing (1990). Yield estimation using regional mb(Pn), *Bull. Seismol. Soc. Am.* 80: 656–674.

Walter, W. R, K. D. Smith, J. L. O'Boyle, T. F. Hauk, F. Ryall, S. D. Ruppert, S. C. Myers, R. Abbot, and D. A. Dodge (2004). An assembled western United States dataset for regional seismic analysis, *Lawrence Livermore National Laboratory* document, UCRL-TR-206630.

Walter, W. R. and S. R. Taylor (2002). A revised magnitude and distance amplitude correction (MDAC2) procedure for regional seismic discriminants, *Lawrence Livermore National Laboratory* document, UCRL-ID-146882.

Walter, W. R., K. M. Mayeda, and H. J. Patton (1995). Phase and spectral ratio discrimination between NTS earthquakes and explosions, Part 1: Empirical observations, *Bull. Seimol. Soc. Am.* 85: 1050–1067.

DEVELOPING AND EXPLOITING A UNIQUE DATASET FROM SOUTH AFRICAN GOLD MINES FOR SOURCE CHARACTERIZATION AND WAVE PROPAGATION

Jordi Julià[1], Andrew A. Nyblade[1], Rengin Gök[2], William R. Walter[2], Lindsay Linzer[3], and Ray Durrheim[3]

Penn State University[1], Lawrence Livermore National Laboratory[2], and
Council for Scientific and Industrial Research[3]

Sponsored by National Nuclear Security Administration

Award Nos. DE-FC52-06NA27320[1] and DE-AC52-07NA27344[2]
Proposal No. BAA06-06

ABSTRACT

In this project, we have developed and exploited a unique seismic dataset to address the characteristics of small seismic events and the associated seismic signals observed at local (< 200 km) and regional (< 2000 km) distances. The dataset has been developed using mining-induced events from three deep gold mines in South Africa recorded on in-mine networks (< 1 km) composed of tens of high-frequency sensors, a network of four broadband stations installed as part of this project at the surface around the mines (1–10 km), and a network of existing broadband seismic stations at local/regional distances (50–1000 km) from the mines. The final dataset includes (i) ~2 years (2007 and 2008) of continuous recording by the surface broadband array and (ii) tens of thousands of mine tremors in the $-3.4 < M_L < 4.4$ local magnitude range recorded by high-frequency in-mine geophones. Events with positive magnitudes are generally well recorded by the surface-mine stations, while magnitudes of 3.0 and larger are seen at regional distances (up to ~600 km) in high-pass filtered recordings.

Significant effort has been devoted to quality control of the in-mine, high-frequency data gathered during this effort. The quality control consisted of (i) identification and analysis of outliers among the P- and S-wave travel-time picks reported by the in-mine network operator and (ii) verification of sensor orientations. The outliers have been identified through a "Wadati filter" developed during this project that searches for the largest subset of P- and S-wave travel-time picks consistent with a medium of uniform wave-speed. We have also detected that trigger times were mistakenly reported as origin times by the in-mine network operator, and corrections have been obtained from the intercept times in the Wadati diagrams. Sensor orientations have been verified by correlating empirically and theoretically rotated P-, SV-, and SH- waveforms. When possible, corrections have been produced through rotations around the vertical components.

Source mechanisms have been investigated by computing full moment tensor solutions for selected events with moment magnitudes in the $0.5 < Mw < 2.6$ range, within the Savuka network volume. The solutions were obtained by inverting P-, SV-, and SH-spectral amplitudes measured on the theoretically rotated waveforms with visually assigned polarities. Most of the solutions revealed the in-mine tremors have a non-zero implosive component (47 out of 76), while a small percentage is purely deviatoric (10 out of 76). The deviatoric component of the moment tensors ranges from pure double couple to pure nondouble couple mechanisms.

Moment tensor solutions and source locations have also been computed for large-magnitude events ($M_L > 3.0$) that were simultaneously recorded by the three in-mine networks and the surface-mine array. During 2007 the high-frequency recordings at one of the mines appeared not to be synchronized with those recorded by the other two mines, so we concentrated our analysis on year 2008. The jointly constrained moment tensor solutions are also dominated by near-vertical, compressional stresses and are more robust than those obtained from the individual in-mine or surface-mine networks. These events are well recorded by AfricaArray stations at local and regional distances.

We have also calibrated the regional stations for seismic coda-derived source spectra and moment magnitude using the envelope methodology of Mayeda (2003). We tie the coda Mw to independent values from waveform modeling. The resulting coda-based source spectra of shallow mining-related events show significant spectral peaking that is not seen in deeper tectonic earthquakes. This coda peaking may be an independent method of identifying shallow events and is similar to coda peaking previously observed for Nevada explosions, where the frequency of the observed spectral peak correlates with the depth of burial (Murphy et al., 2009).

OBJECTIVES

The main objective of this project is to develop and exploit a unique seismic dataset from mine-related events recorded at in-mine (< 3 km), local (3–10 km), and regional (>100 km) distances (Figure 1). The in-mine recordings have been obtained through three in-mine seismic networks consisting of a few tens of high-frequency geophones, which are routinely used to monitor seismic activity in the mines. The local recordings have been acquired through four broadband seismic stations (three Guralp CMG-3T and one Guralp CMG-40T feeding 24-bit RefTek data loggers) deployed under this project and located on the surface of the mining area. And the regional recordings have been acquired mostly through the AfricaArray stations in South Africa and surrounding countries. The dataset that we are assembling is unique in that it contains (1) events spanning several orders of magnitude, (2) events from a range of source depths, and (3) events from a variety of source types (e.g., pillar collapses, tensile fractures, normal and strike-slip faulting, and sources with a significant volumetric component).

We planned to exploit this dataset by using the mining events in 10 related areas of research aimed at improving U.S. operational capabilities to monitor for low-yield nuclear tests: (1) create an event catalog with accurate origin times and locations; (2) determine seismic moment, radiated energy, corner frequency, and stress drop; (3) obtain focal mechanisms from moment tensor inversion; (4) define several categories of event types (shear slip, tensile failure with volumetric component, explosions, pillar collapse) using focal mechanisms and in-mine observations; (5) define and calibrate a coda Mw scale for southern Africa; (6) using calibrated coda techniques, determine Mw for all cataloged events; (7) investigate the effects of depth and source mechanism on the coda-derived source spectra and evaluate the potential of using coda spectral peaking as a depth discriminant; (8) define and calibrate local-to-regional phase (direct P and S, Pn, Pg, Sn, and Lg) propagation characteristics, including the use of the MDAC technique to determine appropriate geometrical spreading and frequency-dependent Q values for the region; (9) characterize relative P and S excitation and source apparent stress resulting from variations in source parameters, including magnitude, mechanism, depth, rock characteristics, and source type; (10) define regional phase ratios that can discriminate between the different source categories, and compare these discriminants and their performance with ongoing work done for other types of mining events, such as in Scandinavia and the western U.S.

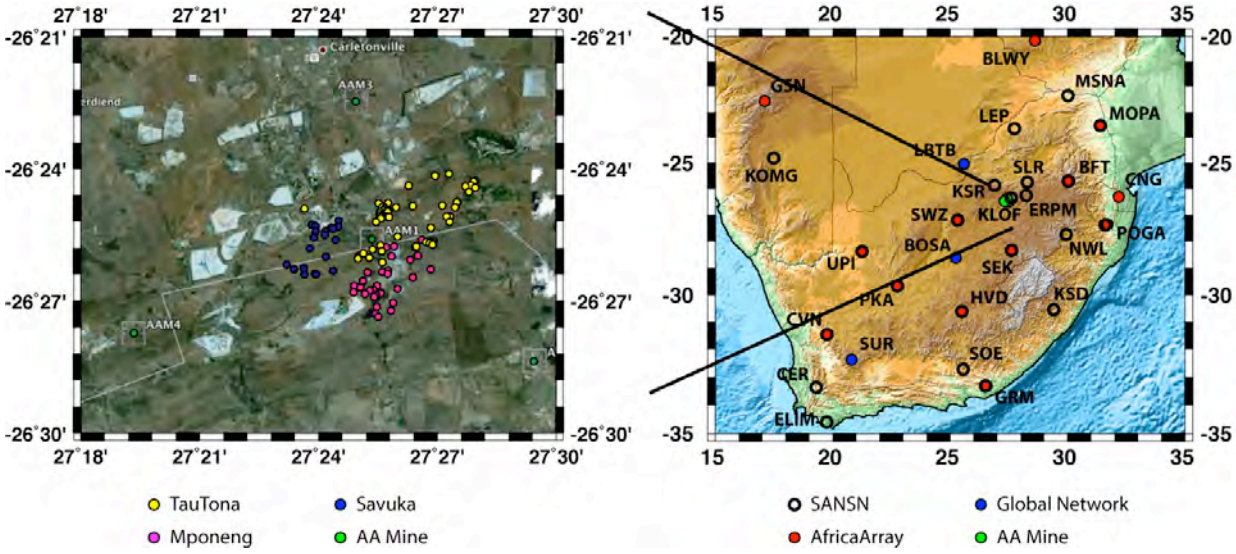

Figure 1. (left) Satellite image from Google Earth showing the Carletonville mining area where the three mines contributing to this project are located. The blue, magenta, and yellow dots are the surface projection of the Savuka, Mponeng, and TauTona in-mine networks, respectively, while the green dots are the surface broadband stations deployed under this effort. (right) Map of broadband stations in South Africa. The red dots are the AfricaArray stations, which are shared with the South Africa National Seismic Network (SANSN) shown as hollow circles, and the blue dots are the three permanent Global Seismographic Network (GSN) stations.

RESEARCH ACCOMPLISHED

A unique dataset of mine-related seismicity to improve U.S. operational capabilities to monitor for low-yield nuclear tests has been developed during this project. The dataset is unique in that it contains events spanning several orders of magnitude ($-3.4 < M_L < 4.4$), recorded at a wide range of epicentral distances, and generated from a variety of source types (mine blasts, pillar collapses, stress fracturing, and faulting events). The collected dataset consists of (i) tens of thousands of high-frequency recordings at near-source distances (< 3 km) from three in-mine networks, (ii) broadband recordings of larger events ($M_L > 1.0$) at local distances (3–10 km) from a surface network in and around the mines, and (iii) broadband recordings of the largest ($M_L > 3.0$) events at near- and far-regional distances (> 200 km) from AfricaArray and Global Seismographic Network (GSN) stations.

The collected dataset has been analyzed to develop (i) event catalogs with accurate event locations (GT1) and origin times, (ii) full moment tensor solutions from spectral amplitudes, and (iii) regional coda-magnitudes and spectra for selected events.

Event Catalogs

Event catalogs for 2007 and 2008 for each mine have been compiled from source locations and local magnitudes provided by the in-mine network operator Integrated Seismic Systems International (ISSI). Locations and origin times were obtained by ISSI from hand picked P- and S-wave arrival times through a ray-tracing algorithm and reported in the local mine-coordinate system and South African local time. We have rebuilt the catalogs to report origin times in Universal Time (UT), epicentral locations in geodetic coordinates (latitude and longitude), and source depths with respect to average mean sea level (a.m.s.l.).

We discovered that the origin times reported by ISSI were actually not origin times but trigger times used to label the events (more precisely, the trigger time corresponding to the first station recording a given event). We were able to obtain origin times from the intercept time in S-P *vs* P travel-time plots (Wadati diagrams) constructed with the hand-picked P- and S-wave travel times provided by ISSI. The accuracy of the origin times was verified during visit to the ISSI branch in TauTona mine in 2008.

Event locations are provided with an accuracy of ~50 m, according to ISSI. Nonetheless, we assessed the hypocentral locations through a simple Geiger inversion of the absolute travel-time picks provided by the in-mine network operator. As we assumed a uniform velocity for the propagating medium, we identified and removed outliers through a "Wadati filter" (Julià et al., 2009a). The "Wadati filter" is a simple search in the (S-P, P) travel-time space that finds the largest subset of (S-P, P) travel-time pairs that follow a straight line (Figure 2), and successfully identifies defective travel-time picks, as well as travel times associated with inhomogeneous ray paths (Julià et al., 2009a). The relocated hypocenters for trial P-wave velocities of 5.8, 5.9, and 6.0 km/s (and

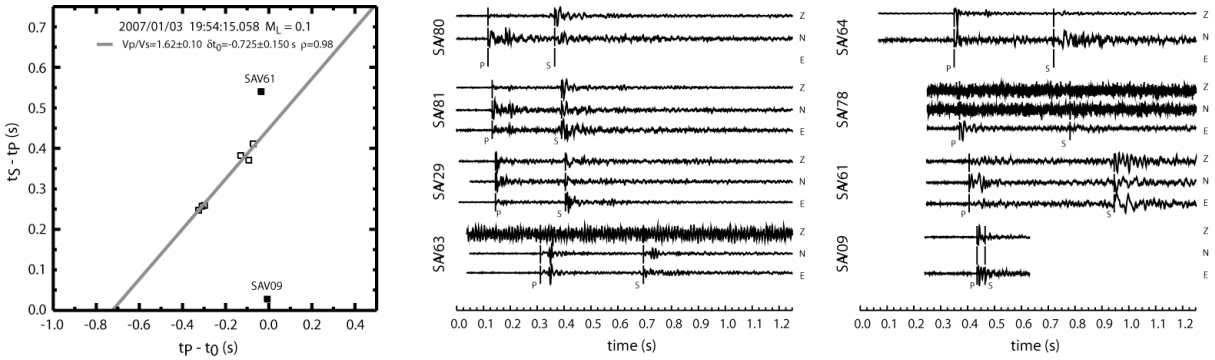

Figure 2. (left) Wadati diagram for a $M_L = 0.4$ event recorded at Savuka mine, South Africa. The solid squares are measurements rejected by the "Wadati filter." The time at the top is a trigger time randomly selected by ISSI to label the event, and used as a reference time in the diagram. (center and right) Recordings for the same events, sorted by P-wave travel time. Note that the waveforms have been normalized to their maximum amplitude. Stations SAV80, SAV63, SAV64, SAV78, and SAV09 have failing channels.

corresponding S-wave velocities computed from a Vp/Vs ratio of 1.64, from the Wadati diagrams) migrated less than 150 m with respect to the original ISSI locations for 50% of the catalog. The origin time corrections obtained from the relocation exercise also correlate well with those obtained from the intercept times in the Wadati diagrams (Figure 3).

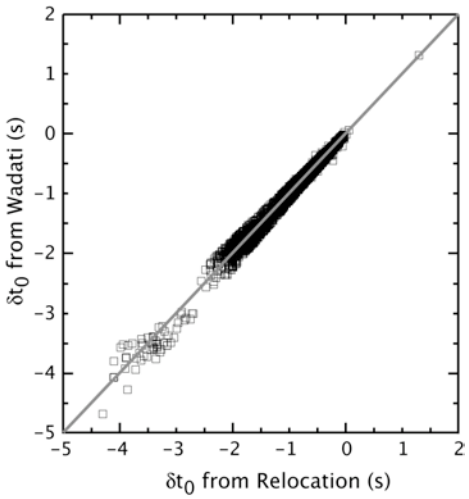

Figure 3. Origin time corrections from the "Wadati filter" vs origin-time corrections from the Geiger relocation (assuming vp = 6.0 km/s).

Savuka Moment Tensor Solutions

We have obtained full moment tensor solutions for 76 events with moment magnitudes between 0.5 and 2.5 by inverting P, SV, and SH spectral amplitudes with polarity attached, as measured on mine tremors recorded by the Savuka in-mine network. We assumed a medium of uniform velocity and density (V_P = 6.0 km/s, V_S = 3.70 km/s, ρ = 2.69 g/cm^3), so the displacements could be expressed as (e.g., Udías, 2000):

$$u_i = G_{ij,k} m_{jk} \quad i,j,k = 1,2,3 \ ,$$

where

$$G_{ij,k} = (1/4\pi\rho v^3 R)\ \gamma_i\gamma_j\gamma_k\ \delta'(t-R/v) \quad \gamma_I = x_i/R$$

and where ρ is density, v is the P- or S-wave velocity, and R is the hypocentral distance. The forward problem was then written by rotating the displacements into the ray-coordinate system and Fourier transforming the resulting equation to obtain spectral amplitudes. This defines a linear problem that was inverted by calculating the natural inverse through a singular value decomposition of the forward problem's matrix (e.g., Menke, 1989).

Spectral amplitudes from the in-mine recordings were obtained through the time-domain procedure of Urbancic et al. (1996). This procedure evaluates the spectral plateau of the P- or S-wave spectrum by computing the ratio

$$\Omega_o = 4(S_{D2})^{3/2}(S_{V2})^{-1/2} \ ,$$

where

$$S_{D2} = 2\int D^2(t)\ dt \quad S_{V2} = 2\int V^2(t)\ dt$$

and D(t) and V(t) are the displacement and velocity, respectively. Following Trifu et al. (2000), the integrals extend between the P- and S-wave travel times, for the P-wave amplitude, and twice the S-P time after the S-wave travel time for the SV and SH amplitudes. The polarity of the spectral amplitudes is assigned visually for each measurement by correlating low-pass filtered waveforms with synthetics.

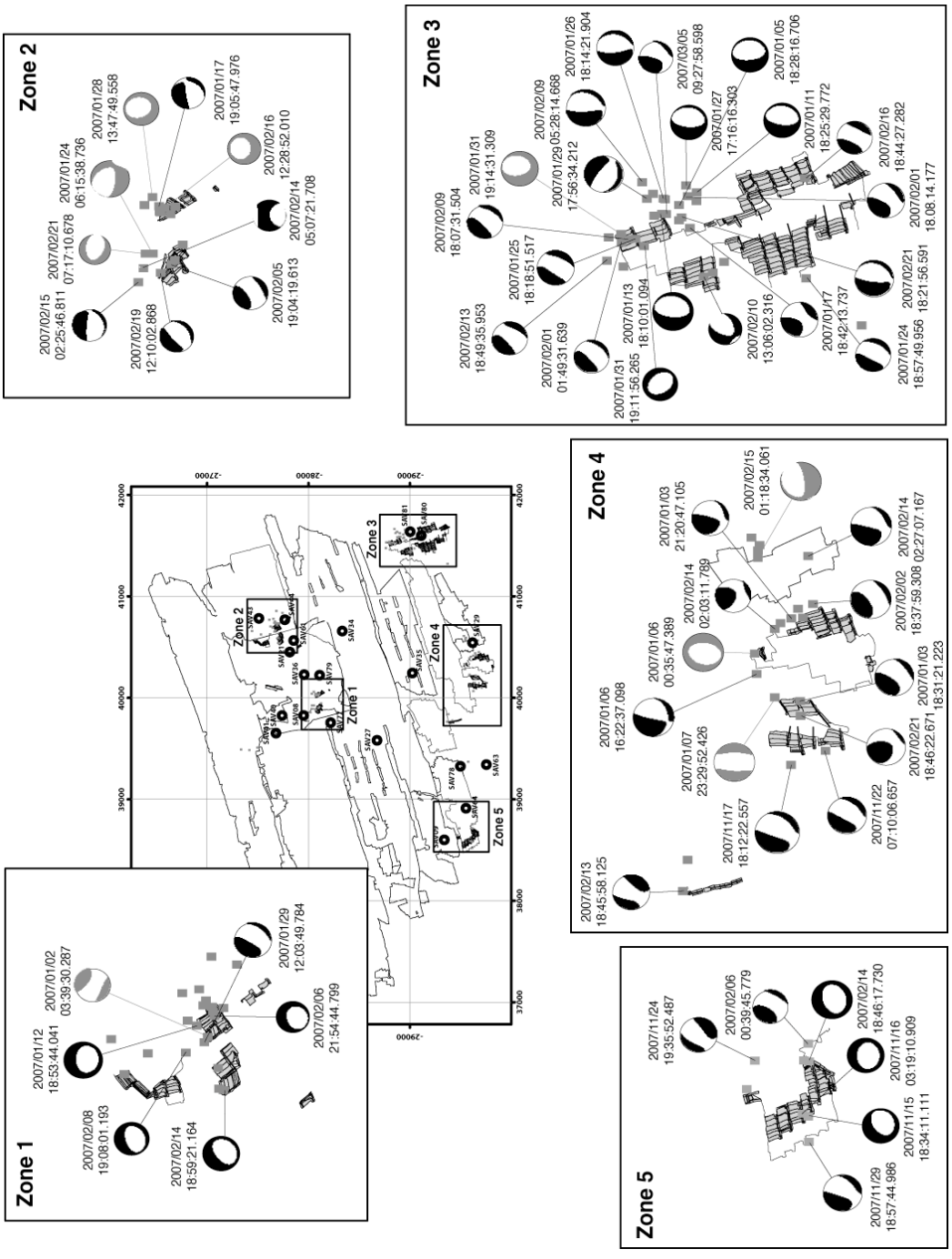

Figure 4. Spatial distribution of the deviatoric focal mechanisms for the Savuka mine events considered in this study (only those events with a well-constrained deviatoric part have been included). The black symbols represent those events with a significant volumetric component (more than 10% of the total scalar moment); the gray symbols represent those events with a near deviatoric solution (less than 10% of the total scalar moment). The mine plan is the same as in Figure 1, with active areas highlighted.

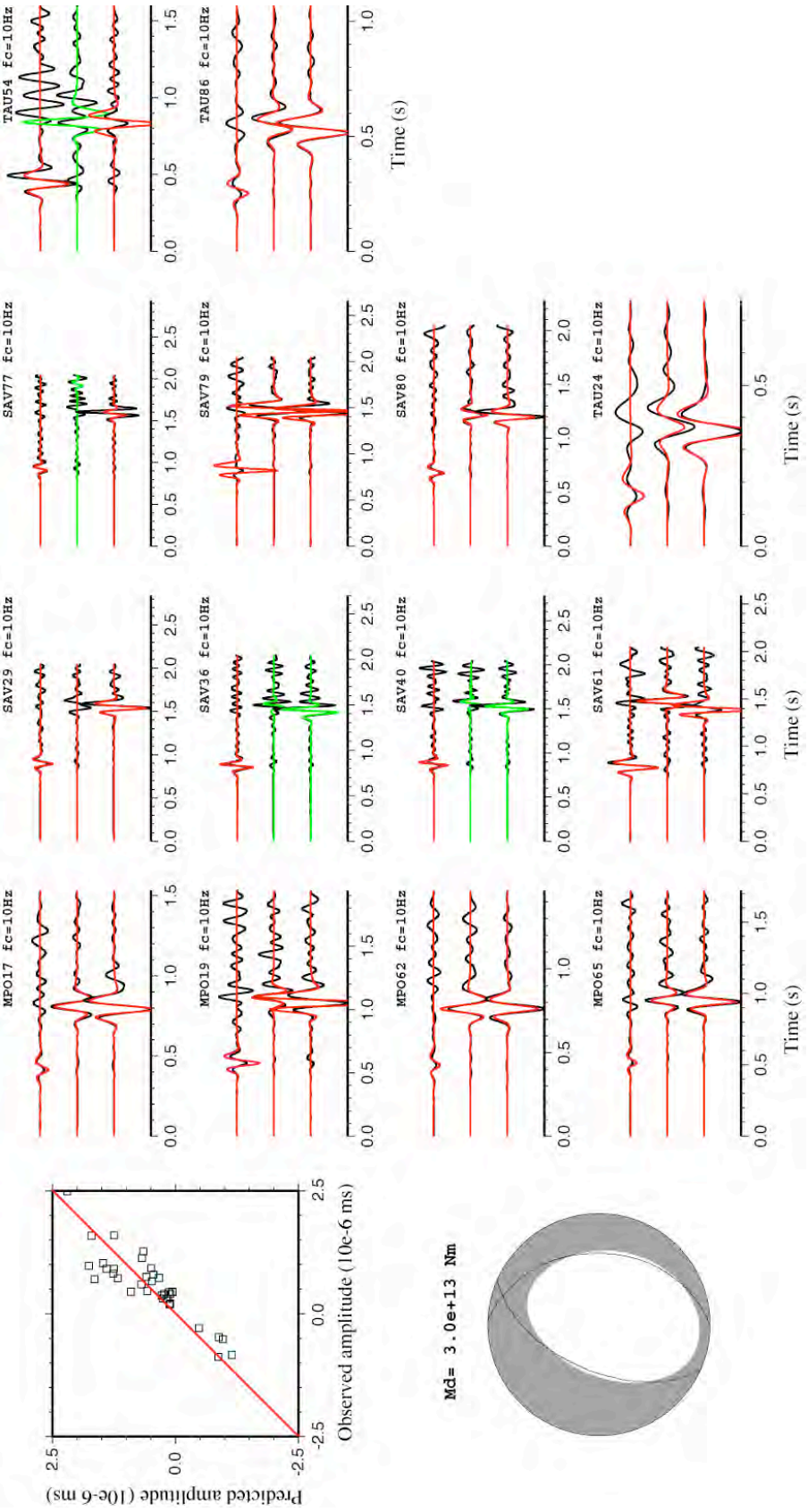

Figure 5. Moment tensor inversion results for a M_L ~3.4 event recorded at the three South African gold mines. The upper left diagram compares predicted and observed spectral amplitudes for P, SV, and SH components. The lower left diagram shows the P-wave radiation pattern for the deviatoric moment tensor. The waveforms on the right are shown to compare the corresponding observed (black) and predicted (red) P, SV and SH amplitudes in the time domain. The green lines are predictions for traces with amplitudes that were not included in the moment tensor inversion. The event origin time is at t = 0 s, and the synthetic waveforms have been shifted to facilitate the comparison with the observations. The time shifts between observed and synthetic waveforms are due to inaccuracies in the event location, assumed wave-speed, and/or anisotropic effects. Note that only spectral amplitudes were inverted, so the observed time shifts did not influence our moment tensor solutions. The waveforms are shown in velocity.

The moment tensor solutions revealed that the largest principal stresses are compressive and oriented near-vertically, consistent with gravity-driven stress conditions in a deep mine and with *in situ* measurements in a nearby deep mine (Pallister et al., 1970). Most of the moment tensor solutions also required a significant implosive component. The robustness of this implosive contribution was assessed by repeating the moment tensor inversion under the additional constraint of a purely deviatoric moment tensor solution, and we found that in 22 occasions the lack of a volumetric component did not degrade the match to the observed spectral amplitudes significantly.

Figure 4 displays the deviatoric "beach-balls" for the 54 events with a well-constrained full moment tensor. The eigenvectors of the deviatoric moment tensor are the same as those for the general moment tensor, so the deviatoric components also have sub-vertical pressure axes and sub-horizontal tension axes. The deviatoric moment tensors can be divided further into two double couples (DCs), consistent with previous works that suggest stresses are relaxed through a combination of co-seismic closure and normal faulting (McGarr, 1992a; 1992b). The deviatoric components can always be decomposed into two DCs, but other decompositions, such as combinations of DC and compensated linear vector dipole (CLVD), are also possible.

The moment tensors for the 76 events recorded by the Savuka in-mine network are reported in Julià et al. (2009b) and can be found online at http://www.geosc.psu.edu/~jjulia/julia-esupp.html.

Joint Inversion of Mine Data

We have selected a total of 43 events with $M_L > 3.5$ (in at least one of the catalogs) that have been well recorded in all the mines in order to determine accurate event locations and moment tensor solutions from the combined dataset. The selection has been performed through sorting and comparison of the event catalogues developed independently for each gold mine for years 2007 and 2008. One of the mines (Mponeng) seems to have had the timing desynchronized with respect to the other mines during 2007, so we are focusing on analyzing events recorded during 2008.

Figure 5 displays a moment tensor inversion from P, SV, and SH spectral amplitudes measured at high-frequency recordings from the three in-mine networks. The eigenvalues are $\sigma_1 = 2.4750 \times 10^{13}$ Nm, $\sigma_2 = 0.4798 \times 10^{13}$ Nm, and $\sigma_3 = -2.9845 \times 10^{13}$ Nm, and the corresponding eigenvectors are $\mathbf{e}_1$ = (-0.2475,0.9524,-0.1778), $\mathbf{e}_2$ = (0.9420,0.2795, 0.1856), and $\mathbf{e}_3$ = (-0.2265,0.1216,0.9664), which have been constrained to be purely deviatoric. The total scalar moment is $\sim 2.98 \times 10^{13}$ Nm, which corresponds with a moment magnitude around 2.9 (Hanks and Kanamori, 1979). The largest principal stress is compressive ($\sigma_3 < 0$) and subvertical, in good agreement with moment tensor solutions obtained for smaller events at Savuka mine (Julià et al, 2009a; Figure 4). The full moment tensor solution includes a volumetric (implosive) component representing ~17% of the total scalar moment, but it does not improve the match to the observed amplitudes significantly.

Regional Coda Magnitudes and Spectra

We have also been looking at the seismic coda from regional events, both natural earthquakes and mine-related events, that are recorded at regional stations across South Africa. Regional coda envelopes are useful to establish a calibrated moment magnitude scale for the area and to study source spectra of events.

We used the coda wave method of Mayeda (2003) to calculate source spectra of earthquakes recorded at GSN broadband stations and the Kaapvaal seismic array. In order to generate a list of seismic events in the South Africa mining districts, we used the seismic bulletins provided by the Council of Geoscience, Pretoria, and the Preliminary Determination of Epicenters (PDE) catalogs. The mining-induced events were found to be concentrated around Welkom, Klerkdorp, (Far West, West, Central, and East) Rand regions. Tectonic events found in the bulletins primarily consisted of a large Mozambique (Mw = 7.2) event and its aftershocks. The early and late coda parameters were obtained for a set of earthquakes in the region. Those parameters are distance dependent at each narrow frequency band (0.05–6 Hz). The raw amplitudes were path corrected using a Street and Herrmann (ESH) method that corrects for geometrical spreading and Q. The path-corrected amplitudes at 1.0–1.5 Hz are shown in Figure 6.

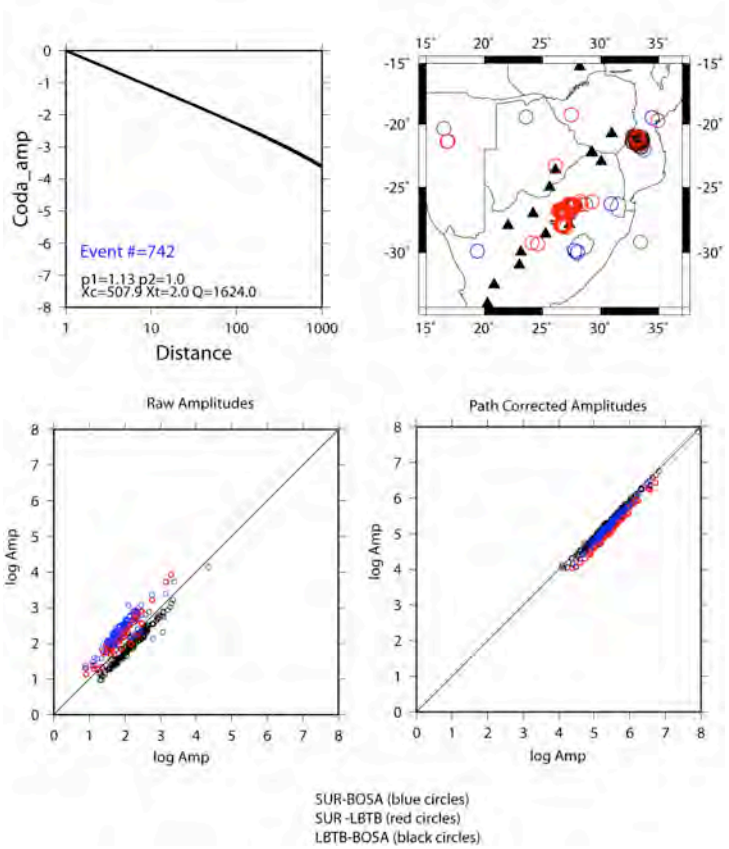

Figure 6. Path calibration at 1.0–1.5 Hz. The upper left panel is the ESH function.

To scale the nondimensional amplitudes to absolute moment, we use independently waveform modeled Mw's. A constant correction factor at each frequency band can then be used to correct for each event to obtain the moment rate function. We performed a grid-search procedure to obtain the body and surface wave fit at long-period levels. The best fitting is obtained at around 1–4 km depth and for a normal fault mechanism. The shallow hypocentral location causes peaking of coda source spectra at 0.4–1.5 Hz. It is probably caused by strong excitation of Rayleigh waves at shallower depth that is then scattered into the coda (Figure 7). The spectral peaking causes overestimated Mw (coda)'s for smaller events where the long period coda levels cannot be measured. Larger-magnitude mining-induced events have coda amplitude values up to a 0.2–0.3 Hz narrow frequency band, where we match the independently waveform-modeled magnitudes. Smaller-magnitude events do not have an amplitude measurement at that frequency. In other words, the coda is abruptly eliminated below 0.2–0.3 Hz for smaller-magnitude events. When we extrapolate the Mw value to the level we expect to measure, then we find an average constant correction factor of 0.4–0.5.

CONCLUSIONS AND RECOMMENDATIONS

We have developed a unique seismic dataset containing events spanning several orders of magnitude ($-3.4 < M_L < 4.4$), recorded at a wide range of epicentral distances and generated from a variety of source types (mine blasts, pillar collapses, stress fracturing, and faulting events). The dataset has been analyzed to determine accurate event locations, full moment tensor solutions, and regional coda magnitudes and spectra. The accuracy of the event locations has been investigated through Geiger-like inversions on select P- and S-wave travel times consistent with a medium of uniform velocity (Julià et al., 2009a), and the moment tensor solutions have been obtained through inversion of P, SV, and SH spectral amplitudes with polarity assigned (Julià et al., 2009b).

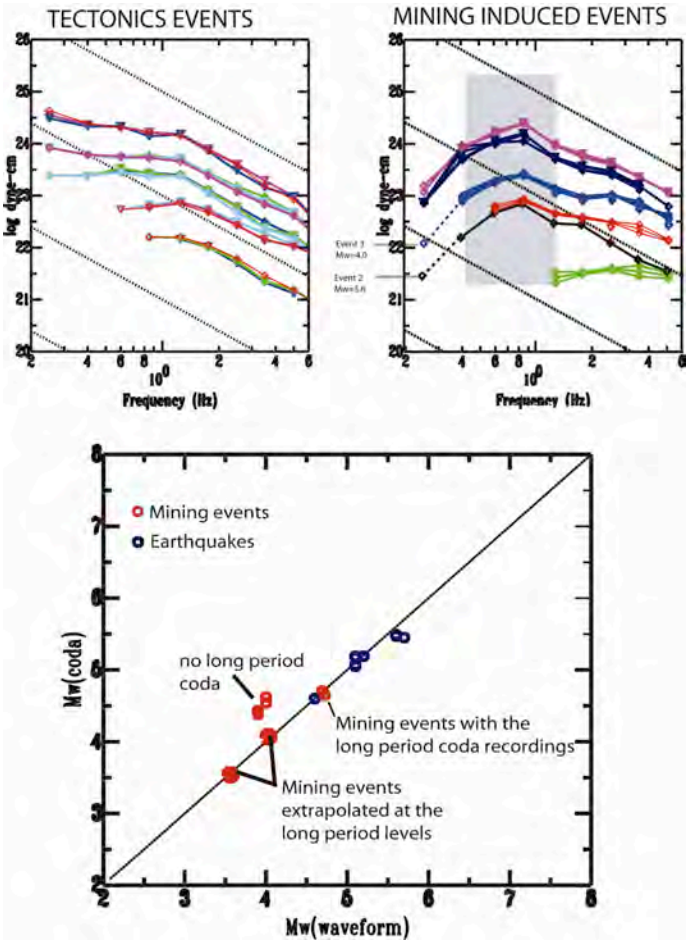

Figure 7. Coda-derived source spectra from earthquakes (left) and mining-induced events (right). The earthquakes have the usual shape: a near constant proportional to the moment at long periods and falling off as frequency^{-2} at the high frequencies. Coda-based Mw's for any event can be determined from the long period level. In contrast, the mine events show an unusual peaked shape, which may be an indicator of shallow depth due to Rg excitation and scattering into the coda. The lowest frequency points shown with dashed lines come from long-period waveform modeling.

We are now constraining moment tensor solutions for large (M_L > 3.5) wells recorded in the three South African mines (Savuka, Mponeng, and TauTona). Preliminary results are consistent with the moment tensor solutions determined for smaller events.

ACKNOWLEDGEMENTS

We thank ISSI and Anglo Gold Ashanti for providing the seismic data and mine plans from the Savuka, Mponeng and TauTona mines. We also thank ISSI and the Council for Scientific and Industrial Research for assisting with event locations and solving other technical issues concerning the in-mine data, and we thank the Council for Geoscience for installing and operating the four broadband stations of the surface mine network. The Data Management Center of the Incorporated Research Institutions (IRIS) for has provided assistance with archiving and distributing data from the permanent AfricaArray seismic stations, including data used in this study.

REFERENCES

Hanks, T. C., and H. Kanamori (1979). A moment magnitude scale, *J. Geophys. Res.* 84: 2348–2350.

Julià, J., A. A. Nyblade, R. J. Durrheim, L. Linzer, R. Gök, W. Walter, S. M. Spottiswoode, and P. Dirks (2009a). A Wadati filter for mine-induced seismicity, *S. Afr. J. Geol.* 112: 371–380.

Julià, J., A. A. Nyblade, R. J. Durrheim, L. Linzer, R. Gök, P. Dirks, and W. Walter (2009b). Source mechanisms of mine-related seismicity, Savuka mine, South Africa, *Bull. Seism. Soc. Am*. 99: 2801–2814.

Mayeda, K. (2003). Stable and transportable regional magnitudes based on coda-derived moment-rate spectra, *Bull. Seism. Soc. Am.* 93: 224–239.

Menke, W. (1989). *Geophysical Data Analysis: Discrete Inverse Theory*. San Diego: Academic Press.

McGarr, A. (1992a). An implosive component in the seismic moment tensor of a mining-induced tremor, *Bull. Seism. Soc. Am.* 19: 1579–1582.

McGarr, A. (1992b). Moment tensors of ten Witwatersrand mine tremors, *Pure Appl. Geophys*. 139: 781–800.

Montalbetti, J. M. and E. R. Kanasewich (1970). Enhancement of teleseismic body waves with a polarization filter, *Geophys. J. R. Astr. Soc.* 21: 119–129.

Murphy, K. R., K. Mayeda, and W. R. Walter (2009), Lg-coda methods applied to Nevada Test Site events: Spectral peaking and yield estimation, *Bull. Seism. Soc. Am.* 99: 441–448.

Pallister, G. F., N. C. Gay, and N. G. W. Cook (1970). Measurements of the virgin state of stress in rock at depth, presented at the 2nd Congress of the International Society for Rock Mechanics, Beograd, 21–26 September 1970.

Trifu, C. I., D. Angus, and V. Shumila (2000). A fast evaluation of the seismic moment tensor for induced seismicity, *Bull. Seism. Soc. Am.* 90: 1521–1527.

Udías, A. (2000). *Principles of Seismology*. Cambridge, UK: Cambridge University Press.

Urbancic, T. I., C. I. Trifu, R. A. Mercer, A.J . Feustel, and J. A. G. Alexander (1996). Automatic time-domain calculation of source parameters for the analysis of induced seismicity, *Bull. Seism. Soc. Am*. 5: 1627–1633.

RE-EXAMINATION OF SURFACE WAVE MAGNITUDE ESTIMATES FOR THE NORTH KOREAN EVENT OF 25 MAY 2009

Karl Koch

Federal Institute for Geosciences and Natural Resources, Hannover, Germany

Sponsored by the German National Data Centre

ABSTRACT

The International Monitoring System (IMS) network of seismic stations detected the event occurring on 25 May 2009 at 00:54 UT in North Korea and corresponding bulletins were released from automatic and interactive analysis. The final Reviewed Event Bulletin (REB) for this event was made up of 72 arrivals from 59 stations being used for event location. From 45 of these recording stations body wave magnitude estimates were reported resulting in a network-averaged event magnitude of mb=4.5. Besides, 15 stations were included with surface wave magnitude estimates yielding a network-averaged magnitude of Ms=3.6. During automatic post-processing event characterization and Standard Event Screening was carried out including screening with the mb-Ms criterion based on these magnitude estimates. As a result, the event was flagged as “not screened out”, but it turned out that it was only marginally off the mb-Ms screening line. The fact that such an event considered to be a nuclear test explosion should be reasonably well discriminated prompted a study to investigate a potential bias of Ms values.

The surface wave magnitudes published in the REB show an interesting clustering of the reported magnitude estimates. Six stations had positive magnitude residuals within 0.2 to 0.5 magnitude units while another seven stations had negative residuals of equivalent size. Only two stations had smaller magnitude residuals. As Ms estimates from stations at shorter distances were found to have negative residuals and more distant stations to have positive residuals, the Ms magnitude estimation procedure applied at the IDC was checked and validated. Reviewing the magnitude estimates a few interesting facts were uncovered. First, the surface wave magnitude at one station (ATTU), even though being in the negative residual group, was determined from a marginal signal. Second, the azimuth dependence of the residuals showed clear pattern in that all positive residuals are from a narrow azimuth window between 290 and 320 degrees from the event, with a single exception (MKAR). Re-analysis of waveforms in the 20 s period range shows that surface wave trains at additional IMS stations in this azimuth range (e.g., KURK, VRAC) can be found well above the background noise. Hence, surface wave magnitude estimates obtained at these stations are relatively high, and the network-averaged surface wave magnitude reported in the REB must be considered a low estimate. Within this scenario it may have been likely that the event would have been screened out under the rules for Standard Event Screening based on the mb-Ms criterion applied at the time.

OBJECTIVES

The event detected by the IMS network occurring on 25 May 2009 at 00:54 UT in North Korea has drawn some attention because initial reports and press releases issued by the Provisional Technical Secretariat (PTS) of the Preparatory Commission for the Nuclear-Test-Ban Treaty Organization (CTBTO) have indicated that the event may have a significant earthquake signature and that it may be difficult to clearly identify it as an underground explosion. One difficulty associated with this event is that there were some observations of surface waves on the tangential component (e.g., BJT station) that are associated with Love wave-type. As it also turned out, a particular difficulty for this event arose from the fact that it was almost screened out during event characterization and standard event screening by the mb-Ms criterion as applied during automatic post-processing, similar to findings from the 2006 event. Therefore the objective of this research is concerned with the re-evaluation of surface wave magnitudes at the stations of the IMS as reported in the Reviewed Event Bulletin (REB) and the identification of any additional surface wave observations at other IMS stations, wherever possible. Furthermore it is intended to evaluate how re-examination and addition of missed surface wave magnitudes will impact on the performance of Standard Event Screening as carried out at the International Data Centre (IDC) of the PTS.

RESEARCH ACCOMPLISHED

On 25 May 2009 at 00:54 UT an event was detected by the International Monitoring System (IMS) network and automatically and interactively located in North Korea near a location of 41.311°N and 129.0464°E (REB parameters) with the depth fixed to the Earth's surface, on the basis of 72 arrivals from 59 stations (see Figure 1). As to the magnitude of the event a body wave magnitude estimate of mb=4.5 and a surface wave magnitude of Ms=3.6 were given, averaged over 45 and 15 station estimates, respectively. Results and assessments were released by the PTS within days, including the data and associated standard products such as the Standard Event Lists (SEL1-3), the REB, the Standard Event Bulletin (SEB) including event characterization parameters, and the Standard Screened Event Bulletin (SSEB) following from application of Standard Event Screening procedures. As pointed out by Selby & Bowers (2009), the set of body and surface wave magnitude values places this event between the Eurasian earthquake and explosions populations and very close to the IDC experimental event screening line, an observation similar to what they had reported for the 2006 event in the same region (Selby & Bowers, 2007; Bonner et al., 2008). This closeness of the event to being screened out during Standard Event Screening may have prompted some concerns (CTBTO, 2009a, b) expressing that the signals from this event would go along with earthquake-like characteristics.

Based on these findings this study sets out to review the published surface wave magnitude and to investigate reasons for the Ms estimate apparently biased high. The initial finding is that the reported station magnitude estimates reported in the REB cluster into two groups (Figure2): a group of six stations with magnitude residuals about 0.2-0.5 magnitude units above the average and seven stations having the same, but negative, residuals. Only two stations showed magnitude estimates that were within 0.1 units of the network average. As most stations showing high estimates were found at larger distances than the group of stations with low estimates (Figure 2a), this effect may be related to the distance correction applied at the IDC (Rezapour & Pearce, 1998). However, the case of MKAR as well as a careful review of the process argue against such a problem.

When plotting the observed station residuals according to station azimuth (Figure 2b) it is found that the group of stations showing high residuals are within a narrow azimuth range between 290° and 320°, i.e., stations to the west and northwest of the epicenter. All stations with low estimates are found at other directions – with the exception of MKAR being within the azimuth range of stations with high estimates. Ford et al. (2009) studied the 2009 event and concluded that an earthquake source is not consistent with the data at frequencies between 10 and 50 s, with the best-fit full seismic moment tensor being predominantly explosive. They argue that non-isotropic radiation is required due to observed Love waves on transverse components, but they also discuss effects from tensile failure models and anisotropic wave propagation. They refer to previous work for the 2006 North Korean explosion and the

similarity of mb-Ms of this event with some Eurasian earthquakes (Bonner et al., 2008) and dissimilarity with NTS and Semipalatinsk explosions (Patton & Taylor, 2008).

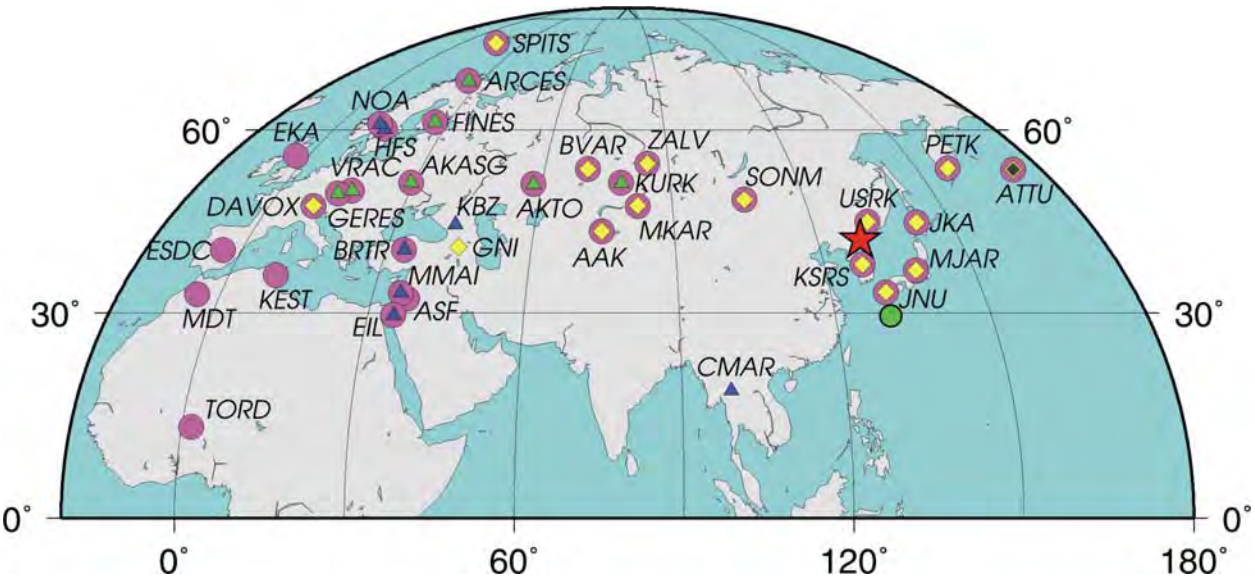

Figure 1. Geographical distribution of stations of the IMS seismic stations recording signals from the 2009 North Korean event. Red dots indicate stations providing defining phases for event location in the Reviewed Event Bulletin (REB). Yellow diamonds symbolize stations with LR observations and associated surface wave magnitude estimates. Triangles (green/blue) represent stations with LR waveforms, whereby green symbols are used for stations with additional surface wave estimates and blue symbols are used where the signals are too marginal for magnitude estimation. The green dot represents a Ryukyu Islands event occurring about 12 mins later which produced the later LR signals shown in the record sections.

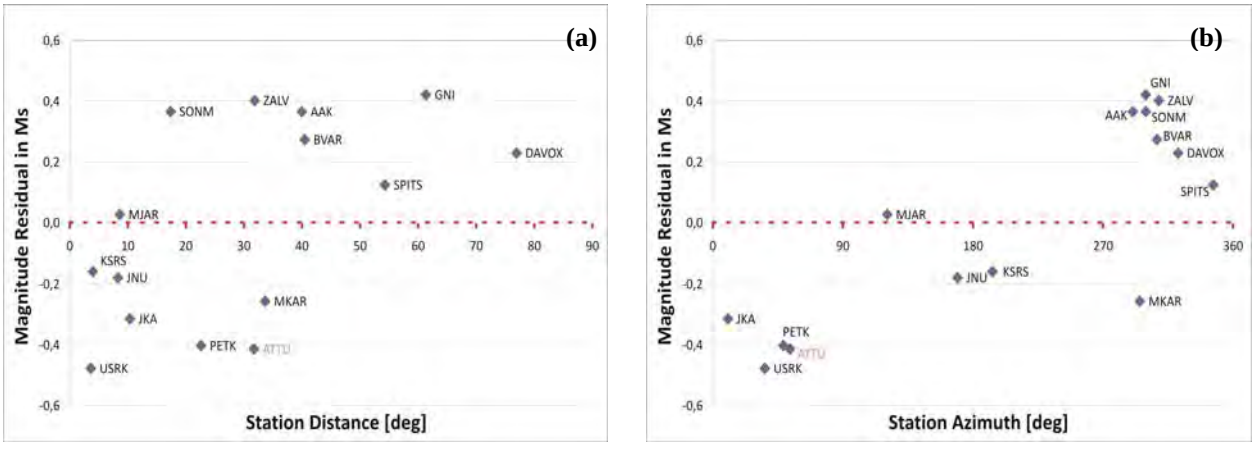

Figure 2. Station surface wave magnitude estimates for 15 IMS stations as contained in the REB and their network-average residuals plotted against epicenter-station distance (a-left) and plotted against station azimuth (from epicenter) (b-right). Note: ATTU is marked differently to indicate its spurious or invalid estimate.

Processing and Analysis Steps

Waveform data for IMS stations included in the REB were downloaded from the IDC. For analyzing the data the SeismicHandler software (Stammler, 1993), which is the standard analysis package at the German National Data Center, was used; in routine teleseismic event analysis amplitudes for surface wave estimation can be measured with this software from SRO-LP simulation records. In order to build corresponding simulation filters, the response files for those stations were requested which showed a potential for a reasonable LR signal. For stations where instrument responses were provided in poles and zeros (PAZ) representation simulation filters could readily be established, while for stations with responses given as frequency, amplitude and phase (FAP) values establishment of corresponding simulations filter is work still in progress. To validate the surface wave estimates in the REB and the procedure for the magnitude determination in this study, the broad-band channels as well as a number of short-period channels were converted to SRO-LP records (see Figure 3) and amplitude and period measurements made and checked for consistency. To calculate surface wave magnitudes the distance correction relation of Rezapour & Pearce (1998) was used, as is at the IDC. While clear surface wave trains are visible for almost all stations reported in the REB, the surface wave train for stations ATTU does not emerge from the background noise.

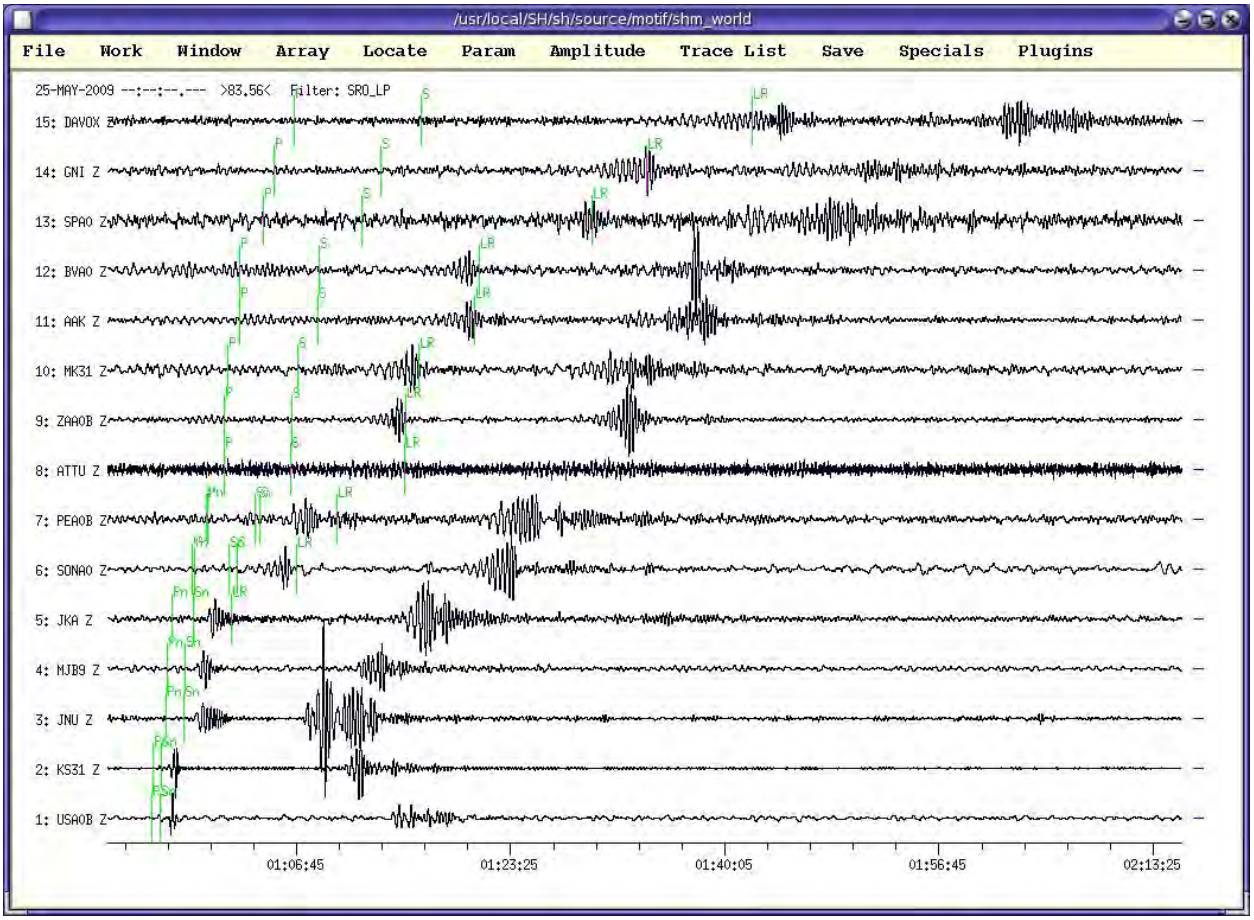

Figure 3. Simulated seismograms for an SRO-LP instrument used to read absolute ground motion amplitudes and periods for the surface wave trains. Note also the somewhat larger surface wave trains from a later event in the Ryukyu Islands region (see also Figure 1).

For stations with potential LR signals the data were initially filtered with a third-order Butterworth bandpass filter for periods between 16 and 25 sec (Figure 4a). From these filtered records it became apparent that fourteen additional IMS stations may be used to obtain additional Ms estimates. Theses stations were located mainly on the Eurasian platform including Scandinavia (see Figure 1). SRO-LP-simulations were done of these stations (Figure 4b) and for another seven stations Ms estimates could be made.

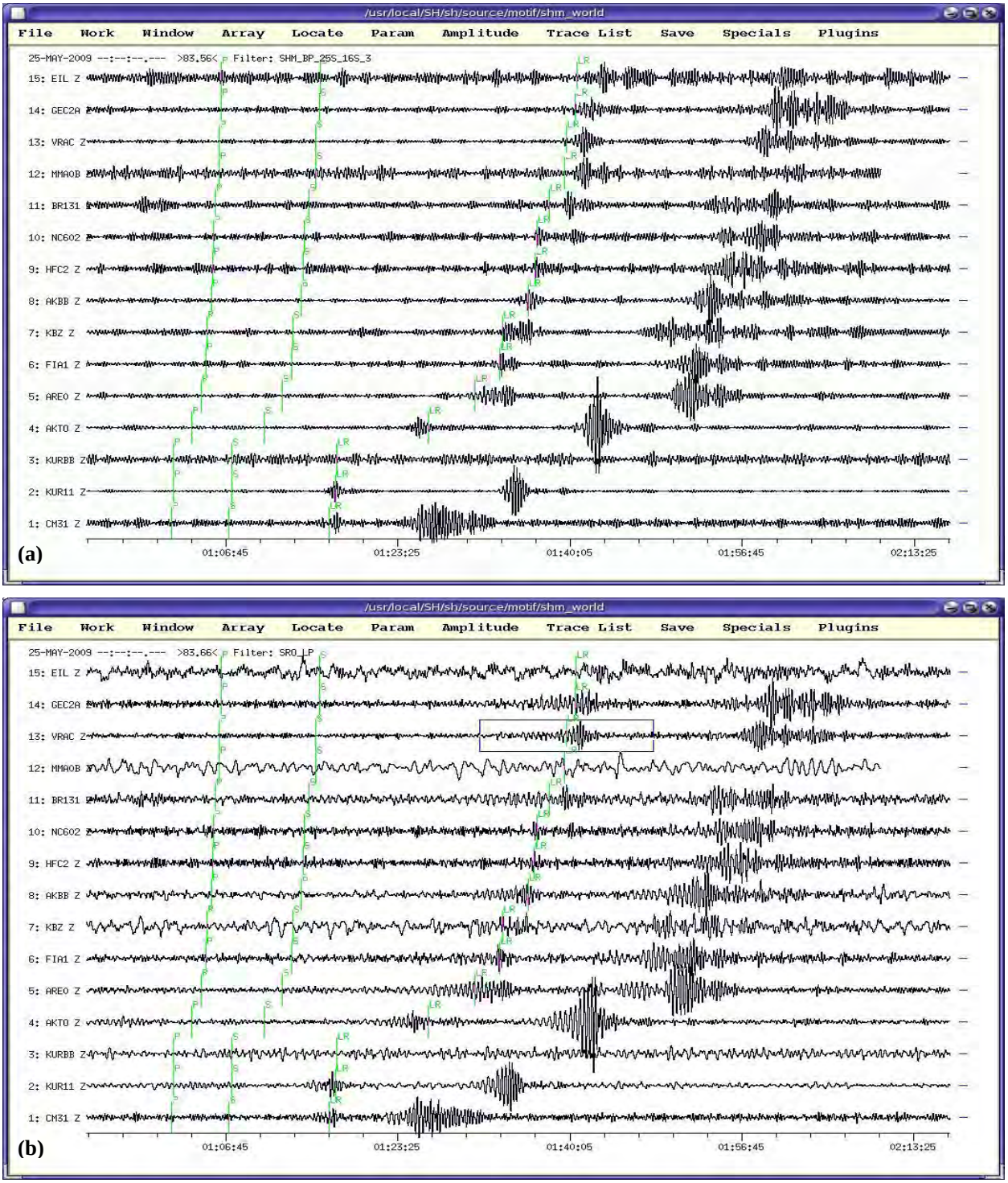

Figure 4. Band-pass filtered seismograms for another 14 IMS stations showing relevant signal levels between 16 and 25 s period (a - upper record section) at LR group velocity. For these stations SRO-LP simulated records were generated (b - lower record section). For seven stations (KURK, AKTO, ARCES, FINES, AKASG, VRAC, GERES) amplitudes can be reliably read, while signals are too marginal for the other stations (CMAR, KBZ, HFS, NOA, MMAI, EIL) (or simulation filters were not reliable from FAP representation).

Results of Surface Wave Magnitude Re-evaluation

Besides re-evaluating the measurements published in the REB (Figure 5a), additional measurements were made at IMS stations and at stations of the German Regional Seismic Network (GRSN) (Figure 5b). Each figure shows the mean Ms values for the particular data sets, plotted near the distance of 89 degrees.

Most Ms estimates of this study are very close to the REB values (Figure 5a), except for USRK. Two estimates for SONM are given: the initial (low) estimate was made on late waveform cycles and some filtering was used to get a measurement close to the signal maximum and which is consistent with the REB value. The results by Selby and Bowers (2009) show more scatter due to their estimation procedure not requiring the measurement to be done within the 18-22 s period band. While the means from the REB values and the values determined by Selby & Bowers are nearly the same, the estimate from this study given in Figure 5a shows a slightly higher value, as three below-average stations (KSRS, ATTU, MKAR) were not used.

The Ms estimates of the seven additional IMS stations, except for FINES, are all above a magnitude value of Ms=3.6 (Figure 5b). The same is found for magnitude values estimated at GRSN stations, except for one (BFO). Therefore the network-average MS values are further increasing, with the mean for all IMS stations used here resulting in Ms=3.74 and the average found for GRSN stations even 0.1 units higher. As can be seen from Figure 1, all the additional stations identified here are within the azimuth segment identified from Figure 2b. The directions are consistent with westerly directions mentioned by Bonner et al. (2008) where they found three stations with large magnitude estimates for the 2006 North Korea event.

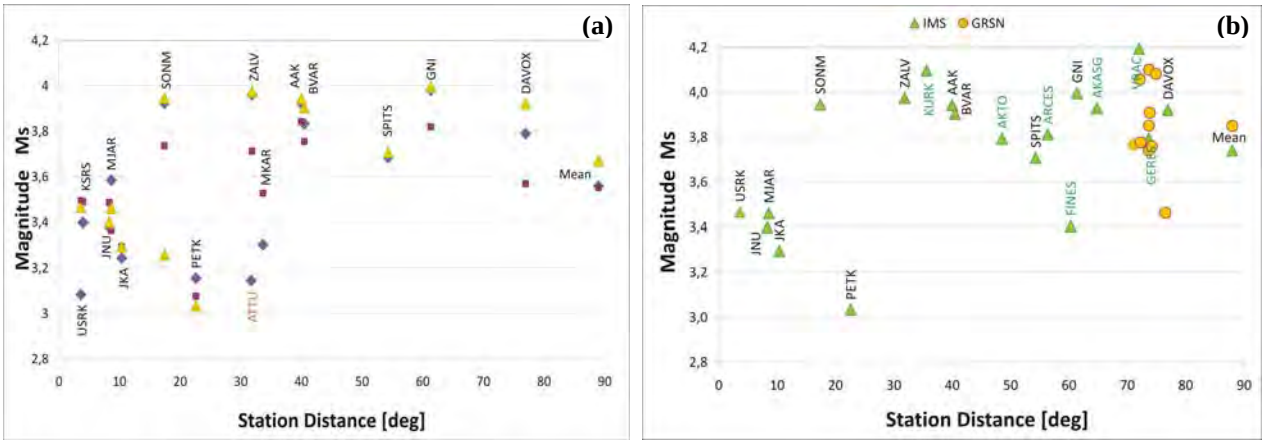

Figure 5. Results of Ms estimation for stations included in the REB with exception of ATTU (no reasonable LR) and KSRS and MKAR (FAP response) (a -left) and for additional IMS stations (lighter font) or GRSN stations (yellow dots) analyzed in this study (b – right). Ms estimates of this study (triangles) are compared to REB values (diamonds) and results by Selby and Bowers (2009) (squares).

During standard event screening carried out at the IDC all events with mb≥3.5 are considered, and if an event lies above the experimental screening line Ms=1.25 mb -2.2 (Figure 6), along with its error tolerances, it is flagged as "screened out" in relation to the mb-Ms criterion. As such the event in North Korea on 25 May 2009 was not screened out by the IDC, due to its proximity to the screening line. Similar results were also obtained by Selby and Bowers (2009). From the results obtained in this study, the event under consideration progressively moves away from the screening line as the data were reprocessed (exclusion of ATTU, KSRS and MKAR) and when including additional stations in Eurasia.

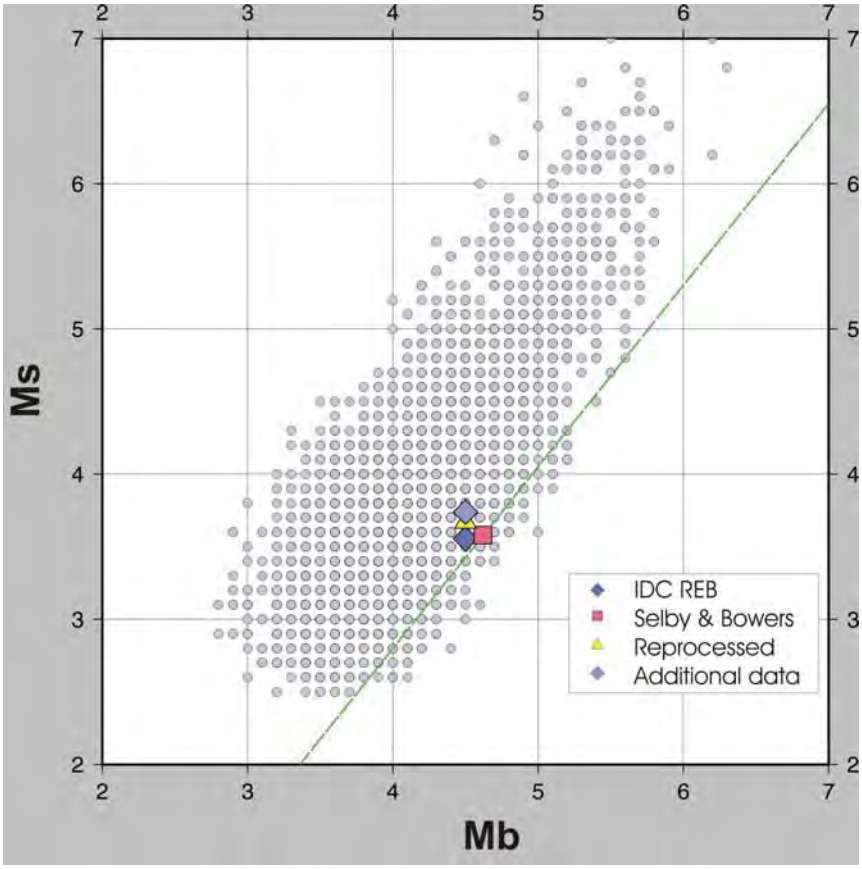

Figure 6. Results of mb versus Ms scaling for all REB events in 2009 yielding mb and Ms estimates. Also shown is the screening line (dashed green line) used in standard event screening at the IDC. Besides the REB results, those by Selby and Bowers (2009) and from this study (for REB stations and when including additional stations) are given.

CONCLUSIONS AND RECOMMENDATIONS

Surface wave magnitude estimates obtained by the IDC were revisited and, in general, the results were confirmed. However, station ATTU's estimate is based on spurious data. Furthermore there is a strong positive Ms magnitude bias for station azimuths between 290 and 320º with the stations located on the Eurasian platform. This information was used to identify additional stations showing LR signals, and corresponding magnitude estimates were made. The new estimates fit into the previously identified pattern of higher than average estimates including stations of the GRSN. The findings indicate that the event could be problematic when applying the standard event screening criterion applied at the time. Questions also arise to what extend the identified positive bias of Ms estimates for stations across the Eurasian platform are a source related effect or that propagation conditions are such that they favor high estimates. If this is the case standard event screening criteria need to be revisited, as has already begun.

REFERENCES

Bonner, J, R.B. Herrmann, D. Harkrider and M. Pasyanos (2008). The surface wave magnitude for the 9 October 2006 North Korea nuclear explosion, *Bull.Seismol.Soc.Am*. 98: 2498–2506, doi: 10.1785/0120080929

CTBTO (2009a). Press release 25 May 2009 (see http://www.ctbto.org/press-centre/press-releases/2009/ctbtos-initial-findings-on-the-dprks-2009-announced-nuclear-test/)

CTBTO (2009b). Press release 27 May 2009 (see http://www.ctbto.org/press-centre/press-releases/2009/next-phase-in-the-analysis-of-the-announced-dprk-nuclear-test/)

Ford, S. R., D. S. Dreger and W. R. Walter (2009). Source analysis of the Memorial Day explosion, Kimchaek, North Korea, *Geophys. Res. Lett*. 36: L21304, doi: 10.1029/2009GL040003

Patton, H.J. and S.R. Taylor (2008). Effects of shock-induced tensile failure on mb-Ms discrimination: Contrasts between historic nuclear explosions and the North Korean test of 9 October 2006, *Geophys. Res.Lett*. 35: L14301, doi: 10.1029/2008GL034211

Rezapour, M. and R.G. Pearce (1998). Bias in surface-wave magnitude Ms due to inadequate distance corrections, *Bull. Seismol. Soc. Am*. 88: 43–61

Selby, N.D. and D. Bowers (2009). Preliminary seismological investigation by the UK NDC of the announced DPRK nuclear test of 25th May 2009, AWE report 508/09, 35 pp.

Stammler, K. (1993). SeismicHandler - Programmable multichannel data handler for interactive and automatic processing of seismological analyses, *Computers & Geosciences* 19: 135–140.

EXAMINATION OF *P/S* SPECTRAL RATIOS FOR SMALL EXPLOSIONS AT LOCAL DISTANCES AND INTERPRETATION OF MOMENT TENSORS ESTIMATED FROM NEAR-SOURCE DATA

Mark R. Leidig[1], Brian W. Stump[2], William R. Walter[3], Anastasia F. Stroujkova[1], Xiaoning Yang[4], and Jessie L. Bonner[1]

Weston Geophysical Corp.[1], Southern Methodist University[2], Lawrence Livermore National Laboratory[3], and Los Alamos National Laboratory[4]

Sponsored by the National Nuclear Security Administration

Contract Nos. DE-AC52-08NA28655[1,2], DE-AC52-07NA27344[3], and DE-AC52-06NA25396[4]
Proposal No. BAA08-97

ABSTRACT

The ratio of 6-8 Hz *P/S* energy is a robust discriminant between earthquakes and explosions at regional distances (e.g., Taylor et al., 1989; Walter et al., 1995; Hartse et al., 1997; Pasyanos et al., 2009). We have examined the *P/S* discriminant at regional and local distances for simultaneously-detonated chemical explosions conducted for the Non-Proliferation Experiment (NPE), Source Phenomenology Experiments in Arizona (SPE Black Mesa and Morenci), Alaska Frozen Rock Experiments (FRE Frozen and Unfrozen), the New England Damage Experiment (NEDE) and other datasets. The shots were conducted at various scaled depths of burial in lithologies ranging from granite to alluvium. Several of these datasets have delay-fired mining explosions detonated in close proximity to the dedicated shots for comparison.

At regional distances, the discrimination analysis includes identifying and picking the onset times of the local and regional phases *Pn*, *Pg*, and *Lg*, making amplitude measurements in a variety of passbands, normalizing those measurements for the effects of source and path using the Magnitude and Distance Amplitude Correction (MDAC) methodology (Walter and Taylor, 2002), and calculating *P/S* ratios for each event. We find that the MDAC-corrected SPE Black Mesa ratios fall in the middle of the nuclear explosion population at station KNB with very little variation due to the differing shot conditions.

At local distances, we windowed the *P*- and *S*-waves based on travel times and particle motion. We then estimated smoothed spectra for the *P*- and *S*-waves and formed *P/S* spectral ratios. The signal quality and difficulty in picking the shear arrival varied between the data sets. The NEDE dataset had the best *S*-wave development, while other datasets were complicated by *P*-coda, small amplitude shear-wave generation, and additional arrivals that were not shear waves based on velocity and polarization analyses. Some of the variability in the *P/S* results could be related to error in the phase picking and analysis.

We typically observed larger *P/S* ratios for confined shots than free-face shots. We also observed larger *P/S* ratios for the NEDE Comp B shots than with ANFO shots. There are a number of interesting and unexplained results including: a) well defined shear waves from the NEDE compared to the other experiments, b) large variations in ratios with distance for SPE Black Mesa Shot 1 and the NEDE black powder shot, c) FRE having the largest ratios at certain distances and near smallest at others, d) the FRE frozen rock shot ratios not consistently larger than the unfrozen rock shots, and e) some well-confined Morenci shots having ratios similar to free-face shots. We plan to address these issues during the final year of this project.

The resolution of moment tensors determined using near-source observations is dependent upon the observations, the propagation path model and source model assumptions. Moment tensors determined from the inversion of near-source data generated by a contained single-fired explosion conducted at SPE Morenci (copper mine) document a strong Compensated Linear Vector Dipole (CLVD) contribution. A set of numerical tests are reviewed that assess the uniqueness of this source interpretation.

OBJECTIVES

We continue to study the physical mechanisms for shear wave generation from small chemical explosions. We are conducting moment tensor inversions and analyzing regional and local distance *P/S* ratios for a variety of different explosion experiments relative to normal production mining explosions, natural earthquakes, and previous nuclear tests at the Nevada Test Site.

RESEARCH ACCOMPLISHED

Interpretation of Near-Source Moment Tensor Inversions

The resolution of the seismic source is dependent upon the source model parameterization, the observational data and propagation path effects. The Source Phenomenology Experiment (SPE) conducted a series of single-fired experiments in a copper mine in Arizona (Morenci) and a coal mine in Arizona (Black Mesa) providing the opportunity to investigate the source characterization of explosions and address the resolution of the source. Here we discuss some of the resolution issues as investigated through source inversions of the copper mine explosions focusing on the effects of observational data and a complementary synthtic study focusing on the importance of the source parameterization. Critical to these studies is the establishment of the importance of isotropic versus nonisotropic source contributions with a goal of improved understanding of *S*-wave generation from explosions.

Zhou et al. (2005) report on moment tensor inversions for a number of the single-fired explosions as part of SPE Morenci showing both the effects of assumed propagation path model as well as the distribution of stations observing the source. One of these moment tensor inversions is summarized below where 8 three-component records from a variety of azimuths (~180^{o} coverage) and distance ranges (~150 to 700 m) were utilized in an inversion for the moment tensor for a contained explosion with a total explosive weight of 13,600 lbs and a scaled depth of 127 m/kt$^{1/3}$ (SPE Morenci Shot 10). The moment tensor that was estimated for this explosion is reproduced in Figure 1. It illustrates the strong contribution from the diagonal elements of the moment tensor characteristic of an explosion but also includes an enhanced M_{zz} component with the ratio of M_{xx}:M_{yy}:M_{zz} approximately 1:1:2 characteristic of a CLVD. This ratio and the relative size of the moment estimates were insensitive to choices of stations used in the inversion. The condition number (Figure 1) from the inversion provides a measure of the adequacy of the station distribution for unique recovery of all elements of the moment tensor as a function of frequency. Typically condition numbers below 100 are satisfactory. The physical interpretation of this source and the uniqueness of the interpretation are further illustrated with some simple numerical experiments reported next.

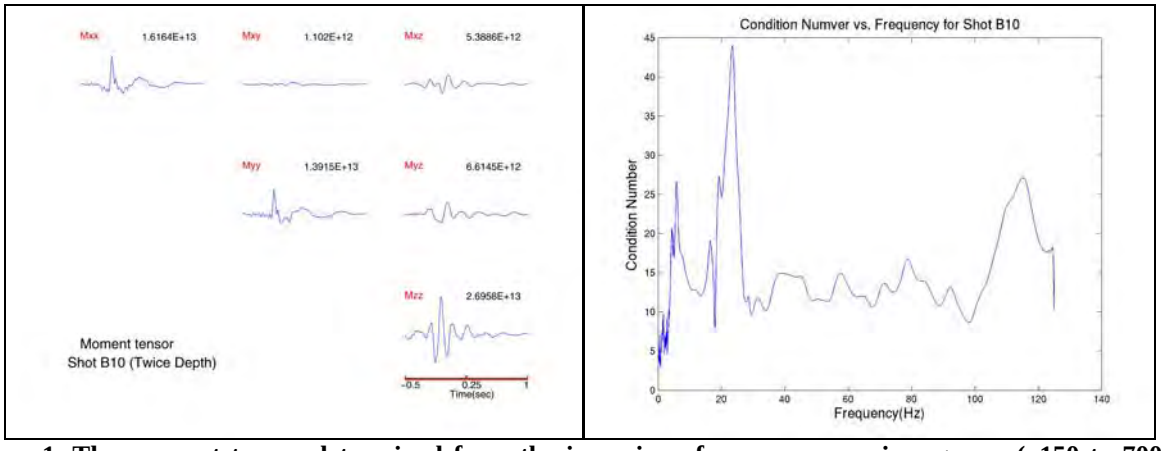

Figure 1. The moment tensor determined from the inversion of near-source seismograms (~150 to 700 m) from Shot B10 (13,600 lbs and scaled depth of 127 m/kt$^{1/3}$) is displayed on the left. The condition number from the inversion is plotted versus frequency in the right figure.

A number of physical models of the source have been proposed for the estimated moment tensor asymmetry documented including the effect of near-surface spallation and more broadly the interaction of the explosion stress waves with the region above the detonation point. The interpretation of the resulting moment tensor is dependent

upon the uniqueness of the moment tensor representation, the resolution of the individual elements of the moment tensor and the importance of assumed source depth in these source inversions.

Spallation that accompanies explosions detonated near the free surface can result from the tensile failure of the near surface layers above the source. This nonlinear failure can re-partition the initially symmetric wave field into waves indicative of cylindrical symmetry. This secondary source can be represented by a set of vertical forces that are applied at a shallower depth than the initial explosion. A set of numerical tests was conducted to illuminate these effects and their relationship to the moment tensor representation. These tests were designed to replicate a contained explosion at a depth of 11.5 m (253 lbs yield) with observations from 50 to 150 m, somewhat similar to the depths and ranges in the SPE inversions. The spallation source was computed for a depth of 3 m. Figure 2 illustrates the similarity of radiated vertical waveforms from the vertical force and waveforms generated by a CLVD. Except for a difference of one temporal differential, the point force and CLVD sources produce very similar waveforms in an elastic half space even with their differences in depth. Comparison of both the radial and vertical synthtics for the two sources produce similar relative amplitudes and decays over a range of distances as demonstrated in Figure 2.

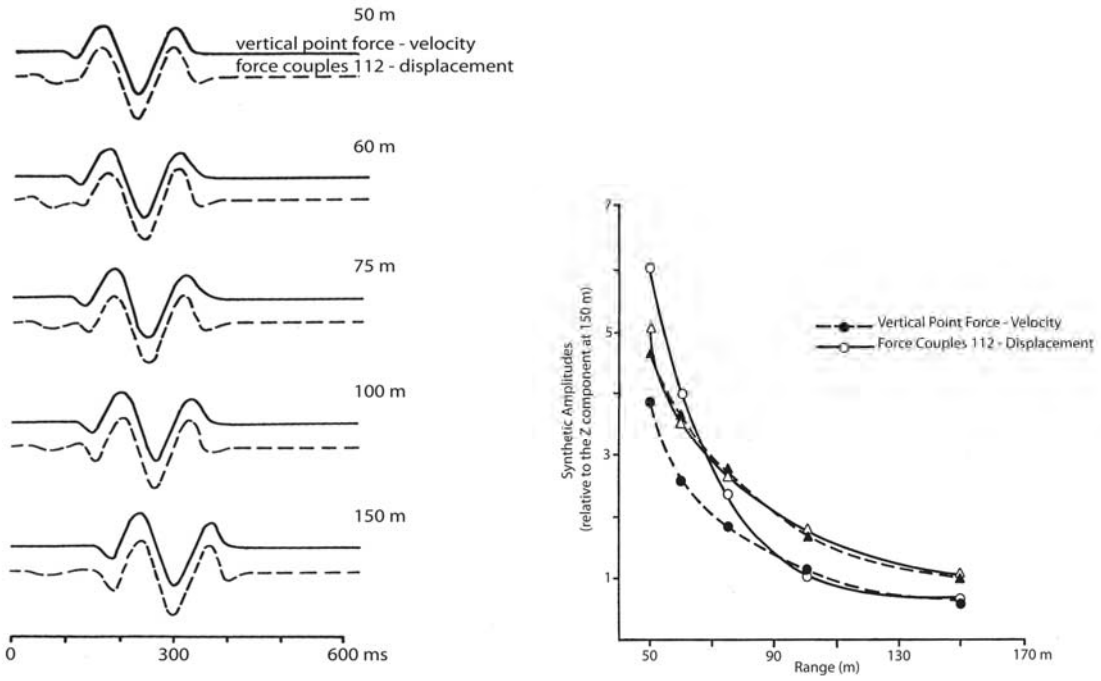

Figure 2. (Left) Comparison of vertical velocity from a vertical point force source at 3m in an elastic half-space to the vertical displacement from a CLVD at 11.5 m illustrating the similarity of waveforms. (Right) The spatial decay of the vertical and radial velocity from the vertical point force and the vertical and radial displacement from the CLVD over the distance range of 50 to 150 m.

These synthetic comparisons illustrate the great similarity of waveforms expected from a CLVD and vertical force source model. They reflect a linearity between the two models that must be taken into account when either completing source inversions or interpreting the resulting representation. As noted earlier, the condition number of moment tensor inversions is one way to quantify these interactions. A set of synthetic seismograms was produced combining a spall source at 3 m and an isotropic explosion at 11.5 m. An inversion that included the moment tensor plus vertical point force was compared to an inversion in which the source was represented only as a moment tensor. The condition numbers for these two inversions are replicated in Figure 3 and illustrates that the strong linearity between the vertical point source and the CLVD results in large condition numbers when the point force is included.

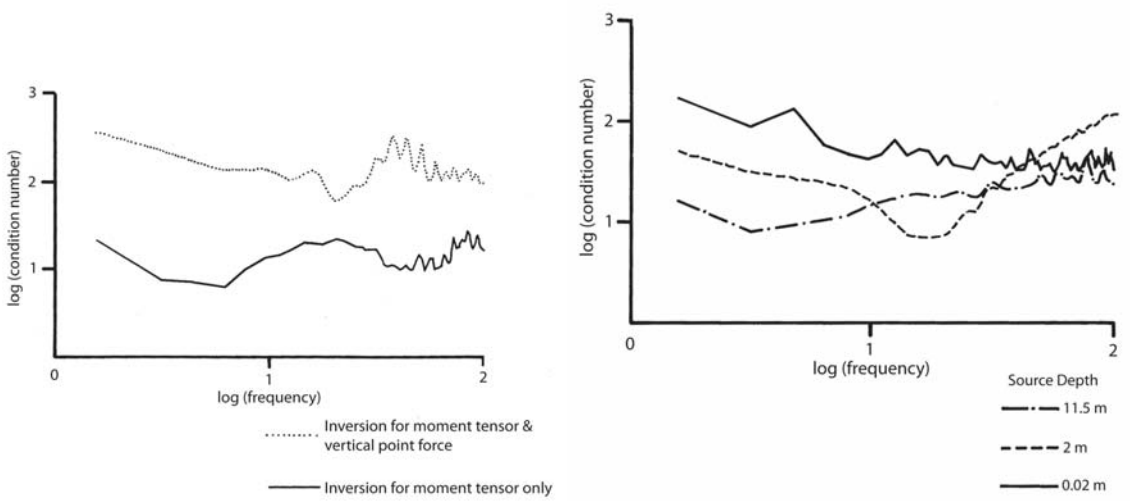

Figure 3. (Left) Condition numbers from a synthetic inversion that includes a moment tensor plus vertical point source representation and an inversion that is represented by only a moment tensors. (Right) Condition numbers for moment tensor inversions with source depths from 11.5 to 0.02 m.

One final synthetic test illustrates additional considerations when conducting near-source moment tensor inversions, the assumption of source depth. As shown earlier in the synthetic waveform comparison (Figure 2), possible differences in source depth for different parts of the source representation may be difficult to resolve with near-source data. As the depth of the source becomes shallower, there is additional non-uniqueness introduced by the free surface. Figure 3 reproduces the condition numbers for a series of near-surface (50 to 150 m range observation) moment tensor inversions at ever-shallower depths. A general increase in condition number with frequency and decreasing source depth documents the problem in fully resolving the moment tensor for shallow explosions.

In conclusion, moment tensor inversions from the SPE explosions detonated in a copper mine show a strong CLVD contribution. Inversions with different distributions of observations suggest that this contribution is not affected by station distribution. Synthetic tests are consistent with this source resulting from a spall contribution although depth resolution of this secondary source may affect a unique physical interpretation of the source. Secondary sources with very shallow depths, especially as they approach the free surface, may be difficult to resolve as indicated by the synthetic tests. Work still remains to be completed to address trade-offs between the assumed propagation path effects and the resulting moment tensors.

Regional Distance *P/S* Ratios

We have examined the behavior of regional discriminants from the Arizona SPE. The discrimination analysis includes identifying and picking the onset times of the local and regional phases *Pn*, *Pg*, and *Lg*, making amplitude measurements in a variety of passbands, normalizing those measurements for the effects of source and path using the MDAC methodology (Walter and Taylor, 2002), and calculating *P/S* ratios for each event. Figure 4 shows the 6-8 Hz *Pg/Lg* ratio results at station KNB (Kanab, Utah) for six of the Black Mesa coal mine SPE shots (diamonds) and production mining explosions (triangles), compared to a set of nuclear tests (stars) and western U.S. earthquakes (circles). We find that the MDAC-corrected production explosions and SPE shots at Black Mesa fall in the middle of the nuclear explosion population with very little variation due to the differing shot conditions. Thus for this particular discriminant at this station, the SPE shots and mining explosions are good surrogates for nuclear explosions, and the differences in depth of burial and single versus multiple shot have only a small effect on the discriminant measures.

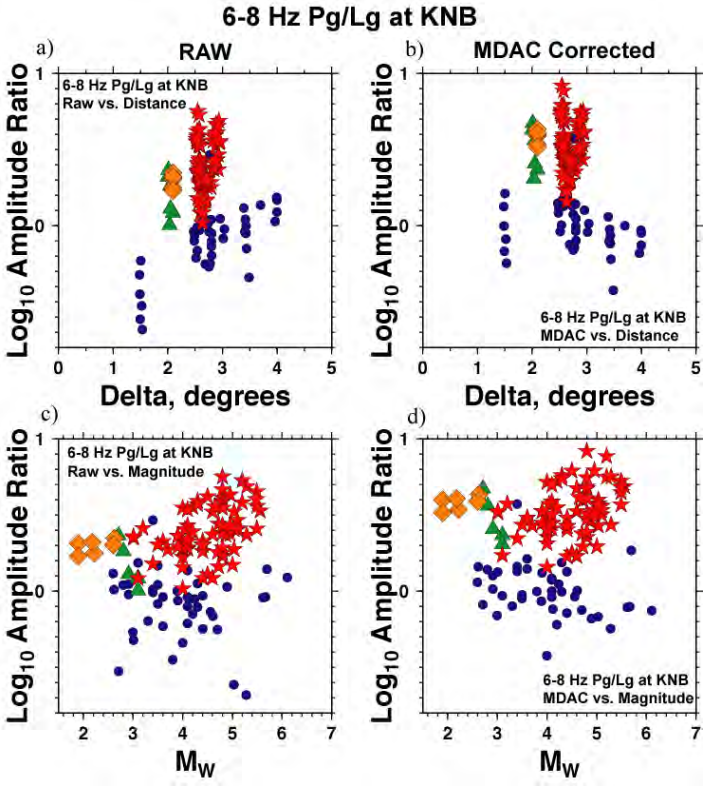

Figure 4. Comparison of six SPE shots from the Black Mesa coal mine (diamonds) with production shots at the same mine (triangles) at station KNB using the 6-8 Hz *Pg/Lg* discriminant (e.g. Walter *et al.*, 1995). The ratios are plotted as either raw (a and c) or MDAC-corrected (b and d) amplitude ratios as a function of distance (a and b) or moment magnitude (c and d). The SPE shots show low variability and have similar values to the mean of the nuclear tests (stars), making them possible surrogates in this discriminant case. Earthquakes are plotted as circles.

Local Distances *P/S* Ratios

Data. We have examined the *P/S* ratios at local distances for simultaneously-detonated chemical explosions conducted for the SPE Morenci and Black Mesa (Bonner et al., 2005), Alaska Frozen Rock Experiments (FRE Frozen and Unfrozen; Bonner et al., 2009), the New England Damage Experiment (NEDE; Leidig et al., 2010) and other datasets. The shots were conducted at various scaled depths of burial in lithologies ranging from granite to alluvium. Several of these datasets have delay-fired mining explosions detonated in close proximity to the dedicated shots for comparison.

Processing. To compare *P* and *S* amplitudes we processed data from the 3-component stations that recorded each of these explosion experiments at local distances. We used remote stations (> 5 km) because *S* and *Rg* phases are not well-separated at distances less than a few kilometers. The initial part of the data processing included correction for the instrument response. The next step in the data processing is identifying *S*-waves. It was done by studying the apparent velocity of the phase (moveout) and the particle motion for the 3C stations. Figure 5 shows the particle motions for NEDE Shot 4 at station SE02 (6 km). At this distance the *S* arrival is separated from the *Rg* phase, which dominates the waveforms at shorter distances. The *P*-wave arrival is polarized approximately parallel to the propagation azimuth. The arrival in the presumed *S*-window in question is polarized approximately perpendicular to the propagation azimuth suggesting that this is indeed an *S* wave.

Signal Quality. The signal quality and difficulty in picking the shear arrival varied between the data sets. The NEDE dataset had the best *S*-wave development, especially at SE02 (Figure 5). The *P* and *S* arrivals are easy to identify in the waveforms and the particle motions show more classic *P* and *S* motion than for the other experiments.

For the SPE data, distinct *S* arrivals were difficult to identify in the waveforms. The *S* windows had little transverse motion, but considerable radial motion indicating possible contamination by *P* coda. Both the SPE Morenci and Black Mesa recordings contained many arrivals other than the simple *P*, *S*, and surface waves. These arrivals could be reflected or refracted *P* waves, but regardless, they make *S* identification more difficult and add noise to the shear wave window.

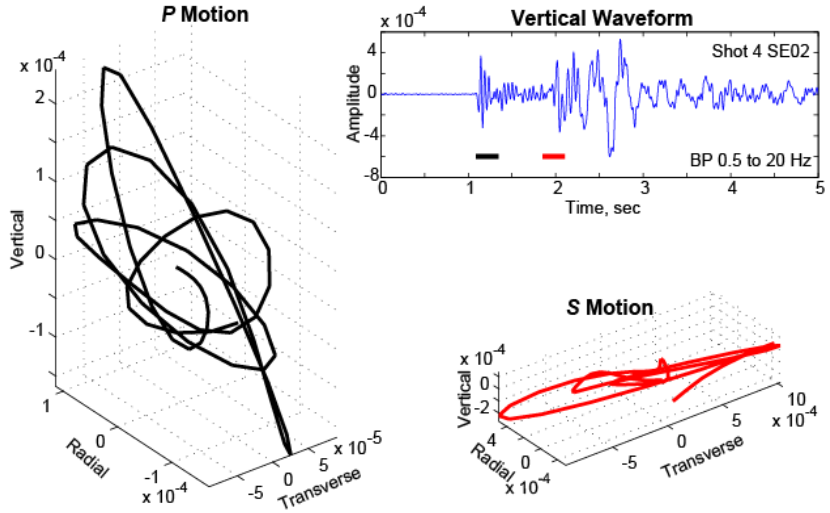

Figure 5. Seismogram (top right) and particle motion plots (left and bottom right) for NEDE Shot 4 records at station SE02.

The *S* waves from the FRE frozen rock shots were extremely difficult to observe in the waveforms, while they were easier to identify from the unfrozen FRE rock shots. The low amplitude *S* window motions resemble *P* motions and again may indicate *P* coda contamination. An interesting arrival only on the transverse component was noted at one station. The arrival came in prior to the expected *S* arrival and could possibly be a *P*-to-*S* conversion somewhere along the travel path.

***P/S* Spectral Ratios.** Once the *P* and *S* windowing were complete, a power spectral density (PSD) using Welch's method was calculated on *P*, *S*, and noise windows from the vertical component. Ratios were then formed using the smoothed spectra. Examination of *P/S* spectral ratios was conducted using equal event-to-station distances to compare different emplacement media. Shot 3 from the Morenci SPE, Shot 7 from the Black Mesa SPE, Shots 2 and 5 from the FRE, and Shot 4 from the NEDE were chosen for comparison as each used ANFO and had similar yields and emplacement depths. Stations at similar distances of 6 and 12 km from each shot were used (Table 1).

Figure 6 shows that the *P/S* spectral ratios at distances of 6 km and 12 km have interesting differences and similarities. For measurements on stations at ~6 km, the ratios are near or below 1 for frequencies below 10 Hz and then gradually build to peak around 30 Hz, except for the Black Mesa curve which peaks at 50 Hz. At 12 km distance, there is a large range of peak ratio frequencies ranging from 9 to 40 Hz. As at 6 km, the Black Mesa shot has the largest peak *P/S* ratio and the NEDE shot has the smallest ratio. The spectra of the two FRE shots have a similar shape, but have a frequency shift with the frozen rock shot peaking at a higher frequency.

In addition, we examined the *P/S* ratios in discrete frequency bands of 1-2, 2-4, 4-8, and 8-16 Hz for all shots and experiments. The ratios were excluded from analysis if the spectra or waveforms were suspected of being affected by the background noise or other 'foreign' signal. Therefore not every shot is represented at every distance. Distances of 6, 12, and 24 km were examined for each experiment. There was not a station near 24 km distance for Black Mesa SPE, so a station at 34 km distance was used. Table 1 lists the stations used and their average distances.

The ratios were compared for each shot as a function of frequency, distance, and yield. The *P/S* ratios in the following plots are color coded by experiment (Table 2) and the symbol shape represents the experiment shot number (Table 3). Note that the Morenci Shot 9 did not detonate so Shot 10 is given the Shot 9 symbol.

Table 1. Analyzed Stations and Distances (km)

SPE Morenci		SPE Black Mesa		FRE		NEDE	
MR02 6	.1	L3A	4.7	MDR	5.5	SE02	6.0
MR04 12	.1	NN24	13.9	PED	13	SE04	12.2
MR08 25	.1	NN23	34.5	ALPAF	22.3	SE08	23.7

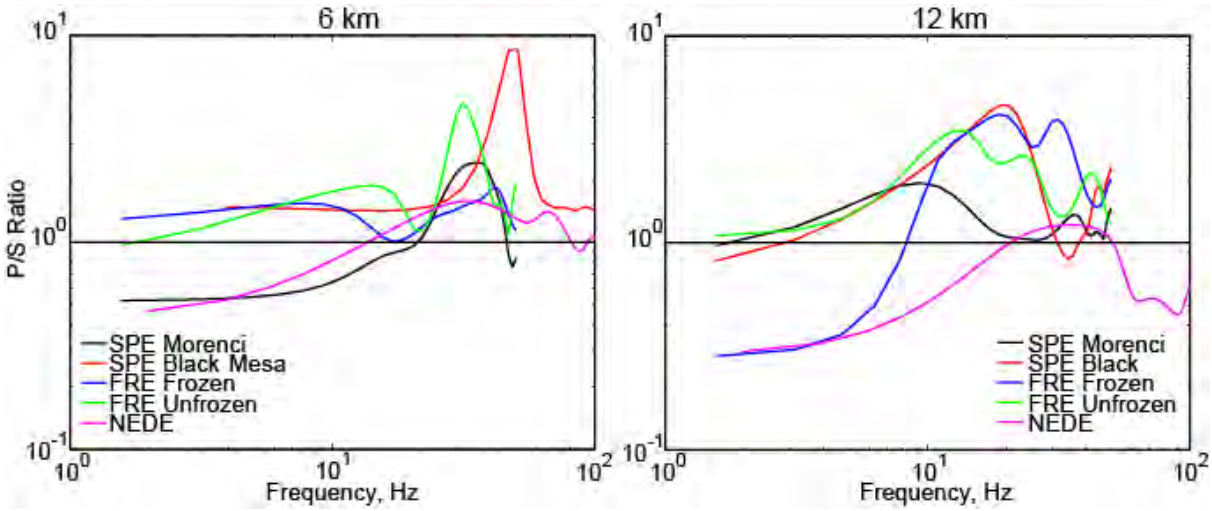

Figure 6. Spectral ratios at equidistant stations of a) 6 km and b) 12 km for the different explosion experiments.

Table 2. Experiment Color Legend

Experiment	Symbol Color
SPE Morenci	Black
SPE Black Mesa	Red
FRE	Blue
NEDE	Green

Table 3. Shot Symbol Legend

Shot #	Symbol
1	+
2	O
3	*
4	□
5	◊
6	△
7	▽
8	☆
9/10	◁

***P/S* Ratio versus Distance.** Figure 7 plots the discrete frequency band *P/S* ratios as a function of distance. At 6 km distance, all ratios are greater than 0.9. The smallest ratios (0.3) and the largest spread of ratios are observed at 12 km distance. By 24/34 km, the scatter is reduced and the minimum ratio value has increased to 0.5. The FRE ratios decrease with distance, while the NEDE ratios decrease from 6 to 12 km but increase out to 24 km. The SPE Black Mesa ratios have a similar characteristic, except they are almost equal amplitude at all distances in the 8 to 16 Hz range. The Morenci ratios show the least variation across the distance ranges. At each distance, the NEDE ratios are typically the smallest. As noted previously, this data set had the most distinct shear wave arrivals, which may explain this observation. At 6 and 12 km, the FRE data set has some of the largest *P/S* ratios, but Morenci shots have the largest ratio at 24 km.

When comparing individual shots in each data set, it is observed that Shots 8 and 5 (2x burden shots) had the largest *P/S* ratios for SPE Morenci. Shots 2, 4, 6, and 7 (free-face and 2x depth shots) had the lowest ratios. Except for the 2x depth shots, these results are not surprising. The SPE Black Mesa shot ratios are tightly packed, with the

exclusion of Shot 1. Shots 8 and 9 (free-face shots) routinely show up near the bottom of the ratios, but this is not consistent and the difference is small. SPE Black Mesa Shot 1 is peculiar. This blast was conducted in a straight line of boreholes detonated near-simultaneously. The *P/S* ratio is at least 50% larger than the other SPE Black Mesa ratios at 6 km, but is barely half the size of the other ratios at 12 km. By 34 km, the ratio is indistinguishable from the other shots. Since this shot least resembled a point source, it is possible that a phase radiation pattern was generated and the station azimuth is affecting the ratios.

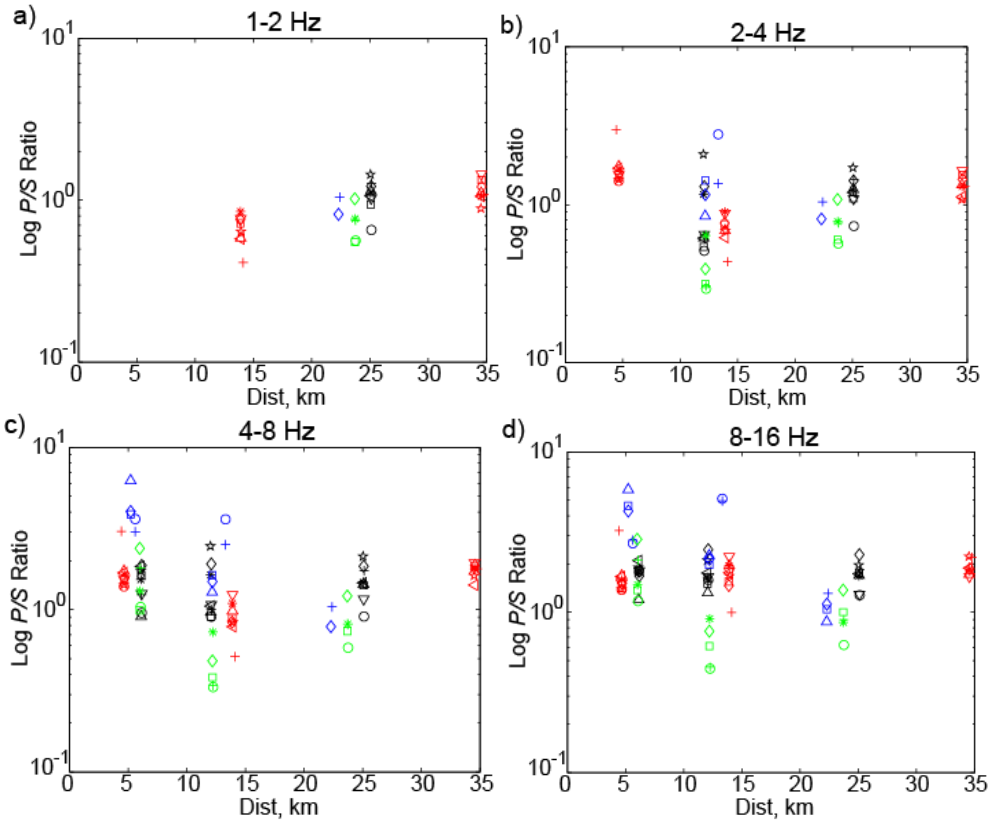

Figure 7. *P/S* spectral ratio as a function of distance. a) 1-2 Hz, b) 2-4 Hz, c) 4-8 Hz, d) 8-16 Hz. The data key is provided in Tables 2 and 3.

At 6 km distance, the FRE unfrozen rock shots have larger ratios (the largest ratios observed for all experiments), but elsewhere the frozen rock shots have larger ratios. The cause of this change is unclear but may be related to the near- source topography. The unfrozen rock shots and the MDR station near 6 km were located on a topographic high, while the frozen rock shots were detonated in a valley below. The ratios at the further stations may have been less affected by the topographic variations. There is not a clear relationship between shot size and *P/S* ratio within either group of frozen and unfrozen rock shots.

The NEDE Comp B shots exhibit the largest *P/S* ratios for that experiment with Shot 5 the largest at 6 and 24 km and Shot 3 the largest at 12 km. The NEDE ANFO Shots 2 and 4 have the smallest ratios at all distances and for all experiments. Shot 2 typically has the smallest ratio. The ratios for these two explosive types of shots behave exactly as anticipated and documented in previous work (Leidig et al., 2009). The Comp B shots lacked the shear wave generating fractures and therefore have a large *P/S* ratio. The NEDE black powder shot has peculiar behavior with distance though. At 6 km distance the ratio is large, at 12 km distance the ratio is similar to that of ANFO Shot 2 as the smallest, and finally at 24 km the ratio equals that of the Comp B Shot 3. However, the black powder shot was very deficient in high frequency energy as evidenced by near-source acceleration recordings.

***P/S* Ratio versus Frequency.** In Figure 8, the ratios are plotted as a function of frequency. A lack of temporal phase separation at the closer stations required shorter phase time windows which reduced the amount of data available in

the 1-2 and 2-4 Hz ranges. The ratios show a clear increase with frequency, particularly at 12 and 24 km distance. The scatter in the ratios is greatly reduced at 24/34 km distance. At this distance the two SPE data sets overlap, while the FRE and NEDE data sets overlap at slightly reduced ratios. At 12 km, FRE has the largest ratios, followed by the overlapped SPE data sets, and finally the NEDE ratios. The changes in ratio order with distance indicate the travel path and/or near receiver effects control the *P/S* ratio more than frequency, and this may provide evidence of shear wave generation away from the source. The frequency ranges at 6 km distance show overlapped ratios for SPE Morenci, SPE Black Mesa, and the NEDE, while the FRE ratios are distinctly larger.

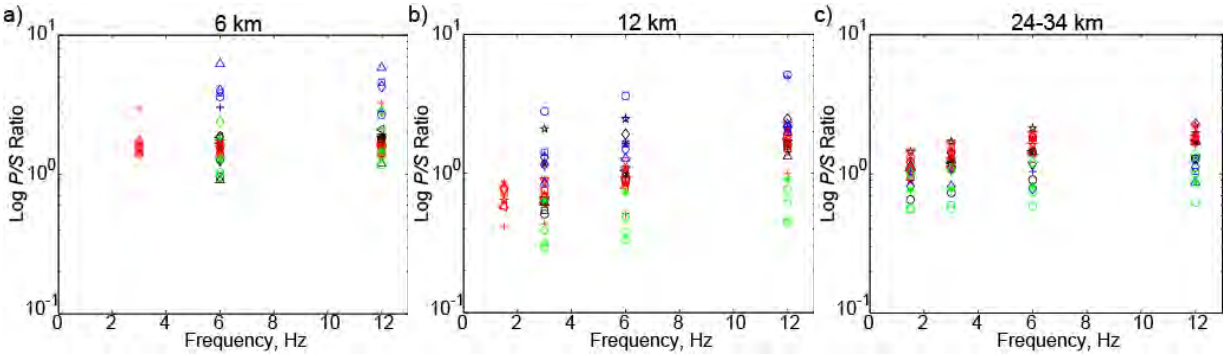

Figure 8. *P/S* spectral ratio as a function of frequency. a) 6 km, b) 12 km, c) 24/34 km. The data key is provided in Tables 2 and 3.

***P/S* Ratio of Single-Fired versus Delay-Fired Shots.** The *P/S* ratios of delay-fired mining blasts were also examined. Partial documentation of 8 production blasts at Morenci was obtained and 3 of these shots were examined. Documentation of 40 production shots at SPE Black Mesa was obtained. Only a handful of these events were recorded by the experiment equipment due to limited installation dates. Most of these shots had very small yield per 8 msec delay and resulted in very noisy recordings not suited for this analysis. Some of the larger yield/delay shots were near simultaneously detonated with other shots resulting in contaminated signals. Only one event was recorded on both L3A and NN24 with good signal-to-noise ratio.

The production shots were not conducted in the same test pits as the experiment explosions which created variations in distance and travel path. For example, station L3A was about 6 km from the SPE Black Mesa single-fired shots, but was more than 12 km from the production shot. Station NN24, which was around 14 km from the SPE blasts, was only about 8 km from the production shot.

Figure 9 plots the SPE single- and delay-fired blasts as a function of distance. Tables 2 and 3 apply to these plots except blue symbols are the Morenci production shots and green symbols are the SPE Black Mesa production shots. The most obvious difference in the *P/S* ratios is that the production ratios are typically less than the experiment blast ratios. In fact, some of the ratios are up to an order of magnitude smaller. This is particularly true at the shorter distances as the production shot ratios increase with distance while the single-fired ratios are more consistent. By 24/34 km distance, it would be nearly impossible to discriminate a single-fired shot from a delay-fired shot using *P/S* ratios, which is consistent with the regional distance data presented in Figure 4. At distances less than 15 km, setting a ratio threshold of 0.8 would do a decent job discriminating the shot types. Between 8 and 16 Hz, this would work well, but the misclassification increases with decreasing frequency.

CONCLUSIONS AND RECOMMENDATIONS

We have finished the first stage of our analysis of local *P/S* ratios from many small explosions in different emplacement media. The next stage will include examining earthquakes at similar distances and adding additional mining explosions. The final results will then be compared with regional MDAC-corrected data for chemical and nuclear explosions, mining explosions, and earthquakes. The largest uncertainty in the local distance *P/S* analysis is the correct identification of the shear wave arrivals by the analyst. Rotated three-component waveforms, hodograms,

record sections, and theoretical arrival times were used to aid the analyst, but the difficulty in confidently identifying the arrival in the filtered waveforms may result in error.

Many of the *P/S* ratios behaved as would be expected, as we observed larger ratios for confined shots than free-face shots and larger ratios for the NEDE Comp B shots than the ANFO shots. There are a number of interesting and unexplained results including: a) well defined shear waves from the NEDE compared to the other experiments, b) large variations in ratios with distance for the linear Black Mesa Shot 1 and the NEDE black powder shot, c) FRE having the largest ratios at certain distances and near smallest at others, d) the FRE frozen rock shot ratios not consistently larger than the unfrozen rock shots, and e) some well-confined Morenci shots having ratios similar to free-face shots. We plan to address these issues during the final year of this project.

Moment tensor inversions suggest a CLVD as a possible major component of the SPE Morenci sources. Synthetic models indicate spall as an additional possible source mechanism component, although reduced depth resolution could reduce the uniqueness of the physical interpretation.

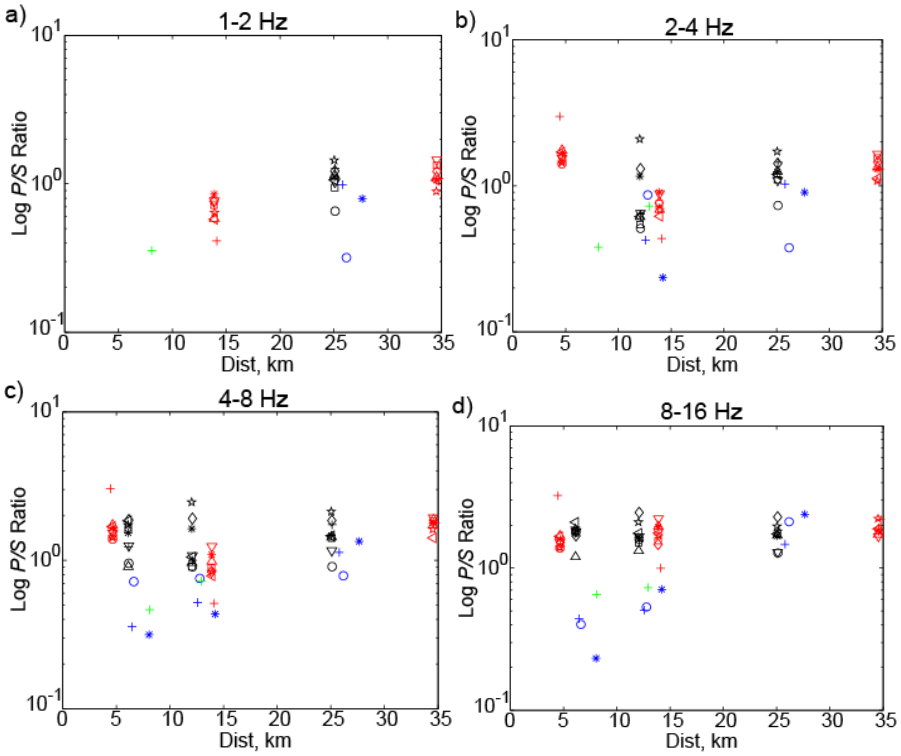

Figure 9. *P/S* spectral ratio as a function of distance for SPE planned and production shots. a) 1-2 Hz, b) 2-4 Hz, c) 4-8 Hz, d) 8-16 Hz. Figure key is shown in Tables 2 and 3, except blue symbols are Morenci production shots and green symbols are Black Mesa production shots.

REFERENCES

Bonner, J. L., B. Stump, M. Leidig, H. Hooper, X. Yang, R. Zhou, T. S. Kim, W. R. Walter, A. Velasco, C. Hayward, D. Baker, C. L. Edwards, S. Harder, T. Glenn, C. Zeiler, J. Britton, and J. F. Lewkowicz (2005). Source Phenomenology Experiments in Arizona, Weston Geophysical Corp. Final Report, 358 p.

Bonner, J. L., M. R. Leidig, C. Sammis, R .J. Martin (2009). Explosion coupling in frozen and unfrozen rock: experimental data collection and analysis. *Bull. Seism. Soc. Am.* 99**:** 830–851.

Hartse, H. E., S. R. Taylor, W. S. Scott, and G. E. Randall (1997). A preliminary study of regional seismic discrimination in central Asia with emphasis in western China, *Bull. Seismol. Soc. Am*. 87: 551–568.

Leidig, M., J. L. Bonner, T. Rath, and D. Murray (2010). Quantification of ground vibration differences from well-confined si ngle-hole ex plosions with va riable vel ocity of detonation, *Int. J. Rock Mech. Min. Sci.,* 47: 42–49.

Leidig, M., R. Mar tin, P. Boyd, J. Bonner, and A. Stroujkova (2009). Qua ntification of rock dam age from small explosions and its effect on shear-wave generation: phase I—homogenous crystalline rock, in *Proceedings of the 2009 Monitoring Research Review*: *Ground-Based Nuclear Explosion Monitoring Technologies*, LA-UR-09-05276, Vol. 1, pp. 492–501.

Pasyanos, M. E., E. M. Matzel, W. R. Walter, and A. J. Rodgers (2009). Broadband *Lg* attenuation modeling in the Middle East, *Geophys. J. Int.* 177: *1166-1176, doi:10.1111/j.1365-246X.2009.04128.x.*

Taylor, S. R., M. D. Denny, E. S. Vergino, and R. E. Glaser (1989). Regional discrimination between NTS explosions and western U.S. earthquakes, *Bull. Seismol. Soc. Am.* 79: 1142–1176.

Walter, W. R., K. Mayeda, and H. J. Patton (1995). Phase and spectral ratio discrimination between NTS earthquakes and explosions, part 1: Emipirical observations, *Bull. Seismol. Soc. Am*. 85: 1050–1067.

Walter, W. R. and S. R. Taylor (2002). A revised Magnitude and Distance Amplitude Correction (MDAC2) procedure for regional seismic discriminants. Lawrence Livermore National Laboratory UCRL-ID-146882.

Zhou, R., B. W. Stump and X. Yang (2005). Moment tensor inversions of single-fired mining explosions at a copper mine in Arizona, *Eos Trans. AGU*, 86(52), Fall Meet. Suppl., Abstract S11B-0166.

CORRELATING NEAR-SOURCE ROCK DAMAGE FROM SINGLE-HOLE EXPLOSIONS TO SEISMIC WAVES

Randolph J. Martin[1], Peter J. Boyd[1], Anastasia F. Stroujkova[2], Mark R. Leidig[2], Lanbo Liu[3], James F. Lewkowicz[2], and Jessie L. Bonner[2]

New England Research Inc. [1], Weston Geophysical Corporation[2], and University of Connecticut[3]

Sponsored by the Air Force Research Laboratory

Award No. FA9453-10-C-0257
Proposal No. BAA10-19

ABSTRACT

We have conducted the Vermont Damage Experiment in central Vermont during July 2008. Five single-hole explosions with yields ranging from 61.5 to 122 kg were detonated in homogeneous, low fracture density granite. The centroid depths for the explosions ranged from ~8 to 13 meters. Explosives with different velocities of detonation (VOD), including black powder (0.53 km/sec), heavy ANFO (4.8 km/sec), and COMP B (8.1 km/sec) were detonated to relate the VOD to seismic wave generation and extent of damage in the source region. The purpose of this paper is to present the analysis of pre- and post-shot corings and borehole imaging in order to relate the microscopic and macroscopic damage caused by the explosions to the frequency-dependent differences in seismic wave generation.

Examination of the ground surface after the blasts found no radial fractures produced by the COMP B explosions, while there were large fractures with displacement from the heavy ANFO and Black Powder shots. Examination of the cores showed few native fractures in the pre-shot medium. Post-shot core was fragmented in the vicinity of the shot point, while intervals above the emplacement depth had less fragmentation. Large scale induced fractures developed for only short distances below the shot points. Blast induced disking of the core was observed in each of the post-shot cores. In addition, visual observation of the post-shot cores showed gross changes in appearance in the vicinity of the working point. The native rock is bluish gray, while the rock recovered near the blasts is lighter colored than the rock outside the working point. The change in appearance is likely due to shattering or crushing of the grains. Density of the rock in the vicinity of the shot points decreased after the blast with a corresponding increase in porosity. Laboratory measurements also show significant changes in rock properties due to blast damage, with higher permeabilities, lower resistivities and acoustic velocity reductions of greater than 20%.

Over 120 seismic stations were deployed to record the explosions at distances between 5 m and 30 km. Analysis of the seismic waves showed distinct differences in amplitudes between the three shots of the equal yields, with the heavy ANFO and COMP B producing larger seismic waves than the Black Powder at frequencies greater than 10 Hz. The slower VOD explosives (e.g., ANFO and Black Powder) produced larger amplitudes than the COMP B at frequencies below 8 Hz.

For the next phase of this study, we will continue to quantify the bulk properties, density, and porosity of the rocks before and after the explosions. We will also evaluate the geophysical properties of the rock at varying stress levels. Intact pieces of core recovered from additional post-shot core holes will also be systematically analyzed to identify distinct damage zones, and define their lateral extent. The variations in these properties at the micro-scale will be combined with macro-scale studies of near source damage by ground penetrating radar (GPR) to image the entire fracture regime. The objective of these studies will be to determine the elastic and effective cavity radii for the explosions as well as motion on the fractures and asymmetries in the damage from the explosions, and relate them to the near and far field seismic responses.

OBJECTIVES

Two of the proposed mechanisms for *S*-wave generation involve processes related to the damage and deformations caused by the explosions. Nonlinear effects in the immediate vicinity of the explosion causes rock damage that can effectively generate shear-waves provided that asymmetries exist in the damage pattern (Johnson and Sammis, 2001; Bykovtsev, 2007). A second proposed mechanism is damage and failure in an inverted conical region above an explosion. Media within the cone deform, fail, or exhibit driven block motions, as envisioned by Masse (1981). The failure in this cone has been modeled with moment tensor representation as a compensated linear vector dipole (CLVD) source (Patton et al., 2005).

Unfortunately, there is a paucity of detailed damage characterization studies from explosions easily available to test these two models of *S*-wave generation. Weston Geophysical Corp. (WGC) and New England Research, Inc. (NER) collected a unique dataset of damage characteristics from explosions in hard, crystalline rock during July 2008. The one year pilot study, called the New England Damage Experiment (NEDE), involved the detonation of five small (61.5 to 122 kg) chemical explosions in relatively unfractured, homogeneous Barre granite in Vermont, USA. Barre granite has been a worldwide standard for homogeneous, low fracture-density granite in commercial, monument, and industrial settings. The emplacement granite was characterized before and after the experiment using borehole cores and acoustic imaging. The explosions were designed with variable velocities of detonations (VOD ranging from 0.53 km/sec to 8.1 km/sec) in order to fracture the rock differently, thus leading to possible variations in *S*-wave generation. The preliminary conclusions from the pilot study (see Leidig et al., 2009):

- Larger amplitude *S*-waves were generated from shots using Black Powder and ANFO (VODs < 5 km/sec) than with COMP-B (VOD~8.1 km/sec);
- No meso-scale surficial damage was observed from the COMP-B shots, whereas large radial cracks with vertical movement were observed from Black Powder and ANFO shots with equivalent yields and source depths;
- Moment tensor inversions indicate a possible CLVD component to the explosions; and
- Meso-scale damage observed in post-shot cores was asymmetrical and had variable characteristics depending on the type of explosive detonated.

The objectives of the current project will include microscopic evaluation of fracturing that occurred during the loading and unloading processes of the explosions. An objective will be to develop a physical model of the non-linear deformation that these rocks incurred. The results will be compared with a macroscopic evaluation of the fracturing from the explosions, which will be completed with additional borehole coring measurements (we only have three post-shot cores currently) as well as ground penetrating radar (GPR) studies to image the fractured regime. The objective of these macro-damage studies will be to determine the elastic and effective cavity radii for the explosions as well as motion on the fractures and asymmetries in the damage from the explosions. Finally, we will combine the results from the damage evaluation with the observed seismic data to examine possible models for differences in the observed *S*-wave generation from the explosions. In the remaining pages, we discuss our research plans and include initial results of the rock damage analysis.

RESEARCH ACCOMPLISHED

Mapping Explosion Damage Using GPR

The cores obtained thus far have provided us with a preliminary assessment of localized damage from three of the NEDE explosions. Observation of surface cracks immediately after the shots showed that the COMP B explosions did not generate radial cracks that reached the surface while the Black Powder and Heavy ANFO shots did (Figure 1). In order to obtain a comprehensive image of the 3D distribution of damage (e.g., cavity and elastic radii), we are conducting a GPR survey (July 2010) to map the large scale aspects of the damage. The objective will be to map the entire test bed and use the resulting data to determine the locations of additional coreholes near Shots 4 and 5.

Figure 1. Radial crack formation from the Black Powder Shot 1 (left) and the Heavy ANFO Shot 2 (right).

Drill Additional Cores

After GPR has imaged the damaged zone to beyond the inelastic radius for the NEDE explosions, we will use the resulting maps to locate additional coreholes. During the first year of the project, an expanded study will concentrate on Shot 4, the 121 kg ANFO shot. New coreholes will be drilled radially outward from the working point, parallel to the rift plain; three coreholes are planned. At least one hole will also be drilled normal to the rift plane. In this way, we should be able to determine whether the intrinsic anisotropy has any effect on the shape of the damage surfaces. During Year 2, similar coreholes will be drilled and studied for Shot 5, the 122 kg COMP B shot. Borehole imaging via optical and acoustical televiewer logs will also be performed in the new coreholes. This will allow for a greater ability to delineate the types and extent of damage, and will assist in determining the overall geometry of the damage. Comparisons of the results of these two shots will help characterize the effects of VOD on the changes in rock mass within the inelastic zone.

Laboratory Analysis of Damaged Barre Granite

Bulk Properties. Data will be collected on additional sections of the pre-shot core, as well as characterization of all post-shot core. We expect that there will be a variation in bulk density and porosity with depth. The spatial variation in porosity will be an initial indication of the degree of damage experienced by the sample due to the detonation of the explosions. Initial analyses show the post-shot porosity increases by a factor of 2-2.5 near the working point of the explosions, and the post-shot permeability can increase by a factor of 8–10 (Figure 2).

Velocities. Compressional- and shear-wave velocities will be measured parallel and normal to the rift plane on all core at ambient conditions. This includes completion of the study of the existing core collected in 2008 and all additional core required to complete the characterization of the damage zones associated with the shots previously detonated at the Barre quarry. Figures 3–6 provide some of the results of the initial velocity analysis completed on our current pre- and post-shot cores.

Geophysical Properties at Stress. Velocity, permeability, and electrical resistivity will be measured on specimens from selected intervals along the core. NER has developed a technique to invert the velocity, permeability, and resisitivity data, as well as image analysis of thin sections, to obtain a pore structure (PSI). For these specimens, we anticipate that the pore spectrum will be fairly simple and be comprised mostly of low aspect ratio (10^{-3}) cracks. By looking at both pre-shot and post-shot specimens, we will be able to determine how the crack length and crack density has changed due to the detonation and how these parameters vary as function of position with respect to the working point. We will model the changes in the length and density of microcracks on specimens collected radially outward from the working point in order to further assist in characterizing the geometry of the damage.

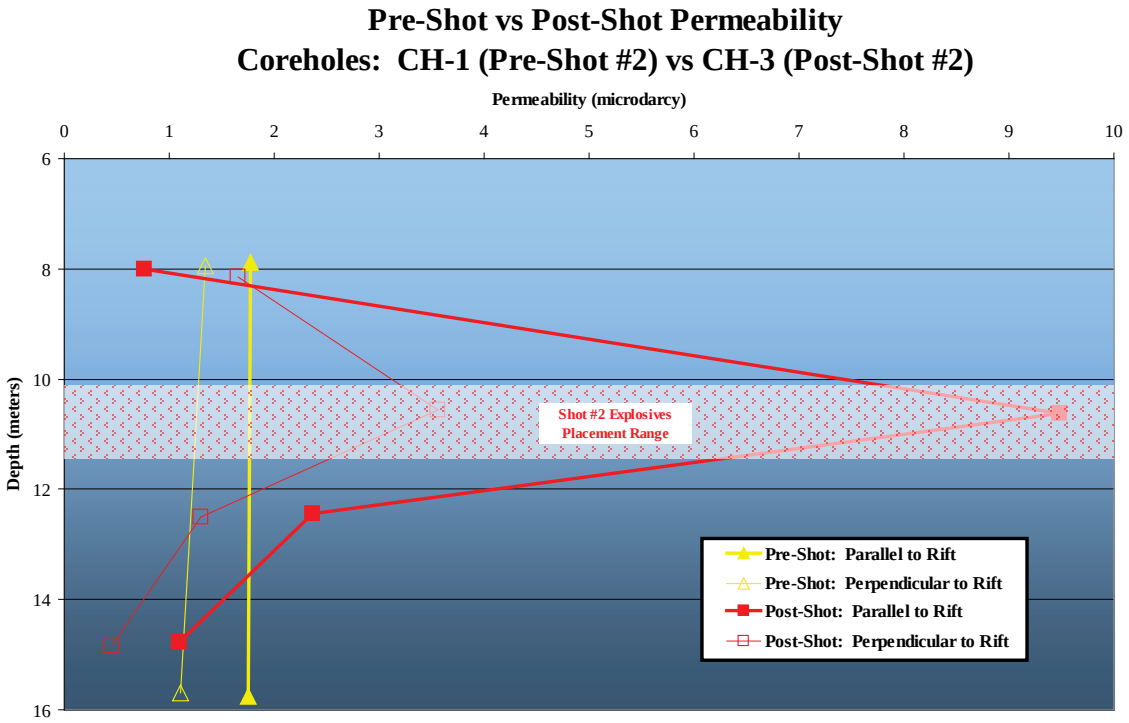

Figure 2. Permeability observed in pre- (yellow) and post-ANFO shot (red) cores parallel (solid symbols) and perpendicular (open symbols) to the rift in the Barre Granite.

Figure 3. Barre granite core that has been partitioned every 5 degrees in order to determine the fast and slow directions of the anisotropy or "rift."

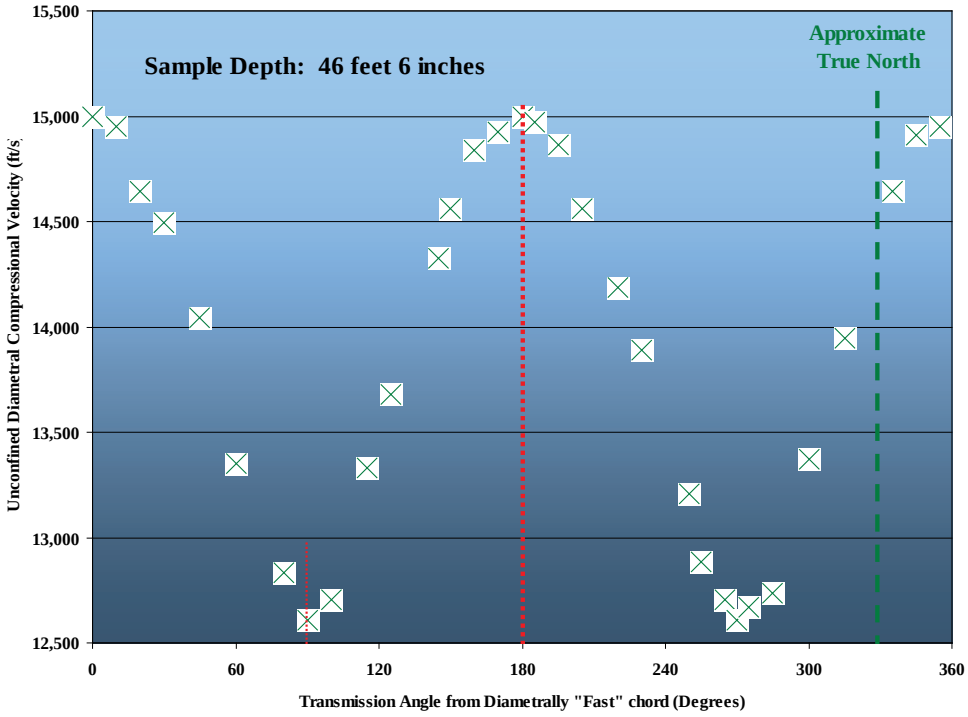

Figure 4. ***P*-wave velocities (in feet per second) for undamaged Barre granite core at a depth of 46 feet and 6 inches. The fast direction was found to be 30 degrees east of true North.**

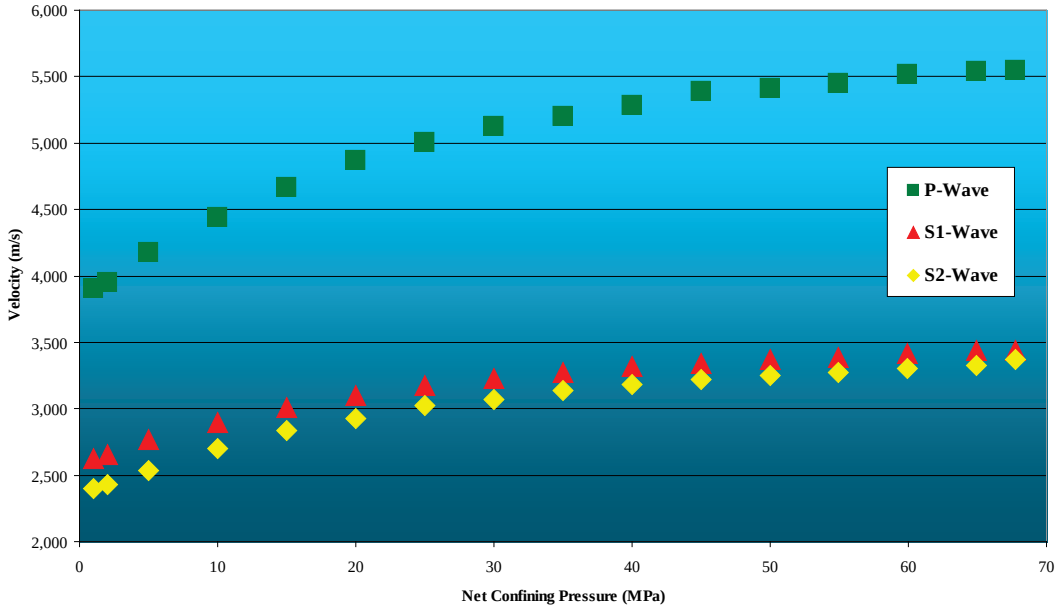

Figure 5. Ultrasonic *P*- and *S*-wave velocities as a function of confining pressure for Barre granite.

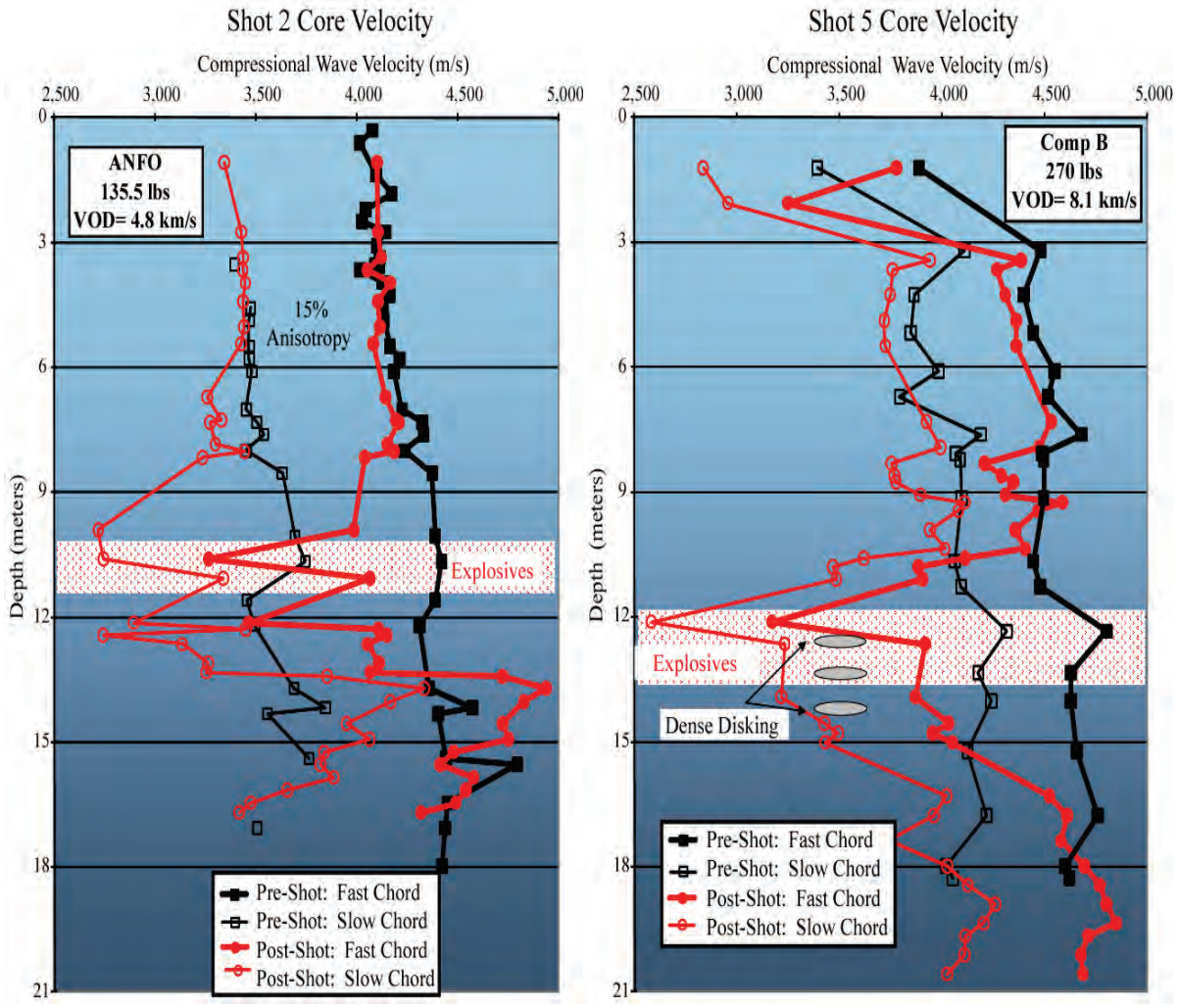

Figure 6. (Left) Velocity data from cores extracted before and after the 61.5 kg (136 lbs) ANFO shot. Because of the rift plane in the Barre granite, there are both "fast" (measured parallel to the rift plane) and "slow" (perpendicular) chords or directions. (Right) Velocity data from cores extracted before and after the 122 kg (269 lbs) COMP B shot. These plots show significant reduction in the seismic wave velocity caused by micro-scale damage from the explosions.

PSI: Pore Structure Inversion – Overview. Details of the pore structure of a rock control many fundamental rock properties including fluid transport, electrical resistivity, seismic velocities, and rheology. While direct imaging of the pore structure of individual cores can provide great insight into physical understanding of a given core, most practical applications involve cases of limited observations. NER's pore structure modeling yields a pore structure of a sample based on measured core scale properties.

The approach is based on the idea that a limited but diverse set of observations provides sufficient constraint to say something meaningful about the pore structure. Simultaneously satisfying observations of a variety of core scale properties can be a powerful constraint because each of the properties is linked to the pore structure in a different way. A schematic illustration of the modeling is shown in Figure 7. The method starts with an assumed generic topology, for which we have adopted a disordered network of tubes connecting nodal pores. Using measurements of velocity, porosity, permeability, resistivity, and compressibility, a description of the pore structure is found, which simultaneously satisfies each of the constraints. Image analysis of the thin section is used to constrain some of the free parameters. The model output is a shape spectrum, describing the smoothest distribution of the throat shapes (for granites, low aspect ratio cracks) and sizes that is consistent with the constraints and model assumptions.

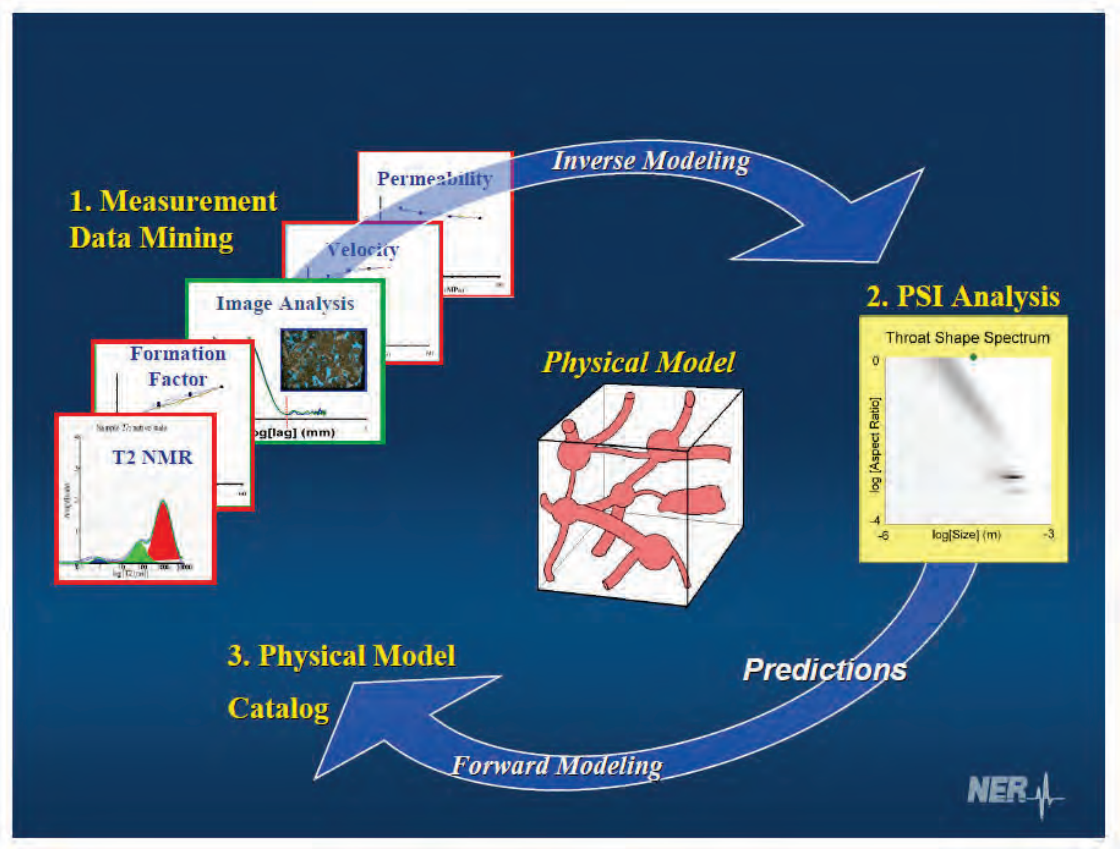

Figure 7. Schematic representation of the pore structure inversion to be performed on Barre granite pre- and post-shot core.

Fragmentation Analyses. In addition to quantifying the variation in microcrack damage in the intact pieces of core recovered from the post-shot core holes, the degree of fragmentation and the size of each fragment need to be systematically analyzed. The specific interests will be the size and shape of each fragment. In this way, it will be possible to determine the amount of granulation occurring between the fragments, and again determine this as a function of position in each of the post-shot coreholes. Presently, this effect has only been documented photographically (Figure 8).

Figure 8. Examples of meso-scale damage observed in cores above the working explosion point.

Identification of Damage Zones. Most models assume that there is a series of concentric shells with varying degrees of damage ranging from the cavity outward to the inelastic radius. The shape of each of these specific zones is not known. In this study, we will integrate collected data to determine the variations of the damage zones surrounding the working point

Testing the Damage Mechanics Model Against the Observed Seismic Data

The shape of the damage zone (e.g., inelastic and cavity radii) and the determination of whether the zones of increasing damage are concentric or variable as a function of depth need to be quantified in order to model the energy distribution throughout the source region. Furthermore, the variations may also occur radially. Note that the rift zone introduces fairly strong anisotropy into the site. The anisotropy may affect the shape of the damage zones in the horizontal plain. Once the data are complete, then the active data modeling, either using the Sammis (2002) model or the CLVD model will be tested.

***S* Waves from Crack Growth.** Ashby and Sammis (1990) formulated a micro-mechanical model for the formation and growth of new fractures from pre-existing cracks under the compressive loading states representative of explosions. Their research has demonstrated that the growth of these fractures contributes to the generation of high-frequency seismic waves from explosions. The Ashby and Sammis (1990) micro-mechanical model has been incorporated into the non-linear explosion codes used by SAIC which have successfully modeled near-source data from the NTS (Rimer *et al*., 1998) and the Degelen Mountain Test Site (DTS; Stevens et al., 2003a).

Sammis (2002) showed that crack growth affects the source in two ways: 1) the increased damage weakens the rock by lowering the elastic modulus and 2) the growing fractures are secondary sources of seismic energy. By combining their micro-mechanical model with a stress field for explosions, they can estimate the growth and seismic moment tensor for each individual crack. While the moment may be small for each crack, integrating them over the entire source volume produces secondary waves that can propagate into the far field. Any asymmetries in the pre-existing shear stress or preferred orientation of the initial cracks can generate *S* waves. Preliminary examination of the post-shot cores for the NEDE does suggest that there were asymmetries in the cracks generated above and below these explosions.

***S* Waves from Spallation and Block Motions.** The presence of the Earth's free surface creates significant asymmetries in rock damage. Above the spherical region of the explosion, there is an inverted conical-shaped damage region with apex at the explosion point source (Masse, 1981). The material inside the cone deforms and fails as a result of tensile stresses caused by the downgoing shock wave reflected off the free surface. Spallation, which usually involves shallow, poorly-coupling geologic strata that open and close with no net displacement, is an example of such failure (Eisler and Chilton, 1964; Stump, 1985). Another example is driven block motions at depth, as envisioned by Masse (1981) and Blouin (1980, 1981). This source might be more important for seismic wave generation than spall if it involves permanent deformations and couples better into the Earth, since its centroid may be located in more competent rock at depths greater than spall.

The region inside the cone of deformation has been modeled extensively using a CLVD moment tensor representation (Knopoff and Randall, 1970). Stevens et al. (2003b) examined *Lg* generation at DTS using non-linear finite difference modeling. Their non-linear seismograms, which incorporate damage in the source region, showed abundant *S*-wave energy on regional distance synthetic seismograms that matched observed data. The researchers then observed they could match the data equally well just by considering an explosion point source plus a shallow point CLVD source.

The CLVD source may excite azimuthally-independent Rayleigh waves. Patton et al. (2005) showed that *Rg* spectra for chemical explosions at the Shagan Test Site could be modeled using a combined monopole explosion and CLVD source. The CLVD source in their study appeared to be more closely related to a driven block motion model envisaged by Masse than spall. *Rg* source amplitudes were consistent with *mb*(*Lg*) measurements at station MAK, as would be expected if near-field *Rg*-to-*S* scattering (Myers et al., 1999) plays a role in generating *S* waves observed at regional distances.

Preliminary research has determined that the amplitudes of M_{xx} and M_{yy} components of the NEDE moment tensors are approximately similar, while the amplitudes of M_{zz} components exceed the horizontals by almost a factor of 2, which could be caused by a CLVD source. We propose to use detailed velocity and attenuation models for this region (currently being developed) coupled with these explosion moment tensors to conduct numerical modeling of recorded near-source, local, and regional seismograms. We will use 1D, 2D, and 3D models, and include topography and stochastic properties of the media in order to quantify possible scattering effects. The goal of this modeling exercise is to determine how much of the local data can be traced back to source effects (e.g., moment tensors which appear to have a strong CLVD component) and what characteristics of the local and regional data are due to path effects.

CONCLUSIONS AND RECOMMENDATIONS

We believe that the datasets that will be obtained from this new study (e.g., meso and micro-fracture analyses, bulk properties under variable stress conditions, pore structure inversions, GPR mapping of meso-fractures, etc.) in conjunction with seismic data collected during the 2008 pilot study will provide the Nuclear Explosion Monitoring community with further data for the development of a more complete explosion source theory model, including *S*-wave generation.

ACKNOWLEDGEMENTS

We wish to thank the following people for their help on this project: Don Murray, Tim Rath, Charlie Sammis, Diane Baker, Sam Huffstetler, Delaine Reiter, James Britton and Katherine Murphy. We also wish to thank these groups for their participation and help: Rock of Ages Corporation, Maxam-North America, Incorporated Research Institutions in Seismology, Hager-Richter, Mike's Boring and Coring, Johnson Artesian, Los Alamos National Laboratory and the Air Force Research Laboratory.

REFERENCES

Ashby, M.F. and C. G. Sammis (1990). The damage mechanics of brittle solids in compressions. *Pure Appl. Geophys*. 133: 489–521.

Blouin, S. E (1981). Prediction of explosively driven displacements in rocks, CRREL Report 81-11.

Blouin, S. E. (1980). Block motion from detonations of buried near-surface explosive arrays, CRREL Report 80–26.

Bykovtsev, A. S. (2007). Mathematical description of the explosion source with a system of cracks. Abs. *Seism. Res. Letts.*

Eisler, J.D. and F. Chilton (1964). Spalling of the earth's surface by underground nuclear explosions*. J. Geophys. Res*., 69: 5285–5293.

Johnson**,** L. R., and C. G. Sammis (2001). Effects of rock damage on seismic waves generated by explosions, *PAGEOPH***,** 158 1869–1908.

Knopoff, L. and M. J. Randall (1970). The compensated linear-vector dipole: A possible mechanism for deep earthquakes, *J. Geophys. Res*. 75: 4957–4963.

Leidig, M. R., R. J. Martin, P. Boyd, J. L. Bonner, and A. Stroujkova (2009). Quantification of rock damage from small explosions and its effect on shear wave generation: Phase I-Homogenous crystalline rock, in *Proceedings of the 2009 Monitoring Research Review: Ground-Based Nuclear Explosion Monitoring Technologies*, LA-UR-09-05276, Vol. 1, pp. 492–501.

Masse, R. P. (1981). Review of seismic source models for underground nuclear explosions, *Bull. Seism. Soc. Am.* 71: 1249–1268.

Myers, S. C., W. R. Walter, K. Mayeda, and L. Glenn (1999). Observations in support of *Rg* scattering as a source for explosion *S* waves: regional and local recordings of the 1997 Kazakhstan depth of burial experiment, *Bull. Seism. Soc. Am.* 89: 544–549.

Mueller, R. A. and J. R. Murphy (1971). Seismic characteristics of underground nulear detonations: Part I, Seismic scaling law of underground detonations, *Bull Seism. Soc. Am.*, 61: 1675.

Patton, H., J. Bonner, and I. Gupta (2005). *Rg* Excitation by Underground Explosions: Insights from Source Modeling the 1997 Kazahkstan Depth of Burial Experiments. *Geophys. J. Int.* doi:10.1111/j.1365-246X.2005.02752.x

Rimer, N., J. L. Stevens, J. R. Murphy, and G. G. Kocharyan (1998). Estimating seismic chracterisitcs of explosions in hard rock using a micro-mechanical damage model, in *Proceedings of the 20th Annual Seismic Research Symposium on Monitoring a Comprehensive Test Ban Treaty*, J. Fantroy, D. Heatley, J. Warren, F. Chavez, and C. Meade (eds). Department of Defense and US Department of Energy, p. 392–400.

Rodean, H. C. (1971). Nuclear-Explosion Seismology, U. S. Atomic Energy Commission, TID-25572, 156 pp.

Sammis, C. G. (2002). Generation of High-Frequency *P* and *S* Wave Energy by Rock Fracture During a Buried Explosion: Its Effect on *P/S* Discriminants at Low Magnitude,in *Proceedings of the 24th Seismic Research Review - Nuclear Explosion Monitoring: Innovation and Integration*, LA-UR-02-5048, Vol 1., pp. 542–551.

Stevens, J. L., N. Rimer, H. Xu, G. E. Baker, and S. M. Day (2003a). Near-field and regional modeling of explosions at the Degelen test site. SAIC Final Report SAIC-02/2050.

Stevens, J. L., G. E. Baker, H. Xu, T. J. Bennett, N. Rimer, and S. M. Day (2003b). The physical basis of *Lg* generation by explosion sources. in *Proceedings of the 25th Seismic Research Review - Nuclear Explosion Monitoring: Building the Knowledge Base*, LA-UR-03-6029, Vol**.** 1, pp. 456–465.

Stump, B. W. (1985). Constraints on explosive sources with spall from near-source waveforms, *Bull. Seism. Soc. Am*. 75: 361–377.

IMPROVED HIGH FREQUENCY DISCRIMINATION: A NEW APPROACH TO CORRECT FOR REGIONAL SOURCE SCALING VARIATIONS

Kevin Mayeda[1], Luca Malagnini[2], William Walter[3], and Rengin Gok[4]

Weston Geophysical Corporation[1], Istituto Nazionale di Geofisica e Vulcanolgia[2], Lawrence Livermore National Laboratory[3], and Los Alamos National Laboratory[4]

Sponsored by the Air Force Research Laboratory

Award No. FA8718-09-C-0014

ABSTRACT

The behavior of earthquake source scaling has been the topic of significant debate in the earthquake source community mainly because current methods require substantial path, site, and source radiation pattern corrections that ultimately yield large variance of the apparent stress (e.g., see review by Abercrombie et al., 2006). The coda ratio method was developed by Mayeda et al., (2007) and subsequently applied to numerous regions (e.g., Chi-Chi, Taiwan; Wells, Nevada, Hector Mine, CA; L'Aquila, Italy; Colfiorito, Italy; San Giuliano, Italy; Fukuoka, Japan etc.). The methodology is similar in every respect to the traditional direct wave spectral ratio methods which take advantage of co-located earthquakes to remove common path and site effects. The significant difference however comes from the fact that the coda envelopes are very stable and not sensitive to both source radiation pattern or source directivity (see Mayeda and Malagnini, 2010). These coda-derived studies provide unprecedented estimates of corner frequency and apparent stress drop, roughly 3-to-4 times less variance than conventional methods, with the advantage of using a minimal number of stations and events. We have also applied the methodology to 3 large magnitude sequences in southern California (San Simeon, Hector Mine, Parkfield) and started a fourth (northern Baja, 2010) as part of a project to delineate 2-D variations in apparent stress and Brune stress drop in the southern California region. We find that only the recent Parkfield sequence obeys self-similarity, whereas the other sequences are consistent with other sequences worldwide that show a curious increase or break at around M_w 5.5. The P.I. and co-authors have found that regional variations in absolute level and scaling can be significant. The methodology has been applied to a variety of tectonic regions and we find clear distinctions between each of them.

OBJECTIVES

The initial study by Mayeda et al. (2007) first compared amplitude ratio performance between local and near-regional *S* and coda waves in the San Francisco Bay region for moderate-sized events, then applied the coda spectral ratio method to the 1999 Hector Mine mainshock and its larger aftershocks. They found: (1) Average amplitude ratio standard deviations using coda are ~0.05 to 0.12, roughly a factor of 3 smaller than direct *S*-waves for $0.2 < f < 15.0$ Hz; (2) Coda spectral ratios for the M_w 7.0 Hector Mine earthquake and its aftershocks show a clear departure from self-similarity, consistent with other studies using the same datasets; (3) Event-pairs (Green's function and target events) can be separated by ~25 km for coda amplitudes without any appreciable degradation, in sharp contrast to direct waves. In almost all regions we find evidence for non-self similar source scaling.

The Magnitude and Distance Amplitude Correction (MDAC) methodology of Walter and Taylor (2001) corrects ratios of regional phase amplitudes for source, path, and site effects and has proven effective for event identification. The MDAC formulation includes a term that describes the earthquake source scaling as the apparent stress variation with magnitude. In almost all regions we find evidence for non-self similar source scaling. The behavior of earthquake source scaling has been the topic of significant debate in the earthquake source community mainly because current methods require substantial path, site, and source radiation pattern corrections that ultimately yield large variance of the apparent stress. A new, state-of-the-art methodology, the coda ratio technique, was developed by Mayeda et al. (2007) and provides unprecedented estimates for corner frequency and apparent stress drop, roughly 3 times less variance than conventional methods using a minimal number of stations and events. Within broad regions it is likely that apparent stress varies with location due to lateral variations in regional stress field, rheology, and degree of tectonic activity. Currently MDAC assumes a single linear apparent stress scaling with moment for a given region, but if we have *a priori* information on lateral variations in apparent stress, then we can use this to lower the amplitude ratio scatter and increase the discrimination capability. The coda ratio methodology has been applied to a variety of tectonic regions and we find clear distinctions between each of them. We will use the coda ratio technique to determine lateral variations in apparent stress and then use them in an updated version of MDAC to reduce discriminant scatter and improve high frequency event identification. We will do a proof of concept test in the western U.S., spanning the Coastal ranges, Sierra Nevada, and Basin & Range province where lateral variation in stress are observed. Next, we will delineate 2-D variations in apparent stress for the Middle East and Korean Peninsula regions. Finally we will extend the techniques across western Eurasia and North Africa.

Conventional direct wave methods of estimating apparent and static stress drop have significant errors, so large in fact that the earthquake source community is divided roughly 50-50 on whether or not self-similarity even holds, a fundamental assumption in many earthquake source models that have been used for roughly 4 decades (i.e., Aki, 1967, Brune, 1970). One such method involves frequency-dependent path, site, and radiation pattern corrections to get at the source spectra. More often than not, these approaches result in corrections that are so large, the resulting estimates on radiated energy and corner frequency are questionable (see reviews by Abercrombie et al., 2004; Ide and Beroza, 2001). One attempt to alleviate some of the problems is to take source ratios of closely spaced events of different magnitude. These can be either a time-domain deconvolution to extract the source-time function (e.g., Hough, 1997) or source spectral ratios (e.g., Izutani and Kanamori, 2001). Figure 1 shows a typical *S*-wave source ratio result from Izutani (2005) for the 2004 M_w 6.7 Niigata, Japan earthquake and selected co-located aftershocks. In spite of a plethora of seismic stations that surround the source region, the scatter on the ratio is huge and estimating corner frequency and apparent stress will have large errors.

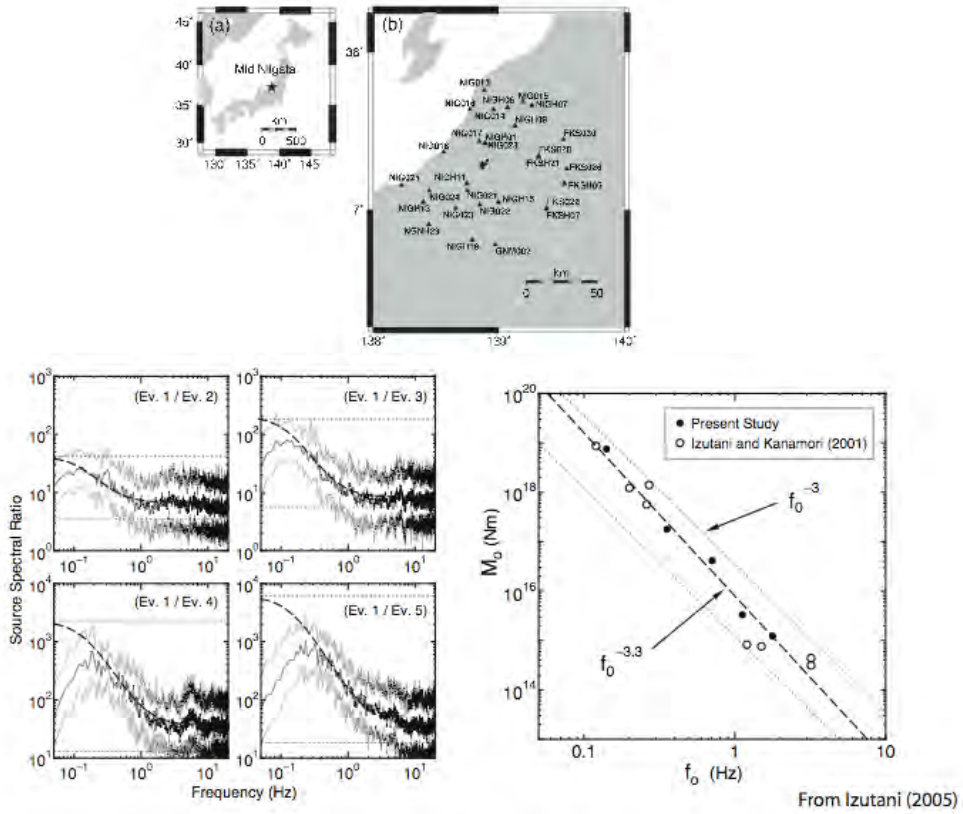

Figure 1. From Izutani (2005) showing direct *S*-wave spectral ratios (lower left) for the 2004 Niigata earthquake in Japan (Ev. 1) relative to four other smaller aftershocks (Ev. 2,3,4,5). Dashed line shows average ratio and dark lines represent +/- 1 σ from the stations shown in above map. Moment versus corner frequency exhibits non-constant scaling ($f^{-3.3}$) however no error estimates are shown, but are presumably large.

In addition to seismic hazard prediction and fundamental research on faulting dynamics, an *a priori* knowledge of apparent stress drop can have a profound influence on high-frequency seismic discrimination. The MDAC methodology of Walter and Taylor (2001) removes source, path, and site effects from regional phase amplitudes ratios used for regional seismic discrimination (Figure 2).

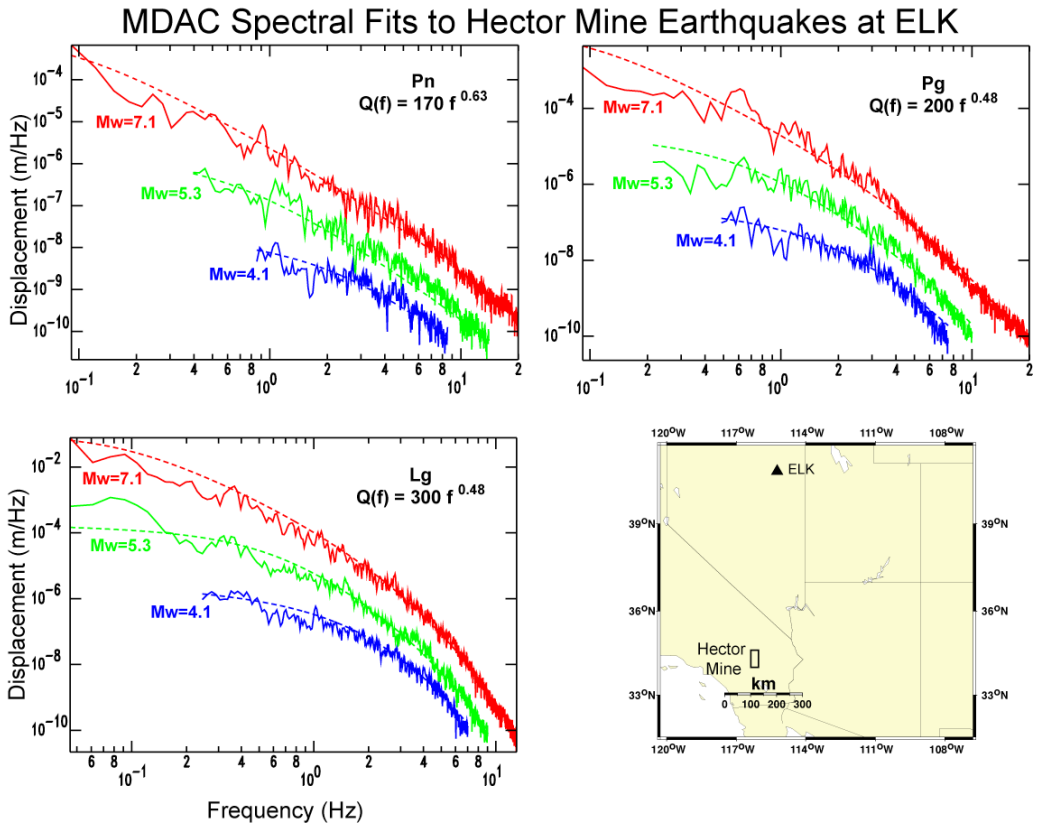

Figure 2. Example of MDAC fits (dashed lines) to observed regional phase amplitude spectra (solid lines) at station ELK for three different size earthquakes in the Hector Mine sequence. MDAC uses an earthquake source spectral model along with path and site corrections to predict amplitudes. In the example shown, part of the path effect is a power law attenuation model that is different for each regional phase type. The MDAC predicted amplitudes are removed from the observed amplitudes leaving residuals that are corrected for source, path and site effects, and ready for use as discriminants, such as in high frequency *P/S* MDAC residual ratios.

MDAC works by correcting observed amplitudes at each frequency by subtracting the predicted earthquake amplitudes based on the distance and magnitude of the source. This requires an independent estimate of the seismic moment, which is usually obtained from regional coda envelopes. Implicit in the MDAC formulation is a term that describes the earthquake source spectra in terms of its apparent stress (e.g., Wyss, 1970). For a given region we usually use either a fixed average apparent stress, or a linear apparent stress relation that increases with seismic moment. We search for the choice that best reduces the earthquake scatter. For example in Figure 3 in the Korea region we use an apparent stress that increases with seismic moment. Despite allowing for this scaling there remains significant scatter in the earthquake population. One source of this scatter may be spatial variations in the apparent stress related to changes in the geology, tectonics and regional stress field.

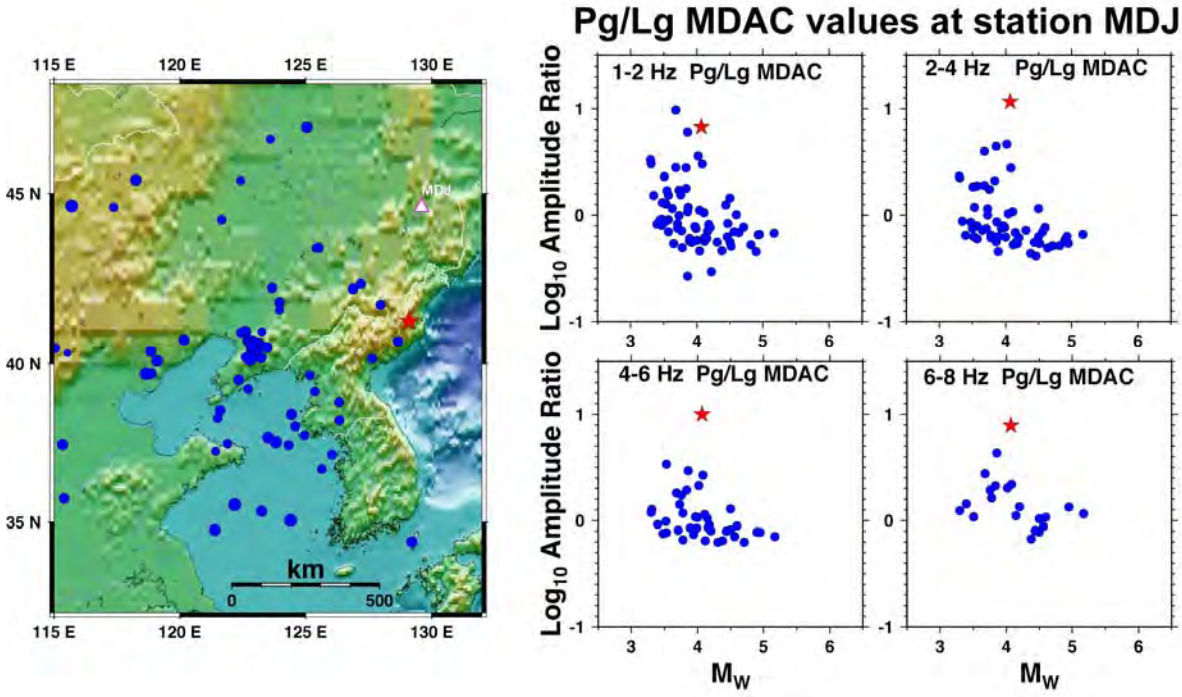

Figure 3. Example of local and regional phase ratios from MDAC for the Yellow Sea/Korean Peninsula for earthquakes (blue circles) and explosions (red star) at station MDJ. Notice the earthquake scatter in all the high frequency discriminants is significant.

To date, in regions of monitoring interest, the apparent stress scaling has been obtained usually through a grid-search or by geophysical analogy (see Equation 3). What is found in almost all regions is that apparent stress appears to increase with magnitude, indicating a non-self similar source scaling. The estimation of earthquake source scaling in general, has been the topic of large debate in the earthquake source community mainly because current methods require substantial path, site, and source radiation pattern corrections that ultimately yield large variance in apparent stress. A new, state-of-the-art methodology has been developed by Mayeda et al. (2007) which provides unprecedented estimates in static and apparent stress drop, roughly 3 times less variance than conventional methods using a minimal number of stations and events. For the broad area, there is every reason to believe that lateral variations in source scaling exist due to lateral variations in regional stress field, rheology, and degree of tectonic activity.

Methodology

Assuming the simple single corner frequency source model (Aki, 1967; Brune, 1970) used in MDAC, the ratio of the moment-rate functions for two events (1 and 2) is given by,

$$\frac{\dot{M}_1(\omega)}{\dot{M}_2(\omega)} = \frac{M_{0_1}\left[1+\left(\omega/\omega_{c_2}\right)^2\right]^{p/2}}{M_{0_2}\left[1+\left(\omega/\omega_{c_1}\right)^2\right]^{p/2}} \qquad (1)$$

where M_0 is the seismic moment and ω_c is the angular corner frequency ($2\pi f_c$) and p is the high frequency decay rate. At the low frequency limit the source ratio shown in equation 1 is proportional to the ratio of the

seismic moments $\left[M_{0_1}/M_{0_2}\right]$, whereas at the high frequency limit, equation 1 is asymptotic to $\left[M_{0_1}/M_{0_2}\right]^{\left(1-\frac{p}{3}\right)}$ under self-similarity. If we follow the usual Brune (1970) omega-square model and set p=2, the exponent of the high-frequency ratio becomes 1/3. However, it has been proposed by Kanamori and Rivera (2004) that the scaling between moment and corner frequency could take on the form,

$$M_o \sim \omega_c^{-(3+\varepsilon)} \qquad (2)$$

where e represents the deviation from self-similarity and is usually thought to be a small positive number. For example, Walter et al. (2006) and Mayeda et al. (2005) found e to be close to 0.5 for the Hector Mine mainshock and its aftershocks using independent spectral methods. For the current study we use the source spectrum portion of the MDAC methodology of Walter and Taylor (2001), which allows for the variation of the corner frequency that does not have to be self-similar. For example,

$$\omega_c = \left(\frac{k\sigma_a}{M_0}\right)^{1/3} \text{ and } \sigma_a = \sigma_a'\left(\frac{M_0}{M_0'}\right)^{\psi} \text{ and } \psi = \frac{\varepsilon}{\varepsilon+3} \qquad (3)$$

where σ_a is the apparent stress (Wyss, 1970), σ_a' and M_0' are the apparent stress and seismic moment of the reference event, and ψ is a scaling parameter. For constant apparent stress, ψ = 0 and e =0, however, Mayeda and Walter (1996) found ψ=0.25 for moderate to large earthquakes in the western United States. By using the corner frequency defined in (3) into equation 1, we can apply a grid search to find the parameters that best fit the spectral ratio data.

RESEARCH ACCOMPLISHED

Figure 4 provides another example of the coda's insensitivity to source directivity, in this case we focus on the recent 2008 Wells, Nevada (M_w 5.9). This figure compares source ratios of the Wells, Nevada mainshock and an M_w 4.5 aftershock using direct *Lg* and its corresponding *Lg*-coda for two bands, 0.3-0.5Hz (0.4Hz) and 1.5-2.0Hz (1.75Hz). For the *Lg*-coda, we used measurement window lengths of roughly 300 seconds for the 0.4Hz band and 150 seconds for the 1.75Hz band for both the mainshock and aftershock, though results using shorter window lengths were not appreciably different. On average, the azimuthal variation in the coda source ratio is 3-to-4 times smaller than for direct *Lg*. For example, the largest variation in the *Lg* source ratio at 0.4Hz for the aftershock is a factor of 8, whereas for the coda the largest variation is a factor of 2.5. At 1.75Hz the differences are even more dramatic, with the coda variation being roughly 0.5 whereas the direct waves are a factor of 5.

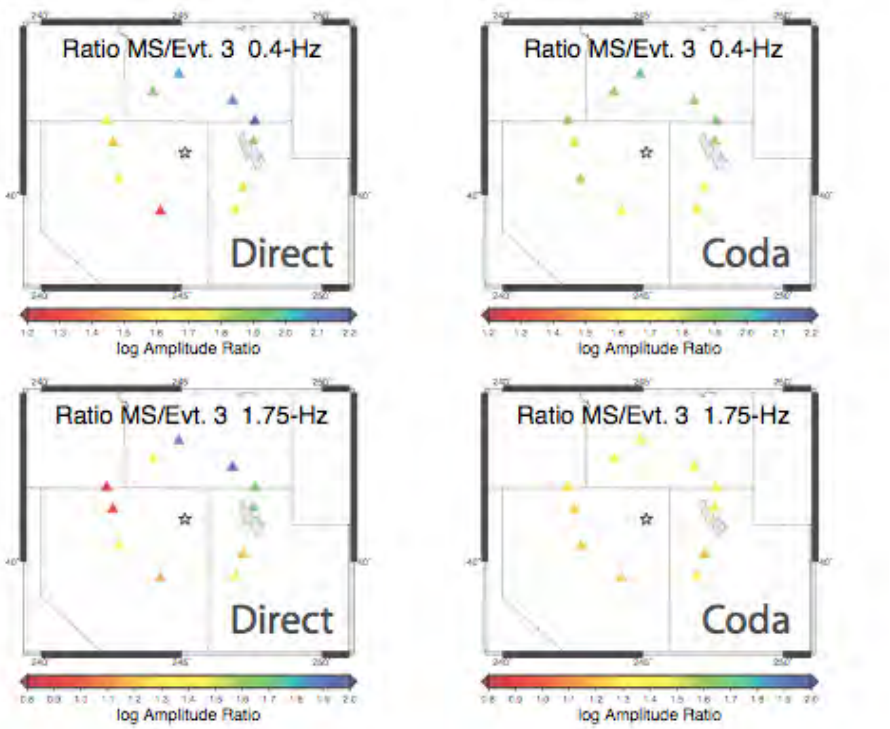

Figure 4. Direct and coda wave amplitude ratios between the Wells mainshock (MS) and an M_w 4.5 aftershock for 11 stations at roughly 200 km epicentral distance. We see that the direct waves show strong variability with azimuth, consistent with finite-fault solutions from Dreger et al. (2009), yet the coda ratios show virtually no variation, proving once again that the coda is virtually insensitive to source heterogeneity (from Mayeda and Malagnini, 2010).

This year we also processed the following sequences for source scaling as part of our plan to study as many varied geo physical regions as possible: Parkfield, CA; San Si meon, C A; W ells, NV; L'Aquila, It aly; Fukuoka, Japan; Niigata, Japan.

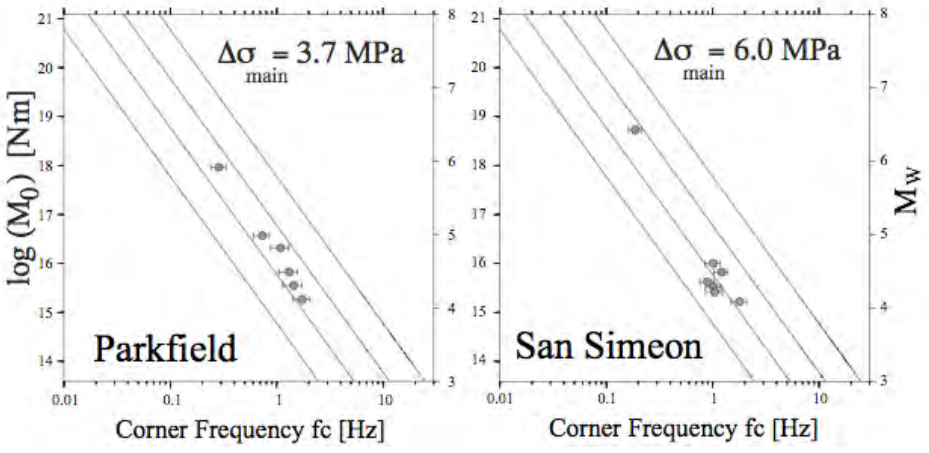

Figure 5a and 5b. Corner frequency vs moment scaling is shown for two sequences in southern California using the coda ratio methodology. The first is the M_w 6.0 2004 Parkfield earthquake and the M_w 6.5 San Simeon earthquake. We see that the Parkfield sequence obeys similarity unlike the San Simeon sequence.

Our results for Parkfield are in some ways a relief since up to this point, virtually all sequences that we have studied were non-self similar. We were wondering if somehow the methodology was biased but this sequence shows that this is not the case. Finally, we completed calibration of the M_w 6.0 2008 Wells, Nevada earthquake and show the results in Figure 6 from Mayeda and Malagnini, 2010.

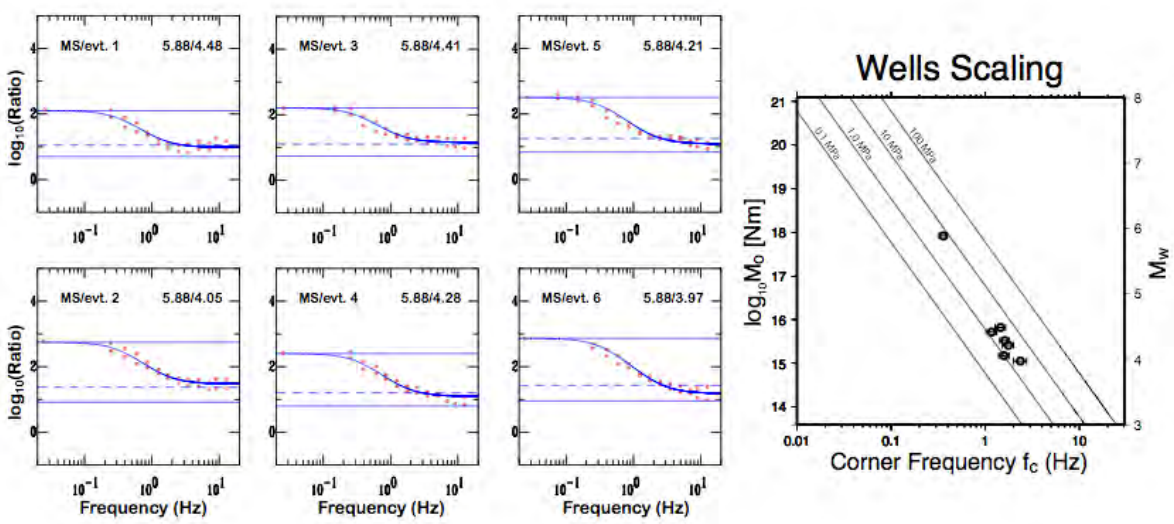

Figure 6. Spectral ratio fits where top horizontal solid line represents the theoretical low-frequency limit based upon the two events' moment estimates, the bottom solid line represents the theoretical high-frequency limit assuming self-similarity, and dashed line is when *p*=1.5 in equation 1. Estimates of f_c and ± 1 standard deviation error bars for the Wells mainshock and 6 aftershocks. Lines represent constant $\Delta\sigma_B$ in MPa.

CONCLUSIONS AND RECOMMENDATIONS

After a delayed start, we are slowly getting back on track and have processed two Japanese sequences in the previous quarter, and have completed, 3 more (Parkfield, San Simeon, and Wells). As discussed previously, we have identified a number of large magnitude events distributed throughout the Middle East region and will embark on selecting events and obtaining waveforms for the coda ratio methodology. Again, we highlight the advantages of the methodology below:

- The coda is not sensitive to lateral variations in structure and effectively homogenizes its energy over a broad area
- Directivity and source radiation pattern will not affect the coda envelope amplitude measurement due to azimuthal averaging
- Unlike direct wave methods that require large amounts of data to average, the coda method can use a minimal number of events and stations.
- The methodology does not require path and site corrections.
- Large amounts of data have already been archived by LLNL and Weston in the regions of monitoring interest and coda envelope shape and velocity parameters have already been derived for all the regions.

REFERENCES

Abercrombie, R.E, A. McGarr, G. Di Toro, and H. Kanamori (2006). *Earthquakes: Radiated Energy and the Physics of Faulting*, *AGU Geophysical Monograph Series*, 170.

Abercrombie, R.E., and J.R. Rice (2005). Can observations of earthquake scaling constrain slip weakening?, *Geophys. J. Int.* 162: 406–424.

Aki, K. (1967), Scaling law of seismic spectrum. *J. Geophys. Res.* 72: 1217–1231.

Brune, J. N. (1970). Tectonic stress and spectra of seismic shear waves from earthquakes, *J. Geophys. Res.* 75: 4997–5009.

Hough, S.E. (1997). Empirical Green's function analysis: Taking the next step, *J. Geophys. Res.* 102: 5369–5384.

Ide, S. and G. C. Beroza (2001). Does apparent stress vary with earthquake size?, *Geophys. Res. Lett.* 28: 3349–3352.

Izutani Y. and Kanamori, H. (2001), Scale-dependence of seismic energy-to-moment ratio for strike-slip earthquakes in Japan, *Geophys. Res. Lett.* 28: 20, 4007–4010.

Izutani, Y. (2005). Radiated energy from the mid Niigata, Japan, earthquake of October 23, 2004 and its aftershocks, *Geophys. Res. Lett.* 32: L21313, doi:10.1029/2005GL024116.

Kanamori H. and L. Rivera (2004). Static and dynamic scaling relations for earthquake and their implications for rupture speed and stress drop, *Bull. Seismol. Soc. Am.* 94: 314–319.

Mayeda, K. M. and W. R. Walter (1996). Moment, energy, stress drop and source spectra of Western U.S. earthquakes from regional coda envelopes, *J. Geophys. Res.* 101: 11,195–11,208.

Mayeda, K., R. Gok, W. R. Walter, and A. Hofstetter (2005). Evidence for non-constant energy/moment scaling from coda derived source spectra, *Geophys. Res. Lett.* 32: L10306, doi:10.1029/2005GL022405.

Mayeda, K., L. Malagnini, and W. R. Walter (2007). A new spectral ratio method using narrow band coda envelopes: Evidence for non-self-similarity in the Hector Mine sequence, *Geophys.Res. Lett.*, doi:10.1029/2007GL030041.

Mayeda, K., and L. Malagnini (2010). Source radiation invariant property of local and near-regional shear-wave coda: Application to source scaling for the Mw 5.9 Wells, Nevada sequence, *Geophys. Res. Lett.* 37: L07306, doi:10.1029/2009GL042148.

Walter, W. R. and S. R. Taylor (2001). A revised Magnitude and Distance Amplitude Correction (MDAC2) procedure for regional seismic discriminants, Lawrence Livermore National Laboratory, Livermore, UCRL-ID-146882.

Walter, W. R., K. Mayeda, R. Gök, A. Hofstetter (2006). The scaling of seismic energy with moment: Simple models compared with observations, Earthquakes: Radiated Energy and the Physics of Faulting, *AGU Geophysical Monograph Series*, 170.

Wyss, M. (1970). Stress estimates of South American shallow and deep earthquakes, *J. Geophys. Res.* 75: 1529–1544.

AN ANALYSIS OF THE SEISMIC SOURCE CHARACTERISTICS OF EXPLOSIONS IN LOW-COUPLING DRY POROUS MEDIA

John R. Murphy and Theron J. Bennett

Science Applications International Corporation

Sponsored by the Air Force Research Laboratory

Contract No. FA8718-09-C-0009.
Proposal No. BAA09-38

ABSTRACT

The dependence of seismic source coupling of underground nuclear explosions on the characteristics of the explosion source medium is an important consideration in any assessment of nuclear test monitoring capability. In particular, while experience has indicated that normal depth explosions in almost all hardrock and water saturated emplacement media (i.e., "good-coupling" media) are roughly consistent with a single m_b/yield relation for any fixed tectonic source region, explosions in dry, porous media, such as the dry tuffs and alluvium found above the water table at the Nevada Test Site (NTS), are typically observed to have m_b values at a given yield that are lower than those in hardrock by about 0.50 ± 0.25 magnitude units. With the exception of the complex cavity decoupling evasion scenario, which is not always feasible, explosions in such low-coupling media define the lower bound on the detection capability required to successfully monitor small, clandestine underground nuclear tests. However, at the present time no fully reliable seismic source model is available to support quantitative analyses of broadband data recorded from such explosions. The technical objectives of this program are to develop a "Mueller/Murphy" frequency dependent seismic source model for underground nuclear explosions in dry, porous media and to then apply this model to a quantitative assessment of seismic yield estimation capability for such explosions as functions of explosion yield and depth of burial, as well as detailed physical properties of the source medium such as compressional wave velocity and percent by volume of air-filled porosity.

Our analyses during the past year have focused on seismic data recorded at the Lawrence Livermore National Laboratory (LLNL) regional network station MNV (Mina Nevada) from nuclear explosions conducted above and below the water table at the Yucca Flat testing area of NTS. P wave spectra over the frequency band 0.5 to 10 Hz have been estimated for a sample of 63 explosions conducted in dry, porous media above the water table at Yucca Flat. The measured gas-filled porosities (Gp) at the working points of these explosions range from near zero to almost 30%, while the associated yield values extend over approximately two orders of magnitude around a mean yield of about 10 kt. Since these explosions were conducted over a fairly narrow range in scaled depth centered on 150 m/kt$^{1/3}$, we analyzed the frequency dependent source scaling as functions of yield and Gp alone. Somewhat surprisingly, it was found that the derived dependence of the observed spectral amplitudes on Gp is essentially independent of frequency over the range 0.5 to 10 Hz, with the logarithm of the spectral amplitude at a fixed frequency decreasing with increasing Gp as -0.024 Gp. That is, the effect of Gp on the seismic source spectrum can be expressed as a frequency independent factor that indicates, for example, that the spectral amplitude levels decrease uniformly by about a factor of 5 as Gp increases from 0% to 30%. In order to compare these results with the well-documented seismic source for explosions conducted below the water table in saturated media, we collected data from a selected sample of explosions conducted below the water table at Yucca Flat and scaled their corresponding station MNV P wave spectra to a yield of 10 kt and a depth of 323 m (i.e., 150 m/kt$^{1/3}$) using the Mueller/Murphy source scaling model. The resulting average spectrum was then divided by the P wave spectra for 10 kt explosions in dry, porous media predicted as a function of Gp using the statistically derived scaling relations. The results of this analysis indicated that the seismic source function for a 10 kt explosion in a dry, porous medium with a Gp value of 25% is expected to be very similar to the corresponding Mueller/Murphy source function for a 10 kt explosion at the same depth in saturated tuff, divided by a frequency independent factor of about 7. In particular, in contrast to some previously published results, both source function estimates show a high frequency rolloff inversely proportional to the square of the frequency. Work is continuing on deriving quantitative estimates of the statistical uncertainty in these results and their implications for general source modeling as functions of yield and source medium Gp value.

OBJECTIVES

The technical objectives of this research program are to develop an analytic approximation for a frequency dependent seismic source model for underground nuclear explosions in dry, porous media analogous to the Mueller/Murphy model for explosions in hardrock and water-saturated media, and to then apply this model to a quantitative assessment of seismic monitoring capability relative to explosions in such media. This is being accomplished by conducting source scaling analyses of broadband seismic data recorded from explosions in such media at NTS to define their frequency dependent source coupling characteristics relative to the already well-documented seismic source coupling of corresponding explosions in "good-coupling" media at that same test site. The ultimate objective is to improve U.S. operational nuclear test monitoring capability by providing a reliable seismic source model that can be used to quantitatively address seismic detection, identification and yield estimation capability as functions of yield, depth of burial and the physical characteristics of the source medium for small underground nuclear tests which might be conducted in such low-coupling media.

RESEARCH ACCOMPLISHED

It has long been recognized that normal depth explosions in almost all hardrock and water-saturated emplacement media (i.e. "good-coupling" media) are roughly consistent with a single m_b/yield relation for any fixed tectonic source region. In fact, the only media which are known to give consistently different results for fully tamped explosions are saturated clay or water and dry, porous media, such as the dry tuff and alluvium found above the water table at NTS. These observations are summarized in Figure 1, where it can be seen that the average m_b value for explosions of fixed low yield in saturated clay or water is expected to be higher by about 0.50 ± 0.25 magnitude units, while that for explosions in dry, porous media is expected to be lower by about 0.50 ± 0.25 magnitude units relative to that for explosions of the same yield in good-coupling media. It follows that, with the exception of cavity decoupled explosions, which are not always technically feasible, small explosions in dry, porous media pose the greatest challenge to effective seismic monitoring.

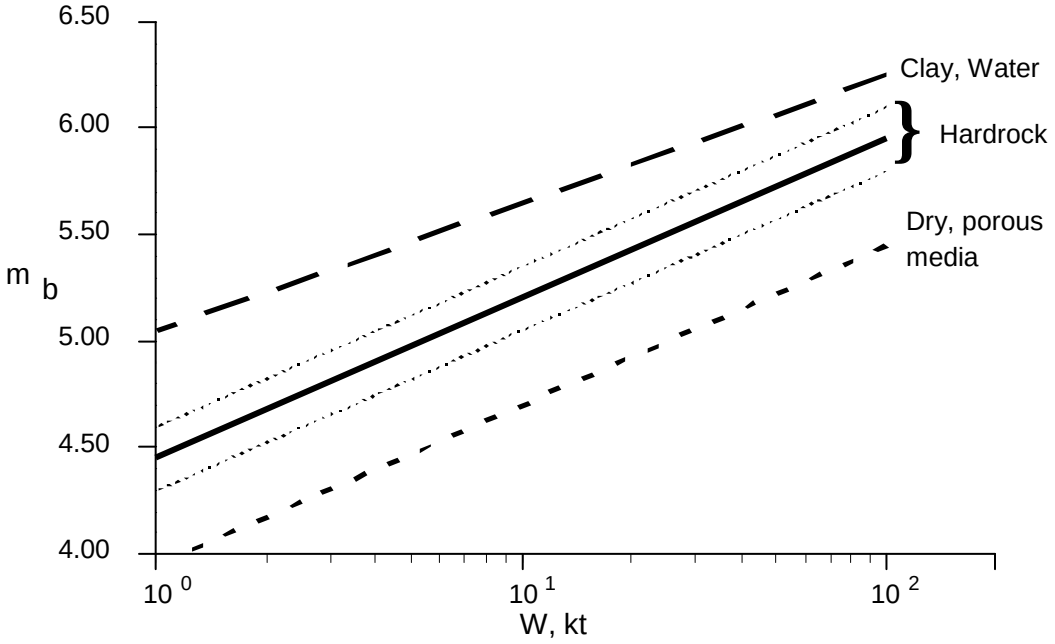

Figure 1. Comparison of m_b/yield relations for fully tamped underground nuclear explosions in a fixed tectonic source environment, illustrating the effects of source medium on seismic coupling. It can be seen that the average m_b value for explosions of fixed low yield in dry, porous media is expected to be lower by about 0.50 ± 0.25 magnitude units relative to that for explosions of the same yield in hardrock media.

During the first year of this two year study program, our analyses have focused on broadband data recorded from NTS explosions at the four near-regional stations of the LLNL seismic network. We currently have digital data recorded at those stations from some 150 NTS explosions, approximately 100 of which were underground nuclear tests conducted above the water table in dry, porous media. These data are generally of excellent quality, as is illustrated in Figure 2 which shows a record section of data recorded from selected Yucca Flat explosions at LLNL station MNV. In this figure, the top ten traces correspond to recordings of low yield (W < 20 kt) explosions in dry, porous media above the water table (above W.T.) at Yucca, while the bottom three traces represent recordings of larger (~140 kt) explosions conducted in saturated tuffs below the water table (below W.T.) at Yucca. It can be seen that the broadband signal to noise ratios are generally quite high, even for the smaller explosions in low coupling media.

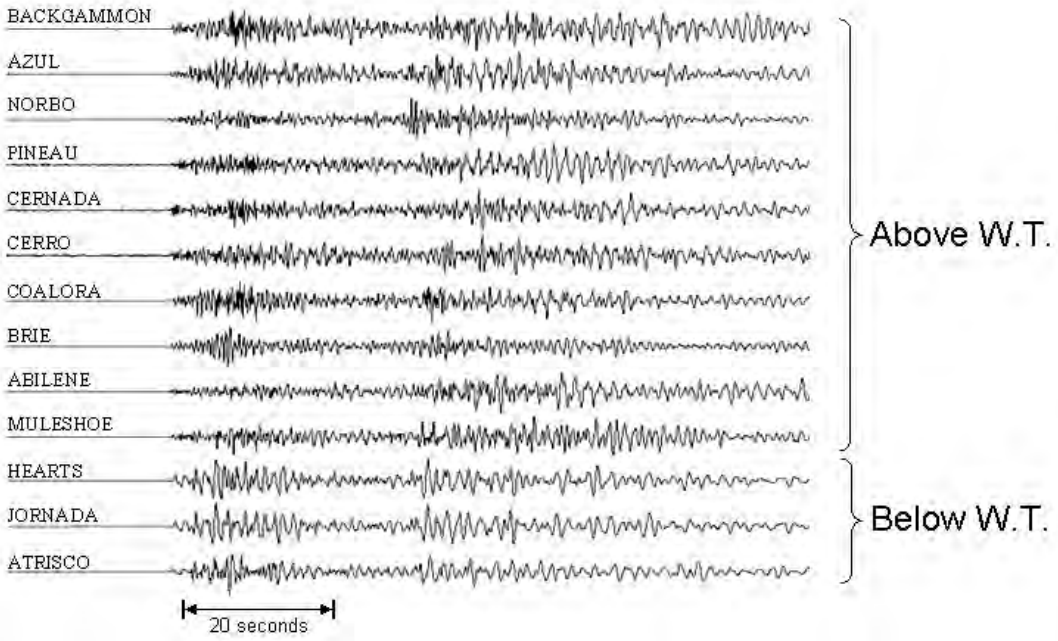

Figure 2. Data recorded from selected Yucca Flat explosions at LLNL station MNV. The top ten traces correspond to recordings of low yield (W < 20 kt) explosions in dry porous media above the water table (above W.T.) at Yucca, while the bottom three traces are recordings of larger explosions conducted in saturated tuff below the water table (below W.T.) at Yucca.

Our initial analyses centered on seismic data recorded at the LLNL near-regional ($\Delta \approx 240$ km) station MNV (Mina, Nevada), for which we have the most complete set of data recorded from explosions conducted above the water table in dry, porous media at Yucca Flat. The distribution of gas-filled porosity (percent by volume) values measured at the working points of these 63 explosions is shown in Figure 3, where it can be seen that the values range from near zero to almost 30%. The mean yield of this sample of explosions is close to 10 kt and their distribution with scaled depth is shown in Figure 4, where it can be seen that the values are fairly tightly clustered around a mean scaled depth of about 150 m/kt$^{1/3}$.

P wave spectra corresponding to the data recorded from these explosions at station MNV were estimated over the frequency band 0.5 to 10 Hz, using the initial 10 seconds of the recorded P waves. Because these explosions were conducted over such a narrow range in scaled depth, it is not possible to explicitly address the depth dependence of the seismic source, and the P wave spectral amplitude level, P(ω), has been represented by the simple scaling relation:

$$P(\omega) = k(\omega)\, W^{a_1(\omega)}\, 10^{a_2(\omega) Gp} \qquad (1)$$

where W is the explosion yield, Gp the percent gas-filled porosity at the working point and k, a_1, a_2 are frequency dependent coefficients to be estimated from the observed spectral data via least squares analysis:

$$\log P(\omega) = \log k(\omega) + a_1(\omega) \log W + a_2(\omega)\, Gp \qquad (2)$$

The assumed functional dependence of the P wave spectral amplitudes on Gp was adopted from the scaling relation proposed previously by Vergino and Mensing (1990) in their prior analysis of m_b(Pn) scaling for explosions in dry, porous media at NTS. Although alternate functional forms could be considered, it has been found that this simple relation provides a good description of the observed variations in P wave spectral amplitude as a function of Gp.

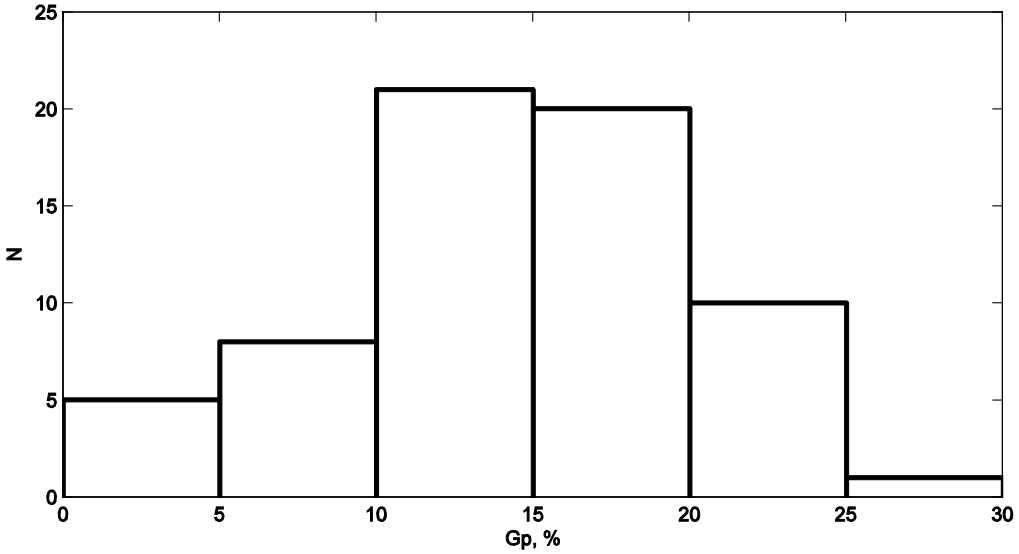

Figure 3. Distribution of observed gas-filled porosity (Gp) values for the selected sample of Yucca Flat explosions recorded at MNV.

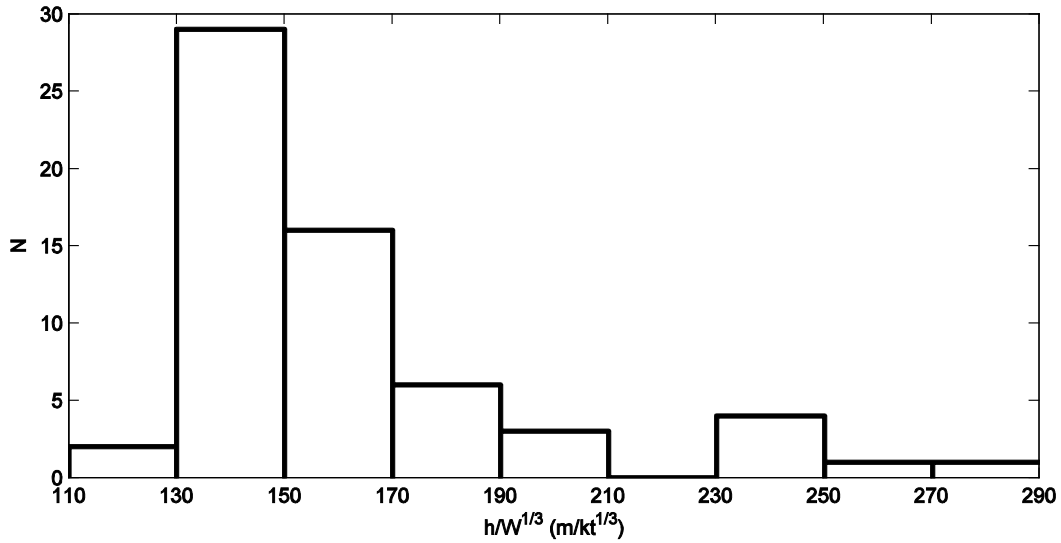

Figure 4. Distribution of scaled depth values for the selected sample of Yucca Flat explosions conducted above the water table and recorded at station MNV. The values are fairly tightly clustered about the mean value of approximately 150 m/kt^{⅓}.

A somewhat surprising result of our scaling analysis has been the finding that the dependence of P wave spectral amplitude on Gp is essentially independent of frequency. This fact is confirmed in Figure 5 which shows a comparison of the prediction σ values as a function of frequency obtained using the statistically derived frequency dependent scaling and a frequency independent scaling in which the coefficient on Gp was held fixed at the average of the frequency dependent values.

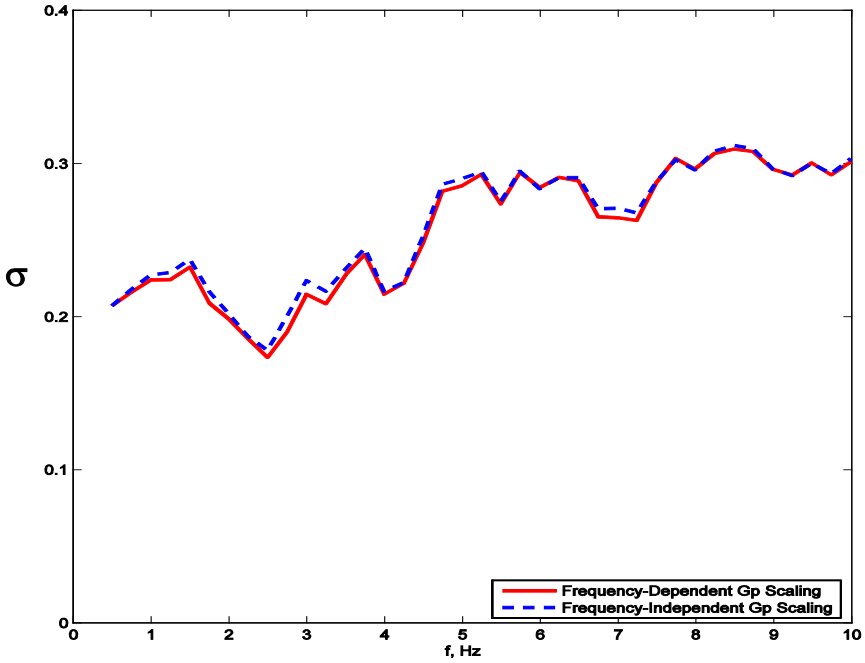

Figure 5. Comparison of prediction standard deviations (σ) as a function of frequency (f) for scaling analyses conducted with frequency dependent (solid) and frequency independent (dashed) Gp scaling. These results indicate that the scaling with Gp is essentially independent of frequency.

It can be seen that the results obtained using these two models are essentially identical, confirming that the Gp scaling is independent of frequency within the uncertainties in the statistically derived scaling coefficients. The average value of the a_2 coefficient in this case is -0.024, which compares with the coefficient values of -0.027 obtained by Vergino and Mensing (1990) from their analysis of the m_b(Pn) scaling dependence on Gp. This finding results in a very significant reduction in the complexity of the source scaling in that it means that the entire P wave source spectrum scales in the same way over the analyzed frequency range from 0.5 to 10 Hz, decreasing by about a factor of five at a fixed yield as Gp varies from near zero to 30%.

It has been found that this statistical scaling model provides quite good predictive capability over the range of source parameters encompassed by the selected sample of explosions. This fact is illustrated in Figures 6 and 7 which show, respectively, comparisons of predicted and observed P wave spectra for explosions of the same yield with significantly different Gp values, and for explosions of the same Gp value (~20%) with m_b(Pn) values (and associated yields) varying over nearly a full order of magnitude. These comparisons confirm that the derived scaling with both yield and Gp are in good agreement with the measured P wave spectral data. In fact, the scaling with Gp appears to be precise enough to identify likely errors in the reported Gp values. An example of this is shown in Figure 8, where the comparison on the left is for the prediction obtained using the reported Gp value of 29% (the highest value in our sample of explosions), while the comparison on the right is for the prediction obtained using a reduced Gp value of 15%. Clearly the fit is much better using the reduced value and the frequency independent nature of the discrepancy strongly points to the Gp variable.

In order to provide a basis for quantitative evaluation of the seismic source for explosions in dry, porous media, we theoretically scaled MNV *P*-wave spectra derived from data recorded from explosions conducted below the water table (BWT) at Yucca Flat to the average sample values of W = 10 kt, h = 323 m (i.e., $h/W^{1/3}$ = 150 $m/kt^{1/3}$) of the dry, porous sample using the Mueller/Murphy (1971) scaling model. Figure 9 shows a comparison of the resulting scaled spectra for an explosion much larger than 10 kt (Jornada) and an explosion smaller than 10 kt (Techado). It can be seen that these scaled spectra are comparable, indicating that we have a good reference level for a 10 kt explosion at a depth of 323 m in saturated tuff.

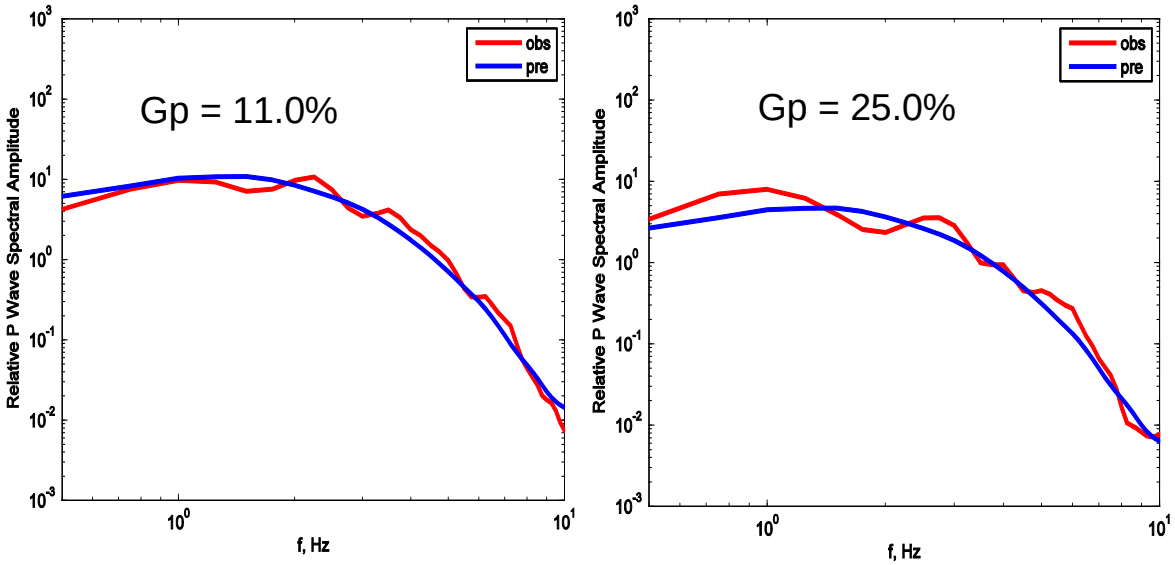

Figure 6. Comparison of predicted and observed MNV P wave spectra for explosions of comparable yield conducted in media with significantly different gas-filled porosity (Gp) values.

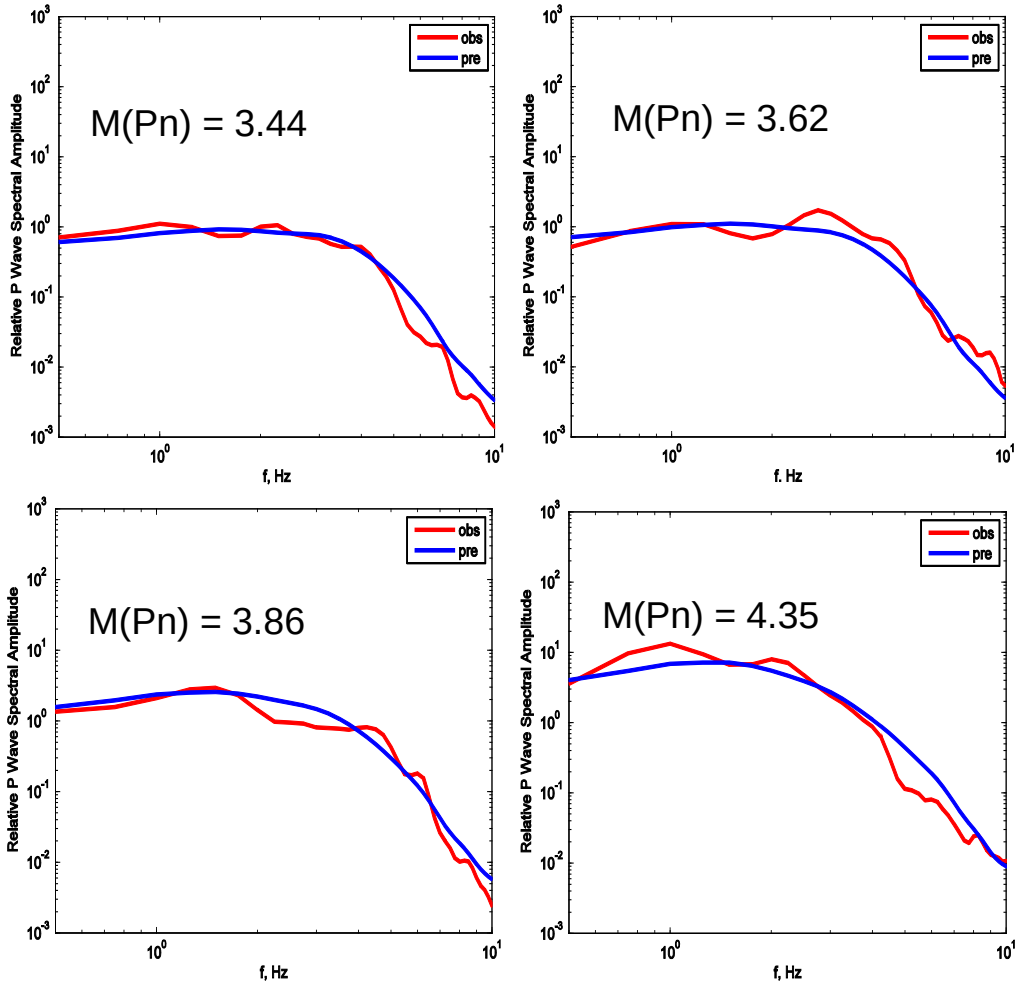

Figure 7. Comparison of predicted and observed MNV P wave spectra for explosions of different yields conducted in media with comparable (Gp ≈ 20%) gas-filled porosity values.

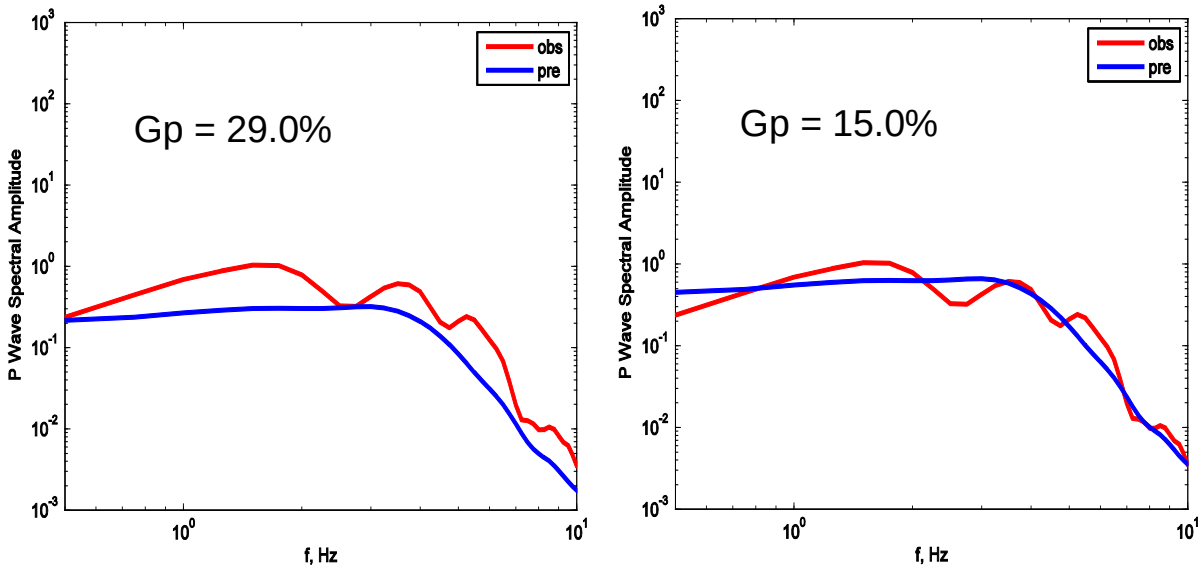

Figure 8. Comparison of observed MNV P wave spectra for an explosion with reported gas-filled porosity (Gp) of 29% with predicted spectra for Gp values of 29% (left) and 15% (right). It can be seen that the derived scaling relations are precise enough to identify likely errors in the reported Gp values.

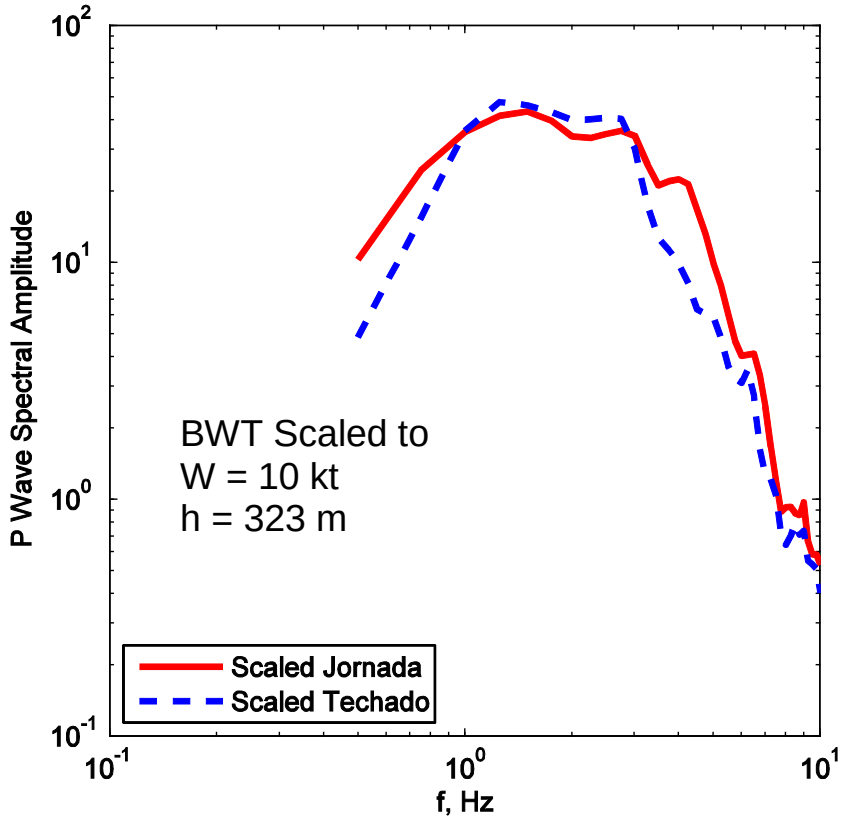

Figure 9. Comparison of station MNV scaled P wave spectra for explosions in saturated tuff below the water table at Yucca Flat with yields significantly larger (Jornada) and smaller (Techado) than the mean yield of approximately 10 kt of the sample of explosions in dry, porous media. It can be seen that the application of the Mueller/Murphy scaling relations brings these two into very good agreement.

Figure 10 shows ratios of the average saturated tuff P wave spectral estimate for a 10 kt explosion at 323 m depth to the corresponding average spectra predicted for the same explosion in dry, porous media with Gp values of 5 and 25%, using the statistically derived scaling laws. It can be seen that these source spectral ratios are approximately independent of frequency over the analyzed band from 0.5 to 10 Hz. Note also that an explosion in a dry, porous medium with very low Gp is not the same as an explosion of the same yield and depth in saturated tuff. That is, the absence of water has some effect on seismic coupling, even for media with very low air-filled porosity values.

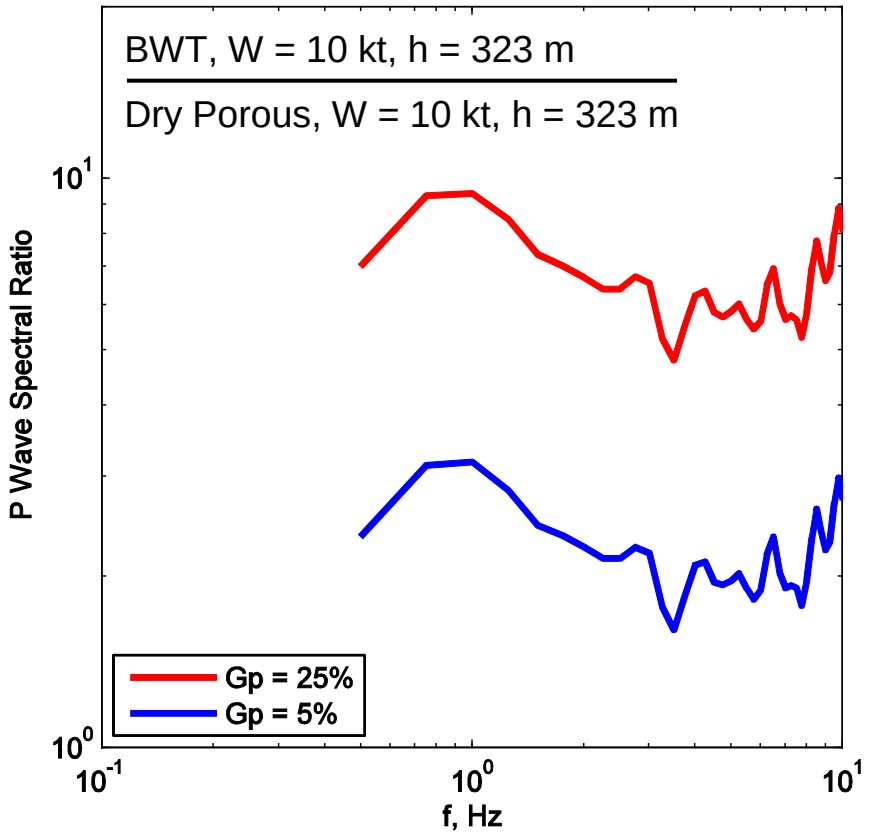

Figure 10. Spectral ratios of the estimated station MNV P wave spectrum for a 10 kt explosion at a depth of 323 m in saturated tuff to the corresponding MNV predicted spectra for 10 kt explosions in dry, porous media characterized by Gp values of 5% and 25%.

Dividing the Mueller/Murphy seismic source function predicted for a 10 kt explosion at a depth of 323 m in saturated tuff by the experimental source spectral ratios shown in Figure 10 gives estimates of the corresponding seismic source functions for the same explosions in dry, porous media. The result for a Gp value of 25% is shown in Figure 11, where it is compared with the result of dividing the Mueller/Murphy saturated tuff source by a frequency independent factor of 6.5. It can be seen that this simple frequency independent shift brings the two source function estimates for a 10 kt explosion at a depth of 323 m in a dry, porous medium characterized by a Gp value of 25% into excellent agreement. In particular, both estimates show about the same corner frequency and a common inverse frequency squared rolloff at high frequency, contrary to the conclusions of some previous studies (e.g., Taylor and Dowla, 1991) which suggested that the rolloff rate is expected to be higher for explosions in dry, porous media.

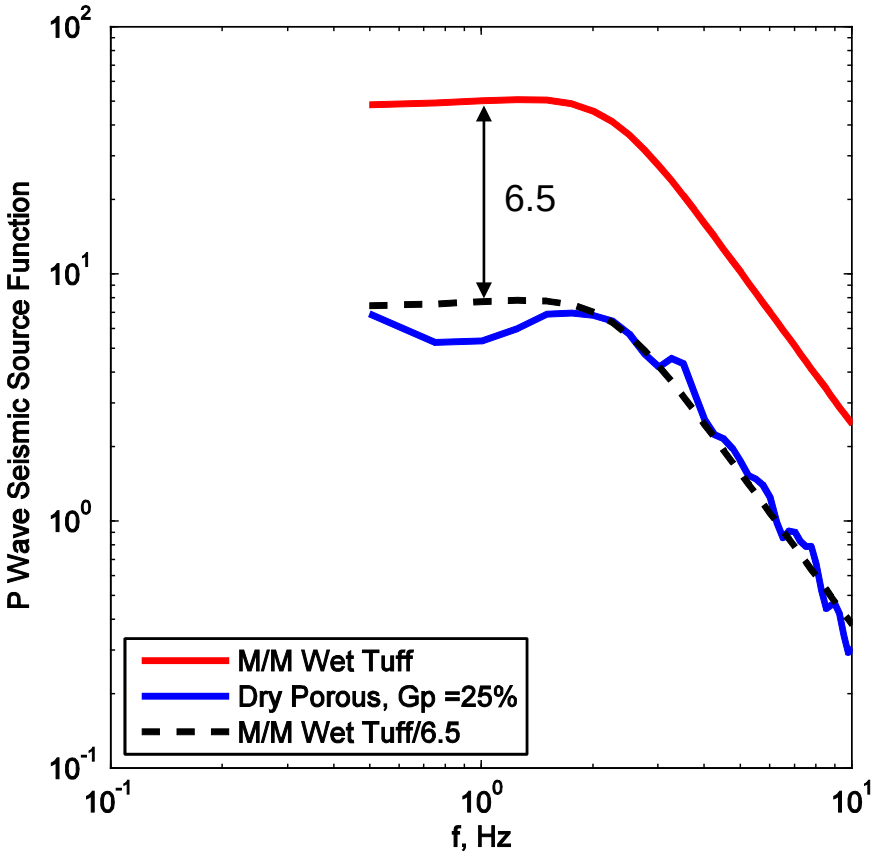

Figure 11. Comparison of the P wave source function estimate for a 10 kt explosion at a depth of 323 m in a dry, porous medium characterized by a Gp value of 25% with the corresponding Mueller/Murphy source function for the same explosion in saturated tuff. It can be seen that these two source function estimates can be reconciled by an essentially frequency independent relative coupling factor of ~ 6.5.

CONCLUSIONS AND RECOMMENDATIONS

The dependence of seismic source coupling of underground nuclear explosions on the characteristics of the explosion source medium is an important consideration in any assessment of nuclear test monitoring capability. While experience has indicated that explosions in almost all hardrock and water-saturated emplacement media are roughly consistent with a single m_b/yield relation in any fixed tectonic source region, explosions in dry, porous media are observed to have low frequency seismic source coupling at a given yield that is as much as an order of magnitude lower than that in hardrock. The objectives of this research study are to develop a "Mueller/Murphy" frequency dependent seismic source model for underground nuclear explosions in such media and to then quantitatively assess the implications of this model with respect to seismic monitoring capability.

Over the past year we have been analyzing seismic data recorded at the LLNL network station MNV from explosions conducted above and below the water table at Yucca Flat. P wave spectra over the frequency band 0.5 to 10 Hz have been estimated for a sample of 63 explosions conducted in dry, porous media above the water table. The measured gas-filled porosities (Gp) at the working points of these explosions range from near zero to almost 30%, while the associated yield values extend over approximately two orders of magnitude around a mean yield of about 10 kt. Statistical scaling analyses of the dependence of the observed spectral amplitudes on explosion yield and Gp indicate that the dependence on Gp is essentially independent of frequency over the entire range from 0.5 to 10 Hz. That is, the effect of Gp on the seismic source spectrum can be expressed as a frequency independent factor that indicates, for example, that the spectral amplitude levels decrease uniformly by about a factor of 5 as Gp increases from 0 to 30%. In order to compare these results with the well-documented seismic source for explosions conducted

in water-saturated media, we analyzed data from a selected sample of explosions conducted below the water table at Yucca Flat and scaled their corresponding station MNV P wave spectra to the mean yield and depth of burial of the sample of explosions in dry, porous media using the Mueller/Murphy source scaling model. The results of this comparison indicate that the seismic source function for a 10 kt explosion in a dry, porous medium with a Gp value of 25% is expected to be very similar to the Mueller/Murphy source function for a 10-kt explosion at the same depth in saturated tuff, divided by a frequency independent factor of about 7. In particular, both source function estimates show a high frequency rolloff proportional to ω^{-2}. Current work is focused on deriving quantitative estimates of the statistical uncertainty in these results and on assessing their implications for general source modeling of explosions in dry, porous media.

REFERENCES

Mueller, R. A. and J. R. Murphy (1971). Seismic characteristics of underground nuclear detonations, I: Seismic spectrum scaling, *Bull. Seism. Soc. Am.* 61: 1675–1692.

Taylor, S. R. and F. U. Dowla (1991). Spectral yield estimation of NTS explosions, *Bull. Seism. Soc. Am.* 81: 1292–1308.

Vergino, E. S. and R. W. Mensing (1990). Yield estimation using regional m_b(Pn), *Bull. Seism. Soc. Am.* 80: 656–674.

EXPLOITATION OF THE IMS AND OTHER DATA FOR A COMPREHENSIVE, ADVANCED ANALYSIS OF THE NORTH KOREAN NUCLEAR TESTS

John R. Murphy, Benjamin C. Kohl, Jeffry L. Stevens, Theron J. Bennett, and Hans G. Israelsson

Science Applications International Corporation

Sponsored by the Department of State

Award No. SAQMMA09C0250

ABSTRACT

On May 25, 2009, the North Koreans conducted a second underground nuclear test in the same area as their initial 2006 test. Preliminary analysis indicated that the explosive yield of the second test was roughly 5 times that of the first, and it was found to have been well-recorded by a variety of globally distributed seismic networks. We carefully analyzed the available short-period seismic data in an attempt to define accurate locations, depths and yields for these two North Korean nuclear tests. In order to determine accurate relative locations for the two events, we made very precise arrival time measurements at 35 stations that recorded both explosions with good signal to noise ratios. The location of the 2006 explosion was then held fixed at the previously determined preferred location and the relative location of the 2009 explosion was estimated using the Joint Hypocenter Determination (JHD), Double Difference (DD) and Differential Waveform Interferometry (DWIF) location algorithms. All of these relative location techniques yielded very similar results, indicating that the 2009 test was conducted about 2.5 km west-northwest of the 2006 test. These relative seismic locations were subsequently integrated with the local topographic data and satellite imagery to define what we believe to be very reasonable and accurate locations for these two explosions.

The corresponding source depths can not be reliably determined using the currently available arrival time data or the observed, narrowband network-averaged teleseismic *P* wave spectral data. Consequently, we implemented a new approach using broadband *P* wave spectral ratios of the two explosions at common regional stations to obtain estimates of the corresponding broadband source spectral ratios. The resulting network-averaged source spectral ratio was then compared with theoretical Mueller/Murphy based source spectral ratios to estimate best-fitting source depths and associated yields. The results of this analysis indicated that the two explosions could not have been detonated at any common depth in the plausible 100 to 800 m depth range and, in fact, the observed spectral ratio data are best fit by source depths of about 200 m for the 2006 test and 550 m for the 2009 test. The corresponding yield estimate for the May 25, 2009, explosion was then found to be about 4.6 kt.

The long-period surface wave Ms magnitudes for both the 2006 and 2009 tests appear to be anomalously large relative to historical experience, producing unreasonably large Ms yield estimates and problematic Ms/mb identification characteristics. A formal moment tensor inversion analysis of the available data indicated that release of tectonic strain energy by the explosion may have contributed somewhat to the observed anomaly. However, current estimates of the likely strength of this tectonic release are not large enough to fully explain the observed anomaly. Additional research will be required to determine whether unresolved CLVD secondary sources may account for the discrepancy. Identification of the 2009 and 2006 events as explosions based on high-frequency Pn/Lg ratios measured at regional stations are unambiguous; however, results for discrimination based on Ms-versus-mb are inconclusive (again probably due to secondary source contamination to Ms).

OBJECTIVES

The North Korean Test of May 25, 2009, was well recorded by the International Monitoring System and other regional and teleseismic stations. However several characteristics of the event were anomalous and warranted further study, in particular with regard to the unknown depth of burial of the event. The objective of the present study was to exploit IMS and other open data sources to conduct comprehensive, advanced analyses of the characteristics of these two North Korean nuclear tests. We focused on refining event locations, estimating source depths and seismic yields and evaluating the effectiveness of the various seismic event identification criteria as applied to these two explosions. Seismic data recorded at stations of the global IMS network were augmented with seismic data from key regional stations (< 20 degrees) obtained from the Incorporated Research Institutions for Seismology (IRIS) data management center, the Ocean Hemisphere Project Data Management Center (OPHDMC) and the Japanese National Research Institute for Earth Science and Disaster Prevention (NIED).

RESEARCH ACCOMPLISHED

Data Resources

The May 25, 2009, underground nuclear test conducted by North Korea (Democratic People's Republic of Korea, DPRK) was located in the same general area of northeastern North Korea where a previous nuclear test was conducted in 2006. The two events appear to have been conducted in the same tunnel complex mined into Mount Mantap. The area is a relatively stable craton (the North China-Korean platform) with a basement of Archean (~2000 Ma BP) and Proterozoic (~1000 Ma BP) granite and metamorphosed rocks which are overlain by up to 1 km of Cenozoic (65 Ma BP - Present) volcanic basalts which are little deformed (USGS, 1967).

Although rather small in magnitude, the 2009 test was recorded by numerous global seismic stations. Seismic locations determined by the International Data Centre (IDC), US Geological Survey (USGS/NEIC), and independently in relative location analyses by SAIC (described below) are located in proximity to a tunnel entrance previously identified from satellite imagery analyses and believed to be associated with the 2006 explosion (GlobalSecurity.org, 2006; Schlittenhadt et al., 2010).

The primary and auxiliary seismic networks of the International Monitoring System (IMS) were the principal sources of data for the analysis conducted in this study. Signals from the 2009 test were detected globally on 56 IMS stations as reported in the Reviewed Event Bulletin of the International Data Centre. We supplemented the IMS data with key regional stations (< 20 degrees) from three sources:

- Incorporated Research Institutions for Seismology (IRIS) data management center
    - Global Seismograph Network (II and IU networks) - numerous stations at regional and teleseismic distances, in particular INCN (Inchon Korea)
    - New Chinese Digital Seismic Network (IC network) - numerous stations at regional distances, in particular MDJ (Mudanjiang, China) the closest station which recorded both events
    - Kazakhstan Network (KZ) - stations at regional distance
    - Kyrgyz Seismic Telemetry Network (KNET) - stations at regional distance
- Ocean Hemisphere Project Data Management Center (OP HDMC) - including TJN (Teajon, Korea) at a distance of about 500 km
- National Research Institute for Earth Science and Disaster Prevention (NIED) - a network of over 40 stations in Japan, all within regional distance.

Emphasis was on obtaining broadband waveform data from stations that recorded signals from both the 2006 and 2009 events. This supported the detailed comparative analysis conducted in much of this report.

Location

The objective of this part of the study was to obtain a best estimate of the absolute locations and depths of both nuclear tests using seismic location methods. The lack of historical calibration data from the North Korea test site limits the accuracy of single event location methods. Even with good regional structure models, biases of several kilometers can be expected. Our approach was to first determine the relative locations between the events. We used three relative location algorithms that complement each other in terms of the data, earth structure model and objective function. In the second stage of our location analysis, we used the relative locations between the events as

a constraint to aid in pinpointing the absolute location. We used high-resolution topographic data along with constraints on depth-of-burial and the relative location to derive the most likely absolute locations of the two events.

Waveform Correlation-Based Relative Location **-** The method builds on the basic concept that the relative location of a new event with respect to one or more reference events can be obtained from differential times of common event-station-phase pairs (Snieder,and Vrijlandt, 2005). Waveform cross-correlation is used to measure the differential times. Rather than pick the lag of the maximum of the correlation trace (which is susceptible to errors due to cycle skipping) to obtain a differential time, the Differential Waveform Interferometry (DWIF) method involves time-shifting the correlation traces for a given event location hypothesis using a slowness model of the source region, and stacking the correlation traces. A grid search is performed to determine the event origin time and hypocenter that maximizes the objective function. The individual correlation traces are weighted by the statistical significance of the correlation results, hence event-station-phase pairs that do not correlate well are implicitly down-weighted and no a priori rejection of data or outlier rejection is required. In the first phase of the processing the correlation processing is performed using phase-dependent rules (filter band, window-length) allowing the use of all common body-wave phases (regional, primary, secondary). All stations with waveform recordings and a good SNR signals for both events were used in the processing.

In the second phase of the processing, the individual correlation traces were time-shifted using a source slowness model, according to a relative location and origin time hypothesis. The peak of the stack of the correlation traces was used as the objective function. A grid search was performed for all relative locations and origin times to maximize the objective function. Figure 1 shows a slice through the objective function grid at fixed relative depth = 0. The breadth of the peak is controlled by the frequency content of the waveform data. For the best location the RMS residual in the peaks of the correlation traces was reduced from about 0.160 seconds to 0.023 seconds.

To assess the uncertainty in the solution we performed a bootstrap experiment. For each case we randomly selected half of the stations and performed the relative location using the same approach as for the full station network. The error ellipse (0.26 x 0.23 km) was defined as the ellipse that enclosed 90% of the bootstrap experiment locations.

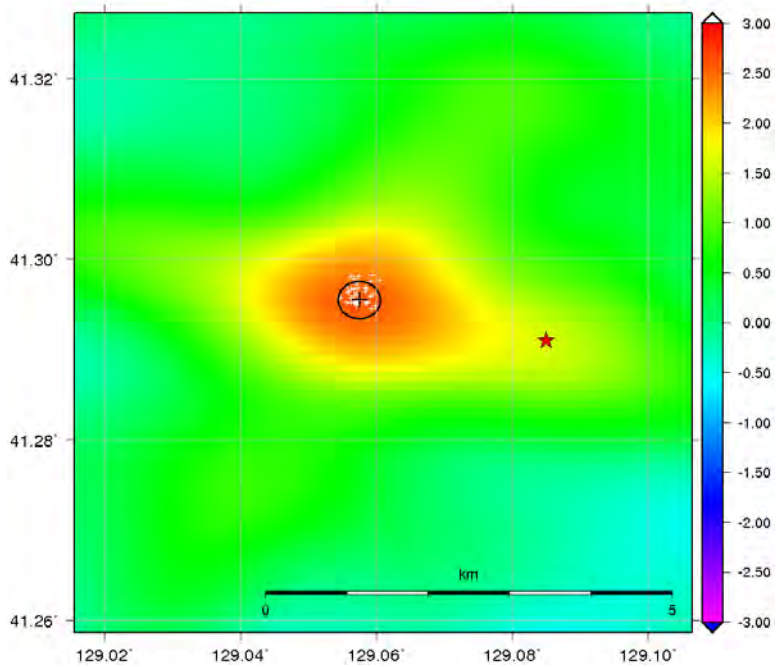

Figure 1. Color-contoured slice through the 3-D objective function grid at constant relative depth (0) at a fixed origin time. The red star marks the location of the October 9, 2006, that was used a fixed reference point in the algorithm. The black "+" marks the best location and the white "+" mark the results of a boot-strap experiment involving subsets of stations to quantify the uncertainty. The black ellipse represents a 90% confidence ellipse based on the bootstrap results.

Waveform Alignment and JHD, DD - Relative arrival times for two events recorded with adequate SNR at a given station can often be measured precisely by waveform alignment either manually or with cross correlation (Fisk, 2002). We measured such relative arrival times manually for all stations with recordings of both explosions. Figure 2 shows the initial part of the waveform sections of the 2009 event (in red) relative to those of the 2006 event (in blue) The difference in arrival times for the station-phase pairs (differential times) picked in this manner were very consistent. Figure 2 plots the residual of the differential times with respect to the average differential time. It shows that the picks for the 2009 event for stations in the north-west quadrant are systematically early relative to the 2006 arrivals, indicating that the 2009 test must have been located to the northwest of the 2006 test.

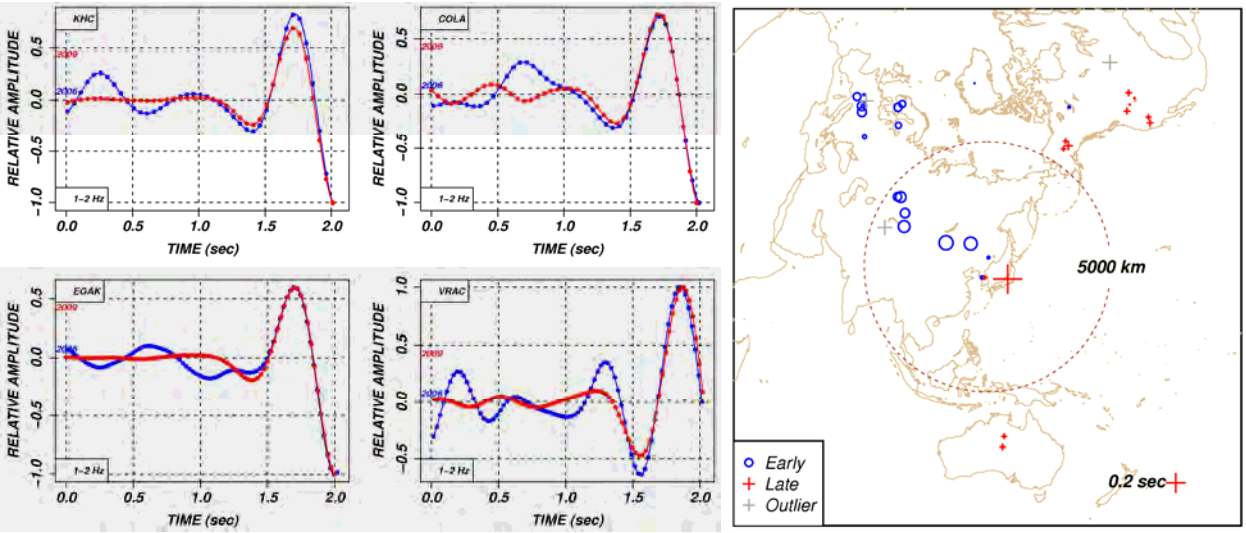

Figure 2. Waveforms for the two explosions at four stations manually aligned (left). Residuals of the differential times plotted for the IMS and IRIS stations (right). The early arrivals for the stations to the northwest support the conclusion that the 2009 event occurred to the northwest of the 2006 event.

We calculated relative epicenters of the two explosions using the algorithm (jhd89) developed by Dewey (1972). Only first arrival *P* phases were used. The epicenter of the 2006 explosions was fixed at 41.291 N and 129.085 E and at zero depth (Bennett et al, 2006) throughout the calculations. To detect and remove possible errors in the data we applied Grubbs' outlier test (Grubbs, 1950). Arrivals for the stations with an outlying residual (p-value larger than 0.05) were removed iteratively before the next JHD run with the arrivals of the remaining stations.

We also applied the double difference method using the hypoDD software (version 1.1) (Waldhauser and Ellsworth, 2000) to data at stations within about 10 degrees. Convergence of the calculations were found to be dependent on the depths of the starting solutions, but epicenters of converging solutions generally agreed with JHD solutions. The epicenter of the 2009 explosion for starting depths at zero for both explosions was 41.2983 N 129.0616 E, after the epicenter solutions of the two explosions were shifted so that the epicenter of the 2006 explosion coincided with the "ground truth" used in the JHD calculations. In all 41 stations were used in this solution after applying an outlier cut-off at 1.96 standard deviations (95%).

Table 1. Comparison of the relative location results. The double difference solution (DD) used regional stations including the NIED stations. JHDNIED used the same stations as the DD run, JHDALL used all stations and JHD used regional and teleseismic IMS and IRIS stations.

Auth	Date Time	Latitude	Longitude	Smaj	Smin	Az
fixed	2006/10/09 01:35:29.90	41.291	129.085	0.13	0.12	90
DD	2009/05/25 00:54:44.90	41.2986	129.0616	0.13	0.12	90
JHDNIED	2009/05/25 00:54:45.30	41.2945	129.0687	0.88	0.22	132
JHDALL	2009/05/25 00:54:45.30	41.2983	129.0608	0.16	0.16	1
JHD	2009/05/25 00:54:45.10	41.2968	129.0605	0.25	0.20	62
DWIF	2009/05/25 00:54:45.17	41.2955	129.0575	0.26	0.23	2

Topographic Analysis **-** The relative location computations yielded a relative location of the May 25, 2009, event of about 2.5 km to the west-northwest of the October 9, 2006, event. All computations were based on fixing the October 9, 2006, to the location of Bennett et al. (2006) as shown in Figure 3. The fixed location reported by Bennett et al. (2006) was estimated as being about 1 km into the mountain from the known tunnel adit in the direction of maximum relief. This placed the 2006 event directly to the north of the adit. This assumed location of the 2006 explosion results in a location for the 2009 on the other side of ridge from the adit (Figure 3). This seems unlikely and suggests that the presumed location of the 2006 may be biased.

We conducted a topographic analysis of the area using ASTER Global Digital Elevation Model. These terrain data are sampled with a posting interval of 30 m, and an accuracy of 7-14 m making them comparable to NIMA DTED level 2. The potential locations of the 2009 event were selected by identifying the areas with sufficient overburden that have positions relative to potential possible 2006 event locations as constrained by the relative location results. The result is shown in Figure 4, i.e. the blue hatched area is the only area that is consistent with all three constraints:

1. The 2006 event had 100 - 300 m of overburden relative to the adit elevation, based on a yield of 1.1 kt and a depth of burial of 200 meters from the Pn spectral ratio analysis (see below)
2. The 2009 event had 350 - 750 m of overburden relative to the adit elevation, based on a yield of 4.6 kt and a depth of burial of 550 meters from the Pn spectral ratio analysis (see below)
3. The 2009 events was about 2.5 km to the west-northwest of the 2006 event (location result)

Much of the hatched area in Figure 4 is beyond the ridge line relative to the adit. Figure 4 shows our best estimate of the locations of both events. This result gives a depth of burial of about 180 meters for the 2006 event and 600 meters for the 2009 event.

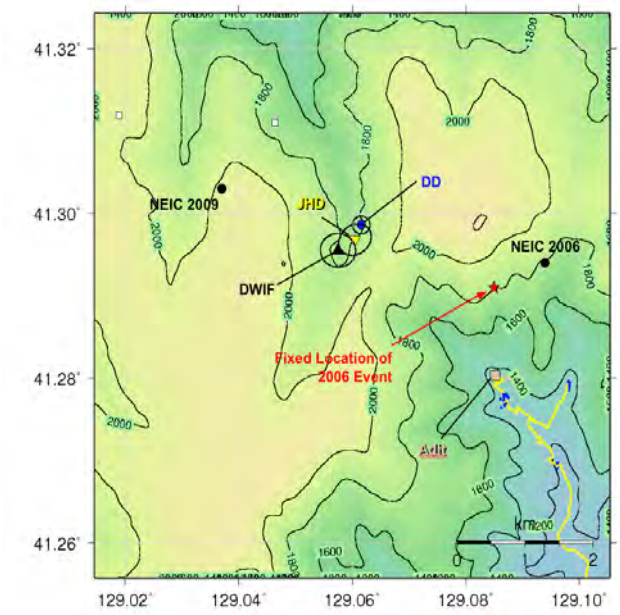

Figure 3. Locations of the May 25, 2009 event assuming a fixed location for the October 9, 2006 event based on Bennett et al. (2006). It places the 2009 event beyond the area of maximum overburden relative to the adit, indicating a probable bias in the fixed location for the 2006 event.

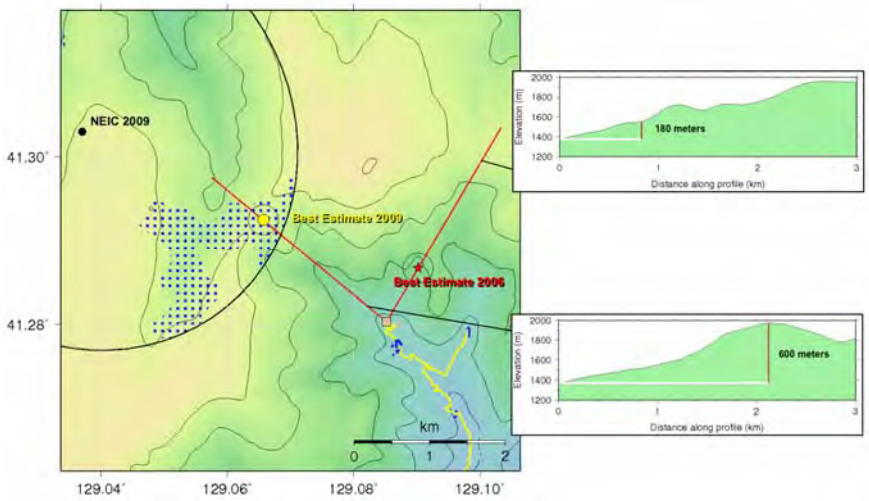

Figure 4. Best estimates for the locations resulting from the topographic analysis, assuming that the tunnel for the 2009 event did not go beyond the area of maximum relief. The best estimates put the 2006 and 2009 events at 41.2867° N, 129.0902° E and 41.2925° N, 129.0657° E respectively.

Yield Estimation from Teleseismic *P* Data

The teleseismic *P* wave data recorded from the May 25, 2009, North Korean nuclear test were analyzed using the model-based network-averaged *P* wave spectral yield estimation procedures summarized by Murphy and Barker (2001). Figure 5 shows a comparison of the observed network - averaged *P* wave spectrum for the May 25, 2009, explosion with that observed for the previous October 9, 2006 North Korean nuclear test based on data recorded at nine common teleseismic stations. The spectral amplitude levels for the 2009 test are about a factor of four larger than those observed from the 2006 test over this short-period band (0.5 - 2.5 Hz). The observed network - averaged teleseismic *P* wave spectrum for the 2009 nuclear test are compared with the corresponding best fitting theoretical predictions obtained using the Mueller/Murphy explosion seismic source model in Figure 6, assuming a source depth of 200 m in hardrock and frequency-dependent attenuation models appropriate to the Semipalatinsk Test Site (Semi) and the Nevada Test Site (NTS). Figure 6 shows that the yield estimate varies by about a factor of two (2.7 kt versus 5.3 kt) depending on the attenuation model. Further, the Semi model with an associated yield estimate of 2.7 kt provides a much better overall fit to the observed spectrum.

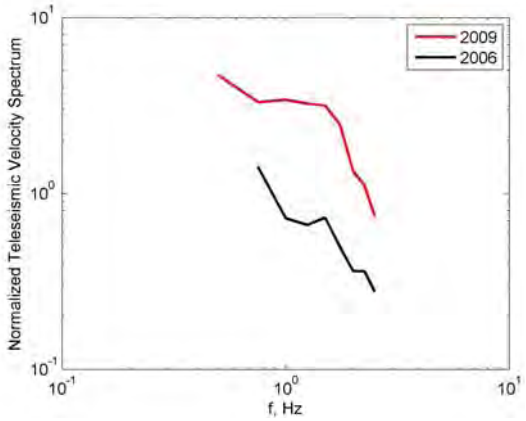

Figure 5. Comparison of the network-averaged, teleseismic *P* wave spectra determined from data recorded at a common set of stations from the North Korean nuclear tests of May 25, 2009, and October 9, 2006. It can be seen that the spectral amplitude levels for the May 25, 2009 test are about a factor of 4 larger, on average, than those for the October 9, 2006 test over the frequency band extending from 0.5 to 2.5 Hz.

The observed network-averaged teleseismic *P* wave spectrum for the 2009 test is compared with the best fitting predictions for hypothetical Mueller/Murphy sources at depths of 200m and 800m in Figure 7. The two theoretical predictions are essentially identical over the available 0.5 to 2.5 Hz frequency band. That is, the observed teleseismic spectral data do not have the resolving power to distinguish between the alternate hypotheses of a 2.7 kt explosion at a depth of 200m and a 4.8 kt explosion at a depth of 800 m.

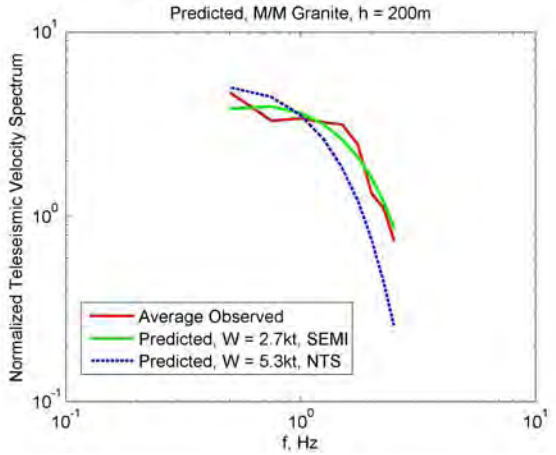

Figure 6. Network-averaged teleseismic *P*-wave spectrum for the May 25, 2009 North Korean nuclear test compared with the best-fitting Mueller/Murphy source models, assuming a depth of 200m and attenuation models for the Semipalatinsk and NTS test sites. The Semipalatinsk model is much more consistent with the observed spectra.

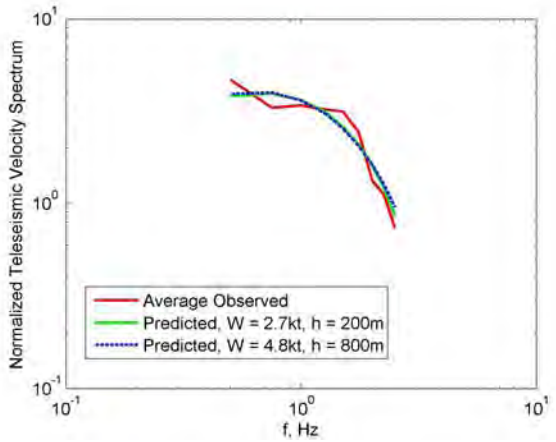

Figure 7. Network-averaged teleseismic *P*-wave spectrum for the May 25, 2009 North Korean test compared with the best-fitting Mueller/Murphy model assuming depths of 200 and 800m. The observed data do not have the resolving power to distinguish between the hypotheses of a 2.7 kt test at 200m depth and a 4.8 kt explosion at 800m.

Source Depth Estimation from *Pn* Spectral Ratio Analysis

In principle, broadband regional *P* wave data recorded from these explosions can provide the information needed to distinguish between different source depth hypotheses. However, in order to use such data to accurately infer source characteristics, it is necessary to first correct for frequency-dependent propagation path effects, and that cannot currently be done with confidence for the regional distance stations that recorded the two North Korean nuclear tests. One approach to eliminating the uncertainties associated with correcting for frequency-dependent propagation effects is to compute *P* wave spectral ratios of the two explosions at common regional stations. For closely-spaced explosions, the propagation path effects are essentially the same, and computing the *P* wave spectral ratios cancels them out to give estimates of the broadband seismic source spectral ratio between these two explosions. The individual regional station *P* wave spectral ratios can then be averaged to obtain a robust estimate of the source spectral ratio that can be compared with the theoretical source spectral ratios predicted by the Mueller/Murphy explosion source model corresponding to different source depth hypotheses for the two explosions.

This analysis procedure was applied to the broadband *P* wave data recorded from the two explosions at regional stations KSRS, MDJ, INCN, TJN and MAJO. The average observed regional *P* wave source spectral ratio, North Korea (2009)/North Korea (2006) is shown in Figure 8 over the frequency range from 1 to 15 Hz, where it is compared with the theoretical Mueller/Murphy source spectral ratios computed by assuming that both explosions were detonated at the same depth of 200m or 800m. The hypothesis that the two North Korean tests were detonated at the same depth anywhere in the plausible depth range is completely inconsistent with the observed spectral ratio data. In fact, it has been found that the observed spectral ratio data are much more consistent with the hypothesis that the 2006 test was conducted at a depth of about 200m, while the 2009 test was conducted at a depth of about 550m. This is shown in Figure 9 where the average observed spectral ratio is compared with the alternate theoretical Mueller/Murphy source spectral ratio obtained by modeling the 2009 test as a 4.6 kt explosion at a depth of 550m and the 2006 test as a 0.9 kt explosion at a depth of 200m.

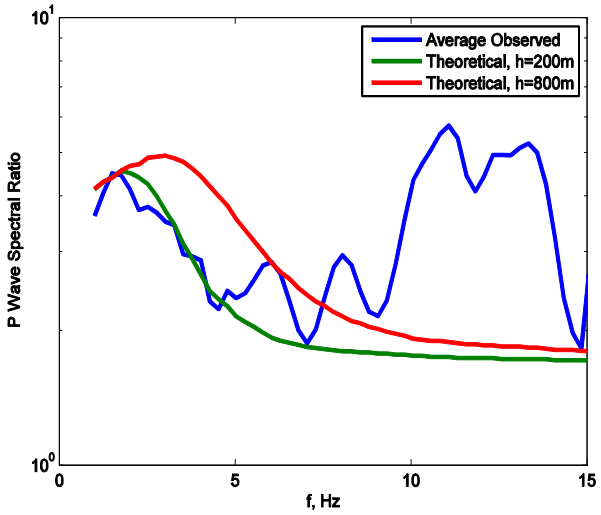

Figure 8. The average observed (KSRS, MDJ, INCN, TJN, MAJO) regional *P*-wave source spectral ratio North Korea(2009)/North Korea(2006) compared with the Mueller/Murphy source spectral ratios computed assuming that both explosions were detonated at 200m depth and at 800m depth. The hypothesis that both tests were detonated at the same depth is inconsistent with the observed high frequency spectral ratio data.

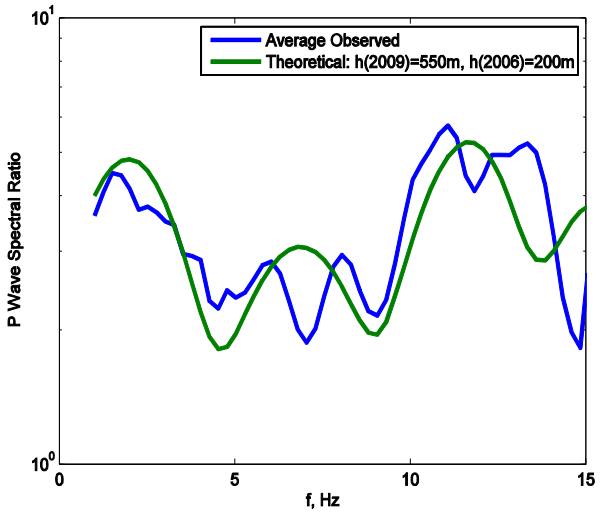

Figure 9. The average observed (KSRS, MDJ, INCN, TJN, MAJO) regional *P*-wave source spectral ratio North Korea(2009)/North Korea(2006) compared with the theoretical Mueller/Murphy source spectral ratio computed assuming that the 2009 test was conducted at 550m (W=4.6kt), while the 2006 test was conducted at 200m (W=0.9kt), with a pP/*P* amplitude ratio of 0.3 for both explosions. The hypothesis of significantly different depths for the two explosions is much more consistent with the observed high frequency spectral ratio data.

Effects of the surface reflected pP phases were included, with the pP/*P* amplitude ratios held at 0.3, consistent with previous experience with shallow explosions at other nuclear test sites (Murphy and Barker, 2001). These calculations predict a source spectral ratio that agrees remarkably well with the average observed spectral ratio over the entire band extending from 1 to 15 Hz. That is, the hypothesis of significantly different source depths for the two North Korea nuclear tests is much more consistent with the observed regional *P*-wave spectral ratio data than is the alternative, that the tests were conducted at the same depth.

Surface Wave Magnitude Anomaly

The two North Korean nuclear tests generated larger than expected surface waves relative to Ms-yield relations derived from historical nuclear explosions. The events were somewhat unusual compared to the body of historical explosion surface wave measurements in that they were small and in high velocity hard rock. Most of the historical events are in lower velocity material at NTS, or larger events at both NTS and foreign test sites. A large fraction of the foreign events were at the Soviet Semipalatinsk test site, and many of those events show evidence of compressive tectonic strain release, which has the effect of reducing surface wave amplitudes. So, it is not immediately clear whether the larger surface waves from the North Korean event are highly anomalous, or incorrectly estimated from larger explosions in different media and tectonic settings.

Ms Measurements **-** We used the Russell (2006) Butterworth filtered surface wave magnitude formula to estimate Ms using measurements from both Rayleigh and Love waves at six regional seismic stations (BJT, ENH, HIA, INCN, KS31 and MDJ) that recorded useable long-period data for both North Korean nuclear tests. Note that for the 2006 test, the Love wave measurements should be regarded as upper bounds as Love waves were close to or below the noise level at all stations. The magnitudes determined for these two events are listed in Table 2. The Ms/yield relation (Ms = 2.10 + 1.0 log W) derived by Stevens and Murphy (2001) results in a yield estimate of 32 kt for the 2009 event which is completely inconsistent with the body-wave estimate from above. The relative Ms-based yields between the 2006 and 2009 are consistent with the relative yield from body wave measurements indicating that the source of the absolute Ms anomaly must be common to both events.

Table 2. Surface wave magnitudes from North Korean explosions (10-20 second average)

Event	Rayleigh $M_{s(b)}$	Love $M_{s(b)}$
Event 1 – 10/9/2006	2.93 ± 0.20	< 2.58 ± 0.27
Event 2 – 5/25/2009	3.66 ± 0.10	3.07 ± 0.11

Analysis of the Ms Anomaly **-** One effect that has been shown to bias Ms values observed from explosions at other test sites is the triggering of the release of pre-existing tectonic strain energy by the explosion. That is, tectonic strain energy stored in the medium prior to the explosion can be released by the effects of the explosion shock waves, producing a secondary source of long-period surface waves that can either add to or subtract from the direct explosion induced surface waves, leading to anomalous Ms values. Since such secondary tectonic sources are expected to produce long-period transverse Love waves, while pure explosions are not, observations of significant transverse component Love waves on recordings from explosions provides strong evidence for explosion-induced "tectonic release." Accurate characterization of any secondary sources of surface waves is important in seismic monitoring, and moment tensor inversion analysis provides the formalism needed to characterize such secondary sources.

To examine the possible effect of tectonic release on surface wave amplitudes observed from the two North Korean tests, we performed moment tensor inversions for the two events. To do this, we performed a search for best fit to all the data in the 10-20 second period band while varying the isotropic moment, CLVD moment and shear moment tensor components, excluding the vertical dip slip moment tensor components which vanish at the free surface. We find the following:

Table 3. Moment tensor inversion results for North Korean explosions ($x10^{14}$ N-m)

Event	Mxx	Myy	Mzz	Mxy
Event 1 – 10/9/2006	4.30	5.56	3.68	-0.50
Event 2 – 5/25/2009	25.12	27.63	18.84	-4.27

Table 4 lists the moment tensor in terms of the isotropic moment and the shear components. The CLVD as defined here will generate larger surface waves if it is positive, since at shallow depths the horizontal strain is the principal generator of surface waves. The CLVD component is small, but is positive and therefore enhances surface waves.

Table 4. Moment tensor inversion results for North Korean explosions (x10^{14} N-m)

Event	M_I	M_{CLVD}	Mxx-Myy	Mxy
Event 1 – 10/9/2006	4.51	1.25	-1.26	-0.50
Event 2 – 5/25/2009	23.86	7.54	-2.51	-4.27

The effects on the individual station Ms values predicted by the tectonic release moment tensor solution for the 2009 test vary from no change up to a change of 0.17 magnitude units. The net effect is predicted to increase the network-averaged Ms value by only 0.06 magnitude units, which is much too small to explain the observed anomaly. However, it should be noted that since the CLVD component does not generate Love waves, it is not well constrained in the inversion; and a larger CLVD component would generate larger Ms. That is, an explosion with the same isotropic moment and a larger CLVD would generate larger surface waves with the same Love waves, no additional Rayleigh wave azimuthal variation and only a small change in spectral shape. This possibility will need to be systematically evaluated in any future studies of the observed Ms anomalies.

In summary, the Ms values observed for the North Korean explosions were much higher than expected based on past experience with explosions at other test sites. The inferred non-isotropic contributions to the long-period sources for the North Korean explosions relative to Semipalatinsk are of opposite sign, and account for part of this difference. Uncertainties in the extrapolation from the experimental database of mostly larger explosions in lower velocity media may also contribute to the apparent anomaly. Nevertheless, it is not clear that there is any plausible combination of these two factors that is adequate to explain the observed offsets. Additional research will be required to more fully investigate possible sources of these observed Ms anomalies for the two North Korean nuclear tests.

CONCLUSIONS AND RECOMMENDATIONS

On May 25, 2009, the North Koreans conducted a second underground nuclear test at a location very close to that of their initial 2006 test in a remote, mountainous region of northeastern North Korea. The objective of the present study was to exploit IMS and other open data sources to conduct comprehensive, advanced analyses of the characteristics of these two North Korean nuclear tests. The focus was on refining event locations, estimating source depths and seismic yields and evaluating the effectiveness of the various seismic event identification criteria as applied to these two explosions. Seismic data recorded at stations of the global IMS network were augmented with seismic data from key regional stations (< 20 degrees) obtained from the Incorporated Research Institutions for Seismology (IRIS) data management center, the OPHDMC and the NIED. The principal findings of these analyses with regard to the characterization of the North Korean nuclear tests can be summarized as follows:

- Available seismic arrival time data from the 2006 and 2009 tests were analyzed using a variety of state-of-the-art relative location techniques. All of the resulting solutions yielded very similar locations, indicating that the 2009 test was conducted about 2.5 km west-northwest of the 2006 test. Supplemental topographic data for the site were used to further constrain the absolute locations with respect to the tunnel adit entry identified from open source overhead imagery.
- Teleseismic *P* wave spectral data were inverted using a model-based procedure to determine the yield of the 2009 test as varying from 2.0 to 4.8 kt. over the plausible depth range from 100 to 800 m.
- Since the uncertainty in source depth leads to considerable uncertainty in the yield estimate, a new technique based on broadband source spectral ratios was developed to better constrain the depths of the 2006 and 2009 explosions. The results of this analysis indicate that the two explosions could not have been conducted at any common depth in the plausible 100 to 800 m range; and, in fact, the observed spectral ratio data are best modeled by source depths of about 200 m for the 2006 test and 550 m for the 2009 test. The corresponding yield estimates for the 2006 and 2009 tests are 0.9 kt and 4.6 kt., respectively.
- The long-period surface wave Ms magnitudes for both the 2006 and 2009 tests appear to be anomalously large relative to historical experience, producing unreasonably large Ms yield estimates and problematic Ms/mb identification characteristics. A formal moment tensor inversion analysis of the available data has indicated that release of tectonic strain energy by the explosion may have contributed somewhat to the observed anomaly. However, current estimates of the likely strength of this tectonic release are not large enough to fully explain the observed anomaly. Additional research will be required to determine whether unresolved CLVD secondary sources any account for the discrepancy.

ACKNOWLEDGEMENTS

Seismic data from the IDC/IMS, OPHDMC, and NIED were used in this study. We are also grateful to Rongsong Jih of the Department of State for his support and recommendations during the course of this project.

REFERENCES

Bennett J, North B, Kohl B, Murphy J, Stevens J, Bondar I, Fisk M, Bahavar M, Barker B, Israelsson H and V Oancea, (2006). Analysis of IMS data from the North Korean (DPRK) Nuclear Test of October 9, 2006, SAIC, *SAIC Technical Report* SAIC-06/2203.

Dewey, J. W. (1972). Seismicity and tectonics of western Venezuela, ***Bull. Seismol. Soc. Am***. 62: 1711–1751.

Fisk, M. D. (2002). Accurate locations of nuclear explosions at the Lop Nor test site using alignment of seismograms and IKONOS satellite imagery, ***Bull. Seism. Soc. Am.*** 92: 2911–2925.

GlobalSecurity.org (2006). Weapons of Mass Destruction (WMD): Possible North Korean nuclear test site near Punggye-yok, online at http://www.globalsecurity.org/wmd/world/dprk/kilju-punggye-yok.htm.

Grubbs, F. E. (1950). Sample criteria for testing outlying observations, ***Ann. Math. Stat***. 21: 27–58.

Mueller, R. A. and J. R. Murphy (1971). Seismic characterization of underground nuclear detonations. Part 1: Seismic scaling law of underground nuclear detonations, ***Bull. Seismol. Soc. Am***. 61: 1675–1692.

Murphy, J. R. and B. W. Barker (2001). Application of network-averaged teleseismic *P*-wave spectra to seismic yield estimation of underground nuclear explosions, ***Pure Appl. Geophys***. (PAGEOPH) 158: 2123–2171.

Russell, D. R. (2006). Development of a time-domain, variable period surface-wave magnitude measurement procedure for application at regional and teleseismic distances. Part I: Theory, ***Bull. Seismol. Soc. Am***. 96: 665–677.

Schlittenhadt, J., M. Canty, and I. Gruenberg (2010). Satellite Earth observations support CTBT monitoring: Case studies including the nuclear test in North Korea of Oct. 9, 2006, and comparison with seismic results, ***Pure Appl. Geophys.*** (PAGEOPH), 10.1007/s00024-009-0036-x.

Snieder, R. and M. Vrijlandt (2005). Constraining the source separation with coda wave interferometry: Theory and application to earthquake doubles in the Hayward fault, California, ***J. Geophys. Res.*** 10: B04301.

Stevens, J. L. and J. R. Murphy (2001). Yield estimation from surface wave amplitudes, ***Pure and Applied Geophysics*** (PAGEOPH) 158: 2227–2251.

US Geological Survey (1966-1969). Military Geology Branch Atlases of Asia and Eastern Europe to Support Detection of Underground Nuclear Testing, prepared for DARPA.

Waldhauser, F. and W. L. Ellsworth, (2000). A double-difference earthquake location algorithm: Method and application to the northern Hayward fault, California, ***Bull. Seismol. Soc. Am*** 90: 1353–1368.

CALIBRATION OF ATTENUATION STRUCTURE IN EURASIA TO IMPROVE DISCRIMINATION AND YIELD

Michael E. Pasyanos, William R. Walter, Eric Matzel, Sean R. Ford,
Rengin Gök, and Arthur J. Rodgers

Lawrence Livermore National Laboratory

Sponsored by the National Nuclear Security Administration

Award No. DE-AC52-07NA27344/LL09-IRP-NDD02

ABSTRACT

It is well known that one-dimensional models do a poor job of predicting both regional amplitudes and travel-times over large and tectonically complicated regions. As a result regional discrimination methods (e.g., high-frequency P/S, M_s:m_b) and magnitude estimates (e.g. coda magnitude) can perform poorly when applied over broad regions. The careful calibration of the earth's attenuation structure is critical to the universal application of event discrimination and yield estimation methods down to very small magnitudes. We have developed and are continuing to improve methods that use the direct amplitudes of the major regional phases (Pn, Pg, Sn, Lg) to determine the attenuation structure of the lithosphere in the Middle East and East Asia. The amplitudes are inverted simultaneously for attenuation parameters (Qp, Qs) of the crust and upper mantle, event source terms, and station site terms, which ensures that parameters, such as seismic moment and apparent stress, are consistent across each phase. We are using these models to correct observed amplitudes for path-dependent variations due to earth structure. Amplitude corrections can be demonstrated to improve high-frequency regional P/S discriminants (e.g., Pn/Lg, Pg/Lg, Pn/Sn) by reducing scatter in the earthquake population and increasing separation from explosions. Better path corrections allow the extension of discrimination to lower frequencies so long as true source differences between events exist at those frequencies.

We are applying similar methodologies to coda amplitudes with the goal of improving magnitude and yield estimation. While coda waves average over large regions and have less variation than direct phases, they too are subject to path-dependent variations in amplitudes. Furthermore, they can be sensitive to changes in the dominant phase (e.g., Sn vs. Lg) over broad regions. We report on our efforts for the 2-D calibration of coda amplitudes in the Middle East. A similar calibration of attenuation structure can be used to improve surface wave amplitudes used in the M_s:m_b discriminant. For small events correcting for attenuation is very important for the regional analog surface wave magnitude M_s(VMAX) because amplitude variations are significantly higher at 7 seconds than at 20 seconds.

All of these attenuation models and their associated source models can be used to predict expected signal-to-noise values for all possible source regions for a given station. We are making use of the models and earthquake source spectral models to create magnitude thresholds maps for regional discriminants such as P/S. This is a natural way to incorporate lithospheric structure into better and more realistic capability assessments.

OBJECTIVES

Our objective is to develop and calibrate methodologies to improve event discrimination and yield estimation down to small magnitudes and for broad regions. Earthquake-explosion discrimination using high-frequency regional P/S amplitude ratios over large and tectonically complicated regions can only be accomplished by properly calibrating the regional attenuation structure. Similar calibration of attenuation structure to coda amplitudes is also necessary to improve the magnitude and yield estimation of smaller events in these complicated regions. Lastly, we will be using the attenuation information in capability assessment.

RESEARCH ACCOMPLISHED

In the past year, we have accomplished a number of research goals in regional amplitude tomography, regional discrimination, coda tomography, and capability assessment.

Regional Amplitude Tomography

Lawrence Livermore National Laboratory (LLNL) has developed a four-phase amplitude tomography which allows us to determine a set of attenuation, site, and source corrections for the primary regional phases of Pn, Pg, Sn, and Lg. Our basic methodology, employed in Pasyanos et al. (2009a) for Lg, uses a magnitude and distance amplitude correction (MDAC) source model (Walter and Taylor, 2001), which more explicitly defines the source expression in terms of an earthquake source model formulated in terms of the seismic moment. One of the advantages of this approach is to easily estimate predicted amplitudes for an event of any given location and size.

In a subsequent paper (Pasyanos et al., 2009b), we applied the technique to simultaneously invert amplitudes of Pn, Pg, Sn and Lg in the Middle East to produce P-wave and S-wave attenuation models of the crust and upper mantle for the region (Figure 1). The attenuation is modeled as P-wave and S-wave attenuation surfaces for the crust, and a similar set for the upper mantle. Inverting all of the phases simultaneously allows us to determine consistent attenuation, site, and source terms for all phases, and eliminates non-physical inconsistencies among them.

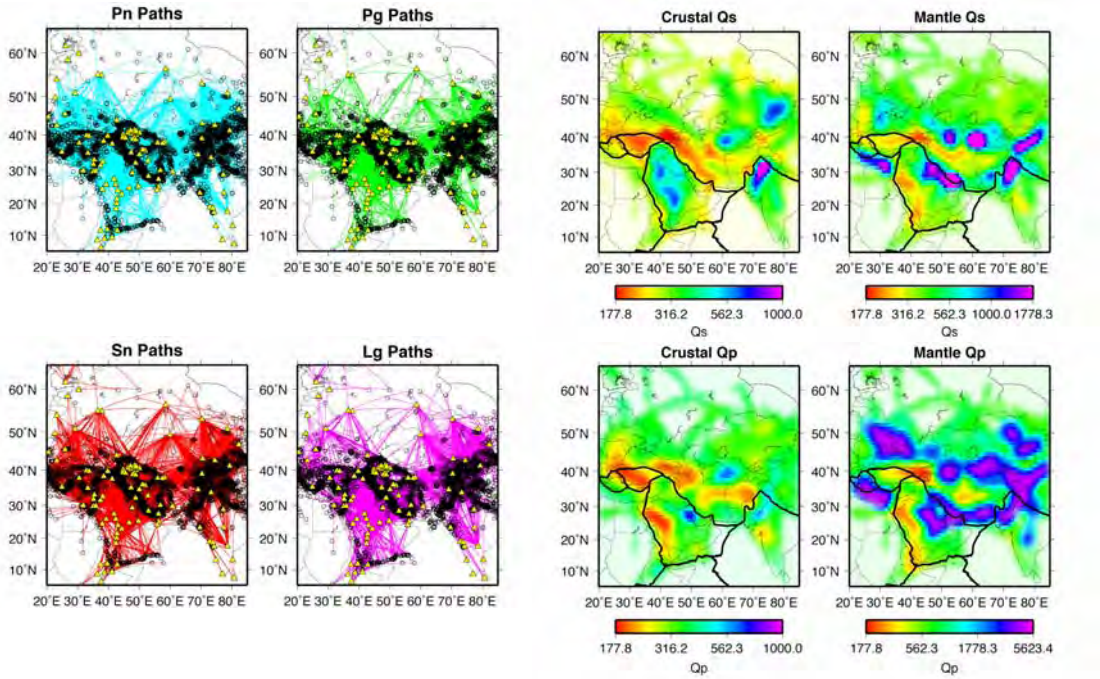

Figure 1. Path map and attenuation results for the Middle East region in the 1-2 Hz passband. a) Path map of Pn, Pg, Sn, and Lg attenuation measurements. b) Attenuation for crustal Qs, mantle Qs, crustal Qp, and mantle Qp (figure from Pasyanos et al., 2009b).

In the past year, we have focused on making improvements to our model-based attenuation tomography. This has been accomplished by making more amplitude measurements and improving the physics of the regional raypath. While we continue to make more measurements in the Middle East, the main focus of measurements for the past year was on amplitudes in East Asia. Applying the tomography to this region forced us to focus on the complex tectonics of the region, including an imbedded region of oceanic crust and subducting slabs in the upper mantle.

One thing we have done to improve the physics of the raypath is to introduce a variable crustal thickness into our inversion. This is particularly important in the Sea of Japan and Pacific Ocean, where the crustal thickness is less than 10 km. Figure 2 shows path and attenuation results in East Asia in the 1-2 Hz passband. Notice the small number of Pg and Lg measurements (passing the signal-to-noise criteria) crossing the Sea of Japan, even though we have picked and measured hundreds of these paths (see Pn and Sn path maps). The tomographic inversion shows relatively simple structure in the Yellow Sea and Korean Peninsula, but gets more complicated outside of this region, particularly to the east. We find low Q in the crust for the Sea of Japan. We also see complicated structure in the mantle that seems to be related to slab structure, but mainly for P-wave attenuation.

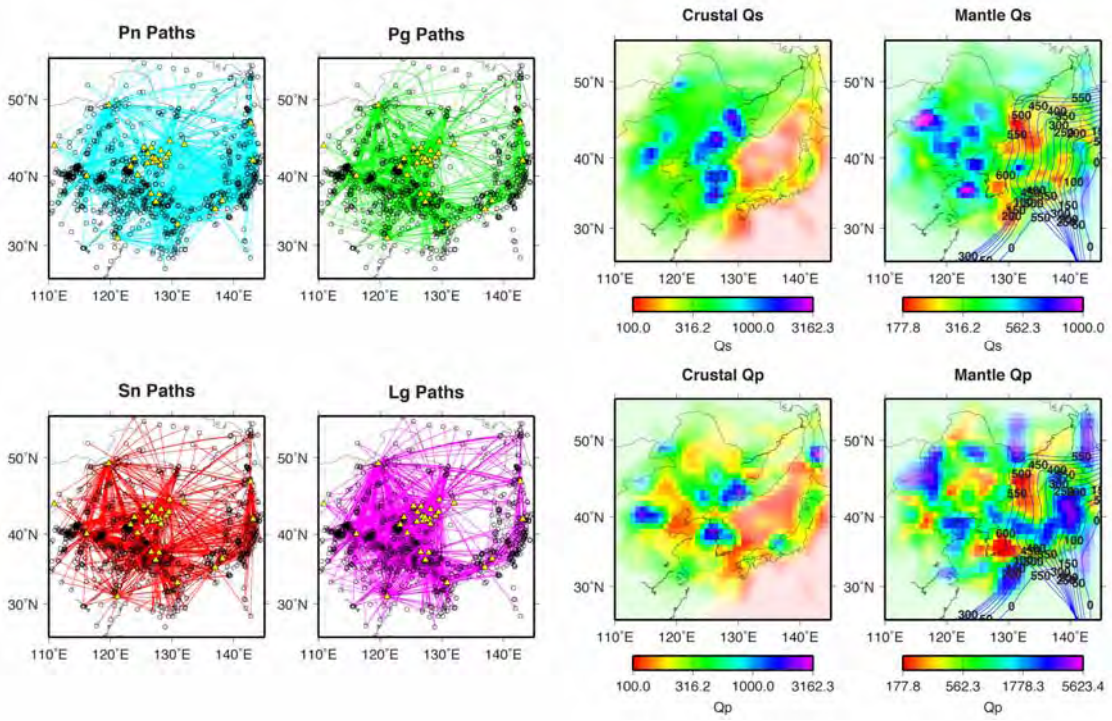

Figure 2. Path map and attenuation results for East Asia in the 1-2 Hz passband. a) Path map of Pn, Pg, Sn, and Lg attenuation measurements. b) Attenuation for crustal Qs, mantle Qs, crustal Qp, and mantle Qp.

We have run a series of tests with the same dataset comparing tomography methods using different choices for raypaths and for geometrical spreading. For the former, we compare a phase-based inversion (which uses a specific attenuation surface for each regional phase) to a model-based inversion (where the path propagates through appropriate attenuation layers of the crust and upper mantle). For the latter, we compare standard geometrical spreading (Street et al., 1975) to the 10-parameter geometrical spreading model of Yang et al. (2007). Using our Middle East amplitude dataset, we find comparable amplitude residuals between phase-based and model-based, although the residuals are lowest when the model-based inversion includes variable crustal thickness. This indicates that we might continue to improve as we more completely capture the true raypath. For the geometrical spreading comparison, the residuals are

comparable for the whole dataset, but increase significantly for short paths near the cross-over (< 400 km) using the Yang geometrical spreading model. Results are shown in Figure 3.

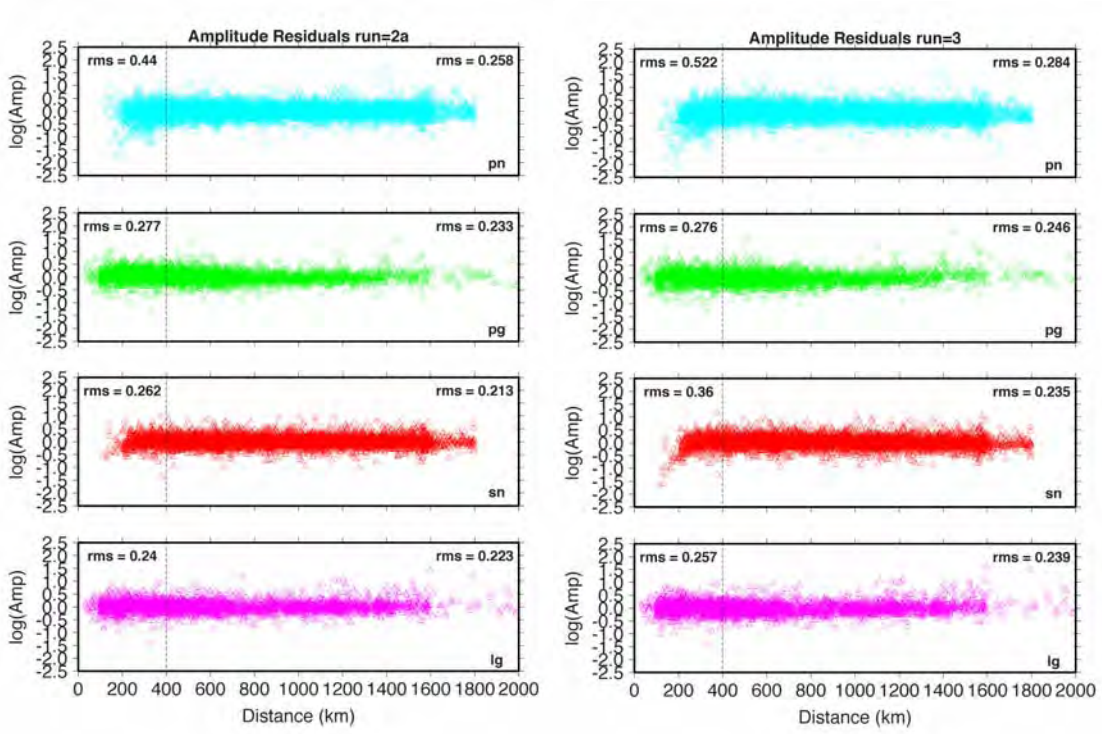

Figure 3. Residuals as a function of distance for phases Pn, Pg, Sn, and Lg. a) Tests performed using a model-based path and standard geometrical spreading. b) Tests performed using a phase-based path and Yang geometrical spreading. RMS in the upper right hand corner are overall residuals, while those in the upper left-hand corner are those for distances less than 400 km.

Regional Discrimination

Applying corrections with the new attenuation models can significantly improve earthquake-explosion discrimination using regional P/S amplitude ratios. P/S discriminants are expressed as the ratio between the P-wave amplitude (A^P) and the S-wave amplitude (A^S) and, because of the large variations, are usually plotted on a log scale. Figure 3 shows the Pn/Lg discriminant in East Asia, for station MDJ in the 2-4 Hz passband. The series of plots first shows the raw discriminant (as a function of magnitude and in map view), then 1-D and 2-D corrected discriminants. In order to correct the phase ratio for path and source effects, we adjust the individual amplitudes assuming an earthquake source. We then form our discriminant using the ratio of the corrected amplitudes. This is a division of the amplitudes or a subtraction in log-space:

$$\text{discriminant} = \log\left[\frac{(A^P/A_0^P)}{(A^S/A_0^S)}\right] = \log\left[\frac{A^P}{A^S}\right] - \log\left[\frac{A_0^P}{A_0^S}\right] \qquad (1)$$

where A_0 are the amplitude predictions for an earthquake of that phase and size. As a result, the corrected discriminant should now have a value around 0 (P/S ratio of 1) for earthquakes. We input a best estimate of the earthquake size by using a moment magnitude, if available, or otherwise estimating Mw using other magnitude estimates.

While the P/S discriminant works reasonable well for the portions of the YSKP region with continental crust (including the Yellow Sea), when we start to include earthquakes from the broader region that includes Japan, most of these events have a high P/S ratio, making them look explosion-like (red circles on the middle panel of Figure 4). A 2-D correction is necessary to account for the high attenuation along these paths. The result is that the high P/S ratio of these events can be explained by earth structure and, when corrected, do not look anomalously explosion-like.

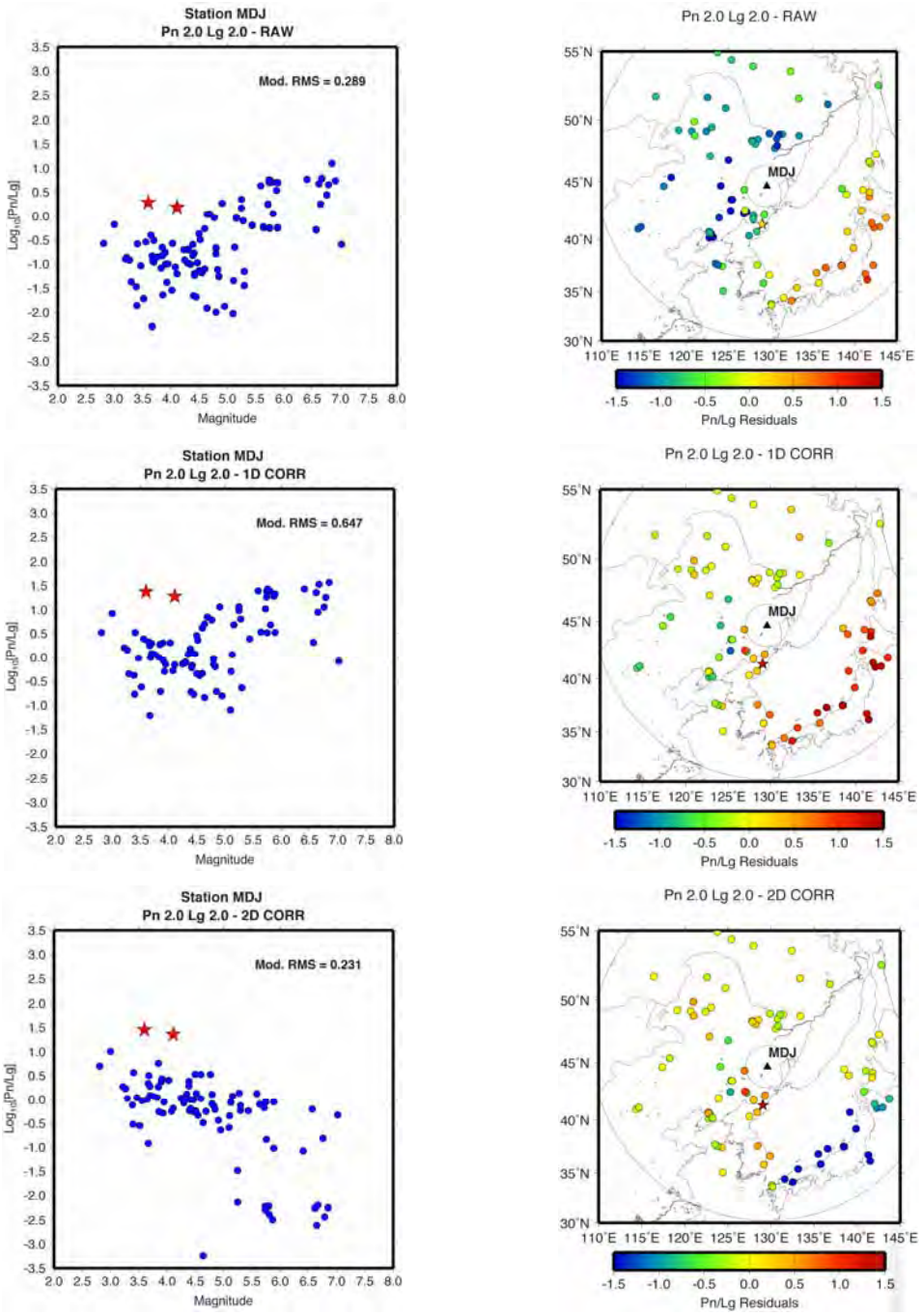

Figure 4. Pn/Lg discriminant in the 2-4 Hz band at station MDJ. Raw measurements shown as a function of magnitude and in map view (top), 1-D corrected amplitudes using calibrations for the on-shore region (middle), 2-D corrected amplitudes (bottom).

Coda Tomography

We are applying similar methodologies to coda amplitudes with the goal of improving magnitude and yield estimation. We analyzed around 500 events between 1996 and 2008 with magnitudes ranging from 3.4 to 7.4. The large number of events provided an opportunity to calibrate for path (attenuation) and site effects. We limited distances to less than 1500 km to avoid triplications in our coda calibration. After forming coda envelopes in 13 narrow frequency bands (ranging from 0.04 – 7 Hz), we estimated the start of the coda envelope by measuring the peaks of each coda envelope. The coda amplitude is estimated using an exponential decay function, and a conic section (specifically, a hyperbola) is used to fit each narrow frequency band coda amplitude (e.g., Mayeda et al., 2003) and the coda shape parameters were estimated with similar techniques for the early and late part of the coda envelopes. The raw amplitudes were corrected for geometrical spreading using the Extended Street and Herrmann (ESH) method (Morasca et al., 2008). The ESH method allows differences at local and regional coda decays to both be considered. To scale those non-dimensional amplitudes to absolute moment we use independently waveform modeled Mw's (G. Ichinose, personal communication). A constant correction factor at each frequency band is used to correct each event to obtain the moment rate function.

The moment rate functions are then used as input in a tomographic inversion of coda Q. An example of some preliminary results are shown in Figure 5. While the initial region covered is relatively small, the maps bear a great resemblance to the results we see from the direct phases (see crustal Qs map in Figure 1). This argues strongly that, while we can calibrate using the coda amplitudes, we might be able to calibrate regions for coda through the analysis of the direct phases as well. The plan is that, in addition to the moment rate functions, we can also incorporate additional information from the raw spectral ratios (e.g., stress drop, corner frequency) to include in the tomography.

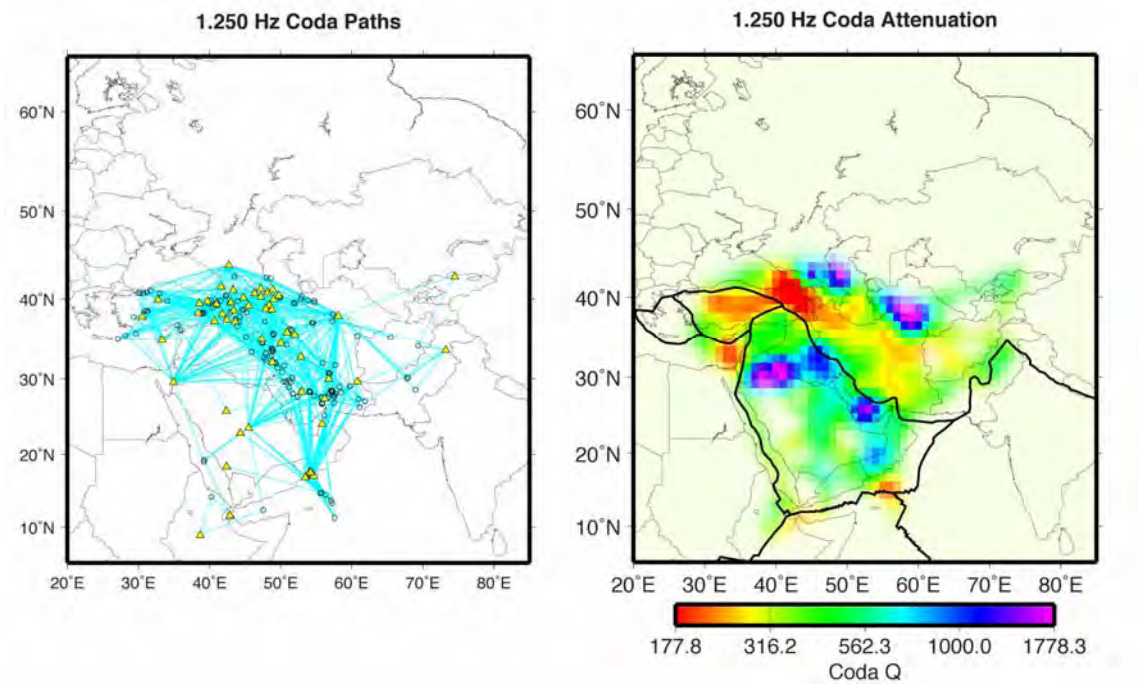

Figure 5. a) Path map of 1.25 Hz coda amplitude measurements in the Middle East. b) Tomographic map of coda Q in the same frequency band.

While we see attenuation variations that can affect coda amplitudes, this is a less significant effect at lower frequencies where larger events are recorded. While we are calibrating the 2-D structure, we have calculated coda magnitudes for many events based on a 1-D coda calibration of the region at frequencies below 0.5 Hz. Figure 6 shows 752 events in the Middle East where we have calculated coda magnitudes. The magnitudes range from Mw 3.1 - 6.4. In order to make more precise measurements of smaller events, 2-D corrections (like those described above) will have to be applied.

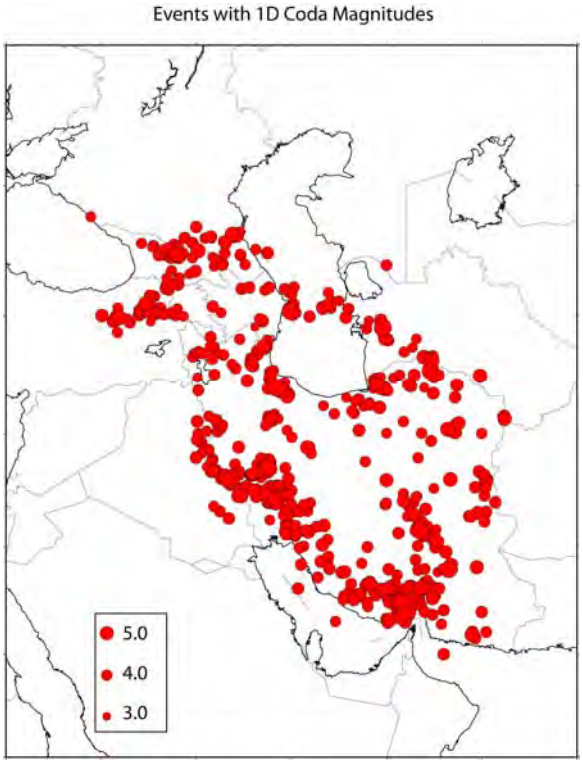

Figure 6. Events in the Middle East for which we have calculated coda magnitudes based on a 1D coda calibration of the region.

Capability Assessment

The ability to detect regional S-waves from earthquakes is key to P/S discrimination capability. Where an explosion would have detectable S-waves, we have a solid P/S discrimination. In situations where an earthquake would have detectable S-waves, but an explosion would not, we have some discrimination. Where even an earthquake would not have a detectable S-wave, we have no ability to discriminate with P/S discriminants.

Techniques like 2D and 3D attenuation methods can map out where and for what magnitude thresholds regional P/S will work as a discriminant and where it does not. Figure 7 shows examples of maps with predicted signal-to-noise recorded at two stations. In the first example, we see the predicted signal-to-noise from a Mw 4.0 event of Lg in the 1-2 Hz passband recorded at station NIL. Where the figure transitions from green to yellow, the expected SNR is dipping below 2.0 and we would not expect to reliably record the signal. The pattern is somewhat symmetric, although we see a clear extension in the SNR to the southwest across the high Q of northern India.

The second example shows a similar map for Lg at station MDJ in the 2-4 Hz passband. We see that station MDJ can record signals well in all directions, except toward the southeast where paths cross the Sea of Japan. We would not expect to see signals from Mw 4.0 events in central Japan, although we might record

them from events in the furthest northern and southern portions of the island chain. The reciprocal relationship, i.e. using stations in Japan as discriminants for events near MDJ, would also apply.

Using this information is critical for regional capability assessment. This should help us to determine which stations, bands and phases to use for regional P/S discrimination.

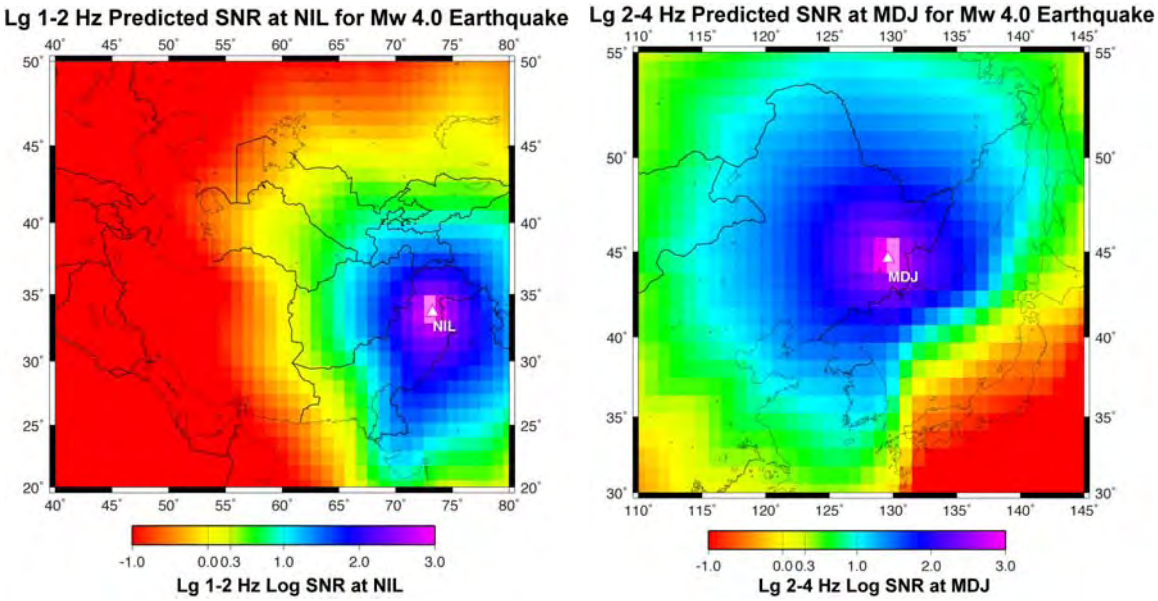

Figure 7. Predicted signal-to-noise ratios from Mw 4.0 earthquake: a) for 1-2 Hz Lg at station NIL and b) for 2-4 Hz Lg at station MDJ.

CONCLUSIONS AND RECOMMENDATIONS

Attenuation tomography can capture the observed variability of regional phase amplitudes (e.g. Phillips and Stead, 2008). The new attenuation tomography method that we have developed allows us to simultaneously invert for the amplitudes of regional phases Pn, Pg, Sn, and Lg (Pasyanos et al., 2009b). We have demonstrated that it is possible to use information about attenuation of the lithosphere to improve regional P/S discriminants. The new attenuation model has the potential to greatly improve earthquake-explosion discrimination across Eurasia. Similarly, we can calibrate the effect of attenuation on coda amplitudes and improve our estimates of magnitude and yield. Finally, we have demonstrated the importance of using amplitude information in regional calibration assessment. Future challenges include calibrating aseismic regions, either using surface waves, or by calibrating attenuation using explosions recorded from these regions.

ACKNOWLEDGEMENTS

We thank Stan Ruppert and Terri Hauk for maintaining the LLNL Seismic Research Database. We thank Doug Dodge and Mike Ganzberger for developing the RBAP code, which is used to make the regional amplitude measurements. We thank Gene Ichinose for the regional moment magnitudes used in the coda calibration.

REFERENCES

Mayeda, K., A. Hofstetter, J. L. O'Boyle, W. R. Walter (2003). Stable and transportable regional magnitudes based on coda-derived moment-rate spectra. *Bull. Seismol. Soc. Am*. 93: 224–239.

Morasca, P., K. Mayeda, R. Gok, S. Phillips, and L. Malagnini (2008). 2D coda and direct-wave attenuation tomography in northern Italy, *Bull. Seismol. Soc. Am*. 98: 1936–1946.

Pasyanos, M.E. and W.R. Walter (2009). Improvements to regional explosion identification using attenuation models of the lithosphere, *Geophys. Res. Lett.,* doi:10.1029/2009GL038505.

Pasyanos, M.E., E.M. Matzel, W.R. Walter, and A.J. Rodgers (2009a). Broad-band Lg attenuation modeling of the Middle East, *Geophys. J. Int.* 177: 1166–1176, doi:10.1111/j.1365-246X.2009.04128.x

Pasyanos, M.E., W. R. Walter, and E. M. Matzel (2009b). A simultaneous multi-phase approach to determine P-wave and S-wave attenuation of the crust and upper mantle, *Bull. Seismol. Soc. Am.*, 99: (6), 3314–3325, doi:10.1785/0120090061.

Phillips, W. S. and R. J. Stead (2008). Attenuation of Lg in the western US using the USArray, *Geophys. Res. Lett.* 35: L07307, doi:10.1029/2007GL032926.

Street, R. L., R. Herrmann, and O. Nuttli (1975). Spectral characteristics of the Lg wave generated by central United States earthquakes, *Geophys. J. R. Astron. Soc*. 41: 51–63.

Walter, W.R. and S.R. Taylor (2001). A revised magnitude and distance amplitude correction (MDAC2) procedure for regional seismic discriminants: theory and testing at NTS, Lawrence Livermore National Laboratory, UCRL-ID-146882, http://www.llnl.gov/tid/lof/documents/pdf/240563.pdf

Yang, X., T. Lay, X.-B. Xie, and M.S. Thorne (2007). Geometric spreading of Pn and Sn in a spherical earth model, *Bull. Seismol. Soc. Am.* 97: 2053–2065, doi:10.1785/0120070031.

EXPLOSION SOURCE MODEL DEVELOPMENT IN SUPPORT OF SEISMIC MONITORING TECHNOLOGIES: APPARENT EXPLOSION MOMENT AND PROSPECTS FOR MOMENT-BASED YIELD ESTIMATION

Howard J. Patton

Los Alamos National Laboratory

Sponsored by National Nuclear Security Administration

Award No. DE-AC52-06NA25396 / LA08-029-NDD02

ABSTRACT

This paper reports on research activities for the third and final year of a project to develop new explosion source models that include the effects of source medium damage, a form of which is deep-seated, shock-induced tensile failure identified in our previous studies. In general, damage will contribute volumetric, compensated linear vector dipole (CLVD), and double-couple (DC) sources of seismic radiation. Our past work has studied the effects of a CLVD source on Rayleigh wave radiation and its impact on the performance of m_b-M_s discrimination. Part I of this paper shifts attention to the volumetric contribution that source medium damage makes. In the model, there are two possible volumetric sources: (1) the traditional source associated with direct effects of explosions creating a cavity with volume *V* and (2) the damage source due to non-linear free-surface interactions and shock-wave rebound causing abrupt changes of elastic moduli and dilating the source medium with volume *U* due to bulking and shear dilatancy. The CLVD represents a non-volumetric, deviatoric source component of damage. *K* is a source parameter measuring the steady-state strength M_{CLVD} of the CLVD with respect to M_I, the isotropic moment. Moment tensor inversion results for NTS explosions show that *K* steadily decreases with yield, approaching values near 1.0 for highest yield shots. A *K* value of 1.0 implies $M_{CLVD} = 0$ and, by inference, small *U*. Our hypothesis is that the force of spall slapdown is great enough at high yields to crush the tuff matrix, reducing *U* while *V* remains intact. Slapdown at low yields is not great enough to do so, leaving both *V* and *U* unaffected. We tested the hypothesis by comparing measurements of M_I with estimates of "classical" moment based on scaling relationships of *V* and velocity models for Pahute Mesa, including the effects of coupling above the water table. The results support the hypothesis and the conclusion that in general, measurements of M_I are composed of two volumetric components: *V* due to cavity formation and *U* related to material damage of the source medium. Thus M_I is an "apparent explosion moment," quite different from the moment predicted by classical theory for a spherical source model.

Part II of this paper revisits the outstanding problem related to estimating yield from seismic moment, highlighted in the 1990s by tectonic release models to explain surface wave observations for Soviet explosions conducted at the Semipalatinsk Test Site. These models failed to provide estimates of M_I that correlated with explosion yield as well as m_b. Something fundamental was missing in explosion source models where the only contributor to source asymmetry was tectonic release represented by a DC force system. Based on the work in Part I, my co-workers (see Acknowledgements) and I think that the missing ingredient is source medium damage and the contributions it makes to the radiated seismic wavefield. It is straight forward to show that by ignoring the effects of source medium damage, past investigations very likely obtained biased estimates of M_I and deduced source models that over-estimate the importance of tectonic release. The 2006 and 2009 North Korean tests provide an opportunity to show the excellent agreement between tradeoff curves for yield versus depth-of-burial based on estimates of M_I and m_b when source medium damage is suppressed (as it is for these tests) or accounted for by new moment-correction methods. This result is motivation for calibrating new M_I-yield relationships corrected for the volumetric contributions due to source medium damage.

OBJECTIVE

The objective is to develop new analytical explosion source models based on seismic moment tensor theory for further improvement and advancement of regional seismic discrimination and yield estimation technologies. Such technologies rely heavily upon the source information contained in high-frequency shear (*S*) waves. The use of coda waves following regional *S* phases to estimate explosion yield is one example of an emerging technology offering great promise for improved nuclear monitoring. Unfortunately, an understanding of how explosions excite *S* waves is quite limited, and a widening gulf between theory and practice undermines our confidence to monitor broad areas at small yields. The new models will provide a physical basis for explosion-generated *S* waves and theoretical insights for advancing yield estimation and discrimination capabilities, thereby closing the gulf between theory and practice.

RESEARCH ACCOMPLISHED

This project builds upon spherical (monopole) explosion source models developed in the 1970's. An important aspect of those models is the theory relating seismic amplitudes of *P* waves directly to yield, depth of burial, and material properties of the source medium. Analytical relationships predicted by the theory draw upon empirical yield scaling behaviors of key model constructs, such as the elastic radius. Furthermore, the analytical nature of these models facilitated their use since they were easy to implement by researchers, and as such, they were widely applied to study the explosion source. Their application continues to this day, but with the recognition that a spherical point source is inadequate to explain *S*-wave generation.

The model under development is a linear superposition of spherical (or monopole), double-couple for relaxation of tectonic pre-stress, and compensated linear vector dipole (CLVD) sources. The CLVD body force system is used to represent the deviatoric source due to material damage which occurs as sudden changes in the source medium's elastic moduli. The source process time for this model is longer than the characteristic time of energy release by the explosion itself because it includes stress wave interactions with the free surface and motions in the source region following spall slapdown. A seismic moment tensor representation is used allowing for the possibility of different centroid depths of moment release and different source-time histories for each source component.

To date, our research has focused on long-period applications where all source components are safely assumed to be coincident in time and space, and share the same source-time histories. Future research will tackle high-frequency applications where those assumptions are no longer valid. The new long-period model moves beyond source models developed in the 1960s, 70s and 80s describing an explosion triggering tectonic strain release with an earthquake double-couple mechanism. In the 80s anomalous surface wave observations for many Soviet tests conducted at the Semipalatinsk Test Site (STS) were reported in the literature, where Rayleigh waves showed polarity reversals and time delays compared to their counterparts excited by normal explosions. For some explosions, all Rayleigh waves, no matter what the azimuth or path recorded on, were found to be reversed, and large Love waves usually accompanied the Rayleigh wave

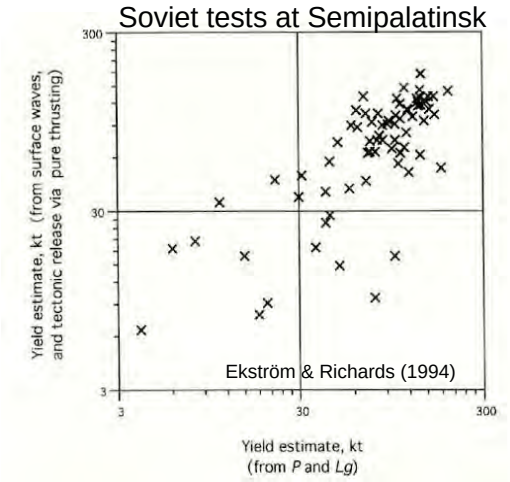

Figure 1. Inferred yields of Balapan tests from estimates of isotropic moment corrected for tectonic release versus empirical m_b-yield relationships for *P* and *Lg* waves (abscissa).

anomalies. These observations were generally accepted to be a consequence of large releases of tectonic strain energy accompanying the detonation of Soviet tests. Sometimes explosions conducted at the Nevada Test Site (NTS) also produced anomalous surface wave observations, but never to the extent found on STS explosions. As such, tectonic release models were put to a test in the 80s and 90s. The failure of these models to explain the surface wave observations and provide estimates of M_I that correlated with explosion yield as well as m_b (see Figure 1) was a disappointment to the monitoring community. At the same time, there was recognition that something fundamental was missing in explosion source models where the only contributor to source asymmetry was tectonic release represented by a double-couple force system (DC).

In the earthquake community, Ben-Zion and Ampuero (2009) renewed interest in the early work of Knopoff and Randall (1970) and others, and demonstrated that the contribution of source medium damage may be comparable to or larger than the contribution from moment release due to slip on earthquake faults and can manifest as a CLVD. Indeed, medium damage can radiate waves as volumetric, CLVD, and DC sources. The implications of damage contributing to seismic radiation from explosion sources are profound for seismic discrimination, as Patton and Taylor (2008; PT08) showed for m_b-M_s, and for yield estimation using isotropic moment, as will be discussed in this paper.

Monopole and CLVD force systems generate Rayleigh waves with opposite polarity below the null frequency f_{null} of the CLVD excitation spectrum, and the waves interfere destructively. Above f_{null}, the interference is constructive. Typically f_{null} is between 0.5 - 2 Hz for a damage centroid located over the explosion at a depth roughly one half the depth of burial. Thus, a CLVD source with a vertical axis in extension superimposed on a monopole reduces long-period Rayleigh-wave amplitudes, reducing the M_s, and making explosions look more explosion-like on a plot of m_b versus M_s. PT08 used this fact to explain why m_b-M_s observations consistently plot below theoretical m_b-M_s relationships for pure explosion sources and why the 2006 North Korean test gave unusually large M_s for its m_b, failing to discriminate. The reason is that this shot was the first to occur in a new test site of a proliferant nation, and the source medium was intact, pristine granite which might have the highest material strength of all geologic materials. That, combined with an emplacement depth quite deep for the yield, would have suppressed material damage mechanisms related to shock-induced deep-seated tensile failure. With damage suppressed and a small amount of tectonic release (Walter *et al*., 2007), this test is very close to being a pure explosion. Its m_b-M_s value should be consistent with a theoretical relationship for a spherical source, which is in fact what was found by PT08.

"Apparent" Explosion Moment and Detection of Volumetric Moment due to Source Medium Damage.
The relative strength of the CLVD compared to the monopole is given by an index *K* defined below.

$$K \equiv \frac{2M_{zz}}{M_{xx} + M_{yy}} \quad , 1)$$

where M_{xx}, M_{yy}, M_{zz} are diagonal elements of the moment tensor. The CLVD is expected to have a vertical axis of symmetry in extension provided that near-by topography is not very great. The reason is that the *T* axis is aligned along the direction of minimum compressive stress, and for explosion source dynamics, this direction is vertical due to tensile stresses set up by rarefactions off the free surface. Explosions "sense" the closest approach to the free surface owing to the interactions of strong shock waves establishing a tensile regime. If relaxation of tectonic stresses occurs only in the horizontal plane, as Toksöz and Kehrer (1972) proposed for NTS, then the ratio between CLVD and isotropic moments equals

$$\frac{M_{CLVD}}{M_I} = \frac{2(K-1)}{K+2} \quad . 2)$$

A K value of 1 means M_{CLVD} is zero, $K > 1$ means permanent extension along the vertical axis and $K < 1$ means permanent contraction along the vertical axis. PT08 inferred that K decreases steadily as yield or m_b increases. This inference was confirmed with moment inversion results for NTS explosions (see Figure 2 of Patton, 2008). Meanwhile, the impulse of materials falling back onto the Earth's surface during spall slapdown increases steadily with yield (Patton, 1990), showing a jump across the water table due to increased coupling at about the same m_b where the rate of fall off of K seems to increase. This suggests a connection between the CLVD source and the dynamics of shock waves impinging on the free surface, resulting in more spalled mass, higher detachment velocities, and larger spall impulse for well-coupled shots below the water table compared to shots above.

During gravitational unloading due to spallation, stock wave rebound induces material bulking and slippage on reverse faults. Slapdown then compacts materials at shallow depths, but may not affect dilation of the source medium due to bulking and block rotations at depth. However, the impulse of slapdown, if sufficiently large as might be the case for the biggest shots on Pahute Mesa, will induce compaction to greater depths, reverse slip on faults, and crush bulked materials that are intrinsically weak, such as volcanic tuffs, or materials weakened by prior damage. Thus, a hypothesis is that for smaller Pahute Mesa explosions with $K > 1$, the impulse of slapdown does not exceed a material strength threshold. On the other hand, spall impulse for large explosions exceeds the threshold. This hypothesis predicts contributions to the volumetric source due to material damage for $K > 1$. For the largest yield tests, the statics are such that the cavity volume, protected by hoop stresses of the containment cage, remains intact, but due to the effects of compaction, the source medium in weakened materials over the shot point has returned to nearly its original volume or has contracted to a somewhat reduced volume.

This prediction or hypothesis was tested; for details, the reader should see Patton and Taylor (2010; PT10). Isotropic moments M_I from moment tensor inversions were compared against estimates of classical moment predicted for a spherical source, $M_t = \rho \cdot \alpha^2 \cdot V_c$, where ρ and α are source medium density and P wave speed, and V_c is cavity volume (Müller, 1973; Richards and Kim, 2005). Density and velocity models for Pahute Mesa are available (Ferguson *et al.*, 1994; Leonard and Johnson, 1987). Cavity radius r_c scaling has been investigated since the 1960s, and there is excellent agreement for normal-buried explosions in tuff using Heard's relationship in Mueller and Murphy (1971), a relationship due to Denny and Johnson (1991; DJ91), and one developed by PT10 specifically for Pahute Mesa. Using depth of burial h_x as a surrogate for yield (*e.g.*, $W = (h_x/120)^3$) and accounting for reduced coupling above the water table, PT10 found that the ratio M_I / M_t is significantly greater than 1 for smaller tests and decreases to values of ~1 or a little less for the largest shots on Pahute Mesa (Figure 2). The scaling relationship for M_I / M_t in DJ91 (eq. 41), after adjustments for

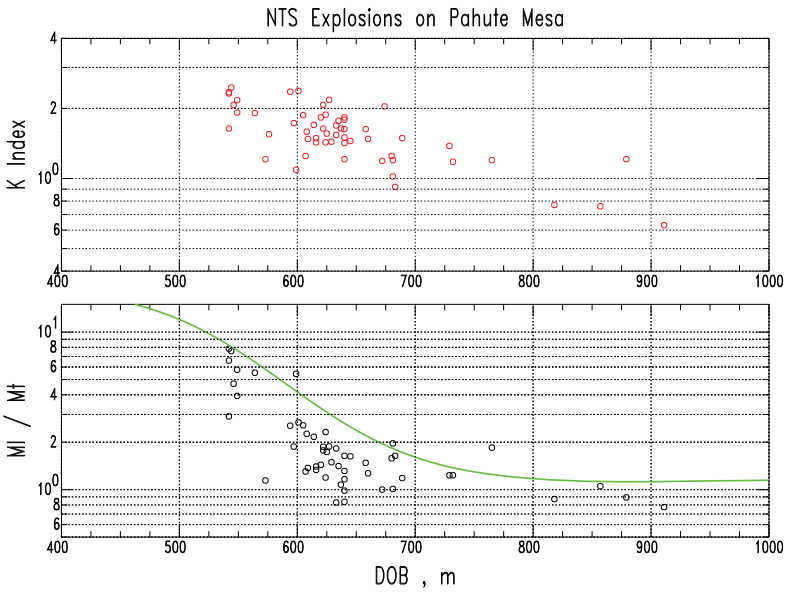

Figure 2. Plots of K and moment ratio M_I / M_t versus depth of burial for explosions on Pahute Mesa. Not shown are 10 very large shots with DOB greater than 1000 m; their K values range from 0.5 to 0.9 and moment ratios between 0.71 and 2.0. The green curve uses equation (41) of DJ91 and corrections for Rayleigh wave coupling as a function of depth from Jones and Taylor (1996) and Taylor (1982).

coupling, is in good agreement with these results. Note the correlation between changes in M_I / M_t and K, and to first order, $M_I / M_t \sim K^{1.5}$. For a K value of two, this relation gives an "apparent" explosion moment three times larger than the moment predicted by cavity creation, implying a volumetric moment due to damage that is significantly greater than the direct effects of the explosion source. The results in Figure 2 are consistent with the slapdown-dynamics hypothesis posited above.

Moment-Yield Scaling: An Outstanding Problem Revisited.

By ignoring the effects of source medium damage, past investigations very likely obtained biased estimates of M_I and deduced source models that over-estimated the importance of tectonic release. To show this, we first write a formula for the Rayleigh wave source term U_1 (Ekström and Richards, 1994) assuming shallow source depths h_x and long periods (note U_1 is proportional to the gain factor A' in PT08; see Patton, 2008, for details).

$$U_1 = \frac{2\beta^2}{\alpha^2} \cdot M_{zz} + \frac{1}{2}(M_{xx} + M_{yy} - 2M_{zz}) - \frac{3\alpha^2 - 4\beta^2}{\alpha^2} \cdot DS \quad , 3)$$

where the source is a sum of axisymmetric and deviatoric moment tensors, the latter representing shear dislocation of arbitrary orientation. M_{xx}, M_{yy}, and M_{zz} are diagonal elements of the axisymmetric tensor, expressed in terms of isotropic and CLVD moments:

$$M_{xx} = M_{yy} = M_I - \frac{1}{2}M_{CLVD} \quad (4)$$

and

$$M_{zz} = M_I + M_{CLVD} \quad . \quad (5)$$

DS and *SS* are defined by Ekström and Richards,

$$DS = \frac{1}{2}M_0 \sin 2\delta \sin\lambda \quad (6)$$

and

$$SS = M_0 \sin\delta \cos\lambda \quad , \quad (7)$$

for tectonic release with moment M_0, slip angle δ, and dip angle λ. Substituting for M_{ij} and *DS* into equation (3) yields

$$U_1 = \frac{2\beta^2}{\alpha^2} \cdot M_I - \frac{3\alpha^2 - 4\beta^2}{2\alpha^2} \cdot (M_{CLVD} + M_0 \sin 2\delta \sin\lambda) \quad . 8)$$

This model (explosion + damage + tectonic release) will be referred to as the "new" model.

The Ekström-Richards model consists of just explosion + tectonic release source components. The isotropic moment for this model is called $\tilde{M}_I$. Noting that tectonic release is the same whether damage is included or not, then

$$U_1 = \frac{2\beta^2}{\alpha^2} \cdot \tilde{M}_I - \frac{3\alpha^2 - 4\beta^2}{2\alpha^2} \cdot M_0 \sin 2\delta \sin\lambda \quad . 9)$$

Since equations (8) and (9) are equal, the relationship between M_I and $\tilde{M}_I$ is

$$M_I = \tilde{M}_I + \frac{5}{4}M_{CLVD} \quad , \quad (10)$$

for a Poisson medium $\alpha^2 = 3\beta^2$. M_I is greater than $\tilde{M}_I$ for a CLVD in extension ($M_{CLVD} > 0$).

The moment ratio $M_I/\tilde{M}_I$ is plotted in Figure 3 as a function of the relative CLVD source strength M_{CLVD}/M_I and K. For M_{CLVD}/M_I of 0.8, $M_I/\tilde{M}_I = \infty$. A moment ratio of infinity is not physical, and results from the fact that equation (3) is an asymptotic approximation for $h_x \to 0$ and $\omega \to 0$; in reality these limits are never attained. The results in Figure 3 illustrate a systematic bias in isotropic moments estimated for models omitting source medium damage.

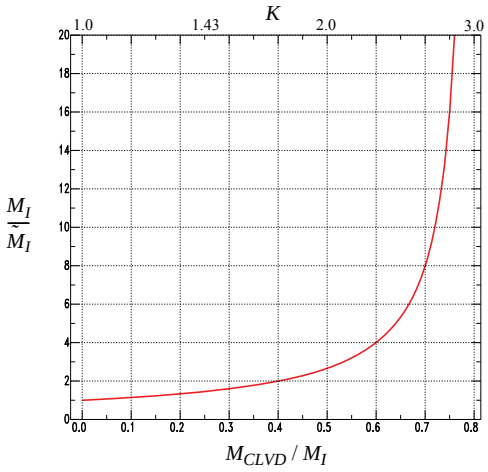

Figure 3. Inferred moment ratio of isotropic moments for models with and without source medium damage. Models without damage will systematically under-estimate the isotropic moment.

Equation 2 above does not strictly apply here because it was defined for a pure strike-slip tectonic release mechanism, while the new model is for tectonic release of arbitrary orientation. Nevertheless, this equation is still applicable to dislocation mechanisms of any orientation, even for the highest levels of tectonic release observed at STS, as will be shown below.

The index F ($= M_0/M_I$) introduced by Toksöz and Kehrer as a relative measure of tectonic release source strength, decreases for models including damage as the inverse moment ratio

$$F = (\tilde{M}_I/M_I) \cdot \tilde{F} \quad . 11)$$

Assuming a nominal K value of 2 for STS explosions, $\tilde{F}$ values are over-estimated by more than a factor of 2. Thus, a vast majority of STS explosions analyzed by Ekström and Richards have smaller F values, averaging only ~0.1, if a nominal amount of source medium damage occurs.

The relationship between K and M_{CLVD}/M_I in equation (2) is based on a strike-slip tectonic mechanism. Let K' be a measure of relative source strength for a general tectonic model. Then, it can be shown that

$$K' \equiv \frac{2M'_{zz}}{(M'_{xx} + M'_{yy})} = \frac{2(M_{zz} + 2DS)}{(M_{xx} + M_{yy} - 2DS)} \quad , \qquad (12)$$

where M_{xx}, M_{yy}, and M_{zz} are defined in equations (4) and (5). Assuming $M_{CLVD}/M_I \approx 0.5$ and denoting $max\{DS\}$ as the maximum absolute value of DS, the following inequalities hold true

$$M_{zz} \approx 1.5M_I \gg 2max\{DS\} = M_0 = FM_I \approx 0.1M_I \qquad (13)$$

and

$$M_{xx} + M_{yy} \approx 1.5M_I \gg 2max\{DS\} = M_0 = FM_I \approx 0.1M_I \quad . \qquad (14)$$

For most STS explosions, $M_{zz} \gg 2DS$ and $M_{xx} + M_{yy} \gg 2DS$ since F values are small. K' will not differ much from K even if tectonic release occurs as a dip-slip thrust mechanism. So equation (2) still applies.

There is little evidence for tectonic release affecting m_b (Bache, 1976). Khalturin *et al*. (2001) found good support for an m_b-log$W$ scaling relationship of the form $m_b = 0.75 \cdot \log W + c_1$ for shots at STS with announced yields. Ringdal *et al*. (1992) discovered that the constant c_1 is different for northeast, southwest, and transition test areas at Balapan. Adopting a M_I-W scaling relationship of the form $\log M_I \sim 0.85 \cdot \log W + c_2$ from DJ91 and substituting $(m_b - c_1)/0.75$ for log$W$, it is of interest to plot the quantity $0.9\log\tilde{M}_I - m_b + c_1$, which is called Δ, against $\tilde{F}$. This

is done in Figure 4 using estimates of $\tilde{M}_I$ and $\tilde{F}$ from Ekström and Richards and m_b from Ringdal *et al.*, adjusted for test areas.

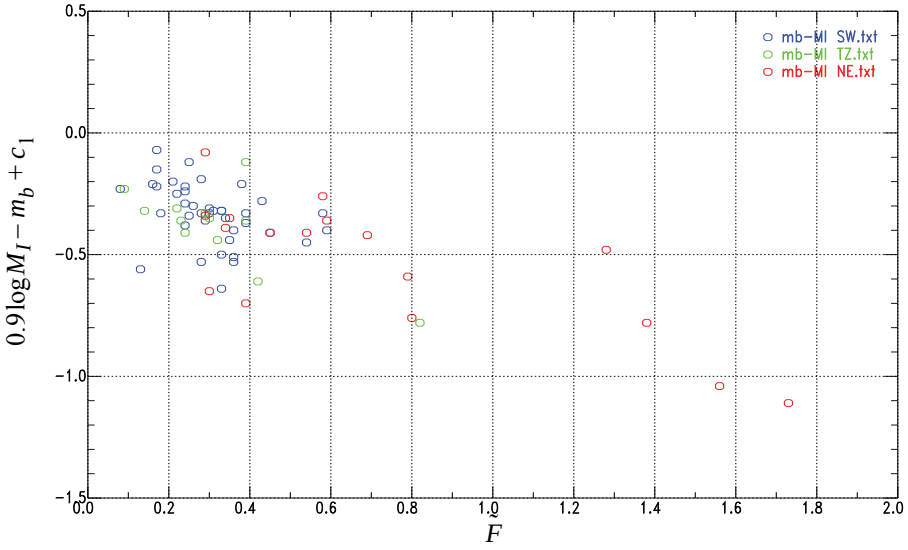

Figure 4. The quantity Δ (= $0.9\log\tilde{M}_I - m_b + c_1$) plotted against $\tilde{F}$ for Balapan explosions analyzed in Ekström and Richards. The constant c_1 was adjusted for test area (NE: 4.35; TZ: 4.43; SW: 4.50) based on the results of Ringdal *et al.* Δ was set equal to 0.0 for $\tilde{F}$ of 0.

An apparent dependence of Δ on $\tilde{F}$ is observed, suggesting an "isotropic moment deficit" increasing with $\tilde{F}$. The deficit is large enough to preclude an effect from m_b (> 0.5 magnitude units for $\tilde{F}$ > 0.6). Our interpretation is that this deficit is caused by under-estimation of $\tilde{M}_I$ due to model bias. If that's the case, then $\tilde{F}$ is systematically overestimated as the deficit grows, and the trend of measurements in Figure 4 is not real, but only apparent.

Several interesting implications can be deduced if the moment deficit is assume to equal Δ. For low tectonic release ($\tilde{F} \approx 0.3$), Δ is ~0.3 log units or a factor of 2, while for moderately high to high levels of tectonic release, the deficits are factors of 5 and 10, respectively. The moment ratio $M_I/\tilde{M}_I$ is set equal to these deficit factors in Table 1. Working backwards using equation (10), the relative source strength of damage M_{CLVD}/M_I can be inferred, and F is inferred by taking the product of the inverse moment ratio and $\tilde{F}$.

Table 1: K' as a Function of Strength of Tectonic Release

Ekström-Richards Model		New Model: Source Medium Damage + Tectonic Release					PT08
$\tilde{F}$	$M_I/\tilde{M}_I$	$\frac{M_{CLVD}}{M_I}$	F	$M_{zz} = M_I+M_{CLVD}$	$2max\{DS\} = F{\cdot}M_I$	K'	K
0.3	× ~2	0.4	0.15	$1.4M_I$	$0.15M_I$	$\approx K$	1.75
0.8	× ~5	0.64	0.16	$1.64M_I$	$0.16M_I$	$\approx K$	2.4
1.5	× ~10	0.72	0.15	$1.72M_I$	$0.15M_I$	$\approx K$	2.7

It can be seen that the inequality $M_{zz} \gg 2DS$ holds true for all cases, as does $M_{xx} + M_{yy} \gg 2DS$. Thus $K' \approx K$ for all three cases in Table 1 and in general for all STS tests studied by Ekström and Richards. Remarkably, F values remain constant and quite small. This result suggests that the appearance of high tectonic release explosions could actually a mirage owing to M_I estimates systematically biased low since the effects of damage were overlooked. Meanwhile, K values increase by about 1 unit showing the tradeoff with $\tilde{F}$ of the Ekström-Richards model.

Yield-depth tradeoff curves for the 2006 North Korean test.

In the absence of significant radiation from damage, the measured isotropic moment should be related to yield through cavity radius scaling using classical theory. While material damage undoubtedly occurred on the 2006 North Korean test, there was no expression of damage in the long-period radiation. As such, this explosion provides an excellent opportunity to test the consistency of yield estimates based on M_I and m_b. Here we follow a procedure similar to one used by Koper *et al*. (2008) to develop tradeoff curves between yield and depth of burial. However, the difference between our approach and the one taken by Koper *et al*. is that we set the measured M_I equal to M_t whereas Koper *et al.* used equation (41) in DJ91 for M_I / M_t, which was calibrated against explosions that suffered source medium damage.

Tradeoff curves are plotted in Figure 5 (see Patton and Taylor, 2010, for details). Their impressive agreement suggests that M_I for the 2006 North Korean test is fully consistent with an explosion source in hard rock medium suffering negligible radiation from either source medium damage or tectonic release. Also plotted in Figure 5 is the tradeoff curve from Koper *et al*. (2008) based on M_I. The difference between this curve and my result is due to the fact that Koper *et al*. employed equation (41) of DJ91 which relates M_I and M_t through additional factors related to overburden and gas porosity. DJ91 used explosions that suffered source medium damage to calibrate this equation, while damage appears not to be a significant source at long periods for the 2006 Korean test. A better physical basis of the source is the reason why I chose the classical formula ($M_t = \rho \cdot \alpha^2 \cdot V_c$) and equated M_I to M_t.

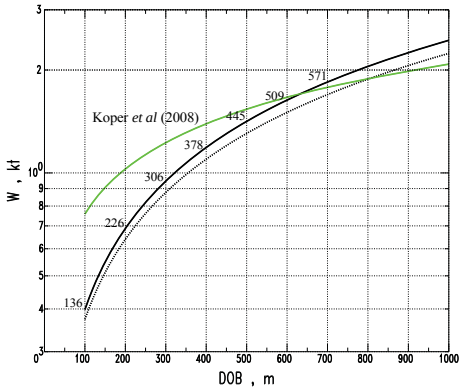

Figure 5. Yield versus depth of burial tradeoff curves for the 2006 North Korean test. Curves plotted with a solid line are based on isotropic moment M_I. The result of Koper *et al.* is the green curve and the result from this study is the black curve. The black dotted curve is based on m_b . Scale depth of burial (h / W$^{1/3}$ in units of m per kt$^{1/3}$) is provided on the M_I curve from this study.

CONCLUSIONS AND RECOMMENDATIONS

Over the course of this three year project, a great deal of progress has been made developing a new explosion source model grounded in a physical basis for seismic wave generation. The source model to date moves beyond simple models describing a spherical explosion releasing stored tectonic strain in the medium. Such tectonic release models were incomplete descriptions of a far more complicated source process. They ignored non-linear failure mechanisms caused by shock wave interactions at the free surface and hydrodynamic flow at depth giving rise to stress-wave rebound and rotational motions on multiple scale lengths. Source medium damage resulting from these non-linear mechanisms is a source of seismic radiation in itself, as pointed out by many researchers in the past. The form of this radiation is consistent with volumetric, CLVD, and DC body-force systems. The model under development has taken into account the radiation from damage, and our investigations have explored the implications for seismic discrimination and yield estimation. As summarized below, the implications are far-reaching and offer the promise for a physical source model for S wave generation, not just for long-periods but for high frequencies too. Also summarized below are recommendations for future research.

• Source medium damage radiating as a CLVD is a source of Rayleigh waves that destructively interfere on all azimuths with Rayleigh waves excited by the spherical explosion source. The resulting interference lowers Rayleigh

wave amplitudes and reduces the M_s making explosions look more explosion-like on a plot of m_b-M_s. The m_b-M_s discriminant owes a large measure of its success to the presence of significant Rayleigh wave radiation from source medium damage. This explanation has implications for test site evolution of the m_b-M_s discriminant. The medium is relatively strong and intact at nascent test sites, where depending on emplacement conditions, seismic radiation from damage is minimal and the m_b-M_s performance is degraded, as seen for North Korean tests. Over time, as the medium is weakened by more testing, the m_b-M_s performance should improve. Another way to state this concept is that the potential for seismic radiation due to damage increases as the source medium of a mature test site is conditioned by previous tests. On the other hand, just the opposite is true for tectonic release since the first explosions release the pre-stress, lowering the potential for tectonic release as testing continues. Research might detect such evolution in a record of m_b-M_s measurements if it is complete enough. The CLVD source of long-period radiation has been quantified for explosions in weak rock; such quantifications are still needed for hard rock explosions.

• The new model predicts two sources of volumetric moment, one from direct effects of the explosion (i.e., cavity formation) and the other from indirect effects related to damage. The volumetric moment due to damage has been detected in the seismic radiation from Pahute Mesa explosions (Patton and Taylor, 2010) by comparing the measured "apparent" explosion moment with estimates of the classical moment based on cavity volume. Such comparisons show that the volumetric moment due to damage can be up to four times larger than the traditional explosion moment due to cavity formation. The net volumetric moment is controlled by dynamics of spallation since the impulse of slapdown can induce compaction at depth, reverse slippage on thrust faults that occurred earlier in the source process, and crush bulked materials that are intrinsically weak, such as volcanic tuffs, or weakened by prior damage. The effects of slapdown are expected to be smaller for explosions in hard rock, which should translate into a weaker yield dependence of the source parameter K than what is observed for NTS explosions. This prediction is supported by preliminary results (Patton, 2008), and future quantifications of the CLVD source will test it by measuring K on hard rock explosions (see previous bullet). It is my opinion that the disappointing past performance of isotropic moment as an indicator of yield is due to the fact that previous source models ignored contributions of source medium damage to the long-period radiation. The prospects of improved methods for moment-based yield estimation rests on a deeper physical understanding of explosion moment, which the new model provides, but much more empirical and theoretical work is needed. A challenge is to extract from observables the volumetric moment due to cavity formation since classical source theory relates this moment to yield through scaling relationships of cavity radius. Developing empirical relationships between apparent and classical moment, such as the one for Pahute Mesa $M_I / M_t \sim K^{1.5}$, is one research avenue worth pursuing since excursions from the relationship for individual explosions could provide clues about material properties and emplacement conditions controlling the extent of damage. But more importantly, there is need for theoretical development of damage models to predict analytical volumetric and CLVD moments caused by changes in material properties. Armed with a physical basis theory for relating the two moments, a correction theory could be developed to extract estimates of damage moment from measurements of apparent explosion moment and K, thereby isolating the moment due to cavity formation. It is worth mentioning that in the absence of significant radiation due to damage, as is the case for the North Korean tests, the measured moment should be related to yield by classical theory. Excellent agreement between moment-based and m_b-based tradeoff curves for yield and depth of burial was shown in this paper. This result is expected if damage is not contributing volumetric moment, and m_b is properly calibrated for measurement of explosion yield at the North Korean test site.

• The ultimate goal is an explosion source prediction capability for P and S radiation across the measurable spectrum of seismic frequencies. Extensions of the current model to higher frequencies is the next evolutionary step in our research agenda. An encouraging sign for a successful outcome of such an agenda is when the basic physics applied in the current model carries over to model extensions for the purpose of explaining other key observations. After all, a unifying explanation for a host of observations is a hallmark of a successful physical model and instills confidence

in the model's utility for broad applications. The source model under development has such encouraging signs since the monopole-CLVD interference phenomenon for long-period Rayleigh waves applies to *Rg* waves too and can explain certain observed features in *Lg* spectra near 1 Hz. These features include amplitude modulations in *Lg* spectral ratios and in *P*/*Lg* ratios for NTS explosions (Gupta and Patton, 2009; Fisk, 2007) and low-frequency amplitude rolloff in what should be the flat portion of the *Lg* spectrum (and corresponding increase in *P*/*Lg* ratios) for Balapan explosions (Patton, 2009; Fisk, 2006). In this case, *Rg*-to-*S* scattering and seismic wave imprinting must be invoked as a mechanism for generating *S* waves at the source. A challenge at high frequencies is to quantify multiple sources of seismic radiation, e.g., direct radiation due to damage and indirect radiation resulting from near-source scattering of *P* and *Rg* waves emitted by a complex source. Such quantification depends critically on source-time functions and Green's function excitation of damage mechanisms. This will require research using nearfield data recorded on historic explosions and new data collected on field experiments devoted to explosion source physics.

ACKNOWLEDGEMENTS

I have benefitted from many helpful discussions with Dr. Steven R. Taylor on a broad suite of issues related to source physics and development of a new explosion source model. The comments of Prof. Paul Richards on the 2008 Patton and Taylor paper motivated some research reported here and focused our attention on a generalized source model with tectonic release of arbitrary orientation and source medium damage.

REFERENCES

Bache, T. C. (1976). The effect of tectonic stress release on explosion *P*-wave signatures, *Bull. Seismol. Soc. Am.* 66: 1441–1457.

Ben-Zion, Y. and Ampuero, J.-P. (2009). Seismic radiation from regions sustaining material damage, *Geophys. J. Int*. 178, 1351–1356, doi: 10.1111/j.1365-246X.2009.04285.x.

Denny, M. D. and L. R. Johnson (1991). The explosion seismic source function: Models and scaling laws reviewed, in *Explosion Source Phenomenology*, *AGU Monograph,* 65, edited by S. Taylor et al., 1-24.

Ekström, G. and P. G. Richards (1994). Empirical measurements of tectonic moment release in nuclear explosions from teleseismic surface waves and body waves, *Geophys. J. Int.,* 117, 120–140.

Ferguson, J. F., A. H. Cogbill, and R. G. Warren (1994). A geophysical-geological transect of the Silent Canyon caldera complex, Pahute Mesa, Nevada, *J. Geophys. Res.* 99: 4323–4339.

Fisk, M. D. (2006). Source spectral modeling of regional *P/S* discriminants at nuclear test sites in China and the former Soviet Union, *Bull. Seismol. Soc. Am.* 96: 2348–2367.

Fisk, M. D. (2007). Corner frequency scaling of regional seismic phases for underground nuclear explosions at the Nevada Test Site, *Bull. Seismol. Soc. Am.* 97: 977–988.

Gupta, I. N. and H. J. Patton (2008). Difference spectrograms: A new method for studying S-wave generation from explosions, *Bull. Seismol. Soc. Am.* 98: 2460–2468.

Khalturin, V. I., T. G. Rautian, and P. G. Richards (2001). A study of small magnitude seismic events during 1961-1989 on and near the Semipalatinsk Test Site, Kazakhstan, *Pure Appl. Geophys.* 158: 143–171.

Knopoff, L. and M. J. Randall (1970). The compensated linear-vector dipole: A possible mechanism for deep earthquakes, *J. Geophys. Res.* 75: 4957–4963.

Koper, K. D., R. B. Herrmann, and H. M. Benz (2008). Overview of open seismic data from the North Korean event of 9 October 2006, *Seismol. Res. Lett.* 79: 178–185

Jones, E. M. and S. R. Taylor (1996). Are Lg spectra from NTS explosions self-similar?, *Bull. Seismol. Soc. Am.* 86: 445–456.

Leonard, M. A. and L. R. Johnson (1987). Velocity structure of Silent Canyon caldera, Nevada Test Site, *Bull. Seismol. Soc. Am.* 77: 597–613.

Mueller, R. A. and J. R. Murphy (1971). Seismic characteristics of underground nuclear detonations, Part I. Seismic spectrum scaling, *Bull. Seismol. Soc. Am.* 61: 1675–1692.

Müller, G. (1973). Seismic moment and long-period radiation of underground nuclear explosions, *Bull. Seismol. Soc. Am.* 63: 847–857.

Patton, H. J. (1990). Characterization of spall from observed strong ground motions on Pahute Mesa, *Bull. Seismol. Soc. Am.* 80: 1326–1345.

Patton, H. J. (2008). Explosion source model development in support of seismic monitoring technologies: New models accounting for shock-induced tensile failure, in *Proceedings of the 30th Monitoring Research Review: Ground-Based Nuclear Explosion Monitoring Technologies*, LA-UR-08-05261, Vol. 1, pp. 649–657.

Patton, H. J. (2009). Explosion source model development in support of seismic monitoring technologies: Applications of new models for shock-induced tensile failure, in *Proceedings of the 2009 Monitoring Research Review: Ground-Based Nuclear Explosion Monitoring Technologies*, LA-UR-09-05276, Vol. 1, pp. 525–535.

Patton, H. J. and S. R. Taylor (2008). Effects of shock-induced tensile failure on m_b - M_s discrimination: Contrasts between historic nuclear explosions and the North Korean test of 9 October 2006, *Geophys. Res. Lett.*, 35: do1:10.1029/2008GL034211.

Patton, H. J. and S. R. Taylor (2010). Apparent explosion moment, Abstr., *Seismol. Res. Lett*. 81: presented at the spring meeting of the Seismological Society America, Portland OR, April; manuscript submitted to *JGR*.

Richards, P. G. and W.-Y. Kim (2005). Equivalent volume sources for explosions at depth: Theory and observations, *Bull. Seismol. Soc. Am*. 95: 401–407.

Ringdal, F., P. D. Marshall, and R. W. Alewine (1992). Seismic yield determination of Soviet underground nuclear explosions at the Shagan River test site, *Geophys. J. Int.* 109: 65–77.

Taylor, S. R. (1982). Calculation of seismic coupling factors at NTS from inversion of regional amplitudes, Abstr., *Earthquake Notes* 53, no. 1, p.8.

Toksöz, M. N. and H. H. Kehrer (1972). Tectonic strain release by underground nuclear explosions and its effect on seismic discrimination, *Geophys. J. R. Astr. Soc.* 31: 141–161.

Walter, W. R., E. Matzel, M. E. Payanos, D. B. Harris, R. Gok, and S. R. Ford (2007). Empirical observations of earthquake-explosion discriminants using *P/S* ratios and implications for the sources of explosion *S*-waves, in *Proceedings of the 29th Monitoring Research Review: Ground-Based Nuclear Explosion Monitoring Technologies*, LA-UR-07-5613, Vol. 1, pp. 683–693.

MODEL DEVELOPMENT FOR BROAD AREA EVENT IDENTIFICATION AND YIELD ESTIMATION

W. Scott Phillips[1], Xiaoning Yang[1], Richard J. Stead[1], Michael L. Begnaud[1], and Kevin M. Mayeda[2]

Los Alamos National Laboratory[1] and Weston Geophysical[2]

Sponsored by the National Nuclear Security Administration

Award Number: DE-AC52-06NA25396/LA10-Yield-NDD02

ABSTRACT

Models of laterally varying attenuation and site effects of regional phases are necessary to correct regional phase and coda amplitudes to reveal source effects of importance to identification and yield estimation procedures. We accomplish this using 2-D amplitude tomography, incorporating ground truth spectral estimates based on relative coda techniques and regional moment tensor inversion. The ground truth spectra allow calibration to absolute levels, and can be used to validate amplitude prediction models. Ground truth spectra may also be used to improve resolution in the margins of raypath coverage where source-path tradeoffs would otherwise dominate. Initial studies using USArray amplitude data show that we can recover frequency dependent, laterally varying attenuation, absolute site terms, moment and apparent stress using constraints based on ground truth spectra from the Wells, Nevada sequence. Tomographic efforts in Asia rely on collections of temporary networks and permanent stations, and preparation includes noise analysis for undocumented instrument changes, relative calibration of channels and array elements, and data culling using manual and automated methods. Network based Pg/Lg discriminants have confirmed earlier results showing that 2-D path calibration improves performance in intermediate bands (2-6 Hz), thus improves discrimination coverage. We applied relative coda methods to Asia sequences to obtain GT spectra. The method generalizes spectral ratio techniques by converting collections of high precision, pairwise relative coda measurements to absolute spectra assuming an omega-2 source model, allowing simultaneous analysis of large numbers of events. Apparent stress results vary significantly for smaller events, and for the Wenchuan sequence, is more heterogeneous over the southern, thrusting segment of the slip plane. The ground truth spectra were used to constrain a joint inversion for frequency dependent attenuation and site terms of the four regional phases, as well as moment and corner frequency of each event. Absolute calibration based on high quality spectral ground truth will allow the examination of test site biases on regional phase and coda amplitudes, and lead to transportable yield estimation techniques. Models may be validated using the spectral ground truth in leave-one-out studies, as is done for traveltime models.

OBJECTIVES

We seek models that will allow the prediction of absolute spectral levels, for purposes of event identification and yield estimation. Models can be constrained and validated using spectral ground truth, obtained using relative coda techniques, with overall levels set by regional moment tensor studies. Spectral ground truth is used to break source-path (corner frequency-Q) tradeoffs, allowing extension of models into poorly covered regions, and can be used for model validation. Models will allow the isolation of near-source effects on explosion spectra, and the evaluation of test site biases, thus enable transportable, regional phase yield estimation.

RESEARCH ACCOMPLISHED

Spectral Ground Truth

Absolute spectral levels can be obtained for event clusters using spectral ratios of coda waves (Mayeda et al., 2007), and direct regional phases (Fisk and Taylor, 2007). These authors show that ratios eliminate common path and site effects, leading to a well-posed inversion for relative moment and corner frequencies. Independently determined moments of one or more cluster events allow absolute levels to be fixed.

We have developed a technique that extends the high precision, relative coda method of Mayeda et al., (2007) to include large numbers of events. Coda amplitudes are compared directly for all event pairs within a preset distance from each other. Minor adjustments are made for differing distance to the station using known variations in envelope peak time, coda shape, and path. Amplitude ($\log_{10}$) differences are stacked for various stations and channels, for each pair, then inverted to determine relative spectral levels for each band, to which we fit moment and corner frequency for each event, as well as a frequency dependent transfer function.

In an initial test, we applied the technique to study source-spectral parameters of over 1000 aftershocks of the Great Wenchuan Earthquake of May 12, 2008 (Figure 1). For this test, we processed envelopes in narrow bands between 0.03 and 8 Hz and used an inter-event cutoff of 50 km for frequencies above 0.5 Hz, increasing to 300 km for the lowest band. CMT scalar moments for many of the larger events were used to set the absolute level. Results show that apparent stress ranged from 0.1 to 10 MPa, and was slightly higher for larger aftershocks (Figure 2). This observation supports conclusions of Mayeda et al., (2007) concerning a break in scaling behavior at magnitude 5.5 or so. Higher stresses for large events are hypothesized by these authors as representing the regional stress state, while the scatter in stress for smaller events, including many low stress events, reflects spatial fluctuation of stress in the source region following the main shock. Envelopes for similar sized, nearby events with greatly differing stress levels show that the scatter is a real effect (Figure 3). Spectra from these events could be used to constrain absolute levels for events throughout this region. In this study, we will use source parameters of the larger Wenchuan events, excluding the mainshock, as well as those from other Asia clusters to constrain multi-band, multi-phase amplitude tomography for 2-D attenuation, site terms, and source parameters.

Amplitude Tomography using Spectral Ground Truth Constraints

Attenuation models are critical for magnitude and yield work (e.g., Nuttli, 1973) and benefit event identification studies through the reduction of discriminant scatter for distributions of earthquakes across large areas. Phillips et al. (1998) showed that 2-D empirical path correction for 0.5-8 Hz Pn, Pg, Sn and Lg phases reduced discriminant scatter in earthquake populations in China, especially for lower and intermediate bands (0.5-6 Hz). The effect in intermediate bands (2-6 Hz) is of particular importance as discrimination performance degrades toward low frequency (Walter et al., 1995; Taylor 1996). Discrimination is known to perform well in high bands (> 6 Hz), but signal-to-noise considerations limit the range at which those bands are observed. Thus, intermediate band discrimination is of importance in extending discrimination to smaller events and larger distances.

Tomographic models are superior to empirical models as attenuation can be constrained in areas without reference events, but that are crossed by raypaths from outside events. The Los Alamos team has been active in producing such models using a wide range of techniques (Phillips et al., 2000, 2005, 2008; Phillips and Stead, 2008), including dual-phase tomography (Phillips et al., 2001), Bayesian approaches (Taylor et al., 2003), accounting for left censored amplitude data (Taylor et al., 2003), and spherical earth spreading models for Pn (Yang et al., 2007). This has and continues to be an active area of research in the community (e.g., Campillo, 1987; Jin and Aki, 1988; Xie et al., 2006; Mitchell et al., 1997; Pei et al., 2006; Mayeda et al., 2005; Ford et al., 2009; Pasyanos et al., 2009).

Here, we describe a tomography scheme that jointly inverts amplitude data for multi-phase, multi-band attenuation, site and source terms, based on the MDAC formulation (Walter and Taylor, 2002). The critical component in the

inversion is to break the tradeoff between source and attenuation using constraints from the ground truth spectra described above. Additional absolute level constraints are applied through collections of regional moments in the area. Absolute levels will be added to the site terms, which become the absolute site terms described by Malagnini et al., (2006). We perform this inversion in two ways: 1) inversion for 2-D Qo and η ($Q=Qo\ f^{\eta}$; f, frequency) and frequency dependent absolute site terms for all phases, and moment and apparent stress (or corner frequency) for each event, and 2) 2-D Q and site terms for all bands and phases, moment and apparent stress for all events. Inversion 1 is the most restrictive as attenuation and source terms are explicit functions of frequency; however, experience with USArray amplitudes has shown us that the restrictions are not particularly harmful in terms of fit to data.

We apply these inversions to a data set of nearly 1.7 million east, central and south Asia Pn, Pg, Sn, and Lg amplitudes, for 12 bands between 0.5 and 10 Hz. We use 979 stations, many from IRIS and PASSCAL collections, and just over 10,000 continental events selected in geographic bins based on catalog quality, including ground truth (GT<=25) events culled from catalog data, magnitude, and coverage. Amplitudes are windowed using picks and predicted arrivals. When first P picks and predictions differ, that time shift is applied to predicted onsets for other phases.

We limit amplitudes to intervals of consistent noise level to avoid contamination by undocumented response changes. Amplitudes are further limited to be within an order of magnitude of fits to regionally varying 1-D models to avoid noise and coda measurements at distance (e.g. Phillips et al., 2008). Relative amplitudes for various channels and array elements are then quantified using common events, and those measurements are combined prior to inversion. A 3-sigma trim is applied to residuals of initial, smooth tomography models to cull remaining outliers.

We show 2-D Qo and η from Inversion 1 in Figures 4-5. The Qo results are similar to 1-Hz results from single-phase inversions presented at past reviews. Frequency dependence terms η are not inversely correlated with Qo. We observed inverse correlation for similar studies of USArray data, with low Qo associated with higher η, and vice versa. Frequency dependence for Pn Q is low, perhaps resulting from the frequency dependent Yang et al. (2007) spreading model used for that phase. Source parameters show typical scaling (Figure 7) with a weak tendency towards scaling that is steeper than self-similar. Pn residuals are highest (Figure 8), followed by Pg, Sn, and Lg. Pn windows are short in this study (8.1 – 7.6 km/s), which may partially explain their higher residuals. Residuals for Inversion 2 are not shown, but they are slightly higher than those depicted. The reason for this is simply that regularization parameters were chosen too large for the latter runs, and no scientific significance is attached to the difference. Figures 8 and 9 show results of a checkerboard test using perfect data. This demonstrates code fidelity and upper limits of spatial resolution with this data set. Synthetic source parameters and site terms were also recovered well.

CONCLUSIONS AND RECOMMENDATIONS

Ground truth spectra can be used in to constrain multi-band, multi-phase amplitude tomography to produce models that predict absolute spectra from regional phase earthquake amplitudes. Further, spectral ground truth can be used to validate propagation models in the same way that location ground truth is used to validate traveltime models. Such models are critical for regional phase magnitude, yield and event identification analyses. Collection of spectral ground truth must be a collaborative effort over time by the community, as has been the case for location ground truth.

ACKNOWLEDGEMENTS

This study relied on IRIS and PASSCAL waveform collections, and we greatly appreciate help from IRIS DMC personnel. Graphics were made with GMT software. Valuable discussions with M. Fisk are acknowledged.

REFERENCES

Campillo, M. (1987). Lg wave propagation in a laterally varying crust and the distribution of the apparent quality factor in central France, *J. Geophys. Res*. 92: 12,604–12,614.

Fisk, M. and S. R. Taylor, (2007). Robust magnitude and path corrections for regional seismic phases in Eurasia by constrained inversion and enhanced kriging techniques, in *Proceedings of the 29th Monitoring Research Review: Ground-Based Nuclear Explosion Monitoring Technologies*, LA-UR-07-5613, Vol. 1, pp. 24–33.

Ford, S.R., W.S. Phillips, W.R. Walter, M.E. Pasyanos, K.M. Mayeda, and D.S. Dreger (2009). Attenuation tomography of the Yellow Sea/Korean Peninsula from coda-source normalized and direct Lg amplitudes, *Pure Appl. Geophys*., doi:10.1007/s00024-009-0023-2.

Jin, A., and K. Aki (1988). Spatial and temporal correlation between coda-Q and seismicity in China, *Bull. Seismol. Soc. Am*. 78: 741–769.

Malagnini, L., P. Bodin, K. Mayeda, A. Akinci (2006). Unbiased moment-rate spectra and absolute site effects in the Kachachh Basin, India, from the analysis of the afters hocks of the 2001 Mw 7.6 Bhuj earthquake, *Bull. Seismol. Soc. Am.* 96: doi:10.1785/0120050089.

Mayeda, K.M., L. Malagnini, W.S. Phillips, W. Walter, and D. Dreger, (2005). 2-D or not 2-D, that is the question: A northern California test, *Geophys. Res. Lett*. 32: L12301, doi:10.1029/2005GL022882.

Mayeda, K., L. Malagnini, W. R. Walter, (2007). A new spectral ratio method using narrow band coda envelopes: Evidence for non-self-similarity in the Hector Mine sequence, *Geophys. Res. Lett.*, doi:10.1029/2007GL030041.

Mitchell, B. J., Y. Pan, J. Xu, and L. Cong (1997). Lg coda Q variation across Eurasia and its relation to crustal evolution, *J. Geophys. Res*. 102: 11767–22779.

Nuttli O. W. (1973). Seismic wave attenuation and magnitude relations for eastern North America, *J. Geophys. Res.* 78: 876–885.

Pasyanos, M.E., W.R. Walter, and E.M. Matzel (2009). A simultaneous multiphase approach to determine P-wave and S-wave attenuation of the crust and upper mantle, *Bull. Seismol. Soc. Am*. 99: 3314–3325.

Pei, S., J. Zhao, C. A. Rowe, S. Wang, T. M. Hearn, Z. Xu, H. Liu, and Y. Sun (2006). M_L amplitude tomography in North China, *Bull. Seismol. Soc. Am.* 96: 1560–1566, doi: 10.1785/0120060021.

Phillips, W. S., G. E. Randall and S. R. Taylor (1998). Path correction using interpolated amplitude residuals: An example from central China, *Geophys. Res. Lett*. 25: 2729–2732.

Phillips, W. S., H. E. Hartse, S. R. Taylor, and G. E. Randall (2000a). 1 Hz Lg Q Tomography in central Asia, *Geophys. Res. Lett*. 27: 3425–3428.

Phillips, W. S., H. E. Hartse, S. R. Taylor, A. A. Velasco, and G.E. Randall (2001). Application of regional phase amplitude tomography to seismic verification, *PAGEOPH*, 158**:** 1189–1206.

Phillips, W. S., H. E. Hartse, and J. T. Rutledge (2005). Amplitude ratio tomography for regional phase Q, *Geophys. Res. Lett*. 32: doi:10.1029/2005GL023870.

Phillips, W. S. and R. J. Stead (2008). Attenuation of Lg in the western US using the USArray, *Geophys. Res. Lett*. 35: L07307, doi:10.1029/2007GL032926.

Phillips, W. S., R. J. Stead, G. E. Randall, H. E. Hartse, and K. Mayeda (2008). Source effects from broad area network calibration of regional distance coda waves, in Advances in Geophysics, 50, *Scattering of Short Period Waves in the Heterogeneous Earth*, H. Sato and M.C. Fehler, Eds., 319–351.

Taylor, S. R. (1996). Analysis of high frequency Pg/Lg ratios from NTS explosions and western US earthquakes, *Bull. Seismol. Soc. Am*. 86: 1042–1053.

Taylor, S. R., X. Yang, and W. S. Phillips (2003). Bayesian Lg attenuation tomography applied to eastern Asia, *Bull. Seismol. Soc. Am*. 93: 795–803.

Walter, W.R., K.M. Mayeda, and H.J. Patton, (1995). Phase and spectral ratio discrimination between NTS earthquakes and explosions: 1. Empirical observations, *Bull. Seismol. Soc. Am*. 85: 1050–1067.

Walter, W. R. and S. R. Taylor (2002). A revised magnitude and distance amplitude correction (MDAC2) procedure for regional seismic discriminants: theory and testing at NTS, Lawrence Livermore National Laboratory, UCRL-ID-146882, pp. 13.

Yang, X., T. Lay, X.-B. Xie, and M. S. Thorne (2007). Geometric spreading of Pn and Sn in a spherical Earth model, *Bull. Seism. Soc. Am.* 97: 6, 2053-2065.

Xie, J. K., Z. Wu, R. Liu, D. Schaff, Y. Liu, and J. Liang (2006). Tomographic regionalization of crustal Lg Q in eastern Eurasia, *Geophys. Res. Lett*. 33: L03315, doi:10.1029/2005GL024410.

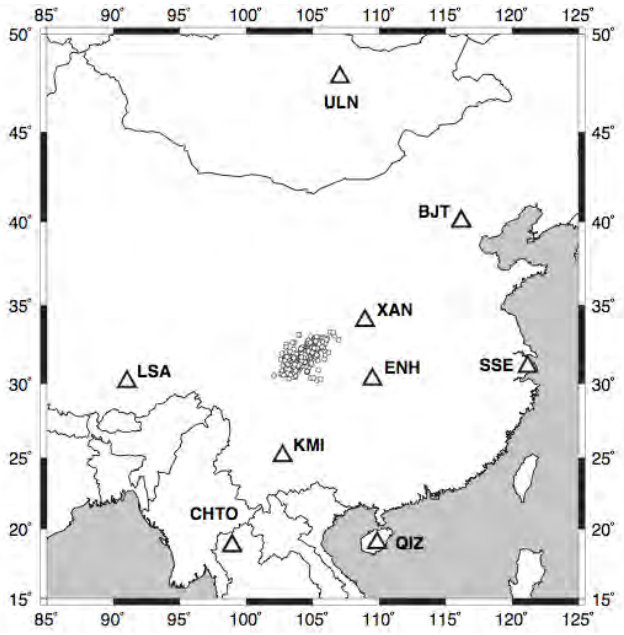

Figure 1. Stations (triangles) and events (EDR bulletin, circles) used in the relative coda source study of Wenchuan aftershocks.

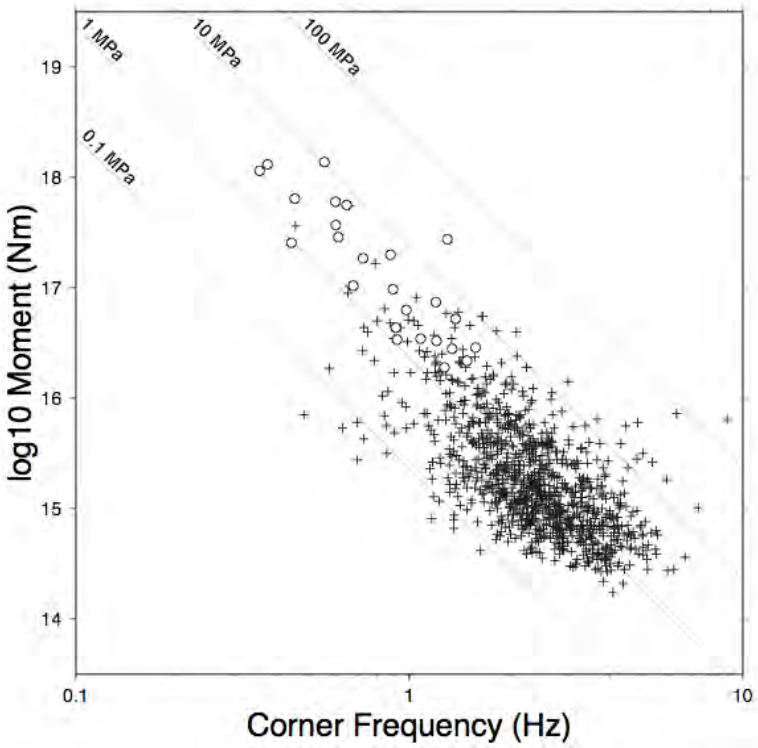

Figure 2. Moments and corner frequencies obtained for Wenchuan aftershocks using the relative coda technique. Open circles represent events for which CMT moments were used as constraints, crosses represent the remainder. Diagonal lines represent apparent stress, as noted.

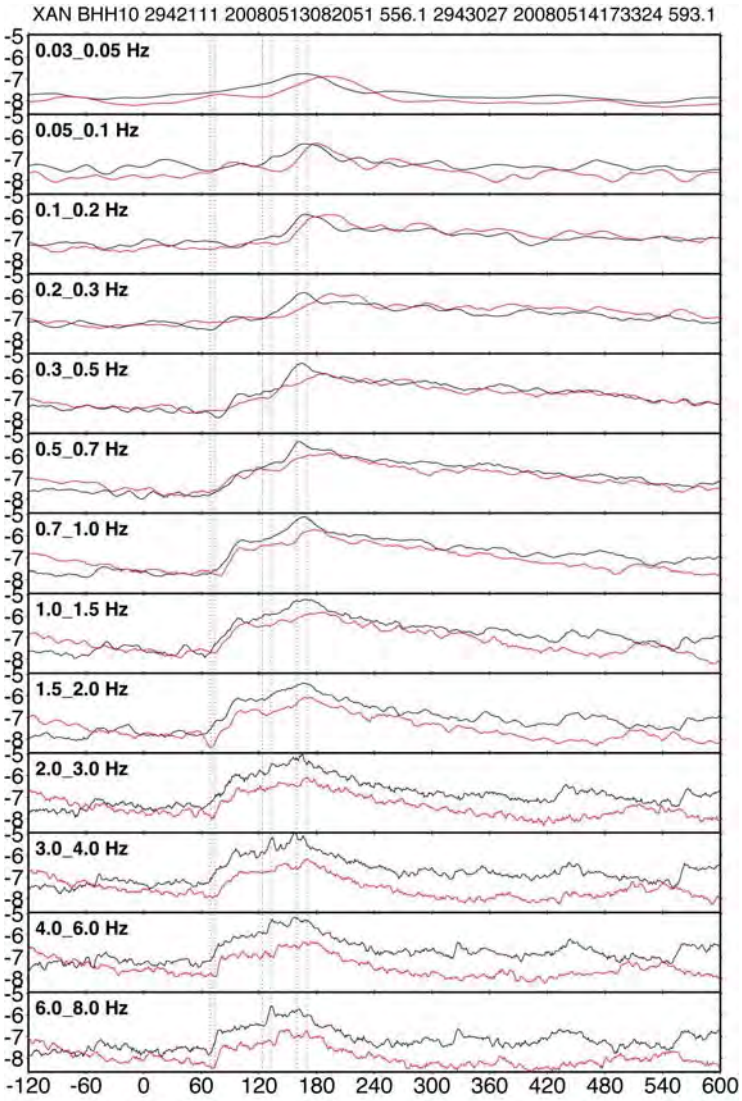

Figure 3. Envelopes for nearby, similar-sized Wenchuan events of differing stress for station XAN (Xian). Predicted P, Sn, and Lg peak envelopes are marked for both events. Band limits are noted. Time is seconds from the origin, envelope units are m/s.

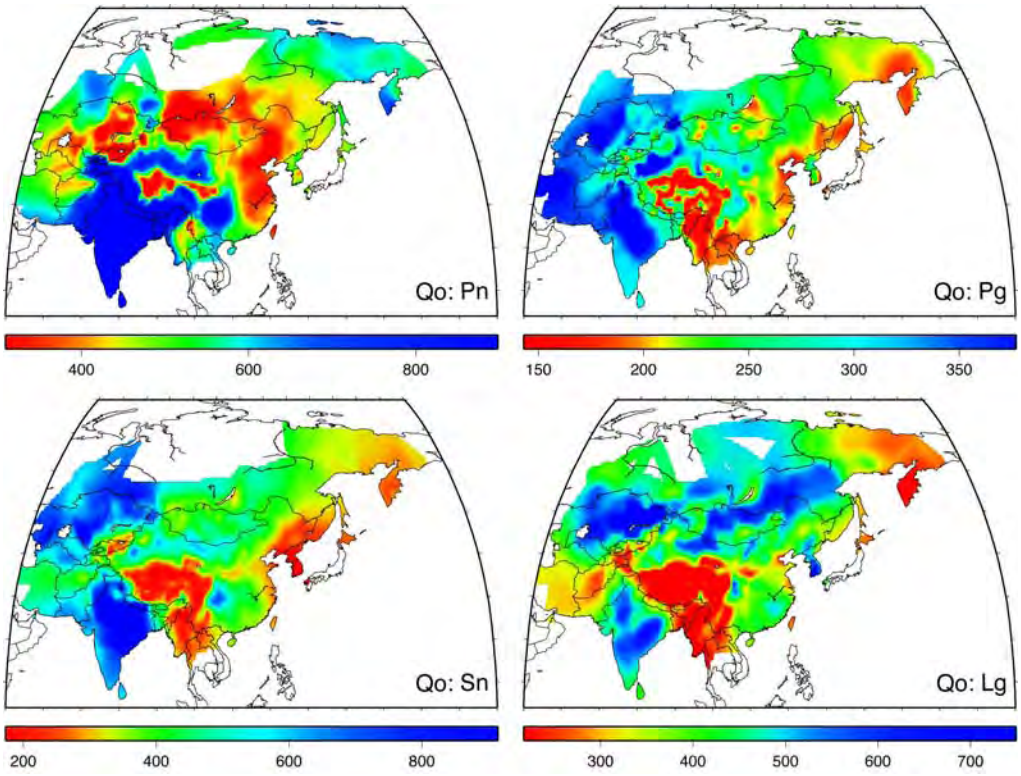

Figure 4. Q at 1 Hz (Qo) for regional phases in central, south and east Asia. Results were obtained using the Yang et al (2007) spreading for Pn, power law spreading of 0.7 for Pg, 1.1 for Sn, and 0.5 for Lg.

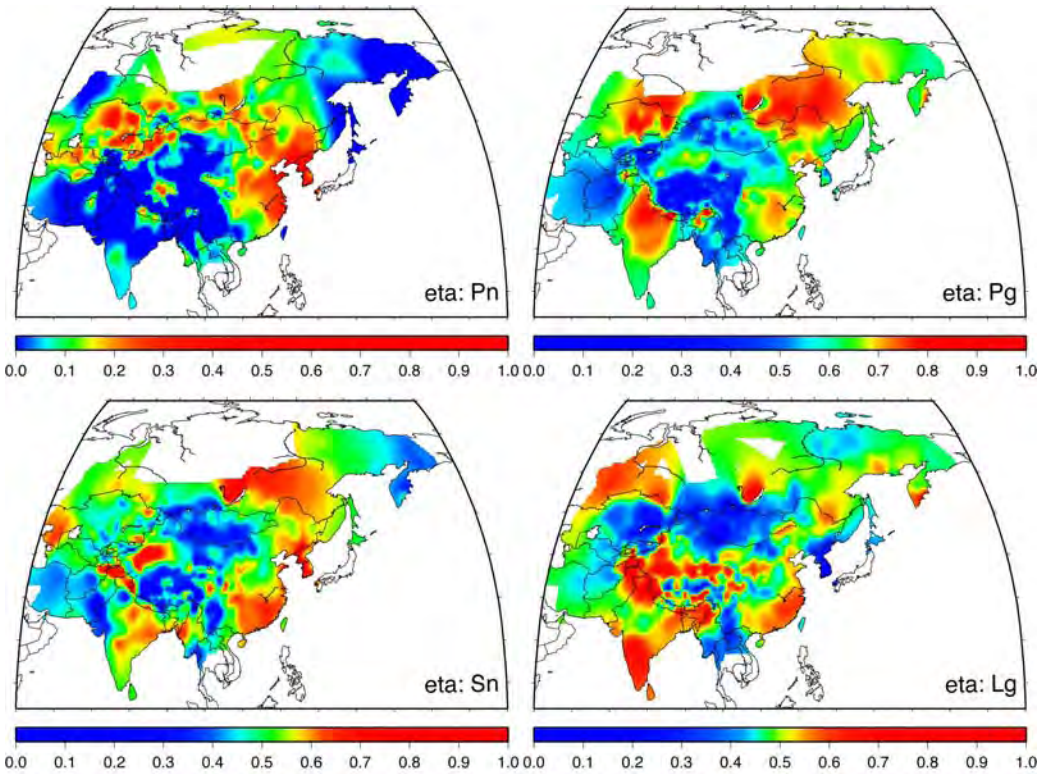

Figure 5. Frequency dependence of Q (η) for regional phases

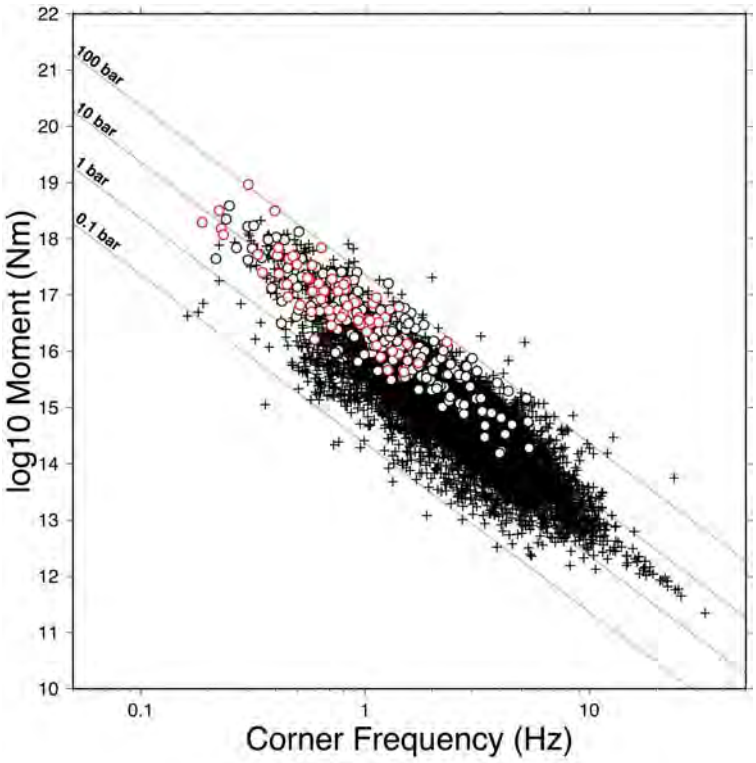

Figure 6. Moment and corner frequency for events used in the inversion. Apparent stress is noted (1 bar = 0.1 MPa). Black circles represent events with scalar moments that were used as constraints. Red circles represent events with ground truth spectra from relative coda studies that were used as constraints. The convergence towards 3 bars for small events is the result of regularizing the inversion to favor self-similar scaling with average stress when corner frequencies cannot be constrained.

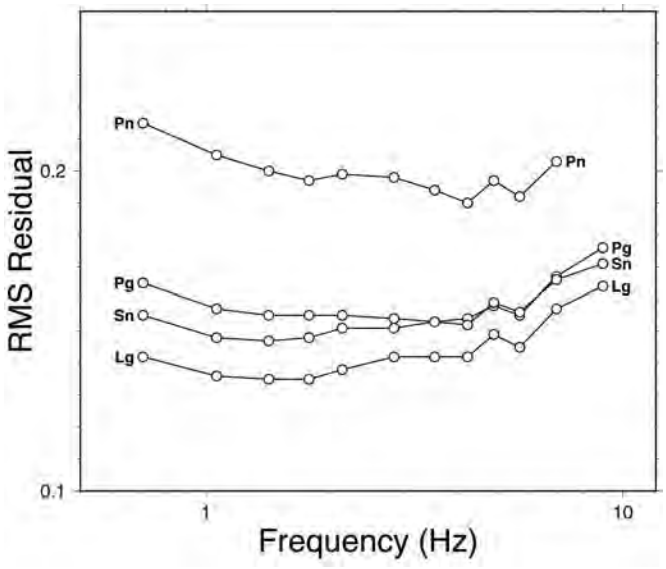

Figure 7. Inversion residuals by band corresponding to results shown in Figures 4-6, for phases as annotated.

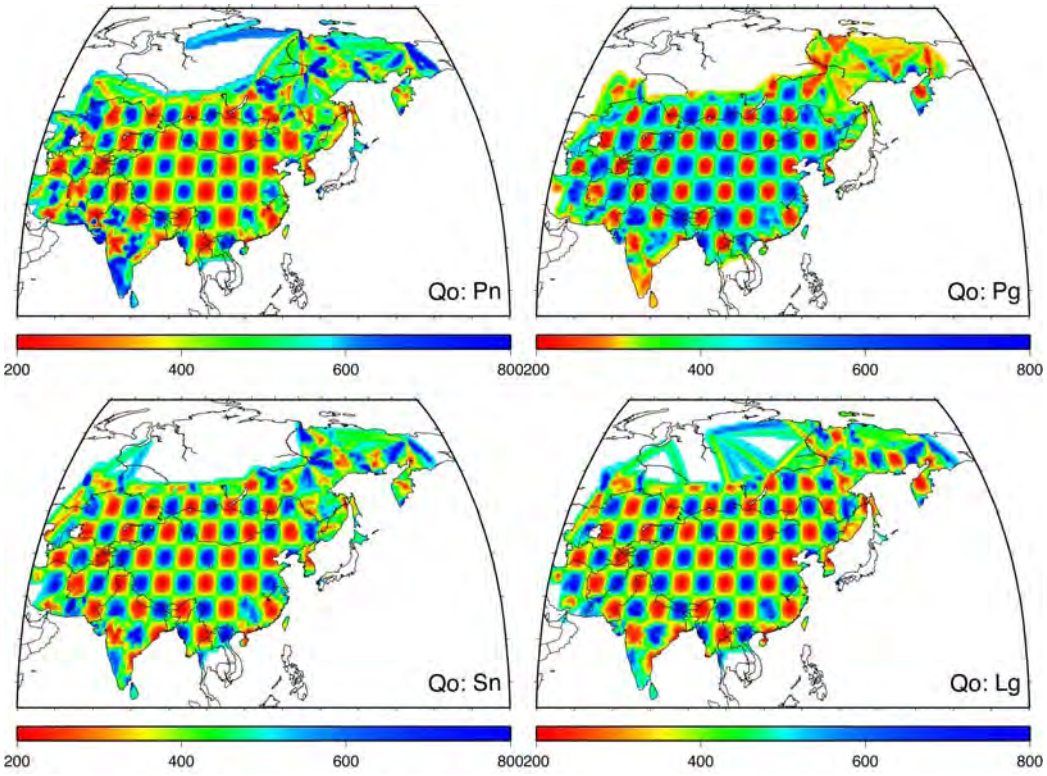

Figure 8. Q at 1 Hz (Qo) for synthetic data test, 5 degree sine model, Q 200 to 800, η 0.3-0.7.

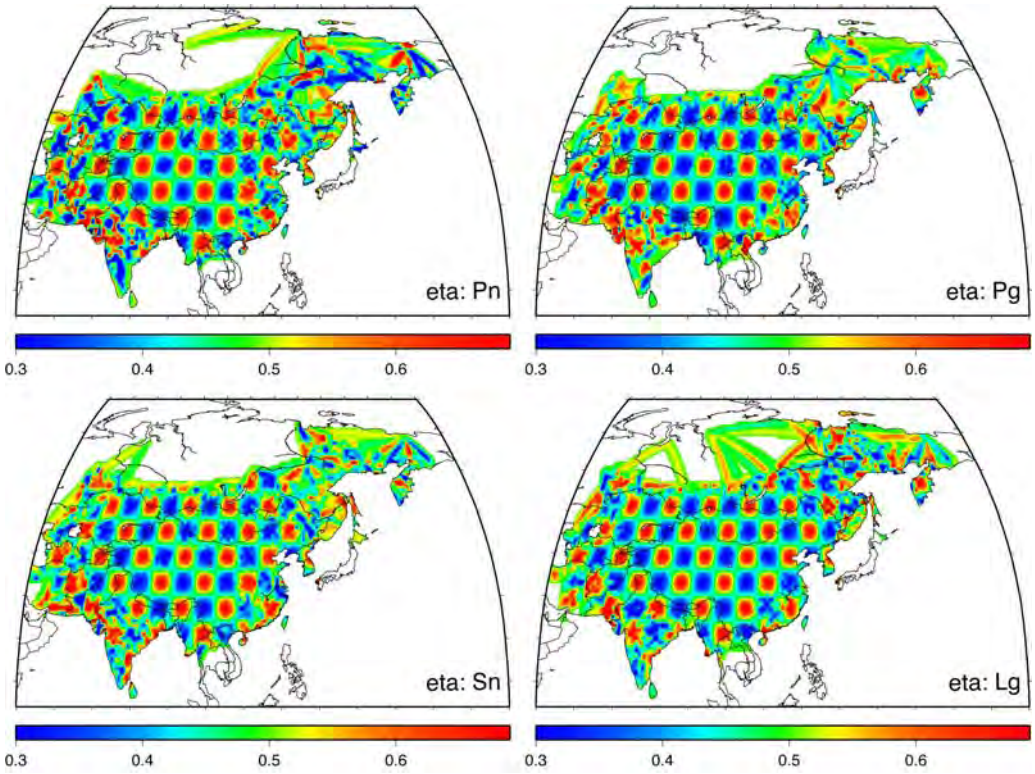

Figure 9. Frequency dependence of Q (η) for synthetic data test as described above.

IDENTIFICATION OF DEEP EARTHQUAKES

George E. Randall and Hans E. Hartse

Los Alamos National Laboratory

Sponsored by the National Nuclear Security Administration

Award No. DE-AC52-06NA25396/LA10-EQID-NDD02

ABSTRACT

The objective of this project is to identify and apply seismic event discriminants that will reliably separate small, crustal earthquakes (magnitudes less than about 4 and depths less than about 40 to 50 km) from small, deep earthquakes (depths between about 50 and 300 km). These deep earthquakes are known to occur in the Asia-India continental collision zone, mostly north of the Indian subcontinent, including far western China. Not only are the depths of these subcrustal earthquakes difficult to reliably estimate using conventional arrival time location methods (when event-station distances are large), but they can also appear with explosion-like characteristics on discrimination plots designed to separate nuclear explosions from crustal earthquakes. Thus, reliably flagging these small, deep events is critical in improving discrimination performance, because deep earthquakes can immediately be removed from further event identification analyses. Further, reliably identifying subcrustal earthquakes will allow us to eliminate deep events (previously misidentified as crustal earthquakes) from research datasets, thereby refining event identification parameters for the Magnitude and Distance Amplitude Correction (MDAC) process, and ultimately leading to more robust capabilities for separating small, crustal earthquakes from explosions.

Our research approach involves 4 primary steps: (1) assemble a "control" data set of waveforms from reliably located, mostly larger earthquakes (both crustal and deep events) from the Hindu Kush region, (2) measure body-wave and coda-wave amplitudes of the "control" earthquakes, (3) experiment with amplitude ratios and other measurements as discriminants for separating crustal and deep events, and (4) apply the discriminants to a data set of small Hindu Kush earthquakes and assess discrimination performance. For selecting a subset of well-located, larger earthquakes we rely on depth constraint provided by the presence of teleseismic depth phases and/or centroid moment tensor (CMT) reports. We also select as "control" events some smaller earthquakes which were recorded by stations KBL and/or NIL, as these stations are within a few hundred km of the zone where deep earthquakes are known to occur. To date we have selected about 300 earthquakes for measurements under step 2 of our project. Wave amplitude measurements are under way. For step 2 we will also measure slownesses of deep and crustal earthquake waves as they cross the seismic arrays within Kazakhstan. We are especially interested in identifying far-local and regional depth phases at arrays and at three-component stations that can be used to constrain earthquake depths during the event location process.

The US National Data Center (USNDC) will be the primary user of these research results. The results of this study also have potential to benefit the current Administration's renewed interest in the Comprehensive Nuclear-Test-Ban Treaty by strengthening the verification regime. Our final research product will be an extension of the Event Classification Matrix (ECM), also known as the Event Categorization Matrix, which currently uses standard teleseismic discriminants to separate seismic events into populations of explosions, shallow earthquakes, deep earthquakes, or unresolved. As we move to regional, broad-area monitoring of smaller events, we will add discriminants to ECM that allow us to categorize deep earthquakes based on regional data alone. This will be essential to resolve small, deep events that may not be categorized as deep using teleseismic discriminants within the current ECM framework.

OBJECTIVES

To meet the United States Government (USG) nuclear explosion monitoring (NEM) requirements with high confidence and a low false-alarm rate, the monitoring community needs new and improved capabilities for analyzing small deep regional seismic events. Many features of regional seismograms can lead to confusion and possible miscategorization as explosions. The primary objective of this work is to identify and apply seismic event discriminants that will reliably separate explosions and small, crustal earthquakes (magnitudes less than about 4 and depths less than about 40 to 50 km) from deep earthquakes (depths between about 50 and 300 km) with particular emphasis on small deep earthquakes. Our end product will be the incorporation of regionally recorded waveform measurements and discriminants into the ECM such that US National Data Center operations can reliably identify and separate deep earthquakes from consideration as potential nuclear explosions.

Deep earthquakes present both a problem and an opportunity for seismic monitoring by the USNDC. The results of this study are intended to also benefit the current Administration's renewed interest in the Comprehensive Nuclear-Test-Ban Treaty by strengthening the verification regime. Standard methods of seismic location are routinely unsuccessful at tightly constraining event depth unless either (1) a number of clear depth phases (near source reflections) are observed, or (2) at least one seismic station reporting phase arrival times is at an epicentral distance no greater than 2 or 3 times the true event depth. Depth phases are extremely difficult to observe for small events as the reflections are often smaller than the direct (first arrival) phase and are either below the noise floor or lost in the reverberant coda of the direct arrival. Seismic event location is an iterative nonlinear least squares estimation problem, and the travel time sensitivity with respect to event depth diminishes rapidly for distances beyond several event depths, requiring manually constrained event depths for a location estimate. Asia has abundant deep seismicity from a number of tectonic collision zones as shown in the map of deep earthquakes in Figure 1. Until recently the seismic station distribution was not favorable for accurate depth estimation in the Hindu-Kush-Pamir deep seismicity region shown on the maps below. Recent installation of station KBL and improvements in the depth estimates of the Global Centroid Moment Tensor Project (based on seismic waveform modeling) finally make it possible for us to build a well-constrained ground truth dataset of deep events seismically recorded at regional distances. Once we construct the ground truth dataset, we can then systematically explore ratios of MDAC-corrected seismic amplitudes to form and test discriminants for deep events using the same tools and formalism we have used to study seismograms for shallow seismic events and explosions. Once we have developed and validated discriminants for categorizing deep events using MDAC and ECM technologies we can easily forward these to the USNDC for their evaluation and implementation.

Our objective is the creation of discriminants for use with the ECM method, which will identify deep earthquakes as separate population, distinct from explosions and normal depth crustal earthquakes using regional seismic data. This will augment the current teleseismic discriminants for deep earthquakes, and allow categorization of smaller events, which may be poorly recorded at teleseismic distances, but well recorded at regional distances. We need to develop a ground truth dataset of earthquakes at both normal crustal depths and earthquakes from subduction zones, below the overlying crust. Many earthquakes catalogs contain events with poorly constrained or fixed depth locations as well as events with well constrained depths, primarily from well recorded depth phases and waveform modeling. We have used the Centroid Moment Tensor (CMT) catalog for deep events as an additional source of ground truth.

RESEARCH ACCOMPLISHED

We first encountered problems with deep earthquakes early in the research program described by Hartse et al. (1997) prior to the development of MDAC and ECM methodologies. We have begun a systematic study regional discrimination of regionally recorded deep earthquakes for integration with MDAC and ECM, with a primary focus on the Pamir and Hindu-Kush zones of deep seismicity. Two recent summaries of the state of knowledge on deep earthquakes by Frohlich (2006) and H. Houston in Schubert (2007) while useful provide little insight into regional discrimination issues. Frohlich (2006) has a useful description of the deep seismicity of the Pamir and Hindu-Kush zones. Active research on the deep seismicity of the Pamir and Hindu-Kush zones spans decades [Roekcker et al. (1980); Chatelain et al. (1980); Verma and Sekhar (1985); Pavlis and Hamburger (1991); Zhao and Helmberger (1993); Fan et al. (1994); Mellors et al. (1995); Zhu et al. (1997); Pegler and Das (1998) and Chu et al. (2009)] but there are no ready answers to the problem of regional discrimination of deep earthquakes from normal crustal earthquakes or explosions. We will focus our efforts on identifying the regional characteristics of seismograms from

deep events that will distinguish them from regional seismograms of crustal earthquakes and explosions, with the goal of incorporating our results into the ECM suite of discriminants.

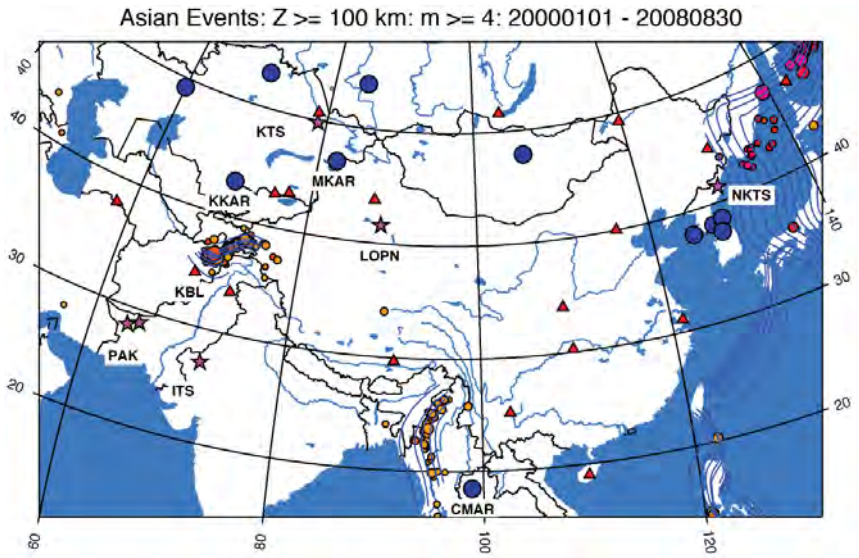

Figure 1. Locations of earthquakes deeper than 100km within the India-Asia collison zone. Also shown are nearby seismic stations and Asian seismic arrays. Blue contours are subducting slab depth associated with seismicity.

Figure 1 shows a map of the deep seismicity of the Asian continent with the contours of event depths and the inferred subducting slabs in the Pamir Hindu-Kush area of Afghanistan/Pakistan as well as deep seismicity in Myanmar near India and in the Korea, Japan and Eastern Siberia regions. Our primary areas of concern are in the Hindu Kush resulting from the Indian subcontinent collision with the landmass of Asia.

Seismic bulletins commonly list seismic events with automatically or manually fixed depths (frequently 0, 10, 15 or 33 km are common) when the travel time location process is unable to estimate depth as a free parameter. Event depth trades off with origin time when depth (or origin time) is unconstrained. Seismic stations in areas of interest are rarely within 2 event depths, but a recently reinstalled station in Afghanistan (KBL) is within 2 event depths of a cluster of deep seismicity. With KBL, the USGS NEIC now locates events with improved accuracy depth estimates from travel times, allowing us to finally build a calibration dataset of well-constrained deep events. We can take advantage of USGS locations using KBL to devise waveform-based discriminants to identify the deep events. We can not reasonably expect KBL to be routinely available in the future given its politically unstable location, and long history of being unavailable. Figure 2 below shows a map of the deep seismicity and the depth contours for the Hindu-Kush region with the nearest available seismic stations. Station KBL is within 2 to 3 event depths of many of the deep events, and is helping constrain the event depths since its reinstallation. Station NIL has had a history of downtime and has not been as useful to constrain event depths. For event locations where KBL is either not close enough or not operating, we will examine the available seismic stations and estimate our own seismic locations using phase arrival time picks that we add and assess the depth from the new location for possible inclusion in out ground truth dataset. This will allow us to exploit our existing archive of event locations and assembled seismograms to create additional ground truth. We will also review and collaborate with the LANL seismic location effort to use existing LANL refined ground truth locations and contribute any additional ground truth locations we may generate.

Deep earthquakes of sufficient magnitude (approximately M > 5) are analyzed and published by the Global Centroid Moment Tensor Project (http://www.globalcmt.org/) which provides estimates of the event depth as well as source mechanism. These estimates are derived from waveform modeling, and have recently included more events with the depth estimated and not fixed. These CMT depth estimates provide another new source of ground truth for larger deep events. We have also used earthquake catalog sources include Earthquake Data Reports (EDR), Reviewed Event Bulletin (REB) and the Kazakh National Data Centre (KNDC) bulletin. We have required 4 or more distinct teleseismic depth phases, such as pP and sS for ground truth event depth. High quality ground truth

will be essential to developing discriminants for deep regional events and subsequent screening of existing event populations to recategorize events with poorly controlled depths. Figure 2a shows all available seismicity since station KBL began reporting and appearing in earthquake locations. Figure 2b shows a dramatically smaller subset of the the data which has had strict event depth criteria applied. We will need to add additional ground truth events over the course of this project.

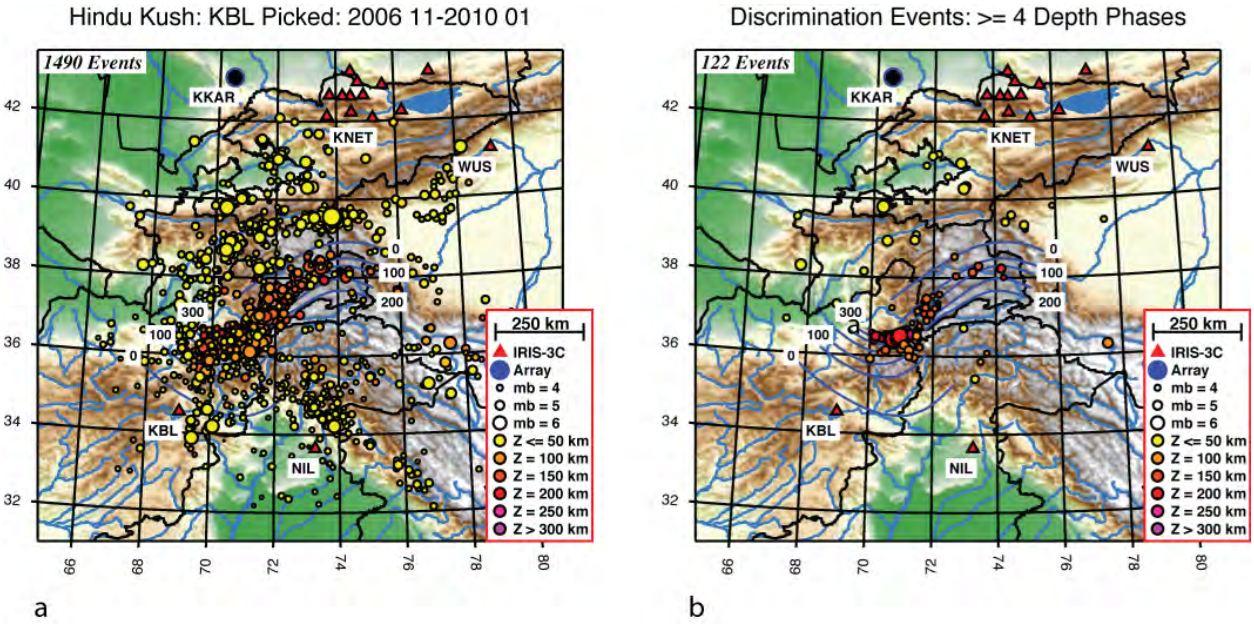

Figure 2. Earthquakes of the Hindu Kush region. Note locations of stations KBL and array KKAR. Blue contours and labels represent depth in km of subducting slabs. In map a (left) are events which we have picked at KBL since KBL began sending data in late 2006. We believe many depths associcated with these reported locations are wrong. In map b (right) are only those events used for our preliminary discrimination analysis (see Figures 4 and 5). We used only events with 4 or more distinct teleseismic depth phases, such as pP and sS. There are 122 events on this map.

The array KKAR is not close enough to constrain event depth, but suffers from a large number of events that are problematic and probably poorly depth constrained. We believe the poor depth control has caused a number of deep earthquakes to be analyzed as if they were shallow crustal events, contaminating our dataset.

A robust quantitative depth estimate can be used to identify a seismic event as an earthquake (too deep to have been a nuclear explosion), reducing the operational burden at the USNDC. Alternatively, deep event discriminants could be formed and ECM could verify the utility of the discriminants for defining the population of deep earthquakes within a formal decision framework. We propose to build a ground truth dataset of events with well-constrained depths using stations close to pockets of deep seismicity, and waveform modeling results for event depth. With a well constrained set of events for both shallow and deep event populations, we will devise event depth discriminants, starting with our ground truth dataset and apply the depth discriminants to all our existing events, identifying and eliminating deep events that are contaminating out datasets for shallow crustal events. After successfully demonstrating useful deep event discriminants with our ground truth dataset, we will move on to look for other deep events in our data for which we do not have a nearby seismic station.

A demonstration of the probable effect of deep events at the array KKAR is shown in Figure 3 below which shows the Magnitude and Distance Corrected (MDAC) amplitude residuals for the P phase versus magnitude on the left and versus distance on the right. The MDAC corrections assume the event is shallow enough to be in the crust and applies corrections for geometric spreading, attenuation and source spectrum assuming a crustal propagation path to the station. Deep events would propagate mostly in the mantle with only a short crustal leg, and our attenuation models are not accurate for the hotter and more attenuating mantle. Also, our magnitudes are derived assuming a crustal path, and may also be incorrect. The vertical arrows show distinctive low residuals at two distance ranges, which we believe correspond to mislocated deep events. The horizontal arrow on the left shows the low residuals are

distributed over a range of magnitudes. In both plots the blue circles are the residuals after the assumed physics of the source, geometrical spreading and attenuation are removed and the red dots are the secondary residuals after linear trends are removed following the physical corrections. Any bias from deep events will contaminate the calibration data and alter the secondary correction.

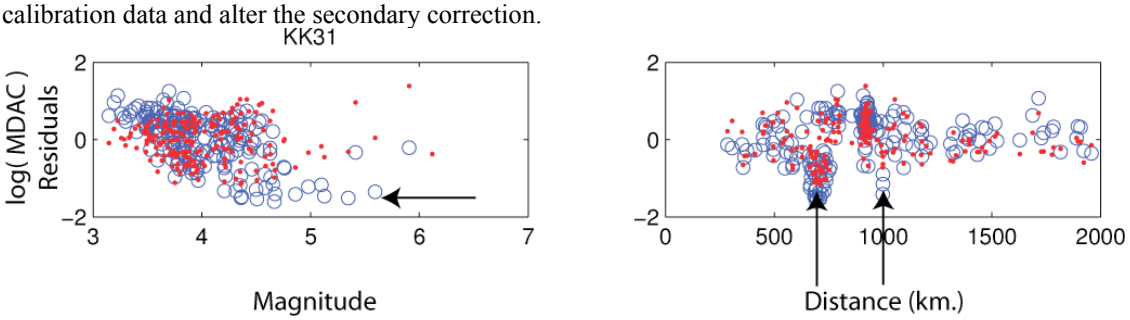

Figure 3. MDAC residuals versus moment magnitude (left) and versus distance (right) for KKAR array element KK31. Blue circles are residuals after removing physical effects of source and path. Red dots are residuals after a final regression. Note low residuals at 700 and 1000 km from KK31. We suspect many of these low-residual earthquakes are sub-crustal, but bulletins listed them at crustal depths.

The residuals should ideally be zero mean if we have accurately removed the effects of the source based on the magnitude and the effects of distance based on geometric spreading and attenuation. These residuals, however, show systematic problems in our MDAC calibration data. We believe that if we can exploit the systematic patterns of residuals with other observables, based on a ground truth set of well constrained deep events, we can develop credible criteria to categorize the events as deep. This will improve the quality of our MDAC residual population, and our event identification results as propagated from MDAC through the ECM products. We anticipate that the shallow, refined event population will show less scatter and bias in terms of MDAC residuals, and will improve the ECM categorization. We also anticipate that we will define MDAC-based discriminants, and possibly other discriminants, that can be applied in the ECM framework, allowing us to recognize deep events based on regional information, even when a nearby station is not available. Hence, we will be able to identify deep earthquakes with small magnitude where teleseismic depth phases are not above noise levels.

As an example of the potential problems with deep events we show the waveforms for a shallow crustal earthquake, a deep sub crustal earthquake, and an explosion in the 1-2 Hz and 6-8 Hz bands all recorded at seismic station MAKZ (shown in Figures 4a and 4b), which is a surrogate for the nearby monitoring array MKAR, and has recorded underground nuclear explosions (UNE's) as well as earthquakes. In the 1-2 Hz band the typical crustal earthquake shows a P wave and a stronger Lg arrival, the deep subcrustal earthquake shows P and S but no discernable Lg, and the UNE shows P, Pg, S. and Lg.

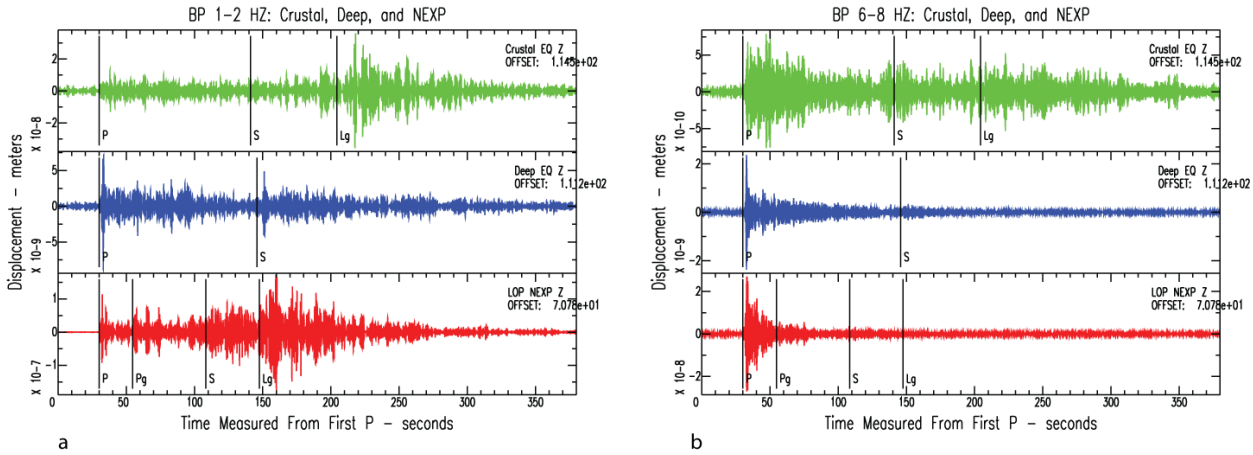

Figure 4. Examples of a crustal earthquakes, a subcrustal earthquakes, and a nuclear explosion from western China recorded at stations MAKZ in Kazakhstan. In (a) all are vertical component seismograms with a 1 to 2 Hz bandpass filter but in (b) bandpass filtered between 6 and 8 Hz. Note the lack of S and Lg for the deep earthquake and the nuclear explosion.

In the 6-8 Hz band (Figure 4b) the appearances change and while the shallow crustal earthquake still shows P and Lg, the S phase is now more visible. In contrast the deep subcrustal earthquake and the UNE now both show only the P wave and visually are not easily distinguished.

We believe that this visual similarity of the UNE and the deep subcrustal earthquake are also reflected in the MDAC residuals, and make the discrimination for ECM potentially complex, requiring additional MDAC ratios. ECM serves as a valuable framework to test hypotheses of a number of MDAC ratios for forming a population of deep subcrustal earthquakes. We can use the Centroid Moment Tensor (CMT) for ground truth estimates of depth (based on the CMT's waveform modeling) as well as the seismic Moment, Mo, and the moment magnitude, Mw, for events large enough for CMT results. The CMT modeling technique has been improved with the inclusion of more regional waveform data, constraining event depths, and producing fewer solutions with fixed depths to stabilize the solution. We may model some events that are too small for the CMT bulletin using our previously developed waveform modeling techniques for estimates of both seismic moment tensor (source mechanism) and event depth. For still smaller sub-CMT sized events, we will rely on accurate depths from events constrained by KBL travel times. Between these depth constraints, we can build a ground truth dataset, make phase amplitude measurements, choose potential MDAC discriminants, and test the utility of these discriminants with the statistically rigorous ECM framework, keeping the most successful discriminants. With CMT (and perhaps also with KBL-constrained events) we will build a set of deep but still crustal earthquakes (i.e., not in the subducting plate at mantle depths below the overriding plate) to test whether deep crustal earthquakes form a unique population or overlap with shallow crustal earthquakes.

In an example event identification plot of MDAC residuals (Figure 5) including the deep event (waveforms shown in Figures 4a and 4b) shown below, with a deep event as a black diamond, nuclear explosions at the Chinese Lop Nor test site as red stars, chemical explosions at the Former Soviet test site in Kazakhstan as blue stars, and earthquakes as yellow or green circles demonstrates the event identification risk of inadvertently including an unknown deep earthquake. The green circles represent earthquakes near the Chinese test site. The deep earthquake was deliberately added to the population for demonstration, as we do not routinely process known deep earthquakes. The MDAC residual for deep earthquakes is at the high end of the earthquake population, overlaps the nuclear explosion population, and exceeds the chemical explosion population. The deep event could be miscategorized as an explosion, and demonstrates that we may well have a number of other unrecognized deep earthquakes contaminating our study dataset. If we can systematically identify and segregate deep earthquakes as a unique population we will be able to provide enhanced event identification capability and improve the performance of ECM.

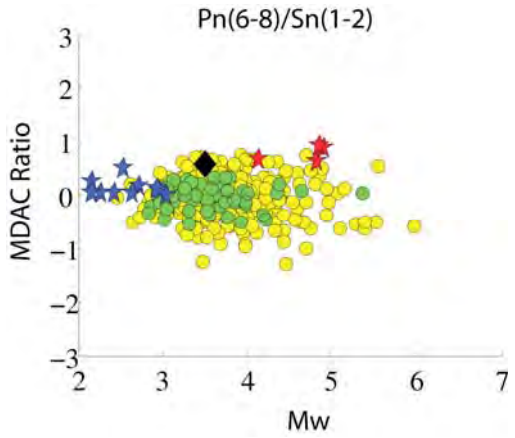

Figure 5. MDAC ratio of Pn in the 6-8Hz band to Sn in the 1-2Hz band for a deep event shown as a black diamond, nuclear explosions as red starts, chemical explosions as blue stars, and earthquakes as yellow and green circles. Earthquakes within 250 km of the nuclear explosions at the Chinese Lop Nor Test site are green. In these and following figures we use data from Global Seismic Network station MAKZ in eastern Kazakhstan, near the IMS array MKAR.

An additional example (Figure 6) for another event with depth ground truth backed up by CMT waveform modeling shows a larger event clearly above the bottom of the nuclear explosion population and in the upper limits of the earthquake population using another MDAC discriminant. This casts suspicion on the higher ratios in the earthquake

population as potentially deep events, which have been mislocated as shallow. The chemical explosions are significantly lower in this example, and we presume that the highest ratio presumed earthquakes are unlikely to be chemical explosions. The lack of solid ground truth for deep events and the potential for significant differences in MDAC ratios for deep events demonstrates the need to carefully develop a ground truth dataset for deep events, and use MDAC ratios to define a separate population of deep events. These example figures show the potential problem of deep events overlapping nuclear explosion populations for these MDAC ratios, and a large population of presumed shallow earthquakes near the explosion population.

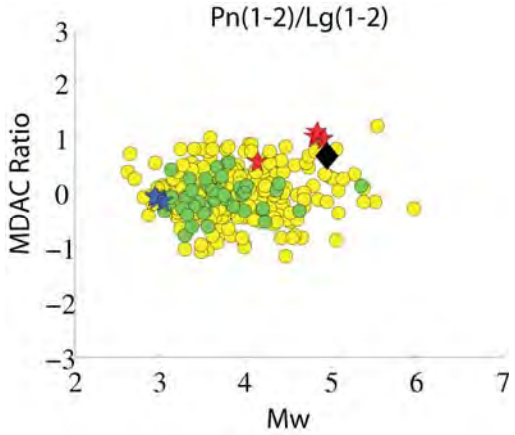

Figure 6. MDAC ratio of Pn 1-2Hz to Pn 6-8Hz which is a candidate for a deep earthquake discriminant. The ground truth deep event clearly is separated from the explosion populations and is near the extreme limits of the earthquake populations. The earthquakes (yellow circles) above the black diamond may be subcrustal events that have been mistakenly located with crustal depths.

In early attempts to find other potential discriminants for deep regional events we have examined other portions of the seismic waveform for amplitudes shown in Figure 7. We observe the lack of Pg relative to Pn for the deeper events.

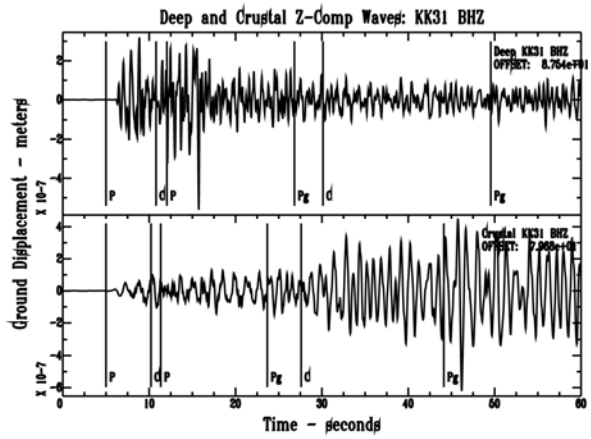

Figure 7. Sample P-waves from station KK31 showing (at top) a deep event (about 180 km) and a crustal event (about 30 km). Both events are about mb 4.8. The shallow event is about 650 km from KK31 and the deep event is about 730 km from KK31. Amplitude measurement windows are marked with "P" (8.2-7.6 km/s) to show the first-P window, "C" (7.7-6.4 km/s) to show the Pn coda window, and "Pg" (6.2-5.2 km/s) to show the Pg window.

We also observe a possible difference between the Pn and Pn coda for shallow and deep events possibly caused by differences in near source scattering. We will need to test all possible discriminants using MDAC for rapid preliminary testing we have used a distance correction which removes observed trends based on ground truth crustal earthquakes. Deep events will have a different propagation path with different attenuation. Figure 8 shows the amplitude ratios for distance corrected amplitudes as a function of both distance and magnitude for two candidate discriminants and shows separation of crustal and deep ground truth earthquake populations. We will want to test

these with full MDAC correction and ECM for performance, and assess datasets with no ground truth depths for possible recategorization of existing mislocated events with poor depth control.

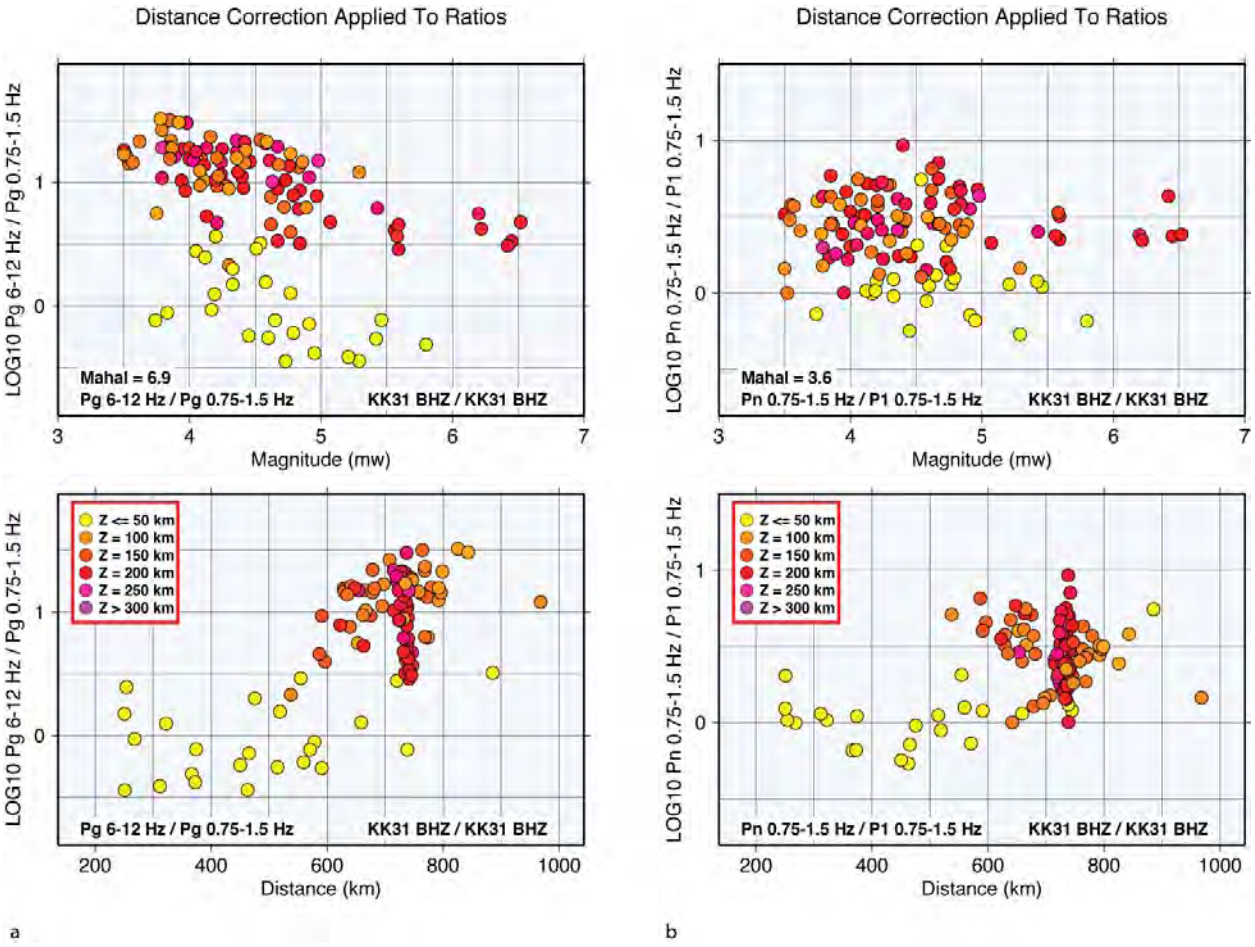

Figure 8. (a) Discrimination plots of Pg spectral ratio (6-12 Hz / 0.75-1.5 Hz) from RMS amplitude measurements (in displacement) made at KK31. Only events with 4 or more teleseismic depth phases were used to make this figure. A distance trend derived from the crustal earthquakes has been removed from all ratios. As the deep events have no true Pg phase, this plot is comparing a phase ratio for the crustal events to a P-coda ratio for the deep events. (b) Discrimination plots of the first-P amplitude in ratio with a P-coda amplitude. See Figure 7 for a description of the P-coda window. Because the P-coda decays more rapidly for deep events compared to crustal events, and because the first-P of the deep events are more impulsive that the crustal events, this discriminant separates the event populations. We will experiment with P-coda window positions and length to attempt to improve this discriminant.

In addition to the separation we continue to observe the systematic variation in residuals for events clustered in a narrow distance range. We will need to investigate this further as it may be an indication of source anomalies for at least a portion of the deep event population. If we can identify and exploit these anomalies, they lead to other candidate discriminants for further evaluation.

CONCLUSIONS AND RECOMMENDATIONS

We developed a small ground truth data set for deep events recorded at regional distances and shown potential discriminants for deep events. We need to develop additional ground truth data for both deep and crustal events in the Pamir Hindu-Kush region with screening events in published earthquake catalogs and merging catalogs with

additional information to relocate events for improved depth control. We also need to pursue all available seismic waveform signatures for deep events recorded at regional distances and test potential discriminants with MDAC and ECM for performance analysis. We further need to use successful discriminants to isolate mislocated deep events from existing calibration datasets and refine the MDAC analysis of those datasets for only the crustal earthquakes to remove any exiting bias from using mislocated deep events.

ACKNOWLEDGEMENTS

We thank Richard Stead for his assistance in updating earthquake catalogs from a variety of sources and updating seismic waveform holdings.

REFERENCES

Chatelain, J. L., S. W. Roecker, S.Hatzfeld and P. Molnar (1980). Microearthquake seismicity and fault plane solutions in the Hindu Kush regionand their tectonic implications, *J. Geophys. Res* 85: No. B3, 1365–1387.

Fan, G., J. F. Ni and T. C. Wallace (1994). Active tectonics of the Pamirs and Karakorum, *J. Geophys. Res* 99: No. B4, 7131–7160.

Frohlich, C. (2006). *Deep Earthquakes*, Cambridge, UK, Cambridge University Press.

Gudmundsson, O. and M. Sambridge (1998). A regionalized upper mantle (RUM) seismic model, *J. Geophys. Res*, 103: No. B4, 7121–7136.

Hartse, H. E., S. R. Taylor, W. S. Phillips, and G. E. Randall (1997). A preliminary study of regional seismic discrimination in central Asia with emphasis on western China, *Bull. Seismol. Soc. Am.* 87: 551–568.

Mellors, R. J., G. L. , M. W. Hamburger, H. J. Al-Shukri and A. A. Lukk (1995). Evidence for a high-velocity slab associated with the Hindu Kush seismic zone, *J. Geophys. Res* 100: No. B3, 4067–4078.

Pavlis, G. L., M. W. Hamburger (1991). Aftershock sequences of intermediate-depth earthquakes in the Pamir-Hindu Kush Seismic zone, *J. Geophys. Res* 96: No. B11, 18,107–18,117.

Pegler, G and S. Das (1998). An enhanced image of the Pamir-Hindu Kush seismic zone from relocated earthquake hypocenters, *Geophys. J. Int.* 134: 573–595.

Roecker, S. W., O. V. Sololeva, I. L. Neresov, A. A. Lukk, D. Hatzfeld, J. L. Chatelain and P. Molnar (1980). Seismicity and fault plane solutions of intermediate depth earthquakes in the Pamir-Hindu Kush region, *J. Geophys. Res* 85: No. B3, 1358–1364.

Schubert, G. (2007). Treatise on Geophysics, Volume 4 Earthquake Seismology, Somewhere, Someplace, Elsevier.

Verma, R.K. and C.C. Sekhar (1985). Seismotectonics and focal mechanisms of earthquakes from Pamir-Hindu Kush regions, *Tectonophysics*, 112, 297–324.

Zhao, L.S. and D.V. Helmberger (1993). Source retrieval from broadband regional seismograms: Hindu Kush region, *Phys. of Earth and Planet. Sci*. 78: 69–95.

Zhu, L, D.V. Helmberer, C.K. Saikia and B.B. Woods (1997). Regional waveform calibration in the Pamir-Hindu Kush region, *J. Geophys. Res*, 102: No. B10, 22,799–22,813.

NUMERICAL SIMULATIONS OF CAVITY RADIUS IN GRANITE: CAVITY BEHAVIOR AS A FUNCTION OF SCALED DEPTH OF BURIAL

Esteban Rougier, Christopher R. Bradley, Howard J. Patton, and Earl. E. Knight.

Los Alamos National Laboratory

Sponsored by the National Nuclear Security Administration

Award No. DE-AC52-06NA25396/LA10-Source-NDD02

ABSTRACT

This paper reports on research activities developed during the first year of this project. The main tasks accomplished and reported in this paper are: a) the development of new computational equation of state (EOS) for granite. One-dimensional calculations using this EOS captures the first principles physics of the near source region and identifies the critical material properties for cavity dynamics. Cavity dynamics are an important consideration for methods that are used to determine accurate estimates of yield under varying emplacement conditions; and b) the extension of the newly developed material models to the analysis of scaled depth of burial and free surface effects in a 2D heterogeneous structure. Efforts in this area are focused on a better understanding of the source stress-cage region as well as free surface Rayleigh and shear wave generation.

A strong motion code for uniform source region structures was used to investigate the dependence of cavity dynamics and final radius on material properties (Young's modulus, shear modulus, gas porosity, overburden, etc.). The material model developed was obtained by taking the PILEDRIVER and the HARDHAT nuclear test events as the main design references. The following aspects of the problem were identified as the driving points when developing the material model: velocity profiles at given stations (near field), source modeling alternatives (iron pill vs. ideal gas vs. Hydses/SESAME), energy partition after the shot, peak velocity and peak displacement attenuation profiles and cavity size as a function of the depth of burial. Previous attempts made with existing material models failed to comply with one or more of the main aspects of the problem. Because of this, a Tillotson type of equation of state with an improved handling of the porosity evolution (crushing and bulking) was implemented, along with a constant yield surface strength model.

The material model developed is used in a set of 2D, axially symmetric simulations aimed at studying the effects of key factors, such as: the variation of the scaled depth of burials (SDoB) and the effects of free surface topography on the cavity dynamics and shear wave generation. A first comparison of the obtained numerical results against the empirical prediction equations shows that the evolution of the calculated final radius of the cavity with the depth of burial is relatively closer to the predictions of Heard's scaling relationship in Mueller and Murphy (1971) than to Denny and Johnson's (1991). Further research needs to be conducted in order to fully understand the cause of the discrepancies between the numerical and the statistical models. Also, the cavity growth, the predicted spall regions, and the seismic radiation associated with the free surface effects are presented.

OBJECTIVES

The NNSA Nuclear Explosion Monitoring Research and Development Roadmaps (2010 these Proceedings) for Ground-Based Systems specifies identification of the sources of waveform signals as an important research and development effort. Source identification is the focus of this project. Understanding the physical basis of seismic wave generation is recognized as the key to advancing our ability to understand and usefully model the explosion source.

The first main objective of the current research is to undertake a series of computer simulations to study the evolution of the cavity radius under different conditions. This phase of computer simulations will employ LANL strong motion codes (CASH) for uniform source region structures (i.e., 1D isotropic velocity models) to investigate the dependence of cavity dynamics and final radius on material properties, such as Young's and shear moduli, gas porosity, overburden (ρgh), regional stresses, etc. The calculations were done using a material having some similarity to the granodiorite that exists at the Democratic People's Republic of Korea (DPRK) test site.

The second main objective of the current work is to perform 2D axially symmetric computer simulations that will introduce 2D sub-surface heterogeneity and free surface topography into the models. Here the focus will be to identify the impact of certain idealized source region structures on the dynamics of cavity growth and on the radiated seismic energy. These 2D structures will be introduced into models of the source region in controlled ways in order to isolate the effects these structures have on the close-in phenomenology and to identify features in the cavity growth and seismic radiation associated with those effects.

RESEARCH ACCOMPLISHED

Modeling an underground nuclear explosion taking into account the propagation of the wave across the elastic region comprises a wide range of physical and thermodynamic phenomena. Four different zones can be identified according to the material behavior. The first zone is called the source region, where the rock and the device material are vaporized due to the huge amount of energy released from the explosion. As the wave created by the explosion propagates outwards the energy dissipates due to mechanical and geometric factors. At a certain range the amount of energy is no longer enough to vaporize the rock but it is sufficient to melt it. This melted region defines the second zone that is called the cavity region. As the wave propagates further the rock material does not melt anymore, but it undergoes plastic deformations. This zone is called the plastic zone. The commonly known *shatter zone* is the first part (closer to the source) of the plastic zone. At a given point located relatively far from the source the material starts behaving elastically, i.e. the elastic zone.

In order to properly account for the wave propagation across all the zones and also for the correct energy deposition in the elastic region of the rock, a series of key constraints concerning each one of the zones must be identified. These constraints are obtained from the available experimental data and are to be employed as design parameters for the purpose of the development of the appropriate material model. In this work, the constraints selected are: velocity and displacement profiles at given stations, energy partition after the shot (for each one of the zones defined above), peak velocity and peak displacement attenuation profiles and cavity size as a function of the depth of burial.

The first part of the modeling effort comprised the development of the material models to be used in the different zones. Regarding the source region, the two most common approaches taken in the past are: iron gas model and the bubble model. The iron gas model assumes that after the explosion an iron gas is formed occupying a relatively small spherical region around the shot point (approximately 1.0 m of radius for a 10 kt source, [Schroeder, 1974]). The initial energy of the explosion is therefore uniformly distributed over this spherical region. The bubble model, on the other hand, considers that the energy of the shot is uniformly distributed over a spherical region with radius equal to the scaled vaporization radius, $r = 2.0\ W^{1/3}$ [Schroeder, 1974], where W is the yield of the explosion, measured in kilotons and r is the radius of the spherical region in meters. Different materials have been used in the past to model the behavior of the "bubble" or source region. The two most common materials employed for this purpose are: ideal gas [Antoun et al., 2001] with a density equal to the density of the rock under consideration, and a tabular equation of state (EOS), i.e., Hydses type of EOS.

The three approaches for modeling the source region that were described in the previous paragraph were tested during the development of the project. However, none of these source models was able to fulfill simultaneously all of the design constraints mentioned before. The results obtained with the bubble model with an ideal gas provided a very good match with the experimental velocity, displacement, peak velocity and peak displacement attenuation profiles. However, it over predicted the final size of the cavity and also the energy distribution at the end of the simulation was not realistic, i.e. the amount of energy remaining in the source region was only 4% of the total

energy of the explosion. It is worth noting that, depending on the size of the "bubble", the amount of energy needed to vaporize the rock contained inside it ranges from 27% to 35% of the total energy of the explosion. On the other hand, the iron pill and the bubble model with the Hydses granite gave reasonably good results for the final cavity size and for the energy distribution across the zones, but both of them under predicted the velocity, displacement, peak velocity and peak displacement attenuation profiles.

The previously described source model approaches arguably do not fully account for the first principle physics of the shock wave continuum from the cavity expansion all the way up to the final energy deposition in the granite elastic region, i.e. there is a gap between the near source region and the near/far field region dynamics. The importance for future studies of this energy deposition and the proper description of the cavity dynamics combined with the shortcomings of the previously available source modeling approaches generated the necessity of finding a different approach regarding the EOS for the source and for the rest of the granite. Because of this, the Tillotson EOS (Tillotson, 1962) was chosen in an effort to find a bridge for the existing gap between the near source physics phenomena and the near/far field observation points. This EOS is an analytical type and it introduces a dependency on the specific internal energy of the material, which makes it suitable to cover all the zones of the simulation grid. The phase change from solid to vapor is also taken into account. According to the state of the material (expansion or compression) and to the level of specific internal energy the Tillotson EOS divides the *p*-*v* space into four different regions, as shown in Figure 1. The Tillotson EOS utilizes a series of parameters to describe the behavior of the material across the different phases. In this work, the parameter set used was based on Melosh, (1989), with some modifications that were introduced in order to adjust the material model to the lab experiment results. The source modeling was done by coupling this newly implemented EOS with the bubble model.

The material model is completed by combining the EOS of the rock with an appropriate strength model. The strength model describes the resistance of the material to shear deformation. For rock-like materials, the shear strength is dependent on the confinement pressure. The main component of the strength model is the so called "yield surface", which describes how the shear strength changes with the confinement pressure. The yield surface used in the current work was derived from the one proposed by Fossum and Brannon (2004). Some modifications were introduced to the original yield surface in order to match the experimental data from the PILEDRIVER and HARDHAT events. It is worth noting that the shear strength material model utilized in this work considers that the yield surface is constant during the whole simulation, i.e. no effects of strain hardening strain softening, high energy states, etc. are taken into account. A more detailed material model is under development, where all of these effects are to be taken into consideration. The yield surface used in the current work is shown in Figure 2.

The PILEDRIVER and HARDHAT events have been extensively studied in the past and very good matches were obtained between the numerical simulation results and the experimental readings for the velocity, displacement, peak velocity and peak displacement profiles (Antoun et al., 2001; Fossum and Brannon, 2004). However, to the authors' knowledge, a complete analysis of these events, where key near source physics parameters, such as the final cavity size and final energy deposition are included along with the near/far field observational data, i.e. peak attenuation profiles and velocity and displacement profiles has not been reported yet. Because of this, the PILEDRIVER and HARDHAT events were revisited in the current work.

The peak displacement and peak velocity attenuation with the scaled range obtained from the numerical simulations using the material model developed are compared to the data from the experiments corresponding to the PILEDRIVER and HARDHAT nuclear events (Rimer et al., 1990) in Figure 3. The material model provides a remarkable good match for the attenuation of the peak displacements of the HARDHAT event. In the case of the attenuation of the peak velocity, the numerical results over estimate the experimental data for HARDHAT. This could be explained by the fact that in the real world there are several dissipation factors that are not currently being considered in the material model, i.e. weathered material, pre existing cracks and faults, non homogeneous material formations, etc. An interesting feature to be extracted from the graphs presented in Figure 3 is the clear demarcation of the elastic limit, i.e. the point where the material ceases to behave plastically (yielding) to start behaving completely elastically. For the material model developed in this work, this threshold is located at a scaled distance of approximately 200 m / $kt^{1/3}$.

The PILEDRIVER event presents a trend that is shifted with respect to the HARDHAT event, even though both of them were conducted on the same type of material (NTS granite). Further research is being conducted to try to explain the discrepancy between the data for PILEDRIVER and HARDHAT.

As the energy from the source propagates across the computational model a certain amount of work due to compression is done on the cells of the model. This work, which is essentially $p\,dv$, where p is the pressure and dv is

the volume change, increases the specific internal energy of the cell, therefore increasing its temperature. When the specific internal energy reaches a given value, the material starts to melt. As it was already pointed out before, in this work, the position of this melting point was selected as the criterion used to identify where the boundary of the cavity area is located, i.e., the last melted cell, counted by starting from the center of the source, is located and the coordinate of its center is taken as the final cavity boundary in that area.

In the first stage of this project the evolution of the final cavity size with the depth of burial was investigated with the help of a 1D spherical computational model. A constant overburden pressure, corresponding to the working point depth, was applied to the whole model. The results obtained for the evolution of the final cavity size as a function of the depth of burial are shown in Figure 4.

It is worth noting that Heard's equation for the cavity radius used for the Mueller and Murphy (1971) curve in Figure 4 was

$$r_c = 16.3\, W^{0.29}\, C\, h^{-0.11} \tag{1}$$

where W is the yield in kilotons, h is the depth of burial in meters and C is a material dependent constant given by

$$C = E^{0.62}\, \rho^{-0.24}\, \mu^{-0.67} \tag{2}$$

where E and μ are the Young's and shear moduli respectively and ρ is the material density. In our calculations

$$C = 1.4616 \tag{3}$$

The equation used for the *Denny and Johnson* [1991] curve in Figure 4 was

$$r_c = \frac{14700 W^{1/3}}{\beta^{0.3848} P_0^{0.2625}} \tag{4}$$

where β is the shear wave velocity in meters per second and P_0 is the overburden pressure in Pascal. The numerical values for the material properties used in this paper are given by

$$\begin{aligned} E &= 73.92 \text{ GPa} \\ \rho &= 2680 \text{ kg/m}^3 \end{aligned} \tag{5}$$

The rest of the variables can be derived from these two. The yield was kept constant at one kiloton.

When the shot is done at deeply over buried locations the calculated cavity size is very close to the predictions of Mueller and Murphy (1971). As the depth of burial gets closer to the nominal value, i.e., 125 m for a 1 kiloton source, the calculated final cavity size gets closer to the predictions done by Denny and Johnson (1991).

For the purpose of validation, a comparison of the calculated final cavity sizes for PILEDRIVER and HARDHAT against the measured quantities is presented in Table 1. The calculated values are within 12% of the measured.

The second part of this year's project effort involves the analysis of the cavity size evolution with the depth of burial utilizing a 2D axially symmetric computational model. These 2D simulations are being processed at the time this paper is being prepared. The first results regarding the final cavity size that were obtained from the 2D simulations are confirming the 1D values shown in Figure 4.

As an example of the 2D results, the wave propagation pattern 0.3 s after the shot is shown in Figure 5. The direct P wave resulting from the explosion is shown, followed by the pP wave, which is a result of the bouncing back of the direct P wave against the free surface. The shear pS wave that is generated as a result of the interaction between the free surface and the main wave can also be seen in Figure 5.

The computational model used to simulate the 2D examples presented in this work does not include the possibility of fracturing or spallation inside the rock. In spite of this, a preliminary prediction of the spall areas can still be made with the existing computational tool. Each material has a certain tensile strength that defines when a tensile fracture would start to develop. Tensile stresses are identified by negative pressures in the computational model. In Figure 6 four different snapshots are shown where the spall regions are marked. In this case, the tensile strength of the rock was assumed to be equal to 10 MPa.

Even if the spall areas can be defined, the actual influence of the fracture of the material on the seismic signals is not being properly captured, i.e. an explicit fracture simulation would be necessary to account for this phenomenon. With respect to this matter and as a result of a project that developed over the last years, a state of the art combined finite-discrete element methodology (FEM-DEM) (Munjiza, 2004) was recently implemented within the CASH hydrocode. This new methodology combines the ability of the discrete element method to deal with a large number of interacting particles while keeping the finite volume ability to model the internal deformation of the material. The areas where fracture and/or fragmentation could occur are modeled as a collection of discrete regions or elements connected among them through their common boundaries, giving a continuum like behavior. This connection between the discrete elements is described through the appropriate material fracture variables, i.e. fracture surface energy, maximum normal and tangential displacements, etc. In this way, if the stress state across the discrete element boundaries is such that the fracture toughness of the material is not exceeded, the material behaves as a continuum. However, if the fracture toughness of the material is passed, a transition from continuum to discrete behavior occurs, with a series of fracture patterns as a result. This capability will be very helpful in the future of the project when spallation areas are to be defined, and their effects to be quantified.

One of the main aspects of the simulation of underground explosion is to be able to properly handle extremely high strain rate phenomena. On this matter, the newly implemented FEM-DEM methodology was tested to the extreme, demonstrating that it is up to the challenge (Rougier and Knight, 2010a; Rougier and Knight, 2010b; Rougier et al., 2010a).

CONCLUSIONS AND RECOMMENDATIONS

The source model approaches used in the past arguably do not fully account for the first principle physics of the shock wave continuum from the cavity expansion all the way up to the final energy deposition in the granite elastic region, i.e. there is a gap between the near source region and the near/far field region dynamics. In an effort to try to close this gap the Tillotson EOS was implemented. The verification and validation of this EOS was done by simulating the PILEDRIVER and HARDHAT events. It was shown that the material model developed is in good agreement with the HARDHAT experimental data: velocity and displacement attenuation profiles as well as final cavity radius prediction and expected energy distribution.

This material model was used to predict the behavior of the final cavity size as a function of the depth of burial for a constant yield of one kiloton. The results obtained showed that the locus of the calculated final cavity size is located between the predicted curves of Denny and Johnson (1991) and Mueller and Murphy (1971), as shown in Figure 4. It can be seen from the figure that Denny and Johnson and Heard's curves from Mueller and Murphy have a stronger dependency on the depth of burial than the results obtained from the numerical calculations.

The next steps on the project will be concentrated on the improvement of the current strength model. The main modifications that are planned to be incorporated are: strain softening, strain hardening and high energy effects. A series of sensitivity studies are to be conducted after the improved material model is implemented. These studies will mainly concentrate on the dependence of the final cavity size on the yield of the explosion and on the main material properties (i.e., Poisson ratio, density, "yield surface", etc.) These studies will improve our understanding of the differences between the statistical and calculated hydrocode results.

The capability demonstrated in the present work provides a valuable tool to estimate the characteristics of unknown sources that have been tested on similar materials, like the case of the DPRK test site.

Further studies utilizing the above defined FEM-DEM capabilities coupled with the newly developed equation of state will enable us to reach a new plateau of understanding of how the seismic shear wave generation is affected by the fracture and fragmentation of the material surrounding the source area, and by the spallation of the material located above the working point.

It is worth noting that this new EOS and material model approach combined with the first principles hydrocode will be applied to the National Center for Nuclear Security (NCNS) 2011 studies at the Nevada Test Site (Rougier et al. 2010b).

REFERENCES

Antoun, T. H., I. N. Lomov, and L. A. Glenn (2001). Development and application of a strength and damage model for rock under dynamic loading, *The 38th U.S. Rock Mechanics Symposium*, UCRL-JC-142748.

Denny, M. D. and L. R. Johnson (1991). The explosion seismic source function: models and scaling laws reviewed, *Explosion source phenomenology. Geophysical monograph 65,* American Geophysical Union: 1–24.

Fossum A. F. and R. M. Brannon (2004) THE SANDIA GEOMODEL: Theory and User's Guide. Sandia National Laboratories.

Melosh, H. J. (1989) Impact cratering. A geologic process. *Oxford Monographs on Geology and Geophysics:* 11.

Mueller, R. A. and J. R. Murphy (1971). Seismic characteristics of underground nuclear detonations. Part I. Seismic spectrum scaling, *Bulletin Seismol. Soc. Am.* 61(6): 1675–1692.

Munjiza, A. (2004). The combined finite-discrete element method, *John Wiley & Sons.*

Rimer, N., J. Stevens, and D. Halda (1990). Modeling of the ground motion from events in genetic rocks, *Modeling and Material Properties Working Group of the CAT,* SSS-DVR-90-11661.

Rougier, E., and E. E. Knight (2010a). Slidelines in CASH. Benchmark Tests and Practical Applications. Los Alamos National Laboratory, LA-UR-10-00908.

Rougier, E., and E. E. Knight (2010b). Fracture in CASH - Benchmark Tests and Practical Applications. Los Alamos National Laboratory, LA-UR-10-03254.

Rougier, E., A. Munjiza, C. Bradley, T. Carney, E. E. Knight, and W. M. Brunish (2010a). Geodynamics and geomechanical analysis using combined finite element and discrete element modeling. Los Alamos National Laboratory, LA-UR-10-04033

Rougier, E., E. E. Knight, and W. M. Brunish (2010b). Source Physics Experiments. HANFO Ground Shock Estimates. Los Alamos National Laboratory, LA-UR-10-04449.

Schroeder, R. C. (1974). A comparison of initial conditions for nuclear explosion calculations, UCRL-51671.

Tillotson, J. H. (1962). Metallic equation of state for hypervelocity impact, AF 29(601)-4759, ARPA Order 251-61.

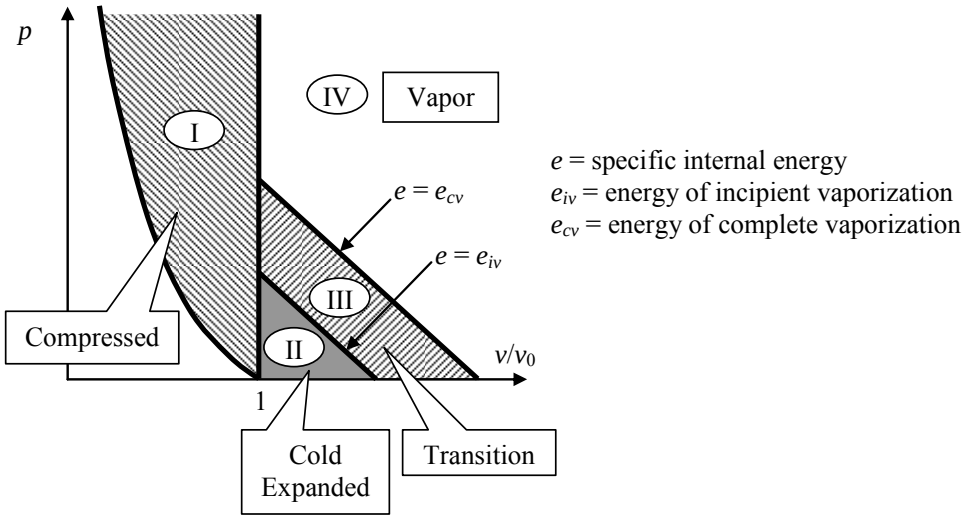

Figure 1. Tillotson EOS. Different phases in the p-v plane. - Phase I: Compressed states for all values of e. Phase II: Expanded state with $e < e_{iv}$. Phase III: Expanded state with partial vaporization $e_{iv} < e < e_{cv}$. Phase IV: Expanded state with complete vaporization $e_{cv} < e$.

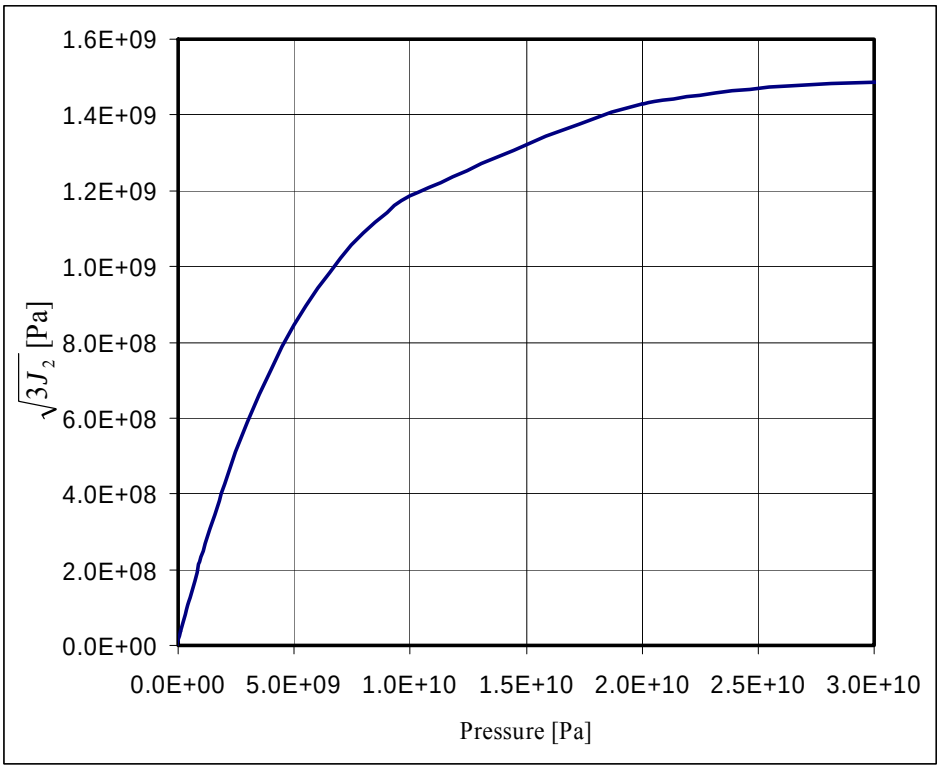

Figure 2. Yield surface used in the simulations presented in the current work.

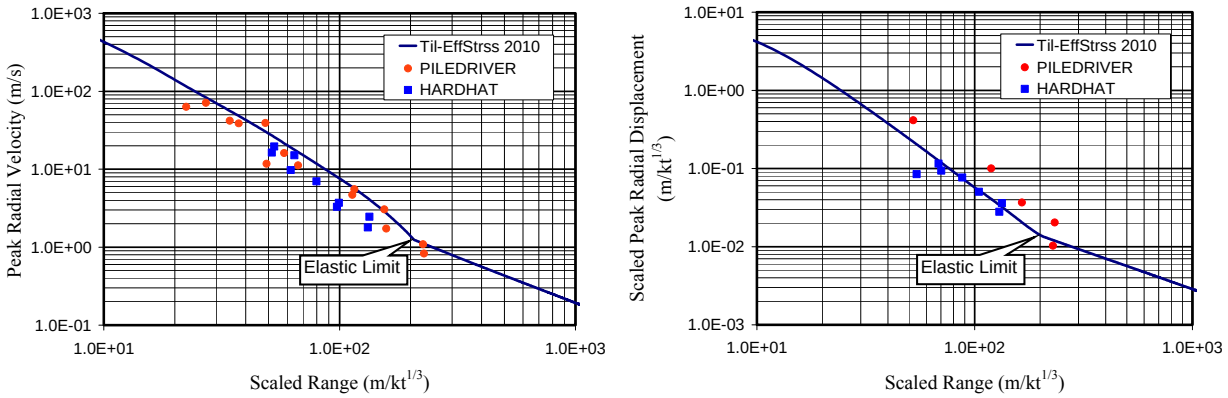

Figure 3. Material model validation: Peak radial velocity (left) and scaled peak radial displacement (right) as a function of the scaled range.

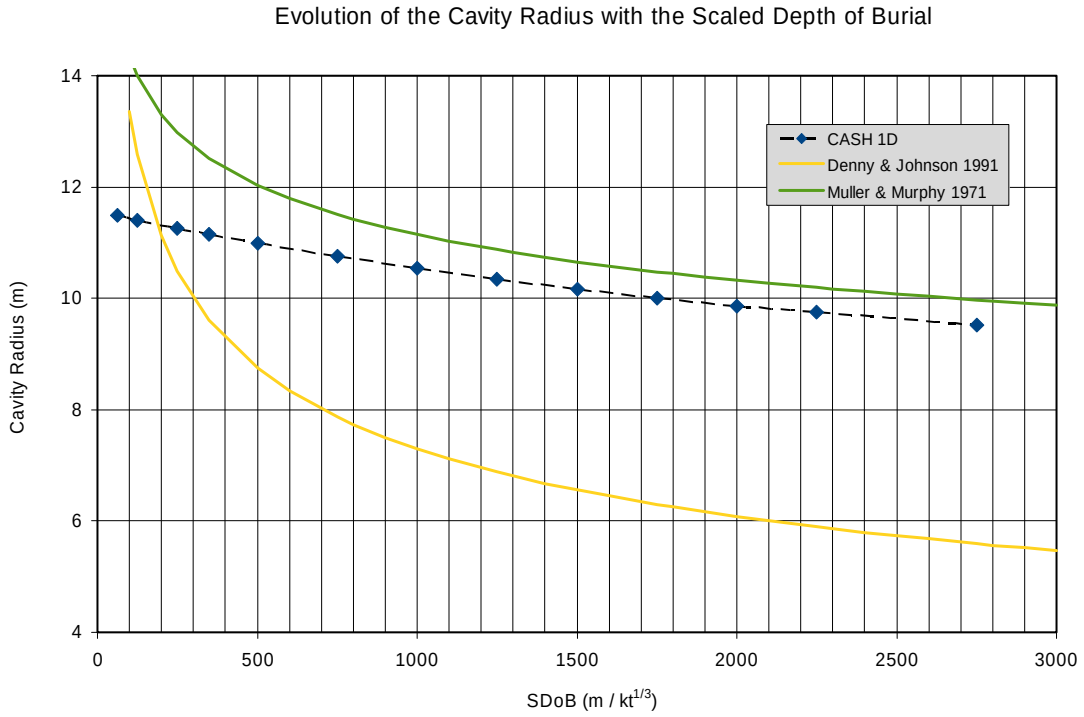

Figure 4. Evolution of the cavity size with the scaled depth of burial. Graphs constructed for a constant yield of 1 kiloton.

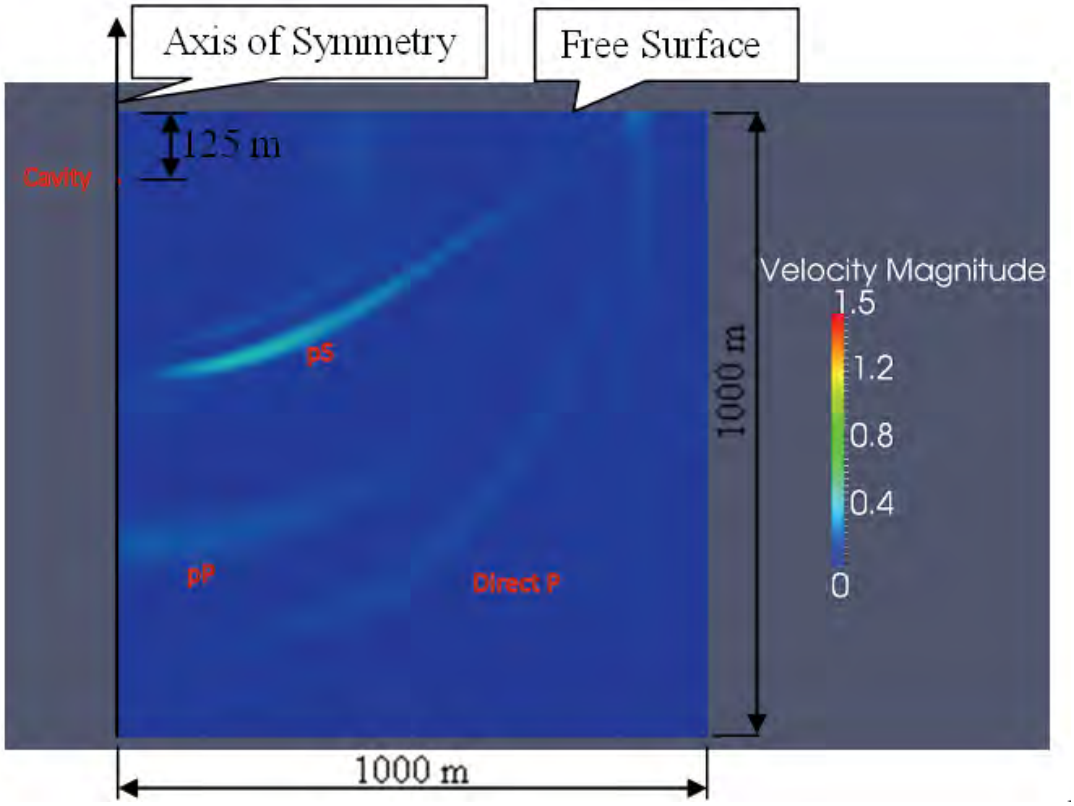

Figure 5. Velocity profile for a 1kt charge buried at nominal DoB (125 m) taken 0.3 sec after the shot.

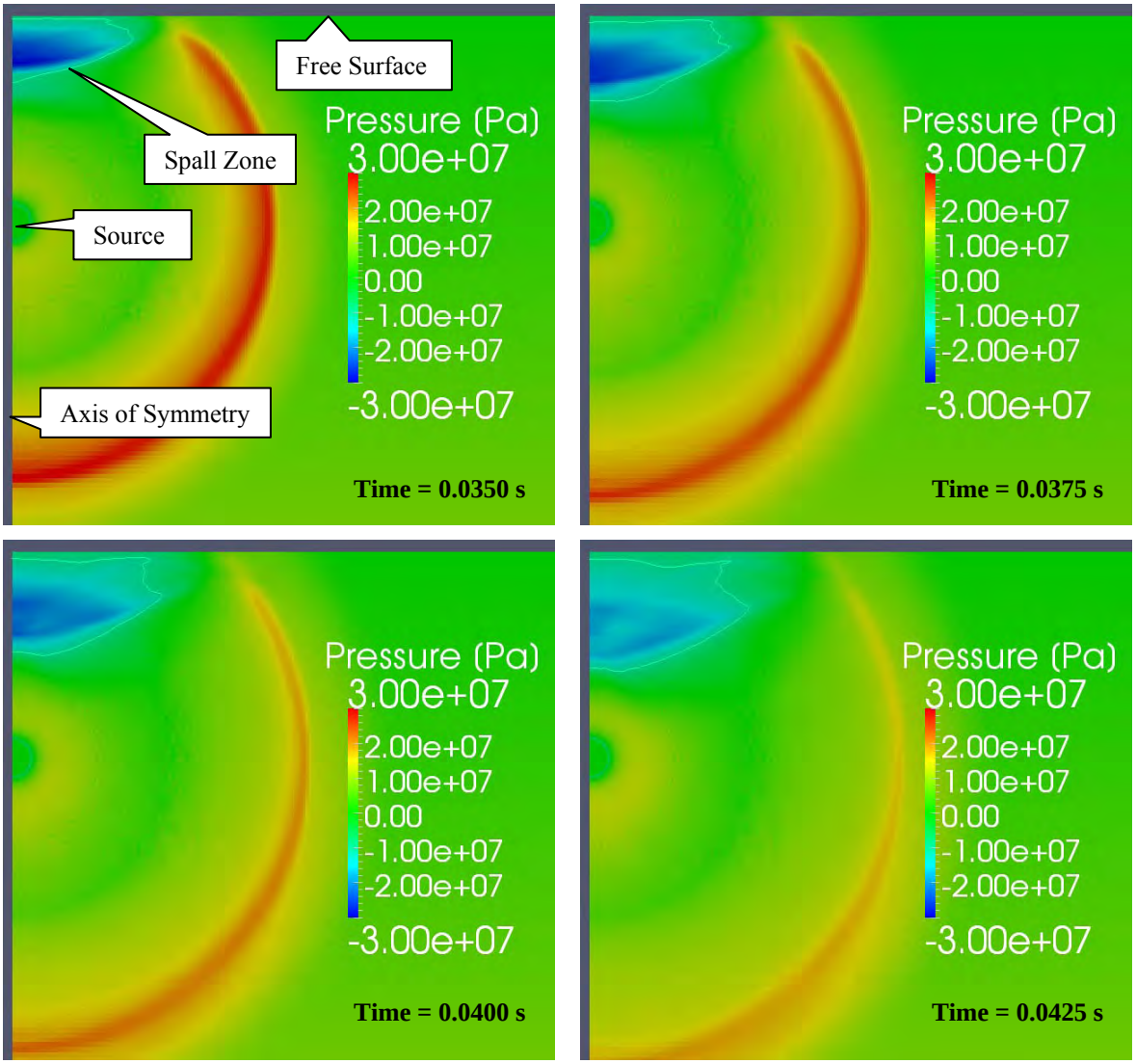

Figure 6. Prediction of the spall zone for a 1kt charge buried at nominal DoB (125 m).

Table 1. Comparison of measured and calculated final cavity radius.

	PILEDRIVER	HARDHAT
Measured Final Cavity Radius (m)	44.5 19	.4
Calculated Final Cavity Radius (m)	42.7 21	.8

MICROMECHANICAL DAMAGE MECHANICS AT HIGH LOADING RATES

Charles G. Sammis[1], Harsha S. Bhat[1,2], and Ares J. Rosakis[2]

University of Southern California[1] and California Institute of Technology[2]

Sponsored by the Air Force Research Laboratory

Award No. FA8718-08-C-0026
Proposal No. BAA08-82

ABSTRACT

Brittle fracture damage in the non-linear source region of a large underground explosion has been shown to make an important contribution to P and S wave radiation, particularly in the near field at frequencies in excess of 1 Hz (Johnson and Sammis, 2001). However, Johnson and Sammis made two simplifications in their model: 1) the stress field produced by the explosion was calculated using an "equivalent elasticity" approximation, and 2) the fracture damage was assumed to be in constant equilibrium with the local stress. Deshpande and Evans (2008) improved on both approximations by 1) calculating the stress field using the ABAQUS dynamic finite element program, and by 2) incorporating a dynamic crack growth law in the Ashby and Sammis (1990) micromechanical damage mechanics. However, the functional form they assume for crack growth is ad hoc and unphysical at very high loading rates. In this paper, we develop a crack growth law based on theoretical models and experimental observations of the nucleation and growth of cracks over a wide range of loading rates. In specific, our new law allows instantaneous acceleration and deceleration of crack growth typically found in explosive shock fronts. We are using the new law to describe dynamic crack growth in the Ashby and Sammis damage mechanics currently implemented in the VUMAT material constitutive subroutine of the ABAQUS finite element program.

OBJECTIVES

The primary objective of this research is to develop and test a physically based constitutive law for the source region of an underground nuclear explosion that is dominated by rock fracture. Our approach is based on micromechanics based damage mechanics in which the nucleation and growth of individual fractures is taken into account and homogenized to obtain a continuum constitutive description. The main advantages of this approach are 1) the size, density and orientations of natural fractures in the rock are physically accounted for in the model and 2) the damage evolution is accounted for by considering the growth of these natural fractures using well-know relations from dynamic fracture mechanics. This model thus offers a natural explanation for the ubiquitous observation of S-wave radiation from explosions. However, our modeling to-date has assumed quasi-static crack growth in which the cracks are always in equilibrium with their surrounding stress field. Experimental observations of crack growth at loading rates comparable to those achieved during nuclear explosions find that crack growth lags behind the applied loads. Our goal, this year, has been to incorporate recent developments in dynamic crack growth into our damage mechanics based constitutive law.

RESEARCH ACCOMPLISHED

Improving the Johnson and Sammis Micromechanical Source Model

Johnson and Sammis (2001) used the Ashby and Sammis (1990) micromechanical damage mechanics to model the Non-Proliferation Experiment (NPE) at the Nevada Test Site in September 1993 (Denny, 1994). They demonstrated that the evolving damage generated significant secondary seismic (P and S-wave) radiation in both near and far-fields. However, an obvious weak point in their approach was the approximate way in which the stresses were calculated, and in particular the empirical way in which the elastic stiffness was adjusted by the evolving damage. However, the most unphysical assumption was the use of the Ashby and Sammis (1990) damage mechanics at the high loading rates that exist in the non-linear source region. The problem is that basic assumption in Ashby and Sammis (1990) is that cracks are assumed to grow quasistatically because the stress intensity factor is always at its critical value. However, at high loading rates, the cracks require a higher value of Coulomb stress to nucleate and, once nucleated, they may not grow fast enough to keep up with the increasing stress. In this case, the stress intensity factor rises above its critical value. The good news is that the accumulation of damage at high loading rates can be modeled since the rate at which the cracks nucleate and grow is a known function of the difference between the instantaneous value of K_I and its critical value K_{IC} and the time rate of change of the stress intensity factor dK_I/dt. Modeling damage accumulation at very high loading rates is one of the primary objectives of the proposed work.

Extending Micromechanical Damage Mechanics to High Loading Rates.

If the history of the crack-tip motion is specified, then the surrounding mechanical fields in an elastic body can be obtained using linear elastic continuum mechanics, as long as the configuration of the body and the details of the loading are specified. However, since the motion of a crack-tip is totally controlled by the deformation state inside the surrounding material, the motion of the crack-tip should not be specified a priori. Due to the fact that the constitutive equation for the material does not include the possibility of material separation, we need a mathematical statement of a crack growth criterion to be added into the governing equations. Such a criterion must be stated as a physical postulate on material behavior at the same level as the kinematical theorems governing deformation, momentum balance principles, as well as the constitutive relation describing material response.

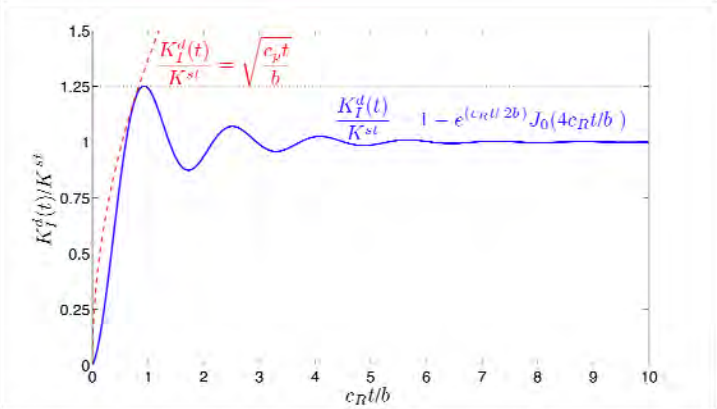

Figure 1. Temporal evolution of the dynamic stress intensity factor, scaled by its static limit.

Thus, to properly solve this problem, one needs to understand the state of stress around a crack-tip (both stationary and propagating) under various loading conditions. These values then need to be compared with experimentally determined fracture toughness of the material, under similar conditions, to develop a crack-growth criterion. The most common form for such a criterion is the requirement that the crack must grow in

such a way that some parameter defined as part of the crack-tip field maintains a value that is specific to the material. This value, representing the resistance of the material to the advance of the crack, is called the fracture toughness (K_{IC}) of the material, and it can be determined through experimental measurements only. In its most general form this can be represented as

$$K_I^d\,[b(t), v(t), P(t), t] = K_{IC}^d\,[v(t), \ldots] \quad (1)$$

where the left hand side of the equation represents the solution obtained from elasticity and the right hand side of the equation represents the material property determined experimentally. Here b, v, and P are the crack length, crack speed, and applied load, respectively.

Dynamic Stress Intensity Factor $K_I^d(t)$

The physical problem at hand involves transient loading of the existing fractures, in the damage mechanics framework, due to an underground explosion. Several authors have studied the problem of transient loading of a crack using analytical and numerical techniques (see Achenbach, 1970; Baker, 1962; Broberg, 1999; Brock, 1991; Freund, 1972a,b, 1973, 1974, 1990; Gross and Seelig, 2006; Kalthoff and Shockey, 1977; Kim, 1979; Kostrov, 1974, 1984; Liu and Rosakis, 1994; Liu et al., 1998; Owen et al., 1998; Ravera and Sih, 1970; Shockey et al., 1983; Sih, 1968; Sih et al., 1972; Zehnder and Rosakis, 1990, among others). The stress intensity factor for transient loading of cracks, referred to as the dynamic stress intensity factor, K_I^d , has two important general characteristics:

1) For a stationary finite crack under transient loading conditions, K_I^d evolves with time following the application of loads. As illustrated in Fig. 1, it rises sharply with time, overshoots the equivalent static value K_{st} by a considerable amount, and then oscillates around the static value with decreasing amplitude. This oscillation is due to the Rayleigh waves traveling back and forth along the surface of the crack with decreasing intensity. This generalized behavior can be summarized by the relationship

$$K_I^d(t) = K_{st}\,\Lambda\,(c_R\,t/b) \quad (2)$$

where Λ is a function of a dimensionless, crack-length-related time $c_R t/b$, describing the oscillation of K_I^d(t) around K_{st}. Here c_R is the Rayleigh wave speed of the material and b is the half-length of the crack. After an early steep increase, Λ reaches a maximum value, and then oscillates around the value 1 with diminishing amplitude, becoming equal to the average value of 1 for longer times. The increase in Λ, before the arrival of reflections, is known analytically (Kostrov, 1974) and is given by

$$K_I^d(t) = K_{st}\,(c_p\,t/b)^{1/2} \quad (3)$$

where c_p is the dilatational or the P-wave speed of the medium. This initial increase and subsequent oscillations can be approximated as

$$\Lambda\,(c_R\,t/b) = 1 - \exp(c_R\,t/2b)\,J_0(4c_R\,t/b) \quad (4)$$

where $J_0(x)$ is the zero'th order Bessel Function. The above equations are plotted in Fig. 1.

2) A second key result was obtained by Freund (1973) who showed that for an unbounded body subjected to time independent loading, the dynamic stress intensity factor at a running crack-tip can be expressed as a universal function of instantaneous crack-tip speed, $v(t)$, multiplied by the equilibrium stress intensity factor for the given applied loading and the instantaneous amount of crack growth i.e.

$$K_I^d\,[v(t)] = k[v(t)]\,K_I\,[b(t)]\;;\;\; k(v) \approx (1 - v/c_R)/(1 - v/c_p)^{1/2} \quad (5)$$

Experimental Observations of K_{IC} at High Loading Rates

As a material parameter, K_{IC} can only be obtained through experimental measurements and is found to vary with loading rate. Under impact loading conditions, high loading rates occur at a pre-existing crack-tip. A parameter $K_{I,\,t}^d$ characterizing the loading rate is defined as

$$K_{I,\,t}^d = K_{IC}\,/\,t_c \quad (6)$$

where K_{IC} is the mode-I critical stress intensity factor at the instant of crack initiation (fracture toughness) and t_c denotes the time from the beginning of loading to the instant at which fracture initiation occurs. Usually, the crack-tip loading rates range from $K_{I,\,t} \sim 1\ MPa\sqrt{ms^{-1}}$ for quasi- static loading to as high as $K_{I,\,t} \sim 10^8$ MPa$\sqrt{\text{ms}^{-1}}$ for impact loading. Due to material inertia and strain rate a material may exhibit totally different behaviors from those under quasistatic loading conditions (Rosakis et al., 1984; Rosakis and Zehnder, 1985). This material property, that depends on the loading rate, is thus called the Dynamic Initiation Toughness, $K_{IC}^{(D)}$, and its quasistatic limit is K_{IC}^{SS}. This can be represented as $K_{IC}^{(D)} = \alpha\, K_{IC}^{SS}$ where $\alpha(\geq 1)$ takes into account the increased initiation toughness due to loading rate and crack-tip bluntness due to plasticity around it (Fig. 2).

Once the crack-tip starts propagating the material resistance ahead of the crack-tip has been shown to depend on the crack-tip speed (Rosakis et al., 1984; Zehnder and Rosakis, 1990). This crack-speed dependent resistance is called Dynamic Propagation Toughness, $K_{IC}^{d}\,(v)$. Liu et al. (1998) explain this in terms of inertial effects associated with the propagating crack-tip. A pre- existing crack in a medium extends in the following way. The stress concentration ahead of the crack-tip loads pre-existing flaws that ultimately fail and coalesce with the crack-tip thus extending it further. If this crack-tip is now moving then the inertial effects will result in less enhanced crack-tip stresses, thus delaying the loading of these flaws, making the material appear more resistant to a growing crack. These experimental observations have been summarized in Fig. 2. Liu and Rosakis (1994) represented this as

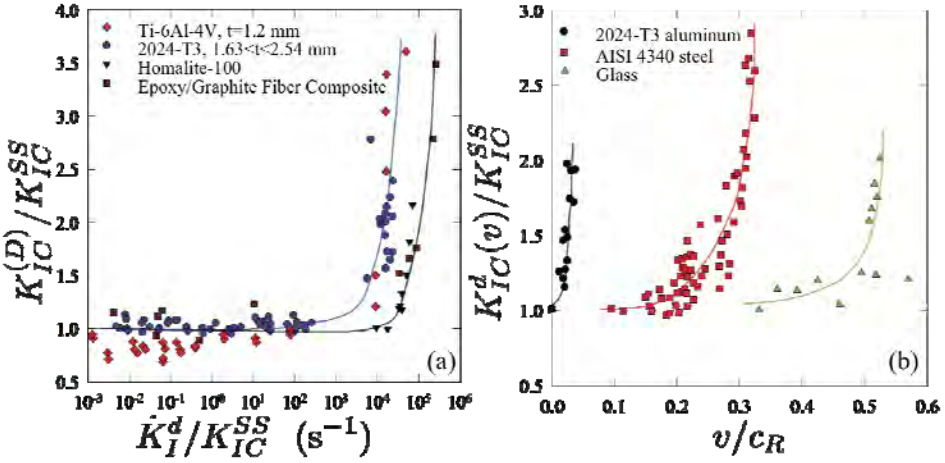

Figure 2. (a) Normalized dynamic $K_{IC}^{(D)}$ for fracture initiation as a function of loading rate for several materials. (b) Normalized K_{IC}^{d} for fracture propagation as a function of crack-tip velocity for various materials.

$$K_{IC}^{d}(v) = f(v)\, K_{IC}^{SS}\ ;\ \ f(v) = [1 + (1/M)\tan(\pi v/2v_m)] \,/\, (1-v/c_p)^{1/2} \qquad (7)$$

where M and v_m are two material constants fit to the data.

Crack-tip Equation of Motion

Based on the experimental observations discussed above we are now in a position to write an expression that describes both the initiation and growth of fractures at high loading rates.

Initiation Criterion: The crack will initiate motion when $K_I^{AS}\,(K_{I,\,t}^{AS}) = K_{IC}^{(D)}$ where K_I^{AS} is the stress intensity factor from Ashby and Sammis (1990).

Growth Criterion: During the process of crack growth, if the small scale yielding condition prevails, the fracture criterion stipulates

$$K_I^{d}\,[t] = K_{IC}^{d} \qquad (8)$$

where the left-hand side is the dynamic stress intensity factor (in principle entirely determined through an analysis of a boundary/initial value problem) and the right-hand side represents a material quantity called the dynamic fracture toughness that can only be determined through experiments. The above equation is an evolution equation for crack growth, i.e., a crack-tip equation of motion, since it represents a nonlinear, first order differential equation for the crack length $a(t)$. For the specific problem at hand, the dynamic stress intensity factor for the propagating crack is given by

$$K_I^d\,[t] = k[v]\,K_I^{AS}\,[D(t)/D_o]\;\Lambda(c_R\,t/b)\;;\;\; k(v) = (1-v/c_R)/(1-v/c_p)^{1/2} \tag{9}$$

where $K_I^{AS}\,[D(t)/D_o]$ is the stress intensity factor from Ashby and Sammis (1990) and D/D_o depends only on the crack length. As for the dynamic fracture toughness, one usually assumes that it is only dependent on the crack-tip velocity and on material characteristics. We can thus express

$$K_{IC}^d(v) = f(v)\,K_{IC}^{SS}\;;\;\; f(v) = [1 + (1/M)\tan(\pi v/2v_m)]\,/\,(1-v/c_p)^{1/2} \tag{10}$$

Combining the above equations, one now gets a non-linear equation for crack-tip motion as,

$$k(v)\,K_I^{AS}\,[D(t)/D_o]\;\Lambda(c_R\,t/b) = f(v)\,K_{IC}^{SS} \tag{11}$$

This expression will be incorporated into the damage module in ABAQUS to replace the ad-hoc growth law currently used by Deshpande and Evans (2008).

CONCLUSIONS AND RECOMMENDATIONS

An accurate calculation of the temporal evolution and spatial extent of rock fracture in the source region of an underground nuclear explosion requires incorporation of dynamic fracture mechanics into the micro-mechanics based constitutive laws currently used to describe the fracture damage dominated regime. Experimental observations of crack nucleation and growth, at a wide range of loading rates, have shown that the material properties pertaining to fracture are sensitive to loading rates, particularly in high loading rate regimes like in underground nuclear explosions. These material properties combined with well known theoretical and numerical observations about dynamic crack growth provide an equation of motion for the crack-tip (crack growth law) that will be implemented in our fracture damage based rheology.

We plan to use this new formulation to recalculate the Johnson and Sammis (2001) simulation of the 1993 Non-Proliferation Experiment, and to simulate recent chemical explosion in a granite quarry conducted by New England Research and Weston Geophysical.

REFERENCES

Achenbach, J. (1970). Extension of a crack by a shear wave, *Z. Angew. Math. Phys.* 21(6): 887–900.

Ashby, M. F., and C. G. Sammis (1990). The damage mechanics of brittle solids in compression, *Pure and Appl. Geophys.* 133: 489–521.

Baker, B. (1962). Dynamic stresses created by a moving crack, *J. Appl. Mech.* 29(3): 449–458.

Broberg, K. B. (1999). *Cracks and Fracture.* Academic Press.

Brock, L. M. (1991). Exact transient results for penny-shaped crack growth under combined loading, *Int. J. Solids. Struct.* 28(4): 517–531.

Denny, M. D. (1994). *Introduction and highlights,in Proceedings of the Symposium on the Non-Proliferation Experiment (NPE): Results and Implications for Test Ban Treaties*, M. D. Denny (editor), CONF-9404100, Department of Energy.

Deshpande, V. S., and A. G. Evans (2008). Inelastic deformation and energy dissipation in ceramics: A mechanism-based constitutive model, *J. Mech. Phys. Solids* 56(10): 3077–3100.

Freund, L. B. (1972a). Crack propagation in an elastic solid subjected to general loading-i. constant rate of extension, *J. Mech. Phys. Solids* 20(3): 129–140.

Freund, L. B. (1972b). Crack propagation in an elastic solid subjected to general loading-ii. non-uniform rate of extension, *J. Mech. Phys. Solids* 20(3): 141–152.

Freund, L. B. (1973). Crack propagation in an elastic solid subjected to general loading-iii. stress wave loading, *J. Mech. Phys. Solids* 21: 47–61.

Freund, L. B. (1974). Crack propagation in an elastic solid subjected to general loading.-iv.obliquely incident stress pulse, *J. Mech. Phys. Solids* 22: 137–146.

Freund, L. B. (1990). *Dynamic Fracture Mechanics*. Cambridge University Press, Cambridge.

Gross, D., and T. Seelig (2006). *Fracture mechanics: With an introduction to micromechanics*. Springer Verlag.

Johnson, L.R. and C.G. Sammis (2001). Effects of rock damage on seismic waves generated by explosions, *Pure Appl. Geophys.* 158(11): 1869-1908.

Kalthoff, J. F., and D. A. Shockey (1977). Instability of cracks under impulse loads, *J. Appl. Phys.* 48: 986–993.

Kim, K. S. (1979). Dynamic propagation of a finite crack, *Int. J. Solids Struct.* 15: 685–699.

Kostrov, B. V. (1974). Propagation of a crack with variable velocity, *Prikl. Mat. Mekh.* 38: 551–560.

Kostrov, B. V. (1984). On the crack propagation with variable velocity, *Int. J. Fract.* 26(4): 370–379.

Liu, C., and A. J. Rosakis (1994). *Investigation of transient effects for dynamically initiating and growing cracks under stress wave loading conditions, in Dynamic Fracture Mechanics*. edited by M. H. Aliabadi, chap. 4, Computational Mechanics Publication, Southhampton, UK; Boston, USA.

Liu, C., W. G. Knauss, and A. J. Rosakis (1998). Loading rates and the dynamic initiation tough- ness in brittle solids, *Int. J. Fract.* 90(1): 103–118.

Owen, D. M., S. Zhuang, A. J. Rosakis, and G. Ravichandran (1998). Experimental determination of dynamic crack initiation and propagation fracture toughness in thin aluminum sheets, *Int. J. Fract.* 90(1): 153–174.

Ravera, R. J., and G. Sih (1970). Transient analysis of stress waves around cracks under antiplane strain, *J. Acoust. Soc. Am.* 47: 875–881.

Rosakis, A., and A. Zehnder (1985). On the dynamic fracture of structural metals, *Int. J. Fract.* 27(3): 169–186.

Rosakis, A. J., J. Duffy, and L. B. Freund (1984). The determination of dynamic fracture toughness of AISI 4340 steel by the shadow spot method, *J. Mech. Phys. Solids* 32(6): 443–460.

Shockey, D. A., J. F. Kalthoff, and D. C. Erlich (1983). Evaluation of dynamic crack instability criteria, *Int. J. Fract.* 22(3): 217–229.

Sih, G. C. (1968). Some elastodynamic problems of cracks, *Int. J. Fract.* 4(1): 51–68.

Sih, G. C., G. T. Embley, and R. S. Ravera (1972). Impact response of a finite crack in plane extension, *Int. J. Solids Struct.* 8(12): 977–993.

Zehnder, A., and A. J. Rosakis (1990). Dynamic fracture initiation and propagation in 4340 steel under impact loading, *Int. J. Fract.* 43(4): 271–285.

WAVE PROPAGATION FROM COMPLEX 3D SOURCES USING THE REPRESENTATION THEOREM

Jeffry L. Stevens and Heming Xu

Science Applications International Corporation

Sponsored by the Air Force Research Laboratory

Award No. FA8718-08-C-0010

ABSTRACT

The objective of this project is to investigate generation of complex seismic waves by explosions in media with 3D heterogeneity using a method based on the exact representation theorem for propagating complex 3D source calculations to the local, regional and teleseismic distances at which they are observed. To accomplish this, we have 1) developed a new three-dimensional nonlinear finite element code CRAM3D, which incorporates all of the nonlinear material models from our well-tested axisymmetric finite difference code CRAM; and 2) developed interface code using the representation theorem to propagate the solution. The interface code uses Green's functions for full-waveform seismograms, modal surface waves and far-field body waves in plane-layered earth models external to the source region and propagates the full 3D solution to any desired location. During the past year, we have implemented a more robust algorithm in the 3D code to improve the grid stability for large grid distortions. Tensile cracking models have also been implemented and tested. As in the 2D code, CRAM3D includes gravity and so can calculate the important nonlinear effects caused by the variation of overburden pressure with depth.

Also during the past year, we implemented the representation theorem for far-field body waves. Although this is the simplest of the three Green's functions, it proved to be the most difficult to implement because it requires exact cancellation of waveforms from different parts of the grid. We reported last year that excellent agreement was obtained between solutions using the representation theorem and analytical solutions for both full-wave solutions and surface wave solutions. The far field body wave solutions (*P, SV,* and *SH* waves) calculated using the representation theorem algorithm are now also in very good agreement with the analytical solutions.

We performed calculations in the presence of topography and lateral elastic and nonlinear heterogeneities in order to look at the effect these variations cause on explosion-generated seismic waves. Two sets of calculations were performed in these heterogeneous structures, the first with a yield of 0.2 kt, the second with yield of 5 kt, each detonated in a spherical cavity with a radius of 5 meters. In the 5 kt explosion, the cavity radius expands to 15 meters above the cavity, 11 meters below and 13 meters to the side. Topography is implemented by gradually distributing offsets of the grid from top to bottom and heterogeneities are implemented by setting different material properties from the background properties in different areas. The results in the presence of topography and lateral heterogeneities show significant tangential wave components due to the asymmetry in the surrounding media in the near field. Nonlinear deformation and tensile cracking are shown to extend to a large distance beyond the cavity radius; about 300 meters varying with direction for the 5 kt explosion. The inelastic regions become non-symmetric, especially near the surface, in the presence of topography and heterogeneities, and cause the tangential motions. The calculations were benchmarked against the equivalent two dimensional axisymmetric calculations for the uniform model, demonstrating the proper numerical implementation of the complex nonlinear materials.

We propagated 3D calculations using the full waveform representation theorem at a local distance of 2.5km, and at a regional distance of 650 km. The results at the local distance show significant tangential motions for the heterogeneous models. For the topographic model the tangential motions are strongly direction dependent and diminish with distance. The surface wave motions are significantly modulated by the topography and lateral heterogeneities whereas the body waves are less affected by the inhomogeneities. We propagate a calculation of a 5 kt explosion at 402 m depth with variable strength across the source region to a distance of 650 km using the representation theorem. There is a strong *SH* component not present in a uniform strength calculation.

OBJECTIVES

The objective of this project is to investigate generation of complex seismic waves by explosions in media with 3D heterogeneity using a method based on the exact representation theorem for propagating complex 3D source calculations to local, regional and teleseismic distances at which they are observed.

RESEARCH ACCOMPLISHED

To accomplish the project objectives, we:

1. Developed a 3D nonlinear finite element code designed for calculation of explosions in 3D heterogeneous media with well-tested material models and including gravity;
2. Implemented interface codes using the representation theorem that propagate the numerical solution from the source region to regional and teleseismic distances;
3. Used the code to evaluate the effect of near source heterogeneity including non-linear material property variations, elastic variability and topography.

The reason that 3D calculations are important for understanding shear wave generation is that symmetry constraints imposed by 1D and 2D calculations act to suppress shear waves. To see this, consider trying to do an explosive experiment in which 2D axisymmetry is imposed. This requires that the motion generated by the explosion be identical in all horizontal directions through propagation of the shock wave, nonlinear deformation of the surrounding material, and rebound to a final state. Since the motion is never identical in all directions, shear waves will always be generated, and in fact shear waves are observed from almost all underground explosions.

An example is shown in Figure 1, which shows near-field radial velocity and displacement from the 12.5-kiloton underground explosion SHOAL, which was detonated at a depth of 370 meters in granite at a location near Fallon, Nevada on October 26, 1963. Seismic instruments were placed in boreholes at shot depth in three directions at a distance of 590 meters from the explosion (Weart, 1965). The observed ground motion was quite different in three directions each separated by about 120º. This asymmetry generates motion across the region of deformation that acts as a secondary seismic source with the form of a horizontal dipole (Stevens and Baker, 2009; Zhou and Harkrider, 1992). Note that the final displacement at station PM-1 to the southwest is negative, while the final displacement at PM-3, to the east-southeast, is positive and large indicating a permanent displacement to the east across the region south of the explosion.

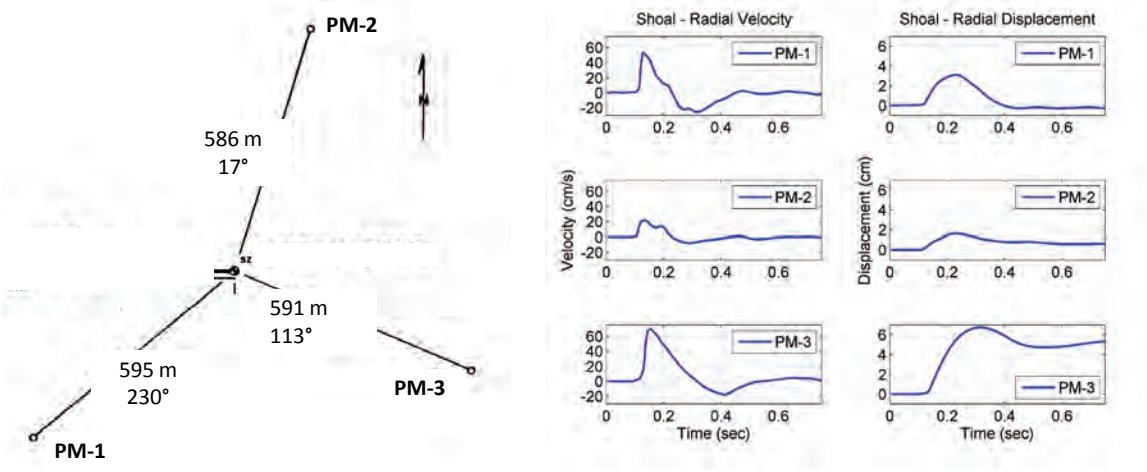

Figure 1. Radial velocity and displacement at shot level in three directions from the 12.5 kiloton underground explosion SHOAL.

The SHOAL example clearly shows substantial heterogeneity in near field motion, and in particular shows motion that differs substantially across the nonlinear region of the event. While the explosion also generates some near-field S that is visible on the vertical and tangential components (not shown), these are high frequency shear waves that may not be visible at regional and teleseismic distances. However, the heterogeneity across the entire source region generates shear waves at lower frequency corresponding to the propagation time across that region. This is

consistent with observations of Fisk (2006, 2007) and Murphy et al. (2009) of *P* and *S* corner frequencies that correspond to the P and S travel times across the source region, respectively.

It is clear that 3D effects in the source region are important and very likely ubiquitous. *SH* waves are commonly observed within a few km of explosions, too close to have been generated by (simple) conversion of vertical and radial components, and often larger than those components. Furthermore, it has not been established what impact 3D effects have on discriminants and on explosion yield estimates. It is important, therefore, to be able to model and understand how 3D source and source region heterogeneity affect the seismic wavefield, and what impact this has on parameters used for nuclear monitoring.

Source Region Calculations and Propagation Using the Representation Theorem

Our approach is to perform 3D explosion source region calculations, and then to propagate the wavefield to local, regional and teleseismic distances using layered earth Green's functions. We are interested in near-source heterogeneities in both the nonlinear and linear regimes, and therefore require both nonlinear and linear 3D codes to model the source region. In previous projects, we have used three nonlinear codes, SKIPPER, STELLAR and CRAM, and the 2D and 3D linear elastic code TRES3D. In the current project, we have developed a 3D finite element code, CRAM3D, based on material models and concepts in axisymmetric CRAM. These codes are described briefly in Table 1.

Table 1. Numerical simulation tools used in this project

Numerical Simulation Tools	
STELLAR	Eulerian finite difference code. Used to simulate the early time history of the explosion shock. It handles material strength correctly, which is difficult for an Eulerian code. Uses second order accurate Riemann solver scheme. 1D, 2D planar and axisymmetric, and 3D.
SKIPPER	One-dimensional spherically symmetric Lagrangian finite difference code. Has been used extensively for free-field explosion modeling.
CRAM	Lagrangian nonlinear finite difference code. Has been used extensively for axisymmetric explosion calculations.
CRAM3D	3D Lagrangian nonlinear finite element code developed during this project. Contains material models also used in CRAM that have been extensively tested.
TRES3D	Elastic finite difference code. 2D planar and axisymmetric, and 3D.
Elastodynamic Representation Theorem	The time dependent displacements and stresses from 3D source region calculations are saved on a monitoring surface located outside of the region of nonlinear response and/or 3D heterogeneity. A numerical implementation of the representation integral is then used to compute the corresponding far-field seismic radiation.

In the three-dimensional numerical finite difference and finite element calculations, we save displacements and stresses due to the seismic source on a monitoring surface on the boundary of a rectangle (5 planar surfaces, excluding the upper surface), and calculate Green's functions from each point on the monitoring surface to the receiver and so the synthetic seismogram at the receiver point *X* outside of the monitoring surface is obtained by integrating over the monitoring surface S_M

$$u_i = \oiint_{S_M} \left\{ G_j^i(\xi; X) * T_j^M(\xi) - u_j^M(\xi) * S_{jk}^i(\xi; X) n_k \right\} dA \qquad (1)$$

in the frequency domain, where $G_j^i(\xi; X)$ and $S_{jk}^i(\xi; X)$ are the Green's function and the stress tensor on the monitoring surface due to a unit impulsive force at *X* in direction *i*, T_j^M is the traction on the monitoring surface due to the seismic source, *u* is the displacement on the monitoring surface, and *n* is the normal to the monitoring surface. The operator * denotes convolution and the summation convention is assumed. We use Green's functions for full waveform seismograms derived from an algorithm based on the work of Luco and Apsel (1983) and Apsel and Luco (1983); modal seismograms using a technique similar to Bache et al. (1982); and far field body waves using a procedure similar to that described by Bache and Harkrider (1976). Our objective in using multiple types of Green's functions is to gain more insight into the nature of the seismic wavefield generated by the source.

Near Field Tests of the 3D Representation Theorem

Two test cases of the representation theorem in 3D are shown below. Figure 2 shows surface motion from a point explosion at 100 meters depth calculated by three different techniques: 1) wavenumber integration; 2) finite difference; 3) finite difference to the surface shown, then by the representation theorem to the receiver. Figure 3 shows the surface motion for an explosion in the same structure plus a low-velocity inclusion between the source and receiver calculated with finite difference and finite difference plus the representation theorem. In both cases, the results are nearly identical, with the largest difference being a reflected phase from the imperfect absorbing boundary in the large finite difference calculations.

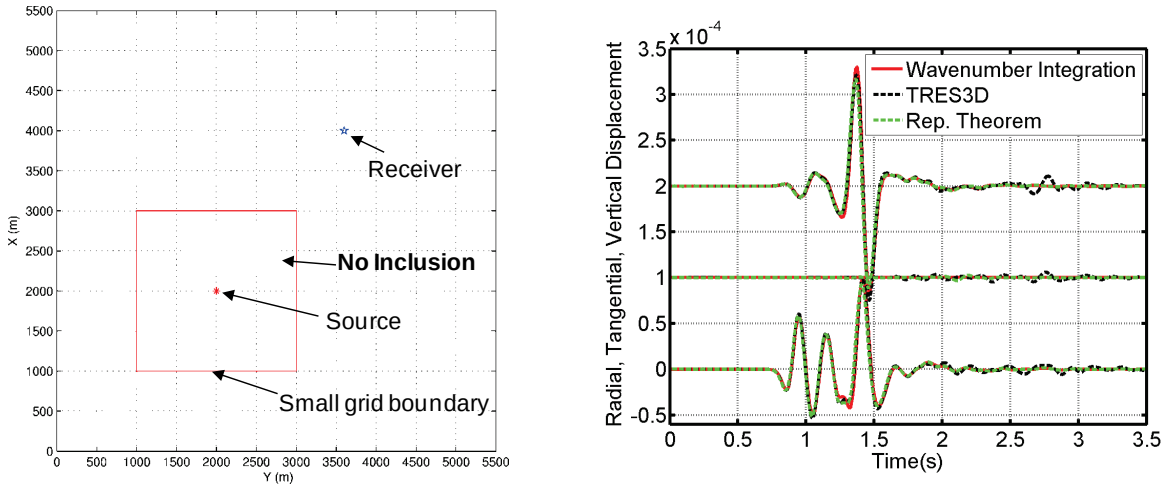

Figure 2. Calculation of surface motion from an explosion source in a plane layered structure by three different methods: wavenumber integration, finite difference and finite difference on the smaller grid plus the representation theorem.

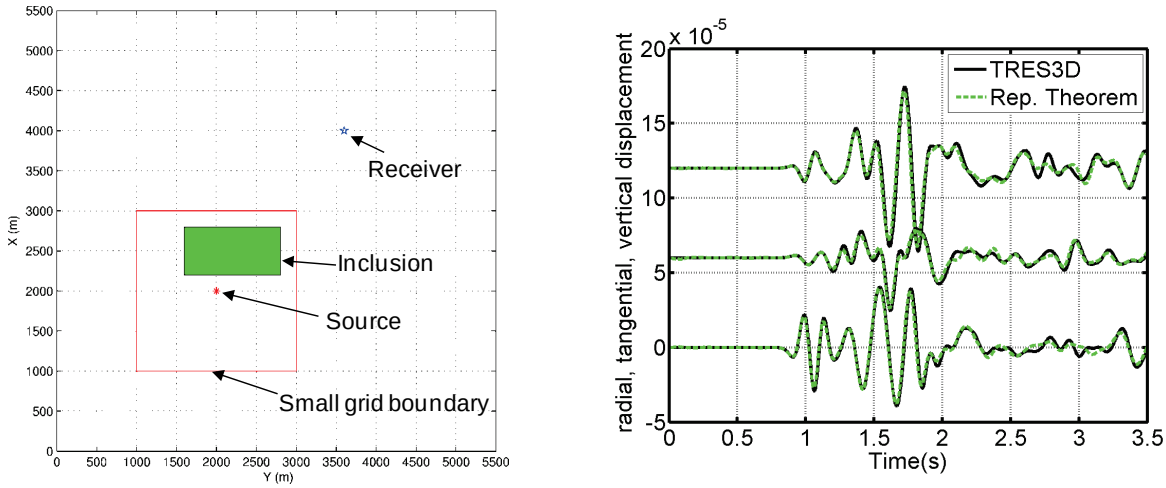

Figure 3. Calculation of surface motion from an explosion source in a plane layered structure with a low velocity inclusion by two different methods: finite difference and finite difference on the smaller grid plus the representation theorem.

CRAM 3D

CRAM 3D is an explicit three-dimensional Lagrangian finite element code designed to run on multiple processors (Stevens and Xu, 2009). For an explosion simulation, the cavity is placed near the center of the grid and is enclosed by a spider grid which facilitates applying the pressure boundary condition and rezoning elements (Figure 4). All of the well-tested nonlinear material models from CRAM 2D have been implemented. The code includes gravity and so includes the important effects that result from variation of overburden pressure with depth. The code also includes tensile cracking. Figure 5 shows a full nonlinear test calculation similar to those discussed earlier for linear elastic calculations.

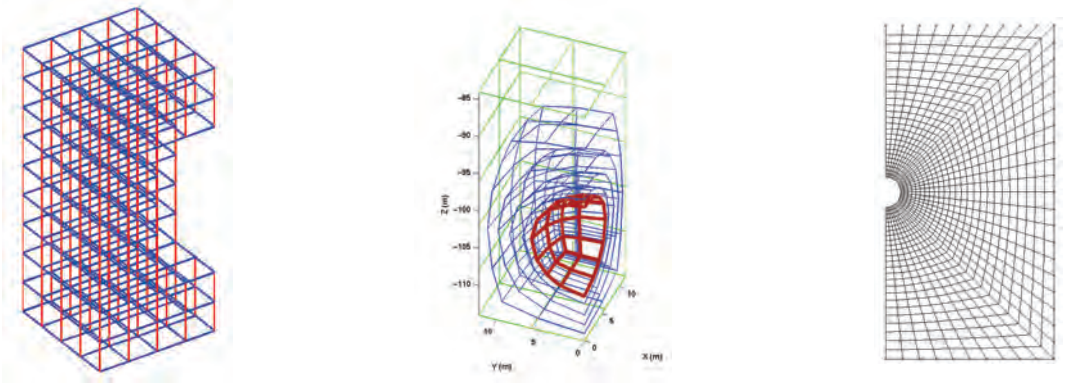

Figure 4. The CRAM 3D finite element outer grid (left) is rectangular. The inner grid (center) is shaped to match the shape of the explosion shock wave. CRAM2D uses a similar axisymmetric spider grid (right) in the region around the explosion.

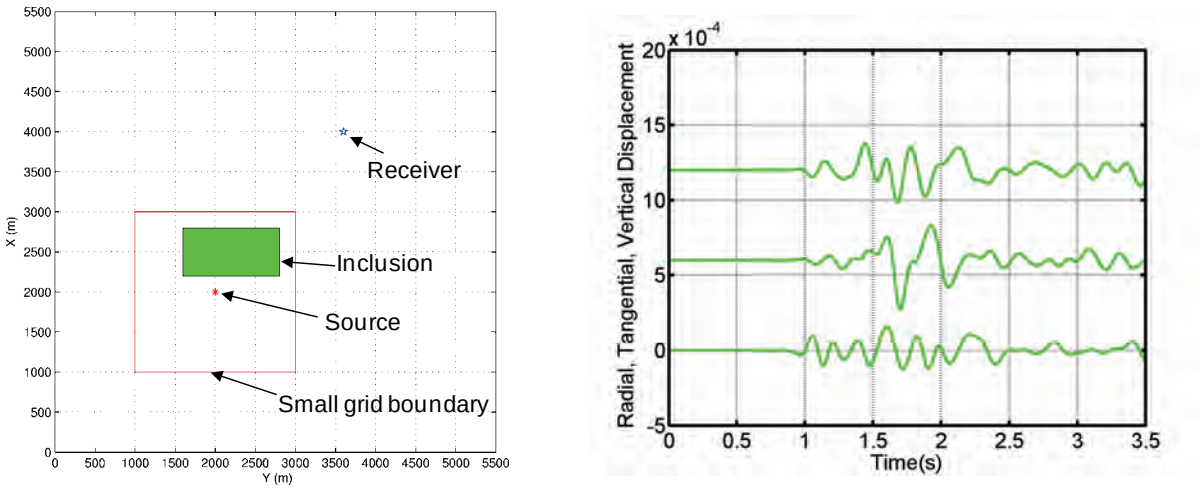

Figure 5. 3D representation theorem test case using CRAM3D with a full nonlinear material model and a 0.5 KT explosion. Initial cavity radius is 5m, which expands to 10.4m. The nonlinear region extends to about 90m. Nonlinear deformation increases the amplitude by about a factor of 6 relative to the linear model (Figure 3). The tangential component is increased more than the vertical and radial.

Figure 6 shows the regions of nonlinear deformation of four 3D nonlinear calculations for a 5 kiloton explosion at 102 meters depth in a half space of Degelen (nonlinear) granite overlain by a shallow linear layer (30m). Calculations were performed for the following four cases: the homogenous (two homogenous layers) medium, a heterogeneous medium with two buried low velocity elastic inclusions, a medium with topography, and a medium with weaker (lower strength) granite on one side of the calculation. In the latter, the weak structure reaches the surface. The heterogeneous model is implemented with homogenous elastic blocks with no nonlinear deformation. The topographic model is implemented with a Gaussian-hill with a peak of 6m, located off the epicenter. Gravity is included in all calculations.

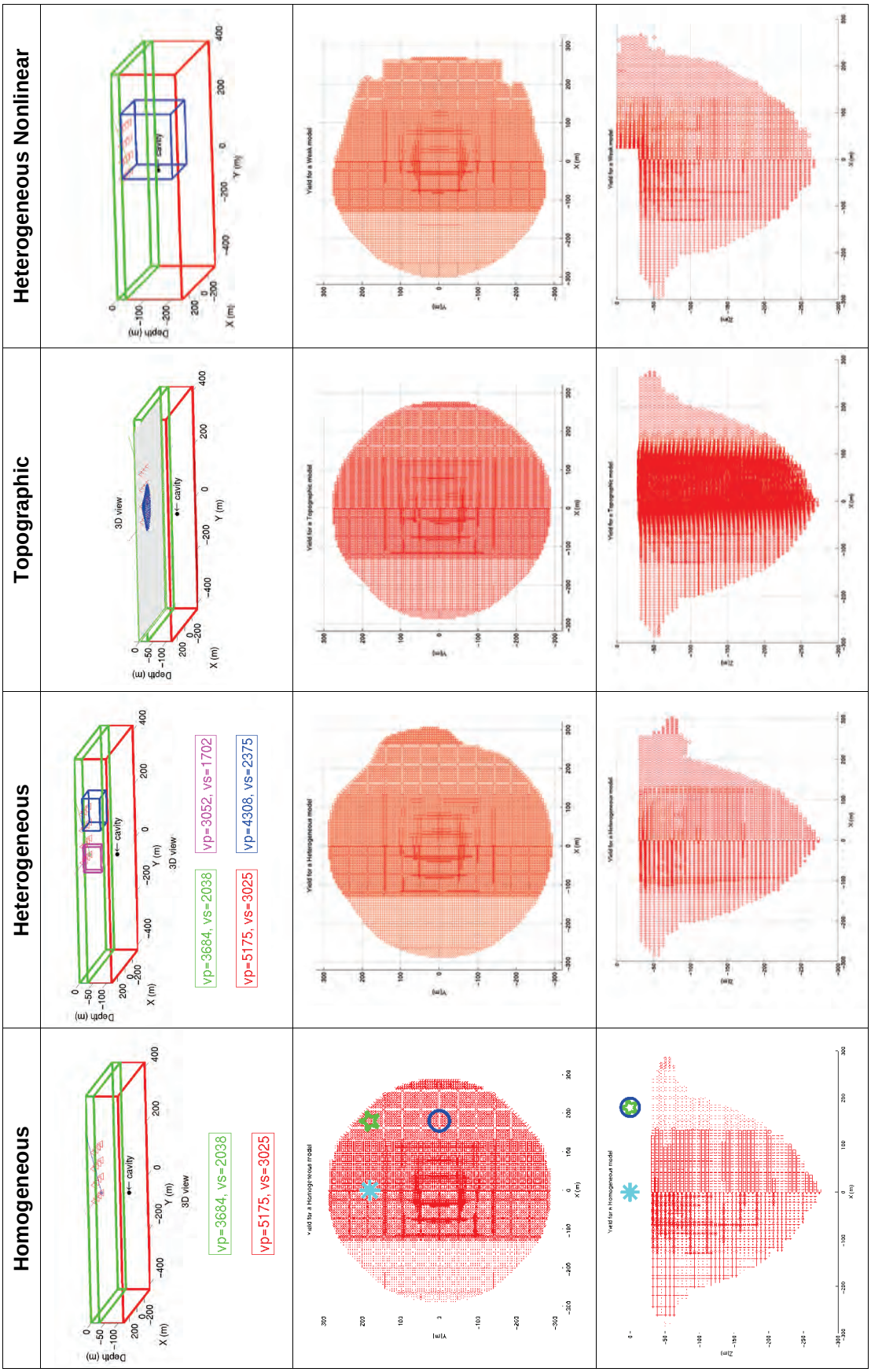

Figure 6. 3D nonlinear calculations for (left to right) a plane-layered structure, a structure with two elastic inclusions within the nonlinear region, a structure with a topographic hill near the explosion, and a plane layered structure with a nonlinear heterogeneity (weakened granite) on one side of the explosion (5 kt). Top row shows the models, the middle row shows a map view of the extent of nonlinear yielding, and the bottom row a cross-section view of the nonlinear region for each calculation. Marks are the location of seismograms shown in Figure 7.

Waveforms from the calculations illustrated in Figure 6 are shown in Figure 7. Note that each of the heterogeneous cases exhibits a substantial tangential component waveform that does not exist in the homogeneous case.

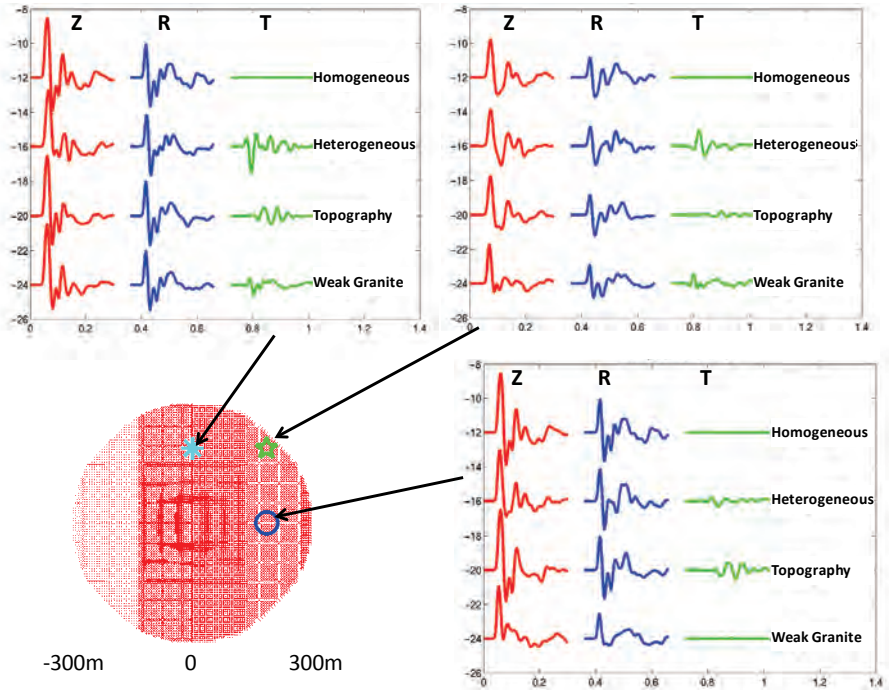

Figure 7. Vertical (red), radial (blue) and tangential (green) waveforms on the free surface at the points indicated by the arrows for the four 5 KT calculations shown in Figure 6.

Tensile Failure

Tensile cracks are calculated using algorithms from Maenchen and Sack (1964) in which crack strains are computed from the applied principal stresses. When the tensile stress exceeds the material's tensile strength, a crack forms normal to the direction of this stress. The 2D algorithms are extended into 3D and the solutions are compared for a spherical cavity in Figure 8. There is good agreement between the solutions at two surface locations 60m and 120m from the epicenter in 2D (red curve) and 3D (blue), demonstrating correct implementation of the crack algorithms extended from 2D to 3D. It also shows that the amplitudes with tensile cracking are higher than without tensile cracking (green curves) due to weakening. Figure 9 shows the tensile crack distributions in 2D and 3D. Both show initiation of tensile cracks near the free surface due to spall and tensile cracks near the pressurized cavity.

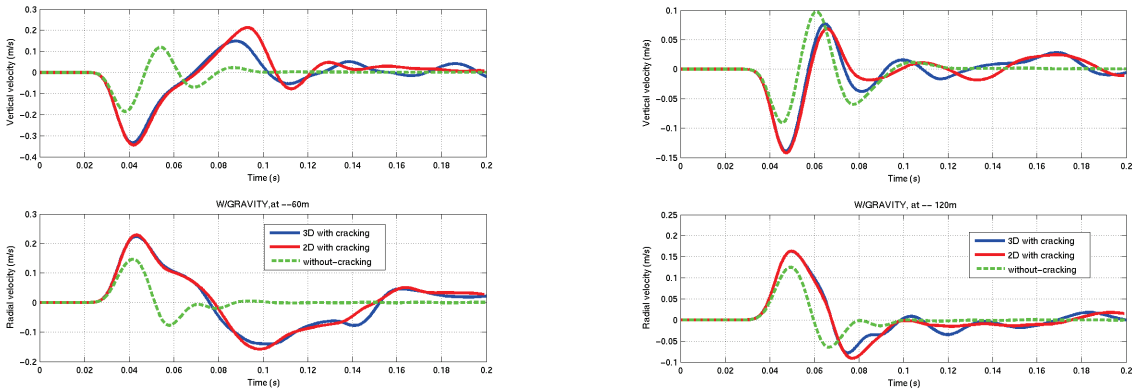

Figure 8. Vertical (top) and Radial (bottom) velocity at the surface at stations 60m (left) and 120m (right) from the point above the explosion. With cracking the velocity at 60m clearly shows evidence of spall as indicated by constant acceleration from 0.04 to 0.10 s. Blue and red curves are 3D and 2D calculations, respectively, with cracking, and the green curve is without. Note the good agreement between the solutions with tensile cracks in 2D and 3D.

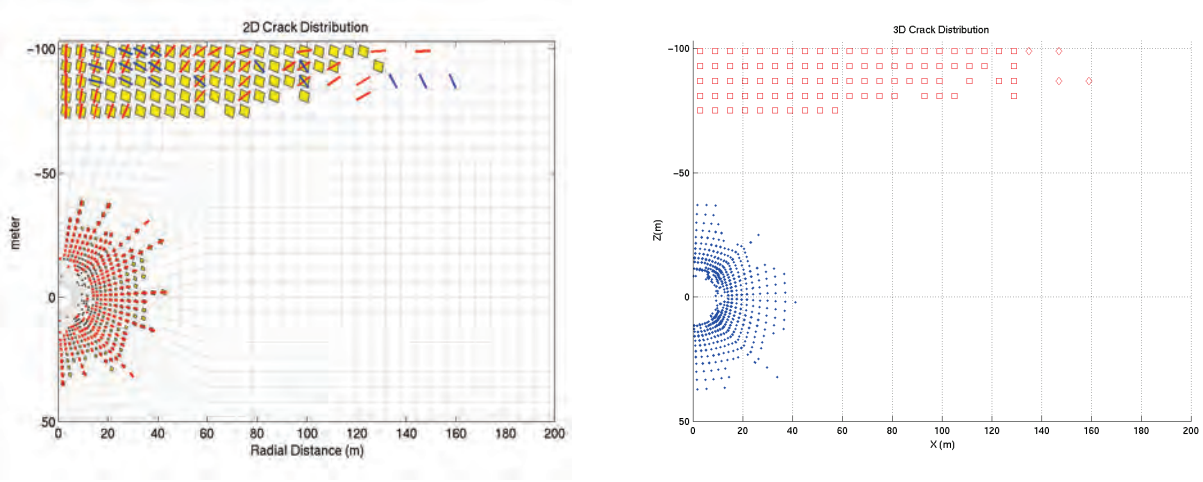

Figure 9. Crack distribution comparisons. Left: 2D crack distribution (symbols indicate the crack opening surfaces); Right: 3D crack distribution in a vertical cross section in which blue symbols indicate the cracks in the inner grid and red squares mark the cracks in the outer grid.

Far Field Propagation of 3D Calculations

Earlier we showed how the representation theorem is used to propagate 3D calculations and showed a full waveform example in the local distance range. Figure 10 shows far-field body waves from two 0.2-kiloton nonlinear calculations: the background structure and the structure with the weak inclusion. The weak rock causes a small amplitude increase in the far-field *P* wave, and otherwise the *P* waves are very similar. However, the heterogeneity causes a substantial *SH* wave to be generated, about 1/3 the size of the direct *P*-wave, which is absent in the background structure. The waveforms in Figure 10 were calculated for a 20º from vertical takeoff angle at an azimuth of 64º. They are broadband waveforms, and so are narrower than observed through typical short-period instruments which filter out the higher frequencies.

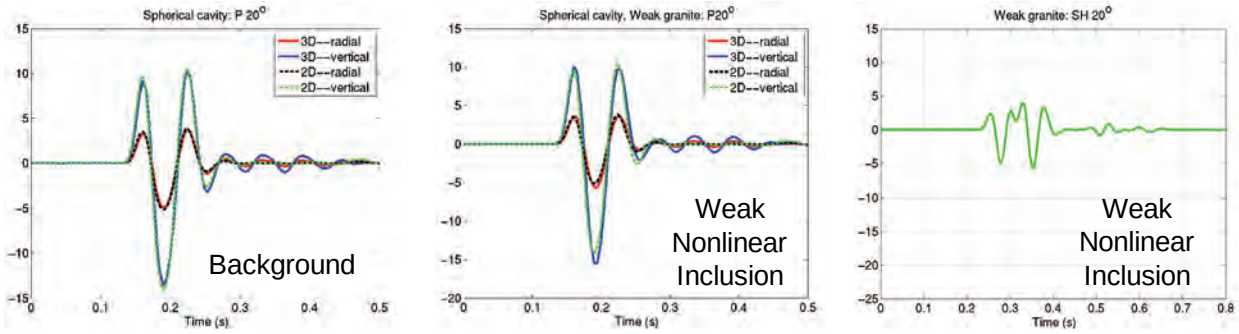

Figure 10. Far field body waves from two 3D nonlinear calculations. Left: *P* waves from the background structure. Middle: *P* waves from the structure with a weak nonlinear inclusion. Right: *SH* waves from the structure with a weak nonlinear inclusion. *P* waves from a 2D axisymmetric calculation in the background structure are shown for comparison on the left and middle figures.

Although the full waveform Green's function generates the entire waveform, the far-field body wave and modal Green's functions are also very useful for gaining insight into the explosion source. The waveforms in Figure 10, for example, are very simple compared to regional full-waveform seismograms and so allow us to distinguish source from propagation effects. Modal Green's functions allow us to separate the fundamental model and higher mode surface waves that are generated at the source.

For a full waveform example at a distance of 650km, we calculate a 5 kt explosion at a depth of 402m in the Degelen structure. The structure layout is similar to the heterogeneous nonlinear structure in Figure 6. The heterogeneous material is weaker than it surroundings. In this calculation, both shear failure and tensile failure are included. Figure 11 shows the nonlinear shear failure extent (top plots) and tensile failure extent (bottom plots) in

the horizontal and vertical views. This demonstrates the asymmetry in nonlinear deformation about the Y axis due to the weak material with symmetry about the X axis. The three rays (blue, green and black) denote the directions of the far field receivers at which the full waveforms are calculated.

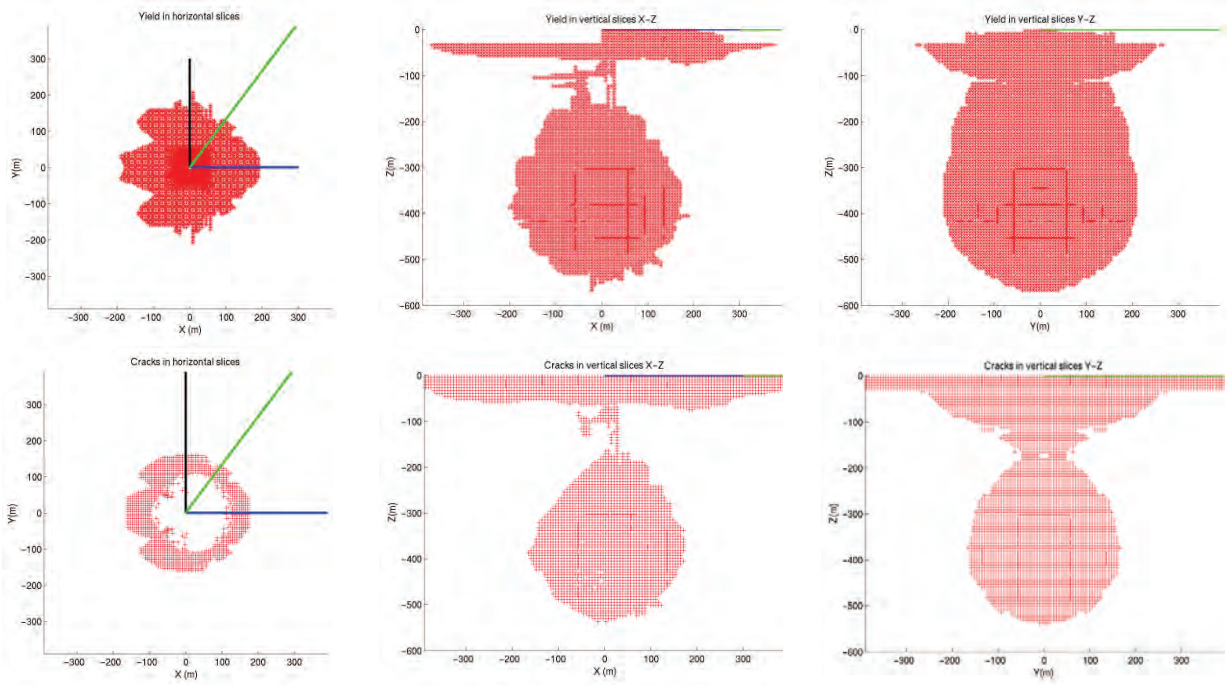

Figure 11. Top: Nonlinear yield extent of a 5 kt explosion. Horizontal and vertical slices are shown from left to right. Bottom: tensile failure. Horizontal slices are at shot level. Note the significant asymmetry about Y of the nonlinear deformation region due to the heterogeneity.

Figure 12 shows these waveforms at 650km. The left, middle and right locations correspond to the directions, black, green and blue, indicated in Figure 11. Each plot shows the radial (red), tangential (green) and vertical components (blue). Due to the heterogeneity and resulting nonlinear deformation asymmetry, these waveforms show significant tangential components for the location on the Y axis although the radial and vertical components show little variations in different directions. The results are consistent with those solutions from a symmetric explosion plus non-zero off diagonal moment components, resulting from the contrast between the weak materials and the adjacent strong Degelen material.

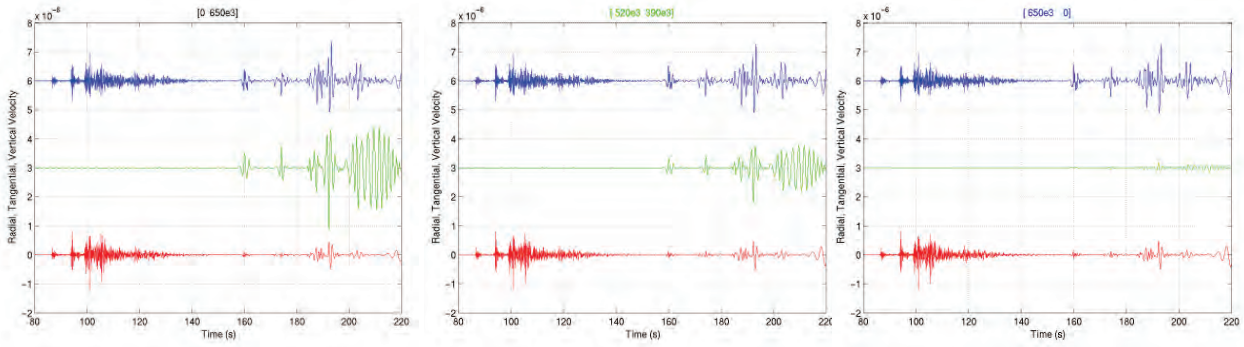

Figure 12. Full waveforms at 650km in the three directions indicated in Figure 11. The left one corresponds to the black line and yields a significant tangential component. The middle corresponds to the green line and the tangential component is reduced. The right one corresponds to the blue line in the symmetry plane so has little tangential component.

CONCLUSIONS AND RECOMMENDATIONS

We have completed development of a 3D version of CRAM, the Lagrangian code used previously for performing axisymmetric calculations of underground explosions. The code includes a tensile crack model and gravity, as well as all of the material models contained in axisymmetric CRAM. We have implemented a procedure for propagating the results of 3D source region calculations to regional and teleseismic distances using the representation theorem to couple source region calculations to wavenumber integration, modal and far-field body wave codes.

Our plans for the remainder of the project are to complete testing of the numerical methods and then perform 3D calculations designed to understand and model the effects of 3D source region heterogeneity and the seismic response to that heterogeneity.

REFERENCES

Apsel, R. J. and J. E. Luco (1983). On the Green's Functions for a Layered Half-Space, Part II, *Bull. Seismol. Soc. Am.* 73: pp. 931–951.

Bache, T. C. and D. G. Harkrider (1976). The Body Waves Due to a General Seismic source in a Layered Earth Model, *Bull. Seismol. Soc. Am.* 66: 1805–1819.

Bache, T. C., S. M. Day and H. J. Swanger (1982), Rayleigh Wave Synthetic Seismograms from Multi-Dimensional Simulations of Underground Explosions, *Bull. Seismol. Soc. Am.* 72: 15–28.

Fisk, M. D. (2006). Source spectral modeling of regional P/S discriminants at nuclear test sites in China and the former Soviet Union, *Bull. Seismol. Soc. Am.* 96: 2348–2367.

Fisk, M. D. (2007). Corner frequency scaling of regional seismic phases for underground nuclear explosions at the Nevada test site, *Bull. Seismol. Soc. Am.* 97: 977–988.

Luco, J. E. and R. J. Apsel (1983). On the Green's Functions for a Layered Half-Space, Part I, *Bull. Seismol. Soc. Am.* 73: 909–929.

Maenchen, G. and S. Sack (1964). The tensor code, in *Methods in Computational Physics*, Vol 3, edited by Berni Alder, 181–210.

Murphy, J. R., B. W. Barker, D. D. Sultanov, and O. P. Kuznetsov (2009). S-Wave Generation by Underground Explosions: Implications from Observed Frequency-Dependent Source Scaling, *Bull. Seismol. Soc. Am.* 99: 809–829, doi: 10.1785/0120080126.

Stevens, J. L., T. G. Barker, S. M. Day, K. L. McLaughlin, N. Rimer, and B. Shkoller (1991). Simulation of teleseismic body waves, regional seismograms, and Rayleigh wave phase shifts using two-dimensional nonlinear models of explosion sources, AGU Geophysical Monograph 65: Explosion Source Phenomenology, S. Taylor, H. Patton, P. Richards, editors, ISBN 0-87590-031-3, 239–252.

Stevens, J. L., N. Rimer, H. Xu, G. E. Baker and S. M. Day (2003). Near field and regional modeling of explosions at the Degelen Test Site, SAIC final report to DTRA, SAIC-02/2050, January.

Stevens, J. L., G. E. Baker, H. Xu, T. J. Bennett, N. Rimer and S. M. Day (2004). The Physical Basis of Lg Generation by Explosion Sources, SAIC Final Report submitted to the National Nuclear Security Administration under contract DE-FC03-02SF22676, December.

Stevens, J. L., S. Gibbons, N. Rimer, H. Xu, C. Lindholm, F. Ringdal, T. Kvaerna, and J. R. Murphy (2006). Analysis and simulation of chemical explosions in nonspherical cavities in granite, *J. Geophys. Res*., 111, B04306, doi:10.1029/2005JB003768.

Stevens, J. L. and G. E. Baker (2009). Seismic wave generation by a non-isotropic explosion source, *J. Geophys. Res.* 114: B12302, doi:10.1029/2008JB005965.

Stevens, Jeffry L. and Heming Xu (2009). Wave propagation from complex 3D sources using the representation theorem, in *Proceedings of the 2009 Monitoring Research Review: Ground-Based Nuclear Explosion Monitoring Technologies*, LA-UR-09-05276, Vol. 1, pp. 574–581.

Weart, Wendell D. (1965). VELA UNIFORM, Project SHOAL, Project 1.1, Free Field Earth Motion and Spalling Measurements in Granite, Sandia Corporation final report VUF-2001 to the Advanced Research Projects Agency, February.

Zhou, L. and D. G. Harkrider (1992). Wave fields from an off-center explosion in an embedded solid sphere, *Bull. Seismol. Soc. Am.* 82: 1927–1955.

RAYLEIGH AND LOVE WAVE MAGNITUDES

Anastasia Stroujkova[1], Jessie Bonner[1], Robert Herrmann[2], and Dale N. Anderson[3]

Weston Geophysical Corporation[1], St. Louis University[2], and Los Alamos National Laboratory[3]

Sponsored by the Air Force Research Laboratory

Award No. FA8718-09-C-0012
Proposal No. BAA09-75

ABSTRACT

We continue to study the M_s(VMAX) surface wave magnitude formula (Russell, 2006). During the past year, we have automated the method for both Rayleigh and Love waves, examined structural effects on the formula in the Middle East, applied the method to Italian earthquakes, and examined performance of the method at the United States Geological Survey National Earthquake Information Center (USGS NEIC). We are also in the process of incorporating a formal discriminant of M_s(VMAX):m_b into the Event Classification Matrix (Anderson et al., 2007). We have applied the M_s (VMAX) analysis (Bonner et al., 2006) using both Love and Rayleigh waves to events in the Middle East, Italy, and the Yellow Sea/Korean Peninsula region.

The Middle East dataset consists of approximately 120 events with reported body wave magnitudes (m_b) between 3.8 and 5.6. We found a significant surface wave magnitude bias between the stations situated to the northwest and northeast from the area of Middle East. We attribute this bias to the surface wave scattering by the Caspian and the Black Seas and the Great Caucasus Mountains.

As a part of this project we examined the validity of the Russell formula for Love waves using the Middle East dataset. We removed the attenuation correction term suggested by the Russell formula and examined the decrease in magnitude as a function of distance for both Rayleigh and Love waves. The attenuation coefficients calculated by fitting a linear regression to uncorrected M_s *(VMAX)* measurements are 0.0037 for the Rayleigh and 0.0042 for the Love waves. Application of the new corrections improves the residuals for the events used in the inversion; however it doesn't improve the RMS residuals for the entire data set.

We studied the relationship between Love and Rayleigh-wave magnitudes for earthquakes occurring in Italy, with a primary focus on the L'Aquila earthquake (6 April 2009 Mw 6.1) and its aftershocks. We have estimated M_s(VMAX) for 125 Italian earthquakes with $2.8 < M_w < 6.1$ at distances ranging from 50 to 414 km. The network-averaged magnitudes show that most of the events (80%) had a Love-wave M_s(VMAX) that was larger (by 0.2 m.u. on average) than the Rayleigh-wave estimate. In addition, we observe larger interstation standard deviation for the Love-wave magnitudes (0.2 m.u.) than for Rayleigh waves (0.17 m.u). Residual M_s(VMAX) estimates (e.g., station minus network average) show no significant distance dependence on the magnitudes; however, there is a clear azimuthal effect on the Rayleigh-wave station residuals.

M_s(VMAX) for Rayleigh waves is currently being tested in the automated USGS NEIC Hydra system. We will present results from the first four months of the test phase, showing comparisons of M_s(VMAX) with other surface wave magnitude formulas and to m_b.

OBJECTIVES

Russell (2006) developed a time-domain method for measuring surface waves with minimum digital processing using zero-phase Butterworth filters. We refer to this technique as M_s(VMAX) for Variable-period, MAXimum amplitude magnitude estimates. The technique was implemented in Matlab (program EVALSURF, Bonner et al., 2006) to estimate variable-period (8 < T < 40 sec) Rayleigh-wave magnitudes for comparison to the historical formulas of Marshall and Basham (1972) and Rezapour and Pearce (1998). The original version of the program requires considerable analyst involvement for the magnitude picking. We recently extended application of the M_s(VMAX) technique to Love waves in attempt to improve seismic event screening using the properties of Rayleigh and Love waves. We are accomplishing this through the development of a Love-wave magnitude formula that is complementary to the Russell (2006) formula for Rayleigh waves

RESEARCH ACCOMPLISHED

Love and Rayleigh Wave M_s(VMAX) in the Middle East

We computed M_s(VMAX) (Bonner et al., 2006) for over 120 seismic events located in the Middle East with reported body wave magnitudes (m_b) between 3.8 and 5.6. The majority of the location and magnitude information (with a few exceptions) was obtained from the NEIC bulletin. The study area (Figure 1) is located in the zone of continental collision between Eurasian, African and Arabian plates. The complex tectonic setting of the region creates highly irregular velocity structure, with rapid changes between the areas with different crustal thicknesses and velocities. One of the world's thickest sedimentary basins is located beneath the Caspian Sea. The South Caspian Basin and has a 15-25 km thick sedimentary layer overlying 10-15 km thick oceanic crust (Neprochnov 1968; Rezanov and Chamo, 1969). This basin forms a deep aseismic depression bounded to the south by the Alborz Mountains in Iran, to the east by the Turkmenistan lowlands and Kopet Dag Mountains of Iran, to the west by the Caucasus Mountains, and to the north by the Apsheron-Balkhan Sill (Priestley and Mangino, 1995).

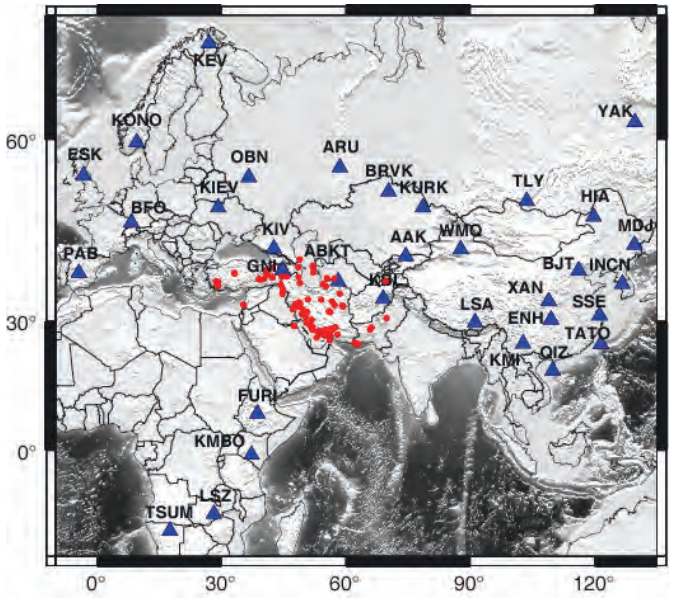

Figure 1. Map of the seismic events (red circles) and stations (blue triangles) used for M_s *(VMAX)* study.

We have applied the M_s (VMAX) analysis to both Love and Rayleigh waves using the Russell (2006) formula:

$$M_s = \log(a_b) + \frac{1}{2}\log(\sin(\Delta)) + .0031\left(\frac{T_0}{T}\right)^{1.8}\Delta - \log(f_c) - 0.43 - 0.66\log\left(\frac{20}{T}\right) \quad (1)$$

The details of the processing used to estimate M_s(VMAX) are described in Bonner et al. (2006). Our initial hope is to be able to use the same formula for both surface wave types.

The M_s(VMAX) computed using Love waves is greater than the magnitude for Rayleigh waves for the majority of the events of larger magnitudes (above m_b~4). For smaller events, however, we observe a large number of events with the Rayleigh M_s(VMAX) exceeding the Love M_s(VMAX). This peculiarity could be caused by either reduced SNR for smaller magnitude events, or by source radiation effects (e.g., due to normal fault mechanisms). In addition regional differences in the wave attenuation and/or anisotropy could cause changes in the amplitudes for the rays traveling in different directions. Since the station coverage is not homogeneous, these propagation effects could potentially result in biases in M_s(VMAX) estimate for smaller events with limited sampling.

Table 1. The average differences between *M_s (VMAX)* measured for each event at a single station and the mean value for all stations. These values represent biases in the magnitude measurements for individual stations.

Station	Bias in M_s *(VMAX)* (in *m.u.*)	
	Rayleigh	Love
ANTO	-0.04	0.13
BFO	-0.16	-0.17
BRVK	0.13	0.07
GNI	-0.05	0.03
KIEV	-0.09	0.02
KIV	-0.17	-0.14

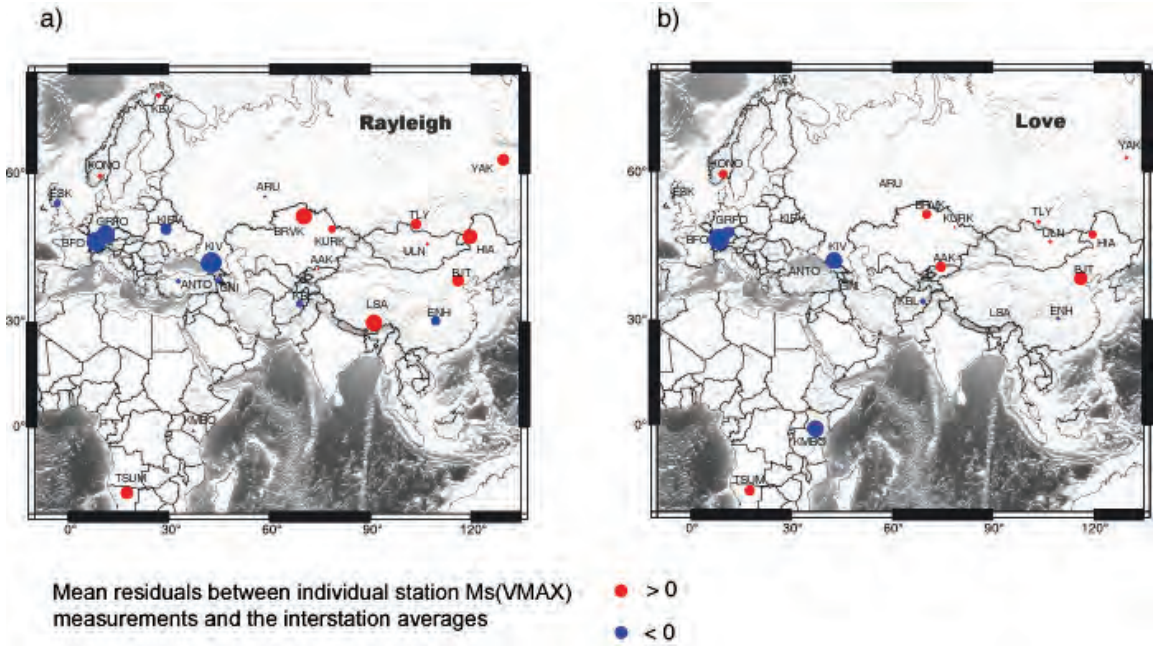

Figure 2. Map of the mean residuals of the station *Ms (VMAX)* estimate as shown in Figure 2: a) *Ms (VMAX)* estimated using Rayleigh waves; b) Love waves.

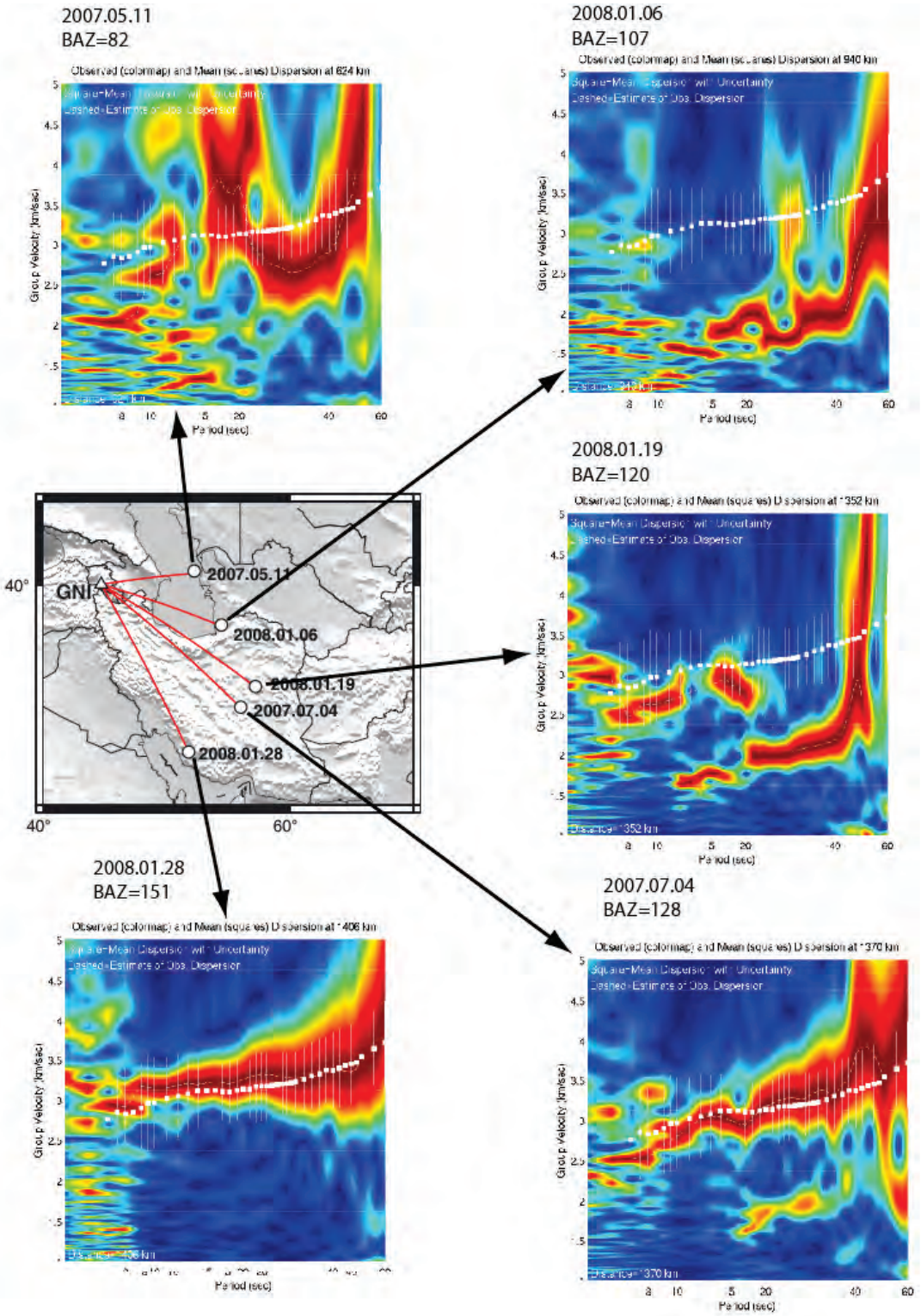

Figure 3. Ray trajectories from selected events to station GNI, showing the influence of the Caspian Sea on Love wave dispersion. The panels surrounding the map show multiple filter analysis results for the Rayleigh waves recorded at the station GNI.

The average M_s *(VMAX)* residuals for each station are shown in Figure 2 with the red circles corresponding to the stations with positive bias, and the blue circles corresponding to the negative bias. Note that the sign of the bias is predominantly negative toward the northwest from the region of study and predominantly positive to the northeast. Negative bias is likely an indication of relatively higher attenuation in that direction. The numerical values of the bias for some of the stations of the region are shown in Table 1. Note that the values of the bias for some stations (e.g., KIV, BFO) are comparable to the M_s *(VMAX)* mean value of the interstation standard deviation computed for the entire dataset (0.2 m.u.). Therefore, determining surface wave magnitudes using different subsets of stations may lead to significant bias, especially for smaller events for which only a limited number of magnitude measurements are available.

To show the effect of the structure variations on the surface wave dispersion, we plotted the results of the multiple filter analysis (MFA), which we used to verify the nature of the phases. Figures 3 show the application of the MFA analysis to the Love waves, in which the dispersion of the trace (illustrated by the colored contours) is compared to the dispersion predicted from the averaged dispersion curve explained earlier (white squares with uncertainty bars connected by the dashed white line). The white dots on each figure show the theoretical (averaged) Love wave group velocities with their error bars. Figures 3 shows rays going trough to Station GNI from different events located to the east from the station, where some of the ray paths cross the Caspian Sea, and others do not. Notice strong dispersion and high velocities for the short periods (less than 20 s) corresponding to the ray paths coming from south and central Iran. The surface waves from events separated by the Caspian Sea, however, are considerably degraded. Notice lowering of the group velocity for short periods (less than 20 s) caused by a thick layer of the sediments. In some cases the maximum of the group velocity becomes less than 2 km/s. The Rayleigh wave results are very similar. Since our processing window for group velocity estimation was between 2 km/s and 4 km/s, the magnitudes for these events could be underestimated. For some ray trajectories (*e.g.* event 2008.01.19) different periods apparently follow separate dispersion curves, which means that these paths go along the boundary between the different tectonic areas. Such complicated wavefield may lead to spurious errors in the magnitude estimation, because the scattered energy adds to the roughness of the spectra used to compute the magnitudes.

Developing Empirical Expressions for Rayleigh and Love Magnitudes

The Russell (2006) M_s formula has opened up new avenues of scientific research, such as the development of improved regional surface wave Q models (Stevens et al., 2006; Levshin et al., 2006; Cong and Mitchell, 2006) that may further reduce interstation variance of the magnitudes. The next step in our project is to either show the validity of Equation 1 for Love waves or to develop a new formula, which takes into account the excitation and attenuation of Love waves. For this task we needed in some instances to use the Russell formula without the attenuation and/or excitation corrections to evaluate the role of each one on Love wave magnitudes. Recalculating M_s(VMAX) without corrections is a time-consuming process, therefore we chose to simply subtract the correction values from already computed M_s(VMAX) values.

In order to find this correction we first need the values without the attenuation and the excitation corrections.

$$M_s(VMAX) = \log(a_b) + \frac{1}{2}\log(\sin(\Delta)) - \log(f_c) - 0.43 \qquad (2)$$

We then solve a system of equations:

$$M_s^{0,i} = M_s^i - a\Delta_j^i \qquad (3)$$

where Δ_j^i is the distance between the i^{th} event and the j^{th} station and $M_s^{0,i}$ is the uncorrected magnitude values obtained from (1) by subtracting the attenuation correction, to obtain the corrected magnitudes M_s^i and the attenuation parameter *a*.

The solution of the inverse problem (3) yields the attenuation coefficient of 0.0037 for the Rayleigh and 0.0042 for the Love waves. We tried to incorporate the dependence on the period *T* into the inverse problem, but it didn't improve the RMS residuals. The final formulas with the distance correction are:

$$M_s^{R^*}(VMAX) = \log(a_b) + \frac{1}{2}\log(\sin(\Delta)) + 0.0037\Delta - \log(f_c) - 0.43 \qquad (4)$$

$$M_s^{L^*}(VMAX) = \log(a_b) + \frac{1}{2}\log(\sin(\Delta)) + 0.0042\Delta - \log(f_c) - 0.43 \quad (5)$$

The attenuation coefficients are very close to the value obtained by Russell (0.0031 in the original formula (Equation 1) vs. 0.0037 for the Rayleigh waves (Equation 4) and 0.0042 for the Love waves (Equation 5).

We compared the magnitude values M_s *(VMAX)* estimated with Russell formula and with Equations 4 and 5. The regression lines are given by the following equations:

$$M_{s_s}^{R^*}(VMAX) = 1.0085 M_s^{RUS}(VMAX) - 0.0424 \quad (6)$$

$$M_s^{L^*}(VMAX) = 1.0201 M_s^{RUS}(VMAX) - 0.0817$$

Application of the new corrections improves the residuals for the events used in the inversion; however it doesn't improve the RMS residuals for the entire data set.

Automatic Detection of Rayleigh and Love Waves

To make automatic surface wave detection and association for the purposes of the magnitude estimate we modified EVALSURF program. In the original version the surface wave dispersion, SNR and the polarization direction for the Rayleigh waves are calculated, but only the degree of fitness of the dispersion curve is used for the decision making process (if the group velocities measured for less than 75% of the periods are outside one standard deviation the entire record is considered unacceptable). Other parameters are used by the analyst in order to visually determine the measurement quality. In the new version we first determine if the polarization of the surface wave is within 30 degrees from the great circle backazimuth. To determine polarization direction of Rayleigh waves we used the Chael (1997) technique based on the elliptical particle motion, while for the Love waves we used principal component analysis. If the record satisfies this condition we find the periods between 8 sec and 40 sec for which the following is satisfied:

1) The signal-to-noise ratio is greater than 3. This is an arbitrary number, which can be changed if we find more appropriate value.
2) The observed group velocity is within an acceptable error of the model-predicted dispersion curve.

The maximum amplitude is then computed only for the periods satisfying these conditions. To further enhance the surface wave detection and association, we are working on a surface wave "quality" measure, similar to the ones proposed by Levshin et al. (1992). We use the wave polarization and the number of periods fitting the dispersion curve to develop a preliminary scale for determining "quality" of the surface wave and the magnitude evaluation. Figure 4 shows an example of the automated magnitude picking for a large event (2006.06.03, *mb=5.4*) using three different stations. For this event the SNR is acceptable for most stations and periods. The largest Rayleigh wave amplitude recorded by station KIV, however, fails the dispersion test; therefore a different magnitude value is picked. Notice that there is a significant difference between the magnitudes estimated at GNI and KIV, even though these stations are separated by approximately 500 km.

Love and Rayleigh Wave M_s(VMAX) in Italy

We applied the M_s(VMAX) measurement technique (Equation 1) to 125 earthquakes in Italy. Many of these events were aftershocks of the damaging L'Aquila mainshock that occurred on 6 April 2009 (M_w=6.1) in central Italy. The analysis resulted in 1449 and 1142 magnitude estimates for Rayleigh and Love waves, respectively, with over 90% of the estimates at source-station of less than 200 km. The dominant period of the measurements was ~8 seconds for Rayleigh waves and between 8 and 12 seconds for the Love waves. The interstation standard deviation for the Rayleigh waves averaged 0.17 m.u., which was slightly lower than for the Love waves (~0.20 m.u.). Comparison of the magnitude residuals with azimuth show the increased variance for the Love waves was due to more complicated radiation patterns. Figure 5a shows the results of the Italian earthquake analysis. The network-averaged magnitudes show that most of the events (80%) had a Love-wave M_s that was larger (average 0.2 m.u.) than the Rayleigh-wave estimate. Relationships between moment magnitude (M_w) and M_s(VMAX) for both Rayleigh and Love waves were estimated using orthogonal regression and include:

$$M_w^R = 0.68 M_s^R(VMAX) + 1.78$$
$$M_w^L = 0.69 M_s^L(VMAX) + 1.64 \quad (7)$$

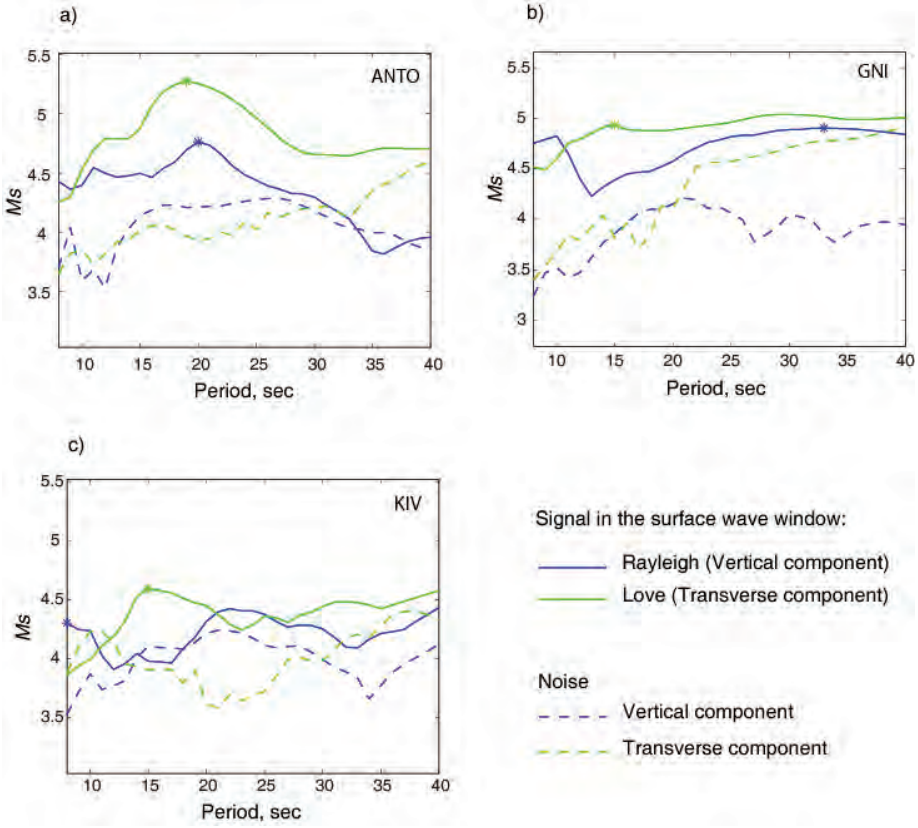

Figure 4. Example of $M_s(VMAX)$ estimate using the new version of the program with automatic picking for event 2006.06.03 (*mb=5.4*): a) Station ANTO, b) Station GNI, and c) Station KIV. The blue lines show the results for Rayleigh waves, the green lines are Love waves.

Love and Rayleigh Wave M_s(VMAX) in the Yellow Sea/Korean Peninsula Region

The last dataset that we used to study the M_s(VMAX) measurement technique originated from the in the Yellow Sea/Korean Peninsula region (YSKP). We found M_s(VMAX) for 31 earthquakes and 2 announced nuclear explosions. The analysis resulted in 266 and 298 magnitude estimates for Rayleigh and Love waves, respectively, with over 90% of the estimates at source-station of less than 700 km. The dominant periods of the measurements for Rayleigh waves less than 13 seconds; however, the Love wave magnitudes equally sampled periods between 8 and 20 seconds. The interstation magnitude standard deviation for the Rayleigh and Love waves averaged 0.11 and 0.22 m.u., respectively. Figure 5b shows the results of the YSKP magnitude analysis. The network-averaged magnitudes show that most of the events (81%) had a Love-wave M_s that was larger than the Rayleigh-wave estimate. For comparison, the M_s(VMAX) was 3.6 and 3.1 for Rayleigh and Love waves, respectively, recorded from the 25 May 2009 announced nuclear explosion. Relationships between moment magnitude (M_w) and M_s(VMAX) were estimated using orthogonal regression and include:

$$M_w^R = 0.60 M_s^R(VMAX) + 2.18$$
$$M_w^L = 0.65 M_s^L(VMAX) + 1.83 \quad (8)$$

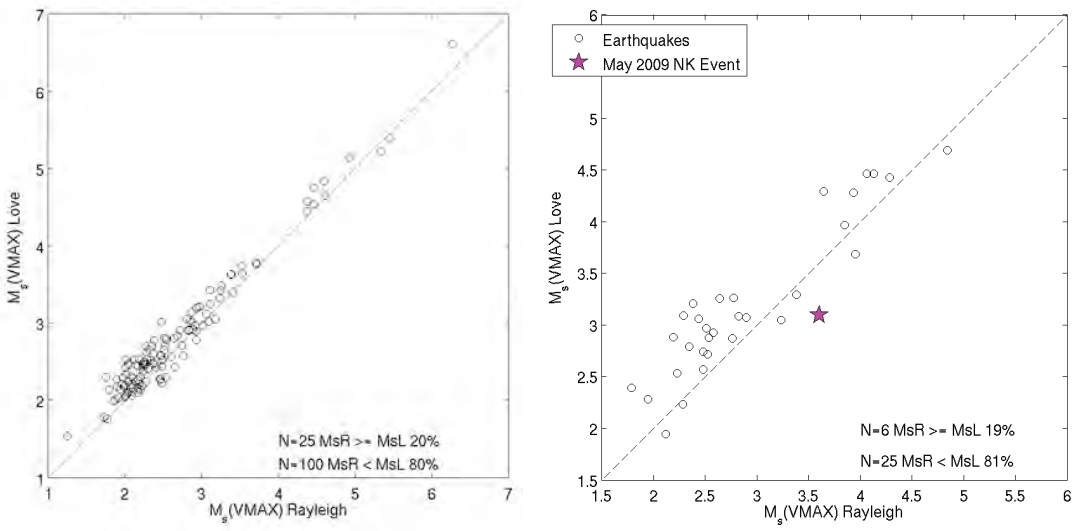

Figure 5. M_s(VMAX) Love versus M_s (VMAX) Rayleigh for 125 events in Italy (left) and 32 events in the YSKP (right).

CONCLUSIONS AND RECOMMENDATIONS

During the past year, we continued studying the application of the M_s(VMAX) magnitude measuring technique (Russell, 2006) to both Rayleigh and Love waves. We have automated the method, examined structural effects on the formula in the Middle East, applied the method to earthquakes in Italy, Korea and Yellow Sea regions, and examined performance of the method at the United States Geological Survey National Earthquake Information Center (USGS NEIC).

While studying the variability of M_s (VMAX) measurements in the Middle East, we found a significant magnitude bias between the stations situated to the northwest and northeast from the area of Middle East. We attribute this bias to the surface wave scattering by the Caspian and the Black Seas and the Great Caucasus Mountains.

We studied the suitability of the Russell formula for Love waves. We computed the attenuation correction by fitting a linear regression to uncorrected M_s *(VMAX)* measurements for both Rayleigh and Love waves. The attenuation coefficients calculated as a result are 0.0037 for the Rayleigh and 0.0042 for the Love waves (compared to 0.0031 in the original formula). Application of the new corrections improves the residuals for the events used in the inversion; however it doesn't improve the RMS residuals for the entire data set.

For the past 50 years, comparing M_s:m_b has been a workhorse in the teleseismic discrimination of earthquakes and explosions. Figure 6 shows the comparison of M_s(VMAX)*:*m_b for the Weston Geophysical Corp. database. We note that the Murphy et al. (1997) screening line, which was developed exclusive of this dataset, does an excellent job of separating the earthquake and explosion populations, with the exception of the announced North Korean nuclear explosions. The two North Korean explosions plot either on or slightly above the descision line; however, when the error of the screening line is considered, the North Korean events would not have been screened as earthquakes. Selby and Bowers (2009) have suggested that a new screening line would ensure that no explosions are screened as earthquakes. Our approach is to consider additional properties of surface waves in the screening process before the Murphy et al. (1997) screening line is abandoned. Our results to date show there is potential event screening information in comparing Rayleigh- and Love-wave magnitudes for earthquakes and explosions. In the final year of this project, we will incorporate a formal discriminant of M_s(VMAX):m_b into the Event Classification Matrix (Anderson et al., 2007) and seek methods of combining those results with new techniques for M_s(Love)*:* M_s(Rayleigh) screening (Figure 6).

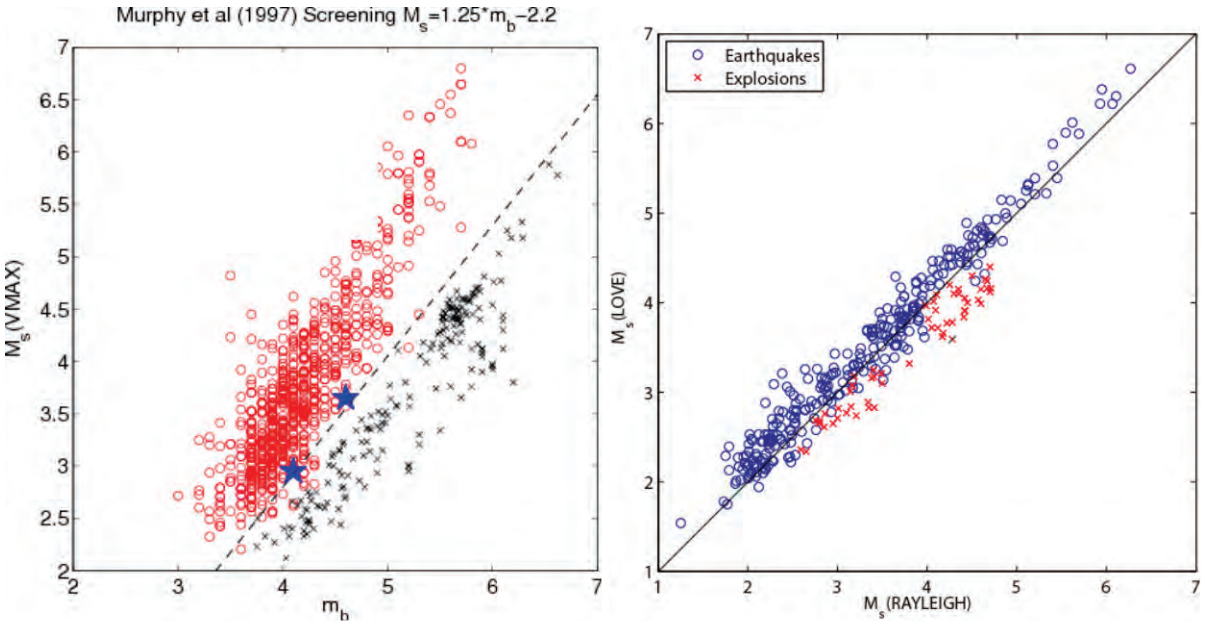

Figure 6. (Left). Traditional M_s(VMAX):m_b discrimination of earthquakes and explosions using the Murphy et al. (1997) screening line. (Right). New techniques that compare M_s(Love) versus M_s(Rayleigh). Of 292 earthquakes, only 58 (20%) have Rayleigh-wave magnitudes larger than the Love wave magnitudes. To date, all of the explosions we have analyzed have exhibited larger Rayleigh-wave magnitudes than Love waves.

REFERENCES

Anderson, D.N., D.K. Fagan, M.A. Tinker, G.D. Kraft and K.D. Hutcheson (2007). A mathematical statistics formulation of the teleseismic explosion identification problem with multiple discriminants. *Bull. Seism. Soc. Am*, 97: 1730–1741.

Bonner, J.L., D. Russell, D. Harkrider, D. Reiter, and R. Herrmann, (2006). Development of a Time-Domain, Variable-Period Surface Wave Magnitude Measurement Procedure for Application at Regional and Teleseismic Distances, Part II: Application and M_s—m_b Performance. *Bull. Seism. Soc. Am.* 96: 678–696

Bonner, J., R.B. Herrmann, and H. Benz (2008). Rapid estimates of seismic moment using variable-period surface-wave magnitudes. *Seism. Res. Letts.* 79: 349.

Bonner, J. L., R. B. Herrmann, D. Harkrider, and M. Pasyanos (2008). The surface wave magnitude for the 9 October 2006 North Korean nuclear explosion. *Bull. Seism. Soc. Am.*, 98: 2598–2506.

Chael, E.P. (1997). An Automated Rayleigh-Wave Detection Algorithm. *Bull. Seism. Soc. Am.*, 87: 157–163.

Cong, L. and B. Mitchell (2006). Continent-wide maps of 5-50 S Rayleigh-wave attenuation for Eurasia inferred from maps of 1-Hz *Lg* Coda Q and its frequency dependence, in *Proceedings of the 28th Seismic Research Review: Ground-Based Nuclear Explosion Monitoring Technologies*, LA-UR-06-5471, Vol. 1, pp. 3–7.

Levshin, A., L. Ratnikova, and J. Berger (1992). Peculiarities of surface wave propagation across central Eurasia. *Bull. Seism. Soc. Am.*, 82: 2464–2493.

Levshin, A., X. Yang, M. Ritzwoller, M. Barmin, and A. Lowry (2006). Toward a Rayleigh wave attenuation model for Central Asia, in *Proceedings of the 28th Seismic Research Review: Ground-Based Nuclear Explosion Monitoring Technologies*, LA-UR-06-5471, Vol. 1, pp. 82–92.

Marshall, P. D. and P. W. Basham (1972). Discrimination between earthquakes and underground explosions employing an improved M_s scale. *Geophys. J. R. Astr. Soc.*, 29: 431–458.

Murphy, J. R., B. W. Barker, and M. E. Marshall (1997). Event screening at the IDC using the M_s/*mb* discriminant. Maxwell Technologies Final Report. 23 p.

Neprochnov, Y. P. (1968). Structure of the earth's crust in epi-continental seas: Caspian, Black, and Mediterranean, *Can. J. Earth. Sci*. 5: 1037–1043.

Priestley, K. and S. Mangino (1995). Seismic studies of the Caspian Basin and surrounding regions. Final Report. *PL-TR-95-2154*. 73 p.

Rezanov, I. A. and S. S. Chamo, (1969). Reasons for absence of a granitic layer in the basins of the South Caspian and Black Sea type. *Can. J. Earth Sci*. 6: 671–678.

Rezapour, M., and R. G. Pearce (1998). Bias in surface-wave magnitude M_s due to inadequate distance correction. *Bull. Seism. Soc. Am.* 88: 43–61.

Russell, D. R. (2006). Development of a time-domain, variable-period surface wave magnitude measurement procedure for application at regional and teleseismic distances. Part I—Theory. *Bull. Seism. Soc. Am*. 96: 665–677.

Selby, N. D. and D. Bowers (2009). UK National Data Centre analysis of the 2006 and 2009 DPRK nuclear tests, and implications for event screening in the context of the CTBT. AGU Abstracts for the Fall 2009 Meeting, Abstract # SW31C-1735.

Stevens, J., J. Given, G. Baker, and H. Xu (2006). Development of surface wave dispersion and attenuation maps and improved methods for measuring surface waves, in *Proceedings of the 28th Seismic Research Review: Ground-Based Nuclear Explosion Monitoring Technologies*, LA-UR-06-5471, Vol. 1, pp. 273–281.

2010

Proceedings of the 2010 Monitoring Research Review:
Ground-Based Nuclear Explosion Monitoring Technologies

Vol. II

Proceedings of the 2010 Monitoring Research Review: Ground-Based Nuclear Explosion Monitoring Technologies

September 21–23, 2010

Orlando, Florida

Volume II

Hydroacoustic Monitoring
Radionuclide Monitoring
Infrasound Monitoring
Data Processing and Analysis

Approved for Public Release; further dissemination unlimited.

National Nuclear Security Administration

AIR FORCE RESEARCH LABORATORY

LA-UR-10-05578

To view these Proceedings online, visit
https://na22.nnsa.doe.gov/mrr/2010

ACKNOWLEDGEMENTS

The National Nuclear Security Administration (NNSA) and the Air Force Research Laboratory (AFRL) gratefully acknowledge the important contributions of the following people for their work to produce the ***Proceedings of the 2010 Monitoring Research Review: Ground-Based Nuclear Explosion Monitoring Technologies***.

Authors of papers for excellent research, technical documentation, and cooperation with electronic submission processes.

Dr. Anton M. Dainty, Mr. Robert J. Raistrick, Dr. Frederick R. Schult, AFRL/RVBYE, and ***Ms. Doris Richards***, 66 ABG/PA, for review and clearance of abstracts and papers related to AFRL contracts.

Dr. Stanley D. Ruppert, Lawrence Livermore National Laboratory (LLNL), for assistance in ensuring that the CDs could be read on a variety of platforms and for burning the CDs.

Ms. Brenda DeVargas, Los Alamos National Laboratory (LANL), for composition of the hardcopy covers and the CD label.

Ms. Eileen F. Patterson, LANL, for technical editing of papers.

Mr. Marvin A. Wetovsky, LANL, managing editor of the Proceedings.

Ms. Leslie A. Casey, NNSA, for review and clearance of abstracts and papers related to NNSA contracts and for NNSA overall support of the Proceedings.

Dr. Sanford (Sandy) Ballard, Sandia National Laboratories (SNL), for providing the 3D Earth model image on the CD label.

Ms. Mary L. Girven, SNL, for making everyone's job easier with web-based technology for abstract and paper submission, on-line review and approval tools, and creation of the master files for the hardcopy, CD, and website versions of the proceedings.

Ms. Guadalupe (Lupe) Massoth and ***Mr. Terry W. Spaulding***, SNL, for providing assistance to Mary Girven on website development and help in creating the master files.

Dr. William R. Walter and ***Dr. Stephen C. Myers***, LLNL; Dr. ***Dale N. Anderson*** and ***Mr. Ward L. Hawkins***, LANL; ***Dr. Theodore W. Bowyer*** and ***Dr. Martin E. Keillor***, Pacific Northwest National Laboratory; and ***Dr. Christopher J. Young***, SNL, for a myriad of internal management and technical reviews of NNSA abstracts and papers.

PREVIOUS PROCEEDINGS

Year	Title of the Proceedings
2009	Proceedings of the 2009 Monitoring Research Review: Ground-Based Nuclear Explosion Monitoring Technologies
2008	Proceedings of the 30th Monitoring Research Review: Ground-Based Nuclear Explosion Monitoring Technologies
2007	Proceedings of the 29th Monitoring Research Review: Ground-Based Nuclear Explosion Monitoring Technologies
2006	Proceedings of the 28th Seismic Research Review: Ground-Based Nuclear Explosion Monitoring Technologies
2005	Proceedings of the 27th Seismic Research Review: Ground-Based Nuclear Explosion Monitoring Technologies
2004	Proceedings of the 26th Seismic Research Review: Trends in Nuclear Explosion Monitoring
2003	Proceedings of the 25th Seismic Research Review: Nuclear Explosion Monitoring: Building the Knowledge Base
2002	Proceedings of the 24th Seismic Research Review: Nuclear Explosion Monitoring: Innovation and Integration
2001	Proceedings of the 23rd Seismic Research Review: Worldwide Monitoring of Nuclear Explosions
2000	Proceedings of the 22nd Annual DoD/DoE Seismic Research Symposium: Planning for Verification of and Compliance with the Comprehensive Nuclear-Test-Ban Treaty (CTBT)
1999	Proceedings of the 21st Seismic Research Symposium: Technologies for Monitoring the Comprehensive Nuclear-Test-Ban Treaty

Table of Contents — Volume II

5. Hydroacoustic Monitoring 539

5-01 **Harben, P. and T. Hauk**
Background Acoustic Noise Models for the IMS Hydroacoustic Stations 541

5-02 **Matsumoto, H., D. Bohnenstiehl, R. Dziak, R. Embley, and M. Park**
Assessment of Hydroacoustic Propagation Using Autonomous Hydrophones in the Scotia Sea 551

5-03 **Prior, M., A. Poplavskiy, R. Le Bras, and J. Given**
Enhancing the Contribution of the T-Stations of the IMS Hydrocoustic Network to IDC Processing and Tsunami Warning 558

6. Radionuclide Monitoring 565

6-01 **Biegalski, S., M. Deinert, C. Rios Perez, and J. Lowrey**
Modeling of Radioxenon Production and Release Pathways 567

6-02 **Cooper, M., C. Aalseth, J. Ely, D. Haas, J. Hayes, J. McIntyre, and B. Schrom**
Digital Data Acquisition Graphical User Interface 577

6-03 **Farsoni, A. and D. Hamby**
Characterizing a Two-Channel Phoswich Detector Using Radioxenon Isotopes Produced in the Oregon State University TRIGA Reactor 585

6-04 **Farsoni, A. and D. Hamby**
Design and Modeling of a Compton-Suppressed Phoswich Detector for Radioxenon Monitoring 595

6-05 **Haas, D., B. Schrom, M. Cooper, J. Ely, A. Flory, J. Hayes, T. Heimbigner, J. McIntyre, D. Saunders, and T. Suckow**
Progress in Advanced Spectral Analysis of Radioxenon 604

6-06 **Keillor, M., C. Aalseth, A. Day, L. Erikson, J. Fast, B. Glasgow, E. Hoppe, T. Hossbach, B. Hyronimus, H. Miley, A. Myers, and A. Seifert**
Initial Results: An Ultra-Low-Background Germanium Crystal Array 609

6-07 **Williams, R., P. Humble, and J. Hayes**
Extraction of Xenon Using Enriching Reflux Pressure Swing Adsorption 619

6-08 **Xie, C., K. Yocum, J. Colaresi, and H. Miley**
Surface Passivation of High Purity Germanium Detectors Using Amorphous Hydrogenated Silicon Films 627

6-09 **Yocum, K., J. Colaresi, and H. Miley**
Improvement in Ge Detector Cooling 636

7. Infrasound Monitoring 645

7-01 **Arai, N., Y. Imanishi, S. Watada, T. Oi, T. Murayama, M. Iwakuni, and M. Nogami**
Dispersion of Infrasound Signals Excited by Explosive Eruptions of the Sakura-jima Volcano 647

7-02 **Arrowsmith, S., H. Hartse, S. Taylor, R. Stead, and R. Whitaker**
Infrasound as a Depth Discriminant 657

7-03 **Arrowsmith, S., I. Che, C. Hayward, and B. Stump**
Multiple-Array Detection, Association and Location of Infrasound and Seismo-Acoustic Events — Utilization of Ground Truth Information 667

7-04 **Gabrielson, T., G. Haralabus, and S. Stefanova**
IMS Infrasound Monitoring Test Site at Trafelberg, Austria: Preliminary Results from In-Situ Response Measurements of Infrasound Elements 678

7-05 **Gibson, R., D. Drob, D. Broutman, and N. Winslow**
Advancement of Techniques for Modeling the Effects of Atmospheric Gravity-Wave-Induced Inhomogeneities on Infrasound Propagation 699

7-06 **Gitterman, Y.**
Sayarim Infrasound Calibration Explosion: Near-Source and Local Observations and Yield Estimation 708

7-07 **Hale, J., S. Arrowsmith, C. Hayward, R. Burlacu, K. Pankow, B. Stump, G. Randall, and S. Taylor**
Infrasound Signal Characteristics from Small Earthquakes 720

8. Data Processing and Analysis 731

8-01 **Bonner, J., R. Herrmann, A. Stroujkova, and M. Leidig**
A Software Toolbox for Systematic Evaluation of Seismometer-Digitizer System Responses 733

8-02 **Dodge, D., M. Ganzberger, T. Hauk, and S. Ruppert**
Enhancing Seismic Calibration Research Through Software Automation and Scientific Information Management 743

8-03 **Gonzales, M. and C. Young**
WavePro: A New Approach to the Design of Data Processing Work Flows 753

8-04 **Hart, D., H. Parks, and R. Rembold**
The Development of Methodologies for Determining Non-Linear Effects in Infrasound Sensors 760

8-05 **Le Bras, R., S. Vaidya, J. Schneider, S. Russell, and N. Arora**
Status of the Machine Learning Efforts at the International Data Centre of the CTBTO 770

8-06 **Ringdal, F., T. Kvaerna, S. Gibbons, S. Mykkeltveit, and J. Schweitzer**
Basic Research on Seismic and Infrasonic Monitoring of the European Arctic 779

8-07 **Taylor, S. and X. Yang**
Development of Software to Digitize Historic Hardcopy Seismograms from Nuclear Explosions 789

Appendices 799

Roadmap Cross Index 801

Acronyms, etc. 807

Guide to Seismic Phases 811

Hydroacoustic Monitoring

BACKGROUND ACOUSTIC NOISE MODELS FOR THE IMS HYDROACOUSTIC STATIONS

Philip E. Harben and Terri F. Hauk

Lawrence Livermore National Laboratory

Sponsored by the National Nuclear Security Administration

Award No. DE-AC52-07NA27344/LL09-IRP-NDD02

ABSTRACT

Background acoustic noise levels in the ocean have been increasing for the past several decades (McDonald, 2006) yet many of our hydroacoustic detection assessment tools use noise models based on data from the 60's and 70's (Urick, 1983). In some ocean basins, noise levels in the monitoring band (1-100 Hz) have risen 15 dB since the 1960's. To address this issue and provide accurate noise models at each of the six International Monitoring System (IMS) hydroacoustic stations, noise models are constructed using historical data from the stations, many now in operation for over 5 years. The analysis procedure consists of computing a power spectral density (PSD) curve for each 2-hour time period and for each hydrophone sensor (28 in all) over the entire archived data history of the stations. There are nearly 20,000 2-hour spectra for some stations. The PSD's are instrument corrected, converted to units of dB relative to 1 micropascal, and accumulated in 1 dB wide bins at each 0.1 Hz increment for each individual hydrophone. This results in a "noise model" matrix for each sensor that can be viewed as hydrophone noise histograms for each 0.1 Hz increment from 1 to 100 Hz. The noise model becomes a probability density model by simply dividing the matrix by the total spectra count. The noise model is used to create maximum probability curves and 90% confidence curves for each sensor that can then be utilized as background noise levels in network capability assessments. The noise models do not support or refute that acoustic noise levels have risen significantly since the stations do not have a long history of measurements to compare with. They do show that noise variation between stations is significant and complex. The noise models document the existence of persistent noise sources at most stations as well as some notable differences in sensor noise within triads. Besides serving as input to network assessment codes, these noise models can also help track and assess the system health of individual sensors over time as well as changes in the ambient background noise.

OBJECTIVES

Accurate assessment of the detection capability (and to a lesser extent location capability) of the IMS hydroacoustic network is necessary in understanding and communicating the strengths and weaknesses of the monitoring network. Assessment tools that model the long-range propagation of acoustic signals, such as HydroCAM (Farrell, 1996), are utilized for this purpose but are only as accurate as the source signal levels and background noise levels provided and the propagation physics implemented. The objective of this work is to improve the accuracy of hydroacoustic network assessments by providing data-driven noise models at each hydroacoustic station based on the archived data history of the station. The noise models will improve the accuracy of assessments by providing background noise levels based on the noise level history of each station rather than using composite ocean noise models that are sweeping averages and, for older models given in textbooks (Urich, 1983), out-of-date due to the anthropogenic changing acoustic noise levels in the ocean.

A secondary objective of this work is to provide a procedure for computing a data-driven probability density noise model for each sensor that can be used to assess the specific noise environment of the sensor and state of health of the sensor and acquisition system. Comparing noise models over a period of time may be used to identify changes in the ambient noise environment and/or the sensor. The methodology can easily be applied to seismic monitoring as well.

RESEARCH ACCOMPLISHED

Background acoustic noise levels in the ocean have been increasing for the past several decades (McDonald, 2006) and this is primarily the result of modern cargo ships that have increased dramatically in number and tonnage, radiating much of their acoustic energy in the 1-100 Hz monitoring band (Arveson, 2000). The increase in acoustic noise levels can be 15 dB higher in some areas than they were in the 1960's (see Figure 1 for the nominal global deep-ocean background noise levels taken from data collected in the 1960's). In addition, a recent study (Hester, 2008) suggests that the acidification of the oceans caused by CO_2 emissions will significantly reduce acoustic attenuation in the ocean, making the oceans acoustically noisier. It is not clear if this will be deleterious for hydroacoustic monitoring since signals will be less attenuated also. The changing acoustic noise field means current noise models are needed in monitoring assessments.

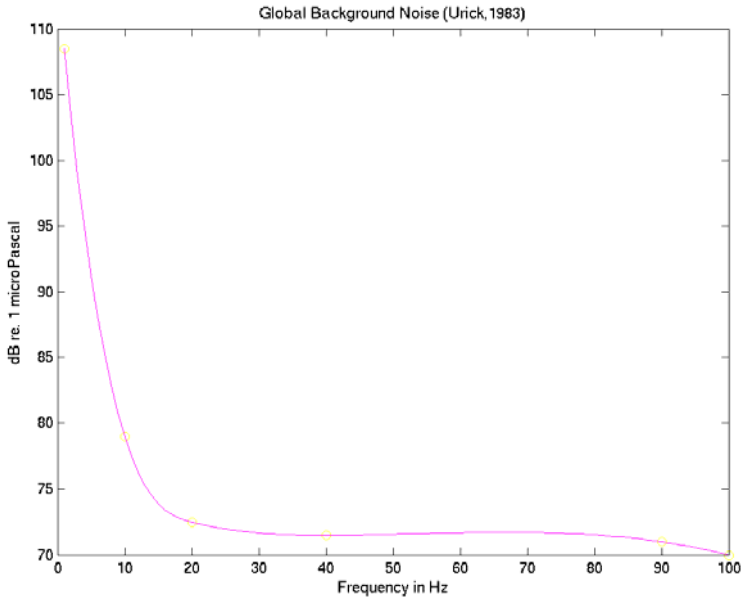

Figure 1. The global background acoustic noise in the deep ocean primarily from data taken in the 1960's. The background noise composite is shown over the full monitoring band (1-100 Hz). Adapted from Urick, 1983.

To address this issue and provide accurate noise models at each of the six IMS hydroacoustic stations, noise models are constructed using historical data from the stations, many now in operation for over 5 years. Due to the large amount of data analyzed, an automated process was developed that utilizes the 2-hour file length records that are typically archived. Sometimes, in an apparently random manner, files were broken up into smaller, unpredictable sizes upstream in the acquisition process. When this occurred the data for that period was rejected from the analysis. Consequently, the data used is less than the full historical archive though it is the vast majority of the archive. It should be noted that the Crozet Island station had a short period of useful operational data and consequently the statistics of the noise models for Crozet are less robust. Table 1 shows the number of spectra calculated and percentage of the historical data used.

Table 1. The number of 2-hour spectra used for the noise models for each sensor are given by year. The final column gives the percent of available data used for each noise model.

SENSOR	2004	2005	2006	2007	2008	2009	TOTAL	POSSIBLE	% of data
ASN1		1340	3060	3036	3744	3336	14516	18816	77
ASN2		1608	3036	3036	3744	3336	14760	18816	78
ASN3		1608	3036	3036	3744	3336	14760	18816	78
ASS1		1596	3012	3036	3648	3264	14556	18816	77
ASS2		1596	3012	3036	3648	3264	14556	18816	77
ASS3		1596	3012	3036	3648	3264	14556	18816	77
DGN1		3228	4200	4212	4116	3756	19512	20820	94
DGN2		3228	4200	4212	4116	3756	19512	20820	94
DGN3		3228	4200	4212	4116	3756	19512	20820	94
DGS1		3204	4164	4152	4044	3744	19308	20820	93
DGS2		3204	4164	4152	4044	3744	19308	20820	93
DGS3		3204	4164	4152	4044	3744	19308	20820	93
WKN1				2232	1392	3828	7452	7884	95
WKN2				2232	1392	3828	7452	7884	95
WKN3				2232	1392	3828	7452	7884	95
WKS1				2196	1380	3792	7368	7884	93
WKS2				2196	1344	3792	7332	7884	93
WKS3				2196	1332	3792	7320	7884	93
CLW1	384	2484	2520	2268	2232	2640	12528	21648	58
CLW2	384	2484	2520	2268	2232	2640	12528	21648	58
CLW3	384	2484	2520	2268	2232	2640	12528	21648	58
JFN1		1308	0	3576	3456	2832	11172	14688	76
JFN2		1308	0	3564	3456	2832	11160	14688	76
JFN3		1308	0	3552	3456	2832	11148	14688	76
CZN1	0	0	0	0	0	0	0	0	N/A
CZN2	443	2550	0	0	0	0	2993	4236	71
CZN3	443	2550	0	0	0	0	2993	4236	71
CZS1	419	1627	444	0	0	0	2490	3256	76
CZS2	0	0	0	0	0	0	0	0	N/A
CZS3	419	1615	444	0	0	0	2478	3256	76

The analysis procedure consists of computing a PSD curve for each 2-hour time period and for each hydrophone sensor (28 in all) over the entire archived data history of the stations. This results in nearly 10,000-20,000 2-hour spectra for some stations. Three hundred 30-sec windows are used to compute the correlation function for each 2-hour time period and the resulting correlation function is used to compute the power density spectra. The spectra are corrected for instrument response, decimated, and converted to units of dB relative to one micro-Pascal, a standard unit of comparison in acoustics. Uncorrected and corrected spectra are saved. The instrument corrections are given as fap (frequency-amplitude-phase) curves with the conversion factor to pressure given at 10 Hz (20 Hz for the Crozet Island station). Each hydrophone sensor was corrected using the specific calibration curve for that sensor but all curves were very similar. Representative amplitude fap curves from each station are shown in Figure 2. It should be noted that although the noise models were constructed for the full monitoring band (1-100 Hz), all data presented here, with the exception of one plot, is in the frequency band 5-95 Hz. This is because, as can be seen in the fap curve plots, the instrument response falls off at the high frequency and, particularly, low frequency extremes where instrument response correction accuracy may be more subject to question.

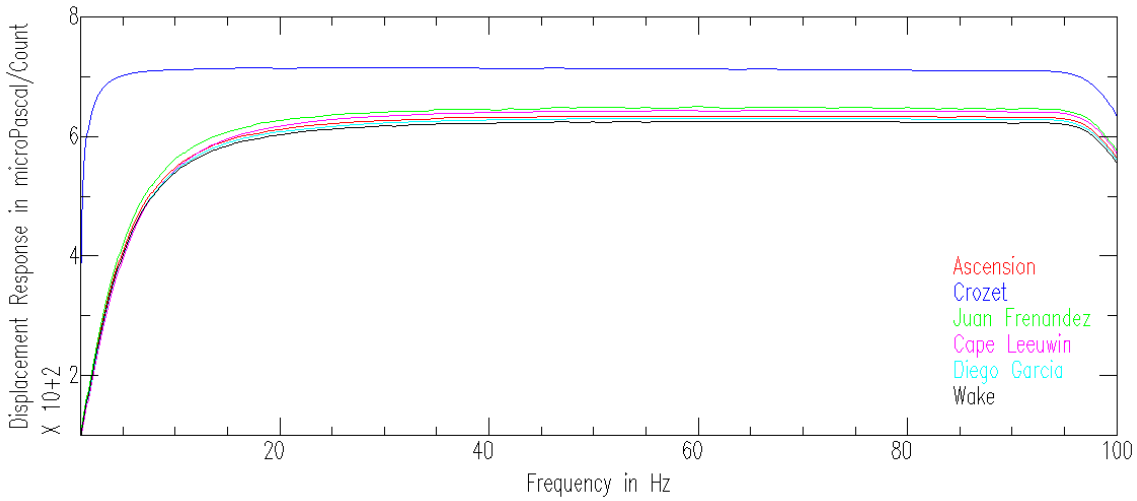

Figure 2. Output amplitude of the hydrophone is shown as a function of frequency for a representative sensor at each station. Excepting Crozet, the instrument responses are nearly identical.

To make noise models from the PSD's we loosely follow an approach used for the U.S. National Seismograph Network (McNamara, 2004). Noise models are created for each spectral frequency between 1 and 100 Hz, in increments of 0.1 Hz. (991 in all) and this is done for every hydrophone in the network. A noise model is the binning of all the PSD's for a particular hydrophone and frequency in 1 dB wide bins by rounding the amplitude in dB to the nearest integer. This results in hydrophone histograms for each 0.1 Hz increment from 1 to 100 Hz. A view of such a frequency slice can be seen in Figure 3. The noise model is simply a 200 X 991 matrix, the row index is the dB bin (1 to 200), the column index is the frequency to the nearest 0.1 Hz (e.g. index 571 is 58 Hz) and the matrix value at the ith row and jth column is the number of spectra at the jth frequency with the ith dB value. Dividing the noise model matrix by the total number of spectra used results in a probability density model.

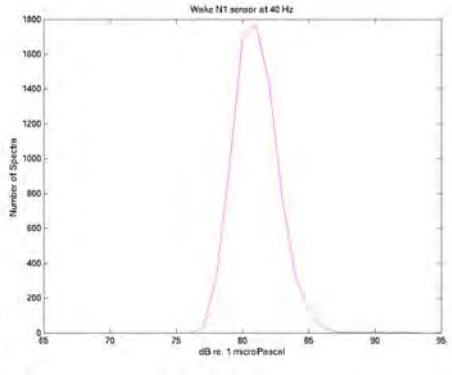

Figure 3. A slice of the noise model for the 1st sensor of the north arm of Wake Station at 40 Hz. Dividing by the total number of spectra would convert to a probability density.

The noise models are shown in the panel of contour plots in Figure 4. The third element of each sensor triad for each station and station arm results in the ten noise models displayed. All plots are to the same scale but the seven contour levels chosen are specific to each model based on the data range of that model.

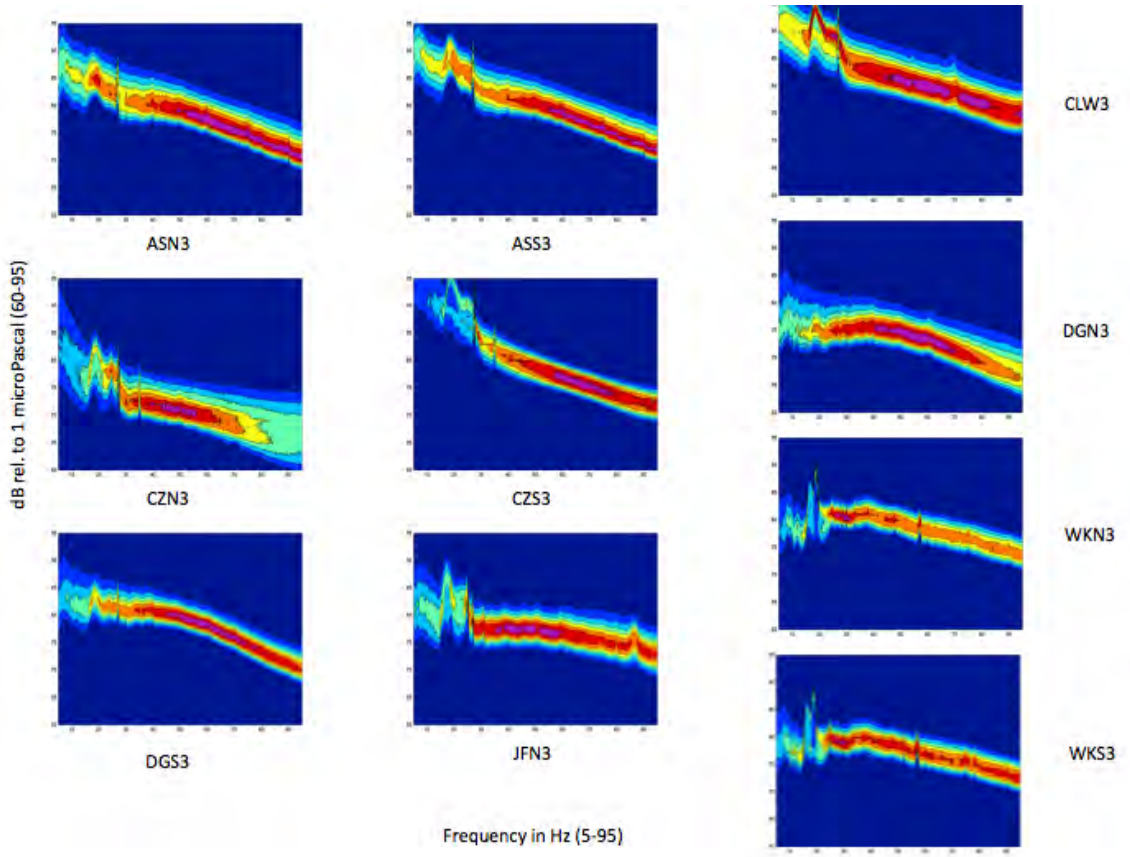

Figure 4. The probability density noise models are displayed here for the 3rd element of each arm as contour plots of probability between 5 and 95 Hz and between 60 and 95 dB. The naming convention uses a two letter identifier and a two character arm/sensor identifier (e.g., CZS3 is the third element of the Crozet Island south arm).

The noise models show some interesting persistent features at many stations. Observe the narrow band 27 Hz peak that is clearly shown on stations CL, AS north and south, CZ north and south, JF north, and DG south but absent from DG north, and WK north and south. Although the blue whale is known to produce strong narrow band calls at 27 Hz (Sirovic, 2007), the persistence and global distribution implied by the noise models would have to be shown to be consistent with blue whale population distribution and calling habits for this to be a viable explanation.

The low-frequency behavior of the stations can be seen in Figure 5. In this figure, the smoothed maximum probability density is plotted for the N1 element of each station. From 1 Hz to 3.5 Hz or so there is relatively little difference in noise levels for the six stations that span most of the world's oceans.

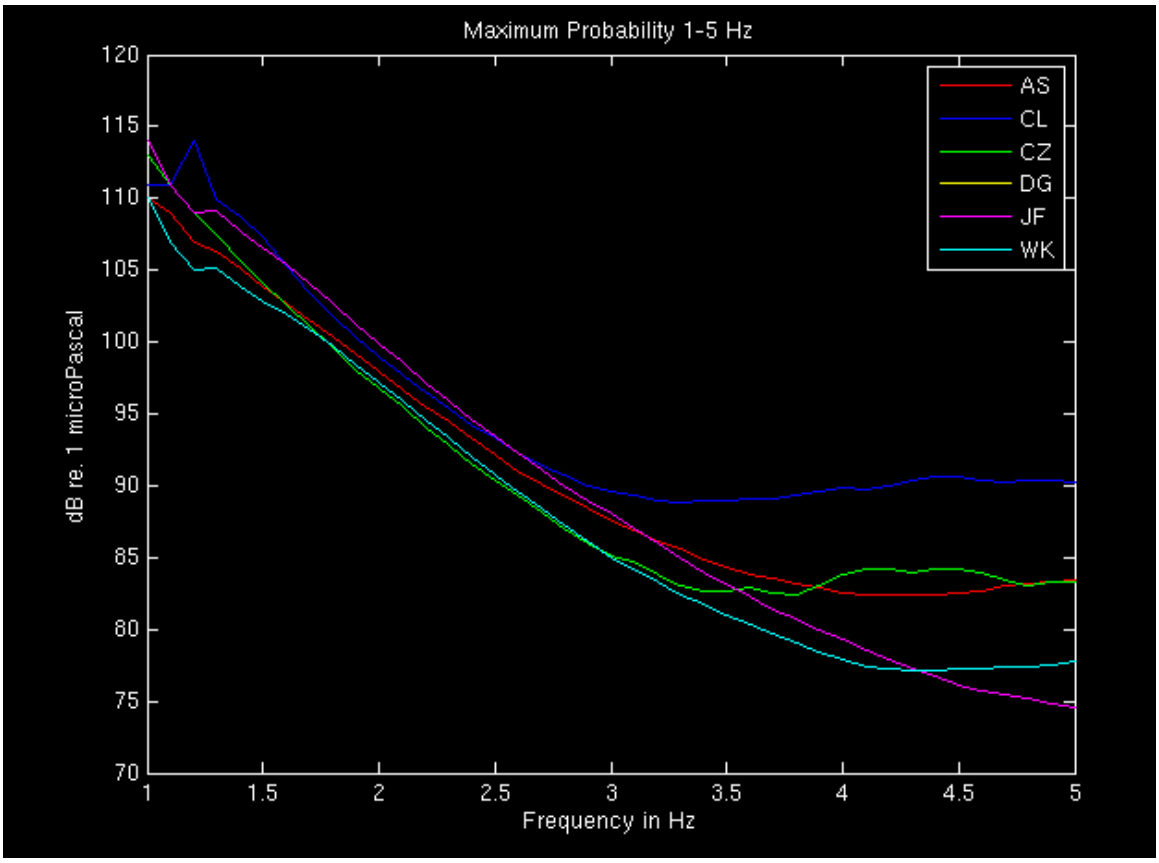

Figure 5. Low-frequency comparison of the N1 (north arm number 1) sensor from each of the six hydroacoustic station.

Since individual sensors composing the triads are separated by less than 2 kilometers, one expects that the noise models for the triads are very similar. Where they are not, installation or sensor/system problems would be likely. The panel of plots in Figure 6 shows each triad with the smoothed maximum probability density plotted for each sensor in the triad. In general, individual sensors within triads do have very similar noise models but there are some small anomalies. The S1 sensor in the Diego Garcia south arm is about 2 dB below the other two sensors over most of the monitoring band. Similarly, the S2 sensor of the Wake south arm is consistently below the other sensors of the south arm. The Ascension north arm shows relatively higher variability among sensors, particularly at low frequencies. Most striking are the differences between arms of the same station, particularly Crozet Island, with the north arm among the lowest broadband noise levels of all stations and the south arm among the highest.

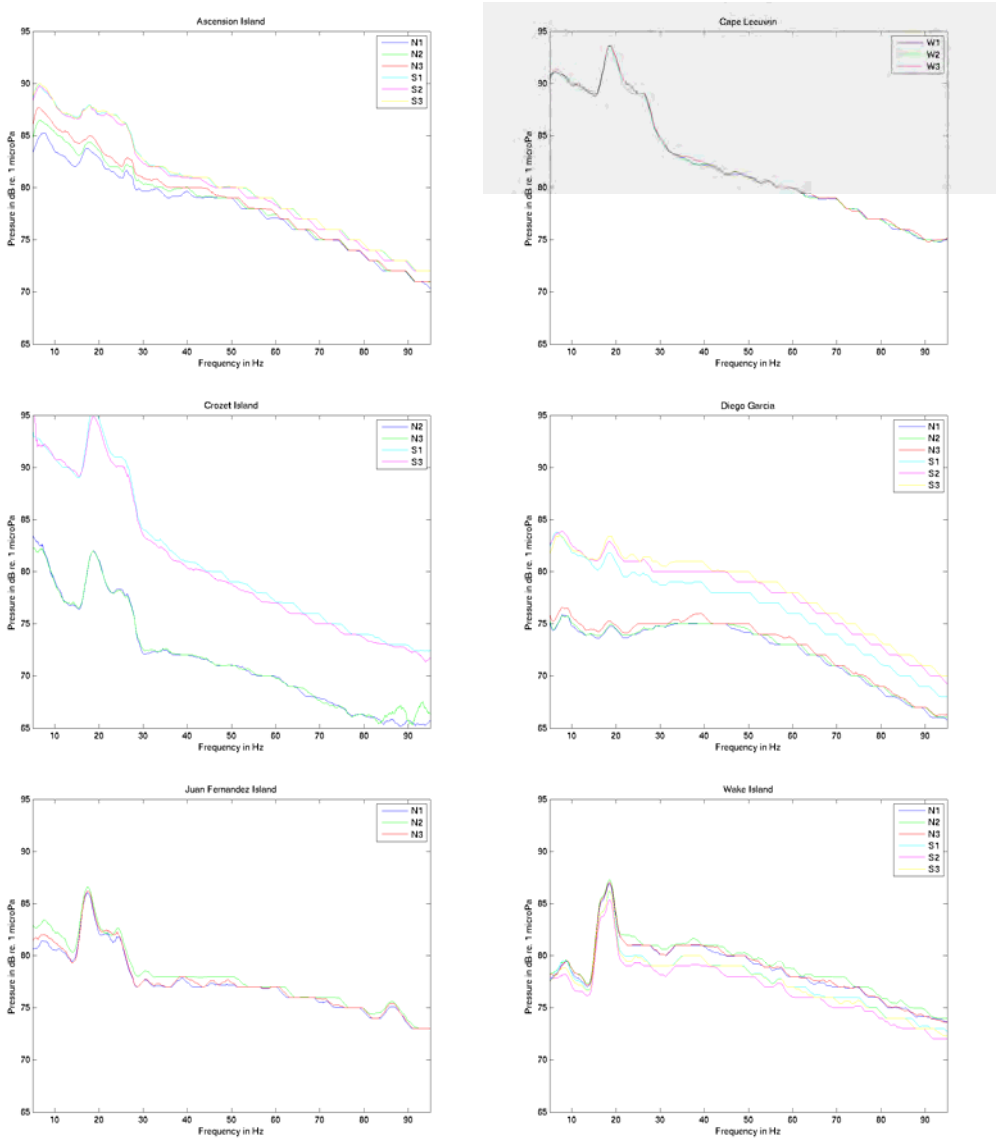

Figure 6. The plot shows the smoothed maximum noise probability for all hydrophones composing that station. We expect noise models of triad sensors to be nearly identical while north and south arms can have different background noise environments, Crozet providing an extreme example.

To use the noise models in an assessment, they must be condensed as in the last figure that uses maximum probability, which is one of many criteria that can be used. In general, the nature and purpose of the assessment will favor different criteria. Figure 7 shows how the criteria selection affects the noise levels. Maximum probability, 10% confidence (i.e., 10% of spectra were lower), and 90% confidence (i.e., 90% of spectra were lower) background noise curves are shown for Diego Garcia South (S3). The maximum probability and 10% confidence curve are coincident at some points and this is due to granularity, the binning into 1 dB increments. It does show that the maximum probability is near the low noise extreme of the model. It also suggests that using a 90% confidence results in a background noise about 5 dB higher than the maximum probability for frequencies above about 20 Hz and up to 15 dB higher at the lowest frequencies.

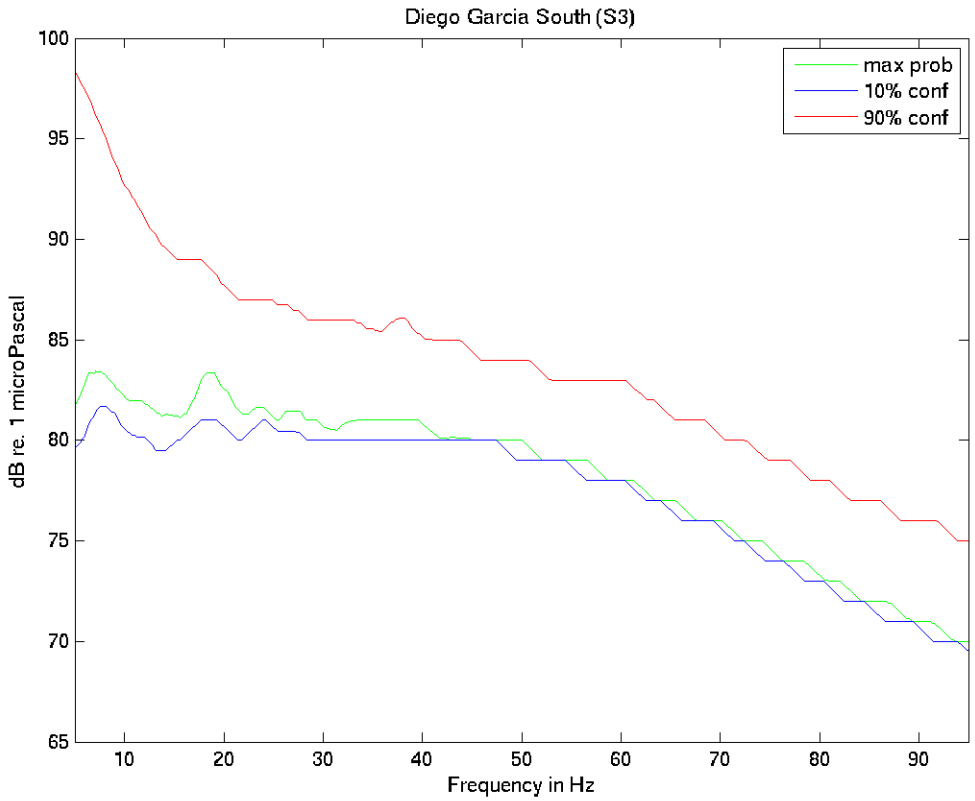

Figure 7. Maximum probability, 90% confidence, and 10% confidence smoothed noise model for Diego Garcia south (S3).

The noise models can easily be constructed for smaller time periods such as yearly or seasonal. Using periods of a month or less would result in only 350 or less spectra for the noise model with consequent poor statistics.
In Figure 8, yearly noise models were calculated for the Ascension Island north N1 sensor, the smoothed maximum probability shown plotted by year. Over the 5 years, no obvious pattern emerges with the exception that 2007 is an anomalously high background noise year.

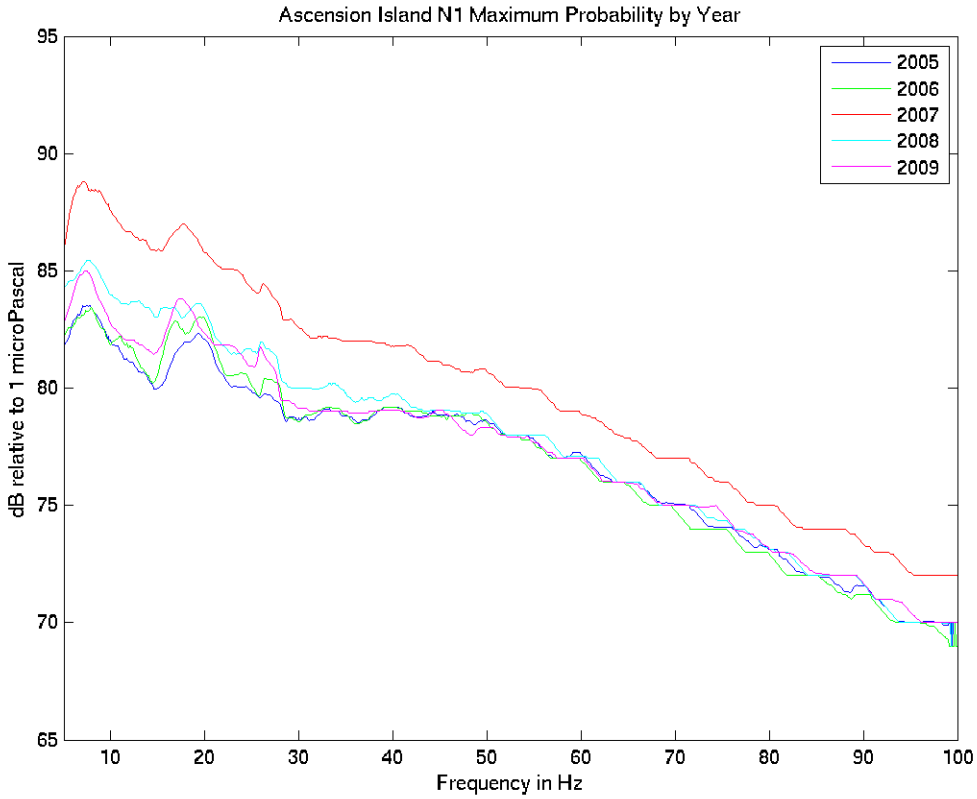

Figure 8. Smoothed maximum probability of yearly noise models for the Ascension Island north hydrophone (N1).

CONCLUSIONS AND RECOMMENDATIONS

Noise models for the IMS hydroacoustic monitoring stations have been developed based on the historical archived data. These models can serve as input to monitoring network assessment codes such as HydroCAM and should improve assessment accuracy by providing more accurate and reliable background noise data. Which noise levels to use (most probable, mean, median, mode, 90^{th} percentile, 10^{th} percentile, etc.) in a network assessment depends on the purpose of the assessment and the underlying question the assessment is trying to answer. The noise models can also be used to quantify temporal changes in the ambient noise environment and to identify persistent narrow band noise features that may be indicative of hydrophone sensor/system malfunction or a continuous noise source in the region of the sensor. Given that ambient background acoustic noise is increasing, it makes good sense to update the noise models periodically. In addition to maintaining accurate values for input to assessment models, the acoustic noise model at each IMS station over time can help in documenting the changing noise field in the world's oceans.

REFERENCES

Arveson, P. T. and D. J. Vendittis (2000). Radiated Noise Characteristics of a Modern Cargo Ship, *J. Acoust. Soc. Am*. 107: Issue (1) 118–129.

Farrell, T., R. and K. D. LePage (1996). Development of a comprehensive hydroacoustic coverage assessment model final report, BBN technical report W1278.

Hester, K. C., E. T. Petlzer, W.J. Kirkwood, and P. G. Brewer (2008). Unanticipated Consequences of Ocean Acidification: A Noisier Ocean, *Geo. Res. Lett*. 35: L19601.

McDonald, M. A., J. A. Hildebrand, and S. W. Wiggins (2006). Increases in the Deep Ocean Ambient Noise in the Northeast Pacific west on San Nicolas Island, California, *J. Acoust. Soc. Am*. 120: (2), pp 711–718.

McNamara, D. E. and R. P. Buland (2004). Ambient Noise Levels in the Continental United States, *Bull. Seismol. Soc. Am*. 94: (4), 1517–1527.

Sirovic, A., J. A. Hildebrand, and S. W. Wiggins (2007). Blue and Fin Whale Call Source Levels and Propagation Range in the Southern Ocean, *J. Acoust. Soc. Am.* 122: (2).

Urick, R. J. (1983). Principles of Underwater Sound, 3rd Edition (McGraw-Hill, New York).

ASSESSMENT OF HYDROACOUSTIC PROPAGATION USING AUTONOMOUS HYDROPHONES IN THE SCOTIA SEA

Haru Matsumoto[1], Del R. Bohnenstiehl[2], Robert P. Dziak[1], Robert W. Embley[3], and Minkyu Park[4]

Cooperative Institute for Marine Resources Studies[1], North Carolina State University[2], Pacific Marine Environmental Laboratory, National Oceanic Administration[3], and Korea Polar Research Institute[4]

Sponsored by the National Nuclear Security Administration

Award No. DE-AI52-08NA28654
Proposal No. BAA08-36

ABSTRACT

The remote area of the Atlantic Ocean near the Antarctic Peninsula and the South Scotia Sea is a region where acoustic surveillance by International Monitoring System hydrophones is at best limited. Sound originating in this area is either blocked or hindered by the South Georgia, South Sandwich Islands and the associated seafloor ridge system, making the region a potential hydroacoustic blind spot. To investigate the sound propagation and interferences affected by these landmasses in the vicinity of the Antarctic polar front, an array of autonomous hydrophones (AUHs) was deployed in the Scotia Sea in December 2007. In January 2009, five AUHs were recovered, completing a 13-month-long acoustic monitoring operation. Four of the recovered instruments continuously recorded low-frequency acoustic signals (1–110 Hz) at a sampling rate of 250 Hz, with one instrument sampling at a rate a rate of 1000 Hz (1–440 Hz band-passed). The submerged moorings utilized autonomous crystal oscillator clocks, with small time shifts that average ~2 seconds per year. Despite the fact that the high-latitude ocean lacks a deep sound channel, low-frequency sound tends to travel relatively efficiently. Regional seismo-acoustic signals (bottom sources) and episodic tremors from large icebergs (near-surface sources) were utilized as natural sound sources. Surface sound sources, e.g., ice-related events, tend to suffer less transmission loss (TL) and dominate the background noise as a result of surface duct transmission and less interaction with seafloor features. On the other hand, earthquake-generated signals (bottom sources) interact more strongly with the shallow arc, and TL tends to be larger. The RAM PE-code (Collins, 1993a,b) was used to model TL, and the AUH data were used to compare with these modeling results. Both the observational and model results indicate a unique acoustic environment of the Scotia Sea, including the evidences of reflected T-waves by the steep slope of the South Georgia Island and efficient P-to-T conversion by the Scotia Ridge system. We found that transmission loss for the shallow-depth sources tends to follow a ~17log10(r) loss model at ranges of 10s to100s km. Seafloor sources are characterized by greater TL, and where the range-dependent bathymetry shallows, the results deviate strongly from a simple $\log_{10}(r)$ relationship. We present two-dimensional path-dependent TL models relative to the hydrophone receivers for near-surface and bottom sources.

OBJECTIVES

The International Monitoring System (IMS) includes a sparse network of sound-channel-moored hydrophones and island-based seismic stations deployed in an effort to monitor the global oceans for signs of explosive tests that may be conducted below or just above the sea surface. Relative to the IMS sites, the most remote portions of the global ocean lie at high polar latitudes. Such settings are unique in that acoustic propagation conditions become surface limited as the deep-ocean sound-channel disappears in response to the nearly isothermal temperature structure of the polar oceans. Moreover, these areas are characterized by high seasonal variability in the background noise field, due in part to the retreat and advance of sea ice and the movement and breakup of drifting icebergs.

This study investigates the acoustic environment at high southern latitudes (~50°–60°) within the Scotia Sea—an area of the southern ocean surrounded by Tierra del Fuego; the Falkland Islands; the South Georgia, South Sandwich, and South Orkney Islands; and the Antarctic Peninsula. It is a tectonic and volcanically active area, providing an abundance of sub-seafloor earthquake sources (T-waves) that produce acoustic energy dominantly in the 5- to 35-Hz band. The surface waters also host a number of drifting icebergs that produce broadband energy with frequencies extending above 125 Hz, with the southern-most hydrophones under sea ice cover during the height of the Austral winter (Matsumoto et al., 2009).

Both earthquake- and ice-generated sound sources within the Scotia Sea were recorded using a network of five autonomous underwater hydrophones (AUHs) (Fox et al., 2001), deployed for a period of ~13 months beginning in December of 2007. The hydrophones recorded continuously with four instruments sampling at 250 Hz (1–110 Hz band passed) and one instrument sampling at a rate of 1000 Hz (1-440 Hz band passed). The submerged instrumentation used autonomous crystal oscillators clocks, with small time shifts that averaging ~2 seconds per year. To avoid the largest of the drifting ice masses in the southern ocean, the AUHs were floated ~500 m below the sea surface. Figure 1 shows a schematic of the polar AUH mooring design.

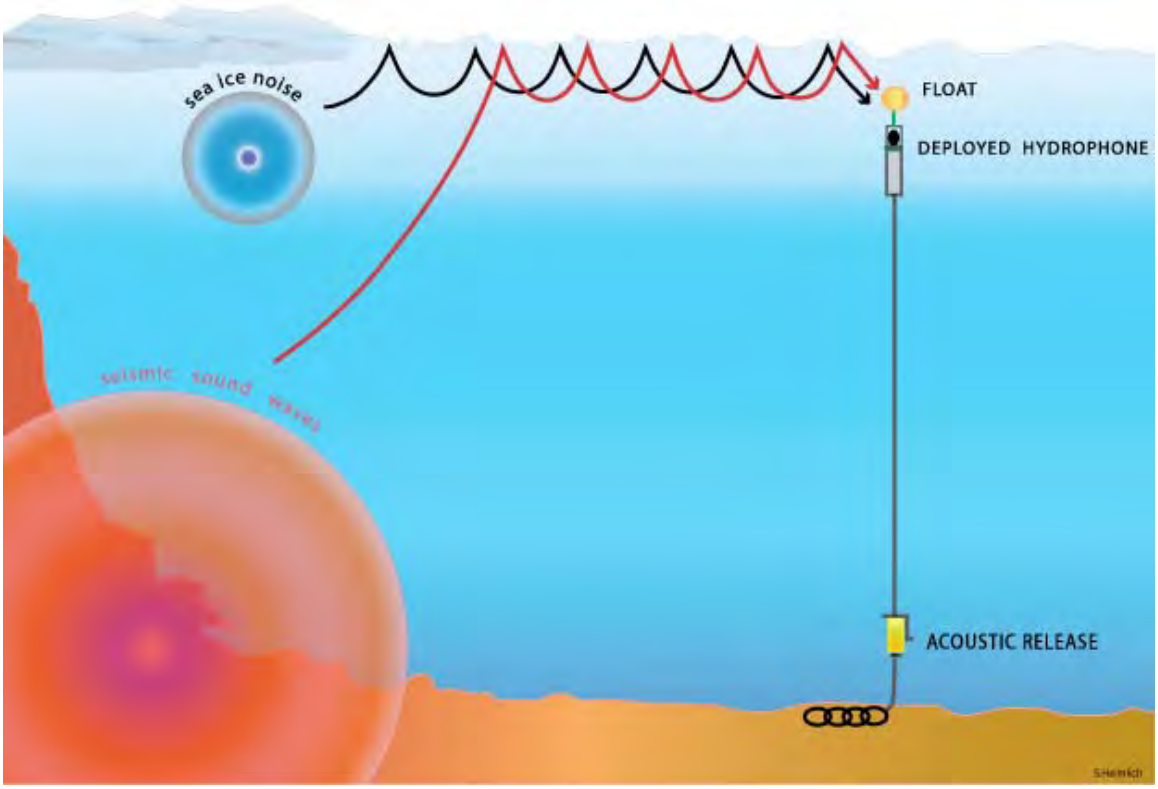

Figure 1. Schematic of high-latitude autonomous hydrophone mooring.

RESEARCH ACCOMPLISHED

Propagation Modeling

Path-dependant TL was modeled using a range-dependent implementation of the RAM PE-code (Collins, 1993a,b). Modeling incorporated the latest global ocean bathymetric data (1 arc-minute resolution) (Amante and Eakins, 2009), annually averaged oceanographic information taken from the 2005 version of the Word Ocean Atlas (WOA-05) (National Oceanographic Data Center, 2008) and National Oceanic and Atmospheric Administration's (NOAA's) 2-arc-minute sediment thickness model (Divins, 2009). The bathymetry and sediment thickness within the Scotia Sea area are shown in Figures 2 and 3. Bathymetry and sediment accumulation patterns primarily reflect the structure of the Scotia subduction zone and volcanic arc.

Model sound sources were located on a ~10 by 10 km grid of points spanning the acoustic environment between 53° and 63° S latitude and 15° and 45° W longitude. Two source depths were considered: (a) 100 m (fixed), simulating the propagation of acoustic energy from a drifting ice mass or an explosion at or near the sea surface, and (b) near sea bottom, where the depth of the source is prescribed based on the local depth at each grid node ($Z^{source} = Z^{bath} + \Delta Z^{model}$). For each source location, the bathymetry and range-dependent sound velocity information were extracted for the relevant databases. Transmission loss was then calculated for each grid relative to the receiver and stored in a matrix. For the models shown here, the source frequency was set at 15 Hz. Signal blockage was assumed if the water depth dropped below ¼ of the acoustic wavelength at any point along the propagation path.

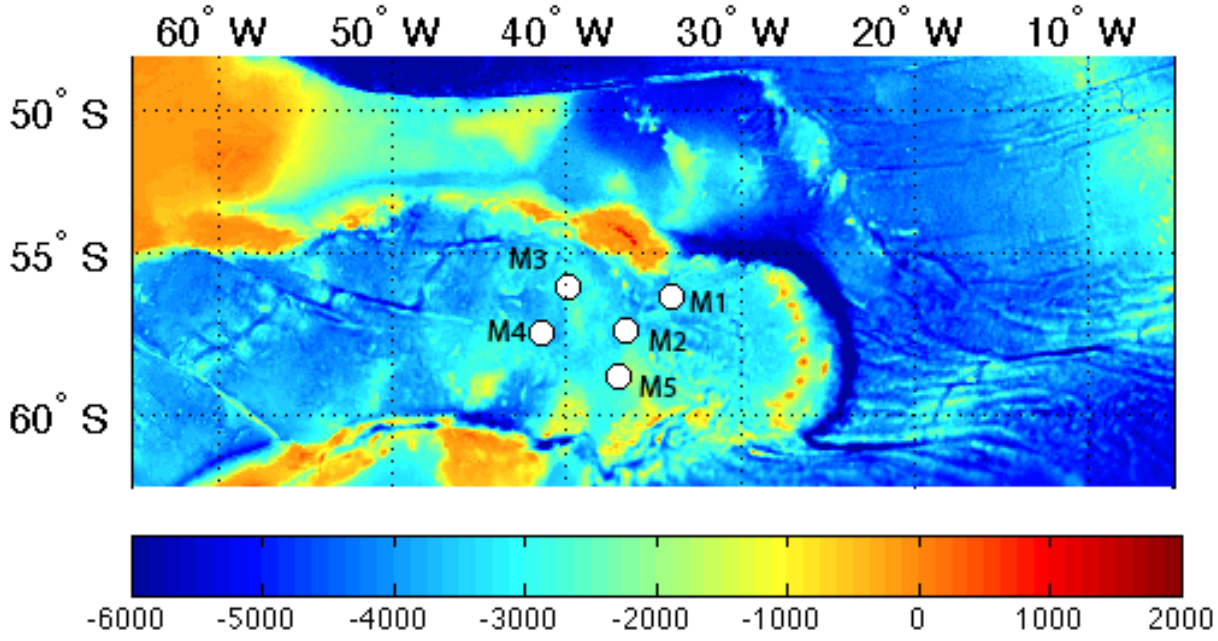

Figure 2. Bathymetry of the Scotia Sea with hydrophones (white circles) labeled M1–M5. Station M1 is sampled at 1000 Hz and the remaining stations at 250 Hz. Depths are displayed in meters. Data are from the ETOPO 1 database (Amante and Eakins, 2009). The amount of ship-based multibeam data is extremely limited in the region.

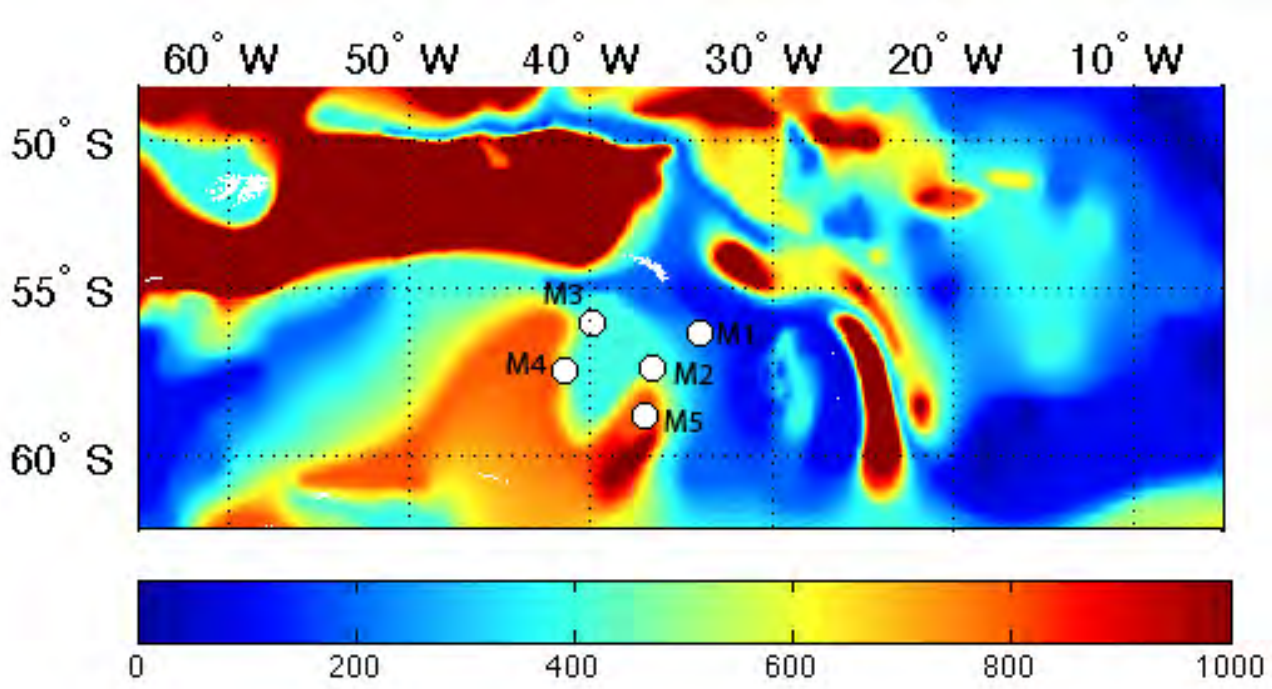

Figure 3. Scotia Sea sediment thicknesses are displayed in meters. Data are from the NOAA sediment thickness compilation (Divins, 2009).

The results of this approach are demonstrated in Figure 4 for station M3. The principal observation that can be made is the difference in TL for the bottom (Figure 4a) and near-surface (Figure 4b) source depths considered. Due to the surface reflected-refracted propagation style, the Scotia Volcanic Arc and the ridges that bound the Scotia Plate to the north and south minimally affect shallow surface-duct sources. Near-bottom earthquake sources, however, interact more strongly with the shallow arc, and TLs are higher as a result.

Matsumoto et al. (2009) previously described a set of double-peaked T-waves representing shallow earthquakes generated to the east of the Scotia Arc. According to their model, the early-arriving phase represents acoustic energy converted between the event epicenter and the station, along the shallow west-facing slope of the volcanic arc. For the bottom source-depth model (Figure 4a), a band of low TL can be seen, indicating the relatively efficient propagation of this signal through down-slope conversion.

Figure 5a examines the TL versus range data for propagation to station M3, with several standard transmission loss models shown for reference. For the ranges investigated here (10-100's km), shallow source depth TL is approximated by a ~17log10(r) model. A pair-wise comparison (Figure 5b) of the shallow and bottom source depth models shows that earthquake sources undergo greater TL at all ranges and these differences increase for paths that cross the Scotia Arc (ranges > 500-600 km). Model results for the other stations show similar patterns.

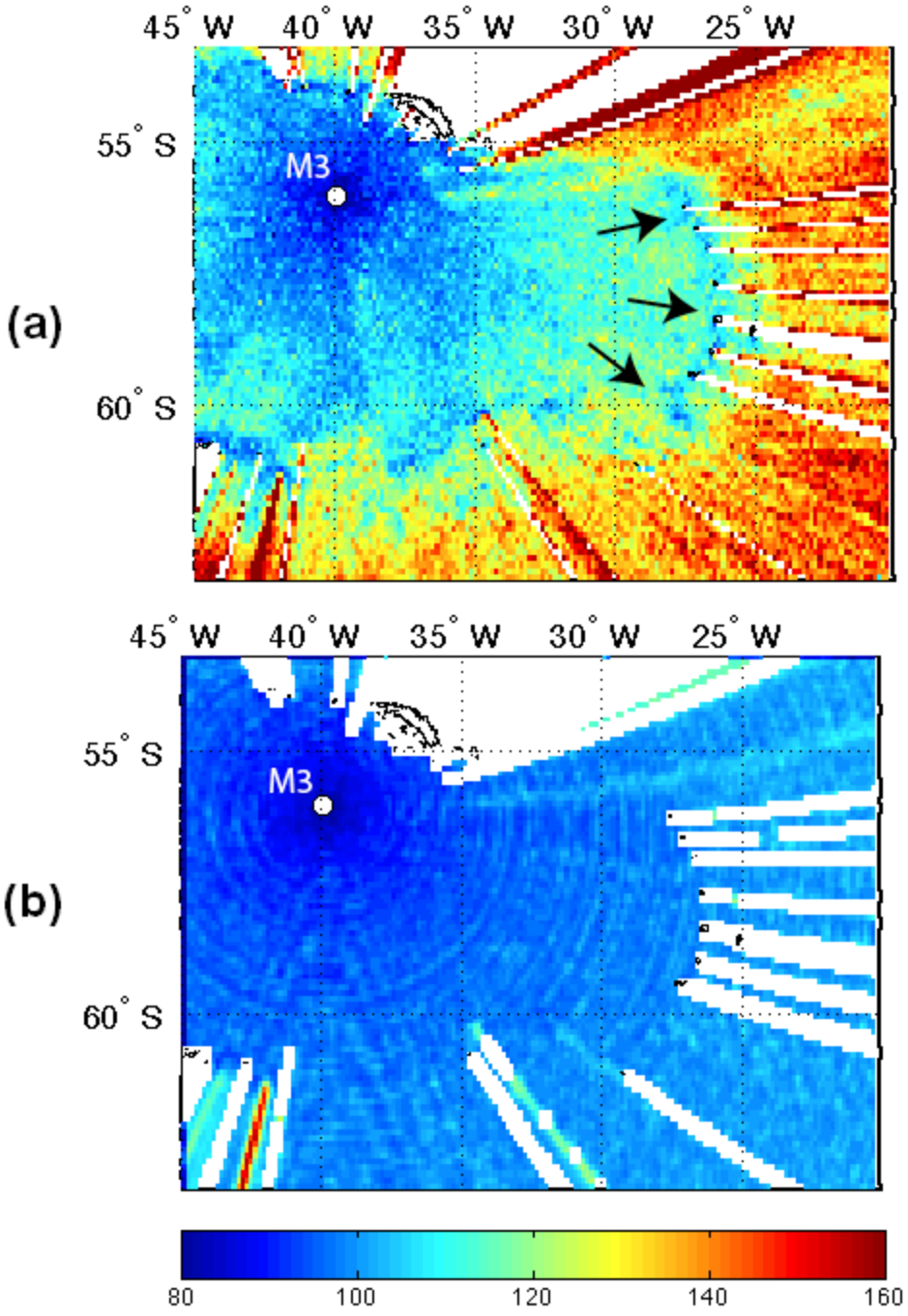

Figure 4. Path-dependent TL model (dB re 1uPa) for (a) bottom and (b) fixed 100-m source depths. Black arrows in (a) highlight the zone of slope conversion along the westward-facing arc.

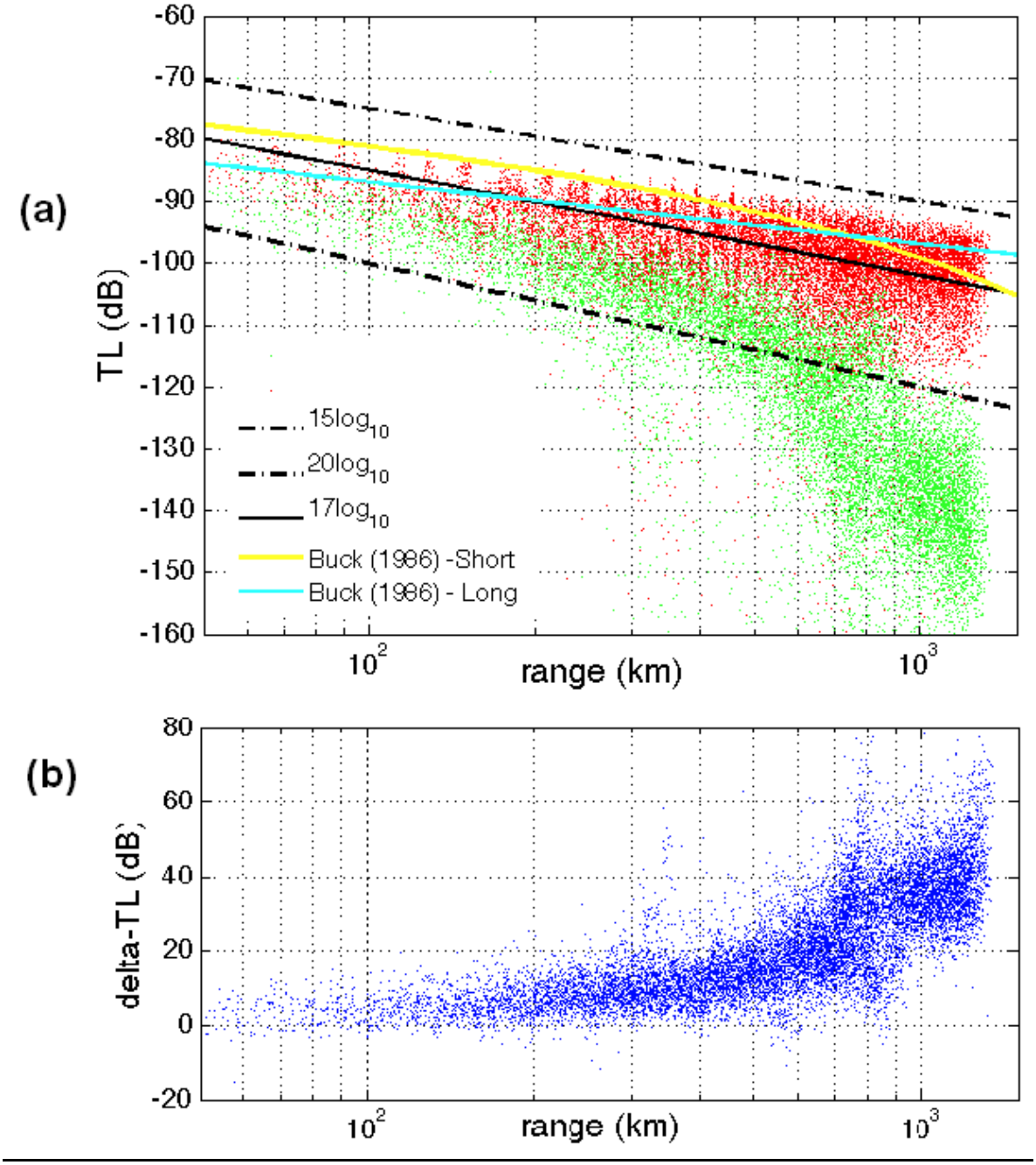

Figure 5. (a) TL versus range with the model domain shown in Figure 4 for station M3 (15 Hz). Red dots are TLs of ice-related surface origin; green dots are of seismic bottom sources. Black lines show reference TL models of 10, 17, and 20*log10(r); yellow and light blue lines show the Arctic propagation model of Buck (1986) at short and long ranges (assume zero ice roughness). (b) TL differences for near-bottom and 100-m depth sources throughout the model domain.

CONCLUSIONS AND RECOMMENDATIONS

Within the Scotia Sea, TL for the shallow-depth sources tends to follow a ~17log10(r) loss model at ranges of 10s to100s km. Near-bottom source depths are characterized by greater TL, and where the range-dependent bathymetry shallows, the results may deviate strongly from a simple $\log_{10}(r)$ relationship. The results demonstrate that the efficiency of acoustic propagation may be strongly source-depth dependant a high latitudes. It also indicates that in the polar region, if a traditional cylindrical-law loss model is applied for the near surface-events, the transmission loss is too small, and as a result yield estimates may be too low.

Traditional line-of-sight blockage maps do not account for this source-depth dependence. Moreover, our model results indicate that empirical blockage maps, which may largely or partially rely on sea-bottom earthquake sources, will tend to over-estimate blockage for high-latitude areas with significant topography. Path-specific TL models overcome these limitations and can be used to improve blockage calculations, validate specific TL versus range relationships, and provide better estimates of T- and H-phase source levels.

ACKOWLEDGEMENTS

We would like to express our gratitude to Dr. Chris Hindley and Dr. Anthony Martin of British Antarctic Survey for carrying out the deployment of M6 in the international waters on the north side of South Georgia Island. We also thank the officers and crew of the *R/V Yuzhmorgeologiya* and *M/V Pharos SG* for deploying and recovering the hydrophones under unfavorable weather conditions. We are also indebted to the base commander Mr. Richard McKee on the Falkland Islands for help coordinating the hydrophone recovery operation. Iceberg position and sea ice extent were provided by the courtesy of Center for Remote Sensing at Brigham Young University. Finally we express our deep gratitude to the Korea Polar Research Institute for providing the ship time and logistic support at the King Sejong Antarctic base.

REFERENCES

Amante, C. and B. W. Eakins (2009). ETOPO1 1 Arc-Minute Global Relief Model: Procedures, Data Sources and Analysis. NOAA technical memorandum NESDIS NGDC-24.

Buck, B. M. (1986), Long term statistical measurements of environmental acoustic parameters in the Arctic, *AEAS Report No. 2—Low Frequency Transmission Loss Measurements in the Central Arctic Ocean*, Polar Research Lab, TR-55.

Collins, M. D. (1993a). A split-step Padé solution for the parabolic equation method, *J. Acoust. Soc. Am*., 93: 1736–1742.

Collins, M. D. (1993b). An energy-conserving parabolic equation for elastic media, *J. Acoust. Soc. Am*., 94: 975–982.

Divins, D. L. (retrieved 2009). NGDC Total Sediment Thickness of the World's Oceans & Marginal Seas, http://www.ngdc.noaa.gov/mgg/sedthick/sedthick.html

Fox, C. G., H. Matsumoto, and T-K. A. Lau (2001). Monitoring Pacific Ocean seismicity from an autonomous hydrophone array, *J. Geophys. Res*., 106: 4183–4206.

Matsumoto, H., D. Bohnenstiehl, R. Dziak, M. Park, and M. Fowler (2009). Hydroacoustic Monitoring of the Scotia Sea: Autonomous Hydrophone Experiment, in *Proceedings of the 2009 Monitoring Research Review: Ground-Based Nuclear Explosion Monitoring Technologies*, LA-UR-09-05276, Vol. 1, pp. 605–612.

National Oceanographic Data Center (retrieved 2008). World Ocean Atlas 2005, http://www.nodc.noaa.gov/OC5/WOA05/pr_woa05.html

ENHANCING THE CONTRIBUTION OF THE T-STATIONS OF THE IMS HYDROACOUSTIC NETWORK TO IDC PROCESSING AND TSUNAMI WARNING

Mark K. Prior, Alexander S. Poplavskiy, Ronan J. Le Bras, and Jeff W. Given

Comprehensive Nuclear-Test-Ban Treaty Organization

ABSTRACT

The Preparatory Commission for the Comprehensive Nuclear-Test-Ban Treaty Organization (CTBTO) is exploring methods to enhance the operational hydroacoustic processing system for its International Monitoring System (IMS). The hydroacoustic IMS network includes two types of stations, the in-water hydroacoustic stations, consisting of multiple sets of hydrophone triplets, and the land-based T-stations, consisting of multiple seismometers. Hydrophone triplets record signals that efficiently propagate in the SOFAR channel over large distances. Processing at the International Data Centre (IDC) classifies these signals into three types (T for underground-generated, H for in-water generated, and N for noise) and determines a direction of propagation, exploiting the multiplicity of sensors. Current efforts are underway to enhance the accuracy of the classification methods. However, the processing in place at the IDC is already quite mature for hydrophone stations. T-stations, on the other hand, present the double disadvantages of a lower detection threshold for in-water propagated hydroacoustic signals and high sensitivity to the geometry and geology of the seismometer emplacements, as opposed to hydrophone triplets located in the much more homogeneous water medium.

In spite of these handicaps, the T-stations do already contribute to the IDC bulletins, mostly by detecting T-phases from events at a higher threshold than hydrophone stations. It would be desirable however to augment the quantity and quality of their contribution to the IDC bulletins. We are presenting the results of attempts at using the multiplicity of seismometers to determine a direction of propagation at the T-stations. In the course of exploring several avenues, including the study of polarization of signals recorded at the two three-component H06 (Socorro Island, Mexico) broad-band seismometers, we have also re-discovered their potential for civil application to tsunami warning because of their recording of long-period horizontally polarized oscillations concomitant with the arrival of the tsunami at the island's coast.

OBJECTIVES

Near-coast seismometer stations (T-stations) are used in the IMS because of their potential (deGroot-Hedlin, 2001) to detect water-borne signals from in-water explosions (H-phases) and crustal events (T-phases). Detection of such signals is complicated by losses in signal intensity and distortions in signal shape incurred when in-water signals couple into seismic waves across the coastal margin. Coastal seismometers suffer further from high levels of surf noise and this problem is particularly strong on horizontal channels. This makes it difficult to estimate arrival azimuth from polarization analysis of seismometer signals. Such azimuth information would be valuable in signal association processing that estimates source time and location, based on observations of arrival properties on spatially distributed sensors. The objective of the research reported here was to investigate two possible methods by which some measure of arrival azimuth could be extracted from seismometer signals from IMS T-stations.

RESEARCH ACCOMPLISHED

Two separate approaches were followed in an attempt to extract arrival azimuth information from seismometer recordings. In the first, polarization analysis was performed on the horizontal channels of coastal seismometers. In the second, envelope correlation was used to determine time lags between signal arrivals at spatially separated seismometers in the same T-station. These approaches are now described separately.

Polarization Analysis

The basic task of the vector signals polarization analysis is the determination of the degree of fluctuation of the linearity of a displacement vector signal and its orientation. The best-known methods of polarization analysis consist of those based on the use of sign and time dependences of orthogonal components of a displacement vector, spectral and covariance methods, etc. They interpret the movement of the end of a displacement vector of a seismic wave either on a line or on an ellipsoidal surface. Such vector signal presentation is not optimal, as it results in the loss of important information concerning polarization structure in a number of cases. A vector harmonic signal polarization is characterized by a flat figure, namely an ellipse, which can degenerate into a line or a circle in some cases. Thus the geometrical parameters of this ellipse such as the location of the plane containing the polarization ellipse in space as well as the ellipse in this plane is often used to estimate the direction to the source or the wave type. When the signal is not harmonic and the vector describes an ellipsoid, this information is lost. In addition, the usual methods of polarization analysis are integral and thus degrade the time resolution. They assume the processing of a part of records with the usual duration of not less than a fluctuation period for finding of the averaged parameters of the equivalent ellipsoid. In cases when the parameters change within a shorter period of time, data connected with these changes is lost.

Thus, it is useful to test the Differential Polarization Analysis (DPA), which is described in Shevchenko, (2002), which allows interpretation of the movement of displacement vector in space along an equivalent polarization ellipse in each point of the real three component seismic records. The standard Flinn's Polarization Analysis (FPA) interprets movement of a displacement vector on a surface equivalent ellipsoid. As a result, the DPA has new specific features: the ability to allocate the current position of a plane containing an ellipse of polarization of a seismic wave. On a normal to this plane, it is possible to search for the direction of the source through the transversal S-waves in the short-period band, and the Rayleigh-LR surface waves in the long period band. This constitutes an advantage over the FPA method.

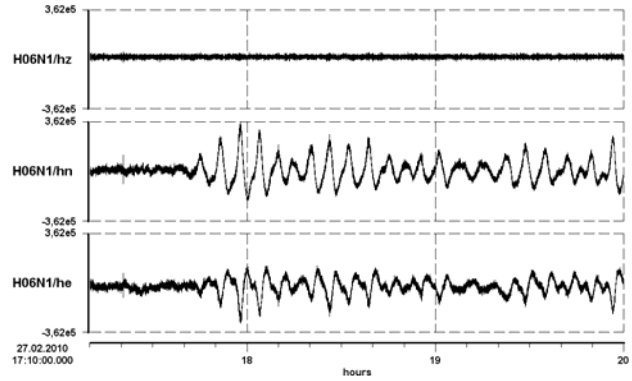

Figure 1. **Long-period fluctuations on the raw broad-band seismograms at station H06N1, beginning at the expected arrival time of the tsunami wave from the Maule event. The wave is seen on the horizontal components (*he* and *hn*), but not on the vertical (*hz*).**

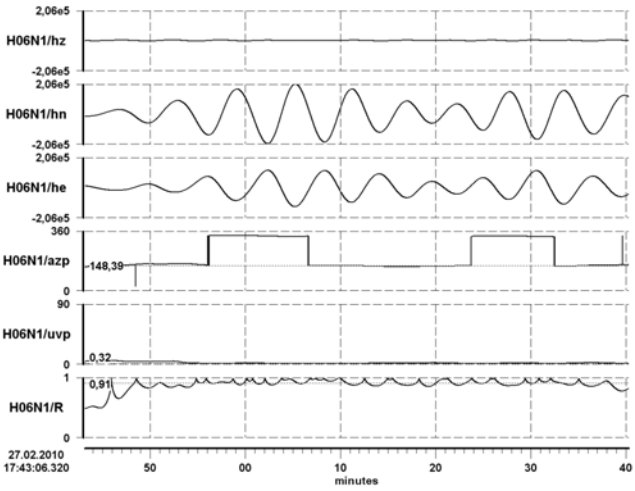

Figure 2. **Long period observations record at stations H06N1 in the 0.001-0.004 Hz frequency band.**

The method was tested on the H06 (Socorro island) T-station to determine if a polarization could be discerned on the three-component seismometer at the time of arrival of T-phases. The results were disappointing. One basic problem noted at T-stations is the strong micro-seismic noise from ocean surf. The noise spectrum occupies a wide frequency band, and the recording of T-phase signals in the short-period band is especially affected by this noise. It has not been possible to determine a direction of polarization for T-phases at T-stations, and therefore no enhancement of the system is possible along these lines.

In the course of investigating the signals at T-stations however, in a frequency pass-band at much lower frequency than the band optimal for T-phases, we re-discovered the potential for T-stations to be used in a tsunami alert system, as was first suggested by Okal (2007) and we made the observation that two of the stations at Socorro observed low-frequency signals on the horizontal components. The signals are associated with the passage of the tsunami wavetrain from two different tsunamigenic events. Figure 1 shows the long period fluctuations recorded by the northern seismometer H06N on Socorro Island during the passage of the tsunami generated by the February 27, 2010, Maule, Chile earthquake. The same components are displayed in Figure 2 along with the rectilinearity trace, *R* and the azimuthal direction trace, *azp* determined by the polarization analysis. The seismic traces are shown filtered in the 0.001-0.004 Hz frequency band in the first hour of the fluctuations. It is clear from this figure that the rectilinearity of these fluctuations is very good and the azimuth of the polarization is constant during that time.

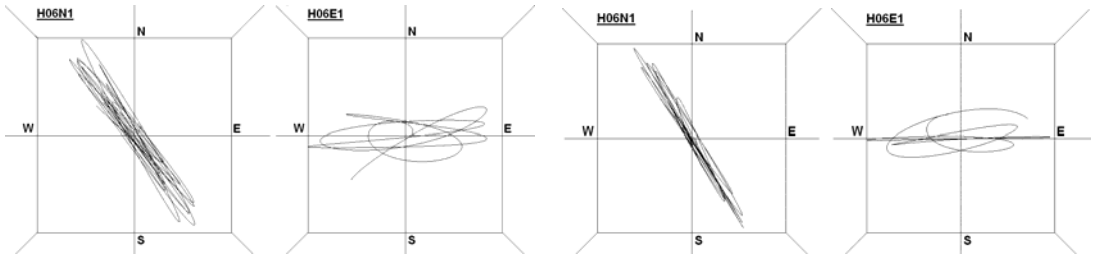

Figure 3. **Particle-motion hodographs in the horizontal plane for long period fluctuations at station H06N1 and at station H06E1 from the Samoa event (left) and the Maule, Chile event (right). Note the similar long-period elastic response to the tsunami loads from two events located at opposite ends of the Pacific.**

Figure 3 shows a particle motion hodograph of the fluctuations during the same time period as shown on Figure 2 for both the H06N and H06E stations. In both cases, the direction of polarization is clear, particularly for the northern station. The direction of polarization for the northern station H06N corresponds quite closely with the direction of propagation of the tsunami from the Maule event, which would fit well with the explanation given by

Okal (2007) for the observation of long period fluctuations coincident with the passage of tsunami waves. This is however purely coincidental, and this is demonstrated by the fact that the same polarization pattern is found for a tsunami generated by the September 29, 2009, earthquake from the Samoa Islands region. Furthermore, the polarization on the H06E station is in a different direction. In both cases, the polarization is the direction of the nearest shoreline. These observations, based on two different tsunamis whose sources are located at opposite ends of the Pacific Ocean indicate that we are observing a local disruption in the strain field of the island due to the passage of the tsunami. Our preferred explanation, elaborated on in a separate future publication, is that the island's strain field is responding elastically to the load of the very long wavelength tsunami on the walls of the island. The wavelength of the open ocean tsunami is long compared to the size of the island and the passage of the tsunami can be modeled as a slow rising and lowering of the water level around the island, inducing lateral pressure on the island's shore at sea level which successively squeezes and releases the body of the island.

Envelope Correlation

Seismic waves generated when in-water sound hits the coast are attenuated rapidly with distance from the coast. For this reason, T-stations in the IMS include multiple seismometers, installed near coastlines that face in different directions. While this geometry is not ideal for the detection of individual signals on multiple seismometers, there remains the possibility that such detections may occur. If the time lag between arrivals at separate seismometers could be estimated reliably then it could be possible to estimate arrival azimuth on the basis of that time lag. Similar lag-based processing is used when processing IMS hydrophone data but the situation is more complicated for seismometer stations for many reasons. First, the seismo-acoustic medium is not homogenous for the seismometer stations and the propagation between sensors may take place partly in water, partly in rock. Second, attenuation in the crust is higher than in the water so a signal clearly detected on one seismometer might be below the noise level at the other if its path has a significantly greater crustal element. Further problems arise from reduced signal-to-noise ratios and increased signal distortions, relative to the hydrophone sensors.

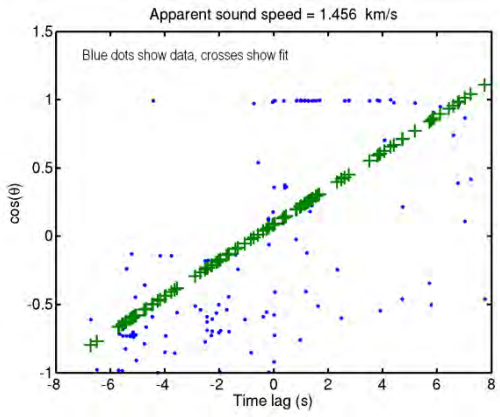

Figure 4. Relationship between time lag between arrival at two seismometers and cosine of angle made with line joining those seismometers.

These considerations meant that it was first necessary to determine if a functional relation actually existed between observed time lag and arrival azimuth. The data in Figure 4 show the results of such an investigation. The Reviewed Event Bulletin (REB) produced from automatic and analyst processing of IMS data was inspected for events that generated T-phases that were detected at both the north and east seismometers of the T-stations at Socorro Island, off the Pacific coast of Mexico. Envelope correlation of these signals was performed and the time lag between signals that showed significant correlation was determined. The arrival azimuth of the signals was taken from the "map azimuth" between the mean seismometer location and the REB event location. The cosine of the angle between the line joining the two seismometers and the arrival's incident direction is plotted on the y-axis in Figure 4 and the time lag is shown on the x-axis. The dots in the figure show the individual points and there is considerable scatter but a noticeable trend from bottom-left to top-right. The crosses show a linear curve fit to the cosine and time-lag data. Evidence for the existence of a functional relationship between cosine of angle and time lag is taken from the slope of the linear fit. For a homogenous medium, this gradient is determined by the seismometer separation and the local sound speed. Since the seismometer separation is known, the gradient of the line can be used to produce an effective local sound speed. As stated in the figure, this value was 1.456 km/s, a value close to a physically sensible estimate for the seawater sound speed.

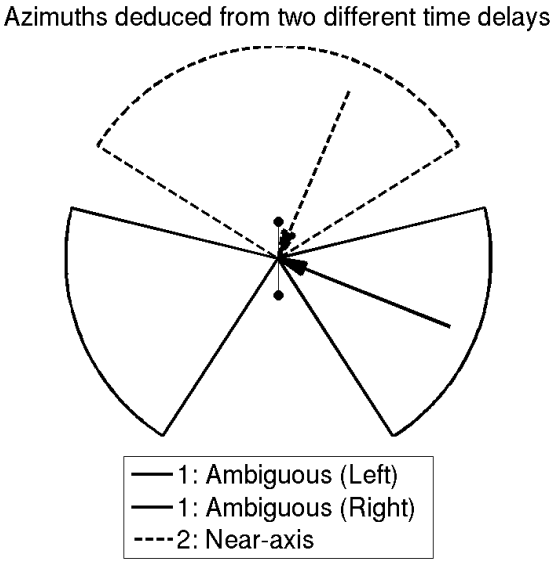

Figure 5. How measurement precision changes with azimuth.

The data shown in the figure were taken as confirmation of a functional – if noisy – relationship between lag and angle and the analysis proceeded. The precision of the relation was taken from the standard deviation of the residual between observed and line-fit values of the cosine. It was deduced that it was possible to determine cosine of incident angle on the basis of an observed time lag to a precision of +/- 0.5.
The important features of the relationship between the arrival azimuth of a signal and the precision to which it can be measured are illustrated in Figure 5. The solid arrow shows the direction at which a signal arrives from the right of the line joining the lower seismometer to the upper. The cosine uncertainty of +/- 0.5 translates into an azimuth uncertainty represented by the sector on the right-hand side, marked in a solid line. However, this single sector does not represent the whole uncertainty since the same time lag would have been observed had the signal arrived from the left-hand side at the same angle to the line joining the seismometers. Thus, the arrival represented by the arrow gives rise to a time lag that identifies the arrival azimuth as being anywhere within the left OR right-hand sectors. This situation represents a left-right ambiguity. If the arrival direction is changed to lie closer to the line joining the two seismometers, two effects occur. First, the width of the two sectors increases as the constant uncertainty in the cosine of the angle equates to an increasingly large uncertainty in that angle. Eventually, the left and right sectors overlap and the conditions for left-right ambiguity are no longer satisfied. Instead, a situation shown by the dashed lines in Figure 5 occurs. Here the signal results in a time lag between the two seismometers that allows the arrival to be located as lying within a single, wide sector. There is no longer any left-right ambiguity for these ‘axial’ arrivals but the angular uncertainty is high.

To investigate the usefulness of this ability to obtain a crude measure of arrival azimuth, a global association code (GA, Hanson et al, 2001) was run twice; first without azimuth information, then with the crude azimuth information quantified as a “delta azimuth” value attached to each arrival. This association process used not only the arrivals at the Socorro IMS station but also all arrivals at all IMS seismic, hydroacoustic and infrasound stations received within the same time period. Signals were extracted from a database to cover the periods of all detections made at Socorro: from March 2006 to June 2010. In cases where arrivals at Socorro were detected at times that indicated the possibility of the same seismic phase being detected at the two seismometers, the waveforms of the arrivals were envelope-correlated and, if the correlation passed a threshold, the two arrivals were paired. The time lag between the pair was then used to estimate the arrival azimuth and the azimuth uncertainty was calculated on the basis of this and the observed uncertainty in cosine of +/- 0.5. For left-right-ambiguous cases, the two arrivals were retained and each was given one of the two possible arrival azimuths, along with the relevant value of “delta azimuth”. For axial arrivals, one arrival was removed from consideration and the other arrival was assigned the deduced azimuth and “delta azimuth” values.

Differences in origins formed by GA in the two cases were observed to be of two types: in some cases the azimuth information allowed new associations to be made, in others it prevented arrivals at Socorro being associated with events for which their arrival times matched event hypotheses but their azimuths did not. In all, the process was

found to affect only a small proportion of events formed during the period of study. A map of event locations is shown in Figure 6, with black circles showing events involving arrivals at Socorro, green circles showing events that had new arrivals associated due to the presence of azimuth information and red circles showing events that had arrivals at Socorro removed because of azimuth information. The color shading in Figure 6 gives travel time to Socorro and ocean areas in white have no unblocked path to the island. Of around 580 events that had arrivals at Socorro associated with them, 7 had arrivals newly associated and 15 had arrivals disassociated due to azimuth information. In the vast majority of cases, no correlated arrivals were observed at the two seismometers and the process can be described as having only a small effect on GA processing.

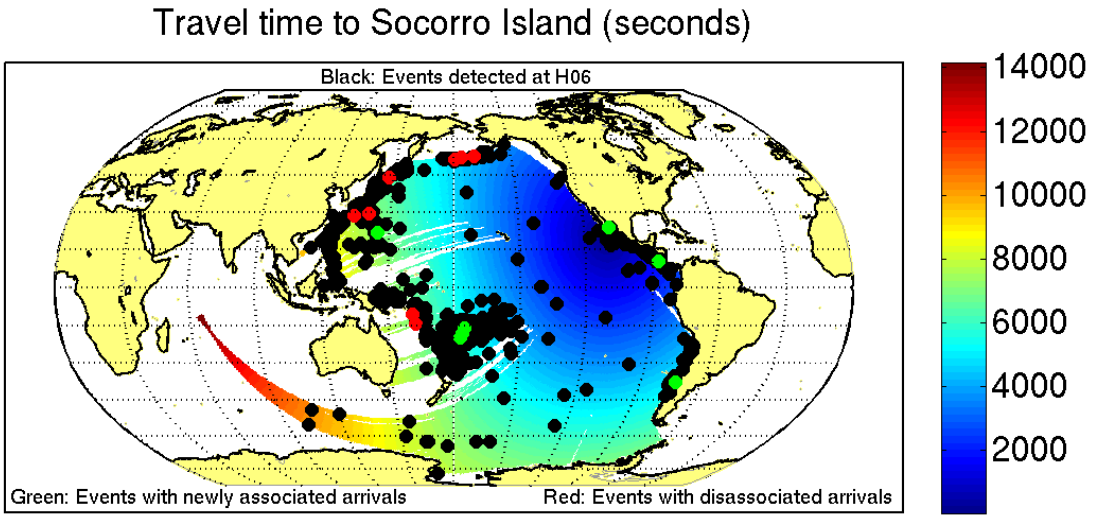

Figure 6. Event locations that included an arrival at Socorro Island (H06) formed by GA during the study period.

CONCLUSIONS AND RECOMMENDATIONS

The envelope correlation of near-simultaneous signals at two seismometers on Socorro Island was shown to allow a crude estimate of arrival azimuth to be derived. Significant correlation was achieved only in a small number of cases, reflecting the fact that the seismometer positions were chosen to give complete azimuth coverage, not to allow multiple detections of the same signal, as would be the case for a seismic array. Estimates of arrival azimuth were shown to change the results of global association processing for only 22 out of 580 events (4%) that were associated with arrivals at Socorro Island.

Polarization analysis in the frequency band of interest for T-phases did not yield any useful results partly due to the presence of surf noise in that frequency band and the lack of clear polarization for the T signals themselves. An unforeseen result of the investigation highlighted the potential use of near-coastal seismometers to complement tsunameters in the real-time tracking of an open ocean tsunami wavetrain. The mechanism generating long period fluctuation on horizontal components of near-coastal seismometers during the passage of a tsunami has now been shown to be very likely of near-field origin, and influenced by the geometry of the nearby coast.

ACKNOWLEDGMENTS

The authors gratefully acknowledge Dr Lassina Zerbo, head of the International Data Centre, for permission to publish the results reported here. The contribution to the tsunami analysis made by Spilio Spiliopoulos, head of the Monitoring and Data Analysis Section of the International Data Centre is also gratefully acknowledged.

REFERENCES

deGroot-Hedlin, C. and Orcutt, J. (Eds) (2001). Monitoring the Comprehensive Nuclear-Test-Ban Treaty: Hydroacoustics, *Pure Appl. Geophys.* 158: (3), 421–626.

Hanson, J., Le Bras, R., Dysart, P., Brumbaugh, D., and Gault, A. (2001). Operational processing of hydroacoustic data at the Prototype International Data Center, *Pure Appl. Geophys.* 158: (3), 425–456.

Okal, E. A. (2007). Seismic records of the 2004 Sumatra and other tsunamis: a quantitative study, *Pure and Applied Geophysics* 164: 325–353.

Shevchenko, V. P. (2002). Methodological principles of differential polarization analysis of vector signals, *Measurement Technique* 12: 14–17

Disclaimer

The views expressed in this paper are those of the authors and do not necessarily reflect the views of the CTBTO Preparatory Commission.

Radionuclide Monitoring

MODELING OF RADIOXENON PRODUCTION AND RELEASE PATHWAYS

Steven R. F. Biegalski, Mark Deinert, Carlos Rios Perez, and Justin D. Lowrey

University of Texas at Austin

Sponsored by National Nuclear Security Administration

Award No. DE-AC52-09NA28608
Proposal No. BAA09-57

ABSTRACT

Models have been developed to calculate the diffusion of radioxenon through porous environmental media such as sand and soil. Initial experiments have also been conducted to determine the feasibility of radioxenon transport through soil and sand columns. The initial studies investigated method detection limits for xenon detection. These results show that stable xenon may be detected through prompt gamma activation analysis (PGAA) with detection limits in the 10-ppm range. New experiments are being designed to measure the diffusion of xenon in a nondestructive temporal manner. The initial goal is to measure an overall diffusion coefficient for each porous medium. The secondary goal is to measure the isotopic fractionation resulting from the process.

OBJECTIVES

The two most recent nuclear weapon tests were conducted by the Democratic People's Republic of Korea (DPRK) in October 2006 and May 2009. Prior to the DPRK tests, India and Pakistan went through a series of nuclear tests in May 1998. It is important to recognize that all of the nuclear tests for more than 12 years have been conducted by countries developing nuclear weapons. The nuclear test yields were relatively small (Nuclear Explosion DataBase, 2010) and were conducted underground.

Radionuclide releases from these nuclear explosions have been minimal. Some of this may be attributed to the low yield of the devices tested, and some may be attributed to underground containment. Radionuclide releases from the DPRK tests have provided only radioxenon measurements from the first test conducted in 2006. Radioxenon measurements showed atmospheric concentrations that at times were close to background levels (Ringbom et al., 2009).

The objective of this work is to develop a better understanding of radioxenon transport after an underground nuclear explosion. The initial source signature of a nuclear weapon may be calculated with previously developed codes. However, there is a considerably larger error in the understanding of how the source signature is perturbed as radionuclides transport in an underground environment. Both chemical fractionation and isotopic fraction may occur. This work focuses on the initial diffusion of xenon through porous media (e.g., soil). The transport times and isotopic fractionation are calculated, and plans are under way to measure this processing utilizing PGAA.

RESEARCH ACCOMPLISHED

The research accomplished may be broken into three areas. The first is the calculation of a radionuclide source term from an underground nuclear explosion. The second area is calculation of diffusion for Xe isotopes. The last area is the initial calculations of detection limits for the measurement of Xe via PGAA.

Source-Term Calculation

As part of this work, models have been developed to calculate the radionuclides produced in a 1-kt nuclear explosion. The code MCNP is utilized to model the neutron transport, while ORIGEN 2.2 is utilized to calculate the production and decay of fission products, activation products, and transuranics resulting from the calculated neutron flux profile. MONTEBURNS is a pearl script that couples the MCNP and ORIGEN 2.2 calculations.

The model used for the source-term calculation is fairly simple. A weapons-grade fissile sphere (k_{eff} ~1.0) is surrounded by a soil or rock shell. For the uranium core case, an 8.7-cm-radius spherical core enriched to 94% ^{235}U was utilized; for the plutonium case, a 5.1-cm-radius spherical core enriched to 93.80% ^{239}Pu was used. MCNP was used to determine the thickness of soil or rock necessary to accurately model the attenuation and capture of neutrons within the media. For most of the soil and rock samples used, a thickness of 150 cm around the core was sufficient, such that less than 1% of neutrons escaped the system. For all cases studied, a soil/rock thickness of 2 m yielded on the order of 0.1% neutrons escaping.

Using MONTEBURNS, a database was complied to include the resulting concentration and activity of every isotope calculated for both a ^{235}U and a ^{239}Pu sphere normalized to a burn of 1 kt. Two different soil compositions and three different rock compositions were utilized in order to model a range of environments and effectively determine a range of resulting activities for the isotopes of concern. The resulting concentrations were then decayed in ORIGEN 2.2 to yield activities at post-burn times from 5 minutes up to 100 days. The results for the radioisotopes of concern are summarized in Tables 1 and 2.

Table 1. Activities in Ci of xenon radioisotopes following modeled 1-kt explosion at various post-burn decay times, assuming both uranium and plutonium cores

		Initial	5 min	1 hr	10 hr	1 day	10 days	30 days	100 days
Uranium Core	^{131m}Xe	1.361E-01	1.384E-01	7.948E-01	2.386E+01	5.972E+01	3.555E+02	2.638E+02	7.439E+00
	^{133}Xe	1.964E+02	3.016E+02	6.481E+03	8.824E+04	1.709E+05	1.127E+05	8.120E+03	7.805E-01
	^{133m}Xe	1.560E+03	1.566E+03	1.984E+03	7.379E+03	1.208E+04	1.743E+03	3.122E+00	7.441E-10
	^{135}Xe	1.109E+05	1.804E+05	6.651E+05	2.000E+06	1.329E+06	1.843E-01	2.334E-17	0.000E+00
Plutonium Core	^{131m}Xe	1.811E-01	1.846E-01	9.736E-01	2.705E+01	6.791E+01	4.147E+02	3.094E+02	8.740E+00
	^{133}Xe	6.991E+02	8.669E+02	7.171E+03	8.886E+04	1.717E+05	1.134E+05	8.178E+03	7.861E-01
	^{133m}Xe	5.446E+03	5.452E+03	5.831E+03	1.078E+04	1.490E+04	1.906E+03	3.425E+00	8.163E-10
	^{135}Xe	2.648E+05	3.722E+05	9.930E+05	2.269E+06	1.459E+06	1.988E-01	2.518E-17	0.000E+00

Table 2. Activities of ^{37}Ar in Ci resulting from modeled 1-kt explosion and subsequent neutron activation in various surrounding soil and rock concentrations

Soil Type		Initial	10 hr	1 day	10 days	30 days	100 days
Uranium Core	Wedepohl	1.014E+03	1.005E+03	9.937E+02	8.316E+02	5.597E+02	1.401E+02
	Taylor	9.455E+02	9.377E+02	9.270E+02	7.757E+02	5.222E+02	1.307E+02
	Mason	4.616E+02	4.579E+02	4.526E+02	3.788E+02	2.549E+02	6.380E+01
	Bowen	3.488E+02	3.460E+02	3.420E+02	2.862E+02	1.926E+02	4.820E+01
	Vinogradov	3.477E+02	3.448E+02	3.409E+02	2.853E+02	1.920E+02	4.805E+01
Plutonium Core	Wedepohl	1.760E+03	1.745E+03	1.725E+03	1.444E+03	9.717E+02	2.432E+02
	Taylor	1.502E+03	1.489E+03	1.472E+03	1.232E+03	8.294E+02	2.075E+02
	Mason	7.241E+02	7.182E+02	7.100E+02	5.941E+02	3.999E+02	1.001E+02
	Bowen	5.021E+02	4.980E+02	4.922E+02	4.119E+02	2.773E+02	6.938E+01
	Vinogradov	5.011E+02	4.970E+02	4.913E+02	4.111E+02	2.767E+02	6.925E+01

Diffusion Coefficients for Xe Isotopes

Although the molecular transport of xenon *in* air would be more accurately modeled as a multicomponent diffusion process, we will use first a binary diffusion scenario to analyze the transport of xenon stable isotopes through a porous medium. Assuming that the molecular motion of each isotope is independent from the presence of other xenon nuclides makes it possible to employ Fick's first law of diffusion in our analysis. This assumption is valid when the amount of all but one species in the gas mixture is small (Deen 1998). Nitrogen will be used as the solvent gas in our analysis because it is an inert gas and is the most abundant element in air. For a nonpolar binary gas mixture at low pressure, the binary diffusion coefficient can be approximated using the correlation proposed by Bird et al. (2007). This formula is presented in Equation 1:

$$2.745x10^{-4}\left[\frac{T}{\left(T_{cXe}T_{cN_2}\right)^{1/2}}\right]^{1.823} = \frac{pD_{XeN_2}}{\left(p_{cXe}p_{cN_2}\right)^{1/3}\left(T_{cXe}T_{cN_2}\right)^{5/12}\left(\frac{1}{M_{Xe}}+\frac{1}{M_{N_2}}\right)^{1/2}} \quad (1)$$

where
p = Total absolute pressure of mixture [atm]
T = Temperature of mixture [K]
D_{XeN_2} = Binary diffusion coefficient of xenon in nitrogen or vice versa.

Table 3 provides a range of diffusion coefficients as calculated by Equation 1 for ^{129}Xe and ^{131}Xe in a binary mixture with N_2. Both ^{129}Xe and ^{131}Xe are stable isotopes with natural abundances of 26.4% and 21.2%, respectively (Molnar, 2004). These two isotopes are chosen for this model because of their higher detection probability through PGAA. Table 3 shows that there is about a 0.1% difference between the diffusion coefficients of ^{129}Xe and ^{131}Xe. While that is not a huge difference, it will result in differential transport over time and distance. Such differences will result in isotopic fractionation and changes in the radioxenon isotopic signature.

Table 3. Binary diffusion coefficients of ^{129}Xe and ^{131}Xe in a binary gas with N_2

				^{129}Xe	^{131}Xe
Ma	**Mb**	**T [K]**	**p [atm]**	D_{XeN_2} **[cm^2 s^{-1}]**	D_{XeN_2} **[cm^2 s^{-1}]**
131	28.013	290	0.9	0.13502	0.13484
131	28.013	290	1	0.12152	0.12135
131	28.013	290	1.1	0.11047	0.11032
131	28.013	290	1.2	0.10127	0.10113
131	28.013	290	1.3	0.09348	0.09335
131	28.013	290	1.4	0.08680	0.08668
131	28.013	290	1.5	0.08101	0.08090
131	28.013	290	1.6	0.07595	0.07585
131	28.013	290	1.7	0.07148	0.07138
131	28.013	290	1.8	0.06751	0.06742
131	28.013	290	1.9	0.06396	0.06387

Analytical Model

The analytical model for the experiment developed for this paper assumes the following:

- The diffusion of xenon isotopes occurs at uniform and constant pressure and temperature and small concentrations.
- The molecular diffusion of xenon isotopes takes place in only one direction (X direction).
- The diffusion coefficient of xenon in nitrogen is independent of the mixture composition.
- The external convection effects are negligible.
- Each xenon isotope is treated as a different species, but all isotopes' molecular diffusion is treated as in a binary system isotope-nitrogen.
- There is no chemical reaction that produces/consumes the xenon isotopes.
- Both xenon and nitrogen have ideal gas behavior.

Based on these assumptions, the molar average velocity is zero, and the equation of continuity of each isotope in molar basis is simplified to

$$\frac{\partial C_{\alpha_{Xe}}}{\partial t} = D_{\alpha_{XeN_2}} \frac{\partial^2 C_{\alpha_{Xe}}}{\partial x^2} \tag{2}$$

where $C_{\alpha_{Xe}}$ is the molar concentration of the isotope $^{\alpha}Xe$, and $D_{\alpha_{XeN_2}}$ is the effective diffusion coefficient. The effective diffusion coefficient takes into account the porosity and tortuosity of the porous medium. Assuming a porosity of 0.3, a tortuosity factor of 1.96 was calculated using the experimental correlation obtained by Matyka et al. (2008). From these two factors, the effective diffusion coefficients for ^{131}Xe and ^{129}Xe obtained are 0.01857 and 0.01854 [cm^2 s^{-1}] respectively.

We will assume that the length of the duct where diffusion occurs is long enough to consider a semi-infinite medium. For this experiment, the initial and boundary conditions are

IC: t = 0, x >0 $C_{\alpha_{Xe}} = 0$

t = 0, x = 0 $C_{\alpha_{Xe}} = C_0$

BC1: t >0, x = 0 $\frac{\partial N_o}{\partial t} = A \cdot D_{\alpha_{XeN_2}} \frac{\partial^2 C_{\alpha_{Xe}}}{\partial x^2}$

BC2: t, x→∞ $C = 0$

where N_o is the initial number of moles of the xenon isotope under analysis ($N_o = C_o V_o$), C_o is the initial concentration of the isotope of interest at x = 0, and A is the cross-sectional area at x = 0.

Equation 3 presents the solution for these preliminary determinations of epicenter (PDEs), and initial and boundary conditions (Takeda et al., 2008):

$$\frac{C_{\alpha_{Xe}}(x,t)}{C_O} = \exp\left(\frac{A^2 D_{\alpha_{XeN_2}} t}{V_o^2} + \frac{Ax}{V_o}\right) \cdot erfc\left(\frac{A\sqrt{D_{\alpha_{XeN_2}} t}}{V_o} + \frac{x}{2\sqrt{D_{\alpha_{XeN_2}} t}}\right). \tag{3}$$

Figures 1 and 2 show the variation of the xenon concentration as a function of time and distance. Figures 3 and 4 show the variation of the ratio of molar concentrations ^{131}Xe and ^{129}Xe with respect to position and time, respectively, for diffusion of 0.0053 kg of natural xenon in a duct of 0.0070 m^2. According to these results, an important ratio between the concentration of ^{131}Xe and ^{129}Xe could be measured at the diffusion. Conversely, at this location, the ratio $C_{\alpha_{Xe}}/C_0$ is very small. For example, at t =1 2 h, a ratio of $C_{^{131}Xe}/C_{^{129}Xe} = 0.7995$ can be measured at x = 1.5 m (the isotopes ratio in natural xenon is 0.803); however, at this location and time, $C_{^{129}Xe}/C_o = 5.749x10^{-5}$ and $C_{^{131}Xe}/C_o = 5.725x10^{-5}$. These small concentrations will make the analysis of differential diffusion at the diffusion front difficult, as will be seen in the following section.

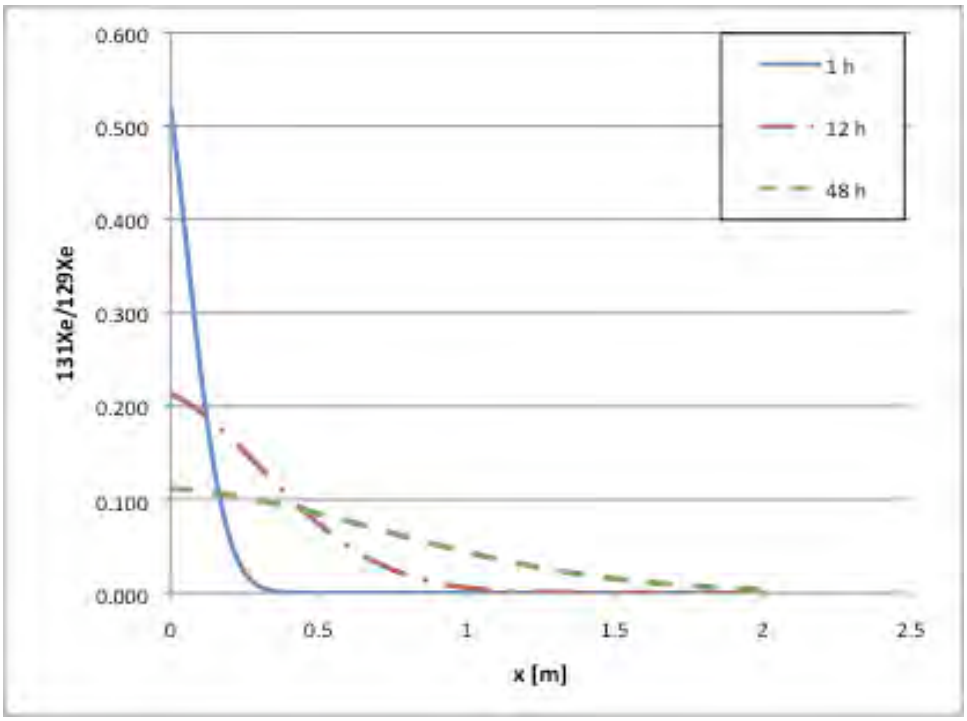

Figure 1. Variation of the Xe concentration profile at 1 h, 12 h, and 48 h.

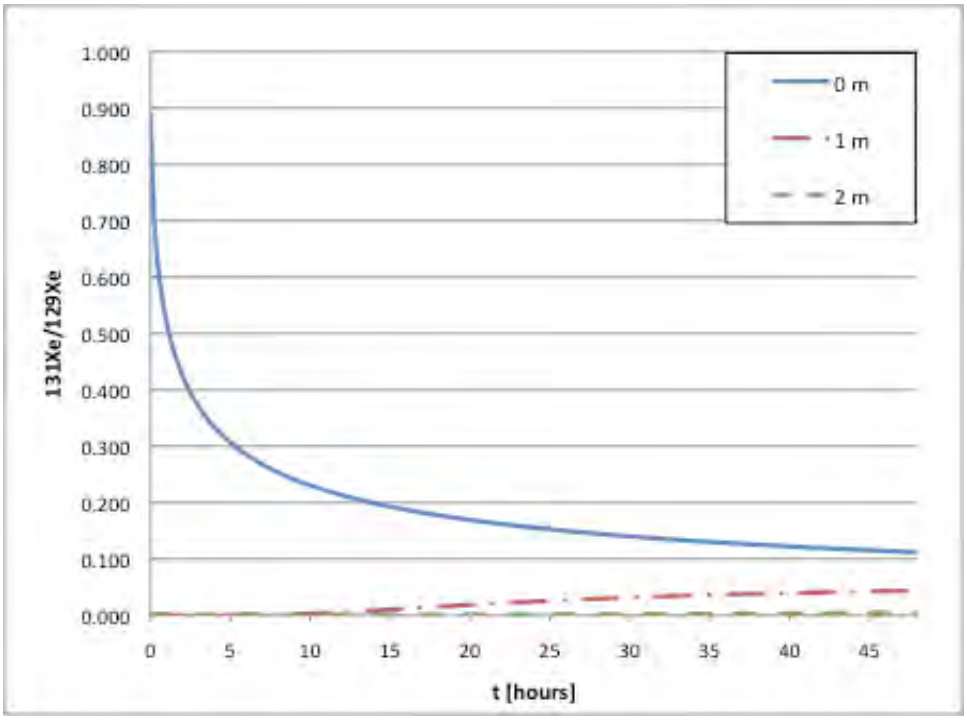

Figure 2. Variation of the Xe concentration with respect to time.

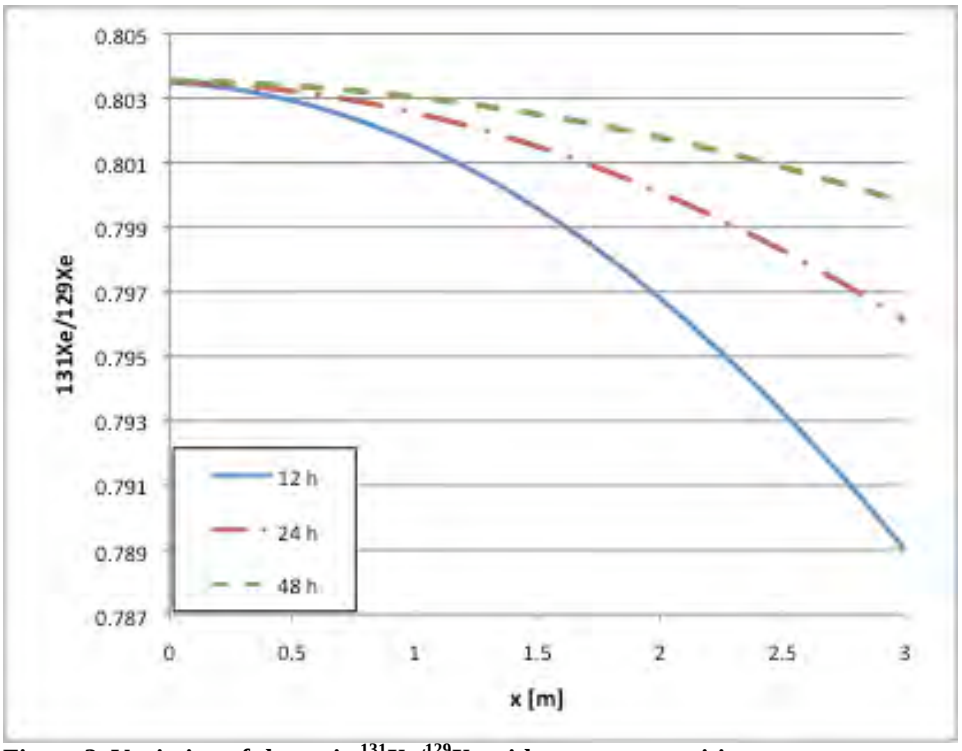

Figure 3. Variation of the ratio $^{131}Xe/^{129}Xe$ with respect to position.

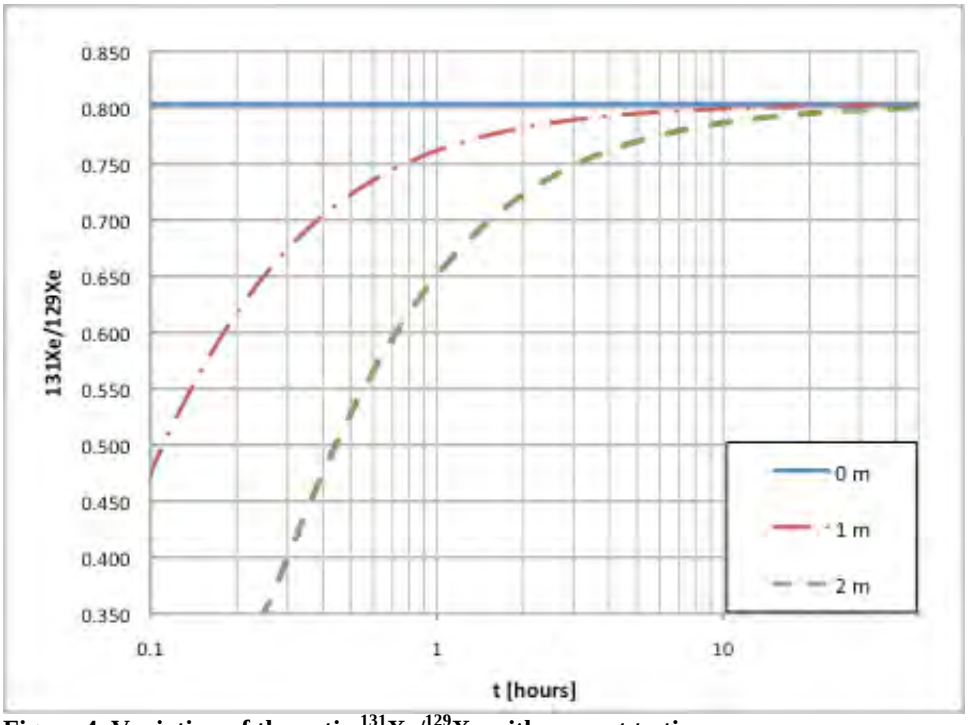

Figure 4. Variation of the ratio $^{131}Xe/^{129}Xe$ with respect to time.

Experimental Validation

This section evaluates the possibility of measuring the differential diffusion of ^{131}Xe and ^{129}Xe in a porous medium such as soil utilizing PGAA. First, the minimum amount of xenon needed for detection is calculated. Second, the effective volume of the sample is approximated. Finally, the minimum concentration of xenon required is obtained, and the feasibility of a xenon differential diffusion testing facility is discussed.

The minimum amount of xenon required to detect ^{131}Xe and ^{129}Xe is calculated from the molar detection limit (L_d) of the equipment and the isotopic composition of the inert gas. Detection limits of 6.3×10^{-5} and 7.7×10^{-5} moles were calculated for ^{129}Xe at 536 keV and ^{131}Xe at 630 keV, for a total efficiency of 0.00145 (This efficiency was estimated from the counting rates analysis of 100% and 20% xenon samples during various time spans). The approximate percentages of ^{131}Xe and ^{129}Xe in natural xenon are 26.4% and 21.2%, respectively. There are two sample volumes that are important for a PGAA: the active and the effective sample volumes (Molnar, 2004). The following assumptions are made to calculate a first approximation of the effective volume of the sample:

- The attenuation of the neutron beam along the sample is negligible (both elements have small (n-γ) cross section).
- The detector has a collimator of 70 mm in diameter (the end-cap diameter of the detector has to be 83 mm or larger in order to have an efficiency of 65% [Rèvay et al., 2007]).

It has been reported that the neutron beam cross section at the sample location is about 2.5×1 cm^2 (Rèvay et al,. 2007). From this, and from the assumptions listed before, the active volume of the sample could be approximated as 6.5 cm × 2.5 cm × 1 cm, i.e., 16.25 cm^3 (see Figure 5). Taking into account the geometric efficiency and the nonuniform intensity of the neutron flux, the effective sample volume is estimated to be 12 cm^3.

From the results calculated above, the minimum molar concentration of xenon required for a PGAA analysis is estimated as 2.5×10^{-5} mol·cm^{-3} (to detect 500 events in 1000 s). Assuming that at x = 0 we have pure xenon gas at 1 atm (molar concentration of 4.5×10^{-5} mol·cm^{-3}), the $C_{\alpha_{Xe}}/C_o$ minimum detectable is 0.556.

From Equation 3, the ratio of $C_{\alpha_{Xe}}/C_o = 0.556$ could be obtained at x = 0 and t = 45 min. Therefore, an accurate analysis at x = 0 m would be difficult to conduct in a noninvasive way since the detection time for the L_d predicted is 1000 s, and the average rate of change of $C_{\alpha_{Xe}}/C_0$ from t = 30 min to t = 45 min is about -6×10^{-5} 1/s.

The analysis of a separated sample would allow us to conduct the PGAA for longer times with smaller detection limits and therefore more accuracy. For example, the L_d for ^{129}Xe at 536 keV in a 7-h PGAA analysis is $2.5 \times 1\ 0^{-6}$ moles, and the $C_{\alpha_{Xe}}/C_o$ minimum detectable in the gas mixture is 0.022. This ratio can be obtained from a sample extracted at x = 0 after more than t = 150 h from initiating the diffusion experiment; i.e., a sample of gas extracted during the first 150 h has larger concentrations of ^{129}Xe than the L_d. Also, at t = 150 h, the ratio $C_{^{131}Xe}/C_{^{129}Xe}$ has changed by 0.07%. Although this change may seem very small, the analysis of the extracted gas may be prolonged in order to reach the desired accuracy without interfering with the diffusion experiment.

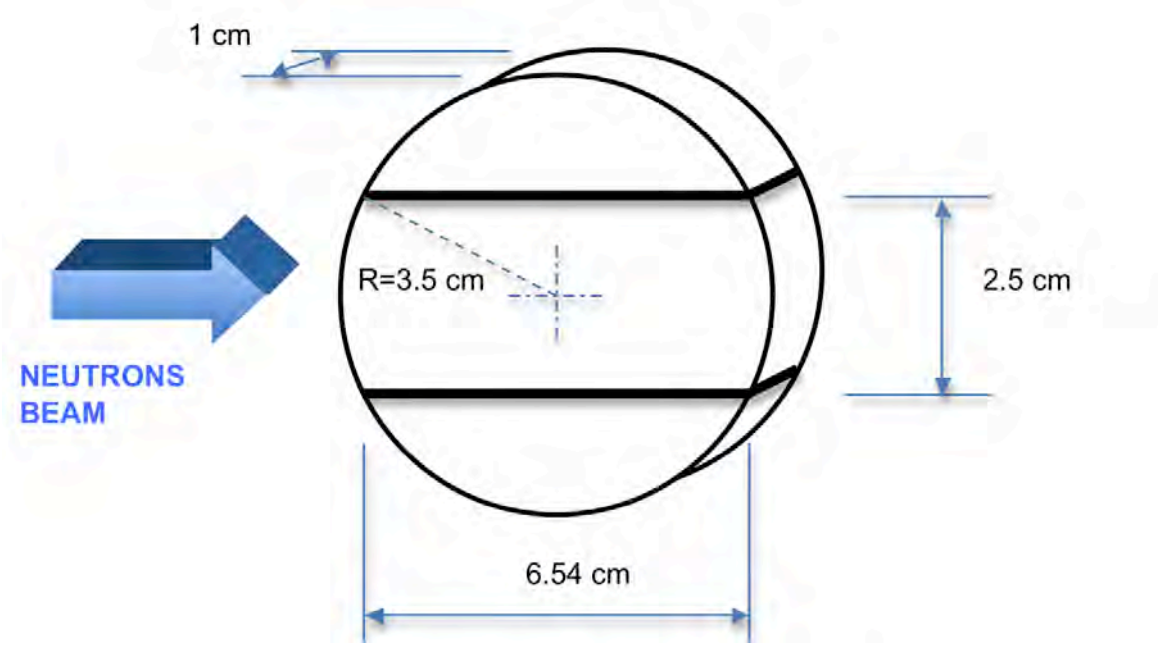

Figure 5. Effective sample volume, assuming a collimator of 7 cm in diameter.

CONCLUSIONS AND RECOMMENDATIONS

The results shown herein lay a foundation for the modeling of Xe transport within a natural soil or sand matrix. The computational results indicate that isotopic fractionation occurs during such transport. This is fundamentally important to understanding the nuclear forensic signature of radioxenon emissions from an underground nuclear explosion.

Experiments are being set up to measure the Xe diffusion through sand and soil media utilizing PGAA. The goal would be to measure the isotopic fractionation that occurs during the diffusion process. However, initial calculations show that measuring the differential diffusion will be a challenge. At a minimum, diffusion coefficients for Xe and the models may be benchmarked with such experiments.

ACKNOWLEDGEMENT

We extend our gratitude to the staff of the Nuclear Engineering Teaching Laboratory at the University of Texas at Austin for experimental support.

REFERENCES

Bird, R. B., W. E. Stewart, and E .N. Lightfoot (2007). *Transport Phenomena*, 2nd edition. New York, NY: John Wiley & Sons, Inc.

Deen, W. M. (1998). *Analysis of Transport Phenomena*. New York: Oxford University Press, Inc.

Matyka, M., A. Khalili, and Z. Koza (2008). Tortuosity-porosity relation in porous media flow, *Phys. Rev. E* 78: 026306.

Molnar, G. L., Ed. (2004). *Handbook of Prompt Gamma Activation Analysis with Neutron Beams*. Kluwer Academic Publishers.

Nuclear Explosion DataBase (2010). http://www.rdss.info/database/nedb/nedb_ent.html

Rèvay, Z., R. K. Harrison, E. Alvarez, S. R. Biegalski, and S. Landsberger (2007). Construction and characterization of the redesigned PGAA facility at the University of Texas at Austin. Nuclear Instruments and Methods in *Phys. Res. Sec. A: Accelerators, Spectrometers, Detectors and Associated Equipment*, 577: 611–618.

Ringbom, A, K. Elmgren, K. Lindh, J. Peterson, T. Bowyer, J. Hayes, J. McIntyre, M. Panisko, and R. Williams (2009). Measurements of radioxenon in ground level air in South Korea following the claimed nuclear test in North Korea on October 9, 2006, *J. Radioanal. Nucl. Chem.* 282: 773–779.

Takeda, M., H. Nakajima, M. Zhang, and T. Hiratsuka (2008). Laboratory longitudinal diffusion tests: 1. Dimensionless formulations and validity of simplified solutions. *J. Contam. Hydrol.* 97: 117–134.

DIGITAL DATA ACQUISITION GRAPHICAL USER INTERFACE

Matthew W Cooper, Craig E Aalseth, James H Ely, Derek A Haas, James C Hayes, Justin I McIntyre, and Brian T Schrom

Pacific Northwest National Laboratory

Sponsored by the National Nuclear Security Administration

Award No. DE-AC05-RLO1830/PL10-ASAR-NDD05

ABSTRACT

Traditional radioxenon measurements have been done by ground-based fixed systems, however in recent years there has been an increased need for systems capable of quick deployment or even complete mobility. Using the Pixie-4 data acquisition (DAQ) system can help reduce the electronics footprint of both current systems, like the radioxenon Radionuclide Laboratory 16 (RL-16) and the Swedish Automatic Unit for Noble Gas Acquisition (SAUNA), as well as future systems. Pacific Northwest National Laboratory (PNNL) has developed a Linux based Nyx graphical user interface (GUI) for Pixie-4 cards. The Nyx software can be installed on various Linux platforms and is written in C++. This software offers a rich user interface for configuring and operating the Pixie4 card and PNNL designed high voltage (HV) cards.

Nyx allows one to quickly get a nuclear detector operational by maintaining the core diagnostic features built into the Pixie-4 cards. First, Nyx maintains the multitude of adjustable parameters accessible in the Pixie-4 cards, which allows one to customize settings to take full advantage of a particular detector. Nyx also maintains an oscilloscope feature which is extremely useful to optimize settings and to verify proper detector behavior and is often the first feature used in Nyx during detector setup. Finally, Nyx allows the user to collect data in several formats including full pulse shapes to basic histograms. Overall, it is the corner stone for the transition of beta-gamma systems to a state-of-the-art digitizing DAQ system.

OBJECTIVES

Ground-based nuclear explosion detection systems currently available range from particulate to radioxenon samplers. There are now several detector packages available to the community in support of nuclear explosion treaty monitoring. These detectors range from β–γ (Reeder, 1998; Cooper, 2005; Cooper, 2007) to high purity germanium (HPGe) detectors, however, despite the differences in detectors, they all have signals that need to be read out and processed. Many of the fielded radioxenon and particulate systems use a combination of CAMAC and NIM. Although these electronics are very flexible they do have fairly large footprints, taking up as much as 45" tall by 24" wide by 31" deep.

Switching to new compact electronics will reduce the physical footprint and also significantly improve the DAQ capabilities through the ability to perform digital signal processing. However, the new data acquisition systems, like those produced by X-ray Instrumentation Associates (XIA) (XIA 2010), do create an interface problem for systems using a Linux operating system. The original systems designs have DAQ interfaces which will need to be reworked for new electronics to be useable. Currently the XIA based Pixie-4 cards (Hennig et al., 2007) run on only Microsoft (MS) Windows operating system (OS), which uses commercially available software as the interface. Since many Radioxenon systems are now using Linux based operating systems, PNNL has developed a Linux based GUI, called Nyx, for the Pixie-4 cards and National Instruments (NI) crate.

RESEARCH ACCOMPLISHED

The Nyx GUI (Schrom, 2009) is a useful tool for rapidly optimizing detector settings and acquiring the measurement data. It uses a number of open source compilers and libraries including Boost (Boost, 2010) and Qt (Qt, 2010) and is written entirely in C++. Nyx uses a modular design, which makes code changes easier by separating the components such as hardware access, the control logic and the graphical user interface. Nyx has been tested under several Linux platforms including Ubuntu, Debian, and Red Hat Enterprise Linux and has shown to be portable between Linux systems.

Nyx uses a tabbed environment to give easy access to each portion of the DAQ. It is organized into sections following a typical experimental flow: setup, configuration, and nuclear detector operation. The High Voltage (HV) tab contains adjustments for the HV. The tab also displays the actual voltage that each channel is set for, allowing some voltage diagnostics of detector performance. The Settings tab is as stated; it is where the user adjusts the majority of the parameters to optimize the signal acquisition from a given detector. The other configuration parameters are a little less straight forward, and control the signal triggering and integration.

Settings Configuration

Configuration parameters that need to be specified are trigger filters, energy filters, thresholds, and coincidence masks and windows. Figure 1 shows the channel sub-tab from on the settings tab. The trigger and energy filters are set based on a typical pulse from the detector of interest. The trigger parameter needs to be set to maximize the number of real pulses triggered as opposed to triggering on noise or missing a real pulse. Typically the threshold is set to reduce or eliminate the noise; it is normal to allow some noise events to be triggered in order to maximize real signal pulses processing. Usually the small amount of noise in the data does not impact the data quality. The energy filter, on the other hand, needs to have the rise time set to match a typical detector pulse rise time, which can be seen in Figure 2. In this particular case, the zoomed in portion of Figure 2 shows the rise time is approximately 0.5 μs. The flat top should be set to be longer than the rise time, however the longer the flat top the better detector energy resolution (maximum flat top length is often determined by the count rate).

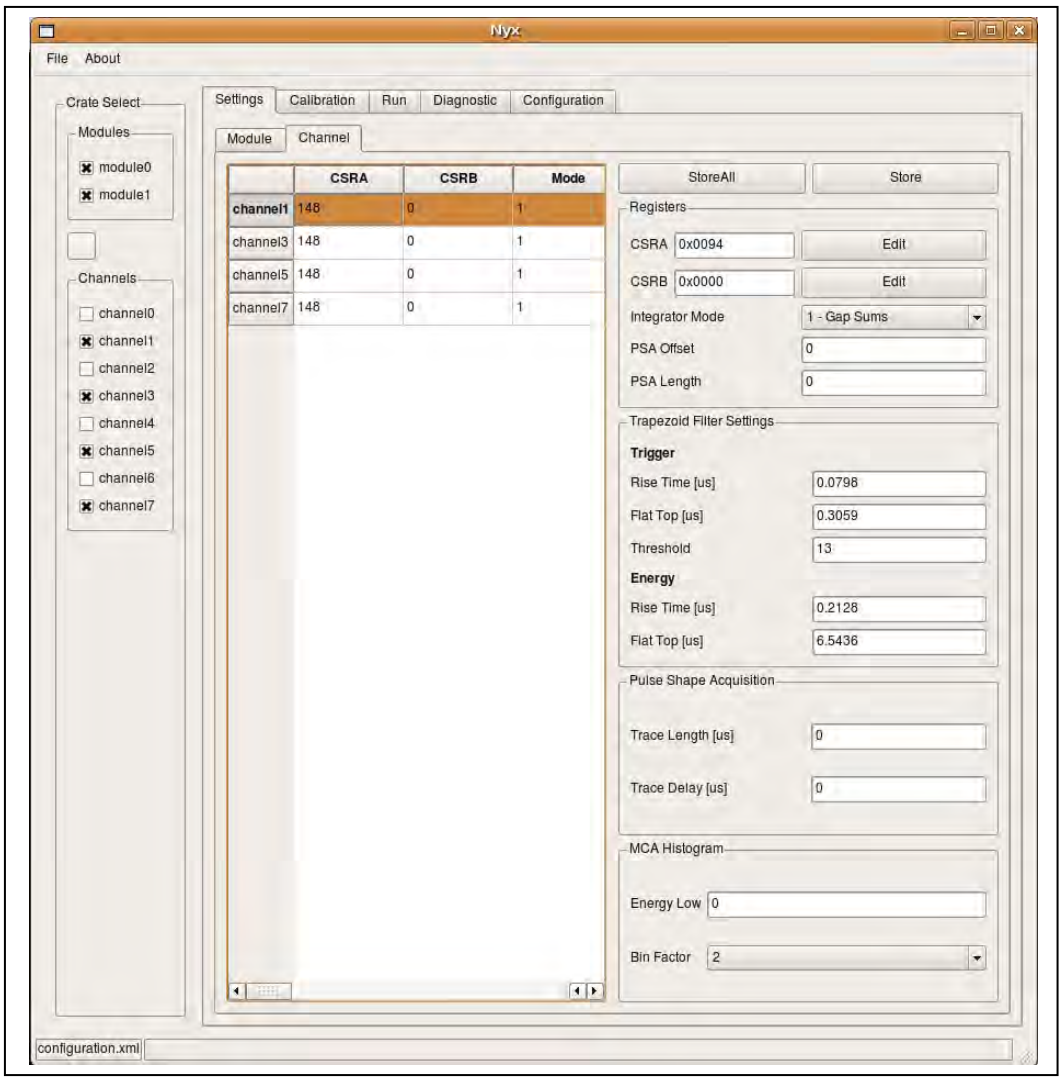

Figure 1. A screenshot of the Nyx settings tab.

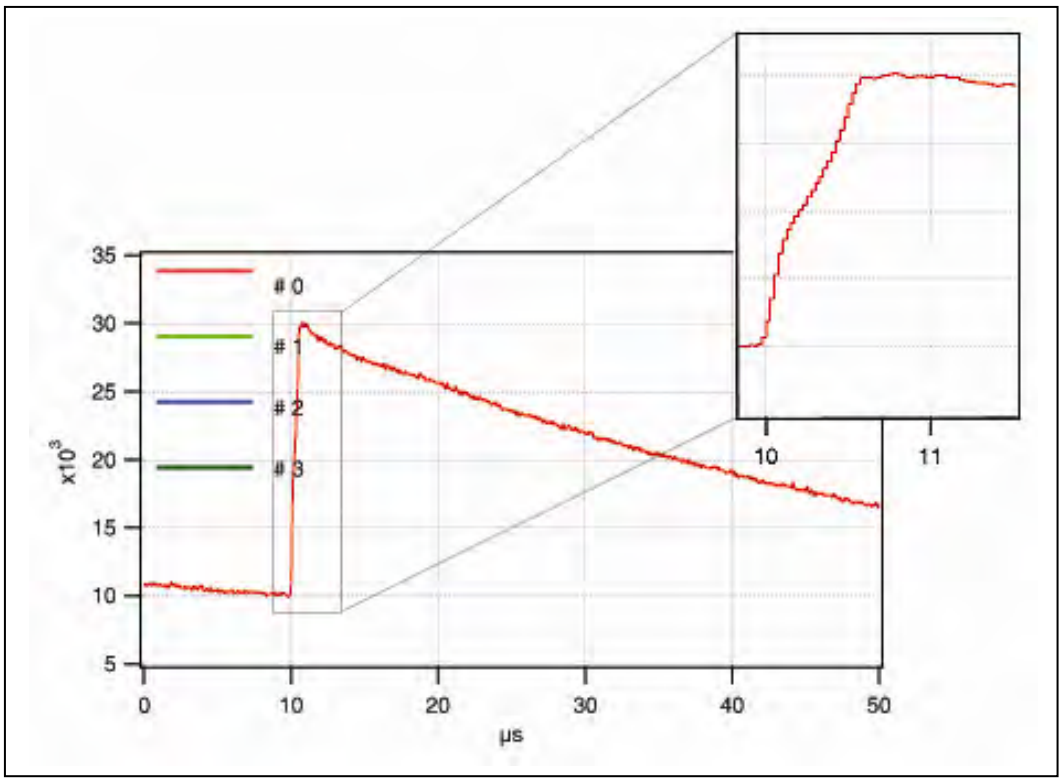

Figure 2. An example of a signal pulse that may be used to set the energy filter.

The second tab section, calibration, enables the researcher to match the dynamic range of the input signal with appropriate gain adjustments. An "oscilloscope" window allows untriggered sampling to capture traces, which are fit to find the preamplifier decay time constant, tau. Figure 3 shows a magnified pulse where tau is being fit using an exponential function built into the fitting routine of the Nyx software. This display also gives an indication of the amount of noise on the input signals. The noise level is indicated by how much variation (peak to peak) there is when a signal pulse is absent. This information can be used as an additional check on threshold settings; however it is usually best to empirically determine the optimal threshold by making several measurements.

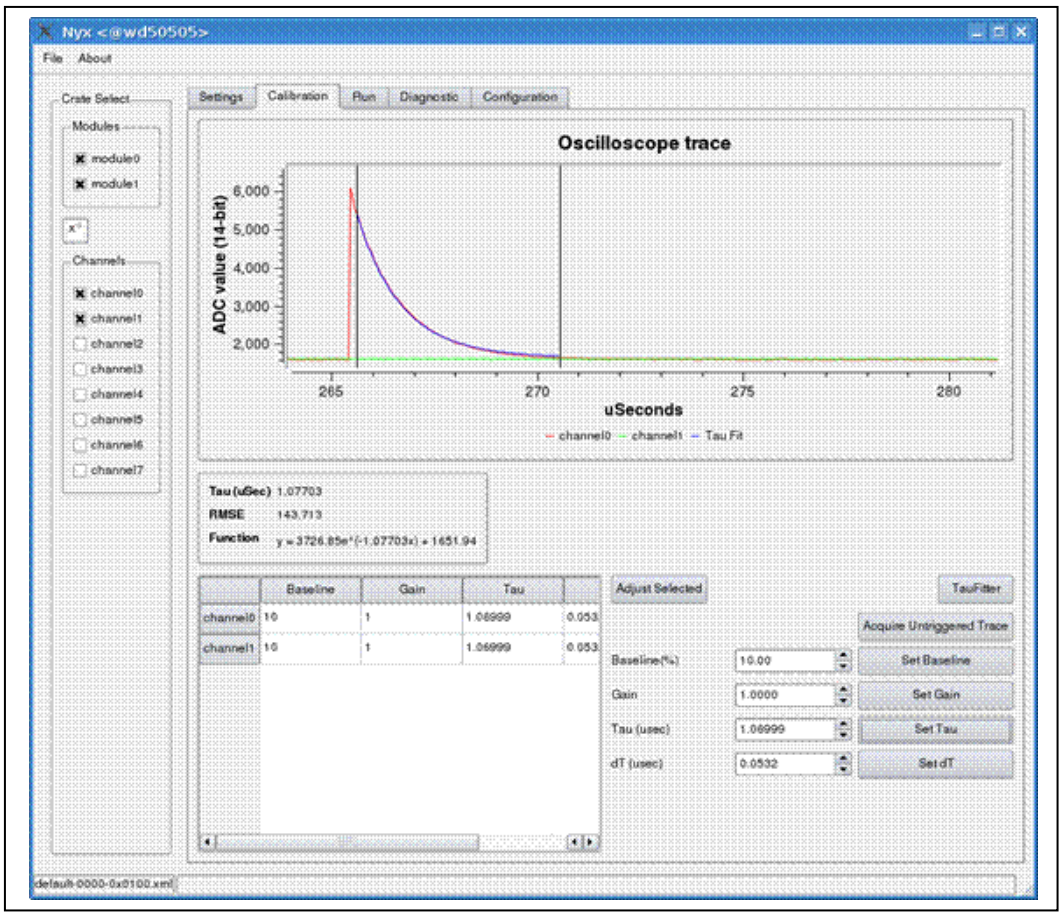

Figure 3. A screenshot of the Nyx calibration tab.

Data Acquisition

The third tab section, Run, controls the data acquisition. A data collection run can acquire the data in histogram mode, list mode or trace data mode. Each data mode uses progressively more storage space, with the trace data using a very large amount of storage. The histogram mode is generally used for either detector diagnostics or for simple experiments. The list mode is often used for experiments that are well characterized, but require some post acquisition processing. Finally, the trace data saves pulse information (shown in Figure 2) and is used in measurements where a sophisticated analysis and post processing is required. For example the trace data mode has been used for pulse shape analysis (Knoll, 1996; Lee, 1999; Gatti 1999; Vetter 2000; Aalseth 2000; Aalseth 2008) of both HPGe for spatial resolution and phoswich research (Farsoni, 2007; Hennig 2005), where a fast beta signal needs to be resolved from a slow gamma signal. Trace data is also frequently taken during initial setup to help determine parameter settings.

During a run there are several real time diagnostic tools available. On the run tab, the count rate and livetime/deadtime can be monitored by clicking on the refresh stats button located 2/3 of the way down the window. This is important to check to ensure the deadtime is not too high (>20%), which may indicate poor data quality or parameters that require further optimization. The other frequently monitored data are the histograms which appear on the diagnostic tab (see Figure 5). Often these are used to make sure the data is being collected properly.

Independent of the data mode being used; a run can be stopped by a particular event or action. Measurements can be stopped at a specified number of recorded events, elapsed time and also by manual stop. At the conclusion of each run, a file set containing the raw data, the complete state of the hardware (including parameter values) and the meta-data for the run is archived. The meta-data includes: parameters from the card, from the system, and parameters that the researcher input for later reference. The archive file can be read in by the Nyx software to load

the settings from that a particular run in order to repeat that measurement and is a typical method for setting the parameters. Figure 4 is a screen capture of the Run window showing typical settings for a run collecting trace data.

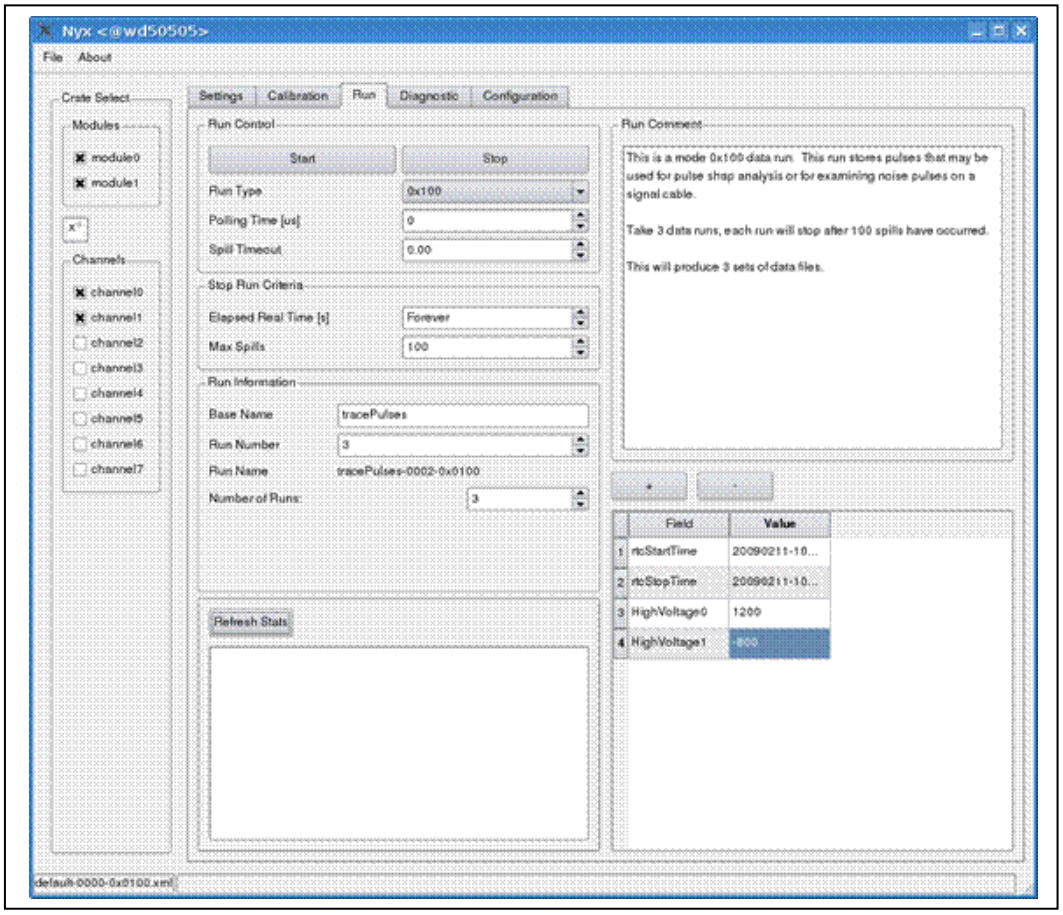

Figure 4. A screenshot of the Nyx run tab.

The fourth tab section, Diagnostic, is for preliminary data analysis that can be used to assess the configuration and operation of the detector. The analysis tools in this section use simplified algorithms (such as a basic Gaussian fitting routine) that are suitable for ensuring valid operation but are not meant for rigorous data analysis. This includes an individual pulse viewer for fine-tuning lower level thresholds and a histogram viewer for verifying both energy resolutions and gain matching. Figure 2 shows a captured pulse in the pulse viewer, while Figure 5 shows the 661.7-keV peak from ^{137}Cs in the histogram before the peaks have been aligned. Aligning the peaks can be done using the gain settings (in the Calibration tab) or adjusting the HV.

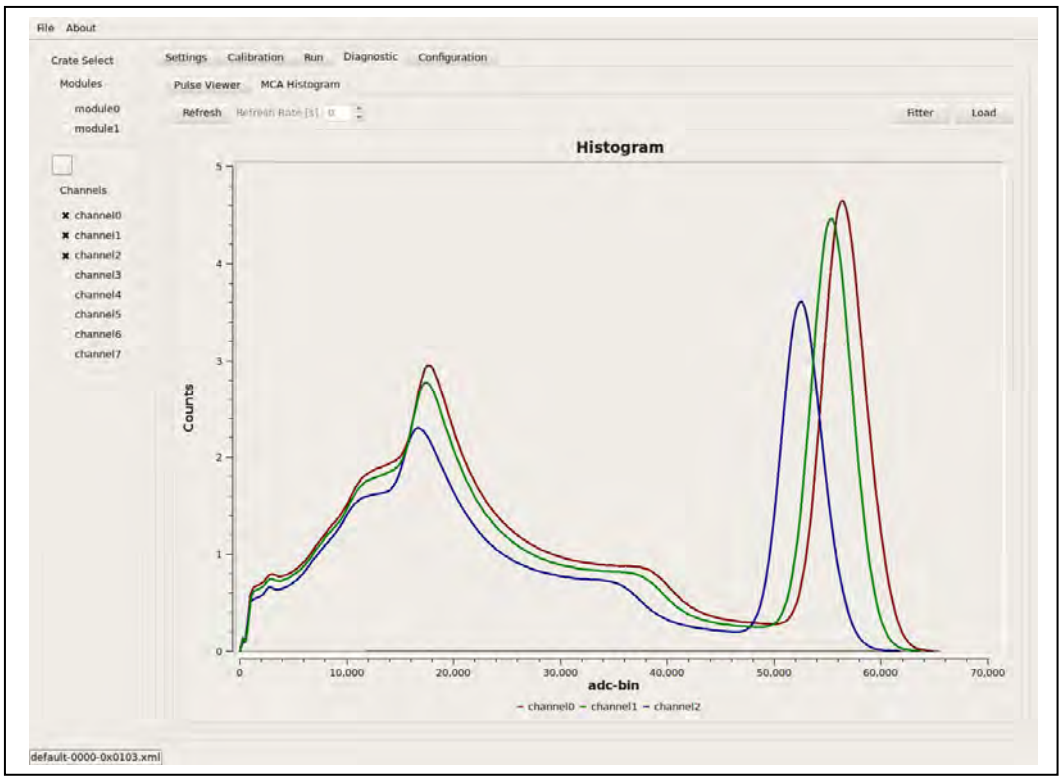

Figure 5. A screenshot of the Nyx diagnostic tab showing ^{137}Cs spectra.

Other Features

The fifth tab, Configuration, is intended for advanced users and will not be discussed in this paper. Finally, one of the commonly used user interface features, which appears independently of which tab is selected, is the module and channel selections. The modules and channels selections are always visible. They allow the user to select what will be displayed on a given screen. For instance, if only one channel has a histogram of interest, then only that channel is selected (checked). This ability to only display selected channels or modules is important when several different detector styles are being used. Each detector will need to be configured independently from the others, so displaying only the channel that is currently being optimized is extremely useful. This transparency, visibility, and selectability makes setting up channels simple and less error prone than other methods whether there are several identical or unique channels.

CONCLUSIONS AND RECOMMENDATIONS

XIA has improved the Pixie4 card by packaging it in a compact peripheral component interconnect (cPCI) bus connector that fits in a National Instruments crate. Pacific Northwest National Laboratory developed a complimentary four channel HV card that fits the same cPCI form factor. The matching HV and data acquisition cards result in a compact multichannel data acquisition system with pulse digitization and large data storage capability. The form factor of the NI crate, Pixie-4 cards and PNNL developed HV cards allows what used to be a physically very large data acquisition system to now be only 8” x 8” x 12” without losing any functionality.

Nyx is the interface with the DAQ system and allows the user to have complete control of the nuclear detector. Nyx interfaces with the Pixie-4 and HV cards, allowing the user to optimize the detectors signal for any particular detector type/style. Nyx maintains a strong emphasis on signal processing and has several tabbed screens to set run parameters. The Nyx software provides fully functional list-mode and pulse-shape data collection, which is critical for applications that either do post processing, pulse shape analysis or pulse shape discrimination. Nyx is a valuable resource for Linux based systems that need a small, yet powerful, DAQ system.

REFERENCES

Aalseth, C.E (2000). Germanium spectrometer pulse-shape discrimination for 76Ge double-beta Decay, Department of Physics and Astronomy, University of South Carolina, Dissertation.

Aalseth, C. E., A. R. Day, J. E. Fast, E. W. Hoppe, T. W. Hossbach, B. J. Hyronimus, M. E. Keillor, KE Litke, and A Seifert (2008). Background rejection by pulse shape discrimination in a low-background, internal-source Proportional counter from electroformed copper. *Methods and Applications of Radioanalytical Chemistry* MARC VIII, Kona.

Boost www.boost.org (2010).

Cooper M. W., A.J. Carman, J.C. Hayes, T. R. Heimbigner, C.W. Hubbard, K. E. Litke, J. I. McIntyre, S. J. Morris, M. D. Ripplinger, and R. Suarez (2005). Improved β-γ coincidence detector for radioxenon detection, in *Proceedings of the 27th Seismic Research Review: Ground-Based Nuclear Explosion Monitoring Technologies*, LA-UR-05-6407, Vol. 2, pp. 779–786.

Cooper MW, JI McIntyre, TW Bowyer, AJ Carman, JC Hayes, TR Heimbigner, CW Hubbard, LS Lidey, KE Litke, SJ Morris, MD Ripplinger, R Suarez, and RC Thompson (2007). *Nucl Instr and Meth*. in Physics Research. Section A, Accelerators, Spectrometers, Detectors and Associated Equipment 579(1) 426.

Farsoni, A., Hamby, D., Ropon, K., & Jones, S (2007). A two-channel phoswich detector for dual and triple coincidence measurements of radioxenon isotopes, in *Proceedings of the 29th Monitoring Research Review: Ground-Based Nuclear Explosion Monitoring*, LA-UR-07-5613, Vol. 2, pp. 747–756.

Gatti, E., G. Casati, A. Geraci, A. Pullia, G. Ripamonti (1999). A pulse-shape analysis approach to 3-D position determination in large-volume segmented HPGe detectors. IEEE *Nucl. Sci. Sym. Conf. Rec*., 346.

Hennig, W., Tan, H., Warburton, W., & McIntyre, J. (2005). Digital pulse shape analysis with phoswich detectors to simplify coincidence measurements of radioactive xenon, in *Proceedings of the 27th Seismic Research Review: Ground-Based Nuclear Explosion Monitoring Technologies*, LA-UR-05-6407, Vol. 2, pp. 787–794.

W. Hennig et al. (2007). Conf. The DGF Pixie-4 spectrometer – compact digital readout electronics for HPGe clover detectors. *NIM B*, 263:1 (2007) 175.

Kröll, T.H., I. Peter, Th. W. Elze, J. Gerl, Th. Happ, M. Kaspar, H. Schaffner, S. Schremmer, R. Schubert, K. Vetter, and H. J. Wollersheim (1996). Analysis of simulated and measured pulse shapes of closed-ended HPGe detectors. *Nucl. Instr. and Meth.* A 371 (1996) 489.

Lee, I.Y., Gamma-ray tracking detectors (1999). *Nucl. Instr. and Meth*. A 422: 195.

P.L. Reeder, T.W. Bowyer, and R.W. Perkins (1998). J. Beta-Gamma Counting System for Xe Fission Products, *Radioanal. Nucl. Chem*. 235: 1-2, 89.

Qt www.nokia.com (2010).

Schrom B.T., C.E. Aalseth, J.C. Hayes, J.I. McIntyre, C.W. Hubbard, R Suarez, and T.R. Heimbigner (2009). Case study: writing Linux control software for XIA's Pixie4 DAQ. MARC, Kona, HI on April 15.

Tepper, G., and J. Losee (1996). A compressed xenon ionization chamber X-ray/gamma-ray detector incorporating both charge and scintillation collection. *NIM A* 368: 862.

Vetter, K., A. Kuhn, M. A. Deleplanque, I. Y. Lee, F. S. Stephens, G.J. Schmid, D. Beckedahl, J. J. Blair, R.M. Clark, M. Cromaz, R. M. Diamond, P. Fallon, G.J. Lane, J. E. Kammeraad, A. O. Macchiavelli, and C. E. Svensson (2000). Three-dimensional position sensitivity in two-dimensionally segmented HP-Ge detectors, *Nucl. Instr. and Meth*. A 452 223.W. Hennig et al. conf., *NIM B*, 263:1, 175.

Warburton, W.K., M. Momayezi, B. Hubbard-Nelson and W. Skulski (2000). Digital Pulse Processing: New Possibilities in Nuclear Spectroscopy, *App Rad and Isot*., 53 (4-5), 913.

XIA. http://www.xia.com/. (2010).

CHARACTERIZING A TWO-CHANNEL PHOSWICH DETECTOR USING RADIOXENON ISOTOPES PRODUCED IN THE OREGON STATE UNIVERSITY TRIGA REACTOR

Abi T. Farsoni and David M. Hamby

Oregon State University

Sponsored by the National Nuclear Security Administration

Award No. DE-FC52-06NA27322
Proposal No. BAA06-36

ABSTRACT

Low concentrations of radioxenon isotopes can be measured with a high sensitivity using beta/gamma coincidence technique. In this technique, a coincidence event is recorded when two signals from beta and gamma detection channels are detected simultaneously. These two coincident signals are then processed to establish a two-dimensional beta/gamma coincidence spectrum in which the four radioxenon isotopes can be measured in the sample. In many beta/gamma coincidence systems, beta and gamma radiations are detected in two separate channels. Another approach is to use a phoswich detector in which both radiations can be detected by one single channel, and simplifying the coincidence system configuration.

To expand the solid angle of the radioxenon detection geometry close to 4π, a two-channel and planar triple-layer phoswich detection system was designed and constructed. In order to characterize the phoswich detection system for radioxenon measurements, we have irradiated enriched stable samples of ^{132}Xe and ^{134}Xe gas with thermal neutrons from the TRIGA reactor at the Oregon State University (OSU). ^{133m}Xe, ^{133}Xe, and ^{135}Xe were successfully produced and injected into the detector gas cell using a simple gas transfer manifold system. To enhance the efficiency of coincidence detection between the two phoswich detectors, a synchronization logic mode was added into the previous firmware of our two-channel digital pulse processor system. In this paper, we will describe xenon neutron irradiation conditions, sample transfer procedures, and beta/gamma coincidence measurements results. Also a brief description of our synchronization logic mode will be covered in this paper.

OBJECTIVE

The Comprehensive Nuclear-Test-Ban Treaty Organization (CTBTO) has established the International Monitoring System (IMS) to monitor underground nuclear weapon tests by several verification means including measuring the concentration of radioactive xenon gas in the atmosphere. Several high-performance detection systems have been developed or are under development to detect the four radioxenon (^{131m}Xe, ^{133m}Xe, ^{133}Xe and ^{135}Xe) in the atmosphere. The Swedish Automatic Unit for Noble gas Acquisition (SAUNA, Ringbom et al., 2003), the SPALAX unit (Fontaine et al., 2004) and Automated Radioxenon Sampler and Analyzer (ARSA, McIntyre et al., 2001) are among these detection systems. Except for the SPLAX unit which uses a high-purity germanium detector to detect only X-rays and gamma-rays, other systems are designed based on beta/gamma coincidence measurement techniques in which both beta particles (or conversion electrons) and gamma-rays (or X-ray) must be detected simultaneously. Albeit with different geometry designs, both the SAUNA and the ARSA systems use two separate scintillation channels for detecting beta-particles and gamma-rays. Since the two scintillation channels in the SAUNA and ARSA systems are optically isolated from each other, scintillation photons are collected with more than one photomultiplier tube (PMT) for each channel. In the SAUNA system, three PMT's are used to detect a coincidence event: two PMT's in the beta channel and one PMT in the gamma channel. In the ARSA system, four PMT's are involved in detecting a coincidence event for each gas cell: two PMT's in the beta channel and two PMT's in the gamma channel.

Beta/gamma coincidence detection can be simplified using phoswich detectors in which both beta-particles and gamma-rays can be detected simultaneously using a single PMT (Ely et al., 2003; Hennig et al., 2005; Farsoni et al., 2007). In phoswich detectors, more than one scintillation material is optically coupled to a PMT. Beta/gamma coincidence events then can be identified using digital pulse shape analysis of the anode pulses. We have developed a two-channel phoswich detection system based on our single-channel prototype phoswich detector (Farsoni et al., 2009). Each phoswich detector consists of three scintillation layers: BC-400, CaF_2 and NaI(Tl) to detect beta-particles (CE), X-rays and gamma-rays, respectively. We have also developed and constructed a two-channel, fast and compact digital pulse processor to capture and analyze complicated anode pulses from the two-channel phoswich detector. The digital pulse processor captures anode pulses with a maximum sampling rate of 250 MHz and an amplitude resolution of 12 bits independently from each channel. All the digital modules and functions such as trigger logic, circular buffer and coincidence detection are implemented in a 1500K gate-equivalent SPARTAN-3 field-programmable gate array (FPGA) from Xilinx Incorporated. The on-board FPGA is automatically programmed via a high-speed USB2.0 port when the processor is connected to the personal computer (PC). Once the FPGA is programmed, the high-speed USB2.0 interface is used either for controlling the processor or transferring data. In this paper, we will present our recent measurements with xenon radioisotopes produced in the TRIGA reactor at the Oregon State University. We also describe our simple procedure to transfer stable and irradiated xenon gas from its vessel to reactor and from there to the detector gas cell. To enhance the coincidence efficiency of the two-channel system, a synchronizing mode was designed and added into the original firmware of the FPGA deployed on the digital pulse processor, a brief description of this mode in capturing coincidence events between the two channel will be presented as well.

RESEARCH ACCOMPLISHED

Detector Design

Based on our previous experiments with a prototype phoswich detector (Farsoni et al., 2009), a two-channel phoswich detection system was designed and constructed. The detector consists of a thin hollow disk (with 2 mm thickness and 76.2 mm diameter) as xenon gas cell, surrounded by two identical planar triple-layer phoswich detectors (Figure 1). The gas cell is completed by an aluminum sleeve which also joins the two detectors (Figure 2). This design provides a solid angle of about 3.4π for the gas cell, close to that of the ARSA system (~ 3.5π). The planar shape of the detectors has several important advantages, among which are the reduced cost due to its simplicity, and because it has a minimum non-uniformity in light collection efficiency, will not unreasonably degrade the beta or gamma energy resolution. Each phoswich detector consists of a plastic scintillator (1.5 mm) for detecting beta and conversion electrons, a CaF_2 crystal (2.0 mm) for X-ray detection and a NaI(Tl) crystal (25.4 mm) for measuring gamma rays.

Previous tests on the ARSA system have shown that latent radioxenon remains in the gas cells even after evacuation of the gases, leading to a memory effect which increases the background level for subsequent measurements.

Research performed at the Pacific Northwest National Laboratory (Seifert et al., 2005) showed that use of a 1-µm aluminum layer on plastic scintillators affectively reduces the memory effect from radioxenon gases remaining in the cells after evacuation. Therefore, to minimize this effect, a very thin layer of aluminum (1 µm) was deposited on the surface of two plastic scintillators (facing the gas cell). The aluminum coating process was performed using vacuum coating process at the Oregon State University. The coated plastic scintillators then were sent to the Saint-Gobain company for final assembly of the phoswich detectors. In addition, the aluminum coating on each plastic scintillator will optically isolate the two phoswich detectors from each other and make a reflection surface for each detector.

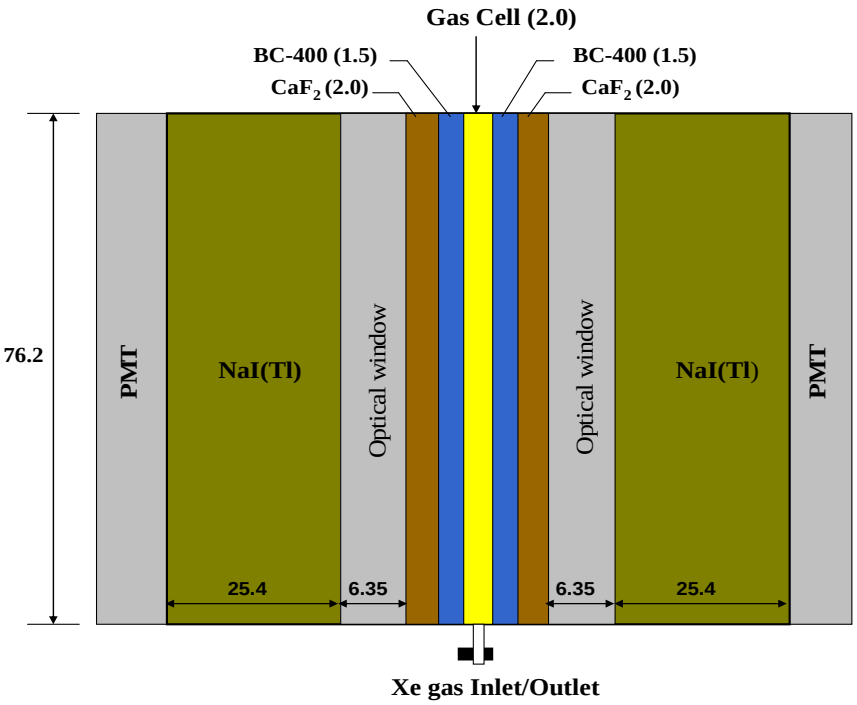

Figure 1. Schematic arrangement of the two-channel phoswich detector. All dimensions are in millimeters.

Radioxenon Production

To characterize our phoswich detectors in measuring xenon radioisotopes, two enriched (> 99%) and stable isotopes of xenon, ^{132}Xe and ^{134}Xe, were purchased. These stable xenon isotopes were activated by thermal neutrons in our TRIGA reactor at the Oregon State University to produce ^{133m}Xe, ^{133}Xe and ^{135}Xe. Our calculations show that irradiating 3 ml of these stable xenon isotopes in a thermal flux of $7x10^{10}$ n . cm^{-2}. sec^{-1} (in the thermal column of the TRIGA reactor) for 30 minutes generates 0.05 µCi of ^{133m}Xe, 0.17 µCi of ^{133}Xe and 1.47 µCi of ^{135}Xe.

Gas Transfer Manifold System

Designing a simple but efficient way to irradiate a small amount of xenon gas was essential for our radioxenon production and measurement work. The simplest way was to use a disposable syringe as a gas irradiation chamber. Polypropylene syringes mainly contain hydrocarbons and do not produce significant activity after neutron irradiation. Then, a low-cost gas transfer manifold system was designed to transfer gas from its cylinder to a disposable polypropylene syringe and from there to the detector gas cell (after neutron activation). The manifold system consists of a vacuum pump, a plastic Luer manifold and polyethylene pipes as depicted in Figure 2. This very simple but handy and efficient arrangement transfers the stable xenon gas from its vessel into a 3 ml disposable polypropylene syringe. The syringe, containing stable xenon, is then irradiated in the thermal column of OSU's

TRIGA reactor. The activated xenon gas is then injected into the phoswich detector using the same manifold as depicted in Figure 2.

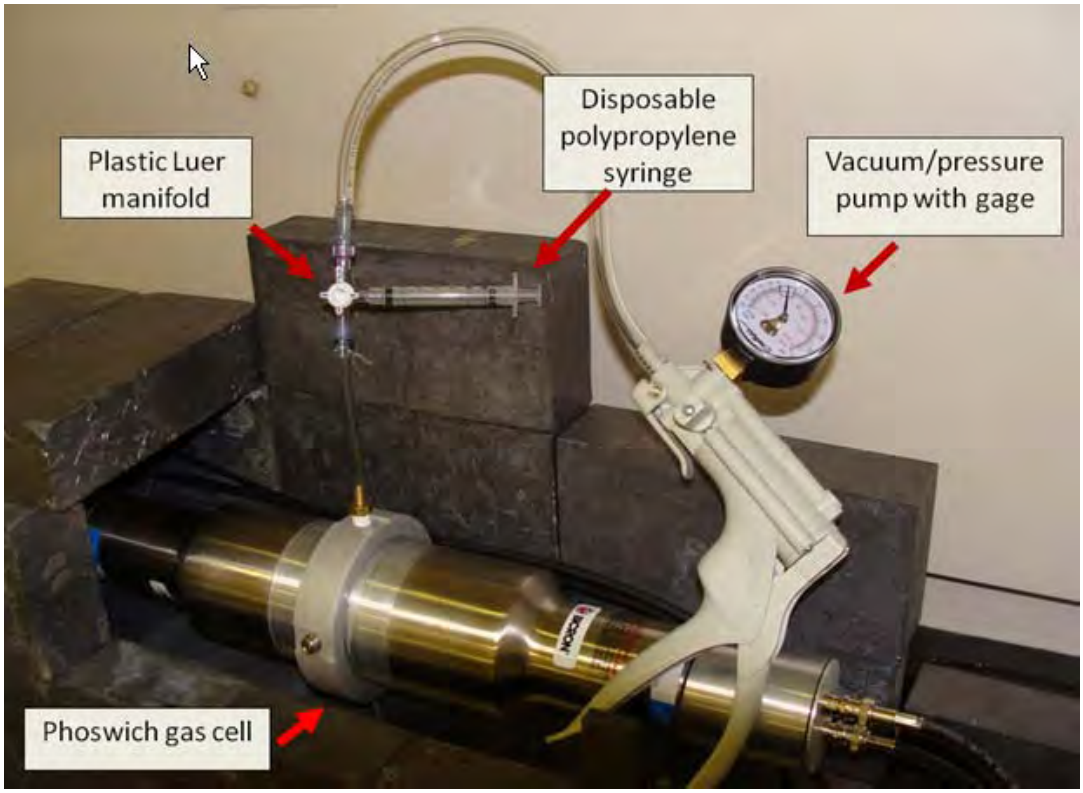

Figure 2. Manifold arrangement to transfer radioactive xenon gas from syringe into the detector gas cell.

Synchronizing Mode

To identify and capture coincidence events between the two channels, instead of using the time stamp method, a coincidence state machine was designed and added into the current FPGA firmware. When two channels are triggered in a predefined coincidence window, those pulses are tagged as coincidence pulses, otherwise as singles. Also for prototyping proposes and to have more flexibility in analyzing anode pulses from the two detectors, all the signal processing analysis are implemented in the PC side. Thus valid pulses from each detector are captured in the digital processor, tagged as either coincidence or single and are uploaded to the PC via high-speed USB interface for further analysis. In high-count rates, when the average time between two events is much less than the USB uploading time, most of the time one channel is waiting to be uploaded while the other channel is ready to be triggered and therefore a small fraction of coincidence events can be practically captured. Obviously, this will reduce the efficiency of our digital processor in capturing coincidence pulses between the two detectors.

To improve the efficiency of capturing coincidence events, the coincidence state machine was designed to work in two modes: (1) Free-Running or (2) Synchronizing modes. In the Free-Running mode, both channels freely and independently can make a trigger for the system. In the Synchronizing mode, however, any channel can be a trigger when the other channel is ready to get triggered (e.g., not being in a wait state for uploading the pulse data to the PC). In very low-count rates, both modes perform similar functionality in terms of capturing coincidence events between the two detectors. In the Synchronizing mode, any free channel will wait until the other channel exits the wait state then is ready to get triggered, making both channels synchronized in capturing coincidence events. Our experimental results using ^{133}Xe confirmed higher coincidence efficiency for high-count rates when using the Synchronizing mode.

To obtain an optimum coincidence window in the Synchronizing mode, ^{133}Xe was injected into the gas cell and the percentage of coincidence events versus coincidence window was recorded. The results of this experiment are

shown in Figure 3. Since the coincidence state machine in the FPGA is clocked with a frequency of 200 MHz (same as the analog-to-digital converter sampling rate), the time resolution for the coincidence window is one clock period or 5 nsec. Zero value for the coincidence window in Figure 3 is referred to capturing the coincidence event in the same clock period. By increasing the coincidence window up to a 9 clock period or 45 nsec, the coincidence percentage increases linearly. After then, it reaches a semi-flat region where we believe any increase in coincidence percentage is a result of random coincidences. Therefore, we decided to set the coincidence window at a 10 clock period or 50 nsec for the rest of experiments as indicated with a vertical and green dashed line in Figure 3. In this experiment, using the Free-Running mode and the coincidence window set at 50 nsec, only 0.68% of events were recorded as coincidence events.

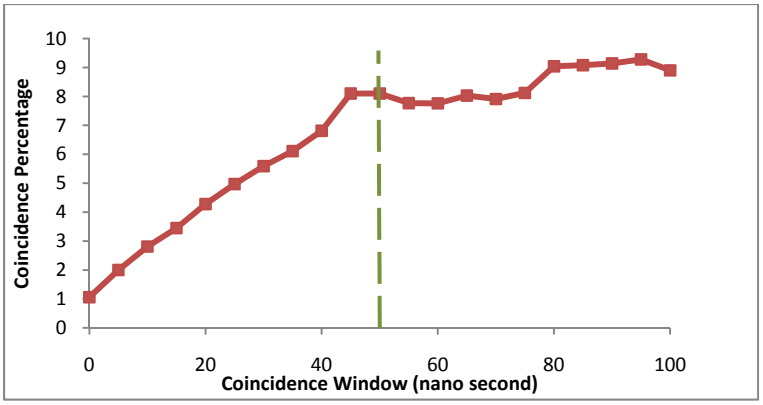

Figure 3. Coincidence percentage between two phoswich detectors versus coincidence window recorded using the Synchronizing mode when ^{133}Xe was injected into the gas cell.

Experimental Results

To minimize the ringing effect (Farsoni et al., 2009), the detector supplier (Saint-Gobain) suggested the replacement of the previous PMT (ET 9305B) with one with a better timing performance (ET 9821B). Before starting our measurements with xenon radioisotopes, the response of two phoswich detectors were examined using radioactive lab sources. For purpose of gain matching, the high voltage for phoswich detectors 1 and 2 was set to 1550 and 1450 V, respectively. Although not completely eliminated, the new detectors still showed a small ringing effect when detectors generate fast pulses from the plastic scintillators. For this reason, correction factors were used in our pulse processing analysis to correct pulse integration when a fast component appeared in the anode pulses.

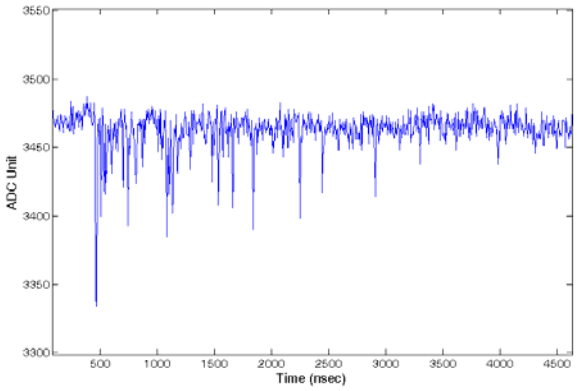

Figure 4. A typical anode pulse when a 30 keV X-ray is absorbed in the CaF_2 crystal.

Comparing to our prototype detector, the new detectors showed lower anode pulse heights (with the same energy deposition at nominal PMT voltages). This affects our pulse shape discrimination analysis, particularly for identifying and measuring 30 keV X-rays from ^{133}Xe and ^{133m}Xe. As mentioned before, pulses from CaF_2 crystal are selectively analyzed to measure the 30 keV X-rays. Regarding the fact that the CaF_2 crystal has a relatively low light yield, this makes the corresponding pulses very close to the noise level and difficult to detect and analyze. To discriminate 30 keV pulses from the noise, the trigger filter used in the FPGA was replaced with a longer filter (150 nsec peaking time). A typical anode pulse from 30 keV X-ray absorbed in CaF_2 crystal, when the phoswich detector was exposed to ^{133}Xe, is shown in Figure 4. This figure shows that the pulse has lost its slow decay shape and instead spikes from single scintillation photons have appeared. This might be due to either low light collection efficiency or low PMT quantum efficiency. We investigated possible relation between the aluminum coating and the light collection efficiency by examining the corresponding channel number of 662 keV photopeak from ^{137}Cs while the source was placed in different positions around the detector. These tests were repeated with a reflective mylar layer attached on the detector's front window (plastic scintillator). No significant differences in the channel number of 662 keV were observed through these experiments.

^{135}Xe measurements

To produce ^{135}Xe, 3 ml of enriched and stable ^{134}Xe was irradiated in the thermal column of the TRIGA reactor for 30 minutes. The thermal neutron flux for this irradiation was $7x10^{10}$ $n.cm^{-2}.sec^{-1}$. The resulting radioxenon activity was calculated to be around 1.47 µCi. Then, using the gas transfer manifold (Figure 2), activated xenon gas was injected into the detector gas cell about 24 hours after the neutron irradiation. Using our high-speed two-channel digital processor (Farsoni et al., 2008), about three million anode pulses were recorded for off-line digital pulse processing. 2-D beta-gamma coincidence energy spectra from ^{135}Xe in each phoswich detectors are shown in Figure 5. Horizontal and vertical axis in this figure represent energy absorption in BC-400 and NaI(Tl), respectively.

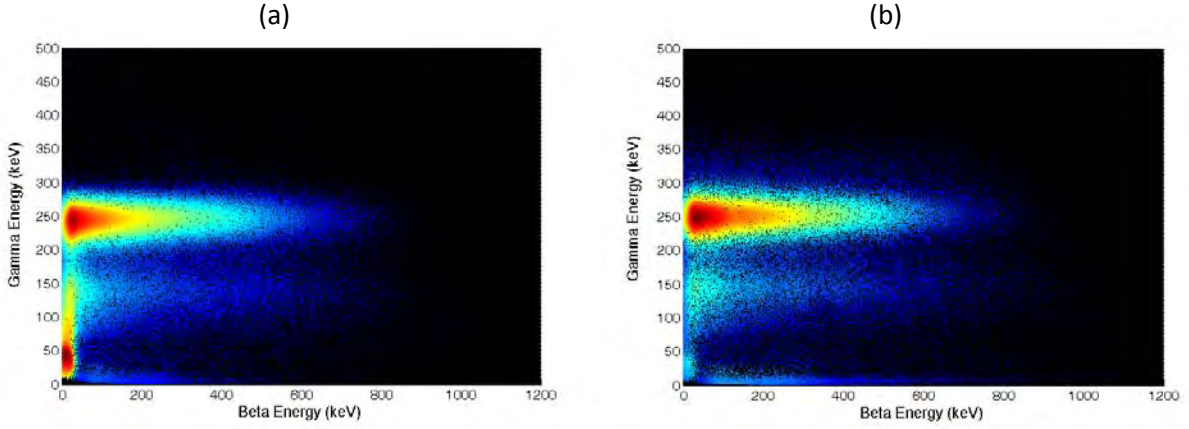

Figure 5. 2-D beta-gamma coincidence energy histograms from ^{135}Xe in channel 1 (a) and channel 2 (b) of the two-channel phoswich detector.

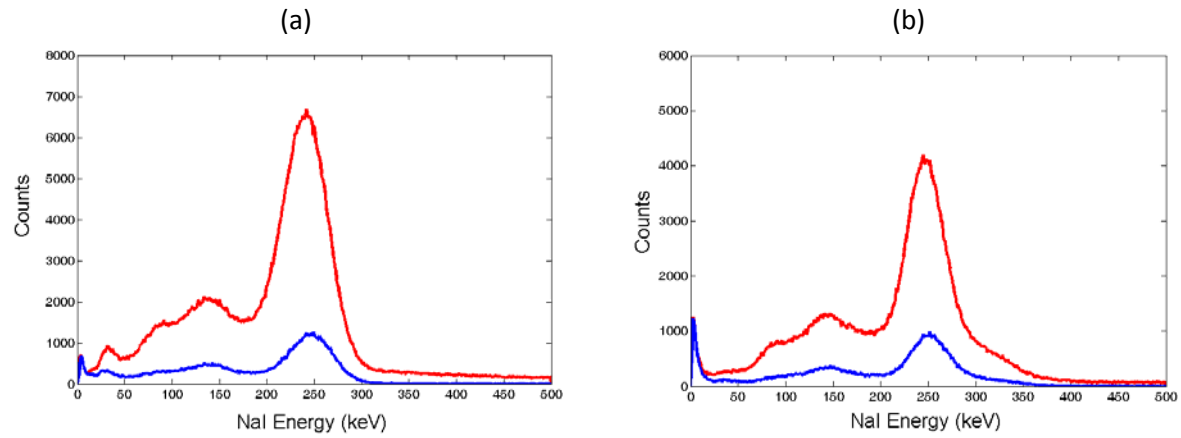

Figure 6. Energy deposition histogram from ^{135}Xe in NaI(Tl) from channel 1 (a) and channel 2 (b) of the two-channel phoswich detector. The red histogram is from NaI(Tl)-only events whereas the blue histogram is from NaI(Tl)-BC400 coincidence events in each channel.

Figure 6 shows the gamma energy deposition in NaI(Tl) from ^{135}Xe in each phoswich channel. The red spectrum is reconstructed from NaI(Tl)-only events. The blue spectrum is also from the NaI(Tl), but when it is in coincidence with an event in the plastic scintillator. The energy resolution of 250 keV from the plastic-NaI(Tl) coincidence histogram was measured to be about 21% for channel 1 and 19% for channel 2. Using the coincidence state machine and synchronizing mode, coincidence events between the two channels were identified and energy histograms (Figure 6) were obtained. Figure 6a shows a 2-D beta-gamma coincidence energy histogram between the two phoswich detectors. This 2-D histogram was updated from single events from both phoswich channels when a coincidence flag was detected by the coincidence state machine. The coincidence window for this experiment was set to 10 clock cycles or 50 nsec. Figure 6b shows a gamma energy histogram from the NaI(Tl) scintillator when a coincidence event was detected between the detectors. The energy resolution of the 250 keV photopeak in this histogram was measured to be 21.6%.

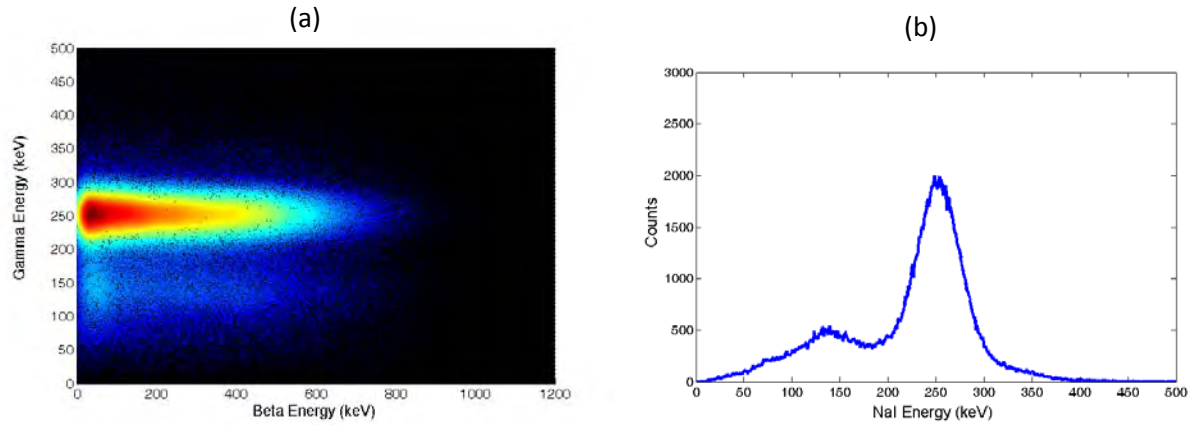

Figure 7. 2-D beta-gamma coincidence energy histogram between the two phoswich detectors (a), and gamma energy histogram from NaI scintillators (b), when the two-channel phoswich detector were exposed to ^{135}Xe.

^{133}Xe and ^{133m}Xe measurements

Three milliliters of enriched and stable ^{132}Xe were irradiated in the thermal column of the TRIGA reactor for 2 hours to produce ^{133}Xe and ^{133m}Xe. Again the thermal neutron flux for this irradiation was $7x10^{10}$ n.cm^{-2}.sec^{-1}. At the end of neutron irradiation, the resulting radioxenon activity was calculated to be around 0.67 and 0.195 µCi for ^{133}Xe and ^{133m}Xe, respectively. An off-line signal processing was then applied on about three million anode pulses from both detectors. Figure 8 shows 2-D beta-gamma coincidence energy spectra collected from both detectors in BC-400/NaI(Tl) after activated xenon gas was injected into the detector gas cell. Horizontal and vertical axes in this figure represent energy absorption in BC-400 and NaI(Tl), respectively. In both channels, 81 keV gamma-ray region is populated with coincidence events. Due to using an optical window (6.35 mm) between NaI (Tl) and CaF_2 crystals, NaI(Tl) crystal was not expected to be as efficient as CaF_2 in detecting 30 keV X-rays. Gamma-ray energy histograms from ^{133}Xe in NaI(Tl) crystal from both channels are depicted in Figure 9. In these histograms, the red histogram is from NaI(Tl)-only events whereas the blue histogram is from NaI(Tl)-BC400 coincidence events. The energy resolution of 81 keV gamma-ray from the plastic-NaI(Tl) coincidence histogram was measured to be about 37% for channel 1 and 26% for channel 2.

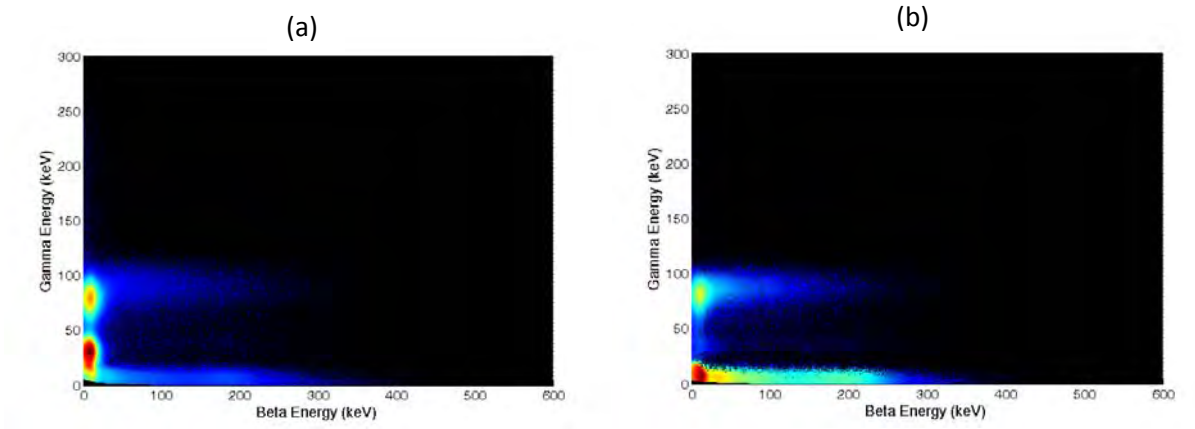

Figure 8. 2-D beta-gamma coincidence energy histograms from ^{133}Xe in channel 1 (a) and channel 2 (b) of the two-channel phoswich detector. Horizontal and vertical axes in this Figure represent energy absorption in BC-400 and NaI(Tl), respectively.

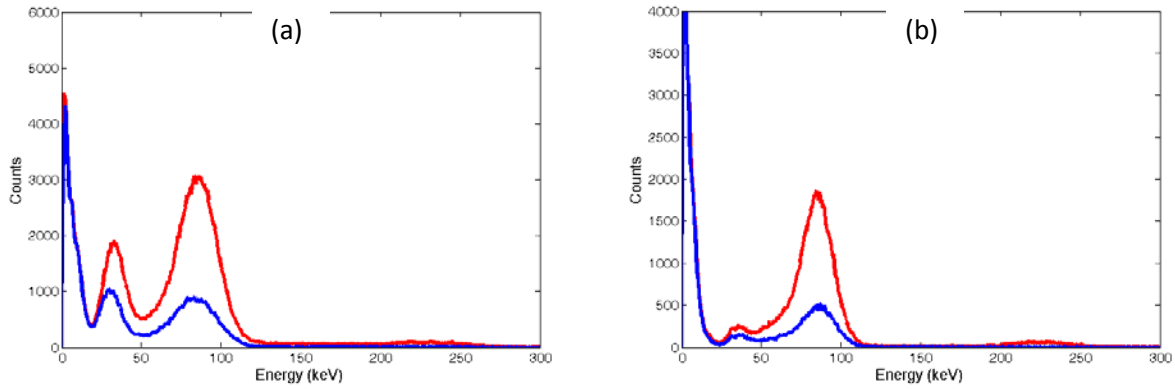

Figure 9. Energy deposition histogram from ^{133}Xe in NaI(Tl) of channel 1 (a) and channel 2 (b) of the two-channel phoswich detector. The red histogram is from NaI(Tl)-only events whereas the blue histogram is from NaI(Tl)-BC400 coincidence events in each channel.

Figure 10 shows 2-D beta-gamma coincidence energy spectra in BC-400/CaF_2 (in channels 1 and 2) when $^{133}Xe/^{133m}Xe$ was injected into the detector gas cell. Due to difficulties in resolving coincidence events from very small pulses (from 30 keV X-rays, see Figure 4) and consequently having poor statistics in energy measurements, the CaF2 spectrum shows a very wide peak for 30 keV X-rays. The corresponding resolution for this peak was measured to be 190% and 200% for channels 1 and 2, respectively. Our previous experiments with a prototype phoswich detector with same design but different PMT (Farsoni et al., 2009) showed a resolution of 43% for 30 keV photopeak in the CaF_2. For both channels, the 2-D coincidence spectrum shows a beta distribution in 30 keV X-ray region. The presence of ^{133m}Xe in the gas sample can be confirmed by observing 199 keV conversion electrons in this region. Beta energy histograms gated with the 30 keV X-ray region from both channels are shown in Figure 11. In each phoswich channel, these histograms were processed from BC-400/CaF_2 coincidence events when a beta event from the plastic is detected in coincidence with 30 keV X-ray from the CaF2. The 30 keV X-ray-gated beta histograms show a peak at 45 keV. This peak represents conversion electrons emitted in coincidence with 30-keV X-rays from ^{133}Xe. In addition, the beta energy histograms in Figure 11 show a peak at about 200 keV. This peak represents 199 keV conversion electrons from ^{133m}Xe when conversion electrons and 30 keV X-rays are detected in coincidence in plastic and CaF_2, respectively.

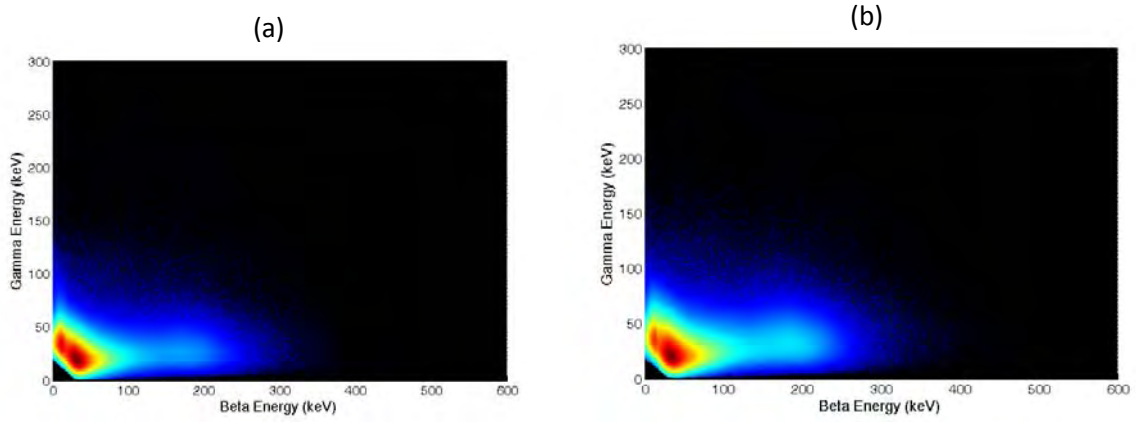

Figure 10. 2-D beta-gamma coincidence energy histograms from $^{133}Xe/^{133m}Xe$ in channel 1 (a) and channel 2 (b) of the two-channel phoswich detector. Horizontal and vertical axes in this Figure represent energy absorption in BC-400 and CaF_2, respectively.

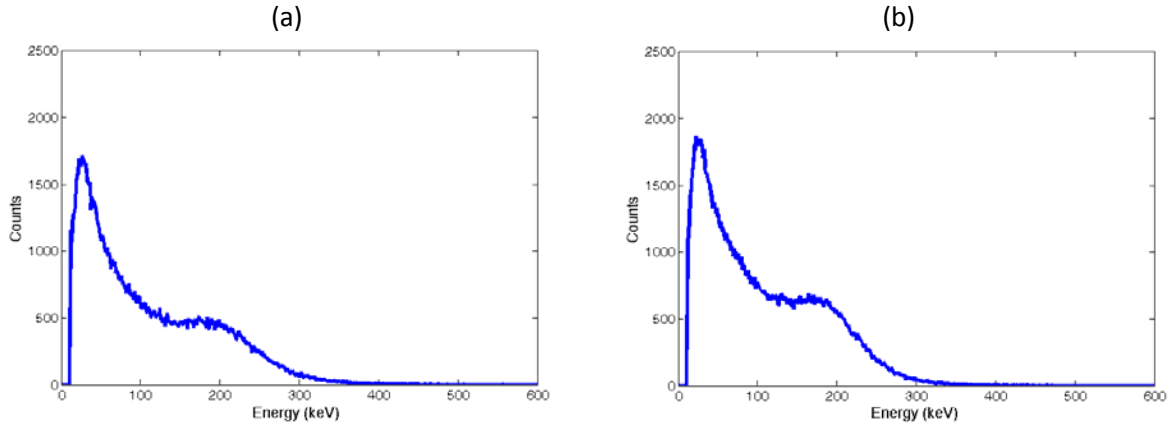

Figure 11. Beta energy histograms (BC-400) from $^{133}Xe/^{133m}Xe$ in plastic scintillator gated with 30-keV X-rays (CaF_2) in channel 1 (a) and channel 2 (b).

CONCLUSION AND RECOMMENDATIONS

In summary, two stable and enriched (>99%) xenon isotopes, ^{134}Xe and ^{132}Xe, were successfully irradiated in the TRIGA reactor to produce xenon radioisotopes ^{135}Xe and ^{133m}Xe and ^{133}Xe for testing a two-channel phoswich detector. Xenon samples in 3-ml polypropylene syringes were irradiated in the thermal column of TRIGA reactor with a thermal neutron flux of $7x10^{10}$ $n.cm^{-2}.sec^{-1}$. A low-cost but efficient gas transfer manifold arrangement was designed to transfer stable xenon gas from its cylinder to a disposable polypropylene syringe and, after neutron irradiation, from there to the detector gas cell. To improve the efficiency of the detection system in capturing coincidence events between the two channels, a synchronizing mode in the FPGA device was designed and characterized. Compared with our prototype detector, the current phoswich-PMT configuration showed a poor energy resolution in detecting 30 keV X-rays with CaF_2 crystal. Use of high-gain PMT's and high-reflective wrapping materials around the phoswich are recommended to improve the resolution.

REFERENCES

Ely, J. H., C. E. Aalseth, J. C. Hayes, T. R. Heimbigner, J. I. McIntyre, H. S. Miley, M. E. Panisko, and M. Ripplinger (2003). Novel Beta-gamma coincidence measurements using phoswich detectors, in *Proceedings of the 25th Seismic Research Review – Nuclear Explosion Monitoring: Building the Knowledge Base*, LA-UR-03-6029, Vol. 2, pp. 533–541.

Farsoni, A. T., D. M. Hamby, K. D. Ropon, and S. E. Jones (2007). A two-channel phoswich detector for dual and triple coincidence measurements of radioxenon isotopes, in *Proceedings of the 29th Seismic Research Review: Ground-Based Nuclear Explosion Monitoring Technologies*, LA-UR-07-5613, Vol. 2, pp. 747–756.

Farsoni, A. T., D. M. Hamby, C. S. Lee, and A. J. Elliott (2008). Preliminary experiments with a triple-layer phoswich detector for radioxenon detection, in *Proceedings of the 2008 Monitoring Research Review: Ground-Based Nuclear Explosion Monitoring Technologies*, LA-UR-08-05261, Vol. 2, pp. 739–748.

Farsoni, A. T., D. M. Hamby (2009). Characterization of triple-layer phoswich detector for radioxenon measurements, in *Proceedings of the 2009 Seismic Research Review: Ground-Based Nuclear Explosion Monitoring Technologies*, LA-UR-09-05276, Vol. 2, pp. 631–640.

Fontaine, J-P., F. Pointurier, X. Blanchard, and T. Taffary (2004). Atmospheric xenon radioactive isotope monitoring, *Journal of Environmental Radioactivity* 72: 129–135

Hennig, W., H. Tan, W. K. Warburton, and J. I. McIntyre (2005). Digital pulse shape analysis with phoswich detectors to simplify coincidence measurements of radioactive xenon, in *Proceedings of the 27th Seismic Research Review: Ground-Based Nuclear Explosion Monitoring Technologies*, LA-UR-05-6407, Vol. 2, pp. 787–794.

McIntyre, J. I., K. H. Able, T. W. Bowyer, J. C. Hayes, T. R. Heimbigner, M. E. Panisko, P. L. Reeder, and R. C. Thompson (2001). Measurements of ambient radioxenon levels using the automated radioxenon sampler/analyzer (ARSA), *J. Radioanal. Nucl. Chem*. 248: 629–635.

Ringbom, A., T. Larson, A. Axelson, K. Elmgren, and C. Johonson (2003). SAUNA - a system for automatic sampling, processing and analysis of radioactive xenon, *Nuclear Instruments and Methods in Physics Research* A 508: 542–553.

Seifert, C. E., J. I. McIntyre, K. C. Antolick, A. J. Carman, M.W. Cooper, J. C. Hayes, T. R. Heimbigner, C. W. Hubbard, K. E. Litke, M. D. Ripplinger, and R. Suarez (2005). Mitigation of memory effects in beta scintillation cells for radioactive gas detection, in *Proceedings of the 27th Seismic Research Review – Nuclear Explosion Monitoring Technologies*, LA-UR-05-6407, Vol. 2, pp. 804–814.

DESIGN AND MODELING OF A COMPTON-SUPPRESSED PHOSWICH DETECTOR FOR RADIOXENON MONITORING

Abi T. Farsoni and David M. Hamby

Oregon State University

Sponsored by the National Nuclear Security Administration

Award No. DE-AC52-09NA29324
Proposal No. BAA09-27

ABSTRACT

By measuring the concentration of four xenon radioisotopes in the atmosphere, the International Monitoring System (IMS) can verify nuclear weapons tests around the world. To measure ultra-low concentrations of radioxenons, many detection systems, such as the Automated Radioxenon Sampler and Analyzer (ARSA) and the Swedish Automatic Unit for Noble gas Acquisition (SAUNA), have been developed and are currently under field tests. These systems employ the beta/gamma coincidence technique to facilitate background rejection. Since all of these systems use two separate detection systems for detecting beta-particles and gamma-rays, the calibration process is usually a tedious task. A phoswich detector, however, can simplify radioxenon detection by measuring both radiations with a single detector.

A phoswich detector with Compton suppression capability for measuring xenon radioisotopes has been designed and simulated. The expected performance of the phoswich detector in suppressing Compton interactions and shielding against background radiation was modeled using MCNPX Version 2.5.0. The Compton suppression mechanism is integrated into the phoswich design to effectively reduce the Compton continuum in 2D gamma/beta coincidence spectra and significantly improve the Minimum Detectable Concentration (MDC) of the xenon radioisotopes. The phoswich detector has been designed with three scintillation layers: a thin plastic scintillator layer to detect beta and conversion electrons, a CsI(Tl) crystal layer for detecting X-rays and gamma-rays and a BGO crystal, which surrounds the CsI(Tl) layer, to identify scattered photons and to shield the CsI(Tl) crystal against external gamma-ray background.

OBJECTIVE

The measurement of radioactive xenon in atmosphere is one of the major techniques employed for monitoring underground nuclear explosion. For compliance with the Comprehensive Nuclear-Test-Ban Treaty (CTBT), the International Monitoring System (IMS) will deploy sensitive automated radioxenon detectors at certain stations around the world to monitor the four xenon radioisotopes: ^{131m}Xe ($\tau_{1/2}$ = 11.9 day), ^{133m}Xe ($\tau_{1/2}$ = 2.2 day), ^{133}Xe ($\tau_{1/2}$ = 5.2 day), and ^{135}Xe ($\tau_{1/2}$ = 9.1 hour).

Within only a few years in the mid-1990s, four automated radioxenon measurement systems have been developed to fulfill the requirements of IMS stations: ARIX (Russia), ARSA (USA), SAUNA (Sweden), and SPALAX (France). In these systems, the atmospheric radioxenon concentration is measured either using high-purity germanium (HPGe) detector (SPALAX) or by a beta/gamma coincidence detection system as deployed in ARIX, ARSA and SAUNA. The systems that use beta/gamma coincidence technique are designed with two separate radiation detection channels: a NaI(Tl) scintillator for detecting gamma-rays and a plastic scintillator for detecting beta-particles (McIntyre et al., 2001). To provide minimal attenuation for beta-particles before they get detected, the gas cell in these systems is made of a plastic scintillator (beta detector). In the beta/gamma coincidence measurements, a two-dimensional beta/gamma coincidence spectrum is updated when the beta and gamma detectors are triggered within a fixed time window. The concentration of xenon radioisotopes then can be calculated through regions of interest corresponding to the four xenon radioisotopes in the 2D spectrum.

An alternative solution to measure beta/gamma coincidence events from radioactive xenon is to use phoswich detectors (Hennig et al., 2005; Farsoni et al., 2009) in which more than one scintillation layer is optically coupled to a single photomultiplier tube (PMT). To facilitate the pulse shape discrimination process in phoswich detectors (usually using digital pulse shape analysis), scintillators are selected from among those materials that have sufficient different decay times. In these detectors, a fast plastic scintillator is used for measuring beta-particles whereas a more dense and slower scintillator, such as NaI(Tl) or CsI(Tl), is used to detect gamma-rays.

In this work, a phoswich detector with Compton suppression capability has been designed and modeled to enhance the radioxenon measurements. Without using a secondary detector, the Compton suppression mechanism is integrated into the phoswich design to effectively reduce the Compton continuum in 2D gamma/beta coincidence spectra and significantly improve the Minimum Detectable Concentration (MDC) of the xenon radioisotopes. The expected performance of the phoswich detector in suppressing Compton interactions and shielding against background radiation was modeled using MCNPX Version 2.5.0.

RESEARCH ACCOMPLISHED

Compton Suppression Mechanism and Detector Design

In a beta/gamma coincidence detection system such as the ARSA system, as depicted in Figure 1, a two-dimensional beta/gamma coincidence spectrum is constructed to measure xenon radioisotopes. There are three boxed areas (in the absence of any radon daughters) from which the concentration of four xenon radioisotopes can be calculated. These areas are located at three gamma/x-ray energies; 30, 80, and 250 keV.

Although employing the beta/gamma coincidence measurement technique significantly increases the sensitivity of the detection system and improves the measurement of ultra-low radioactivity such as atmospheric isotopes of radioxenon in a high background field, there is still some probability for high-energy gamma-rays to be scattered through Compton scattering in the gamma detector. These interactions will add unwanted background for regions of interest at lower energies, e.g., at 30, 80, and 250 keV gamma-ray lines, in the two-dimensional beta/gamma spectrum. For instance, some of these coincidence events are indicated by a white arrow in Figure 1.
The high-energy gamma-rays could originate from either external or internal (from radon daughters or radioxenon itself in the gas sample) gamma-ray sources. These events will ultimately reduce sensitivity of the detection system and increase the MDC of radioxenon (McIntyre et al., 2006).

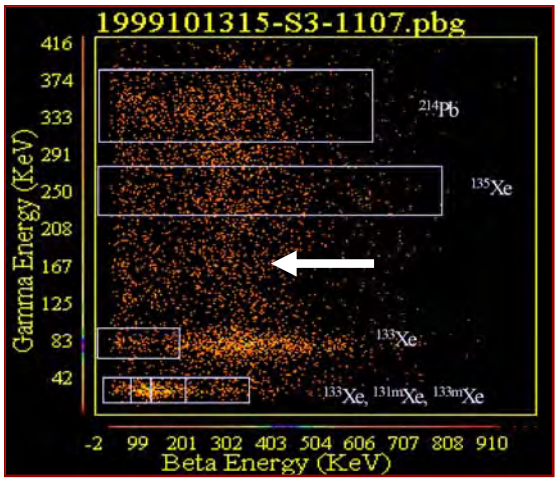

Figure 1. Two-dimensional beta/gamma spectrum from the ARSA system (taken from McIntyre et al., 2006). A white arrow in this Figure shows coincidence events recorded from beta absorption in the plastic scintillator and Compton scattering from higher energies (e.g., 250 keV from ^{135}Xe or 352 keV from ^{214}Pb) in the NaI(Tl) detector of the ARSA system.

The main objective of this research is to integrate an active Compton suppression mechanism into the phoswich design to further advance radioxenon detection and measurement by reducing the Compton background in the regions of interest of gamma-ray spectra. This feature will not require a secondary detector, sensor, electronics or additional photomultiplier tube. Figure 2 shows the schematic diagram of the phoswich detector. In this paper, we will call this detector an Actively-Shielded Phoswich (ASP) detector.

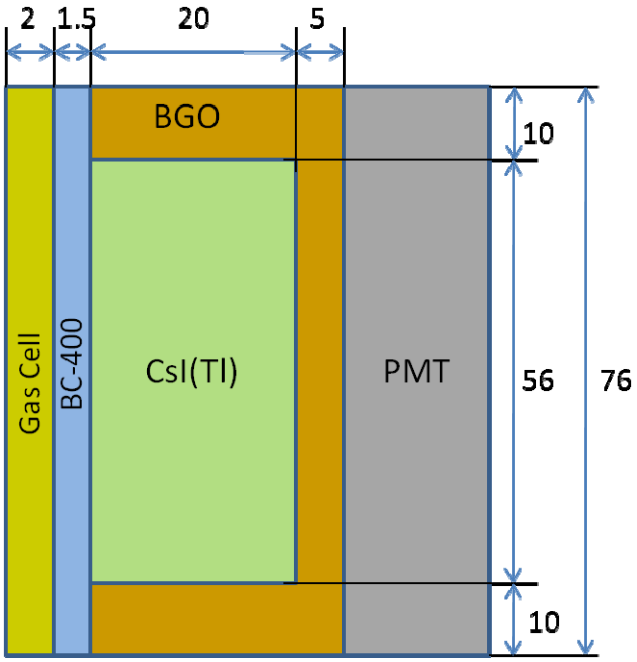

Figure 2. Schematic diagram of ASP detector designed to reduce Compton continuum in the regions of interest and shield the gamma detector against background radiation. All dimensions are in millimetres.

The ASP detector has been designed with three scintillation layers (see Figure 2): a thin plastic scintillator layer, BC-400, to detect beta and conversion electrons, a CsI(Tl) crystal layer for detecting X-rays and gamma-rays and a BGO crystal, which surrounds the CsI(Tl) layer, to identify scattered photons and to shield the CsI(Tl) crystal against external background gamma-rays. The BGO crystal is a high-density (7.13 g/cm^3) and high-efficient scintillator and is commonly used in Compton suppression systems. We integrate this crystal into our phoswich detector to identify unwanted Compton scatters from internal and external gamma-ray sources which could generate background into the beta/gamma coincidence spectra. Since the scintillation photons generated in this layer will be collected by the same PMT used for the other two layers, no additional light sensor or PMT is required for this task. The decay time of BGO crystal (300 nsec) is quite different from the other two scintillators (2.4 nsec of BC-400 and ~1,000 nsec of CsI(Tl)); this will facilitate our digital pulse shape analysis algorithm in discriminating the origin of radiation interactions.

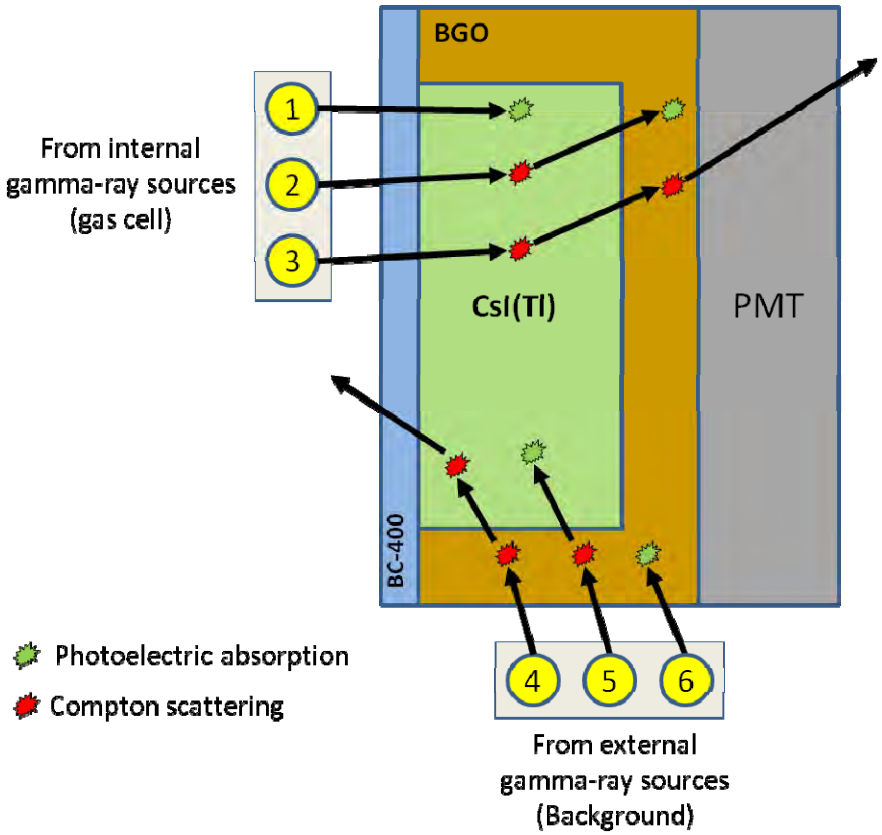

Figure 3. Major interaction scenarios in the ASP detector from internal and external gamma-ray sources. When accompanied with a coincident beta absorption in plastic scintillator, interaction scenarios 2 and 3 generate coincident pulses which are most likely responsible for Compton background in the two-dimensional beta/gamma coincidence spectrum. Corresponding pulses will be identified and rejected in our digital pulse processor (anti-coincidence logic).

Major interaction scenarios in the ASP detector from internal and external gamma-ray sources are illustrated in Figure. 3. Photons emitted from the sample source in scenarios 1, 2, and 3 are assumed to be coincident with a beta absorption in the plastic scintillator. In scenario 1, a gamma-ray from the sample source undergoes a photoelectric interaction and is fully absorbed in the CsI(Tl) crystal. If the resulting slow pulse is accompanied with a fast component from the plastic scintillator, the pulse will be identified as a valid beta/gamma coincidence event and the corresponding energy bin will be recorded in the 2-dimensional energy spectrum. A single gamma-ray may also generate such a coincidence pulse when it is fully absorbed in the CsI(Tl) after an scatter in the plastic scintillator. Since the plastic has a low Z and is very thin, the probability of this event is low. These mischaracterized events,

however, will form a diagonal line in the 2-D spectrum and therefore can be easily identified. In scenarios 2 and 3, a gamma-ray from the source is scattered in the CsI(Tl) crystal and will be either absorbed or scattered in the BGO crystal. When accompanied with a coincident beta absorption in plastic scintillator, interaction scenarios 2 and 3 generate coincident pulses which are most likely responsible for Compton background in the two-dimensional beta/gamma coincidence spectrum. These events can be identified and rejected (suppressed) by our digital pulse shape analysis (anti-coincidence logic).

One other advantage of using a BGO crystal in the ASP detector is to shield the CsI(Tl) crystal from background sources. Scenarios 4, 5, and 6 in Figure 3 show some events in which external gamma-rays from background radiation interact with the ASP detector. In scenarios 4 and 5, a gamma-ray from the external source is scattered in the BGO crystal and will be either absorbed or scattered in the CsI(Tl) crystal. In scenario 6, with no scattering, the external gamma-ray is fully absorbed in the BGO crystal. Pulses resulted from these scenarios will be rejected and will not contribute into the 2D energy spectra.

DETECTOR MODELING

The anti-coincidence feature of the MCNPX Version 2.5.0 was used to study the Compton suppression capability of the ASP detector. This study focuses on the evaluation of Compton suppression on three regions of interest of gamma-ray spectra for measuring the xenon radioisotopes. These regions are 30 keV X-ray, 81 keV, and 250 kev gamma-rays and are indicated by ΔE(30 keV), ΔE(81 keV) and ΔE(250 keV) in Figures 4-7. Approximately, one FWHM of these gamma-ray lines in the CsI(Tl) crystal were used to define these regions (Hennig et al, 2005, 2007, and 2008). Ranges for these regions of interest were 25-35 keV, 73-89 keV and 228-272 keV, respectively. The green distribution in Figures 4-7 shows the energy absorption in CsI(Tl) crystal with no event rejection (unsuppressed). The blue distribution shows the energy absorption in CsI(Tl) crystal when no energy absorption in the BGO crystal has been detected in coincidence with the CsI(Tl) crystal (suppressed).

For modeling the internal sources in Figures 4-7, three gamma-ray sources were used: ^{135}Xe (250 keV), ^{214}Pb (351.9 and 295.1 keV), and ^{214}Bi (609.3 keV). 250 keV from ^{135}Xe scattered in the CsI (Tl) crystal can generate Compton background in 30 and 81 keV regions. The two later sources, ^{214}Pb and ^{214}Bi, are two ^{222}Rn daughters which are readily observed by the beta/gamma counting systems. These beta-decaying isotopes emit high-energy gamma-rays (in coincidence with beta-particle) and are mainly responsible for Compton continuum in those three regions of interest (Bowyer et al., 1999). In Figures 4-6, a peak at about 74 keV in CsI(Tl) spectrum is observed. This peak is believed to be a characteristic X-ray of bismuth emitted after a photoelectric absorption in the BGO crystal.

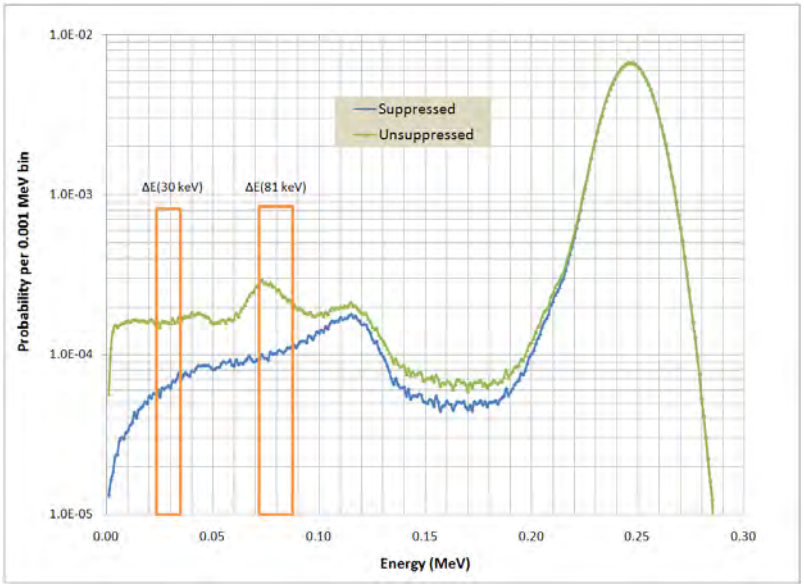

Figure 4. Suppressed and unsuppressed energy deposition spectra in CsI(Tl) crystal from 250 keV gamma-ray (from ^{135}Xe) modeled using the MCNPX.

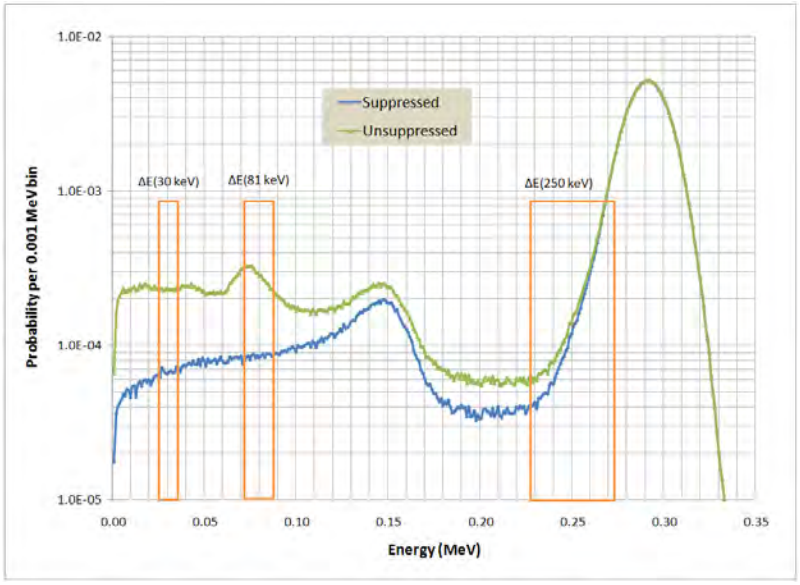

Figure 5. Suppressed and unsuppressed energy deposition spectra in CsI(Tl) crystal from 295.1 keV gamma-ray (from ^{214}Pb, a Radon daughter) modeled using the MCNPX.

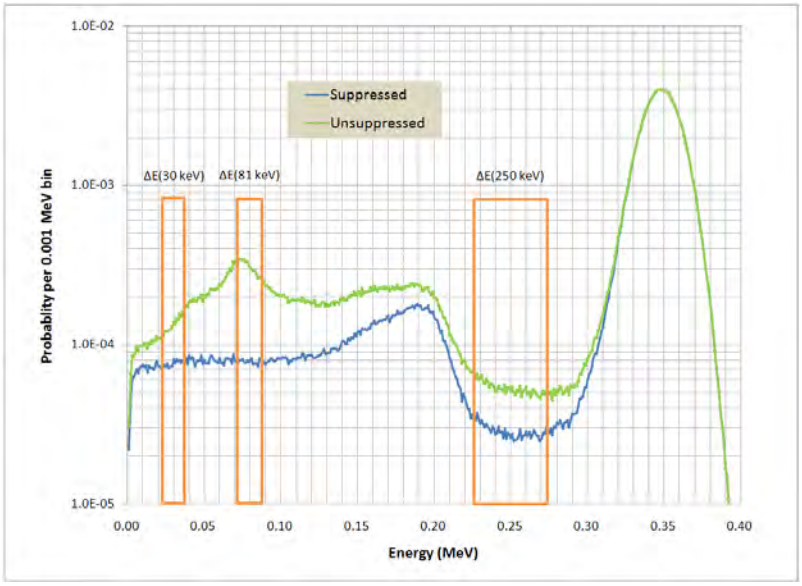

Figure 6. Suppressed and unsuppressed energy deposition spectra in CsI(Tl) crystal from 351.9 keV gamma-ray (from ^{214}Pb, a Radon daughter) modeled using the MCNPX.

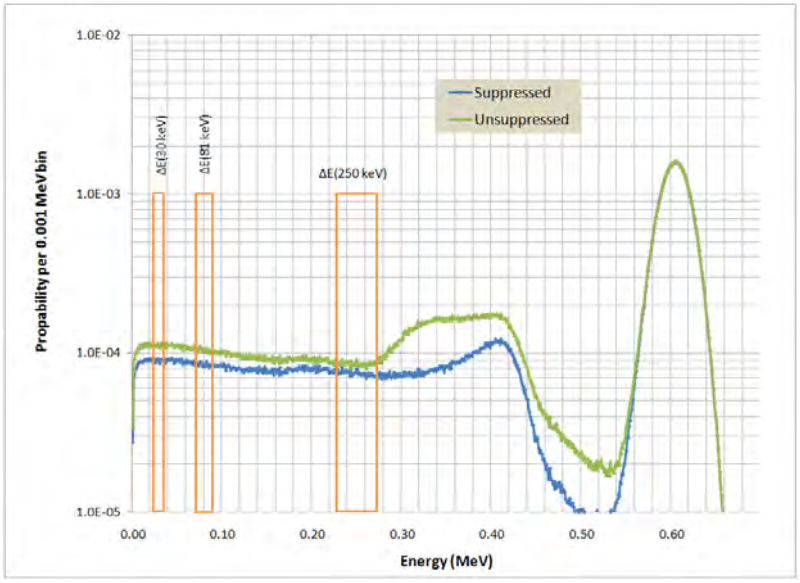

Figure 7. Suppressed and unsuppressed energy deposition spectra in CsI(Tl) crystal from 609.3 keV gamma-ray (from ^{214}Bi, a Radon daughter) modeled using the MCNPX.

The figure of merit used to measure the efficiency of the modeled suppression performance for each region of interest is the suppression factor, defined by:

$$\text{Suppression Factor} = \frac{\varepsilon_u(\Delta E) - \varepsilon_s(\Delta E)}{\varepsilon_u(\Delta E)} \times 100$$

where:

$\varepsilon_u(\Delta E)$ is the efficiency of events in the energy range of ΔE without using suppression (suppressed spectrum)

$\varepsilon_s(\Delta E)$ is the efficiency of events in the energy range of ΔE using suppression (unsuppressed spectrum)

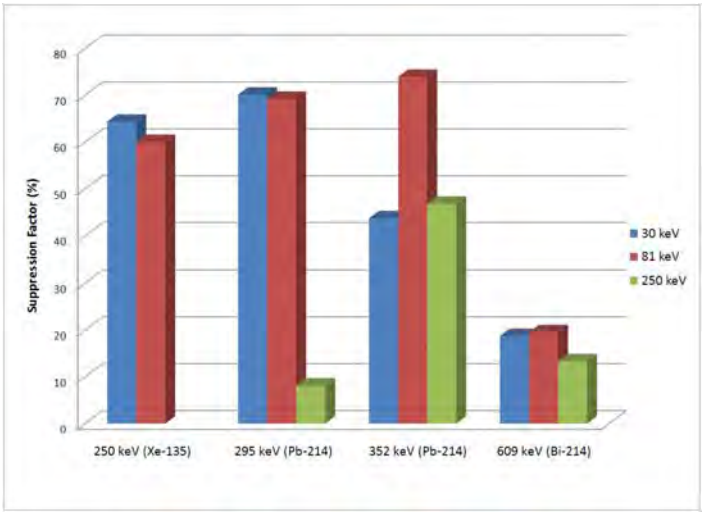

Figure 8. Suppression Factor in energy deposition spectra in CsI(Tl) crystal for three regions of interest from 250 keV, 295 keV, 352 keV and 609.3 keV gamma-rays modeled using the MCNPX.

The suppression factors calculated from four gamma-ray energy spectra given in Figures 4-7 are illustrated in Figure 8. As predicted in this Figure, for example, the Compton suppression mechanism integrated in the ASP detector reduces the Compton background in 30 keV and 81 keV regions (due to 250 keV gamma-rays from ^{135}Xe) by a factor of 64.3% and 60.0%, respectively. This factor is maximum (73.9%) for suppressing the Compton background at 81 keV region from 352 keV of ^{214}Pb. As expected, the suppression factor for all regions is dropped (13% to 20%) for high-energy gamma-rays from ^{214}Bi (609 keV), a daughter of radon.

To evaluate the phoswich detector in shielding against external sources (ambient background), a 2-mm disk source (1,460 keV from ^{40}K) was modeled on the back side of the detector, where the PMT is located in Figure 1. The source emits gamma-rays only in parallel with the detector axis. To study the effect of BGO layer in shielding the CsI (Tl) crystal against the background radiation, two simulations were performed with this high-energy gamma-ray source: (1) with BGO crystal as depicted in Figure 1, and (2) with BGO replaced by air. Figure 9 shows the results of these simulations. The green spectrum shows the energy deposition in CsI(Tl) crystal when the BGO crystal was replaced by air. The blue and red spectra are suppressed and unsuppressed energy spectra in CsI (Tl) crystal, respectively, when the phoswich was modeled with the BGO crystal. In addition of single- and double-escape peaks in these spectra, the unsuppressed energy spectrum with the BGO crystal (red spectrum) shows a significant peak at the Compton edge. This peak does not appear in the suppressed spectrum. Considering a non-isotropic source used in this simulation, low-angle scattered photons from the BGO crystal have a more chance to be absorbed in the CsI(Tl) crystal and therefore it might be a reason to have a pronounced Compton edge in the unsuppressed spectrum. Our calculations from this modeling show that the BGO layer (5 mm, at the back side) reduces the total efficiency of CsI(Tl) crystal in absorbing 1,460 keV from ^{40}K as much as 51.2%, when the suppressed (blue) spectrum is used. This is only 38.7% reduction when the unsuppressed (red) spectrum is used.

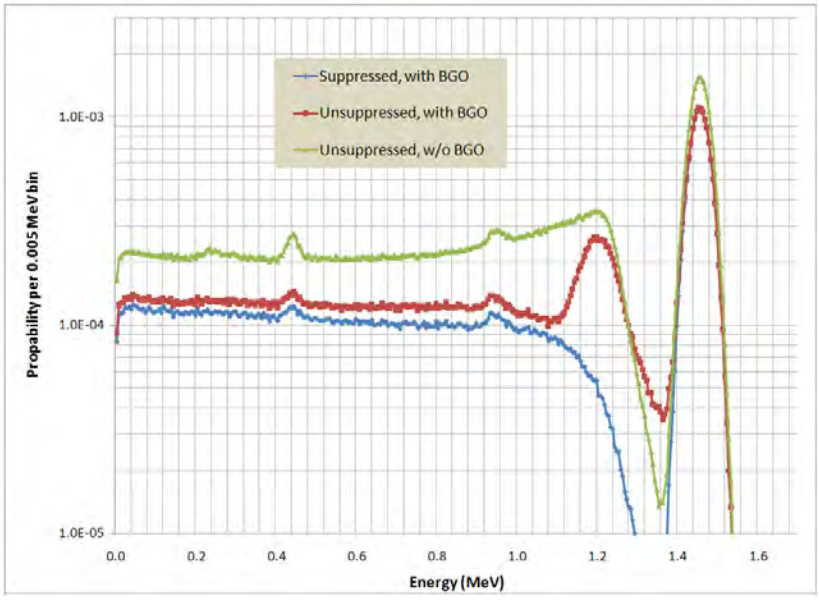

Figure 9. Energy deposition spectra in CsI(Tl) crystal from a ^{40}K external source. The blue and red spectra are suppressed and unsuppressed energy spectra, respectively, when the phoswich was modeled with the BGO crystal. The green spectrum was obtained when the BGO crystal was replaced by air.

A prototype detector with dimensions illustrated in Figure 1 is currently under construction. To have more flexibility in testing the detector with different PMT's, this detector is planned to be assembled in our laboratory. To do so, the required scintillation crystals have been ordered through the Saint-Gobain company. Due to their long lead-time, the prototype detector was not ready when this paper was prepared for publication. Other geometry designs such as well-type or two-channel versions, however, will be considered after our preliminary experiments with this simpler design.

CONCLUSION

The expected performance of a phoswich detector in suppressing Compton interactions was modeled using anti-coincidence feature of the MCNPX Version 2.5.0. The Compton suppression mechanism is integrated into the phoswich design to effectively reduce the Compton continuum and improve the Minimum Detectable Concentration (MDC) in measuring xenon radioisotopes. The phoswich detector has been designed with three scintillation layers: a thin plastic scintillator layer (coated with a 1-μ aluminum layer to minimize the memory effect) to detect beta and conversion electrons; a CsI(Tl) crystal for detecting X-rays and gamma-rays; and a BGO crystal, which surrounds the CsI(Tl) layer, to identify scattered photons and to shield the CsI(Tl) crystal against ambient background. Our modeling shows that when the phoswich detector is exposed to a gamma source of 250 kev from ^{135}Xe, the Compton suppression mechanism reduces the Compton background in 30 keV and 81 keV regions by a factor of 0.64 and 0.60, respectively. This factor is about 0.74 in 81 keV region when the detector is exposed to a gamma source of 352 keV from ^{214}Pb. Our modeling also predicts that the BGO layer (5 mm, at the back side of detector) reduces the total efficiency of CsI(Tl) crystal in absorbing 1,460 keV from ^{40}K as much as 51.2%, when the suppressed spectrum (anti-coincidence logic between pulses from CsI(Tl) and BGO crystals) is used.

REFERENCES

Bowyer, T. W., J. I. McIntyre, P. L. Reeder (1999). High-sensitivity detection of xenon isotopes via beta-gamma coincidence counting, in Proceeding of the 21st Seismic Research Review: *Ground-Based Nuclear Explosion Monitoring Technologies*, LA-UR-99-4700, Vol. 2, pp. 231–241.

Farsoni, A. T., D. M. Hamby (2009). Characterization of triple-layer phoswich detector for radioxenon measurements, in *Proceedings of the 2009 Seismic Research Review: Ground-Based Nuclear Explosion Monitoring Technologies*, LA-UR-09-05276, Vol. 2, pp. 631–640.

Hennig, W., H. Tan, W. K. Warburton, and J. I. McIntyre (2005). Digital pulse shape analysis with phoswich detectors to simplify coincidence measurements of radioactive xenon, in *Proceedings of the 27th Seismic Research Review: Ground-Based Nuclear Explosion Monitoring Technologies*, LA-UR-05-6407, Vol. 2, pp. 787–794.

Hennig, W., H. Tan, W. K. Warburton, A. Fallu-Labruyere, K. Sabourov, J. I. McIntyre, M. W. Cooper, and A. Gleyzer (2007). Characterization of phoswich well detectors for radioxenon monitoring, in *Proceedings of the 29th Monitoring Research Review: Nuclear Explosion Monitoring Technologies*, LA-UR-07-5613, Vol. 2, pp. 757–763.

Hennig, W., H. Tan, W. Warburton, A. Fallu-Labruyere, K. Sabourov, M. Cooper, J. McIntyre, and A. Gleyzer (2008). Development of a COTS Radioxenon Detector System Using Phoswich Detectors and Pulse Shape Analysis, in *Proceedings of the 30th Monitoring Research Review: Ground Based Nuclear Explosion Monitoring Technologies*, LA-UR-08-05261, Vol. 2, pp. 758–767

McIntyre, J. I., K. H. Able, T. W. Bowyer, J. C. Hayes, T. R. Heimbigner, M. E. Panisko, P. L. Reeder, R. C. Thompson (2001). Measurements of ambient radioxenon levels using the automated radioxenon sampler/analyzer (ARSA), *J. of Radioanalytical and Nuclear Chemistry*, 248: (3)629–635.

McIntyre, J. I., T. W. Bowyer, P. L. Reeder (2006). Calculation of minimum detectable concentration levels of radioxenon isotopes using the PNLL ARSA system, Technical Report, PNNL-13102.

PROGRESS IN ADVANCED SPECTRAL ANALYSIS OF RADIOXENON

Derek A. Haas, Brian T. Schrom, Matthew W. Cooper, James Ely, Adam E. Flory, James C. Hayes, Tom R. Heimbigner, Justin I. McIntyre, Danielle L. Saunders, and Thomas J. Suckow

Pacific Northwest National Laboratory

Sponsored by the National Nuclear Security Administration

Award No. DE-AC05-76RL0183/PL10-ASAR-NDD05

ABSTRACT

Improvements to a Java based software package developed at Pacific Northwest National Laboratory (PNNL) for display and analysis of radioxenon spectra acquired by the International Monitoring System (IMS) are described here. The current version of the Radioxenon JavaViewer implements the region of interest (ROI) method for analysis of beta-gamma coincidence data. Upgrades to the Radioxenon JavaViewer will include routines to analyze high-purity germanium detector (HPGe) data, Standard Spectrum Method to analyze beta-gamma coincidence data and calibration routines to characterize beta-gamma coincidence detectors. These upgrades are currently under development; the status and initial results will be presented. Implementation of these routines into the JavaViewer and subsequent release is planned for FY 2011-2012.

OBJECTIVES

As the IMS radionuclide stations become fully populated and certified, the data collected will become more profuse. Collection and measurement of radioxenon is an important aspect for verification of treaties (Bowyer, 2002). Analysis tools that can process, display, and provide rapid calculations will be required to keep up with the data flow. The research performed by the radioxenon JavaViewer project will provide the US National Data Center (NDC) with a radioxenon viewer/analyzer for displaying and analyzing noble gas data. Additionally, the JavaViewer will provide a framework for PNNL to investigate alternative radionuclide analysis methods and, when appropriate, update the NDC analysis package with the improved methods.

Since the IMS stations use nuclear detector materials including high purity germanium (HPGe), sodium or cesium iodide and plastic scintillator the analysis software needs to be highly flexible. Currently, the JavaViewer is capable of loading and analyzing $\beta-\gamma$ data (using the sodium/cesium iodide and plastic scintillator) from the NDC. However, it is also necessary to incorporate analysis algorithms for HPGe detectors from radioxenon stations like the IMS Systéme de Prélèvements et d'Analyse en Ligne d'Air pour quantifier le Xénon (SPALAX™) (Fontaine et al., 2004) and possibly particulate stations like the Radionuclide Aerosol Sampler/Analyzer (RASA) systems in the future. This will provide the NDC with a comprehensive analysis capability and data management solution.

Two other functionalities within the current scope of the project also need to be implemented. The first functionality is the standard spectrum fitting method (Biegalski, 2007; Cooper, 2008). The first nuclear weapon test by North Korea demonstrated the need to perform spectral fitting -instead of the typical regions of interest - for samples with very low activity. To address this, standard spectral fitting is being investigated. Standard spectral analysis may be integrated into the JavaViewer, but will require significant cross checking with the current accepted analysis methods. The second functionality to be implemented into the JavaViewer is the $\beta-\gamma$ detector calibration calculations. Integrating PNNL calibration methodologies (McIntrye, 2009) into the JavaViewer will provide the calibration calculation routines to analysts and researchers in a single and consistent manner. It may potentially lead to an automated calibration routine which can be used by basic users as opposed to requiring an expert to perform the calibration.

Finally, isotopic ratio analysis and trending displays will be added to the JavaViewer beta version. Ratios between the various radioxenon isotopes can be used to better illuminate changes in the concentrations from a specific station, and help differentiate between releases from a medical isotope production facility from other sources (Carman, 2002; Bowyer, 2007). Displays of the concentrations over selected periods of time in history will provide a quick method to perform trend analysis and understand any changes to a particular station.

RESEARCH ACCOMPLISHED

The initial beta version of the JavaViewer program has been installed and is being used at the NDC. Feedback from the first 6 months of use has been received and is currently being incorporated into an update, which will be released at a later date. The feedback was primarily for changes to optimize the graphical user interface (GUI) for efficient workflow.

Currently, the new version of the JavaViewer is capable of displaying data generated from the SPALAX HPGe (see **Figure 1**) with the correct energy calibration. Work is ongoing to implement fitting routines for the data analysis. This will take the form of Gaussian peak fitting and background subtraction. Once the data fitting routine is complete and the isotopes can be resolved, concentration calculations will be implemented. The concentration calculations for the HPGe data will necessarily need to be different than for other detector material types.

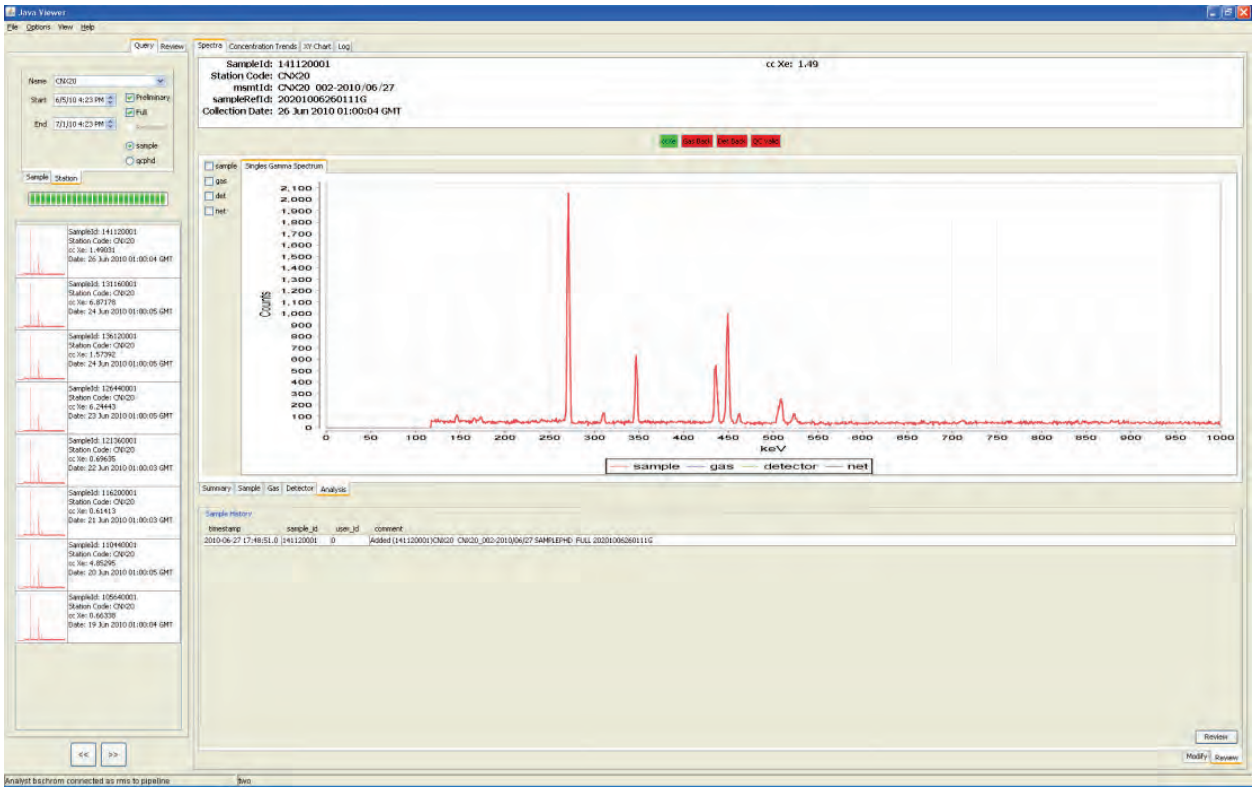

Figure 1. HPGe data from a SPALAX system as loaded and displayed in the JavaViewer software.

As part of the software development process, PNNL staff visited the International Data Center (IDC) in Vienna, Austria to receive a demonstration of the current analysis code, Simulation Assisted Interactive Nuclide Review Tool II (SAINT II). This code will be used to cross-check and validate the HPGe analysis in the JavaViewer.

Work has begun on implementing an evaluation version of the standard spectrum analysis method for use in analyzing radioxenon beta-gamma coincidence spectra. This incorporates the work of Biegalski et al. and in the first stage will add a robust user interface to a stand-alone version. The new user interface will undergo validation testing by comparing analysis results to the existing ROI analysis method. In the future, the standard spectrum fitting routines will be incorporated into the JavaViewer program itself.

Work is also underway to incorporate PNNL calibration programs into the JavaViewer. The calibration routine will determine, from appropriate data files, the ROI ratios and efficiency for a detector. The initial intent is to calibrate PNNL developed β−γ detector systems but could be broadened to include other detectors as well. This routine is only meant to be an aid for an expert analyst who will be required to ensure the energy calibration is correct.

An update to the beta version of the JavaViewer is currently undergoing testing which will help further refine the calculation accuracy and the graphical user interface.

A station history display tab has been added to the beta version of the JavaViewer to provide a display for trending analysis. Currently, the station history of radioxenon isotopic concentrations is displayed for the range of dates queried in the JavaViewer. This includes measured values as well as minimum detectable concentrations (MDC). The user interface plots activity concentration, in millibecquerel per standard cubic meter of air (mBq/SCM), versus time. The screen capture below shows the xenon concentrations for IMS station JPX38 during June 2010. The black line is the measured concentration and the red line is the MDC. As can be seen in the figure there is one day during the month which had an event above background. This plot demonstrates the importance of data trending; it shows that Xe-135 concentrations for this system likely have a positive bias.

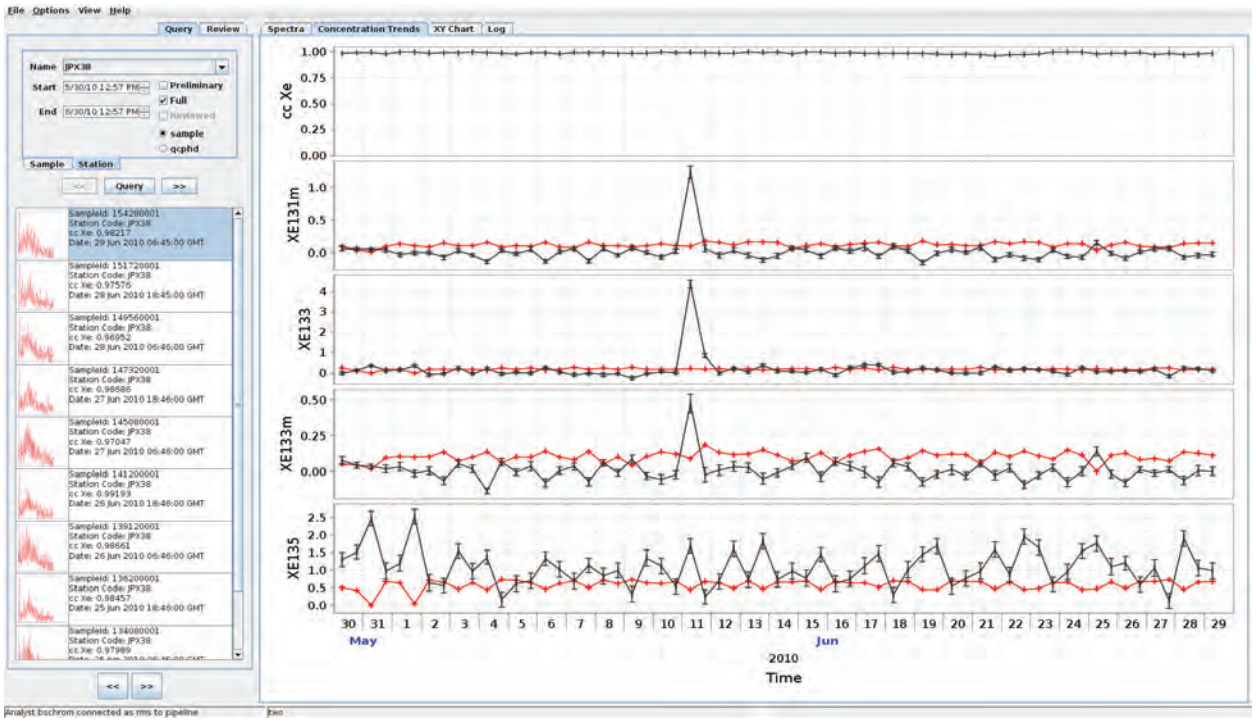

Figure 2. Screenshot of the station history function from the JavaViewer.

CONCLUSIONS AND RECOMMENDATIONS

The research presented here extends the development of the Radioxenon JavaViewer and provides a more comprehensive analysis of data produced by the IMS radioxenon network. The JavaViewer already demonstrates several features that clearly show the need for and usefulness of the application. Further work will result in a more complete data analysis system and a test bed for future improvements.

REFERENCES

Bowyer T. W., C. Schlosser, K. H. Abel, M. Auer, J. C. Hayes, T. R. Heimbigner, J. I. McIntyre, M. E. Panisko, P. L. Reeder, H. Satorius, J. Schulze, and W. Weiss (2002). Detection and analysis of xenon isotopes for the Comprehensive Nuclear-Test-Ban Treaty International Monitoring System. *J. Environ. Radioact.* 59(2):139–151.

Biegalski, K. M. Foltz, S. R. Biegalski, and D. A. Haas (2008). Performance evaluation of spectral deconvolution analysis tool (SDAT) software used for nuclear explosion radionuclide measurements. *J. Radioanal. Nucl. Chem*. 276(2):407–413.

Fontaine, J. P., F. Pointurier, X. Blanchard, and T. Taffary (2004). Atmospheric xenon radioactive isotope monitoring. *J. Environ. Radioact*. 72: 129–135.

Carman A, J., T. W. Bowyer, J. C. Hayes, T. R. Heimbigner, J. I. McIntyre, and M. E. Panisko (2002). Discrimination between anthropogenic sources of atmospheric radioxenon, American Nuclear Society, Winter Conference. Washington DC, PNNL-SA-37760, Pacific Northwest National Laboratory, Richland, Washington, Trans. of the ANS, 87: 89–90.

Bowyer T. W., J. C. Hayes, and J. I. McIntyre (2007). Environmental measurements of Radioxenon, in *Environmental Radiochemical Analysis III*, no. 312, ed. P Warwick, pp. 44-51. RSC Publishing, Cambridge, United Kingdom.

Cooper M. W., T. W. Bowyer, J. C. Hayes, T. R. Heimbigner, C. W. Hubbard, J. I. McIntyre, and B. T. Schrom (2008). Spectral Analysis of Radioxenon, in *Proceedings of the 30th Monitoring Research Review: Ground-Based Nuclear Explosion Monitoring Technologies*, LA-UR-08-05261, Vol. 2, pp. 733–738.

McIntyre JI, MW Cooper, AJ Carman, TW Bowyer, AR Day, DA Haas, JC Hayes, TR Heimbigner, CW Hubbard, KE Litke, MD Ripplinger, and R Suarez (2009). Concentration Independent Calibration of a β-γ Coincidence Detector Using 131mXe and 133Xe. *J. Radioanal. Nucl. Chem*. 282(3):755–759.

INITIAL RESULTS: AN ULTRA-LOW-BACKGROUND GERMANIUM CRYSTAL ARRAY

Martin E. Keillor, Craig E. Aalseth, Anthony R. Day, Luke E. Erikson, James E. Fast, Brian D. Glasgow, Eric W. Hoppe, Todd W. Hossbach, Brian J. Hyronimus, Harry S. Miley, Allan W. Myers, and Allen Seifert

Pacific Northwest National Laboratory

Sponsored by the National Nuclear Security Administration

Award No. DE-AC05-RLO1830/PL10-CASCADES-NDD05

ABSTRACT

Treaty verification techniques, environmental surveillance, and physics experiments continue to require increased sensitivity for detecting and quantifying radionuclides of interest. This can be accomplished with new detector designs that establish high detection efficiency and reduced instrument backgrounds. Current research is producing an intrinsic germanium (HPGe) array designed for high detection efficiency, ultra-low-background performance, and sensitive γ-γ coincidence detection. The system design is optimized to accommodate filter paper samples, e.g., samples collected by the Radionuclide Aerosol Sampler/Analyzer (RASA). The system will provide high sensitivity for weak collections on atmospheric filter samples (e.g., $< 10^5$ fissions), as well as offering the potential to gather additional information from higher-activity filters using gamma cascade coincidence detection. The first of two HPGe crystal arrays in ultra-low-background vacuum cryostats has been assembled, with the second in progress. Traditional methods for constructing ultra-low-background detectors were followed, including use of materials known to be low in radioactive contaminants, use of ultra-pure reagents, and use of a clean room assembly. The cryostat is constructed mainly from copper electroformed into near-final geometry at Pacific Northwest National Laboratory. Details of the detector assembly, vacuum and thermal performance testing, and initial measurement results are presented.

OBJECTIVES

The objective for the "Radionuclide Laboratories " (RN Labs) project was to build an instrument utilizing two germanium arrays in ultra-low-background cryostats to surround the sample being measured. The follow-on "CASCADES" project aims to develop a multicoincidence data-analysis package and make robust fission-product demonstration measurements to establish system capabilities. The design and performance expectations for this instrument have been discussed previously (Keillor, et al., 2008, 2009). Each cryostat houses seven high-purity germanium crystals (HPGe); these cryostats are built using a limited set of materials known to have very low levels of radioactive impurities. The vast majority of each cryostat is made from pure copper (< 1μBq/kg, see Aalseth, et al., 2009) electroformed into near-final geometry at Pacific Northwest National Laboratory (PNNL) under class 1000 clean room conditions.

The instrument is designed to take advantage of low background performance, high detection efficiency, and γ-γ coincidence signatures to provide unprecedented gamma spectroscopy sensitivity. This effort is focused on improving gamma analysis capabilities for nuclear detonation detection (NDD) applications, e.g., nuclear treaty monitoring. The instrument also has the potential to contribute to basic nuclear physics research. For example, the potential for this detector to measure the half-life of predicted rare decay modes of ^{130}Te is being investigated.

RESEARCH ACCOMPLISHED

This paper details assembly and initial characterization of the active anti-cosmic shield, assembly of the first seven-crystal array into its ultra-low-background cryostat, results of system thermal tests, and initial spectroscopic performance of the array. Initial spectral analysis results obtained with the analysis package in development under the CASCADES project are also presented.

Active Anti-Cosmic Shield

To reduce backgrounds, an active cosmic veto shield composed of 12 BC-408 plastic scintillator panels was installed on the left, right, rear, and top surfaces of the passive lead shield. Panels will be added to the front and bottom sides to complete the active shield when the system is moved to the new shallow underground laboratory at PNNL; the move is scheduled for ~September 2010. The goal of this veto system is to detect and exclude cosmic-ray generated interactions within the germanium array. Each plastic panel is roughly 17.5" × 2" × 70" and makes use of a single photomultiplier tube to detect the scintillation light (widths and heights vary slightly to accommodate the shield dimensions). On each side protected by the active veto, the signals from three panels are combined into one Canberra model 2005 preampifier; the signal is subsequently read out by an XIA PIXIE-4 waveform digitizer. Figure 1 shows an example of a typical energy spectrum produced by a gain-matched side of the cosmic-ray veto (the red line is a fit to the cosmic-ray muon through-peak).

Various preliminary performance studies have been conducted with the current veto system. The time resolution of the system was of particular importance because the effects of a poor time resolution will increase the number of legitimate events improperly excluded during data collection. The waveform digitizer system also requires additional configuration to properly handle coincident signals across PIXIE-4 cards. In the system's initial configuration, our results suggest that the time resolution of the veto system is approximately 200 ns (see Figure 2) or better; planned changes to the signal processing should significantly improve this performance. The rejection efficiency for the active veto will be determined in the near future.

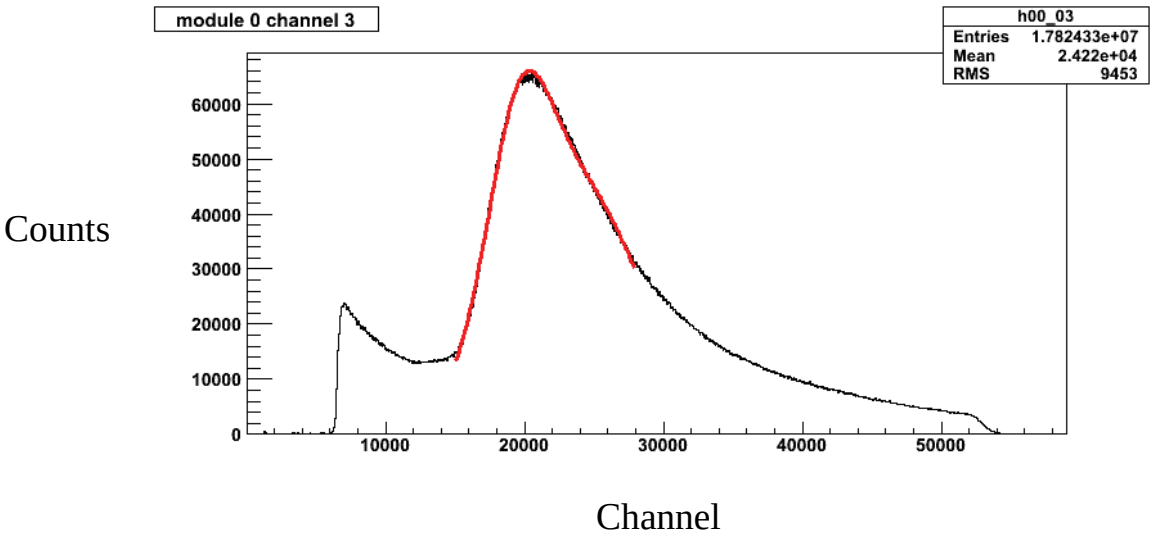

Figure 1. Muon spectrum collected with three 2"-thick plastic scintillator panels "T'ed" together. These are the panels making up the active veto on the top surface of the lead shield. The lower energy threshold, as set in this figure, will accept some gamma background to ensure a high rate of muon exclusion.

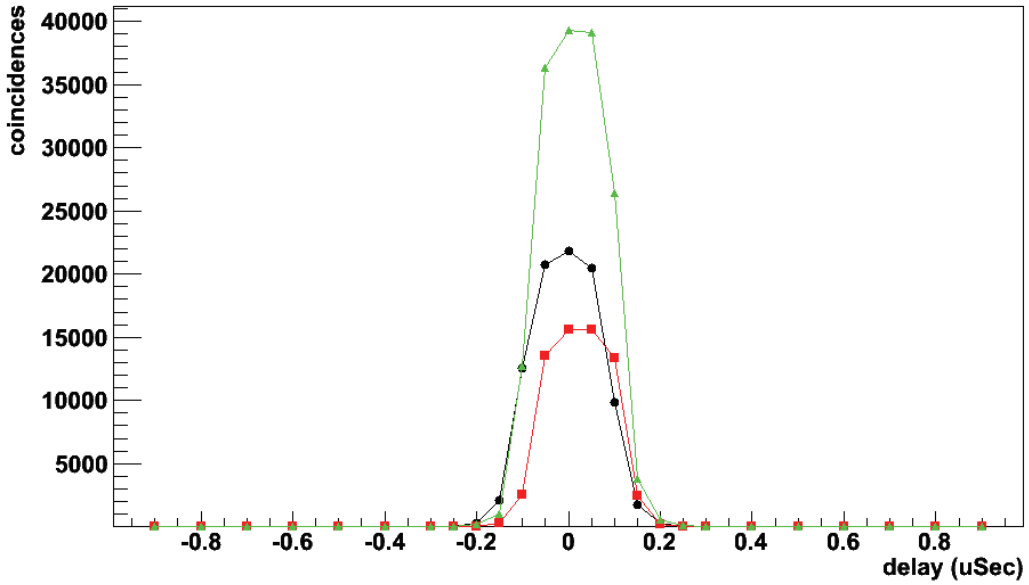

Figure 2. Cosmic-ray coincidence data collected to investigate the single-card PIXIE time resolution for veto signals. Black circles are events collected in coincidence between panels on adjacent sides of the shield, red squares are between opposite sides of the shield, and the green triangles are coincident events from a side and the top of the shield.

Cryostat and HPGe Array Assembly

The first cryostat was initially assembled with all components except the IR shield and crystals in their mounting hardware. This includes installation of the low-background, front-end electronics package (LFEP); wiring; and preamplifiers. Cryostat vacuum and thermal performance were tested prior to installation of the seven HPGe crystals.

At MRR2009, we also reported challenges with electroforming of the thin IR shields and the domed entrance window for the system (Keillor, 2009). During the past year, both of these difficulties have been resolved. Our typical approach to removing an electroformed piece from its stainless steel mandrel is to heat the piece to ~ 300^{o}C, then rapidly cool it. We believe this heating process may contribute to accelerated electrochemical processes that result in the production of holes through thin pieces. This is specifically associated with parts electroformed on 304 stainless steel (SS) mandrels and has not been observed to affect parts on 316 SS mandrels. We have not completed a detailed study to verify this effect; however, we were able to solve the issues that delayed production of the IR shields. Rather than using the heating and quench process, electroformed IR shields were removed from their 304 SS mandrels by running a roller over the surface of the piece. This stretched the thin copper sufficiently to allow its release from the mandrel. The solution for the entrance window followed the method proposed in the MRR2009 paper: the thin window was electroformed separately, then e-beam welded into an annular plate to form the required part. This process allowed us to produce an entrance window that is ~0.04" (~ 1 mm) thick over a 5"-diameter window. Prior to installation of HPGe crystals, the cryostat was successfully cycled between vacuum and atmospheric pressure more than 15 times to verify that it would not fatigue and fail under vacuum or vacuum cycling. Figure 3 shows a cryostat assembled with the completed entrance window.

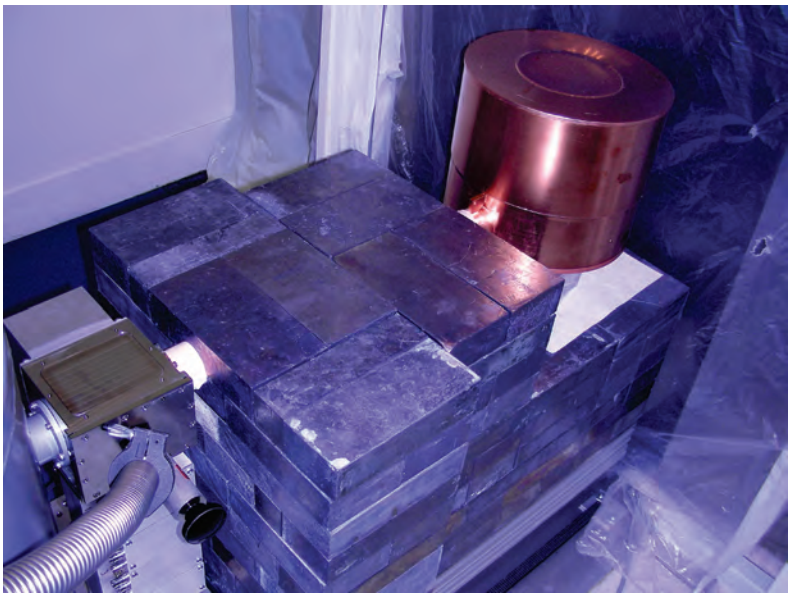

Figure 3. Assembled cryostat with dished entrance window. The window is 5" in diameter and ~ 0.04" (1 mm) thick.

Seven P-type coaxial HPGe crystals, nominally 63 mm in diameter by 70 mm high, were installed into the cryostat in mid-May 2010. This was completed in a clean room with the cryostat disconnected from the Dewar. The installation of each crystal assembly was relatively simple: signal wire was attached to the center connection of the crystal, then the HV wire was fed through the appropriate hole in the cold plate and attached. Following this, the crystal was placed on the cold plate and secured with electroformed copper nuts on the three posts. Once a crystal was secured, the cryostat was inverted to allow crimping of the signal wire to a lead attached to the gate of the LFEP. This sequence was repeated until all seven crystals were installed. Crystal installation was accomplished in a single session in the clean room, in less than 4 hours. Figure 4 shows a sequence of photos taken during the installation.

Vacuum and Thermal Performance

For thermal testing, the cryostat was instrumented with four silicon resistance temperature detectors (RTDs) located along the cold path from the Dewar to the cold plate, as well as a Zener diode on the cold plate to allow injection of a known thermal load. Initial thermal tests showed that the cryostat did not cool sufficiently for operation of HPGe crystals. Two problems were corrected to improve cooling of the cold plate. First, a thermal short between the cold finger and cross arm was eliminated by modifying the copper piece that connects directly to the Dewar (the “nub”).

After elimination of the thermal short, the steel bolts holding a clamp that connects the nub to the cold finger were changed from 304 SS to 18-8 SS to eliminate loosening during thermal cycles. These changes allowed the cold plate to reach a temperature of 89.5K, deemed sufficient to proceed with installation of the HPGe crystals. We have noted that the aluminum-to-copper connection at the Dewar produces the largest single temperature change across a material interface ($\Delta T \sim 6$ K); at the next opportunity, we will attempt to improve thermal performance of this interface by inserting gold foil between the aluminum and copper.

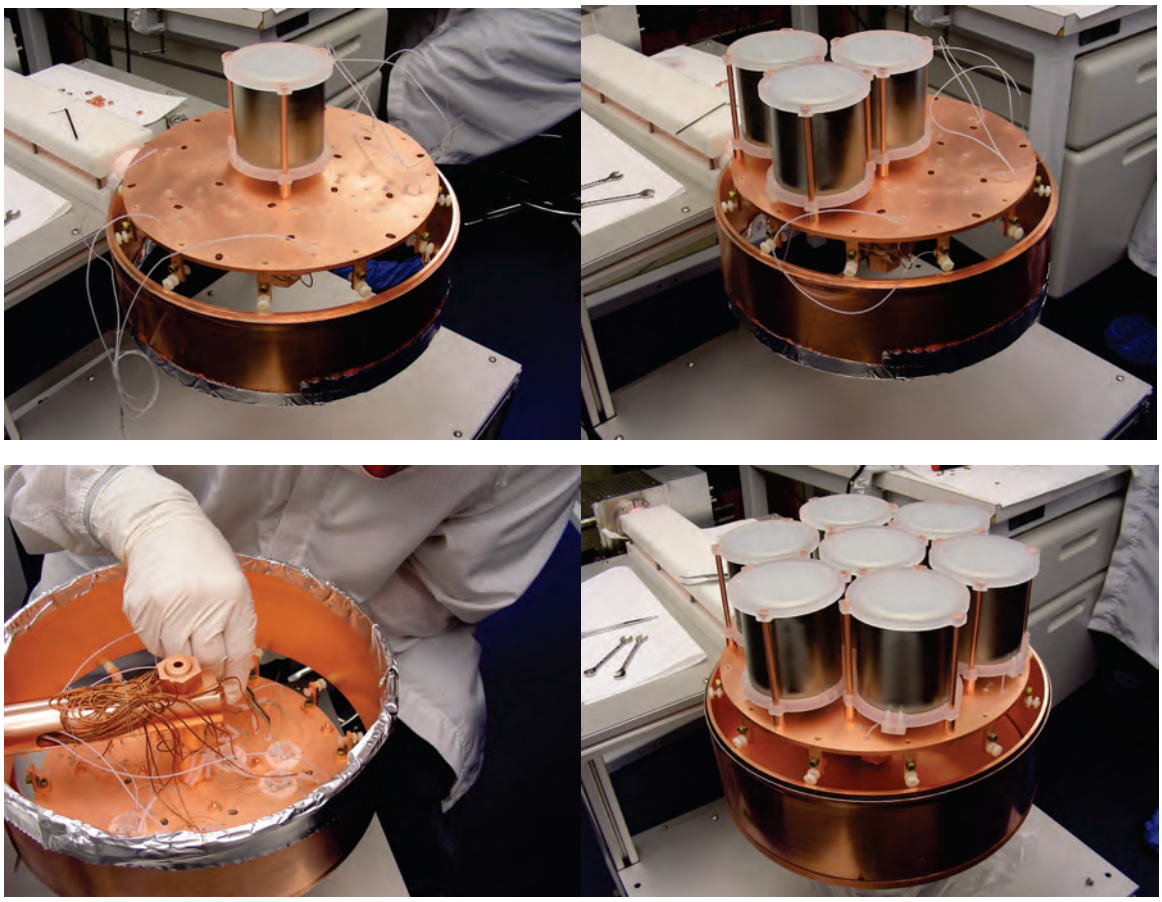

Figure 4. This sequence of photos shows the progress of installation of the HPGe crystals. The frame in the lower left shows the cryostat inverted to allow easier access for crimping the signal wire.

Cooling for the cryostat is provided by a liquid nitrogen (LN) Dewar, custom built by Technifab Corporation, with a 100-L capacity. Initial tests of this Dewar indicate that it uses about 1 kg of LN per day, with no external load. LN use with the cryostat attached is about 4 L/day, or 3.25 kg/day. Thus, the Dewar itself consumes about 2.3 W, while the cryostat represents a thermal load slightly above 5 W. This thermal load is consistent with our expectations. In the completed system, both cryostats will be cooled by the same Dewar; total LN use should be on the order of 7 L/day after installation of the second cryostat.

Results of previous vacuum testing were reported at MRR2009 (Keillor, 2009), and similar results were achieved with the fully assembled cryostat. Vacuum behavior was not as stable as expected during the first couple of attempts to cool the array after installation of the crystals; an epoxy patch was applied to a joint in the neck of the LN Dewar, but later discovery of a loose vacuum flange was the likely culprit. Despite the loose flange, the array was successfully cooled for testing and is currently holding in the temperature range of 82.5K–83.5K at the nub.

Data Acquisition

The signal-processing path consists of PNNL LFEP sockets mounted near each crystal, on the opposite side of the cold plate, through Belden 8700 micro-coaxial cable (with insulation stripped to reduce background contribution) to a 50-pin vacuum feedthrough. Seven PGT RG-11 preamplifiers are mounted on a housing covering the outside of the vacuum feedthrough. Preamplifier power is supplied from Ortec 4003 preamplifier power supplies (NIM). Preamplifier signals are processed with a PXI crate holding five XIA PIXIE-4 digitizers. Software control of the data acquisition hardware uses an in-house PNNL data acquisition program called NYX (Cooper 2010). NYX provides much the same functionality as the Windows-based software supplied by XIA; however, it is based on Linux to provide a higher degree of stability. This acquisition system allows the user to specify different levels of data collection, with three key modes being (1) basic MCA-style spectra for each crystal, (2) time and energy list mode data, and (3) digitized waveform data for each observed pulse. The system also records coincident hit pattern information for modes 2 and 3.

Development of Analysis Framework

When this system is complete, each measurement will contain data from 14 germanium crystals, coincidence hit pattern information, and the status of the active anti-cosmic shield. The availability of this robust dataset will make it possible to reconstruct the event data in many ways. This adds significant complexity to the analysis, when compared with traditional "singles" gamma-ray spectroscopy. We are developing an analysis framework to streamline the process so that the analyst can reach a final result within a reasonable time frame.

This software is being developed using the C++ programming language and relies on the library of tools provided by the ROOT framework available on the CERN website (http://root.cern.ch/drupal/), as well as Qt (http://qt.nokia.com/) for graphical user interface functionality. We anticipate drawing upon capabilities developed in two previous PNNL analysis developments, the Coincidence Lookup Library (CLL) for nuclear data (focused on γ -γ coincidence signatures) (Smith et al., 2004) and the Multi-Isotope Coincidence Analysis code (MICA) (Warren et al., 2006).

The current effort, with the working name "Melusine," consists of a data preprocessor and an analysis engine. The preprocessor (Melusine1) converts measurement results from the native XIA data format into a ROOT data structure. The analysis code (Melusine2) will provide the functionality to analyze both one- and two-dimensional spectra to establish isotope identifications and activity results. This development is in the early phases; current capabilities consist mainly of the preprocessor, various data reconstruction capabilities for both one- and two-dimensional spectra, and peak fitting in one-dimensional spectra. We are currently focused on tasks to simplify both the energy and efficiency calibration for the system.

Initial Spectroscopic Results

We collected the first spectroscopic data with the array on June 22, 2010. The first results were very encouraging, with all seven channels active. However, initial performance showed significant intermittent high-frequency noise on the baseline for all seven crystals; quiet periods allowed collection of spectra, with several crystals achieving ~3.4-keV FWHM at 1332 keV.

Within several days of collecting these initial results, the loose flange mentioned above was located and tightened, eliminating the intermittent noise. Subsequent tests have shown five crystals operating with energy resolution in the range of 2.2–2.4 keV at 1332 keV, while one crystal cannot be fully biased due to apparent high leakage current, and one crystal continues to suffer from poor energy resolution due to high-frequency noise on the baseline. The crystal with high leakage current can be biased sufficiently to provide ~3.3 keV energy resolution at 1332 keV, and we expect to locate and eliminate the source of noise affecting the other poorly performing crystal. We note that the initial performance of the detector array is better than expected, with useful data available from all seven crystals.

As of this writing, all data has been acquired with the array outside of the shield; the background for these measurements is, understandably, significant. Figure 5 shows a 5-minute background measurement prior to gain matching of the channels. The 1460-keV ^{40}K peak and the 2615-keV ^{208}Tl were easily indentified in the spectrum,

and provided a means to gain match the channels, as well as establish a quick energy calibration to verify that the peaks were correctly identified. Figure 6 is a 10-hour room background spectrum, taken after gain matching. The most prominent peak in the spectrum is the 1460-keV peak of ^{40}K, while the other peaks are associated with the natural uranium and neptunium decay series. Figure 7 shows a close-up of the ^{40}K peaks for the crystals; five of the crystals show good energy resolution, while broadening of the peak for the two crystals with degraded performance is obvious.

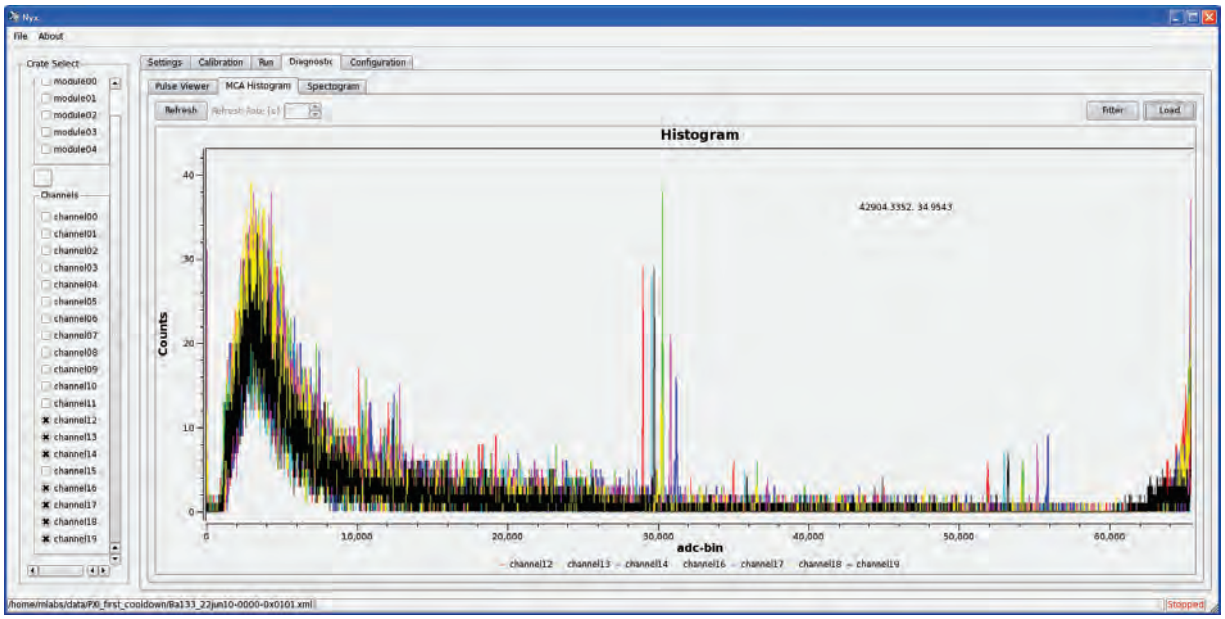

Figure 5. A 5-minute room background spectrum acquired prior to gain matching the channels. The peaks around channel 30,000 are the 1460 keV ^{40}K line.

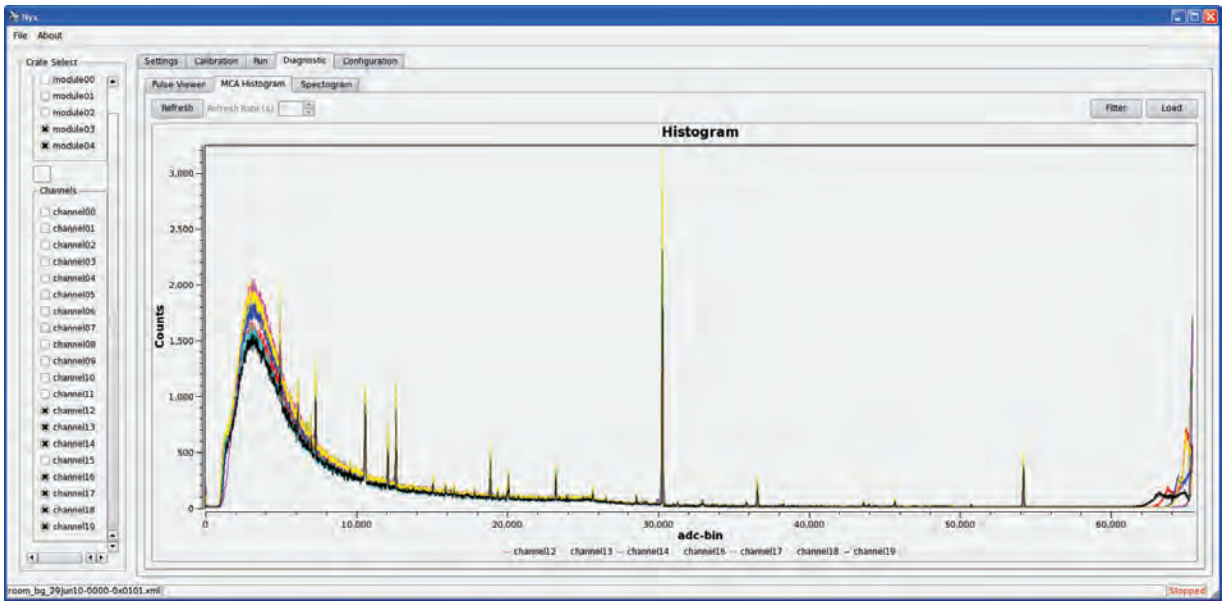

Figure 6. Room background collected with all seven crystals for 10 hours. The variation in the height of the continuum at low energies appears to be correlated with position of the crystal relative to the nearby shield. The continuum is lowest for those crystals closest to the cave. Data were collected and displayed with NYX.

Figure 8 and Figure 9 show products from the Melusine analysis package. These are examples of the one-dimensional peak fitting and two-dimensional data reconstructions available with Melusine. The current version of the code still requires setting a number of manual parameters to generate such products; however, we envision a product requiring minimal user intervention to enable rapid analysis of each dataset.

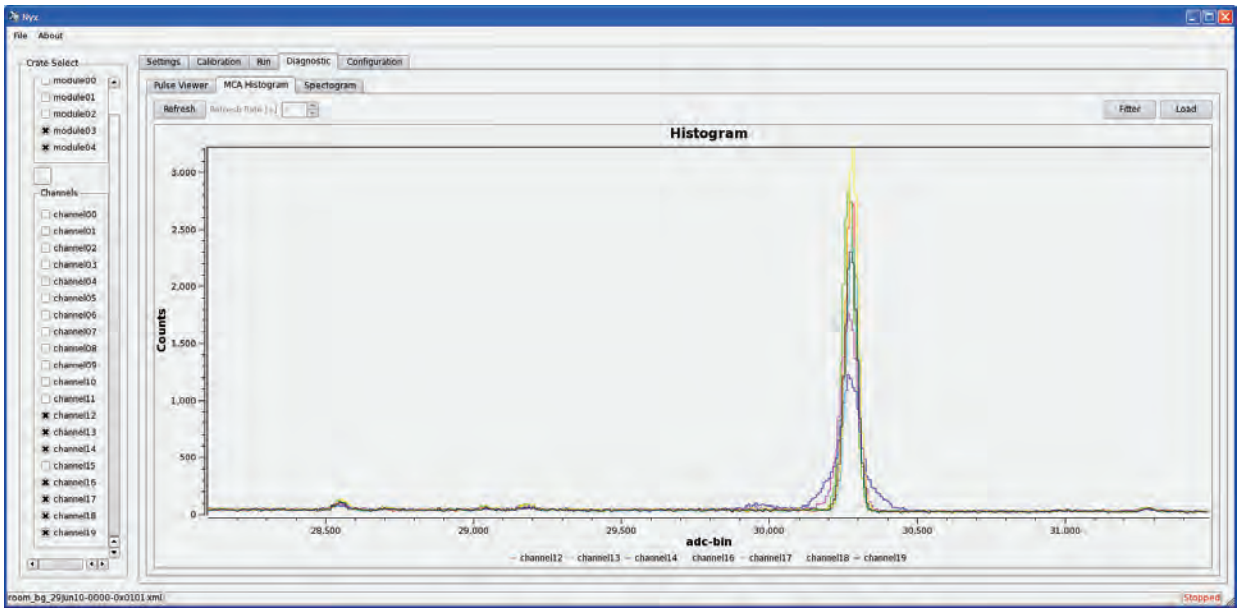

Figure 7. This figure highlights the ^{40}K 1460-keV peak from the background spectra of Figure 6. The traces from the two crystals with poorer resolution are apparent.

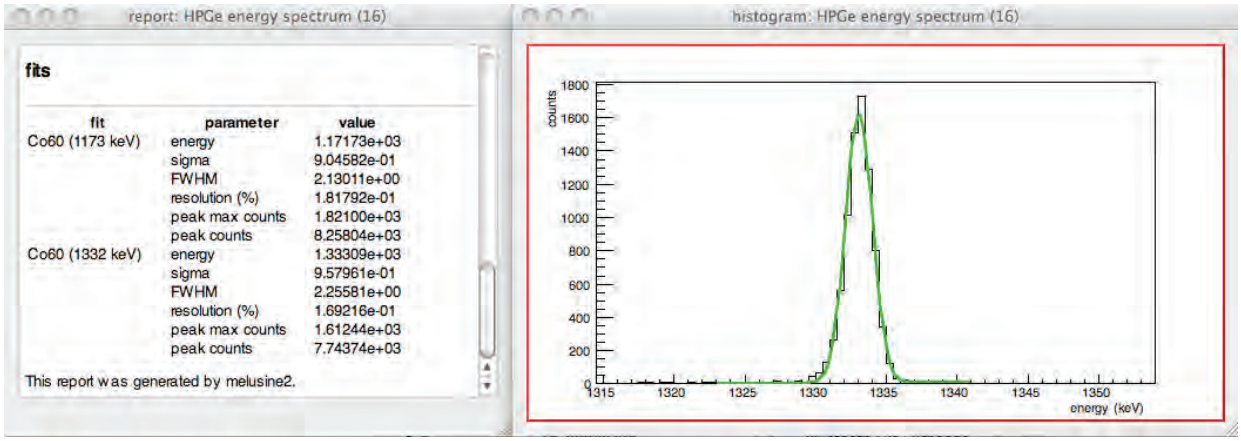

Figure 8. An analysis product from Melusine2. The image on the right is a fit to a measured ^{60}Co source peak, while the left-hand panel provides the results for fits to the 1173- and 2332-keV peaks. The energy calibration is off slightly because it is based on a linear fit to one of the other crystals and the rough gain matching discussed earlier in the article.

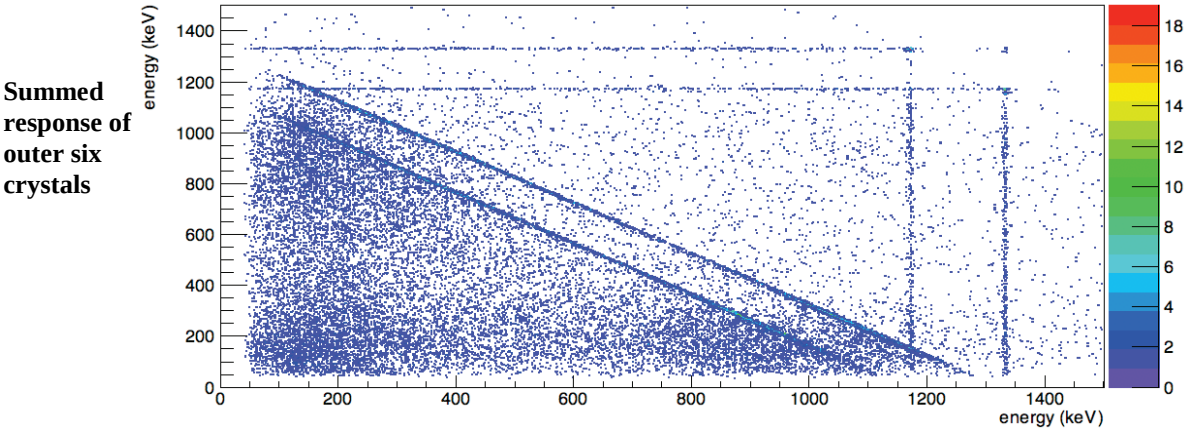

Figure 9. This figure shows a reconstruction of a short ^{60}Co measurement; coincidence between detections in the center crystal (x-axis) and event-by-event energy summed detection in the other six crystals (y-axis) is shown. This data reconstruction was produced using Melusine2.

CONCLUSIONS AND RECOMMENDATIONS

An array of seven HPGe crystals has been successfully assembled in a cryostat designed and constructed using ultra-low-background materials and techniques. Background performance, as well as the effectiveness of the active anti-cosmic veto, will be determined after the system is moved to a new shallow underground laboratory (~35 m.w.e.) at PNNL. All copper parts for the second cryostat have been electroformed; electron beam welding of subassemblies is in progress.

Initial data collected from this crystal array show that the instrument is functioning extremely well for its debut performance. Five of the crystals perform with energy resolution typical of ultra-low-background cryostats. Elimination of minor remaining ground-loop issues and optimization of the Pixie4 acquisition parameters may allow us to improve upon this performance; however, slightly broadened peaks are expected in ultra-low-background setups due to the long cross arm and potential for increased baseline noise in a multicrystal cryostat. One crystal continues to suffer from significant energy resolution degradation due to high-frequency noise; we hope that the cause of this issue will be straightforward and easily corrected, perhaps something as simple as a bad signal cable. Despite suffering from apparent high-leakage current that is limiting the bias voltage we can apply, the seventh crystal provides useable measurement data.

Collecting this initial data has provided us with valuable measurement datasets to process through the Melusine data analysis package currently under development. This effort is early in its development but can already provide significant capabilities for reconstructing data acquired with the array in multiple ways. Current efforts are focused on streamlining energy and efficiency calibration routines. The long-term vision is that the system will be capable of performing multiple parallel analyses to establish the most sensitive data reconstruction for an isotope-by-isotope measurement.

REFERENCES

Aalseth, C. E., O. T. Farmer, J. E. Fast, E. W. Hoppe, T. W. Hossbach, J. D. Kephart, K. E. Litke, M. Liezers, H. S. Miley, E. E. Mintzer, and J. S. Reeves (2009). *Nucl. Instrum. Methods Phys. Res. A* (submitted).

Cooper, M. W., C. E. Aalseth, D. A. Haas, J. C. Hayes, J. I. McIntyre, and B. T. Schrom (2010). Digital data acquisition graphical user interface, these Proceedings.

Keillor, M. E., C. E. Aalseth, A. R. Day, J. E. Fast, E. W. Hoppe, T. W. Hossbach, B. J. Hyronimus, H. S. Miley, A. Seifert, and G. A. Warren (2008). Design and construction of an ultra-low-background 14 germanium crystal array for high efficiency and coincidence measurements, in *Proceedings of the 30th Monitoring Research Review: Ground-Based Nuclear Explosion Monitoring Technologies*, LA-UR-08-05261, Vol. 2. pp. 778–786.

Keillor, M. E., C .E. Aalseth, A. R. Day, J. E. Fast, E. W. Hoppe, T. W. Hossbach, B. J. Hyronimus, H. S. Miley, and A. Seifert (2009). Design and construction of an ultra-low-background 14-crystal germanium array for high efficiency and coincidence measurements, *J. Radioanal. Nucl. Chem*. 282: 703–708.

Smith, L. E., E. J. Ellis, A. E. Valsan, C. E. Aalseth, and H. S. Miley (2004). A coincidence signature library for multicoincidence radionuclide analysis systems, *IEEE Trans. Nucl. Sci.* 51: 1044–1048.

Warren, G. A., L. E. Smith, C. E. Aalseth, E. J. Ellis, A. E. Valsan, and W. Mengesha (2006). Generalized multicoincidence analysis methods, *IEEE Trans. Nucl. Sci*. 53: 351–355.

EXTRACTION OF XENON USING ENRICHING REFLUX PRESSURE SWING ADSORPTION

Richard M. Williams, Paul H. Humble, and James C. Hayes

Pacific Northwest National Laboratory

Sponsored by the National Nuclear Security Administration

Award No. DE-AC05-RLO1830/PL07-ZINC-NDD02

ABSTRACT

Measuring radioactive xenon isotopes in the atmosphere is an important technique used for monitoring within the Comprehensive Nuclear-Test-Ban Treaty (CTBT). Several process steps are needed to capture and prepare a xenon sample suitable for transfer to a nuclear detector. These processes include air drying, xenon collection, concentration, and purification. The ideal xenon sampling system would be small, have low power consumption, not use consumables (such as helium gas or liquid nitrogen), and be fully automated, robust, and dependable. Due to the low concentration of xenon in the air, the most energy-intensive part of the gas processing is the first stage collection and concentration. Pacific Northwest National Laboratory has developed a batch-mode enriching-reflux pressure-swing-adsorption (ER-PSA) process that shows promise as a xenon collection and concentration technique. The development of this process was guided by finite element models of the process chemistry. The modeling showed that minimizing the xenon dispersion in the adsorption columns is critical to achieving a good separation. Prior to hardware construction, models were used to determine appropriate trap dimensions, adsorbent particle size, and optimum process variables such as cycle steps, step times, and flow rates. A benchtop ER-PSA unit was constructed, and testing under various operating conditions has begun. The results obtained in these initial parametric experiments have provided insight into the physics of the process and have refined the mathematical models. The combination of modeling and experiment provides a better understanding of process physics than either experiment or models alone. The benchtop system has demonstrated room-temperature collection of xenon with a xenon enrichment of 1000 (starting from air) and a modest pressure ratio of 7–10, resulting in an energy-efficient separation technique. The technique does not use exotic adsorbents, cryogenic temperatures, or high-pressure compressors, enabling a small, low-power, robust system. This ER-PSA process is an enabling technology for small energy-efficient xenon collectors, desirable qualities for next-generation international xenon systems.

OBJECTIVE

The objective of this research project is to build and test a unique gas collection scheme aimed at preconcentrating xenon without the use of any form of cooling. The collection scheme utilizes activated charcoal (AC), a well-proven, reliable, and easily obtained adsorbent material. To achieve this task a basic experimental apparatus was designed and built based on results from realistic computer simulations of the process chemistry. Initial tests were conducted to demonstrate that, in fact, the gases of interest could be collected. These early results are very encouraging and confirm that AC can be used to preconcentrate xenon to useful levels without cooling.

RESEARCH ACCOMPLISHED

Pressure Swing Adsorption

The gas preconcentrating approach that has been explored here is a special variant of a pressure swing adsorption (PSA) method, a common approach used in many small- and large-scale gas-separation applications (e.g., heatless air drying, N_2/O_2 separations, methane and hydrogen purification). The basic notion behind any PSA scheme is that the adsorption capacity of a given material is greater at high pressure than at lower pressure. Additionally, if there is a difference in the capacity of the adsorbent material for two (or more) different adsorbing species (adsorbates), it is possible to develop a separations scheme that takes advantage of the selectivity of the material and the pressure dependence of the adsorption capacity. Figure 1 shows a series of conceptual curves representing “typical” adsorption isotherms that can be used to further explain the phenomena behind PSA. In this diagram, temperature is also an adjustable variable (between adsorption and desorption) that can be used to enhance the relative difference in capacity between adsorption and desorption. Maximizing this difference leads to improved collection efficiency for a given trap size. For a given isothermal system, it can be seen that if adsorption occurs at high pressure, where capacity is large, then the capacity of the adsorbent drops if the trap is suddenly depressurized, and the previously adsorbed species must be released into the gas phase. This forms the basis of a PSA cycle: adsorption at high pressure followed by desorption at lower pressure. Typical PSA systems consist of two adsorption beds, one operating at high pressure (adsorbing mode) and the other at low pressure (desorbing or regenerating mode). In such a dual-bed configuration, the system can operate continuously by cycling back and forth between the two beds. Other PSA schemes have multiple beds used in more-complex arrangements to maximize yield.

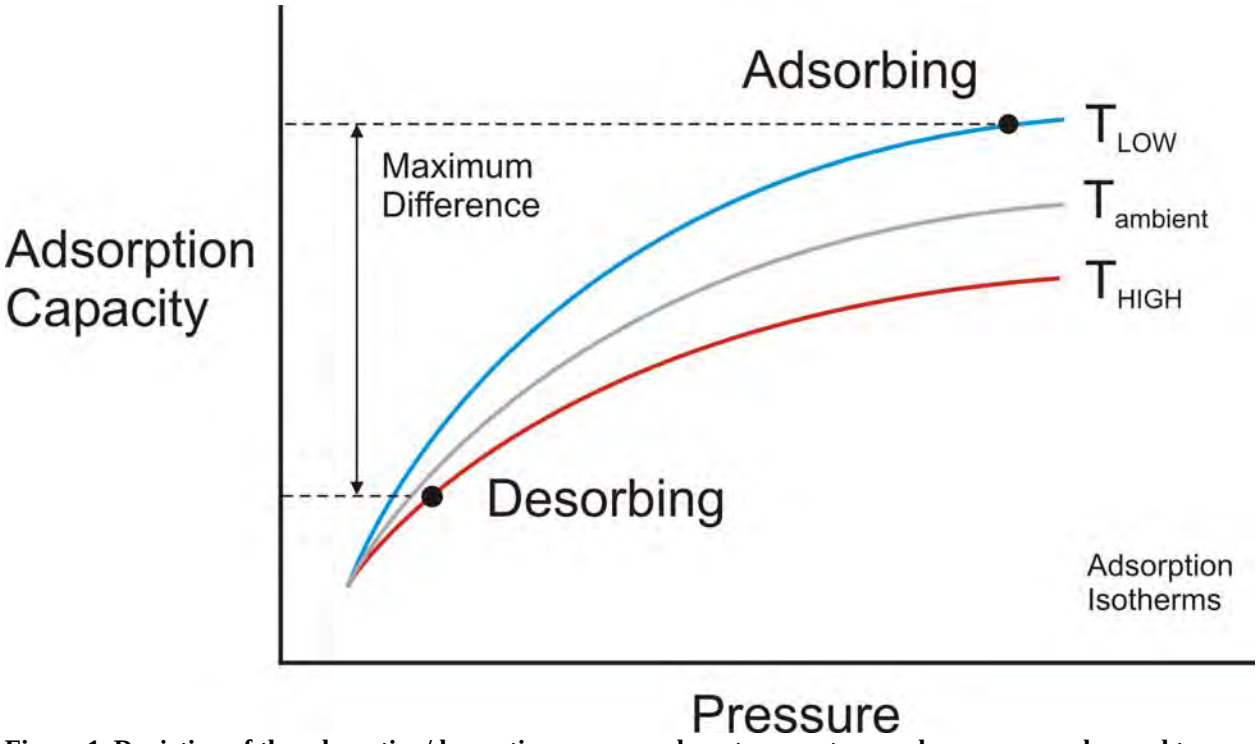

Figure 1. Depiction of the adsorption/desorption process, where temperature and pressure can be used to maximize the relative difference between adsorption capacity.

In order to develop a separations or selective pre-concentration process using PSA, it is useful that a difference exist in adsorption capacity of the adsorbent material for the different chemical species involved; this is referred to as selectivity. While a difference in capacity is useful, it is not completely necessary for a selective separations process to be practical. This is because the adsorption capacity of a given material is considered an equilibrium property. In a PSA system, gases are flowing at high rates through the beds, and the cycling between the beds can occur on short time scales. Under these nonequilibrium conditions, kinetic factors of the different chemical species begin to play a significant role in the actual separations performance of the system. The most common practical example of this difference between equilibrium and kinetic behavior is in the industrial separation of N_2 and O_2 using carbon molecular sieve (CMS) adsorbent in a PSA scheme. Evaluation of the equilibrium adsorption isotherms for these adsorbates on CMS suggests that separations would not be practical; however, it was found that the differences in kinetic behavior between these two species was sufficiently large that a separations process was economically viable, and many PSA air-separation units are now in large-scale production. On the other hand, PSA air driers function on the principle of equilibrium adsorption of water onto a zeolite molecular sieve while letting the rest of the air components pass through; kinetics play a small role in the function of PSA air driers.

In devising a new PSA gas-separations process, it is key to have a complete understanding of both the equilibrium and kinetic behavior of the gases involved. This information can then be fed into numerical simulations of the PSA scheme to predict the overall behavior and performance of the process. The simulation approach is extremely valuable and can save considerable time when designing a process and also during initial testing, as many of the variables can be optimized in the simulation first and then verified on a test bench system.

Enriching-Reflux Pressure-Swing-Adsorption (ER-PSA)

Before describing the specific process that has been studied here, it is useful to focus more on how a traditional PSA system operates. Typically, the input gas stream is compressed up to a high pressure (e.g., several atm), then passed through an adsorbent bed that retains some of the gas species while passing others to yield a “purified” product stream. A portion of this product stream is split off and used to purge a second depressurized adsorbent bed. The PSA system cycles back and forth between the two beds; in this way the high-pressure bed is always yielding a

product stream while the low-pressure bed is being regenerated prior to the next cycle. The gases that are removed are usually referred to as the heavy products, typically the more-retained species, while the lesser-retained species are referred to as the light products. In a PSA air drier, for example, the light-product stream is dry air and the discarded waste stream is wet air (the heavy product being actual water vapor) coming from the low-pressure bed being regenerated by a supply of dry air split off from the product stream. It is important to note here that in a traditional PSA unit, the heavy products are not recovered for further use and are treated as waste. Therefore, if the desired outcome were to recover the water vapor from this traditional PSA air-drying system, it would be challenging because *the heavy product is rediluted and lost on every cycle of the system*.

The gas separations process that is relevant to this project is one in which xenon from the atmosphere needs to be concentrated and then passed onto a secondary unit for purification, etc. In this case, the light products are nitrogen and oxygen, while xenon is the heavy product. The overall goal is not to dilute and vent the xenon heavy product in the waste stream, but rather to continuously increase its concentration up to a high level within the system, then extract it a batch mode for further processing. This can be accomplished by recycling the xenon heavy product back into the PSA system on each cycle (rather than venting it); this process is referred to as enriching reflux (ER).

Enriching-reflux pressure-swing-adsorption (ER-PSA) has previously been demonstrated to preconcentrate trace atmospheric species by several hundred times (Yoshida et al., 2003). In ER-PSA the feed air comes into an atmospheric pressure bed and is used to strip or purge the adsorbed heavy products from the previous high-pressure adsorption cycle. The exit stream from this low-pressure bed is then directed to the inlet of an air compressor, which boosts the pressure up to 80–100 psig and feeds it into the high-pressure adsorption bed. The flow continues for a duration set by the cycle period, and then the flow is reversed; the cycle continues in this manner for however long is required. Upon each cycle, fresh atmospheric air is used to strip off the xenon from the low-pressure bed and sweep it into the compressor, where it is boosted to a higher pressure and readsorbed in the high-pressure bed. In addition to adsorbing the previously retained xenon during this phase of the cycle, an additional new amount of xenon is added to the adsorption bed from the incoming air stream (this is not adsorbed in the first bed because it is operated at a low pressure).

The notional concept behind ER-PSA is that adsorption of xenon occurs in the high-pressure bed, just as in any PSA scheme, but rather than its being vented during the subsequent purge, it is recycled back into the adjacent bed during the next cycle. In this way, the heavy product builds up within the system during each cycle and (in theory) would continue to build up until the bed reached saturation. However, the maximum concentration in the system will be limited by the dispersion of the gases, which causes them to “bleed out” or “break through” the exit of the high-pressure adsorption bed before the cycle is complete. Ideally, the xenon would stay physically isolated on the feed ends of the two adsorption beds as the system cycles back and forth and not migrate toward the exit ports, where it would be lost in the light-product stream. The mechanism that controls this migration or physical concentration profile of the gas is the dispersion of the adsorbing species within the bed. Higher dispersion causes the concentration profile to “smear” out along the length of the bed during the adsorption step. Several factors influence the dispersion of gases in adsorbent beds, including gas-flow velocity, particle size, and the diffusivity of the gas in the various pores of the adsorbent. Particle size and flow velocity are factors that can be adjusted for a given system, while diffusivity is an adsorbate/adsorbent physical relationship.

The objective of this research was to design, construct, and conduct preliminary tests of a prototype ER-PSA system to determine if xenon in air could be preconcentrated using activated charcoal at room temperature. These results are presented below and show that these early tests appear very promising and that useful quantities of xenon were recovered from both 2- and 4-hour collection intervals using PSA cycles of less than 2 minutes.

ER-PSA System Research

As mentioned earlier, a prototype ER-PSA system was designed and constructed. In order to provide for maximum flexibility, a three-bed system was built with individually controlled electronic valves. Figure 2 is a flow schematic for an ER-PSA prototype; this flow schematic is also used in the web-based graphical user interface, where all the functions of the system can be either independently controlled by an operator or set to run in an automated process mode.

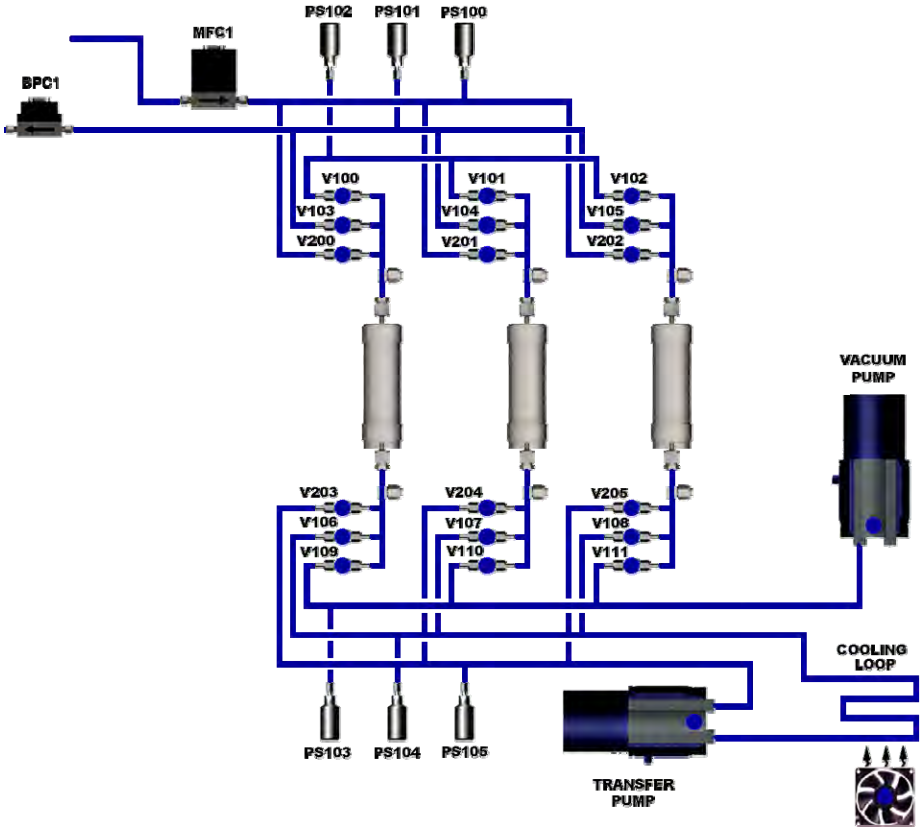

Figure 2. Flow schematic and GUI display of the ER-PSA prototype.

In the ER-PSA system, air flow enters the system through a mass flow controller and is directed through one of the low-pressure beds (filled with ~200 grams of AC). This flow is routed to the inlet of the transfer pump (compressor), where it is boosted up to 80 psig and routed into the high-pressure adsorption bed. The pressure in this bed is kept high with the use of a back-pressure regulator located at the flow exit of the system. Adsorption is cycled back and forth between two of the beds with cycles times as short as 8 seconds and as long as desired (typically less than 3 minutes). Build-up of xenon was monitored in real time by sampling the outlet of the compressor with a capillary connected to a quadrupole mass spectrometer. Initial experiments were conducted in which the cycle time and/or flow rate were varied and the build-up of product monitored. Very recently a secondary module was added to the test bench, which allows for manual batch-mode extraction of the xenon into a small-volume charcoal trap after some number of cycles have been completed (usually 2 or 4 hours). This step was added so that the samples could be concentrated further (by removing excess nitrogen and oxygen) and be analyzed on a commercial gas chromatograph (GC) for a more quantitative evaluation of the system performance. To date, samples have been extracted from the system and analyzed on a separate mass spectrometer but not yet on a calibrated GC. Figure 3 shows a recent photo of the ER-PSA test bench. The instrumentation on the right in Figure 3 is the quadrupole mass spectrometer used to measure the real-time build-up of xenon. The small tubing, traps, and manual valves on the left are part of the secondary collection portion used for quantifying the gas collected. No consideration was given to the overall size or weight of this test bench. Rather, it was designed for maximum flexibility and ease of access to all the elements; however, it can be seen that a system this simple could be easily engineered to be relatively compact.

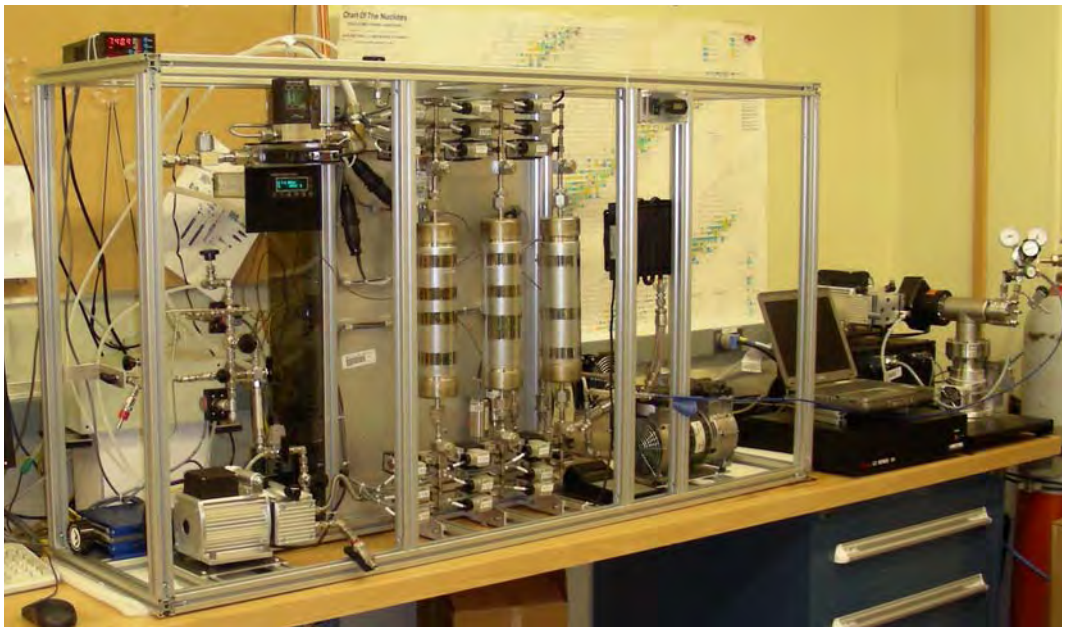

Figure 3. Photo of the ER-PSA test bench, along with the mass spectrometer and manual secondary collection module for sample quantification.

ER-PSA Results

Figure 4 shows the xenon build-up from one of the preliminary tests of the ER-PSA. In this particular comparison, the only change that was made was in the inlet flow rate. The upper black trace shows the gas-phase xenon concentration build-up under an inlet flow of 35 standard liters per minute (SLPM), while the blue trace is at half the previous flow (or 17.5 SLPM). In both experiments the cycle time was fixed at 30 seconds. The lower-flow-rate experiment was allowed to operate for twice as long so that the total amount of air that moved through the system was the same (i.e., 4.2 std. m^3 of air). If the system retained xenon with the same overall efficiency under these two conditions, it is expected that the measured xenon concentration for the lower flow rate at 240 minutes would match the xenon level from the higher flow rate at 120 minutes because both experiments would have processed the same amount of whole air. It can be seen from the data that the system was less efficient at collecting xenon at the lower flow rate than it was at the higher flow rate. The results suggest that xenon dispersion in the bed is not the likely cause of product loss, as dispersion (and breakthrough) would have occurred to a higher degree in the higher-flow-rate experiment. In addition to potential product loss from dispersion, a second source of loss in the ER-PSA system arises from the pressure equalization step that occurs just prior to switching flow between the two adsorption beds. During these first trial experiments of the ER-PSA system, the pressure equalization occurred through the feed ends of the adsorption beds. This involved gas exiting the high-pressure adsorption bed from the end near the zone of highest xenon enrichment and flowing at high rate directly into the low-pressure bed. This turns out to be a very inefficient pressure-equalization process due to the fact that the desorbing xenon from the high-pressure bed flows into the low-pressure bed and ends up being distributed throughout the entire column. Under an ideal pressure-equalization step, the enriched gas would be transferred to only the feed end of the low-pressure column prior to flow. With the product being dispersed throughout the whole column, a significant fraction is then lost (out of the vent) during the subsequent adsorption cycle. A series of experiments is planned that will explore alternative pressure-equalization schemes that minimize (or eliminate) loss due to pressure equalization prior to column switching.

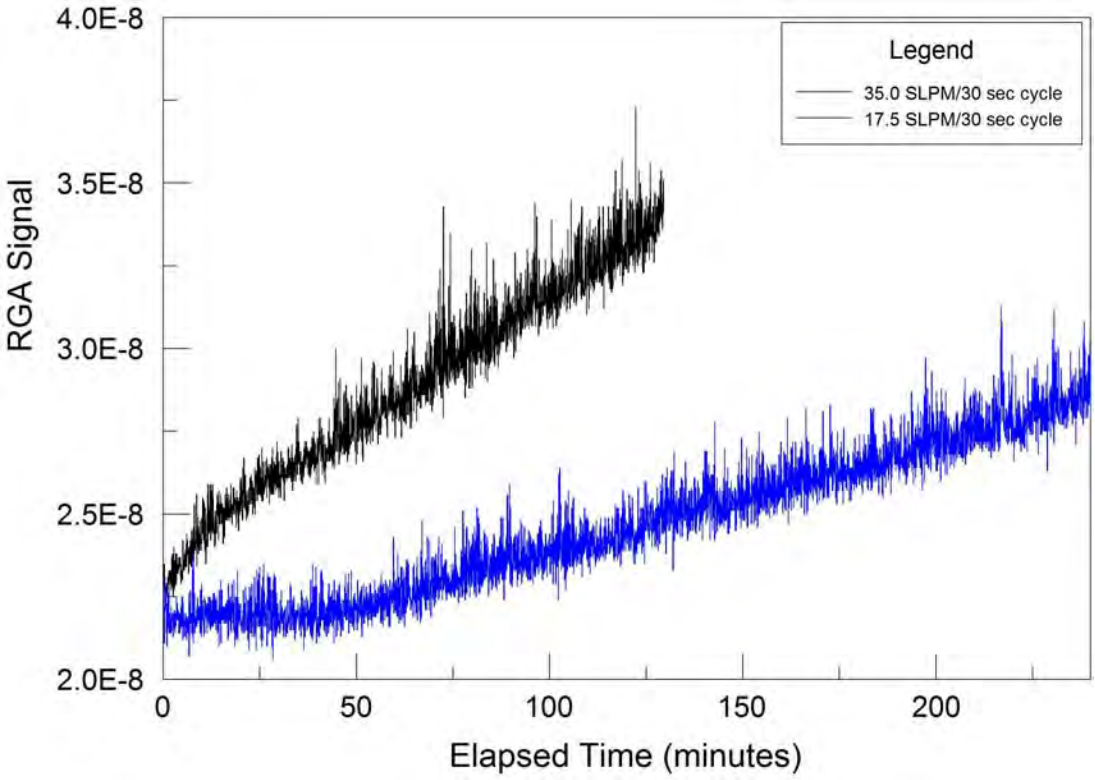

Figure 4. Build-up curves for xenon in the ER-PSA test bench under different flow-rate conditions.

As mentioned previously, a secondary module was added to the test bench, which allows the preconcentrated gases to be extracted from the ER-PSA system at the end of a collection run and transferred into a small container for further analysis. This secondary re-concentration system consists of a small-volume AC trap designed to be submerged in liquid nitrogen for complete adsorption of xenon. A small 13-X zeolite trap is installed before the AC trap to collect adsorbed CO_2 and water, which also build up in the ER-PSA system. This re-concentration module is very efficient because it reduces the total gas volume from ~ 10 std. liters of gas (in the entire ER-PSA system after collection) down to < 0.1 std. liters, while maintaining high recovery of xenon. Following this re-concentration step, the sample can be taken to a separate quadrupole mass spectrometer or gas chromatograph for analysis and comparison against a standard sample. To date the mass spectrometer approach has allowed for semi-quantitative assessment of the percent recovery of xenon in the initial trial experiments on the ER-PSA system. At the time of this writing, only a few tests runs have been completed, but all show promising results and also suggest that changes made to the running parameters do have a impact on recovery, suggesting improvements in system performance can be made with further testing. Table 1 summarizes four ER-PSA runs in the which the collected gas was analyzed using the mass spectroscopy method mentioned above.

Table 1. Summary of early test results for the ER-PSA system. Percent recovery is defined as the total volume of gas collected compared to the total possible.

Flow Rate (SLPM)	Cycle Time (sec)	Collection Duration (min)	% Xenon Recovery
35	30	120	33%
17.5	30	240	18%
17.5	15	240	18%
17.5	15	120	28%

Other experiments have been conducted with the ER-PSA system in which the flow rate and cycle time are varied and the percent recovery is measured. The results thus far suggest two likely causes of product loss during collection. In both of these scenarios, a portion of the xenon is lost out of the system exhaust vent during the

adsorption cycle. The first mechanism is basic dispersion of the xenon concentration profile during the duration of the adsorption cycle. This dispersion causes the concentration profile to smear out along the adsorption bed (rather than being focused near the inlet). During the duration of the adsorption cycle, some of this xenon reaches the exit prior to the switching of the beds and is therefore lost; shortening the adsorption cycle can reduce the loss associated with this mechanism. A second loss factor that may be affecting the performance of the current ER-PSA scheme is the pressure equalization step mentioned and described earlier.

Addressing these two loss mechanisms is an important next step in improving the overall efficiency of ER-PSA for extraction of xenon from ambient whole air. Dispersion can be mitigated with modifications to the adsorption beds. The current bed design was based on the best available estimates of the kinetic behavior of xenon in AC because no experimental kinetic data are available. As the percent recovery is lower than expected, this suggests that the values used for the mass transfer coefficients (i.e., the kinetic parameters) in the simulation may have been incorrect, and the resulting dispersion in the bed is higher than expected. Methods to reduce dispersion in the bed include increasing the diameter, which causes the flow velocity to drop, and reducing the adsorbent particle size, thereby reducing the time for gases to reach the adsorption sites. Reducing particle size would have the effect of increasing the pressure drop across the column. Since the results also suggest xenon loss during the pressure-equalization step, new approaches should be investigated. Presently, several new pressure-equalization steps have been discussed that can be easily implemented on the ER-PSA test bench in the future.

CONCLUSIONS AND RECOMMENDATIONS

An ER-PSA test bench has been designed and built, and initial tests have been conducted aimed at demonstrating pre-concentration of xenon using AC (a basic adsorbent) at room temperature. Measurements have been made showing significant build-up of xenon during the collection interval. Additionally, a secondary module was added to the system, allowing for the processing of the gases after the collection duration. The module allowed for semi-quantitative analysis of the collected xenon. This analysis has shown that for this initial design the percent recovery for xenon was greater than 30%. These results show that the ER-PSA concept is capable of the original objective of room-temperature collection of xenon from ambient air. The results also point to the likely cause of product loss, that is, dispersion loss of products as they move back and forth through the beds. Several design factors can be modified now that this effect has been observed and it is expected that with a new bed design the percent recovery will increase significantly. These design modifications include beds with reduced flow velocity and smaller particle size. New pressure-equalization schemes can also be implemented aimed at reducing product loss during bed switchover.

ACKNOWLEDGEMENT

The authors would like to acknowledge and thank Rey Suarez, Charlie Hubbard, Jennifer Mendez, Kevin Litke, Mike Ripplinger, and Bill Sliger for their assistance in design and assembly of the ER-PSA test bench.

REFERENCE

Yoshida, M., J. A. Ritter, A. Kodama, M. Goto, and T. Hirose (2003). Enriching reflux and parallel equalization PSA process for concentrating trace components in air, *Ind. Eng. Chem. Res.* 42: 17951803.

SURFACE PASSIVATION OF HIGH PURITY GERMANIUM DETECTORS USING AMORPHOUS HYDROGENATED SILICON FILMS

Changkun Xie[1], K. Michael Yocum[1], James F. Colaresi[1], and Harry S. Miley[2]

CANBERRA Industries, Inc.[1] and Pacific Northwest National Laboratory[2]

Sponsored by the National Nuclear Security Administration

Award No. DE-AC52-08NA28650
Proposal No. BAA08-10

ABSTRACT

High purity germanium (HPGe) detectors used in Radionuclide Aerosol Sampler/Analyzer (RASA) systems must be operational unattended for long durations. To fulfill the critical requirement, our work strives to improve HPGe detector long term reliability and resolution performance through investigating new surface passivation techniques to passivate and protect the surface area between electrical contacts.

Amorphous hydrogenated silicon (AHSi) films as the passivation alternative to CANBERRA standard silicon oxides for germanium detectors have been investigated. The AHSi films are deposited on germanium surfaces using a radio frequency (RF) magnetron sputtering technique in an environment of argon and hydrogen gas mixture. Sample analysis shows that the hydrogen atoms are well incorporated into the amorphous films and play an essential role in saturating dangling bonds and minimizing surface states on germanium surfaces. Excellent AHSi passivation films have been attained with this technique.

Two HPGe detectors with AHSi films as the passivant have been successfully fabricated. Test results demonstrate that the AHSi films have the following characteristics in passivating HPGe detectors: low leakage current, low noise contribution, good temperature stability of resolution and noise, ability to withstand thermal stress and maintain physical integrity, and ruggedness in atmospheric rapid thermal cycle and aging tests. Amorphous hydrogenated germanium (AHGe) film as a passivant deposited by sputtering techniques will be investigated later in this project.

OBJECTIVES

The objective of this research is to develop passivation techniques that provide superior resolution and reliability in HPGe detectors. The research is driven by the critical need in radionuclide assay systems such as Radionuclide Aerosol Sampler/Analyzer (RASA) systems that HPGe detectors must be in operation unattended for long periods of time. Current commercially available germanium detectors using the SiOx (x~2) passivation technique have demonstrated acceptable performance and reliability for most laboratory applications in radiation detection and measurement. However, for remote deployments such as RASA systems designed for nuclear detonation detection and analysis, detector performance and reliability must be further improved to achieve superior resolution and noise as wells as enhanced durability for long-term operation.

Passivation of germanium surfaces is one of the key factors that affect the performance and reliability of HPGe detectors. The germanium surface between the electrical contacts must be passivated to minimize surface related leakage current. Also, the intercontact surface must generate little dielectric noise. Both surface leakage noise and passivant dielectric noise must remain low to achieve an acceptable signal–to-noise ratio. Unlike native oxides on silicon surfaces which provide excellent passivation, naturally formed germanium oxides on germanium surfaces have unacceptable stoichiometries which may result in charged states. Charged oxide states may cause an inversion layer in P-type germanium or an accumulation layer in N-type germanium (Brown, 1953). Traditionally, a SiOx film deposited by a well-controlled SiO evaporation process in an oxygen-rich environment is used to passivate germanium surfaces (Holland, 1970). The SiO_x process has been a standard technique for commercial detector products at CANBERRA. However, some variabilities in reverse leakage currents as well as dielectric noise associated with the intercontact surfaces have been observed. Surface issues resulting from the evaporated SiO on germanium have been previously investigated (Bardeen et al., 1956; Dinger, 1976). Controlling the surface chemistry and passivating germanium surfaces to achieve a consistently neutral intercontact surface is of paramount importance in the success of HPGe detector manufacturing processes (Martin, et al., 2008; Martin, et al 2009).

In this work, the feasibility and performance of AHSi films as a passivation alternative to CANBERRA standard silicon oxides for germanium detectors were investigated. AHSi films are considered to be effective passivants in the microelectronics and photovoltaic industries (Searle, 1998). The incorporation of hydrogen in amorphous films effectively compensates dangling bonds within the film as well as on the substrate surface. The result on a single crystal germanium surface is to reduce the surface density of states at near mid-band gap. In this research AHSi films were deposited onto germanium surfaces in an argon and hydrogen gas mixture using a sputtered film technique. HPGe detectors fabricated with the AHSi films as the passivant demonstrated excellent resolution performance and reliability.

RESEARCH ACCOMPLISHED

Characterization of sputtered AHSi passivation films

AHSi films were grown using a RF magnetron sputtering technique. The composition and chemistry of the films were characterized by standard analysis techniques to ensure high-quality films were deposited. Germanium test samples were prepared for the growth of AHSi films. The pre-etched samples were transferred into our sputtering chamber at CANBERRA. The vacuum chamber was pumped down to a vacuum level in the range of 10^{-6} Torr and a silicon target was sputtered. An argon / hydrogen gas blend was used as the deposition plasma to create the amorphous films. The film samples were sent to Evans Analytical Group of Sunnyvale, CA to examine the film composition and quality. The laboratory analysis, utilizing state-of-art scientific instruments, investigated the film surface morphology, thickness, atomic concentration, and physical and chemical states.

Figure 1 shows the test samples prepared for laboratory analysis and a scanning electron microscopy (SEM) surface image of our sputtered AHSi film on a germanium substrate. The surface topography of the initially sputtered film was poor presenting with non-uniformities manifested by defects such as bubbles and circular holes. The dark circles appeared to be areas that were beginning to bubble but had not yet flaked off. The circular holes were the areas where the film was missing. It is extremely important to obtain a dense and homogenous film for passivation on germanium surfaces, so that the surfaces become impervious to ambient atmosphere. The partial coating of germanium surfaces could deleteriously compromise germanium detector performance and reliability. The presence of circular holes penetrating the sputtered films is possibly due to several reasons such as poor surface preparation,

compressive stress, or embedment of deposition gases. To eliminate these adverse effects, several sputtering tests to optimize the growth conditions were carried out. In RF sputtering techniques, gas pressure, RF power, sample to target distance, and sputtering time are the four critical parameters for achieving high quality sputtered films. With optimized conditions, excellent passivation films have been successfully grown. The bubble-like defects found on the germanium test samples are not present on germanium surfaces in our newly fabricated germanium detectors with AHSi films as the passivants.

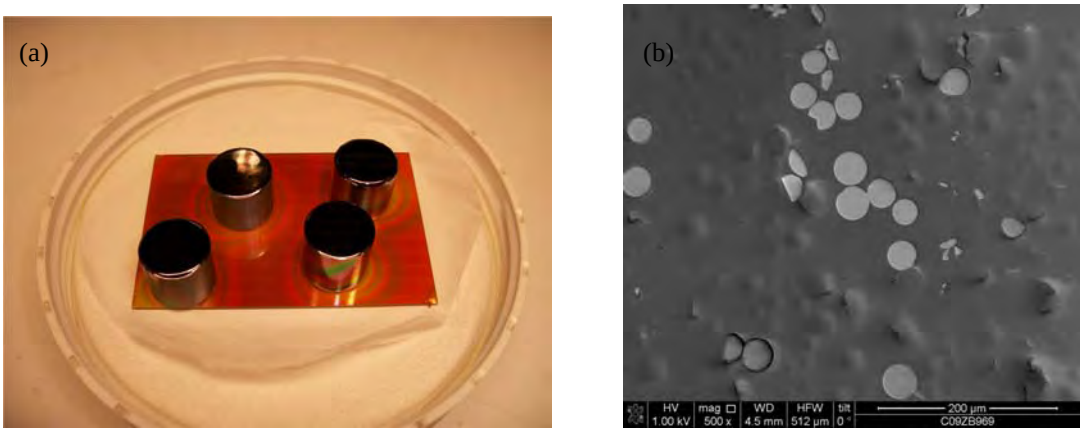

Figure 1. (a) Sputtered AHSi film test samples deposited on germanium substrates (b) Scanning electron micrographs of sputtered AHSi film grown on a HPGe substrate. The film shows the bubble-like defects on germanium surfaces.

The thickness and the elemental composition of the AHSi film were determined by Rutherford Backscattering Spectrometry (RBS) analysis, and the surface chemistry was examined by X-ray photoelectron spectroscopy (XPS). We are mostly interested in how much hydrogen was actually incorporated into the film during the deposition. Table 1 summarizes the results from the RBS analysis showing that the atomic concentration of hydrogen in AHSi films is about 21%. XPS results also suggest that the sputtered film on the germanium substrate is composed primarily of elemental Si with lower levels of SiO_2, indicating that the silicon atoms are bonded/clustered with the hydrogen atoms. The success of high percentage incorporation of hydrogen into the films is instrumental to our study in compensating the dangling bonds on germanium surfaces, suggestive of a high quality AHSi passivant for germanium surfaces.

Table 1. RBS analysis of the sputtered AHSi films

Depth (Å)	Atomic concentration (%)			Density (at/cc)
	Si	H	Ge	
6500	78.8	21.2	-	6.70×10^{22}
Bulk	-	-	100	4.42×10^{22}

Detector Fabrication using AHSi Passivation Films

Standard electrode germanium (SEGe) detectors P84648A and P3488B were fabricated using the sputtered AHSi technique to evaluate the passivation performance of the films. The detectors had been evaluated in the past with different passivation techniques which resulted in good resolution and low noise performance. Previously the core hole was implanted with boron ions to form a thin p^+ contact, and an outside wraparound thick Li layer was produced to form a rugged n^+ contact. After both detectors received a nitric/hydrofluoric acid solution etch of the groove surface to obtain a clean germanium surface, they were immediately transferred into a vacuum process

chamber for AHSi film depositions. Figure 2-a shows the SEGe detector P3488B where the intercontact surface was passivated with an AHSi film. The film presented a dense and uniform coating on the germanium intercontact surface. No visible porous or fissure defects were found in the film with microscopy inspections, which makes this detector surface passivation nearly impervious to ambient atmospheric conditions. Figure 2-b shows the I-V and C-V measurements at liquid argon temperature for detector P3488B. The leakage currents are generally low but with a gradual increase as the reverse bias increases from 3000 V to 5000 V. The depletion voltage is around 3400 V, and the capacitance after depletion is about 34 pF. These results suggest that the AHSi passivation technique results in low leakage current necessary for high resolution germanium detectors. The AHSi passivant withstands high electric field between the two electrical contacts, and induces low or no density of charged surface states which would result in surface leakage current.

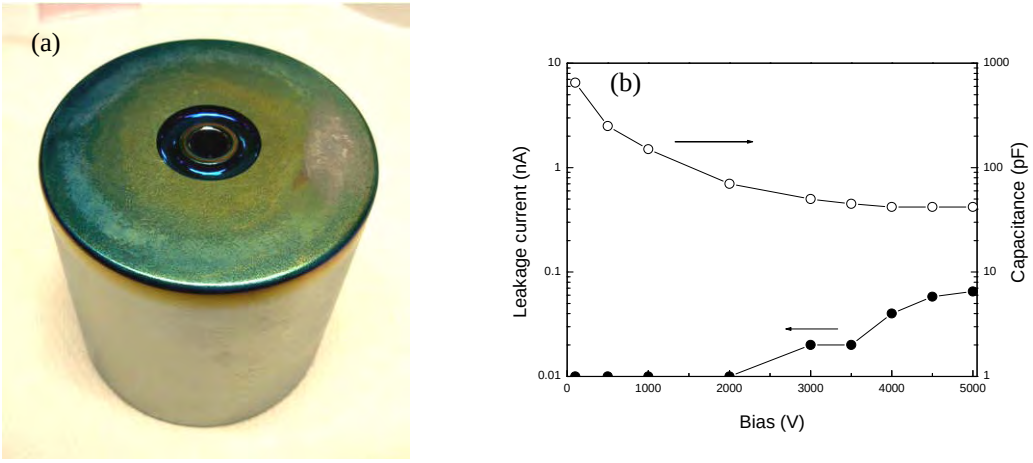

Figure 2. (a) SEGe detector P3488B for which the intercontact surface was passivated with the sputtered AHSi film. (b) C-V and I-V characteristics for the SEGe detector P3488B at liquid argon temperature (87 K).

Detector Resolution and Noise

To measure the detector resolution and performance, the detector P84648A was mounted into a CANBERRA 7500SL dipstick cryostat. The cryostat cold finger was inserted into a liquid nitrogen Dewar for detector performance tests and then placed into a liquid argon Dewar for re-evaluation. Table 2 shows test results of detector P84648A as a function of reverse bias including detector resolution, noise, peak-to-Compton ratio, and detector efficiency. Detector resolution is represented by full width at half maximum (FWHM) and full width at tenth maximum (FWTM) of ^{60}Co (1.33 MeV) and ^{57}Co (122 keV) and the electronic noise by the FWHM of an injected pulser signal. Increasing the reverse bias appears to slightly worsen the detector resolution. At 3.5 kV bias, the FWHM of ^{60}Co at 1.33 MeV and ^{57}Co at 122 keV are 1.68 keV and 0.87 keV, respectively. While at 5.0 kV bias, the FWHM of ^{60}Co at 1.33 MeV and ^{57}Co at 122 keV are 1.73 keV and 0.95 keV, respectively. The deterioration of detector noise is related to the increase of the parallel noise due to the effect of increased detector leakage current. The detector relative efficiency is 21%, which is in agreement with the previous result where the wet chemical oxide (WCO) passivation was employed (Martin et al., 2009). The detector maintained constant resolution and efficiency while being biased over a period of 12 hours. Finally, the cryostat was placed into a liquid argon Dewar to warm the detector by 10 K. Subsequent measurements showed that the detector's resolution and relative efficiency were consistent with the LN_2 measurements, suggesting good temperature stability of the detector performance.

Detector P3488B was mounted into a CANBERRA Cryo-Pulse® 5 (CP-5) electrically cooled system. The CP-5 cryocooler allows controlled variation of the detector temperature over a wider range than permitted by a liquid cryogen cooled cryostat. Detector test results at a temperature of 93 K are listed in Table 3. The resolution is approximately 2 keV at 1.33 MeV for ^{60}Co, and 1.25 keV at 122 keV for ^{57}Co. The injected pulser signal resolution is 1.18 keV. The detector relative efficiency is approximately 100% consistent with the active volume the detector, and the peak-to-Compton (P/C) ratio is 73:1.

Table 2. Detector evaluation for detector P84648A with shaping time of 6 µs.

Bias (kV)	RESOLUTION (keV) ^{60}Co		^{57}Co		Pulser	P/C	Eff.	Comment
3.5	1.68	3.11	0.87	1.63	0.75	53.5	20.6%	Test in LN_2
4.0	1.70	3.10	0.86	1.58	0.74	52.5		
4.5	1.70	3.12	0.91	1.70	0.78	51.8		
5.0	1.73	3.19	0.95	1.72	0.78	53.5		
Bias overnight								
3.5	1.65	3.06	0.84	1.53	0.72	54.8	20.4%	
3.5	1.71	3.10	0.84	1.55	0.76	52.5	20.5%	Test in LAr

Table 3. Detector evaluation for detector P3488B with shaping time of 6 µs.

Bias(kV)	RESOLUTION (keV) ^{60}Co		^{57}Co		Pulser	P/C	Eff.	Det. Temperature
4.0	2.01	3.77	1.25	2.25	1.14	73.2	95.4%	93 K
Bias overnight								
4.0	1.99	3.69	1.25	2.30	1.17		97.9%	

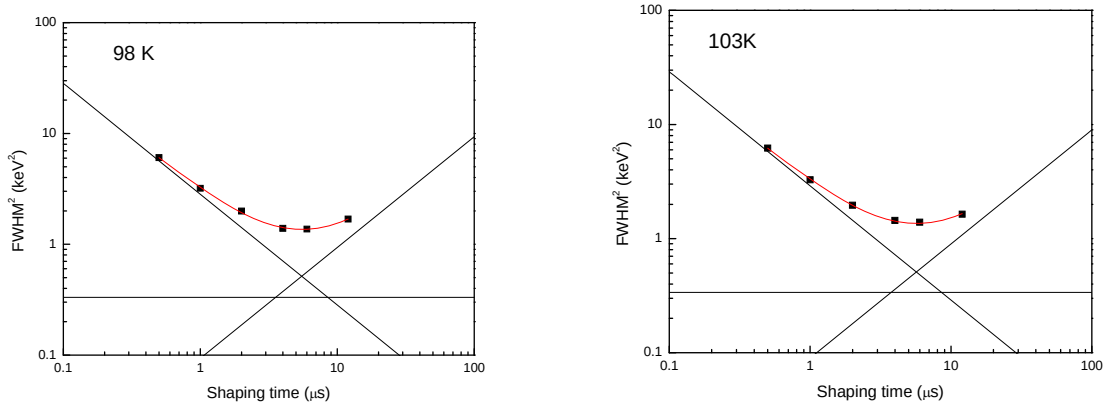

Figure 3. Noise analysis of detector P3488B. The pulser FWHM measurements were carried out at 98 K and 103 K, respectively. The three straight lines in each figure represent series, parallel, and 1/f noise, respectively.

Sources of electronic noise in germanium detectors are associated with detector capacitance, leakage current, and intercontact surface noise. Therefore, the total noise encompasses three independent categories which sum in quadrature as given by the following expression

$$FWHM_{pulser}{}^2 = N_{series}^2 + N_{parallel}^2 + N_{1/f}^2 = \frac{k_1}{\tau} + k_2\tau + k_3 \ . \qquad (1)$$

Series and parallel noise correspond to detector capacitance and leakage current, respectively, and are functions of amplifier shaping time. The 1/f noise component is partly contributed by the detector intercontact surface and is not a function of amplifier shaping time (Bertolini and Coche, 1968). The pulser FWHM data as a function of shaping time from 0.25 µs to 10 µs were measured for the detector P3488B at 98 K and 103 K. The data ($FWHM_{pulser}{}^2$) were fitted with equation (1) using a nonlinear least squares method. The fitted curves are shown in Figure 3. The three components of the noise are individually shown in both figures as straight lines. At 98 K, the fitting parameters

k_1, k_2 and k_3 are 2.82, 0.09, and 0.33, respectively, and at 103 K, the fitting parameters k_1, k_2 and k_3 are 2.89, 0.09, and 0.34, respectively. The *1/f* noise contribution from AHSi passivation is lower than that for the detector previously fabricated with the standard SiOx passivation technique where k_3 was 0.61 (Martin, et al.,2009).

Temperature stability

Surface channel effects can greatly compromise detector performance if germanium surfaces are not effectively passivated. In addition surface channels may be temperature sensitive which can further deteriorate HPGe detector performance at higher operating temperatures (Hull, et al., 1995). Depending on the efficacy of a surface passivation in eliminating surface channels, the detector resolution and noise can be greatly improved if the passivation is stable over a broad temperature range. This may not only improve detector resolution at higher temperatures, but also reduce the input power of the cryocooler and mitigate the associated microphonics noise.

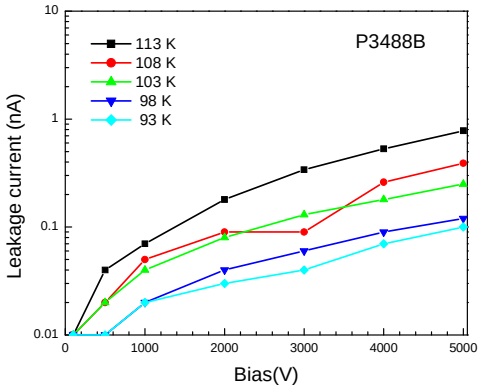

Figure 4. I-V characteristics of detector P3488B at various detector temperatures.

Lowering the cooling power of the CP-5 allowed the progressive increase of the detector temperature from 93 K to 113 K. At each temperature, the detector leakage current and resolution were measured to determine the temperature effect on detector performance. Figure 4 shows the detector leakage current as a function of reverse bias at various temperatures. As can be determined from the graphs, the leakage current gradually increases as the temperature increases. However, it is observed that increasing detector temperature by 20 K from 93K does not compromise its resolution and noise performance. As shown in Table 4, the FWHM and FWTM for ^{60}Co (1.33 MeV) and ^{57}Co (122 keV) sources and FWHM for pulser, as well as the P/C ratio and relative efficiency for the detector P3488B at various temperatures do not change significantly. Compared to the standard SiOx passivant from previous investigations, detector P3488B with AHSi as its passivant demonstrates excellent resolution and noise performance over a wide temperature range. Our earlier data for the detector with the standard SiOx passivant showed that the detector became much noisier once the detector was warmed to above 103 K. The improved temperature stability reported here is due to the unique properties of the AHSi films produced by the sputtering technique developed during this research.

Table 4. Detector evaluation for detector P3488B at various detector temperatures.

Bias (kV)	RESOLUTION (keV) ^{60}Co		^{57}Co		Pulser	P/C	Eff.	Det. Temperature
4.0	1.99	3.69	1.24	2.30	1.17	70.0	100%	98 K
4.0	1.96	3.64	1.24	2.33	1.18	69.0	98.1%	103 K
4.0	1.95	3.60	1.26	2.39	1.16			108 K
4.0	1.97	3.62	1.26	2.31	1.14			113 K

Detector Ruggedness

To examine the AHSi passivation method for ruggedness, two tests were carried out for both detectors P84648A and P3488B: rapid thermal cycles and atmospheric aging. Plots of leakage current as a function of reverse bias for the ruggedness tests are shown in Figure 5 for both devices. The leakage current characteristics before and after the ruggedness tests were measured, providing a direct comparison of leakage performance. Five rapid thermal cycle tests were performed for each detector from 87 K to approximately 300 K. No change of film color and morphology were observed during the tests. The leakage current of detector P84648A showed no change after five thermal cycles, however, a slight increase of leakage current for detector P3488B occurred after five rapid thermal cycles.

The atmospheric aging test was carried out by storing both detectors in a nitrogen-purged dry box over an extended period of time. After one month of dry box aging, the leakage current for detector P84648A increased at 3000 V reverse bias from 0.01 nA to 0.04 nA. The increase in leakage current was negligible since a subsequent retest showed the same resolution and noise as they were prior to the ruggedness tests. For the device P3488B, the leakage current improved during the one month aging test, indicating a moderate improvement of the surface condition. The AHSi passivant performance was not compromised by storage/aging in a clean and dry storage environment, which contrasts with the standard SiOx passivant. Our previous results had shown that the standard SiOx passivant introduced much more leakage current and noise after a four week aging process. These results demonstrate that the detector fabricated with the new AHSi technique as its passivant can have a much longer shelf lifetime than the one with SiOx.

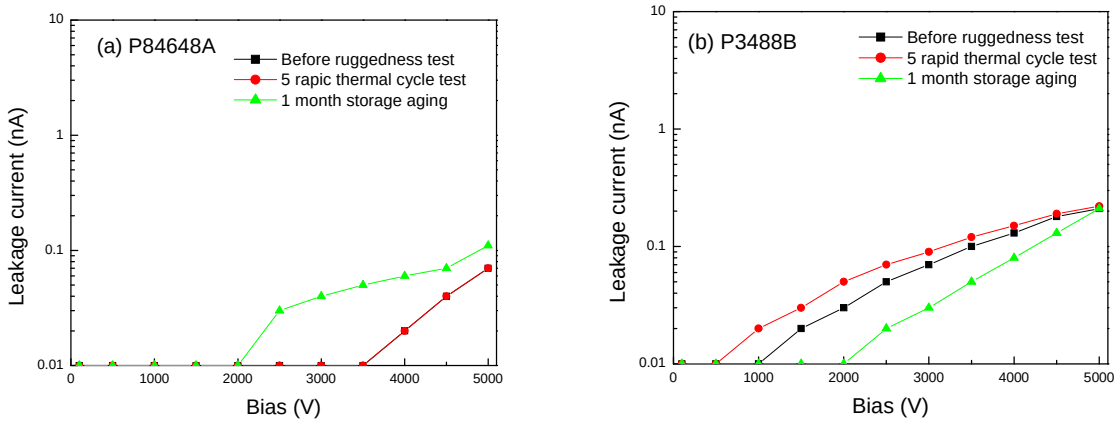

Figure 5. I-V ruggedness tests including five rapid thermal cycles and one month storage aging for the two SEGe detectors (a) P84648A and (b) P3488B, respectively.

CONCLUSIONS AND RECOMMENDATIONS

Two HPGe detectors were successfully fabricated with AHSi film as the intercontact surface passivant using a RF magnetron sputtering technique. Detector test results demonstrated acceptable resolution and noise performance, suggesting the effectiveness of a sputtered AHSi technique in passivating germanium surfaces for high resolution germanium detectors. The fabricated detectors tolerated temperature cycling between room temperature and cryogenic temperatures, were stable with time without compromising resolution or efficiency, and tolerated ruggedness tests by maintaining acceptable performance after thermal quenches and atmospheric aging. Low leakage current was achieved suggesting that AHSi films are electrically stable and are capable of withstanding strong electric fields. Excellent temperature stability of resolution and noise will allow detectors to operate at higher temperatures. This will help to mitigate microphonics induced by cryocoolers by allowing them to operate at lower input power. Low 1/f noise contribution from the intercontact surface will greatly benefit small germanium detectors for which ultra-low noise is required.

This research demonstrated that amorphous hydrogenated semiconductor films can be used as passivants for germanium surfaces for high resolution germanium detectors. In the next phase of this research the feasibility and performance of AHGe films will be investigated. It is expected that AHGe may have better performance in passivating germanium surfaces than AHSi. It is intuitive to believe that superior interface between germanium surfaces and AHGe passivant can be achieved since interface bonding stoichiometry should be better. At the interface, the ordered Ge atomic lattice may seamlessly morph into a disordered Ge network that removes strained Ge–Ge bonds. Any unsatisfied bonds created during the film deposition will be mitigated by the creation of Ge–H bonds. Figure 6 displays initial results of the sputtered AHGe film as the passivant for a HPGe detector along with the collected ^{57}Co spectrum. Low leakage current and acceptable resolution and noise have been accomplished, suggesting that AHGe films may be useful in passivating germanium surfaces for HPGe detectors.

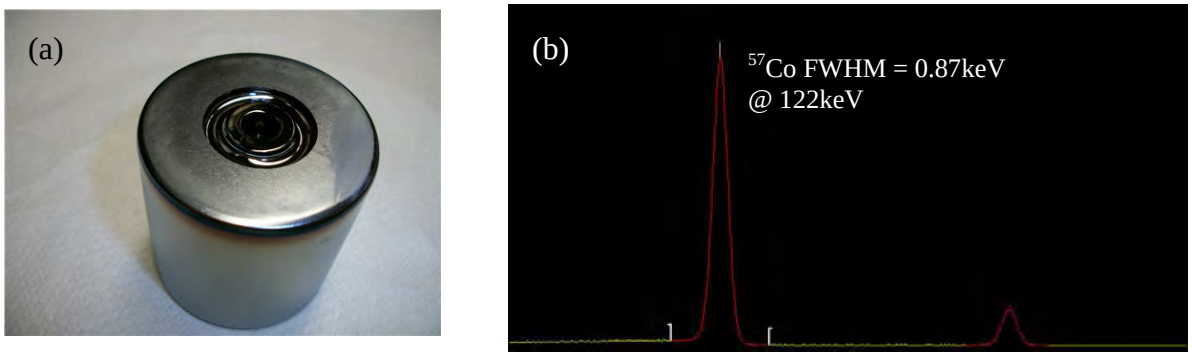

Figure 6. (a) SEGe detector P84648A for which the intercontact surface was passivated with the sputtered AHGe film. (b) ^{57}Co spectrum showing a resolution of 0.87 keV at 122 keV.

ACKNOWLEDGEMENTS

Thanks to the CANBERRA Detector R&D team for laborious support in this project. Thanks to Audrey Carmichael for project management. C. Xie is particularly grateful to Greg Martin for enlightening discussions.

REFERENCES

Bardeen, J., R. E. Coovert, S. R. Morrison, J. R. Schrieffer, and R. Sun (1956). Surface conductance and the field effect on germanium, *Physical Review* 104: 47–51.

Bertolini G. and A. Coche (1968). *Semiconductor Detectors*, Wiley Interscience, New York

Brown, W. L. (1953). N-type surface conductivity on p-type germanium, *Physical Review* 91: 518–527.

Dinger, R. J. (1976). Effect of evaporated dielectric materials on the surface of high purity germanium, *J.Electrochem. Soc.: Solid-State Science and Technology* 123: 1398–1404.

Holland, L. (1970). *Vacuum Deposition of Thin Films*, Chapman & Hall Ltd.

Hull E.L., R.H. Pehl, N.W. Madden, P.N. Luke, C.P. Cork, D.L. Malone, J.S. Xing, K. Komisarcik, J.D. Vanderwerp, and D.L. Friesel (1995). Temperature sensitivity of surface channel effects on high-purity germanium detectors, *Nuclear Instruments and Methods in Physics Research Section A: Accelerators, Spectrometers, Detectors and Associated Equipment*, 364:488–495

Martin, G. N., K. M. Yocum, J. F. Colaresi, and H. S. Miley (2008). Improving germanium detector resolution and reliability, in *proceedings of the 30th Monitoring Research Review: Ground-Based Nuclear Explosion Monitoring Technologies*, LA-UR-08-05261, Vol. 2, pp.787–792.

Martin, G. N., C. K. Xie, K. M. Yocum, J. F. Colaresi, and H. S. Miley (2009). Improving germanium detector resolution and reliability, in *Proceedings of the 2009 Monitoring Research Review: Ground-Based Nuclear Explosion Monitoring Technologies*, LA-UR-09-05276, Vol. 2, pp.677–685.

Searle, T. (1998). *Amorphous silicon and its alloys*, INSPEC, London.

IMPROVEMENT IN GE DETECTOR COOLING

K. Michael Yocum[1], James Colaresi[1], and Harry S. Miley[2]

Canberra Industries, Inc.[1] and Pacific Northwest Laboratory[2]

Sponsored by the National Nuclear Security Administration

Award No. DE-AC52-08NA28656
Proposal No. BAA08-09

ABSTRACT

High Purity Germanium (HPGe) detectors used in International Monitoring System (IMS) radionuclide monitoring stations must operate unattended in remote locations for up to six months between maintenance intervals. Recent technology advances have resulted in availability of Stirling and pulse tube cryocoolers with lifetimes well in excess of 20,000 hours. The Cryo-Cycle™ and Cryo-Pulse® 5 are two such commercial products being modified and evaluated for application in IMS Radionuclide Aerosol Sampler/Analyzer (RASA) systems. The Cryo-Pulse® 5 makes use of pulse tube cryocooler technology for the direct cooling of germanium detectors. Improvements are being implemented by the addition of ultra-high vacuum detector chamber technology, inclusive of all metal vacuum seals, to increase reliability and decrease downtime following brief power outages. A remote detector chamber (RDC) is incorporated to reduce the streaming path and decrease interference due to background radiation. The detector chamber is sized to accept large detectors in excess of 100% relative efficiency at 1.33MeV. The Cryo-Cycle™ is a hybrid cryostat having a liquid nitrogen (LN) reservoir and self contained Stirling cryocooler that condenses boil-off gas to maintain the LN supply indefinitely and provide a seven day cooling buffer in the event of component or power failures. The Cryo-Cycle™ is being integrated with a nitrogen generator for initial remote filling and top-off of LN to improve remote use and long term reliability. Details on the progress of both efforts are presented.

OBJECTIVES

The RASA Mark 4 and implementation of the Cryo-Pulse® 5 and Cryo-Cycle™ have been described previously by Yocum et al., (2008, 2009). The RASA was developed at the Pacific Northwest National Laboratory (PNNL) in the 1990s to meet Comprehensive Nuclear-Test-Ban Treaty (CTBT) requirements for aerosol radionuclide measurements, as described by Bowyer et al. (1997) and Miley et al. (1998). The electromechanically cooled HPGe detectors incorporated into aerosol samplers currently operating in the field rely mainly on Joule-Thomson direct coolers. Performance of Joule-Thomson (J-T) coolers for this application has been problematic. The standard Cryo-Pulse® 5 has been under evaluation and operating successfully in a prototype RASA system for two years at Patrick AFB, Florida.

The goal of this project is to investigate improvements in HPGe detector cooling technology for use in the RASA Mark 4. Explorations in both direct pulse tube cooling and hybrid Stirling cooling are being conducted. CANBERRA Cryo-Pulse® 5 and the Cryo-Cycle™ standard products provide the starting point for this effort. UHV technology is being incorporated in the Cryo-Pulse® 5 to improve long-term vacuum integrity and to eliminate the possibility of partial thermal cycles. This includes the use of metal vacuum seals, onboard vacuum pumps such as non-evaporable getter (NEG) pumps and ion pumps, improvements in cryostat end cap sealing, and use of UHV compatible internal components. Vibration isolation and mitigation techniques are being investigated to further enhance overall performance.

A nitrogen (N_2) gas generator is being integrated with the Cryo-Cycle™ cooler to maintain a seven-day cooling buffer in the event of a power outage. An uninterruptible power supply (UPS) will be used with both direct and hybrid coolers to provide redundant protection against partial thermal cycles and to keep the Cryo-Pulse® 5 at operating temperature in the event of short power outages.

RESEARCH ACCOMPLISHED

The UHV Cryo-Pulse® 5 design described previously has been implemented and progress on the final assembly of the hardware is reported. The results of our tests on the Cryo-Cycle™ hybrid cryostat with an integral nitrogen gas generator are also detailed.

Direct Electric Cryo-cooling Improvements

For the RASA application a 4.0 inch diameter detector chamber was designed to fit inside the 4.3 inch diameter shield penetration of the RASA Mark 4. Figure 1 is an outline drawing showing the UHV Cryo-Pulse® 5 in relation to the RASA shield and filter paper. The RASA uses radiation shielding to reduce interference from background radiation and to increase sensitivity. To maximize the effectiveness of the shielding, a RDC is incorporated. The RDC allows the shield penetration to be effectively closed by insertion of lead back shielding directly behind the detector chamber after it is assembled into the shield (i.e. no-stream-path design). Back shielding in close proximity to the detector element further reduces the background and increases the sensitivity when compared to long end cap detector chambers. The benefit of the RDC and back shielding is clearly illustrated in Figure 1. The RDC is designed to accept germanium detector elements greater than 100% relative efficiency. All materials used within the vacuum envelope are UHV compatible for added vacuum reliability and to allow quick recovery from short power outages.

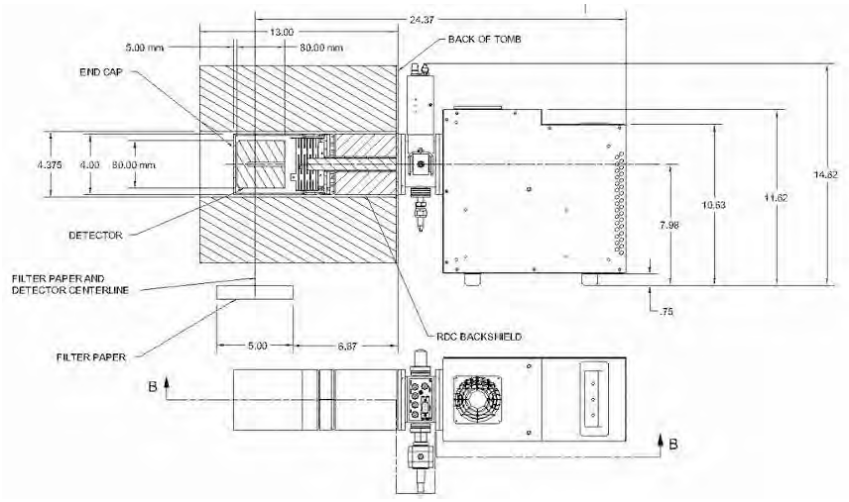

Figure 1. UHV Cryo-Pulse® 5 (Units are in inches unless otherwise indicated.)

Long term reliability of the UHV Cryo-Pulse® 5 is primarily dependant on the cooler reliability and the vacuum integrity. Historically these have been the two most common failure modes for RASA detectors. Pulse tube cooler reliability has reached the point that the lifetime is expected to exceed 50,000 hours, and a 5-year prorated warranty is offered as a standard feature. Vacuum integrity is improved by use of UHV materials and assembly techniques. The vacuum enclosure is made of stainless steel, aluminum, and copper with ceramic electrical feedthroughs. All fixed joints are welded or brazed with careful attention to weldment design to eliminate trapped gasses and virtual leaks. Demountable vacuum seals comprise metal knife edge seals (i.e., Conflat), indium compression seals, and swaged pinch seals. Internal hardware is made of copper, stainless steel, aluminum, and ceramic. The AC coupled FET assembly consists primarily of ceramic components assembled on a ceramic printed circuit board. Solder connections are made using 96% tin with 4% silver. The insulation for the high and low voltage wires inside the cryostat is one area of compromise; wires are insulated with polyimide resin. The UHV Cryo-Pulse® 5 assembly with and without the end cap in place is shown in Figure 2.

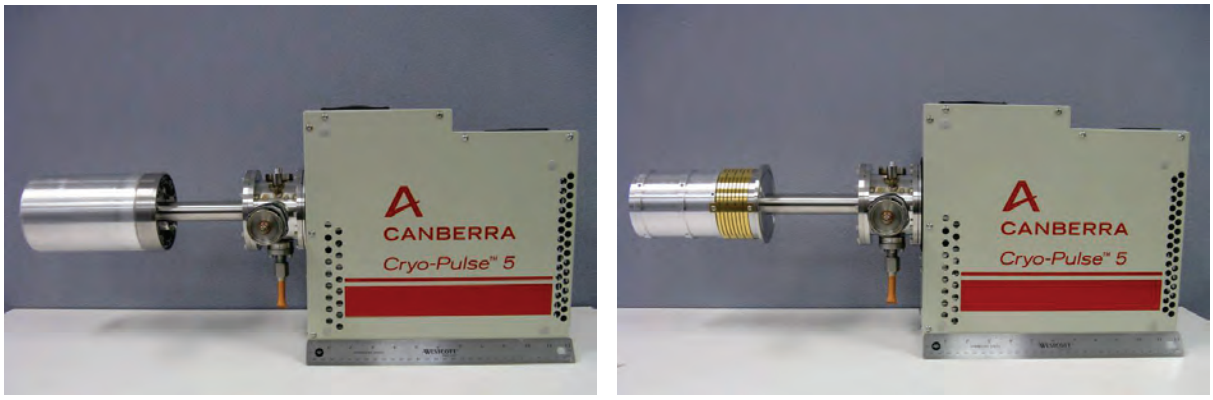

Figure 2. UHV Cryo-Pulse® 5 shown with and without end cap.

The vacuum integrity of the cryostat depends on proper use of materials and assembly techniques, as well as the method used to manage the residual gas evolution inside the cryostat. The UHV Cryo-Pulse® 5 incorporates a non-evaporable getter (NEG) pump and an ion pump. The NEG pump is effective at permanently removing chemically reactive gases such as carbon, oxygen, and nitrogen. Hydrogen is reversibly pumped by NEG pumps, but is only released in quantity by heating the getter to temperatures well in excess of 100 °C. NEG pumps may be regenerated by heating to approximately 200 °C at which point the hydrogen is released and must be pumped away. The adsorbed reactive gasses diffuse into the bulk of the getter leaving a clean reactive surface layer. Non-reactive gasses such as helium and other noble gasses are controlled by use of an ion pump. The ion pump ionizes residual gas atoms that are then accelerated by an intense electric field. The energetic ions impinge on metal electrode plates

where they chemically react or become buried by sputtering of the electrodes. The ion pump on the Cryo-Pulse® 5 has a pumping speed of approximately 0.5 liters/second.

The cryostat components have been fabricated and tested and assembly is nearly complete. Residual gas analysis, vibration analysis, and thermal characterization of the system will be performed prior to mounting the detector element. Evaluation of detector performance will conclude the tests.

Circuitry to Mitigate Microphonics Response (MR)

Tests have been performed to determine that an AC coupled preamplifier is sufficiently low in noise and gives satisfactory MR performance for the RASA application. The final cooled FET assembly has been built and installed in the cryostat. Additional test were performed to demonstrate the benefit of increasing the second stage filter capacitance to reduce the effective MR caused by the relative motion of the high voltage components to ground surfaces inside the cryostat. In addition lead routing and electrical isolation of low and high impedance leads have also been designed to minimize MR.

Mechanical Vibration Isolation

Vibrations in the high voltage circuit and or high impedance portions of the low voltage signal circuit inside the cryostat cause MR induced noise in germanium (Ge) detector systems. Capacitive coupling between these circuits and nearby conductors at a different potential results in a modulation of charge in the signal circuit. This ΔQ is amplified along with the signal. The signal-to-noise ratio is degraded to a degree dependant upon the frequency, amplitude, and repeatability of the resultant perturbations. High frequency vibration in the range of 10's of kHz and higher can be effectively filtered by shaping amplifiers typically used in spectroscopy systems. Random frequencies in the audio range down to 10's of Hz are difficult to filter or suppress without degrading the signal.

The most common approach to mitigating MR originating inside the cryostat is to reduce the transfer of vibration to high voltage components, high impedance leads and components, and nearby ground planes. This can be accomplished externally by reducing the vibration from external sources such as fans or the pulse tube compressor. Coupling of external vibrations to the cryostat body can be reduced by inertial damping or mechanical isolation techniques such as the addition of mass or insertion of flexible couplings at strategic locations. Similarly vibrations that make their way to the external vacuum enclosure can be reduced or prevented from transferring through the mechanical connections to the high impedance detector circuit inside the cryostat by isolating, damping, or restraining circuit components. The mechanical flexures that support the internal components provide flexible vibration isolation and thermal isolation while providing mechanical support. All of these methods have been incorporated into our design to mitigate the effects of the compressor and pulse tube vibrations.

Cryo-Cycle™ Hybrid Cryostat Improvements

The Cryo-Cycle™ HPGe detector cooler is a closed-system N_2 re-liquefier incorporating a 15 Watt free-piston linear Stirling cooler manufactured by SunPower, Inc., Athens, Ohio. This hybrid system has the same footprint as a standard 30-liter LN_2 Dewar and receives dipstick HPGe detector cryostats like those commonly used in other LN_2-based systems. The Cryo-Cycle™ continually condenses the LN boil-off inside a closed Dewar to maintain a 22-liter reservoir of LN. Once charged, the system does not require additional N_2 except in the event of a long-duration power outage or to replace gas loss due to seal leakage. Make-up can be added by topping off with LN or by adding N_2 gas. A N_2 gas generator was integrated with the standard Cryo-Cycle™ to allow unattended operation in the RASA. In controlled environments such as the instrument bay inside RASA systems, the only maintenance required will be semi-annual filter cleaning for both the Cryo-Cycle™- and Cryo-Pulse® 5-based systems.

A Domnick Hunter Model G1, N_2 gas generator was procured for integration with the Cryo-Cycle™. The G1 generator is a self-contained unit that uses 115 V, 60 Hz power and produces 0.75 liters/min. of N_2 gas containing less than 10 ppm oxygen (O_2). Filter cleaning or changes are required on a semi-annual basis at a cost of about $100. The internal compressor requires replacement every 2-3 years at a cost of $600. The molecular sieve beds are expected to last 10 years. Cost of the unit is $7,500 and it comes with a 2-year manufacturer's warranty. The specifications for the Domnick Hunter G1 N_2 gas generator can be viewed at: www.domnickhunter.com/documents/products/174004740_01_EN.pdf.

The gas extractor is connected to the cryostat as shown schematically in Figure 3 and Figure 4. In the configuration shown the G1 gas generator operates continually to provide high purity N_2 gas to Cryo-Cycle™ through a gas solenoid valve. A time-delay-relay circuit must be added if the gas generator is to be operated intermittently because

the G1 requires 6-12 hours to achieve acceptable purity of the N_2 gas after start-up. As tested here, a Canberra model 7186 liquid nitrogen level (LN) controller senses the level of the LN in the Cryo-Cycle™ Dewar and operates the solenoid valve that directs the gas flow to either the Dewar or a vent. A precision pressure regulator maintains the pressure of the gas feed to precisely 2.5 psig. This pressure forces the Cryo-Cycle™ cooler into high power cooling mode so the maximum 15 W cooling capacity of the Stirling cooler is made available to liquefy the N_2 gas. When the gas flow is diverted to the vent the Cryo-Cycle™ returns to its normal operating pressure of 1.5 psig and the Stirling cooler operates at a lower cooling power sufficient to condense the boil-off gas and maintain the LN level in the Dewar.

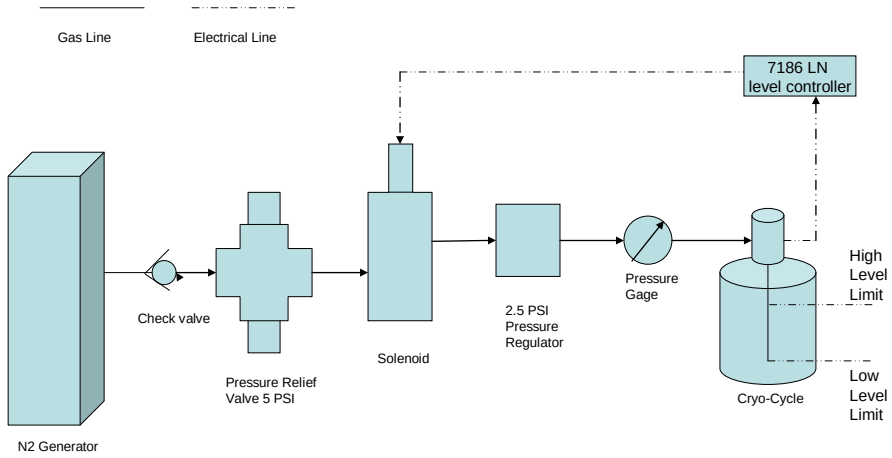

Figure 3. Block diagram of the nitrogen gas generator test assembly.

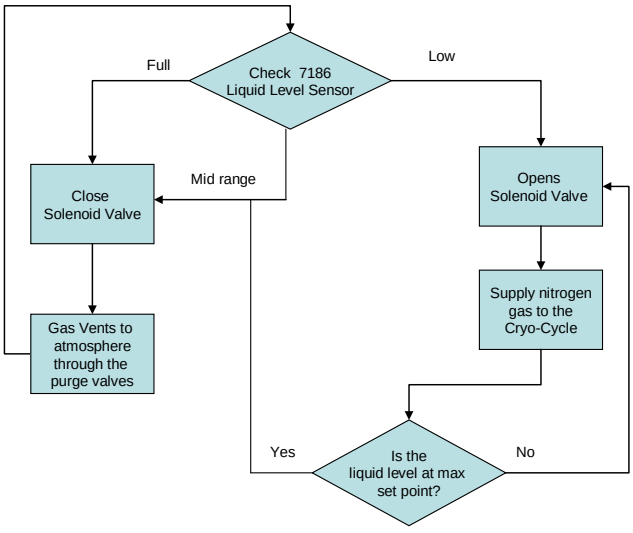

Figure 4. Flow chart showing the operation of the gas extractor with the Canberra 7186 LN level controller and hybrid cryostat.

Tests were performed to characterize the total heat load of the Cryo-Cycle™ and the operation of the system described above. The test setup is shown in Figure 5. The heat load was determined by measuring weight loss vs. time for the system with the Stirling cooler turned off. The results of this test are shown in Figure 6. A liter of LN weighs 1.78 lb so the loss rate from the graph is 2.2 liter/day. Since the heat of vaporization for LN is 199 J/g then 2.2 liter/day is equivalent to a heat load of 4.1 W. If the cooling power of the Stirling cooler is 15 W this implies that

when the system is operating there should be excess cooling power of 10.1 W available for converting externally supplied N_2 gas to LN.

Figure 5. LN Level Controller, N_2 generator, and Cryo-Cycle™ test setup.

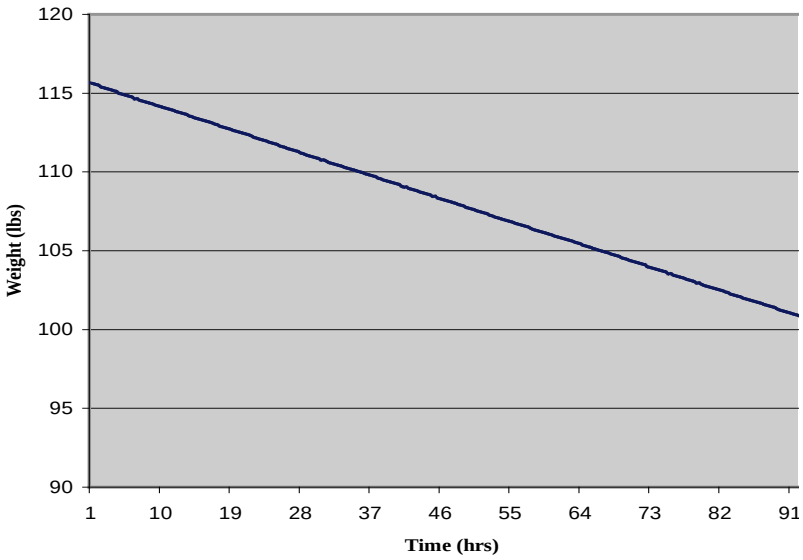

Figure 6. Cryo-Cycle™ weight vs. time with the Stirling cooler off.

The ability of the Cryo-Cycle™ to cool from room temperature with the G1 gas generator providing the N_2 gas was measured by monitoring the weight of the system with the Stirling cooler operating at full power. A 2 kg detector was mounted in the cryostat and the detector temperature was monitored during the cooldown. The results are shown in Figure 7. The data show that LN began accumulating in the Dewar approximately 24 h after the beginning of the cooldown. The slope appears to be linear after about 40 h. The temperature readings on the detector holder indicated that equilibrium temperature of 95 K was reached about 43 h after the beginning of cooldown. When the system reached equilibrium it was observed that the Stirling cooler was cycling on and off indicating that the supply of N_2 was insufficient to utilize all of the available cooling capacity. The cooldown curve from 55 h to 118 h indicates that LN was accumulating at a rate of about 2.4 lb/d. This means that N_2 was being supplied at a rate of 650 cm^3/min, which is well below the specified production rate of 750 cm^3/min for the G1 gas generator. Subsequent tests with a flow meter confirmed the N_2 production rate of 650 cm^3/min.

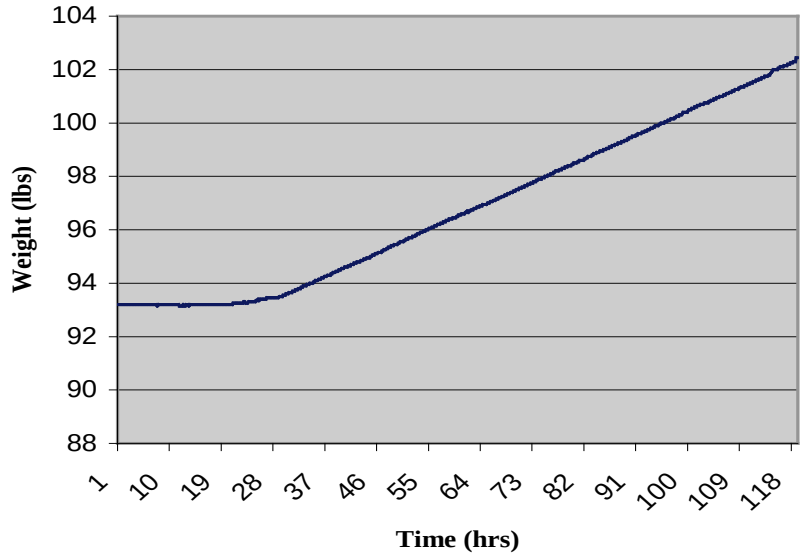

Figure 7. Cryo-Cycle™ cooldown from room temperature with nitrogen generator feed.

When gas is introduced into a cold, operating Cryo-Cycle™, it must first be cooled from room temperature to 77 K before it is condensed to liquid. The specific heat capacity of nitrogen gas at room temperature is 1.039 kJ/kg-K and varies only slightly down to 77 K. Therefore, cooling 808 g of gas over 24 h requires 2.16 W of cooling power. When gas is introduced into a cold, operating Cryo-Cycle™, the cooling power required to cool the gas and liquefy 1 l/day of LN is the combination of 2.16 W to cool the gas from room temperature to 77 K and 1.86 W to liquefy the gas, for a total of ~4 W. Given the excess cooling capacity that was calculated above the test unit should be able to make roughly 2.5 l/d of LN in addition to keeping the detector cold. The maximum that can be expected in this test setup is 1.34 l/d because of the limited 650 cm^3/min N_2 gas production rate of the nitrogen generator. The time required to cool the detector and fill the Dewar to its 22 liter capacity is roughly 18 days for this system. The detector is usable two days after cool down begins.

CONCLUSIONS AND RECOMMENDATIONS

Improvements to the Cryo-Pulse® 5 have been designed and fabricated. Testing and assembly of the mechanical and electrical components are complete with the exception of connecting the detector chamber and service body assembly to the cooler vacuum housing. Residual gas analysis, vibration analysis, thermal, and detector performance evaluation will be performed following completion of the assembly.

The Cryo-Cycle™ has been tested with a N_2 gas generator. Cool down from room temperature and maintenance of the LN level with the 1786 LN level controller has been demonstrated. Long term testing will continue. Operation with a UPS will be performed and susceptibility of the system to long and short term power outages will be investigated.

ACKNOWLEDGEMENTS

Thanks go to the CANBERRA Detector R&D staff for their tireless efforts and insightful investigations. Thanks to George Rybicki, Patrick AFB for his hospitality and help with the mechanical details of the RASA Mark 4 and the application. And finally, thanks go to our sponsor the NNSA for providing us with the opportunity and means to pursue this work.

REFERENCES

Bowyer, S. M., H. S. Miley, R. C. Thompson, and C. W. Hubbard (1997). Automated particulate sampler for comprehensive-test-ban treaty verification (the DOE radionuclide sampler/analyzer), *IEEE Trans. Nuc. Sci.*, NS-44, 3: 551–556.

Miley, H. S., S. M. Bowyer, C. W. Hubbard, A. D. McKinnon, R. W. Perkins, R. C. Thompson, and R. A. Warner (1998). Automated aerosol sampling and analysis for the comprehensive-test-ban treaty, *IEEE Trans. Nuc. Sci.*, NS-45: 3, 1034–1039.

Yocum, K. M., J. F. Colaresi, and H. S. Miley (2009). Improvements in Ge Detector Cooling, in *Proceedings of the 30th Monitoring Research Review: Ground-Based Nuclear Explosion Monitoring Technologies*, LA-UR-09-05276, Vol. 2, pp. 686–694.

Yocum, K. M., G. N. Martin, J. F. Colaresi, and H. S. Miley (2008). Improvements in Ge Detector Cooling, in *Proceedings of the 30th Monitoring Research Review: Ground-Based Nuclear Explosion Monitoring Technologies*, LA-UR-08-05261, Vol. 2, pp. 824–833.

Infrasound Monitoring

DISPERSION OF INFRASOUND SIGNALS EXCITED BY EXPLOSIVE ERUPTIONS OF THE SAKURA-JIMA VOLCANO

Nobuo Arai[1], Yuichi Imanishi[2], Shingo Watada[2], Takuma Oi[3], Takahiko Murayama[1], Makiko Iwakuni[1], and Mami Nogami[1]

Japan Weather Association[1], University of Tokyo[2], and Toho Mercantile Co., Ltd.[3]

ABSTRACT

The Sakura-jima volcano in the southern part of Japan has been erupting actively since 2009. The activity is characterized by intermittent Vulcanian-type explosive eruptions and volcanic ash emissions. As a component of the International Monitoring System verification scheme for the Comprehensive Nuclear-Test-Ban Treaty (CTBT), an observation system of arrays for detecting infrasound signals was installed at Isumi, Chiba Pref. (60 km SE of the Tokyo metropolitan area) in November 2004. The infrasound wave trains excited by the eruption of the Sakura-jima volcano are sometimes observed at Isumi (I30JP), which is about 1000 km from the volcano.

The shape of infrasound signals observed at the monitoring station closest to Sakura-jima (about 4 km from the summit crater) evinced the obvious characteristic of an explosive event: quickly increasing pressure and followed by an alleviating process. On the other hand, the shape of infrasound wave trains observed at I30JP looked complex and we supposed that it showed the characteristic of dispersion.

For the purpose of understanding the dispersion process of infrasound wave trains propagated over a long distance, we deployed infrasound sensors between the Sakura-jima volcano and I30JP, specifically, Kirishima (44 km away from volcano), the Kii-Peninsula (530 km away) and the Izu-Peninsula (870 km away). A barometer sensor (model 6000-16B, Paroscientific, Inc.) was deployed at each site as an infrasound sensor, instead of MB2000, which was installed at I30JP. Before the deployment, the sensitivity and stability of the model 6000-16B barometer sensor had been determined through the comparison with MB2000.

When a large explosive eruption occurred in the Sakura-jima volcano, wave trains were observed at distant stations. From the results of octave band analysis, a dispersion of infrasound signals was detected, making it clear that estimated dispersion curves were consistent with the velocity profile of an acoustic wave.

OBJECTIVES

To understand characteristics of observed infrasound wave trains, both the source process and the path effect for infrasound signals should be revealed quantitatively.

The Sakura-jima volcano in the southern part of Japan is active now, and its activity is characterized by intermittent Vulcanian-type explosive eruptions. When a large explosive eruption occurs, infrasound wave trains are sometimes observed at infrasound station I30JP, which is a component of the International Monitoring System for the CTBT verification scheme and is about 1000 km from the volcano. Wave trains observed at I30JP seem to have dispersed.

The objective of this research is to realize the dispersion process of infrasound signals propagated over a distance.

RESEARCH ACCOMPLISHED

Temporal Observation System

The layout of each temporary observation system is schematically shown in Figure 1. Each system is composed of an absolute barometer sensor, a notebook PC as a data logger, GPS for correcting the PC's clock, and hose arrays as a wind-noise reducing system. The digital quartz resonator sensor Model 6000-16B, which is produced by Paroscientific, Inc., was adopted as an absolute barometer sensor for this observation. Hose arrays were composed of three (3) 10-meter hoses.

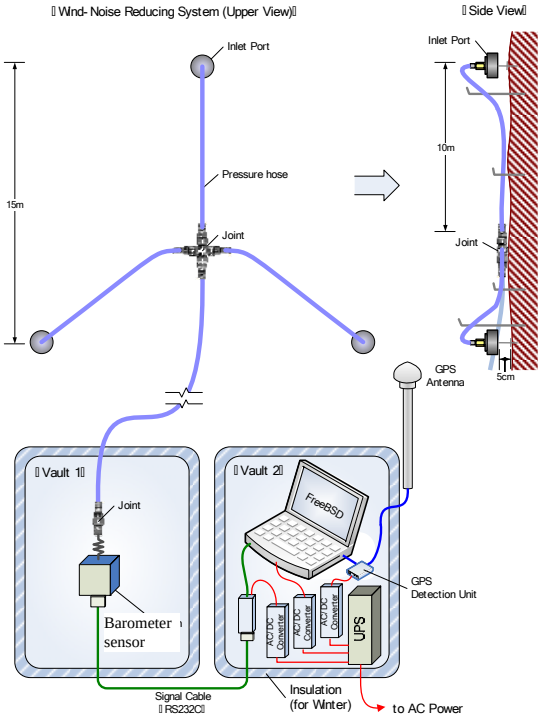

Figure 1.Temporal observation system.

Before the temporary observation, an absolute barometer sensor Model 6000-16B was examined from the viewpoint of its sensitivity and stability by comparison with the MB2000 barometer sensor that was installed at I30JP. Figure 2 indicates the power spectral density of both sensors' data under low wind conditions. A high-cut filter whose corner frequency is 5.5 Hz had been adapted to Model 6000-16B data, and a high-cut filter whose corner frequency is 8.5 Hz had been adapted to MB2000. The remarkable similarity of the spectra between Model 6000-16B and MB2000 warrants that the Model 6000-16B barometer sensor bears enough sensitivity for infrasound observation. According to the amplitude of power spectrum in Figure 2, the resolution of the Model 6000-16B barometer sensor seemed to be about 10^{-3} Pa.

The Model 6000-16B sensor worked well during the comparison test, which was carried out for about 1.5 month, so we also concluded that the Model 6000-16B sensor had enough stability for field observation.

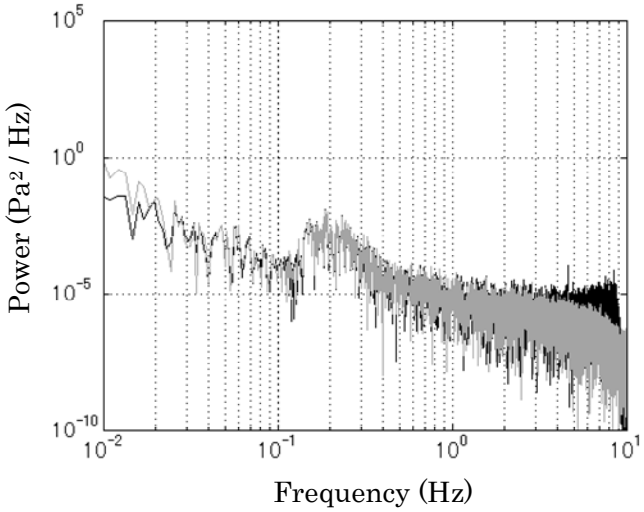

Figure 2. Power spectral density of time series observed by Model 6000-16B barometer sensor with a pipe array (gray line) and MB2000 (black line) when wind speed was less than 0.6 m/s.

A few infrasound wave trains corresponding to explosive eruptions of the Sakura-jima volcano were observed by both the Model 6000-16B barometer sensor and the MB2000 microbarometer during the comparison test (Figure 3). From the comparison in the time domain, as shown in Figure 3, we could also conclude that the temporal observation system had enough resolution for infrasound observation.

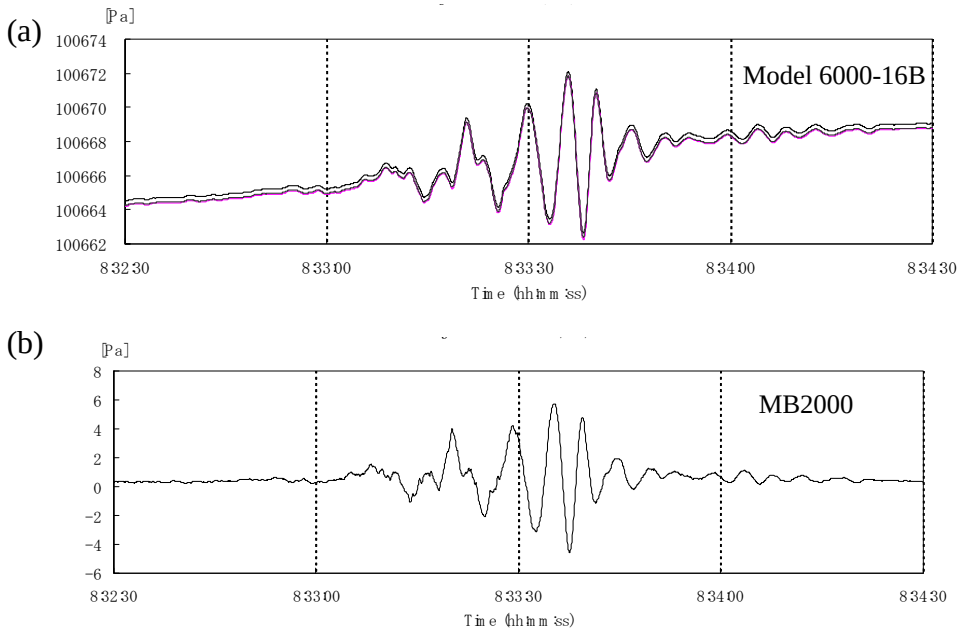

Figure 3. Infrasound wave trains, which were recorded (a) by a temporary observation system with the Model 6000-16B barometer sensors and (b) by the MB2000 microbarometer, corresponding to the explosive eruption that occurred at the Sakura-jima volcano (Oct. 3, 2009). During the comparison test, three Model 6000-16B sensors were examined, so three traces were drawn in the upper figure.

Temporary Observation between Sakura-jima and I30JP

On Oct. 3, 2009, a large explosive eruption occurred at the Sakura-jima volcano. The infrasound waveform observed at Kurokami, which is 4 km from the summit, and a waveform observed at I30JP, which is about 1000 km from the volcano, are indicated in Figure 4. The waveform at Kurokami shows an explosive event, characterized by a quick pressure increase, followed by an alleviating process. On the other hand, the waveform observed at I30JP seems to have dispersed.

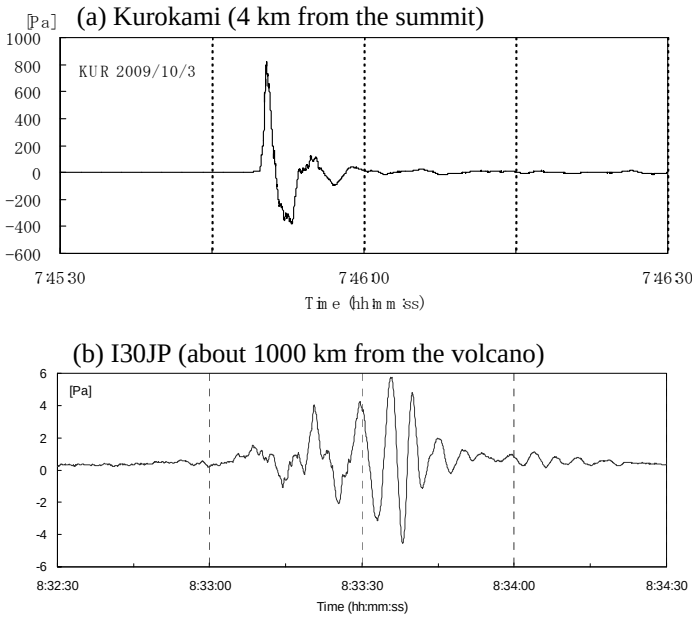

Figure 4. Infrasound signals observed on Oct. 3, 2009, at (a) Kurokami, which is 4 km from the summit, and (b) I30JP, which is 1000 km from the volcano.

For the purpose of understanding the dispersion process of infrasound wave trains over long-distance propagation, we temporarily deployed three (3) infrasound sensors between the Sakura-jima volcano and I30JP. The temporary observation sites were Kirishima, Kozagawa, and Okuno (see Figure 5 and Table 1).

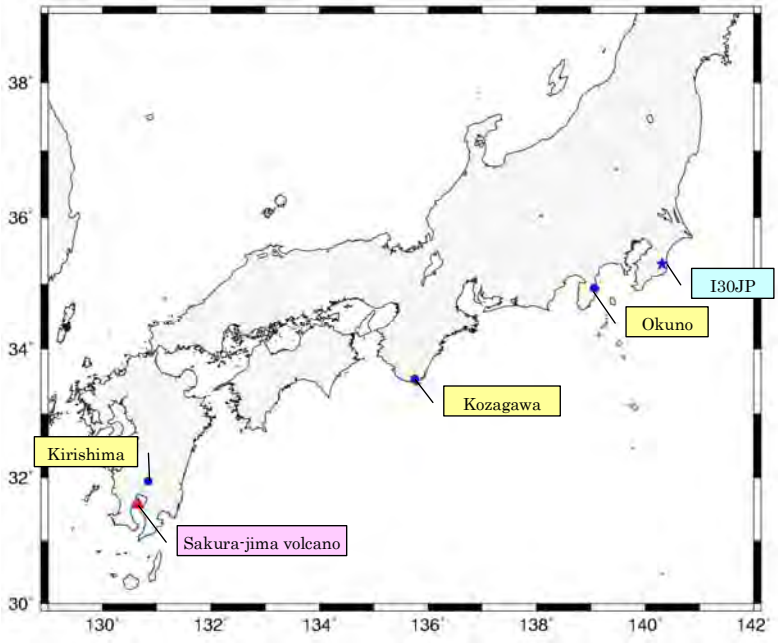

Figure 5. Locations of the Sakura-jima volcano and observation sites.

Table 1. Locations of the Sakura-jima volcano and observation sites

Site name	Latitude	Longitude	Distance*	Back-Azimuth
Sakura-jima volcano	N31.57722	E130.65889	-	-
Kirishima	N31.94746	E130.83927	44 km	203 deg
Kozagawa	N33.54030	E135.75887	526 km	247 deg
Okuno	N34.94031	E139.06035	867 km	247 deg
I30JP	N35.30770	E140.31380	988 km	248 deg

* The distance between each site and the Sakura-jima volcano

All three sites were working simultaneously from February 25 through March 22. The Sakura-jima volcano frequently erupted explosively during the period when the three temporary systems were working. However, the explosions were not large, so remarkable infrasound signals were not observed at distant stations. Figure 6 shows an example of observed wave trains during the temporary observation period.

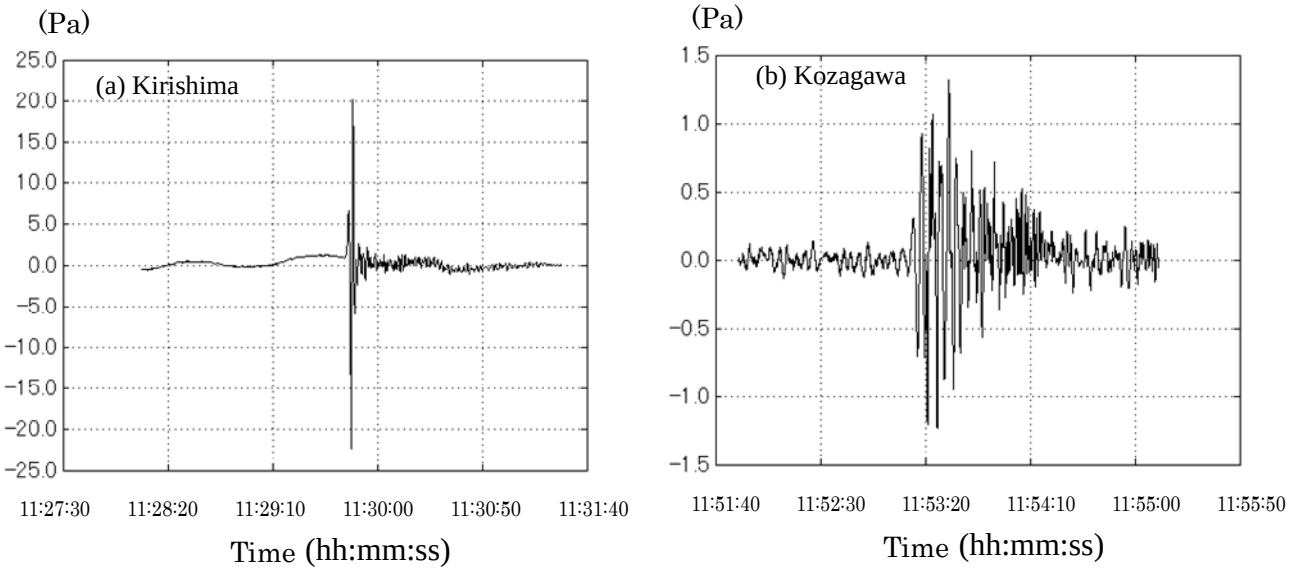

Figure 6. Infrasound signals corresponding with the explosive eruption that occurred at 11:27, Feb. 28, 2010. (a) Signal observed at Kirishima. (b) Wave trains observed at Kozagawa.

Octave Band Analysis

On Feb. 28, relatively large explosions occurred at 11:27 and 13:04; signals having good S/N ratio were observed at Kirishima and Kozagawa. Therefore, we tried to analyze these two (2) explosions' data by using the octave band analysis method. The 1/5 octave band-pass filter was adopted in the analysis. Figure 7 shows results of the octave band analysis. The "f_0" in Figure 7 means the central frequency of each band-pass filter adopted.

From each spindle-shaped envelope extracted by a 1/5 octave band-pass filter, the onset time (having maximum amplitude) was picked up. The onset time when the impulse signal was detected at the closest station (4 km from the volcano) was assumed to be the time when the eruption occurred (origin time); the group velocity at f_0 was calculated for Kirishima and Kozagawa data, respectively. These results are shown in Figure 8.

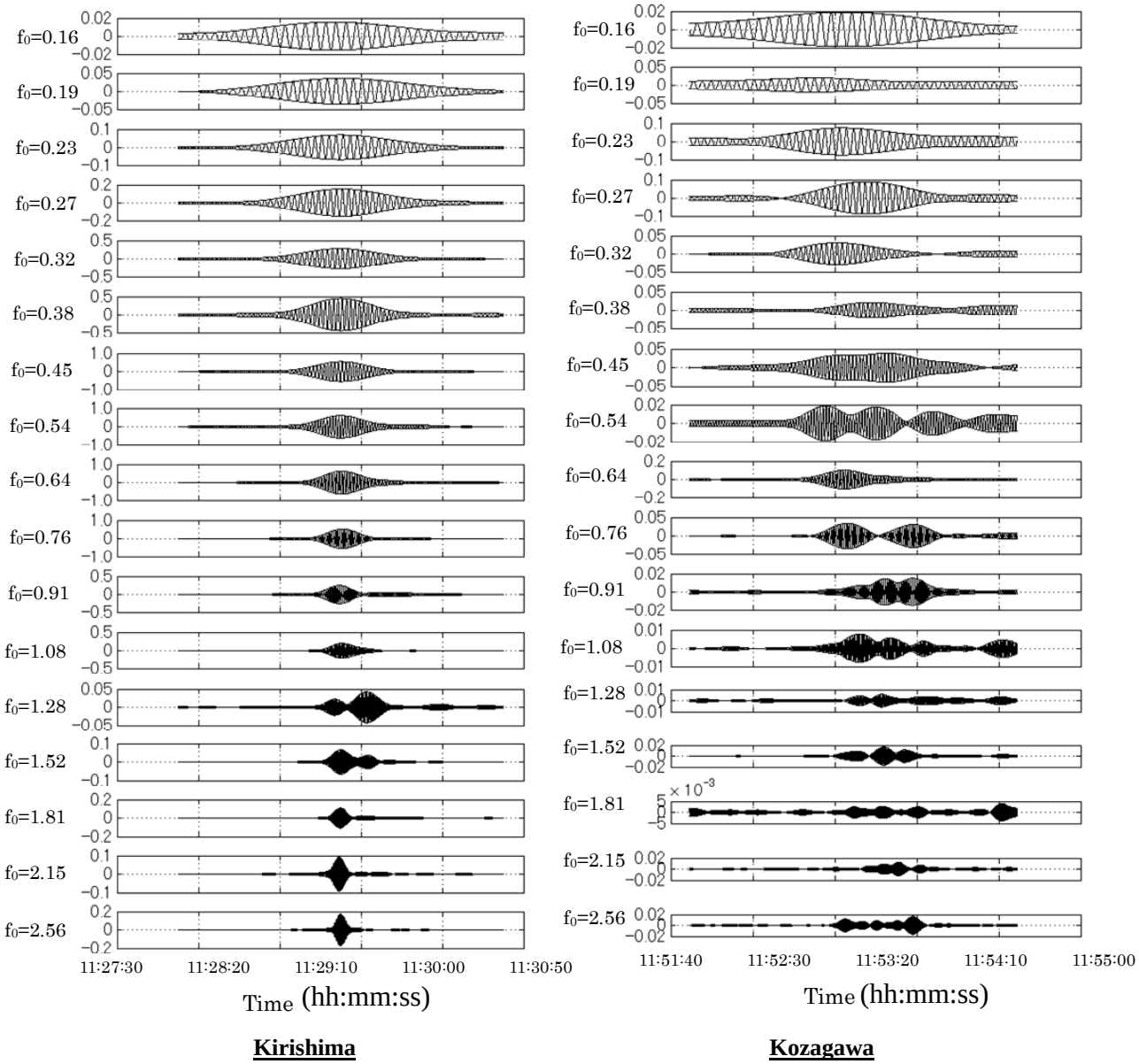

Figure 7. (a) Time series extracted by 1/5 octave band-pass filters. The "f_0" indicates the central frequency of each band-pass filter adopted. Waveforms were generated by the explosive eruption that occurred at 11:27, Feb. 28: (left) Kirishima and (right) Kozagawa.

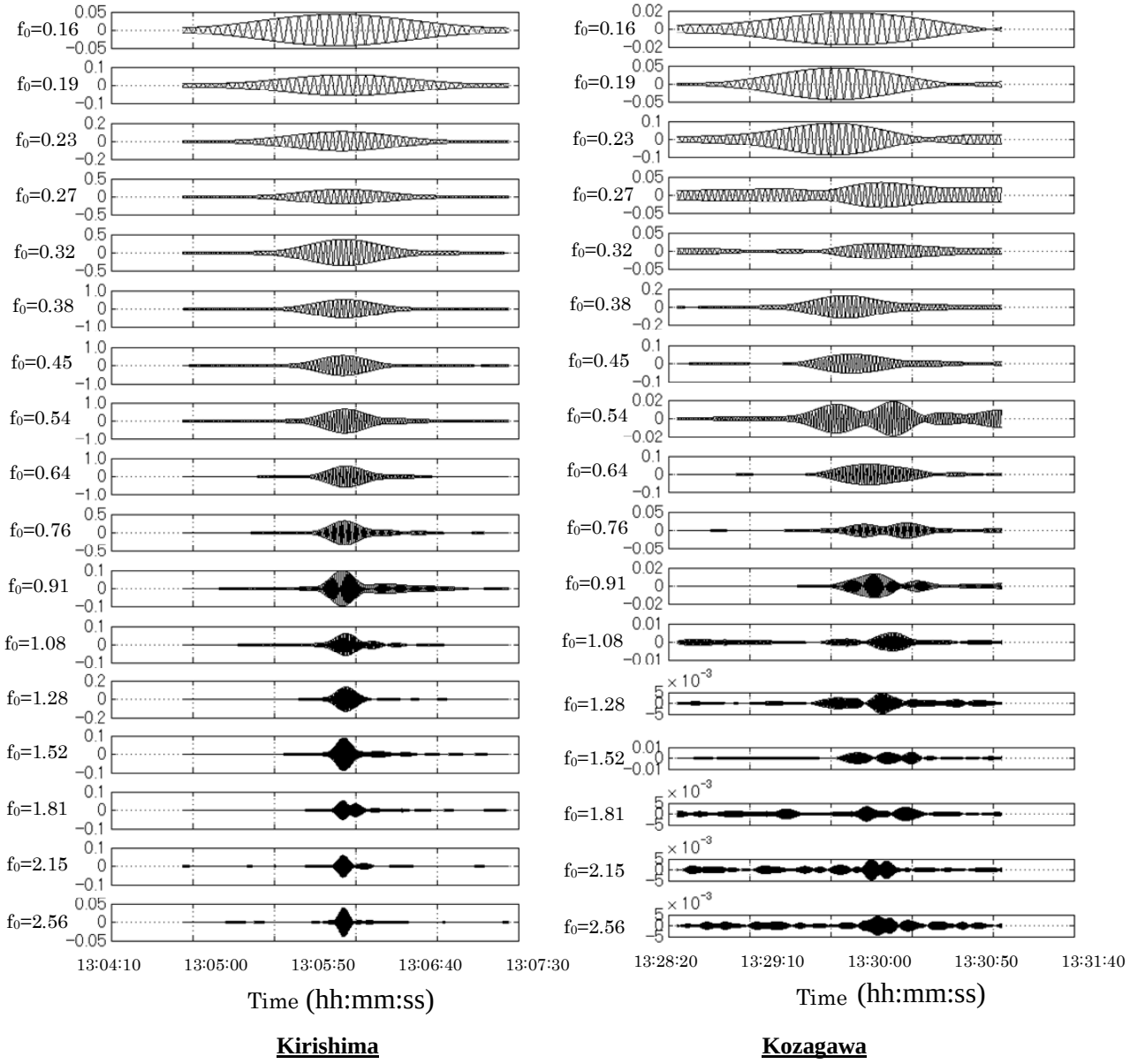

Figure 7. (b) Time series extracted by 1/5 octave band-pass filters. The "f_0" indicates the central frequency of each band-pass filter adopted. Waveforms were generated by the explosive eruption that occurred at 13:04, Feb. 28: (left) Kirishima and (right) Kozagawa.

In Kirishima's results (Figure 8a), the measured group velocity looks almost the same through all periods analyzed. On the other hand, in the results for Kozagawa (Figure 8b), longer-period waves tend to have higher group velocities, indicating the effect of the normal dispersion of infrasound. This effect may not have been evident at Kirishima because of the shorter distance from the volcano.

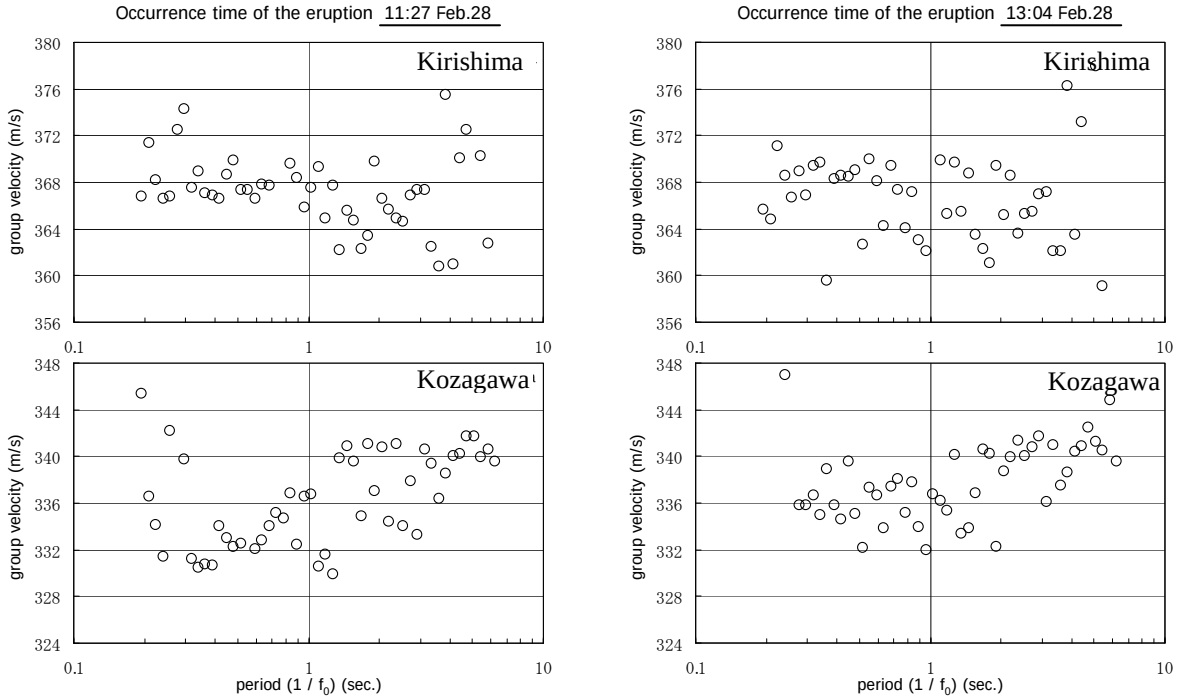

Figure 8. Infrasound group velocity measured at (a, upper panels) Kirishima and (b, lower panels) Kozagawa.

Group velocities estimated at Kirishima were about 365 m/s through the all-period range in analysis (see Figure 8 a). In this estimation, the time when an impulsive signal was detected at the closest station was assumed to be the origin time of the explosion. Kirishima site was only 44 km from the volcano. The time it takes for propagation from the crater to the closest station (propagation length was about 4 km) may be significant for evaluating group velocity. Assuming the effective sound speed was 340 m/s along the propagation path between the crater and the closest site, it took about 12 s for propagation. Considering this time (12 s) for an estimation of group velocity of infrasound signals, group velocity in Kirishima would be reduced to about 330 m/s.

Discussion

Upper-air observations are conducted by the Japan Meteorological Agency. The radio-sonde, a balloon-borne instrument platform with a radio transmitting device, covers the upper air to a maximum of 30 km from the surface and measures temperature, pressure, humidity, and wind. Radio-sonde observations are carried out twice a day at 0000 and 1200 UTC. The upper-air observation network consists of 18 aerological observatories.

Considering the locations of our temporary infrasound observation sites, upper-air data observed at Kagoshima and Shiono-misaki were used for estimating sound speed profiles. Figure 9 shows the locations of the Kagoshima and Shiono-misaki aerological observatories. Infrasound signals corresponding to explosive eruptions that occurred at 11:27 and 13:04 on Feb. 28 were analyzed, so upper-air data observed at 12:00, Feb. 28, were used for estimating sound speed profiles. The effective sound speed along the propagation direction (direction from Sakura-jima to I30JP) was calculated by using temperature, wind speed, and wind direction at each height. Estimated sound speed up to 30 km at Kagoshima and Shiono-misaki is shown in Figure 10.

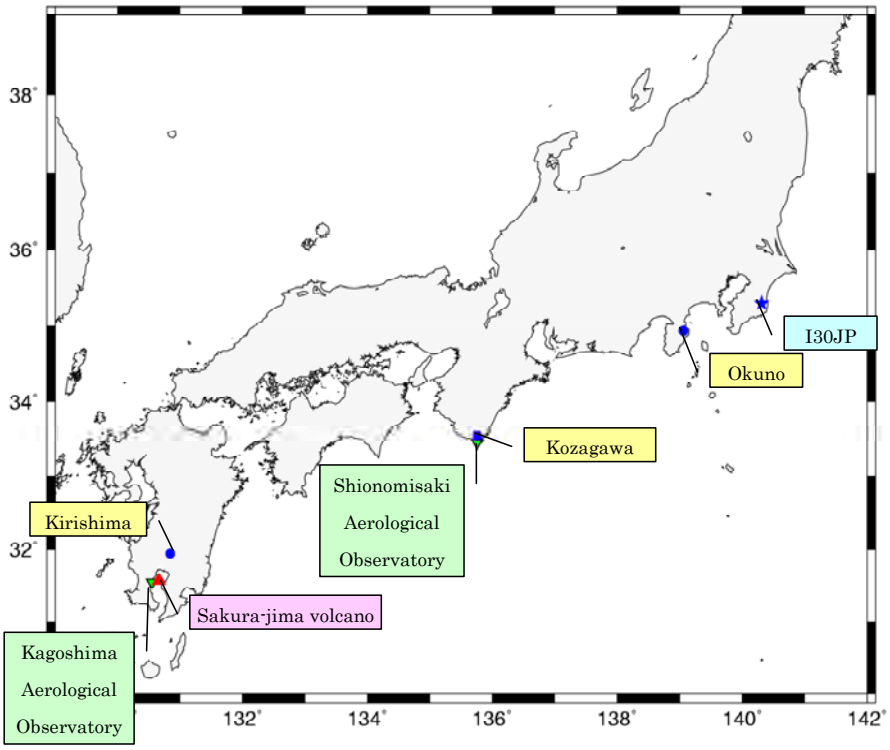

Figure 9. Locations of aerological observatories whose upper-air data were referenced for the estimation of effective sound speed profiles.

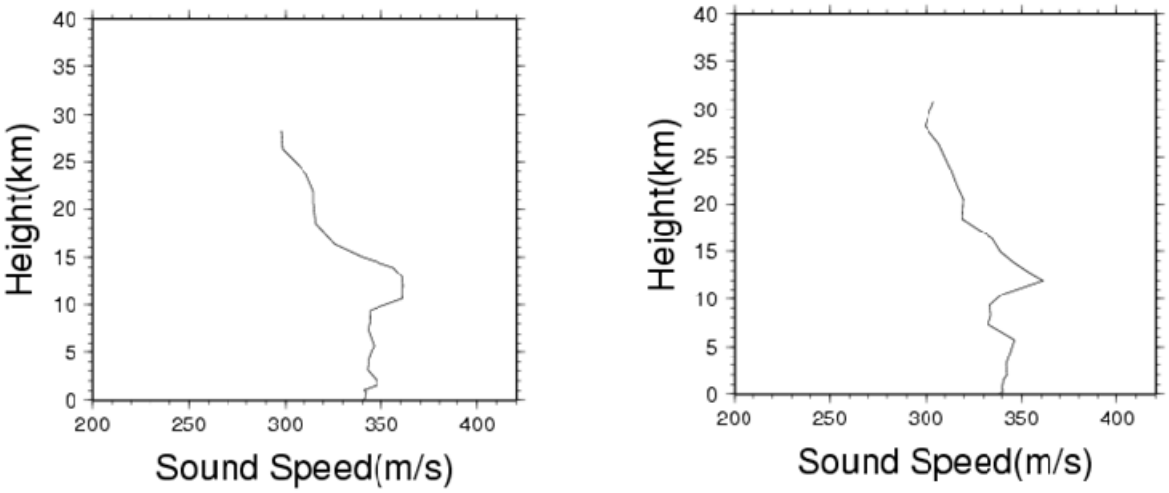

(a) Kagoshima **(b)Shiono-misaki**

Figure 10. Effective sound speed profiles along the propagation direction (direction from the Sakura-jima volcano to I30JP) at 12:00 on Feb. 28: (a) Kagoshima Aerological Observatory and (b) Shiono-misaki Aerological Observatory.

According to the estimated effective sound speed profiles shown in Figure 10, sound speed in the layer between 10 and 15 km high was significantly faster than sound speed near the surface. Because the explosions occurred near the surface, the infrasound signals must have propagated through a duct established within the troposphere (the duct might have been established between the surface and a place in the atmosphere about 10 km above the surface). Short-period infrasound signals might have propagated with average sound speed in the troposphere; on the other hand, long-period infrasound waves might be affected by a high-speed layer around the upper boundary of the troposphere and might have propagated with faster speed than the average within the troposphere.

CONCLUSIONS AND RECOMMENDATIONS

Temporary observation systems were deployed between the Sakura-jima volcano and I30JP, and infrasound signals excited by explosive eruptions at the volcano were observed. According to the results of the octave band analysis, dispersion of infrasound signals was detected. The estimated dispersion curve at Kozagawa would be consistent with sound speed profile.

To understand the dispersion process of infrasound waves quantitatively, waveforms observed in other conditions (other seasons, other directions, etc.) shall be analyzed.

ACKNOWLEDGEMENT

We are grateful to the Earthquake Research Institute at the University of Tokyo for allowing us to use its observatories (Kirishima Volcano Observatory, Kozagawa,, and Okuno) to deploy our temporary observation systems.

REFERENCES

Japan Meteorological Agency (2010), Upper-air observation data (http://www.data.jma.go.jp/obd/stats/etrn/upper/).

INFRASOUND AS A DEPTH DISCRIMINANT

Stephen J. Arrowsmith[1], Hans E. Hartse[1], Steven R. Taylor[2], Richard J. Stead[1], and Rod W. Whitaker[1]

Los Alamos National Laboratory[1] and Rocky Mountain Geophysics, LLC[2]

Sponsored by the National Nuclear Security Administration

Award No. DE-AC52-06NA25396/LA09-Depth-NDD02

ABSTRACT

The identification of a signature relating depth to a remotely recorded infrasound signal requires a dataset of earthquakes, recorded infrasonically, with well-constrained depths. Although the premise is simple, five significant complications arise: (1) Earthquakes can generate infrasound via a variety of processes, which have occasionally been confused in past studies due to the complexity of the process; (2) mining explosions are efficient infrasound generators and can be mistaken for earthquakes; (3) coherent noise on infrasound arrays can be confused with transient signals; (4) atmospheric path effects must be adequately accounted for; and (5) seismic estimates of depth trade-off with origin time without a measurement in the near-epicentral region. This study provides a comprehensive framework for addressing these limitations, building on a focused study of the Wells, Nevada earthquake sequence that was performed as part of the previous year of this research effort (Arrowsmith et al., 2009). Such an approach is necessary to robustly identify a depth signature within a signal that incorporates various source, path, and receiver effects. In addition, we outline a complementary seismo-acoustic modeling approach, also being explored as part of this study, which should provide insight into the physical basis of an infrasonic depth signature.

OBJECTIVES

The depth of an event is an important tool in event classification and is used in the Event Classification Matrix (ECM) as a discriminant. Seismic depths can be uncertain unless a seismometer happens to be located near the epicenter, because there is a trade-off between event depth and origin time in routine location algorithms. The fundamental objective of this research is to determine whether infrasound can be used to provide information on event depth. Towards this goal we aim to empirically search for a depth signature in real infrasound data. Coupled with this focus, we aim to model the generation of infrasound from earthquakes in order to provide an improved understanding of the physical basis of the generation of infrasound.

RESEARCH ACCOMPLISHED

Dataset

The completed dataset for this study comprises a regional component (Western US) and a global component.

(a) Regional Dataset

Arrowsmith et al. (2009) outlined the initial development of a dataset with the following requirements: (1) Each event must be recorded at >1 infrasound array, (2) each event must have accurate source constraints, and (3) a high-resolution atmospheric model must be available. The final regional dataset is shown in Figure 1 (care was taken to ensure earthquakes were not misidentified mine blasts; regions of mining activity are also depicted in Figure 1). From an initial dataset of 353 earthquakes (Figure 1), synchronous with data availability in our holdings at two or more arrays within 1500 km, we observed 7 earthquakes at multiple arrays (red stars in Figure 1), with magnitudes ranging from 3.7 to 5.8.

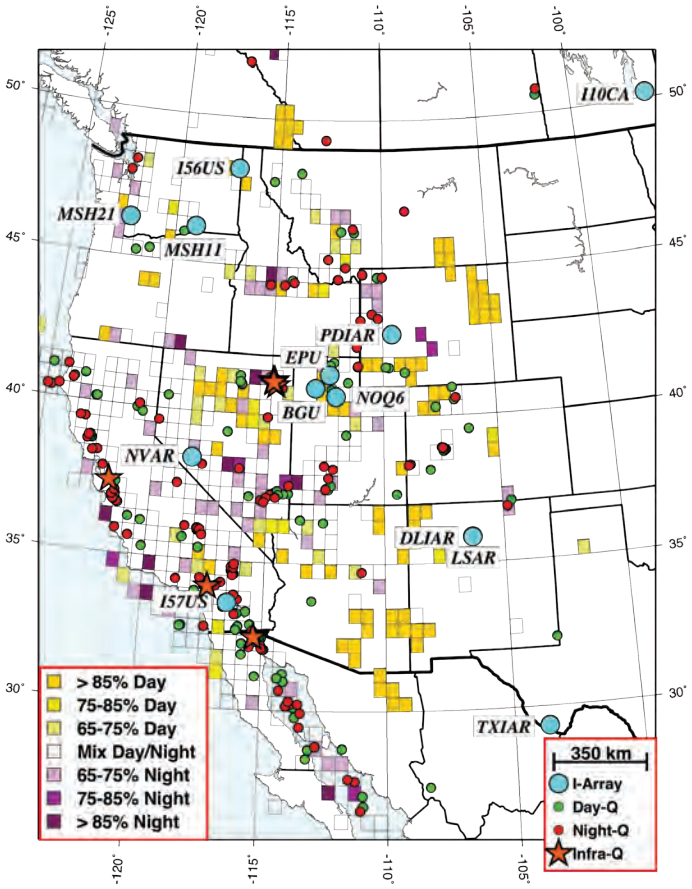

Figure 1. Map of the regional dataset in the Western US. Red stars are detected earthquakes, green circles and red circles are undetected day and night earthquakes. Infrasound arrays in our database are depicted as blue circles.

(b) Global Dataset

To extend the limited regional dataset, we have undertaken an extensive search for large earthquakes (M>5) in our global data holdings. By focusing on large earthquakes near infrasound arrays, we minimize the likelihood of mis-association (the purpose of constraint 1 above). Thus, we have compiled a list of earthquakes with the following constraints:

- Origin location between 100 and 400 km from any infrasound array;
- Mw > 5.0;
- Synchronous with data availability from the array.

The resultant catalog of earthquakes is plotted in Figure 2. We distinguish between shallow earthquakes and deep earthquakes using a depth boundary of 50 km. In total, there are 37 earthquakes that range in depth from 3 to 189 km. For each earthquake, we have obtained the USGS earthquake catalog information, the Harvard CMT solution (where available), and the G2S model specifications appropriate for the source-receiver path. These constraints provide a *starting point*, but are being refined upon as described in detail below.

The global dataset comprises earthquake swarms in South America, East Africa, and Japan (Figure 2). Working with earthquake swarms is advantageous, as outlined in more detail below, because the repeating source facilitates phase identification. Further, if a cluster of events is close enough in time and space, the individual events can be considered to have sampled the same atmosphere, removing the need for a path correction.

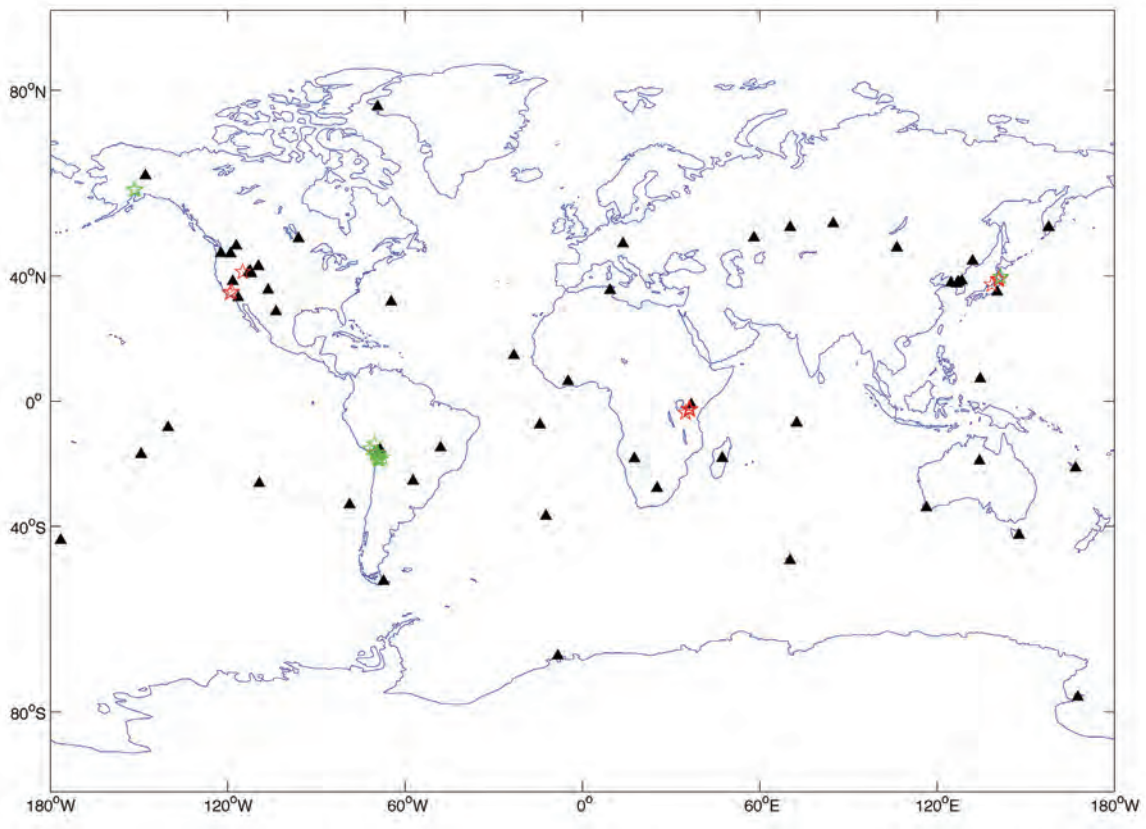

Figure 2. Map showing the locations of infrasound arrays available for this study (black triangles) and earthquakes with M>5.0 at distances between 100 and 400 km from each array (stars). Waveform data has been obtained and stored for all earthquakes shown in this plot. Red stars denote shallow (< 50 km) earthquakes, while green stars denote deep (> 50 km) earthquakes.

Data Analysis

An overall comparison of the detectability of shallow and deep earthquakes is given in Figure 3 (noting that this plot has been constructed for all earthquakes in the global dataset, i.e., M>5.0 and signals were detected at a single array at distances between 100 and 400 km). Based on this plot, two notable conclusions are made: (1) very deep earthquakes can generate infrasound, (2) the probability of detecting a shallow earthquake is >> 0.5 while the probability of detecting a deep earthquake is < 0.5. These findings indicate that infrasound has potential as a depth discriminant, but that further research is required to characterize the difference between infrasonic signatures from shallow and deep earthquakes.

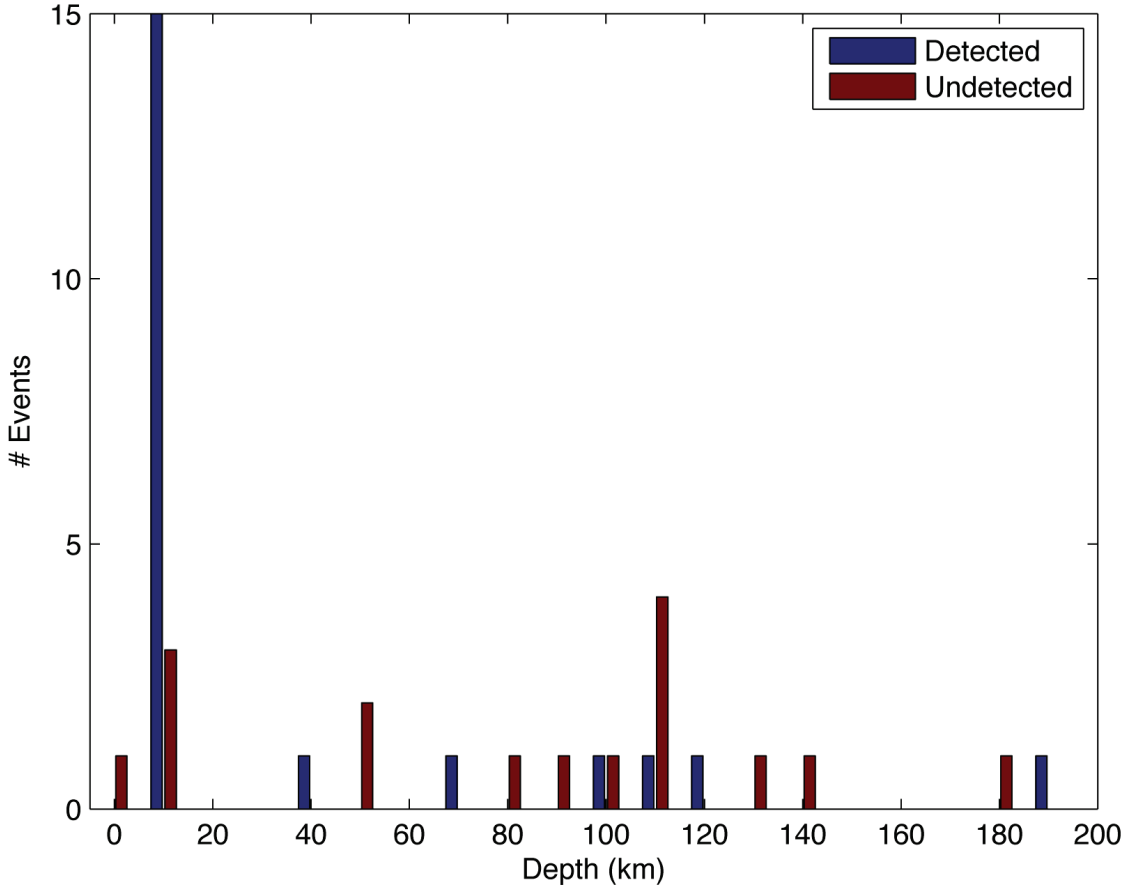

Figure 3. Histogram providing a comparison between the depths of detected (blue) and undetected earthquakes (red). While a majority of shallow earthquakes at these ranges and magnitudes are detected, the majority of deep earthquakes are undetected. Further research is needed to characterize the difference between signals from detected shallow and deep earthquakes.

A swarm of earthquakes in Tanzania provides a clear illustration of the effects of variations in source and path effects. As shown in Figure 4, while local infrasound (infrasound generated at the receiver by seismic waves) is similar from event to event, epicentral infrasound (which has propagated through the atmosphere) shows clear variations, reflecting the dynamic nature of the atmospheric path. While arrivals with group velocities of 0.27–0.31 km/s are persistent, later arriving signals with group velocities of ~0.25 km/s – which are much stronger in amplitude – are only observed for some of the events. This example clearly illustrates the value of using earthquake sequences (repeating sources), for identifying and separating different phases.

Preliminary measurements of these signals, and associated earthquake source parameters, are provided in Table 1 (noting that we are working on improving the earthquake source parameters as described in the next section). Peak-to-peak amplitudes, associated phase and group velocities, and periods, have been measured for the maximum

infrasound signal on each trace, discounting the local infrasound (Table 1). The component of the stratospheric wind from source to receiver, averaged between 45 and 55 km, is denoted v_d and also provided in Table 1. Positive values of v_d indicate that the wind component is in the direction of propagation, while negative values indicate that the wind component is in the opposite direction. Mutschlecner et al. (1999) developed an empirical formula for using this term to normalize for the effects of winds on the amplitudes of stratospheric returns. Using this formula, provided in Mutschlecner and Whitaker (2005), the winds normalized for the effects of distance and winds, A_N, are also provided in Table 1 for phases with stratospheric group velocity (0.27 – 0.31 km/s).

An example of an infrasound detection from a deep earthquake is provided in Figure 5. In this example, both local infrasound and epicentral infrasound are clearly detected—with backazimuths consistent with the great-circle backazimuth—above the background noise. The signal amplitudes are relatively low, but sufficient for reliable measurement by an analyst. This clear detection of a deep earthquake highlights the need to obtain an improved understanding of the generation of infrasound from earthquakes.

Source/Path/Receiver effects

One way in which this study aims to improve upon earlier studies is by improving the confidence with which we account for source, path, and receiver effects. The approach taken, relevant to each of these components, is described below.

(a) Source Effects

Studies by Mutschlecner and Whitaker (2005) and ReVelle (2005) utilized the USGS earthquake catalog to provide *a priori* information on earthquake magnitude, location, and depth. Here, we aim to determine high-resolution estimates of earthquake depth, in addition to mechanism, by modeling the seismic waveforms using a reflectivity method (Randall, 1989).

(b) Path Effects

Mutschlecner and Whitaker (2005) utilized available rocketsonde data to determine averaged zonal and meridional winds at elevations between 45 and 55 km. Due to the temporal and spatial sparseness of rocketsonde data, this required interpolation to obtain wind data suitable for a given location and time. Here, we aim to improve upon this correction by using the Ground-To-Space (G2S) model for the precise location and to the nearest hour. The use of earthquake sequences (repeating sources) also helps to better characterize and separate path effects.

(c) Receiver Effects

The goal here is to provide accurate and appropriate measurements that minimize the effect of ambient noise and are suitable for the purpose of depth estimation. The prior requirement is accomplished by making all measurements on the beam trace, and by only utilizing large earthquakes (M>5.0) to enhance signal/noise ratios. The latter requirement is more complex but should be based in part on a coupled modeling effort to determine what measurements would be representative of depth based on an improved understanding of the physical mechanism of infrasound generation (e.g., peak to peak amplitude, rms amplitude, period, duration, etc.)

Modeling

We plan to leverage R&D reported by Whitaker (2007, 2008, and 2009) on modeling the near-source infrasound generated by an underground source. Whitaker outlined the use of a Rayleigh Integral (RI) method, and a finite difference computational fluid dynamics program (CAVEAT), to predict the infrasound generated by an input ground acceleration model. Using a 3D finite difference code for the solid earth, E3D (Larsen and Schultz, 1995),we have begun to predict surface ground motions from earthquakes at two different depths (7 km and 15 km) and with three orthogonal source mechanisms (e.g., Figure 6). These ground motions will then provide the initial conditions for RI/CAVEAT. Through E3D-RI/CAVEAT, we hope to tie this modeling to the observational data described above.

As an example, Figure 6 shows the output from an E3D simulation for a pure strike-slip earthquake using the SCEC 1D model for the LA Basin (future research will utilize representative models for regions where we have data, such as Tanzania). The earthquake was located at 7 km depth. Displacement seismograms for a transect of hypothetical receivers clearly show the arrivals of P-wave, S-wave, and Surface wave energy.

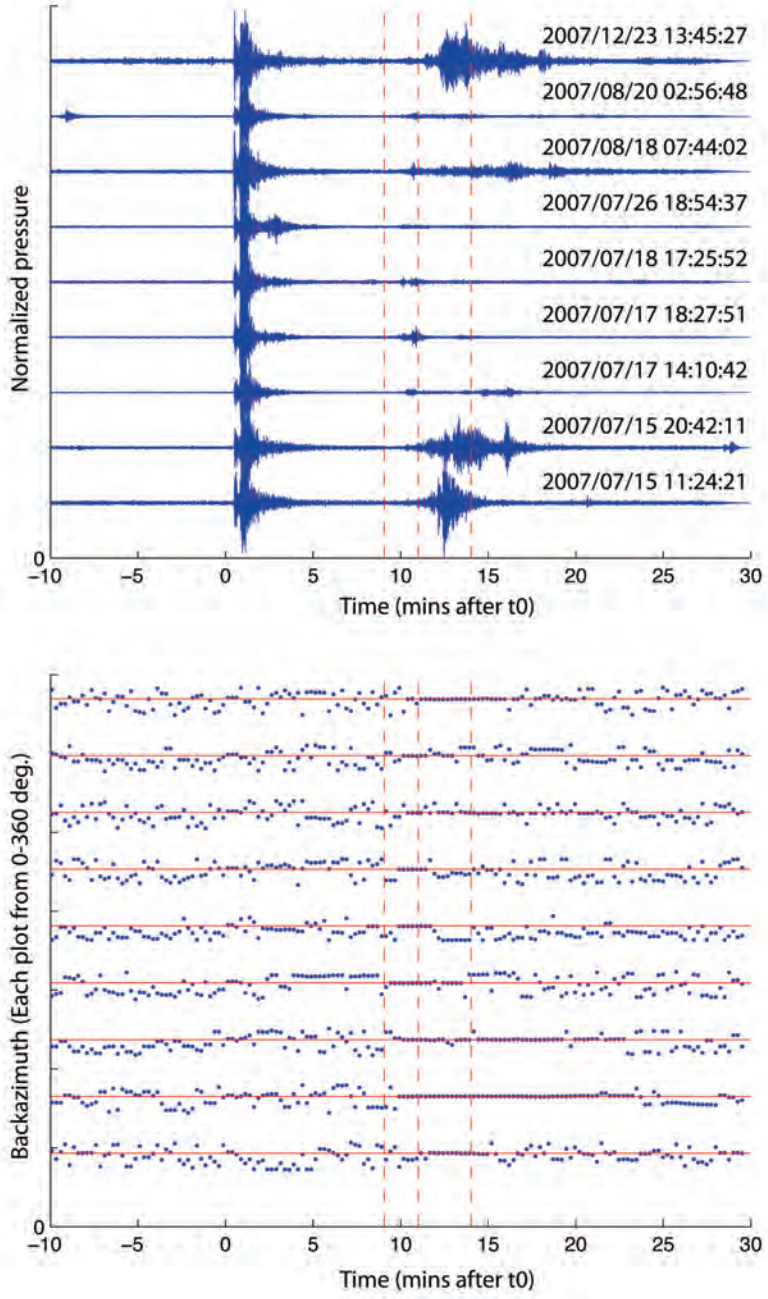

Figure 4. Detailed plot showing the waveforms associated with detected earthquakes in Tanzania (top) and corresponding derived backazimuths, with great-circle backazimuths shown by horizontal red lines (bottom). Measurements of all earthquakes in this sequence are provided in Table 1. Dashed red lines (vertical) indicate group velocities of 0.34, 0.28, and 0.22 km/s, assuming the source of infrasound corresponds to the origin time.

Table 1. Summary of observations from Tanzania. Italicized earthquakes are of unknown phase.

Origin Time	Location	Mw	Depth (km)	Slip (°)	d (km)	A (Pa)	v_d (m/s)	A_N	T (s)	v_p (m/s)	v_g (m/s)
2007/07/15 11:24:21	*-2.93, 36.24*	*5.3*	*17.9*	*57.0*	*198.7*	*0.192*	*6.72*		*0.65*	*0.34*	*0.26*
2007/07/15 20:42:11	*-2.88, 36.16*	*5.4*	*12.0*	*80.0*	*196.6*	*0.105*	*5.01*		*0.83*	*0.34*	*0.25*
2007/07/17 14:10:42	-2.73, 36.36	5.9	12.0	86.5	173.4	0.059	-0.13	0.0047	1.17	0.35	0.28
2007/07/17 18:27:51	-2.78, 36.19	5.3	12.0	89.0	185.1	0.105	-1.39	0.0096	0.59	0.35	0.29
2007/07/18 17:25:52	-2.77, 36.09	5.1	12.4	81.5	188.6	0.033	2.38	0.0027	1.10	0.35	0.31
2007/07/26 18:54:37	-2.68, 36.01	5.2	17.0	65.0	183.9	0.020	-7.31	0.0023	0.72	0.35	0.30
2007/08/18 07:44:02	-2.83, 36.21	5.2	12.0	82.0	189.4	0.034	3.50	0.0026	1.64	0.35	0.29
2007/08/20 02:56:48	-2.71, 36.29	5.4	12.0	83.5	173.8	0.032	0.70	0.0025	0.60	0.35	0.27
2007/12/23 13:45:27	*-2.78, 36.20*	*5.2*	*12.3*	*81.5*	*184.7*	*0.333*	*-10.34*		*0.74*	*0.36*	*0.25*

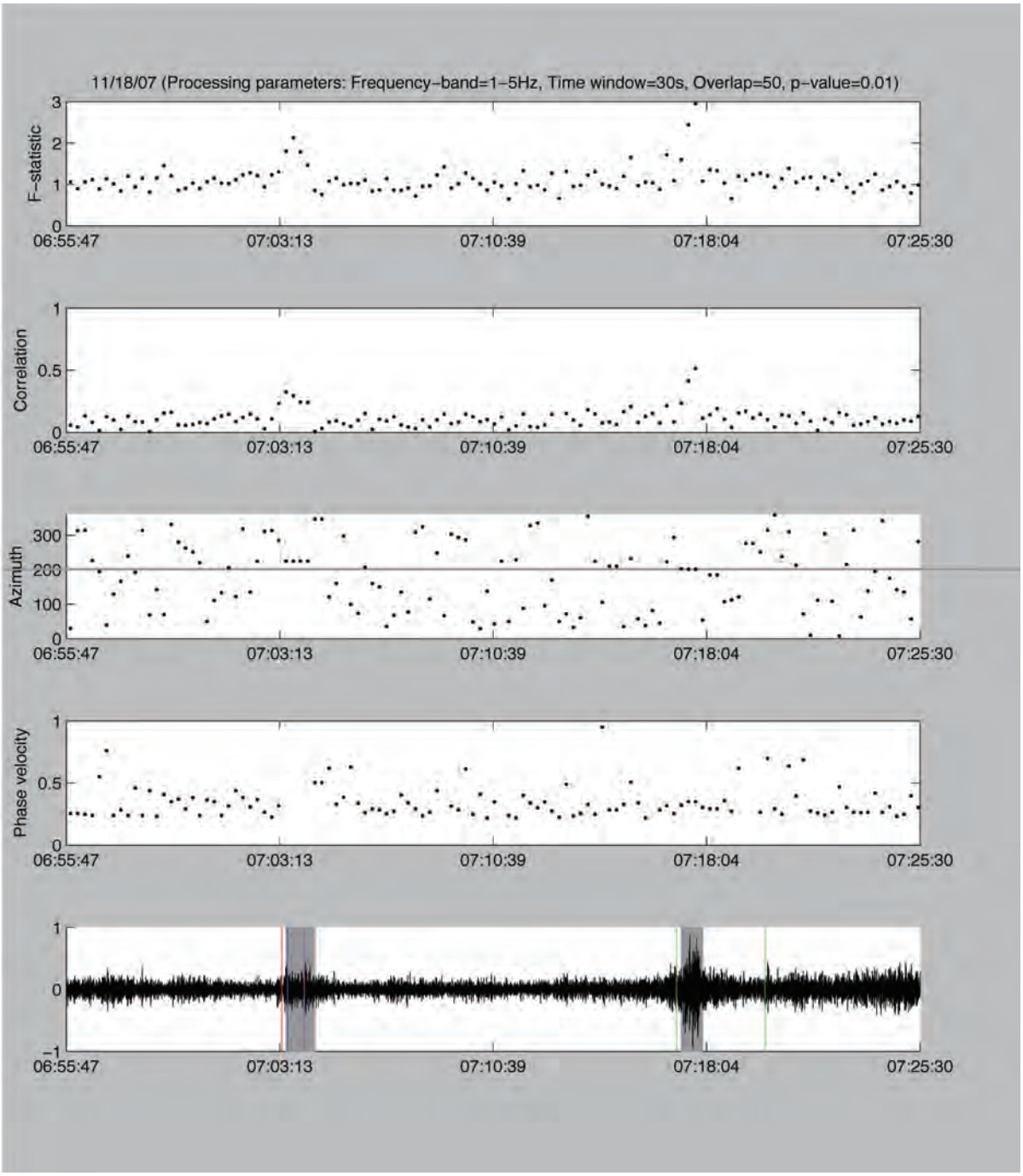

Figure 5. ***InfraMonitor*** **plot showing the normalized beam trace (bottom panel) and derived waveform parameters (top four panels) for a deep earthquake (Depth = 98.4 km) recorded at the I08BO array in Bolivia. Gray boxes denote automatic detections corresponding to the arrival of the seismic wave (left) and stratospheric infrasound (right).**

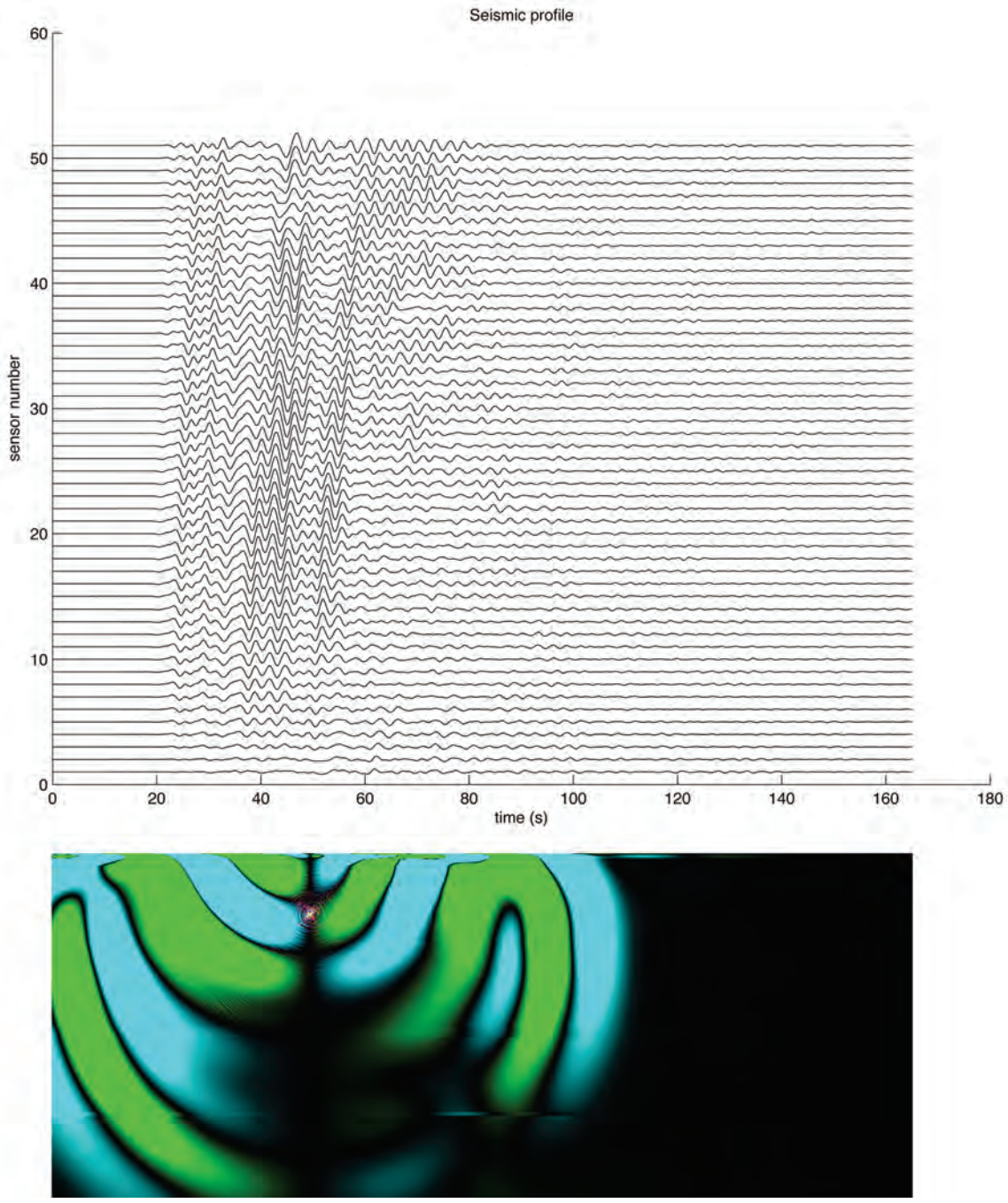

Figure 6. Illustration of seismic E3D modeling. Bottom panel is a snapshot of the model at a given time, for a pure strike-slip earthquake at 7 km depth. A simple 1D velocity model has been used, representative of the LA Basin. Green and blue colors represent positive and negative S-wave energy. Top panel is a transect over the surface showing predicted ground displacement as a function of time at a series of hypothetical receivers.

CONCLUSIONS AND RECOMMENDATIONS

This paper is a report on continuing progress towards an infrasonic depth discriminant. We have completed the acquisition of a high-quality dataset comprising both regional (Western US) and global components. An analysis of detectability highlights the fact that very deep earthquakes can generate infrasound, but that the probability of detection for shallow earthquakes (depth < 50 km) is much higher than for deeper earthquakes, where only relatively few events are detected. We highlight the utility of earthquake sequences for providing reliable phase identification through analysis of the variability of the repeating source. We discuss steps that are being taken to better constrain source, path, and receiver effects. Finally, we report on the initial modeling R&D, which utilizes a seismo-acoustic modeling scheme that combines a seismic finite difference code (E3D) with techniques for converting ground accelerations to acoustic pressure in the near field.

REFERENCES

Arrowsmith, S. J., H. E. Hartse, G. E. Randall, and S. R. Taylor (2009). Infrasound as a Depth Discriminant: Construction of a Unique Dataset and Preliminary Analyses, in *Proceedings of the* 2009 Monitoring Research Review: Ground-Based Nuclear Explosion Technologies, LA-UR-09-05276, Vol. 2, pp. 697–705.

Larsen, S., and C. A. Schultz (1995). ELAS3D: 2D/3D elastic finite-difference wave propagation code, Lawrence Livermore National Laboratory Technical Report No. UCRL-MA-121792.

Mutschlecner, J. P., R. W. Whitaker, and L. H. Auer (1999). An empirical study of infrasound propagation, Tech. Rep. LA-13620-MS, Los Alamos Natl. Lab., Los Alamos, N.M.

Mutschlecner, J. P., and R. W. Whitaker (2005). Infrasound from earthquakes, *J. Geophys. Res*. 110: doi:10.1029/2004JD005067.

Randall, G. E. (1989). Efficient calculation of differential seismograms for lithospheric receiver functions, *Geophys. J. Int*. 99: 469–481.

ReVelle, D. O. (2005). Additional Infrasonic Studies of Earthquakes and Mining Blasts Discrimination, in *Proceedings of the 27th Seismic Research Review: Ground-Based Nuclear Explosion Monitoring Technologies*, LA-UR-05-6407, Vol. 2, pp. 845–854.

Whitaker, R. W. (2007). Infrasound Signals as Basis for Event Discriminants, in Proceedings of the 29th Monitoring Research Review:Ground-Based Nuclear Explosion Monitoring Technologies, LA-UR-07-5613, Vol. 2, pp. 905–913.

Whitaker, R. W. (2008). Infrasound Signals from Ground-Motion Sources, in *Proceedings of the 30th Monitoring Research Review: Ground-Based Nuclear Explosion Monitoring Technologies*, LA-UR-08-05261, Vol. 2, pp. 912–920.

Whitaker, R. W. (2009). Infrasound Signals from Ground Motion Sources, in *Proceedings of the 2009 Monitoring Research Review: Ground-Based Nuclear Explosion Monitoring Technologies*, LA-UR-09-05276, Vol.2, pp. 750–758.

MULTIPLE-ARRAY DETECTION, ASSOCIATION AND LOCATION OF INFRASOUND AND SEISMO-ACOUSTIC EVENTS – UTILIZATION OF GROUND TRUTH INFORMATION

Stephen J. Arrowsmith[1], Il-Young Che[2], Christopher T. Hayward[3], and Brian W. Stump[3]

Los Alamos National Laboratory[1], Korea Institute of Geoscience and Mineral Resources[2] and Southern Methodist University[3]

Sponsored by the Air Force Research Laboratory and the National Nuclear Security Administration

Contract Nos. DE-AC52-06NA25396[1] and FA8718-08-C-008[2,3]

ABSTRACT

This work is intended to provide automated methodology for processing seismic and infrasound data from seismo-acoustic arrays and apply the methodology to regional networks for validation with ground truth information. In the initial year of the project automated techniques for detecting, associating and locating infrasound signals were developed. Recently, the location procedure has been cast into a Bayesian framework.

Work this year has focused on assessment of sets of robust regional infrasound signals in order to optimize the location algorithms. Quantification of the importance of model and empirical travel times, backazimuth estimation (including errors) and signal detectability have all been undertaken and are reported. Two specific studies are reported.

Infrasound from a static rocket test conducted at Promontory, Utah on11/01/2007, was observed on USArray seismographs up to a distance of 600 km. Signal durations were broadly consistent with the duration of the test, 123 s, and signal envelopes correlated with variations in thrust in some cases. The effect of adding Gaussian noise to wind profiles is investigated for the purpose of phase identification. It is shown that all observations can be predicted through the combination of simulations using different noise levels, suggesting that a probabilistic approach to phase identification is possible. These results have important implications for how atmospheric models might be utilized in source location in particular how they might be implemented into the Bayesian location framework of Modrak et al. (2010).

The deterministic dependence of infrasound propagation on the season and path environment was quantified by the analysis of more than 1,000 repetitive infrasonic ground-truth events at an active, open-pit mine in Korea over 2 years. Blast-associated infrasonic signals were analyzed from two infrasound arrays (CHNAR and ULDAR) located at similar distances of 181 and 169 km, respectively from the source but in different azimuthal directions and with different path environments. The CHNAR array is located to the NW of the source area with primarily a continental path, whereas the ULDAR is located E of the source with a path dominated by open ocean. As a result, CHNAR observations were dominated by stratospheric phases with characteristic celerities (group velocities) of 260 to 289 m/s and large seasonal variations in the travel time, whereas data from ULDAR consisted primarily of tropospheric phases with larger celerities from 322 to 361 m/s and larger daily than seasonal variation in the travel time. Ray tracing using atmospheric models incorporating daily weather balloon data that characterizes the shallow atmosphere for the 2 years of the study verifies the interpretation of these observations. Finally, experimental celerity models that included seasonal path effects were constructed from the long-term dataset. These experimental celerity models were used to constrain travel time variations in infrasonic location algorithms providing improved location estimates as illustrated with the empirical dataset.

OBJECTIVES

There are two primary objectives to our efforts in the second and third year of this contract. Each objective builds on the automatic algorithms for detection, association, and location of infrasound events developed in the first year of this project, the further development of these techniques in year two and the preliminary analysis of ground truth data in assessing atmospheric propagation models.

- **Validation and utilization of atmospheric models**. Initial efforts in this contract focused exclusively on infrasound detection, association, and location without requiring the use of atmospheric models. R&D this year has focused on how best to use prediction models (comprising the combination of atmospheric and propagation models) for enhancing source localization. In this paper we outline two different approaches: a stochastic approach and a deterministic approach, for using atmospheric specifications in event location.
- **Extended analysis of infrasound propagation effects using ground-truth data from Korea.** A primary focus in the last year has been in the careful analysis and modeling of infrasound observations associated with the ground truth data acquired in the earlier stages of the study. These data have been compared to detailed propagation path models for the Korean peninsula and provide a basis for assessing the types of empirical data that can improve location estimates based exclusively on infrasonic data and seismic and infrasonic data in combination.

RESEARCH ACCOMPLISHED

A Strategy for Enhancing the Bayesian Infrasonic Source Location (BISL) Method

The BISL framework, outlined in Modrak et al. (2010), provides a robust framework for infrasound location without requiring a prediction model. This is accomplished in part by defining a uniform prior PDF on celerity (group velocity) as follows:

$$p(v) = \begin{cases} 16.67 & 0.22 \text{ km/s} \le v \le 0.34 \text{ km/s} \\ 0 & \text{otherwise} \end{cases}.$$

This Bayesian prior term effectively takes a worst-case scenario: we have no expectation of the celerity for a given observed arrival, and can therefore only place bounds on celerity (noting that these bounds might be more restrictive if, for example, we can rule out a thermospheric return on some basis). In the absence of a reliable prediction model that is capable of predicting infrasound phases, this appears to be the best we can do for now. But is it really?

Prediction Models

Real time state-of-the-art atmospheric models, such as the Ground-to-Space (G2S) model are thought to capture the day-to-day and hourly variability in temperatures and winds at horizontal resolutions of approximately $1 \times 1°$. However, they do not attempt to resolve fine-scale atmospheric structures such as sub-grid scale gravity waves, turbulence, and wind gusts. It has been demonstrated that the combination of such atmospheric models with existing infrasound propagation models do not always reliably predict observations (e.g., Arrowsmith et al.; 2007; Evers, 2009). This is a particular problem in the zone-of-silence, a region that extends from approximately 50 to 200 km. Two factors influence this limitation: (1) the fidelity of atmospheric models, and (2) the fidelity of propagation models.

For routine infrasound location, we require a good blend of simplicity and physical thoroughness, to balance the need to be useful in operational processing and capture sufficient propagation physics. As outlined by Drob et al. (2010), the TauP method (e.g., Garcés et al., 1998; Drob et al., 2010) provides a good balance of simplicity and physical thoroughness to make it the propagation model of choice for automatic location algorithms. Other methods – such those based on Parabolic Equations or Normal Modes (see Whitaker and Norris, 2008, for a summary) – account for additional wave physics, such as diffraction effects, but are impractical for current automated techniques due to the high computational costs.

Using Prediction Models in BISL

The simple question is this: Given some smoothed realization of the atmosphere at a given place and time, how can we use that information to better constrain the group velocity? With the knowledge that we cannot

reliably predict arrivals deterministically, we need to somehow account for the unknown effects of gravity waves, turbulence, and wind gusts – as well as limitations in propagation physics – in a stochastic way. A simple way to do this is to add noise to G2S wind profiles, constrained by empirical data. We note here that Gibson et al. (2009) have used spectral models for gravity waves to perturb atmospheric models with some success, using a Time Domain Parabolic Equation method. Since our strategy is to account for multiple sources of error for event location, a simple Gaussian noise model is used here. Incorporating additional constraints such as the gravity wave spectral model of Gardner (1995) could refine this model.

Based on the fact that the dense network of seismic stations in the USArray can be used for detecting infrasound (e.g., de Groot-Hedlin et al., 2008), we can leverage this unprecedented sampling of the infrasound wavefield to test the effect of adding different levels of noise to the zonal and meridional wind components, and determine what standard deviation of noise is needed to predict the observations. A static rocket test, conducted at Promontory, Utah, at 19:00 UT on 11/01/2007 was well recorded by USArray and easy to identify on the single-channel seismic data owing to its unique source-time function of duration equal to 123 s (Figure 1).

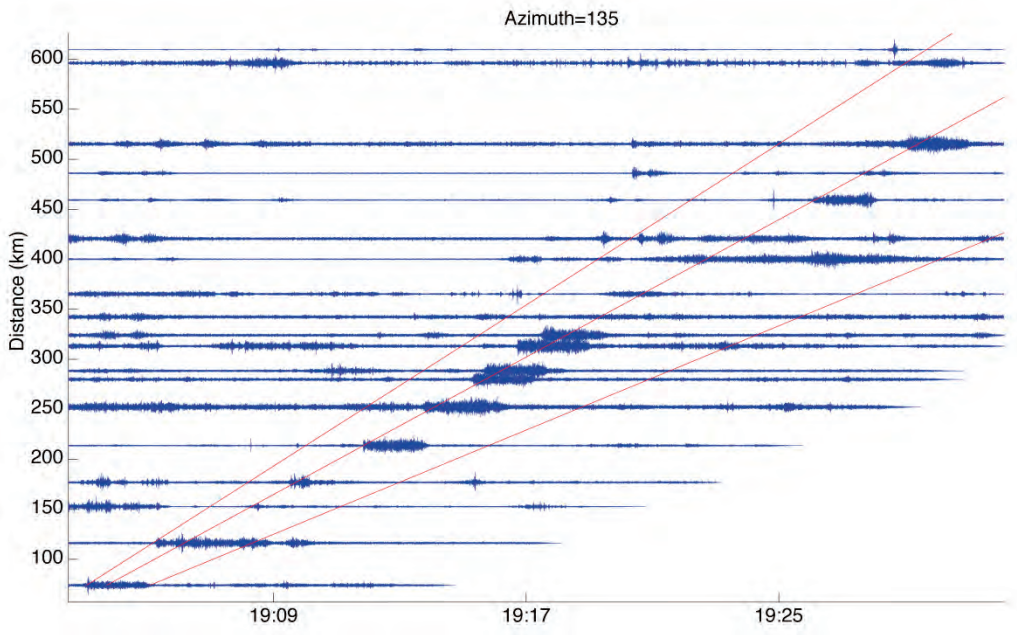

Figure 1. Record section taken along a great-circle azimuth of 135°. All stations within 20° of the great-circle azimuth are projected onto the great-circle path. Vertical component waveforms are plotted, bandpass filtered from 3-10 Hz. Red lines correspond to group velocities of 0.34 km/s, 0.29 km/s, and 0.22 km/s.

We add noise to the wind components only, since the uncertainties in temperature in the G2S model are lower (Drob et al., 2010). The implementation is simple: Mathematically, $u(z) = u_0(z) + \eta$ and $v(z) = v_0(z) + \eta$, where u_0 and v_0 are the unperturbed G2S wind profiles and η is the noise vector. Figure 2 illustrates the addition of noise by comparing zonal and meridional winds with and without Gaussian noise with a standard deviation of 5 m/s.

A comparison between the observations and predictions, for different levels of added noise, is shown in Figure 3. Gaussian noise with σ equal to 5 m/s, 10 m/s, and 20 m/s have been added to the unperturbed wind profiles in Figure 2. The uncertainties used are within the approximate range of estimated uncertainties in G2S models (Drob et al., 2010), although the variation in uncertainty with height is not accounted for here. The predictions estimated here do not include direct arrivals -- only ducted arrivals are considered. Furthermore, multiple bounces are not considered in this study, eliminating the added complexity of accounting for topography (Arrowsmith et al., 2007). Multiple atmospheric realizations have been computed at each noise level, with similar ray-tracing results obtained each time. The results

presented below correspond to single realizations, but these are broadly representative of multiple runs in terms of the highlighted regions where predictions match (see Figure 3).

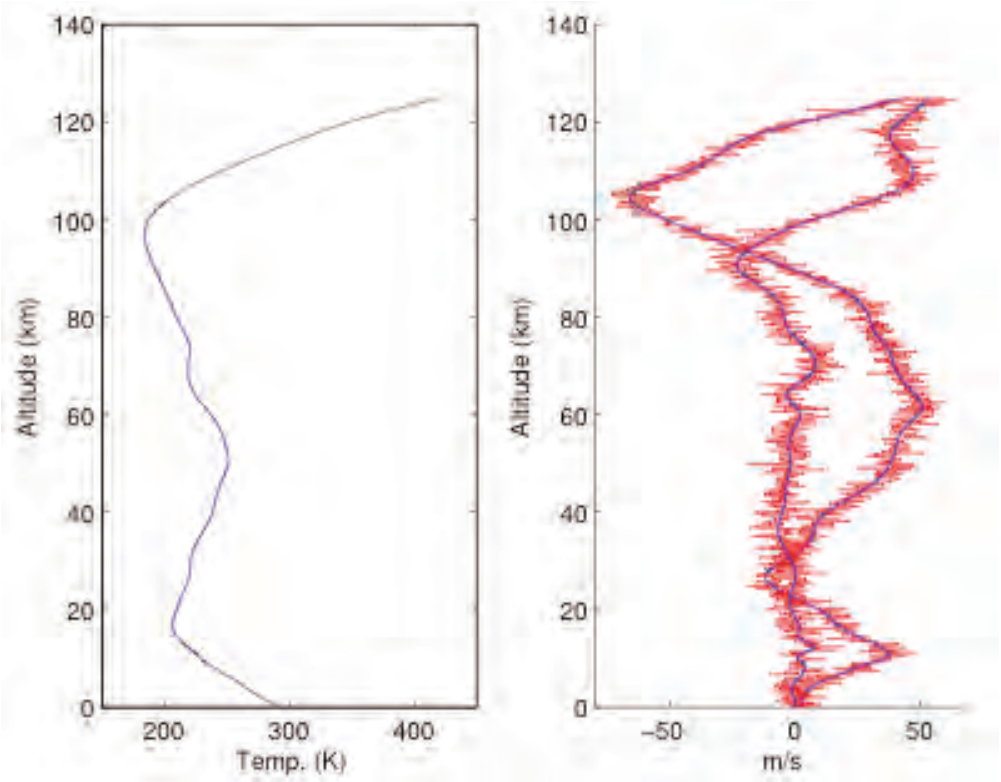

Figure 2. Profiles of the 1D temperature (left panel) and winds (right panel) extracted from the G2S model for 19:00 on 11/01/2007 at the test location. Unperturbed zonal and meridional winds are represented by blue lines, while perturbed wind profiles (using $\sigma = 5$ m/s) are shown in red.

The predicted bounce-points (locations where rays are predicted to hit the ground), which are shown in Figure 3, assume an omni-directional source and do not account for the known source directivity. The bounce-points were predicted by shooting a suite of rays at azimuths of 0–355°, and launch angles of 0–90°, with 5° spacing in both azimuth and launch angle. With no added noise, the geographic distribution of bounce-points reflects the strong positive zonal wind in the stratosphere, common at this latitude during the winter months, which enhances the stratospheric duct to the east and destroys the stratospheric duct to the west (noting that stratospheric group velocities are typically 0.28 km/s–0.31 km/s).

The results shown in Figure 3 highlight that, although some arrivals are not predicted using the unperturbed G2S profiles, they can be predicted when noise is added to the profiles. For example, observations with v_g = 0.28 km/s to the southwest of the test are only predicted with σ = 5-10 m/s; observations with v_g < 0.27 to the northeast of the test are only predicted with σ = 20 m/s. As would be expected, with increasing noise, returns are predicted at ever-closer distances. However, due to the strong zonal winds that favor propagation to the east, few returns are predicted towards the west at these noise levels, with the exception of thermospheric returns.

The full suite of observations can only be explained through the combination of simulations with varying noise levels. This detail is important because it implies that, for phase identification (and thus also for location purposes), a probabilistic approach is necessary. For example, an observed arrival may be explained as either a stratospheric, or tropospheric, arrival depending on the standard deviation of the wind perturbation addition.

Our contention is that if we can reliably predict arrivals through the addition of noise to atmospheric wind models, the simple uniform prior of Modrak et al. (2010) may be refined using a stochastic prediction model. By the principle of reciprocity, the Tau-P equations can be calculated from the receiver perspective by integrating the ray equations with a negative time step. Thus, by tying the standard deviation of wind perturbations to probability (where more probable predictions are based on smaller standard deviations of additive noise), we can develop a non-uniform prior PDF, for a given signal backazimuth and arrival time, based on Tau-P predictions. In effect, we can directly relate celerity to the standard deviation of wind perturbations, and subsequently relate wind noise probabilities to group velocity probabilities. Further research is needed to develop this R&D concept, implementing prediction model simulations into BISL2.0.

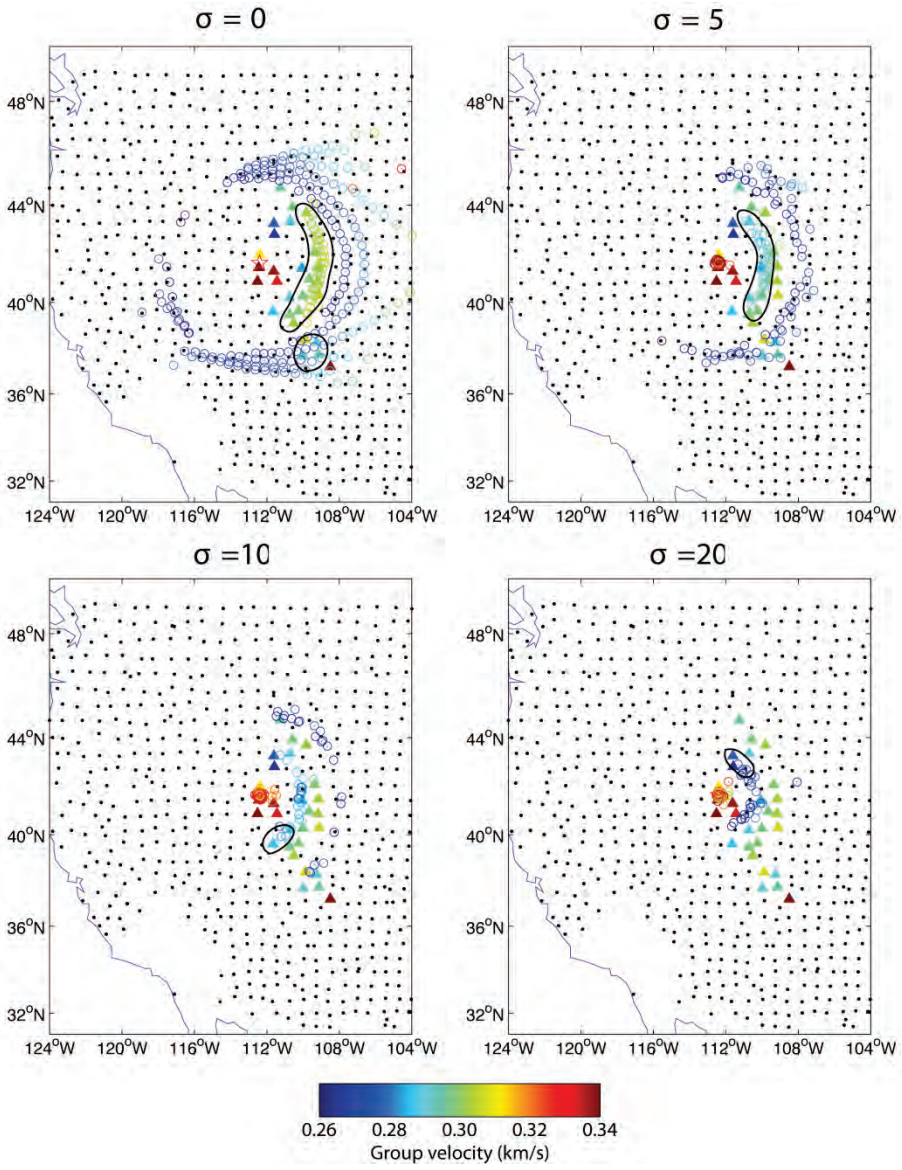

Figure 3. Plots comparing predictions (open circles) and observations (filled triangles) for different levels of noise added to the atmospheric data. Black dots represent stations that did not record the test. The predictions and observations are plotted on the same color scale, which represents group velocity. Thermospheric predictions have been removed for clarity. Observations enclosed by black lines are uniquely predicted for that given noise level.

Experimental Characterization of Seasonal Variations in Infrasonic Travel Times in the Korean Peninsula with Implications for Infrasound Location

The purpose of this component of our work is to experimentally characterize infrasonic travel time and construct quantitative celerity models that depend on the season and propagation path. In support of this deterministic approach to travel-time assessment we collected nearly daily repetitive infrasonic observations over a two-year time period from ground-truth events at an active mine. These events included more than 1,000 surface blasts that occurred daily, with multiple events on active days, over the 2 years. Variations in infrasound propagation based on the data are quantified at the two infrasound arrays CHNAR and ULDAR in Korea (Figure 4), both located at similar distances from the mine but with different propagation environments - one path dominated by the continent and the other by the ocean.

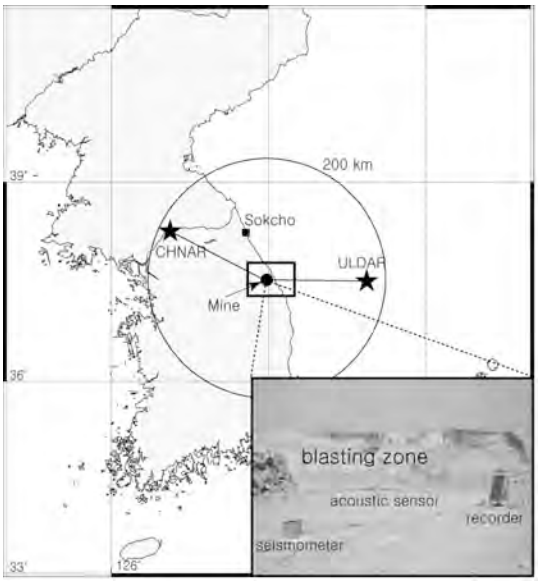

Figure 4. Locations of the open-pit mine (circle), two infrasound arrays (stars) and weather balloon station (square) used in this study. A photograph of one in-mine seismo-acoustic station is shown in the lower right.

Array processing based on the progressive multi-channel correlation (PMCC) (Cansi, 1995), is used to detect and analyze the blast-associated infrasonic signals and to construct a celerity model for each path. Characteristics of the two sets of experimental celerity models include seasonal dependent path effects to each array. Ray tracing using long-term atmospheric models supplemented by shallow atmosphere constraints provided by weather balloon data was performed for comparison with the observations.

Variations of infrasound propagation. During the two years of in-mine sensor operation, 1,066 blasts were detonated, more than one blast per day on average. 97% of the blasts occurred at or around 03 UTC (12 pm local time). The origin time and approximate location of each event was estimated using the seismic and infrasound observations from the in-mine stations. Infrasonic array data were analyzed using the PMCC method, in order to detect blast-associated infrasonic signals. The wave parameters of each detected signal, including the arrival time and azimuth, were then estimated at each array. Figure 5 displays the waveforms and analysis results for one set of the ground-truth events. The left figure shows near-field seismic and acoustic signals recorded at the two in-mine stations (ACE3 and ACE7). The acoustic signals in this case were clipped due to instrument dynamic range and the close distance to the 10-ton blast. We simply used the center of the main blasting zone as a source location for all blasts. PMCC results are also shown in the figure. WinPMCC v2.1 was used to make the regional wavefield estimates focusing on a phase velocity range of 0.25-0.40 km/s using a window length 20 s, and a frequency band 0.5–5 Hz. After signal association, we compiled travel times and wave parameters determined from PMCC.

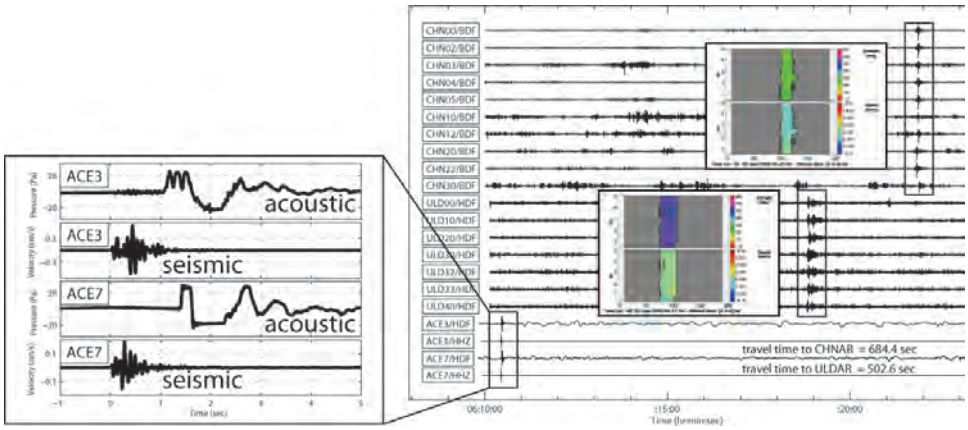

Figure 5. Example data for a blast charged with 10 tons of explosives. (left) The four waveforms from the blast are the near-field seismic and acoustic signals recorded in the mine. (right) Boxes mark the blast-associated infrasound signals recorded at the two regional arrays with the upper ten waveforms from CHNAR, excluding one bad channel (CHN32), and next seven waveforms from ULDAR. The corresponding PMCC results display the estimates of azimuth (upper) and apparent velocity (lower) for the detected signals. Measured travel times for both infrasonic signals are listed in the lower right.

Figure 6 documents the variation of infrasound travel times and azimuths to the two arrays for all the ground-truth events that were observed over the 2 years. Despite similar propagation distances, the average travel times were significantly different to the two arrays, with arrivals at ULDAR on average 150 seconds earlier than those at CHNAR. For CHNAR, the celerities calculated from the distances and travel times ranged from 260 to 289 m/s, which corresponds to the characteristic value of stratospheric returns (Evers and Haak, 2007).

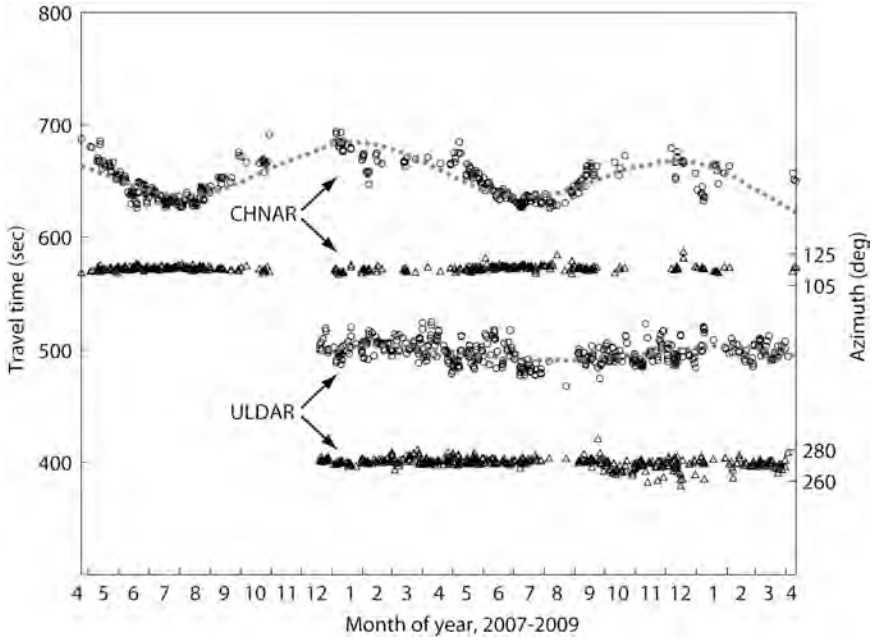

Figure 6. Variations of travel times (circles) and azimuths (triangles) estimated at both arrays from the ground-truth events recorded over the 2 years of the study. The dotted lines superimposed on the observed travel times are sinusoidal celerity models that were fit to the observations. Note that ULDAR was installed in December 2007 and so there is a shorter time period of observation.

In addition, the travel times showed systematic seasonal variations with signals arriving up to 68 seconds faster in the summer. Thus, the celerity showed a smoothly varying cyclical change with time, with

velocities of ~0.26, ~0.29, and ~0.27 km/s in the winter–spring, summer, and fall seasons, respectively. This systematic variation in observed celerity is consistent with the contention that the travel times of infrasound signals are strongly dependent on the seasonal ambient sound speed along the path. In contrast, the infrasound signals arriving at ULDAR showed relatively large celerities (322 to 361 m/s), characteristic of tropospheric returns. The travel times to ULDAR show little seasonal variation but document larger daily variations of up to 56 second in the travel times between days. These observations can be partially attributed to the dominant effect of the ocean on temperatures at the ocean–atmosphere boundary.

Path variations also impact the ability to detect the arrivals. Signals at CHNAR were most likely to be detected in the summer. Many signals were not detected during the fall–winter–spring seasons, even though strong source signals were identified at the in-mine stations for these times. Detection at ULDAR was low in summer (August) but stable during the other seasons. Thus, the seasonal detection at the two arrays was complementary, as shown in Figure 6 as result of the azimuthal differences of the two arrays relative to the mine. This variation in detection can be partially explained by seasonal changes in the atmospheric wave duct attributable to known seasonal wind in and around the Korean Peninsula with winds northwesterly in the winter and southeasterly in the summer. In contrast to the variation of travel times, the azimuth estimates showed little variation with season at either array (Figure 7). The mean and variance of the azimuth estimates were 115.6±1.6^o at CHNAR (115.8^o of true azimuth) and 271.5±3.1^o at ULDAR (271.7^o), respectively. The insensitivity of backazimuth to seasonal variations is consistent with the relatively weak meridional winds (5.9% and 27.2% of annual average zonal wind speed at 10 and 30 km above the mine, respectively, estimated from Horizontal Wind Models (Drob et al., 2008) in the region, which are normal to the dominantly EW propagation paths in this study.

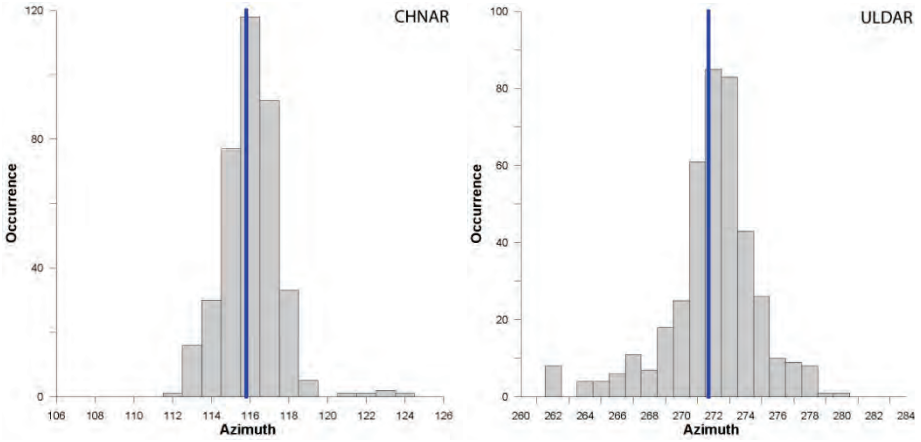

Figure 7. Distribution of backazimuth estimates at CHNAR (left) and ULDAR (right) for all the ground truth events observed at the two arrays. The blue line represents the true backazimuth to the mine where the events occurred.

Modeling of Infrasonic Propagation. Atmospheric ray tracing was performed for all the observations over the 2 years of the study using a combination of empirical atmospheric models (Horizontal Wind Model/Mass Spectrometer, Incoherent Scatter: HWM07 (Drob et al., 2008)/MSISE-90 (Hedin et al., 1991) for the upper atmosphere and weather balloon data for the lower atmosphere. The lower part of the effective sound velocity profiles (ESVP) used for ray tracing (Hagerty et al., 2002) was based on the weather balloon data from the Sokcho station, which is closer to both the mine and arrays than other stations operated by the KMA. The measurement height of the balloon data depended on the day, but data were usually available to an approximate altitude of 30 km and included temperature, wind direction, and wind speed. Data acquired at 00 UTC was used for the modeling because it is within 3 hours of the average time of the blasts. Ray tracings at a 0.1^o intervals were computed for each day of the experimental period and included models for 726 days at CHNAR and 484 days at ULDAR (smaller number of days for ULDAR reflects its more recent installation, December 2007). When trajectories of a ray passed within 1 km (capture radius) of the array, the ray was identified as an eigenray for the infrasonic phase. Of the eigenrays computed on a given day, the ray with highest turning height was selected as a representative

eigenray for the day. In case of CHNAR, the total rays from the simulations were grouped into four dominant classes: (1) in 43.8% of the cases there exists a thermospheric phase but CHNAR is located in a acoustic shadow zone for the rays, *It_shadow*; (2) in 36.9% of the cases there exists a stratospheric phase but CHNAR is again located in a shadow zone, *Is_shadow*; (3) in 16.7% of the cases there was a tropospheric phase that was predicted to return to CHNAR, *Iw_eigen*; and (4) in 2.6% of the cases there was predicted a stratospheric phase that is predictable to return to CHNAR, *Is_eigen* . In case of ULDAR, four dominant cases were identified and included *It_shadow* (9.9%), *Is_shadow* (5.4%), *Iw_shadow* (3.1%), and *Iw_eigen* (81.6%). Unlike the other shadowing phase, the *Iw_shadow* phases jumped ULDAR with bounces at the surface.

Figure 8 displays the variation of ESVP for the 2 years of the study along with the ray-tracing results. The refraction altitudes of each daily eigenray from the mine to the individual arrays are superimposed on the ESVP.

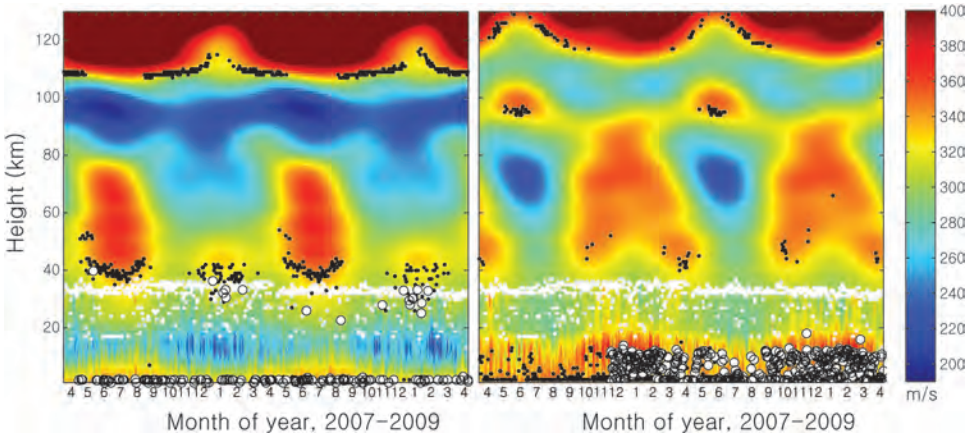

Figure 8. Ray tracing results using effective sound velocity profiles (ESVP) for the path from the mine to CHNAR (left) and to ULDAR (right) for the 2 years of the study. White dots indicate boundary heights between balloon data and the empirical data used for the ray tracing. Black dots indicate the lowest possible refraction heights where the sound speed is larger than that at source. White circles indicate turning points in the atmosphere from the predicted eigenrays for each day at 00 UTC.

For CHNAR, ray tracing predicted a smaller number of eigenrays representative of stratospheric returns than that documented in Figure 6. Although many stratospheric returns were predicted from ray tracing (the black dots around 40 km altitude), CHNAR was in the so-called zone of silence in most of these prediction. This comparison implies that the ESVP, particularly the empirical models with stratospheric returns, were not sufficient to predict the real observations or that the capture radius was too small, even though the predictions for the *Is_eigen* are increased by widening the capture radius, for example 4.7% for 5 km and 14.5% for 10 km of capture radius. Most *Is_eigen* phases at CHNAR were predicted during the winter (see January of 2008 and 2009) with refraction altitudes corresponding to heights sampled by the balloon data. These predictions can be explained by not only the slow sound speed at the ground but also the slightly higher velocity channel at stratospheric heights during this season. The higher level of signal detection predicted for the mid-winter (January) in comparison to the spring and fall seasons was consistent with the observations detailed in Figure 6. The calculations also predicted many *Iw_eigen* phases that refracted at very low altitudes and experienced bounces at the ground surface but the corresponding phases were not clearly observed in the ground truth data. This second result suggests that the *Iw* phase may have limited horizontal propagation along the continental path which includes significant topographic variation between the mine and CHNAR. In contrast, many eigenrays returned to ULDAR by refraction at altitudes lower than 20 km. These altitudes were in the range where the balloon data were collected.

Infrasound Location of Ground Truth Events. Infrasonic signals from 130 blasts were detected by both arrays. In this study, we calculated two different location sets for these selected blasts. The first set of location estimates were determined by assuming common stratospheric phase for both arrays with constant celerity of 0.3 km/s for all seasons in the least-square method. The second set of location estimates were

calculated using simple sinusoidal celerity model which were fit to the observation (dotted lines in Figure 6), and includes seasonal dependences as described. The location results are summarized in Figure 9 with the blue squares representing the first set of locations and the red ones the second location set using the seasonal dependent celerity models. 95% confidence ellipses for each location set are also included in the figure. The centroid for the location of the first set is biased about 17.8 km to the east of the mine due to the discrepancies between the assumed constant celerity and observed celerities shown in Figure 6. The average location estimates using the experimentally determined celerity models that included seasonal path effects showed only a 1.7 km offset from the mine location. This result suggests that, for infrasonic source location at regional distances, the dependence of infrasound propagations on seasons and path environments should be quantified and its effects incorporated into the infrasound location method in order to produce improved location estimates. In the figure, black circles indicate seismic locations for the blasts extracted from the seismological catalog of the KEMS. Of the total ground truth dataset used in this study, the KEMS detected 589 events (open circles) with local magnitude ranging from 0.5 to 1.8 M_L. Yellow circles in the figure indicate the 100 seismic locations which correspond to the 130 blasts located using only the infrasound signals as described above. It is interesting to note that there were 30 events in the infrasound set that did not produce seismic events in the database. Comparing the infrasonic location with the seismic location, suggests that the infrasonic location including seasonal path effects are at least comparable to seismic location in case of small-magnitude surface explosions at regional distances.

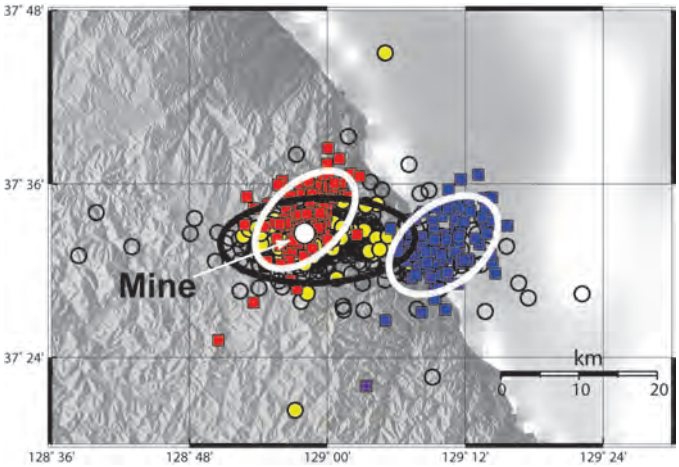

Figure 9. Two infrasonic locations results for selected ground truth events using constant celerity model (blue squares) and sinusoidal model (red squares). Circles indicate seismic locations of the ground truth events determined by the KEMS.

CONCLUSIONS AND RECOMMENDATIONS

The stochastic study suggests that one can reliably predict arrivals through the addition of noise to atmospheric wind models. The implication is that the simple uniform prior of Modrak et al. (2010) may be refined using a stochastic prediction model. By the principle of reciprocity, the Tau-P equations can be calculated from the receiver perspective by integrating the ray equations with a negative time step. Thus, by tying the standard deviation of wind perturbations to probability (where more probable predictions are based on smaller standard deviations of additive noise), we can develop a non-uniform prior PDF, for a given signal backazimuth and arrival time, based on Tau-P predictions. In effect, we can directly relate celerity to the standard deviation of wind perturbations, and subsequently relate wind noise probabilities to group velocity probabilities.

The complementary two-year deterministic study of infrasound wave propagation has utilized ground truth events collected at an active mine in Korea. The dataset included 1,066 blasts and highlights the variation of infrasonic propagation due to the seasonal variation of atmospheric structures and propagation path environments. The blast-associated infrasonic signals were analyzed at two distant infrasound arrays, which

were located at similar distances (zone of silence) from the mine but pointed in different azimuth directions over different path environments (continental and open ocean). Infrasonic waves traveling NW toward CHNAR over the continent propagated as guided waves between the ground and stratosphere, with a characteristic celerity range of 260–289 m/s. These observations documented seasonal cyclical variations in travel time. The infrasonic waves traveling E to ULDAR also propagated as guided waves, but observed celerities indicated that wave ducts were formed at relatively low heights in the troposphere. The celerity range was correspondingly large (322–361 m/s), even though the propagation distances to both arrays were similar. ULDAR showed more daily variation in travel time than seasonal variation. The lower refractions were compared and verified by ray tracings with balloon data constraining the lower atmosphere. In particular, the observations at ULDAR support the existence of an ephemeral 'SOFAR' layer in the atmosphere (Herrin et al., 2006) throughout the year over the open ocean. Finally, the dataset illustrates that a celerity model that captures the seasonal path effects can substantially improve infrasound location procedures. The infrasound only location resulted in improved locations when compared routine seismic locations for these small-magnitude surface explosions observed at regional distances.

ACKNOWLEDGEMENTS

We would like to thank Mr. Kwan Kyo Chung, section manager of the mine office for his thoughtful supports during the experiment. We used atmospheric data collected by the Korea Meteorological Administration (www.kma.go.kr). This work was also supported by the Basic Research Project of the Korea Institute of Geoscience and Mineral Resources funded by the Ministry of Knowledge Economy of Korea.

REFERENCES

Arrowsmith, S. J., D. Drob, M. A. H. Hedlin, and W. Edwards (2007). A joint seismic and acoustic study of the Washington State bolide, *J. Geophys. Res*., 112, doi:10.1029/2006JD008001.

Cansi, Y. (1995). An automatic seismic event processing for detection and location: the PMCC method, *Geophys. Res. Lett.* 22: 1021–1024.

de Groot-Hedlin, C. D., M. A. H. Hedlin, and K. T. Walker (2008). Evaluation of infrasound signals from the shuttle Atlantis using a large seismic network, *J. Acoust. Soc. Am*. 124: 1442–1451, doi:10.1121/1.2956475.

Drob, D. P., et al. (2008). An empirical model of the Earth's horizontal wind fields: HWM07, *J. Geophys. Res*. 113: A12304, doi:10.1029/2008JA013668.

Drob, D., Garcés, M., Hedlin, M., and Brachet, N. (2010). The temporal morphology of infrasound propagation. *Pure Appl. Geophys.* 167: 437–453.

Evers, L. G., and H. W. Haak (2007b). Infrasonic forerunners: Exceptionally fast acoustic phases, *Geophys. Res. Lett*. 34: L10806, doi:10.1029/2007GL029353.

Evers, L. G. (2009). Imaging of the atmosphere with infrasound, *Proceedings of Internoise, 2009*, Ottawa, Canada, August 23-26, 2009.

Garces, M. A., Hansen, R. A., and Lindquist, K. G. (1998). Traveltimes for infrasonic waves propagating in a stratified atmosphere, *Geophys. J. Int.* 135: 255–263.

Gardner, C. (1993). Gravity Wave Models for the Horizontal Wave Number Spectra of Atmospheric Velocity and Density Fluctuations, *JGR* 98; D1, 1035–1049.

Gibson, R .G., Drob, D. P., and Broutman, D. (2009). Advancement of Techniques for Modeling the Effects of Fine-Scale Atmospheric Inhomogeneities on Infrasound Propagation, in *Proceedings of the 2009 Monitoring Research Review*: *Ground-Based Nuclear Explosion Technologies*, LA-UR-09-05276, Vol. 2, pp. 714–723.

Hagerty, M. T., W. Y. Kim, and P. Martysevich (2002). Infrasound detection of large mining blasts in Kazakstan, *Pure Appl. Geophys*., 159: 1063–1079.

Hedin, A. E. (1991). Extension of the MSIS thermosphere model into the middle and lower atmosphere, *J. Geophys. Res*., 96(A2), 1159–1172.

Herrin, E. T., T. S. Kim, and B. W. Stump (2006). Evidence for an infrasound waveguide, *Geophys. Res. Lett*. 33: L07815, doi:10.1029/2005GL025491.

Modrak, R. T., S. J. Arrowsmith, and D. N. Anderson (2010). A Bayesian framework for infrasound location, *Geophys. J. Int*., 181: doi:10.1111/j.1365-246X.2010.04499.x

Whitaker, R. W. and Norris, D. E. (2008). Infrasound Propagation, in *Handbook of Signal Processing in Acoustics*, Springer, New York.

IMS INFRASOUND MONITORING TEST SITE AT TRAFELBERG, AUSTRIA: PRELIMINARY RESULTS FROM IN-SITU RESPONSE MEASUREMENTS OF INFRASOUND ELEMENTS

Thomas Gabrielson[1], Georgios Haralabus[2], and Stefi Stefanova[2]

Penn State University[1] and the Comprehensive Nuclear-Test-Ban Treaty Organization[2]

ABSTRACT

The International Monitoring System (IMS) of the Comprehensive Nuclear Test-Ban Treaty Organization (CTBTO) has a unique infrasound test site (I99AT) with four wind-noise-reduction pipe-array systems in close enough proximity to allow simultaneous measurements under similar environmental conditions. It was designed as a facility to study the effectiveness of various wind-noise-reduction systems so it is clear of trees, vegetation, or other wind breaks. The persistent winds presented a challenge for response measurement by reference-microphone comparison; however, there were several suitable periods during the eight days of continuous recording from 19 May to 27 May 2010.

Reasonable estimates for the magnitude and phase response of all four infrasound elements at I99 were made from 0.008 Hz to several Hz. For all four elements, from 0.01 to 0.1 Hz, the measured magnitude and phase correspond closely to the manufacturer's specifications for the MB2005. Above 1 Hz, the effects of the pipe system produce a significant change in the phase response compared to the MB2005. Below 0.01 Hz, the phase also changes somewhat faster than expected. A preliminary investigation of the effects of non-acoustic turbulence and the associated scale sizes was performed and an apparent drop in the magnitude response of the larger elements below 0.08 Hz was tentatively associated with area-averaging of non-acoustic pressure fluctuations. Finally, in windy conditions, the large hexagonal element showed higher spectral levels from 0.2 to 3 Hz than the small element.

OBJECTIVES

This progress report covers eight days of reference-microphone measurements at the I99AT infrasound test bed in Trafelberg, Austria. The I99 infrasound test bed comprises four complete pipe-array elements. Two of the elements are rosettes – 18 and 36 meters overall dimension – and are placed so that their geometric centers are coincident. The other two elements are close-packed hexagonal configurations – 18 and 36 meters overall – also with coincident geometric centers. They are located in an area surrounded by trees and hills; however, there are no trees or other vegetation in the immediate area of the elements.

Since the hexagonal and rosette systems are only 44 meters apart, reference microphones could be deployed at all four systems for simultaneous evaluation. Four reference microphones were used with three microphones in a triangular configuration at the hexagonal-pair center and the fourth microphone at the rosette-pair center. Halfway through the deployment, the positions of the three microphones and the single microphone were reversed. The overall configuration is shown in Figure 1 below. This configuration of I99 elements and reference microphones meant that a number of different spatial scales could be investigated under nearly the same conditions.

For part of the deployment period, two portable systems provided by the PTS were placed near the center of the rosette pair. One of these systems was run with its port open, the other with its port connected by a length of hose to a quad-plate reference port. The I99 systems and the portable systems all use the MB2005. The reference microphones are all GRAS 40AZ cartridges with 26CG preamplifiers and a custom power supply and gain stage.

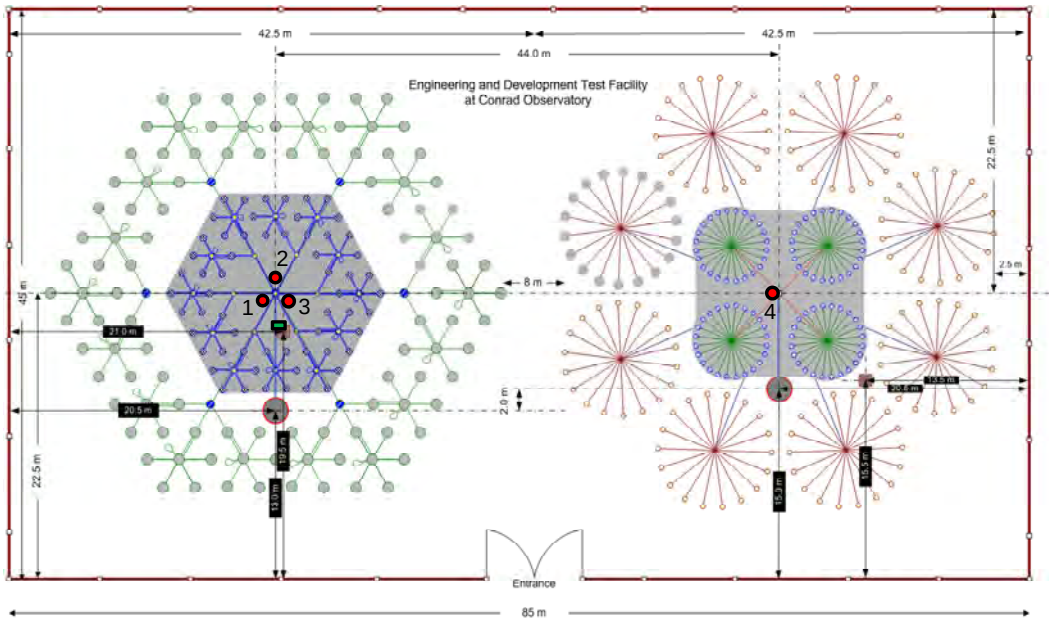

Figure 1. Schematic diagram of the elements at I99AT and the reference microphones. The two hexagonal close-packed arrays are on the left; the two rosette systems are on the right. For dimensional reference, the two sets of elements are 44 meters from center to center. The Reference Microphones 1-3 (red) were placed on a 1.5-meter radius circle coincident with the geometric center of the element. Reference Microphone 4 was placed close to the center of the rosette systems. The green rectangle represents the data-acquisition hardware. For the second half of the deployment, the three microphones were moved to the rosette and the single reference to the hexagonal element. During the second half of the measurement period, two portable microbarometer systems were deployed near the center of the rosette pair. Results from those systems will be included in a later report. (Site diagram from P. Grenard.)

The reference microphones were installed on 19 May 2010 (Day 139) with recording started at 10:11 UTC. Data were recorded continuously until 27 May 2010 (Day 147) at 08:43 UTC for a total of about 190 hours. The first half of the deployment period was characterized by moderate to high gusty winds and periods of heavy rain; during the second half, the winds dropped somewhat but the periods of rain continued. Consequently, the reference-microphone data are often dominated by wind noise. There were, however, several periods of sufficiently calm winds that a response reconstruction could be performed.

Figure 2. Deployment of the three reference microphones on a 1.5-meter radius circle centered on the hexagonal element pair. The three microphones in their wind screens are to the right of the meteorological instrumentation tower and the data acquisition unit is at the base of that tower.

Figure 3. View from near the center of the hexagonal elements toward the rosette elements. The pad on which the four I99 elements are installed is clear of all vegetation. The forested area starts somewhat outside the fenced pad.

Basic Frequency Response Estimation

Periods with low winds were rare; however, there were quiet periods on both 25 May and 27 May in the early morning hours. The period used here was about 50 minutes long starting at 01:42 UTC on Day 145 (25 May). At this time, Microphones 1-3 were located at the center of the hexagonal element pair and Microphone 4 was located at the center of the rosette pair.

The I99 elements have the following general characteristics:

Type	Channel Designation	Overall Size	Number of Inlets
small rosette	V1-BFH	18 m	96
large rosette	V1-BFL	36 m	144
small hexagon	V2-BFH	18 m	72
large hexagon	V2-BFL	36 m	108

For response estimation, the averaged cross-spectral density between the relevant I99 element and the co-located microphone (or microphone combination) was calculated using 10-minute records overlapped by 50%. The averaged auto-spectra for the I99 element and for the reference channel were also calculated. From these spectral densities, the coherence was calculated and the response of the I99 element was calculated. The response calculation also depends on the laboratory calibration of the reference microphone system. Details of the response estimation procedure are available elsewhere.

When three microphones are used, their outputs are summed (in the time domain), which forms a virtual microphone with a phase center at the geometric center of the I99 element. When a single microphone is used, that microphone is placed as close as practical to the geometric center of the element. The issue of physical offset from the geometric center of the I99 element is only significant near the upper end of the frequency range; even there, the error from a one- to two-meter offset is small. The virtual microphone formed by the sum of three microphones does have a small degree of noise rejection compared to a single microphone.

The next eight figures show the magnitude and phase estimates for each of the four I99 elements. Those plots are coded by coherence value. The blue curve is the response estimate made regardless of the value of coherence. The red circles correspond to coherence greater than 0.9 and the black circles to coherence between 0.75 and 0.9. This coding gives some indication of the reliability of the results. The blue curve should be ignored; the red circles should be reliable estimates. The solid green curve is the expected response[1] of the MB2005 and digitizer anti-aliasing filter. Differences between the green curve and the red/black circles indicate either response deviations in the microbarometer system or effects of the wind-noise-reduction piping network. The effects of the piping network are expected to be most significant toward the higher frequencies.

[1] MB2005 response from the Martec CEA MB2005 User Manual, 14643-B January 2006, section 5.5.1.

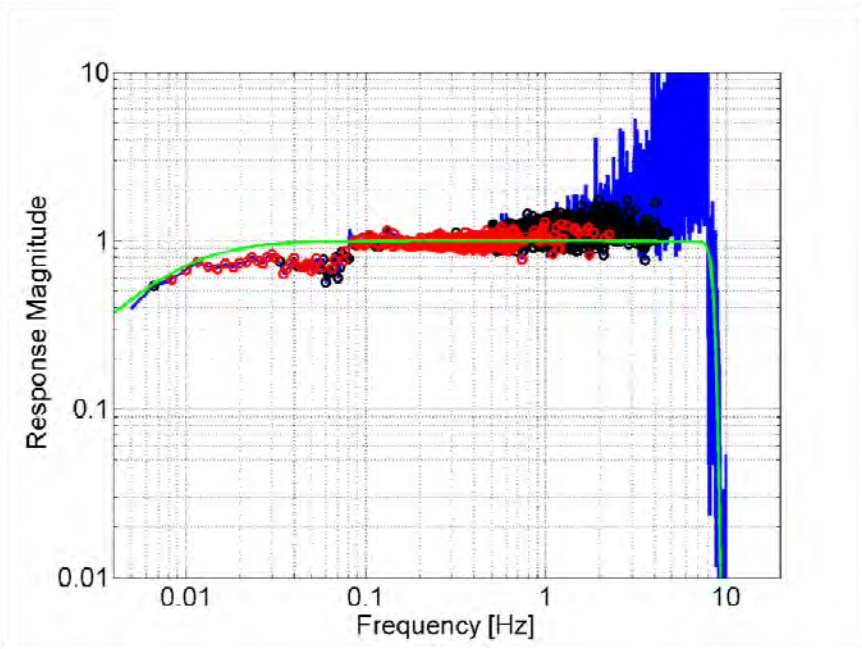

Figure 4. Magnitude response calculation for the large hexagonal element (V2-BFL). The calculation represents a 50-minute period starting at Day 145 01:42 UTC. The reference channel is the sum of Microphones 1, 2, and 3. The apparent offset in magnitude response that appears from 0.01 to 0.08 Hz is discussed in the text below.

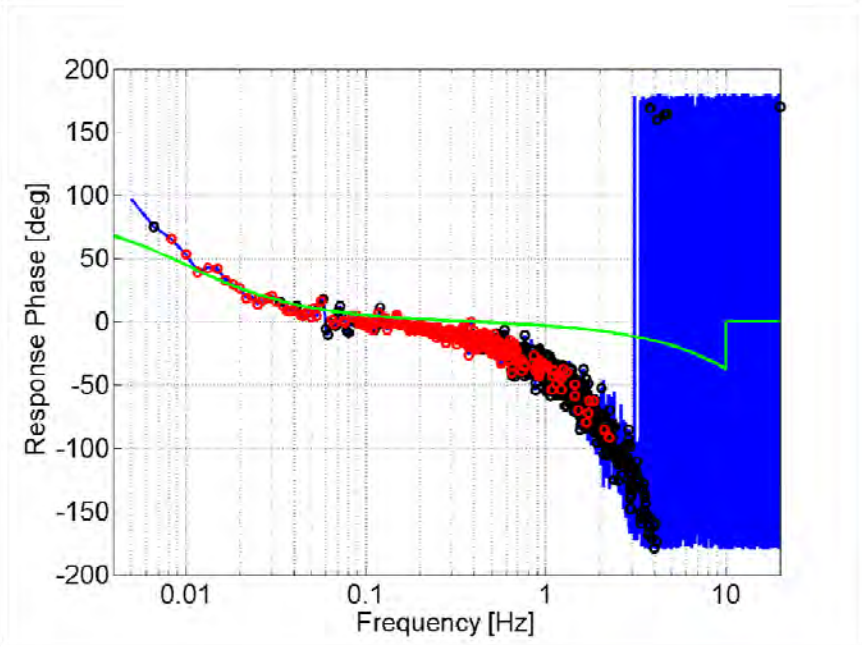

Figure 5. Phase response for the large hexagonal element (V2-BFL) corresponding to the magnitude plot above. The effects of the pipe network show up most clearly in the phase response as a departure from the MB2005 phase above 0.1 Hz. Notice that there is no offset in the phase in the 0.01 to 0.08 Hz region but there is an increase in the scatter near 0.08 Hz.

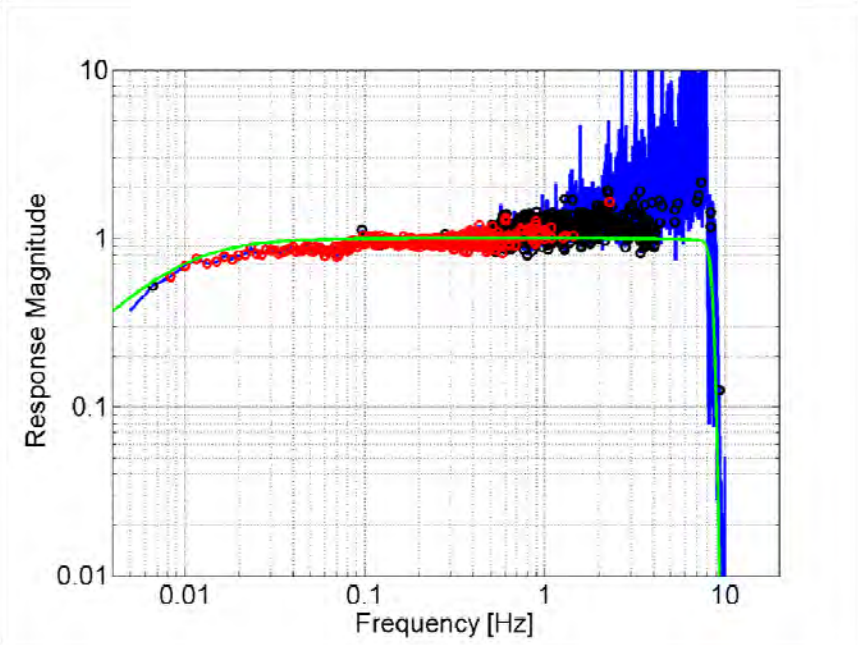

Figure 6. Magnitude response calculation for the small hexagonal element (V2-BFH). The calculation represents a 50-minute period starting at Day 145 01:42 UTC. The reference channel is the sum of Microphones 1, 2, and 3. Notice that the apparent offset in magnitude response below 0.08 Hz is considerably smaller than for the large element (V2-BFL).

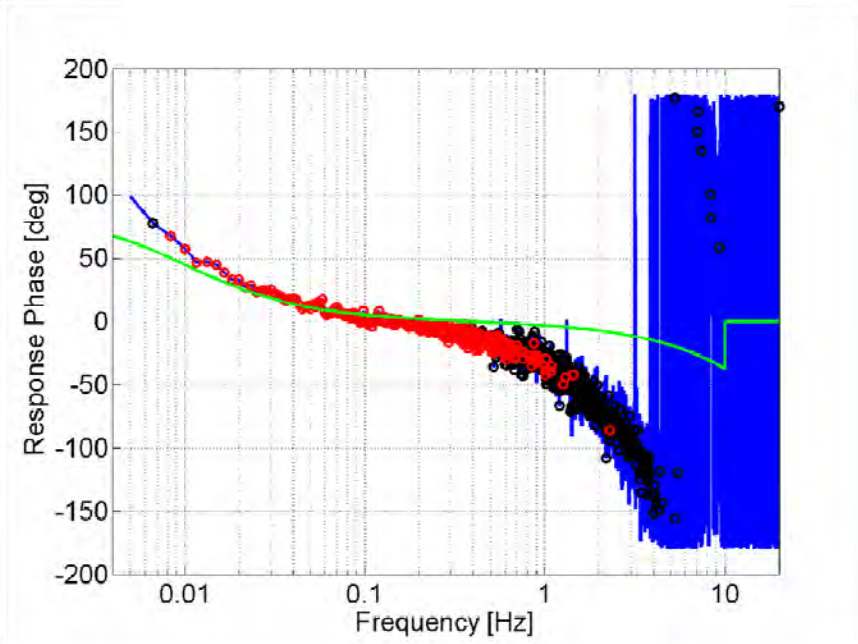

Figure 7. Phase response for the small hexagonal element (V2-BFH) corresponding to the magnitude plot above. The effects of the pipe network show up most clearly in the phase response as a departure from the MB2005 phase above 0.1 Hz.

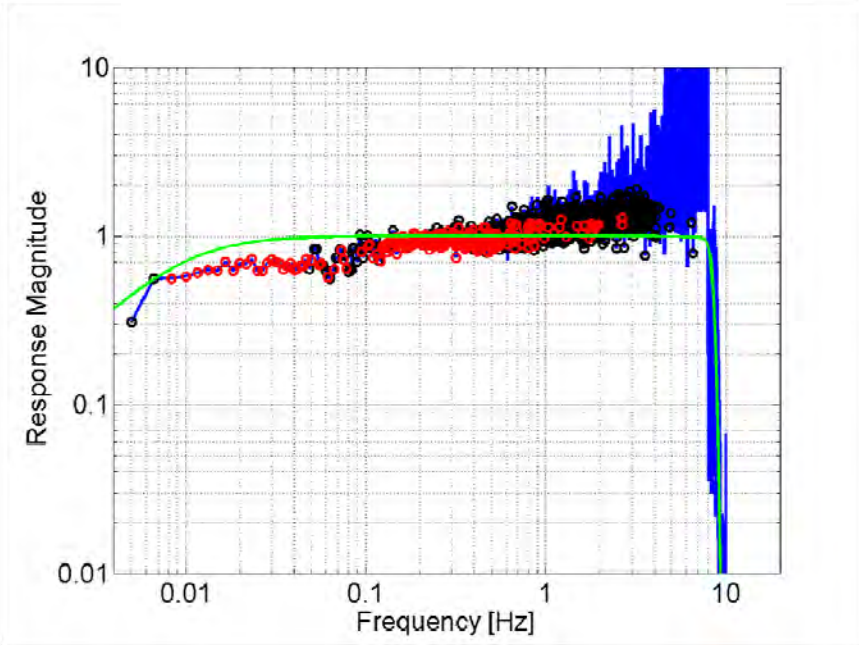

Figure 8. Magnitude response calculation for the large rosette element (V1-BFL). The calculation represents a 50-minute period starting at Day 145 01:42 UTC. The reference channel is Microphone 4. An apparent offset in magnitude response, similar to that for the large hexagonal element, appears in the 0.008 to 0.08 Hz range.

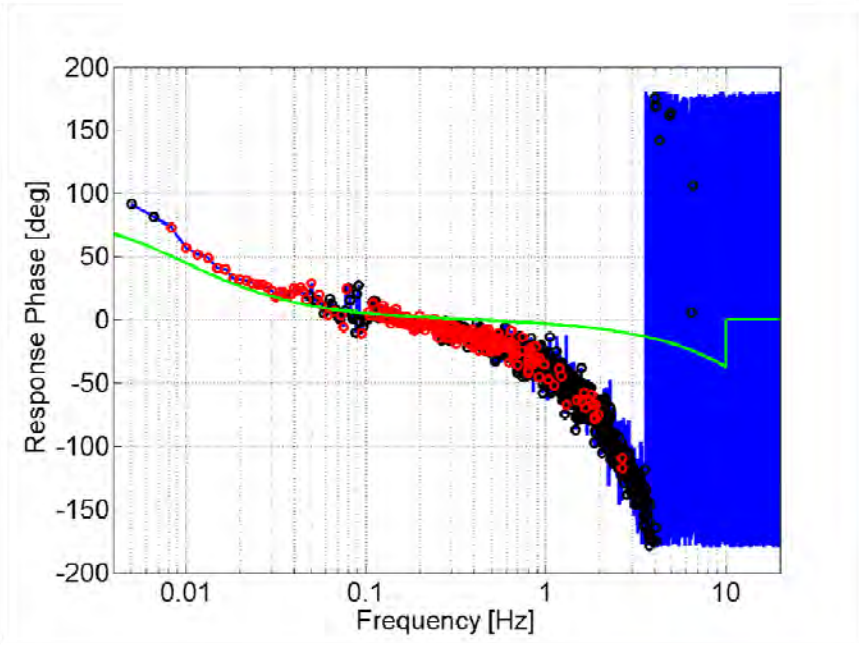

Figure 9. Phase response for the large rosette element (V1-BFL) corresponding to the magnitude plot above. Notice the increase in scatter near 0.08 Hz but the lack of an offset. The effects of the pipe network show up most clearly in the phase response as a departure from the MB2005 phase above 0.1 Hz.

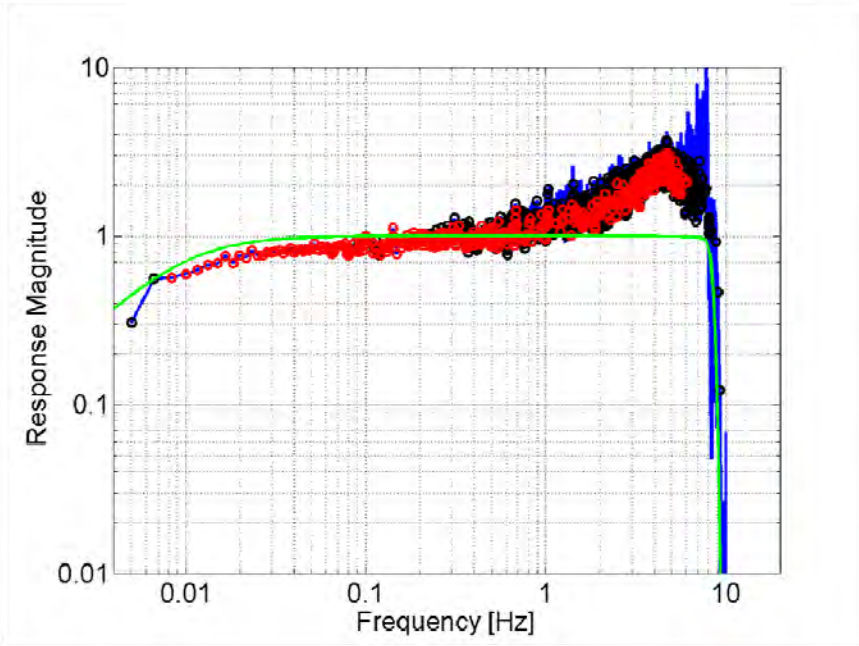

Figure 10. Magnitude response calculation for the small rosette element (V1-BFH). The calculation represents a 50-minute period starting at Day 145 01:42 UTC. The reference channel is Microphone 4. For this element, the magnitude response shows an increase at the high-frequency end that is characteristic of a resonance in the system.

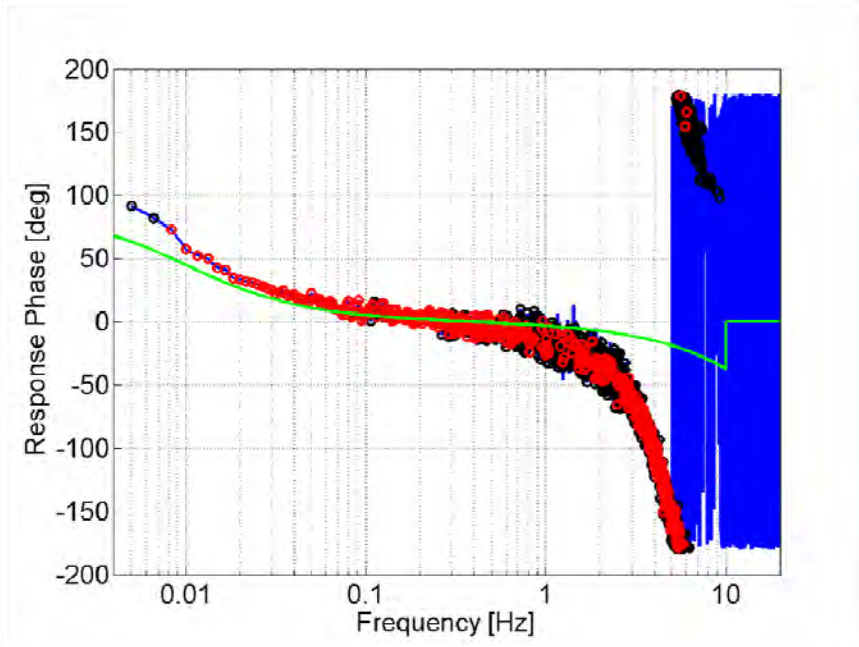

Figure 11. Phase response for the small rosette element (V1-BFH) corresponding to the magnitude plot above. The phase at higher frequencies is consistent with a resonance. Compared to the other phase plots, the phase departs more slowly above 0.1 Hz initially; however, the rate of change of phase at the highest valid frequencies is greater than for the other elements.

Influence of Non-Acoustic Pressure Fluctuations

Perhaps the most striking feature of the response estimates is the apparent jump in magnitude near 0.08 Hz for both of the 36-meter elements (with some suggestion of a smaller magnitude shift in the two 18-meter elements). In attempting to understand this behavior, it is important to identify the pressure field being sensed at different frequencies. The plot below is a typical coherence plot; the coherence is computed between the reference channel and the I99 element channel.

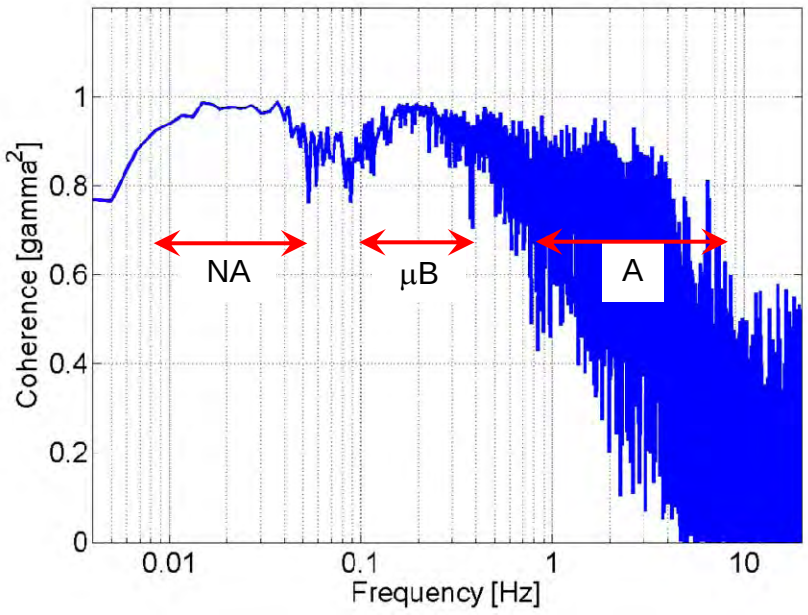

Figure 12. Coherence between the co-located reference microphone (Microphone 4) and the large rosette (V1-BFL). If the wind is low enough, the region between 0.1 and 0.4 Hz is often dominated by microbaroms (μB). Frequently, the region above the microbarom range is dominated by anthropogenic (A) sources of sound. At the I99 site, excitation above 1 Hz was generally weak. Although less well established, the region below 0.1 Hz may be dominated by non-acoustic (NA) pressure fluctuations advected past the sensor by wind.

The microbarometers and the reference microphones respond to pressure fluctuations regardless of their cause. Ideally, we would like to excite the systems with acoustic waves over the entire range of frequencies; however, this is not always possible. Certainly, when the wind is strong, the entire spectrum may be registering the passage of non-acoustic turbulence-related fluctuations. In this case, we would expect low coherence as long as the scale size of the turbulence is smaller than the wind-noise-reduction system.

Observations at a number of infrasound sites (including I99) suggest that there are several distinct regions of source mechanism across the spectrum. When winds are weak (or the system is well shielded by trees and undergrowth), the ambient background from about 0.1 Hz and above seems to be dominated by acoustic pressure fluctuations – microbaroms from 0.1 to 0.4 Hz, then various sources (typically anthropogenic) of acoustic waves above that.

Under exceptionally calm conditions, the region below 0.1 Hz may be the result of acoustic disturbances but it seems likely that in many cases, the ambient background below 0.1 Hz is the result of local non-acoustic pressure fluctuations. These non-acoustic fluctuations travel with the local wind rather than at the speed of sound.

Consequently, their effective "wavelength[2]" at a given frequency can be quite short and the area averaging of pipe-array networks can influence the apparent received level.

With respect to non-acoustic pressure fluctuations, then, the relationship of the scale size of these fluctuations to the dimensions of the sensor is critical. With a steady average wind, a pressure disturbance with large physical dimension would appear at a lower frequency than a disturbance with small physical dimension. We would expect the following:

(a) Below some frequency, the pressure disturbance "wavelength" would be larger than the pipe network and both the pipe system and the smaller reference microphone would respond in like manner with high coherence.

(b) Above that frequency, the spatial scale of the pressure fluctuation becomes smaller than the wind-noise-reduction pipe network but still larger than the reference microphone wind screen. Here, the pipe network samples both positive and negative phases of the pressure fluctuation and the apparent level at the microbarometer is reduced over that sensed by the reference microphone. The magnitude of the response of the element would appear to drop.

(c) At higher frequencies, the spatial scale of the pressure fluctuations would drop below the effective spacing of the inlets of the wind-noise-reduction network. The noise "gain" of the pipe network would reach its limiting value.

(d) Eventually, the spatial scale would drop below the size of the reference microphone wind screen and the reference microphone wind screen would start to average out (and, therefore, reduce) the fluctuations.

If wind noise dominates over the entire spectrum, then we would see low coherence over most of the spectrum; however, the coherence would still be high at frequencies sufficiently low that the pressure-fluctuation spatial scale was larger than the wind-noise-reduction pipe network. For example, Figure 13 below shows the coherence between the reference-microphone channel and one of the I99 elements during a period of moderate wind. Below 0.1 Hz, the coherence is high. If this region is dominated by non-acoustic pressure fluctuations, then the coherence should drop significantly if the reference microphone is displaced from the center of the I99 element. This drop in coherence is shown in Figure 14 for which Microphone 2, located 44 meters from the V1-BFH element center, is used as reference. The spatial scale[3] of non-acoustic disturbances below 0.1 Hz is smaller than the offset of the reference so the coherence drops. For an acoustic field below 0.1 Hz, the coherence would remain high even with the 44-meter offset in reference microphone.

[2] It is more conventional to describe the spatial scales in terms of wave number; however, wavelength is more intuitive in the context of area averaging. The wavelength is 2π divided by the wave number whether the disturbance is acoustic or not.

[3] To be precise: the coherence length.

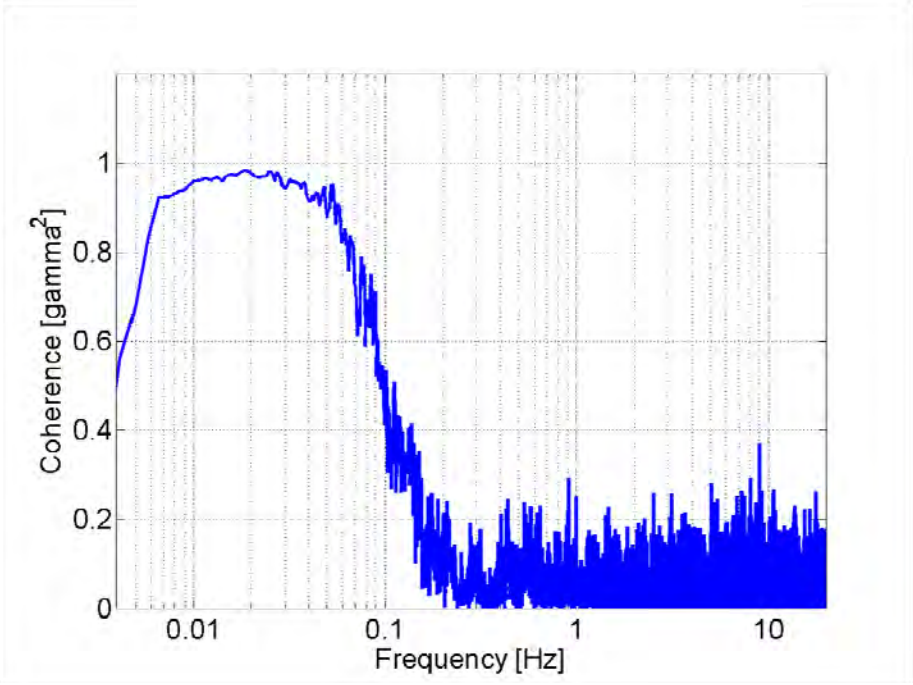

Figure 13. Coherence between the co-located reference microphone (Microphone 4) and the small rosette (V1-BFH) during a period of moderate wind. The coherence is still high below 0.07 Hz but is very low above 0.1 Hz.

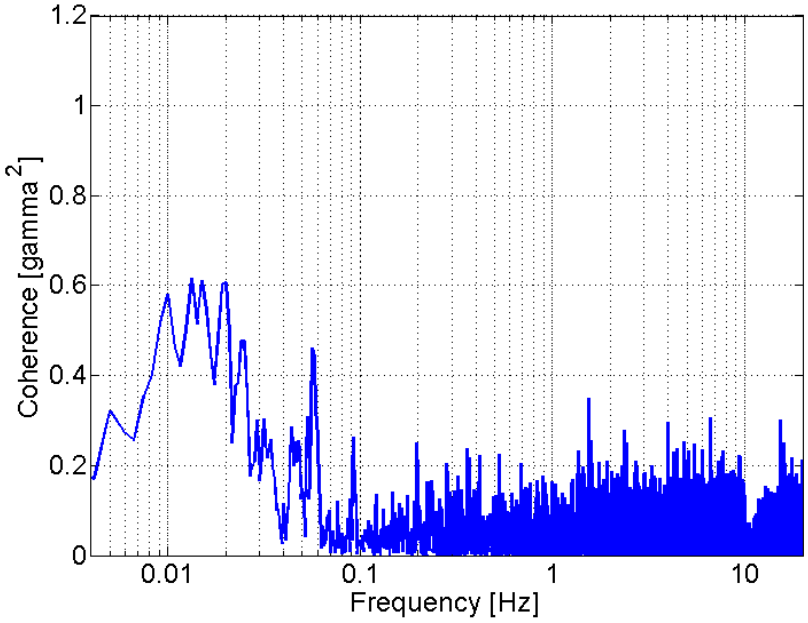

Figure 14. Coherence between a reference microphone (Microphone 2) 44 meters from the center of the small rosette and the small rosette (V1-BFH) during a period of moderate wind. The coherence is much lower below 0.1 Hz than that shown in Figure 13. If the ambient below 0.1 Hz was acoustic, the coherence would still be high.

Another approach for considering the impact of spatial scales of turbulence is an examination of the pressure spectral density. In the figure below, the pressure spectral densities of the small rosette (V1-BFH) and of the co-located reference microphone are shown.

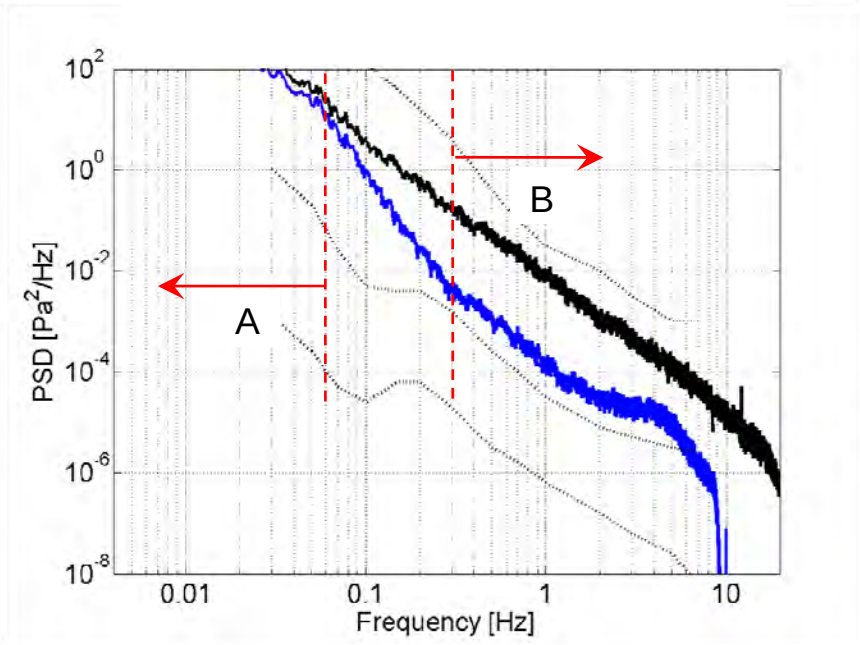

Figure 15. Pressure spectral densities for the small rosette (blue) and for the co-located reference microphone (black) for the same windy period as for Figures 13 and 14. Below 0.06 Hz (A), the spectra are nearly identical; from 0.3 to 2 Hz (B), the spectra are parallel.

Notice at the lowest frequencies that the spectral densities for the reference microphone and for the I99 element are nearly the same. In this example, below about 0.06 Hz, the scale sizes of the non-acoustic pressure fluctuations are large enough that the small rosette is too small to be effective in area averaging those fluctuations. When that happens, the single reference microphone and the extended-area rosette produce virtually the same result. Above 0.06 Hz, the turbulence scale size drops below the overall size of the rosette and the rosette spectral density starts to drop below that of the reference microphone – the result of averaging over the rosette's spatial extent. Once the scale size of the turbulence drops below the effective inlet spacing[4] of the rosette, the area averaging reaches its maximum value and the rosette spectrum parallels the microphone spectrum. For this example, this occurs at about 0.3 Hz.

If the scale-size argument is valid, then the large rosette would maintain area averaging to lower frequency (perhaps a factor of two lower – 0.03 Hz – if the averaging scales directly with overall dimension) than the small rosette. Figure 16 – comparable to Figure 15 but for the large rosette – shows that this may be the case. Figure 16 also shows the additional degree of inlet averaging (as evidenced by the larger difference in levels) above 0.3 Hz associated with the larger number of inlets in the large rosette (144 compared to 96).

[4] For a non-uniform inlet distribution, there is some question as to the appropriate value for the "effective" inlet spacing.

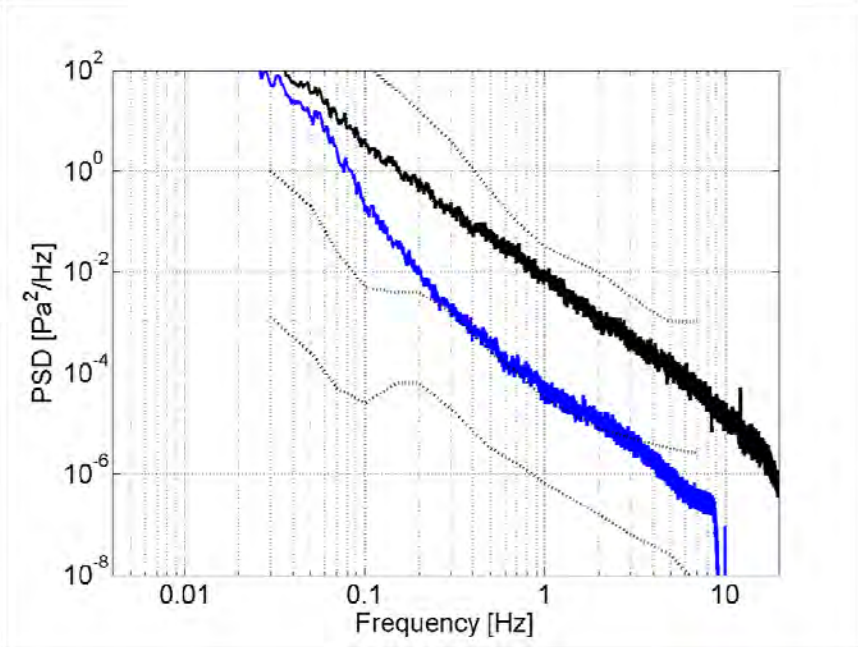

Figure 16. Pressure spectral densities for the large rosette (blue) and for the co-located reference microphone (black) for the same windy period as for Figure 15. Notice that the blue curve is lower for the large rosette than for the small rosette in the region where it parallels the single-microphone spectrum. Further, notice that the blue curve approaches the black curve at a lower frequency than for the small rosette.

If it is true (for these measurements) that the source mechanism below 0.1 Hz is non-acoustic pressure fluctuation, then the apparent frequency response of the I99 element would be affected. In that case, we would see the actual MB2005 response at the very lowest frequencies since, for those frequencies, the scale size of the fluctuations is larger than the pipe array. As the frequency increases, the scale size of the fluctuations decreases (assuming roughly constant average wind) and, at some point, the extended pipe array starts to average over positive and negative fluctuations. This would appear as a decrease in the magnitude of the response; however, the basic response of the MB2005 is still increasing toward its "mid-band" value; therefore, the net effect is a roughly flat response somewhat below the expected acoustic response.

Once the frequency has increased to the point where microbaroms start to dominate, the dominant source mechanism becomes acoustic, the wavelength is very large compared to the pipe array, and there is no longer any reduction in response from averaging over the much shorter "wavelength" non-acoustic fluctuations. In the frequency response reconstruction, this would appear as a jump in the response magnitude. That jump should be larger for the larger pipe arrays (since the onset of area averaging occurs at a lower frequency for the larger systems) and that is, in fact, what appears when comparing Figure 4 to Figure 6 or Figure 8 to Figure 10.

The actual acoustic response is correctly estimated when the source mechanism is acoustic or when the scale of the non-acoustic fluctuations is so large that the responses of the extended pipe array and the single microphone (or virtual microphone) are equivalent.

Figure 4 above illustrates this the most clearly. At the lowest frequencies, the estimated response is very close to the expected MB2005 low-end response. Above the "jump" in magnitude response at 0.08 Hz, the response is, again, close to the expected mid-band response. In the region between 0.01 and 0.08 Hz, the competing effects of area averaging by the extended pipe array and the low-frequency roll-off of the MB2005 produce a relatively flat response that is about 20% lower than the expected mid-band response.

It is important to recognize that the measured *phase* response is not affected by area averaging of non-acoustic fluctuations. The phase response does not reflect any noticeable discontinuity at the same frequency as the magnitude jump. This is one of the most compelling arguments that the magnitude jump is not a "real" jump in the

acoustic response of the system. If the actual acoustic response showed a jump in magnitude, causality would require a corresponding change in the phase response. In this case, *the magnitude jump reflects a difference in the structure of the field external to the pipe array*. However, because the phase centers of the reference microphone and of the I99 element are coincident, the phase response is estimated accurately.

In fact, from observations at a number of sites, the phase appears to be a more reliable estimator of true acoustic response than the magnitude. In addition to the bias associated with area averaging of non-acoustic fluctuations, the magnitude estimate can be biased by incoherent noise whereas incoherent noise only increases the scatter of the phase estimate without introducing a bias. Consequently, the phase can be used to guide reconstruction of the actual acoustic response.

We can gain further insight into the impact of scale size by exploiting the co-location of two pipe arrays of different size. If the pressure field below 0.1 Hz is predominantly non-acoustic pressure fluctuations with small "wavelength" (i.e., large wave number), then the larger of the two pipe systems should appear to drop somewhat in response compared to the smaller system from the lowest frequencies up toward 0.1 Hz. Figure 17 below was constructed by taking the smaller of the two pipe systems as the reference and calculating the response of the larger array relative to the smaller one. For acoustic waves, the relative response should be one at all frequencies. Notice, however, that below 0.1 Hz, we see a drop in response that is consistent with the onset of area averaging for the larger system at a lower frequency than for the smaller system.

For both the rosette-to-rosette comparison and for the hexagonal-to-hexagonal comparison, the coherence shows a dip just below 0.1 Hz that is consistent with a change in the nature of the pressure field from non-acoustic pressure fluctuations below 0.1 Hz to microbaroms above 0.1 Hz. At the lowest frequencies and above 0.1 Hz, the relative magnitude of the response is one for both pairs of pipe arrays. (Also, notice that, above 1 Hz, the relative response for the rosette systems shows the difference in high-frequency response illustrated explicitly in Figure 10.) The high coherence above 10 Hz is an artifact introduced by the up-sampling process[5] applied to the element data.

[5] The reference microphone signal is sampled at 250 samples per second and the I99 element signal is sampled at 20 samples per second. In order to characterize the element response through the anti-alias filter roll-off at 8 to 10 Hz, the data are processed at 50 samples per second. The reference signal is down-sampled and the element signal is up-sampled so that their sample rates match.

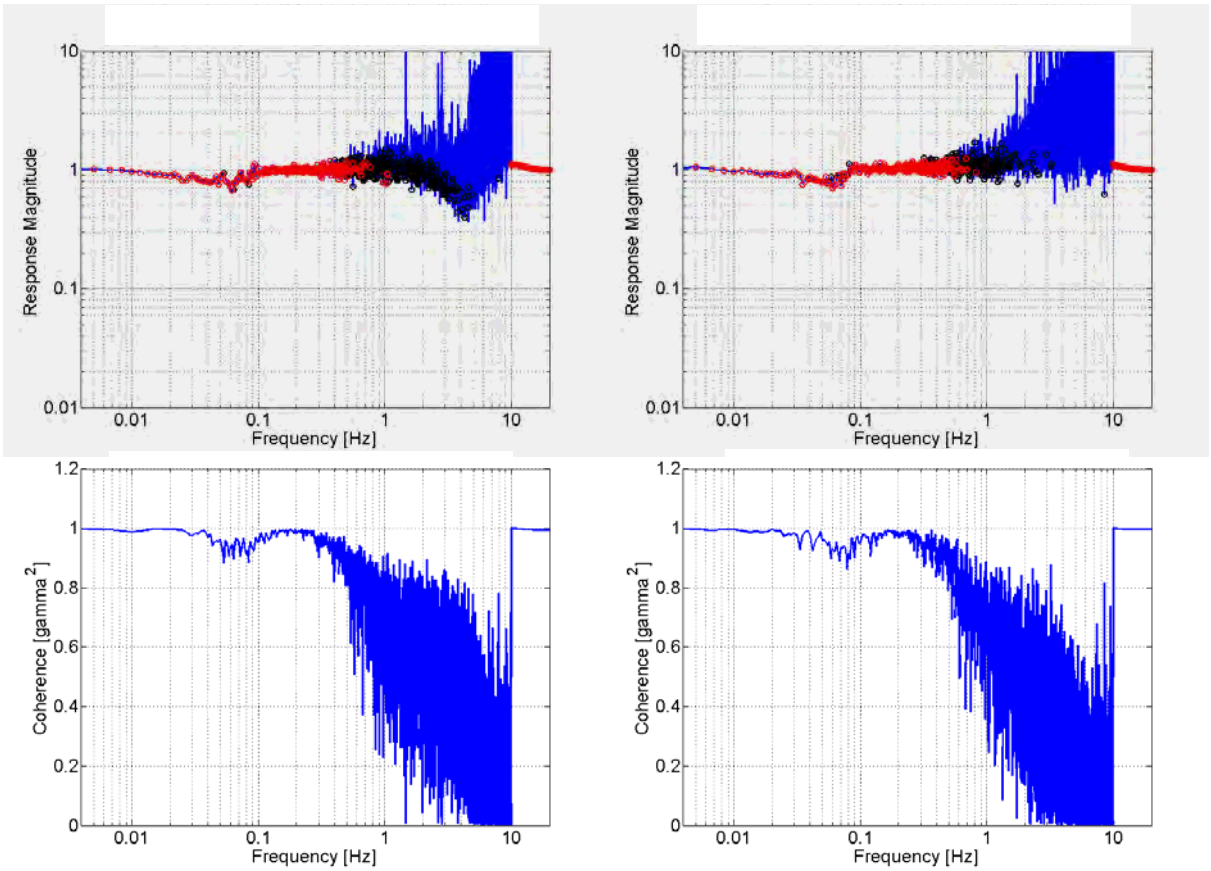

Figure 17. Magnitude response reconstructions for the larger pipe arrays using the corresponding smaller pipe array as the reference. Upper left: magnitude response of V1-BFL relative to V1-BFH; lower left: corresponding coherence; upper right: magnitude response of V2-BFL relative to V2-BFH; lower right: corresponding coherence. (The high coherence above 10 Hz is an artifact introduced by the up-sampling of the original data.)

Extended Low-Frequency Response Estimation

If these speculative conclusions regarding non-acoustic fluctuations are valid, then the very lowest frequency response can be determined even in windy conditions. To illustrate, we can take a long period (12 hours) during relatively strong winds, average using longer records (4800 seconds), and concentrate on the low-frequency response. This was done for the small hexagonal element in the figures below. Figure 18 shows the coherence; Figure 19 and Figure 20 give the magnitude and phase response. Even though this period is much "noisier" than the period selected for the response estimates in Figures 4-10, the low-frequency results compare closely with the corresponding results in Figures 6 and 7.

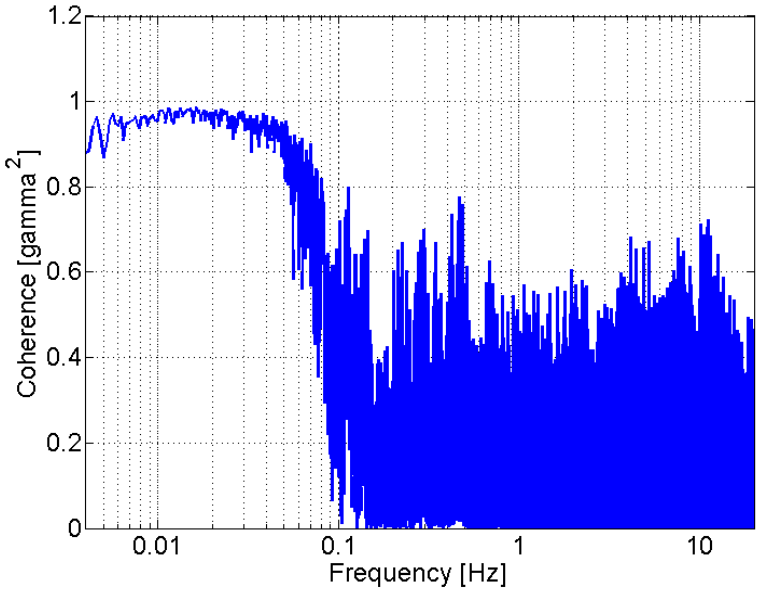

Figure 18. Coherence between the small hexagonal element and the virtual reference microphone for a 12-hour period of moderate winds. The record length is lengthened to 80 minutes in order to better resolve the lower frequencies. The coherence is greater than 0.9 from 0.006 to 0.05 Hz.

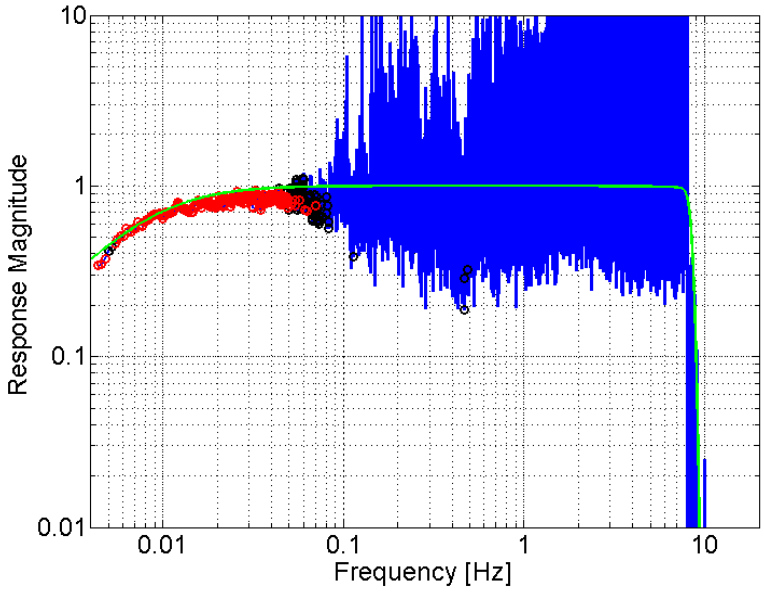

Figure 19. Magnitude response reconstruction for the small hexagonal element for low frequencies. Compare this result to the corresponding result in Figure 6.

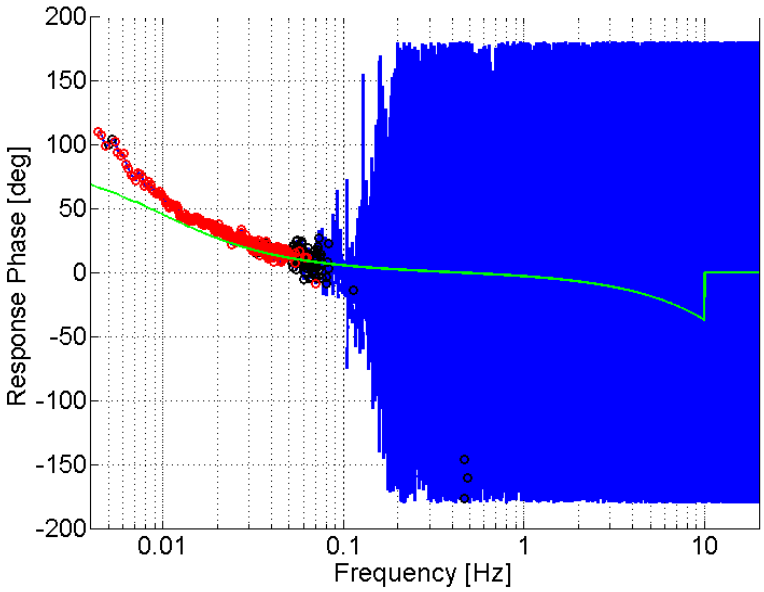

Figure 20. Phase response reconstruction for the small hexagonal element for low frequencies. The departure from the expected MB2005 response (green) at the lowest frequencies suggests the presence of another pole in the low-frequency response. Compare to Figure 7.

Element-to-Element Comparisons

An examination of the pressure spectral densities for all four I99 elements is worthwhile. One-hour averaged (100-second records) spectra were generated for every hour of the measurement period. The figure below is typical of those results. Below 0.1 Hz, the spectral density seems directly related to the overall size of the array with the two 18-meter arrays giving about the same levels and the two 36-meter arrays giving about the same levels. Above 0.1 Hz, the effects of averaging over the inlet geometry control the spectral shape.

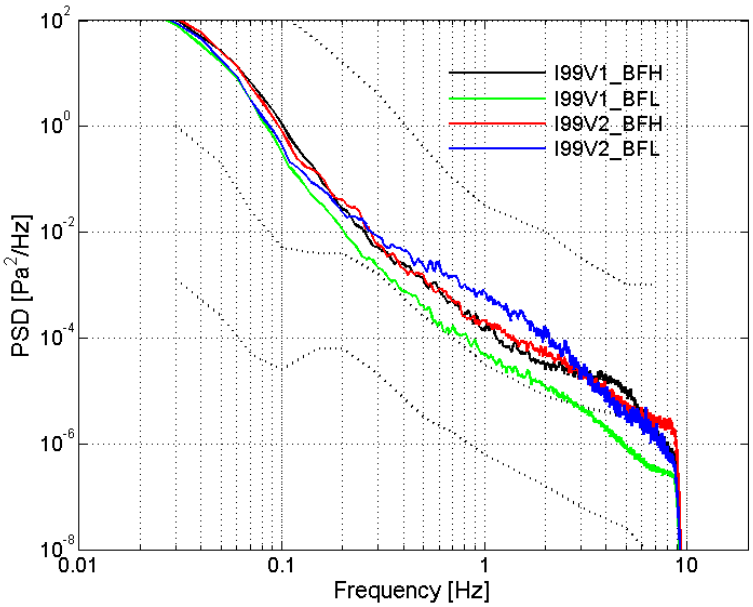

Figure 21. Pressure spectral densities from the four I99 elements. The period of 6 hours starting at 00:00 UTC on 21 May (Day 141) was a period of strong and gusty wind as evidenced by the levels shown here. The four elements are: 18-meter rosette (V1-BFH, 96 inlets), 36-meter rosette (V1-BFL, 144 inlets), 18-meter hexagonal (V2-BFH, 72 inlets), and 36-meter hexagonal (V2-BFL, 108 inlets). The dotted black lines are low-, medium-, and high-noise averages from many IMS arrays (Bowman, Baker, and Bahavar, 2005). Compare this plot to Figure A-1 in Appendix A for an example of much lower wind conditions.

A surprising result is that the highest spectral levels above 0.3 Hz belong consistently to the *larger* hexagonal array. This may suggest a problem in the large hexagonal array or it may be associated with the specific inlet geometry. We can synthesize another array by combining the large and small hexagonal array outputs (as a time-domain average weighted by the number of inlets in the two "sub-arrays"). This synthetic array has a more uniform distribution of inlets than the large hexagonal array – the large array has a void in the center (see Figure 1).

As Figure 22 shows, the synthetic array (with 180 inlets) produces a spectral density generally as low as or lower than either the small or large hexagonal array. This suggests that there is no fault in the large hexagon but, rather, that the spectral levels depend in a more complicated manner on the geometry of the inlet distribution than a simplistic N-inlet average suggests.

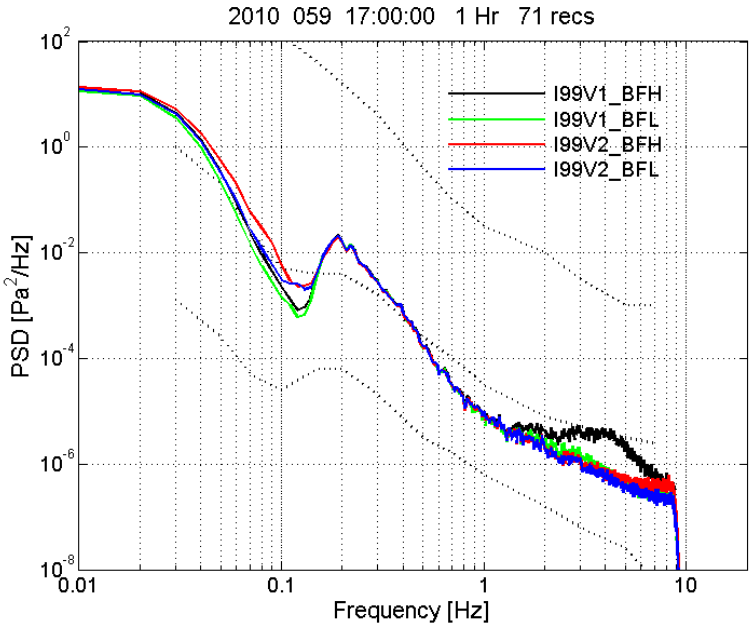

Figure 22. Pressure spectral densities for the four elements at I99 for a period of relatively low wind from 01 March 2010. Compare this to Figure 21 in the text. Notice that the small rosette (V1-BFH) appears to have a higher response above 1 Hz than the other elements. Notice also how closely matched the elements are from 0.13 to 1.2 Hz and the divergence below 0.13 Hz. This further supports the hypothesis that the region below 0.1 Hz is non-acoustic even for low-wind conditions.

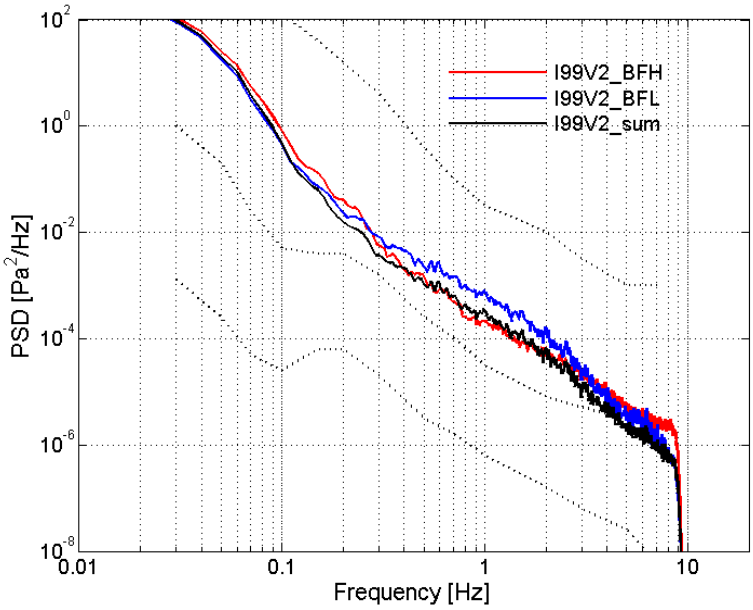

Figure 23. Pressure spectral densities from the two hexagonal I99 elements and a synthetic array formed by an inlet-weighted sum. The time period and averaging are the same as in Figure 21. (Notice that the black curve represents the combination element here but, in Figure 21, black represents the small rosette.)

CONCLUSIONS

The preliminary results of this work can be summarized as follows:

- Reasonable estimates for the magnitude and phase response of all four infrasound elements at I99 were made from 0.008 Hz to several hertz. The scatter in the results is higher than typical for similar measurements at more sheltered sites.
- For all four elements, from 0.01 to 0.1 Hz, the measured magnitude and phase correspond closely to the manufacturer's specifications for the MB2005. Above 1 Hz, the effects of the pipe system produce a significant change in the phase response compared to the MB2005. Below 0.01 Hz, the phase also changes somewhat faster than expected (as if there is another pole at very low frequency in the system).
- Resonance suppressors are installed in all four elements; however, both the magnitude and phase response of the small rosette element show indications of an incompletely suppressed resonance above a few hertz.
- A preliminary investigation of the effects of non-acoustic turbulence and the associated scale sizes was performed and an apparent drop in the magnitude response of the larger elements below 0.08 Hz was tentatively associated with area-averaging of non-acoustic pressure fluctuations.
- Non-acoustic fluctuations may be useful for determining element response at very low frequency – below 0.05 Hz – even in windy conditions.
- The effects of inlet distribution particularly for the large hexagonal element appear to be more complicated than simple incoherent summation of isotropic turbulence: in windy conditions, the large hexagonal element showed higher spectral levels from 0.2 to 3 Hz than the small element but a virtual element formed by coherent summation of the large and small hexagons showed levels more consistent with expectations.
- Aside from the caveat above, the wind-noise-reduction performance of the various elements seems consistent with a model based on overall dimension for the lower frequencies and on inlet density for the middle frequencies.

ACKNOWLEDGEMENTS

These measurements would not have been possible without the support of Patrick Grenard, Ekrem Demirovic, Pavel Martysevich, Viatcheslav Bereza, Reinhard Jelinek, and Eva Graham of the CTBTO/PTS and Norbert Blaumoser of the ZAMG (Conrad Observatory). The CTBTO provided the travel and living expenses and the US Army Space and Missile Defense Command provided the salary support.

REFERENCES

Bowman, J. R., G. E. Baker, and M. Bahavar (2005). Ambient infrasound noise, *Geophys. Res. Lett*. 32: L09803.

ADVANCEMENT OF TECHNIQUES FOR MODELING THE EFFECTS OF ATMOSPHERIC GRAVITY-WAVE-INDUCED INHOMOGENEITIES ON INFRASOUND PROPAGATION

Robert G. Gibson[1], Douglas P. Drob[2], David Broutman[2] and Nathan W. Winslow[1]

BBN Technologies[1] and Naval Research Laboratory[2]

Sponsored by National Nuclear Security Administration

Award Nos. DE-AC52-08NA28652[1] and DE-AI52-08NA28653[2]
Proposal No. BAA08-05

ABSTRACT

Propagation studies of a growing number of infrasound observations indicate that fine-scale atmospheric inhomogeneities contribute to infrasonic arrivals that are not predicted by standard modeling techniques. In particular, gravity waves, or buoyancy waves, are believed to contribute to the multipath nature of infrasound propagation and to cause penetration of infrasound into the classical shadow zones that are predicted by conventional modeling techniques. Propagation modeling studies using basic parameterizations of gravity wave spectra suggest that gravity waves represent the primary component of fine-scale atmospheric inhomogeneity that affects infrasonic arrivals at regional ranges.

The influence of atmospheric gravity waves on the upper and middle atmosphere provides a significant source of uncertainty in atmospheric specifications. A large fraction of the gravity wave spectrum in operational numerical weather prediction models is either filtered out during the data assimilation process or else not resolved by the models. Prior approaches to modeling infrasound through gravity waves have relied on one-dimensional vertical wavenumber spectral models of gravity waves; this simplified model approach captures the vertical spatial scales in gravity waves as a function of height. Our recent research has developed improved resolution of these wave fields through more sophisticated computational techniques to achieve more complete spectral parameterization.

Atmospheric specification techniques have been developed that incorporate realistic models of gravity waves that are self-consistent with the background flow field and that include effects of altitude, range-dependence, and time-dependence over relevant scales. One shortcoming of prior gravity wave field models recently used with infrasound propagation models is that they ignore the typically strong refraction of the background gravity waves by variations in the mean winds and mean stratification above 15 km. These limitations are addressed in this research by including the refraction effects of the gravity wave field by the background atmosphere as defined by the Naval Research Laboratory-ground-to-space (NRL-G2S) semi-empirical specification. A local atmospheric gravity wave field is represented using the summation of vertical eigenfunctions approximated by a computationally efficient Fourier-space ray-tracing technique. Using this methodology, wave perturbation fields (horizontal wind components, pressure, density, and temperature) are calculated that are self-consistent with the background atmospheric flow.

Broadband, full-wave infrasound predictions computed using the parabolic equation (PE) method are used to model atmospheric infrasound from explosions at ranges of 100s to 1000s of km. Model predictions using the PE method are conducted using range-dependent specifications of the atmospheric wind and temperature from NRL-G2S that are modified by the addition of perturbation terms representing the gravity wave field, in order to characterize the fine-scale atmospheric structure not resolved by numerical weather prediction models. Synthesized infrasound waveforms, obtained using the Fourier-synthesis time-domain PE method, are compared with observed infrasound signals from ground-truth events in order to evaluate the modeling capabilities.

OBJECTIVES

The objective of this research effort is to improve understanding of the effects of gravity waves and other fine-scale atmospheric inhomogeneities on infrasound propagation. The improved understanding of the relevant atmospheric and infrasonic physics will result in enhanced capabilities for modeling infrasound features and waveforms.

It is evident that existing propagation modeling, coupled with state-of-the-art atmospheric characterizations, fails to adequately predict infrasonic arrivals in certain circumstances. In particular, there have been numerous events for which infrasound arrivals are observed by sensors in regions that are predicted by standard modeling techniques to be in zones of silence (e.g., Bhattacharyya et al., 2003; Kulichkov, 2004; Mutschlecner and Whitaker, 2006). This issue is relevant over both local and regional ranges. Recent scientific work in gravity waves, long-range acoustic propagation, and infrasound has indicated that fine-scale atmospheric inhomogeneities contribute to unexpected infrasonic arrivals. We address this issue through systematic evaluation of the relevant atmospheric phenomena, advancement of the state of the art of modeling the interactions between infrasound and fine-scale atmospheric inhomogeneities such as gravity waves, improved atmospheric specification, and model validation.

Specifically, the objectives are as follows:

- Review recent scientific progress in the understanding of gravity waves, their temporal and spatial variability, and their statistics, in order to develop an improved model of the characteristics of gravity waves that are relevant to infrasound propagation.
- Develop atmospheric specification techniques that incorporate realistic models of gravity waves in a manner that maintains self-consistency with the background flow field and that includes effects of latitude, longitude, and time-evolution over relevant scales.
- Exercise the improved gravity wave models with infrasound propagation models. Examine variability of infrasound predictions over a statistical ensemble of gravity wave realizations. Perform sensitivity studies to establish the effects of key atmospheric model variables on infrasound prediction.
- Perform model validation studies using ground truth datasets, focusing on local and regional ranges.

The effort is anticipated to increase understanding of the regional and local propagation of infrasound through the dynamic atmosphere and also to improve the capability to predict infrasound arrivals and features relevant to phase classification. Research results include spectral-based atmospheric variability specifications; numerical modeling subroutines that enable improved propagation modeling via incorporation of effects of gravity waves and related fine-scale atmospheric structure phenomena; and model/data comparisons.

RESEARCH ACCOMPLISHED

Atmospheric Specification

The atmospheric structure responsible for the propagation of infrasound can change rapidly. Global climatological models have largely been replaced in current infrasound modeling practice by the NRL G2S model of Drob et al. (2003) and Drob (2004), which was developed to provide background atmospheric information for the Nuclear Explosion Monitoring Research and Development program. The G2S data processing system combines operational numerical weather prediction (NWP) specifications with the upper atmospheric empirical models, NRLMSISE-00 and HWM-93 (Picone et al., 2002; Hedin et al., 1996). The near-real-time system incorporates 1ºx1º and 1ºx1.25º resolution global NWP input fields to the nearest 6-hour interval in the lower atmosphere. The HWM-93 model was recently upgraded to HWM-07 by Drob et al. (2008) via the assimilation of recent upper atmospheric research satellite-based measurements and ground-based measurements.

However, these specifications are unable to resolve all fine-scale stochastic phenomena, e.g., atmospheric irregularities smaller than the model resolution, fine-scale structures above 35 km, and gravity wave fluctuations that cannot be deterministically measured or internally generated by the model. Fine-scale atmospheric structure not characterized by near-real-time atmospheric models such as G2S has been identified as a likely source of refraction, advection and scattering effects that may play a significant role in infrasound propagation. In particular, gravity waves are of interest because their spatial scales are of the same order as infrasonic wavelengths. Gravity waves result from oscillations of air parcels displaced by buoyancy and restored by gravity. The oscillations have time scales ranging from minutes to tens of hours. Vertical length scales of gravity waves are in the range of 0.1 to 15 km, and horizontal scales can span from 10 to 1,000 km. The multi-scale nature of gravity waves presents a

challenge to quantification of their properties. Owing to the important influences of gravity waves on the atmosphere's general circulation, vertical structure, and spatiotemporal variability, gravity wave dynamics is a significant atmospheric science research topic area. Recent research progress includes a better understanding of gravity wave source characteristics and evolution with altitude due to changes in wind conditions and atmospheric stability (e.g., Fritts and Alexander, 2003). The development of high-fidelity physically-based gravity wave parameterizations is an active research area.

BBN has previously developed a baseline wind variability model (Norris and Gibson, 2002; Gibson, et al., 2008) for predicting infrasound deviations due to atmospheric effects that are not resolved by the existing atmospheric specifications. The basic variability model uses a power-law wind perturbation spectrum based on the spectral gravity wave model of Gardner (1995, 1993) and generates realizations of horizontal wind perturbation profiles due to gravity waves. A source spectrum is defined near the ground, and as the wave spectrum is propagated up in height, attenuation is modeled by introduction of diffusive damping. Therefore, height-dependent gravity wave dependencies are modeled. Range-dependent effects can be approximated by selecting a dominant horizontal correlation length and combining wind perturbation profiles using Gaussian weighting functions.

Approaches to Improved Gravity Wave Modeling

As discussed above, baseline approaches to modeling infrasound through gravity waves have relied primarily on one-dimensional vertical wavenumber spectral models. This simplified model approach captures the vertical spatial scales in gravity waves as a function of height. During this research effort we have extended this capability by accounting for additional dimensional variability, including horizontal wavenumber. Furthermore, we have extended the capability of the spectral model by allowing input parameters to vary to account for spatial and temporal dependencies. For example, model parameters may be quantified based on latitude and Julian day, whereas the baseline implementation of the Gardner model does not account for the fact that gravity wave fields can vary dramatically with altitude, latitude, and season (e.g., Eckermann, 1995).

The technical approach to the improved gravity wave model has been discussed in Gibson et al. (2009). The modeling technique accounts for the typically strong refraction of gravity waves by variations in the mean winds and the mean stratification above 15 km. The refraction effects of the gravity wave field are calculated using the background atmosphere as defined by the G2S specification. This approach accounts for spatial and temporal variability by defining gravity wave fields based on the background atmospheric temperature and wind profiles. Using this methodology, wave perturbation fields are calculated that are self-consistent with the background atmospheric flow. As described in Gibson et al. (2009), the formulation involves ray tracing in Fourier space, in a way that efficiently approximates the vertical eigenfunctions for a given background. The ray solutions are then Fourier synthesized to give the spatial solution. Since wave phases are also computed, a wide range of problems can be considered, from deterministic mountain waves, to semi-deterministic gravity waves generated by convection, to fully random wave fields. Additional theoretical details of the Fourier gravity wave ray tracing method implemented here are presented in Broutman et al. (2003, 2006, and 2009).

The stochastic gravity wave field is calculated using a realistic gravity wave spectrum based on Warner and McIntyre (2001). Wave fields are typically calculated for altitudes up to 150 km. Integration is typically performed over a range of source frequencies from 2**f* to N/$\sqrt{5}$, where *f* is the Coriolis frequency and N is the Brunt-Vaisala frequency. The model includes gravity wave propagation effects of: multiple reflections at turning points; Airy function amplitude approximation at caustics; critical layer filtering; wave field saturation; anelastic amplitude scaling in the dispersion relationship; and dissipation by molecular viscosity in the lower thermosphere. Heuristics have been included to limit horizontal phase velocities to less than 90 m/s as suggested by observation. There are readily tunable free parameters for: source altitude and average source region wave variance; control of the horizontal extent and resolution of the model domain; and arbitrary number of spectral frequencies. We have also begun to systematically examine the numerical parameter space for the source spectrum shape constants, empirical wave amplitude normalization scale factors, and the optimal source spectrum seeding altitude.

An example below (Figure 1) presents and compares two representative sets of atmospheric profiles that include gravity wave perturbation fields computed for regional scenarios. Each gravity wave field is self-consistent with the G2S background atmosphere. Specifically, the figure shows wind profiles, perturbed by gravity wave fields, computed for events with two seasonally different background wind field characteristics. The panel on the left

shows the zonal and meridional wind profiles corresponding to the Ghislenghien, Belgium gas pipe explosion event on 30-July-2004. The panel on the right shows the wind profiles in the vicinity of the Gerdec, Albania ammunition explosion event, which occurred on 15-April-2008. These examples highlight the seasonal and latitudinal dependence of the newly developed stochastic gravity wave field fluctuation model as compared to the time- and space-independent gravity wave perturbation model that exists in BBN's current baseline implementation.

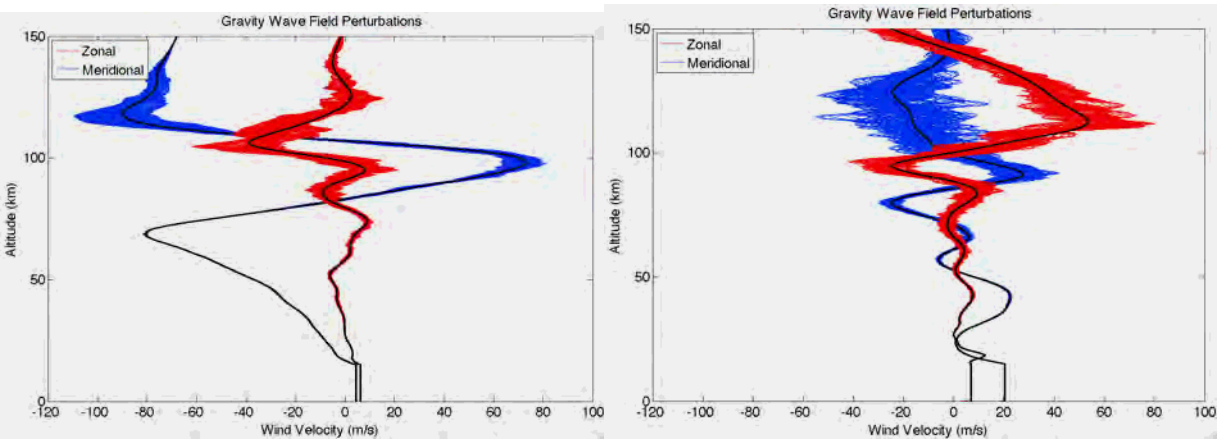

Figure 1. Zonal and meridional wind profiles, including gravity wave perturbations, for two scenarios: the Ghislenghien, Belgium event [50.6566 N, 3.879 E], which occurred on 07/30/2004 at approximately 07:00 UT (left panel); and the Gerdec, Albania event [41.394 N, 19.655 E], which occurred on 04/15/2008 at approximately 11:00 UT (right panel).

Research has included tuning gravity wave model results to published observational datasets. This enables an improved capability to define the recommended range of values for the free model parameters over a range of latitudes and seasons. Examples of seasonal, latitudinal, and altitudinal dependence of the gravity wave perturbations are shown in Figures 2 and 3. Figure 2 shows seasonal variation of the standard deviation of the zonal wind component of the gravity wave perturbation profile at fixed latitude. Figure 3 shows latitudinal variation of the standard deviation of the meridional wind component of the gravity wave perturbation profile for a fixed date.

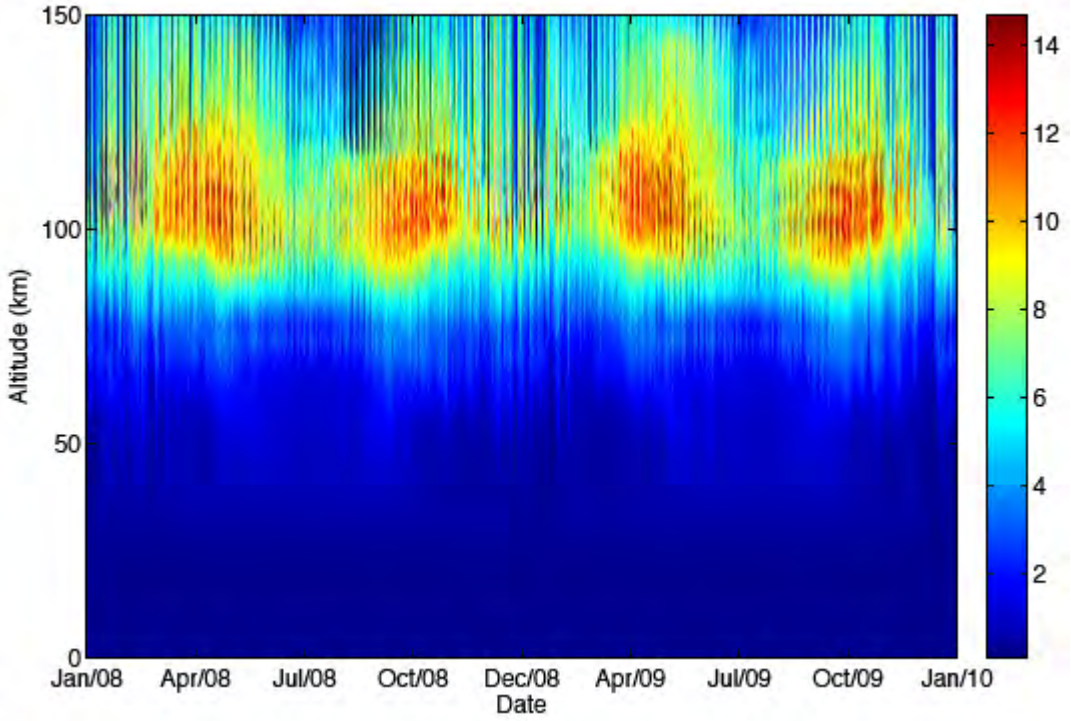

Figure 2. Seasonal variation of standard deviation (in m/s) of the zonal wind component of the gravity wave perturbation $\sigma_{u'}$ at 55° N.

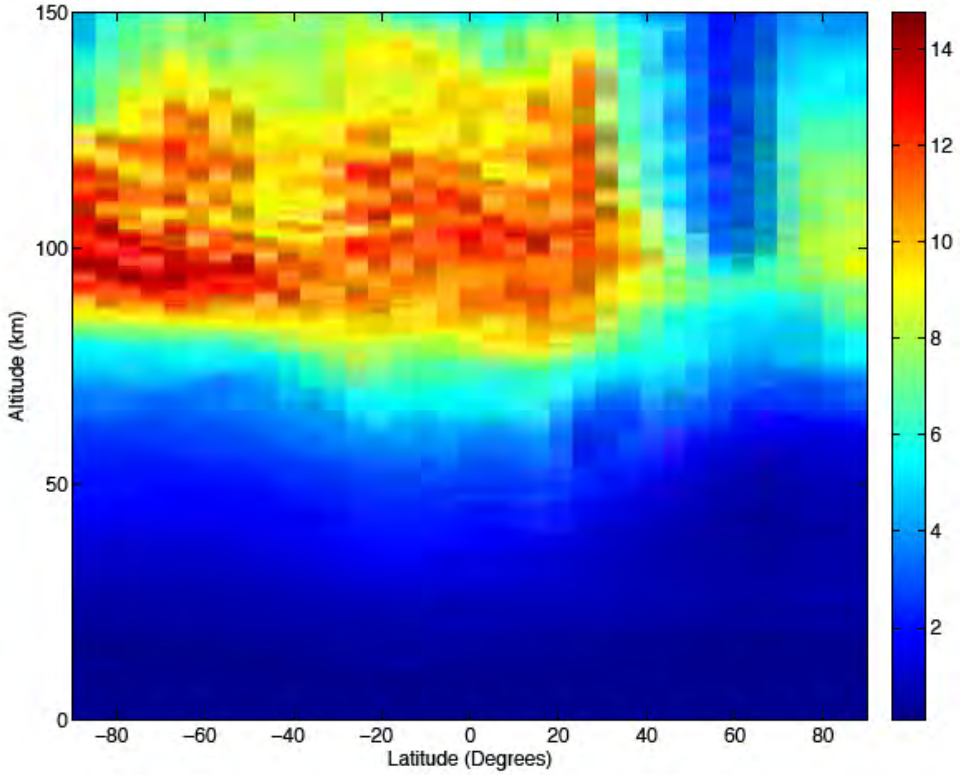

Figure 3. Latitudinal variation of standard deviation (in m/s) of the meridional wind component of the gravity wave perturbation $\sigma_{v'}$ for a fixed date.

Applications to Infrasound Propagation Modeling for Ground-Truth Events

The G2S atmospheric specifications described above, the baseline gravity wave models due to Gardner, and a suite of infrasound propagation models (including 3D ray-tracing, PE, time-domain parabolic equation [TDPE], and normal modes) are currently integrated into the tool kit InfraMAP (Gibson and Norris, 2002; Norris and Gibson, 2004). InfraMAP (*Infrasonic Modeling of Atmospheric Propagation*) has been developed by BBN for use in the study of infrasound propagation and monitoring. InfraMAP can be applied to predict attenuation, travel times, bearings, amplitudes, and waveforms for infrasonic events. The most recent version of InfraMAP includes TDPE waveform prediction capabilities (Tappert et al., 1995) based on either a canonical blast wave (Pierce and Posey, 1970) or any user-defined source waveform. PE and TDPE calculations incorporate effects of horizontal wind components (both mean and perturbations) by utilizing the effective sound speed approximation. Capabilities have also been developed for performing propagation calculations using the new gravity wave model.

Using the baseline gravity wave model, propagation studies have been conducted for various scenarios and ground truth events. These include explosive events at: Nevada Test Site, US (2002); Neyshabur, Iran (2004); Ghislinghien, Belgium (2004); Snohomish, WA bolide, US (2004); Buncefield, UK (2005); Novaky, Slovakia (2007); Gerdec, Albania (2008); Chelopechene, Bulgaria (2008); Sayarim, Israel (2007/2008); and others. Examples from studies that show comparisons of TDPE model output with observed waveforms have been presented by Gibson and Drob (2009) and Gibson (2009).

An example to quantify gravity wave effects on infrasound propagation is the Chelopechene, Bulgaria arms depot explosions (3 July 2008) detected at arrays throughout Europe and northern Africa. Observed infrasound arrivals from this event contain considerably more complexity than simple stratospheric and/or thermospheric phases. Regional observations at both I26DE (Germany) and I48TN (Tunisia) are characterized by multiple discrete arrivals ("pulses") within an extended infrasound signal of duration ~10 minutes (Green et al., 2008). Conventional propagation modeling using G2S predicts a weak stratospheric waveguide and does not predict either the early arrival time or the extended, multi-pulse features. Results of TDPE modeling over a 0-2 Hz bandwidth using a realization of a range-dependent gravity wave field are shown in Figure 4 for the path to I26DE at range of 1017 km and the path to I48TN at a range of 1440 km. A source yield of 100 tons is assumed in the synthetic waveform calculation, based on analyses by Green et al. (2008). The mean atmospheric profiles were defined using range-dependent G2S specifications. The propagation modeling includes effects of atmospheric absorption in the thermosphere (Sutherland and Bass, 2004). The agreement between data and model in arrival time, amplitude, number of pulses, and waveform envelope is striking.

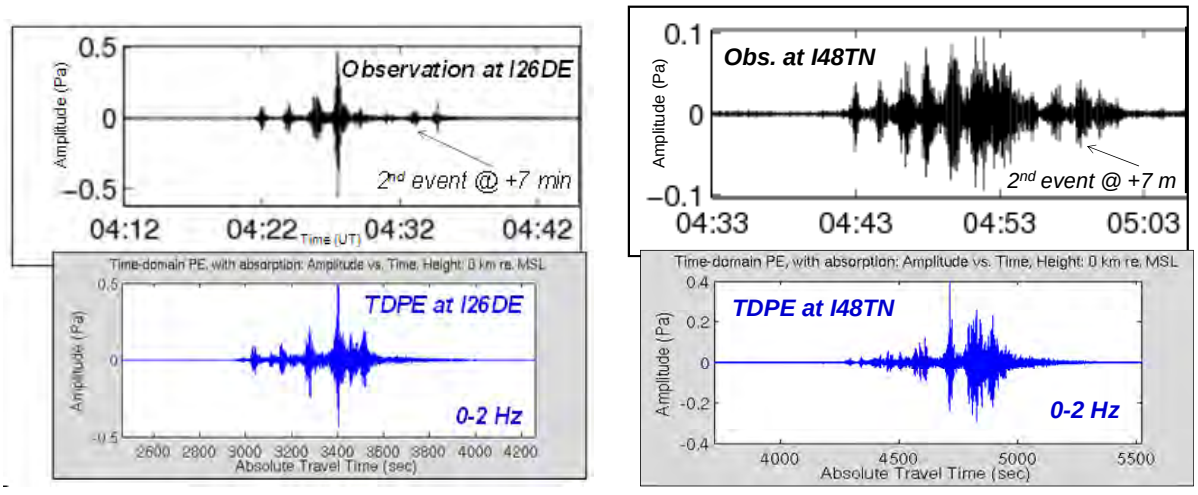

Figure 4. Comparisons between observed infrasound waveforms from the Chelopechene explosion and TDPE synthetic waveforms, including gravity wave perturbation effects. Upper panels (from Green et al., 2008): observations at I26DE (left) and at I48TN (right). Lower panels: synthetic waveforms, computed over a bandwidth of 0-2.0 Hz, and time-aligned with the waveforms in the upper panels.

An additional example is presented for one of the controlled explosions in the test series conducted at Sayarim, Israel, specifically the event of 23-Jul-2007 (Gitterman et al., 2009). This event was a surface explosion of approximately 6 tons yield. It was detected at arrays in Europe and northern Africa. Here we consider the 2460 km path to I48TN (Tunisia). Similar to the Chelopechene event, observations at I48TN are characterized by multiple pulses arriving over a period of several minutes. Analysis of the observed waveform, reproduced from Gitterman et al. (2009), is presented in the upper panel of Figure 5. Figure 5 also shows the TDPE simulation computed over a bandwidth of 0-2 Hz, including the effects of a realization of a range-dependent gravity wave field. The mean atmospheric profiles were defined using range-dependent G2S specifications, and effects of thermospheric absorption are included. Multiple arrivals are predicted in the synthetic waveform, and the arrival times and duration of these pulses are consistent with those in the observation as reported by Gitterman et al. (2009). Amplitudes are underpredicted somewhat, compared to the observation, in this example.

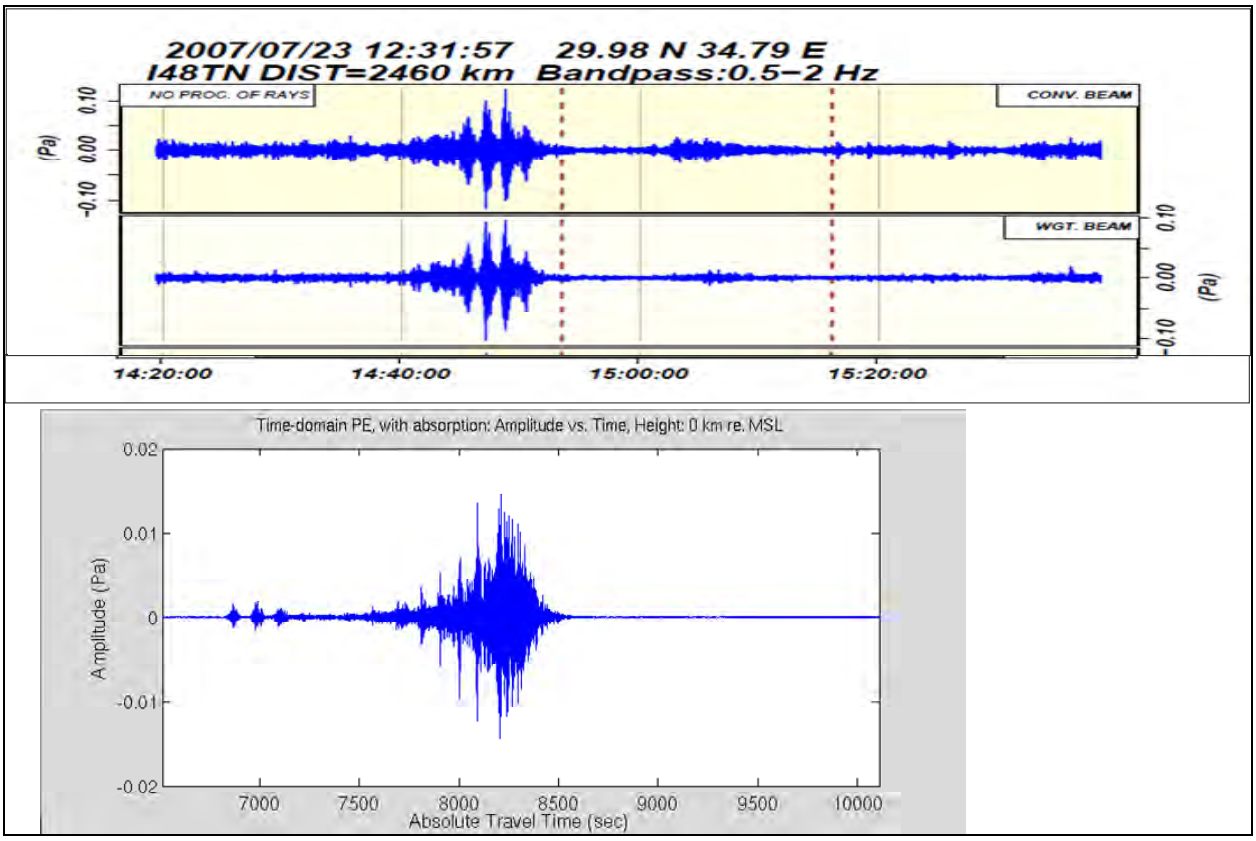

Figure 5. Comparison between observed infrasound waveforms from one of the Sayarim test explosions (23-Jul-2007) and a TDPE synthetic waveform, including gravity wave perturbation effects. Upper panel (from Gitterman et al., 2009): observation at I48TN. Lower panel: synthetic waveform, computed over a bandwidth of 0-2.0 Hz, time-aligned with the waveforms in the upper panel.

Waveform synthetics shown above have been calculated using our baseline gravity wave modeling technique. Modeling of infrasound from ground-truth events has also been conducted using our new stochastic gravity wave field fluctuation model, and comparisons with observations are in progress. Simulations have also been conducted using multiple realizations of gravity wave fields in order to assess consistency and repeatability of predictions and to develop statistical assessments as a part of the model validation activity.

CONCLUSIONS AND RECOMMENDATIONS

Substantial evidence for the importance of specification of atmospheric variability due to fine-scale inhomogeneity has been indicated by TDPE waveform predictions of ground-truth events observed at regional ranges. In several

instances, conventional propagation modeling that ignores fine-scale atmospheric structure has failed to predict observed arrivals due to the lack of a stratospheric duct in the baseline atmospheric characterization; these observations exist in so-called "zones of silence." However, modeled infrasound arrivals that consider energy refracted or scattered from gravity waves agree well in waveform envelope, duration and arrival time with observations. Progress has also been made in the ability to predict infrasound signal amplitude. These results indicate the considerable benefit to regional monitoring that is to be gained by understanding effects of gravity waves on infrasound. Implementation of our existing baseline gravity wave model enables accurate prediction of many observed infrasound features. The model for gravity wave fields has been improved during this research to incorporate additional physical effects. The new gravity wave fields have also been incorporated with existing infrasound propagation models. Testing of the new formulations should continue, including assessment of improvements against baseline models, study of additional infrasound ground truth events of interest, and extensive data/model comparison studies in order to quantify the performance of the techniques and identify research needs.

We recommend continuing extension of the new gravity wave calculation technique to address the latitudinal and seasonal variability of the gravity wave spectrum source function, focusing on effects in the troposphere, and to improve our ability to model it accurately through proper selection of model parameters. Model results should be tuned to the measured seasonal and latitudinal gravity wave characteristics (e.g., wave amplitudes, wavelengths, variances) published in the recent scientific literature. Research should also continue to explore the numerical parameter space for source spectrum shape constants, empirical wave amplitude normalization scale factors, wave-breaking, viscosity characterization, and the optimal source spectrum seeding altitude. By better defining the spatial scales and amplitudes of the relevant gravity wave perturbations, better estimates of the stochastic properties of infrasound propagation will be obtained.

REFERENCES

Bhattacharyya, J., H. Bass, D. Drob, R. Whitaker, D. ReVelle, and T. Sandoval (2003). Description and Analysis of Infrasound and Seismic Signals Recorded from the Watusi Explosive Experiment, in *Proceedings of the 25th Seismic Research Review—Nuclear Explosion Monitoring: Building the Knowledge Base*, LA-UR-03-6029, Vol. 2, pp. 587–596.

Broutman, D., J. W. Rottman, and S. D. Eckermann (2003). A simplified Fourier method for nonhydrostatic mountain waves. *J. Atmos. Sci*., 60: 2686–2696.

Broutman, D., J. Ma, S.D. Eckermann, and J. Lindeman (2006). Fourier-ray modeling of transient trapped lee waves. *Mon. Wea. Rev*. 134: 2849–2856.

Broutman, D., S. D. Eckermann, and J. W. Rottman (2009). Practical application of two turning-point theory to mountain-wave transmission through a wind jet, *J. Atmos. Sci*., 66: 481–494.

Drob, D. P., J. M. Picone, and M. A. Garcés (2003). The Global Morphology of Infrasound Propagation, *J. Geophys. Res.* 108: doi:10.1029/2002JD003307.

Drob, D. P. (2004). Atmospheric Specifications for Infrasound Calculations, *Inframatics*, No. 5.

Drob, D.P., J. T. Emmert, G. Crowley, J. M. Picone, G. G. Shepherd, W. Skinner, P. Hays, R. J. Niciejewski, M. Larsen, C. Y. she, J. W. Meriwether, G. Hernandez, M. J. Jarvis, D. P. Sipler, C. A. Tepley, M. S. O'Brien, J. R. Bowman, Q. Wu, Y. Murayama, S. Kawamura, I. M. Ried, and R. A. Vincent (2008). An empirical model of the Earth's horizontal wind fields: HWM07, *J. Geophys. Res.*, 113, A12304, doi:10.1029/2008JA013668.

Eckermann, S. D. (1995). Effect of background winds on vertical wavenumber spectra of atmospheric gravity waves, *J. Geophys. Res.* 100: 14,097–14,112.

Fritts, D. C., and J. M. Alexander (2003). Gravity Wave Dynamics and Effects in the Middle Atmosphere, *Rev. of Geophys.* 41: 1, 1003.

Gardner, C. (1993). Gravity Wave Models for the Horizontal Wave Number Spectra of Atmospheric Velocity and Density Fluctuations, *JGR* 98; D1, 1035–1049.

Gardner, C. (1995). Scale-Independent Diffusive Filtering Theory of Gravity Wave Spectra in the Atmosphere, *The Upper Mesosphere and Lower Thermosphere: A Review of Experiment and Theory*, Geophysical Monograph 87, AGU.

Gibson, R., and D. Norris (2002). Development of an Infrasound Propagation Modeling Tool Kit, *Defense Threat Reduction Agency Technical Report DTRA-TR-99-47*, Alexandria, VA.

Gibson, R. G., D. E. Norris and D. P. Drob (2008). Investigation of the effects of fine-scale atmospheric inhomogeneities on infrasound propagation, in *Proceedings of the 30th Seismic Research Review—Ground-Based Nuclear Explosion Monitoring Technologies*, LA-UR-08-05261, Vol. 2, pp. 872–881.

Gibson, R. and D. Drob (2009). Full-Wave Modeling of Infrasound from Explosions Using the Parabolic Equation Method and Realistic Atmospheric Specifications, in *Proceedings of the International Scientific Studies Conference*, Vienna, Austria.

Gibson, R., D. Drob and D. Broutman (2009). Advancement of Techniques for Modeling the Effects of Fine-Scale Atmospheric Inhomogeneities on Infrasound Propagation, in *Proceedings of the 2009 Monitoring Research Review—Ground-Based Nuclear Explosion Monitoring Technologies*, LA-UR-09-05276, Vol. 2, pp. 714–723.

Gibson, R. (2009). Recent Applications of Full-Wave Infrasound Modeling from Explosions, *Proceedings of the Infrasound Technology Workshop*, Brasilia.

Gitterman, Y., M.A. Garces, J.R. Bowman, D. Fee, H.G. Israelsson, R. Hofstetter, and V.I. Pinsky (2009). Near-source and far-regional infrasound observations for Sayarim test explosions, in *Proceedings of the 2009 Monitoring Research Review—Ground-Based Nuclear Explosion Monitoring Technologies*, LA-UR-09-05276, Vol. 2, pp. 724–734.

Green, D. et al. (2008). Analyzing multiple explosions in Europe: Signal characteristics and propagation modeling, *Proceedings of the Infrasound Technology Workshop*, Bermuda.

Hedin, A. E., E. L. Fleming, A. H. Manson, F. J. Scmidlin, S. K. Avery, R. R. Clark, S. J. Franke, G. J. Fraser, T. Tsunda, F. Vial, and R. A. Vincent (1996). Empirical Wind Model for the Upper, Middle, and Lower Atmosphere, *J. Atmos. Terr. Phys.* 58: 1421–1447.

Kulichkov, S.N. (2004). Long-range propagation and scattering of low-frequency sound pulses in the middle atmosphere, *Met. Atmos. Phys*. 85: No. 1–3, pp. 47–60.

Mutschlecner, J., and R. Whitaker (2006). *Infrasonic Signals from the Henderson, Nevada, Chemical Explosion*, LA-UR-06-6458.

Norris, D. and R. Gibson (2002). InfraMAP Enhancements: Environmental/Propagation Variability and Localization Accuracy of Infrasonic Networks, in *Proceedings of the 24th Seismic Research Review—Nuclear Explosion Monitoring: Innovation and Integration*, LA-UR-02-5048, Vol. 2, pp. 809–813.

Norris, D., and R. Gibson (2004). Advanced Tools for Infrasonic Modeling, *Inframatics*, No. 5.

Picone, J., A. Hedin, D. Drob, and A. Aiken (2002). NRLMSISE-00 empirical model of the atmosphere: statistical comparisons and scientific issues, *J. Geophys. Res.* 107: 1468.

Pierce, A. D., and J. W. Posey (1970). Theoretical Prediction of Acoustic-Gravity Pressure Waveforms Generated by Large Explosions in the Atmosphere. Technical Report AFCRL-70-0134, Air Force Cambridge Research Laboratories, Bedford, Mass.

Sutherland, L. and H. Bass (2004). Atmospheric absorption in the atmosphere up to 160 km. *J. Acoust. Soc. Am.* 115: 1012–1032.

Tappert, F., J.L. Spiesberger, and L. Boden (1995). New full-wave approximation for ocean acoustic travel time predictions, *J. Acoust. Soc. Am*. 97: 2771–2782.

Warner, C.D., and M.E. McIntyre (2001). An ultrasimple spectral parameterization for nonorographic gravity waves, *J. Atmos. Sci.* 58: (14), 1837–1857.

SAYARIM INFRASOUND CALIBRATION EXPLOSION: NEAR-SOURCE AND LOCAL OBSERVATIONS AND YIELD ESTIMATION

Yefim Gitterman

Geophysical Institute of Israel

Sponsored by the Army Space and Missile Defense Command

Award No. W9113M-07-C-0189
Proposal No. BAA07-52

ABSTRACT

A large-scale calibration explosion of about 82 tons of high explosives (HE), assembled as a pyramid on a soft sediment surface, was successfully conducted by the Geophysical Institute of Israel (GII) at Sayarim Military Range (SMR), Negev Desert, Israel, on 26 August 2009.

Near-source high-pressure values, measured in the range 200–600 m, were higher than predicted, whereas the resulting crater and the seismic magnitude were smaller than expected for this on-surface charge. These results confirm that the explosives, charge design, and upward detonation generated the necessary explosion energy and partition: a maximum of energy to the atmosphere and a minimum to the ground.

The high-pressure observations were utilized for reliable estimation of the important ground truth parameter—TNT equivalent yield of about 0.1 kt, based on a stable integral characteristic of air-blast waves—the positive phase impulse. As with near-source pressure gauges, anomalous enhanced peak pressure amplitudes were found at local infrasound stations, indicating possible an upward directivity effect and asymmetric energy radiation to the atmosphere.

Clear infrasound signals were well observed at distances up to 3,500 km at numerous portable and permanent stations in Israel, Mediterranean countries, and north-central Europe, including two International Monitoring System (IMS) stations I26DE and I48TN, which provided for this region the first full GT0 source dataset for on-surface, large-scale explosions recorded by infrasound stations of IMS.

Additional estimations of the explosion yield, based on empirical scaling relations for the peak amplitude, dominant period, and crater dimensions, were analyzed. Yield estimations from far-regional IMS infrasound stations, obtained at the International Data Centre (IDC) using trial published empirical yield-range-amplitude attenuation laws, were significantly overestimated, thus indicating the need for refinement and tuning of the monitoring procedures.

Observations jointly obtained with GT0 source parameters provided an extensive dataset for analysis and modeling of long-range atmospheric propagation of infrasound signals, detection, source location, and yield estimation.

OBJECTIVES

1) To conduct a surface explosion of 80 tons, providing the first large-scale GT0 infrasound source for Middle East/Mediterranean/Europe region for calibration of IMS and national infrasound stations and improvement of monitoring capabilities
2) To develop a charge design, providing maximum explosion energy to the atmosphere
3) To provide an extensive infrasound dataset from stations deployed at a broad of distances (0.1–3000 km)
4) To provide a reliable yield estimation of the explosion based on near-source observations and compare that estimation with estimations from local and far-regional distances

RESEARCH ACCOMPLISHED

Activities and research during the project's second year included final preparations for conducting the main surface calibration explosion at Sayarim and observing infrasound waves in a broad distance range. Obtained data and records were used to analyze empirical scaling relations for the peak amplitude, dominant period, and crater dimensions and to evaluate the TNT equivalent yield.

Testing the Feasibility of New Explosives and Charge Design

New HE explosives supplied by IMI Ltd. were used as the charge main agent for the Sayarim Calibration Explosion. The explosives were composed of recuperated TNT and some other HE components. Laboratory testing by IMI showed an average detonation velocity of ~7500 m/s, much higher than for standard TNT (6800 m/s). The cast explosives were supplied in big cardboard barrels (each one 315 kg). The last test was conducted several days before the main explosion (Table 1) to estimate energy release in the charge units (barrels) and transfer of the upward detonation through layers of charge. Two barrels were assembled as a tower on a wooden platform (Figure 1). The booster (mine M15, 10 kg of Composition B) was placed upside down (to provide an additional upward cumulative effect) beneath the platform. Two Bikini mechanical gauges were used for characterizing near-source high pressures.

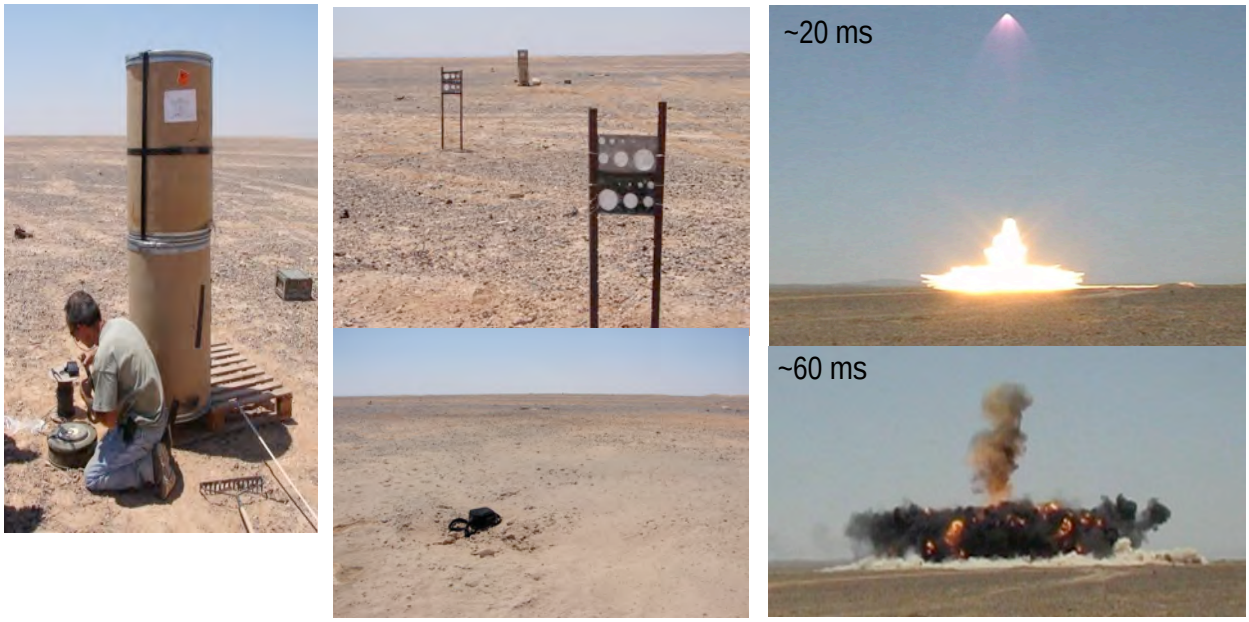

Figure 1. Preparation of the test shot charge of 640 kg (left) and observations: two Bikini gauges with two sets of holes glued by paper membranes and the explosion crater with a camera bag for scale (center); and snapshots from a home video recording, with the time after the detonation shown (right).

The gauges showed higher pressures than predicted for the equal TNT charge, and a very small crater was created. Both these features were evidence of a high efficiency for the selected explosives, charge design, and upward detonation conception, resulting in enhanced energy radiation to the atmosphere and low coupling to the ground.

Table 1. Parameters of explosions, conducted at Sayarim Military Range (SMR), Negev Desert, Israel

Explosion	Date	Detonation Time, GMT	Altitude, m	Latitude	Longitude
Test 640 kg	18/08/09	10:10:40.16*	563	29.99522N	34.80792E
Main shot	26/08/09	06:31:54.00	556	30.00057N	34.81351E

* Estimated by the Israel Seismic Network (ISN)

Main Charge Design.

Major design conceptions, elaborated by GII, were maximal concentration of explosives in the charge to provide release of maximal energy to the atmosphere. Figure 2 shows the following features of the charge design: big barrels filled up to the top with strong, cast HE explosives (315 kg); minimal air voids between the barrels (accomplished by filling the voids with plastic bags of HE bulk explosives); minimal air voids between six charge layers (accomplished by removing wooden platforms, except for those under the first layer); approximately hemispherical (pyramidal), compact shape (actual measured dimensions: base 5.8 × 5.9 m, height 5.5 m); strong booster with 52 M15 mines on the ground, upside down to provide the upward detonation, and 63 mines on the central platform in the first layer; and a multiple (22-point) initiation scheme.

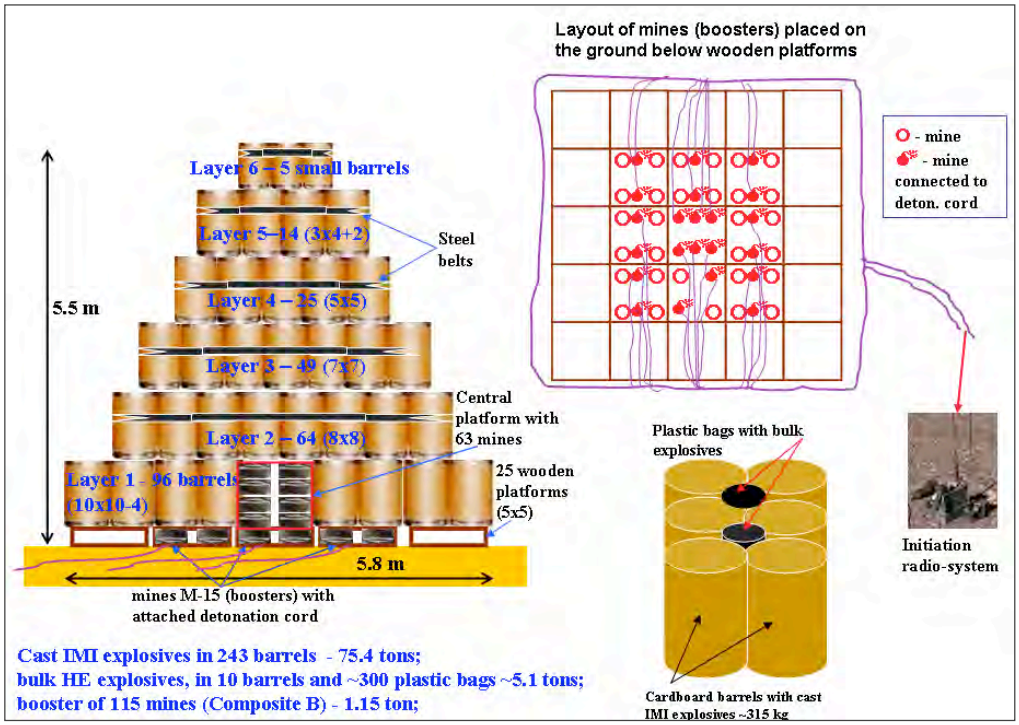

Figure 2. Charge shape and booster configuration and 22-point initiation design scheme.

The main charge was composed mostly of new, cast HE explosives by IMI, bulk HE explosives of different types, and Composition B in M15 mines, with the total nominal explosives weight of 81,664 kg. After the charge units on the platforms were specially prepared (in about 3 days), the charge was assembled during 1.5 days. The details of charge assembling and configuration are important for understanding the observed explosion effects and energy generation.

Conducting the Explosion and Near-Source Observations

The explosion was detonated on August 26, 2009, at ~9:30 AM local time. The day and time were chosen due to favorable wind conditions for infrasound propagation (Garces et al., 2009; Bowman et al., 2009). No wind was

observed during the explosion, evidenced by the vertical column of dust and gases (Figure 3). Accurately measured Greenwich Mean Time (GMT) for the detonation and GPS coordinates are presented in Table 1. Different measuring and observation systems were deployed at close distances: pressure gauges, accelerometers, and video cameras. The explosion layout and the locations of the systems are shown on Figure 3.

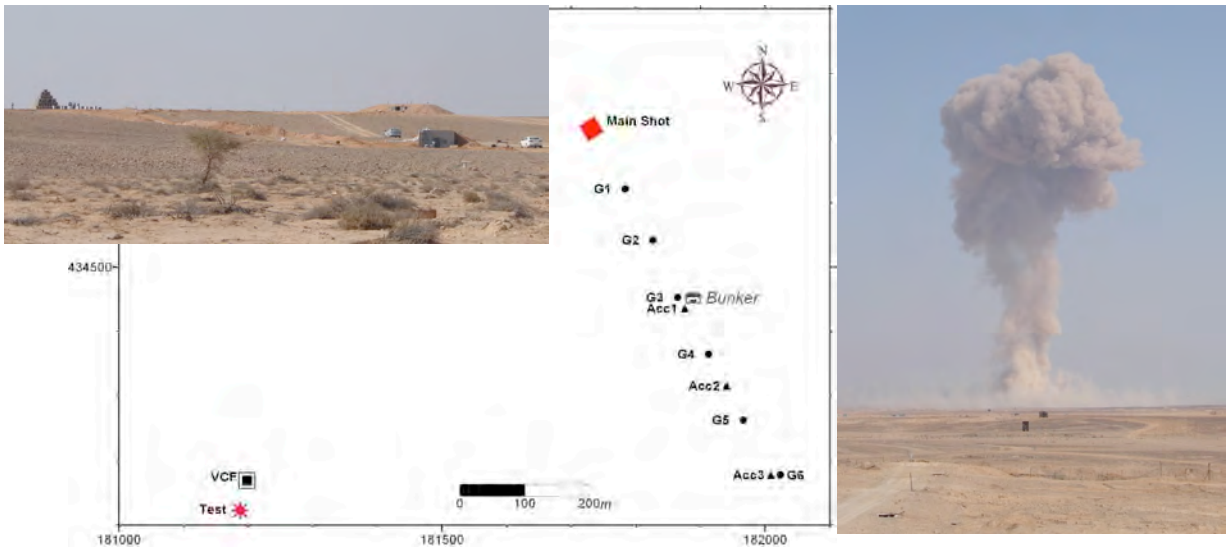

Figure 3. Explosion site view and layout, showing locations of the shots, the pressure gauges (G1–G6), accelerometers (Acc1–Acc3), and the speed video camera VCF (left); vertical light column of dust and gases of ~2 km height observed from the Command Post 5.8 km from the test and ~3 min after the detonation (right).

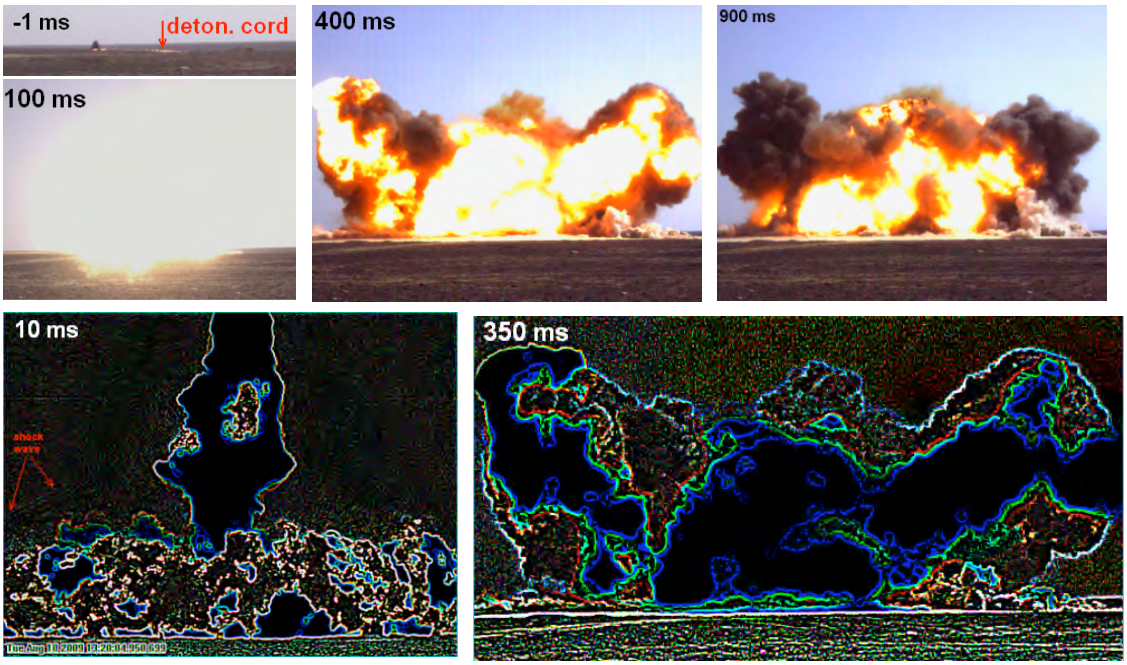

Figure 4. Sample snapshots from a speed video recording during the first second of the detonation (top). The explosion view using a *Edge Laplacian 5x5* filter: the test 640 kg shot (bottom left, see also Figure 1) and the main explosion (bottom right).

Speed Video Records

The speed camera Phantom v5.1 was placed at ~750 m; the actual frame rate was 3902 fps. Sample snapshots are presented in Figure 4. The Cine Viewer 675 software was used for processing and visual analysis of raw data.

Unfavorable lighting conditions prevented aerial observation of the shock wave. As for the test shot (Figure 4), it was revealed only on the ground, close to the camera, at ~1.5 seconds after the detonation. Observed anomalous nonuniform expanding of the fireball and detonation products indicates possible nonlinear directivity effects.

Observation of the Explosion Crater

Initial coarse estimations by measuring tape showed a crater radius of R ~13.5 m (Figure 5). The Survey of Israel team conducted accurate GPS crater measurements just after the explosion and provided appropriate crater 2D and 3D images, confirming the radius value and a depth estimation of H ~5 m (Figure 5).

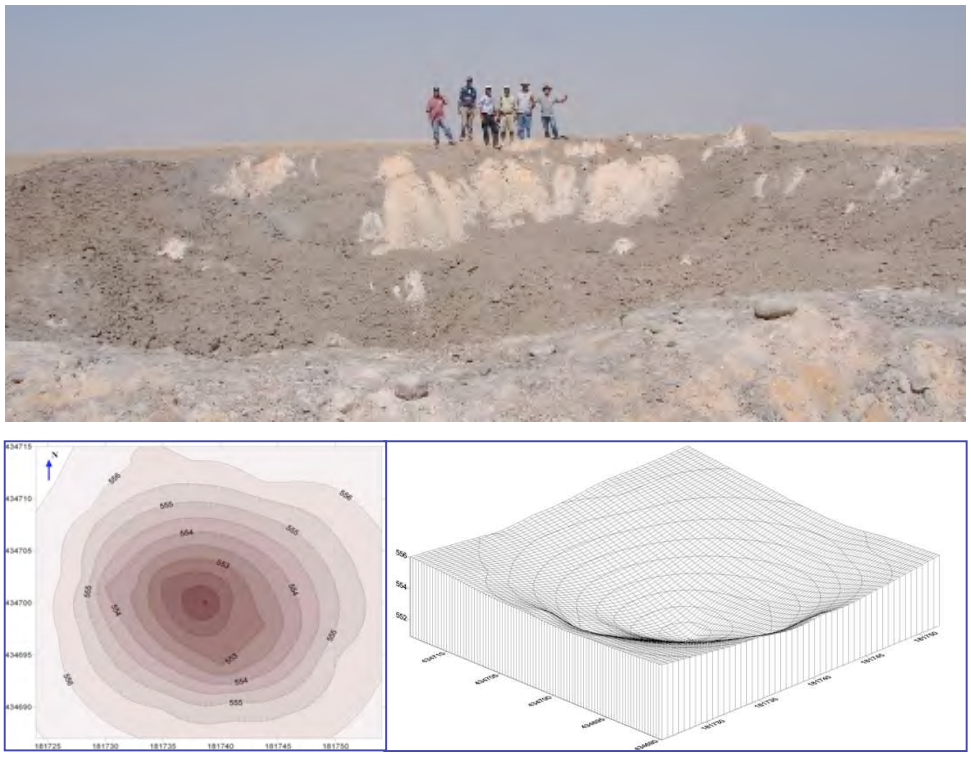

Figure 5. Crater created by the calibration explosion (top); 2D and 3D images provided by the Survey of Israel (bottom).

A similar hemispherical surface explosion of 90.7 tons of TNT, on alluvium, in the US Army Waterways Experiment (1962) created a much larger crater with R = 21.3 m, H =6 .3 m (CraterDatabase, 2004). For comparison, we also used empirical equations for craters of large-scale explosions on soft soil (Adushkin and Khristoforov, 2004):

$$R = 3.36W^{0.336}; \quad H = 1.78W^{0.316}, \qquad (1)$$

where W is TNT equivalent yield, in tons.

According to Eq.(1), the measured radius 13.5 m fits to a charge of 63 ton, and the depth 5 m fits ~30 tons, whereas a charge of 82 tons should provide R ~15 m, H ~7 m. Thus the created crater was smaller than expected for this on-surface charge, according to similar explosions, indicating decreased coupling of explosive energy to the ground, supposedly due to the specific charge design and especially the upward detonation.

Accelerometer Measurements

Three K2 accelerometers of Kinemetrics were deployed prior to the explosion; Acc1 and Acc3 were co-located with pressure gauges (Figures 3, 6). The accelerometers were placed on the surface and were subjected to the impact of the strong air-shock wave on the sensor. Vertical acceleration of more than 4 g was measured at the closest Acc1, corresponding to the first shock; weaker secondary shocks were also found (Figure 7).

High-Pressure Measurements

High-pressure measurements were intended to evaluate energy generation for the new IMI explosives and the elaborated charge design and to provide a TNT yield estimation of the explosion. Six pressure gauges XTL-190-5G/50A/100A were installed in a line in the distance range of 100–600 m; the recording system (with a sampling rate of 2 MHz) was deployed in the half-buried concrete bunker at ~300 m (Figure 3).

Shock waves for the new explosives were expected to be weaker than for TNT, but all pressure gauges measured significantly larger free-field side-on peak pressure and positive phase impulse and more speed propagation, compared with predictions for the equal TNT charge (Figures 7–8). The closest sensor G1 was knocked down, and the unreliable record was excluded from the analysis (Figure 6).

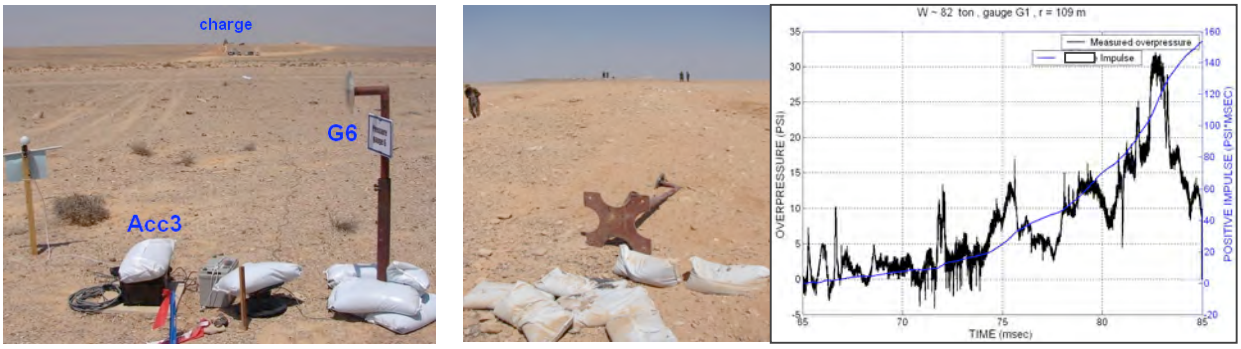

Figure 6. The most remote co-located accelerometer Acc3 and pressure gauge G6 at 611 m (left). The closest gauge G1 at 109 m after the explosion (center) and the record (right)

For all pressure gauges, a distinct secondary shock (SS) wave was observed during the negative phase portion of the pressure-time curves (Figure 7), showing positive peak amplitudes, as opposed to the case of surface ANFO shots 20 and 100 tons in Alberta, Canada, where all SS peak amplitudes were negative (Swisdak and Sadwin, 1970).

This SS phase clearly also occurred at all accelerograms, with appropriate time delay (Figure 7). We estimated from the records basic parameters of the air-blast wave: Time of Arrival T_A, Peak Pressure P_m, Positive Phase Impulse I_+, Positive Phase Duration τ_+, and (T_A, P_m) for the Secondary Shock. Due to some irregularities in the high-pressure time history, it was approximated by 2- or 3-exponent fit curves, for more reliable estimation of P_m and τ_+ values.

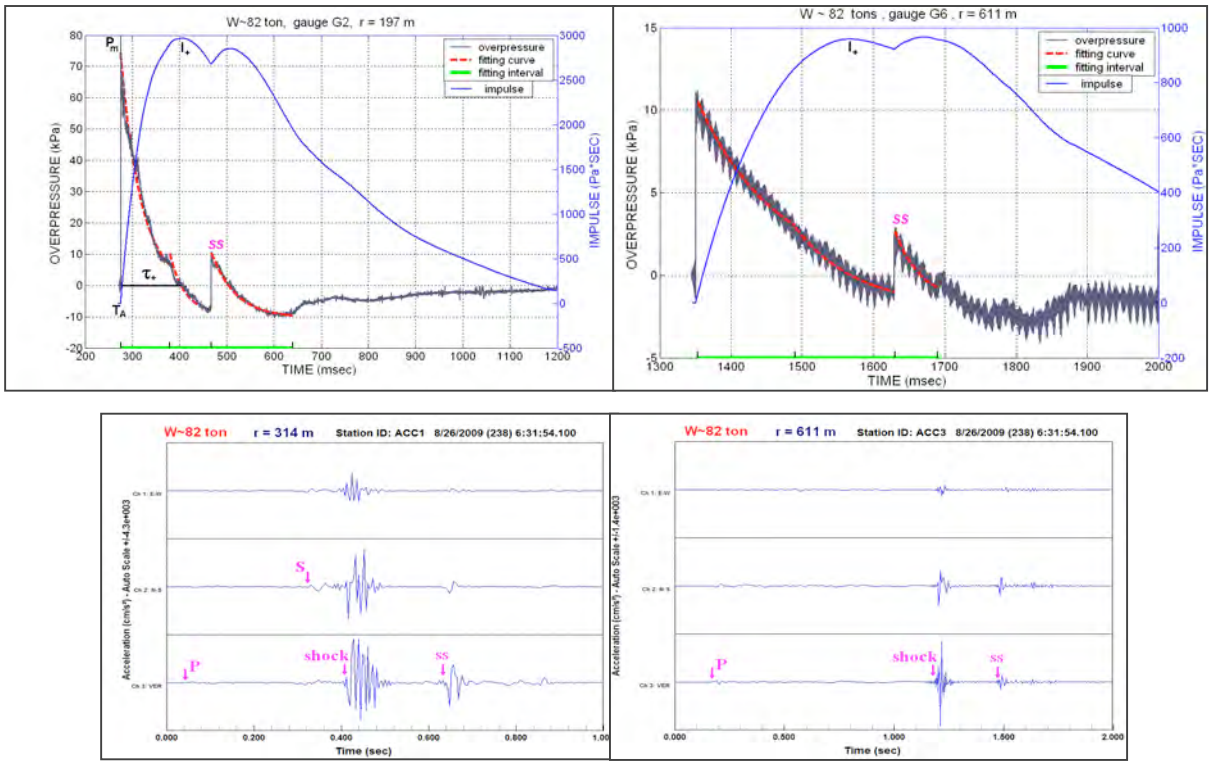

Figure 7. Sample records at two pressure gauges (top) co-located with accelerometers (bottom).

We used the DDESB Blast Effects Computer Version 4.0 (BECV4), an Excel template (Swisdak, 2000), for predicting the Sayarim air-blast parameters for the equal weight TNT charge of W = 81, 664 kg, actual altitude H = 556 m, and T = 35°C. Figure 8 shows a comparison of measured parameters P_m, τ_+, I_+, and T_A and the predicted values at different distances, where all parameters are evidence that the actual TNT equivalent yield was larger than the nominal charge weight. Comparison of measured P_m and T_A for the main and secondary shocks is also presented, where P_m for SS was calculated as the difference (the jump) between fit maximal and minimal amplitudes on the arrival time.

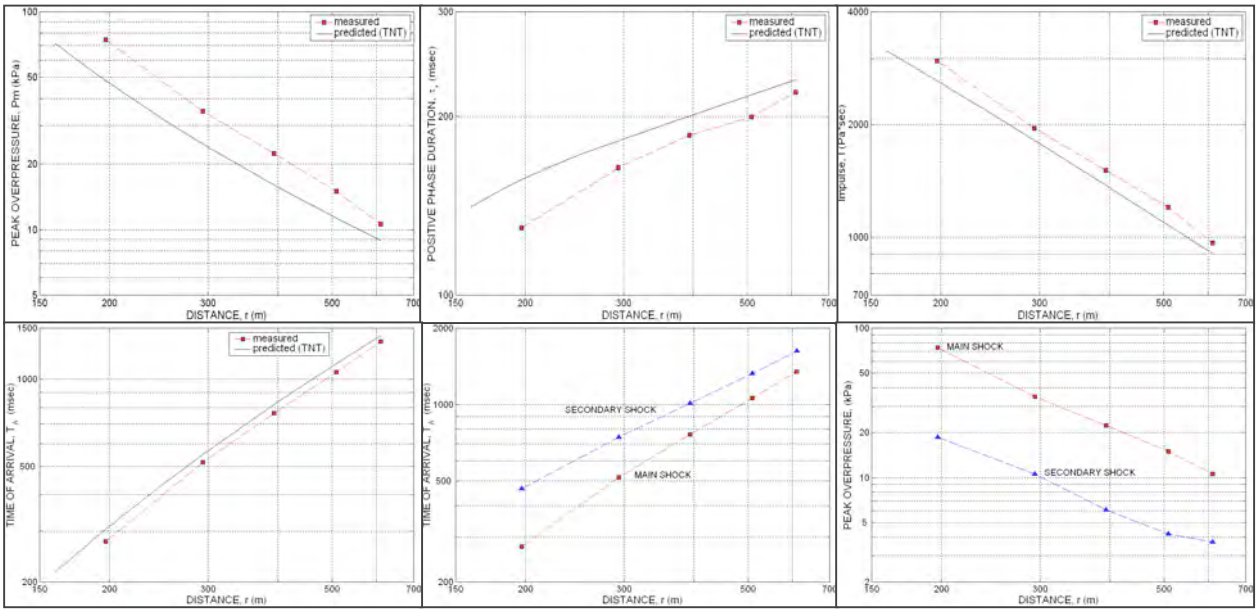

Figure 8. Comparison of measured free-field air-blast parameters with values predicted by BECV4 procedure for the surface explosion of 81,664 kg of TNT (H = 556 m, T = 35°C). Comparison of measured parameters for the main and secondary shocks is also shown.

Estimations of Equivalent TNT Yield

Estimations of equivalent TNT yield were obtained, using BECV4 procedure (Swisdak, 2000), for altitude 556 m, T = 35°C, based on measured airbast values, averaged over 5 gauges (Table 2). Increased P_m and decreased τ_+ values (Figure 8) resulted in appropriately overestimated and underestimated yields. The positive phase impulse I_+ is the integral and stable characteristic of the air-blast wave (unlike the one-point peak amplitude), and we consider the impulse-based estimation of 96 tons (~0.1 kt) as the most reliable. Note that it is close to the average of estimations by both parameters (P_m and τ_+) because the impulse is about proportional to their multiplication.

Table 2. Estimation of the TNT equivalent yield based on air-blast measurements (H = 556 m, T = 35°C).

Gauge	Distance, m	Peak Over-Pressure P_m		Positive Phase Duration τ_+		Positive Phase Impulse I_+	
		Measured, kPa	Yield, tons	Measured, msec	Yield, tons	Measured, Pa*sec	Yield, tons
G2	197	74.4	164	129.9	33	2963	101
G3	294	34.9	157	163.9	52	1953	93
G4	394	22.3	163	185.6	59	1508	95
G5	509	15.0	155	199.6	57	1202	98
G6	611	10.6	123	219.5	67	966	92
AVERAGE			**152**	**54**		**96**	

The obtained yield estimation is about 20% more than the nominal weight of the charge; we assume several possible factors of enhanced air-blast energy and the appropriate enlarged TNT yield: (1) high concentration of explosives, with minimal air voids between the charge units; (2) a very strong booster and multiple initiation scheme; (3) upward detonation of the charge; and (4) high detonation velocity (~10% higher than TNT).

Observations at Local Distances.

Seismic and acoustic signals were recorded at numerous permanent and portable stations in Israel, installed by GII. We also used data from an infrasound array deployed at Mt. Meron (IMA) by Israel NDC and an array at Cyprus (CYPR) and a close station UMUF, deployed by the Universities of Mississippi and Alaska (Fairbanks) (Figure 9). Seismic signals were recorded at ISN stations at 15–340 km, and strong acoustic phases (T) were observed at several close stations (up to 70 km) (Figure 9). At some stations amplitudes of acoustic phases were higher than the amplitudes of seismic signals. The estimated local (duration) magnitude of 2.5 was smaller than expected (~2.7–2.8)

for this on-surface charge; old ammunition shots with downward detonation showed maximal vertical amplitudes in P-waves, whereas for the calibration explosion with upward detonation, P-waves are much smaller than surface waves (Figure 9)—two more indications of a decreased impact on the ground due to the enhanced explosives energy coupling to the atmosphere.

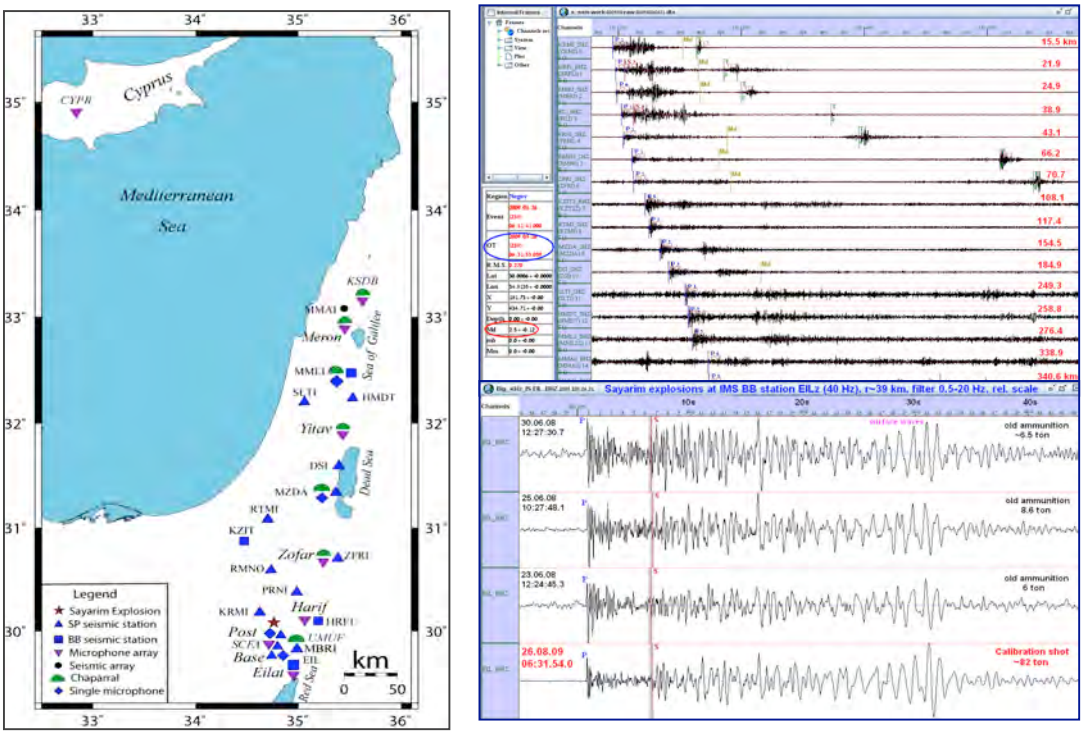

Figure 9. Map of recording stations used (left); seismic and acoustic phases (T) at ISN stations (top right); comparison of seismic waves (in relative scale) at IMS BB station EILz from three old ammunition shots (see Gitterman and Hofstetter, 2008) with the main explosion (bottom right).

Dominant Periods, Filtering Raw Records, and Yield Estimation

An empirical relationship between the yield Y_0 (tons) and the dominant period of the infrasound signal T_0 (sec) was derived by the U.S. Air Force Technical Applications Center from nuclear explosions above ground at the Nevada Test Site (ReVelle et al., 1998):

$$Y_0 = (2)\times 2.63 \times T_0^{3.34} \ , \qquad (2)$$

where T_0 is the period at the signal maximal amplitude, and the doubling factor in brackets compensates for the nonnuclear nature of the explosions. The physical basis for this relation is found in the increased acoustic transit time of the blast radius with increased yield. The period is not influenced much by propagation like peak amplitudes. According to Eq. (2), for charges ~100 tons the dominant period should be T_0~2.4 sec, or f_0~0.4 Hz. Then, the high-pass filter frequency should be much lower, such as 0.1 Hz, in order not to cut the signal energy and distort waveforms.

When processing records of the Sayarim Calibration Explosion, filters 0.3–6 Hz for local Israel stations and 0.3–4 Hz for the far-regional I48TN station were used (O'Brien et al., 2010). Empirical yield-range-amplitude attenuation laws use the peak-to-peak amplitude (Pa) of the dominant stratospheric return at IMS stations, filtered from 0.5 to 3.0 Hz (Brown et al., 2009a). Table 3 shows that for these filter bands the energy and peak amplitude of infrasound signal was reduced notably, compared with the filter band 0.1–5 Hz, which we used when measuring dominant periods and peak pressure amplitudes of the signals.

Table 3. Peak amplitudes at Cyprus infrasound station (array) for different band-pass filtering

Sensor	Peak amplitude, units		Peak amplitude reduction, %	Peak amplitude, counts	Peak amplitude reduction, %
	Filter 0.1-5Hz	Filter 0.3-4Hz		Filter 0.5-3Hz	
CYPR1	13905	10447	25	8818	37
CYPR2	19258	13968	27	9108	53
CYPR3	65386	57940	11.4	43641	33

For the yield estimation, we utilized a dataset of Israel and Cyprus infrasound stations a range of 150–570 km, where single, clear main arrivals were observed. Dominant periods of the signals were accurately determined, using zero crossings; in some cases sinusoidal extrapolations were used to find the crossing of a signal curve with the zero level (Figure 10, Table 4). Yield estimation based on the average of dominant periods of infrasound signals is obtained: 128 tons of TNT. This value is also higher than the nominal charge weight of 82 tons and is relatively close to the estimated yield of ~0.1 kt, based on air-blast measurements.

Table 4. Measured dominant periods for the main explosion and the yield estimation

Station	Sensor type	Distance, km	Dominant period, sec
MZDB	Chaparral25	154	2.52
MMLB	Chaparral25	276	3.0
IMA1-5	MB2000	338	2.50,2.57,2.53, 2.50, 2.48
Meron_GII	Chaparral25	340	2.53
CYPR1-3	UM sensors	576	2.56,2.71,2.66
Average period T_0			**2.60**
standard deviation σ			0.106
Y_0 in formula (2)			**128 tons**

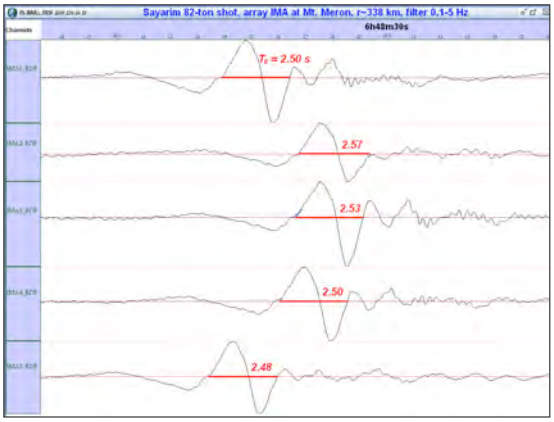

Figure 10. Sample of measuring the dominant period at IMA array.

Analysis of the Peak Amplitudes for Israel Stations

The most common empirical amplitude-yield scaling relation is based on data from a series of large-scale explosive tests at White Sands Missile Range (WSMR) during 1981–1993 with the charge range of 24–4880 tons of ANFO, recorded at distance range of 250–5300 km, with addition of the Watusi explosion (Whitaker et al., 2003), referenced also as LANL2003:

$$P = 5945.7\times(SR)^{-1.4072} \qquad SR = R/(2*W)^{0.5}, \tag{3}$$

where P is peak-to-peak, wind-corrected amplitude in Pa and SR is scaled range, W is yield in kilotons, and R is range in kilometers. The empirical wind-correction factor is given by $10^{-0.019v}$, where v is wind-component at 50 km altitude in m/s.

The peak amplitudes for the main explosion were measured at well-calibrated stations that recorded good-quality signals and wind-corrected using along-path wind v = 15 m/s, based on G2S specifications (O'Brien et al., 2010) and local radiosonde data. The signal at the close UMUF station was very strong and therefore clipped, and the peak value was extrapolated. The group velocity of the maximal (first) arrival at selected stations was ~340 m/s (except for UMUF ~350 m/s). Scaled range is calculated for W = 0.1 kt. The results are presented in Table 5 and Figure 11, demonstrating 3–5 times higher amplitudes, compared with the LANL2003 curve, thus indicating a possible upward directivity effect and asymmetric energy radiation to the atmosphere, appeared at these local distances. Using a

different new measure of the source-receiver wind showed that wind-corrected amplitudes for the main SMR shot (with W = 82 tons) agree closely with the LANL2003 relation at far-regional stations (O'Brien et al., 2010).

Table 5. Measured wind-corrected amplitudes at Israel stations (W = 0.1kT, *v* = 15 m/s, filter 0.1–5 Hz)

Station	Range R, km	Scaled range SR, km/kT$^{1/2}$	Peak-to-peak measured amplitude, Pa	
			raw	wind-corrected
UMUF	22.5	50.3	~280	~145
Zofar	72	161	23.5	12.19
MZDB	154	344	15.3	7.94
MMLB	276	617	7.48	3.88
IMA(aver)	338	756	3.93	2.04
Meron	340	760	4.23	2.19

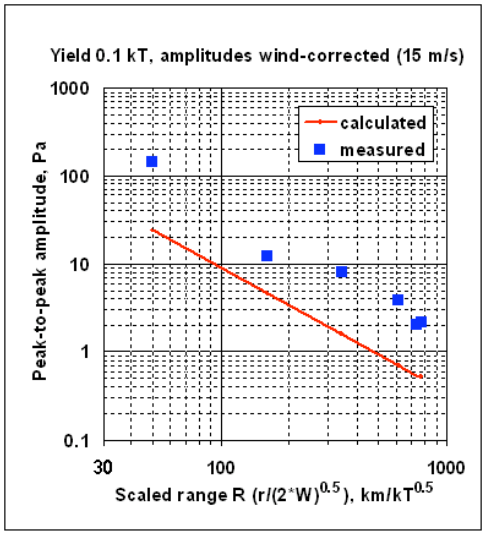

Figure 11. Measured wind-corrected amplitudes at Israel stations for the main SMR shot, compared with the LANL2003 curve (red).

Other Yield Estimations

An overestimated yield of 0.3–0.5 kT was obtained at IDC, using wind-corrected amplitudes at two far-regional IMS stations I26DE and I48TN, applied to several yield-range-amplitude attenuation laws, including LANL2003 (Brown et al., 2009b). Using a new-developed parabolic-equation-based semi-empirical relation, a reasonable value of ~0.1 kt at the dominant frequency was estimated from IS48 data (Le Pichon et al., 2010).

CONCLUSIONS AND RECOMMENDATIONS

A charge of about 82 tons of HE explosives, assembled as a special design pyramid on a soft sediment surface, was successfully detonated. Enhanced peak pressures at all distances and smaller crater and seismic magnitude confirmed that the developed charge design provided a strong explosion energy generation and necessary partition: more energy to the atmosphere and less to the ground. The estimated yield of 0.1 kt, based on the measured positive phase impulse in air-blast waves at near-source distances, can be considered as Ground Truth parameter.

The main goal of the Sayarim Calibration Experiment was reached: infrasound signals were observed at numerous stations at distances up to 3500 km (much more than planned) (Garces et al., 2009, Bowman et al., 2009), thus establishing the first Ground Truth GT0 infrasound dataset for Middle East/Mediterranean/ Europe region.
More similar explosions are necessary, in different seasons, to provide more data and some statistics, for refining and tuning IDC evaluation procedures of infrasound monitoring (especially yield estimation).

ACKNOWLEDGEMENTS

The Experiment Division of Israel Defense Forces provided the territory and valuable technical and logistic support (in preparation for the explosion), speed video recording, and high-pressure measurements. Private companies supplied effective HE explosives (IMI Ltd.) and prepared and assembled the charge (Elita Security Ltd.). The Israel NDC provided infrasound array observations at Mt. Meron. The Universities of Mississippi and Alaska (Fairbanks) installed the close station UMUF and the array at Cyprus. The Survey of Israel provided accurate crater measurements. The GII personnel conducted local measurements (U. Peled) and provided all necessary organizational support (R. Hofstetter) and the processing and graphic presentation of air-blast data (N. Perelman).

REFERENCES

Adushkin, V. V. and B. D. Khristoforov (2004). Craters of large-scale surface explosions, *Combust, Explo. Shock Waves* 40: 674–678.

Bowman, J. R., H. Israelsson, G. Shields, M. O'Brien, and Y. Gitterman (2009). Detection and characterization of infrasound signals at IMS stations from explosions at the Sayarim Military Range, Israel: 2005–2009, Infrasound Technology Workshop, Brasilia, Brazil, November 2–6, 2009.

Brown, D., I. Kitov, N. Brachet, P. Mialle, and R. Le Bras (2009). Enhancements to the CTBTO infrasound processing system, Infrasound Technology Workshop, Brasilia, Brazil, November 2–6, 2009.

CraterDatabase_V1.3, (2004). http://keith.aa.washington.edu/craterdata/

Garces M., D. Fee, R. Waxler, C. Hetzer, J. Assink, D. Drob, A. Le Pichon, Y. Gitterman, and R. Hofstetter (2009). The Sayarim Calibration Experiment: Theory and observations, Infrasound Technology Workshop, Brasilia, Brazil, November 2–6, 2009.

Gitterman, Y. and R. Hofstetter (2008). Infrasound Calibration Experiment in Israel: preparation and test shots, in *Proceedings of the 30th Monitoring Research Review: Ground-Based Nuclear Explosion Monitoring Technologies*, LA-UR-08-05261, Vol. 2, pp. 872–881.

Le Pichon A., J. Vergoz, L. Ceranna, D. Brown, G. Aubert, P. Mialle, and N. Brachet (2010). Towards an enhanced picture of the detection capability of the IMS infrasound network, EGU General Assembly 2010.

O'Brien M. S., J. R. Bowman, and G. Shields (2010). Infrasound signals from explosions at the Sayarim Military Range, Israel: 2005–2009, *Report SAIC-10/3001*.

ReVelle, D., R. Whitaker, and W. Armstrong (1998). Infrasound from the El Paso super-bolide of October 9, 1997, Los Alamos National Laboratory report LA-UR-98-2983.

Swisdak, M. and L. Sadwin (1970). Blast Characteristics of 20 and 100 ton hemispherical AN/FO charges, NOL data report, NOL TR 70-32, 17 Mar 1970.

Swisdak, M. (2000). DDESB Blast Effects Computer, Version 4.0.

Whitaker, R. W., T. D. Sandoval, and J. P. Mutschlechner (2003). Recent infrasound analysis, in *Proceedings of the 25th Seismic Research Symposium—Nuclear Explosion Monitoring: Building the Knowledge Base*, LA-UR-03-6029, Vol. 2, pp. 646–654.

INFRASOUND SIGNAL CHARACTERISTICS FROM SMALL EARTHQUAKES

J. Mark Hale[1], Stephen J. Arrowsmith[2], Chris Hayward[3], Relu Burlacu[1], Kristine L. Pankow[1], Brian W. Stump[3], George E. Randall[2], and Steven R. Taylor[4]

University of Utah[1], Los Alamos National Laboratory[2], Southern Methodist University[3], and Rocky Mountain Geophysics[4]

Sponsored by the National Nuclear Security Administration

Award No. DE-AR52-08NA28608
Proposal No. BAA09-49

ABSTRACT

Understanding the source properties responsible for infrasound generation is critical to developing a seismo-acoustic data discriminant to distinguish between near-surface explosions and earthquakes. The regional seismicity, complex topography, open-pit quarries, and subsurface mining in the Utah region create a unique setting for the study of near-field infrasound. The Utah network has been operating three permanent infrasound arrays collocated with seismic stations NOQ (2006), BGU (2007), and EPU (2007). Additionally, four new arrays were installed and collocated with existing seismic stations BRPU, FSUT, HWUT, and WMUT. This summer three additional arrays will be collocated at stations LCMT, PSUT, and RCJ. Each array consists of four infrasound sensors with an average spacing of ~100 m, recording at 100 samples/s, and all data is telemetered to the University of Utah in near-real-time. This increased array coverage provides greater likelihood for independent locations of infrasound sources using crossing backazimuth estimates. The data from the arrays are being processed with InfraMonitor, which generates lists of detections and catalogs of located infrasound sources. Once processing is complete, the detections will be used to correlate and model the infrasound generation by earthquakes utilizing preexisting earthquake scaling relations dependent on depth, magnitude, and mechanism. The observations made during this study will contribute to refining the source excitation model for infrasound.

OBJECTIVES

An understanding of the mechanism involved in infrasound generation by earthquakes is critical for the development of seismo-acoustic discriminants that distinguish between surface explosions and earthquakes. The generation of infrasound from surface explosions has been documented by many groups, e.g., McKenna et al. (2007), Che et al. (2002), and Sorrells et al. (1997). These studies show that infrasound detections can be path dependent (Arrowsmith et al., 2008) and depend on time-varying atmospheric conditions (Garcés et al., 1998). These results suggest that with just a single array many potential infrasound detections might go unrecorded. Previous studies on earthquake-generated infrasound have largely been limited to medium-to-large earthquakes recorded at distances greater than 220 km (e.g., Kim et al., 2004, Mutschlecner and Whitaker, 2005, and Le Pichon et al., 2006). From these studies there is a suggestion of a linear relationship between earthquake magnitude ($M > 4$) and the duration of stratospheric returns as well as a linear relationship between earthquake magnitude and the log of amplitude for stratospheric returns corrected for winds and scaled to a reference distance (Mutschlecner and Whitaker, 2005 and Le Pichon et al., 2006).

Due to the sparseness of historical infrasound deployments, most previous studies of earthquake-generated infrasound studies have focused on only single-array observations; consideration of magnitude scaling relations, while neglecting the effects of earthquake depth, focal mechanism, and local geology; large earthquakes, omitting earthquakes $M < 4$; and observations limited to distances > 220 km. The goal of this project is to expand on previous work as follows:

- **Installing a dense network of seismo-acoustic arrays within 220 km of a major earthquake zone.** All of the arrays are (or will be installed) in the state of Utah within ~115 km of the axis of the Intermountain Seismic Belt (Smith and Arabasz, 1991), a zone of seismicity that extends from Nevada and Arizona northeast to Montana (Figure 1). In addition to the seismicity, the region is marked by complex topography, open-pit quarries, and subsurface coal mining, resulting in diverse seismo-acoustic signals. The network design should reduce the sensitivity to path effects documented from the previous explosion studies and increase the likelihood of acquiring detections on multiple arrays, which will allow robust associations with seismic events (Arrowsmith et al., 2008). The close distance to the sources will allow for analysis of infrasound propagation in the shadow zone where standard atmospheric models predict no infrasound arrivals and where Stump et al. (2007) observed strong variability in infrasound amplitudes.
- **Extending the analysis to earthquakes with $M < 4.0$.** This will be done to determine if similar linear scaling documented by Mutschlecner and Whitaker (2005) and Le Pichon et al. (2006) holds for the smaller magnitudes and if there exists a threshold magnitude or minimum ground motion for generating infrasound.
- **Analyzing source characteristics and earthquake ground motions for earthquakes generating infrasound**. Earthquakes will be analyzed to determine peak ground motions using a combination of observations and predictive ground-motion relations, to refine depth estimates, and, when possible, to determine source mechanisms with a goal of relating these additional source characteristics to the infrasound observations.

Here we report on progress to date that includes the installation of the new arrays, details of the routine data processing that will be applied to the new dataset, and preliminary analysis from two days of processing, each day containing a significant event.

RESEARCH ACCOMPLISHED

Deployment

Network design and array installation have been the focus during this first year of a three-year project. The original plan was to add three arrays to the existing network (NOQ, BGU, and EPU) of infrasound arrays embedded in the Utah Regional Seismic Network (Stump et al., 2009), which were installed in 2006 and 2007. However, instrumentation has been secured with support from PASSCAL such that a total of seven new arrays (see Figure 1 and Table 1) will be installed by the end of September 2010. Four of these new arrays have been installed to date. Data from all arrays are telemetered in near-real-time to the University of Utah and archived at the Incorporated Research Institutions for Seismology's Data Management Center (IRIS DMC) for easy access by all members of the research group. The data are also archived to DVD at the University of Utah.

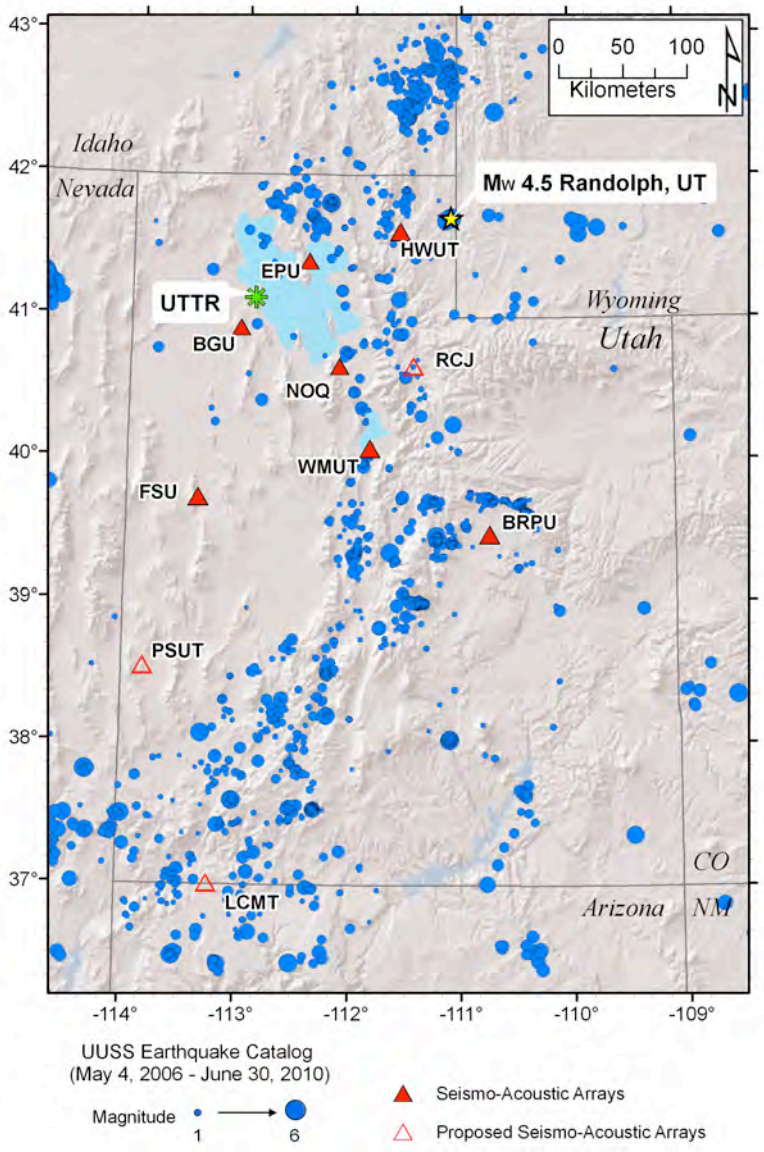

Figure 1. Study area with locations of infrasound arrays and earthquakes M > 1.5 located by the University of Utah seismograph stations between 5/4/2006 and 6/30/2010 (N = 4381). Earthquakes are scaled by magnitude. The seismicity immediately north and west of array BRPU is related to underground coal mining and will not be included in this study. The two events analyzed (Randolph earthquake and the Utah Test and Training Range detonation) are also shown.

Each station consists of four acoustic sensors, with ~100 m spacing, with one acoustic sensor being collocated with a seismic sensor. Figure 2 shows the location and sensor distribution for the array WMUT, which is representative of the general layout of each array in the network. See Table 1 for a complete list of the sensors and telemetry for each array.

The three arrays installed in 2006 and 2007 use Chaparral 2 and Chaparral 2.5c sensors modified by Southern Methodist Univeristy (SMU) to operate on 12 volts rather than 24 volts. This modification includes reducing the sensitivity of the unit from 400 mV/Pa to 200 mV/Pa. Nominal response and self-noise remain the same. In 2006, prior to installation, SMU matched the sensor phase response such that the phase mismatch among the Chaparral sensors in an array was less than 10° in the 0.1- to 5-Hz band. While we expect that the mismatch above 5 Hz is well within 10°, this was not confirmed with laboratory tests.

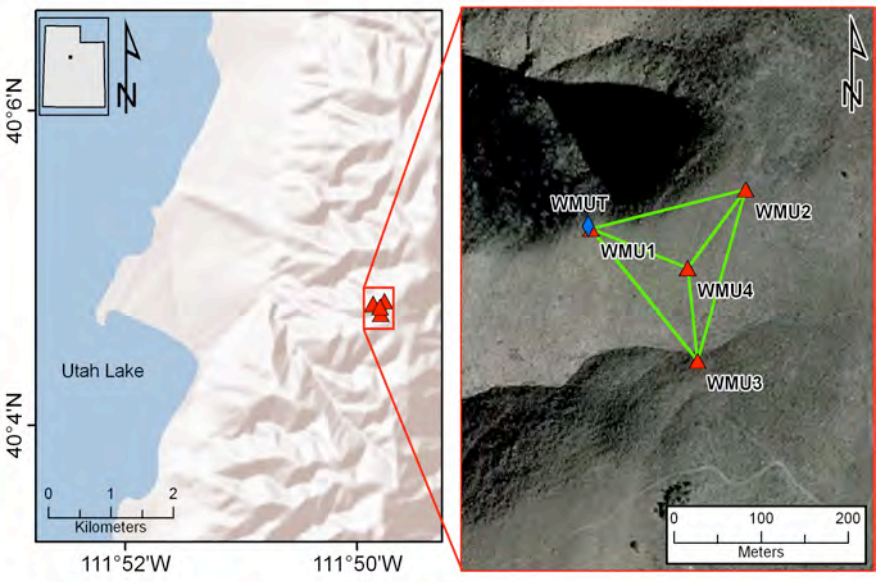

Figure 2. Left: Location of seismo-acoustic array WMUT acoustic sensors shown as red triangles. Right: Overhead view of WMUT acoustic array configuration with ~100 m spacing and northwest element (WMU1) collocated with an existing seismometer (blue diamond).

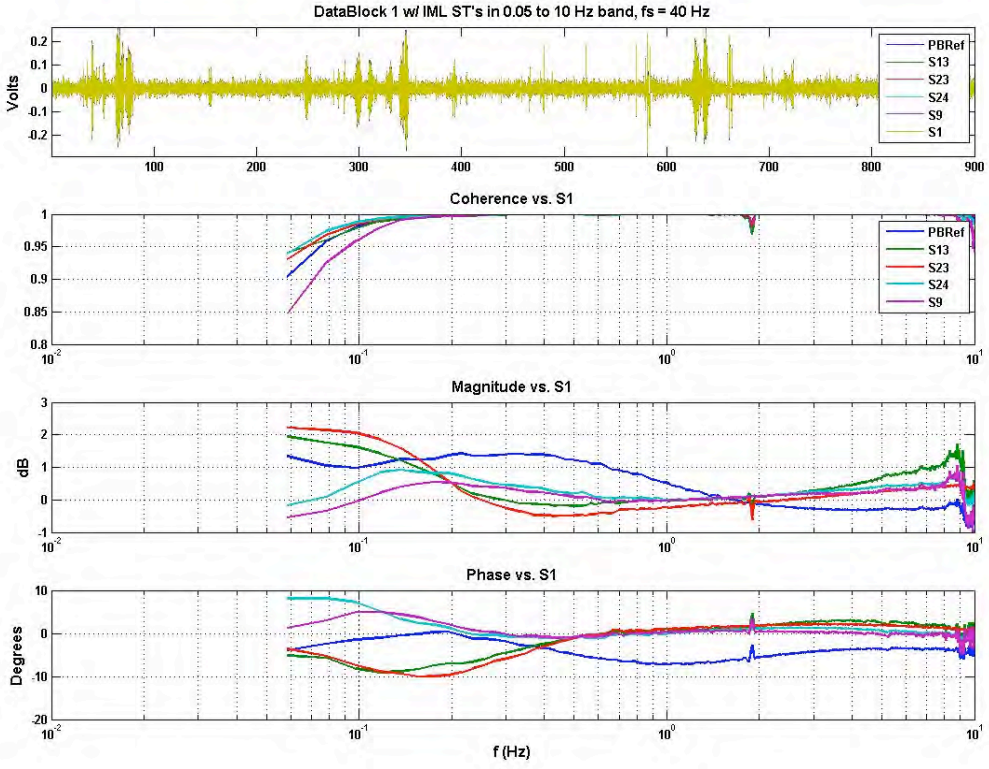

Figure 3. Relative responses of one group of Inter-Mountain Laboratories (IML) sensors from IML's in-house testing and adjustment. The dark blue is a laboratory reference IML used for tracking differences between groups of sensors. (Figure provided by IML.)

For arrays using Chaparral sensors, the sensors are connected to 10-port manifolds with Fiskars-brand 25-ft, 5/8-in. soaker hoses on each port. This forms the standard wind noise filter. Because the original Fiskars-brand hoses are no longer available, the hoses on the existing arrays have not been replaced since installation. In other locations, aging hoses sometimes result in additional wind noise due to cracks and holes in the hose. Thus, it is important to recognize the difference between a detection failure due to low or no signal as opposed to a wind noise–blinded conditions.

The arrays installed under this project use IML Seattle-T (IML-ST) sensors, an improved sensor relative to the earlier IML Seattle-S sensor used as part of an infrasound avalanche detector. Although the IML does not have the flat low-frequency response of the Chaparral, previous tests of the IML Seattle-S sensor by SMU and by Sandia have indicated that it is useful down to 0.10 Hz and up to at least 10 Hz. The IML-ST model has an improved response and is suitable for direct connections to digitizers. The IML models used for this project use 8-port manifolds with the same 25-ft Fiskars-brand hoses.

The IML-ST systems were ordered from IML with a requested phase match at 0.5 Hz. IML sorted the sensors into six groups of four sensors and then adjusted the phase response of the sensors to match within 5° at 0.5 Hz and 3-dB amplitude at 1 Hz (Figure 3). In review, most of the groups were matched better than these nominal values.

Table 1. Instrumentation

	Seismometer	Microphones	Telemetry	Install Date
NOQ	Broadband Nanometrics Trillium 120	Chaparral 2	RADIO	May 4, 2006
BGU	Broadband Nanometrics Trillium 120	Chaparral 2	RADIO	April 17, 2007
EPU	Short-period vertical Mark Products L-4C	Chaparral 2.5	RADIO	July 13, 2007
BRPU	Broadband Nanometrics Trillium 240	Inter-Mountain Labs Model ST	CELL MODEM	April 16, 2010
WMUT	Short-period Vertical Mark Products L-4C	Inter-Mountain Labs Model ST	CELL MODEM	May 8, 2010
HWUT	Broadband Streckheisen STS-2	Inter-Mountain Labs Model ST	RADIO	May 14, 2010
FSUT	Short-period Vertical Mark Products L-4C	Inter-Mountain Labs Model ST	RADIO TO A CELL MODEM	June 10, 2010
PSUT	Broadband Nanometrics Trillium 120	Inter-Mountain Labs Model ST **	RADIO OR CELL MODEM	Planned for July 2010
LCMT	Broadband Guralp CMG-3T	Inter-Mountain Labs Model ST**	RADIO OR CELL MODEM	Planned for July 2010
RCJ*	Short-period vertical Geotech S-13	Inter-Mountain Labs Model ST**	RADIO OR CELL MODEM	Planned for September 2010

** RCJ or nearby site **Planned sensors*

SMU duplicated IML's response results, and compared responses to an additional Chaparral 2.5 sensor that has been used as a reference in adjusting the Chaparrals at the three 2006 arrays and to a Setra Model 239 as a reference to absolute pressure. These results will be incorporated into the SEED dataset header for the delivered datasets.

Data Processing

Continuous data for all arrays are being processed using the Los Alamos National Laboratory InfraMonitor software package (Arrowsmith and Whitaker, 2008). The software uses multiple arrays to detect, associate, and locate infrasound-generating sources. A strength of InfraMonitor is its use of an adaptive noise approach to account for variations in ambient noise. The spatial and azimuthal distribution of the network of arrays with respect to the seismic zone increases the likelihood of acquiring multiple array detections and provides tighter constraints on the infrasound source location (increased number of crossing backazimuths), which is needed to obtain robust associations with seismic events.

For the purpose of example, we have processed two days of data and report on the analysis of two events. The first day, April 16, 2010, contains the recordings from a local M_W-4.5 earthquake located near Randolph, Utah. The second day, June 28, 2010, contains a rocket motor detonation at the Utah Test and Training Range (UTTR). This ground-truth event is used for calibration.

Randolph Earthquake

The Randolph earthquake (M_W 4.5) was the largest recorded earthquake located in the state of Utah since 1992. The earthquake was widely felt throughout northern Utah and parts of Wyoming and Idaho. It was a normal faulting event on a generally north-striking fault (Hermann, undated) and reportedly produced local liquefaction features. Peak horizontal and vertical accelerations (peak ground acceleration [PGA]) recorded at the closest station for this event (HWUT, Δ = 38km) were 0.7% g and 0.2% g, respectively. Using the Pankow and Pechmann (2004) ground-motion relation and the distribution of observed maximum horizontal PGA, the predicted horizontal ground motion at the source approaches 10% g (Figure 4). For an earthquake of this magnitude, the linear relations developed by Le Pichon et al. (2006) predict an infrasound signal with an amplitude of ~0.04 μbars and a duration of ~6 minutes for stratospheric returns.

No infrasound-generated waves were detected for this event at any of the three arrays operational in Utah (BGU, EPU, and NOQ), with distances varying from 115 km to 185 km to the earthquake epicenter. Ground-to-space (G2S) atmospheric profiles extracted for this date at the location of the epicenter (see Figure 1) are shown in Figure 5 for each of the three arrays. The three profiles have been computed by summing the wind in the direction of propagation with the sound speed due to temperature. In order to form a duct, the effective sound speed must exceed the sound speed at the surface (~350 m/s). For this date and location, this only occurs in the thermosphere (~110 km), which would produce returns at horizontal distances greater than those separating the epicenter and the operational arrays. Given the atmospheric conditions, even if the Randolph earthquake generated strong infrasound, the probability of detection by these three arrays would be very low. Had the array at BRPU (distance ~250 km) been installed one day earlier—since the effective sound speed along that path in the stratosphere is greater than for the other arrays (Figure 5)—the probability of detection would have been greater. However, no duct is predicted for that path either, based purely on the unperturbed G2S model. Since the earthquake was located at the edge of our network, the azimuths to each array are similar (south–southwest), and path effects, therefore, are similar. Thus, if path effects are unfavorable, in this case, they are unfavorable to all arrays. This clearly validates our strategy of deploying a dense network of arrays to ensure that the Intermountain Seismic Belt in Utah is well sampled at different directions and azimuths.

Utah Test and Training Range Blast

The UTTR blast was well recorded at five of seven arrays operational at the time of detonation (Figure 6) and was used as a calibration source for the new instrumentation. Array EPU was operating but not telemetering due to vandalism, and array NOQ did not detect the event. Figure 7 shows the data from WMUT processed with

InfraMonitor. At the expected time for epicentral infrasonic arrivals (green bars), there is a peak in both the correlation and F-statistic (Blandford, 1974) parameters corresponding to these arrivals. The backazimuth is also consistent with the known location of the UTTR blast zone. To take advantage of the network of infrasonic arrays, the backazimuth estimate and the infrasonic arrival times from WMUT are combined with the results determined from the four other arrays that detected the blast using the Bayesian Infrasound Source Location (BISL) algorithm developed by Modrak et al. (2010). The results are presented in Figure 8 and provide confirmation of the validity of the algorithm, the success of the array installations, and the accuracy of array metadata. The regions enclosed by the credibility contours are 135 km^2 (at 0.75), 391 km^2 (at 0.9) and 610 km^2 (at 0.95).

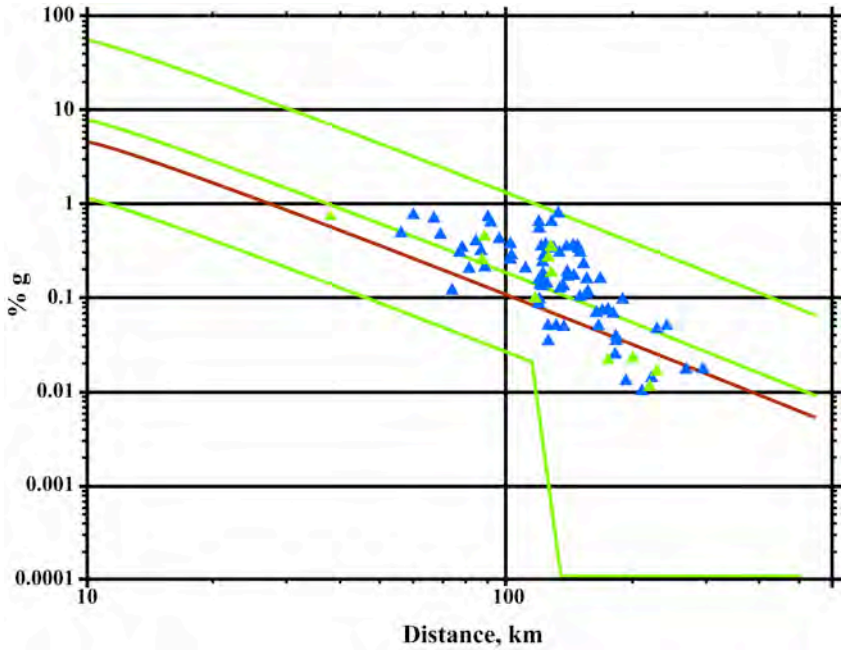

Figure 4. Distribution of maximum horizontal PGA recorded by the Utah Regional Seismic Network (blue triangles = UU stations; green triangles = US and NP stations) for the Randolph earthquake. The red line is the ground motion as a function of distance predicted by Pankow and Pechmann (2004). The green lines are the ground-motion prediction and standard deviation determined by adjusting for the calculated bias in the distribution of measured PGA. This is the method used in ShakeMap (Wald et al., 2005).

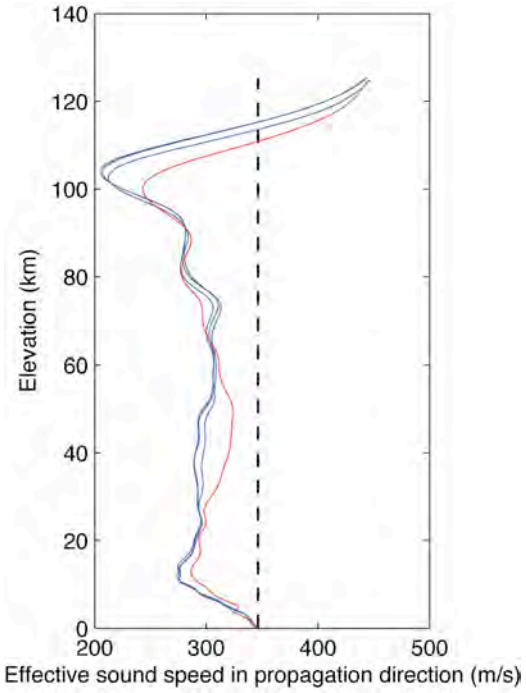

Figure 5. Ground-to-space profiles for April 16, 2010, 00:00 UTC, at the location of the Randolph earthquake epicenter. The three profiles for BGU, EPU, and NOQ (blue) and BRPU (red) have been computed by summing the wind in the direction of propagation with the sound speed due to temperature. The dashed bar represents the sound speed at the ground that must be exceeded to expect local-to-regional returns.

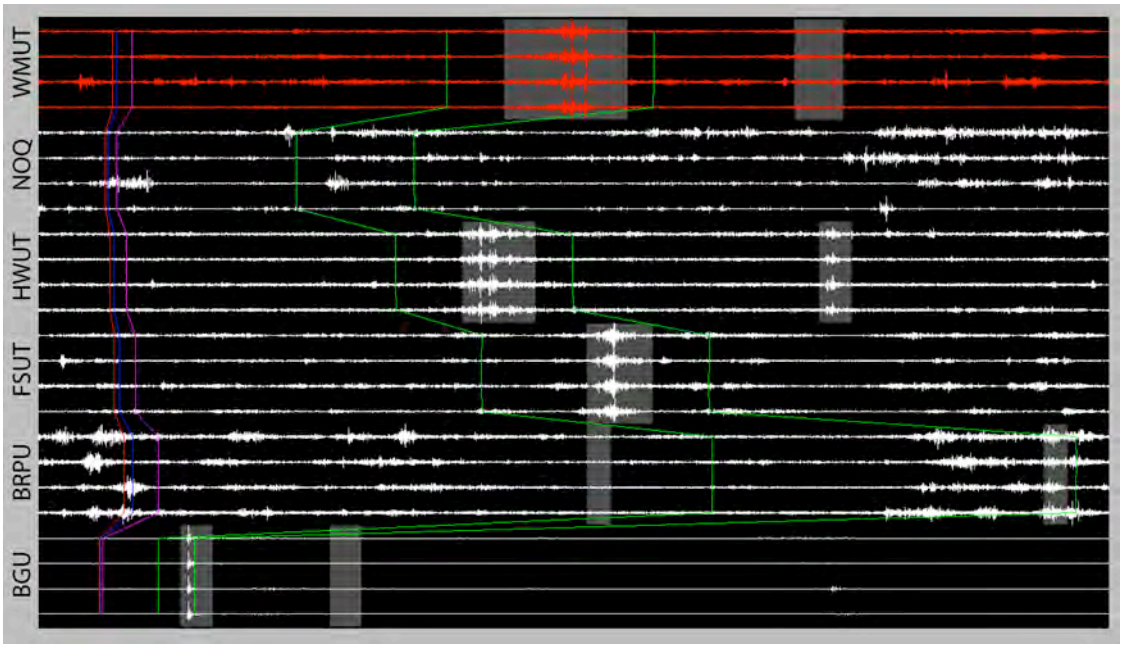

Figure 6. InfraMonitor output of acoustic data recorded from a UTTR blast on June 28, 2010. Expected times for seismic and infrasonic arrivals are denoted by purple and green colored lines, respectively.

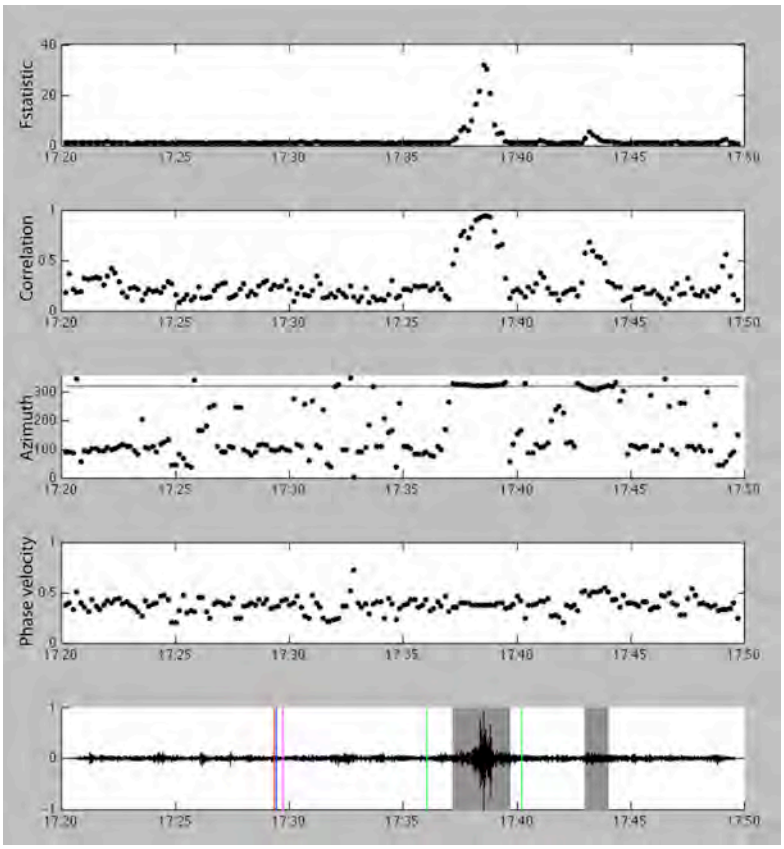

Figure 7. InfraMonitor plot showing the array processing of the June 28, 2010, UTTR blast, recorded at WMUT. The lower panel shows the normalized beam trace (filtered from 1–5 Hz), and the upper four panels show the InfraMonitor-derived array parameters. The purple bars show the expected seismic arrivals, while the green bars show the expected time of epicentral infrasonic arrivals.

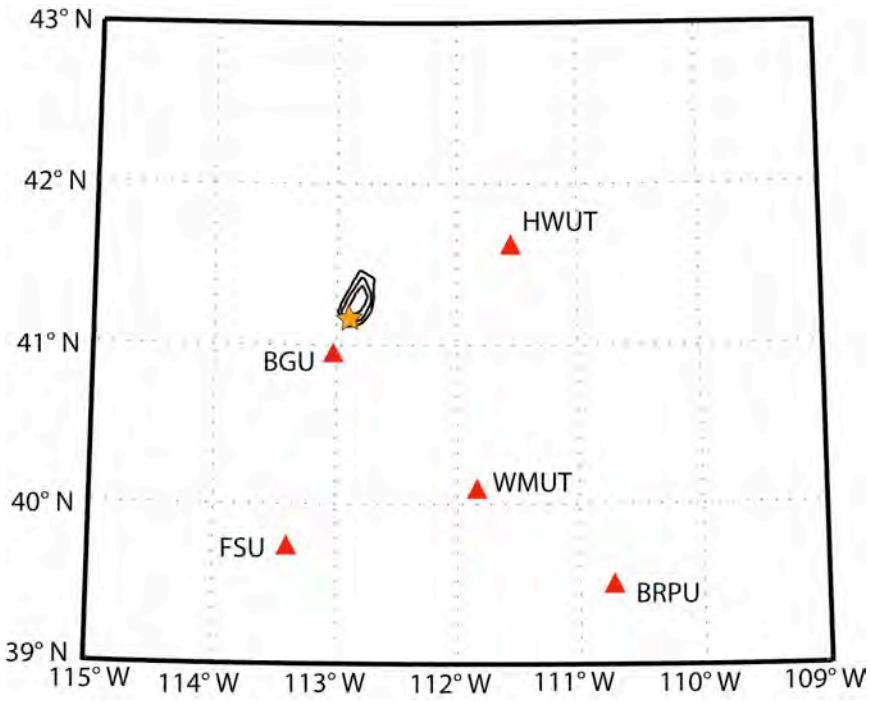

Figure 8. Location of the June 28, 2010, UTTR blast, determined using the BISL algorithm. Triangles show locations of arrays contributing to the location. The source location is shown as 75%, 90%, and 95% credibility contours from the algorithm. The star symbol represents the ground-truth detonation location.

CONCLUSIONS AND RECOMMENDATIONS

The major focus of the first year has been deployment of infrasound arrays, collocated with seismometers within the Utah Regional Seismic Network. When completed, the Utah infrasound network (seven new and three existing arrays) will consist of the most densely spaced local seismo-acoustic array network to date. The arrays are located within a seismic zone, making it possible for possible local infrasonic arrivals, previously overlooked, to be studied. Data from each of the arrays either are or will be telemetered in near-real-time to the University of Utah, where they will be processed and archived at the IRIS-DMC. While the density does not change the likelihood of an infrasound-generating earthquake occurring, the spatial coverage will provide a greater possibility of obtaining multiple observations from smaller earthquakes than in past studies. Continuous data from 2006 to the present are being processed with InfraMonitor in order to generate both lists of detections and catalogs of infrasound source locations using the smaller three-array infrasound network. We provide examples from both an explosion and an earthquake, utilizing data from the new arrays, which confirm that the array installations to date have been successful. Future work will concentrate on the continued processing of the continuous infrasound data and the correlation of identified signals with source characteristics and earthquake ground motions to further refine the source excitation model for infrasound from earthquakes.

ACKNOWLEDGEMENTS

We would like to thank the following for their assistance and continued support throughout this project: Mike Thorne, Dave Drobeck, Peter O'Neill, Wesley O'Keefe, Hans Andersen and William Pomerleau. Dataloggers and materials support are being provided by PASSCAL.

REFERENCES

Arrowsmith, S. J. and R. Whitaker (2008). InfraMonitor: A tool for regional infrasound monitoring, in *Proceedings of the 30th Monitoring Research Review: Ground-Based Nuclear Explosion Monitoring Technologies,* LA-UR-08-05261, pp. 837–843.

Arrowsmith, S. J., R. Whitaker, S. R. Taylor, R. Burlacu, B. Stump, M. Hedlin, G. Randall, C. Hayward, and D. ReVelle (2008). Regional monitoring of infrasound events using multiple arrays: Application to Utah and Washington State, *Geophys. J. Int.* 175: 291–300.

Blandford, R. R. (1974). An automatic event detector at the Tonto Forest Seismic Observatory, *Geophysics* 39: 633–643.

Che, I.-Y., M.-S. Jun, J.-S. Jeon, and K. Min (2002). Analysis of seismo-acoustic events in the Korean Peninsula. *Geophys. Res. Lett.* 29.

Garcés, M., R. Hansen, and K. Lindquist (1998). Traveltimes for infrasonic waves propagating in a stratified atmosphere, *Geophys. J. Int.* 135: 255–263.

Hermann, R. B. (undated, accessed July 2010). Focal mechanism determinations for U.S. http://www.eas.slu.edu/Earthquake_Center/recenteq.html

Kim, T. S., C. Hayward, and B. Stump (2004). Local infrasound signals from the Tokachi-Oki Earthquake, *Geophys. Res. Lett.* 31: L20605 10.1029/2004GL021178.

Le Pichon, A., P. Mialle, J. Guilbert, and J. Vergoz (2006). Multistation infrasonic observations of the Chilean earthquake of 2005 June 13, *Geophys. J. Int.* 167: 838–844.

McKenna, M. H., B. W. Stump, S. Hayek, J. R. McKenna, and T. R. Stanton (2007). Tele-infrasonic studies of hard-rock mining explosions, *J. Acoust. Soc. Am.* 122: 97–106.

Modrak, R. T., S. J. Arrowsmith, and D. N. Anderson (2010). A Bayesian framework for infrasound location, *Geophys. J. Int*. 181: 399–405.

Mutschlecner, J. P. and R. W. Whitaker (2005). Infrasound from earthquakes, *J. Geophys. Res*. 110: D01108, doi:10.1029/2004JD0050067.

Pankow, K. L. and J. C. Pechmann (2004). The SEA99 ground-motion predictive relations for extensional tectonic regimes: Revisions and a new peak ground velocity relation, *Bull. Seism. Soc. Am.* 94: 341–348.

Smith, R. B. and W. J. Arabasz (1991). Seismicity of the intermountain seismic belt, in *Neotectonics of North America*, D. B. Slemmons, E. R. Engdahl, M. L. Zoback, and D. D. Blackwell, Eds. Boulder, CO: Geol. Soc. Am.

Sorrells, G. G., E. Herrin, and J. L. Bonner (1997). Construction of regional ground-truth data base, *Seismo. Res. Lett.* 68: 743–752.

Stump, B., R. Burlacu, C. Hayward, K. Pankow, S. Nava, J. Bonner, S. Hock, D. Whiteman, A. Fisher, T. S. Kim, R. Kubacki, M. Leidig, J. Britton, D. Drobeck, P. O'Neill, K. Jensen, K. Whipp, G. Johnson, P. Roberson, R. Read, R. Brogan, and S. Masters (2007). Seismic and Infrasonic Energy Generation and Propagation at Local and Regional Distances: Phase I—Divine Strake Experiment, Air Force Research Laboratory report, AFRL-RV-HA-TR-2007-1188.

Stump, B., Hayward C., Arrowsmith S., Randall G., Pankow K., Burlacu R., and Taylor S. R (2009). Infrasound from earthquakes: Signal characterizations, in *Proceedings of the 2009 Monitoring Research Review*: *Ground-Based Nuclear Explosion Monitoring Technologies,* LA-UR-09-05276, Vol. 2, pp. 742–749.

Wald, D. J., B. C. Worden, V. Quitoriano, and K. L. Pankow (2005). *ShakeMap Manual: Technical Manual, User's Guide, and Software Guide.* U. S. Geological survey.

Data Processing and Analysis

A SOFTWARE TOOLBOX FOR SYSTEMATIC EVALUATION OF SEISMOMETER-DIGITIZER SYSTEM RESPONSES

Jessie L. Bonner[1], Robert B. Herrmann[2], Anastasia F. Stroujkova[1], and Mark R. Leidig[1]

Weston Geophysical Corporation[1] and St. Louis University[2]

Sponsored by the National Nuclear Security Administration

Award No. DE-FG02-09ER85548/Phase_I

ABSTRACT

Measurement of the absolute amplitudes of a seismic signal requires accurate knowledge of the seismometer-digitizer response. When the seismometer and digitizer characteristics are known, deconvolution of the digital system response is relatively straightforward. However, even with a known response, problems in timing and incorrect polarities can often contaminate any calibration parameters derived from these data. When either one or both components of the response for a seismometer system are unknown, the data are often not considered suitable for seismological tasks that require absolute amplitude measurements.

We have developed a set of software tools that can recover the sensor/digitizer response function from raw data when the response is either unknown or incorrectly known. These software tools include:

- **SACPSD**: a power spectral density (PSD) estimator for background noise spectra at a seismic station. SACPSD differs from the current PSD used by NEIC and IRIS in that the smoothed spectra are derived by smoothing over linear frequencies rather than logarithmic periods, resulting in smoothed PSD that tracks the unsmoothed PSD rather than exhibiting a bias where the raw PSD drops rapidly with increasing period. SACPSD is fast and can be used routinely to monitor network performance and metadata validity,

- **NOISETRAN**: a prototype method of estimating the broadband seismic system response for a seismic station based on the background noise at a nearby reference station,

- **GUIs/SCRIPTS**: we have developed Graphical User Interfaces (GUIs) and shell scripts that provide seismologists with easy access to the software in the system response recovery toolbox.

During Phase I of this Small Business Innovative Research (SBIR) project, we have also compiled an extensive database of seismic sensors and recorders that are in use or have been developed. Information on each instrument includes sensitivities, bit weights, and gains. The database also contains station information and response corrections for many stations actively or previously installed around the world. The information in this database provides another step in determining the proper response correction for an unknown station.

Our results indicate that our Phase I project demonstrated both technical feasibility and a high potential to achieve the GNEM R&D goals for system response recovery of important seismic datasets.

INTRODUCTION

For this Phase I SBIR FY2009 project, we began the development of a software toolbox to estimate, assess, and chronicle the seismometer and digitizer response from recorded seismic data. The specific technical objectives included developing a comprehensive database of known seismometer and digitizer responses. Next, we have assembled a set of seismic analysis tools (Figure 1) to iteratively recover the instrument response (either precisely or rough order-of-magnitude). We estimate a station response transfer function by fitting the seismic data at an unknown station to the background noise and recorded signals from nearby stations with known responses. We have also investigated tools for metadata validation and initiated development of an easy-to-use graphical-user-interface to assist the user in running the programs.

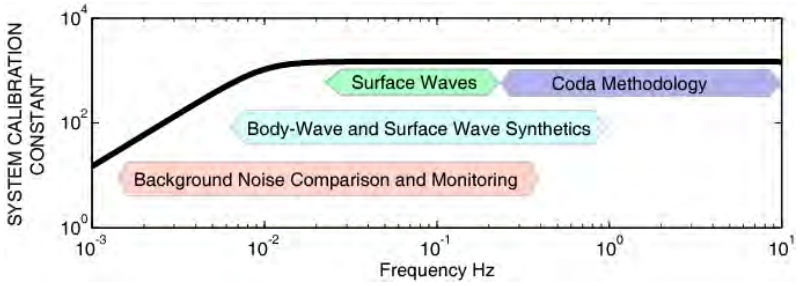

Figure 1. Schematic showing our techniques for recovering the seismometer-digitizer response for recorded seismic data. The methods include developing transfer functions using noise, surface wave and coda methods, developing synthetics for comparison to the observed data, and monitoring broadband background noise for timing, gain changes, and metadata discrepancies.

RESEARCH ACCOMPLISHED

Seismometer-Digitizer Database

During Phase I of the project, we compiled an extensive database of seismic sensors and recorders that are in use or have been developed. Information on each instrument includes sensitivities, bit weights, and gains. The database also contains station information and response corrections for many stations actively or previously installed around the world. The information in this database provides an initial step in determining the proper response correction for a station with unknown response.

The database consists of 400 seismometer, accelerometer, and infrasound sensors. Almost every sensor in the database includes the response sensitivity, with 107 instruments having more than one possible manufactured sensitivity. A more complete instrument response definition in the form of a pole/zero file is available for 21% of the sensors. There are 50 digitizers in the database, but only a small number of these are traditionally used for seismic recording. The bit weight needed to convert the digitized signal back to that output from the sensor was acquired for these most common recorders. Approximately half of the recorders can record at more than one gain setting.

The database contains varying amounts of information on over 16000 actively and previously deployed stations from around the world. Information includes the station name, location, dates of operation, instrumentation deployed, and instrument responses. A map of the 4016 stations with instrument response information is shown in Figure 2. These stations with known responses can be used to correct data recorded nearby with unknown responses. Examples of the amplitude responses for many of the United States National Seismic Network (USNSN) stations are shown in Figure 3.

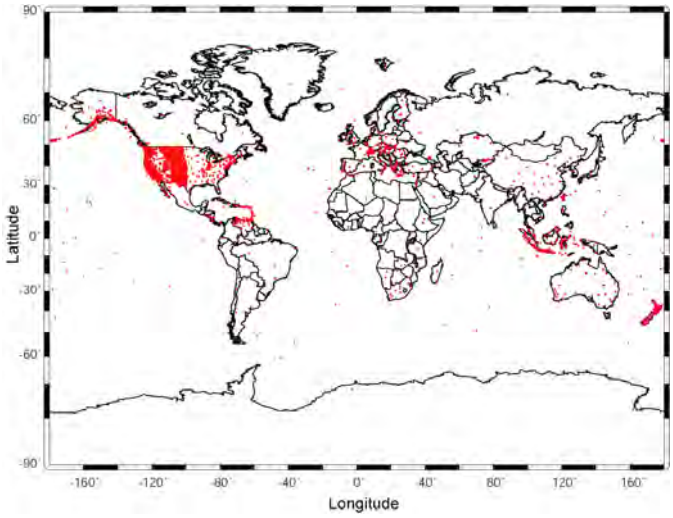

Figure 2. Map of pertinent stations (red dots) with instrument response correction information in the database.

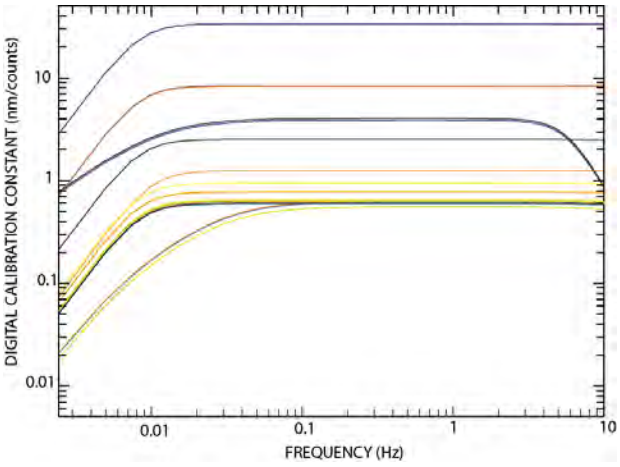

Figure 3. Seismometer-digitizer responses for United States National Seismic Network (USNSN) broadband stations (vertical component). There are 63 different stations plotted.

SACPSD

The determination of PSD of Earth noise is a useful tool for monitoring noise sources and for the performance estimation of seismic instruments (McNamara and Buland, 2004). As part of the Phase I project, we developed SACPSD, a GSAC program that calculates power spectral densities for seismic data. The program allows the use of routine PSD measurements as a tool for verifying the metadata for digital instrumentation and for checking on instrument performance. We also use SACPSD to help recover system responses based on noise estimates from a reference station—further discussed in the NOISETRAN section of this proposal.

The computation of power spectra follows Ifeachor and Jervis (1993). Given a time series x_k, we first correct that series to have a zero mean, apply a window, w_k, and correct amplitudes for the windowing function. Their equation (10.16) defines the corrected time series, s_k, as

$$s_k = c_2 w_k (x_k - c_1), \quad (1)$$

where the constants are defined as

$$c_1 = \frac{\sum_{k=0}^{N-1} w_k x_k}{\sum_{k=0}^{N-1} w_k} \text{ and } c_2^2 = \frac{N}{\sum_{k=0}^{N-1} w_k^2}, \quad (2)$$

and N is the number of equally spaced observations, with sampling interval Δt. In SACPSD, the user may select either a Hanning window or a 10% sine taper for the windowing function.

Using an N-point discrete Fourier transform (DFT), the transform of s(k) is S(n), which is defined as

$$S_n = \sum_{k=1}^{N-1} s_k \exp(-j2\pi\, ft)\,\Delta t = \sum_{k=1}^{N-1} s_k \exp(-j2\pi nk / N)\Delta t \quad (3)$$

where n=0,...,N-1 , t = k Δt and f=n Δf. Because of the definitions of the forward and inverse DFT's, both s_k and S_n are periodic. The power spectrum density is defined as

$$PSD(f = n\Delta f) = 2S_n^2 / T \quad (4)$$

where the time window $T = N\Delta t$. The factor 2 accounts for the negative frequency contribution.

For actual processing, the initial time series is assumed to consist of more than N=16384 points. Then using successive N point segments that overlap by N/2 points, the individual PSD's are summed and finally averaged by dividing by the number of segments, NSEG. The stacking and averaging reduces the variance in the PSD estimate, yielding a smoother PSD.

The estimate of the ground noise uses the frequency dependent modulus of acceleration sensitivity of the sensor, G (in counts/m/s^2) to give the noise estimate in decibels through the relation

$$N(f) = 10\log_{10}\frac{1}{NSEG}\sum_{i=1}^{NSEG}\frac{PSD_i}{G^2} \quad (5)$$

For comparison with other noise-PSD algorithms, a smoothed noise spectrum is computed from

$$\frac{1}{NSEG}\sum_{i=1}^{NSEG}\frac{PSD_i}{G^2} \quad (6)$$

by applying a simple smoother, currently a 5-point averaging operation in the equi-spaced frequency domain. Other smoothers may be implemented in the future. We note that McNamara and Buland (2004) apply a smoothing operation over period. Finally the smoothed noise spectrum is linearly interpolated to yield estimates at periods that are multiples of $2^{1/8}$ and then converted to decibels. To make the output independent of sampling rate, the multiples are always with respect to a period of 1.0 seconds. This smoothed version is always plotted as an overlay onto the N(f).

SACPSD is written in C and then easily transformable to other languages (e.g., JAVA or MATLAB). SACPSD is lean, easily adapted to field use and requires only that the acceleration sensitivity of the instrument be known. It is fast on laptops and could easily be used in the field for rapid estimation of noise power spectral densities (e.g., on noise studies for array siting).

Processing scripts have been developed to use SACPSD for a variety of different applications. We have used the method to examine errors and inconsistencies in metadata that accompany downloaded data from seismic networks. Similar analysis is performed routinely at NEIC and at IRIS to focus on individual channel performance with time. The purposes of the current implementation of SACPSD is a) to focus on individual network performance, since the actual noise field at certain periods should be the same for a network covering a relatively small geographical area and b) to note inconsistencies that may have to be addressed by the data/metadata generator or by the data/metadata servers. Figure 4 compares the noise PSDs for 568 vertical component traces. The overlay plot shows the high and low noise model limits (Peterson, 1993) and the individual station PSDs.

The color coding provides a means for identifying a curve. There are obviously a few outliers which can be examined in more detail by analyzing the SACPSD results of individual sub-networks.

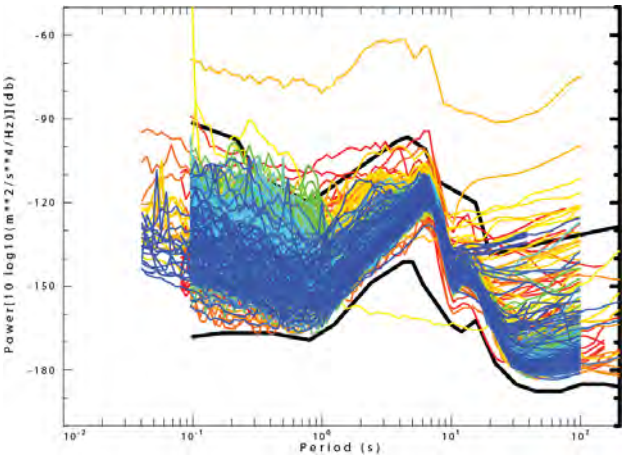

Figure 4. An overlay of 568 individual noise PSD's of USGS Network data based on the one-hour segment starting at 2010/02/17-01:00:00. The colors are used to distinguish individual estimates. The two black lines represent the new low and high noise models (Peterson, 1993). Note that the comparisons are a reflection solely of the waveform data at the USGS and of the existing metadata on the day that this comparison was run, e.g., February 21, 2010.

Figure 5 shows the result of running SACPSD for the New Madrid (NM) network in the central United States. For the NM network operators, the positive aspect of this plot is that all systems, except PBMO, show the same noise levels between 6 and 20 seconds. Clearly PBMO behaves differently having a gain of about 6db (a factor of 2) higher than the others. At long periods, the PBMO response differs greatly, indicating a sensor problem.

The short-period noise at PVMO (neon green in Figure 5) is very high, as is expected since this is a deep sediment site, just a short distance (200 meters) from a railroad. A visual examination of the hour-long segment shows that there is a significant noise burst, possibly from a train.

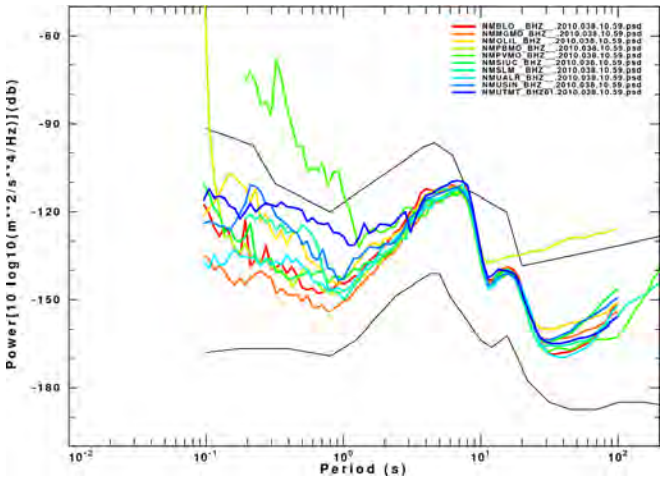

Figure 5. Result of running the SACPSD program for the BHZ components of the New Madrid network. The reason that different components cover different period ranges is due to the variable sample rates. PVMO has a rate of 20 Hz while the others have a rate of 40 Hz.

At a period of 0.1 sec, the curve for PBMO (light green in Figure 5) is very high. We know that this station has a sample rate of 40 Hz, but this behavior is indicative of using the response for a 20 Hz sampling interval which is indicated in the RESP file. This was not expected since the station was upgraded in November, 2009 to 40 Hz. We then verified that the correct metadata had not yet been loaded into the NEIC metadata server.

Results of applying SACPSD to the Cal Tech network data for February 21, 2010 is shown in Figure 6. Interestingly, the top five stations differ from the final four by ~12 db, which would translate into a factor of 4. A station map shows that this difference is not due to proximity to the ocean. We have yet to determine the reason behind this difference, but one suggestion is that the data are being sampled with Quanterra HR digitizers with a metadata response file for a non-HR digitizer.

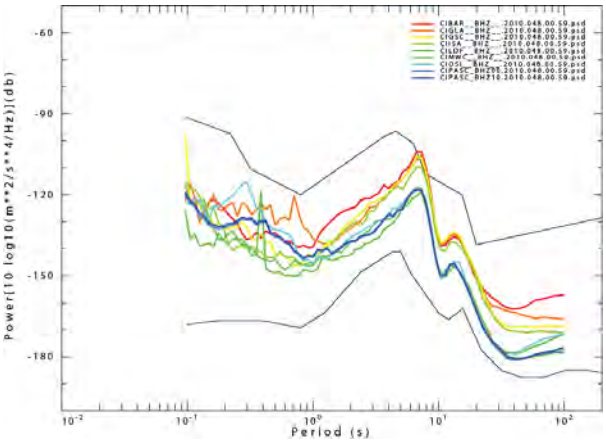

Figure 6. Result of running the SACPSD program for the BHZ components of the Cal Tech (USA) network showing two distinct sets of noise curves separated by ~12 db.

NOISETRAN: Noise Transfer Functions for Pseudo-Response Estimation

Important calibration datasets may be obtained in which no metadata accompany the waveforms. We are examining methods that attempt to determine a rough order-of-magnitude (ROM) estimate of the seismometer-digitizer response by considering the background seismic noise at a nearby seismic station with a known response (e.g., the "reference" station). We refer to this method as NOISETRAN, as we attempt to estimate a *transfer function* $T(\omega)$ to convert the background seismic *noise* at a station ($R_1(\omega)$) with unknown response (henceforth referred to as the "candidate" station) to the background noise levels at a reference station $R_2(\omega)$. The transfer function can be estimated using:

$$R_1(\omega)=R_2(\omega)*T(\omega). \quad (7)$$

Once the ROM system response $R_1(\omega)$ has been recovered, we can then use waveform modeling techniques to further refine the system response.

Our assumption for attempting the NOISETRAN technique is that the actual noise field at certain periods should be the same or similar for a network covering a relatively small geographical area. McNamara and Buland (2004) showed the geographical distribution of noise in three different period bands (e.g., 0.125-0.0625 sec, 8-4 sec, and 64-32 sec) in North America. They observed the strongest geographical variations at periods > 1 second due to cultural noise, especially near large population centers. Proximity to oceans dominates the variations in the microseism band (8-40 sec). They note that at longer periods (64-32 sec), the geographic variations decrease, and that the responses are more a function of the installation characteristics (e.g., borehole vs. surface installation) than the actual seismic noise characteristics. These results suggest that our best results of NOISETRAN will most likely occur at periods longer than 1 sec. We did not correct for possible noise sources during the Phase I project, but believe that our results suggest improvements could be made during the Phase II research based on noise prediction for the candidate stations.

NOISETRAN is initiated by manually selecting a reference station. The considerations for choosing a reference station should include: 1) a well-established background noise model for the reference stations (e.g., such as those provided by Berger *et al*. 2004; McNamara and Buland, 2004, and others), 2) proximity to the stations of interest, and 3) whenever possible, a similar noise background level between the reference and unknown stations.

The choice of a pre-determined background level at the reference station based on a yearly average was based on a Phase I objective that the data at the reference station and unknown station need not overlap. However, the noise stationarity becomes an issue in this case, because the noise PSD varies depending on the time of day, year, weather, etc. For example, the noise in the microseism band has significant annual variations (15-20 dB) according to McNamara and Buland (2004). In order to find an asymptotically unbiased estimate of the PSD one has to use very long time intervals (> 1 year).

If the shorter time interval is used, the PSD can be expressed as a sum of a mean value m_{PSD} and some quasi-periodic function d_{PSD}. If the seasonal variations are similar between the reference station and the unknown station, it may be possible to estimate the PSD for both stations during the same time intervals, which might minimize the error associated with these long-period variations. For the Phase II project, we will determine if NOISETRAN can be improved by calculating SACPSDs on data recorded from the same date and time at the reference and unknown stations; however, this procedure requires accurate knowledge of the system response at the reference station.

For the examples presented in the Phase I research, we chose to recover the ROM system response of a 19-station proprietary dataset from the Middle East obtained in 2008 by Weston Geophysical Corporation. Due to the sensitivity of these data, we do not provide a map of the candidate stations or the reference station, which was selected because it was the only open Global Seismographic Network (GSN) station with both a well-known seismometer-digitizer response and published background noise levels within 10 degrees of the proprietary seismic network. The reference station was located at distances between 183 and 612 km from the candidate stations. No metadata accompanied the initial delivery of the candidate waveform database to Weston Geophysical Corp, thus we did not know if the data were in counts or volts, velocity or acceleration. We chose to develop the NOISETRAN functions for this unknown network by comparing it to the 50th percentile background noise levels at the reference station as estimated by Berger et al. (2004).

For the next stage of NOISETRAN, the SACPSDs for the raw data recorded by the candidate stations are estimated and compared to the noise PSD of the reference station (Figure 7). For this case, we have chosen the Berger et al. (2004) supplied noise curve for the reference station, which are typically provided at frequencies between 0.01 to 10 Hz. The spectral division between the candidate and the reference station yields the noise-based transfer function, which can be used to convert the unknown units to the units of the reference station. Because seismologists are often more familiar with the velocity response for many broadband instruments (see Figure 3), we convert the transfer functions to velocity and plot each NOISETRAN in Figure 7. Each of these curves can be used to convert the raw data to “approximate” units of velocity in m/sec. We emphasize that NOISETRAN will not provide the true ground velocity unless the noise between the reference and station of interest are exactly the same. We maintain that NOISETRAN can provide seismologists with a broadband ROM estimate of the response that may be improved with additional tools to be developed during the Phase II project.

We did know that the instruments that comprised this proprietary dataset were broadband instruments all from the same manufacturer (Guralp), thus the response for each should be very similar with only small differences in the calibration values. The NOISETRAN results provide somewhat conflicting information. At frequencies between 0.05 and 0.8 Hz, the scatter between the curves is reduced, and it would be possible to fit these curves reasonably well with a single instrument response. At frequencies above 1 Hz and below 0.05 Hz, the scatter between the transfer functions is increased and a single-response would seem implausible. These frequency ranges are somewhat in agreement with the geographical variations of noise as a function of frequency suggested by McNamara and Buland (2004). NOISETRAN seems to be providing reliable system-response recovery in the microseism bandwidth for these stations, which are all located at least 500 km from the nearest ocean. It is outside this band, where cultural noise and site effects are providing the increased scatter in the NOISETRAN method.

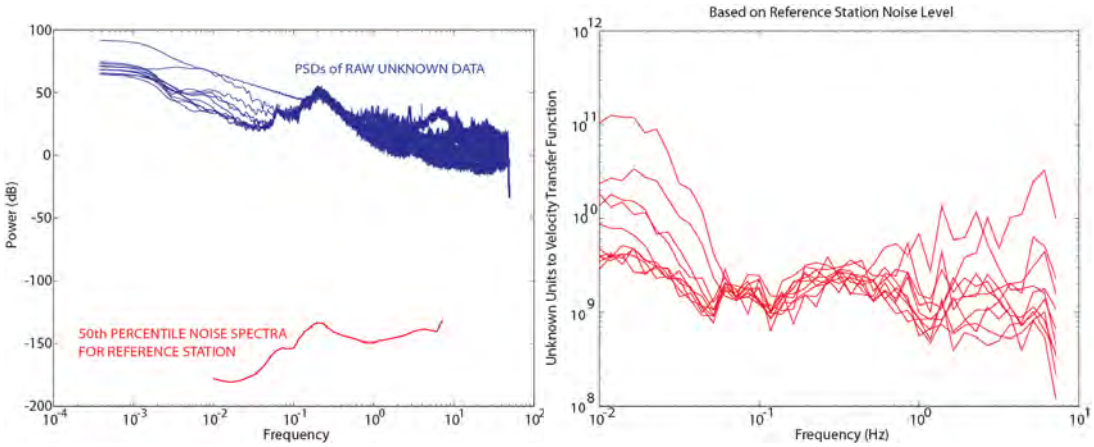

Figure 7. (Left) SACPSDs of raw data (blue) from a 2008 dataset that originally had no accompanying metadata. The red line is the 50% percentile noise estimate (Berger et al., 2004) at a reference station located between 183 and 612 km from the stations candidate stations. The reference data PSD are in units of acceleration while we did not know the units for the candidate stations. (Right) NOISETRAN-estimated transfer function that transforms the candidate data from unknown units to either acceleration or (in the case above) velocity (m/sec) by correcting the data to the 50% noise level at the reference station.

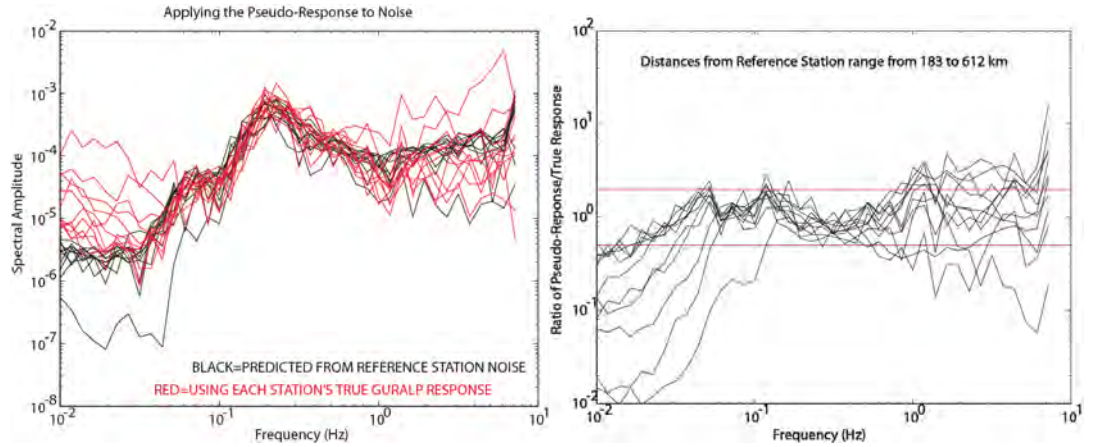

Figure 8. (Left) Comparison of our pseudo-response corrected data (black) to the true response calculations (red). We eventually obtained some metadata, including company-supplied PZ files, for the stations in this dataset. We corrected the data for the instrument response and then compared to our NOISETRAN-estimated responses obtained from noise levels at the reference station. The spectral ratios for the individual stations (pseudo-response/true-response) are shown at right.

Eventually, we were able to obtain nominal instrument response data for the candidate sensors from the manufacturer. We generated poles and zeros (PZ) files for each station and corrected the data for the true instrument response using the *transfer* command in GSAC (Herrmann, 2008). Figure 9 provides a comparison of background noise that has been converted to spectral amplitudes using NOISETRAN (black) and the true response (red). As suspected from Figure 7, NOISETRAN provides reliable estimates of the background noise at frequencies between 0.05 and 0.8 Hz and less reliable estimates outside this band. When spectral ratios between the NOISETRAN and true response estimates are formed (Figure 8), we note that most of the spectral ratios are within a factor of ±2 of an exact fit between the true response and NOISETRAN method across the entire frequency band. It is surprising and worth additional study as to why the worst fit is at frequencies less than 0.05 Hz. One thing to note is that the scatter

in these spectral ratios would have been reduced more had we used the 90th percentile noise estimate for the reference station in the initial steps of NOISETRAN. In other words, it was a quiet day at the reference station at the time the candidate PSDs were estimated. This led us to postulate that the more appropriate method might be to use data from the reference station at the same time as the data from the candidate stations when forming the transfer functions. We hope to examine this further in Phase II.

We present Figure 9 to show how well NOISETRAN works when applied to actual earthquake signals recorded on the proprietary network. For regional recordings of this earthquake, we applied NOISETRAN and the true seismometer-digitizer responses to the signals. We then estimated a surface wave magnitude using data at periods between 8 and 40 seconds. We note only a difference of ~0.1 magnitude unit between the NOISETRAN-corrected and known pole-zero-corrected waveforms (e.g., 5.65 vs. 5.56). These results indicate technical feasibility and warrant further analysis and possible refinement during the Phase II project.

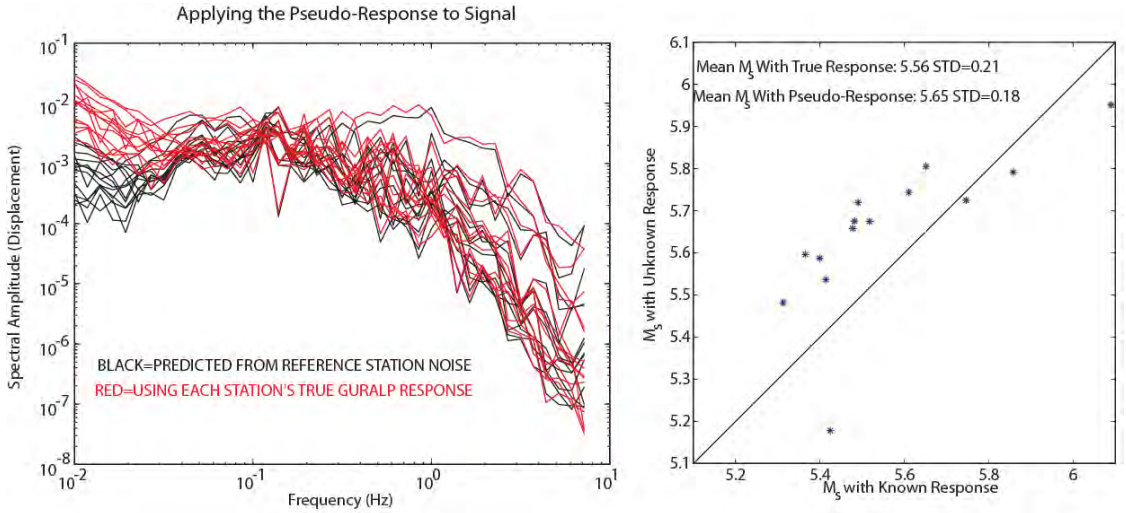

Figure 9. Results of applying the NOISETRAN response functions to an earthquake recorded on the proprietary network. The surface wave magnitude estimated using the NOISETRAN-estimated response is approximately 0.1 m.u. larger than the estimate from the true response.

Graphical User Interface

To facilitate the procedures required for an effective system for monitoring system response, Weston Geophysical Corp. has implemented an easy-to-use GUI in MATLAB. The Phase I toolbox currently includes 1) a database of known seismometer and digitizer responses and 2) methods for estimating response "transfer" functions between stations with and without known responses. The program is written in Matlab™ and uses SAC files as an input. The features implemented in the software package during the Phase I project include:

Seismometer-Digitizer Database. Figure 10 shows the GUI layout highlighting access to the instrument response database. The pull-down menu on the right shows a list of the instruments currently in the database. In this example, the pole-zero diagram is presented on the lower right of the GUI and shows the poles (red crosses) and zeros (blue circles) for a Guralp 3T seismometer. The amplitude response for the systems is shown to the left.

NOISETRAN. This feature provides a GUI for calculating the NOISETRAN functions. Figure 11 shows the response transfer function is obtained for station ANMO (Albuquerque, New Mexico, United States) using the TUC (Tucson, Arizona, United States) noise floor.

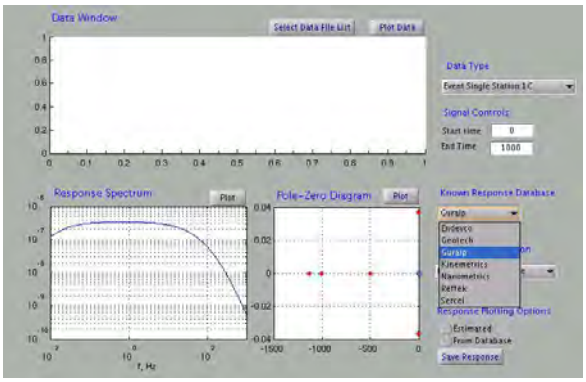

Figure 10. GUI layout with shown access to the database of known responses. In this example the pole-zero diagram (bottom right) corresponds to the response function (bottom left) for Guralp 3T as an example.

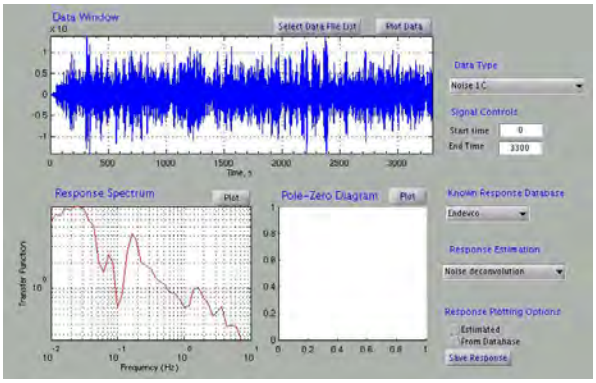

Figure 11. Acceleration NOISETRAN for station ANMO obtained by dividing the spectrum of the noise shown in the window by the noise floor computed for TUC (e.g., Berger et al, 2004).

CONCLUSIONS AND RECOMMENDATIONS

Under the DOE SBIR/STTR FY 2009 Phase I program, we have developed a set of software tools that can recover a ROM sensor/digitizer response function from raw data when the response is either unknown or incorrectly known. Our results indicate that our Phase I project demonstrated both technical feasibility and a high potential to achieve the GNEM R&D goals for system response recovery of important seismic datasets. For the Phase II project, we plan to further enhance the software tools initiated during the Phase I. We will focus on the development of an easy-to-use interface (either using GUIs or scripts) for the seismologist to apply these software tools to their dataset of interest. We will Alpha test the updated version of the system response recovery toolbox on several proprietary datasets recently acquired from the Middle East by Weston Geophysical that have response and metadata inconsistencies. The final component of the Phase II project would include Beta testing of the software toolbox at another data center.

REFERENCES

Berger, J., P. Davis, and G. Ekstrom (2004). Ambient earth noise: a survey of the Global Seismographic Network, *J. Geophys. Res.* 109: B11307.

Ifeachor E. C. and B. W. Jervis (1993). *Digital Signal Processing - A Practical Approach.* Addison-Wesley Publishing Company, Wokingham, England, 492–505.

Herrmann, R. B. (2008). *Computer Programs in Seismology.* St. Louis University.

McNamara, D. E. and R. P Buland (2004). Ambient noise levels in the continental United States, *Bull. Seism. Soc. Am.* 94**:** 1517–1527.

Peterson, J. (1993). Observation and modeling of seismic background noise, *U. S. Geol. Surv. Tech. Rept. 93-322*, 1-95.

ENHANCING SEISMIC CALIBRATION RESEARCH THROUGH SOFTWARE AUTOMATION AND SCIENTIFIC INFORMATION MANAGEMENT

Douglas A. Dodge, Michael D. Ganzberger, Teresa F. Hauk, and Stanley D. Ruppert

Lawrence Livermore National Laboratory

Sponsored by the National Nuclear Security Administration

Award No. DE-AC52-07NA27344/LL09-IRP-NDD02

ABSTRACT

The National Nuclear Security Administration (NNSA) Ground-Based Nuclear Explosion Monitoring Research and Development (GNEMRD) Program at Lawrence Livermore National Laboratory (LLNL) continues to make significant progress enhancing the process of deriving seismic calibrations and performing scientific integration, analysis, and information management with software automation tools. Our tool efforts address the problematic issues of very large datasets and varied formats encountered during seismic calibration research. New information management and analysis tools have resulted in demonstrated gains in efficiency of producing scientific data products and improved accuracy of derived seismic calibrations. Data automation facilitates research data integration and validation.

This year most of our development work has been directed toward additional automation of our data ingestion capabilities. Our specific automation methodology and tools improve the researchers' ability to assemble quality-controlled research products for delivery into the Knowledge Base (KB). The software and scientific automation tasks provide the robust foundation upon which synergistic and efficient development of GNEMRD Program seismic calibration research may be built. Three new Java programs, BulletinLoader (seismic bulletins), SegmentLoader (seismic waveforms), and MTLoader (moment tensor information) have been developed that replace older C/C++ codes and extend the capabilities of those codes to reduce the amount of required human supervision. This allows resources to be focused on analysis and production of calibration products.

The BulletinLoader tool is a Java replacement for the C++ program ORLOADER which we have been using for many years to load earthquake catalogs. Currently, BulletinLoader supports 16 bulletin formats. More importantly, it runs autonomously, retrieving bulletins as they become available on the Internet. BulletinLoader also can retrieve data from remote databases, and can be configured to automatically retrieve such data as they are added to the remote database. The SegmentLoader tool is a new Java application that replaces existing (C/C++) applications DDLOAD and UPDATEMRG. SegmentLoader loads waveform data from various flat file formats as well as from remote databases. It has the capability to cut segments from continuous sources or to load segments that have been created by other means. SegmentLoader leverages part of its code base with the WaveformRetriever and extends its functionality. In addition, we are creating a generic application layer that will allow clients to identify and retrieve needed bulletin and waveform data, load data as required into our database, and then display the new data in the client. The moment tensor loading tool (MTLoader) utilizes the recently-implemented GNEMRD schema for moment tensors. The tool allows loading of moment tensor information in a number of formats and can be run autonomously to retrieve moment tensor information from external network sources as soon as data become available. The Surface Wave Amplitude Processor (SWAP) tool produces high quality amplitude measurements of surface wave amplitudes. It leverages GNEMRD moment tensor schemas and is our first client software that uses the NASA World Wind software (http://worldwind.arc.nasa.gov/java/) for interactive mapping capability that produces fully interactive, 3-D imagery-based maps with excellent resolution.

These new applications comprise a significant re-engineering of our data management software suite designed to leverage new data distribution technologies that have been developed by data providers in the last few years. Exploitation of the new methods has resulted in demonstrated gains in efficiency and reduction in time required to identify, acquire, process raw data essential for calibration research. Improved process efficiency has potential applicability beyond GNEMRD.

OBJECTIVES

As the LLNL GNEMRD database and supporting software have matured, we have continually found more opportunities for automating pieces of our processing flow. Initially, our efforts were devoted mainly to replacing data-loading scripts with software specialized for the task of loading waveforms and bulletins. Later we developed automated procedures for identifying and publishing ground-truth information in newly ingested data.

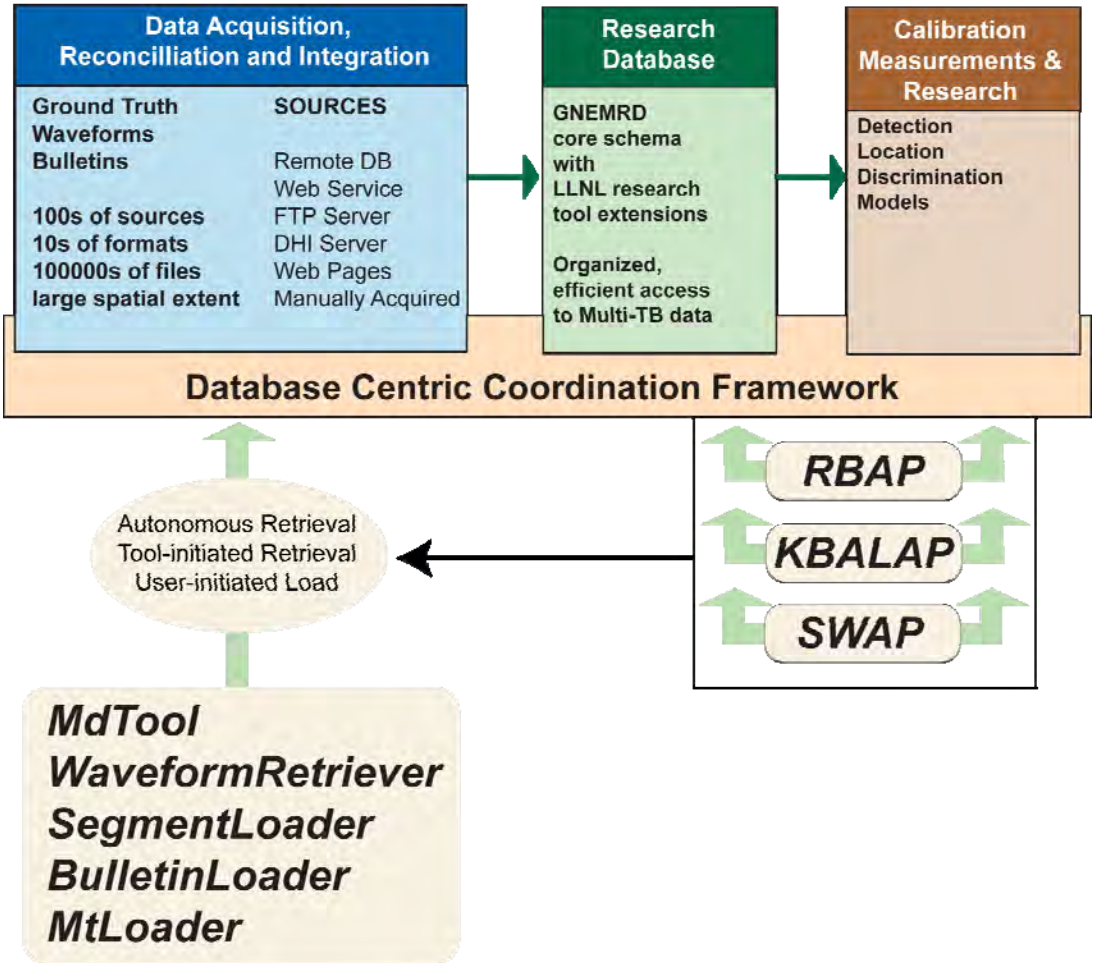

Figure 1. Software support for automated ingestion and integration of seismic data in bulk mode and as requested by analysis tools.

Still later, we developed analysis tools such as RBAP for amplitude measurement and KBALAP for travel-time measurement to help researchers produce calibration information from the steadily-growing raw data stored in the database.

Over the last two years we have shifted our focus back to the beginning of our data flow and worked on codes that help automate both the retrieval and ingestion of raw data. The bulk of such efforts this year have been on the development of the BulletinLoader, SegmentLoader, and MtLoader tools. In addition, we have begun development on a new client application for measuring surface wave amplitudes. These new tools directly facilitate and enable more efficient data integration and evaluation of scientific datasets from numerous sources.

RESEARCH ACCOMPLISHED

BulletinLoader

The BulletinLoader program is a Java program used for loading earthquake bulletin data into the LLNL GNEMRD schema. It is a replacement for the ORLOADER program, but it also includes a number of new capabilities. These include

- Raw bulletin (text) data is now archived in the database for all single-file source types. These data may be accessed on a per-orid basis using the ArchiveReader program.
- Bulletins may be retrieved and loaded directly from a number of public internet sources.
- The program may be run in an autonomous mode where it continually checks for new content.
- Events may be loaded directly from an external database account, possibly residing on a remote instance.
- Events may be loaded automatically from a remote instance based on entries in the DB.REMOTE_DB_EVID_MAP table. The map table is populated by a DBMS job, and automatically gets updated as new events are added in the remote database. This option allows the target schema to be synchronized with the remote instance.
- Extensive QC checks are applied to new bulletin data prior to insertion into the target schema. Where possible, BulletinLoader will modify invalid data as required to make it compatible and consistent. Where this is not possible, the program will pause, inform the user of the problems requiring attention, and resume when the problems have been addressed.
- BulletinLoader can be set to notify selected email addresses when data meeting certain criteria are loaded.

Loading Data from Internet Sources
BulletinLoader is able to retrieve and load bulletin data from several Internet sources. The currently-supported sources are

- NEIC
    - Weekly and Monthly PDE
    - Weekly and Monthly EDR
    - M2.5+ earthquake data feed
    - Hourly and 7-day latest earthquakes
    - US Mines bulletins
- ISC Monthly Bulletins
- NORSAR Reviewed Bulletins
- University of Helsinki Regional Bulletins

BulletinLoader remembers what it has retrieved previously from each of these sources, so when you direct BulletinLoader to retrieve data from Internet sources, it only brings back new data. In addition, BulletinLoader keeps track of the last time it visited a source, and for those that only update occasionally, if enough time has not elapsed since the last visit, the source is skipped.

QC Operations
BulletinLoader attempts to ensure that all the data it loads are consistent and meet the constraints in the LLNL GNEMRD schema while at the same time being robust to inconsistent or unexpected data values. Rather than loading data directly into the target, BulletinLoader first loads into stage tables in the ORLOADER schema. These tables have no column constraints, so unexpected data will not cause a constraint violation to occur. Next, the program checks the staged arrivals against the SITE table target to identify any arrivals that would not join to the SITE table. Any problems are presented to the user, and must be addressed either by removing the offending arrivals or by modifications to the target SITE table before execution can continue.

Next, the program identifies all the column constraints currently in effect by querying the USER_CONSTRAINTS view in the target schema and then checks each table-column affected by the constraints. Progress cannot continue until any problems are addressed. The principal advantage of this approach compared to hard-coding the tests, is that it isolates the source code from changes in the database and allows the same code to be used with different databases having different constraints.

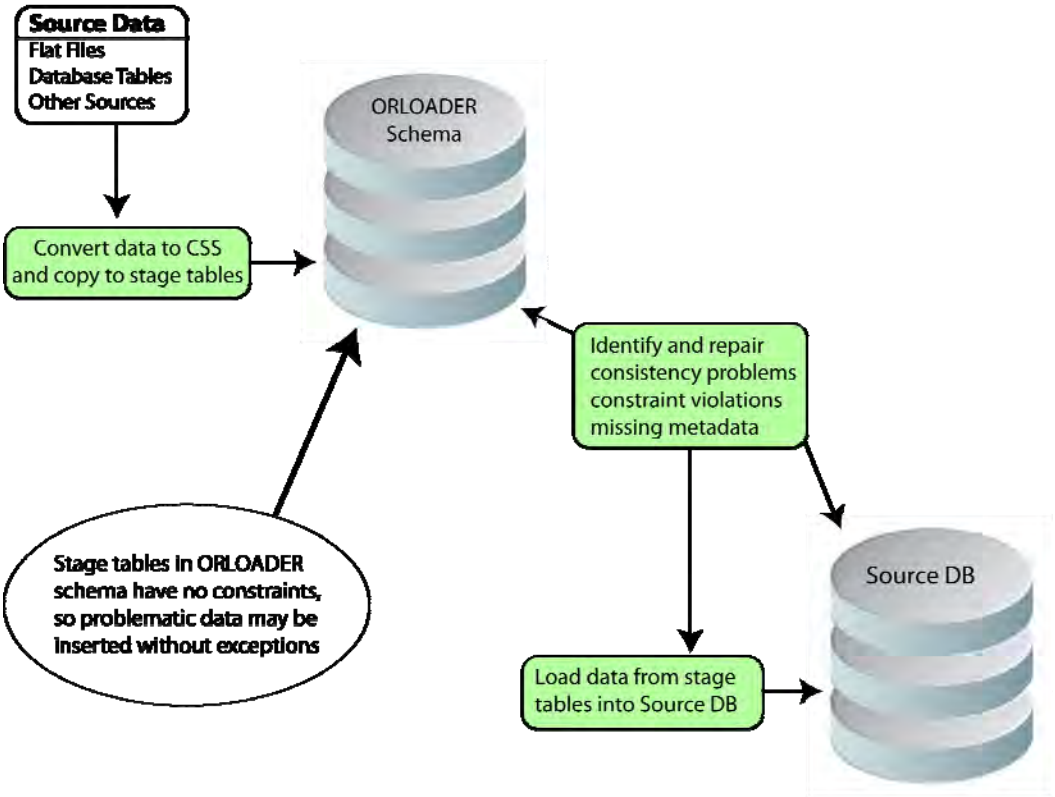

Figure 2. BulletinLoader data flow.

Autonomous Mode

In autonomous mode, BulletinLoader runs continuously. Most of the time the program is sleeping, but periodically, it wakes up and checks sources to see if new data are available. If so, it retrieves the data and loads it. In autonomous mode, BulletinLoader can retrieve from both Internet sources and from remote database instances. Retrieval from internet sources is governed by the mechanism discussed in a previous section. Retrieval from a remote database instance is governed by entries in the DB.REMOTE_DB_EVID_MAP table.

This table is populated by a DBMS_JOB that runs periodically in the target account. Each time the job runs it queries each database listed in the REMOTE_DB_REMAP_BASE table to find events that have been added since the last job execution and that meet certain user criteria. For each such event an entry is created in the REMOTE_DB_EVID_MAP table. If any origins in the event correlate with an origin already in the target schema, then the target EVID is entered along with the correlation information. Otherwise the information is left null.

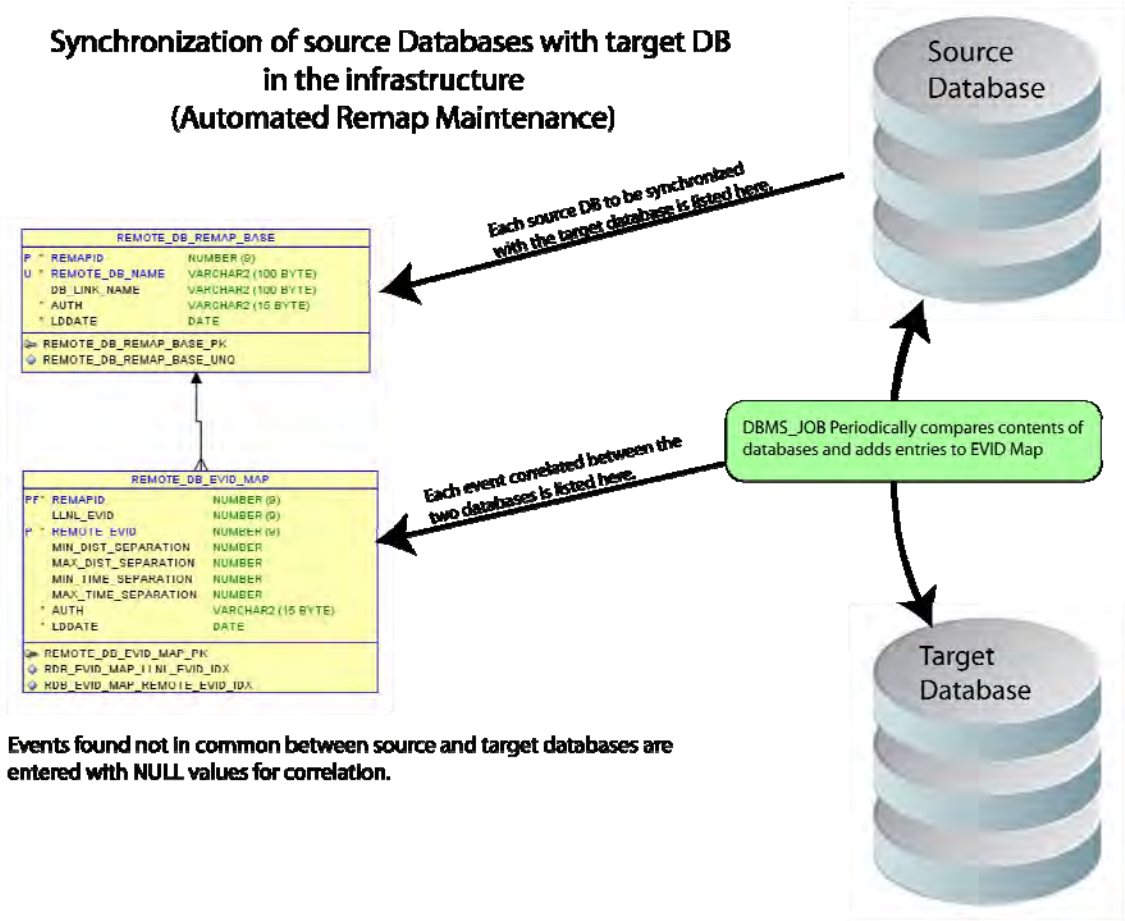

Figure 3. Management of the REMOTE_DB_EVID_MAP table used to govern retrieval of data from a remote instance.

BulletinLoader identifies new events to load from remote instance(s) by choosing rows in the REMOTE_DB_EVID_MAP that have a null DB_EVID. For those rows, BulletinLoader retrieves the data from the remote instance and loads it into the DB schema. After the data are loaded, BulletinLoader updates the REMOTE_DB_EVID_MAP with the correlation information.

SegmentLoader

The SegmentLoader program is a utility for adding data to the DB.WFDISC table. It combines the functions of the DDLOAD (waveform segment production and staging) and UPDATEMRG (updating the WFDISC table with new waveforms) programs. SegmentLoader currently supports three input sources:

1. Wfdisc flat files (and associated .w files)
2. Wfdisc tables (and associated .w files)
3. Wfdisc/Wftag pre-segmented data.

In cases 1 and 2 the data are considered to be un-segmented. For these, SegmentLoader will identify time segments that are appropriate for events that exist in the DB.EVENT table, extract the corresponding waveforms, and merge them into the DB.WFDISC table. For case 3, the program assumes that the data are pre-segmented and that the WFTAG evid tagid values are correct for the target schema. In this mode, the program functions like the old UPDATEMRG software. Continuous WFDISC data may be loaded from a table in the current instance or from a

table in a different instance. Any user with an account in the instance containing the target account may run the program provided that they have been granted the WAVEFORM_LOADER role and have appropriate file system permissions in the target directory.

Event Screening

When loading data from a continuous WFDISC source, SegmentLoader identifies all the events in the DB.EVENT table that fall within the time frame of the source WFDISC table. However, in general only a few of the possible events will have a usable signal for many of the channels in the source. To avoid loading a lot of noise, SegmentLoader applies a screen to each event-station combination, to determine whether to extract the data.

Segment Merge details

In the simplest case, there is no segment in DB.WFDISC for a new source segment. In that case, SegmentLoader simply writes the new segment, and creates WFDISC and SEARCH_LINK rows. Often, though, there is pre-existing data for the EVID-STA-CHAN. In these cases, SegmentLoader must merge the new data with the existing data.

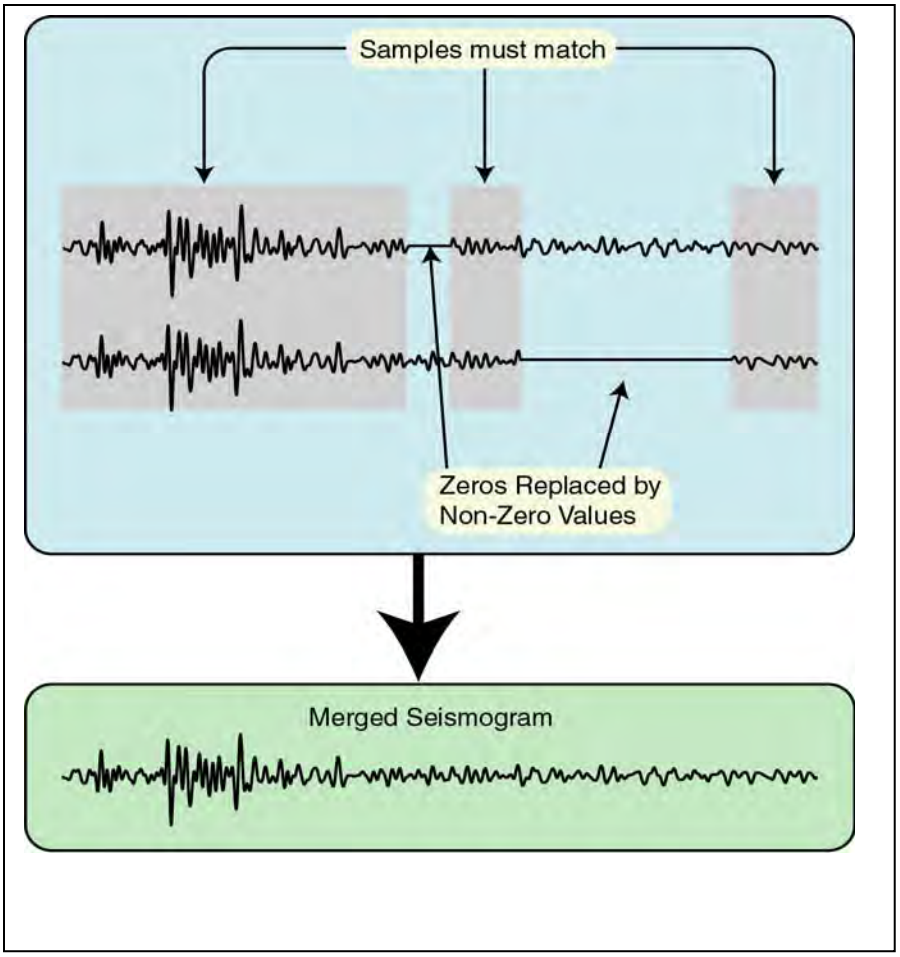

Figure 4. Schematic illustration of the process by which SegmentLoader merges waveforms.

The process is illustrated in Figure 4. The program starts the merge by reading the existing segment from disk and comparing the samples to those of the new segment. If all samples match, the program reports that the data are an exact match, and moves on. Otherwise, the program verifies that the sample rates are comparable and then aligns the

data on common time samples. Then over the range of samples in the union of the two traces the following algorithm is applied:

- If one trace has a value and the other does not, then the value is copied to the merged trace.
- If both traces have a value then
    - If the values are the same, the common value is copied to the merged trace.
    - If one value is zero and the other is non-zero, then the non-zero value is copied to the merged trace.
    - If both values are non-zero, but do not match, then a MergeException is thrown. This exception will be reported in the log, and the new data will not be merged into the target, but SegmentLoader will continue processing the remaining waveform segments.

MtLoader

The moment tensor loading tool (MtLoader) was developed to load data into the recently-implemented GNEMRD schema for moment tensors. The tool allows manual loading of moment tensor information in a number of formats. It can also run autonomously and retrieve moment tensor information from various Internet sources as the data become available. So far, we have loaded ~57,000 moment tensor solutions with this tool. The primary database tables populated by this tool are:

- MOMENT
- FOCAL_PLANE
- MOMENT_VERSION

The tool also populates the ORIGIN and NETMAG tables as required, and by means of an insert trigger on NETMAG, populates the PREFERRED_MAGNITUDE table as well.

Input formats read by MTLOADER vary in their completeness of the moment tensor description. At one extreme, the NDK format supplies data for most of the columns in the MOMENT and FOCAL_PLANE tables. At the other extreme, a solution may be expressed as a (strike, dip, rake, scalar moment) tuple. Where the tensor elements are specified, the units may be CGS or MKS and the coordinate systems may vary as well. MTLOADER always translates moment tensor data as required into MKS and (X,Y,Z) reference frame.

For incompletely specified solutions, MTLOADER will calculate a number of additional columns as well. These can include the eigenvalues and eigenvectors, PISO, PCLVD,PDC, EPSILON, and the auxiliary plane parameters. Therefore in using the values in these tables, it is important to know that not all values are necessarily reported by the author of a given row.

We are currently extending MTLOADER so that it can accept as a source a MOMENT table and FOCAL_PLANE table from a different schema, possibly residing on a different instance. This will facilitate importing solutions produced by other organizations using the GNEMRD tables.

SWAP

The Surface Wave Amplitude Processor (SWAP) tool is intended to aid in the production of high quality amplitude measurements of surface wave amplitudes. In addition to being the first client software to use the GNEMRD moment tensor schema, it is our first client software that uses the NASA World Wind software (http://worldwind.arc.nasa.gov/java/) for interactive mapping capability. With this software, applications can produce fully interactive, 3-D imagery-based maps with resolution in some places as high as 0.2 meters per pixel. Display of World Wind imagery requires a connection to one or more WMS servers for image and geographic data. By default, the imagery is served from a NASA server. However, for installations in which it is not possible to have a connection to the public Internet, the imagery can be stored locally in a cache pack or can be served from a locally-administered WMS server.

SWAP uses World Wind to display stations for which we have both moment tensor solutions and 3-component waveform data. (Both are required for producing the measurements.) For selected stations, World Wind is used to display the events for which we have both moment tensor solutions and 3-component waveform data.

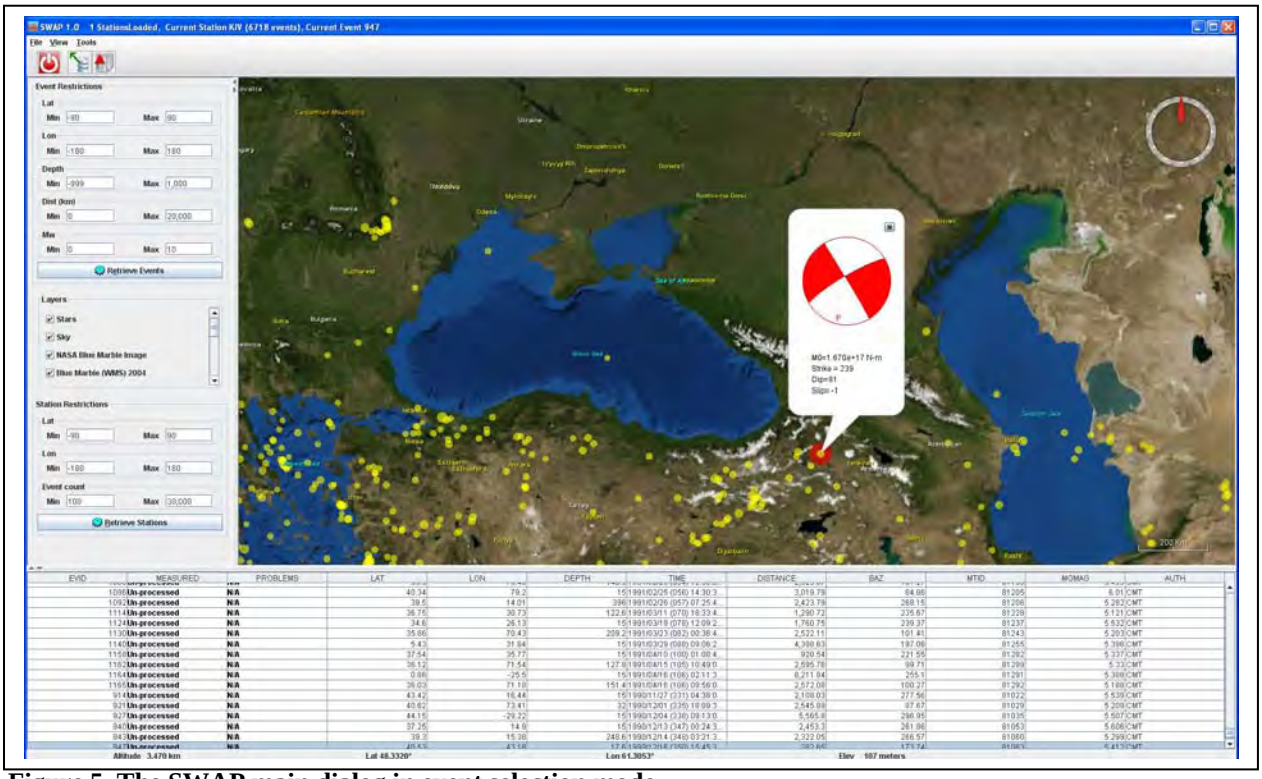

Figure 5. The SWAP main dialog in event selection mode.

Figure 5 shows the main dialog after a station has been selected and a set of events recorded at the station have also been selected. The events are shown on the map as colored circles scaled by magnitude. The color of the circle indicates the processing status. In the example, all stations are unprocessed. Events may be selected for processing by clicking on them in the map or alternatively, by selecting them in the table underneath the map.

Selecting an event loads it into the waveform dialog (Figure 6). In this dialog, all available 3-component trace sets are displayed on the left-hand-side, each separated from the others by a splitter. By making all sets available next to each other, the user has the opportunity to select the best (largest bandwidth, fewest data problems) set for measurement.

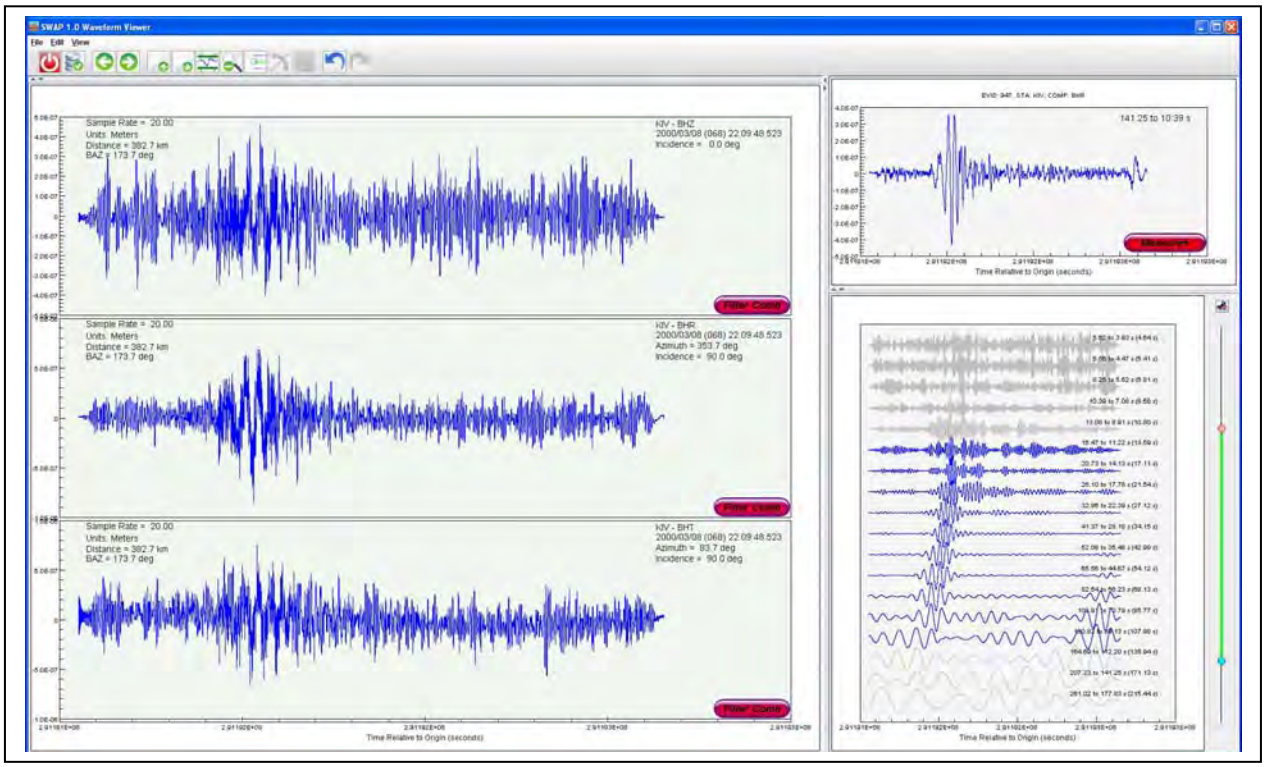

Figure 6 The SWAP waveform dialog showing the 3-component seismograms (left), the band selection control (lower-right), and the band-pass filtered component ready for measurement (upper-right).

After selecting the trace set to be measured, the user removes the instrument response and rotates the horizontal components into radial and transverse orientation.

After the user selects a trace it is narrow-band filtered and presented in the filter comb view shown in the lower right of Figure 6. This view provides controls to easily select the band of frequencies over which surface wave measurements are to be performed. The resultant filtered seismogram is displayed in the upper-right of Figure 6.

This is as far as we have developed SWAP to date. The next steps include adding a module for managing velocity models and adding the actual measurement code.

CONCLUSIONS AND RECOMMENDATIONS

This year most of our development work has been directed toward additional automation of our data ingestion capabilities. Our specific automation methodology and tools improve the researchers' ability to assemble quality-controlled research products for delivery into the Knowledge Base (KB). The software and scientific automation tasks provide the robust foundation upon which synergistic and efficient development of GNEMRD Program seismic calibration research may be built. Three new Java programs, BulletinLoader (seismic bulletins), SegmentLoader (seismic waveforms), and MTLoader (moment tensor information) have been developed that replace older C/C++ codes and extend the capabilities of those codes to reduce the amount of required human supervision. This allows resources to be focused on analysis and production of calibration products.

These new applications comprise a significant re-engineering of our data management software suite designed to leverage new data distribution technologies that have been developed by data providers in the last few years. Exploitation of the new methods has resulted in demonstrated gains in efficiency and reduction in time required to identify, acquire, process raw data essential for calibration research.

ACKNOWLEDGEMENTS

We acknowledge the assistance of the LLNL computer support unit, Stan Ruppert and Laura Long, in implementing and managing our computational infrastructure. We would also like to thank G. Ichinose for invaluable information regarding the NNSA schema gleaned from personal communication, 30 June 2010.

REFERENCES

Ruppert, S. D., D. A. Dodge, T. F. Hauk, M. D. Ganzberger, D. B. Harris, and E. M. Matzel (2009). Enhancing seismic calibration research through software automation and scientific information management, in *Proceedings of the 2009 Monitoring Research Review: Ground-Based Nuclear Explosion Monitoring Technologies*, LA-UR-09-05276, Vol. 2, pp. 808–817.

World Wind JAVA SDK 15.75K. NASA. 8 October 2009. <http://worldwind.arc.nasa.gov/java/>

WAVEPRO: A NEW APPROACH TO THE DESIGN OF DATA PROCESSING WORK FLOWS

Mark A. Gonzales and Christopher J. Young

Sandia National Laboratories

Sponsored by the National Nuclear Security Administration

Award No. DE-AC04-94AL8500/SL08-IRP-NDD02

ABSTRACT

For the most part, both the types and the sequences of signal processing algorithms (work flows) used to process waveform data for the basic nuclear explosion monitoring tasks are well established and efficiently implemented in the major monitoring systems. However, the methods and tools provided to design or modify a workflow, can be improved to make these tasks easier and less time-consuming. In keeping with well-designed commercial software that most of us use on a daily basis, the work flow can be presented graphically, with each signal processing algorithm shown as an icon, and with the data flow indicated by lines linking these together. Even a complex data processing workflow can be understood at a glance, and changing parameters for any of the algorithms can be accomplished by clicking on the corresponding icon to access a well-formatted display with each parameter clearly labeled. We have begun to explore this idea, using modern software design techniques and tools. In this paper, we will present our original project goals, show the design that we developed to meet these goals, and then present and discuss the software package (WavePro) that we have implemented that realizes this design. We show how WavePro can be used to develop work flows for basic data processing tasks, and in turn how these low-level workflows can be cloned and assembled to easily form more complex work flows for an entire network. WavePro is coded in Java so it is platform independent, and it utilizes "drag and drop" technology to enhance the use of the user interface. In addition, the software is being designed as a pluggable framework in order that new signal processing algorithms can be added to the package without redelivery or recompilation of the software. WavePro uses multi-threading to exploit the multi-core technology that is available on virtually all current generation computers. Further, the package is designed to be compatible with distributed computing using the JPPF package, so WavePro can be used to develop efficient implementations for complex, computationally demanding work flows.

OBJECTIVES

The idea behind the WavePro software application came from observing the difficulty that many researchers encounter in setting up and testing even relatively simple signal processing algorithms using existing software. Though there is high-quality software available to *execute* data processing workflows for monitoring, to our knowledge there is no software designed to aid in the *development* or *modification* of such workflows.

Our WavePro development has two major goals that we believe are essential for the software to prove useful. First, the WavePro application must include a framework to allow for new software modules to be added to the existing application without recompiling or redistributing the existing WavePro software. A software framework that allows for the dynamic adding of software in this manner is called a "pluggable" framework and the software modules added are called "plug-ins". Imagine an application with a software framework in which new signal processing algorithms could be added dynamically as a plug-in and work seamlessly within that application. Throughout this paper we will refer to a plug-in that is a signal processing algorithm as a code module. The second WavePro goal is to allow for signal processing workflows to be created and modified by a user in an intuitive manner without knowledge of a programming language; i.e. a user can arrange, integrate and interchange, via a user interface, well-defined code modules to achieve their signal processing needs.

RESEARCH ACCOMPLISHED

Creating a Graphical Workflow

Currently, the methods and tools provided to design or modify a workflow are much more difficult and time consuming than need be. In a typical current generation system, the users must navigate their way through a confusing hierarchy of directories to find the appropriate parameter files (often poorly indexed), which then must be brought up in an editor and scanned to find the parameters of interest. In an effort to improve this process, the WavePro application represents workflows graphically with signal processing algorithms (code modules) represented as icons that can be connected to form workflows. Using WavePro, a typical workflow design process would be as follows:

1. Start the application. The code modules are automatically loaded into framework and displayed as icons in a panel to the left.

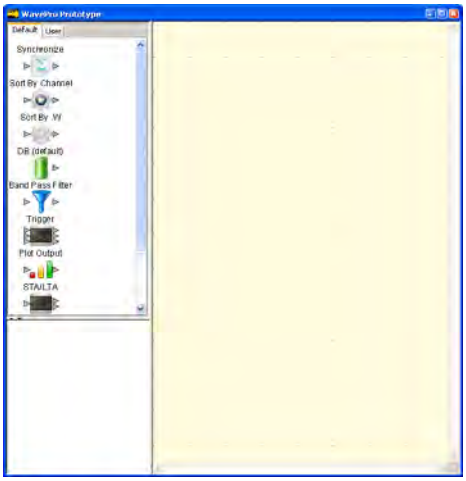

2. Build workflow by dragging icons over to workspace.

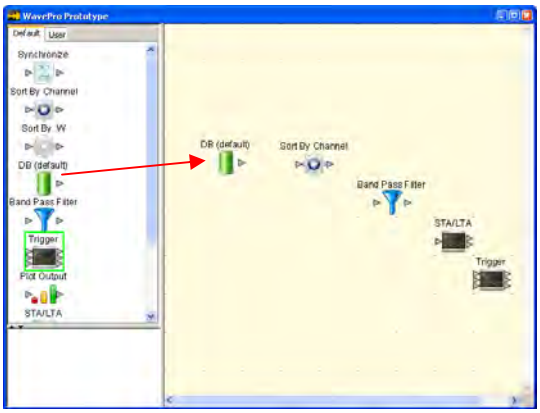

3. Connect code modules by selecting output and dragging to an input to form a workflow.

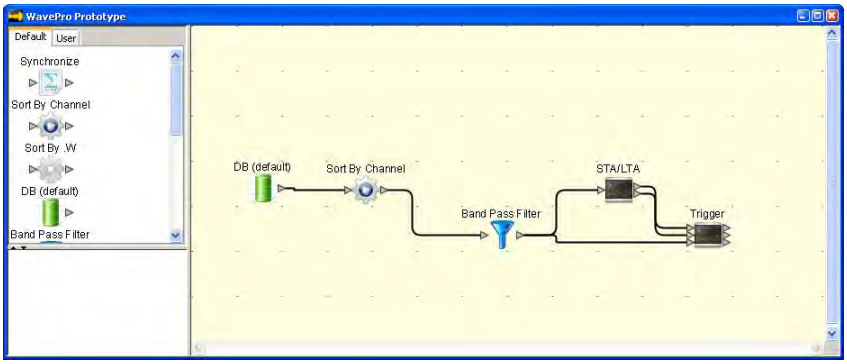

4. Modify algorithm parameters by right clicking on individual icons.

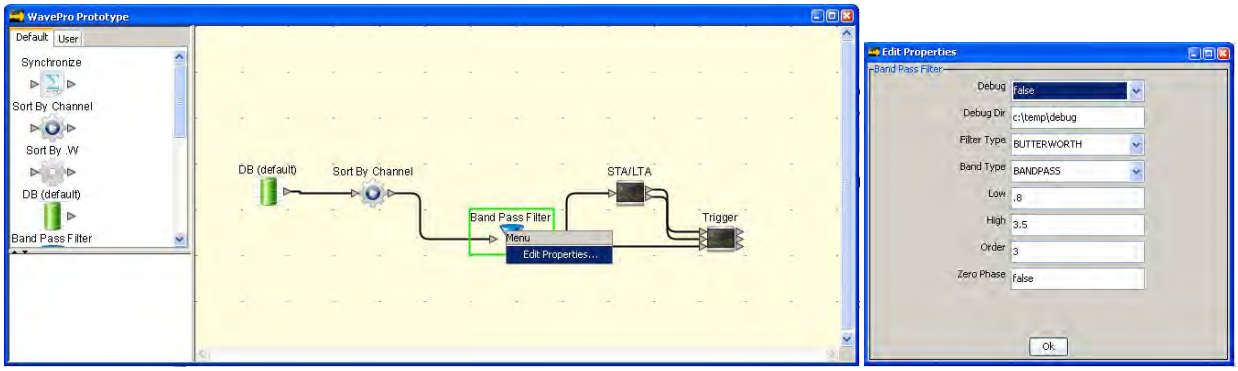

5. Select waveform data by right clicking on data source icon.

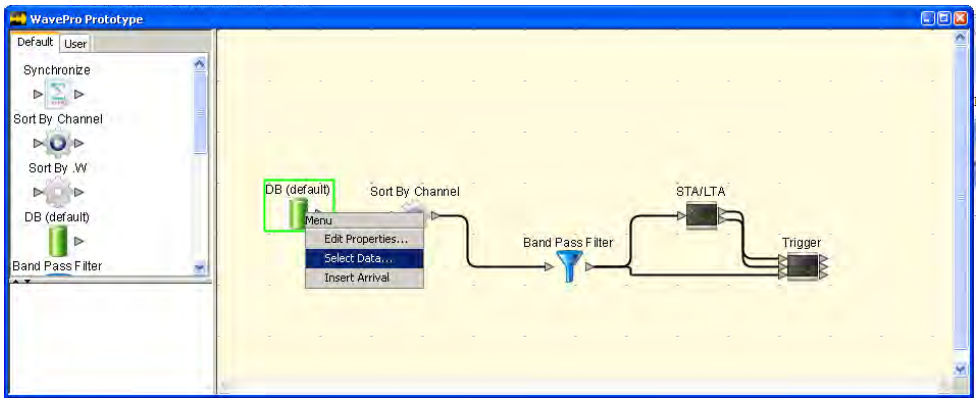

6. Execute workflow by right clicking workspace.

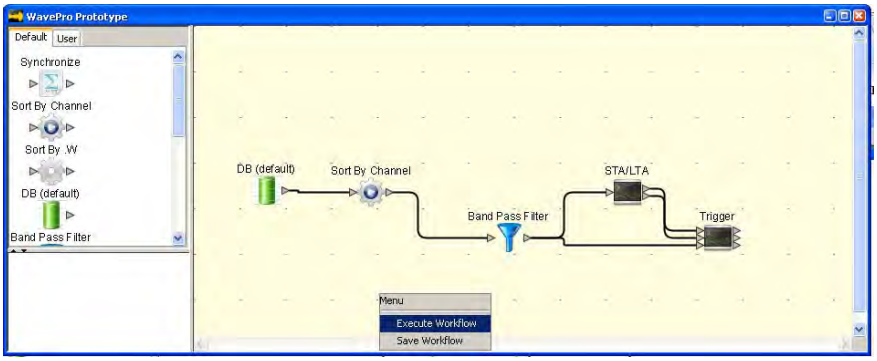

Analyzing A Workflow

To understand whether a workflow is working as intended, the researcher may have a need to view the output of the algorithms at various points. Our application allows for picking "plot points" within the workflow to view data. The researcher selects the output port of the signal processing icon and selects a plot point. For example, in the workflow shown below, the user selects the "Band Pass Filter" icon to send the output of the filter step to a plot.

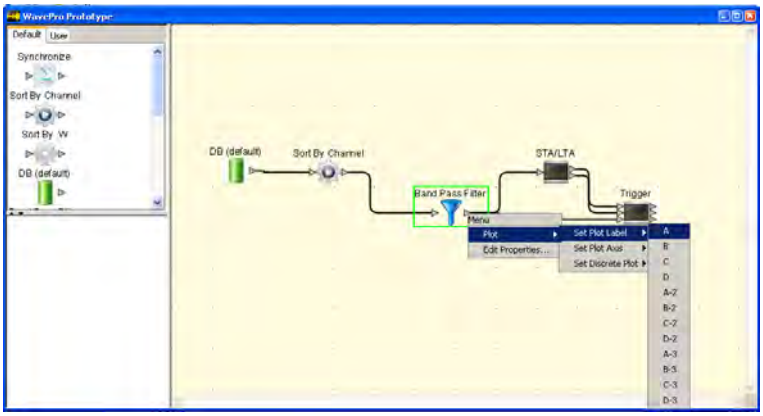

When the workflow is executed, the application produces the specified output plot.

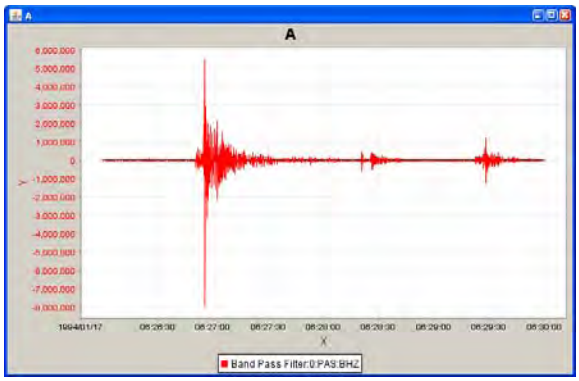

The concept of picking plot points within the workflow is just one idea of how to help researchers analyze a workflow. Other concepts within the WavePro framework include: plotting multiple plot points on the same graph (e.g., original waveform and STA/LTA output), dumping output at specific points within the workflow to files and databases, easily modifying workflows by deleting links between icons, replacing signal processing icons with different ones by deleting and dragging a new icon over, and saving workflows to a library in order to recall them for later use.

Pluggable Framework

In addition to the suite of algorithms available within WavePro, the application can be readily extended to allow researchers to develop their own signal processing algorithms and to automatically add them for use. The extendibility capability is possible because the WavePro software is implemented as a pluggable framework.

The goal of using a pluggable framework is to make your application extendable by adding functionality to already existing functionality. For example, suppose that a software package had an existing signal processing workflow with a Band Pass Filter and an STA/LTA processor. The pluggable framework will allow for a third algorithm, e.g. a Detector, to be developed outside of the existing software and added to the framework so that it can become part of the workflow. The extendibility of the software allows researchers to develop individual signal processing algorithms outside of the framework and be able to plug those algorithms into the framework. This gives researchers the ability to develop algorithms without having to worry about how to connect them within a workflow. Thus, the researcher could focus the majority of their time developing the algorithm, not on worrying how to integrate it into WavePro. In order for researchers to be productive using this method, the process of adding functionality must be easy to use.

WavePro utilizes an open source project called Java Plug-in Framework (JPF) to create the plug-in capability. JPF uses a concept of extension points and extensions. Extension points are the parts in the main software framework where new software can be inserted. The main software framework must define its own extension points. An extension is the software that exists outside of the main software framework that can be inserted into the extension point. Any piece of software that is an extension is called a plug-in. Currently, the WavePro software framework defines three extension points: *CodeModule*, *DatasourceModule*, and *ExecuteModule*. The *CodeModule* extension point is the interface that allows individual signal processing algorithms to be inserted as pieces of software called *code modules*. In addition to having the ability to plug-in signal processing algorithms, there are other software modules that are needed to process data. In order to process data, you need to get the data from some source. Therefore, the extension point *DatasourceModule* is the interface used to insert software modules that are designed to obtain waveform data. Currently, the WavePro software framework defines default *DatasourceModules* that get waveform data from databases and files. The final extension point defined is the *ExecuteModule*. The *ExecuteModule* interface is used to insert software that controls the execution of the workflow. This includes sorting the data received from the *DatasourceModule*, executing the code modules in the workflow, and receiving results from execution of the workflow. The *ExecuteModule* extension point was added as a need to interchange the way data is sorted and passed through a workflow. For example, the current WavePro application has three default *ExecuteModules*. There is an *ExecuteModule* that sorts data by station and channel, an *ExecuteModule* that sorts data by Wfdisc file, and an *ExecuteModule* that sorts data by breaking up the data into time segments. Using these

three extension points it is possible to create a fully function workflow that obtains signal data, sorts the data, processes the data and obtains the results.

Extending JPF

As mentioned above, the process for the WavePro software framework to start up, find plug-ins and automatically insert them into the framework must be simple. JPF uses a boot library that follows the following flow chart.

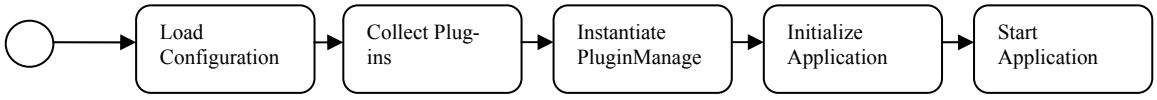

During the Load Configuration phase, the framework loads a configuration properties file. In the properties file, the user specifies the location of where to look for plug-in software. The Collect Plug-ins phase uses an XML Plugin Collector to locate the plug-in software and attempts to load it into the framework. The XML Plugin Collector is able to load plug-ins by searching for an xml manifest file. The xml manifest file is deployed with the plug-in software and contains all the metadata used to define the plug-in. The xml file defines the location of the plug-in framework file (a Java file needed for configuration), the location and definition of the plug-in extension point file (i.e., the signal processing algorithm software), and all of the library files that the plug-in will need to work.

While this type of configuration works, it is not simple. In order to simplify, the WavePro application extends the JPF framework by creating and using its own Annotation Plugin Collector in place of the JPF XML Plugin Collector. The Annotation Plugin Collector is similar to the XML Plugin Collector except that it finds plug-in software by searching the Java binary code for Java Annotations. Java Annotations are special metadata embedded in the Java code, hence eliminating the need for an xml file. In addition, the WavePro application takes advantage of object oriented techniques to combine the plug-in framework Java file and plug-in extension point file into one Java file. Therefore, by putting the Java annotations into the plug-in extension point file, the configuration for creating a plug-in requires only one file instead of three. For example, researchers can create a signal processing algorithm plug-in using one Java file similar to the one below:

```
@Module(type="CodeModule", name="Norm", iconName="filter2.png",
version = "1.0.0")
Public class NormalizeModule extends WaveformProcessor {
        @Override
        public void execute() throws ExcecuteException {
            ...signal processing code goes here
        }
}
```

1. Java annotations replace xml file
2. Object oriented extension allows for one file.
3. Custom user-provided algorithm.

Notice the "type" annotation variable specifies that this software is to implement the extension point CodeModule as defined by the WavePro framework, thus making it a signal processing algorithm plug-in. In addition, the annotation variables define the name and icon to be displayed and the version of this particular plug-in.

Therefore, with one Java source file it is possible to create a signal processing plug-in that can be easily added to the WavePro framework and inserted into workflows. With this type of system researchers can create, modify, and test algorithms quickly.

Exploiting Multicore Technology

In recent years there has been a shift in hardware processor design research and development away from increasing clock speeds and toward expanding the number of cores per processor. One of our design goals for the WavePro application is to exploit this new multi-core architecture. WavePro is being designed to execute workflows in parallel using the concurrent (i.e., multi-threaded) capabilities within the Java programming language, as well as using distributed systems such as the Java Parallel Processing Framework (JPPF) that can execute on more than one

machine. While work on executing software in parallel is ongoing, the WavePro software currently implements a concurrent and distributed system. For example, WavePro has default *ExecuteModules* that work in the following manner on a single multi-core machine:

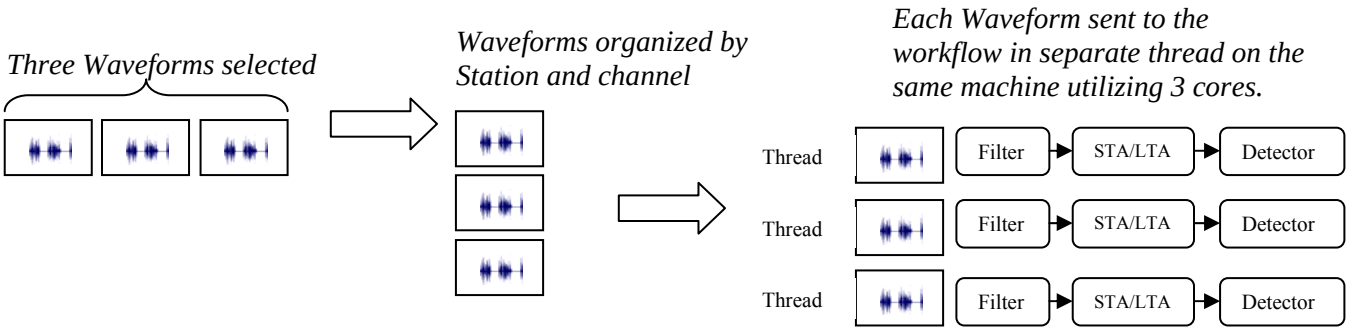

Hence, the parallelism occurs because the data is broken up into pieces sending each piece of data to a different thread then each executes at the same time among multiple cores. The same kind of parallelism can be achieved on a grander scale by using a distributed system such as JPPF. In this case the data is organized by station and channel and sent, via JPPF, to multiple cores on multiple machines. This approach is similar to the concurrent solution, but can allow for much more data to be processed in a similar amount of time.

CONCLUSIONS AND RECOMMENDATIONS

The purpose of WavePro software development project is to address the need for software specifically to aid in the design and maintenance of data processing workflows for nuclear explosion monitoring. Due to improvements in computer hardware, a robust signal processing workflow for a large networks of stations (such as the International Monitoring System) that a decade or so ago would have required processing on several workstations can now be easily executed on one or two commodity machines. However, the process involved in setting up such a workflow has not kept pace with other improvements. This project seeks to remedy that situation.

Our WavePro development so far has succeeded in achieving our two primary design goals:
1) WavePro allows signal processing workflows to be created and modified by a user in an intuitive manner without knowledge of a programming language. WavePro is designed to present the work flow graphically, with each signal processing algorithm shown as an icon, and with the data flow indicated by lines linking these together. Even a complex data processing workflow can be understood at a glance, and changing parameters for any of the algorithms can be accomplished by clicking on the corresponding icon to access a well-formatted display with each parameter clearly labeled.
2) WavePro includes a framework to allow for new software modules to be added to the existing application without recompiling or redistributing the existing WavePro software. This sort of framework is known in computer science as a "pluggable" framework and the software modules added are called "plug-ins".

ACKNOWLEDGEMENTS

We thank all of our GNEMRD colleagues at SNL for their helpful feedback on WavePro throughout the design and testing process.

REFERENCES

Java Plug-in Framework . Retrieved from http://jpf.sourceforge.net/

Java Parallel Processing Framework. Retrieved from http://www.jppf.org/

THE DEVELOPMENT OF METHODOLOGIES FOR DETERMINING NON-LINEAR EFFECTS IN INFRASOUND SENSORS

Darren M. Hart, Harold V. Parks, and Randy K. Rembold

Sandia National Laboratories

Sponsored by the National Nuclear Security Administration

Award No. DE-AC04-94AL85000/SL10-CE-NDD02

ABSTRACT

The Ground-Based Nuclear Explosion Monitoring Research and Development (GNEM R&D) program at Sandia National Laboratories (SNL) is regarded as a primary center for unbiased expertise in testing and evaluation of geophysical sensors and instrumentation for nuclear explosion monitoring. Over the past year, four new infrasound sensor designs were evaluated for common performance characteristics, i.e., power consumption, response (amplitude and phase), noise, full-scale, and dynamic range. In the process of evaluating a fifth infrasound sensor, which is an update of an original design, SNL has observed a higher than expected variability in the sensor's analog output sensitivity as measured in units of volts per pascal. Variations in sensitivity by as much as 15% were observed within one hour. This is an issue because of the International Monitoring System infrasound sensor requirement for the uncertainty in the measurement to be less than 5%. An infrasound two-tone test and an extended duration single tone test demonstrated that this variability was due to large amplitude low-frequency weather signals affecting the response due to a non-linearity in the sensor.

OBJECTIVES

Over the past three years several infrasound sensor designs have been evaluated for basic performance of sensitivity, linearity, response verification and self-noise. Of these the sensitivity, the conversion factor of the analog sensor's voltage output to measured geophysical unit (i.e., differential pressure for infrasound), should vary in a linear manner when compared to different external influences. Sandia identified one sensor that was observed to vary in its output sensitivity by as over 10% during one hour test. A typical expectation is the sensitivity of the sensors should vary less than 1% when tested against different external variables (e.g., temperature, humidity, barometric pressure, magnetic fields, etc.). Due to requirements to have known responses to within 5%, this sensor design should not be used at monitoring stations. Through two sequences of tests, an infrasound two-tone test and an extended duration single tone test, the initial observations of high variability in sensitivity were confirmed, and allowed us to speculate that the sensor design may have possible issues with non-linear components, out-of-band signal influencing in-band signals, or environmental sensitivities. The following sections describe our investigation into further understanding the observation made while evaluating this specific sensor design.

The research for this paper was separated into two main areas:

1. Summary of Results
2. Two-Tone Infrasound Test

RESEARCH ACCOMPLISHED

Summary of Results

We describe here our evaluation of a new infrasound sensor design (NSD). Initial tests of the sensors over various frequency and amplitude ranges produced inconsistent results. For example while running piston phone tests to try to measure variations in the sensitivity versus amplitude of a NSD sensor, the sensitivity was observed to vary by as much as 10% from run to run.

We believe that this variability in the NSD sensitivity is related to nonlinearity in the sensor response. Weather changes can easily cause pressure changes of tens of Pa over 10 minutes. The low frequency acoustic response of the NSD can be modeled by a single pole with a corner below 0.01 Hz. This allows the transducer to see pressure fluctuations of several Pa due to meteorological effects and any non-linearity in the transducer response will cause an apparent modulation of a high frequency signal riding on the low frequency background. Our tests were performed in a sealed chamber, but small leaks allow very low frequency signals to couple through efficiently.

To test this hypothesis, we performed a two-tone infrasound piston-phone test, where a 0.8 Pa 1 Hz tone was superimposed on a 9 Pa 0.02 Hz tone. The amplitude of the 1 Hz tone as measured by the NSD showed a 40% modulation in amplitude caused by the 0.02 Hz tone, while reference microphones (a Chaparral 25 and a MB2000) showed a much smaller modulation. We also ran a long duration sine test, where a single 1 Hz tone was applied for 7 hrs. The reference MB2000 sensor showed only a 0.25% variation in the 1 Hz tone amplitude over the duration of the test. The amplitude as measured by the NSD varied by 8%, and is clearly correlated with low frequency fluctuations in the piston-phone chamber pressure.

Two-Tone Infrasound Test

The two tone infrasound linearity test was parameterized to observe how a high amplitude (~9 Pa) low frequency (0.02 Hz) tonal signal can influence the secondary low amplitude (~0.8 Pa) and higher frequency (1.0 Hz) tonal signal. Under our initial assumption that the NSD is a linear system, then we should observe no change of the 1 Hz tone (in amplitude, frequency or phase distortion) on a time scale of the primary tone (i.e., 50 seconds).

Test Configuration

The signal source for this test is the low-frequency low-distortion oscillator (LFLDO) was input to the voice-coil driven piston of our piston phone chamber.. The equipment was configured to output a two-tone signal. The first signal was set for 0.02 Hz and 1.3 Volts zero-to-peak sine. The second signal was set for 1.0 Hz and 0.3 volts zero-to-peak sine. A HP3458A multi-meter was used as a calibrated reference to record and verify the linearity of LFLDO two-tone signal. Figure 1 show results of performing sine fit on two cycles of 0.02 Hz tone LFLDO data.

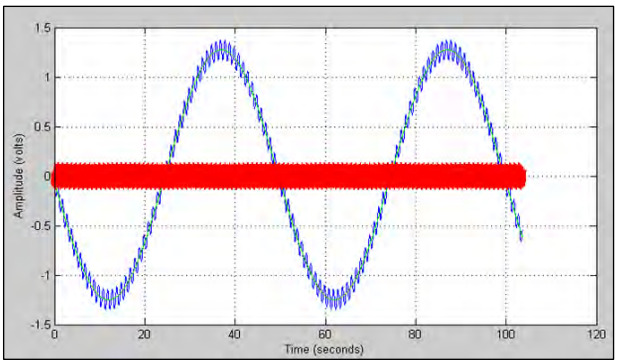

Figure 1. Results from sine fit algorithm for two cycles of 0.02 Hz tone data from the LFLDO during two-tone test. Blue line is output from LFLDO sensor, the green line is the best-fit 0.02 Hz sine model, and the red markers are the misfit between the raw data and the model fit which includes only the 0.02 Hz tone (leaving the unmodulated 1 Hz tone).

From Figure 2 we observe a well centered fit to the 50 second tone, with the misfit residuals on the order of the secondary 1 Hz tone. By bandpass filtering the data from 0.6 to 2 Hz we can also look at the sine fit characteristics of the 1 Hz tone. Figure 3 shows the results of performing the moving window sine fit analysis on two minutes of the LFLDO data set.

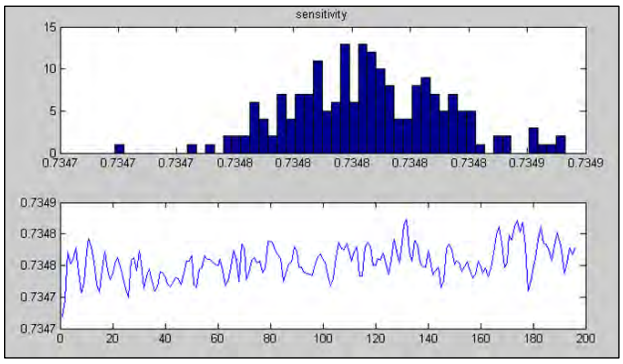

Figure 2 shows the 1 Hz secondary tone has no observable distortion related to the primary 0.02 Hz tone. The distribution has the expected Gaussian shape, with small standard deviation of 2.3e-5 volts.

Figure 2. Results from moving window sine fit algorithm for two minutes of LFLDO data. Data were processed using two cycles of 1 Hz data and 50% window overlap (i.e., 1 cycle overlap). Upper plot is histogram of sine fit amplitudes for two minute window; lower plot is sine fit amplitude as function time along waveform.

Sensor Data

Several days of testing were spent addressing the two tone test set up and data processing for results interpretation. The following data set summarizes observations made during analysis of the complete set of tests.

Test data: 2/25/2010
The digitizer channel to sensor mapping for this test were:
Channel 1 C1P: MB2000 Absolute Pressure attached to chamber
Channel 1 C2P: GRAS 42 AE Microphone attached to chamber
Channel 3 C3P: No sensor
Channel 4 C4P: NSD - 051722 attached to chamber
Channel 5 C5P: Chaparral Physics model 25 082058 attached to chamber
Channel 6 C6P: MB2000 Filtered output attached to chamber
Figure 3 shows the raw data on channels C1P to C6P (waveform index 1-6) and the bandpass filtered, from 0.6 to 3 Hz, data for channels C3PBP to C6PBP (waveform index 7-10). The NSD, Chaparral 25 and MB2000 have been selected (as indicated by the red waveform color), a window 150 seconds (three sine cycles of 50 seconds period) has been set for processing. The GRAS 42AE microphone was not reported on, due to low SNR of the 0.02 Hz signal.

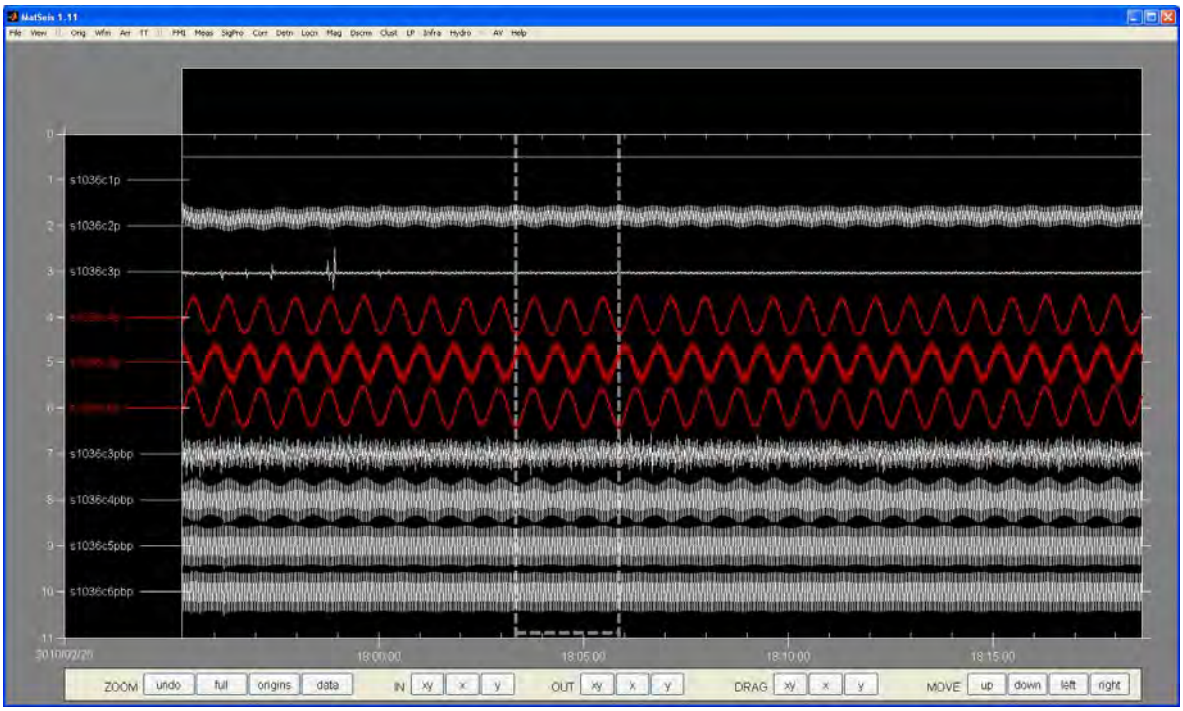

Figure 3. Screen shot of two tone linearity test data. Top six waveforms are raw data from two tone test in which the 0.02 Hz signal dominates. The lower four waveforms are the bandpass (0.6 to 2 Hz) filtered showing the 1 Hz secondary signal. The third trace from the bottom shows the 1 Hz signal from the NSD. The NSD displays a clear modulation in amplitude which is not present on the signals from the two reference sensors immediately below.

Figures 4a-c show the results of a sine fit to the 0.02 Hz signal for the NSD, the MB2000, and the Chaparral 25. The MB2000 and chaparral 25 shows slight drift over time, but no correlation to the primary tone of 0.02 Hz. Observed zero-to-peak pressure of the MB2000 was 7.7 Pa for the Primary 0.02 Hz tone. The NSD has a misfit residual with clear correlation to the primary frequency of 0.02 Hz, with a period of ~25 seconds; this is twice the primary period of 50 seconds, typically called the first harmonic. The SNR differences observed in the Figures 4a-c are due to the different response characteristics of the three sensors.

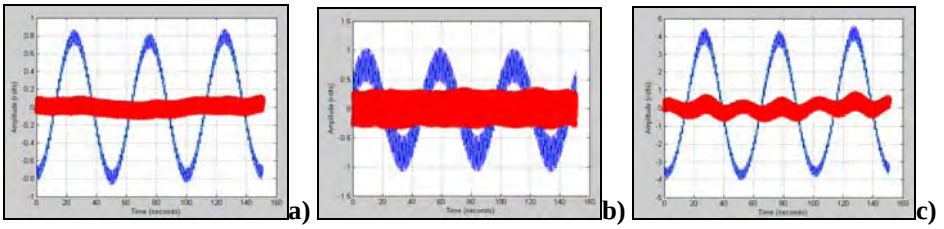

a) b) c)

Figure 4a-c. a) MB2000 filtered output showing two-tone signal output in blue, best-fit sine in green, and the RMS residual in red. Misfit uncorrelated, by observation, to primary signal. b) Chaparral 25 output showing two-tone signal output in blue, best-fit sine in green, and the RMS residual in red. Misfit correlated to primary signals by first harmonic (observed as period of misfit). Note that the 1 Hz signal appears much larger relative to the 0.02 Hz signal than for the NSD or the MB2000. This is because the Chaparral 25 response has begins to roll off below 0.1 Hz. c) NSD output showing two-tone signal output in blue, best-fit sine in green, and the RMS residual in red. Misfit correlated to primary signals by first harmonic (observed as period of misfit).

When a narrow bandpass filter is applied to the raw data to remove the primary 0.02 Hz frequency, an interesting observation is made on the NSD and Chaparral 25 output for the 1 Hz tone. First, the NSD's 1 Hz signal has strong amplitude modulation, which can be measured by the modulation index (MI). The modulation index (MI) is calculated by taking one minus the ratio of the minimum (zero-to-peak) amplitude to the maximum (zero-to-peak)

amplitude obtained from a common analysis technique, e.g., our IEEE sine fit method. This was done for the four sensors: the MB2000, NSD and Chaparral 25, and the GRAS 42AE. The modulation indexes are given in Table 1.

Table 1. Modulation index of 1 Hz low amplitude secondary tone.

Sensor M	inimum Amplitude (V)	Maximum Amplitude (V)	Modulation Index
MB2000	0.080 0.	083	0.04
Chaparral 25	0.278 0.	308	0.10
NSD	0.300 0.	450	0.33
GRAS 42AE	0.043 0.	045	0.04

From Table 1 the observations of amplitude modulation are quantified and we see relative differences between the sensors in this test. The MI values represent the amount the carrier amplitude varies by above and below its unmodulated level. The NSD and Chaparral 25 have the largest MI values at 33% and 10 % respectively; where both the MB2000 and GRAS both have relatively low MI values at 4%. The zero-to-peak pressure observed on the MB2000 for the 1Hz secondary tone was 0.8 Pa, approximately a factor of 10 less than the primary tone.

The results of this two-tone acoustic linearity test lead us to speculate on the possible reason for the observed MI observed on the NSD and Chaparral 25 sensors. If one starts under the assumption that the each sensor is a linear system, then one should be able to input a two-tone signal into a system and get same two-tone signal out of the system, with only relative amplitude changes based on sensor to sensor differences in output sensitivity. The simplest way to get amplitude modulated output of a two-tone signal is to introduce the first non-linear term in the Taylor series expansion of the model of the sensor. The quadratic term provides a modulation term (the product of two sinusoids of different frequencies) with the coefficient determining the relative strengths it plays in the sensors performance.

This sensor response can be approximates as:

$$V(t) = A * p(t) + B * p^2(t). \qquad (1)$$

The V(t) represents the voltage output of the sensors over time, p(t) is the pressure input in the acoustic pass band of the sensor, A is the linear component of the sensors output, and B is the first order non-linear term.

For the two tone test, the input signal is:

$$P(t) = a_1 * \sin(\omega_1 t) + a_2 * \sin(\omega_2 t). \quad (2)$$

If this is inserted into the nonlinear sensor response equation for V(t), then the $p^2(t)$ term causes a modulation in the high frequency signal due to the low frequency signal.

Since all of the analysis has been done in the time domain, a longer duration two-tone test was run to look at the spectral content of the two-tone signals to make observations between the sensors. Two known effects of non-linear behavior are harmonic and intermodulation distortions. If harmonic or intermodulation distortions are observed in the spectral analysis, the non-linear explanation for the observations is further supported. Approximately an hour of data were collected. Individual sensor instrument responses were deconvolved from the time domain waveforms and power spectrum computed. The results are shown in Figure 5 for four sensors and the LF LDO. **Note: The LFLDO does not have a transfer function to pressure, but is plotted along with the infrasound sensors.** The Acoustic low noise model of Bowman (2004) was added for reference.

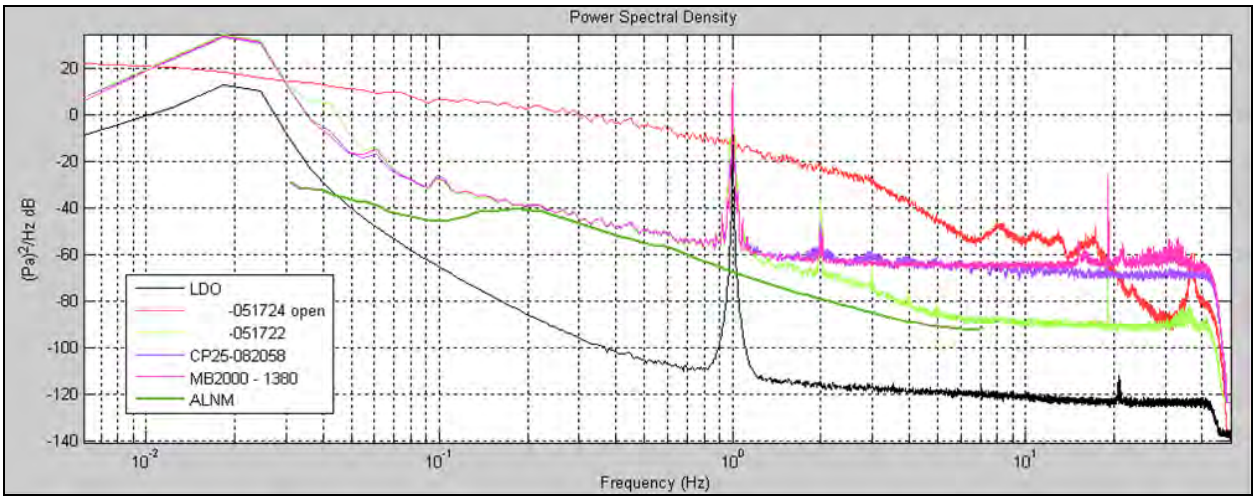

Figure 5. Spectral plot of an hour of two-tone data collected with three sensors attached to the test volume and one recording acoustic background. The red line is a NSD (051724) open to acoustic background, the black is the LFLDO output, the green line is the NSD (051722), the purple line is the chaparral 25 (082058), and the magenta is the MB2000.

From the broad observation the two tones are present in the spectral domain. If we zoom in to each of the tone, more information is obtained. Figure 6 shows the primary frequency of 0.02 Hz, we have less frequency resolution due frequency bin size. But over the broad sense, the spectral results match well except for the NSD. The NSD has extra energy (~10dB) in the area of the first harmonic (~25 seconds).

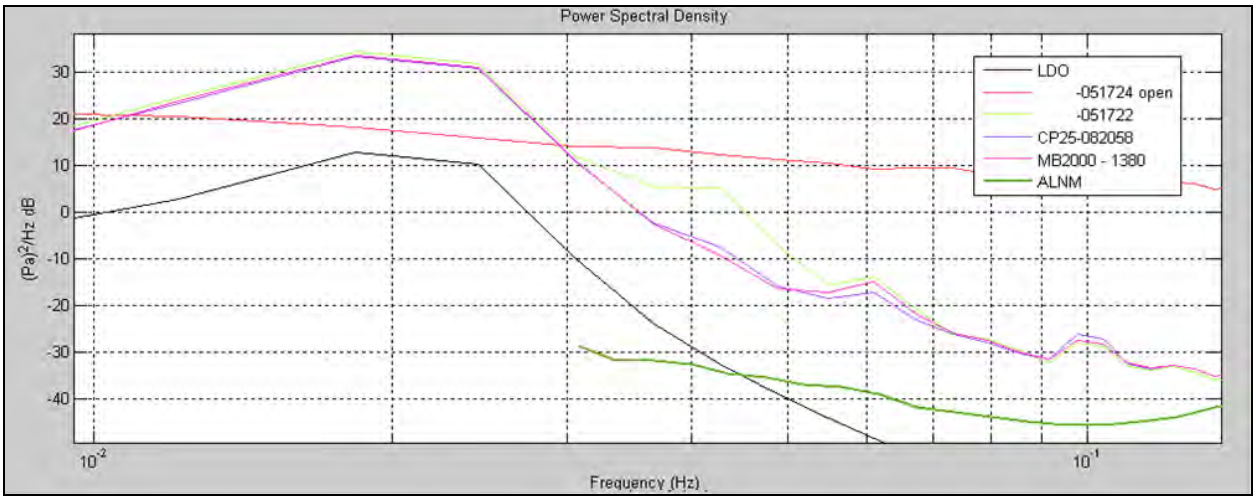

Figure 6. An enlarged view around the primary tone of 0.02 Hz from Figure 5; highlighting the spectral similarities and differences among the three sensor designs.

Figure 7 shows the secondary frequency of 1 Hz, now we have plenty of frequency resolution due frequency bin size. The spectral results match well at 1 Hz, but we observe several differences between the sensors spectral signatures. Each sensor has a second harmonic present, but the observed second harmonic is the largest on the NSD. The NSD also has a strong inter-modulation component, as observed by the spectral shoulders at 0.98 and 1.02 Hz on the green spectral line for the NSD attached to the test volume.

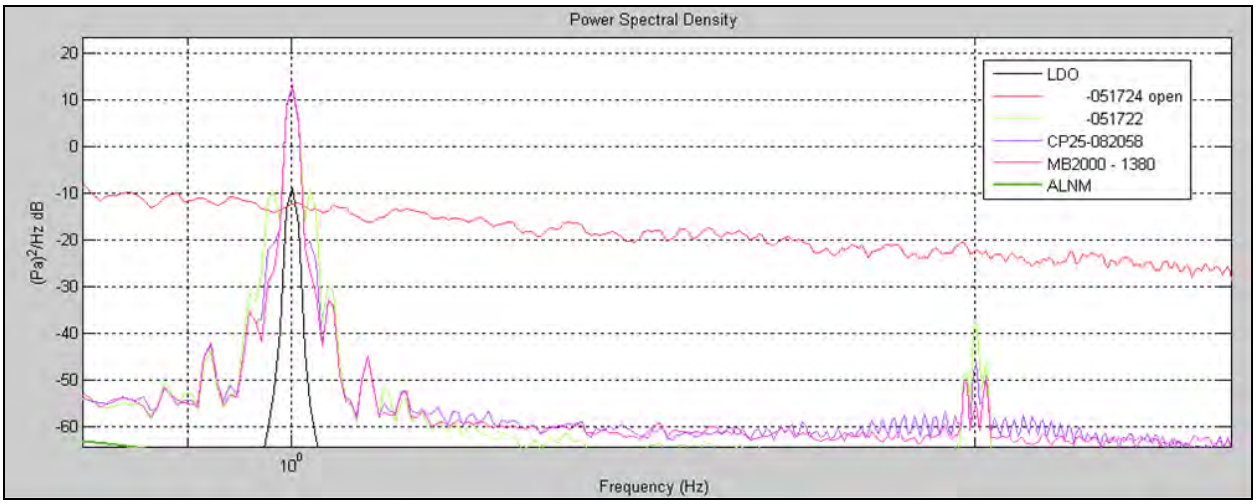

Figure 7. An enlarged view around the secondary tone of 1 Hz from Figure 5; highlighting the spectral similarities and differences among the three sensor designs.

Long Duration Sine Test

The long duration sine test was proposed to characterize the long term variability of the sine fit technique as the technique is applied to different sensors. Five sensors were configured to record the long duration acoustic sine signal. Figure 8 shows the 7 hours of data for this test.

The digitizer channel to sensor mapping for this test were:
Channel 1 C1P: MB2000 Absolute Pressure attached to chamber
Channel 1 C2P: GRAS 42 AE Microphone attached to chamber
Channel 3 C3P: NSD 051724 open to acoustic input
Channel 4 C4P: NSD 051722 attached to chamber
Channel 5 C5P: Chaparral Physics model 25 082058 attached to chamber
Channel 6 C6P: MB2000 Filtered output attached to chamber

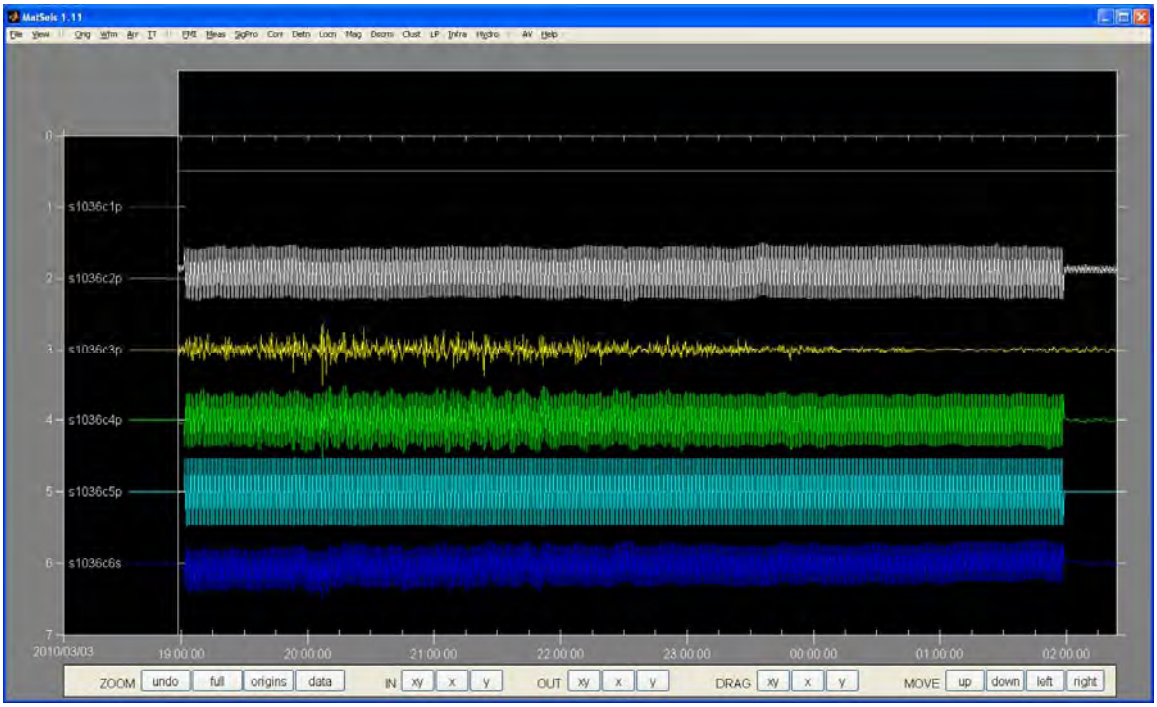

Figure 8. Illustration of the long duration sine test data.

From the raw data we can make a few observations:

1. The NSD open to acoustic background observed a significant change in background activity over the duration of the test. Strong background effects are observed from 20100/3/3 19:00 to 2010/3/4 00:00.
2. The NSD attached to the chamber observed the highest amount of variability of the sine tone over the duration of the test. Variations appear to correlate to observed background changes as seen on the NSD open to acoustic input.
3. The MB2000 filtered output was observed to have a moderate amount of variability of the sine tone over the duration of the test. Variations appear to correlate to observed background changes as seen on the NSD open to acoustic input.
4. The CP 25 attached to the chamber observed the least amount of variability of the sine tone over the duration of the test.

Processing: The data were processed using a standardized IEEE sine fit algorithm. First, a large window is defined which includes the full amount of tonal data to be processed. A smaller window of length defined by two sine cycles with 50% overlap is applied to each waveform and the sine fit parameters (i.e., amplitude, frequency, phase, RMS error, and SNR) are compiled for each realization. Amplitudes were normalized to the average observed amplitude and plots made for the MB2000 filtered output, NSD 051722. Figure 10a shows the results of applying a smoothing technique to remove the 1 Hz signal on the MB2000 filtered output signal. Figure 10b is absolute pressure within the test chamber as measured by the MB2000 absolute pressure output. Figures 10c and 11 shows the reported amplitude values obtained from the sine fit processing for the MB2000 filtered output and NSD 051722 over the seven hours of data.

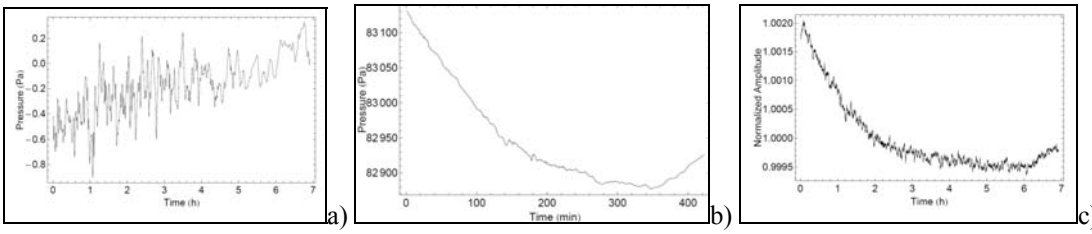

a) b) c)

Figure 9a-c. a) MB2000 Filtered output with 1 Hz signal removed using smoothing filter. This is what the raw signal from the MB2000 would have looked like had the 1 Hz signal not been present. b) MB2000 observed absolute pressure within test chamber for long duration sine test. c) Normalized amplitudes obtained from sine fit algorithm for MB2000 filtered output for long duration sine test.

Noteworthy observations from Figure 9a:

1. Small pressure fluctuations (~1 Pa) were observed by sensors attached to chamber as documented by MB2000 filtered output with 1 Hz signal removed.
2. Background is coupling into chamber, via leak or transmission coefficient.

Noteworthy observations from Figures 9b and 9c:

1. Normalized amplitudes change by small amount over duration of test, on the order of 0.25%.
2. Strong correlation exists to the observed acoustic background coupled into the test chamber when compared to MB2000 absolute pressure output of Figure 9b. This is because the piston phone output is proportional to the ambient chamber pressure.

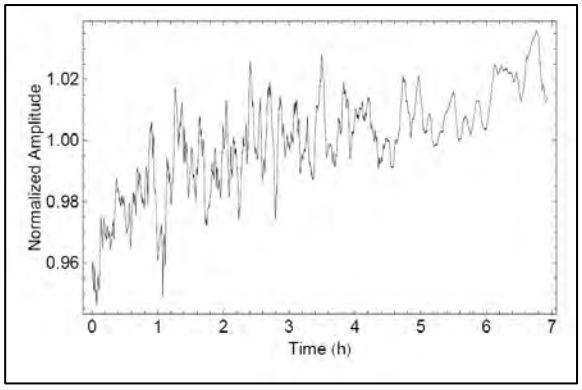

Figure 10. Normalized amplitudes obtained from sine fit algorithm for NSD - 051722 for long duration sine test. This signal looks very similar to Figure 10a, but it is from a different sensor processed in a different way. Figure 9a shows the background signal as seen by the MB2000 absent the 1 Hz signal. This plot shows the modulations in the 1 Hz signal that are present in the NSD output.

Noteworthy observations between Figures 9a and 10:

1. Normalized amplitudes change by significant amount over duration of test, on the order of 8%.
2. Strong correlation to coupled acoustic background observed on MB2000 filtered output shown in Figure 10a.

From the above results we observe the normalized sine fit amplitudes for the NSD and MB2000 filtered output are not correlated. Yet, the MB2000 filtered output background signal (once the 1Hz signal is removed) and the NSD 1 Hz amplitude are strongly correlated.

For comparison, the MB2000 1 Hz signal removed filtered output (Figure 9a) data was biased and scaled (i.e., scaled by 8% and added 1) and plotted with the normalized output from the NSD 051722. Figure 11 shows this comparison with the NSD data in black and the MB2000 AP data in red.

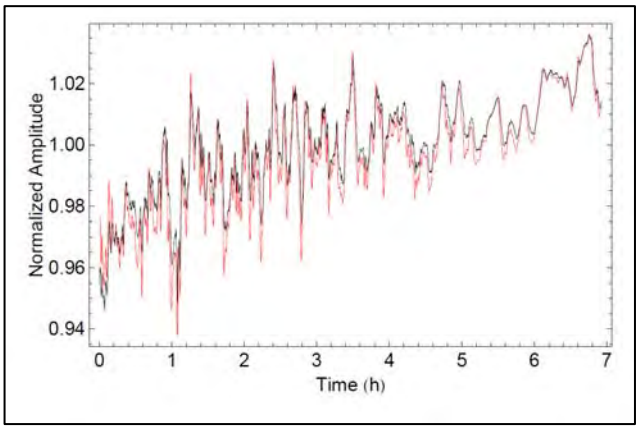

Figure 11. Normalized amplitudes from sine fit algorithm for NSD - 051722 are shown in black. Background pressure fluctuations measured by the MB2000 are shown in red (the red trace was generated by taking the MB2000 filtered output and removing the 1 Hz signal). A very strong correlation between the NSD amplitude modulations and the background pressure fluctuations is observed.

The strong correlation between the background pressure fluctuations and the NSD is clear. This leads us to believe the NSD sensitivity is influenced by the pressure fluctuations, as observed from within the test chamber. As with the two tone test, the low frequency background causes a modulation in the apparent amplitude of the high frequency test signal as seen by the NSD. We note that we can filter the 1 Hz signal from the NSD output. Background fluctuations similar to those seen in Figure 10a are apparent but they do not exactly match the signals plotted in Figure 11. This is because the electronic filtering in the NSD distorts the low frequency signal that comes directly from the diaphragm. However the single electronic pole in the MB2000 low frequency response closely matches the single pole acoustic filter that is built into the NSD due to the leak between the fore and back volumes.

CONCLUSIONS AND RECOMMENDATIONS

To summarize, the two-tone test allows us to observe harmonic and inter-modulation distortion on varying levels for the sensors in this test. Both harmonic and inter-modulation distortions were observed and are known as measures of non-linearity. The long duration sine test allowed us to show the NSD design has a clear correlation between the background pressure fluctuations and the observed amplitude modulation. The results of this investigation have been forwarded to the manufacture and were immediately addressed. The primary non-linear component was identified and modifications were made to replace this component. Future work should focus on quantifying the non-linearity quantity of modulation index for different sensors designs using this newly developed two-tone infrasound linearity test.

REFERENCES

1. Bowman, R. J., G. E. Baker, and M. Bahavar (2004). Infrasound station ambient noise estimates, in *Proceedings of the 26th Seismic Research Review: Trends in Nuclear Explosion Monitoring*, LA-UR-04-5801, Vol. 1, pp.608–617.

STATUS OF THE MACHINE LEARNING EFFORTS AT THE INTERNATIONAL DATA CENTRE OF THE CTBTO

Ronan J. Le Bras[1], Sheila Vaidya[2], Jeff Schneider[3], Stuart Russell[4], and Nimar Arora[4]

Comprehensive Nuclear-Test-Ban Treaty Organization[1], Lawrence Livermore National Laboratories[2], Carnegie Mellon University[3], and the University of California at Berkeley[4]

ABSTRACT

Machine learning projects were conceived in March 2009 as part of the International Scientific Studies Project initiative at the Provisional Technical Secretariat of the Comprehensive Nuclear-Test-Ban Treaty Organization (CTBTO) and initiated a few months later. Some of the projects are intended to aim at short to medium term operational applications. These include the identification of seismic and hydroacoustic phase names using a large number of features extracted from the waveforms, and the labeling of automatic events as real or false depending again on a large number of features from the automatic events. Concrete research results using International Data Centre (IDC) data are available for these two sets of projects. Seismic phase identification is shown to have the potential to improve its accuracy by 23 %, and the software developed for the project on false events identification has been tested at the IDC and shown to correctly label 80% of the false alarms. Some projects are aimed at the longer term. This is the case of a Bayesian approach to the automatic seismic network processing problem and a distributed database approach to the waveform cross-correlation problem. The first project is well under way and has surpassed the current operational system by 14 % in accuracy for the same false alarm rate. The second has shown the potential of distributed systems to solve efficiency issues.

OBJECTIVES

The objective of this project is to investigate the application of Machine Learning techniques to the processing of waveform data at the IDC of the CTBTO. The initial motivation was that a large database of waveform and parametric data has been accumulated in the last ten years and this database is currently hardly exploited in terms of its potential to improve on existing models and processing techniques. Analyst knowledge has been captured in the archive but is not used in the current automatic system which tends to treat an incoming event as if it is seeing it for the first time without the benefit of recalling information pertaining to events in similar locations that have previously been recorded. In addition, methods that were too computationally intensive just a few years ago could now be used on a real-time basis and inserted into the IDC processing pipeline.

The ISS09 project initiated by the CTBTO in 2008 included a *Data Mining/Machine Learning* component, which was a new area of investigation for the organization. A workshop in March 2009, in preparation for the June 2009 conference, identified a number of objectives that could be fulfilled in the near term with a high probability of success and others that would take a longer effort to bear fruit in the operational system.

- The projects with operational short term goals included:
  - False Events Identification (FEI) using Support Vector Machine (SVM) methods (Mackey et al., 2009)
  - Hydroacoustic and Seismic phase identification (Tuma M. and Igel C., 2009; Schneider et al., 2010)

- The projects with operational long term goals included:
  - Vertically Integrated Seismic Analysis (VISA) detection, association, and location (Arora et al., 2009a, 2009b)
  - Distributed database approach to the waveform cross-correlation problem

Figure 1 shows the areas of impact of four of these projects within the context of the IDC waveform processing.

RESEARCH ACCOMPLISHED

The various short-term and long-term projects tackled in the Machine Learning area during the last year have led to a number of publications illustrating the benefits that can be obtained from applying concepts in that field to the problem of processing of seismic and hydroacoustic data at the IDC.

False Events Identification

The first short-term project which was tackled was the false event identification (FEI) in the SEL3 bulletin based on features of the detections and associations that comprise each hypothesized event. The problem was formulated as a classification problem of labeling SEL3 events as either true or false based on a large set of features. Several variants of the SVM methods as well as the naive Bayes methods were tested in order to identify the most promising approach.

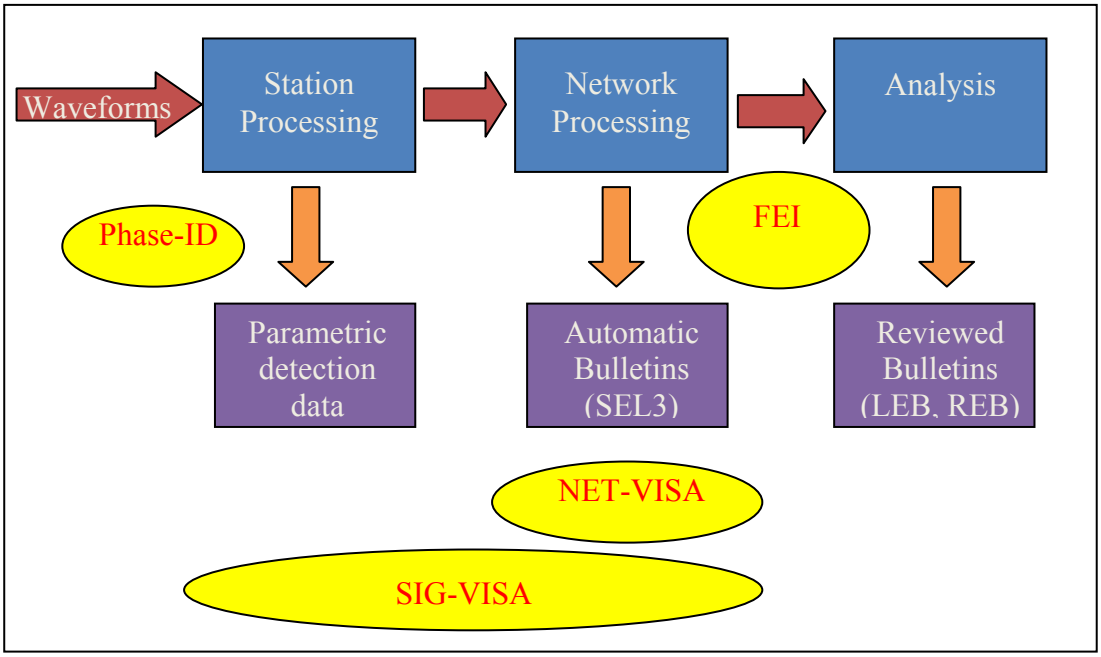

Figure 1. Simplified context diagram situating the various projects undertaken in the Machine Learning area and applied to the processing of seismic and hydroacoustic data at the IDC.

The classifiers were trained on parametric data which included both automated event bulletins (SEL3) and the corresponding analyst-reviewed bulletins, *late event bulletins* (LEB). Each bulletin includes data for both events and arrivals, as well as associated information. The parametric data used to train the classifiers consists of a long list of attributes related to the arrivals and associations. This list is detailed in Table 1.

Table 1. List of attributes used to form the feature vector to characterize SEL3 events.

Origin table fields: lat, lon, depth, time, nass, ndef, ndp, grn, srn (vectorized), dtype (vectorized), mb, ms, ml
Origerr table fields: sxx, syy, szz, stt, sxy, sxz, syz, stx, sty, stz, sdobs,
smajax, sminax, strike, sdepth, stime
Number of associated arrivals at each station
Haversine distance from origin location to each station
Counts of associated Assoc.delta values in six-degree bins
Counts of associated Arrival.qual values
Counts of associated Assoc.phase values
Counts of associated Arrival.iphase values
Number of times Assoc.phase != Arrival.iphase for associated arrivals
Number of time defining associated arrivals
Fraction of time defining associated arrivals
Number of azimuth defining associated arrivals
Fraction of azimuth defining associated arrivals
Number of slowness defining associated arrivals
Fraction of slowness defining associated arrivals

Mean of absolute value of associated Assoc.timeres values
Mean of absolute value of associated Assoc.azres values
Mean of absolute value of associated Assoc.slores values
Mean of associated Arrival.snr values
Variance of associated Arrival.snr values
Mean of associated Arrival.deltim value
Variance of associated Arrival.deltim values
Mean of associated Arrival.delaz value
Variance of associated Arrival.delaz values
Mean of associated Arrival.delslo value
Variance of associated Arrival.delslo values

The three-month dataset used in the study consisted of IDC parametric data for mid-March to mid-June 2009. It included 13,254 SEL3 events with 150,275 associated arrivals. The LEB bulletin for that time period included 9,961 events with 169,981 associated arrivals. Of these LEB arrivals, 114,464 were automatically generated (i.e., retained by analysts from SEL3) and 55,517 were added by analysts.

A set of SEL3 events for use by the classification procedures is obtained by featuring numeric values that informatively summarize the parametric data describing each SEL3 event, including residuals, error ellipses, number of defining phases, signal-to-noise ratios, and other quantities (see Table 1 for the list of features). The set of such values for a given SEL3 event forms a real vector, with which a binary label is associated indicating whether or not that event was subsequently discarded by analysts. For evaluation, a data set is built that excludes parametric data based on non-seismic stations. The first 75% of SEL3 events are used for training, and the final 25% of SEL3 events are used as a test set. To evaluate a given classification procedure, it is first trained to learn a classifier. Subsequently, the classifier is evaluated to determine which previously unseen events will be discarded by analysts by applying it to the test set.

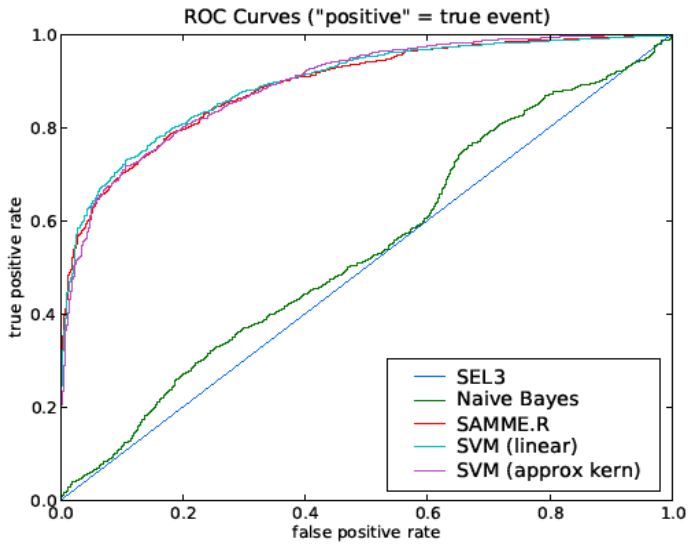

Figure 2. ROC for the different false events classifiers tested in this study (after Kleiner et al., 2009).

The primary metric used to assess the performance of the classification procedures is *accuracy*: the fraction of events in the test set that are correctly classified. The receiver operating characteristic (ROC) curves measure the tradeoff between false positive and false negative rates. Figure 2 summarizes the performance metrics for the different classifiers tested along with the SEL3 bulletin performance. The accuracy of the SEL3 bulletin under this measure is 65.41%. The classification procedures yield significant improvements. Among them, the linear L2 SVM yields the best performance with 81.47% accuracy. Other methods considered, such as boosted decision stumps and the non-linear L2 SVM, achieve similar performance, though the linear SVM enjoys the additional advantages of efficiency and interpretability. It is also worth noting that the simpler Naive Bayes procedure provides some improvement over SEL3 but significantly underperforms its more sophisticated counterparts.

Seismic Phase Identification

The second short-term project presented here is the identification of seismic phases on three-component seismic stations using features extracted from the waveform. This project aims at assessing potential improvements in the current operational system at the level of station processing, as shown on Figure 1 (Phase_ID label). A data set consisting of 117,181 detections at 3-component stations during 2009 was compiled from a number of IDC tables. The attributes used to perform the classification and their definitions are shown in Table 2. The ground truth phase for these detections is taken from the analyst-reviewed association table. For this study, only 8 phases were considered (Lg, P, PKP, Pg, Pn, Rg, S, Sn). In most cases, P and PKP are grouped together and the problem treated is a 7-class problem. One of the difficulties with this problem is that the P and PKP phases overwhelmingly dominate the statistics in terms of their numbers (75.7% of the records) and that other phases—Rg in particular—are very rare.

ddet60	Number of detections in a 60s window before and after the current detection
dtime60	Average time between detections in a 60s window before and after the current detection
Hmxmn	Maximum to minimum horizontal ratio
htov0.25	Horizontal to vertical ratio at 0.25 Hz
htov0.5 H	orizontal to vertical ratio at 0.5 Hz
htov1 H	orizontal to vertical ratio at 1.0 Hz
htov2 H	orizontal to vertical ratio at 2.0 Hz
htov4 H	orizontal to vertical ratio at 4.0 Hz
Hvrat	S-phase horizontal to vertical ratio
Hvratp	P-phase horizontal to vertical ratio
inang1	Long-axis incidence angle
inang3	Short-axis incidence angle
Per Dom	inant period
Plans S-phase	planarity
Rect Rectilin	earity
Slow Sl	owness

Table 2. Attributes used in the classification of different seismic phases detected on three-component stations.

Several classifiers were assessed against the analyst ground-truth and they are included in the following list:

Support Vector Machines – SVM algorithms identify a linear decision boundary in the feature space between two classes. Among all possible linear decision boundaries, they choose the one that maximizes the margin between the two classes. The solution allows for a number of points to lie on the wrong side of the boundary and assesses a penalty on them. In order to create a non-linear decision boundary in the original space, a kernel is used to generate additional features from the original ones. The 7-class problem is handled by building 7 binary classifiers that separate each class from all the others. For each new sample, all 7 classifiers are queried and the class corresponding to the one giving the highest prediction is chosen. See Cristianini et al. (2000) for more details on SVMs. The implementation used for this test was the LIBLINEAR library available at http://www.csie.ntu.edu.tw/~cjlin/liblinear/

Decision Trees – These are trees where the root and the other internal nodes contain a test of one of the features, which specifies whether a data point belongs to the left or right sub-tree of that node. The training data points are stored at the leaves of the trees. In order to classify a new test sample, the tests are used to find the correct leaf for the sample and the majority class of the training samples in that leaf is predicted. Learning of the decision trees is done by a greedy information-gain based procedure. See Hastie et al. (2000) for more details on decision trees.

Bagging – Bagging takes multiple bootstrap samples of the training data and learns a separate model from each bootstrap sample. The final prediction is made by averaging or voting the predictions of each model. Bagging may be applied to any classifier, but is commonly used in conjunction with decision trees to handle problems with over-fitting, which is what we did in this study.

Boosting – Boosting is conceptually similar to bagging except that each new model is constructed by reweighting the training data points according to how much prediction error they have in the current set of models. We tested a version called AdaBoost.

The methods were tested using the first 60% (in time) of the data for training and the last 40% for testing. There were two modes of modeling. The "single-task" mode lumps all the data together and learns a single model to be used at all stations. The "multi-task" mode learns a station-specific model using only the data for that station. A summary of the accuracy in predicting the phases for the test set is shown in Table 3.

Table 3. Accuracy results of testing six different classifying methods. The first column (single-task) shows the results of classifying independently of the station. The second column (multi-task) shows the results of classifying using station-specific classifiers.

Method	One predictor for all stations	One predictor per station
Multi-class SVM	76.09	82.32
Multi-class SVM with normalization	77.53	83.47
Real AdaBoost, 1vsAll	80.22	83.17
Gental AdaBoost, 1vsAll	80.31	83.42
Bagged decision trees	79.66	84.05
Bagged decision trees with kernels	**79.82**	**84.18**

The best performing models were those using bagged decision trees (shown in bold in Table 3). The kernel used to produce the best result was one that generates all quadratic features (i.e., the product of all pairs of features). Based on this empirical study, a supervised classification method using bagged decision trees with additional features generated by a quadratic kernel yields the best results. The best performance is obtained by training a separate classifier for each station.

Vertically Integrated Seismic Association

The goal of this project is to investigate if improvements can be made to the existing IDC seismic processing system using modern methods based on Bayesian inference. In a first stage, as indicated in Figure 1, the method is applied at the stage where parametric detection data is processed to obtain automatic bulletins. This initial project leads to the building of the NET-VISA prototype and the current results are presented here. A second stage, SIG-VISA, will include the detection and phase identification stage leading to the parametric data into the inference construct.

The probabilistic model in NET-VISA is based on a generative forward model which consists of:

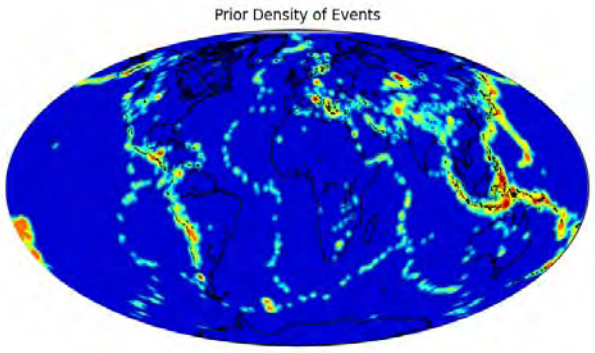

Figure 3. Prior distribution of events used in the event distribution generative model.

- Spatial, temporal, and magnitude probabilistic models for event generation. The temporal model is a Poisson process. The spatial model is based on a prior spatial distribution of seismicity (shown in Figure 3) to which is added a uniform spatial distribution to take into account the possibility of an event occurring at a place where it never occurred before, as in the case of a newly developed nuclear test site. The magnitude model is based on the Gutenberg-Richter distribution.

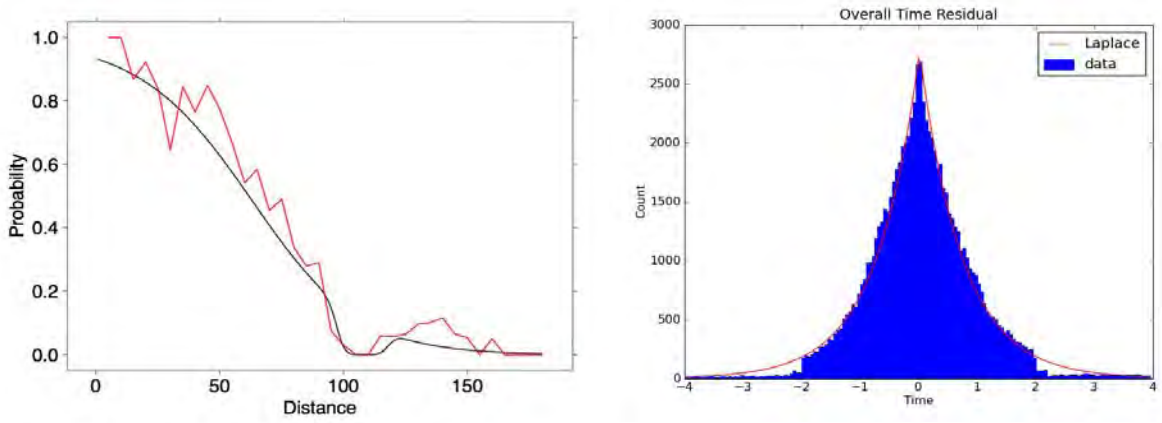

Figure 4. The curve to the left is the probability of detection of a P phase at station ASAR as a function of distance for an event of magnitude between 3 and 4. The analytical curve (in black) used in the calculations is shown superimposed on the observations (in red). The histogram to the right shows the overall (over all stations) travel time residuals distribution. Note the good fit to a Laplace distribution.

- Detection generation model at a given station knowing the location and magnitude of the event. This includes the phase-dependent probability that the event be detected at the station and the phase-dependent probability that the detection be of a certain amplitude and at a certain time around the mean time of arrival from the specific phase. Figure 4 shows on the left the analytical curve used in the probability of detection calculations and how it calibrates well against the observations. The right side of the figure shows the overall distribution of arrival time residual for P phases. Note that it fits very closely the Laplace distribution used in the modeling. Slowness and azimuth residuals are also modeled using a Laplace distribution.

- False detection. To take into account the fact that many false detections are made and may coincidentally be associated with an event, false detections are modeled into the generative forward model. The result is that the inference process takes into account the possibility of a false association. This is superior to the current operational model where any match between event and detection is assumed to be a positive match independently of the potential for the detection to be false. This leads to spurious association and degradation of location capability.

Using this probabilistic generative model, consisting of the product of all aforementioned probabilities, an inference engine is used to build event hypotheses consistent with the parametric observations. The general manner in which event set hypotheses are improved is that the current state is updated using a limited set of moves. The different moves used within the inference engine are listed below and give an intuitive view of the various steps leading to incremental improvements in the set of event hypotheses.

1. **Birth Move**: The birth move is executed only once in each event window. To propose the birth move events are searched on a fixed grid of points. The grid consists in 1-degree longitude and latitude buckets, 100-km depth buckets, 5-second time buckets within the event window, and 0.5-magnitude steps. At each of these grid points an event is hypothesized and the best detections added to it. At each station, the best detection with a score > 1 is added. Finally, the score of all the possible events is computed and the event with the greatest score > 1 is picked. If an event is found, then it is added to a list and all of its associated detections are marked unavailable. The algorithm is repeated over the same grid of events but with fewer associated detections. Finally, when no more events are found, the list of events is added to the hypothesis. The events are added to the hypothesis without any associated detections. Therefore this move is technically a downhill move. However, it is followed by other moves which will either add detections and make these events viable or kill them.

2. **Improve Detections Move**: For each detection in the detection window, all possible events up to the time of the detection are considered as well as all possible phases for these events to find the best event-phase for it. If the best event-phase has a score < 1 or the best event-phase already has another detection with a higher score then this detection is changed to a false detection.

3. **Death Move**: Any event with a score < 1 is killed and all its detections are marked as noise.

4. **Improve Events Move**: For each event we look for 1000 points chosen uniformly at random in a small ball around the event (5 degrees in longitude and latitude, 200 km in depth, 50 seconds in time, and 1 units of magnitude) for an event with a higher score. If such an event is found, the event parameters are changed.

5. **Final Pruning**: Before outputting events a final round of pruning to remove some duplicate events is performed. Any event which has another event with a higher score and within 5 degree distance and 50 second time is pruned. The reason for these spurious events is that true events have a long waveform coda within which detections are made at each site. These detections don't correspond to any event-phase of the original event but taken together they do suggest a new event at about the same location and time as the original event. Our model does allow for false detections but not false detections which are associated with a true event. Thus we need to explicitly prune these events for now. A later, more realistic model might be envisioned where the most probable detections within the coda are modeled.

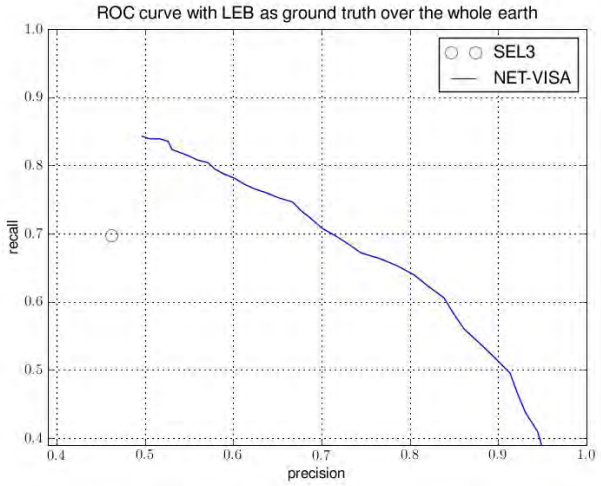

Figure 5. Receiver Operating Characteristics (ROC) for NET-VISA (in blue) and the location on the SEL3 bulletin in the precision/recall space.

The current results of the prototype are very promising when compared to the IDC operational results (see Figure 5). NET-VISA has a 14% higher recall (obtained events) at a slightly higher precision (automatic event that match an LEB event) than global association (GA), the current network processing program, and a 24% higher precision rate at the same recall rate as GA. A full assessment of the prototype cannot be achieved without analyst review of its results. There is tantalizing suggestion that this may prove very interesting since some of the events formed by NET-VISA (and missed by LEB) have been confirmed by bulletins (National Earthquake Information Center) independent of the IDC bulletin. It should be noted that an LEB bulletin based on the results of NET-VISA has the potential to be quite different especially at magnitudes between 3 and 4, and perhaps more accurate than the currently produced LEB which takes as starting point for analysis the SEL3 produced by GA.

CONCLUSIONS AND RECOMMENDATIONS

The few projects initiated in the Machine Learning area at the IDC of the CTBTO have proven that bringing innovative components to the current operating system should strengthen it and increase the precision of the automatic results which in turn should greatly increase the productivity of analysis and allow more precise bulletins to be produced. Some of the methods can be applied to some extent as a tuning exercise of the existing system, since it was found that some projects presented in this paper would benefit from station-dependent adjustment in parameterization of the algorithms. The NET-VISA project has shown the benefit of a radical overhaul of a key component of the system, and how new paradigms can be applied operationally with the increased computing power available to us over a decade after the development of the current IDC operational system.

A crucial step before a complete proof-of-concept for these projects can be presented to the member states of the CTBTO is to involve seasoned analysts in the evaluation of these new algorithms.

Another conclusion of these positive results of the current machine learning efforts is that more problems of interest to the CTBTO could be tackled such as infrasound phase identification, event screening, and on-site-inspection data sifting.

ACKNOWLEDGEMENTS

We thank Dr. Lassina Zerbo, IDC Director, for allowing us to publish this research and for his support of the machine learning efforts at the IDC and Misrak Fisseha for her analyst expertise and efforts in evaluating the FEI software delivered at the IDC.

REFERENCES

Arora, N., Jordan, M., Russell, S., and Sudderth, E., 2009, Vertically Integrated Seismological Analysis I: Modeling

Arora, N., Jordan, M., Russell, S., and Sudderth, E., 2009, Vertically Integrated Seismological Analysis II: Inference

Cristianini N. and J. Shawe-Taylor (2000). An Introduction to Support Vector Machines and other kernel-based learning methods. Cambridge University Press.

Hastie, T., Tibshirani, R., and Friedman, J. H. (2009). The elements of statistical learning: Data mining, inference, and prediction (Second Edition). New York: Springer Verlag.

Mackey, L.; Kleiner, A.; Jordan, M. I., 2009, Improved Automated Seismic Event Extraction Using Machine Learning**,** American Geophysical Union, Fall Meeting 2009, abstract #S31B-1714.

Schneider J., Given, J., Le Bras, R., and Fisseha, M., 2010, Supervised Classification Methods for Seismic Phase Identification, EGU abstract, EGU2010-6269

Tuma, M. and Igel, C., 2009, Kernel-based machine learning techniques for hydroacoustic signal classification, ISS09 Conference.

Disclaimer

The views expressed in this paper are those of the authors and do not necessarily reflect the views of the CTBTO Preparatory Commission.

BASIC RESEARCH ON SEISMIC AND INFRASONIC MONITORING OF THE EUROPEAN ARCTIC

Frode Ringdal, Tormod Kværna, Steven J. Gibbons, Svein Mykkeltveit, and Johannes Schweitzer

NORSAR

Sponsored by the Army Space and Missile Defense Command

Award No. W9113M-05-C-0224

ABSTRACT

This project is a research effort aimed at improving seismic and infrasonic monitoring tools at regional distances, with emphasis on the European Arctic region, which includes the former Novaya Zemlya test site. The project has three main components: a) to improve seismic processing in this region using the regional seismic arrays installed in northern Europe, b) to investigate the potential of using combined seismic/infrasonic processing to characterize events in this region and c) to carry out experimental operation, evaluation and tuning of the seismic threshold monitoring technique.

On 11 November 2009, signals from a magnitude 3.2 event in the eastern Barents Sea were recorded by seismic stations in the Nordic countries and in NW Russia. This part of the Barents Sea has no known history of significant earthquake activity. However, over the past decades, several seismic events at various locations in this region have been detected, and several of these have been confidently associated with anthropogenic activity, like the Kursk submarine accident. As to the source type of the 11 November 2009 event, we are not in a position to draw a firm conclusion. Observations at the ARCES array, at a distance of 800 km, show signal energy up to 40 Hz and show no indication of spectral banding or cepstral peaks. This is quite different from the characteristics of underwater explosions in this area, suggesting that the event is more likely to be an earthquake. This study further illustrates the very efficient high-frequency seismic energy propagation characteristics of the Barents Sea area.

Seismic and infrasound signals at ARCES have recently been associated with blasting at the Suurikuusikko gold mine in northern Finland, approximately 10 km to the west of Hukkakero. This mine started operations in the summer of 2006 and, in order to develop a database of explosions, multi-channel waveform correlation detectors were initiated using ARCES seismic signals as templates. Many hundreds of clear detections have been made indicating several events per week. The absence of detections prior to June 2006, and the absence of detections outside of characteristic times of days, indicate a low false alarm rate. A majority of the over 500 events detected since June 2006 have been associated with infrasound detections at ARCES and at stations of the infrasound networks of Sweden, Finland, and Russia, all at regional distances from the source and with a fortuitous coverage of directions from the mine. While the events appear to be less efficient generators of infrasound than the military munitions explosions at Hukkakero, the blasts occur throughout the year and so will sample a far greater spectrum of atmospheric profiles. Examining long time-series of observations from these well-constrained sources will hopefully improve our understanding of the conditions under which infrasound is observed within and on the edge of the so-called “Zone of Silence”.

International news media reported in July 2009 on an unsuccessful launch of the new Russian intercontinental Bulava missile. The missile was launched from a submarine in the White Sea on 15 July 2009, and was reported to self-destruct during the first stage of flight. The effect of another launch failure of the Bulava missile was visually observed in northern Scandinavia on 9 December 2009, in terms of strange light phenomena in the sky. This caused considerable public attention, and it was reported after some time that the phenomena were believed to originate from an engine failure and self-destruction in the third stage of a Bulava missile. Infrasound signals from both of these launches were well recorded at several infrasound arrays in the region. Array analysis followed by tracing of the estimated back-azimuths located both infrasound sources to the White Sea. During recent years, infrasound signals been observed in the Nordic region from several rocket launches and meteors entering the atmosphere. Establishing a database of such events is important for future studies of infrasound wave propagation.

OBJECTIVE

The objective of the project is to carry out research to improve the current capabilities for monitoring small seismic events in the European Arctic, which includes the former Russian test site at Novaya Zemlya. The project has three main components: a) to improve seismic processing in this region using the regional seismic arrays installed in northern Europe, b) to investigate the potential of using combined seismic/infrasonic processing to characterize events in this region and c) to carry out experimental operation, evaluation and tuning of the seismic threshold monitoring technique, with application to various regions of monitoring interest.

RESEARCH ACCOMPLISHED

On 11 November 2009, at 04:18 GMT, signals from a seismic event in the eastern Barents Sea were recorded by seismic stations in the Nordic countries as well as in NW Russia. This part of the Barents Sea has no known history of significant earthquake activity. However, over the past decades, NORSAR has recorded several seismic events at various locations in this region as listed in the NORSAR reviewed regional seismic bulletin. Since January 2006, five small seismic events near Novaya Zemlya have been detected (Table 1 and Figure 1).

Table 1. Seismic events near Novaya Zemlya detected during 01/2006-01/2010

Date	Origin time	Latitude (N)	Longitude (E)	Magnitude (mb)
05/03/2006	23:17:35.7	76.80	66.04	2.65
14/03/2006	20:57:02.4	75.07	53.05	2.23
30/03/2006	10:46:02.8	70.79	51.50	2.30
26/06/2007	03:19:05.0	73.45	53.43	2.75
11/11/2009	04:18:21.0	71.58	46.09	3.20

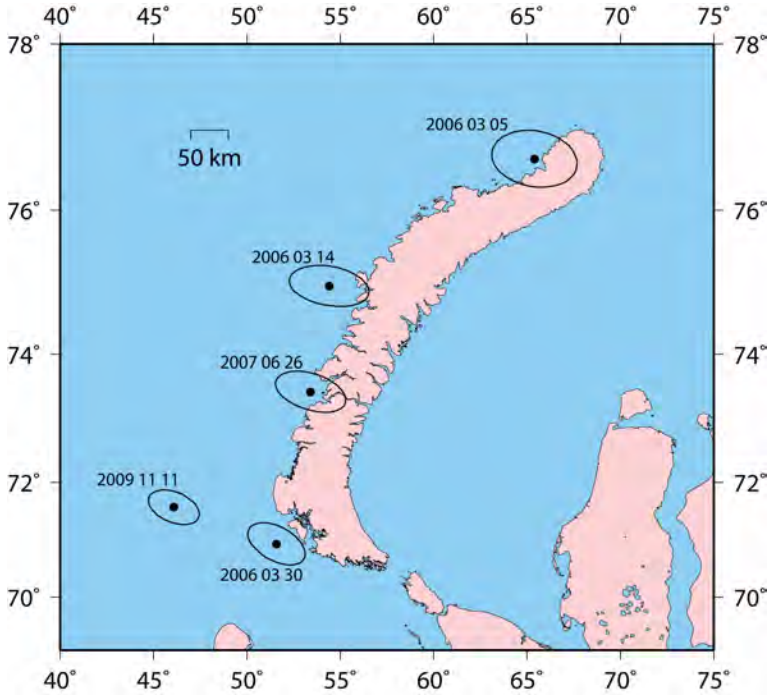

Figure 1. Location of seismic events near Novaya Zemlya between 2006 and 2010 as published in the regional NORSAR bulletin. The 95% location confidence ellipses are indicated for each event.

Observations at ARCES

We have analyzed data from the ARCES array in northern Norway recorded for the event on 11 November 2009. Figure 2 shows filtered recordings (2-16 Hz) of the three-component center seismometer of ARCES. The characteristics of the traces are similar to previous events from this region, with clear Pn and Sn phases, whereas the Pg and Lg phases are not discernible, at least not in this frequency band. We also note that the direction of the event is nearly due east of ARCES, and that consequently the radial component (se) of the Pn-phase is about as strong as the vertical component, while the Sn phase is by far the most prominent on the transverse (sn) component. This is an important confirmation of the advantages of using the transverse component of the seismogram to increase the probability of detecting S-type phases.

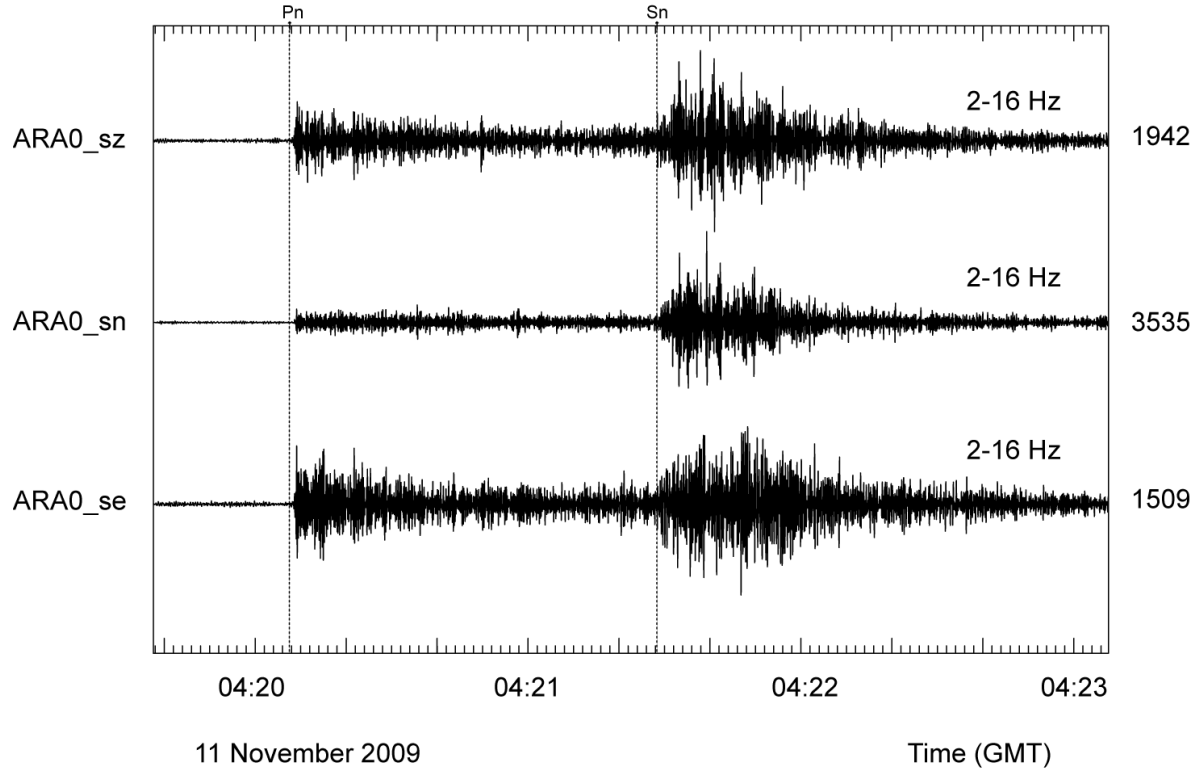

Figure 2. Recordings by the three-component center seismometer of the ARCES array of the seismic event in the Barents Sea on 11 November 2009. The traces have been filtered in the 2-16 Hz frequency band.

The event on 11 November 2009 is of special importance since it is the first event near Novaya Zemlya since the high frequency element was installed at ARCES in early 2008. As noted by Ringdal et al. (2008) in their initial study of high frequency ARCES recordings, the available high-frequency data at that time did not include recordings of distant events to the east and north-east of the ARCES array, and the high-frequency propagation from the Novaya Zemlya region to ARCES could therefore not be assessed.

We have therefore made a special analysis of the associated ARCES high frequency recordings for the event on 11 November 2009, as described in Kværna and Ringdal (2010). Figure 3 shows spectra of the Pn and Sn phases as well as the spectrum of noise preceding the event. We note the significant high-frequency energy of the Pn and Sn phases, with the signal exceeding the noise for frequencies all the way up to 40 Hz for the Pn phase, and even above 40 Hz for the Sn phase.

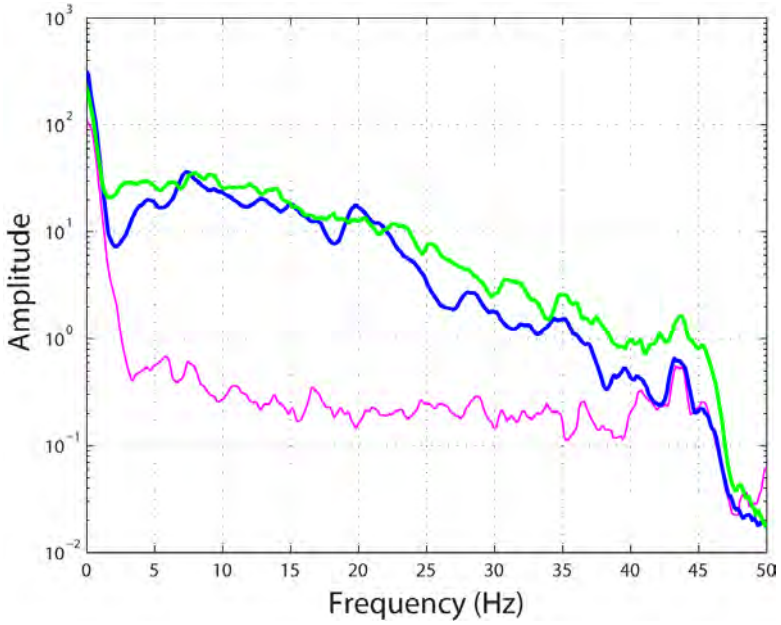

Figure 3. Spectra from the ARCES vertical high-frequency element of the Pn (blue) and Sn (green) phases of the 2009 event. The noise spectrum (magenta) preceding the event is also shown.

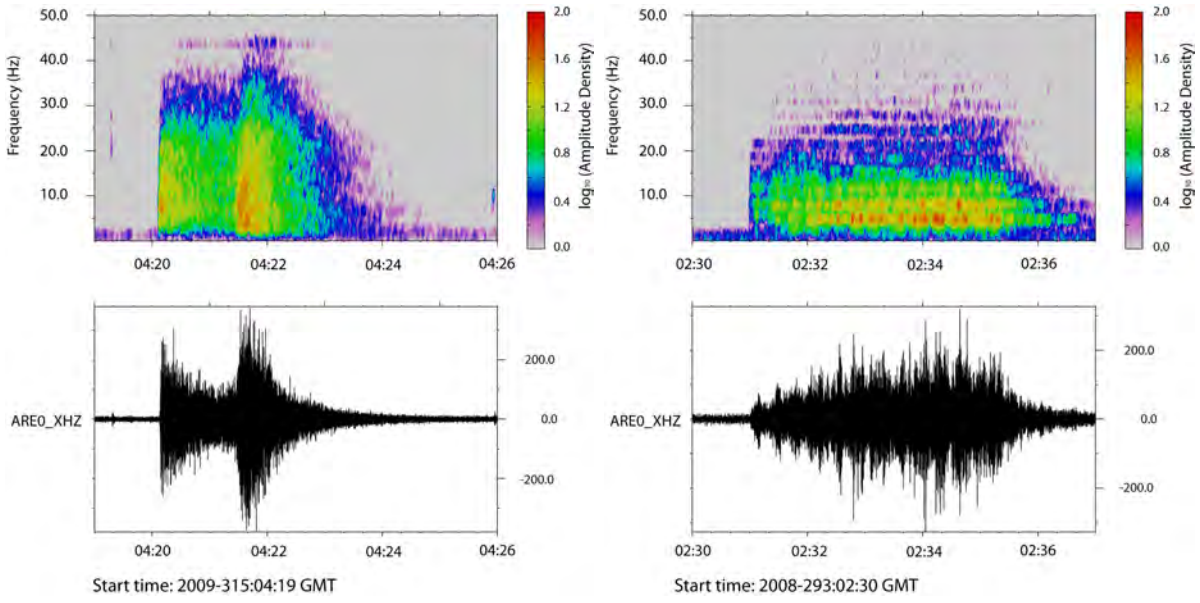

Figure 4. Spectrograms from the ARCES vertical high-frequency element of seismic events in the Barents Sea. The left plot shows the seismic event on 11 November 2009. The plot to the right shows a sequence of presumed underwater explosions near the northern coast of the Kola Peninsula on 19 October 2008. The traces have been high-pass filtered at 2.2 Hz. Note the significant differences between the two plots.

After the ARCES high-frequency element was installed, there have been a number of seismic events in or near the mining regions of NW Russia. However, the distance from ARCES to these events are 300 km or less, whereas the epicentral distance of the 11 November 2009 event was as large as 800 km. Nevertheless, it is of interest to compare the latter event to some of the presumed underwater explosions at about 300 km distance. One way to make such a

comparison is illustrated in Figure 4. This figure shows spectrograms from the ARCES vertical high-frequency element of the 11 November 2009 event as well as a sequence of presumed underwater explosions near the northern coast of the Kola Peninsula on 19 October 2008. We note that the presumed explosions in 2008 have their dominant energy at much lower frequencies than the event in 2009, even though the latter event is at a much larger distance from ARCES. The spectral scalloping evident in the 2008 plot is typical of many underwater explosions, and is associated with multiple reflections from the bottom and surface of the water (e.g., Baumgardt and Der, 1998).

Kværna and Ringdal (2010) applied the software described by Oberg et al. (2004) to compare the cepstral peaks associated with various categories of events in the Barents Sea region. They concluded that the recordings from the 11 November 2009 event were more consistent with previous earthquake recordings than with recordings of known underwater explosions, although they noted that it is difficult to discriminate reliably using this criterion only.

Infrasound studies

The site of military explosions at Hukkakero, northern Finland (67.934 N, 25.832 E) has raised significant interest in recent years due to the generation of infrasound (Gibbons et al., 2007). Hukkakero is the site of between 20 and 50 near-surface explosions every year for the destruction of expired ammunition. The events occur on consecutive days in August and September and provide a useful data set for the study of infrasound propagation for a number of reasons:

- The location of the events is known. All explosions are known to take place within approximately 300 meters of the coordinates stated.
- The sources are almost identical both in terms of yield (approximately 20000 kg per explosion) and source-time function (there are no multiple or ripple-fired explosions as are common in open-cast mining).
- The similarity of the waveforms makes the events amenable to detection using waveform correlation detectors (Gibbons and Ringdal, 2006). This means that every event can be detected with an almost negligible false alarm rate and also that the origin times of explosions can be constrained very accurately.

On October 2, 2009 we noted an event which occurred shortly after the end of the 2009 Hukkakero explosion sequence and was reported by the NORSAR Event Warning System (Schweitzer, 2003). Due to the event origin time and poor signal correlation with known events, this event was deemed unlikely to be from the same source location. Using seismic waveforms from stations of the Finnish national seismic network, in addition to ARCES, indicated an event location approximately 10 km to the west of the Hukkakero site. A consultation with colleagues at the Institute of Seismology at the University of Helsinki concluded that the source of the October 2 event was almost certainly the Kittilä Gold Mine, operated by Agnico-Eagle, at Suurikuusikko (67.90 N, 25.39 E). Figure 5 displays the location of the sources together with waveforms from one event from each of the two explosion sites.

The magnitude estimate for the seismic event on October 2, 2009, was just in excess of 1.0 and, while such events are routinely detected and included in the fully automatic seismic event bulletins at NORSAR, they are not large enough to be reviewed manually and included in the published analyst bulletin. We therefore use a correlation detector to try to catch as many occurrences as possible of seismic events at this mine.

Gibbons and Ringdal (2006) demonstrated that seismic arrays have a tremendous advantage over single stations for correlation detectors. Firstly, there is a great suppression of the background noise made possible by a stacking of the correlation coefficient traces. Secondly, we can perform a post-processing of detections by examining the alignment of the cross-correlation coefficients from the different channels and large numbers of false alarms can be eliminated in this way.

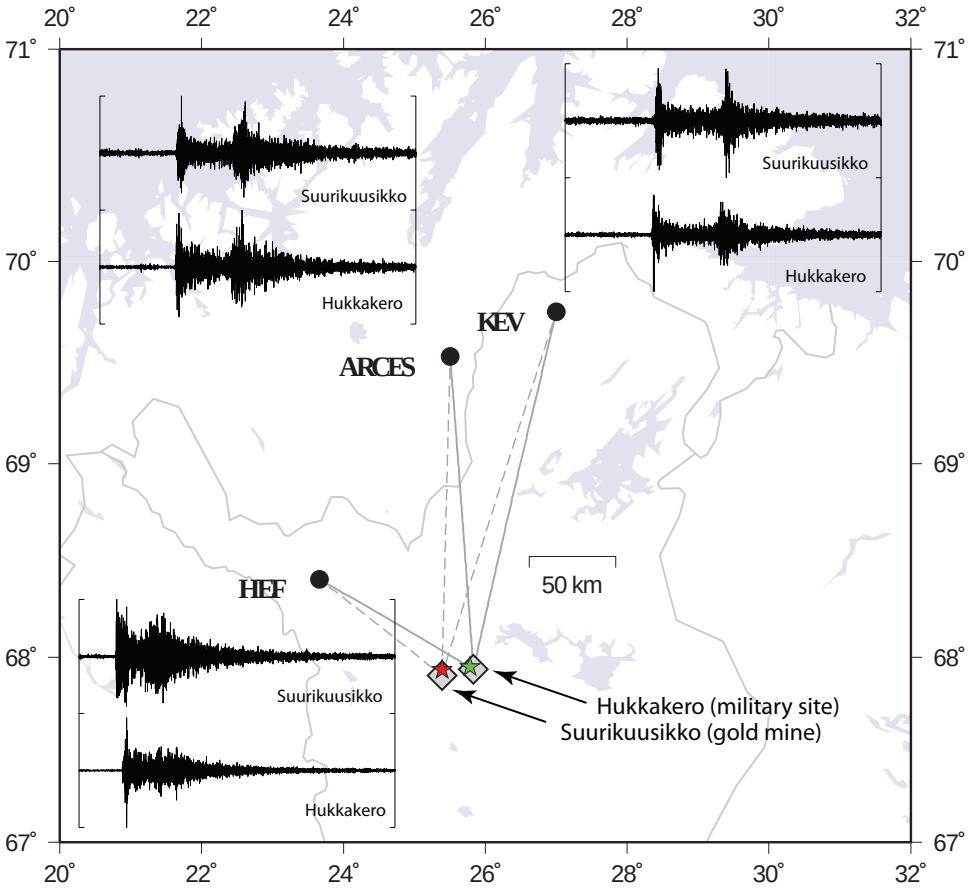

Figure 5. Locations of the Hukkakero military explosion site (67.934 N, 25.832 E) and the Suurikuusikko gold mine (67.902 N, 25.391 E) in relation to the ARCES seismic array and the HEF and KEV 3-component stations of the Finnish seismic network. Two minutes of data are displayed for each trace beginning at the estimated event origin time and all waveforms are bandpass filtered 3-16 Hz. The green and red stars denote event location estimates for a Hukkakero and a Suurikuusikko event respectively using the network displayed.

Figure 6 displays all of the detections attained since 2006 using a correlation detector with signal at ARCES from the October 2, 2009, event as a template. A total of 493 detections have been made in the period shown. No convincing detections were made prior to July 2006, and a consultation with the information provided by Agnico-Eagle confirms that this is consistent with the operational history of the mine. The detections displayed in Figure 6 have yet to be screened manually for false alarms, but have been filtered using the criteria described by Gibbons and Ringdal (2006). The concentration of detections at particular times of day and the absence of detections at night time suggest that the false alarm rate is very low.

The detection of infrasound signals at ARCES following many events in this sequence indicates that this source may be of great interest for the study of sound propagation of regional distances. The mine location is fortuitous in relation to the network of infrasound sensors in Norway, Sweden, Finland and Russia (Figure 7) which provide an almost optimal coverage of the different directions from the source. Some of the stations are located either at the edge of or well within the so-called “Zone of Silence” within which the propagation of infrasound is currently very poorly understood. While initial indications are that the Suurikuusikko mine is a less efficient generator of infrasound than the military explosions at Hukkakero, the new data set has a great advantage in that the events occur throughout the year, and so will sample many different atmospheric profiles, and may contribute more to understanding the conditions under which infrasound is observed from explosions at a known location.

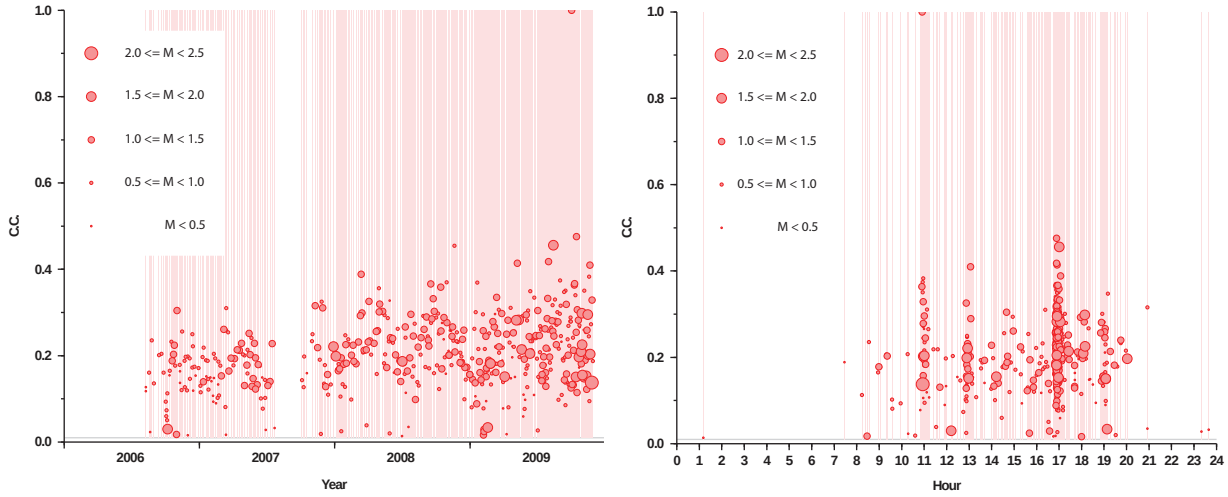

Figure 6. Correlation detections on the ARCES array using a template of the signal from the October 2, 2009, event. The left plot shows detections chronologically, the right plot shows detections by local time of day at ARCES. The detector was run on archived data from years prior to 2006 and the very few detections prior to July 2006 were all demonstrated to be false alarms. The time-of-day plot shows very clear clusters of events close to 1100, 1300, 1700 and 1900 hours. There are almost no detections between 2000 and 0800 hours which also suggests that the false alarm rate among these detections is probably very low.

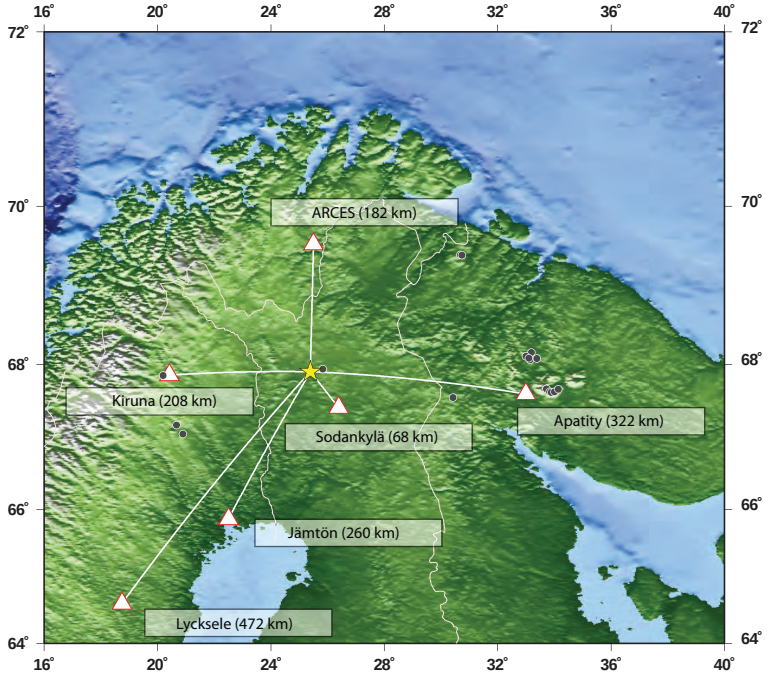

Figure 7. Location of the Suurikuusikko gold mine in Central Lapland in relation to the ARCES and Apatity seismic/infrasonic arrays and the microphone arrays at Kiruna, Lycksele, Jämtön and Sodankylä.

The Sodankylä microphone array is located at only 68 km from the source (to the south). This station is located within the so-called “zone of silence” although it is accepted that infrasound can propagate to these distances in the lower atmosphere (the troposphere) given favorable wind and temperature profiles. Very clear infrasound signals have been observed for many of these events at Sodankylä (see Figure 8) and it will be the subject of future research to understand the conditions under which infrasound is and is not detected at this and the other stations shown.

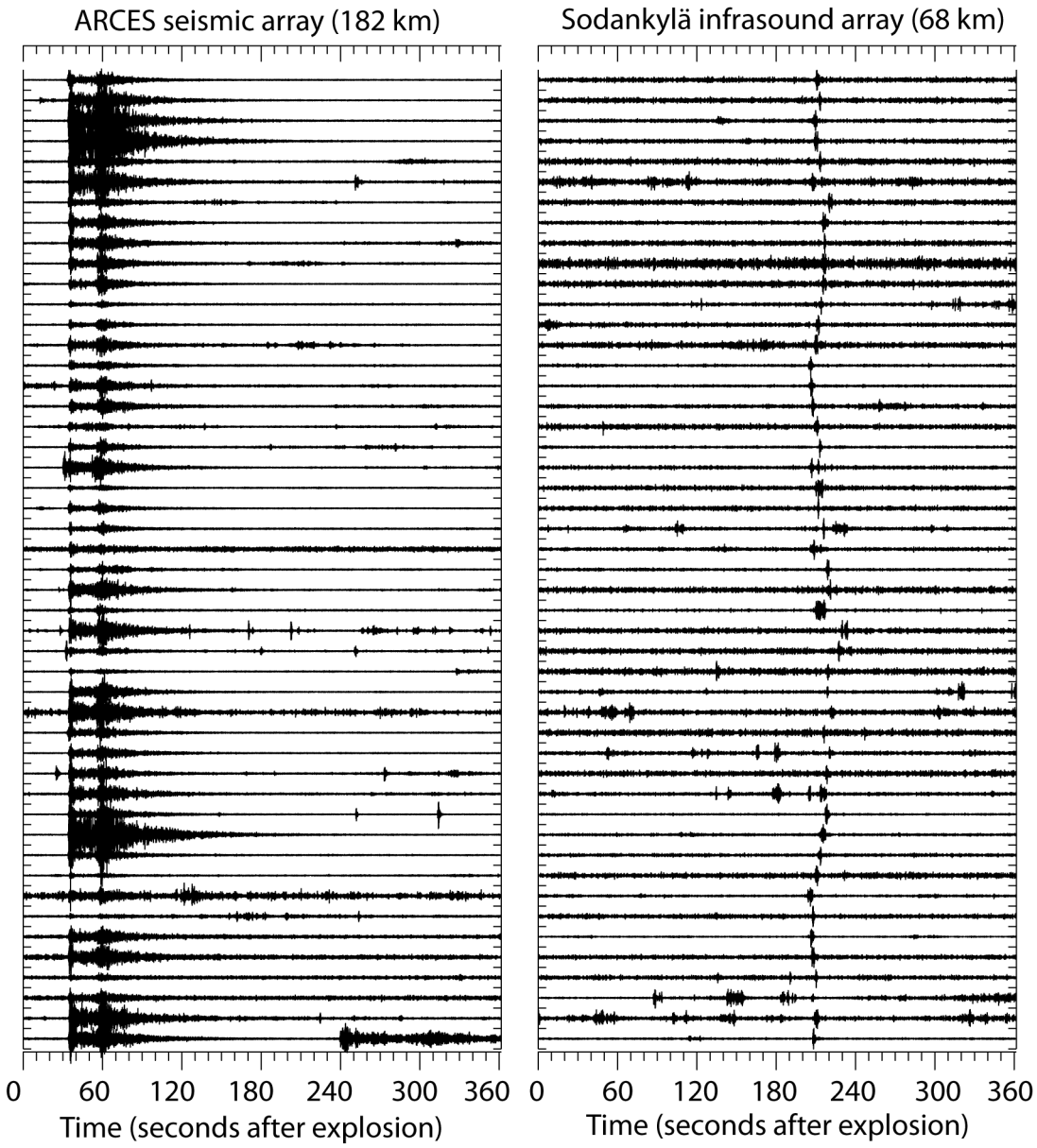

Figure 8. Waveforms at the ARCES seismic array (ARA0_sz channel, bandpass filtered 4-16 Hz) and the Sodankylä microphone array (SDA1_MI channel, bandpass filtered 2-5 Hz) for the 50 events with the greatest coherence of the associated infrasound signals. The ARCES waveforms are drawn to a common scale, demonstrating the variation in the event magnitudes. Each channel of the Sodankylä data is scaled individually. (Note that infrasound signals at ARCES arrive later than displayed here.)

Infrasound Recordings of the Bulava Missile

International news media reported in July 2009 on an unsuccessful launch of the new Russian intercontinental Bulava missile. The missile was launched from a submarine in the White Sea on 15 July. Infrasound signals associated with this launch were recorded at NORSAR's experimental infrasound station at ARCES (Roth et al., 2008) and the four stations in Sweden and Finland operated by the Swedish Institute of Space Physics (IRF). Another Bulava launch took place on 9 December 2009. Around 6:50 UTC on that day, strange light phenomena were observed in northern Norway. These observations caused a lot of attention in the news media, and after a while it became evident that the phenomena were associated with this launch. According to the Russian Defence Ministry there was an engine failure

in the third stage of the flight that caused the problem. According to recent information provided by the Norwegian Ministry of Defence, they believe that the missile exploded at an altitude between 100 and 300 km above the Novaya Zemlya region, and that the missile was launched from a submarine in the north-eastern part of the White Sea. Infrasound signals believed to originate from this missile launch were observed at ARCES as well as at the infrasound station in Apatity on the Kola peninsula. No infrasound signals were found at the stations of the IRF network for the 9 December event.

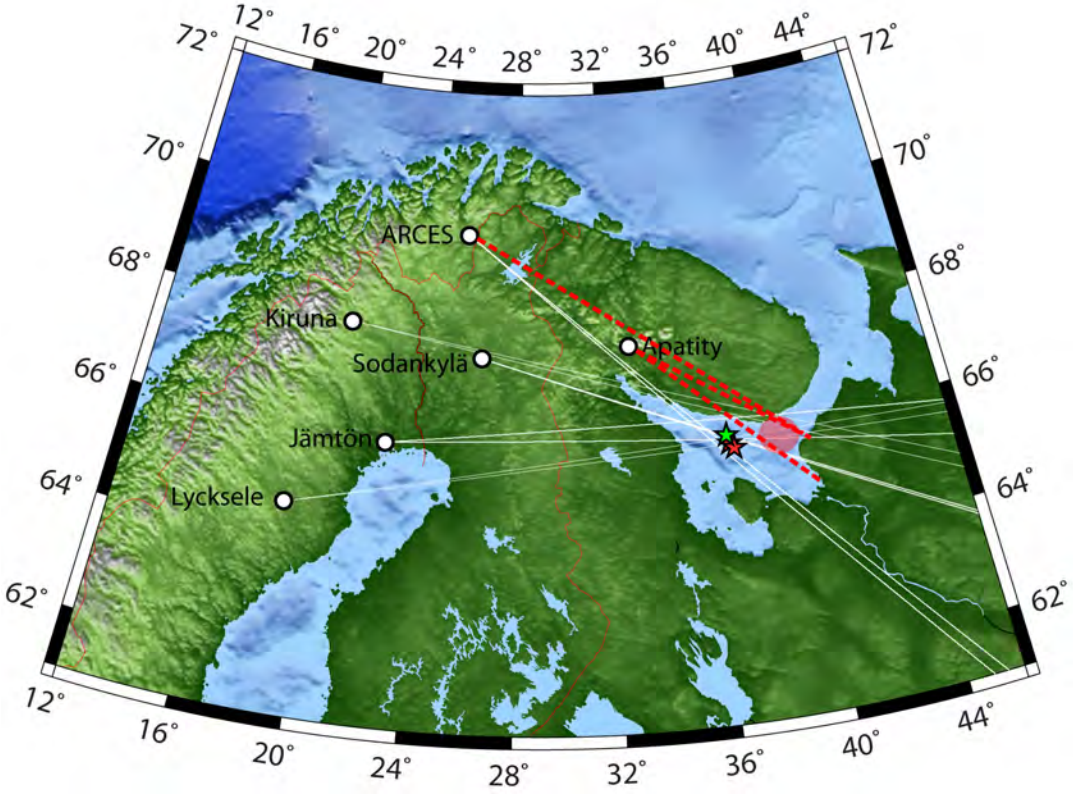

Figure 9. The dashed red lines show estimated back-azimuths from the ARCES and Apatity infrasound arrays for the 9 December 2009 event. See text for details.

Figure 9 shows the results of our analysis of these two events. The approximate source region of the 9 December event is indicated by the red ellipse. For comparison, the red and green stars show the estimated locations of the 15 July 2009 event. The red stars show locations provided by Prof. L. Liszka of the Swedish Institute of Space Physics, and the green star is from the study by Kværna (2010).

CONCLUSIONS AND RECOMMENDATIONS

Seismic events in the eastern Barents Sea are rare, and the event on 11 November 2009 is therefore of considerable interest. It is the first recorded seismic event in this region since the new high-frequency system was installed at the ARCES array on 23 March 2008. Our analysis of this event confirms the preliminary results of Ringdal et al. (2008) that there is a remarkably efficient propagation from regional events recorded at ARCES at frequencies up to 30 Hz and above.

This result is similar to what has been previously observed at the Spitsbergen array for paths from Novaya Zemlya crossing the Barents Sea. The Spitsbergen studies showed that energy up to 30 Hz and above can be recorded with good signal-to-noise ratio even for small events at epicentral distances as large as 1000 km and we see a similar result in this study, although the event is at a slightly shorter distance (800 km). We consider that there is still much to be gained by making improved use of the high-frequency recordings in the European Arctic, and we recommend that a systematic mapping of the high-frequency propagation characteristics of this region be undertaken.

As discussed by Ringdal et al. (2008), there are several advantages of high-frequency recordings in a nuclear monitoring context. Although the best filter band for event detection over paths across the Barents region generally appears to be either 4-8 Hz or 8-16 Hz, the most remarkable result shown in our previous papers as well as the current study is the strong SNR even at the highest frequencies (up to 40 Hz). While such frequencies would not be used for detection purposes, the high frequency data could be very important for signal characterization, as also pointed out by Bowers et. al. (2001) in their paper discussing the level of deterrence to possible CTBT violations in the Novaya Zemlya region provided by data from the Spitsbergen array. In fact, it appears from the present study that similar advantages are provided by the ARCES array.

The infrasound databases that have been developed based on the explosions in northern Finland provides a unique resource for studies of infrasonic propagation from well-constrained sources. One of the main topics to be studied is the surprising observations of various infrasound phases in what is often denoted a “zone of silence” (less than 200 km distance). We plan to carry out various modelling exercises in order to further investigate the propagation of infrasound phases at local distances. At the same time we recommend that the ongoing accumulation of ground truth data of a variety of infrasound sources should be continued.

During recent years, infrasound signals been observed in the Nordic region from several rocket launches and meteors entering the atmosphere. Establishing a database of such events is important for future studies of infrasound wave propagation.

REFERENCES

Baumgardt, D.R. and Der, Z. (1998). Identification of presumed shallow under-water chemical explosions using land-based regional arrays. *Bull. Seismol. Soc. Am*. 88:581–595.

Bowers, D., P. D. Marshall, and A. Douglas (2001). The level of deterrence provided by data from the SPITS seismometer array to possible violations of the Comprehensive Test Ban in the Novaya Zemlya region, *Geophys. J. Int.* 146: 425–438.

Gibbons, S. J. and Ringdal, F. (2006). The detection of low magnitude seismic events using array-based waveform correlation, *Geophys. J. Int.* 165: 149–166.

Gibbons, S. J., Ringdal, F., and Kværna, T. (2007). Joint seismic-infrasonic processing of recordings from a repeating source of atmospheric explosions. *J. Acoust. Soc. Am.* 122: EL158-EL164.

Kværna, T. (2010). Infrasound signals from recent rocket launches in the White Sea. *In NORSAR Scientific Report No. 1-2010: Semiannual Technical Summary, NORSAR, Kjeller, Norway.* pp. 35–43.

Kværna, T. and Ringdal, F. (2010). Seismic event in the eastern Barents Sea, 11 November 2009. *In NORSAR Scientific Report No. 1-2010: Semiannual Technical Summary, NORSAR, Kjeller, Norway.* pp. 26–34.

Oberg, D., Kværna, T. and Ringdal, F. (2004). Discriminants for seismic monitoring. *In NORSAR Scientific Report No. 2-2004: Semiannual Technical Summary, NORSAR, Kjeller, Norway.* pp. 57–69.

Ringdal, F., Kværna, T., and Gibbons, S. J. (2008). Initial studies of high-frequency signals recorded at ARCES. *In NORSAR Scientific Report No. 2-2008: Semiannual Technical Summary, NORSAR, Kjeller, Norway.* pp. 27–51.

Roth, M., Fyen, J., and Larsen, P. W. (2008). Setup of an experimental infrasound deployment within the ARCES array. *In NORSAR Scientific Report No. 2-2008: Semiannual Technical Summary, NORSAR, Kjeller, Norway.* pp. 52–59.

Schweitzer, J. (2003). NORSAR’s Event Warning System (NEWS), *In NORSAR Scientific Report No. 1-2003: Semiannual Technical Summary, NORSAR, Kjeller, Norway.* pp. 27-32.

DEVELOPMENT OF SOFTWARE TO DIGITIZE HISTORIC HARDCOPY SEISMOGRAMS FROM NUCLEAR EXPLOSIONS

Steven R. Taylor[1] and Xiaoning (David) Yang[2]

Rocky Mountain Geophysics, LLC[1] and Los Alamos National Laboratory[2]

Sponsored by the National Nuclear Security Administration

Award No. DE-FG02-09ER85428

ABSTRACT

One main issue associated with nuclear explosion monitoring research is the paucity of seismic recordings to be used for calibration purposes. The problem is particularly acute for nuclear explosions that occurred in the pre-digital seismic era. Many of these historic explosions have been detonated under a wide variety of geologic and emplacement conditions and it is important to revisit them in the context of broad area monitoring. Our Phase I work has demonstrated the feasibility of developing software for the digitization of historic hardcopy seismograms from nuclear explosions. We have already begun development of a prototype MATLAB® based Graphical User Interface (GUI) computer code called *DigiSeis* that is specifically designed to meet this goal. Importantly, our project is conducted by seismologists who have a long history of nuclear explosion monitoring with intimate understanding of the nuances of the signal aspects that are important to this field.

The key element of our approach is to use mathematical statistics to automatically determine specified tuning parameters in order to develop spatially adaptive thresholding parameters, accurate timing and calibration information, and signal reconstruction schemes that maintain waveform fidelity. We have implemented some of the statistics algorithms in the current version of *DigiSeis* and have successfully applied *DigiSeis* to digitize some WWSSN LP recordings of NTS explosions. Human interaction with the program is facilitated via a graphical user interface. Scanned photographic images can be read in, cropped and rotated. Image processing techniques are used for adaptive contrast enhancement and horizontal noise trace removal prior to digitization. The core methodology used in *DigiSeis* is global and local histogram enhancement techniques combined with median-value processing. Specialized peak tracking techniques have been developed to isolate high-frequency features such as *P*-wave arrivals where pixel resolution becomes a problem. A Wiggins Interpolator is used to convert pixels to uniform sampling and to fill in signal segments that are not tracked due to various reasons. Digitized seismograms are written to Seismic Analysis Code (SAC) files with timing information estimated through pixel analysis of minute marks.

OBJECTIVES

The technical objective of this study is the development of software for the digitization of historic hardcopy seismograms from nuclear explosions.

RESEARCH ACCOMPLISHED

Our Phase I work has demonstrated the feasibility of developing software for the digitization of historic hardcopy seismograms from nuclear explosions. We have begun development of a prototype MATLAB® based GUI computer code called *DigiSeis* that is specifically designed to meet this goal. Those of us who are old enough to have had the tedious misfortune of having to hand-digitize seismograms, are well aware of the difficulties encountered in dealing with hard-copy seismograms. Importantly, our project is conducted by seismologists who have a long history of nuclear explosion monitoring with intimate understanding of the nuances of the signal aspects that are important to this field. In order to increase the data availability of digital seismic data for nuclear explosion monitoring research it is important to consider systematically scanning and digitizing hardcopy seismograms (both paper and photographic) from historic explosions. Portions (e.g., either *P* waves, *S* waves or surface waves) of particular nuclear explosions have been hand-digitized for specific studies (e.g., Helmberger and Hadley, 1981 as one of many examples). Most available historic seismic data from nuclear explosions comes from the World Wide Standardized Seismographic Network (WWSSN) that began operation in 1961 (e.g., Lee et al., 2005). The SeismoArchives project initiated by W.H.K. Lee is under the auspices of the International Committee for Preservation of WWSSN and Historical Seismograms (ICPWHS) in collaboration with the Incorporated Research Institutions for Seismology (IRIS) Data Management Center (DMC). The original records were photographed and stored on 70 x 120 mm film chips and are available from Lamont-Doherty Earth Observatory and the USGS Albuquerque Seismic Laboratory (ASL). Current scanning programs are underway at the Incorporated Research Institutions for Seismology (IRIS) Data Management Center (DMC; Lee et al., 2005). As discussed by Lee et al., (2005), some early historic nuclear explosion film chip scanning was performed at the ASL for 78 earthquakes and 156 nuclear explosions (about 30,000 film chips were scanned). However, most recent scanning efforts have been focused on significant historic earthquakes.

There is already some existing software for digitizing seismogram images, e.g., SeisDig (Bromirski and Chuang, 2003) and Teseo^2 (Michelini and the Sismos Team, 2005). Nuclear explosions typically have a distinctive character (which is why they can be discriminated from earthquakes) and our goal is to develop a software package that can be tuned to particular signals (including, but not limited to, seismic signals from nuclear explosions). The key element of our approach is to use mathematical statistics to automatically determine specified tuning parameters in order to develop spatially adaptive thresholding parameters, accurate timing and calibration information, and signal reconstruction schemes that maintain waveform fidelity. We have implemented some of the statistics algorithms in the current version of *DigiSeis* and have successfully applied *DigiSeis* to digitize some WWSSN LP recordings of NTS explosions. Human interaction with the program is facilitated via a GUI. Scanned photographic images can be read in, cropped and rotated. Image processing techniques are used for adaptive contrast enhancement and horizontal noise trace removal prior to digitization. The core methodology used in *DigiSeis* is global and local histogram enhancement techniques combined with median-value processing. Specialized peak tracking techniques have been developed to isolate high-frequency features such as *P*-wave arrivals where pixel resolution becomes a problem. A Wiggins Interpolator (Wiggins, 1976) is used to convert pixels to uniform sampling and to fill in signal segments that are not tracked due to various reasons. Digitized seismograms are written to SAC, (http://www.iris.edu/software/sac/) files with timing information estimated through pixel analysis of minute marks.

Because of the large quantity of seismograms that have already been scanned, and the many more that potentially could be scanned, their digitization must be as automated as possible. This is quite challenging because of the varying quality of the photographic records**.** Figure 1 shows one of the earliest seismograms from a nuclear test illustrating many of the difficulties associated with scanned paper records. For example, it appears that the left portion of the image may have been exposed to sunlight and the background contrasts with the right portion. As will be discussed below, this complicates the preparation of the image for subsequent digitization because background threshold values are spatially dependent. Another phenomenon is that the high-frequency signals have low contrast with the background color, which makes them difficult to track.

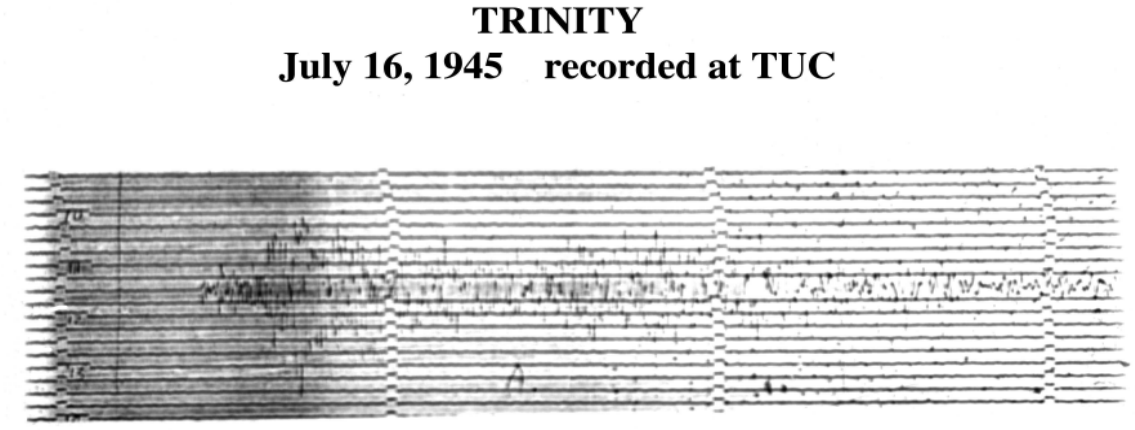

Figure 1. **Low-resolution scan of paper record seismogram recorded at TUC (Tucson, AZ) from the atmospheric TRINITY nuclear test at the Alamogordo Test Range, on the Jornada del Muerto (Journey of Death) desert, NM, on July 16, 1945 (courtesy of Terry Wallace)**.

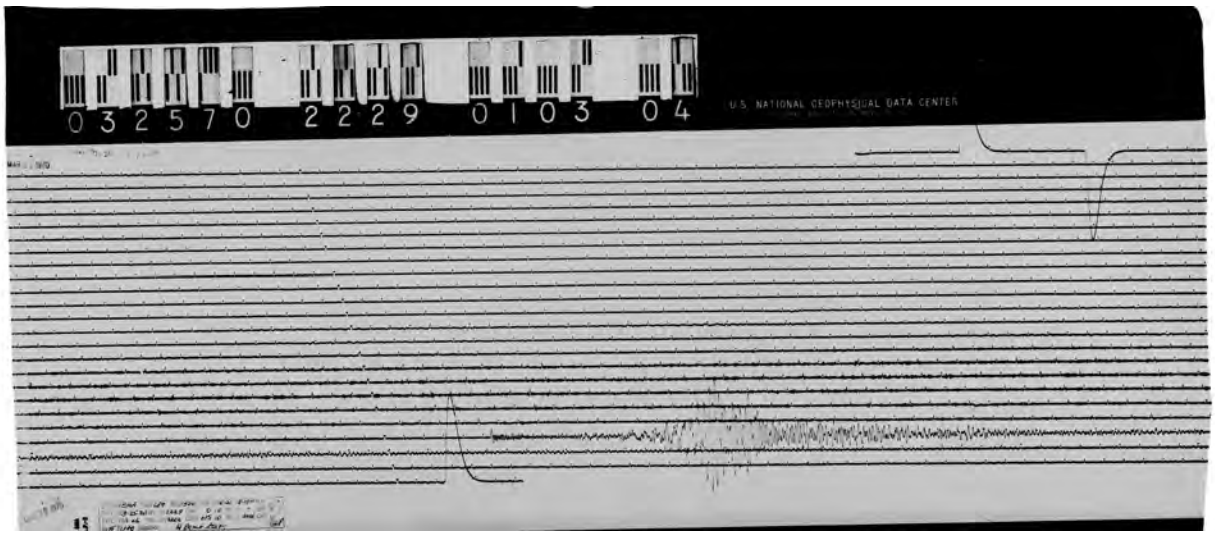

Figure 2. **Scanned image of the m_b = 6.5 Handley nuclear explosion at NTS of March 26, 1970 at the long-period WWSSN station SHA (Spring Hill, Alabama; Δ ~ 24°).**

As an illustration of our Phase I effort to develop the basic digitization methodology and the prototype software package *DigiSeis*, we use *DigiSeis* to digitize the long-period (LP) WWSSN seismogram of the Handley nuclear explosion and describe the procedure and the results below. Figure 2 shows a scanned seismogram obtained from the IRIS SeismoArchives from the m_b = 6.5 Handley NTS nuclear explosion of March 26, 1970, on the LP vertical component at the WWSSN station SHA (Spring Hill, Alabama; Δ ~ 24°). The seismograms were recorded on a rotating circular drum and consist of a single day's worth of record. The stamp in the lower left-hand corner gives information such as the station name, start and end times, natural period of the seismometer and galvanometer, and magnification (gain). Early in the signal are calibration pulses that can be used to check the amplitude and phase calibration (e.g., Mitchell and Landisman, 1969). Timing marks (ticks) from crystal oscillator clocks mark every minute and wider ticks for each hour. Every sixth hour has no hour mark. The WWSSN 70 x 120 mm film chips were scanned with a resolution of 3200 dpi (Lee et al., 2005).

Figure 3 is a screen shot of the *DigiSeis* GUI with the Handley seismogram displayed. The GUI consists of four figure panels and three groups of function buttons. The *Image* panel displays the original loaded image or the processed image. The *Digitize* panel displays the digitized trace along with the image for comparison. Since no digitization has been done in Figure 3, this panel, as well as the *TraceSelection* and *Threshold* panels, is blank. We will explain in detail the functions of different buttons and other GUI elements below. Once a seismogram image is read into *DigiSeis*, the user can crop the image to include only the portion of the image that contains the signal of interest. If the image is skewed, as is the Handley seismogram shown in Figure 3, the user can rotate the image by selecting two points to define the axis of rotation. These functions are fulfilled by clicking the *Crop* and the *Rotate* buttons. Figure 4 shows the image after cropping and rotation.

There are numerous ways that the seismogram image shown in Figure 4 can be digitized (e.g., Gonzalez and Woods, 2002). Figure 5 is a screen shot of *DigiSeis* illustrating the digitization process. The basic technique that we use for the digitization is called thresholding, in which image pixels are divided based on their grayscale values. We first construct a histogram of the normalized grayscale values from the image shown in the *Image* panel of Figure 3. The histogram is plotted in the *Threshold* panel in Figure 5 where black pixels have a value of 0 and white pixels have a value of 1 (note the gradation indicated by the horizontal bar below the histogram). The histogram shows a single large peak centered at about 0.82 units, which results from the gray image background. The small number of pixels having values of 0.3 and below represent the darker lines associated with the horizontal signal and noise traces. In applying the thresholding, we set a grayscale-value threshold and remove all pixels that have values larger than the threshold. This threshold is indicated by the vertical red line in the *Threshold* panel. After thresholding, we then use the locations of small-valued pixels that survived the thresholding to calculate the locations (row numbers) of the signal trace using a median-value technique, in which we compute the median of pixel grayscale values for each pixel column, find the row location of the corresponding pixel and use this location as the location of the signal trace that we digitize. Using the median, instead of the mean, reduces the effect of extraneous noise that may appear in outlying rows. The user can adjust the threshold either by moving the slider bar, by entering a value, or by dragging the vertical red line. As the threshold value is adjusted, the digitized trace, shown as the red line in the *Digitize* panel, is recalculated and the plot is updated, thus providing an effective method for selecting a proper global threshold value.

Oftentimes the cropped image contains multiple noise traces in addition to the signal trace to be digitized, as Figure 4 shows. We implemented a technique in *DigiSeis* to mask the noise traces (the *SelectTrace* button). The procedure is often necessary because of the median processing technique that we use to track the signal. In *SelectTrace*, we first calculate the sums of grayscale values along the rows of the image shown in Figure 4 and plot the result in the *TraceSelection* panel in the lower left-hand of the *DigiSeis* GUI (Figure 5). In the plot, each peak corresponds to a narrow, horizontal and dark region of the image, such as a signal trace. We use a cutoff value (the blue line) to identify the peaks (traces) in the plot. The user can then select which trace to unmask using the bottom slider bar. Once *TraceSelection* is completed, white masks will appear on the image in *Image* panel (Figure 5) indicating that these horizontal swaths will not be used in the digitization processing. As will be described below, we have been testing an alternative method for removing horizontal noise traces by accurately tracking and masking noise traces themselves rather than masking with horizontal swaths. Our preliminary results indicate that this method may improve the ability to detect signal peaks that are very close to the noise traces.

After trace selection and grayscale-histogram calculation, we choose a global threshold value of 0.7 based on the histogram, which appears to give a good tradeoff between signal resolution and randomly distributed noise pixels for the Handley seismogram. The *Digitize* panel in Figure 5 shows the digitized trace (the red line) superimposed on the original image following the application of the global thresholding.

In studies of nuclear explosions (e.g., Wallace et al., 1983), it is critically important to accurately digitize the *P* waves. Subtle differences in the P waveform contain important information regarding emplacement depth and nature of the explosion source (e.g., Lay, 1991). Figure 5 shows a good tracking of the overall waveform for Handley however; close examination of the P wave illustrates deficiencies that must be remediated through specialized processing. We implemented several pre-processing techniques in *DigiSeis* to enhance image contrast between signal and background pixels (see additional function buttons in the *Image* button group in Figure 3). These techniques become particularly important in cases where a fast moving galvanometer or pen results in a low contrast between the background and the signal. We plot the cropped *P* wave from the Handley explosion in Figure 6 to illustrate the problem.

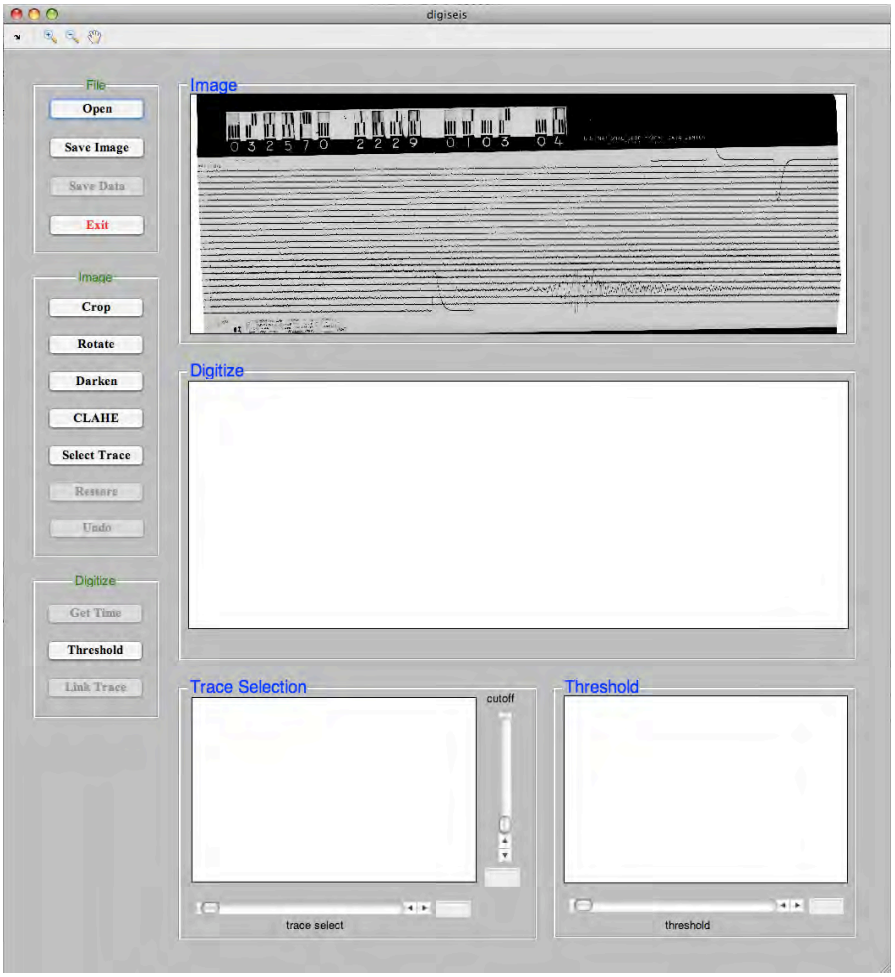

Figure 3. A computer screen shot of the *DigiSeis* GUI with the Handley nuclear-explosion seismogram displayed.

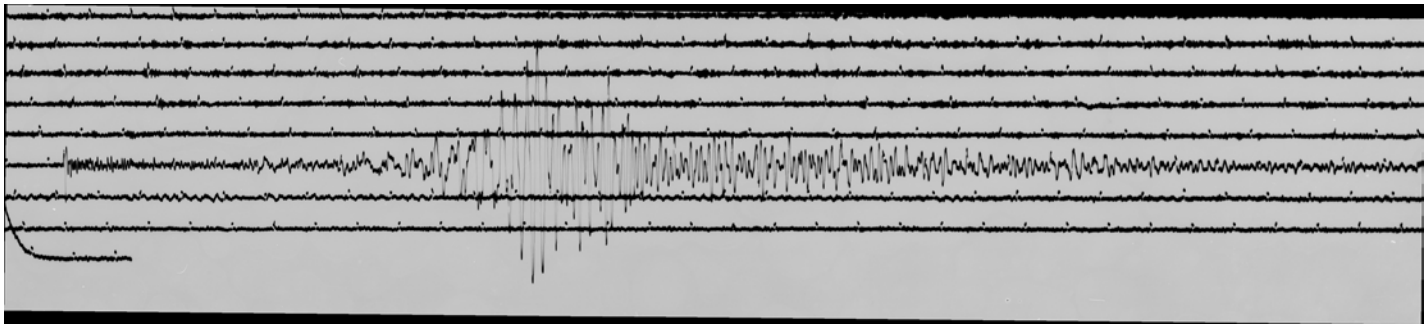

Figure 4. Cropped and rotated portion of Handley explosion seismogram.

The left panel of Figure 6 shows an enlargement of the *P* wave from Handley using the global thresholding parameter of 0.7. Although the tracking of the full seismogram in Figure 5 is quite good, it is seen that the global thresholding does not pick up the faint rapid downswing of the *P* wave. Additionally, the tracked first upswing does not track image well by being too gradual. The reason for this is seen by examination of the image histogram in the lower right portion of Figure 5. The broad peak above the assigned threshold of 0.7 represents light gray associated with the image background. Pixel values of the downswing are only slightly less than 0.7 indicating that some contrast enhancement techniques are required. Additionally, the width of the downswing and subsequent upswing is only about 10 pixels.

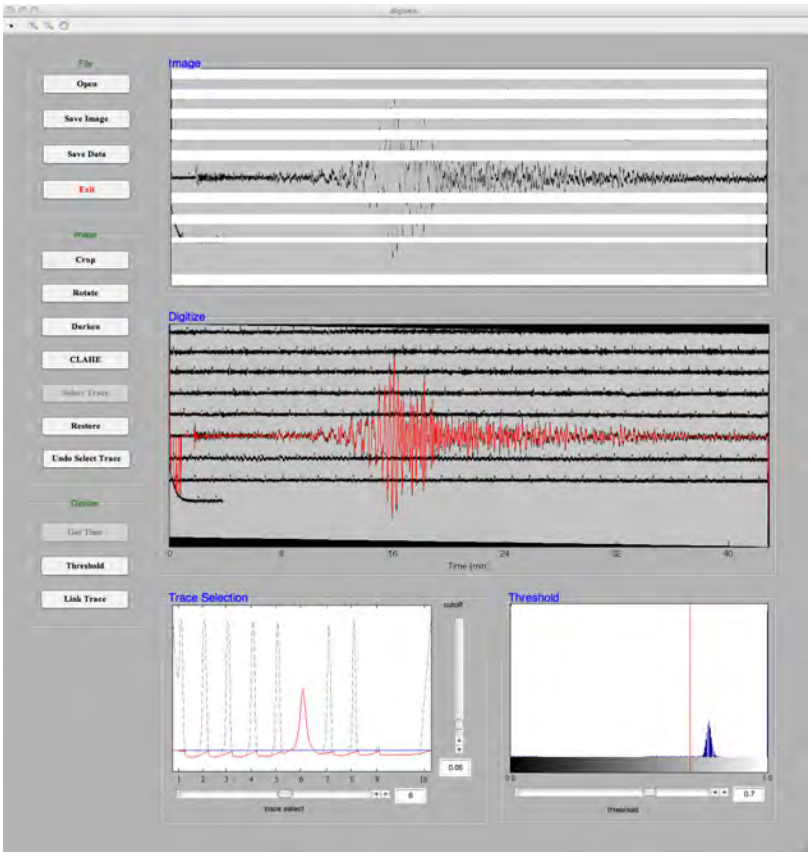

Figure 5. Screen shot of *DigiSeis* showing various processing steps using the cropped and rotated image shown in Figure 4.

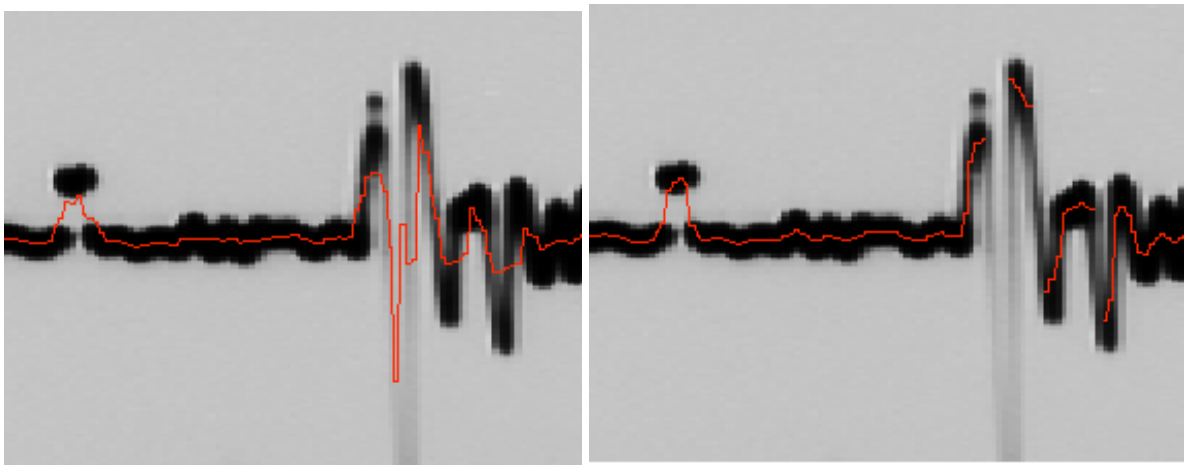

Figure 6. Close up of Handley *P* wave using global thesholding values of 0.7 (left) and 0.15 (right).

In the right panel of Figure 6, we have lowered the global threshold parameter down to 0.15. Now the high frequency portions of the waveform are tracked better including the first upswing. However, low contrast features such as the first downswing do not survive the thresholding and are not tracked. This is further illustrated in Figure **7** showing the row and column matrix representation of the image after thresholding. The above example suggests that local processing techniques are required in certain situations to adjust to small nuances associated with specific signal and background characteristics of the image. We have tested a number of methods and find that a *Darken* and *Contrast-Limited Adaptive Histogram Equalization* (CLAHE) appear to give the best results. The *Darken* button can be used to enhance dark pixels associated with signals using a power-law transformation of the form

$$g(x,y) = f(x,y)^{\frac{1}{1+\beta}} \quad (1)$$

where $f(x,y)$ is the input image, $g(x,y)$ is the output image and $-1 < \beta \leq 0$ is a user selectable parameter. Global contrast enhancement uses a whitening transform to make a given image histogram approach a uniform distribution (e.g., Gonzales and Woods, 2002). *CLAHE* is a modification of global contrast enhancement whereby a small region is moved along the image and a local contrast enhancement is performed at each spatial point (e.g., Pizer et al., 1987). Figure 8 shows an example where we have applied *CHAHE* to the Handley P wave. In addition, we have developed a specialized peak finding algorithm (*LinkTrace* button in the *DigiSeis* GUI) that can be used to trace waveforms that are very similar to background. *LinkTrace* first automatically finds the columns of the untracked waveform segments, runs a smoothing operator across each row and at each time (column), and finds the pixel having the minimum value for the corresponding column. Close examination of Figure 8 shows that *LinkTrace* works as desired. We will further show below that if the peaks (troughs) of the signal can be identified, then the Wiggins interpolator algorithm that we use actually can track the rapid swings quite well.

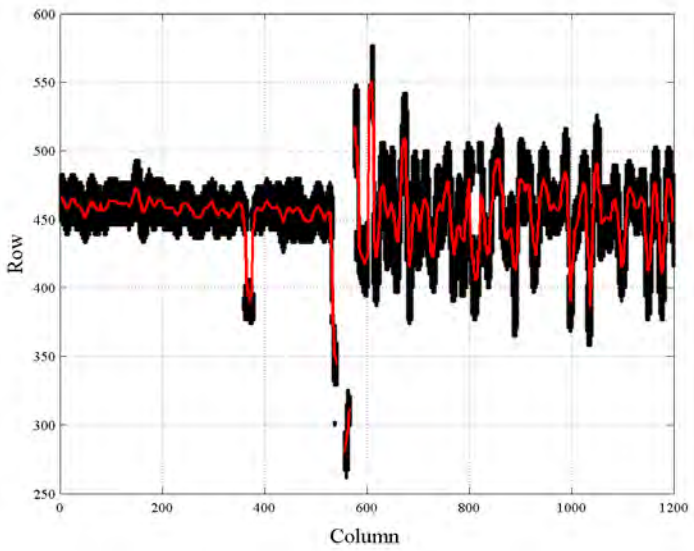

Figure 7. Row and column matrix representation of the *P* wave in the right panel of Figure 6. Dark corresponds to pixels less than the global threshold parameter of 0.15. Red line corresponds to tracked median row value. Note that because of the matrix storage, the polarity appears reversed.

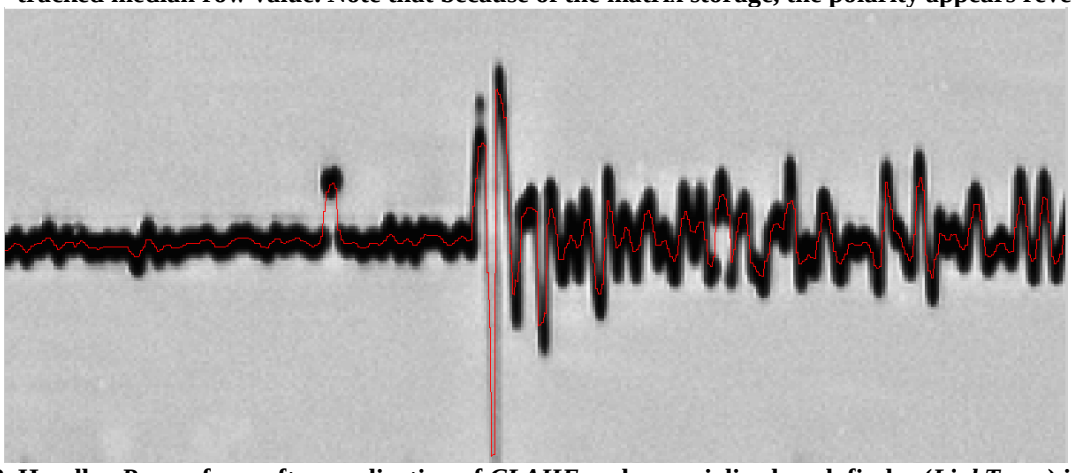

Figure 8. Handley *P* waveform after application of *CLAHE* and a specialized peak finder (*LinkTrace*) in DigiSeis.

Another critical aspect of P-waves from nuclear explosions is that m_b measurements need to be accurately estimated both for discrimination (e.g., m_b - M_s) and for yield estimation. Magnitude measurements require a peak-to-peak measure (and sometimes corresponding period) so that the digitized *P* waveform has to be as precise as possible. Figure 9 shows a *DigiSeis* screen shot of the Handley *P* wave and adjacent noise traces. Note that the first downswing barely crosses the underlying noise trace. We have been testing an alternative technique to remove just the adjoining noise traces (see white out lines in the *Image* panel of Figure 9), instead of wide swaths of pixels around the noise traces, in order to retain signal peaks and troughs that are very close to the noise traces. We use the global thresholding to accomplish this. In Figure 9, we have not used *LinkTrace*, and it can be seen that only the later half of the P-wave downswing is tracked. However, we will show below that once a peak or a trough has been identified, our Wiggins interpolation method will capture the other half of the downswing.

Once a signal image has been digitized, it is necessary to output the result into a commonly used seismic data format such as SEED (Standard for the Exchange of Earthquake Data), SAC (Seismic Analysis Code), or CSS (Center for Seismic Studies). Currently, *DigiSeis* outputs SAC files with timing obtained from minute marks (the *SaveData* and *GetTime* buttons). The user uses *SelectTrace* to select a quiet noise trace with clear minute marks to estimate the time scale. The average number of pixels per minute across the trace is computed and subsequently used to convert pixel separation into time. Figure 10 shows the window that pops up when *GetTime* button is clicked. This method of obtaining timing information is still crude and we will develop more accurate techniques for time estimation in the Phase II of the project. The *SaveData* button is used to save the digitized signal. Currently, only SAC file format is supported. Segments of the signal that were not tracked due various reasons are filled with values interpolated from adjacent tracked segments using a Wiggins Interpolator (Wiggins, 1976). The Wiggins interpolator uses a weighted-average-slope method that was specifically designed by seismologists to interpolate hand-digitized seismograms. Figure 11 shows a SAC plot of the digitized Handley seismogram from the image shown in Figure 4. At this point the unit of the signal is in pixels. As part of Phase II project, we will develop methods to derive instrument responses from the calibration pulses and convert the digitized signal to ground displacements or velocity.

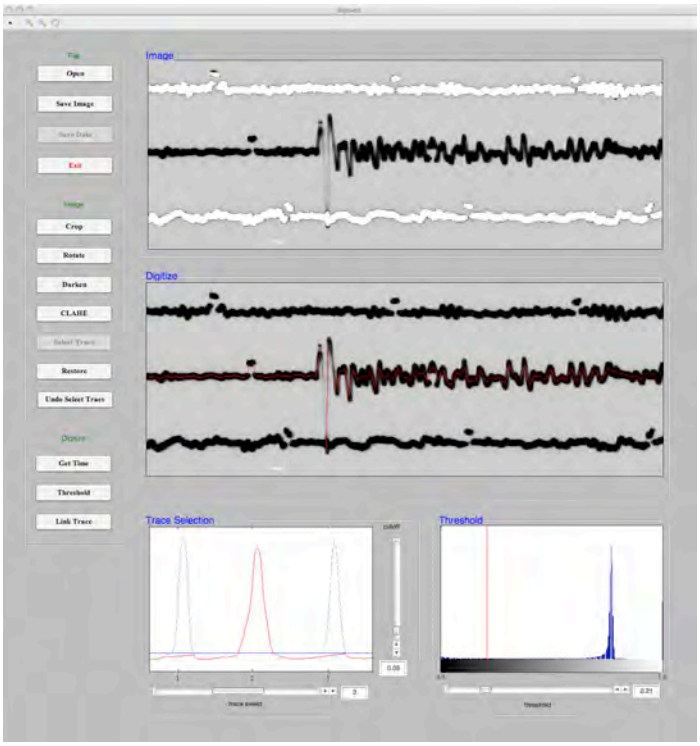

Figure 9. ***DigiSeis* screen shot showing Handley *P* wave and adjacent noise traces. Note that the first downswing barely crosses the underlying noise trace. We have been testing an alternative technique to remove adjoining noise traces (see white out lines in the *Image* panel) to isolate peaks and troughs in the signal, which are very close to the adjacent noise traces. Accurate tracking of *P*-wave amplitudes is important in m_b estimation, which is critical to both discrimination and yield estimation.**

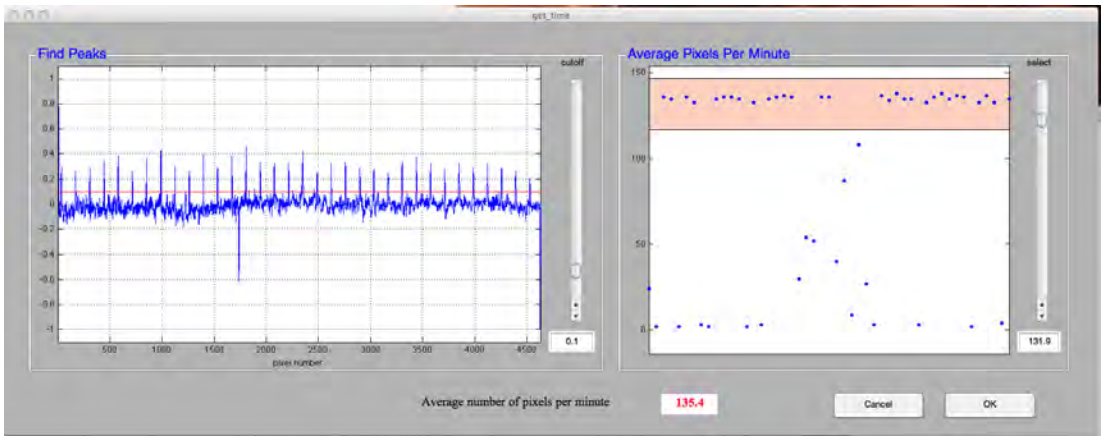

Figure 10. **Screen shot of the window that pops up when *GetTime* button of *DigiSeis* (Figure 3) is clicked. Minute marks manifested as peaks in the left panel are found and average number of pixels between these peaks is calculated (right panel). The average value is then used to convert pixel numbers into time intervals.**

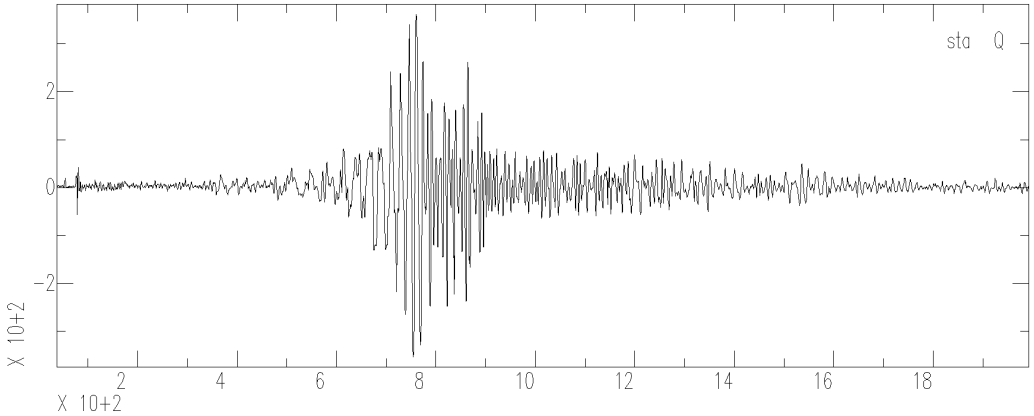

Figure 11. **SAC plot of digitized Handley seismogram (pixels; see Figure 4). The signal is interpolated using the Wiggins interpolator (Wiggins, 1976).**

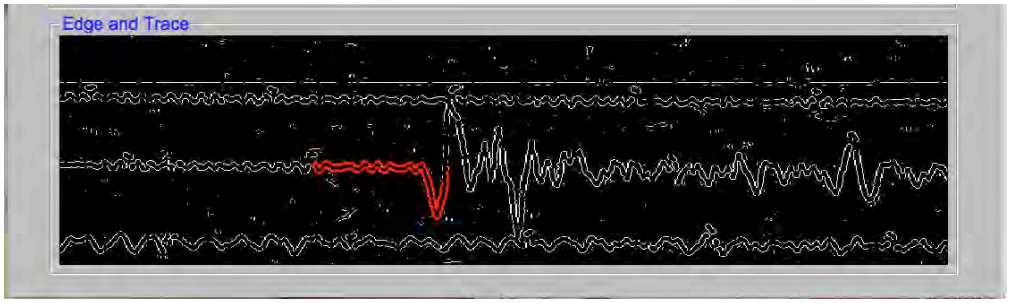

Figure 12. **Boundary of signal edge (red line) superimposed on a *P*-wave image. The white lines correspond to edges detected using the LoG Laplacian gradient operator.**

We have tested an edge detection and tracking algorithm with mixed results. The algorithm takes the Laplacian of a Gaussian (LoG) mapping rapid changes in the image grayscale level and detecting edges. Figure 12 shows a portion of an early version of *DigiSeis* where we had implemented the edge detector. The white lines in the *EdgeAndTrace* panel are the edges defined by the application of the LoG Laplacian gradient edge detector. After the application of LoG, we used an edge tracking and boundary mapping methodology to link the edge boundaries. Figure 12 illustrates that edge detection and boundary tracking is not as robust as the basic global thresholding. For example, the signal on the first main upswing cannot be successfully tracked. Of course the LoG operator can be tuned to better define these rapid swings, but at the expense of increasing noise and false contours.

CONCLUSIONS AND RECOMMENDATIONS

We have developed a prototype MATLAB® based Graphical User Interface (GUI) computer code called *DigiSeis* for the digitization of historic nuclear explosions from hardcopy records.

ACKNOWLEDGEMENTS

We have utilized scanned seismograms from the SeismoArchives scanning project of the Incorporated Research Institutions for Seismology; http://www.iris.washington.edu/data/historical.

REFERENCES

Bromirski P. D. and S. Chuang (2003). SeisDig: Software to digitize scanned analog seismogram images, Users Manual, *Scripps Institution of Oceanography Technical Report*, San Diego, CA.

Gonzalez, R. C. and R. E. Woods (2002). *Digital Image Processing*, Pearson Prentice Hall, Upper Saddle River, NJ.

Helmberger, D. V. and D. M Hadley (1981). Seismic source functions and attenuation from local and teleseismic observations of the NTS events JORUM and HANDLEY, *Bull. Seism. Soc. Am.*, 71: 56–67.

Lay, T. (1991). The teleseismic manifestation of pP: Problems and paradoxes, in *Explosion Source Phenomenology*, *Geophys. Monograph* 65, S. R. Taylor, H. J. Patton and P. G. Richards, eds., 127–140.

Lee, W. H. K., C. R. Hutt, T. K. Ahern, D. Barnes, R.Benson, T. Knight and J. Schweitzer (2005). Constructing SeismoArchives at the IRIS DMC, Appendix to ICSU report.

Michelini, A. and the SISMOS Team (2005). Collection, digitization and distribution of historical seismological data at INGV, *Trans. Am. Geophys. Un*., 86.

Mitchell, B. J. and M. Landisman (1969). Electromagnetic seismograph constants by least-squares inversion, *Bull. Seism. Soc. Am.*, 59: 1335–1348.

Pizer, S. M., E. P. Amburn, J. D. Austin, R. Cromartie, A. Geselowitz, T. Greer, B. H. Romeny, J. B. Zimmerman, and K. Zuiderveld (1987). Adaptive histogram equalization and its variations, *Comp. Vision, Graphics, and Image Proc*., 39: 355–368.

Wallace, T.C., D.V. Helmberger, G.R. Engen (1983). Evidence of tectonic release from underground nuclear explosions in long-period *P* waves, *Bull. Seism. Soc. Am.* 73: 593–613.

Wiggins, R.A. (1976). Interpolation of digitized curves, *Bull. Seism. Soc. Am.* 66: 2077–2081.

Appendices

Roadmap Cross Index

Overview Papers (2):

1-01 **Casey, L. and R. Bell**
Nuclear Explosion Monitoring Research and Development Roadmaps 3

1-02 **Grenard, P. and T. Steeghs**
Science and Technology Foresight for the Provisional Technical Secretariat of the Comprehensive Nuclear-Test-Ban Treaty Organization 14

Source Physics Papers (22):

4-01 **Anderson, D., H. Patton, S. Taylor, and J. Bonner**
Isolating Source Information in mb and Ms with Model-Based Corrections: New mb Versus Ms Discriminant Formulations 361

7-02 **Arrowsmith, S., H. Hartse, S. Taylor, R. Stead, and R. Whitaker**
Infrasound as a Depth Discriminant 657

4-02 **Brunish, W., W. Hawkins, D. Coblentz, H. Patton, J. Zucca, J. Sweeney, C. Carrigan, T. Antoun, C. Seifert, K. Wohletz, C. Bradley, A. Sussman, T. Bowyer, R. Corbell, R. Abbott, C. Snelson, and P. Lee**
Source Physics Experiments at the Nevada Test Site 370

4-03 **Dreger, D., S. Ford, and W. Walter**
Identifying Isotropic Events Using a Regional Moment Tensor Inversion Technique 381

4-04 **Ford, S., W. Walter, S. Ruppert, E. Matzel, T. Hauk, and R. Gok**
Toward an Empirically-Based Parametric Explosion Spectral Model 390

7-04 **Gabrielson, T., G. Haralabus, and S. Stefanova**
IMS Infrasound Monitoring Test Site at Trafelberg, Austria: Preliminary Results from In-Situ Response Measurements of Infrasound Elements 678

7-06 **Gitterman, Y.**
Sayarim Infrasound Calibration Explosion: Near-Source and Local Observations and Yield Estimation 708

7-07 **Hale, J., S. Arrowsmith, C. Hayward, R. Burlacu, K. Pankow, B. Stump, G. Randall, and S. Taylor**
Infrasound Signal Characteristics from Small Earthquakes 720

4-05 **Julia, J., A. Nyblade, R. Gok, W. Walter, L. Linzer, and R. Durrheim**
Developing and Exploiting a Unique Dataset from South African Gold Mines for Source Characterization and Wave Propagation 398

4-07 **Leidig, M., B. Stump, W. Walter, A. Stroujkova, X. Yang, and J. Bonner**
Examination of P/S Spectral Ratios for Small Explosions at Local Distances and Interpretation of Moment Tensors Estimated from Near-Source Data *416*

4-08 **Martin, R., P. Boyd, A. Stroujkova, M. Leidig, L. Liu, J. Lewkowicz, and J. Bonner**
Correlating Near-Source Rock Damage from Single-Hole Explosions to Seismic Waves *427*

4-09 **Mayeda, K., L. Malagnini, W. Walter, and R. Gok**
Improved High Frequency Discrimination: A New Approach to Correct for Regional Source Scaling Variations *437*

4-10 **Murphy, J. and T. Bennett**
An Analysis of the Seismic Source Characteristics of Explosions in Low-Coupling Dry Porous Media *446*

4-13 **Patton, H.**
Explosion Source Model Development in Support of Seismic Monitoring Technologies: Apparent Explosion Moment and Prospects for Moment-Based Yield Estimation *475*

4-14 **Phillips, W., X. Yang, R. Stead, M. Begnaud, and K. Mayeda**
Model Development for Broad Area Event Identification and Yield Estimation *486*

2-16 **Pollitz, F., J. Rubinstein, and W. Ellsworth**
Analysis and Modeling of the Wavefield Generated by Explosions at the San Andreas Fault Observatory at Depth *170*

4-15 **Randall, G. and H. Hartse**
Identification of Deep Earthquakes *495*

8-06 **Ringdal, F., T. Kvaerna, S. Gibbons, S. Mykkeltveit, and J. Schweitzer**
Basic Research on Seismic and Infrasonic Monitoring of the European Arctic *779*

2-18 **Rodgers, A., O. Vorobiev, N. Petersson, B. Sjogreen, and W. Foxall**
Progress in Three-Dimensional Simulations of Explosions and Earthquakes *188*

4-16 **Rougier, E., C. Bradley, H. Patton, and E. Knight**
Numerical Simulations of Cavity Radius in Granite: Cavity Behavior as a Function of Scaled Depth of Burial *504*

4-17 **Sammis, C., H. Bhat, and A. Rosakis**
Micromechanical Damage Mechanics at High Loading Rates *513*

4-19 **Stroujkova, A., J. Bonner, R. Herrmann, and D. Anderson**
Rayleigh and Love Wave Magnitudes *529*

Signal Propagation Papers (31):

2-01 **Ammon, C., M. Maceira, and M. Cleveland**
3D Modeling of Iran and Surrounding Areas from Simultaneous Inversion of Multiple Geophysical Datasets *21*

7-01 **Arai, N., Y. Imanishi, S. Watada, T. Oi, T. Murayama, M. Iwakuni, and M. Nogami**
Dispersion of Infrasound Signals Excited by Explosive Eruptions of the Sakura-jima Volcano 647

7-02 **Arrowsmith, S., I. Che, C. Hayward, and B. Stump**
Multiple-Array Detection, Association and Location of Infrasound and Seismo-Acoustic Events — Utilization of Ground Truth Information 657

3-01 **Bergman, E., E. Engdahl, M. Ritzwoller, and S. Myers**
Earthquake Location Accuracy in the Arabian-Eurasian Collision Zone 249

6-01 **Biegalski, S., M. Deinert, C. Rios Perez, and J. Lowrey**
Modeling of Radioxenon Production and Release Pathways 567

3-02 **Brazier, R., K. Boomer, S. Myers, A. Nyblade, and J. Kokoska**
Establishing and Validating Empirically-Based Ground Truth Criteria for Seismic Events Located Using Regional Networks 259

2-03 **Chen, P., Y. Chen, and W. Chan**
Joint Inversion for Crustal and Upper Mantle Shear-Wave Velocity and Attenuation Structure in Eastern Eurasia Using Three-Dimensional Full-Wave Frechet Kernels 40

2-04 **Fisk, M. and W. Phillips**
A Stepwise, Iterative Procedure to Constrain Stress Drop, Regional Attenuation Models, and Site Effects 57

7-05 **Gibson, R., D. Drob, D. Broutman, and N. Winslow**
Advancement of Techniques for Modeling the Effects of Atmospheric Gravity-Wave-Induced Inhomogeneities on Infrasound Propagation 699

2-05 **Gritto, R., M. Sibol, P. Caron, H. Ghalib, R. Herrmann, G. Aleqabi, B. Ali, and A. Ali**
Crustal Velocity Models of the Zagros-Bitlis Zone from Body- and Surface Wave Analyses 67

2-06 **Hauser, J., K. Dyer, M. Pasyanos, H. Bungum, J. Faleide, and S. Clark**
Development and Tuning of a 3D Stochastic Inversion Methodology to the European Arctic 77

2-07 **Julia, J., A. Nyblade, A. Rodgers, and E. Matzel**
Developing Regionalized Models of Lithospheric Thickness and Velocity Structure Across Eurasia and the Middle East from Jointly Inverting P-Wave and S-Wave Receiver Functions with Rayleigh Wave Group and Phase Velocities 87

4-06 **Koch, K.**
Re-Examination of Surface Wave Magnitude Estimates for the North Korean Event of 25 May 2009 408

2-08 **Maceira, M., H. Zhang, R. Modrak, C. Rowe, and M. Begnaud**
Advanced Multivariate Inversion Techniques for High Resolution 3D Geophysical Modeling 97

2-09 **Mackey, K., H. Hartse, K. Fujita, M. Pasyanos, and M. Begnaud**
Seismic and Geophysical Characterization of Northern Asia 108

2-10 **Martin, R., L. Gulen, Y. Sun, and M. Toksoz**
The Crustal and Mantle Velocity Structure in Central Asia from 3D Travel Time Tomography 118

2-11 **Masters, T., Z. Ma, G. Laske, and M. Pasyanos**
LITHO1.0: An Updated Crust and Lithosphere Model of the Earth 128

5-02 **Matsumoto, H., D. Bohnenstiehl, R. Dziak, R. Embley, and M. Park**
Assessment of Hydroacoustic Propagation Using Autonomous Hydrophones in the Scotia Sea 551

2-12 **Mayeda, K. and W. Phillips**
Transitioning the Coda Methodology to Full 2-D for P and S Codas 138

3-07 **Myers, S., G. Johannesson, and N. Simmons**
Bayesloc Multiple-Event Location Applied to a Global Data Set 299

2-14 **Nabelek, J., S. Carpenter, P. Monigle, J. Braunmiller, and W. Phillips**
Source and Path Calibration in Regions of Poor Crustal Propagation Using Temporary, Large-Aperture, High-Resolution Seismic Arrays 150

2-15 **Nowack, R., W. Chen, J. Griffin, A. Bakir, and T. Tseng**
The Propagation of Pn in Western China 161

2-17 **Reiter, D., W. Rodi, and S. Myers**
Estimating the Uncertainty and Predictive Capabilities of Three-Dimensional Earth Models 180

3-11 **Rodi, W., D. Reiter, S. Myers, and N. Simmons**
A Unified Approach to Joint Regional/Teleseismic Calibration and Event Location with a 3D Earth Model 338

2-19 **Sandvol, E., X. Bao, J. Ni, T. Hearn, and W. Phillips**
High-Resolution Seismic Velocity and Attenuation Models of Western China 197

2-20 **Savage, B., D. Peter, B. Covellone, A. Rodgers, and J. Tromp**
Next Generation, Waveform Based Three-Dimensional Models and Metrics to Improve Nuclear Explosion Monitoring in the Middle East 207

2-21 **Sen, M., J. Pulliam, U. Dutta, R. Ghosh, R. Gok, and M. Pasyanos**
Seismic Velocity Estimation in the Middle East from Multiple Waveform Functionals: P & S Receiver Functions, Waveform Fitting, and Surface Wave Dispersion 214

3-12 **Simmons, N., S. Myers, and G. Johannesson**
Global-Scale P-Wave Tomography Designed for Accurate Prediction of Regional and Teleseismic Travel Times for Middle East Events 348

2-22 **Song, X., Z. Xu, L. Zhu, and Y. Zhou**
Joint Inversion of Crustal and Uppermost Mantle Structure in Western China 224

4-18 **Stevens, J. and H. Xu**
Wave Propagation from Complex 3D Sources Using the Representation Theorem 519

2-23 **Zhang, J., P. Gerstoft, and S. Taylor**
Body-Wave Arrivals from Seismic Noise 232

Sensors Papers: (10)

3-03 **Carr, D., P. Baldwin, S. Knapp-Kleinsorge, H. Milburn, and D. Robinson**
A Laser Interferometric Miniature Seismometer 268

6-03 **Farsoni, A. and D. Hamby**
Characterizing a Two-Channel Phoswich Detector Using Radioxenon Isotopes Produced in the Oregon State University TRIGA Reactor 585

6-04 **Farsoni, A. and D. Hamby**
Design and Modeling of a Compton-Suppressed Phoswich Detector for Radioxenon Monitoring 595

3-04 **Fourguette, D., M. Otugen, L. Larocque, G. Ritter, J. Meeusen, and T. Ioppolo**
Optical MEMS-Based Seismometer "WhiGS" 272

3-05 **Garcia, C., G. Onaran, B. Avenson, B. Yocom, and N. Hall**
Micro-Seismometers via Advanced Meso-Scale Fabrication 280

8-04 **Hart, D., H. Parks, and R. Rembold**
The Development of Methodologies for Determining Non-Linear Effects in Infrasound Sensors 760

6-06 **Keillor, M., C. Aalseth, A. Day, L. Erikson, J. Fast, B. Glasgow, E. Hoppe, T. Hossbach, B. Hyronimus, H. Miley, A. Myers, and A. Seifert**
Initial Results: An Ultra-Low-Background Germanium Crystal Array 609

6-07 **Williams, R., P. Humble, and J. Hayes**
Extraction of Xenon Using Enriching Reflux Pressure Swing Adsorption 619

6-08 **Xie, C., K. Yocum, J. Colaresi, and H. Miley**
Surface Passivation of High Purity Germanium Detectors Using Amorphous Hydrogenated Silicon Films 627

6-09 **Yocum, K., J. Colaresi, and H. Miley**
Improvement in Ge Detector Cooling 636

Signal Analysis Papers (17):

2-02 **Ballard, S., M. Begnaud, C. Young, J. Hipp, M. Chang, A. Encarnacao, C. Rowe, W. Phillips, and L. Steck**
A Global 3D P-Velocity Model of the Earth's Crust and Mantle for Improved Event Location — SALSA3D 31

8-01 **Bonner, J., R. Herrmann, A. Stroujkova, and M. Leidig**
A Software Toolbox for Systematic Evaluation of Seismometer-Digitizer System Responses 733

6-02 **Cooper, M., C. Aalseth, J. Ely, D. Haas, J. Hayes, J. McIntyre, and B. Schrom**
Digital Data Acquisition Graphical User Interface 577

8-02 **Dodge, D., M. Ganzberger, T. Hauk, and S. Ruppert**
Enhancing Seismic Calibration Research Through Software Automation and Scientific Information Management 743

8-03 **Gonzales, M. and C. Young**
WavePro: A New Approach to the Design of Data Processing Work Flows 753

6-05 **Haas, D., B. Schrom, M. Cooper, J. Ely, A. Flory, J. Hayes, T. Heimbigner, J. McIntyre, D. Saunders, and T. Suckow**
Progress in Advanced Spectral Analysis of Radioxenon 604

5-01 **Harben, P. and T. Hauk**
Background Acoustic Noise Models for the IMS Hydroacoustic Stations 541

3-06 **Kvaerna, T., S. Gibbons, D. Harris, and D. Dodge**
A Matched Field Processing Framework for Coherent Detection Over Local and Regional Networks 289

8-05 **Le Bras, R., S. Vaidya, J. Schneider, S. Russell, and N. Arora**
Status of the Machine Learning Efforts at the International Data Centre (IDC) of the CTBTO 770

2-13 **Miller, K., M. Arrowsmith, W. Phillips, S. Harder, L. Worthington, A. Sheehan, and M. Anderson**
Assessment of Regional Explosion Discriminants Using Datasets of Unparalleled Spatial Sampling: The Big Horns Array Seismic Experiment (BASE) 145

4-11 **Murphy, J., B. Kohl, J. Stevens, T. Bennett, and H. Israelsson**
Exploitation of the IMS and Other Data for a Comprehensive, Advanced Analysis of the North Korean Nuclear Tests 456

3-08 **Myers, S., M. Begnaud, S. Ballard, A. Ramirez, W. Phillips, M. Pasyanos, H. Benz, and R. Buland**
A Regional Seismic Travel Time Model for North America 308

4-12 **Pasyanos, M., W. Walter, E. Matzel, S. Ford, R. Gok, and A. Rodgers**
Calibration of Attenuation Structure in Eurasia to Improve Discrimination and Yield 466

5-03 **Prior, M., A. Poplavskiy, R. Le Bras, and J. Given**
Enhancing the Contribution of the T-Stations of the IMS Hydrocoustic Network to IDC Processing and Tsunami Warning 558

3-09 **Ringdal, F., D. Harris, T. Kvaerna, and S. Gibbons**
Expanding Coherent Array Processing to Larger Apertures Using Empirical Matched Field Processing 318

3-10 **Ritzwoller, M., M. Barmin, A. Levshin, and Y. Yang**
Epicentral Location of Regional Seismic Events Based on Empirical Green's Functions from Ambient Noise 328

8-07 **Taylor, S. and X. Yang**
Development of Software to Digitize Historic Hardcopy Seismograms from Nuclear Explosions 789

Acronyms, etc.

Acronym	Definition
ADC	analog-to-digital converter
AFRL	Air Force Research Laboratory
AFTAC	Air Force Technical Applications Center
ANFO	ammonium nitrate fuel oil
ARSA	Automated Radioxenon Sampler/Analyzer
BAA	Broad Agency Announcement
CC	correlation coefficient
CLVD	compensated linear vector dipole
CMT	Harvard centroid moment tensor
CTBT	Comprehensive Nuclear-Test-Ban Treaty
CTBTO	Comprehensive Nuclear-Test-Ban Treaty Organization
DC	double couple
DD	double difference
DMC	Data Management Center (IRIS)
DOB	depth of burial
DoD	Department of Defense
DOE	Department of Energy
DOS	Department of State
DPRK	Democratic People's Republic of Korea
DSS	deep seismic sounding
ECM	Event Classification Matrix (or Event Categorization Matrix)
EDR	Earthquake Data Reports - a USGS publication
EGF	Empirical Green's Function
EHB	Engdahl, E.R., van der Hilst, R. & Buland, R., 1998. Global teleseismic earthquake relocation with improved travel times and procedures for depth determination, *Bull. Seismol. Soc. Am* . 88: 722-743
EMP	electromagnetic pulse
EOS	equation of state
ETOPO	earth topographic (database)
EventID	tool to implement event discrimination (Hartse et al., 1997; Walter et al., 1999)
FD	finite difference
FE	finite element
FFT	Fast Fourier Transform
FSU	Former Soviet Union
FWHM	full width at half maximum
G2S	ground-to-space
GA	global association
GIS	geographical information system
GMT	generic mapping tool
GNEMRD	Ground-Based Nuclear Explosion Monitoring Research and Development Program
GPR	ground-penetrating radar
GSN	global seismographic network
GTx	ground truth information of accuracy x km
HDC	hypocentroidal decomposition
HE	high explosive
HPGe	high purity germanium
HPXe	high-pressure xenon
HV	high voltage
Hz	hertz

Acronym	Definition
IASPEI	International Association of Seismology and Physics of the Earth's Interior
iasp91	standard earth model
IDC	International Data Centre
IMS	International Monitoring System
IRIS	Incorporated Research Institutions for Seismology
ISC	International Seismological Centre
ISS	International Scientific Studies
JHD	joint hypocenter determination
JVE	U.S.-Soviet Joint Verification Experiment
KB	Knowledge Base
LANL	Los Alamos National Laboratory
LLNL	Lawrence Livermore National Laboratory
MatSeis	seismic analysis package developed by SNL using Matlab
mb	body wave magnitude
MDAC	magnitude and distance amplitude corrections
MDC	minimum detectable concentration
MEMS	microelectromechanical systems
MFA	multiple filter analysis
Ms	surface wave magnitude
Mw	moment magnitude
NA-22	Office of Nonproliferation and Verification Research and Development in NNSA
NDC	National Data Center
NEIC	National Earthquake Information Center
NEM R&D	Nuclear Explosion Monitoring Research and Development
Nm	newton-meters
NNSA	National Nuclear Security Administration
NORSAR	Norwegian Seismic Array
NPE	Nonproliferation Experiment
NRL	Naval Research Laboratory
NSF	National Science Foundation
NTS	Nevada Test Site
ORFEUS	Observatories and Research Facilities for European Seismology
OSI	on-site inspections
PASSCAL	Program for the Array Seismic Studies of the Continental Lithosphere
PDE	preliminary determination of epicenters
PE	parabolic equation
PMCC	progressive multi-channel correlation
PMT	photomultiplier tube
PNE	peaceful nuclear explosions
PNNL	Pacific Northwest National Laboratory
PSD	power spectral density
PTS	Provisional Technical Secretariat
Q	Seismic Q factor (reciprocal of attenuation)
RASA	Radionuclide Aerosol Sampler Analyzer
REB	Reviewed Event Bulletin - an IDC report
RMS	root mean square (errors)
ROC	receiver operating characteristic
RSTT	regional seismic travel-time model
SAC	seismic analysis code
SASC	Slowness and Azimuth Station Correction
SAUNA	Swedish Automatic Unit for Noble Gas Acquisition

Acronym	Definition
SBIR	Small Business Innovation Research
SEM	spectral element method
SLBM	Seismic Location Baseline Model
SMDC	Space Missile Defense Command (Army)
SNL	Sandia National Laboratories
SNR	signal-to-noise ratio
SOFAR Channel	SOund Fixing And Ranging - primary sound channel in the ocean
SPE	source phenomenology experiments
SSEB	Standard Screened Event Bulletin
STA/LTA	short-term average/long-term average
t* (t-star)	A measure of the "damping" or attenuation along a path. T* is the ratio of the travel time along a ray path to the average Q (seismic "quality" factor) along it.
UNE	underground nuclear explosions
USAEDS	United States Atomic Energy Detection System
USGS	United States Geological Survey
USNDC	United States National Data Center
VOD	velocity of detonation
WWSSN	World Wide Standardized Seismographic Network
YSKP	Yellow Sea and Korean Peninsula

Guide to Seismic Phases

The change of seismic velocities within Earth, as well as the possibility of conversions between compressional (P) waves and shear (S) waves, results in many possible wave paths. Each path produces a separate seismic phase on seismograms. Seismic phases are described with one or more letters, each of which describes a part of the wave path. Upper case letters denote travel through a part of the earth (e.g. P or S), and lower case letters denote reflections from boundaries. A complete, standardized nomenclature for seismic wave paths is available at the web site: http://www.isc.ac.uk/doc/analysis/2003p13/index.html. This information has also been published [Storchak, D.A., J. Schweitzer, P. Bormann (2003), "The IASPEI Standard Seismic Phase List", Seismol. Res. Lett. 74, 6, 761-772], and a pdf file of this publication is available from the same web site.

In the verification context, wave propagation in Earth is divided into *teleseismic* (distances greater than 2000 kilometers) paths and *regional* (distances less than 2000 kilometers) paths.

Teleseismic Phases

In these plots, the seismic event is at the left, and seismic ray paths are shown to possible stations at several angular distances from the event.

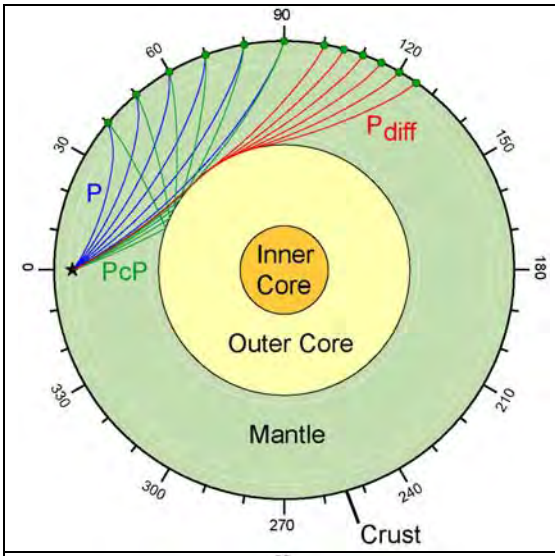

P A primary (compressional) wave that follows a simple path from event source to the station.

PcP A P wave that goes downward through the mantle (the first "P"), is reflected from the top of the outer core ("c") and goes upward through the mantle to the station (second "P").

P_{diff} A P wave that has been bent (diffracted) around the outer core boundary and arrives at a station in the ray "shadow" of the outer core.

S A secondary (shear) wave that follows a path similar to the P wave (not shown).

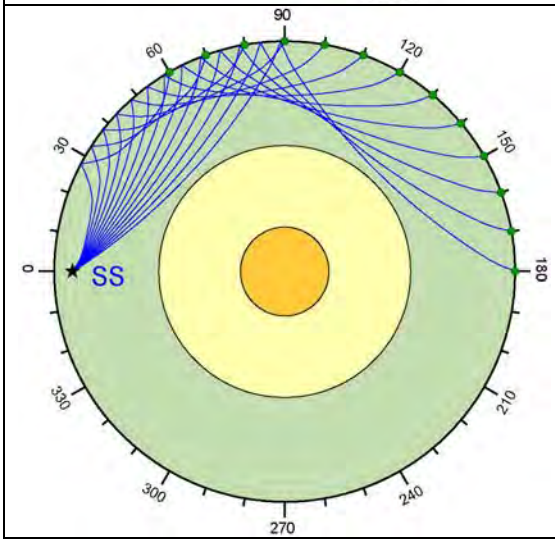

SS A shear wave that has traveled through the mantle ("S"), undergone one reflection from the underside of Earth's surface and traveled again through the mantle (second "S"). Unlike with most other reflected waves, there is no separate letter to denote the reflection at the surface; it is implicit.

PP A compressional wave that follows paths similar to those of SS (not shown).

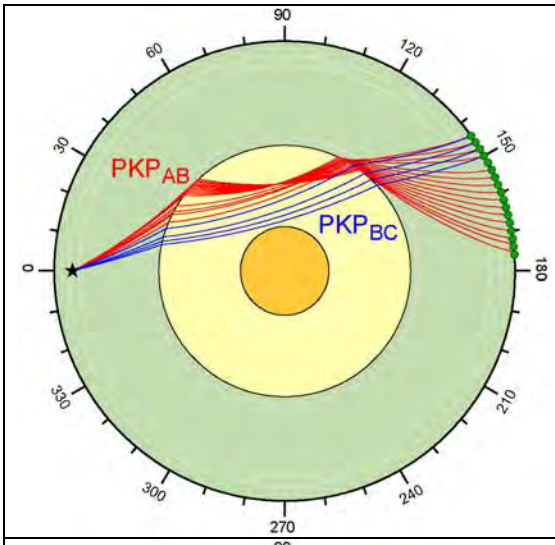	**PKP** A P wave that has traveled through the mantle ("P"), been transmitted across the mantle-outer core boundary and traveled through the outer core ("K"), transmitted back across the outer core-mantle boundary and traveled as a P wave to the station ("P"). Because of the large difference between the P wave velocity in the mantle and the outer core, this wave is bent (refracted) strongly at the boundary. Seismic waves can follow slightly different paths (labeled PKP_{AB}, PKP_{BC}) and still arrive at about the same time.
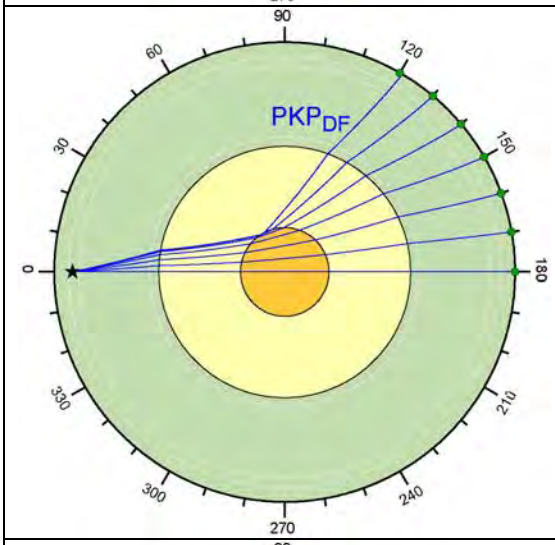	**PKIKP** A P wave that has traveled through the mantle ("P"), been transmitted across the mantle-outer core boundary ("K"), crossed the outer-core inner-core boundary and traveled through the inner core as a P wave ("I"), then followed a similar path in reverse to get from the inner core to the station (the second "KP"). An alternate name for this phase is PKP_{DF} (shown in the path illustration).
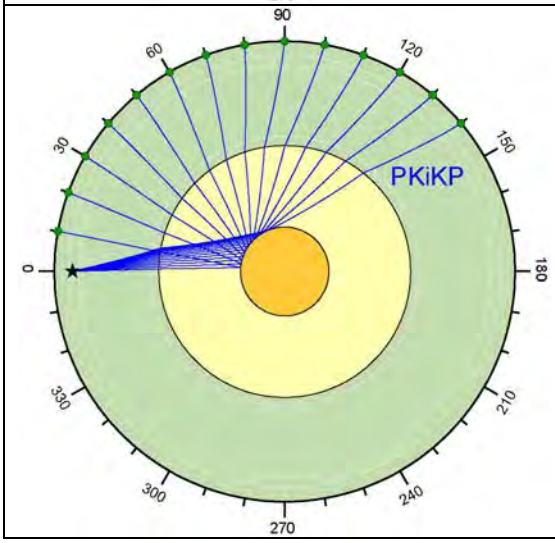	**PKiKP** This phase has followed a series of paths similar to the PKIKP phase, except it was reflected off the top of the inner core-outer core boundary (this is the "i" part of the path), rather than being transmitted through the inner core.

Figures courtesy of Ed Garnero, Arizona State University (http://garnero.asu.edu/research_images/index.html)

Depth Phases

A number of "depth" phases are referred to in the proceedings. The paths of these phases are nearly the same as P waves. The depth phases all result from a reflection from the Earth's surface near the epicenter of the event. The time delay between the P wave and the depth phase is proportional to the depth of the event (hence the term "depth" phase).

pP A P wave that started out upward from the source ("p"), reflected off the Earth's surface, and traveled to the station as a P wave ("P").

sP An S wave that started out upward from the source ("s"), reflected off the earth's surface and also converted to a P wave, which then traveled to the station as a P wave ("P").

pwP Similar to the pP phase. A P wave that started out upward from the source ("p"), reflected off the ocean surface ("w" - water) and traveled to the station as a P wave ("P").

Regional Phases

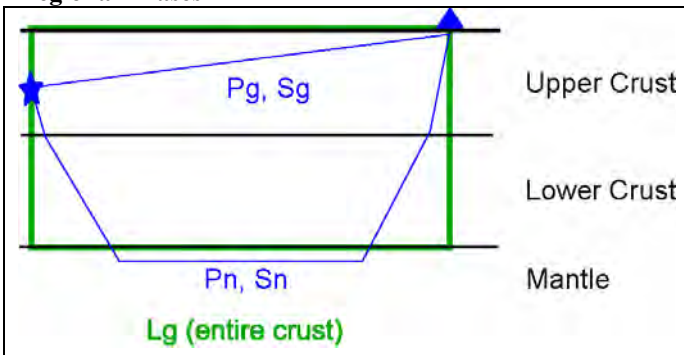

A highly simplified representation of the crust of Earth, which is seldom so simple and flat. Changes of crustal thickness and velocities can disrupt crustal phases, notably Lg.

Pg (Sg) At short event-station distances, an upgoing P (S) wave from a source in the upper crust (depicted here) or a P (S) wave bottoming in the upper crust. At larger distances the Pg phase includes arrivals resulting from multiple P-wave reverberations within the entire crust that propagate at a group velocity around 5.8 km/s.

Pn (Sn) A P (S) wave bottoming in the uppermost mantle or an upgoing P wave from a source in the uppermost mantle

Lg A wave group observed at larger regional distances and caused by superposition of multiple S-wave reverberations and S to P and/or P to S conversions inside the whole crust. The maximum energy travels with a group velocity around 3.5 km/s